Australian Government
Geoscience Australia

Report 1 of 5
Final Report
July 2012

BROKEN HILL MANAGED AQUIFER RECHARGE (BHMAR) PROJECT

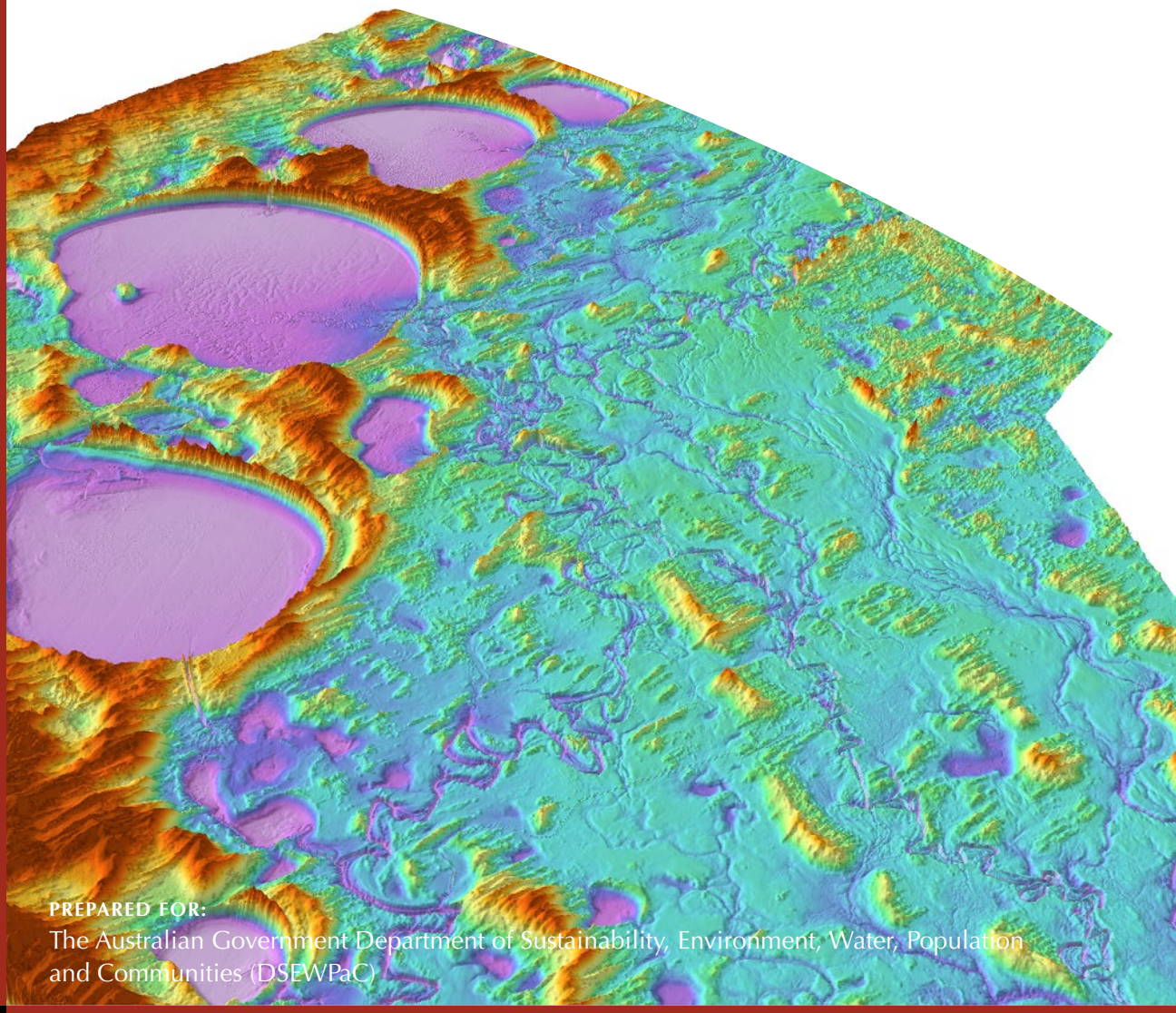
# Securing Broken Hill's Water Supply: Assessment of Conjunctive Water Supply Options Involving Managed Aquifer Recharge and/or Groundwater Extraction at Menindee Lakes

## Data acquisition, processing, analysis and interpretation methods

*Lawrie, K.C., Brodie R.S., Tan, K.P., Gibson, D., Magee, J., Clarke, J.D.A., Halas, L., Gow, L., Somerville, P., Apps, H.E., Christensen, N.B., Brodie, R.C., Abraham, J., Smith, M, Page, D., Dillon, P., Vanderzalm, J., Miotlinski, K., Hostetler, S., Davis, A., Ley-Cooper, A.Y., Schoning, G., Barry, K. & Levett, K.*

Record
2012/11

GeoCat #
73819



PREPARED FOR:
The Australian Government Department of Sustainability, Environment, Water, Population and Communities (DSEWPaC)

# Broken Hill Managed Aquifer Recharge (BHMAR) Project

# SECURING BROKEN HILL'S WATER SUPPLY: ASSESSMENT OF CONJUNCTIVE WATER SUPPLY OPTIONS INVOLVING MANAGED AQUIFER RECHARGE AND/OR GROUNDWATER EXTRACTION AT MENINDEE LAKES

## DATA ACQUISITION, PROCESSING, ANALYSIS AND INTERPRETATION METHODS

## GEOSCIENCE AUSTRALIA RECORD 2012/11

By:

Lawrie, K.C.[1], Brodie, R.S.[1], Tan, K.P.[1], Gibson, D.[1], Magee, J.[1], Clarke, J.D.A.[1], Halas, L.[1], Gow, L[1]., Somerville, P.[1], Apps, H.E.[1], Christensen, N.B.[2], Brodie, R.C.[3], Abraham, J.[4], Smith, M.[1], Page, D.[5], Dillon, P.[5], Vanderzalm, J.[5], Miotlinski, K.[5], Hostetler, S.[6], Davis, A.[7], Ley-Cooper, A.Y.[7], Schoning, G.[1], Barry, K.[5] and Levett, K. [5].



Australian Government
Geoscience Australia

[1] Groundwater Group, Geoscience Australia, Canberra ACT Australia; [2] Department of Earth Sciences, Aarhus University, Aarhus, Denmark; [3] Minerals and Geohazards Division, Geoscience Australia, Canberra ACT Australia; [4] U.S. Geological Survey, Crustal Geophysics and Geochemistry Science Center, Denver, Colorado, USA.; [5] CSIRO Water for a Healthy Country Flagship, Adelaide, SA; [6] FrOG Tech, Canberra ACT Australia; [7] Formerly Geoscience Australia, currently CSIRO, Perth, WA

**Department of Industry**

Minister for Industry: The Hon Ian Macfarlane MP
Parliamentary Secretary: The Hon Bob Baldwin MP
Secretary: Ms Glenys Beauchamp PSM

**Geoscience Australia**

Chief Executive Officer: Dr Chris Pigram

This paper is published with the permission of the CEO, Geoscience Australia



© Commonwealth of Australia (Geoscience Australia) 2012

With the exception of the Commonwealth Coat of Arms and where otherwise noted, all material in this publication is provided under a Creative Commons Attribution 3.0 Australia Licence (http://www.creativecommons.org/licenses/by/3.0/au/)

Geoscience Australia has tried to make the information in this product as accurate as possible. However, it does not guarantee that the information is totally accurate or complete. Therefore, you should not solely rely on this information when making a commercial decision.

Please note: This version of the report replaces the version released on 12th December 2013. Inconsistent labelling of stress orientations on structural diagrams have been corrected and relevant figure captions modified accordingly. Identified report formatting issues have also been resolved.

**ISSN 1448-2177**

**ISBN 978-1-922103-41-3**

**ISBN web: 978-1-921954-87-0**

**GeoCat # 73819**

Geoscience Australia acknowledges funding of this project by the Australian Government Department of the Environment.

**Bibliographic reference**: Lawrie, K.C., Brodie, R.S., Tan, K.P., Gibson, D., Magee, J., Clarke, J.D.A., Halas, L., Gow, L., Somerville, P., Apps, H.E., Christensen, N.B., Brodie, R.C., Abraham, J., Smith, M., Page, D., Dillon, P., Vanderzalm, J., Miotlinski, K., Hostetler, S., Davis, A., Ley-Cooper, A.Y., Schoning, G., Barry, K. and Levett, K. 2012. *BHMAR Project: Data acquisition, processing, analysis and interpretation methods*. Geoscience Australia Record 2012/11. 824p.

# Summary

## PROJECT BACKGROUND

The Broken Hill Managed Aquifer Recharge (BHMAR) project was commissioned in 2008 as part of an Australian Government election policy commitment to invest up to $400 million to reduce evaporation and improve water efficiency at the MLS, secure Broken Hill's water supply, protect the local environment and heritage, and return up to 200 GL to the Basin. The study area is located on the Darling Floodplain near Menindee in far western New South Wales. The project is managed by the Australian Government Department of the Environment, previously the Department of Sustainability, Environment, Water, Population and Communities (SEWPaC).

As part of a broader suite of scientific and technical investigations, the Broken Hill Managed Aquifer Recharge (BHMAR) project was tasked with identifying and assessing:

- Alternative groundwater-related water supply options for Broken Hill that could provide enhanced drought security for periods up to 3 years (~30 GL), within 20 km of existing water and energy infrastructure at Menindee.
- Potential MAR opportunities and groundwater resources that could provide enhanced drought security and promote regional development for communities and industries (e.g. agriculture and mining) across a larger area (~7,500 km$^2$) of the Darling Floodplain.

In managed aquifer recharge (MAR), a water source, such as natural water from a lake or river, is used to 'recharge' an aquifer with water under controlled conditions (Dillon, 2005; Dillon *et al*., 2005, Dillon *et al*., 2009). The aquifer is used to store surplus water (e.g. available during flood events) for later use that may include community water supplies, industry or agriculture, or environmental benefit. In this project, all of the MAR and groundwater extraction options for Broken Hill were considered within a framework of conjunctive water management. This approach means that Broken Hill would continue to access water stored within the Menindee Lakes Storages (MLS) when surface water is abundant, with groundwater extraction from aquifers if/when the MLS become dry in the future. In this way, groundwater would provide enhanced water security for Broken Hill (and regional communities) during drought conditions.

The BHMAR project followed a 5-phase work plan, based on the staged approach to MAR assessment identified in the national MAR guidelines for major projects (NRMMC-EPHC-NHMRC, 2009). The first 3 phases of the project have been completed:

- **Phase 1: Assessment of pre-existing data and overall technical risk assessment for the project;**
- **Phase 2: Acquisition and interpretation of regional baseline hydrological and geological data;**
- **Phase 3: Assessment of MAR storage and groundwater extraction options for a priority site to provide enhanced drought security for Broken Hill.**
- Phase 4: Implement and test preferred groundwater extraction and storage options at a small operational scale.
- Phase 5: Construct and operate groundwater extraction/storage option.

This report summarises the scientific research methods and data acquisition undertaken in the BHMAR study Phases 1-3. This report is supported by three accompanying scientific and technical reports (Lawrie *et al.,* 2012b, c, d). The overall findings of the BHMAR study are contained in a project summary report (Lawrie *et al*., 2012e). Additional data and sub-contractor reports are included in fifteen accompanying appendix volumes (see Section 1.2), and in the BHMAR project GIS (Gow *et al*., 2012a). 3D models of the data are also contained in the project GIS. The data and interpretations in these final reports supersede all previous interpretations contained in earlier interim reports (Lawrie *et al.,* 2008a; 2009a; 2010a, b, 2011).

The final project reports have been reviewed internally by scientific experts within Geoscience Australia (GA) and the CSIRO; externally reviewed by independent consultants within Australia, as well as by an expert panel from the United States Geological Survey (USGS). The project was guided by a Steering Committee with representatives from the Australian and New South Wales governments. The BHMAR project is managed by the Australian Government Department of the Environment, previously the Department of Sustainability, Environment, Water, Population and Communities (SEWPaC).

## KEY FINDINGS- DATA ACQUISITION AND RESEARCH METHODOLOGIES

1. The BHMAR study area was recognised prior to commencement of the project as a data-poor area from the perspective of identifying and assessing suitable groundwater targets. A comprehensive review of pre-existing biophysical (e.g. geological, hydrogeological, hydrogeophysical, hydrogeochemical, landscape, vegetation, cultural and environmental) data found relevant to the identification and assessment of potential MAR and groundwater resource targets helped to identify critical data gaps and assisted with the design of a data acquisition strategy.
2. A data acquisition program was undertaken utilising the national MAR guidelines as a reference framework. A phased approach to data acquisition was undertaken, with regional scale data acquired in an initial campaign designed to map and assess groundwater resources and MAR opportunities in 4 main aquifers, with the primary focus being the intermediate depth Pliocene aquifers.
3. In the BHMAR study, an evolution in project management from multi-disciplinary, to inter-disciplinary and finally a trans-disciplinary approach was critical to developing a robust hydrogeological conceptual model as well as the successful completion of pre-commissioning maximal and residual risk assessments for a proposed MAR site at Jimargil.
    i. A multi-disciplinary approach guided the initial data acquisition and project design phases. However, multi-disciplinary and inter-disciplinary approaches left many science questions unresolved.
    ii. A trans-disciplinary approach is a more integrative process, and permits a more comprehensive analysis of all data and interpretation. This approach enabled the team to recognise fundamental problems in discipline approaches, helped identify critical data gaps, led to significant innovation across discipline boundaries, and was critical in the development of new science methods and a hydrogeological conceptual model that underpinned MAR assessment.
    iii. More specifically, integration of the 3D mapping with hydrochemical and hydrodynamic data provides critical new insights into surface-groundwater interactions and groundwater flow. Using a trans-disciplinary approach, it has been possible to develop a new understanding of recharge processes, and identify potential recharge and groundwater flow pathways.
4. Previously, the high cost of investigations, low level of knowledge of risk, and time taken to fill hydrogeological knowledge gaps have been a deterrent to development of MAR options, especially in pioneering projects in greenfield and/or more remote locations like Menindee. To overcome these issues, the project used AEM to map a large, data-poor area (7,541.5 $km^2$) of the Darling floodplain. AEM data acquisition was completed within a nine-week period, with data available to target drilling and field investigations in the same timeframe. It is our understanding that this is the first use of AEM for MAR identification and assessment.
5. The use of airborne electromagnetics (AEM) for hydrogeological investigations often requires high-resolution data. Optimisation of AEM data therefore requires careful consideration of AEM system suitability, calibration, validation and inversion methods. Over the past decade, several new airborne electromagnetic (AEM) systems have become available for commercial surveying, and when a new survey involving AEM is planned, one of the crucial choices is to select an appropriate system for the mapping task. In this study, the choice of an appropriate AEM system for a given task was based on a staged approach utilising:
    i. A derivative analysis approach to comparing various AEM systems, including forward modelling of system responses, based on geo-electric models derived from ground TEM and borehole induction profiles in the candidate areas (Lawrie *et al*., 2008, 2009a);
    ii. A comparative analysis of candidate systems, consisting of both theoretical considerations and field studies including AEM test lines (Christensen *et al*., 2009; Lawrie *et al*., 2009c; Christensen & Lawrie, 2012). Comparative analysis of short-listed systems included:
        a. Acquisition of AEM test lines for 2 systems (TEMPEST and SkyTEM), short-listed based on the derivative analysis approach;
        b. Fiducial Point (FID point) analysis of test line data utilising conductivity data from 8 individual boreholes on the test lines versus the nearest FID point from each of the 2 systems using contractor supplied inversion products, and in the case of TEMPEST data, some additional inversions carried out by GA staff. The FID point analysis involved

comparing conductivity values averaged over 4 m intervals for all 8 boreholes vs averaged values from nearest FID points for all the inversion products.

c. Comparison of existing ground EM and AEM system responses for all the inversion products from both the TEMPEST and SkyTEM systems.

iii. Specific target analysis. This involved assessment of the ability of each system/inversion method to map each of the 3 primary MAR targets (Primary Pliocene Sands, Secondary Lower Renmark Group Sands, and Tertiary Menindee Formation Sands), utilising all the available inversion products. This involved comparing data from all the inverted test line data (in 20 km line sections) to get an overview perspective on hydrogeological features that need to be mapped.

iv. Additional hydrogeological data including boreholes close to the test lines were also incorporated into this analysis. System responses for each of the features listed above were tabulated.

v. Assessment of the ability of the contractor to meet project timing requirements. This included:

a. Ability of the contractor to deliver surveys within the specified timeframes– i.e. system availability;

b. The demonstrated ability of the contractor to provide field processed data (as inverted conductivity depth sections ) under survey conditions, within 48 hrs of acquisition;

c. Historical performance of the contractor to provide final data within the required timeframes.

vi. Consideration of the cost of the survey (line km) and the impact on the whole project timeframes and budget based on project acquisition timeframes.

Overall, the success of the methodology is witnessed by the project results, with rapid data acquisition and delivery, with the selected system detecting all the key features of the hydrogeological system (see below).

6. This study has demonstrated the importance of selecting the most appropriate AEM system and optimizing the AEM inversions for generating a wide range of customized interpretation products.

i. New inversion code (WANDA) has been developed for rapid inversion of the AEM data. This permitted rapid trialling of different constraints.

ii. A lateral correlation procedure was developed to correlate AEM data strictly horizontally.

iii. Development of the WANDA inversion code enabled rapid experimentation with regularization and lateral smoothing constraints, and combined with numerical modelling, this enabled the settings to be adjusted until there was a close match with the known geology, even in the shallow sub-surface.

iv. New procedures were developed for borehole induction logging and calibration. These provided greater confidence in the borehole geophysical conductivity measurements. This method offers an extension of previous calibration methods in that it uses a suite of calibration experiments to derive a statistically robust transfer function between measured voltage and conductivity.

v. Hover tests were used in conjunction with a ground geophysical (WalkTEM) survey to assist with AEM data calibration and inversion.

vi. A new, more consistent concept with an uncertainty-normalised quantitative measure of misfit was developed for the comparison between AEM inversion model conductivities and borehole conductivity logs and applied to 92 boreholes within the BHMAR area. With the exception of about 10% of the boreholes, the estimated average difference is of the same order of magnitude as the uncertainty of the parameters. An $R^2 > 0.98$ was obtained for new bores used as inversion constraints, while an $R^2 > 0.94$ was obtained for FID point comparisons with bores distributed throughout the project area that were not used as inversion constraints.

vii. Bayesian inference via a reversible jump Markov Chain Monte Carlo (RJ-McMC) inversion for nine selected AEM data sets provided useful (quantitative) assessment of the final inversion models. Sixteen independent Markov chains were sampled in parallel in the inversion of each data set. In each chain 200,000 samples were acquired. Models were accumulated into the posterior probability and change-point histograms after the burn-in period of 10,000 samples. Therefore a total of 3.04 million (190,000 x 16) samples were acquired after the burn-in period.

Overall, the borehole conductivity log and the AEM inversion model lie around the centre of the McMC likelihood interval, with a few exceptions. This analysis provided increased confidence in the final WANDA inversions.

viii. Conductivity products produced using the final WANDA inversions, include:

- Conductivity depth (model) sections (for all flight line sections);
- Analysis sections showing estimates of the relative uncertainty on the related conductivities for all conductivity depth (model) sections. These innovative plots show where the conductivities are well determined and vice versa, and provided the interpreters an additional means of assessing the certainty on mapped structures and hydrostratigraphy;
- Conductivity depth slices based on 30-layer conductivity models generated using the WANDA inversion;
- A number of 'synthetic' conductivity sections derived from the 3D conductivity model that were constructed to show regional stratigraphic relationships;
- A GoCAD model showing the modelled conductivity distribution in 3D;
- Conductivity depth slices for the central project area, inverted using the WANDA inversion using different line spacings: 600 m, 1 km, 2 km, 5 km and 10 km. These inversions were gridded using both Nearest Neighbour (NN) and Lateral Parameter Correlation (LPC) methods, and were used to assess the widest line spacing that could be used to map key elements of the hydrogeology, MAR and groundwater resource targets.

7. A suite of customized interpretation products were produced through integration of AEM data with other project datasets, notably the information from 40 new rotary mud and 60 sonic-cored holes. Data obtained from the drilling program includes: sedimentary facies, textures (including grain size), mineralogy, redox state and whole rock geochemistry; hydrogeophysical data (nuclear magnetic resonance (NMR), induction and gamma logs); hydraulic data (from slug and pump tests), hydrochemistry (from groundwater and pore fluid samples), and hydrodynamic data from the monitoring of groundwater levels in 40 boreholes pre- and post-flooding in 2010-2011. Customised interpretation products developed through integration of the modelled conductivity data integrated with these datasets include maps of hydrostratigraphy, sedimentary textural classes, structures including neotectonic elements, groundwater salinity, zones of inter-aquifer leakage, aquifer porosity, aquifer transmissivity, and MAR and groundwater storage volumes.

8. In the Broken Hill Managed Aquifer Recharge project, a new method has been developed for surface-materials and geomorphic mapping. These have been essential for assisting hydrogeological investigations, including recharge predictions, salinity hazard and the identification of potential infiltration basins.

i. Prior to landform identification, the LiDAR DEM data was levelled using trend surfaces to eliminate regional slope (~20 m). As a consequence of this, an ArcGIS interactive contour tool could be used to identify specific breaks in elevation associated with landform features. Multivariate image analysis of elevation, high resolution SPOT and Landsat-derived wetness further enhanced the contrast between geomorphic elements to confirm mapping boundaries.

ii. While specific landforms can be characterised by particular surface materials, these sediments can vary within a single geomorphic feature. Consequently, SPOT multispectral satellite imagery was used to identify surface materials using principal component analysis and unsupervised classification. This approach generated 20 classes; each assigned a preliminary cover/landform attribute using SPOT imagery. Field data (surface and borehole sample, and observations at shallow pits) were used to refine the classification approach.

iii. Interactive mapping using a de-trended DEM provided a rapid, effective and accurate alternative to time consuming manual landform digitisation. The combination of these two new products – surface-materials and geomorphic maps – has assisted in the identification of potential recharge sites and naturally occurring infiltration sites.

iv. Overall, this innovative approach significantly increased the speed and the level of detail of geomorphic mapping when compared to previous methods.

9. Mapping of geological structures across the BHMAR study area has entailed a multi-scale mapping approach involving the analysis of AEM, airborne magnetic, regional gravity, LiDAR, landsat (vegetation condition) and geomorphology data in cross-sections and maps. Identification of Neogene tectonics was facilitated by the identification (in the AEM data) of structural off-sets in the lacustrine Blanchetown Clay. The correspondence of faults in multiple, independent datasets, validated by drilling data, provided increased confidence in the structural analysis.
10. Ground direct current/induced polarization (DC/IP) surveys were undertaken largely to assess borefield scale heterogeneity in the hydrogeological system, and in particular, to determine whether the AEM system was mapping 'holes' in the confining aquitards.
    i. These ground surveys were limited by access, cultural heritage and environmental issues, with the survey design compromised in a number of locations because of these factors. In particular, it was not possible to extend the surveys either side of boreholes in a number of locations, limiting the utility of borehole datasets for calibration purposes.
    ii. One particular issue of note is that the IP data (and borehole nuclear magnetic resonance (NMR) data) may be affected by the extensive ferruginisation of the aquifer materials. Further tests are required to establish the effects on the IP (and NMR) response.
    iii. Two inversions of the ground DC/IP surveys were carried out. These inversions did not match the AEM or borehole IP data particularly well, and further inversions are required using different inversion constraints. One issue of note is that the upper confining aquitard in the Jimargil area is particularly indurated and relatively dry, and this was not factored into the inversion interpretation. The inversions did however appear to reveal some heterogeneity in the hydrogeological system at a scale not observed in the AEM data.
11. In the BHMAR project, sensitivity analysis was used to help define uncertainty for key parameters, such as estimates of aquifer storage volumes at both the regional target and potential borefield scale. These parameters are critical to economic viability of a project (which is not addressed in any National Water Quality Management Strategy (NWQMS) Guidelines). The new multi-scale methodology developed to estimate groundwater quality and storage volumes, was applied to the Pliocene aquifers. This methodology is a significant improvement on previous approaches that rely upon extrapolation from limited borehole data.
    i. Salinity class thresholds were estimated by comparing the downhole pore fluid data with the AEM response at a borehole scale. Bulk volumes for each water quality class in a target were then calculated using these thresholds on an AEM depth slice basis, which had been mapped into textural classes. An effective porosity range for each textural class was developed by integrating borehole nuclear magnetic resonance (NMR) data and laboratory porosity data (from Lexan-encapsulated core samples). These effective porosity ranges were used to convert the depth-slice bulk volume estimates to stored groundwater volumes.
    ii. Sensitivity analysis revealed that there are still significant uncertainties in volume estimates using this approach. There can be order-of-magnitude differences in the volume calculations depending on the AEM technology, inversions and constraints used. Significant variations were also found when different AEM conductivity thresholds were used to map groundwater salinity. Low, medium and high estimates of effective porosity were derived to represent the inherent geological heterogeneity.
    iii. Due to this uncertainty, the groundwater storage volumes should only be considered as indicative estimates. The estimates are still useful in a relative sense, as a tool to prioritise the groundwater targets and to scope the potential aquifer storage capacity for MAR options.
12. Difficulty in obtaining regulatory permissions for long-term pump tests necessitated the use of alternative methods for gathering information on the hydraulic properties of aquifers and aquitards.
    i. Using the 33 ms $T_2$ cut-off and the resulting calculation of the bound, free, and total water from NMR logging permitted a detailed perspective of the downhole variation in water-filled porosity for sites throughout the BHMAR area. This downhole measurement of water content and pore geometries is difficult and/or impossible with any other geophysical tool. Caution needs to be exercised in detailed examination of these logs to be certain that the measurements have accrued within the saturated portion of the sequence. The assumptions built into the calculations assume that the system contains only water and that system is fully saturated. The NMR method could not be used on shallower partially saturated sediments.

ii. Empirical relationships between the NMR data and laboratory permeameter measurements of relevant sonic core samples across various sediment types allowed estimation of hydraulic conductivity (K) at the resolution of the NMR measurements (0.5 m). This was achieved using the Schlumberger-Doll Research (SDR) equation, involving definition of formation coefficients ($C_{ave}$) for key sediment textures. For each borehole, the NMR derived K values were then aggregated over the screened interval so that an NMR derived transmissivity ($T_{SDR}$) could be compared with the transmissivity estimated from the borehole slug test ($T_{Slug}$). However, as with other empirical measurements errors occur due to a mismatch between the NMR measurement scale and the permeameter and slug test calibration scales. The petroleum industry has faced this issue for decades with the use of these empirical relationships. They have reduced the problems of scale by characterising producing aquifers with a multitude of laboratory measurements. Also, the $K_{SDR}$ values are based on published and accepted physical relationships between $T_2$ distributions and permeability. These values are calibrated with laboratory measurements of area specific materials. Although the measurements scales are different, there is a consistency between the NMR derived transmissivities and the slug test transmissivities.

iii. The NMR logs provide surrogates for effective porosity and hydraulic conductivity at a downhole resolution not possible using traditional methods. Overall, borehole NMR provides a rapid way of mapping the variations in effective porosity and hydraulic conductivity in unconsolidated medium and coarse-textured siliciclastic sediments. However, effective porosities measurements (using the matric potential method) derived from Lexan-encapsulated core materials demonstrated that the NMR method significantly over-estimates hydraulic conductivities in fine-textured materials (fine sands, silts and muds).

   a. From comparisons of permeameter data obtained from drillcores and NMR data, it is concluded that the SDR equation is not valid for fine-textured materials, with the K values of the clays and silts consistently over-estimated (by several orders of magnitude). This is likely to be because the mineralogy (surface relaxivity) of the clays is different from the coarser materials. Also, the physics of the flow and the relationship between permeability and the NMR sensitive parameters (surface-area and electrical permeability) can be very different when comparing a dense clay and coarse sand. A lithology specific calibration will certainly get you closer to the mean, but more interestingly, it could allow you to better characterize and distinguish a very-low-K clay from a low-K clay.

   b. Initial NMR logging used an echo spacing of 2.25 ms, while a second phase of logging used an echo spacing of 1.5 ms. Even with the latter configuration, it appears that a significant amount of the clay signal is not be detected, and so to some extent the data are impacted by a measurement limitation rather than a fundamental physics limitation. Reducing the echo spacing further can only improve characterization of these very low K materials.

13. Sonic drilling has been used successfully to obtain 4.5 km of core materials in the BHMAR study area.

i. Although the method effectively fluidises unconsolidated materials, with consequential loss of some detailed bedding information, core recoveries of over 99% were obtained in the unconsolidated sands and gravels, inter-layered clay-sand sequences and indurated layers and bedrock to depths of 206 m.

ii. The core was sufficiently well preserved to allow ±5 cm accuracy in the location of geological contacts, thinly interbedded sand and silt units. Preservation of small-scale sedimentary structures such as ripples, root casts, intra-clasts, and burrows aided detailed facies interpretation. The sonic cored material also proved an ideal sampling medium for geological analyses, such as grainsize distribution (sieve and laser), bulk density, X-ray fluorescence, X-ray diffraction and palynology. It was also useful in laboratory tests requiring relatively intact samples, such as permeameter and porosity measurements and column tests to assess clogging potential in MAR studies.

iii. Pore fluids were also extracted from core sub-samples using hydraulic presses, for analysis of electrical conductivity (EC), pH, alkalinity and major cations and anions. The principal purpose was to interpret the pore fluid EC, with core moisture content and porosity data, to infer relationships between groundwater salinity and downhole log and AEM conductivities.

Although the pore fluids have been subjected to oxidation and $CO_2$ degassing during their recovery, the pore fluid chemistry obtained from sonic cores was still found to be useful in assessing key hydrogeological processes such as recharge. Although not indicative of in situ conditions, the pore fluid chemistry could be used to identify potential water-rock interactions that could occur with the injection of oxygenated water into the aquifer during MAR operations.

iv. However, there are limitations with the method. Sands, in particular, are disturbed when they are vibrated out of the core barrel into the flexible plastic sampling tube. There can be changes to moisture content, pore fluid chemistry and sediment mineralogy on exposure to the atmosphere, even when the samples are processed and analysed soon after collection.

v. To obtain less disturbed core materials in selected locations, a number of additional sonic cores were obtained by encapsulating the core in rigid polycarbonate lexan tubes. Although this increases costs and reduces drilling rates, atmospheric exposure of the core during drilling is reduced to the ends of the lexan tubes before being capped. Lexan coring is best carried out below the watertable as the heat from drilling dry clays can cause the polycarbonate to melt. This method was used to obtain additional pore fluids (salinity, major ions, trace metals, stable isotopes) and mineral phases (XRD, XRF). The major advantage was the recovery of encapsulated and intact sediment intervals for determining hydraulic conductivity by centrifuge or falling head permeameter methods. Similar samples were also despatched to external laboratories for porosity measurements. By painting some tubes black, sand samples were also successfully obtained for optically stimulated luminescence (OSL) dating.

vi. Recovery of high quality core using the sonic drilling technique has enabled confident interpretation of the hydrostratigraphy, and detailed hydrogeochemical analysis (Lawrie *et al*., 2012a, b, c, d).

14. A new remote sensing vegetation mapping approach was developed at part of the BHMAR Project. This method utilised 25 years of historic Landsat imagery, processed to highlight medium and long-term trends in vegetation condition. Innovative elements of this method include:

i. This study combined Landsat Normalised Difference Vegetation Index (NDVI) time series data with hydrogeological, hydrogeochemical and hydrogeophysical data to assess the relative importance of hydrological processes and groundwater characteristics.

   a. Identification and application of Normalised Difference Vegetation Index (NDVI) thresholds derived from LiDAR vegetation structural mapping;
   b. Minimisation of short-term fluctuations in vegetation condition (associated with rainfall) by extracting average annual minimum NDVI values;
   c. Specific, tailored drought-summary products that focused on statistical trends in NDVI over the 2002-2009 drought; and
   d. Integration of subsurface data including groundwater depths and quality, hydrostratigraphy and tectonic processes.

ii. This new methodology has resulted in a greater understanding of processes driving the spatial distribution of woody vegetation as well as observed changes to condition. At a project scale, the vegetation assessment study has implications for:

   a. The development of any future groundwater schemes including the susceptibility of vegetation communities to changes in groundwater availability or quality; and
   b. The impact of existing surface water management schemes on vegetation condition including the Menindee Lakes Scheme and environmental flows.

iii. More broadly, this vegetation assessment methodology provides a case study for the type of integrated remote sensing temporal analysis required to better understand vegetation variability, in particular a focus on vegetation behaviour during water-limited conditions. Furthermore, the results of this assessment have tantalisingly alluded to the importance of structural features in vegetation distribution and condition that may be applicable elsewhere in the Murray-Darling Basin.

iv. Finally, this method can be applied relatively cheaply, retrospectively and over large areas, making it an excellent first-pass assessment of vegetation behaviour. With continued advances in image processing and computing power, such analysis is also increasingly becoming quicker to generate.

15. In this study, predictive flood modelling and flood-risk assessment used a static modelling approach and a 1 m resolution LiDAR Digital Elevation Model (DEM). To produce accurate predictions of flood inundation and calculations of flood volume in a range of flooding scenarios, a number of steps were undertaken:

i. The DEM was initially levelled to the Darling River floodplain by subtracting an interpolated floodplain elevation trend surface from the DEM. This produced a de-trended flood plain surface.

ii. The levelled DEM surface was then adjusted to the water level reading at the Darling River gauging station (Site 425012), upstream of Weir 32, at the time when the LiDAR was acquired.

iii. Flood extents were then derived by elevation slicing of the adjusted levelled DEM up to any chosen river level. River-level readings from historical and current events were extracted from the NSW Office of Water real time river data website[1].

iv. The flood-depth dataset is an inverted version of the flood extent grid. Predicted flood depth and extent were classified by depth/elevation slice ranges of the adjusted de-trended DEM with 25 and 50 cm increments.

v. Predicted flood extents were validated by comparisons to satellite images from the 1990 floods, and photographs of inundation from recent flood events. In all cases, imagery and photo validation proved that predicted extents are accurate. The flood-risk predictions were then applied to a number of river level scenarios. These included:

a. Examination of the extent of flooding at the highest historical level;

b. Determination of the river level required to completely inundate the Coonambidgal Formation scroll plain in the GWR1 study area (probable maximum recharge potential); and

c. An assessment of flood impacts in 0.5 m increments from 5.5 to 7 m of river level rise at the Site 425012 gauging station.

vi. This flood inundation modelling only shows the theoretical extent of inundation due to river-level rise based only on elevation and does not take into account flow pathways and impediments to flow or loss of water due to evaporation, soil wetting, and leakage via faults or surface cracks. This may lead to an overestimation, however results of the quantitative validation suggest this only affects a small percentage of the landscape. However modelling the impact of flooding in and around the Menindee Lakes is problematic as the lakes are regulated and do not necessarily, fill under natural flood conditions.

vii. The accuracy of flood modelling decreases with distance from the river gauge station. Validation of the methodology in the central section of the project area indicates good accuracy. More broadly, there appears to be under-estimation in the north, particularly in relation to Talyawalka Creek; and over-estimation in the south, along both the Darling River and the Darling Anabranch. In these areas, flood extent can instead be derived from the Landsat water classification.

viii. There are also limitations with utilising Landsat imagery for flood modelling. Landsat has a repeat cycle of approximately every 16 days, and is affected by cloud cover – both of which limit the number of suitable scenes for analysis. As a consequence of this, Landsat images are not always available for key flood events. Landsat also has a spatial resolution of 30 m as opposed to the LiDAR DEM using in this study (5 m spatial resolution). This causes issues with mixed pixel responses, for example when a single pixel is in reality both wet and dry. The water body extraction algorithm can only essentially assign wet or not wet. Finally, the ability of Landsat to detect surface water can be affected by dense canopy cover (Wang *et al*., 2002). Only

[1] http://waterinfo.nsw.gov.au/water.shtml?ppbm=SURFACE_WATER&rs&3&rskm_url

the Darling River channel is associated with anything other than open forest hence this is unlikely to affect the analysis considerably. These products are also unable to provide any information about the depth of water inundating any surface which is a strength of the LiDAR products.

ix. Overall, the flood modelling methodology used in this project successfully predicted the extent and depth of water coverage in the central project area of the Darling floodplain under different scenarios, and to identify the geomorphic features prone to inundation in different flooding regimes. The flood predictions were also used as inputs to recharge potential mapping and for borefield and pipeline planning.

16. A comprehensive hydrochemistry campaign involved the sampling of cumulative rainfall, surface water (river, lake storages and treated water supply), groundwater and pore fluids extracted from the sonic core.
    i. A field sampling protocol involving low-flow pump operation, monitoring of field parameters, the taking of routine, replicate and spiked samples, sample preservation and storage and chain of custody processes was established for the project.
    ii. The suite of hydrochemical analyses was comprehensive and included field parameters, major and minor ions, trace metals, nutrients, organic carbon and radon. These were used to assess the quality of groundwater and potential MAR source water against the national drinking water guidelines (ADWG 2011). More specific analyses such as pesticide screens were also undertaken on selected samples.
    iii. The analysis suite also included supplementary parameters useful for the MAR risk assessment. This included the field spectrophotometry of specific ions (ferrous iron, total iron and sulfide), biodegradable dissolved organic carbon, total suspended solids and particle size distribution. These data were also used in the assessment of potential MAR-related issues such as metal remobilisation and clogging. This assessment involved geochemical modelling using the PHREEQC code (Parkhurst & Appelo, 1999).
    iv. Many of these water quality parameters (such as major ions, trace metals, EC, pH) can also be used in the hydrochemical assessment of key groundwater processes such as recharge. These data was supplemented by the analysis of stable isotopes (oxygen-18 and deuterium), radiocarbon, chlorofluorocarbons and strontium isotopes. The stable isotopes for groundwaters were particularly useful as the data could be integrated with pre-existing monitoring for rainfall and Darling River surface water. The radiocarbon analyses best captured the spectrum of groundwater ages evident within the shallow and semi-confined aquifers.
17. A new methodology, integrating fuzzy-k means (FCM) cluster analysis with conventional hydrochemical and hydrodynamic analysis provides invaluable new insights into groundwater processes. Surface water and groundwater sampling with pore fluid analysis of cored sediments, combined with fuzzy-k means (FCM) cluster analysis, provides a novel, relatively simple but powerful tool to assist with interpretation of groundwater processes.
    i. Pore fluids were extracted from sediments from 60 sonic-cored bores, and together with rainfall, surface water and groundwater samples, provided a hydrochemical dataset with over 1600 samples and 25 analytes.
    ii. The FCM cluster analysis used analytes that were present in at least 60% of samples and resulted in samples being classified into eight classes (or hydrochemical facies). Pore fluids and groundwater with the greatest affinity to the surface water samples were easily identified. In this way, sites with significant active recharge, principally by river leakage, were mapped.
    iii. Downhole plots of the pore fluid FCM classes provided additional insights into groundwater processes. Comparing the FCM classification of pore fluids within the target (semi)confined aquifer with those from the overlying clay aquitard and shallow aquifer allowed the assessment of vertical inter-aquifer leakage or diffusion processes. The FCM cluster analysis also assigns indices to each sample as indicators of how well it relates to each of the eight classes. A simple recharge index was calculated from these FCM indices.

iv. In summary, fuzzy-k means (FCM) cluster analysis, combined with conventional hydrochemical and hydrodynamic analysis provides invaluable new insights into groundwater recharge processes.

18. MAR assessment requires the hydraulic characterisation of key aquifers and aquitards, involving the estimation of parameters such as effective porosity, hydraulic conductivity, transmissivity and storativity. For the BHMAR project, various approaches at different scales were applied.
    i. A slug test was routinely undertaken following the construction of each of the 100 project bores. A time series of the groundwater level response during the test was collected using a pressure transducer and processed for input into AQTESOLV, for interpretation, curve fitting and transmissivity estimation of the screened interval. The method provided a relatively cheap, rapid and consistent approach to estimating aquifer properties.
    ii. Two aquifer pump tests were undertaken using production bores constructed into the Calivil Formation aquifer at Jimargil, supplemented by monitoring bores established in the overlaying shallow aquifer, the target aquifer and the underlying Renmark Formation. These tests were limited to 7 days due to regulatory constraints. However, the tests provided useful insights into the level of aquifer confinement, the degree of potential inter-aquifer leakage as well as estimates of key aquifer hydraulic properties that were incorporated into preliminary groundwater flow and solute transport modelling.
    iii. As discussed above, nuclear magnetic resonance (NMR) logging provided a complimentary dataset to these more traditional approaches. The logging could provide a downhole hydraulic conductivity profile at 0.5 m resolution, whilst the slug and pump tests provided aggregated properties of the screened aquifer interval. The logging was also logistically simpler compared to the requirements of an aquifer pump test (including suitable production and monitoring bores and appropriate disposal of pumped groundwater).
    iv. The collection of lexan-encapsulated sonic core allowed the opportunity to have laboratory measurements of porosity and permeability undertaken on relatively undisturbed columns of sediments across a range of textural classes. Due to scale issues, this data was particularly useful in validating the NMR logging.
19. Pressure transducer loggers have been installed in a subset of the monitoring bores constructed by the project. Barometric loggers have also been installed to enable correction of the time-series groundwater level data.
    i. Loggers have been installed in bores screened in different aquifers, along different reaches of the Darling River and Talyawalka Creek and at varying distances from potential sources of surface water leakage. The network is designed to characterise the groundwater response to episodic flood events and associated filling of the Menindee Lakes.
    ii. The network was installed prior to the 2010-11 Darling River flood and this provided an opportunity to monitor groundwater replenishment following a significant drought period. The borehole hydrograph data provided evidence for actual recharge into the Calivil Formation, although the aquifer is ostensibly overlain by a significant regional aquitard.
    iii. The groundwater level data, combined with manual measurements and historic data was used in the contouring of the shallow watertable and Pliocene Sands potentiometric surfaces.
20. Preliminary groundwater flow and solute transport modelling has been undertaken for the Jimargil borefield site.
    i. Two simple models were constructed to represent the radial conditions at sites BHMAR33 and 80A, which were the production bores used in the aquifer pump tests. The estimates of aquifer and aquitards hydraulic properties from the pump tests were used as input parameters for FEFLOW radial models at these two locations.
    ii. The models considered an ASR scenario of two years of continuous injection of fresh source water (EC= 250 µS/cm), followed by 2 years of storage and 2 years of recovery at the same rate as the injection. Two model runs used injection/recovery rates of 25L/s and 50 L/s.
    iii. The modelling was undertaken early in the site investigations and helped scope the requirements and scale of a potential MAR borefield and in the MAR risk assessment process.

21. To define the water quality criteria and minimum pre-treatment requirements to allow recharge at an acceptable scale during Aquifer Storage and Recovery, a new methodology was developed using laboratory column studies. In these studies, four types of treated source water were used at constant temperature (19°C) with light excluded, to determine the potential for near-well clogging for a proposed ASR scheme. Due to time constraints, a limited number of representative geological materials were packed into cylinders for this experiment. Overall, this method provided some useful results, however an improvement in the confidence in the results would likely be obtained if the results were performed on undisturbed lexan core, and run over a greater time period.

22. The potential for geochemical reactions to cause aquifer clogging or detrimental water quality changes was assessed for MAR options at the priority Jimargil borefield site.

    i. The assessment used ambient groundwater quality from the target Calivil Formation aquifer, as well as from the shallow unconfined aquifers; Darling River source water quality; and mineralogy and geochemistry of sonic-cored aquifer samples. PHREEQC was used to examine the impact of mixing and interaction between these end-members. This methodology enabled the potential for chemical and physical clogging of the aquifer, and potential for metal mobilisation under a range of different pe redox states within the Calivil Formation aquifer.

    ii. This evaluation has also provided insights into source water pre-treatment requirements, the use of redox mapping to optimise MAR bore-field design, appropriate monitoring for assessing aquifer clogging and water quality changes, and the appropriate contingency plans for treatment of recovered water if required.

23. The BHMAR projects used various approaches to assess different recharge mechanisms to the shallow watertable aquifers and the target Calivil Formation aquifer.

    i. The routine measurement of chloride concentration in groundwater and pore fluid samples enabled the application of the chloride mass balance method to estimate steady-state diffuse recharge from rainfall. This is a simple and rapid technique that has minimal data requirements.

    ii. The watertable fluctuation method is also a simple approach and was applied using the hydrographic responses observed in boreholes monitoring the shallow watertable aquifers near the Darling River or Menindee Lakes. Assigning an appropriate specific yield represented the greatest source of uncertainty for the method.

    iii. The steady state groundwater mounding equation of Hantush (1967) was used based on the geometry and hydraulic properties of representative cross sections for the shallow unconfined aquifer orthogonal to the Darling River.

    iv. Radiocarbon depth models to estimate steady state recharge rates to the unconfined aquifer (Walker and Cook, 1991) and the semi-confined aquifer (Cook and Bohlke, 2000) were applied, using the comprehensive groundwater radiocarbon ($^{14}C$) analyses.

24. The BHMAR project provided the opportunity to apply and test the national MAR guidelines (NRMMC-EPHC-NHMRC, 2009) in the evaluation of a range of MAR options, and a proposed large –scale ASR scheme. Key points about the MAR guideline methodologies are briefly summarised below, however detailed discussion and conclusions can be found in Lawrie *et al*. (2012c).

    i. Overall, the project found that the guidelines provided a very useful framework for entry-level and pre-commissioning MAR assessments. However, the guidelines assume that a potential MAR site has already been identified, necessitating the development of new methodologies to map and select MAR sites in a data-poor, hydrogeologically complex area.

    ii. The project found the application of the entry-level assessment framework from the MAR guidelines to be a particularly useful tool for the assessment of multiple targets. The degree of difficulty assessments were particularly helpful in the identification of critical data and knowledge gaps, and the prioritisation of candidate sites.

    iii. At an early stage in investigations, the BHMAR project developed a method for evaluating aquifer suitability for MAR using conceptual targets based on the pre-existing understanding of hydrostratigraphy and recharge processes (Lawrie *et al*., 2009). This was useful in identifying targets not just in terms of aquifers with appropriate storage, but also the presence of bounding aquitards and potential recharge mechanisms. These conceptual models were also used to define the requirements of the data acquisition program. This was a useful process as it enabled the

definition and prioritisation of a range of potential MAR targets, rather than having project success relying on assessment of a single target.

iv. In parallel with the above approach, the BHMAR project developed a technical risk assessment (TRA) methodology to prioritise regional investigations and evaluate the viability of MAR options in different aquifers (Lawrie *et al*., 2009). This TRA matrix was based on the two key criteria of:

- Likelihood of technical success – accounting for the probability that the required groundwater resource is likely to be present, discoverable with the available technology, and the water supply alternative can be implemented.
- Likelihood of negative consequences – accounting for the potential and significance of impacts to the water resource, ecosystems and other groundwater users if the option was to be implemented.

This approach was successfully used to assess the relative viability of various options, defined by a combination of target formations, water supply strategy and the ability to map and characterise the targets. This allowed elimination of a number of options at an early stage, as well as the identification of critical data gaps. Broader than a MAR human health and environmental risk assessment, the matrix approach was useful in prioritising aquifer targets and aided design of the data acquisition program and assessing the suitability of various technologies (such as AEM survey requirements).

25. Acquisition of a high-resolution LiDAR dataset has been essential in developing a range of geomorphic, geological and hydrogeological interpretation and planning products. For example, the LiDAR dataset provides a high resolution surface datum over which remote sensing data (e.g. Landsat) data be draped for vegetation structure and health mapping, and a datum at an appropriate high resolution to reference the sub-surface datasets including AEM, ground geophysical, and borehole data.

i. Ground validation has demonstrated that the LiDAR data is an accurate representation of the terrain at the time of the survey. However, due to localised flooding at the time of survey (which provided returns from the surface of turbid waters), the LiDAR data is inaccurate in some small, partially inundated landscapes around Lake Wetherell.

ii. Fundamental vertical accuracy (at 95% confidence level) of the LiDAR derived 5 m DEM dataset was found to be 0.52 m, due to inherent inaccuracies of the methodology, insufficient and erroneous ground control points and cumulative errors including the transformation to the vertical reference datum and re-sampling procedures. These vertical inaccuracies need to be factored in to flood modelling, and in utilisation of LiDAR datasets as an absolute height datum. Even considering this factor, flood inundation extent mapping of the central project area has a 93% compatibility with corresponding Landsat TM 5 imagery.

iii. Three digital elevation models (DEMs) were used within the BHMAR Project: 1, 5 and 10 m spatial resolution. These surfaces were fundamental to the interpretation of both surface and subsurface geomorphic, geological and hydrogeological features. BHMAR Project spatial analysis datasets could not have been generated from pre-existing elevation data (e.g. SRTM DEM) due to inadequate spatial resolution and vertical accuracy.

a. The 1 m DEM has the greatest accuracy and highest level of detail but is a very large file which impacts on processing time. It was consequently only used at the borefield scale for the generation of products such as flood inundation and river incision where minor topographic variation was important.

b. The 5 m DEM was more appropriate at the target scale. This product still retained good spatial resolution but was considerably smaller in size and thus quicker to process. This DEM was used for geomorphic mapping, AEM-derived products such as depth to formations and stratigraphic units and interpreted cross sections, and also displaying topography.

c. The 10 m DEM was re-sampled twice thus has slight greater inherent vertical error of the three DEM products. This is was particularly evident where topographic variation was considerable over a small area (i.e. river banks). Consequently this surface was used at the

regional scale and when combined with coarse resolution products such as the depth to the watertable.

d. The acquisition of a high resolution LiDAR dataset has also enabled:
   - Key elements of the floodplain geomorphology to be mapped. The LiDAR dataset has also been critical in guiding the siting of pits and trenches for dating of the near-surface geomorphic units.
   - Fault scarps to be identified in the landscape. The high resolution of the dataset further enables the timing of faulting relative to scroll plain deposition to be ascertained.
   - Integration of river bed mapping with floodplain elevation data.
   - Flood inundation modelling to be carried out at a range of scales, including local borefield scales.
   - Assessment of infiltration options for MAR.
   - Assessment of the potential impact of groundwater extraction and MAR on groundwater dependent vegetation.
   - Cultural heritage and environmental surveys to be carried out with a high degree of spatial accuracy. This was essential for planning all field activities.
   - Design of conceptual borefields.
   - Planning of surface water engineering works at the MLS.

26. In this study, two hyperspectral instruments were used on sonic-cored drillhole materials to assess the value of hyperspectral methods for hydrogeological investigations:
    i. The Portable Infrared Mineral Analyser (PIMA). The PIMA is used on individual samples, and was used to cross-check SWIR results from the Hylogger. Further validation of the methods was carried out using XRD analysis of selected samples.
    ii. The Hylogger core scanner. The Hylogger provides continuous coverage down the logged sonic cores in the visible to near-infrared (VNIR), short wavelength infrared (SWIR), and thermal infrared (TIR) bands. The Hylogging method successfully mapped the distribution of clays and oxides in both the aquitards and aquifers.

27. A number of issues have been identified with using laser grain size analysis of BHMAR core materials. More specifically, samples from mud- and clay-sized textural classes, as determined by laser grain size analysis, were found to often contain sand-sized or larger mud- and clay-particle aggregates if they have been dried (either naturally of in the laboratory) or contain secondary carbonate (or other) cementation. Air drying is sufficient to produce aggregates and it should be noted that the same process turns wet mud into adobe bricks. The study has concluded that standard minimal dispersion regime used in the GA Sedimentology Laboratory does not disaggregate these secondary particles. However, the standard dispersion regime does successfully determine the correct modal grainsize of the clay-fraction of samples that contain significant sand-sized clay- and mud-aggregates.

28. To facilitate effective communication of large and complex geoscience datasets and project results to a wide range of stakeholders, the BHMAR project an interactive 3D virtual globe viewer built on NASA's open source World Wind Java Software Development Kit (SDK) was developed to display complex 3D hydrogeological, hydrogeophysical and hydrogeochemical data (points, lines, 2D surface and 3D shapes).
    i. The final product includes support for a variety of geo-referenced raster data formats, as well as vector data such as ESRI shapefiles and native support for a variety of GOCAD data types including TSurf, SGrid, Voxet and PLine. It also supports borehole data including attribute-based styling of log features and the ability to include legends and descriptions of data within the user interface
    ii. An easy-to-use interface has been customised for navigation of data in 3D space using a virtual globe model, with powerful keyframe based animation tools used to generate flythrough animations for use in knowledge communication workshops.

A 3D hydrogeological systems approach has successfully delineated key functional elements of the Darling Floodplain hydrogeological system (e.g. aquifers, aquitards and faults), mapped heterogeneity (and ‘holes’)

within the aquitards, and hydraulic classes and transmissivities within the main aquifers, as well as groundwater salinities (Lawrie *et al*., 2012b). An even greater heterogeneity of the hydrogeological system is revealed by ground geophysics and drilling data at a borefield scale.

The new datasets, knowledge and hydrogeological conceptual models generated in the project have provided a reliable basis for the identification, characterisation and initial assessment of groundwater resources and MAR options. In particular, AEM data, informed by facies analysis of sonic cores, have been used to target high-yielding palaeochannels, greatly assisting with the rapid identification and prioritisation of groundwater resources and MAR targets.

The products and knowledge generated will also provide important inputs to assist with the parameterisation of groundwater flow and solute transport models that are critical to the next steps in the assessment of MAR and groundwater extraction options in the area. It is our understanding that this is the first use of a trans-disciplinary approach utilising AEM for MAR identification and assessment.

Lessons from the BHMAR study in terms of MAR site identification, characterisation and assessment, have the potential to reduce the timeframes for similar studies, and the scientific investigative costs, even in data-poor areas. Hydrogeological systems mapping approach and the integrated workflows developed in the BHMAR Project can provide rapid and comprehensive assessments of MAR options, in comparison with more traditional methods. In particular, the integrated use of AEM, ground electrical methods, and borehole NMR, enables the rapid characterisation of complex hydrogeological systems, including the key groundwater storage parameters necessary for assessing MAR options. This methodology has the potential for application in many Australian landscapes (and more broadly).

Overall, a multi-scale approach provides a reliable platform for the development of new geological and hydrogeological conceptual models, and a framework for understanding complex hydrogeological and hydrogeochemical processes (Lawrie *et al*., 2012b). Using a holistic systems analysis approach, integration of the 3D mapping with hydrochemical and hydrodynamic data provides critical new insights into surface-groundwater interactions. This approach has been fundamental to developing a new understanding of recharge processes, and the identification of potential recharge and groundwater flow pathways.

# RECOMMENDATIONS- METHODOLOGIES

1. A number of recommendations are made about the use of AEM technology for the high resolution mapping of near-surface hydrogeological systems and the identification and assessment of MAR targets:
    i. AEM data acquisition should be considered as part of any data acquisition strategy in data-poor areas. These data can map large near-surface areas rapidly, maximising the likelihood of identifying multiple MAR targets.
    ii. The mapping and assessment of MAR targets often requires high-resolution geophysical data to resolve the complexities of the hydrogeological system. Traditional derivative analysis approaches for AEM technology selection are inadequate for assessing the ability of candidate systems to map MAR targets. A comparative analysis of candidate systems, consisting of both theoretical considerations and field studies including test lines over representative hydrostratigraphic targets is recommended.
    iii. Optimisation of AEM data for MAR investigations should also involve careful consideration of AEM data acquisition strategy, AEM system calibration, validation and inversion methods.
    iv. It is recommended that a phased approach to AEM data acquisition be trialled to decrease the costs of acquiring AEM data for MAR target mapping. Depending on the nature of the target and the size of the area of investigation, initial reconnaissance mapping of MAR targets could utilise wide line-spaced data to identify potential MAR targets in Australia's major river basins.
        a. As shown in this study, one risk of using this phased approach is that wide line-spacing data may identify targets that on closer inspection may not pass assessments. To minimise these risks, a swath-mapping approach, with 3-5 closely-spaced (e.g. 200 m) flight lines separated by wider line spaced data (e.g. 1-2 km), could be trialled to give more opportunity for key elements of the hydrogeological system to be mapped and assessed.
        b. It should be noted however, that for logistic reasons, it is not always possible to acquire data in phased approaches, however the potential benefits of using such an approach for MAR mapping and assessment should be investigated in future investigations.
        c. The area surveyed should be sufficient to allow for assessment of multiple targets, given the likelihood of failure of some targets on hydrogeological, economic, environmental or social factors.
        d. Depending on the hydrogeological system, it is likely that high density line spacing and/or follow up high resolution ground geophysics would be required to provide sufficient data to resolve the complexities of many Australian hydrogeological systems.
2. An initial assessment concluded that the BHMAR project required a high resolution DEM with a vertical resolution <0.20 m absolute vertical accuracy for the purposes of aquifer potentiometric mapping, flood modelling, and to map key landscape and geomorphic features across the Darling floodplain. However, this was translated as an absolute vertical accuracy of < 0.2 m (RMSE) or < 0.39 m (FVA - Fundamental Vertical Accuracy) when the contract with the provider was finalised. To avoid confusion in the future, it is recommended that all vertical accuracies should be reported as Fundamental Vertical Accuracy (FVA) representing 95% confidence levels, rather than RMSE values representing 1 sigma or 68% confidence levels. The latter are inadequate for hydrological and hydrogeological applications in most Australian landscape settings. Based largely on the BHMAR project experiences, a number of additional recommendations are made with regard to the acquisition, processing, calibration and validation of remote sensing technologies used for high-resolution elevation surveys.
    i. The selection of the appropriate elevation survey technology has to be driven by a clear understanding of project requirements. There are a range of satellite and aircraft-mounted systems available, all with different resolution and accuracy capabilities
        a. It is recommended that future projects clearly identify the immediate project requirements, while also paying some heed to the likely future uses of the datasets as part of the project planning phase. Publically-funded datasets should generally anticipate that

these datasets will be used for a range of purposes beyond the initial scope, and attempt to adhere to the highest standards in terms of precision, accuracy and metadata description.

b. For hydrological investigations, it is recommended that particular attention be paid to the vertical accuracy requirements and definitions. In most Australian floodplain landscapes it is recommended that datasets with < 0.2 m vertical accuracies with respect to an application appropriate vertical reference datum, e.g. the national Geoid model, are obtained.

c. It is recommended that guidelines be drafted providing clear guidance on the resolution capabilities of different systems (precision and accuracy), the limitations of the techniques, and the steps that are required to calibrate these datasets. Such guidelines are required to better inform stakeholders on the potential and limitations of the different technology platforms, and to provide some guidance on the ancillary steps required to ensure the datasets are fit for purpose and adequately calibrated.

ii. Complementary techniques. There are a number of elevation mapping techniques that provide different measurements of surface (and sub-surface) datums with geoscience applications. The following recommendations are made:

a. For hydrological investigations, it is recommended that inSAR techniques be deployed where measurements of temporal variations in land surface heights are required. This includes instances of subsidence and /or 'floodplain breathing'.

b. More specifically, it is recommended that inSAR techniques be trialled in the BHMAR study area to assess the degree of floodplain breathing as a consequence of episodic flooding.

c. It is also recommended that inSAR techniques be trialled in the BHMAR study area to assess the capability of InSAR techniques for mapping watertable fluctuations in unconfined aquifers under Australian landscape conditions.

iii. Ground techniques such as Global Navigation Satellite System (GNSS), geodetic levelling, ground based gravity and other geodetic observing techniques might also complement InSAR mapping techniques. To provide reference surfaces for hydrological applications.

a. Currently, the Australian Height Datum (AHD msl) is used as the reference surface for elevation applications across Australia. While AHD meets the needs of most users, and is used extensively throughout Australia, there must be a recognition within the hydrological community that is not suited for many hydrological applications due to its errors and its definition (msl) that results in a north–south slope (~1 m) arising as a consequence of sea surface topography. It is therefore recommended that for hydrological applications an appropriate vertical reference datum be adopted. This might be the national Geoid model, which is derived from the national gravity network.

b. Efforts should be made to capture and archive all elevation surfaces in an ellipsoidal datum, as described in the ICSM LiDAR Acquisition and Tender Templatei, to future proof their use and facilitate their future improvement as the national Geoid model and height datum is improved.

c. Ellipsoid-geoid transformations are an important source of error in digital elevation modelling applications. In part, this error stems from limitations in the national Geoid model. It is recommended that further observational and modelling efforts be directed toward improvement of the Australian national Geoid model. The contribution of errors associated with the ellipsoid-Geoid transformation in elevation mapping applications is currently poorly understood and also requires additional research.

iv. There are a number of recommendations made with respect to the acquisition of airborne LiDAR and derived products. The current ICSM LiDAR Specifications and Tender Template[2] should be modified to incorporate learnings from the BHMAR project. These changes include:

[2] http://www.icsm.gov.au/elevation/LiDAR_Specifications_and_Tender_Template.pdf

a. Clearly stating the requirement for vertical accuracy in terms of Fundamental Vertical Accuracy (FVA). An FVA of < +/-20cm 95% confidence interval (1.96 x RMSE) is the most appropriate for hydrological modelling in floodplain environments.

b. Incorporate options for derived products, specifically for hydrological modelling. All derived surfaces should be provided with ellipsoidal and orthometric heights. Orthometric heights should be relative to the AUSGeoid Gravity Model, not the Australian Height Datum 1971 (AHD).

c. Improved requirements for ground control.

i. Aircraft trajectories must be computed with reference to local base stations and precise ephemeris data (ITRF), and then subsequently transformed to GDA94.

ii. Where existing CORS are not within range to ensure fixed ambiguity solutions for trajectories, new base station sites are to be established with permanent marking. The Precise Point Positioning (PPP) technique is not acceptable either as a primary or fall-back solution.

iii. The GDA94 ellipsoid heights for these sites are to be determined using the AUSPOS Online GPS Processing Service (final orbit product) with a minimum of two 6 hour observations sessions.

iv. If the setup is a tripod, then it must be reset with a different height between sessions. Refer also to Section 13.4 below for GNSS base station data delivery requirements.

d. A minimum standard for LiDAR classification of Level 3 ground correction should be stipulated to ensure that all derivative surfaces provide the best possible representation of the ground surface.

e. A minimum point density of 2 points per square metre is recommended at nadir to improve the chances of obtaining a ground measurement.

f. There should be a requirement to capture coincident imagery to ensure Level 3 classification is achieved and assist with water masking.

3. Darling Floodplain strategic science site. The BHMAR project area is the most data-rich site in Australia from a hydrology-hydrogeology-geomorphology-neotectonics perspective. A groundwater observation network (40 bores) has been established, and sites established for the trialling of new geophysical and remote sensing technologies.

i. It is recommended this site be recognised as a strategic science site for the trialling of a range of new geophysical, remote sensing technologies, and science methods.

ii. More specifically, it is recommended that a number of monitoring sites (e.g. tiltmeters, microseismic monitoring stations, GNSS reference station) be established at strategic locations within this area to provide baseline stations for future technology and science trials.

iii. It is also recommended that InSAR techniques be trialled in the BHMAR study area to assess the degree of floodplain breathing as a consequence of episodic flooding.

iv. It is also recommended that inSAR techniques be trialled in the BHMAR study area to assess the capability of InSAR techniques for mapping watertable fluctuations in unconfined aquifers under Australian landscape conditions.

4. With regard to the flood modelling, the paucity of river gauge data and issues with the vertical accuracy of the LiDAR dataset limit the accuracy of the modelled flood extent surfaces. Flood predictions could be improved by:

i. Developing an automated process for removing areas disconnected from the river;

ii. Collecting additional ground control points to recalibrate the LiDAR dataset may be useful if sub-20cm vertical resolution is required. This would have to take into account temporal shifts in the elevation of the land surface during the 2010-11 flooding.

iii. Using alternative mapping and prediction methods. These methods could include:

a. Generation of continuous surface flow networks in discretized stretches of the river. This could also be trialled in the northern and southern portions of the BHMAR Project area to reduce over- and under-estimation.

b. Hydrodynamic modelling utilising the extensive data obtained over the course of the BHMAR Project.

5. For mapping and assessing vegetation condition, particularly with respect to groundwater dependent vegetation (GDV), it is recommended that:
   i. A temporal, integrated approach similar to that utilised in the BHMAR study be applied when considering any new (or modified) groundwater developments including for urban supply, irrigation or mining/extraction purposes such as coal or coal seam gas.
   ii. Furthermore, it is strongly recommended that any such study be undertaken in conjunction with a vegetation field program, measuring compatible biophysical parameters under varying climatic/seasonal conditions. This will result in a more robust, quantitative analysis. Other, complimentary remote methods could also be undertaken to strengthen the analysis and increase the spatial resolution such as aerial photography, different satellite or airborne imagery (e.g. Quickbird) or derived products (e.g. fractional cover).
6. A trans-disciplinary systems approach, and integrated workflows developed in the BHMAR Project, should be considered for future hydrogeological investigations and the assessment of MAR options in Australia, and in shallow sedimentary systems in particular. These methods provide the integrative framework required to address the many inter-related issues encountered in assessing MAR options, particularly in hydrogeologically and hydrogeochemically complex areas.
7. Structural mapping in the BHMAR study area and in the larger area covering the Western Murray Porous Rock Aquifer, combined with other recent tectonic studies, have revealed that Neogene tectonics (and neotectonics) may be more extensive than previously thought in the Murray-Darling Basin and Australia more generally. Neogene and more recent faulting activity may play an important role in inter-aquifer leakage and recharge processes. It is therefore recommended that future hydrogeological and MAR studies should consider tectonic studies as an integral part of future investigations and assessments.
8. The key learnings and recommendations from applying various methods to estimate recharge are outlined below.
   i. There are many different methods for estimating groundwater recharge. Some of these provide estimates of potential recharge or deep drainage, which is the flux below the root zone that has the potential to reach the watertable over varying periods of time. Other methods focus on groundwater responses where recharge accessions have actually reached the watertable. Many of these methods apply only to the unconfined aquifer and cannot be extrapolated to estimating groundwater recharge to confined or semi-confined aquifers. An understanding of the geometry and structure of the hydrostratigraphy, including any overlying aquitards is recommended to ensure that the recharge method is appropriate.
   ii. It is important to understand the assumptions inherent in any recharge estimation method and the implications of these on method suitability. This is important to ensure that the recharge method is appropriate to the conceptual model developed for the groundwater system. For example, the groundwater chloride mass balance method assumes that the chloride in groundwater originates from rainfall, with no other subsurface chloride sources. It also assumes that surface water leakage to the aquifer is absent. With river/lake leakage interpreted as the dominant recharge mechanism, these assumptions are not met for the BHMAR study area so the derived potential recharge estimates are not valid. A verification of the underlying assumptions of the recharge method against the conceptual model is recommended.
   iii. Recharge to the Calivil Formation is dominated by episodic leakage during high river flows and via structurally controlled disruptions to the regional overlying aquitards. This results in significant variations in recharge rates in both space and time, resulting in significant challenges in terms of extrapolating point-based recharge estimates. To address this spatial and temporal variability in recharge, it is recommended that a transient groundwater flow model be constructed and calibrated to the hydrographic responses to a series of flood events.
9. The hydrographic network established by the BHMAR project enabled comprehensive monitoring of the groundwater response to the 2010-11 Darling River flood. This provided a critical dataset that provided evidence that recharge is predominantly the result of river leakage during high flow events. Based on the importance of long-term hydrographic monitoring of critical episodic events it is therefore recommended that:

i. The newly established hydrographic and barometric network should be maintained in the study area, to monitor the groundwater response to streamflow events of varying magnitude on both Talyawalka Creek and the Darling River;

ii. Current bore data loggers should be upgraded to include improved temperature sensors, and key bore monitoring stations telemeterised to provide real-time monitoring of groundwater levels.

iii. Stream gauges be established for Talyawalka Creek to assist with measuring the frequency and magnitude of flows, and to calculate losses to the groundwater system.

iv. Additional stream gauges are required for the Darling River upstream of Lake Wetherell to enable losses to the groundwater system to be calibrated.

v. Trial the installation of additional logger technologies in the monitoring bores to collect time series data of complimentary parameters (such as groundwater electrical conductivity).

10. A number of recommendations are made with respect to water sampling and analysis:

i. In future sonic drilling programs, investigate further the use of suitable field methods or instrumentation (such as hand-held meters) to measure key hydrochemical parameters including EC, pH and Eh at the time of drilling and core retrieval.

ii. Establish protocols for the appropriate preservation of core material, notably to reduce exposure to the atmosphere. This is important to retain the integrity of redox-sensitive species in the pore fluids and to reduce post-drilling water-rock interactions as much as possible. Different approaches could be taken depending on whether conventional plastic sleeves or more specialised lexan tubing is used in core collection.

iii. Expand the routine hydrochemical analysis of pore fluids to include the stable isotopes of oxygen-18 and deuterium to help provide insights into groundwater flow paths and processes. This will require reviewing of pore fluid extraction and preservation protocols to ensure suitable sample integrity, particularly the minimisation of post-drilling evaporation.

iv. Integrate with the existing regular sampling of the Darling River and Menindee Lakes by Country Water staff, to enable regular surface water samples for complimentary analyses, particularly for water stable isotopes.

v. Extend the groundwater sampling regime to the collection of dissolved or entrained gases, particularly carbon dioxide and methane. Gas analyses can provide insights on biogenic processes such as methanogenesis and assist in the mapping of redox zones in the aquifer. This is important in assessing and managing risks such as clogging and metal remobilisation associated with injection of treated source water.

vi. The project borehole network provides the opportunity to trial alternative approaches to groundwater sampling, considering the routine use of low-flow pumping during the BHMAR project.

11. Recommendations with respect to the use of tracers and age dating include:

i. Trial alternative groundwater age dating techniques (such as sulfur hexafluoride $SF_6$) to test and extend the interpretations based on the use of carbon-14 and chlorofluorocarbon analyses.

ii. When using chlorofluorocarbon as a tracer tool, analysis of CFC-113 is recommended in addition to the conventional analysis of CFC-11 and CFC-12. This would improve evaluation of groundwater mixing fractions between the fresh river leakage and the saline regional groundwaters.

iii. Investigate the use of heat as a tracer for interactions between the river (or lakes) and the shallow unconfined aquifer. This can include the installation of infrastructure to monitor temperature in the river and also within the near-river sediments.

12. Hydraulic testing of aquifers in the target borefield has involved the extensive use of slug tests and two short-term pump tests. This has been supplemented by downhole profiles of hydraulic properties derived from NMR logging, as well as permeameter and porosity testing on selected core samples. The next phase of investigations could include the following recommendations:

i. Implement longer-term (> 1 month) aquifer pump tests in the potential borefield target to quantify key aquifer hydraulic properties (such as transmissivity and storativity), assess inter-aquifer leakage and river-aquifer connectivity.

ii. Such aquifer pump tests should not only include monitoring of groundwater levels in monitoring bores in the target Calivil Formation, the overlying unconfined aquifer and the underlying Renmark Formation, but also monitoring of the hydrochemistry of the pumped groundwater. This includes regular field chemistry measurements (e.g. EC, pH, Eh, alkalinity, $Fe^{2+}$, etc.), water quality indicators (major ions, trace metals, nutrients etc.) and isotopes (oxygen-18, deuterium etc.). This hydrochemistry data can be used to assess the potential mobilisation of poor quality groundwater with pumping and the identification of groundwater flow paths.

iii. The existing infrastructure of production and monitoring bores can equally be used in aquifer injection trials at the Jimargil borefield site. Like the aquifer pump tests, this would involve monitoring the hydraulic response in the shallow watertable aquifer, the target Calivil Formation aquifer and the underlying Renmark Formation aquifer. Hydrochemical monitoring and sampling would also be undertaken to map the progress of the injectant plume and secondary processes such as redox, water-rock and source water-groundwater reactions. Monitoring of injection flow rates would be used to assess potential clogging. Such an injection trial would preferably involve the temporary installation of a mobile treatment plant to replicate the use of appropriately treated Darling River source water, as envisaged in an operational MAR scheme.

iv. The monitoring bore network provides an opportunity to trial other approaches to hydraulic characterisation. One such approach is using an electromagnetic borehole flowmeter to measure variations in hydraulic conductivity within the screened interval. This would provide independent data to better define the conversion of NMR logging data to downhole estimates of hydraulic conductivity.

13. Hydrographic Monitoring and analysis

    i. Continue to collect time-series groundwater level and barometric data from the existing project monitoring network. The monitoring of the groundwater response to flood events of varying magnitude is required to better quantify recharge dynamics.

    ii. Trial the installation of additional logger technologies in the monitoring bores to collect time series data of complimentary parameters (such as groundwater electrical conductivity or temperature).

14. Unfortunately due to time and resource constraints, both phases of geomorphic mapping were only completed in the central, higher priority area. It is thus recommended that detailed geomorphic mapping be finalised across the entire BHMAR study area. More broadly, in areas where the trend in the floodplain dictates, it is recommended that the regional digital elevation model be levelled prior to geomorphic mapping. This will then facilitate the generation of both rapid and highly detailed geomorphic mapping of the floodplain using a semi-automated contouring tool.

15. With respect to laboratory grain size analysis, the following recommendations are made:

    i. To improve the reliability of the laser grain size analysis, stronger pre-treatment regimes (including acid) and dispersion protocols can more effectively disaggregate secondary particles but must necessarily add to laboratory time and therefore costs. In future, stronger pre-treatment (including acid) and dispersion regimes should be used for mud- and clay-rich samples which are dry or are known to have dried in the past and/or contain secondary cementation. Moisture analyses and quantitative XRD mineralogy determinations can help inform the decision to select samples requiring these processes. Sand-sized sediments have issues with repeatability of results, due to the difficulty of obtaining representative samples because of the small sample requirements of the measuring instrument. This constraint is likely to increase with coarser textured samples.

    ii. New laboratory procedures are recommended for sample preparation prior to carrying out laser grain size analysis of core materials. More specifically, representative samples should be tested prior to routine analyses to determine the most appropriate disaggregation method for a batch of samples; routine treatment with HCl where carbonate cementation is possible. Methodologies should also be established for dealing with non-carbonate cementation; and sample splitting methods are necessary to ensure statistically representative sub-sampling.

16. With respect to laboratory clogging tests it is recommended that future studies should consider a greater number of samples distributed over representative textural classes in the aquifer of interest. It is also recommended that wherever possible, undisturbed drillcore materials be used in the experiments to provide a more realistic simulation of hydraulic conductivity and water-rock interactions.

Consideration of the column sizes that are appropriate to the grain size distributions is also recommended.

17. The following recommendations are based on the successful trialling of in-river surveys and sampling by the BHMAR project.
    i. The data and observations from the in-river survey were critical in finessing the conceptual model for river-aquifer connectivity in the Jimargil target area. This data included mapping of river bathymetry which could be compared against the existing understanding of underlying hydrostratigraphy, as well as the identifying and sampling of riverbed depressions.
    ii. The survey boat is a useful platform where additional data collection could be incorporated. This could include systematic photography of the river banks, regular river water sampling and the towing of water quality sondes (such as EC, pH and DO). Reconnaissance survey data could then be used to target more detailed investigations such as shallow coring or the installation of pressure or temperature loggers in the water column and river sediments. Such data is important in understanding the spatial and temporal changes in groundwater-surface water connectivity. The in-river data also has relevance to other disciplines (such as aquatic ecology, engineering and landscape remediation)
18. Preliminary groundwater modelling was undertaken as part of Phase 3 investigations of the Jimargil borefield target, for which the following recommendations are based:
    i. The use of rapid, simple but robust (parsimonious) groundwater flow and solute transport models is recommended at relatively early stages of data acquisition and interpretation. Such models are useful in (1) a sensitivity analysis to define key data gaps, (2) in testing the validity of a range of potential conceptual models about the hydrogeological system and key groundwater processes and (3) in scoping the broad MAR requirements and potential impacts such defining the required target size or highlighting zones of inter-aquifer leakage;
    ii. A review of the available data and conceptual understanding be made at a decision point concerning the development of a more sophisticated 3D multi-layered transient groundwater flow and solute transport model to support any future borefield design and operation. Such modelling will need to take account of (1) the episodic flow-dependent nature of river leakage including change in river bed conductance (2) the localised nature of recharge to the target Calivil Formation aquifer via structural or erosional gaps in the overlying Blanchetown Clay (3) the preferential distribution of Calivil Formation aquifer sands and gravels in palaeovalley fill (4) the mapping of the shallow aquifer as generations of alluvial deposits that are structurally controlled and disrupted (5) the distribution of native vegetation that has been interpreted to have a degree of dependency on shallow groundwater (6) possible variability in the hydraulic connectivity between the target Calivil Formation aquifer and the underlying Renmark Formation (7) the potential with pumping for vertical and lateral ingress from mapped zones of brackish to saline groundwater.
19. To improve the reliability of the laser grain size analysis, stronger pre-treatment regimes (including acid) and dispersion protocols can more effectively disaggregate these secondary particles but must necessarily add to laboratory time and therefore costs. In future, stronger pre-treatment (including acid) and dispersion regimes should be used for mud- and clay-rich samples which are dry or are known to have dried in the past and/or contain secondary cementation. Moisture analyses and quantitative XRD mineralogy determinations can help inform the decision to select samples requiring these processes. Sand-sized sediments have issues with repeatability of results, due to the difficulty of obtaining representative samples because of the small sample requirements of the measuring instrument. This constraint is likely to increase with coarser textured samples.
20. New laboratory procedures are recommended for sample preparation prior to carrying out laser grain size analysis of core materials. More specifically, representative samples should be tested prior to routine analyses to determine the most appropriate disaggregation method for a batch of samples; routine treatment with HCl where carbonate cementation is possible. Methodologies should also be established for dealing with non-carbonate cementation; and sample splitting methods are necessary to ensure statistically representative sub-sampling.
21. The MAR guidelines (NRMMC-EPHC-NHMRC, 2009) are a component of the National Water Quality Management Strategy (NWQMS) and as such have a specific focus on human health and environment protection. Experience in the BHMAR project suggests that there is a strong case that the MAR guidelines be complemented by supporting documentation that would provide complementary

advice on a broader range of issues not covered in the existing Guidelines. This supporting documentation, covering MAR site selection and best practice advice on the adequacy of geological and hydrogeological data for MAR site assessment, may include:

i. Advice on technical risk assessment frameworks for selecting the most appropriate technologies and methods for MAR mapping and assessment.

ii. This document should also provide 'best practice' advice on how to assess the adequacy of geological and hydrogeological data, and the inherent variability of key geological and hydrogeological parameters, be written to guide MAR proponents. This document should also address issues such as the potential impact on the level of confidence in proceeding through the MAR assessment stages. This should include guidance on the data density and data quality required to map critical geological, hydrochemical and hydraulic properties could also be provided in the supporting document.

iii. Advice on assessing the uncertainty associated with the hydrogeological and hydrochemical characterisation, including sensitivity analysis approaches, would also be useful.

iv. This document should stress the importance of assessing multiple targets. This was highlighted by the failure of many sites in the BHMAR study. Failure to identify multiple candidate sites may lead to significant delays in MAR project implementation, if scientific investigations required to address the questions in Stage 2 assessments are undertaken sequentially rather than concurrently

v. Advice on how groundwater flow and solute transport modelling could be incorporated into the MAR assessment process is also warranted. As the case for the BHMAR project, relatively simple models constructed early in the process can greatly assist with the MAR viability or degree of difficulty assessment and the defining of key information gaps. As data acquisition proceeds, more sophisticated models could be constructed to provide a more realistic evaluation of operational options and potential third party or environmental impacts.

vi. The document would aim more broadly to assist proponents with all stages of MAR selection and assessment.

22. A trans-disciplinary systems approach, and integrated workflows developed in the BHMAR Project, should be considered for future hydrogeological investigations and the assessment of MAR options in Australia, and in shallow sedimentary systems in particular. These methods provide the integrative framework required to address the many inter-related issues encountered in assessing MAR options, particularly in hydrogeologically and hydrogeochemically complex areas.

# Contents

Summary ..... i
Contents ..... xxiii
List of Figures ..... xxviii
List of Tables ..... xxxvii
1 Introduction ..... 1
1.1 Project Background ..... 1
1.1.1 Previous Geoscience Australia Investigations ..... 2
1.1.2 The BHMAR Project ..... 3
1.2 Purpose and Scope of This Report ..... 5
2 BHMAR Project Workflows ..... 7
2.1 BHMAR Project Phases ..... 7
2.2 BHMAR Phase 1 ..... 11
2.2.1 Hydrogeological Data Compilation ..... 11
2.2.2 New Data Acquisition ..... 12
2.2.3 Hydrogeological Assessment ..... 12
2.2.4 AEM Technology Evaluation and Risk Assessment ..... 16
2.2.5 AEM (and LiDAR) Survey Design and Costing ..... 17
2.3 BHMAR Phase 2 ..... 17
2.3.1 New Data Acquisition ..... 18
2.4 BHMAR Phase 3a ..... 18
2.4.1 Phase 3a Data Acquisition ..... 19
2.5 Research Methodology and Project Management ..... 20
2.6 Using AEM to Map MAR and Groundwater Resource Targets ..... 22
2.6.1 3D Mapping of Hydrostratigraphy, Structure and Groundwater Salinity ..... 24
2.6.2 Customised Interpretation Products ..... 25
3 Managed Aquifer Recharge and Water Quality Guidelines, and Cultural Heritage ..... 26
3.1 MAR Options and Assessment Guidelines ..... 26
3.1.1 MAR Options Considered in the BHMAR Project ..... 26
3.1.2 MAR Risk Assessment Framework Used in BHMAR Phase 1 ..... 29
3.2 National MAR Risk Assessment Framework Used in BHMAR Phases 2-3a ..... 29
3.2.1 MAR Viability Assessments ..... 33
3.2.2 Degree of Difficulty Assessments ..... 35
3.2.3 BHMAR Phase 2 Assessment ..... 36
3.2.4 BHMAR Phase 3 Assessment ..... 36
3.3 Water Quality Guidelines ..... 37
3.4 Indigenous Cultural Heritage ..... 40
4 Assessment of Pre-existing Data ..... 42
4.1.1 Borehole Data ..... 42
4.2 Regional Geophysics ..... 56
4.2.1 Airborne Magnetic and Gamma Radiometric Data ..... 56
4.3 Digital Elevation Data ..... 59
4.4 Remotely Sensed Satellite Data ..... 60
4.5 Land Use and Cadastral Mapping ..... 61
4.6 Summary Assessment of Pre-existing Data ..... 66
5 LiDAR Data ..... 69
5.1 LiDAR Data Acquisition ..... 69
5.2 Calibration and Data Processing ..... 73
5.2.1 Vegetation Capture Issues ..... 73
5.2.2 Gouging or Reduced Terrain around Trees ..... 73
5.2.3 Classification of Wetland Environments ..... 77
5.2.4 Dataset Merging ..... 79
5.2.5 Assessment of Vertical Accuracy ..... 85
5.3 Utility of the High Resolution LiDAR Dataset in the BHMAR Study Area ..... 95
5.4 DEM Summary ..... 96
6 Airborne Electromagnetics (AEM) ..... 98
6.1 Using AEM to Map Key Elements of the Hydrogeological System ..... 98

6.1.1 Introduction ..... 98
6.1.2 Groundwater Salinity and Hydrostratigraphic Mapping in Australia's Salinized Landscapes ..... 98
6.1.3 Use of AEM as Part of Trans-disciplinary Systems Studies of Groundwater Systems in Australia 100
6.2 AEM System Selection for the BHMAR Survey ..... 101
6.2.1 Introduction ..... 101
6.2.2 Step 1: Derivative Analysis Approach Including Ground TEM and Borehole Induction Models and Forward Modelling of System Responses ..... 102
6.2.3 Step 2: Comparative Analysis Utilising Theoretical Considerations and Field Studies Including Test Lines ..... 104
6.2.4 Discussion ..... 107
6.3 SKYTEM TDHEM System ..... 110
6.3.1 System Configuration ..... 113
6.3.2 Transmitter and Receivers ..... 114
6.3.3 In-field Data Processing ..... 116
6.3.4 BHMAR AEM Survey Logistics ..... 116
6.4 AEM System Resolution and Sensitivity ..... 119
6.4.1 Principle of the TEM Method ..... 119
6.4.2 Significance of Transmitter Moment and Turnoff Time ..... 119
6.4.3 Resolution Limits ..... 120
6.4.4 Sensitivity Functions ..... 120
6.4.5 What Depths can be Mapped to with the SkyTEM System? ..... 125
6.4.6 An Analysis of the Resolution Capability of the AEM Data to Map the Blanchetown Clay ..... 125
6.5 SKYTEM System Calibration ..... 128
6.5.1 Establishing a Reference Model ..... 128
6.5.2 Airborne Hover Test ..... 129
6.5.3 SKYTEM Technical Specifications and Data Processing and Inversion ..... 132
6.5.4 Processing of River Flight Lines ..... 136
6.6 BHMAR AEM Inversions ..... 137
6.6.1 Initial Contractor's Inversion ..... 139
6.6.2 Initial Aarhus WorkBench Inversion ..... 143
6.6.3 LCI WorkBench Inversion (Aarhus University Hydrogeophysics Group) ..... 144
6.6.4 Test Inversion of the GWR Area ..... 160
6.6.5 A 3D Inversion Approach ..... 165
6.7 Final (WANDA) Inversion Products ..... 165
6.7.1 Introduction ..... 165
6.7.2 Data Post-processing ..... 169
6.7.3 Final (WANDA) Inversions: Forward and Inverse Modelling, Correlation and Analysis ..... 169
6.7.4 An Analysis of the Residuals of the BHMAR Inversion ..... 193
6.8 Comparison of Borehole EM Data with the Final Inversion ..... 242
6.8.1 Introduction ..... 242
6.8.2 Comparing Borehole Conductivity Logs and Final AEM Inversion Results ..... 244
6.8.3 A Comparison with Pre-existing Borehole Induction Log Data ..... 264
6.9 Trans-dimensional Markov Chain Monte Carlo Uncertainty Analysis ..... 274
6.10 Re-gridding the BHMAR Inversion Results Using Increasingly Sparse Data ..... 277
6.10.1 Background ..... 277
6.10.2 The Re-gridding Experiment ..... 277
6.11 Summary ..... 293
7 Borehole Geophysics ..... 295
7.1 Induction Conductivity Logging ..... 295
7.1.1 Logging Procedures ..... 297
7.1.2 Calibration ..... 298
7.1.3 Processing ..... 302
7.2 Natural Gamma Logging ..... 302
7.3 Nuclear Magnetic Resonance (NMR) Logging ..... 303
7.3.1 Why NMR Logging in the BHMAR Area? ..... 303
7.3.2 NMR Background ..... 303
7.3.3 Borehole NMR Measurements ..... 304
7.3.4 NMR Field Acquisition Method ..... 307
7.3.5 NMR Derived Hydraulic Conductivity ..... 326
7.3.6 NMR Logs of Total-, Free- and Bound-water, and Hydraulic Conductivity ..... 339

7.3.7 Recommendations for Future NMR Applications ... 341
8 Ground Geophysics ... 342
8.1 Time Series Monitoring of Aquifer Pump Tests ... 342
8.2 Ground Resistivity and Induced Polarisation Surveys ... 344
8.2.1 Menindee Common ... 344
8.2.2 Jimargil-East Bootingee ... 347
8.3 Aarhus University Inversions of the Ground Geophysical Data at Jimargil ... 347
8.3.1 Time Domain Induced Polarization ... 347
8.3.2 Survey and Data Processing ... 349
8.3.3 Inversion ... 353
8.3.4 Results ... 359
8.3.5 AEM, Induction and Gamma Log Comparison ... 362
8.3.6 Geological Comparison ... 367
8.3.7 Discussion and Conclusions ... 368
8.3.8 Recommendations and Future Work ... 369
9 In-River Geophysical Surveys and Sediment Sampling ... 372
9.1 Project Requirements and Survey Options ... 372
9.1.1 Background ... 372
9.1.2 Technologies for In-river Surveys ... 372
9.2 Multibeam Sonar Riverbed Mapping ... 373
9.2.1 Introduction ... 373
9.2.2 Methodology ... 375
9.2.3 Data Processing ... 382
9.2.4 Processed Data Products and Formats ... 383
9.3 Results ... 383
9.3.1 Single Beam Echo Sounder Data ... 383
9.4 Multibeam Echo Sounder Data ... 384
10 Drilling Program ... 390
10.1 Drilling Phases ... 390
10.2 Rotary Mud Drilling ... 390
10.3 Sonic Drilling ... 391
10.3.1 Benefits of Using Sonic Core ... 395
10.4 Bore Construction ... 400
11 Sonic Core Logging, Sampling and Analysis ... 401
11.1 Core Description and Sampling ... 401
11.2 Pore Fluid Analysis ... 402
11.2.1 Potential Contamination ... 402
11.2.2 Extraction ... 406
11.2.3 Compatibility Between Different Extraction Methods ... 408
11.3 Physical Properties ... 409
11.3.1 Grainsize Analysis ... 409
11.3.2 Moisture Content ... 419
11.3.3 Bulk Density Determination ... 420
11.4 Palynology ... 420
11.5 Rock Chemistry and Mineralogy ... 421
11.5.1 Preparation ... 421
11.5.2 XRF ... 421
11.5.3 ICP-MS ... 423
11.5.4 XRD ... 424
11.5.5 Hyperspectral Studies of Core Materials ... 424
11.5.6 HyLogger ... 425
11.5.7 PIMA ... 427
11.6 MAR Clogging Potential (CSIRO) ... 428
11.7 Laboratory Hydraulic Conductivity Tests ... 430
11.7.1 Preparation ... 430
11.7.2 Analysis ... 431
11.8 Total and Effective Porosity ... 434
11.8.1 Helium Injection Method ... 434
11.8.2 Kerosene Saturation Method ... 435
11.8.3 Matric Potential Method ... 435

11.8.4 Results ... 437
12 Sampling and Analysis of Near-Surface Units ... 439
12.1 Field Sampling ... 439
12.1.1 Natural Exposures ... 439
12.1.2 Tractor Excavated Pits ... 439
12.1.3 Hand-auger Holes ... 439
12.2 Quaternary Fluvial-unit Geochronology ... 441
12.2.1 OSL Dating ... 441
12.2.2 Sediment Radiocarbon Dating ... 446
13 Hydraulic Testing ... 450
13.1 Air Lift Tests ... 450
13.2 Slug testing ... 452
13.3 Pump Tests ... 458
13.3.1 Pumping Bores ... 460
13.3.2 Pumping and Pipeline Infrastructure ... 463
13.3.3 Pump Test Discharge ... 467
13.3.4 Groundwater Level Monitoring ... 468
13.3.5 Pumped Flow Monitoring ... 469
14 Water Sampling and Analysis ... 471
14.1 Groundwater Sampling ... 475
14.2 Surface Water and Rainfall Sampling ... 479
14.3 Pore Fluid Sampling ... 480
14.4 Quality Control Procedures ... 480
14.4.1 Internal QA/QC ... 480
14.4.2 ALS QA/QC ... 481
14.5 Hydrochemical Data Processing and Analysis ... 484
14.5.1 Fuzzy-k Means Cluster Analysis ... 485
14.6 Geochemical Modelling (CSIRO) ... 487
14.6.1 Sediment Chemistry ... 488
14.6.2 Groundwater Chemistry ... 489
14.6.3 Source Water Chemistry ... 489
14.6.4 Geochemical Modelling ... 490
14.6.5 Statistical Analysis ... 491
15 Hydrographic Monitoring and Analysis ... 492
15.1 Groundwater Level and Temperature Monitoring ... 492
15.1.1 Data Collection ... 492
15.1.2 Data Processing and Interpretation ... 496
15.2 Potentiometric Surfaces ... 498
15.3 Groundwater Modelling (CSIRO) ... 499
16 Recharge Studies ... 502
16.1 Background ... 502
16.2 Estimating Groundwater Resoures in Data-Poor Areas Project ... 502
16.2.1 Method of Last Resort (MOLR) ... 502
16.2.2 Percentage Clay Method ... 502
16.2.3 Chloride Mass Balance Method ... 503
16.3 Watertable Fluctuation Method ... 504
16.4 Groundwater Mounding Model ... 505
16.5 Flood Frequency Analysis ... 507
16.6 Radiocarbon Depth Models ... 509
16.7 Recommendations ... 510
17 Data Integration and Mapped Products ... 511
17.1 Flood Inundation Mapping ... 511
17.1.1 Introduction ... 511
17.1.2 LiDAR-derived Potential Flood Extents ... 512
17.2 Vegetation Health and Groundwater Dependence Mapping ... 533
17.2.1 Introduction ... 533
17.2.2 Acquisition, Basic Processing and Existing Datasets ... 533
17.2.3 Advanced Processing and Derived Products ... 540
17.2.4 Future Recommendations ... 562
17.3 Lineaments and Structural Mapping ... 565

17.3.1 Structural Mapping Using the AEM Inversion Products ..... 565
17.3.2 Recognition of Lineaments on LiDAR ..... 579
17.4 Surface Geomorphology and Landform Mapping ..... 585
17.4.1 Landform Mapping ..... 585
17.4.2 Surface-materials Mapping ..... 587
17.5 Identifying the Blanchetown Clay ..... 590
17.5.1 Introduction ..... 590
17.5.2 Methodology ..... 590
17.6 Stratigraphic mapping ..... 600
17.6.1 Blanchetown Clay ..... 601
17.6.2 Mapping the Deeper Intervals ..... 601
17.6.3 Mapping the Shallower Intervals ..... 604
17.6.4 Reconciling the Stratigraphic units ..... 605
17.7 Mapping Hydraulic Textural Classes ..... 605
17.7.1 Input Datasets ..... 606
17.7.2 Methodology ..... 608
17.8 Hydrostratigraphic Mapping ..... 626
17.8.1 Thickness and Depth to Top of Hydrostratigraphic Units ..... 628
17.9 Hydraulic Conductivity of Sediments ..... 638
17.9.1 Data Exclusion ..... 639
17.9.2 AEM and Lithology ..... 639
17.9.3 Map of Hydraulic Conductivity ..... 640
17.10 Transmissivity ..... 640
17.11 Effective Porosity ..... 652
17.11.1 NMR Datasets ..... 652
17.11.2 Laboratory Porosity Measurements ..... 653
17.11.3 Comparison of NMR and Porosity Datasets ..... 655
17.12 Diffusion Rate Within Upper Confining Aquitard ..... 677
17.13 Groundwater Volume Estimation ..... 683
17.13.1 Groundwater Salinity Thresholds ..... 683
17.13.2 Aquifer Bulk Volumes ..... 692
17.13.3 Effective Porosity ..... 693
17.13.4 Groundwater Volume Estimates ..... 694
17.13.5 Uncertainty Analysis of Groundwater Storage Volume Estimates ..... 697
17.14 Calculating the Salt Store in the Unsaturated Zone ..... 707
17.14.1 Calculations ..... 707
17.15 Recharge Potential Mapping ..... 712
17.15.1 Introduction ..... 712
17.15.2 Recharge Mapping ..... 712
17.15.3 Application ..... 719
17.16 Graphic Display of Borehole Geological, Geophysical and Geochemical Data ..... 720
17.16.1 Data Collation ..... 720
17.16.2 Production of Strater Logs ..... 720
17.16.3 Textural Bar Graph Anomalies ..... 721
17.17 3D Geological Model and Visualisation ..... 733
18 Conclusions ..... 734
19 Recommendations ..... 745
References ..... 753
Acknowledgements ..... 772
Glossary ..... 776

# List of Figures

**Figure 1-1.** Location of the BHMAR project area relative to the Murray -Darling Drainage Basin ..... 2
**Figure 1-2.** Location of the BHMAR project area relative to Menindee and Broken Hill ..... 4
**Figure 2-1.** Datasets acquired during the BHMAR project, grouped by theme. ..... 9
**Figure 2-2.** Simplified BHMAR project workflow ..... 10
**Figure 2-3.** Hydrogeological cross-section through the Darling River Floodplain ..... 13
**Figure 2-4.** Map showing location of hydrogeological cross-section ..... 14
**Figure 2-5.** Salinity-yield mapping for the priority aquifers ..... 15
**Figure 2-6.** Map showing data reliability for the aquifer salinity-yield mapping ..... 16
**Figure 3-1.** Schematic diagrams showing MAR options. ..... 28
**Figure 3-2.** Stages in establishing a MAR project in accordance with MAR Guidelines ..... 31
**Figure 3-3.** MAR viability assessment decision flow chart. ..... 34
**Figure 3-4.** Previously recognised cultural heritage sites in the BHMAR project area ..... 41
**Figure 4-1.** Pre-existing boreholes located in or adjacent to the BHMAR project area ..... 43
**Figure 4-2.** Pre-existing boreholes classified by borehole ownership. ..... 44
**Figure 4-3.** Maximum depth of pre-existing boreholes ..... 45
**Figure 4-4.** Pre-existing boreholes with useable lithological information ..... 46
**Figure 4-5.** Maximum depth of pre-existing PVC-lined boreholes ..... 49
**Figure 4-6.** Pre-existing PVC-lined boreholes that intercept shallow aquifers ..... 50
**Figure 4-7.** Pre-existing PVC-lined boreholes that intercept the Pliocene aquifer ..... 51
**Figure 4-8.** Pre-existing PVC-lined boreholes that intercept the upper Renmark Formation aquifer ..... 52
**Figure 4-9.** Pre-existing PVC-lined boreholes that intercept the middle Renmark Formation aquifer ..... 53
**Figure 4-10.** Pre-existing PVC-lined boreholes that intercept the lower Renmark Formation aquifer ..... 54
**Figure 4-11.** Downhole gamma and induction logging of borehole T2:0702 and T2:0703. ..... 55
**Figure 4-12.** Distribution and line-spacing of lower resolution (>300 m line spacing) airborne magnetic, gamma radiometric and elevation dataset ..... 56
**Figure 4-13.** Distribution and line-spacing of high resolution (<150 m line spacing) airborne magnetic, gamma radiometric and elevation datasets ..... 57
**Figure 4-14.** Total magnetic intensity of airborne magnetics dataset ..... 58
**Figure 4-15.** First vertical derivative of airborne magnetics dataset ..... 58
**Figure 4-16.** A ternary gamma radiometric image for the Broken Hill area ..... 59
**Figure 4-17.** SRTM 1 second dataset for the Broken Hill area ..... 60
**Figure 4-18.** ALOS image availability for the Broken Hill area ..... 61
**Figure 4-19.** Map showing Kinchega National Park, Timber Reserve and Water Supply Reserve Boundaries. ..... 62
**Figure 4-20.** Exploration lease areas prior to and during a) 1970 and b) 1980 ..... 63
**Figure 4-21.** Exploration lease areas for a) 1990 and b) 2000. ..... 64
**Figure 4-22.** Exploration lease areas for a) 2010 and b) current mineral and petroleum exploration titles and applications. ..... 65
**Figure 5-1.** LiDAR survey area ..... 70
**Figure 5-2.** View of the Menindee Lakes from the AAMHatch survey aircraft. ..... 71
**Figure 5-3.** LiDAR survey grounded at Broken Hill airport due to dust storm activity. ..... 72
**Figure 5-4.** Partially submerged vegetation in Lake Wetherell ..... 74
**Figure 5-5.** LiDAR vegetation removal issues ..... 75
**Figure 5-6.** Vegetation laser strike removal ..... 76
**Figure 5-7.** Wetland environment with turbid water and a complex land cover. ..... 77
**Figure 5-8.** LiDAR water body image before and after classification correction ..... 78
**Figure 5-9.** LiDAR wetland image before and after classification correction ..... 78
**Figure 5-10.** Vertical accuracy of base datasets and final compilation surfaces. ..... 81
**Figure 5-11.** Full point clouds from the Thiess 2003 and AAMHatch 2009 surveys. ..... 83
**Figure 5-12.** Extent and location of the various base datasets. ..... 84
**Figure 5-13.** Vertical accuracy analysis of DEMs using 1:250,000 spot heights. ..... 87
**Figure 5-14.** Vertical accuracy analysis of DEMs using SCIMS benchmarks ..... 88
**Figure 5-15.** Vertical accuracy analysis of DEMs using 2009 LiDAR control points ..... 89
**Figure 5-16.** Vertical accuracy analysis of DEMs using all borehole collar elevations. ..... 90
**Figure 5-17.** Correlation between surveyed elevation and LiDAR DEM elevation. ..... 91
**Figure 5-18.** Location of surveyed bores used in the analysis of LiDAR DEM accuracy. ..... 92
**Figure 5-19.** Comparison between 5m, 15m DEMs and LiDAR ground returns from 2003 Lake Wetherell Survey ..... 93
**Figure 5-20.** Three examples of the diversity of land cover classes ..... 95

**Figure 6-1.** Risk plot of aquifer management options expressed as likelihood of technical success against likelihood of negative consequences. ....103
**Figure 6-2.** Conductivity depth section through two MAR targets identified by ground TEM and drilling prior to the test flights....105
**Figure 6-3.** Conductivity depth sections from two different AEM systems ....107
**Figure 6-4.** Analysis templates for layer resistivities....109
**Figure 6-5.** The components of the SkyTEM airborne electromagnetic system in flight ....111
**Figure 6-6.** Operating principles of the SkyTEM AEM system ....112
**Figure 6-7.** SkyTEM acquisition system on the ground at Menindee....114
**Figure 6-8.** Map showing main AEM survey blocks (1-4) and flight line orientations. ....118
**Figure 6-9.** SkyTEM field crew with members of the BHMAR team at Menindee ....119
**Figure 6-10.** Vertical section through the flight line for the normalised 3D step response sensitivity functions for the SkyTEM system....122
**Figure 6-11.** Plane section through the normalised 3D step response sensitivity functions for the SkyTEM system. ....123
**Figure 6-12.** Normalised 1D step response sensitivity functions for the SkyTEM system....124
**Figure 6-13.** Plots of the analysed Blanchetown Clay models....128
**Figure 6-14.** Plan view showing layout of ground TEM loops centres around borehole BHMAR19-1....129
**Figure 6-15.** Diagrammatic representation of hover test configurations ....130
**Figure 6-16.** Low moment data, Forward data and SkyTEM data after calibration ....131
**Figure 6-17.** High Moment data, Forward data and SkyTEM data after calibration ....131
**Figure 6-18.** iTEM results of processing raw data with and without channels 4 and 11 ....135
**Figure 6-19.** Inversion of north section of area 2, with and without bias response on the late time channels....136
**Figure 6-20.** Schematic representation of helicopter time domain EM data acquisition and interpretation ....138
**Figure 6-21.** An iTEM flight line conductivity depth section....140
**Figure 6-22.** An iTEM flight line conductivity depth section....141
**Figure 6-23.** An iTEM flight line conductivity depth section....142
**Figure 6-24.** SCI conductivity depth section for the BHMAR88 drill site ....143
**Figure 6-25.** LCI 5-layer model sections ....145
**Figure 6-26.** LCI 19-layer model section....146
**Figure 6-27.** Borehole conductivity log for borehole BHMAR18-1....149
**Figure 6-28.** Comparison of depth-averaged borehole conductivity to 19-layer AEM inversion conductivities over 34 boreholes....150
**Figure 6-29.** Borehole and AEM inversion conductivity data using a laterally constrained inversion....153
**Figure 6-30.** Borehole and AEM inversion conductivity data using a spatially constrained inversion without borehole constraints....154
**Figure 6-31.** Borehole and AEM inversion conductivity data using a spatially constrained inversion with borehole constraints....155
**Figure 6-32.** Comparison of a borehole conductivity log to various AEM inversions ....157
**Figure 6-33.** Comparison of iTEM inversion to conductivity log for BHMAR64-1 ....158
**Figure 6-34.** Comparison of iTEM layer conductivities to the layer-averaged conductivities from borehole log for BHMAR64-1 ....159
**Figure 6-35.** Comparison of the layer-averaged borehole conductivity values to the AEM inversion conductivity values from the borehole and spatially-constrained (SCI-bore) inversion product over 5 bores....160
**Figure 6-36.** LCI conductivity depth section through the Jimargil borefield site ....161
**Figure 6-37.** East-West cross-sections through the Menindee Common borefield site ....163
**Figure 6-38.** Conductivity depth sections for the 23421 flight line for various inversion schemes....166
**Figure 6-39.** Conductivity depth slices for 23421 flight line using the new WANDA inversion procedure....167
**Figure 6-40.** Elevation of top of the upper aquitard in the Jimargil borefield area....168
**Figure 6-41.** Plot of the time/wavenumber domain halfspace response ....172
**Figure 6-42.** Comparison between WANDA step responses and exact step responses....175
**Figure 6-43.** Discretisation of the plane around a line segment of length 30 units....182
**Figure 6-44.** Profile Line 23290 inverted with different constraints ....185
**Figure 6-45.** Maps from the Jimargil area of the likelihood of the resistivity of the 16th model layer in the depth interval 18.54-22 m being below a limiting value ....187
**Figure 6-46.** Plots of the distribution over all flight lines of the average along-line distance between soundings.191
**Figure 6-47.** Comparison of model sections from the Jimargil area from inversion of the data set with 13 m and 26 m along-line sampling distance ....192
**Figure 6-48.** Histogram of the distribution of normalized residuals for the survey area ....193
**Figure 6-49.** Histograms of the distribution of normalized residuals for the 39 gates....195

**Figure 6-50.** Map of topography for the BHMAR study area....199
**Figure 6-51.** Map of fitting error for the total residual for the BHMAR study area. ....210
**Figure 6-52.** Map of fitting error for the data residual for the BHMAR study area. ....201
**Figure 6-53.** Maps of fitting error for the first Low Moment (LM) gate and second LM gate....203
**Figure 6-54.** Maps of fitting error for the 3rd Low Moment (LM) gate and 4th LM gate....205
**Figure 6-55.** Maps of fitting error for the 5th Low Moment (LM) gate and 6th LM gate....207
**Figure 6-56.** Maps of fitting error for the 7th Low Moment (LM) gate and 8th LM gate....209
**Figure 6-57.** Maps of fitting error for the 9th Low Moment (LM) gate and 10th LM gate....211
**Figure 6-58.** Maps of fitting error for the 11th Low Moment (LM) gate and 12th LM gate....213
**Figure 6-59.** Maps of fitting error for the 13th Low Moment (LM) gate and 14th LM gate....215
**Figure 6-60.** Maps of fitting error for the 15th Low Moment (LM) gate and 16th LM gate....217
**Figure 6-61.** Maps of fitting error for the 17th Low Moment (LM) gate and 18th LM gate....219
**Figure 6-62.** Maps of fitting error for the first High Moment (HM) gate 19 and second HM gate 20....221
**Figure 6-63.** Maps of fitting error for the 3rd HM gate 21 and 4th HM gate 22....223
**Figure 6-64.** Maps of fitting error for the 5th HM gate 23 and 6th HM gate 24....225
**Figure 6-65.** Maps of fitting error for the 7th HM gate 25 and 8th HM gate 26....227
**Figure 6-66.** Maps of fitting error for the 9th HM gate 27 and 10th HM gate 28....229
**Figure 6-67.** Maps of fitting error for the 11th HM gate 29 and 12th HM gate 30....231
**Figure 6-68.** Maps of fitting error for the 13th HM gate 31 and 14th HM gate 32....233
**Figure 6-69.** Maps of fitting error for the 15th HM gate 33 and 16th HM gate 34....235
**Figure 6-70.** Maps of fitting error for the 17th HM gate 35 and 18th HM gate 36....237
**Figure 6-71.** Maps of fitting error for the 19th HM gate 37 and 20th HM gate 38....239
**Figure 6-72.** Map of fitting error for the 21st HM gate 39 for the BHMAR. ....241
**Figure 6-73.** 2D sensitivity function of the borehole conductivity tool....243
**Figure 6-74.** ModMod comparison for BHMAR33-7 ....247
**Figure 6-75.** DatDat comparison for BHMAR33-7....248
**Figure 6-76.** ModMod comparison plot for BHMAR03B-1....249
**Figure 6-77.** DatDat comparison plot for BHMAR03B-1 ....250
**Figure 6-78.** ModMod residuals as a function of the distance between the borehole and the closest AEM sounding ....251
**Figure 6-79.** Histogram showing the distribution of ModMod residuals....252
**Figure 6-80.** Histogram showing the distribution of DatDat residuals ....252
**Figure 6-81.** Histogram showing the distribution of the AEM data residuals ....253
**Figure 6-82.** Cross plot with error bars of AEM model conductivity with borehole model conductivity. ....256
**Figure 6-83.** Cross plot of AEM model conductivity with borehole model conductivity....257
**Figure 6-84.** Cross plot with error bars of AEM model conductivity with borehole model conductivity for model layers with relative uncertainty of conductivity less than 0.2....260
**Figure 6-85.** Cross plot of AEM model conductivity with borehole model conductivity for model layers with relative uncertainty of conductivity less than 0.2 ....261
**Figure 6-86.** Cross plot with error bars of AEM conductivity with borehole conductivity. ....262
**Figure 6-87.** Cross plot of AEM conductivity with borehole conductivity ....263
**Figure 6-88.** ModMod comparison plot for GW36812 borehole....265
**Figure 6-89.** ModMod comparison plot for GW36812 borehole....266
**Figure 6-90.** ModMod comparison plot for GW36891 borehole....267
**Figure 6-91.** DatDat comparison plot for the GW36891 borehole ....268
**Figure 6-92.** Cross plot with error bars of AEM model conductivity with borehole model conductivity. ....270
**Figure 6-93.** Cross plot of AEM model conductivity with borehole model conductivity....271
**Figure 6-94.** Cross plot with error bars of AEM conductivity with borehole conductivity. ....272
**Figure 6-95.** Cross plot of AEM conductivity with borehole conductivity ....273
**Figure 6-96.** Summary of the RJ-McMC inversion of the AEM data set nearest to borehole BHMAR08-1. ....276
**Figure 6-97.** Delaunay triangulation....279
**Figure 6-98.** Overlapping areas between the Voronoi cell of the interpolation point and the neighbouring Voronoi cells....280
**Figure 6-99.** Results from 200 m and 600 m line spacing using NN interpolation in layer 11 (7.22-9.24 m). ....281
**Figure 6-100.** Results from 1 km and 2 km line spacing using NN interpolation in layer 11 (7.22-9.24 m). ....282
**Figure 6-101.** Results from 5 km and10 km line spacing using NN interpolation in layer 11 (7.22-9.24 m) ....283
**Figure 6-102.** Results from 200 m and 600 m line spacing using NN interpolation in layer 22 (51.52-61.04m)..284
**Figure 6-103.** Results from 1 km and 2km line spacing using NN interpolation in layer 22 (51.52-61.04 m)....285
**Figure 6-104.** Results from 5 km and10 km line spacing using NN interpolation in layer 22 (51.52-61.04 m)....286
**Figure 6-105.** Results from 200 m and 600 m line spacing using LPC interpolation in layer 11 (7.22-9.24 m)...287

**Figure 6-106.** Results from 1 km and 2 km line spacing using LPC interpolation in layer 11 (7.22-9.24 m). .....288
**Figure 6-107.** Results from 5 km and 10 km line spacing using LPC interpolation in layer 11 (7.22-9.24 m). ....289
**Figure 6-108.** Results from 200 m and 600 m line spacing using LPC interpolation in layer 22 (51.52-61.04m).290
**Figure 6-109.** Results from 1 km and 2 km line spacing using LPC interpolation in layer 22 (51.52-61.04 m). ..291
**Figure 6-110.** Results from 5 km and 10 km line spacing using LPC interpolation in layer 22 (51.52-61.04m). .292
**Figure 7-1.** Photograph of borehole logging set-up in the field. .....299
**Figure 7-2.** Calibration ring position on the induction conductivity tool during a calibration experiment .....300
**Figure 7-3.** Secondary voltage versus calibration ring jig value for every calibration experiment .....301
**Figure 7-4.** Results of a functional fit to the calibration data using a form of $\sigma = ax^b+c$ .....301
**Figure 7-5.** Speed of relaxation which depends on how often protons collide with grains, governed by the surface to volume (S/V) ratio. .....305
**Figure 7-6.** CPMG pulse sequence used to generate a spin-echo train. .....306
**Figure 7-7.** Diagram of the impact of 100% water saturated pores on T2. .....306
**Figure 7-8.** Vista Clara Javelin NMR logging system. .....307
**Figure 7-9.** Field NMR water tank experiment .....308
**Figure 7-10.** NMR measurement timing diagram .....310
**Figure 7-11.** CPMG decay curves versus depth for an entire log, shown as a colour map. .....312
**Figure 7-12.** Multi-exponential fit window of the time series CPMG decay curve and multi-exponential inversion result .....312
**Figure 7-13.** CPMG decay curve data with the multi-exponential fit and resulting T2 distribution for a fine grained silt layer and coarse grained sand layer. .....315
**Figure 7-14.** T2 distributions in BHMAR58-1 with the regulation factor varied. .....316
**Figure 7-15.** BHMAR58-1 logging with the regulation factor varied. .....318
**Figure 7-16.** The T2 distribution composed of free and bound-water in a saturated aquifer .....319
**Figure 7-17.** Location of the water in the pores influencing the T2 distribution .....320
**Figure 7-18.** NMR free-water and bound-water for two depth intervals in BHMAR58-1. .....321
**Figure 7-19.** BHMAR99-1 2011 and 2013 mobile water plots with depth .....322
**Figure 7-20.** Comparison between corrected 2012 total water, 2013 total water and uncorrected 2011 total water for BHMAR80A-2 .....324
**Figure 7-21.** Comparison between corrected 2011 mobile water, 2013 mobile water and uncorrected 2011 mobile water for BHMAR99-1 .....325
**Figure 7-22.** Comparison between corrected 2011 total water, 2013 total water and uncorrected 2011 total water for BHMAR77-2 .....326
**Figure 7-23.** Calculated transmissivity based on a single C = 46,000 versus transmissivity from the slug tests. .330
**Figure 7-24.** Calculated transmissivity based on the initial hydraulic classes C values from the permeameter tests versus transmissivity from the slug tests .....331
**Figure 7-25.** Calculated transmissivity based on the final hydraulic classes NMR derived Cave values, versus transmissivity from the slug tests. .....332
**Figure 7-26.** Plot of the median versus the mode for grain size analyses from the BHMAR study .....336
**Figure 7-27.** Downhole plots of bound-water, free-water and the $K_{SDR}$ for BHMAR58-1. .....340
**Figure 8-1.** Google Earth image of BHMAR33 ground resistivity survey lines. .....343
**Figure 8-2.** Oblique 3D view showing the baseline data from the resistivity survey at BHMAR33 site .....343
**Figure 8-3.** Google Earth image of the Menindee Common resistivity survey .....344
**Figure 8-4.** IP and resistivity inversions compared with AEM conductivity data for survey line 1700N .....346
**Figure 8-5.** Overview map of the collected IP and resistivity data at Jimargil. .....347
**Figure 8-6.** Basic principles of time domain DC/IP acquisition .....348
**Figure 8-7.** Resistivity data for Line 6 showing removal of bad data points .....350
**Figure 8-8.** Example vertical electrical sounding curve from Line 6 .....351
**Figure 8-9.** Examples of IP decay curves from Line 6. .....352
**Figure 8-10.** Laterally constrained inversion (LCI) methodology .....353
**Figure 8-11.** Sensitivities calculated for a re-discretized version of the model .....355
**Figure 8-12.** Chargeability section for Line 6 showing DOI .....357
**Figure 8-13.** Chargeability section for Line 6 showing DOI and uncertainty analysis .....357
**Figure 8-14.** Example DC sounding curve and IP decay curves .....359
**Figure 8-15.** Sections for Line 8 .....361
**Figure 8-16.** Map showing AEM profiles and DC/IP lines .....363
**Figure 8-17.** Comparison between AEM inversions and DC/IP line 3 .....365
**Figure 8-18.** Comparison between inverted conductivity (initial Christensen) AEM, SCI AEM, DC and the induction log BHMAR33-8. .....366
**Figure 8-19.** Comparison between the normalized integral chargeability and the gamma log BHMAR33-8. .....367

**Figure 8-20.** IP sections for Lines 1 and 2 ..... 370
**Figure 8-21.** IP sections for Lines 3 and 4 ..... 371
**Figure 9-1.** Extent of in-river survey ..... 374
**Figure 9-2.** Trees overhanging the river the cause of GNSS satellite reception difficulties. ..... 376
**Figure 9-3.** The survey vessel underway ..... 377
**Figure 9-4.** Survey vessel setup showing instrument locations ..... 378
**Figure 9-5.** Survey vessel setup showing antenna locations ..... 378
**Figure 9-6.** Survey system electronics setup on the vessel. ..... 379
**Figure 9-7.** GPS base station 300 m south of Bootingee Homestead. ..... 380
**Figure 9-8.** Optical dumpy levelling of the river waterline to the GPS base station ..... 382
**Figure 9-9.** In-river survey single beam echo sounder data draped over LiDAR dataset. ..... 383
**Figure 9-10.** Photograph of the Darling River bed in drought. ..... 384
**Figure 9-11.** Example of transverse sand waves in bed of Darling River. ..... 385
**Figure 9-12.** Multi-beam backscatter image of transverse sand waves in Darling River bed. ..... 386
**Figure 9-13.** Sand waves exposed by lower water levels along Darling River bed. ..... 386
**Figure 9-14.** Coarse lag of calcrete fragments and woody debris at sediment site 7. ..... 387
**Figure 9-15.** Multi-beam image of large river bed depression on sharp river bend ..... 387
**Figure 9-16.** Multi-beam image of river bed depression on Jimargil Station ..... 388
**Figure 9-17.** Multi-beam image of large woody debris in bed of Darling River ..... 389
**Figure 10-1.** Rotary rig engaged in well development. ..... 391
**Figure 10-2.** Sonic drilling rig operating on the Darling Floodplain ..... 392
**Figure 10-3.** Sonic drilling rig operating 24 hrs per day with 2 crews ..... 392
**Figure 10-4.** Sonic drilling rig, with vibration head on the mast and drill rod attached. ..... 393
**Figure 10-5.** Ross S. Brodie and Elder from the Indigenous community examine drillcore. ..... 393
**Figure 10-6.** Visual comparisons of materials and geological detail obtained using the sonic drilling technique and rotary mud drilling ..... 398
**Figure 10-7.** Comparisons of geological detail obtained from rotary mud drilling versus the sonic drilling technique at adjacent bores at site BHMAR75 ..... 399
**Figure 11-1.** Photograph of sonic core prepared for sampling ..... 402
**Figure 11-2.** Sonic core sampling approach ..... 402
**Figure 11-3.** Contaminated zone in BHMAR19 sonic core ..... 403
**Figure 11-4.** Contaminated zone in BHMAR08 sonic core ..... 403
**Figure 11-5.** Sample point at least 60 cm below top of sonic core run in BHMAR58 ..... 404
**Figure 11-6.** Six borehole plots representing the only sonic cores where pore fluid contamination may be observed. ..... 405
**Figure 11-7.** Comparison between original laser textural analysis results using the Laboratory Dispersion Protocol and the Magee Dispersion Protocol ..... 413
**Figure 11-8.** Comparison between original laser textural analysis results using the Laboratory Dispersion Protocol and the Magee Dispersion Protocol ..... 414
**Figure 11-9.** Workflow diagram for investigating the BHMAR sample laser grainsize analysis ..... 415
**Figure 11-10.** Laser grainsize analysis for BHMAR75-8, 12.4-12.5 m ..... 416
**Figure 11-11.** Laser grainsize analysis for BHMAR75-8, 15.5-15.6 m. ..... 417
**Figure 11-12.** Resin setting of core. ..... 431
**Figure 11-13.** Bench-top falling head permeameter ..... 432
**Figure 11-14.** Photographs of the centrifuge permeameter ..... 433
**Figure 11-15.** Water retention graph for fine textured samples. ..... 436
**Figure 11-16.** Water retention graph for medium- to coarse textured sand samples.. ..... 436
**Figure 12-1.** Wheel loader excavating trench DR03 on the Darling River scroll plain ..... 440
**Figure 12-2.** Hand augering on dunes at the eastern margin of the Three Mile Creek floodplain. ..... 440
**Figure 12-3.** Hand-auger OSL sample tubes and end cups. ..... 443
**Figure 12-4.** Sonic drilling Lexan-encapsulated tube OSL sample and sub-sampling protocol ..... 444
**Figure 12-5.** Blackened wood sample in fluvial sand at 8.7 m depth in BHMAR79A-2 ..... 448
**Figure 13-1.** Slug testing of project bores. ..... 453
**Figure 13-2.** Typical data logger response during a slug test ..... 454
**Figure 13-3.** Oscillatory water level response during a slug test ..... 454
**Figure 13-4.** Map showing the infrastructure for the BHMAR33-5 aquifer test. ..... 458
**Figure 13-5.** Map showing the infrastructure for the BHMAR80A-5 aquifer test. ..... 459
**Figure 13-6.** Construction details of the BHMAR33-5 aquifer test bore. ..... 461
**Figure 13-7.** Construction details of the BHMAR80A-5 aquifer test bore. ..... 463
**Figure 13-8.** Pumping equipment used for the BHMAR33-5 aquifer test. ..... 465

**Figure 13-9.** Staff and contractors at the BHMAR33-5 headworks during aquifer testing .....466
**Figure 13-10.** Groundwater discharge into the river via the diffuser array during aquifer test .....466
**Figure 13-11.** Cross section design view of floating diffuser platform used to discharge test groundwater. .....467
**Figure 13-12.** Overhead design view of floating diffuser platform used to discharge test groundwater. .....468
**Figure 14-1.** Radon sampling procedure.....474
**Figure 14-2.** Groundwater sampling in progress .....477
**Figure 14-3.** General workflow for the collection of groundwater samples .....478
**Figure 14-4.** Components of the cumulative rainfall collector .....480
**Figure 14-5.** Graph showing original and duplicate results for dissolved metals in all groundwater samples. .....482
**Figure 14-6.** Graph showing original and duplicate results for dissolved metals in pore fluid samples.....483
**Figure 14-7.** Charge balance for major ion analyses of surface water, rainfall and groundwater samples.....484
**Figure 14-8.** Charge balance for BHMAR major ion analyses of pore fluid samples. .....484
**Figure 14-9.** Interface of the FuzME software used for fuzzy k-means cluster analysis. .....486
**Figure 14-10.** Plot of the cluster validation index FPI with the number of resulting data clusters (or classes). .....487
**Figure 15-1.** Location of groundwater level monitoring network.....495
**Figure 15-2.** Input parameters used for FEFLOW modelling of ASR scenarios at sites BHMAR 33 and 80A. ....500
**Figure 16-1.** Section showing geometry and parameters for calculating the groundwater mound below a long infiltration area (strip) of width W.....506
**Figure 16-2.** Number and proportion of stream flow events exceeding stream flow thresholds for Darling River at Weir 32 .....508
**Figure 17-1.** LiDAR DEM surface showing a 20 m difference between the upper and lower reaches of the Darling River within the study area .....513
**Figure 17-2.** Elevation drop grid highlighting flat areas or areas with minimal continuing change along a flow path. .....514
**Figure 17-3.** Floodplain trend surface overlain by original DEM and flat areas or areas with minimal continuing change identified in the drop grid. .....514
**Figure 17-4.** Comparison between the original DEM and the levelled DEM. .....515
**Figure 17-5.** Location and extent of Landsat scenes 95/82 and 95/83 .....516
**Figure 17-6.** Modelled flood extent and Landsat image showing area flooded on May 8, 1990. .....517
**Figure 17-7.** Modelled flood extent and Landsat image showing area flooded on September 29, 1990. .....518
**Figure 17-8.** Modelled flood extent and Landsat image showing area flooded on December 2, 1990. .....519
**Figure 17-9.** Modelled flood extent and Landsat image showing area flooded on the March 16, 2011. .....520
**Figure 17-10.** Modelled flood extent at a river level of 5.18 m recorded on October 25, 2010 compared to on-ground photographs of inundation. .....521
**Figure 17-11.** Modelled flood extent at a river level of 5.6 m recorded on October 28, 2010 compared to on-ground photographs of inundation. .....522
**Figure 17-12.** Validation of modelled flood extent on the March 15, 2011 .....523
**Figure 17-13.** Quantitative comparison between Landsat and LiDAR-derived flood extents on April 8, 1990. ....525
**Figure 17-14.** Quantitative comparison between Landsat and LiDAR-derived flood extents on June 25, 1990. ..527
**Figure 17-15.** Quantitative comparison between Landsat and LiDAR-derived flood extents on September 29, 1990 .....529
**Figure 17-16.** Comparison between the LiDAR-derived and Landsat-derived flood extent for the 1990 event. ..532
**Figure 17-17.** Flow chart describing the workflow for analysing the remote sensing data .....534
**Figure 17-18.** Location of vegetation field sites within the BHMAR study area .....535
**Figure 17-19.** FPC and CEM measurements .....537
**Figure 17-20.** Geomorphic-based regionalisation.....539
**Figure 17-21.** Unique stratum structural classes identified in the central study area.....541
**Figure 17-22.** Unique sub-stratum structural classes for Lake Cawndilla .....542
**Figure 17-23.** Location of vegetation field sites and comparison with LiDAR vegetation structural mapping ....544
**Figure 17-24.** NDVI time series for typical grassland and forest pixel .....547
**Figure 17-25.** Annual NDVI statistics and individual 'comprehensive' average NDVI values for each scene ....548
**Figure 17-26.** Distribution of vegetation structural/land cover classes (Hierarchy Level 2). .....549
**Figure 17-27.** Flow chart representing the segmentation process.....550
**Figure 17-28.** Final Landsat derived vegetation classification and LiDAR derived vegetation structure mapping. .....552
**Figure 17-29.** Comparison between Landsat and LiDAR-derived vegetation mapping products .....554
**Figure 17-30.** Time series profile of floodplain vegetation .....556
**Figure 17-31.** Condition of vegetation at the conclusion of the drought (2009).....557
**Figure 17-32.** Comparison of vegetation condition at the beginning and end of drought .....558
**Figure 17-33.** Indication of the variability in vegetation condition during drought.....559

**Figure 17-34.** Inferred volume and reliability of source water ....561
**Figure 17-35.** Flood frequency for 2010 as generated from the Landsat flood inundation surfaces. ....563
**Figure 17-36.** Flood frequency for 2010 as generated from the LiDAR DEM potential flood inundation surfaces. ....564
**Figure 17-37.** Series of conductivity depth sections for the 23421 flight line ....566
**Figure 17-38.** Two conductivity depth sections produced using the new Wave Number Domain Approximate (WANDA) inversion procedure ....567
**Figure 17-39.** Conductivity depth section produced using the new lateral parameter correlation procedures. ....568
**Figure 17-40.** Conductivity depth section for Line 23261 ....568
**Figure 17-41.** Conductivity depth section showing an interpretation of the hydrostratigraphy and faulting ....569
**Figure 17-42.** Top picks for the Blanchetown Clay and fault picks in a conductivity depth section ....569
**Figure 17-43.** Density of data points acquired from mapping the top of the Blanchetown Clay ....571
**Figure 17-44.** Elevation of top of the upper confining aquitard in metres AHD ....573
**Figure 17-45.** Data point density acquired from mapping the top of the Blanchetown Clay ....574
**Figure 17-46.** Map of faults offsetting the upper confining aquitard at the Jimargil site. ....575
**Figure 17-47.** Tiled conductivity depth sections with 200 m spacing between flight lines for an area near Menindee ....577
**Figure 17-48.** LiDAR image showing the Talyawalka Scarp ....579
**Figure 17-49.** LiDAR image of the Darling River near Bootingee ....580
**Figure 17-50.** View of Lakes Menindee and Cawndilla and part of GWR1 ....581
**Figure 17-51.** Map of the top Blanchetown Clay surface showing contoured elevations and interpreted faults ....582
**Figure 17-52.** LiDAR image with mapped lineaments and TMI first vertical derivative image for a reach of the lower Yampoola Creek floodplain ....583
**Figure 17-53.** The Jimargil-East Bootingee borefield showing a comparison between lineaments interpreted from the LiDAR and faults interpreted from AEM flight line section analysis of the upper-confining aquifer (UCA). 584
**Figure 17-54.** Landform mapping with combined regional and detailed products. ....586
**Figure 17-55.** Surface materials map including field sites used for validation. ....589
**Figure 17-56.** Map of coordinates of picks for the top of the Blanchetown Clay conductivity anomaly ....592
**Figure 17-57.** AEM conductivity section along part of flight line 22520 showing top and bottom picks for Blanchetown Clay conductivity anomaly ....593
**Figure 17-58.** Map of coordinates picks for the base of the Blanchetown Clay conductivity anomaly ....594
**Figure 17-59.** Map of flight lines over SPOT image and AEM conductivity section along part of flight line 223100 beneath Menindee Lake. ....595
**Figure 17-60.** AEM conductivity section along part of flight line 22110 across Lake Pamamaroo ....597
**Figure 17-61.** AEM conductivity section along part of flight line 24550 ....598
**Figure 17-62.** AEM conductivity section along part of flight line 30120 ....599
**Figure 17-63.** Schematic diagram showing the mapping of stratigraphic units ....601
**Figure 17-64.** Traverse of local and regional AEM conductivity and stratigraphic interpretation cross section ....602
**Figure 17-65.** Stratigraphic units present at 61.0m to 72.3m depths in the southern part of the study area. ....603
**Figure 17-66.** Extent of AEM survey, geomorphic mapping and LiDAR DEM. ....607
**Figure 17-67.** Average apparent conductivity values for each texture class in each depth slice. ....608
**Figure 17-68.** Averaged AEM apparent conductivity for each texture class at each depth slice interval ....609
**Figure 17-69.** AEM apparent conductivity depth slice, 2.8 m to 3.5 m. ....610
**Figure 17-70.** AEM depth slice grid 2.8 m – 3.5 m overlain with geomorphic units. ....611
**Figure 17-71.** Elevation relative to the scroll plains based on residual analysis of the LiDAR DEM data. ....612
**Figure 17-72.** Averaged AEM conductivity for each hydraulic texture class at each depth slice interval ....617
**Figure 17-73.** AEM depth slice 43.5 m to 51.5 m with threshold classes ....624
**Figure 17-74.** AEM depth slice 43.5 m to 51.5 m with interpreted texture classes based on AEM conductivity threshold ranges. ....625
**Figure 17-75.** Textural composition of the Coonambidgal Formation, Menindee Formation and Willotia beds ....627
**Figure 17-76.** Depth to the top of the shallow unconfined aquifer ....629
**Figure 17-77.** Depth to the top of the upper confining aquitard ....630
**Figure 17-78.** Depth to the top of the semi-confined aquifer ....631
**Figure 17-79.** Depth to the top of the lower confining aquitard ....632
**Figure 17-80.** Thickness of the shallow unconfined aquifer ....633
**Figure 17-81.** Thickness of the semi-confined aquifer ....634
**Figure 17-82.** Near-surface mud drape thickness ....635
**Figure 17-83.** Percent mud thickness between ground surface and base of Talyawalka Creek (5 m depth) ....636
**Figure 17-84.** Percent mud thickness between ground surface and base of the Darling River (9 m depth) ....637
**Figure 17-85.** Borehole NMR data for 43.5-51.5m AEM depth slice ....641

**Figure 17-86.** Calculated transmissivity (TSDR) based on the final hydraulic classes NMR derived Cave values, versus transmissivity (TSlug) from the slug tests. ....642
**Figure 17-87.** Box and whisker plots of hydraulic conductivity for five hydraulic textural classes....642
**Figure 17-88.** Lower estimate of transmissivity ($m^2$/d) for 51.5m to 61.0m depth slice. ....645
**Figure 17-89.** Upper estimate of transmissivity ($m^2$/d) for 51.5m to 61.0m depth slice....646
**Figure 17-90.** Range between lower and upper estimate of transmissivity ($m^2$/d) for 51.5m to 61.0m depth slice. ....647
**Figure 17-91.** Lower estimate of transmissivity ($m^2$/d) for the shallow unconfined aquifer ....648
**Figure 17-92.** Upper estimate of transmissivity ($m^2$/d) for the shallow unconfined aquifer ....649
**Figure 17-93.** Lower estimate of transmissivity ($m^2$/d) for the semi-confined aquifer....650
**Figure 17-94.** The upper estimate of transmissivity ($m^2$/d) for the semi-confined aquifer....651
**Figure 17-95.** Box plot of the gravimetric water content data by hydraulic class ....654
**Figure 17-96.** Downhole plot of gravimetric data and NMR total water for BHMAR88-3 ....655
**Figure 17-97.** Downhole plot of gravimetric data, 2011 NMR total water and 2011 mobile water coded by texture class for BHMAR83-2. ....656
**Figure 17-98.** Box plots of the porosity values from the matric potential of 10, 70, 200 kPa of suction and the calculated total porosity for texture classes 5, 4, and 3. ....658
**Figure 17-99.** Box plots of the porosity values from the matric potential of 10, 70, 200 kPa of suction and the calculated total porosity for texture classes 2 and 1 ....659
**Figure 17-100.** NMR total water and total porosity for texture class 5: Coarse sand to gravel ....660
**Figure 17-101.** NMR total water and total porosity for texture class 4: Medium sand....661
**Figure 17-102.** NMR total water and total porosity for texture class 3: Fine sand ....661
**Figure 17-103.** NMR total water and total porosity for texture class 2: Muddy sand....662
**Figure 17-104.** NMR total water and total porosity for texture class 1: Mud....662
**Figure 17-105.** NMR mobile water and total porosity for texture class 5: Coarse sand to gravel ....664
**Figure 17-106.** NMR mobile water and total porosity for texture class 4: Medium sand....664
**Figure 17-107.** NMR mobile water and total porosity for texture class 3: Fine sand ....665
**Figure 17-108.** NMR mobile water and total porosity for texture class 2: Muddy sand....665
**Figure 17-109.** NMR mobile water and total porosity for texture class 1: Mud. ....666
**Figure 17-110.** Box plots of the NMR water contents for two different inter-echo spacing versus the laboratory porosity measurements, for texture class 5: Coarse sand to gravel for BHMAR33-9. ....667
**Figure 17-111.** Box plots of the NMR water contents for two different inter-echo spacing versus the laboratory porosity measurements, for texture class 4: Medium sand for BHMAR33-9....667
**Figure 17-112.** Box plots of the NMR water contents for two different inter-echo spacing versus the laboratory porosity measurements, for texture class 3: Fine sand for BHMAR33-9. ....668
**Figure 17-113.** Box plots of the NMR water contents for two different inter-echo spacing versus the laboratory porosity measurements, for hydraulic class 5: Coarse sand to gravel for BHMAR75-8. ....668
**Figure 17-114.** Box plots of the NMR water contents for two different inter-echo spacing versus the laboratory porosity measurements, for texture class 4: Medium sand for BHMAR75-8....669
**Figure 17-115.** Box plots of the NMR water contents for the two different inter-echo spacing versus the laboratory porosity measurements, for texture class 3: Fine sand for BHMAR75-8....669
**Figure 17-116.** Box plots of NMR mobile water distribution for texture class 5 across various data groups. ....672
**Figure 17-117.** Box plots of NMR mobile water distribution for texture class 4 across various data groups. ....673
**Figure 17-118.** Box plots of NMR mobile water distribution for texture class 3 across various data groups. ....674
**Figure 17-119.** Box plots of NMR mobile water distribution for texture class 2 across various data groups ....675
**Figure 17-120.** Box plots of NMR mobile water distribution for texture class 1 across various data groups. ....676
**Figure 17-121.** Relationship between power exponent and effective dispersion coefficient....678
**Figure 17-122.** Box and whisker plot of salinity of Blanchetown Clay pore fluids ....678
**Figure 17-123.** Diffusion distance over different time frames for the Blanchetown Clay....679
**Figure 17-124.** Plots of diffusion distance against diffusion time for the upper confining aquitard ....680
**Figure 17-125.** Time required for complete diffusion for the upper confining aquitard using a low estimate. ....681
**Figure 17-126.** Time required for complete diffusion for the upper confining aquitard using a high estimate ....682
**Figure 17-127.** Workflow for estimating target/borefield groundwater storage volumes for salinity thresholds..684
**Figure 17-128.** Cross plot of the AEM model conductivity as a function of the borehole model (BH) conductivity ....685
**Figure 17-129.** Reversible Jump Markov Chain Monte Carlo (RJ-McMC) inversion of one of 9 representative sections in the AEM data ....686
**Figure 17-130.** Example of interpolating pore fluid salinity and deriving averages for AEM depth slices....687
**Figure 17-131.** Relationship between average pore fluid salinity and corresponding AEM depth slice conductivity value ....687

**Figure 17-132.** Relationship between average pore fluid salinity and corresponding AEM depth slice conductivity value for Calivil-dominant AEM depth slices (22-61 m) ..... 689
**Figure 17-133.** Predicted groundwater salinity mapping for the AEM depth slice 43.5-51.5 m based on AEM conductivity thresholds. ..... 691
**Figure 17-134.** Map showing the distribution of groundwater resource (GWR) targets in Pliocene (Calivil and Loxton-Parilla Sand Formation) aquifers. ..... 696
**Figure 17-135.** Comparison of target bulk volumes calculated from different AEM inversions ..... 699
**Figure 17-136.** Comparison of target bulk volumes calculated from AEM inversions using different constraints ..... 700
**Figure 17-137.** Comparison of target bulk volumes calculated using different groundwater salinity thresholds. . 700
**Figure 17-138.** Comparison of target bulk volumes calculated using different groundwater salinity thresholds. . 701
**Figure 17-139.** Comparison of target bulk volumes calculated with (and without) applying additional limits based on texture and saturation classes. ..... 701
**Figure 17-140.** Comparison of target bulk volumes calculated using different ranges in the AEM depth slices . . 702
**Figure 17-141.** Comparison of borefield bulk volumes calculated from different AEM inversions ..... 703
**Figure 17-142.** Comparison of borefield bulk volumes calculated from AEM inversions using different constraints. ..... 703
**Figure 17-143.** Comparison of borefield bulk volumes calculated using different groundwater salinity thresholds. ..... 704
**Figure 17-144.** Comparison of borefield bulk volumes calculated using different groundwater salinity thresholds ..... 704
**Figure 17-145.** Comparison of borefield bulk volumes calculated with (and without) applying additional limits based on texture and saturation classes ..... 705
**Figure 17-146.** Comparison of borefield bulk volumes calculated using different ranges in the AEM depth slices ..... 705
**Figure 17-147.** Salt store and electrical conductivity of mud-rich and sand-rich sediments ..... 708
**Figure 17-148.** Salt store and electrical conductivity of sediment grouped by NMR total water contents for depth slices 1.6 m to 5.3 m. ..... 709
**Figure 17-149.** Salt store and electrical conductivity of sediment grouped by NMR total water content for depth slices 5.3 m to 13.1 m. ..... 710
**Figure 17-150.** Salt store and electrical conductivity of sediment grouped by NMR total water contents for depth slices 13.1 m to 22.0 m. ..... 711
**Figure 17-151.** Predicted groundwater salinity map for the BHMAR project area ..... 713
**Figure 17-152.** Thickness of the upper confining aquitard including areas where it is absent or non-interpreted 714
**Figure 17-153.** Thickness of the upper aquitard (clay-drape) ..... 715
**Figure 17-154.** Thickness of the shallow unconfined aquifer ..... 716
**Figure 17-155.** Extent of flooding during the 1990 flood derived from Landsat imagery ..... 717
**Figure 17-156.** Recharge potential and pathway classification for the 14 groundwater resource targets. ..... 719
**Figure 17-157.** Borehole graphical logs including well construction details, stratigraphy, lithology and hydraulic conductivity ..... 723
**Figure 17-158.** Borehole graphical logs including hydrochemical major ion data obtained from pore fluid analysis. ..... 725
**Figure 17-159.** Borehole graphical logs including hydrochemical trace ion data obtained from pore fluid analysis. ..... 727
**Figure 17-160.** Borehole graphical logs including solid major element geochemistry ..... 729
**Figure 17-161.** Borehole graphical logs including solid trace element geochemistry ..... 731
**Figure 17-162.** Perspective view of BHMAR Project AEM 3D conductivity model ..... 733

# List of Tables

**Table 2-1.** Definitions of scientific orientation of research teams ....21
**Table 3-1.** The 4-stage approach for assessing risks in MAR projects ....32
**Table 3-2.** Details of the activities proposed in the 4-stage approach for assessing risks in MAR projects ....33
**Table 3-3.** Entry-level assessment ....36
**Table 3-4.** ADWG2011 guideline values for physical and chemical parameters. ....38
**Table 4-1.** Completion status and drilling type of boreholes in or adjacent to the BHMAR priority project areas .47
**Table 5-1.** LiDAR survey data acquisition parameters ....71
**Table 5-2.** Control point datasets used to quantify vertical accuracy. ....85
**Table 5-3.** Vertical accuracy for input datasets ....85
**Table 6-1.** Parameters of the test models ....108
**Table 6-2.** Gate delay times for High Moment (HM) and Low Moment (LM) modes ....115
**Table 6-3.** Sk1 and Sk2 roster and coverage ....117
**Table 6-4.** Flight line naming convention. ....117
**Table 6-5.** Summary of SkyTEM survey logistics ....118
**Table 6-6.** Depth extent and horizontal extent of the 1D step response sensitivity functions for the SkyTEM system ....124
**Table 6-7.** Distribution of relative uncertainty for the Blanchetown Clay models. ....126
**Table 6-8.** Borehole models and analysis ....127
**Table 6-9.** System transmitter specifications ....133
**Table 6-10.** System receiver specifications ....133
**Table 6-11.** Thickness and depths of the layers used in the 19-layer inversion models. ....147
**Table 6-12.** ModMod and DatDat residuals for all 92 boreholes with the data residual of the AEM inversion ....253
**Table 6-13.** ModMod and DatDat residuals for 11 pre-existing boreholes with the data residual of the AEM inversion ....268
**Table 6-14.** Vertex coordinates used in the re-gridding experiment. ....277
**Table 6-15.** Parameters used in the re-gridding experiment. ....278
**Table 7-1.** Physical and operational characteristics of A034 induction conductivity tool ....295
**Table 7-2.** The physical and operational characteristics of A631 gamma tool ....302
**Table 7-3.** NMR borehole data acquired in 2011 using the Javelin logging system ....309
**Table 7-4.** Operator settings of the BHMAR project NMR logging program. ....310
**Table 7-5.** NMR data acquired in April 2013 using the Javelin logging system for the BHMAR project ....311
**Table 7-6.** User input parameters for the Interpret Javelin Log version 1.1.0a software. ....313
**Table 7-7.** Scaling factor applied to 2011 NMR data to make it comparable to 2013 data. ....323
**Table 7-8.** Permeameter results from preserved sonic core samples. ....327
**Table 7-9.** Initial Kave and Cave values for the hydraulic texture classes ....328
**Table 7-10.** BHMAR boreholes either coincident or adjacent to NMR data location ....328
**Table 7-11.** Final Kave and Cave values for the hydraulic texture classes ....331
**Table 7-12.** Magnetic susceptibility summary for BHMAR80A-2 and BHMAR99-1 ....333
**Table 7-13.** Core intervals selected for Hylogging. ....334
**Table 7-14.** Summary PIMA results ....335
**Table 8-1.** Inversion settings for LCI smooth setup. ....358
**Table 8-2.** Inversion settings for smooth SCI setup ....364
**Table 10-1.** Facies differentiation from different drilling technologies ....396
**Table 10-2.** Comparison in data quality between specific sonic and rotary mud holes ....400
**Table 11-1.** Volume of pore-water required as a function of electrical conductivity (EC). ....406
**Table 11-2.** Procedures and analyses for the saturation extract, slurry, hydraulic press and reference methods. ..409
**Table 11-3.** Procedures for comparing the sieve and laser diffraction techniques. ....410
**Table 11-4.** Mineralogy percentages for BHMAR75-8 samples determined by quantitative XRD analyses ....416
**Table 11-5.** XRF major oxides ....422
**Table 11-6.** Titrimetry. ....422
**Table 11-7.** XRF trace detection limits (ppm). ....422
**Table 11-8.** Detection limits of ICP-MS trace element analyses. ....424
**Table 11-9.** Core intervals selected for Hylogging. ....426
**Table 11-10.** Clay mineralogy in bores predicted from Kernel Function. ....426
**Table 11-11.** Samples selected for PIMA analysis. ....428
**Table 11-12.** Samples of lexan-encapsulated sonic core for measurement of total and effective porosity ....435
**Table 11-13.** Total porosity of lexan core samples using three different methods. ....437
**Table 11-14.** Partial porosity at specific matric potentials for lexan core samples ....438

**Table 12-1.** Details of nineteen OSL-dated samples....446
**Table 13-1.** Summary of air-lift development of project monitoring bores. ....460
**Table 13-2.** Summary of slug test interpretations for BHMAR project bores. ....455
**Table 13-3.** Construction summary for BHMAR33-5 aquifer test bore. ....461
**Table 13-4.** Construction summary of BHMAR80A-5 aquifer test bore. ....462
**Table 13-5.** Specification of equipment used for BHMAR33-5 and 80A-5 aquifer tests. ....464
**Table 13-6.** Summary of project monitoring bores used for the BHMAR33-5 and BHMAR80A-5 aquifer tests.469
**Table 14-1.** Hydrochemical analysis suite used in BHMAR water sampling program ....471
**Table 14-2.** Sampling requirements for hydrochemical analysis suite....473
**Table 14-3.** Sampled NSW State Water surface water monitoring sites....479
**Table 14-4.** Model simulations and the subroutines implemented in PHREEQC. ....490
**Table 15-1.** Status of groundwater level monitoring in the BHMAR project area ....493
**Table 15-2.** Analysis of time lags and hydrographic responses in BHMAR project bores. ....497
**Table 15-3.** Parameters of the numerical model of ASR system ....501
**Table 16-1.** Recharge estimates for unconfined aquifers based on watertable fluctuation method. ....505
**Table 16-2.** Summary of estimates of infiltration rates using Bouwer (2002) groundwater mounding equation. .506
**Table 16-3.** Summary of events exceeding flow thresholds for the Darling River at Weir 32 gauge record ....507
**Table 16-4.** Summary of radiocarbon recharge estimates for selected Jimargil-East Bootingee bores. ....510
**Table 17-1.** Satellite images used to validate LiDAR-derived flood extents....516
**Table 17-2.** Results of a quantitative analysis of the LiDAR-derived modelled flood extents. ....524
**Table 17-3.** Recorded water levels at Lakes Wetherell, Menindee and Cawndilla....524
**Table 17-4.** LiDAR survey data acquisition parameters ....536
**Table 17-5.** Number of Landsat scenes acquired for each year ....538
**Table 17-6.** Vegetation structural classes and associated CEM and FPC ranges....543
**Table 17-7.** Annual minimum NDVI thresholds used to differentiate non-woody and woody cover, and different woody vegetation structural classes....551
**Table 17-8.** Example of scene by scene Landsat NDVI statistics....552
**Table 17-9.** Example of annualized NDVI statistics....553
**Table 17-10.** Combination of vegetation structural classes considered to be a moderate or poor match ....553
**Table 17-11.** Annual minimum NDVI thresholds used to further sub-divide the open forest vegetation structural class. ....556
**Table 17-12.** Classification of variability in vegetation condition based on calculated standard deviations. ....559
**Table 17-13.** Two variables of overall trend in condition and variability in vegetation condition throughout the drought....560
**Table 17-14.** Vegetation condition at the end of the drought used as an indicator of available water volumes ....560
**Table 17-15.** Landform/cover and surface materials classification approaches....588
**Table 17-16.** Stratigraphic units present in the study area starting with the youngest. ....600
**Table 17-17.** AEM depth slice intervals and thicknesses....600
**Table 17-18.** The 25 regional cross sections referenced for stratigraphic mapping. ....601
**Table 17-19.** Relative height above lowest part of the floodplain and the grid used to delineate surfaces across the respective depth slice interval....604
**Table 17-20.** The 14 AEM depth slice grids and the threshold values used in the hydraulic texture class mapping of the near surface sediment. ....610
**Table 17-21.** Geomorphic units and codes for dividing the AEM threshold grids into spatial domains ....611
**Table 17-22.** Elevation classes of the relative elevation grids and the corresponding AEM depth slices. ....612
**Table 17-23.** Hydraulic texture classes populated across the AEM threshold and geomorphic domain matrix ....614
**Table 17-24.** Hydraulic texture classes populated across the AEM threshold and geomorphic domain matrix for first two depth slices. ....617
**Table 17-25.** The 20 BHMAR sites used to derive the textural class conductivity thresholds ....618
**Table 17-26.** The seven AEM depth slice grids and the threshold values used in the hydraulic texture class mapping of the deeper sediment. ....618
**Table 17-27.** AEM threshold values, texture classes and number of polygons in depth slice 22.0 - 26.1m. ....619
**Table 17-28.** AEM threshold values, texture classes and number of polygons in depth slice 26.1 - 30.9m. ....620
**Table 17-29.** AEM threshold values, texture classes and number of polygons in depth slice 30.9 – 36.7m. ....620
**Table 17-30.** AEM threshold values, texture classes and number of polygons in depth slice 36.7 – 43.5m. ....621
**Table 17-31.** AEM threshold values, texture classes and number of polygons in depth slice 43.5 – 51.5m. ....622
**Table 17-32.** AEM threshold values, texture classes and number of polygons in depth slice 51.5 – 61.0m. ....622
**Table 17-33.** AEM threshold values, texture classes and number of polygons in depth slice 61.0 – 72.3m. ....623
**Table 17-34.** Assigning of hydrogeological units based on stratigraphy, hydraulic texture class and depth. ....626
**Table 17-35.** NMR borehole data acquired using the Javelin logging system. ....638

**Table 17-36.** Number of NMR derived hydraulic conductivity values for AEM depth slices.....639
**Table 17-37.** Four types of interbedded units and the code assigned to each texture combination .....643
**Table 17-38.** Summary of NMR borehole data acquired in 2011 .....653
**Table 17-39.** Summary of NMR borehole data acquired in 2013 .....653
**Table 17-40.** Comparison of NMR and laboratory porosity data.....657
**Table 17-41.** Comparative groupings of NMR mobile water content survey data.....670
**Table 17-42.** Summary statistics of NMR mobile water for Class 5 coarse sand to gravel .....672
**Table 17-43.** Summary statistics of NMR free water for Class 4 medium sands .....673
**Table 17-44.** Summary statistics of NMR mobile water for Class 3 fine sands .....674
**Table 17-45.** Summary statistics of NMR mobile water for Class 2 muddy sands.....675
**Table 17-46.** Summary statistics of NMR mobile water for Class 1 muds.....676
**Table 17-47.** Summary statistics for salinity of Blanchetown Clay pore fluids.....679
**Table 17-48.** Combinations of De and C/C0 used to derive diffusion distances in the upper confining aquitard. 680
**Table 17-49.** Proportion of pore fluid data points in AEM depth slices that are within the Calivil Formation .....688
**Table 17-50.** Statistics of average pore fluid salinities relating to increments of AEM conductivity, for Calivil-dominant AEM depth slices (22-61 m).....690
**Table 17-51.** Effective porosity statistics and associated scaling factors for each of the textural classes. .....693
**Table 17-52.** Estimated groundwater volumes in BHMAR groundwater resource targets.....694
**Table 17-53.** AEM inversions used in bulk volume analysis.....697
**Table 17-54.** Versions of groundwater quality thresholds used in bulk volume uncertainty analysis. .....698
**Table 17-55.** Presence or absence of surface water and recharge pathways at each groundwater resource target.718
**Table 17-56.** Amount of watertable response observed from bores within each groundwater resource target. ....718
**Table 17-57.** Calculated recharge potential for each groundwater resource target. .....718
**Table 17-58.** The data types used in Strater® .....720

# 1 Introduction

## 1.1 PROJECT BACKGROUND

Recent periods of prolonged drought and predictions of a drier future for the southern half of Australia under a number of climate change scenarios (Barron *et al*., 2011) have led to the search for innovative strategies to identify more secure water supplies for regional communities and industries, while also delivering environmental benefits to threatened river systems. These issues are particularly pressing in the Murray-Darling Basin (the Basin), where the recent Millennium Drought (late 1990's - 2010) adversely affected many communities, industries and the environment (MDBA, 2010). While subsequent heavy rains and flooding associated with La Niña cycles broke the drought in late 2010-2012, there is general recognition of the need to provide longer-term strategic solutions to achieve a healthier working Basin (MDBA, 2011a, b).

It has long been recognised that one of the areas with the greatest potential to contribute water savings in the Basin is at the Menindee Lakes Storages (MLS), located on the lower section of the Darling River in far western New South Wales, adjacent to the township of Menindee (Figure 1-1). The MLS provide the main water supply storage of up to 2,100 gigalitres (GL) in the lower Murray-Darling River system, and play a significant role in meeting South Australia's water requirements. The MLS are also the principal water supply storage for the City of Broken Hill, which is supplied via a 110 km pipeline (Figure 1-1). The MLS also provide water locally near Menindee for irrigators and stock and domestic use.

The shallow nature of the lakes in this hot and windy semi-arid environment results in significant evaporation (Evans *et al*., 2009; MDBA, 2010; Chiew *et al.,* 2002). It is estimated that the average evaporation loss for the MLS as a whole is in the order of 420 GL per year, and a nominal market value of some $420 m. This quantity is nearly 10% of the entire surface water diversion in the Basin for the last three years (MDBA, 2010), and is similar to the 500 GL/yr figure identified for recovery under the Living Murray Program (MDBA, 2010). Moreover, evaporative losses increase to approximately 700 GL/yr when the Lakes are full (Maunsell, 2007). The opportunity cost of this water evaporating each year is realised by downstream irrigators, communities and ecosystems.

Currently, management of the MLS aims to maintain a minimum storage of 300 GL in order to secure Broken Hill's water requirements (of <10 GL/yr) in times of drought. This volume is estimated to guarantee a 21 month supply, and when the supply is depleted to 18 months the upper river intakes are managed to attempt to regain the 21 month supply. However, during the recent Millennium Drought even this storage has proven insufficient to provide a secure supply of suitable quality water to Broken Hill. For example, in 2002-2003, reservoirs at Broken Hill were empty, and there was insufficient storage in Lake Wetherell in the MLS (Country Water, pers. comm., 2009). This led to sourcing of water from the residual pool of water at Lake Menindee. This water was of poor quality (2,300 EC), yet was supplied to the residents of Broken Hill, despite being significantly above the 1500 EC limit deemed acceptable for human consumption (Country Water, pers. comm., 2009). With even that source in danger of running dry, plans were made to bring in water supplies by train at significant cost, while a Reverse Osmosis (RO) plant was constructed (but never commissioned). The situation was only saved when floodwaters came down the Darling River (Country Water, pers. comm., 2009).

Changing the management of the MLS to provide enhanced water security for Broken Hill, reduce these evaporative losses, and provide downstream economic and environmental benefits is possible, but Broken Hill's water supply would first need to become less reliant on the MLS. To address these issues, in 2008 the Australian Government confirmed its 2007 election policy commitment to invest in water saving infrastructure from the National Plan for Water Security and to invest up to $400 million to reduce evaporation and improve water efficiency at Menindee Lakes on the Darling River in Western New South Wales, secure Broken Hill's water supply, protect the local environment and heritage and return up to 200 billion litres to the Murray Darling Basin. This included a commitment to work with the New South Wales (NSW) Government and the local community to improve the Menindee Lakes water storage system.

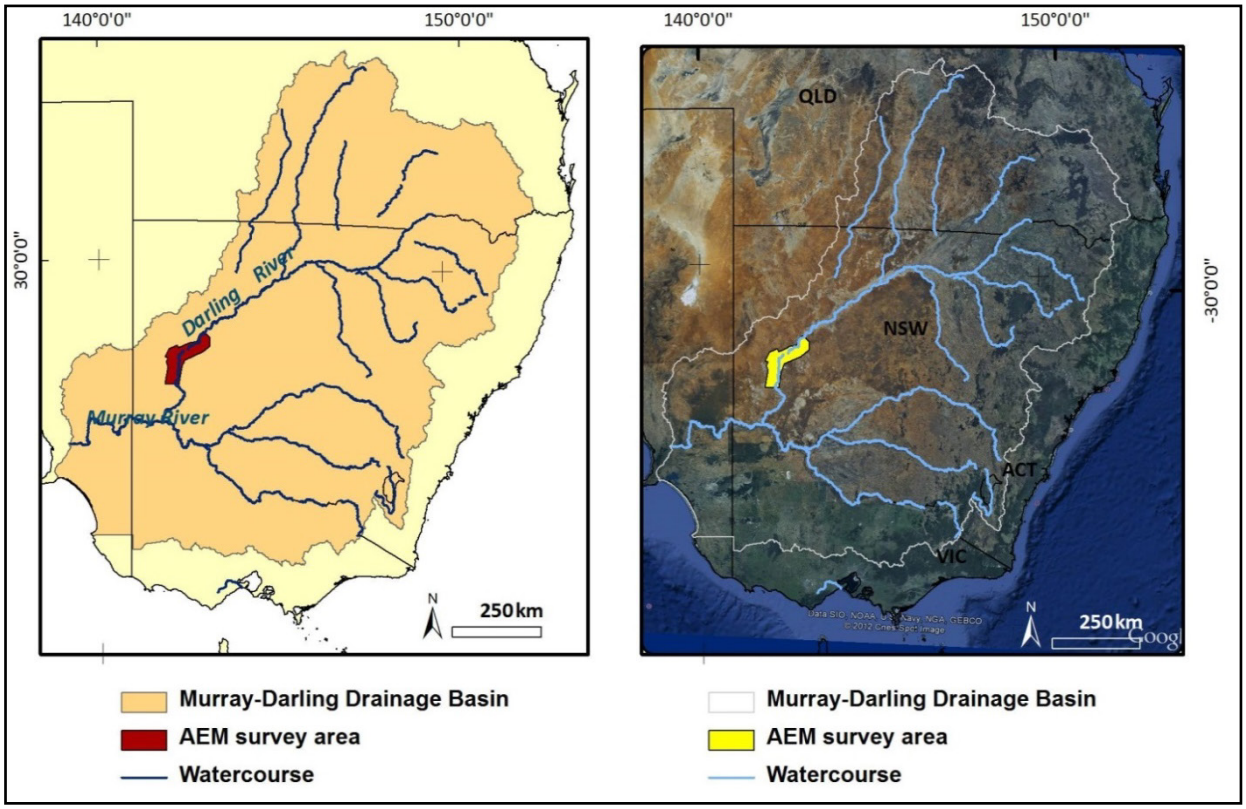



**Figure 1-1.** *Location of the BHMAR project area relative to the Murray -Darling Drainage Basin in south-eastern Australia.*

### 1.1.1 Previous Geoscience Australia Investigations

Central to the plan to realise water savings from the MLS is the identification of alternative water supply options to ensure Broken Hill's water supply during periods of prolonged drought. To this end, in 2008 the Department of Sustainability, Environment, Water, Population and Communities (SEWPaC) initially funded a regional groundwater assessment project (the Broken Hill Groundwater Assessment (BHGA) project).

The BHGA Project (Lewis *et al*., 2008), found that the opportunity existed to develop an integrated water supply strategy to secure Broken Hill's water supply and allow for significant amounts of water currently stored at Menindee Lakes to be returned to the environment by developing Managed Aquifer Recharge (MAR) options. The study concluded that this could be achieved by integrating the existing surface water operations at the Menindee Lakes Storages and the Stephens Creek and Umberumberka Reservoirs with groundwater options.

Lewis *et al*. (2008) identified nine potential areas for further groundwater investigation in the Broken Hill region, although subsequent considerations of the hydrogeology and infrastructure costs reduced this to five priority areas (Lawrie *et al*., 2009a). Among the measures suggested was MAR; the purposeful recharge of water to aquifers for subsequent recovery and/or environmental benefit. MAR encompasses a wide variety of methods usually adapted to local situations which are governed by water quality, the type of aquifer available, topography, land use, and the intended uses of the recovered water (Dillon *et al*., 2009). Other options identified included the direct extraction of groundwater resources, and/or desalinisation of brackish groundwater (Lewis *et al*., 2008).

The BHGA study also concluded that the quality and extent of groundwater in the Broken Hill area is poorly understood, and the potential for sourcing significant quantities of previously unallocated fresh and brackish groundwater is thought to be relatively high (Lewis *et al*., 2008). The BHGA study recognised that any future investigations would necessarily entail significant new hydrogeological investigations. A future work plan was identified to assess the potential for MAR and groundwater resource options in the region, and

SEWPaC commissioned Geoscience Australia to undertake further scientific investigations (the Broken Hill Managed Aquifer Recharge (BHMAR) project).

### 1.1.2 The BHMAR Project

The primary objective of the Broken Hill Managed Aquifer Recharge (BHMAR) project is to identify potential MAR and/or groundwater resource options to provide a more secure alternative water supply for Broken Hill during droughts. This would reduce the amount of water required to be stored in the MLS, and identify water-saving measures for the Darling River system. The options assessed include MAR schemes such as infiltration basins, Aquifer Storage and Recovery (ASR), Aquifer Storage, Transport and Recovery (ATSR), bank infiltration, as well as groundwater extraction. Any new option would involve retaining a (reduced) capacity within the MLS, with water supply arrangements operating as a conjunctive use scheme with MAR and/or groundwater extraction providing a vital drought-security component. A secondary objective of the project was the identification of other groundwater resources and MAR targets in the Darling Floodplain region to provide improved drought security for local communities and industries (e.g. agriculture and mining).

The boundary of the overall BHMAR project area relative to the major drainage features including the Menindee Lakes System (MLS) as shown in Figure 1-2. The project area covers 7,541.5 $km^2$ and was defined primarily by the groundwater salinity-yield mapping from previous investigations (Lewis *et al*., 2008; Lawrie *et al*., 2008a, 2009a, b). While the search for alternative water supply options for Broken Hill was initially on an area within 50 km of Menindee, a relatively larger project area was scoped to identify additional groundwater resources and MAR options to underpin regional development (for agriculture and mining) as well as enhanced water security for regional communities. The size of the project area was also determined by the need to consider the groundwater system holistically, including the broader regional hydrogeological impacts of groundwater use and replenishment on environmental assets. Scientific, technical and logistic considerations and limitations were also taken into consideration, with the project area reduced in size at the end of preliminary assessments, given the short timeframe to complete scientific investigations and interpretation to high confidence levels in such a data-poor area.

For the MAR assessment component of the project, investigations have adhered to the stringent assessment framework set out in the Australian Guidelines for Managed Aquifer Recharge (NRMMC–EPHC–NHMRC, 2009) and Water Recycling: Augmentation of Drinking Water Supplies (NRMMC–EPHC–NHMRC, 2008). The BHMAR project was the first project in Australia to apply these new guidelines, with the assessment framework reflected in a 5-phase work plan designed in accordance with the MAR guidelines (see Section 3):

- Phase 1 (Oct. 2008 - Feb. 2009): Study area finalisation and technical risk assessment / AEM technology selection exercise for six potential project areas for MAR options near Broken Hill;
- Phase 2 (Apr. 2009- Mar. 2012): Acquisition of baseline hydrogeological and geological data to derive a new conceptual groundwater model and identify potential MAR and groundwater resource targets and options across the project area;
- Phase 3a (Jul. 2010- May 2012): Acquisition of additional hydrogeological and geoscientific data to assess the feasibility of MAR and groundwater extraction options at a priority borefield target within 20 km of Menindee, and assess groundwater extraction-only options;
- Phase 3b: Carry out the necessary groundwater modelling and engineering design to optimise borefield design;
- Phase 4: Implement and test preferred groundwater extraction and storage options at a small operational scale;
- Phase 5: Construct and operate groundwater extraction/storage option.

To date, Phases 1, 2 and 3a have been implemented for the BHMAR project.

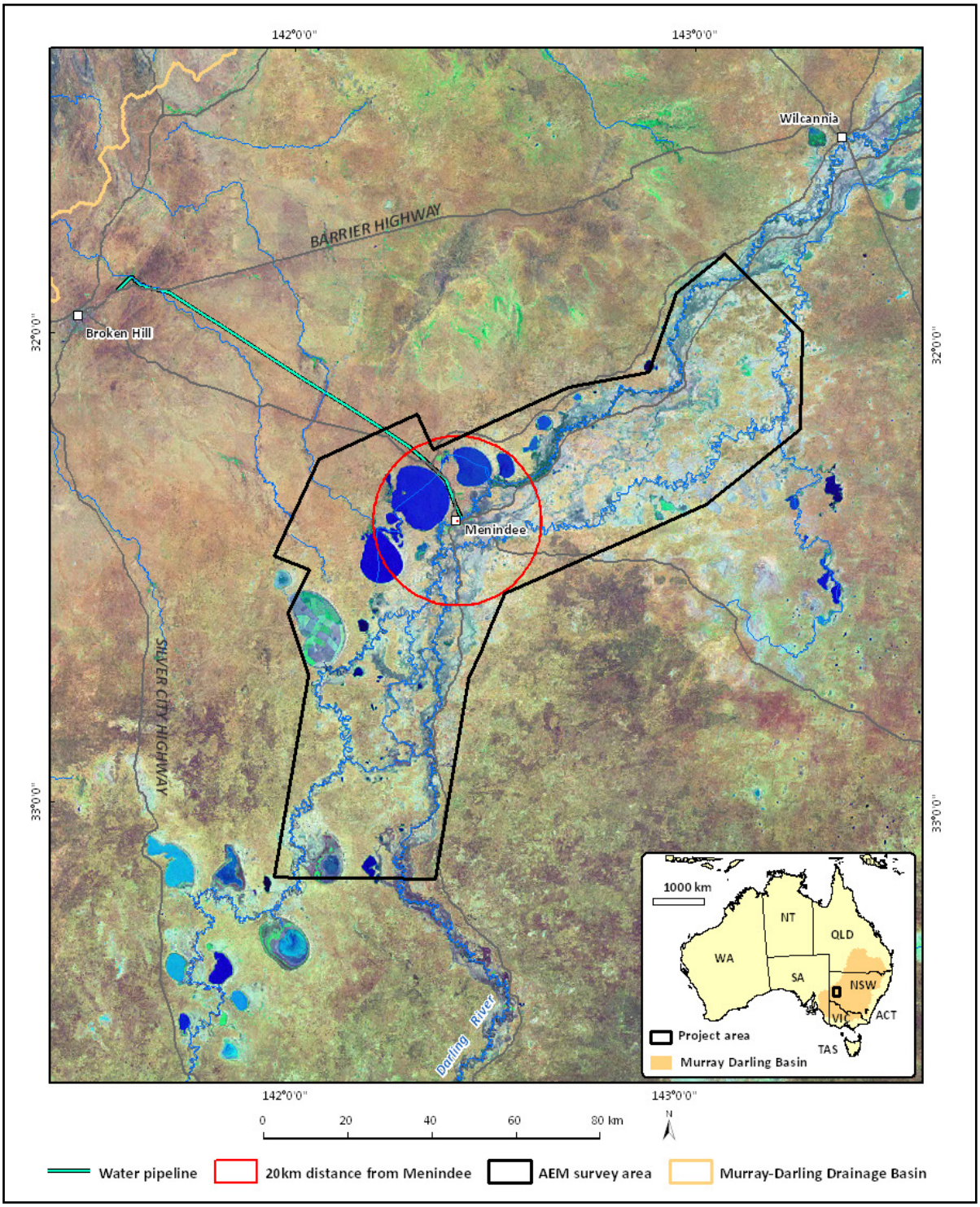



**Figure 1-2.** *Location of the BHMAR project area relative to Menindee and Broken Hill.*

## 1.2 PURPOSE AND SCOPE OF THIS REPORT

This report documents the data acquisition, processing, and interpretation methods undertaken in the three completed phases of the BHMAR study. The report integrates the project workflows previously presented in a number of interim reports (Lawrie *et al*., 2008, 2009a, 2010b, 2011). This final report supersedes the earlier documenting of data acquisition and assessment methods in these interim reports. It provides details of the investigative program that formed the baseline for the other four accompanying scientific and technical reports for the project (Lawrie *et al*., 2012b, c, d & e), namely:

- Final Report 2: Lawrie *et al*. (2012b). BHMAR Project: Geological and Hydrogeological Framework and Conceptual Model. This report details the results from geological, hydrogeological and hydrogeochemical investigations, and sets out 3D geological and hydrogeological frameworks and new hydrogeological conceptual model for the area.
- Final Report 3: Lawrie *et al*. (2012c). BHMAR Project: Securing Broken Hill's Water Supply: Assessment of Conjunctive Water Supply Options Involving Managed Aquifer Recharge Options at Menindee Lakes. This report details the findings of investigations into finding groundwater-related water supply options for Broken Hill within a 20 km radius of Menindee. These options include groundwater extraction and MAR.
- Final Report 4: Lawrie *et al*. (2012d). BHMAR Project: Assessment of Potential Groundwater Resources and Underground Storage Options in the Darling Floodplain. This report details the results of investigations to identify groundwater resources potential MAR options in the greater BHMAR study area within the Darling Floodplain.
- Final Report 5: Lawrie *et al*. (2012e). BHMAR Project: Assessment of Conjunctive water supply options to enhance the drought security of Broken Hill, regional communities and industries – Summary Report. This is the overall summary report outlining the key findings and recommendations for the BHMAR project

All the supporting data, analytical, interpretation and product generation methods are included in fifteen accompanying appendix volumes, and all project data and products are available in the BHMAR project GIS (Gow *et al*., 2012). All ancillary publications are listed below:

- Appendix 1: Halas *et al*. (2012a). Graphical display of borehole geological and geophysical logs and hydrogeochemical data;
- Appendix 2: Spulak *et al*. (2012). Core photographs;
- Appendix 3: Apps *et al*. (2012f). Borehole geophysical and geological data;
- Appendix 4: Apps *et al*. (2012c). AEM data: acquisition reports, inversion and calibration, and basic conductivity map and cross-section products;
- Appendix 5: Apps *et al*. (2012b). AEM-based interpretation products: maps and cross-sections
- Appendix 6: Somerville *et al*. (2012). Hydrological, climate, hydrochemical and hydrodynamic data;
- Appendix 7: Apps *et al*. (2012e). Age dating;
- Appendix 8: Apps *et al*. (2012a). Recharge models and data;
- Appendix 9: Gow *et al*. (2012). Remote sensing /vegetation health analysis background data and intermediate products;
- Appendix 10: Apps *et al*. (2012d). Ground and in-river geophysics and supporting data;
- Appendix 11: Apps and Lawrie (2012). CSIRO MAR reports;
- Appendix 12: Apps and Gibson (2012). Drilling construction, location and remediation data and reports;
- Appendix 13: Apps *et al*. (2012g). Borehole Hydraulic Data (contractor reports);
- Appendix 14: Lawrie *et al*. (2012f). LIDAR acquisition and processing contractor reports; and

- Appendix 15: Magee *et al*. (2012). Cultural Heritage and environmental clearance surveys.

Other final products include:

- Halas *et al*. (2012b). Broken Hill Managed Aquifer Recharge Project 3D GoCAD Model.
- De Hoog *et al*. (2012). Broken Hill Managed Aquifer Recharge Project WORLDWIND virtual globe model.
- Caldwell *et al*. (2012). Broken Hill Managed Aquifer Recharge Project. Fly-through movie

# 2 BHMAR Project Workflows

## 2.1 BHMAR PROJECT PHASES

The BHMAR project has involved the acquisition, processing, integration and interpretation of significant new geological, hydrogeological, hydrogeophysical and hydrochemical datasets. The project is the largest single hydrogeological investigation project undertaken by the Australian Government over the past 30 years. Data acquisition in the BHMAR Project involved a phased approach, with investigations initially at a regional scale, with subsequent investigations at more local scales as potential groundwater resource and MAR targets were identified and assessed.

Phase 1 of the BHMAR Project was completed in 2009 and largely involved assessment of pre-existing datasets for five possible study areas (Lawrie *et al*., 2009a). Publicly available geological, geophysical and hydrogeological data from mineral exploration companies as well as State and Federal agencies were compiled and assessed, and limited fieldwork carried out in a 6-week period to address specific questions (Lawrie *et al*., 2009a). New data acquisition included reconnaissance geomorphic mapping, borehole and ground geophysics, and groundwater and surface water sampling. The Phase 1 study identified the Darling Floodplain as the area most likely to yield groundwater resource and/or MAR storage options (Lawrie *et al*., 2009a).

Phase 2 of the BHMAR project involved major new data acquisition between 2009 and 2012, over an area of approximately 7,500 km$^2$ (Lawrie *et al*., 2010b, 2011). Acquisition included an AEM survey, a light detection and ranging (LIDAR) survey, a drilling program of 44 sonic and rotary mud holes, borehole geophysics (EM and gamma logging), field mapping, aquifer slug and pump tests, and field and laboratory hydrogeochemical investigations. The Phase 2 study identified potential groundwater resource and MAR targets, and an excellent aquifer (the Calivil Formation), on which subsequent investigations focussed.

Phase 3a of the project commenced in mid-July 2010, with the specific aim of determining, with a defined level of confidence, whether at least 3 years water supply (~30 GL), at a similar salinity to that already available for Broken Hill would be available at all times through new groundwater-related arrangements. While a number of targets were identified (Lawrie *et al*., 2010c, 2011), ranking of targets led investigations to focus on a single priority MAR target (GWR1), south and within 20 km of Menindee township (Figure 1-2). The target was the semi-confined to confined Pliocene Calivil Formation aquifer at depths of 30-80 m below ground surface.

Phase 3a investigations initially focussed in two small sub-areas (Jimargil and Menindee Common) within this target. These sub-areas were chosen to assess bank filtration, basin infiltration and aquifer storage and recovery (ASR) options, and contain two end members of the hydrogeological system within the aquifer. Both sites were considered representative of potential future borefield sites. Subsequently, work focussed primarily on the Jimargil site, with the Menindee Common site found to be less suitable. The Jimargil site (and surrounding area), has the appropriate hydrostratigraphy, significant native fresh groundwater, and was accessible in the project timeframes. The interim findings of these investigations have previously been reported (Lawrie *et al.,* 2010c, 2011).

Phase 3a investigations have involved detailed characterisation of the hydrogeological system at these sub-areas, achieved through the drilling of 56 new boreholes, groundwater pump tests, hydrogeological, hydrogeophysical (ground and borehole geophysics including borehole NMR), hydrogeochemical sampling and analysis, modelling and interpretation. Pre-commissioning maximal and residual risk assessments have also been undertaken in accordance with national MAR guidelines (NRMMC–EPHC–NHMRC, 2009). This includes accounting for human health risks in water supply, and environmental risks in relation to surface water-groundwater interaction and sustaining groundwater-dependent vegetation.

In the second half of 2011, the emphasis on investigations shifted somewhat, with a request from SEWPaC to explore a greater range of water supply options including assessment of a greater range of MAR options (including a re-examination of infiltration options), as well as groundwater extraction-only options. In 2012, a further request was made to include assessment of drought security options over shorter time periods (3

months and up to 3 years). Estimates of groundwater resources across the whole project area were also requested. The datasets acquired in BHMAR phases 1-3a, and a simplified project workflow showing the relationship of datasets are summarised in Figure 2-1 and Figure 2-2 respectively.

In summary, the BHMAR Project has acquired the following key datasets:

- A 31,834 line km airborne electromagnetic (AEM) survey using the SkyTEM heliTEM system to map the electrical conductivity of the geological profile and groundwater systems;
- A high resolution LiDAR digital elevation survey (~50cm vertical resolution) over the ~7,500 $km^2$ project area;
- 100 bores in a 7.5km drilling program, including 60 sonic bores to obtain good quality core material for analysis;
- Construction of a piezometer network, including installation of automated data loggers in 40 bores, with groundwater levels manually checked every 3-4 months;
- A hydrochemical sampling program of rainfall, surface water, groundwater and pore fluids. This entailed analysis of about 1600 hydrochemical samples (25 analytes and including trace metals);
- Stable isotopic characterisation of rainfall, river, lake and groundwater to help understand hydrological processes;
- A program of groundwater age dating using radiocarbon ($^{14}C$) and chlorofluorocarbon (CFC) tracers, to assess where and how often groundwater systems are being recharged;
- Limited (7-day) pump tests, and more extensive slug tests to obtain estimates of aquifer hydraulic properties;
- Ground resistivity and IP surveys of potential borefield sites to provide more detailed hydrogeological characterisation of potential borefield sites;
- In-river mapping of the Darling River bed using multi-beam sonar (echo sounder) and sub-bottom profiler methods to map river bed bathymetry and composition, as baseline data to assess river-aquifer connectivity;
- Borehole geophysics including gamma, induction, and nuclear magnetic resonance (NMR) logging, to provide information on sediment textures, salinity and hydraulic properties;
- Age dating of geological materials with optical stimulated luminescence (OSL), radiocarbon and palynology, to better understand sediment depositional history and hydrogeological variability;
- Laboratory column tests to assess aquifer storage and recovery (ASR) clogging potential;
- Laboratory permeameter and porosity testing of drill core materials;
- Geochemical analysis (major and trace elements) of drill core materials, to assess potential water-rock interactions during MAR operations;
- Scanning electron microscopy (SEM), x-ray diffraction (XRD), portable infrared mineral analyser (PIMA) and Hylogging multi-spectral analysis of drill core materials for fine-scale mineralogical analysis;
- Limited groundwater and water-rock interaction modelling;
- Surface geomorphic mapping, trenching and hand augering, to assess near-surface geology including infiltration characteristics; and
- Mapping of Indigenous cultural heritage sites, to ensure protection during field operations.

The acquisition, processing, and interpretation of such large, varied and complex datasets involved a trans-disciplinary systems analysis approach involving a trans-disciplinary team. There was a core team of 10 scientists within Geoscience Australia, and with an additional 20 staff and 40+ contractors involved at various stages in data acquisition and processing. The data acquisition and key activities of the three completed phases of the BHMAR project are outlined in greater detail below.

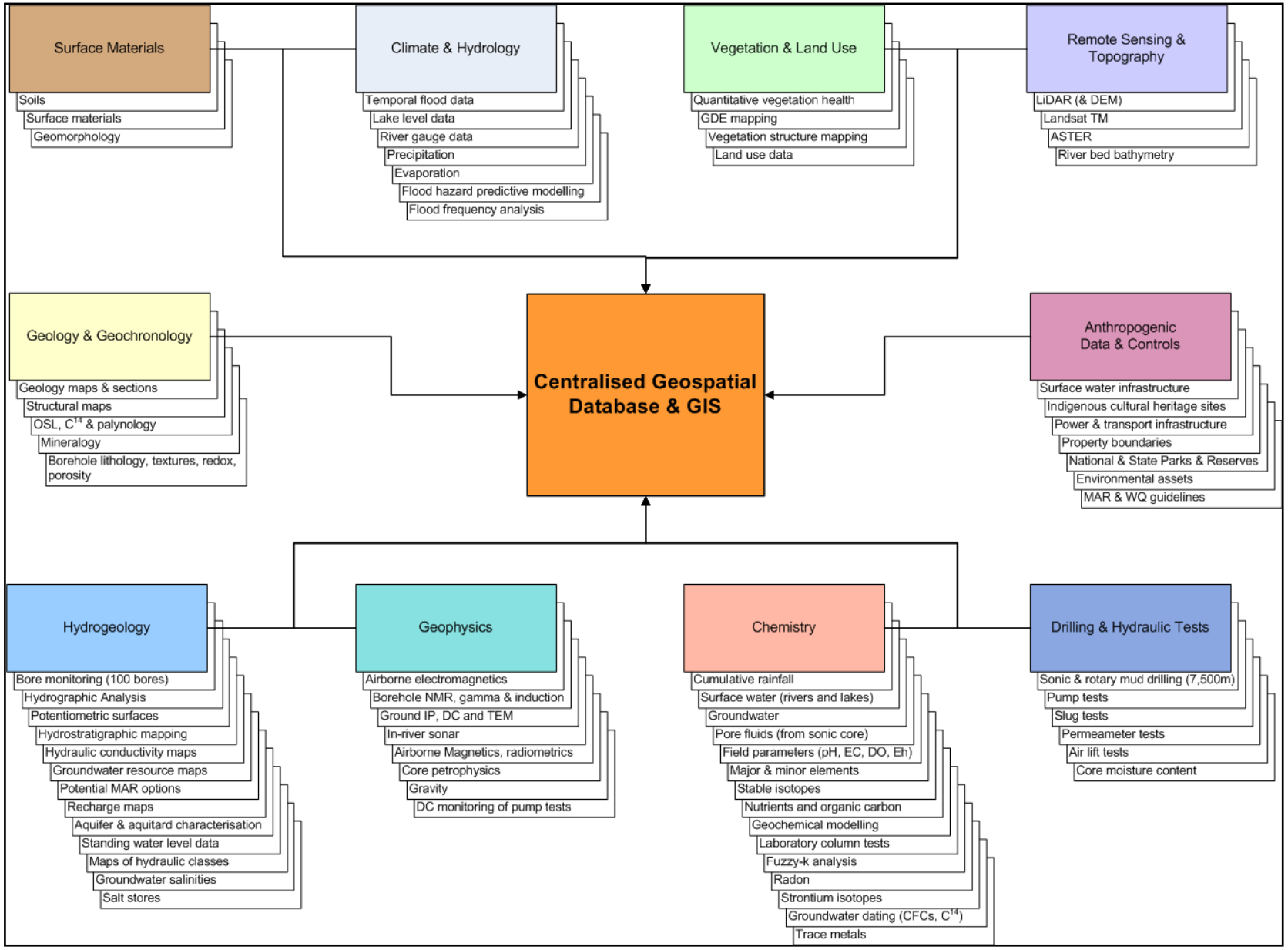



**Figure 2-1.** *Datasets acquired during the BHMAR project, grouped by theme.*

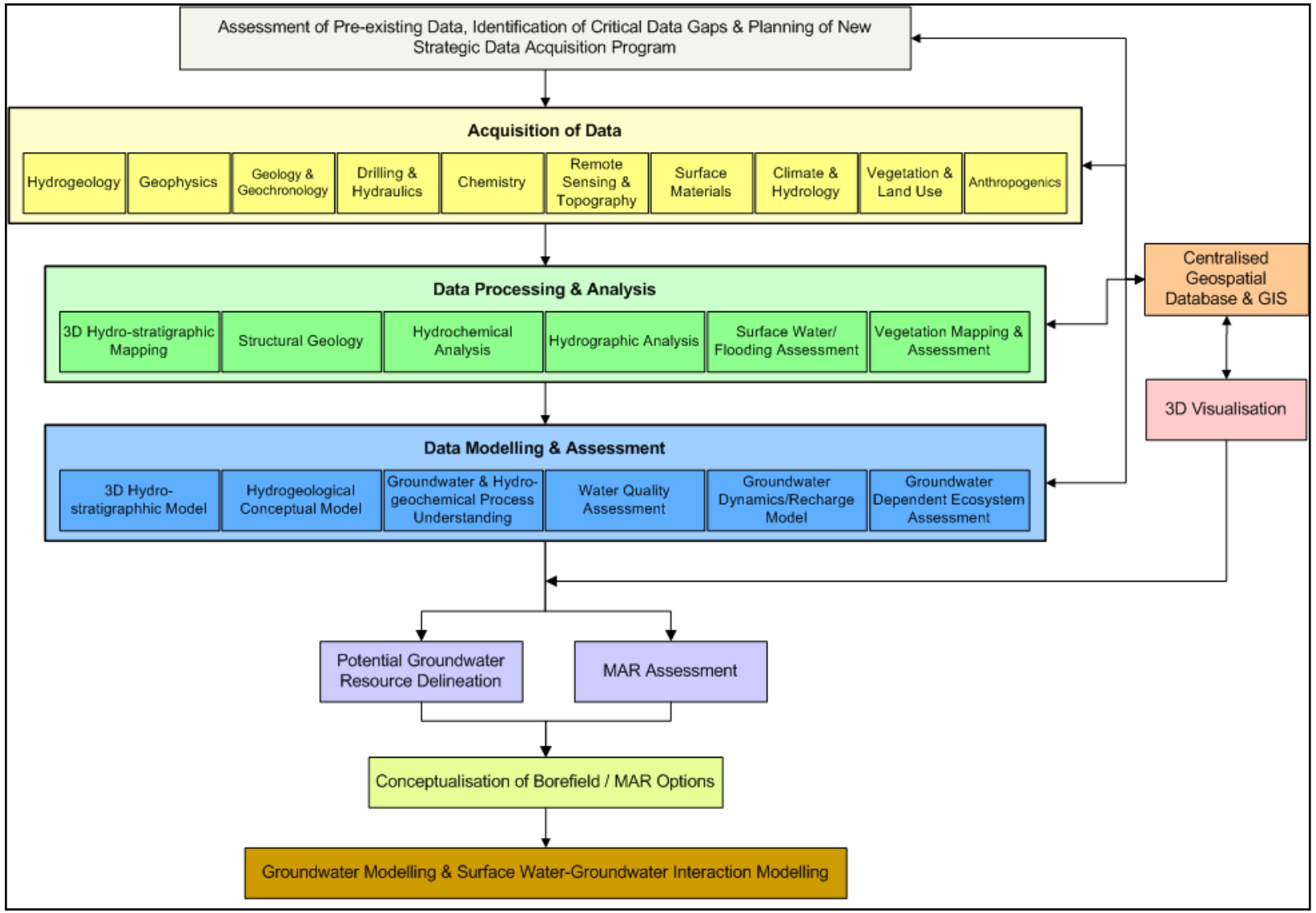



**Figure 2-2.** *Simplified BHMAR project workflow. Those themes listed under acquisition of data relate to Figure 2-1.*

## 2.2 BHMAR PHASE 1

The principal objective of Phase 1 of the BHMAR Project was to select a final project area from nine options identified in the BHGA study (Lewis *et al*., 2008). The areas assessed in Phase 1 are documented in Lawrie *et al.* (2008, 2009a).To meet the challenge of rapidly identifying and assessing potential MAR targets and groundwater resources over large, data-poor areas within a short timeframe, it was recommended that the only cost-effective method with the ability to resolve key elements of the hydrostratigraphy in the top 300 m was airborne electromagnetics (AEM).

A technical risk assessment was therefore carried out to evaluate the suitability of AEM for defining aquifer systems and potential MAR aquifer targets in the BHGA-identified priority areas. This entailed an assessment of existing geophysical and remote sensing technologies to map:

- Particular aquifers (to depths of ~330 m), including their lower (and upper) boundaries and their lateral extent;
- The internal textural characteristics of each of the aquifers, at an appropriate scale (variable with depth);
- Water quality and its variability within the individual aquifers, including the extent of river flush zones;
- Inter-aquifer leakage (i.e. vertical connectivity between aquifers);
- The connectivity of river and lake waters to the shallower aquifer systems; and
- Recharge of surface waters through the floodplain to shallow aquifers (with particular focus on sites for preferential recharge, storage and recovery).

Due to the timeframe available for this phase of the project (four months), the study was largely limited to an analysis of relevant pre-existing hydrogeological data. The key activities of Phase 1 included:

- The compilation and technical assessment of existing borehole, hydrogeological and relevant geospatial data;
- Limited data acquisition involving downhole geophysical logging, ground geophysical transects, water sampling and reconnaissance mapping;
- An assessment of the hydrostratigraphy and aquifer characteristics;
- Construction of hydrogeological and geo-electrical conceptual models of aquifer targets;
- Forward modelling of geophysical data;
- A risk assessment of AEM technology and its suitability for mapping critical elements of the aquifer system; and
- Preparation of technical and summary reports, with recommendations on the design and costing of AEM and ancillary data acquisition.

### 2.2.1 Hydrogeological Data Compilation

Relevant pre-existing hydrogeological, geological and ground geophysical data, including borehole data, from natural resource management (NRM) and mineral exploration sources were compiled for the regional study area. A technical assessment of data was carried out, and relevant filtered data entered into a database linked to the project GIS. All relevant pre-existing airborne geophysical and other remote sensing data (available DEMs, Landsat, airborne magnetics, airborne gamma radiometrics, AEM, ALOS, ASTER and topographic and relevant cultural data), were also compiled, entered into the project GIS, and used in the technical assessment. A summary and assessment of the pre-existing data is contained in Section 4.

### 2.2.2 New Data Acquisition

Limited additional geophysical, geomorphic and hydrogeological data was collected where this was deemed essential for the technical assessment. New data included:

- The acquisition of new borehole (induction and gamma borehole logging) data in existing boreholes on the Darling River Floodplain;
- A spaced moving loop ground time domain electromagnetic (TEM) survey in a series of transects adjacent to the MLS on the Darling River Floodplain; and additional soundings elsewhere in the project areas;
- Groundwater sampling from pre-existing boreholes;
- Surface water sampling from the Darling River and the MLS;
- Reconnaissance geomorphic mapping on the Talyawalka and Darling Rivers and the area adjacent to the MLS.

### 2.2.3 Hydrogeological Assessment

Lewis *et al*. (2008) summarised some of the key characteristics of the aquifers in the Broken Hill area. However, a further review of aquifer systems architecture and inter-connectivity was deemed necessary to assist with defining geophysical targets and providing data on assumed aquifer hydraulic properties. The hydrogeological assessments largely relied on existing geospatial and hydrogeological datasets. New data and analysis compiled as part of Phase 1 are to be found in Lawrie *et al*. (2009a).

The assessment paid particular attention to identifying the aquifers and aquitards, the internal architecture of the aquifers units and their bounding relationships as deduced from existing sedimentological and geomorphological studies. Prior to the commencement of the BHMAR study, the hydrostratigraphy was only established at a generalised regional scale. Figure 2-3 is a hydrogeological cross-section through the Darling River Floodplain showing the pre-BHMAR study understanding of the hydrostratigraphy, and groundwater salinity.

Previously, Lewis *et al*. (2008) reported that of the 198 bores in the Darling alluvial aquifers, only half (84 of the 198) have salinity information, provided in broad categories of 0–500 mg/L, 0–1000 mg/L, 0–14,000 mg/L, 1000–10,000 mg/L and 10,000–100,000 mg/L, rather than specific measurements. Salinity-yield mapping (from Lewis *et al*., 2008; adapted from Brodie, 1994) for the principal aquifers are shown in Figure 2-5. The distribution of bores and corresponding salinity values indicates that groundwater freshens proximal to surface water bodies, such as the Darling River. A general positive relationship between increasing depth and salinity is also apparent. These findings are consistent with previous investigations of the Darling floodplain (Brodie, 1994; Kellett, 1994; Jewell, 2007), and support our conceptual understanding of groundwater systems in this region. However, the data reliability for these maps is based on the availability of historic data and shown in Figure 2-6, and clearly demonstrates the paucity of data points from which these maps were drawn.

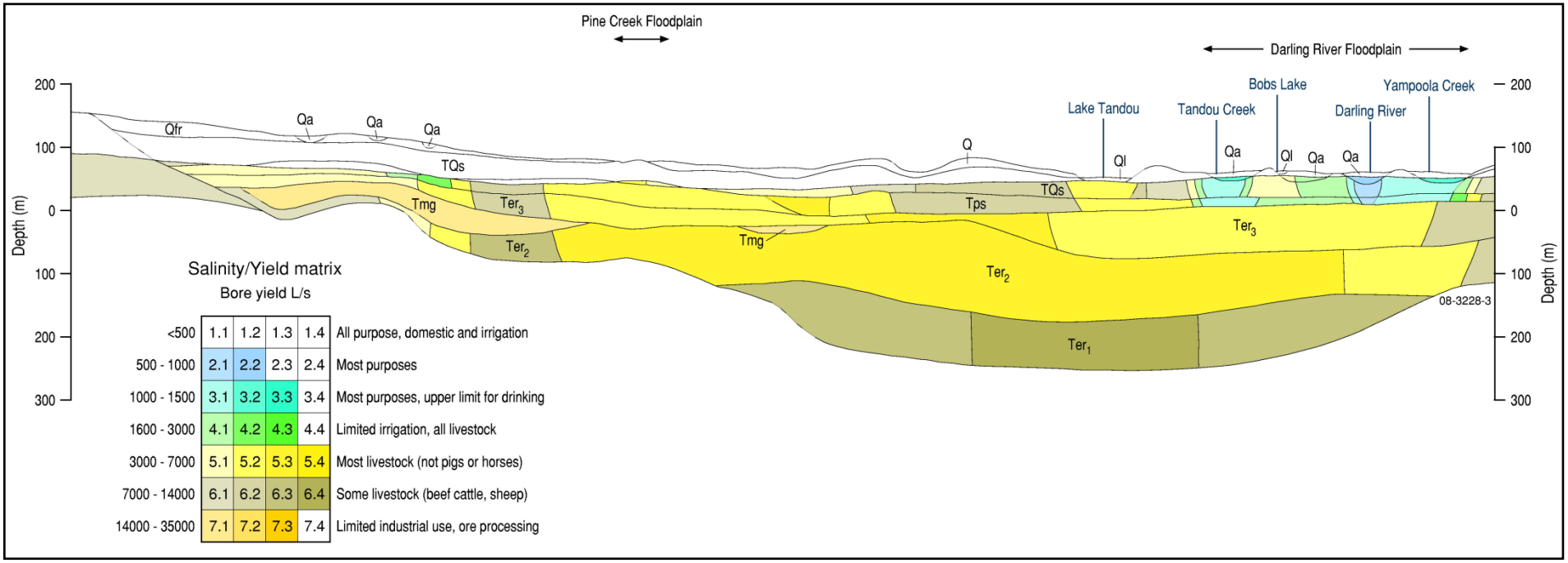



**Figure 2-3.** *Hydrogeological cross-section through the Darling River Floodplain showing water quality dilution zones developed to depth and laterally around the River Darling and its anabranches. From Brodie (1994).*

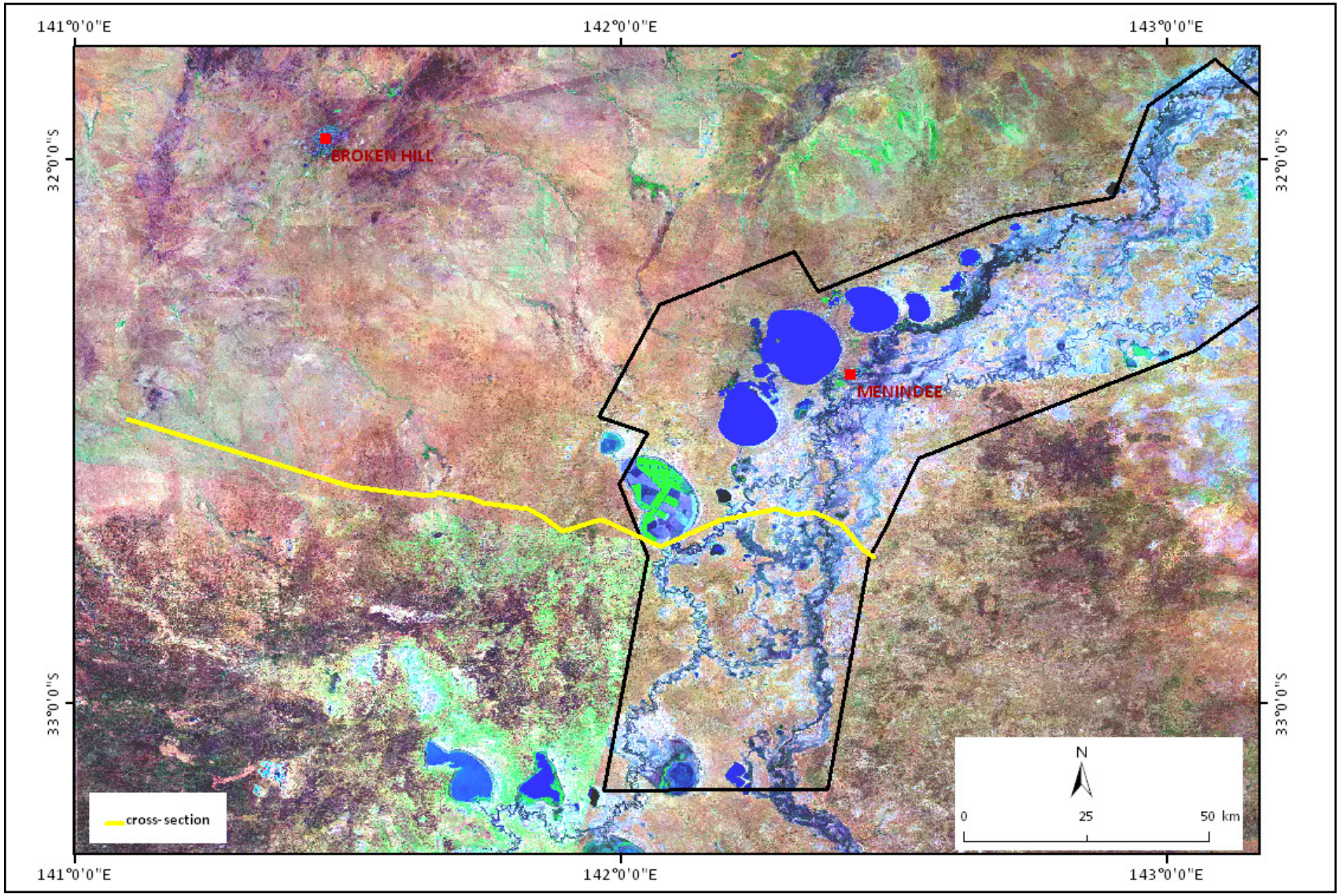



**Figure 2-4.** *Map showing location of hydrogeological cross-section (*Figure 2-3*) through the Darling River Floodplain.*

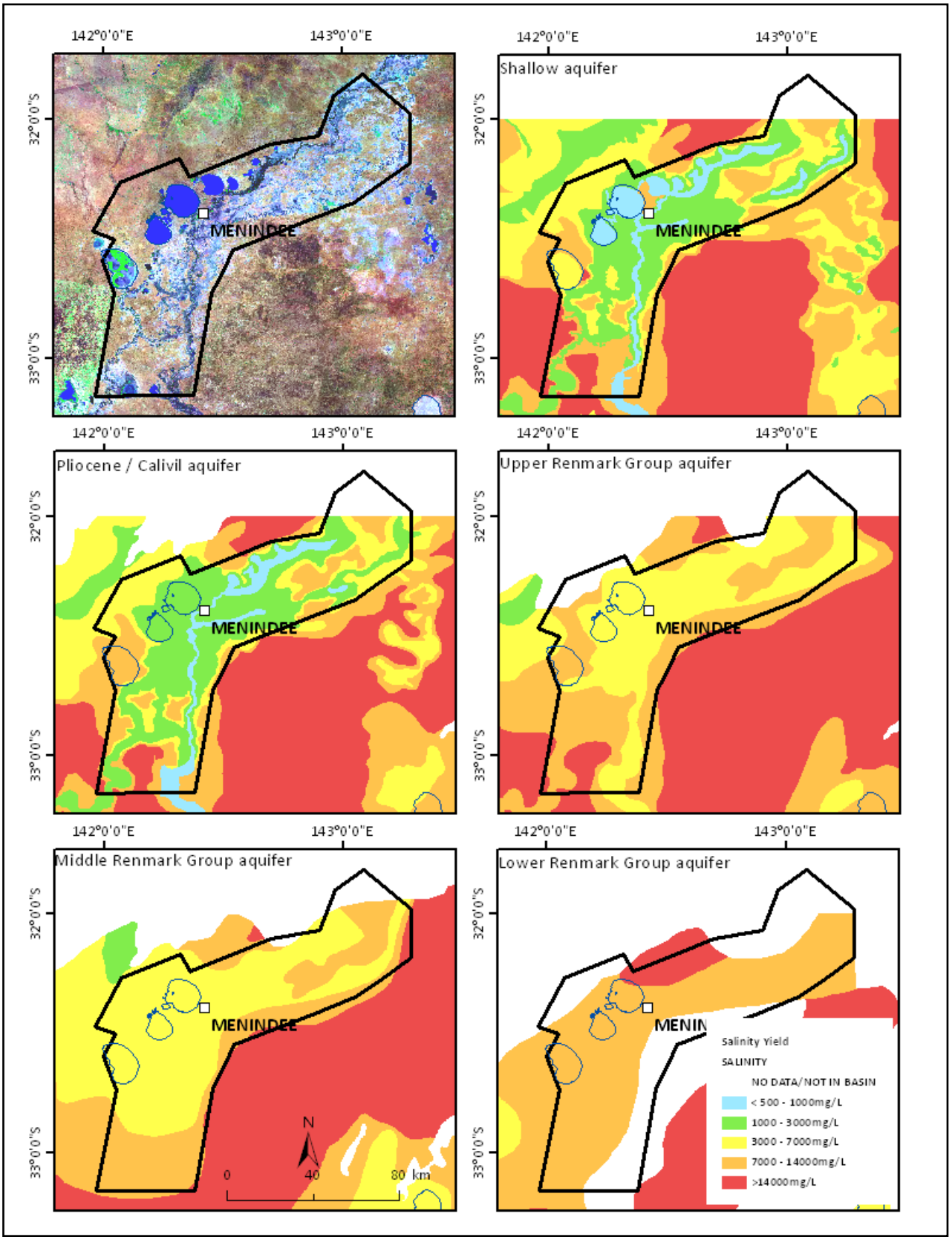



**Figure 2-5.** *Salinity-yield mapping for the priority aquifers. Adapted from Lewis et al. (2008).*

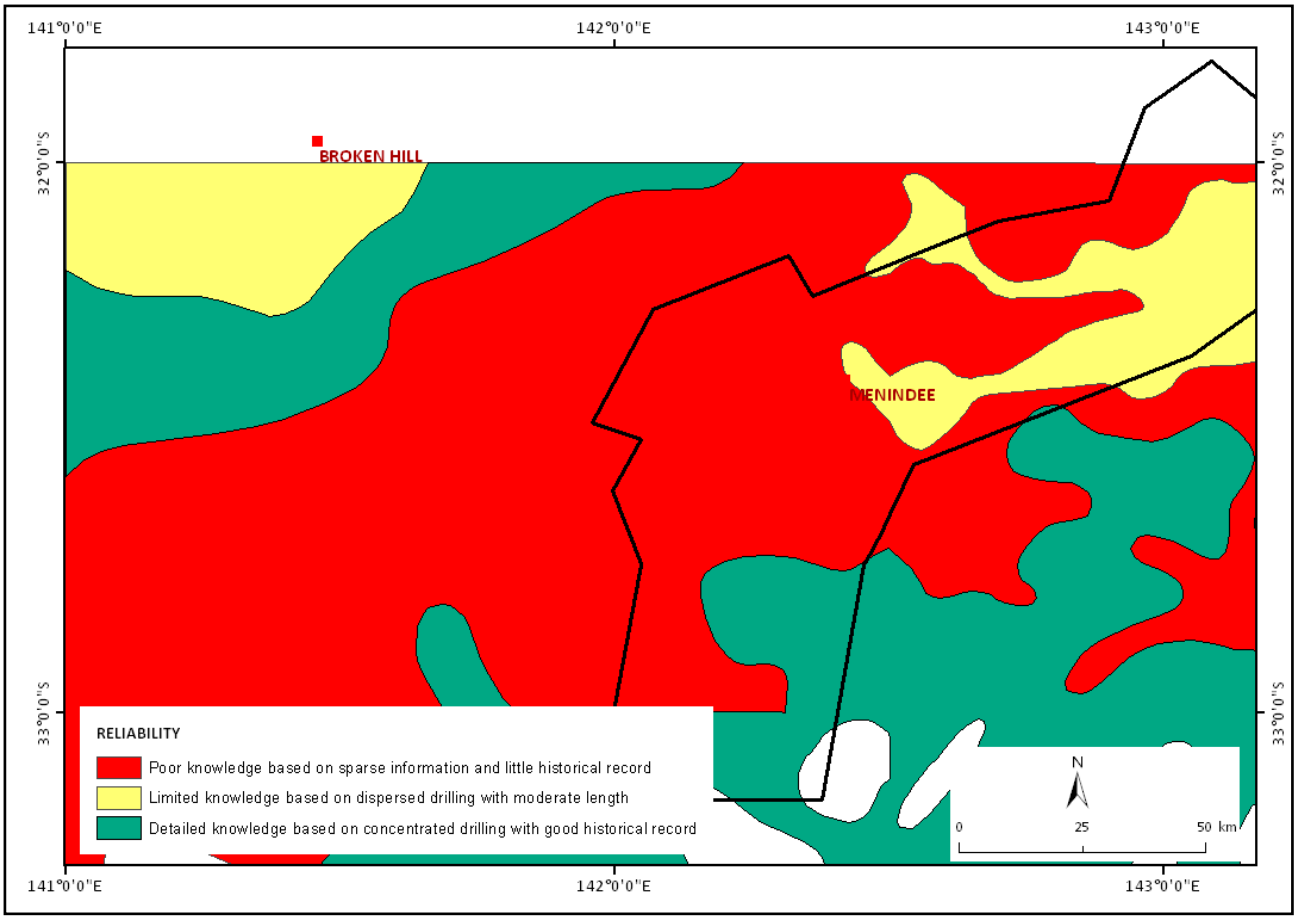



**Figure 2-6.** *Map showing data reliability for the aquifer salinity-yield mapping. This map shows the poor certainty in most of the project area on the distribution of aquifers and groundwater quality variations. Modified from Lewis et al. (2008).*

### 2.2.4 AEM Technology Evaluation and Risk Assessment

The specific tasks undertaken in the evaluation of AEM technology were:

- A review of aquifer systems architecture and inter-connectivity to define geophysical targets;
- construction of conceptual hydrogeological models of aquifer targets including surface-groundwater connectivity;
- Estimation of aquifer hydraulic properties and assumed hydraulic gradients using existing data. These were a key component in construction of hydrogeological and geo-electrical models;
- A reconnaissance water sampling program of existing boreholes (including groundwater level and field chemistry parameters) and surface waters to assess water quality (salinity) distribution. These data were essential for the development of electrical conductivity models and aided the interpretation of geophysical data;
- A study of aquifer texture characteristics to help define electrical conductivity responses;
- construction of geo-electrical models of aquifer targets;
- With assistance by CSIRO, a full technical evaluation of AEM suitability for mapping the Broken Hill aquifer systems;
- Integration of the borehole induction and gamma logs, ground geophysical soundings and available borehole lithologies to produce a summary report of geo-electrical characteristics of Broken Hill aquifers This report outlined the findings of the AEM evaluation, including recommendations on AEM (and associated airborne geophysical) data acquisition;

- A full technical risk assessment for the BHMAR Project, taking into consideration existing data on groundwater aquifer systems, AEM technology suitability, recharge potential and aquifer characteristics; and
- Presentation of Phase 1 report findings in meetings and other forums.

### 2.2.5 AEM (and LiDAR) Survey Design and Costing

The specific tasks and outputs were:

- A technical assessment with recommendations on the optimal survey area for MAR options and Broken Hill groundwater resources to be investigated in BHMAR Phase 2;
- With assistance by CSIRO, a detailed survey plan with estimated costs for the acquisition of AEM data in BHMAR Phase 2;
- Recommendations on acquisition of LiDAR and borehole data acquisition, including a costed plan for acquisition of LiDAR data in BHMAR Phase 2; and
- A cost estimate and workplan for borehole data acquisition in BHMAR Phase 2.

Phase 1 of the BHMAR project recognised the Darling River Floodplain as the area most likely to yield MAR storage options and groundwater resources.

## 2.3 BHMAR PHASE 2

Phase 2 of the project was funded to acquire the baseline hydrogeological and geological data to identify potential MAR and groundwater resource targets and options in the project area. The boundary of the BHMAR Phase 2 project area relative to the major drainage features including the Menindee Lakes System (MLS) is shown in Figure 1-2. The project area covers 7,541.5 $km^2$ and was selected primarily based on the salinity-yield mapping from previous investigations (Lewis *et al*., 2008; Lawrie *et al*., 2008, 2009a, b).

Initially, the project was tasked with identifying MAR targets within a 50 km radius of Menindee township and groundwater resources throughout the project area. However, in a parallel investigation, the DRWSP Part B MAR study reported on a conceptual design and preliminary (conceptual) cost estimate for a MAR scheme to provide water supply for Broken Hill and other high security water users (SKM, 2010). This assessment was used for comparison with other surface water supply options being developed as part of the DRWSP Part B study (SKM, 2010).

The Darling River Water Savings Project (DRWSP) found MAR using borehole injection into shallow aquifers to be the most cost-effective option when compared to alternative surface water options within 5km of existing infrastructure, and infiltration options to be the least expensive within 20 km of Menindee. However, due to a paucity of data at the time, the DRWSP Part B MAR study was only able to assess a very limited number of potential MAR options, and of necessity had to make a number of wide-ranging assumptions about potential treatment costs and options. In light of preliminary findings that there were many more conceptual MAR targets in the region (Lawrie *et al*., 2009c), including a wide range of potential infiltration options, the project team were directed by SEWPaC to focus on an area within a 40 km radius of Menindee. Subsequently, the primary objective was narrowed to identifying MAR targets and options within a 20 km radius of Menindee township. Identification of potential groundwater resources and other potential MAR targets throughout the remainder of the study area remained as a secondary, lower priority, and have been identified and assessed at a reconnaissance level.

### 2.3.1 New Data Acquisition

Earlier scoping studies found that the BHMAR project area was an area with significant hydrogeological data gaps. In order to move forward with an assessment of MAR potential in this area, a number of new datasets were commissioned in Phase 2 of the project. Data acquisition covered a large area, and was designed to map and assess both MAR and groundwater resource potential in a large tract of the Darling Floodplain centred on Menindee. The activities and new datasets include:

- A light detection and ranging (LiDAR) survey;
- An airborne electro-magnetic (AEM) survey (helicopter-borne SkyTEM transient EM system);
- Drilling program (sonic and rotary mud drilling);
- Hydraulic testing of aquifers (including slug and pump tests);
- Surface and groundwater characterisation (including chemistry and age dating);
- A program of borehole geophysics (Induction, Gamma Radiometrics and Nuclear Magnetic Resonance (NMR));
- Petrophysics including permeameter tests;
- Laboratory analysis including groundwater characterisation (major anions and cations, trace metals, tracers and age dating);
- Surface geomorphic mapping (including digging of pits and shallow augering);
- Geochronology (OSL and radiocarbon and palynology) of sedimentary materials;
- Monitoring (data loggers) and measuring of groundwater levels, temperature and salinity;
- Quantitative temporal analysis of vegetation health using remote sensing (LiDAR and Landsat data).

More details on acquisition of these datasets are provided later in this report and in accompanying appendices.

## 2.4 BHMAR PHASE 3A

Phase 2 of the BHMAR project identified a number of potential MAR and groundwater resource targets across the Darling Floodplain, including 7 sites within 20 km of Menindee (Lawrie *et al*., 2009c; Lawrie *et al*., 2010b & c). This led to fast-tracking of Phase 3 of the project, which commenced in mid-July 2010. Specifically, Phase 3 was therefore charged with determining, with a defined level of confidence, whether at least 3 years water supply (~30 GL), at a similar salinity to that already available for Broken Hill would be available at all times from a MAR and/or groundwater extraction borefield at a specific target (GWR1). This target covers an area of 144.38 $km^2$, and lies within a 20 km radius SSW of Menindee.

The focus of investigations within this target is the Calivil Formation aquifer at depths of 30-80 m below ground surface. Investigations were focussed on two small sub-areas (Jimargil and Menindee Common) within the GWR1 target. These sub-areas were chosen to address bank filtration, basin infiltration and aquifer storage and recovery (ASR) options, and contain two end members of the hydrogeological system within the aquifer. Both sites were considered representative of potential future borefield sites. Subsequently, work was focussed primarily on the Jimargil site, as the Menindee Common site was found to be less suitable. The Jimargil site (and surrounding area), has the appropriate hydrostratigraphy, significant native fresh groundwater, and was accessible in the project timeframes. In this report, this target is referred to as the Jimargil sub-area, which is a larger area than the Jimargil borefield test site originally identified in the BHMAR Phase 3a Interim Report (Lawrie *et al*., 2010c).

Subsequent to releasing interim findings (April, 2011) of Phase 3 investigations, the project team was recently (February 2012) asked to scope a wider range of options in the final reports. These include a wider range of supply duration options (3 months up to a 3-year supply), from a greater range of targets within a 20

km radius of Menindee township. The water supply delivered through these new arrangements would need to be available at all times through these new arrangements, with a capacity to supply water through a pipeline to Menindee at 250 L/sec.

### 2.4.1 Phase 3a Data Acquisition

Phase 3a investigations have involved detailed characterisation of the hydrogeological system at the two key sub-areas in the GWR1 target. This has been through the drilling of 56 new boreholes, pump and slug tests, water sampling and analysis, borehole geophysics, ground geophysics (EM and IP), petrophysics including permeameter tests, surface geomorphic mapping, geochronology (OSL, radiocarbon and palynology), hydrographic monitoring, modelling and interpretation. Pre-commissioning maximal and residual risk assessments have also been undertaken in accordance with MAR guidelines (NRMMC–EPHC–NHMRC, 2009). This includes accounting for human health risks in water supply, and environmental risks in relation to surface water-groundwater interaction and sustaining groundwater-dependent vegetation.

The specific Phase 3a activities are documented in more detail below:

- Drilling campaign and piezometer construction. An investigative drilling program was undertaken to obtain geological samples, define stratigraphic profiles, and construct bores. A combination of sonic and rotary mud drilling was used to complete production and monitoring bore arrays at key sites. Sonic core samples assisted with screen locations in target aquifers and in overall aquifer characterisation, while core samples were taken for pore fluids, mineralogical analysis and facies interpretation. Core sediment samples were also critical for laboratory analyses designed to address specific ASR issues, such as vulnerability to clogging or chemical compatibility with source water.
- Borehole geophysical logging. Downhole logging of EM induction, passive gamma radiometrics and nuclear magnetic resonance (NMR) was undertaken on BHMAR bores and other existing suitable boreholes.
- Surface and groundwater sampling and monitoring program. Comprehensive water sampling (including rainfall, river, lake and groundwater) was carried out to assess and monitor water quality criteria and undertake hydrochemical analysis to understand hydrological processes. Water quality parameters such as pH, EC, dissolved oxygen and Eh were routinely taken in the field. Analytes included major, minor and trace elements and isotopes (such as deuterium and oxygen-18), nutrients, organic carbon, radon, radiocarbon, chlorofluorocarbon and on a less frequent basis, pesticides. More specialised analyses used for MAR assessment, such as particle size distribution, membrane filtration index (MFI) and organic carbon speciation were undertaken on selected samples.
- Laboratory analysis of geological materials and pore fluid samples. Sonic core samples were analysed for a range of rock and hydraulic properties. This included grainsize analysis (sieve and laser techniques), x-ray diffraction, x-ray fluorescence and PIMA analysis for mineralogy. Palynology, permeameter tests and Hylogging were also undertaken on selected intervals. Pore fluids were routinely extracted from the core for measurement of electrical conductivity (salinity) and pH and in some cases, major ion analyses.
- Hydraulic testing. Slug tests were undertaken on all BHMAR bores with the data used to derive estimates of aquifer transmissivity. Two pump tests were undertaken at the Jimargil site to better define the hydraulic properties and response to pumping for the target Calivil Formation aquifer.
- In-river surveying. A multi-beam sonar and sub-bottom profiler was used to map the bathymetry of the Darling River bed and identify deeper holes at the river base. River sediment sampling was also undertaken at selected sites. This data was used in the assessment of river–aquifer connectivity.
- Groundwater geochemical analysis and modelling. Surface water and groundwater chemistry and mineralogical data were used as inputs into PHREEQC geochemical modelling by CSIRO to better understand potential hydrochemical processes such as water-rock interactions and to assess potential risks associated with ASR operations.

- Groundwater flow and solute transport modelling. Preliminary groundwater models at a borehole scale using FEFLOW were constructed by CSIRO to simulate potential MAR scenarios (e.g. 3 year injection and 3 year recovery) at the Jimargil site. The models were used to estimate recovery efficiencies for potential ASR operations.
- Assessment of clogging and water treatment requirements. A laboratory column study using homogenised core material of the Calivil Formation aquifer was undertaken by CSIRO to investigate potential clogging issues associated with ASR injection. The study used four types of potential source water of (a) bank filtered water, (b) Menindee town water, (c) Menindee town water treated with granular activated carbon filtration, and (d) untreated Darling River water with suspended solids kept in suspension.
- Processing and interpretation of satellite imagery to support key mapping datasets. Examples include time-series analysis of vegetation health (particularly maintenance of vigour during prolonged dry periods) to establish recharge and discharge zones on the floodplain and the extent of lateral river flush zones. Other image processing techniques were used to map flood inundation and surface clay distribution.
- Borehole-calibrated inversions and 3D inversions of the AEM data. New drilling results and geophysical logging of the new boreholes were used to produce a revised borehole spatially-constrained inversion of the AEM data. This was required to produce the range of AEM-based interpretation and map products. Due to topographic effects associated with the steep river banks and certain dune features in the target area, a customised 3D inversion of the AEM data in a swath along the Darling River was undertaken.
- Analysis, synthesis, interpretation, reporting and product generation. This involved combining the regional and local-scale datasets to produce a range of 2D and 3D digital map products and interpretation reports.

Further details on the acquisition, processing and analysis of these datasets are provided as separate sections in this report as well as in accompanying appendices.

## 2.5 RESEARCH METHODOLOGY AND PROJECT MANAGEMENT

In the BHMAR project, investigations involved an integrated, multi-scale hydrogeophysical, hydrogeochemical and hydrogeological systems approach to map and assess near-surface (<100 m) aquifers and aquitards in unconsolidated alluvial sediments beneath the Darling River floodplain (Lawrie *et al*., 2012b). Data acquisition, integration and interpretation involved a large (>50) multi-disciplinary group of geoscientists (geomorphologists, sedimentologists, regolith geoscientists, hydrogeologists, hydrogeophysicists, hydrogeochemists, geospatial analysts, remote sensing specialists, geochronologists, groundwater modellers and structural geologists; Figure 2-1), working in a team to understand the hydrological system and identify MAR and potential groundwater resource targets (Figure 2-2). The research team was based largely at Geoscience Australia in Canberra, however, key researchers included colleagues elsewhere in Canberra, Adelaide and Perth in Australia, in Denmark, and in the United States of America.

Critical to successful completion of MAR pre-commissioning maximal and residual risk assessments was an evolution in team science and project management from multi-disciplinary, to inter-disciplinary and finally a trans-disciplinary approach (Table 2-1). Multi-disciplinary and inter-disciplinary approaches left many science questions unresolved. In the BHMAR study, the SkyTEM system has successfully mapped key functional elements of the hydrogeological system critical to the identification and assessment of managed aquifer recharge (MAR) sites and potential groundwater resource targets.

Multi-disciplinarity is a process where researchers from disparate fields work independently or sequentially, periodically coming together to share their individual perspectives for purposes of achieving broader-gauged analyses of common research problems (Rosenfeld, 1992). Participants in multi-disciplinary teams remain firmly anchored in the concepts and methods of their respective fields. Inter-disciplinarity is a more robust approach to scientific integration in the sense that team members not only combine or juxtapose concepts

and methods drawn from their different fields, but also work more intensively to integrate their divergent perspectives, even while remaining anchored in their own respective fields (Stokols *et al*., 2008).

**Table 2-1.** *Definitions of scientific orientation of research teams (from Rosenfeild, 1992).*

| Scientific Origin | Definition |
|---|---|
| Unidisciplinarity | Unidisciplinarity is a process in which researchers from a single discipline work together to address a common research problem. |
| Multi-disciplinarity | Multi-disciplinarity is a sequential process whereby researchers in different disciplines work independently, each from his or her own discipline-specific perspective, with a goal of eventually combining efforts to address a common research problem. |
| Inter-disciplinarity | Inter-disciplinarity is an interactive process in which researchers work jointly, each drawing from his or her own discipline-specific perspective, to address a common research problem. |
| Trans-disciplinarity | Trans-disciplinarity is an integrative process in which researchers work jointly to develop and use a shared conceptual framework that synthesizes and extends discipline-specific theories, concepts, methods, or all three to create new models and language to address a common research problem. |

Trans-disciplinarity is a process in which team members representing different fields work together over extended periods to develop shared conceptual and methodological frameworks that not only integrate but also transcend their respective disciplinary perspectives (Rosenfeld, 1992). Trans-disciplinary collaborations have significant potential to produce highly novel and generative scientific outcomes, but they are more difficult to achieve and sustain than unidisciplinary, multi-disciplinary, and inter-disciplinary projects due to their greater complexity of the research, and the challenges in bring individuals and teams prepared to question their own discipline orthodoxy to achieve supra-disciplinary integrations (Stokols *et al*., 2003; Nash, 2008; Klein, 2008; Hirsch *et al*., 2008). Overall, a trans-disciplinary approach is a more integrative process, and permits a more comprehensive analysis of all data and interpretation (Stokols *et al*., 2008).

Using the trans-disciplinary approach, a process was established for confirming and negating established discipline-based methods and assumptions, and conceptual models. This approach enabled the team to recognise fundamental problems in discipline approaches, helped identify critical data gaps, led to significant innovation across discipline boundaries, and was critical in the development of a hydrogeological conceptual model that underpinned MAR assessment (Lawrie *et al*., 2012b, c). The approach was facilitated by advances in geophysical and sensor technologies, and supercomputing.

The success of a trans-disciplinary approach is illustrated by the evolution in AEM inversions throughout the project. Initially, Fast Approximate Inversions (FAI) provided within 48 hours of acquisition were used to target the drilling program used in part for AEM calibration and validation. Subsequently, a number of different (Laterally and Spatially Constrained) inversions of the AEM data were carried out, with refinements made as additional information on vertical and lateral constraints became available. Finally, a Wave Number Domain Approximate (WANDA) Inversion procedure with a 1D multi-layer model and constraints in 3D, was used to produce a 3D conductivity model. This inversion procedure only takes days to run, enabling the rapid trialing to select the most appropriate vertical and horizontal constraints. Comparison of borehole induction logs with adjacent AEM fiduciary points confirms high confidence levels in the final inversion, however, the hydrostratigraphy mapped using all of these inversions was unable to resolve fundamental aspects of the hydrogeological system, particularly in the near-surface (top 20 m), where hydrodynamic data indicated a connection between the major rivers and the underlying aquifers, either through incision and/or through faults (and bypass flow).

To resolve these issues, a trans-disciplinary approach (Stokols *et al*., 2008) was used to investigate all underlying assumptions within discipline and inter-disciplinary approaches, including the regularization used in the AEM inversion. In modern laterally-correlated inversion of AEM data, the usefulness of the resulting inversion models depends critically on an optimal choice of the vertical and horizontal regularization of the inversion. Set the constraints too tight, and the resulting models will become overly smooth and potential resolution is lost. Set the constraints too loose, and spurious model details will appear that have no bearing on the hydrogeology. There are several approaches to an automatic choice of the regularization level in AEM

inversion based predominantly on obtaining a certain pre-defined data misfit with the smoothest possible model.

In this study, we used a pragmatic approach to optimizing the constraints by an iterative procedure involving all available geological, hydrogeological, geochemical, hydraulic and morphological data and understanding. In this approach, in a process of both confirming and negating established interpretations and underlying assumptions, the inversion results are judged by their ability to support a coherent conceptual model based on all available information. This approach is dependent on integrating a team of scientists, where all facets of data and interpretation are considered and questioned in a trans-disciplinary analysis of the hydrological system. Necessary elements for this approach to succeed are the experience and professional insights of the scientists involved and a willingness and ability of scientists from diverse areas to establish a dialogue that will question and refine the inversion constraints and the quality of the final hydrogeological conceptual model.

The trans-disciplinary approach has been essential to resolving many of the more complex biophysical and hydrological systems interactions, and essential in the assessment of MAR and groundwater extraction options. The resultant improved 3D conductivity model revealed details of the hydrostratigraphy and neotectonics. Prior to the mapping of near-surface hydrostratigraphy and structural features, it had not been possible to explain apparently contradictory data, nor develop a plausible hydrogeological conceptual model. A pragmatic approach to optimizing the constraints was achieved using an iterative procedure involving all available geological, hydrogeological, geochemical, hydraulic and morphological data and understanding. In this approach, in a process of both confirming and negating established interpretations and underlying assumptions, the inversion results are judged by their ability to support a coherent conceptual model based on all available information.

In summary, a trans-disciplinary 3D hydrological systems mapping approach (Lawrie *et al*., 2000, 2008), has been developed in this project to guide development of new geological and hydrogeological conceptual models, and to provide a framework for understanding complex hydrogeological and hydrogeochemical processes (Lawrie *et al*., 2012b). Integration of the 3D mapping with hydrochemical and hydrodynamic data provides critical new insights into surface-groundwater interactions and groundwater flow. Using this approach, it has been possible to develop a new understanding of recharge processes, and identify potential recharge and groundwater flow pathways (Lawrie *et al*., 2012b).

The new datasets, knowledge and hydrogeological conceptual models generated in the project have provided a reliable basis for the identification, characterisation and initial assessment of groundwater resources and MAR options (Lawrie *et al*., 2012c, d). The products and knowledge generated will also provide important inputs to assist with the parameterisation of groundwater and solute transfer models (Lawrie *et al*., 2012b) that are critical to the next steps in the assessment of MAR and groundwater extraction options in the area.

## 2.6 USING AEM TO MAP MAR AND GROUNDWATER RESOURCE TARGETS

Previously, the high cost of investigations, low level of knowledge of risk, and time taken to fill hydrogeological knowledge gaps have been a deterrent to development of MAR options, especially in pioneering projects in new and/or more remote locations. In the BHMAR project, the initial scoping study concluded that despite the paucity of data, there were a number of possible MAR and groundwater resource targets in the Darling Floodplain near Menindee (Lawrie *et al*., 2008a, 2009a, b).

To meet the challenge of rapid identification and assessment of potential MAR targets and groundwater resources over a large area (7,541.5 $km^2$) within relatively short timeframes (18 months), it was concluded that the only cost-effective method with the ability to resolve features in this depth range was airborne electromagnetics (AEM) (Lawrie *et al*., 2009a, b).

AEM methods for near-surface hydrogeological investigations have undergone significant improvements in the past 10-15 years (Auken *et al*., 2006; Thompson *et al*., 2007; McNae, 2007). The depth of investigation and spatial resolution of these AEM systems varies significantly with system type and depending on ground

conditions (Spies & Woodgate, 2005; Sorensen & Auken, 2004; Munday, 2008). AEM methods have been used successfully to map the hydrogeology and variations in groundwater salinity in a range of geological environments (Siemon *et al*., 2009; Viezzoli *et al*., 2011; Abraham *et al*., 2012). Successful applications include the mapping of seawater intrusion interfaces in both clastic and carbonate aquifer systems (Fitterman & Deszcz-Pan, 1998; D'Ozouville *et al*., 2008; Supper *et al*., 2009; Siemon & Steuer, 2011), saline groundwater plumes (Paine, 2003), freshwater-salt water interfaces beneath inland lakes (Martinez & Pitcher, 2008), and surface-groundwater interaction associated with rivers (Paine *et al*., 2009). AEM methods have also been used to map karstic aquifer systems (Doll *et al*., 2000; Smith *et al*., 2003, 2005, 2008) and key elements of the hydrostratigraphy in clastic sedimentary systems (Abraham *et al*., 2011a), including faults (Bedrosian *et al*., 2012).

In Australia, the application of electromagnetic (EM) methods for hydrogeological investigation is made more complex by the highly salinized nature of many of the landscapes, which can also be often deeply and variably weathered. In many instances, the electrical conductivity distribution does not equate with formation (and/or hydrogeological) boundaries, but instead to a combination of groundwater salinity and formation composition and texture (Lawrie *et al*., 2000, 2003a, 2009). A review facilitated by the Australian Academy of Sciences and the Australian Academy of Technological Sciences and Engineering for the Australian Federal Government's Natural Resource Management Ministerial Council found that, despite the additional challenges posed by regolith and groundwater salinization, AEM is the only broadacre technique that can detect and resolve hydrostratigraphy and groundwater quality (salinity) in the sub-surface deeper than the root zone (Spies & Woodgate, 2005).

The processing of AEM data and the presentation of conductivity data as maps and sections is now routine, and particularly effective in regolith and flat to shallow-dipping sedimentary environments (Lane, 2000, 2002; Lawrie *et al*., 2000), at the scale of the 'footprint' of most AEM systems (Munday, 2008). AEM methods are particularly relevant for regional scale mapping, with ground EM methods required for higher resolution mapping at local scales (Lawrie *et al*., 2009c, 2012a).

The complex electrical structure of Australia's near-surface landscapes and the presence of conductive layers and basement in many regolith terrains, has necessitated the development of constrained inversion approaches that utilise a priori geological, hydrogeological and hydrogeophysical data (Green & Munday, 2004; Lane *et al*., 2004; Lawrie *et al*., 2012). Constrained inversions, combined with rigorous technology selection, and appropriate calibration and validation procedures (Christensen & Lawrie, 2012), have enabled key elements of the hydrostratigraphy and variability in groundwater salinities to be resolved in many of Australia's unique landscape settings (Lane *et al*., 2004; Lawrie *et al*., 2008, 2009c, 2010c). These approaches have enabled successful mapping and assessment of groundwater salinity hazard in a range of floodplain environments (George *et al*., 1998; Lawrie *et al*., 2000, 2003a, b, 2004, 2008b, 2009c, 2010c; Lane *et al*., 2004; Chamberlain & Wilkinson, 2004; Walker *et al*., 2004; Munday *et al*., 2006, 2007, 2012; Cresswell *et al*., 2007; Palamera *et al*., 2010; Munday, 2010; Tan *et al*., 2012). Using similar approaches, AEM surveys have also been used to detect potential groundwater resources (George *et al*., 1998; Edwards & McAuley, 2008; Lawrie *et al*., 2009c; Fitzpatrick *et al*., 2010) and seawater intrusion interfaces (Fitzpatrick & Munday, 2006; Munday, 2010; Tan *et al*., 2012), despite near-surface salinisation.

Importantly, studies in Australia have also demonstrated that the benefits from new AEM technologies and constrained inversion modeling are maximised when these technologies are employed within trans-disciplinary, systems-based approaches to the analysis of problems and the development of customised interpretation products (Lawrie *et al*., 2000, 2003a, b, 2009c, 2010c; George *et al*., 2003; Spies & Woodgate, 2005). Systems-based approaches incorporate an understanding of landscape evolution and scale, utilise modern investigative approaches to the conceptualisation of groundwater systems, and incorporate data on mineralogy, petrophysics, hydrology, ecology, topography, hydrogeochemistry and hydrodynamics. Within this trans-disciplinary research framework, the power and long-term value of AEM-based datasets for groundwater management lies largely in providing stakeholders with a range of customized interpretation products derived from the integration of electrical conductivity data with other hydrogeological, hydrogeophysical and hydrochemical datasets (George *et al*., 2003; Lawrie *et al*., 2000, 2008, 2009c, 2010c).

Over the past five years, a staged approach to survey design combined with forward modelling studies has ensured that appropriate AEM technologies are selected to match the target objectives (Green & Munday, 2004; Lawrie, 2006; Munday *et al*., 2007, 2008d; Lawrie *et al*., 2009b, c, 2010c). In Australian landscape settings AEM-based products have proven effective at providing high resolution baseline data on the spatial distribution of aquifers and aquitards as well as water quality and salt stores in shallow (<120 m) floodplain sediments (Tan *et al*., 2005; Munday *et al*., 2006, 2007; Lawrie *et al*., 2009c, 2010c; Mullen *et al*., 2007). However, while these datasets and information products address specific gaps in the biophysical knowledge framework, addressing salinity and land management questions usually requires an understanding of underlying biophysical processes and dynamics that often cannot reliably be determined from analysis of spatial patters of conductivity alone (Cresswell *et al*., 2007, Lawrie *et al*., 2010c).

The BHMAR AEM survey has built significantly on the principles, methodologies, experience and products developed for salinity mapping and management in Australia. In particular, the staged approach to technology selection and survey design (Lawrie, 2006; Lawrie *et al*., 2009c, 2010c), and the use of a 4D systems approach to integrate complex datasets and develop a range of customised information products for use in subsequent hydrogeological and geotechnical modelling was recognised as critical to the success of the survey. The BHMAR survey would appear to be the first use of AEM methods in MAR investigation and assessment.

### 2.6.1 3D Mapping of Hydrostratigraphy, Structure and Groundwater Salinity

To meet the challenge of rapid identification and assessment of potential MAR targets and groundwater resources over a large area (7,541.5 km$^2$) within relatively short timeframes (18 months), it was concluded that the only cost-effective method with the ability to resolve key features of the hydrogeological system in the 0-150 m depth range with the density of information (and certainty) required, was airborne electromagnetics (AEM) (Lawrie *et al*., 2009a, b).

In Australia's salinized landscapes, AEM has been used effectively to map hydrostratigraphy, groundwater salinity, salinity hazard and risk, and groundwater resources, in a number of floodplain environments, including the Basin. In the BHMAR study, it was necessary to select an AEM system with the capability of mapping key functional elements of the hydrogeological system critical to the success in identifying and assessing suitable MAR and groundwater resource targets. This necessitated selecting an AEM system capable of mapping heterogeneities in the hydrostratigraphy and hydrogeology, and more specifically, the:

- Thickness and extent of near-surface unconfined aquifers and aquitards that might provide recharge pathways or inhibit surface-groundwater connectivity;
- Thickness, extent and internal textural variability of Pliocene sand aquifers;
- Thickness, extent and internal variability in upper (Blanchetown Clay) and lower (upper Renmark Group) confining aquitards that 'sandwich' the Pliocene sand aquifers;
- 3D distribution of groundwater salinity (to help define fresh and brackish groundwater resources);
- Faults that might act as discrete recharge and groundwater flow pathways; and
- Zones of inter-aquifer leakage.

Experience over the past 15 years has demonstrated that the use of AEM for near-surface hydrogeological investigations often requires higher resolution data than typically used in regional mineral exploration. High resolution data over large areas are required to map key functional elements of often complex hydrogeological systems (Spies & Woodgate, 2005; Auken *et al*., 2006; Lawrie *et al*., 2009e). Optimization of AEM data therefore requires careful consideration of AEM system suitability, calibration, validation and inversion methods (Green & Munday, 2004; Lane *et al*., 2004; Christensen & Lawrie, 2012).

In the BHMAR project, the helicopter-borne SkyTEM transient EM system was selected after forward modeling of system responses and comparative assessment of test line data from two systems over potential

targets (Lawrie *et al*., 2009b). The SkyTEM system is a high-resolution helicopter-borne time-domain electromagnetic system, and was developed specifically for high-resolution groundwater and environmental investigations. It was developed as a rapid alternative to ground-based TEM surveying and has the advantage of delivering much higher data density and spatial area coverage.

The BHMAR survey involved acquisition of 31,834 line km of data over an area of 7,500 $km^2$ of the River Darling Floodplain, and was acquired by two systems over a 9-week period. Initially the geophysical data was inverted (modelled) using "Fast Approximate Inversions (FAI)" software, in order to generate data that could be viewed as flight–line sections within 48 hours of acquisition, and gridded to provide maps to guide a field investigation program. More information regarding the survey is included in Lawrie *et al*. (2012a).

The AEM data were used to target 100 sonic and rotary mud holes that were used for calibration and validation of the survey results. Subsequently, a number of different (Laterally and Spatially Constrained) inversions of the AEM data were carried out, with refinements made as additional information on vertical and lateral constraints became available. Finally, a "Wave Number Domain Approximate Inversion" procedure (Christensen, 2012; Lawrie *et al*., 2012a), with a 1D multi-layer model and constraints in 3D, was used to produce a 3D conductivity model (Lawrie *et al*., 2012a). This inversion procedure only takes days to run, enabling rapid trialing to select the most appropriate spatial constraints. Methods pertaining to the generation of the inversions and derivative products are documented in detail in Lawrie *et al*. (2012a).

### 2.6.2 Customised Interpretation Products

A suite of customized interpretation products were produced through integration of AEM data with the other project datasets, notably the information from 40 new rotary mud and 60 sonic-cored holes. Data obtained from the drilling program includes: sedimentary facies, textures (including grain size), mineralogy, redox state and whole rock geochemistry; hydrogeophysical data (nuclear magnetic resonance (NMR), induction and gamma logs); hydraulic data (from slug and pump tests), hydrochemistry (from groundwater and porefluid samples), and hydrodynamic data from the monitoring of groundwater levels in 40 boreholes pre- and post-flooding in 2010-2011.

Customised interpretation products developed through integration of these datasets include maps of:

- The sedimentary system including the location of palaeochannels with favourable hydraulic properties;
- Hydrostratigraphy including the thickness, extent and depth to unconfined and confined aquifers;
- The thickness, extent, depth to, and holes in confining aquitards;
- Textural classes within the clastic sedimentary system;
- Neotectonic elements including faults that might act as potential recharge, inter-aquifer leakage and groundwater flow pathways;
- Groundwater salinity (to help define fresh, 'acceptable' and brackish groundwater resources, and potential zones of salinity ingress), and salt store in the unsaturated zone;
- Zones of inter-aquifer leakage;
- Aquifer transmissivity;
- MAR storage volumes;
- Groundwater storage estimates in various water quality classes (0-600; 600-1200; and 1200-3000 mg/L).

Development of these customised interpretation products was critical to the completion of MAR risk assessments and the assessment of potential groundwater resources.

# 3 Managed Aquifer Recharge and Water Quality Guidelines, and Cultural Heritage

The data acquisition and scientific investigations of the BHMAR project were undertaken within frameworks defined by national guidelines and State and Federal regulatory requirements. In terms of MAR assessment, the project applied the framework established by the Australian Guidelines for Managed Aquifer Recharge (NRMMC–EPHC–NHMRC, 2009) and Water Recycling: Augmentation of Drinking Water Supplies (NRMMC–EPHC–NHMRC, 2008). The water chemistry data were evaluated against the recently updated Australian Drinking Water Guidelines (NHMRC-NRMMC, 2011).

The on-ground activities associated with drilling, bore construction and pump testing required licensing and permissions by NSW State land and water regulatory agencies. This included implementing strategies for the assessment and protection of any indigenous culturally significant sites, the protection of significant vegetation communities and ecosystems, the rehabilitation of disturbed ground, the containment of drilling muds and the appropriate discharge of pumped groundwater, amongst other logistical issues.

This section describes these national and State-based guidelines and regulatory frameworks in greater detail.

## 3.1 MAR OPTIONS AND ASSESSMENT GUIDELINES

### 3.1.1 MAR Options Considered in the BHMAR Project

Managed Aquifer Recharge (MAR) covers a range of on-ground works that seek to deliberately increase the volume of water stored in an aquifer for recovery at a later date. Groundwater recharge is enhanced, rather than solely relying on natural processes such as rainfall or river leakage to replenish the aquifer storage. Figure 3-1 provides schematics of the various types of MAR options (Dillon *et al*., 2005).

Aquifer Storage and Recovery (ASR) involves injection of water into an aquifer via a well, and recovery from the same well (Figure 3-1a). The aquifer may be confined or unconfined. This is useful in brackish aquifers, where storage is the primary goal and water treatment is a smaller consideration. Aquifer Storage, Transport and Recovery (ASTR) uses an adjacent well to draw the water through the aquifer which extends the residence time in the aquifer beyond that of a single well, increasing the opportunity for water quality treatment (Figure 3-1b). The most likely MAR scheme to be implemented in the study area is ASR, using the Calivil Formation aquifer in particular. The potential design and cost of implementing and operating an ASR scheme at Menindee has been previously considered (SKM, 2010, Lawrie *et al*., 2010c) and was further developed in the latter phases of the BHMAR project.

Bank filtration makes use of hydraulic connections between the river and the shallow alluvial aquifer (Figure 3-1c). Pumping from near-river shallow bores or caissons can induce infiltration from the river and through the shallow aquifer. The adsorptive capacity of the aquifer provides the potential for improved and more consistent water quality by removing impurities (such as suspended solids, nutrients or pathogens). There is potential to apply bank filtration using shallow bores (or caissons, horizontal wells or galleries) in the Coonambidgal or Menindee Formation aquifers. Pumping, particularly during high flows in the Darling, could provide additional source water that could be of better quality (in terms of turbidity, nutrients and organic carbon) than the raw river water. This would reduce treatment requirements for ASR injection into the target Calivil Formation aquifer.

Dune filtration is used primarily for water treatment where water is pumped into a dune swale and then harvested at a lower level after gravity transport through the dune sands (Figure 3-1d). This can have water quality benefits by removing organic material, nutrients or pathogens, but can also potentially provide pathways for recharge to underlying aquifers. Detailed geomorphic mapping across the Darling floodplain recognised several dune morphology types and ages. AEM mapping validated by drilling and augering, shows that there is commonly a thick mud drape beneath the dunes, with minor localised groundwater

perching. There are also cemented hardpan layers in many of the dunes. The dunes do not appear to provide a recharge pathway to suitable aquifers at depth. Dunes in the study area often contain sites of cultural and heritage sensitivity. The overall assessment is that dune filtration is not an effective MAR option in the study area.

Basin infiltration involves pumping or diverting water onto a permeable surface area above the target aquifer to allow vertical infiltration to the shallow watertable (Figure 3-1e). Near-river infiltration basins or channels can be constructed, allowing controlled diversion from the river during favourable flow conditions. The advantage of shallow basins is that they are readily accessible in terms of the removal of any veneers of mud or organic material which accumulate and impede infiltration. Laboratory experiments of clogging were carried out as part of the BHMAR study, and a number of field sites examined to assess infiltration rates. Particular attention was paid to observations of infiltration and aquifer responses during flooding. Near-surface mud horizons as well as the laterally extensive Blanchetown Clay make the locating of suitable sites for infiltration basins difficult across the Darling floodplain. However, the AEM and interpreted mapping projects are invaluable in targeting sites of preferential leakage in the floodplain, particularly defining pathways to the target Calivil Formation aquifer.

More sophisticated infiltration galleries are geotechnically-stabilised buried trenches (such as with polythene cells or slotted pipes) in permeable media (Figure 3-1j). Dry wells are used where the watertable is relatively deep (Figure 3-1k). Like infiltration basins, these structures facilitate infiltration through the unsaturated zone to the unconfined aquifer. However, they lack the ease of maintenance in terms of removal of clogging material and because of this would likely require pre-treatment of the source water.

Soil aquifer treatment is a specific application of infiltration basin where treated sewage effluent is intermittently introduced to a basin to facilitate leakage to the watertable. The objective of water treatment, relying on transport through the unsaturated zone to facilitate removal of nutrients and pathogens. For the BHMAR study, the Darling River water is the most readily available source water for MAR operations, with the availability of treated sewage effluent limited.

Percolation tanks are dams constructed across ephemeral streams to retain water and facilitate infiltration to the unconfined aquifer (Figure 3-1g). There are ephemeral streams in the study area, particularly draining off the Broken Hill Block to the northwest. However, the large distances between potential sites for percolation tanks and the existing water supply infrastructure and pipeline would make these an uneconomic option. The overall water budgets of these streams are minor compared to the potential MAR source water availability in the Menindee Lakes Storages. These issues also apply for sand dams where structures across ephemeral streams are designed to trap sediment to create suitable aquifer material (Figure 3-1h) as well as for recharge releases, where water is released from dams on ephemeral streams (Figure 3-1i).

In summary, of the range of MAR strategies, the BHMAR project has considered dune filtration, bank filtration, infiltration basin, Aquifer Storage and Recovery (ASR), and Aquifer Storage, Transport and Recovery (ASTR) options (Figure 3-1).

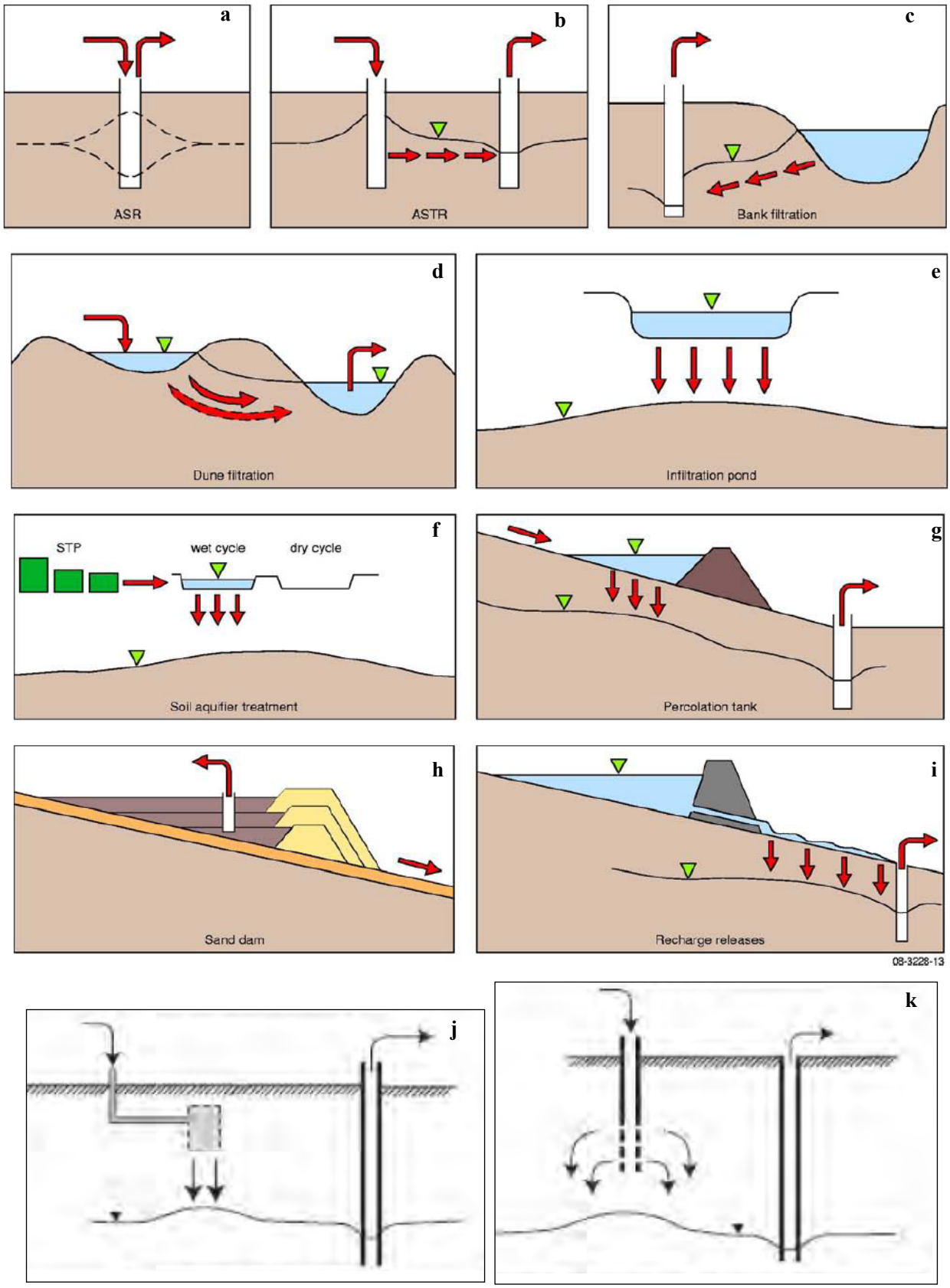



**Figure 3-1.** *Schematic diagrams showing MAR options (a) Aquifer Storage and Recovery, ASR (b) Aquifer Storage, Transport and Recovery, ASTR (c) bank filtration (d) dune filtration (e) infiltration pond (f) soil aquifer treatment (g) percolation tank (h) sand dam (i) recharge releases (j) infiltration gallery (k) dry well (from Dillon et al., 2005).*

### 3.1.2 MAR Risk Assessment Framework Used in BHMAR Phase 1

In Phase 1 of the BHMAR project, a novel assessment framework was developed for MAR site selection in data poor areas (Lawrie *et al*., 2009a). An initial scoping study identified five broad areas within a 150 km radius of Broken Hill where MAR storage options and/or groundwater extraction could provide alternative sources of water for the town (Lewis *et al*., 2008). However, in order to select a single area, and focus the next phase of hydrogeological investigations, an assessment framework was developed for MAR site selection.

Specific options assessed, included:

- Enhanced recharge or extraction of fresh to brackish quality water from near-surface (0-30 m) alluvial aquifers and river flush zones.
- Extraction of fresh to saline groundwater from intermediate-level (30-120 m) aquifers; and/or use of these formations for MAR.
- Extraction of brackish groundwater or use of storage in deeper (>250 m) aquifers.
- Groundwater resource and MAR potential of alluvial fan systems.
- Capture of groundwater seepage from existing reservoirs.

The assessment framework utilised a matrix approach, and prioritised two key criteria:

- The likelihood of technical success: accounting for the probability that the required groundwater resource is likely to be present, discoverable with the available technology, and the water supply alternative can be implemented.
- The likelihood of negative consequences: accounting for the potential and significance of impacts to the water resource, ecosystems and other groundwater users if the option was to be implemented.

The approach also included an analysis of the characteristics of key aquifer systems in each of the five priority areas, with a focus on a review of their internal architecture and yield potential, in addition to their bounding relationships. As a result of this risk assessment, the Darling Floodplain was ranked as the highest priority, and the BHMAR Project Phase 2 was established. Final project boundaries were chosen based on the use of salinity-yield maps to delineate zones of possible fresh to brackish groundwater in target aquifers.

## 3.2 NATIONAL MAR RISK ASSESSMENT FRAMEWORK USED IN BHMAR PHASES 2-3A

In Australia, a stringent risk assessment framework for consideration of MAR schemes was adopted in 2008-2009. The national risk assessment framework is set out in the Australian Guidelines for Water Recycling: Augmentation of Drinking Water Supplies (NRMMC–EPHC–NHMRC, 2008) and Managed Aquifer Recharge (NRMMC–EPHC–NHMRC, 2009). Importantly, this approach, and the detailed steps outlined within, were developed after commencement of Phase 2 of the BHMAR Project, and hence there is not an exact match between the 5-Phase approach identified in the BHMAR project (Lewis *et al*., 2008, Lawrie *et al*., 2009a), and the 4-step risk management approach assessment approach identified in the new national MAR risk management framework (NRMMC-EPHC-NHMRC, 2009).

The national guidelines ensure that considerable investigative effort is undertaken to assess the viability of proposed schemes, and to ensure the engineering design meets all requirements and standards. In particular, hydrogeological investigations are undertaken in a phased approached to ensure aquifer suitability. These investigations take time, and rigorous risk assessments are carried out at each stage in the investigations to ensure all aspects of MAR viability are considered in a timely and cost-effective manner. The new national approach provides a useful framework for assessing MAR options, and for assessing suitability against water quality guidelines in particular.

Essentially, the risk assessment framework encompasses four stages of project development and assessment, with the information required for assessment at each stage increasing in complexity. The four stages are shown in Figure 3-2. Phase 2 and 3 of the BHMAR Project were completed using these new guidelines. Interim assessments carried out against Stage 1 of the national assessment framework for the BHMAR project were reported in Lawrie *et al*. (2010b, c), with interim findings for Stage 2 assessments for a priority area reported in Lawrie *et al*. (2011). Final assessments are documented more fully in Lawrie *et al*. (2012c), with assessments for the highest priority sites and options summarised later in this report.

The four assessment MAR stages (Figure 3-2) identify:

- Entry-level risk assessment. This involves gathering information that is normally readily available within the locale of the project and performing a basic desktop assessment to determine whether the project is viable and the likely degree of difficulty. This indicates the extent of field investigations required in Stage 2.
- Maximal risk assessment. These baseline investigations and site-specific data reveal inherent risks associated with a checklist of key hazards. This assessment will reveal whether preventive measures are required (as is normally the case).
- Residual risk assessment (pre-commissioning). This assessment identifies proposed preventive measures and operational procedures that will ensure acceptably low residual risks to human health and the environment from constructing and commissioning the project. This assessment also informs on hazards or aspects that require validation monitoring during commissioning trials.
- Residual risk assessment (operational). This is based on the results of commissioning trials and determines whether the ongoing operation of the project has acceptably low residual risks to human health and the environment. This assessment also informs the risk management plan including types and levels of verification and operational monitoring for ongoing operation of the project.

The detailed objectives of each of these risk assessment steps are shown in Table 3-1 and Table 3-2. Stage 1 of the national MAR risk assessment approach (Figure 3-2) envisages that an Entry-level risk assessment can be completed using existing information in a desktop study (Table 3-2). Unfortunately, this approach does not fully take into consideration regional MAR investigations in large data-poor areas such as the Darling Floodplain. In the BHMAR project area, an Entry-level risk assessment was not deemed feasible without the acquisition of new hydrogeological datasets.

New hydrogeological investigations and groundwater modelling have been identified as necessary in Stage 2 of the new risk assessment framework (Table 3-1 and Table 3-2; NRMMC-EPHC-NHMRC, 2009). However, the investigative phase of Stage 2 in the new risk assessment approach is designed to characterise specific sites in detail, while Phase 2 of the BHMAR Project is restricted to a detection and assessment of MAR options at a regional scale, with limited data on individual potential targets. Furthermore, Stage 2 of the new risk management approach (Figure 3-2) incorporates site-specific hydrogeochemical, water-rock interaction and groundwater modelling studies, while these have been earmarked for Phase 3 of the BHMAR study (Figure 3-2).

In summary, the acquisition and interpretation of new hydrological and geoscientific datasets in Phase 2 of the BHMAR Project, enabled an entry-level risk assessment of MAR options to be carried out for a number of sites and options. Entry-level risk assessment evaluates the apparent viability of managed aquifer recharge, and is undertaken in two parts:

- A viability assessment, which is intended to inform proponents of any fatal flaws in their intended project, based on existing, readily available information; and
- Assessment of the likely degree of difficulty of the project, which is intended to provide information about the amount of effort likely to be needed to achieve public health and environmental approvals from the relevant jurisdiction.

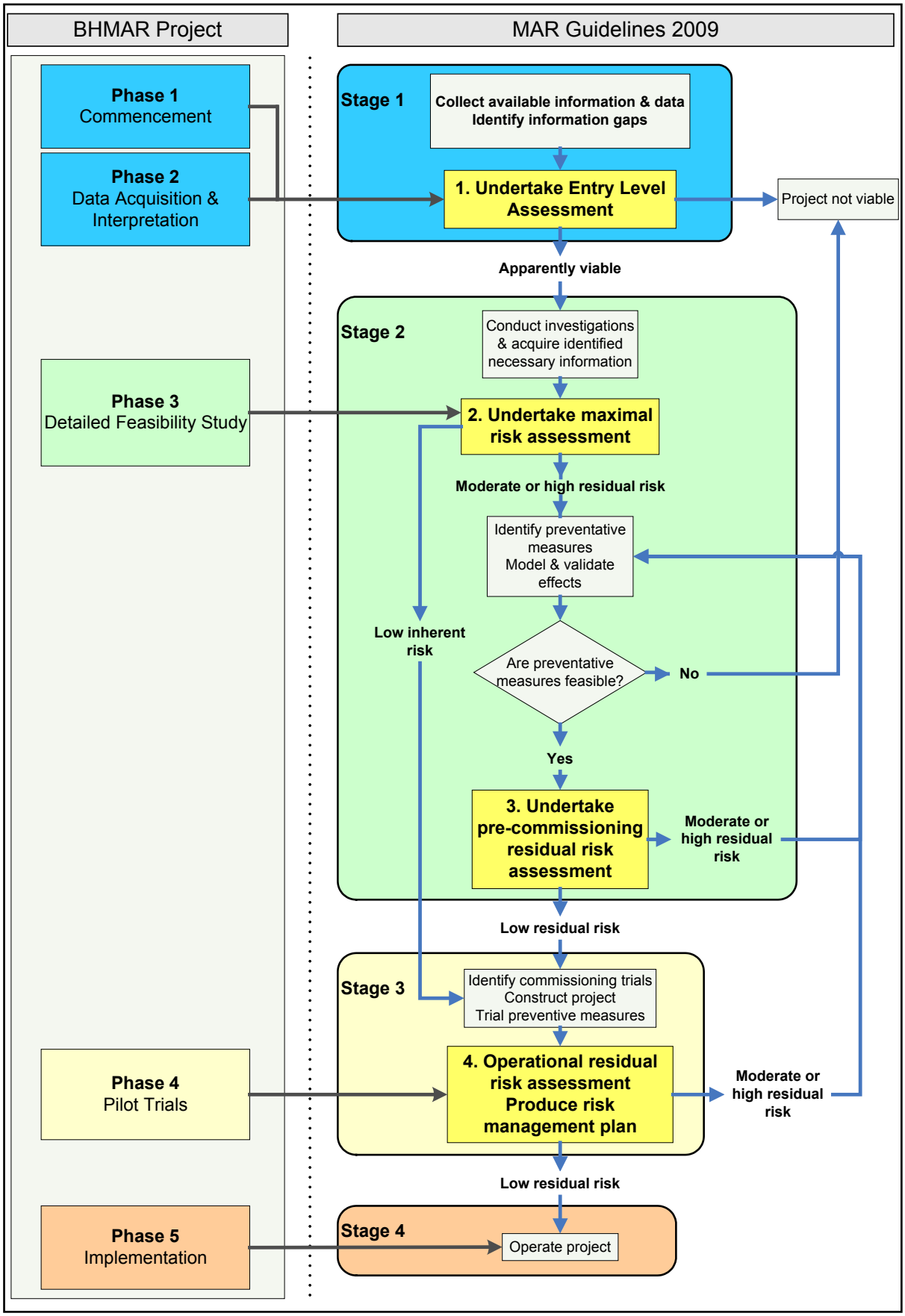



**Figure 3-2.** *Stages in establishing a MAR project to meet human health and environmental needs in accordance with MAR Guidelines (NRMMC-EPHC-NHMRC, 2009).*

**Table 3-1.** *The 4-stage approach for assessing risks in MAR projects. From the National MAR Guidelines (NRMMC-EPHC-NHMRC, 2009).*

| Assessment Stage | Information Available | Objectives |
|---|---|---|
| 1. Entry-level risk assessment | Existing information and regulations<br>(Stage 1) | To assess likely presence of a suitable aquifer<br>To assess conformity with catchment and aquifer management plans and local government requirements<br>To identify, using only rudimentary information, the likely degree of difficulty of the managed aquifer recharge project; this will inform the extent of investigations and level of operational expertise likely to be required at Stage 2 |
| 2. Maximal risk assessment | Investigations (Stage 2) plus Stage 1 | To assess whether the project has low maximal (inherent) human health and environmental risks based on investigation data<br>In low maximal risk cases, planning for construction and commissioning is simplified. This avoids the requirement for additional preventive measures and pre-commissioning residual risk assessment<br>In moderate or high maximal risk cases, preventive measures must be identified |
| 3. Residual risk assessment: precommissioning | Investigations (Stage 2) plus Stage 1 | To assess whether proposed preventive measures and operational procedures ensure acceptably low residual risks to human health and the environment from constructing and commissioning the project<br>To inform on hazards or aspects that may require validation monitoring during commissioning trials |
| 4. Residual risk assessment: operational | Validation data from commissioning (Stage 3) plus Stages 1 and 2 | To assess whether ongoing operation of the project has acceptably low human health and environmental risks<br>To inform the management plan, including operational and verification monitoring for ongoing operation (Stage 4) |

**Table 3-2.** *Details of the activities proposed to be undertaken in the 4-stage approach for assessing risks in MAR projects. From the National MAR Guidelines (NRMMC-EPHC-NHMRC, 2009).*

| Assessment Stage | Issues Addressed |
|---|---|
| **Desktop** | Type and scale of scheme<br>Source-water availability<br>Compatibility with catchment and groundwater management plans<br>Intended uses of recovered water<br>Existence of a suitable aquifer<br>Source water, native groundwater and end-use environmental values<br>Similarity to successful projects<br>Management capability<br>Planning and development requirements<br>Preliminary evaluation of project viability and degree of difficulty |
| **Investigations, drilling, basic modelling** | Source-water quality<br>Source-water catchment land use assessment<br>Groundwater quality<br>Soil, aquifer and aquitard characteristics, and fate of recharged water<br>Aquifer storage competence<br>Groundwater pressures and gradients<br>Reactions between recharge water, groundwater and aquifer minerals<br>Water treatment options and effectiveness<br>Management of clogging<br>Biodegradation and inactivation of contaminants |
| **Trials, detailed modelling** | Effectiveness of preventive measures and operational controls<br>Suitability of recovered water for intended uses<br>Size of attenuation and impact zones<br>Recovery efficiency<br>Targeted studies covering identified hazards |

### 3.2.1 MAR Viability Assessments

At the most fundamental level, there are five critical elements for a successful MAR project (Dillon *et al*., 2009). These are:

- A sufficient demand for recovered water;
- An adequate source of water for recharge;
- A suitable aquifer in which to store and recover the water;
- Sufficient land to harvest and treat water;
- Capability to effectively manage a project.

Addressing these five key questions is the first step in an entry-level MAR assessment, and is termed a MAR Viability Assessment. These five criteria are explained below, and an example of the decision process given in Figure 3-3.

**Demand:** The volumetric demand for recovered water (within an economic scale) or a clearly defined environmental benefit of recharge is essential for MAR. The purposes for which water will be recovered also need to be defined. Generally, this will provide the revenue stream to pay for the water supply cost elements of the project.

**Source:** Entitlement to water to be used for recharge needs to be secured. Mean annual volume of recharge should exceed mean annual demand with sufficient excesses to build up a buffer storage to meet reliability and quality requirements. In an over-allocated catchment it is unlikely that an entitlement to surface water would be available.

**Aquifer:** A suitable aquifer is critical for MAR. It needs to have an adequate rate of recharge, sufficient storage capacity and be capable of retaining the water where it can be recovered. Low salinity and marginally brackish aquifers are preferred so that mixing with fresh recharge water should still allow recovered water to be fit for use. Maps of MAR opportunity will assist in determining likelihood of one or more suitable aquifers being present at the proposed site.

**Detention Storage:** There should be open space, or dams, wetlands, ponds or basins to detain sufficient water without causing flood damage to enable the target volume of recharge to be achieved. Similarly, there needs to be space available for whatever treatment process, if any, is subsequently determined to be required.

**Management capability:** Hydrogeological and geotechnical knowledge, as well as knowledge on water storage and treatment design, water quality management, water sensitive urban design, hydrology and modelling, monitoring and reporting are all required to meet governance requirements. Such expertise will be required from Stage 2 and a growing number of consultants are experienced in investigations and design of MAR projects. National guidelines have been developed.

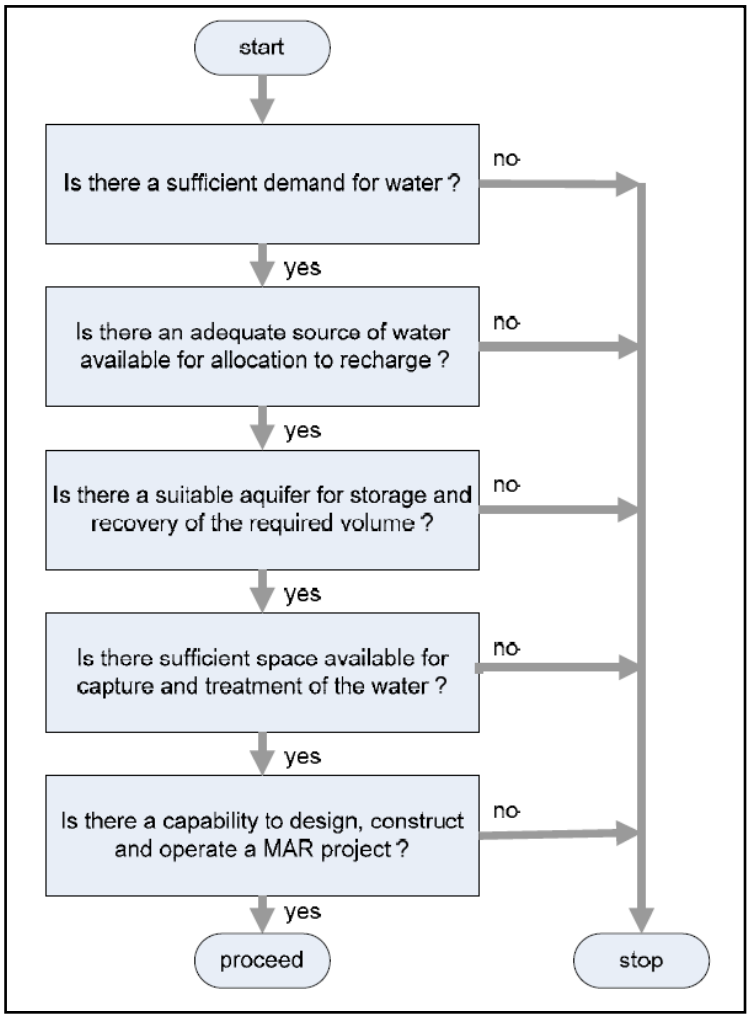



**Figure 3-3.** *MAR viability assessment decision flow chart.*

If the answer to **all** of the questions given in Figure 3-3 is *'Yes'*, proponents then proceed to determine the *degree of difficulty*. In the BHMAR project, the project scope was restricted to an assessment of hydrogeological issues, with consideration of water entitlements and management capacity the remit of the Department of the Environment and the broader Darling River Water Savings Project (DRWSP).

### 3.2.2 Degree of Difficulty Assessments

The second part of the **entry-level** assessment is intended to inform stakeholders of the degree of difficulty of the proposed project (NRMMC-EPHC-NHMRC, 2009). It also serves as a preliminary indicator of human health and environmental risks. The entry-level assessment is intended to help proponents to make better informed decisions about whether to proceed with the Stage 2 investigations that would allow a more rigorous risk assessment (of specific sites).

The template for the degree of difficulty assessment provides 14 questions related to information needs, and the answers determine the scope of Stage 2 (site-specific) investigations. The 14 questions are detailed below. The number of questions for which additional information is required in Stage 2 is a further qualitative indicator of the degree of difficulty of a project. It is also an indicator of the order of magnitude of resources likely to be required for investigations and for the preventive measures that would be needed to result in a low level of risk at a subsequent pre-commissioning risk assessment, which in turn would enable construction and trials (NRMMC-EPHC-NHMRC, 2009).

Answers to the questions asked in these assessments are indicative only, and suggest the level of effort required for next stage investigations (and subsequent maximal and residual risk assessments prior to commissioning). Some criteria are more onerous than for subsequent assessments (e.g. depth to watertable for infiltration systems), because considerably more information on sub-surface conditions is needed than is presumed to be available at the entry-level stage in order to be able to assess actual risk. By answering these entry-level questions, proponents will discover the types of information that will subsequently be required. Projects that have a high degree of difficulty for a large number of questions will require substantial Stage 2 investigations and/or preventive measures. In such cases, reconsideration of the project concept or location may potentially be more cost effective.

Also of note is the method chosen for recharge depends on site-specific conditions. If aquifers are confined, then well-injection methods are preferred; these include ASR and ASTR. If infiltration is restricted by surficial mud, then galleries, ponds, sumps or wells may be constructed to completely penetrate the low-permeability layer, exposing underlying formations that have higher permeability. The chosen configuration and size will depend on a range of factors, including the depth to the base of the confining mud layer (Lawrie *et al*., 2010c, 2012c). The guidelines have produced a risk matrix to help with assessments (Table 3-3). However, it should be noted that is this is followed prescriptively, all intended drinking water uses are assessed as a high risk, and need to be further qualified.

The assessment method outlined above has enabled confidence estimates to be placed on the viability of implementing a MAR system in the Menindee region. The approach adopted in the BHMAR Phase 2 study enabled potential MAR sites to be identified, and enabled the identification of specific issues for further detailed investigation and modelling of prioritised sites in Phase 3.

It is further noted that to complete **maximal risk** and **pre-commissioning residual risk assessments** (identified in Stage 2 of the national risk assessment framework), infill drilling, and site-specific hydrogeochemical, water-rock interaction and groundwater modelling studies, were required. Other investigations necessary for the completion of site-specific **maximal risk** assessments included studies of aquifer storage, groundwater pressures and gradients, reactions between recharge water, groundwater and aquifer minerals, water treatment options and effectiveness, management of clogging, and biodegradation and inactivation of contaminants.

These modelling activities and infill data gathering require significant investigative effort, and hence have been applied to high priority sites and options only during Phase 3 of the BHMAR Project. For this project, MAR storage of 30 GL is sought to secure a three-year drought security supply for Broken Hill when surface storage at the MLS is low. The only previous MAR study in this area has modelled a scenario with one-year injection, storage for 8 years, and extraction over an 18 month period SKM (2009).

**Table 3-3.** *Entry-level assessment, indicating relative degree of difficulty in relation to specific environmental values of the aquifer and intended uses of recovered water (From Table A1.2, NRMMC-EPHC-NHMRC, 2009).*

| Recovered water environmental values | Aquifer environmental values | | | | | | | |
|---|---|---|---|---|---|---|---|---|
| | Aquatic ecosystems 1[a] | Aquatic ecosystems 2[b] | Aquatic ecosystems 3[c] | Drinking | Aquaculture | Recreation | Irrigation | Livestock |
| **Aquatic ecosystems 1a** | H | H | H | H | H | H | H | H |
| **Aquatic ecosystems 2b** | H | M | M | H | M | M | M | M |
| **Aquatic ecosystems 3c** | H | M | L | H | M | M | L | L |
| **Drinking** | H | H | H | H | H | H | H | H |
| **Aquaculture** | H | M | M | H | M | M | M | M |
| **Recreation** | H | M | M | H | M | M | M | M |
| **Irrigation** | H | M | L | H | M | M | L | L |
| **Livestock** | H | M | L | H | M | M | L | L |

H = higher difficulty, generally corresponding with high risk;

M = moderate difficulty, generally corresponding with moderate risk;

L = lower difficulty, generally corresponding with low risk.

[a]Aquatic ecosystems 1 = high conservation or ecological values.

[b]Aquatic ecosystems 2 = slightly to moderately disturbed systems.

[c]Aquatic ecosystems 3 = highly disturbed systems.

### 3.2.3 BHMAR Phase 2 Assessment

In Phase 2 of the BHMAR study, initial Viability Assessments for MAR options in the Menindee area were positive, with the caveat that issues of source water entitlements and licensing are outside the remit of this project (Lawrie *et al.,* 2010b &, c). It was therefore decided to carry out the Part 2 Degree of Difficulty Assessments based on this positive assessment.

The results of the Part 2 Degree of Difficult Assessment demonstrated there is a moderate to high degree of difficulty in developing MAR options in this region (Lawrie *et al*., 2010b & c; 2012c). In part, this is due to the data paucity and the pioneering nature of the project. The hydrogeological complexity in the area provides a diversity of potential MAR alternatives but also brings with it the challenges of understanding key processes. The analysis identified a number of issues that warranted further analysis, both in source water quality suitability, and in groundwater hydrogeochemistry (Lawrie *et al*., 2010c).

In Phase 2 of the project, Degree of Difficulty' and 'Entry level' assessments were carried out for a large number of potential MAR sites and options distributed across the project area (Lawrie *et al*., 2010b, c). A number of sites were favourably assessed (Lawrie *et al.*, 2010b, c), and the recommendation made to proceed to Phase 3 of the project, with an emphasis on investigating MAR opportunities close to Menindee in order to secure Broken Hill's water supply.

### 3.2.4 BHMAR Phase 3 Assessment

Significant additional scientific and technical investigations are required to carry out Maximal Risk Assessments and Pre-Commissioning Residual Risk Assessments under the national MAR guidelines (NRMMC–EPHC–NHMRC 2009). Pre-commissioning semi-quantitative residual risk assessments include an assessment of 12 hazard types and all the barriers: source control; bank filtration or engineered pre-

treatment (coagulation/flocculation and chlorination); aquifer treatment; engineered post-treatment (coagulation/flocculation, rapid sand filtration, UV disinfection, chlorination and powdered activated carbon dosing if required). In the BHMAR project, special emphasis was placed on pathogen risks consistent with the Augmentation of Drinking Water Supplies Guidelines. Analysis of the summary results also gives a rationale for further risk-based studies to support a future pilot trial and also prior to connecting BHMAR water to the Broken Hill mains water supply.

Initially, Phase 3 of the project assessed aquifer storage and recovery (ASR), aquifer storage, transport and recovery (ASTR), bank filtration and infiltration basin options, within a 40 km radius of Menindee township. However, parallel assessments of MAR options and costs (SKM, 2010), led to BHMAR investigations being narrowed to a radius of within 20 km from Menindee.

Subsequently, after consideration of eight targets, sites at Jimargil and Menindee Common were prioritised for further detailed hydrogeological investigations and MAR assessment. After significant endeavour, work at the site at Menindee Common was curtailed as a number of hydrogeochemical and hydrogeological issues emerged which increased the difficulty of developing MAR options at this site (Lawrie *et al.*, 2011; 2012c). Consequently, Maximal and Pre-Commissioning Residual Risk Assessments have only been fully completed for an ASR option at the highest priority site (Jimargil).

While the Jimargil (EB-J-W) site is identified as the highest priority site for potential development, three additional sites: north Lake Menindee (LM), Larloona (L1) and Kinchega National park (KNP 1a, b and 2 a, b) have also been identified. These should be considered only as back-up sites should problems be encountered with the Jimargil site. There is insufficient drilling and complementary data to complete pre-commissioning residual risk assessments of other options at these additional sites, as well as other lower priority sites identified across the BHMAR study area

The overall assessments of the MAR options therefore reflect a varying level of confidence commensurate with the level of investigations. A comprehensive assessment of the MAR options at these sites and at other sites across the study area, is presented in Lawrie *et al.* (2012c). Degree of difficulty and entry level assessments of other sites within 20 km of Menindee which were assessed unfavourably (e.g. Lake Wetherell, Southern Lake Menindee, Eastern Larloona and Appin Station), are also detailed in Lawrie *et al.* (2012c).

## 3.3 WATER QUALITY GUIDELINES

The BHMAR project aims to provide a mechanism to secure the water supply for Broken Hill, without relying on a drought surface water reserve in the Menindee Lakes Storages. This entails investigating a conjunctive approach where groundwater-related options are incorporated with the MLS. As provision of potable-quality water for Broken Hill is the ultimate objective, the Australian Drinking Water Guidelines 6 (NHMRC-NRMMC, 2011) were applied in the assessment. The ADWG2011 applies to any water intended for drinking (with the exception of bottled or packaged water), regardless of the source. In the case of the BHMAR project, the following assessments used the drinking water criteria established by the ADWG2011:

- Suitability of raw surface water in the Darling River and the MLS as source water for Broken Hill water supply, including identification of key treatment requirements.
- Pre-treatment requirements for using the Darling River (and MLS) as sources for injection water for potential ASR operations
- The key water quality issues and suitability of groundwater as source water for potable water supply
- The potential water quality issues associated with oxygenation, using the pore fluid samples as an analogue
- The key water quality issues and potential ADWG exceedances defined by geochemical modelling of water-rock interactions associated with ASR scenarios.

- Definition of thresholds for the mapping of groundwater salinity
- Definition of thresholds associated with modelling of recovery efficiencies of potential ASR scenarios at the Jimargil priority site.

Table 3-4 summarises the ADWG2011 criteria for the water quality parameters assessed in the BHMAR project. The ADWG2011 includes two types of threshold values, namely:

- A health-related guideline value, which is the concentration that, based on present knowledge, does not result in any significant risk to the health of the consumer over a lifetime of consumption; and
- An aesthetic guideline value, which is the concentration that is associated with acceptability of water to the consumer (such as appearance, taste and odour).

**Table 3-4.** *ADWG2011 guideline values for physical and chemical parameters measured in the BHMAR project (from NHMRC-NRMMC, 2011).*

| Parameter | Guideline Values (mg/L unless otherwise specified | | Comments |
|---|---|---|---|
| | Health | Aesthetic | |
| Aluminium | c | 0.2 | Guideline value based on post-flocculation problems; < 0.1 mg/L desirable. Lower levels needed for renal dialysis. No health-based guideline value can be established currently. |
| Ammonia (as $NH_3$) | c | 0.5 | Presence may indicate sewage contamination and/or microbial activity. High levels may corrode copper pipes and fittings. |
| Antimony | 0.003 | | Exposure may rise with increasing use of antimony–tin solder. |
| Arsenic | 0.01 | | From natural sources and mining/industrial/agricultural wastes. |
| Barium | 2 | | Primarily from natural sources. |
| Beryllium | 0.06 | | From weathering of rocks, atmospheric deposition (burning of fossil fuels) discharges. |
| Boron | 4 | | From natural leaching of minerals and contamination. <1 mg/L in uncontaminated sources; higher levels may be associated with seawater intrusion. |
| Cadmium | 0.002 | | Indicates industrial or agricultural contamination; from impurities in galvanised (zinc) fittings, solders and brasses. |
| Chloride | c | 250 | From natural mineral salts, effluent contamination. High concentrations more common in groundwater and certain catchments. |
| Chromium (as Cr(VI)) | 0.05 | | From industrial/agricultural contamination of raw water or corrosion of materials in distribution system/plumbing. If guideline value exceeded, analyse for hexavalent chromium. |
| Copper | 2 | 1 | From corrosion of pipes/fittings by salt, low pH water. Taste threshold 3 mg/L. High concentrations colour water blue/green. >1 mg/L may stain fittings. >2 mg/L can cause ill effects in some people. |
| Dissolved Oxygen | Not necessary | >85% | Low concentrations allow growth of nuisance microorganisms (iron/ manganese/sulfate/nitrate-reducing bacteria), causing taste and odour problems, staining, corrosion. Low oxygen concentrations are normal in groundwater supplies and the guideline value may not be achievable. |
| Fluoride | 1.5 | | Occurs naturally in some water from fluoride-containing rocks. Often added at up to 1 mg/L to protect against dental caries. >1.5 mg/L can cause dental fluorosis. >4 mg/L can cause skeletal fluorosis. |
| Hardness (as $CaCO_3$) | Not necessary | 200 | Caused by calcium and magnesium salts. Hard water is difficult to lather. <60 mg/L $CaCO_3$ – soft but possibly corrosive. 60-200 mg/L $CaCO_3$ – good quality. 200-500 mg/L $CaCO_3$ – increasing scaling problems. >500 mg/L $CaCO_3$ – severe scaling. |
| Iron | c | 0.3 | Occurs naturally in water, usually at <1 mg/L, but up to 100 mg/L in oxygen-depleted groundwater. Taste threshold 0.3 mg/L. High concentrations stain laundry and fittings. Iron bacteria cause blockages, taste/odour, corrosion. |

| | | | |
|---|---|---|---|
| Lead | 0.01 | | Occurs in water via dissolution from natural sources or household plumbing containing lead (e.g. pipes, solder). |
| Manganese | 0.5 | 0.1 | Occurs naturally in water; low in surface water, higher in oxygen depleted water (e.g. groundwater at bottom of deep storages). >0.1 mg/L causes taste, staining. <0.05 mg/L desirable. |
| Mercury | 0.001 | | From industrial emissions/spills. Very low concentrations occur naturally. Organic forms most toxic, but these are associated with biota, not water. |
| Molybdenum | 0.05 | | Concentrations usually <0.01 mg/L; higher concentrations from mining, agriculture, or fly-ash deposits from coal-fuelled power stations. |
| Nickel | 0.02 | | Concentrations usually very low; but up to 0.5 mg/L reported after prolonged contact of water with nickel-plated fittings. |
| Nitrate (as $NO_3$) | 50 | | Occurs naturally. Increasing in some waters (particularly groundwater) from intensive farming and sewage effluent. Guideline value will protect bottle-fed infants under 3 months from methaemoglobinaemia. Adults and children over 3 months can safely drink water with up to 100 mg/L nitrate. |
| Nitrite (as $NO_2$) | 3 | | Rapidly oxidised to nitrate (see above). |
| pH | c | pH 6.5-8.5 | While extreme pH values (<4 and >11) may adversely affect health, there are insufficient data to set a health guideline value. <6.5 may be corrosive. >8 progressively decreases efficiency of chlorination. >8.5 may cause scale and taste problems. New concrete tanks and cement-mortar lined pipes can significantly increase pH and a value up to 9.2 may be tolerated provided monitoring indicates no deterioration in microbial quality. |
| Radon-222 | 100 Bq/L | | applies to the concentration of radon at the point of use of the water, not at the source, because of the significant decrease in concentration which can occur due to radioactive decay during storage, treatment and reticulation. |
| Selenium | 0.01 | | Generally very low concentrations in natural water. |
| Silica | | 80 | An important characteristic for both aesthetics and treatment processes. Can form films on glass and can also affect reverse osmosis. |
| Silver | 0.1 | | Concentrations generally very low. Silver and silver salts occasionally used for disinfection. |
| Sodium | Not Necessary | 180 | Natural component of water. Guideline value is taste threshold. |
| Sulfate | 500 | 250 | Natural component of water, and may be added via treatment chemicals. Guideline value is taste threshold. >500 mg/L can have purgative effects. |
| Temperature | Not necessary | No value set | Generally impractical to control; rapid changes can bring complaints |
| Tin | Not necessary | | Concentrations in water very low; one of the least toxic metals. |
| Total dissolved solids | Not necessary | 600 | Based on taste: <600 mg/L is regarded as good quality drinking water. 600-900 mg/L is regarded as fair quality. 900-1200 mg/L is regarded as poor quality. >1200 mg/L is regarded as unacceptable. |
| Turbidity | c | 5 NTU | NTU is just noticeable in a glass. <0.2 NTU is the target for effective filtration of Cryptosporidium and Giardia. <1 NTU is the target for effective disinfection. |
| Uranium | 0.017 | | Occurs naturally, or from release from mill tailings, combustion of coal and phosphate fertilizers. |
| Zinc | c | 3 | Usually from corrosion of galvanised pipes/fittings and brasses. Natural concentrations generally <0.01 mg/L. Taste problems >3 mg/L. |

C = Insufficient data to set a guideline value based on health considerations

## 3.4 INDIGENOUS CULTURAL HERITAGE

The BHMAR project area is one of great cultural sensitivity to the local Indigenous community (Figure 3-4; Lawrie *et al.,* 2010b; Appendix 15, Magee *et al*., 2012). Local Indigenous cultural beliefs and traditions were recognised at the commencement as a very important aspect of the project, and all team members were made aware of these issues and asked to respect these values. Several of the project team members have significant experience in working with Indigenous communities in the study area and nationally, both informally and through formal consultation processes, and their counsel was important in ensuring appropriate procedures were put in place during fieldwork.

At the commencement of the project, a meeting was held with elders and members of the local Indigenous community (Menindee Local Aboriginal Land Council).

For the fieldwork component of this study, the local Indigenous community were consulted about the process of carrying out assessments for field investigations and drilling activities. Consequently, detailed cultural assessments were undertaken by archaeologists Sarah Martin and Wilfred Shawcross. Members of the local Indigenous community were employed through Menindee Local Aboriginal Land Council (coordinated by Noeline Ferguson) to provide advice at all fieldwork sites. In accordance with the wishes of the local Indigenous community, and to obtain permissions from the NSW Lands Department, cultural heritage assessments were conducted at each proposed drilling site.

Members of the local Indigenous Community were also employed to assist with monitoring any potential site disturbance during drilling activities, and to assist geologists on-site with core recovery. From a Geoscience Australia perspective, the employment of members of the local Indigenous community has been extremely successful.

Reports on cultural heritage at each proposed drilling site were submitted along with other technical information to the NSW Lands Department as part of the drilling approval process. Sites deemed too sensitive were not drilled, and alternative sites identified. A similar process has been identified for obtaining approvals for disposal of groundwater associated with 7-day pump tests. All cultural heritage and environmental assessment reports for the project are contained in Appendix 15 (Magee *et al.,* 2012).

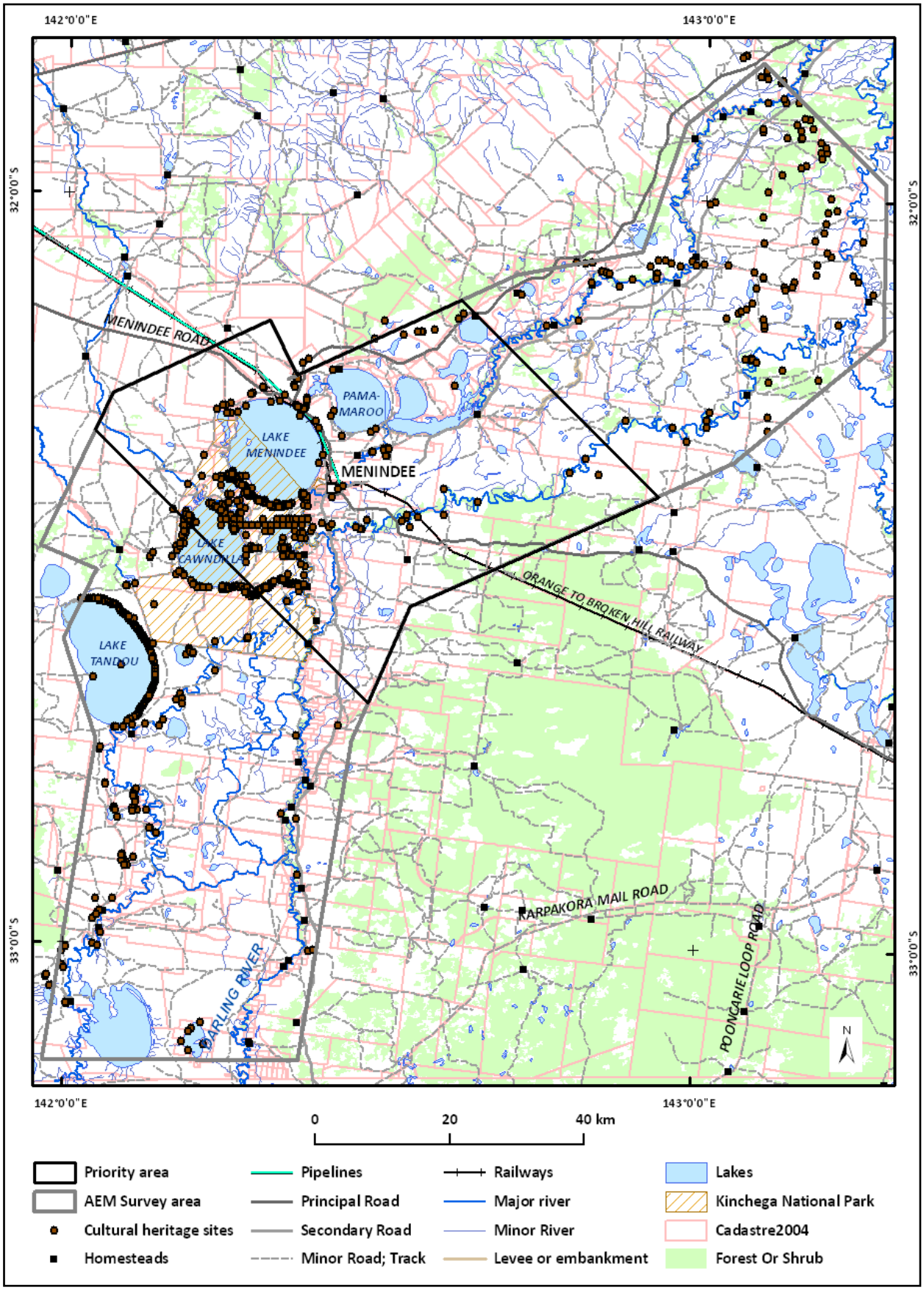



**Figure 3-4.** *Previously recognised cultural heritage sites in the BHMAR project area obtained from the Aboriginal Heritage Information Management System.*

# 4 Assessment of Pre-existing Data

The compilation of pre-existing data for the BHMAR study area was an important initial step in the project. Due to the limited timeframes available for Phase 1 (4 months), initial assessments of the hydrogeology of candidate areas relied heavily upon an analysis of existing geospatial and hydrogeological datasets. All pre-existing and new data incorporated in the BHMAR study are contained in the project GIS (Gow *et al*., 2012). A full assessment of pre-existing geospatial and hydrogeological data analysed for all potential project areas is detailed elsewhere (Lawrie *et al*., 2008; 2009a). In this section, only the data relevant to the final BHMAR study area are reported.

### 4.1.1 Borehole Data

Lewis *et al*. (2008) summarised the status of hydrogeological data available in the NSW Groundwater Works Database and relevant to the Broken Hill region. They found that the database lacked sufficient detailed information on the nature of the local groundwater resources and aquifers to draw any significant conclusions. The BHMAR study broadened the data search to include the available mineral exploration data.

At first glance, there appeared to be a significant number of pre-existing boreholes in the Broken Hill area suitable for the Phase 1 Risk Assessment (Figure 4-1). A total of 3292 boreholes were identified either within or adjacent to six Phase 1 priority areas (Lawrie *et al*., 2008, 2009a). Of these, 1200 were drilled by the NSW State Government and/or Country Energy, or were drilled by private landowners, and 2092 were drilled by various Mineral and Petroleum exploration companies (Figure 4-1). More detailed summary data on these boreholes is contained in Lawrie *et al*. (2009a). All the publicly available pre-existing data on these boreholes is included in the BHMAR Project GIS (Gow *et al*., 2012).

Closer analysis revealed that most boreholes in the priority areas were drilled to relatively shallow depths (Figure 4-3). The exception is the Mundi Mundi area, although most of these boreholes were drilled for the minerals exploration industry and have been back-filled. A few deeper boreholes adjacent to the priority areas were drilled for petroleum exploration and only a small subset have been completed to permit groundwater pumping and sampling. In the priority areas, the majority of boreholes have been drilled to depths of <50 m, tapping groundwater sources in the upper alluvial aquifers.

No diamond core of the aquifer intervals has been preserved, and geological descriptions are highly variable, with most descriptions inadequate for the purposes of a detailed assessment of aquifer properties for MAR. In summary, most of the existing data from minerals industry sources is of limited use in terms of adding value to groundwater resource assessments in this area of interest. A map showing the distribution of boreholes (<200) with some useable information in terms of descriptions of downhole lithology, texture, and/or colour etc. is shown in Figure 4-4.

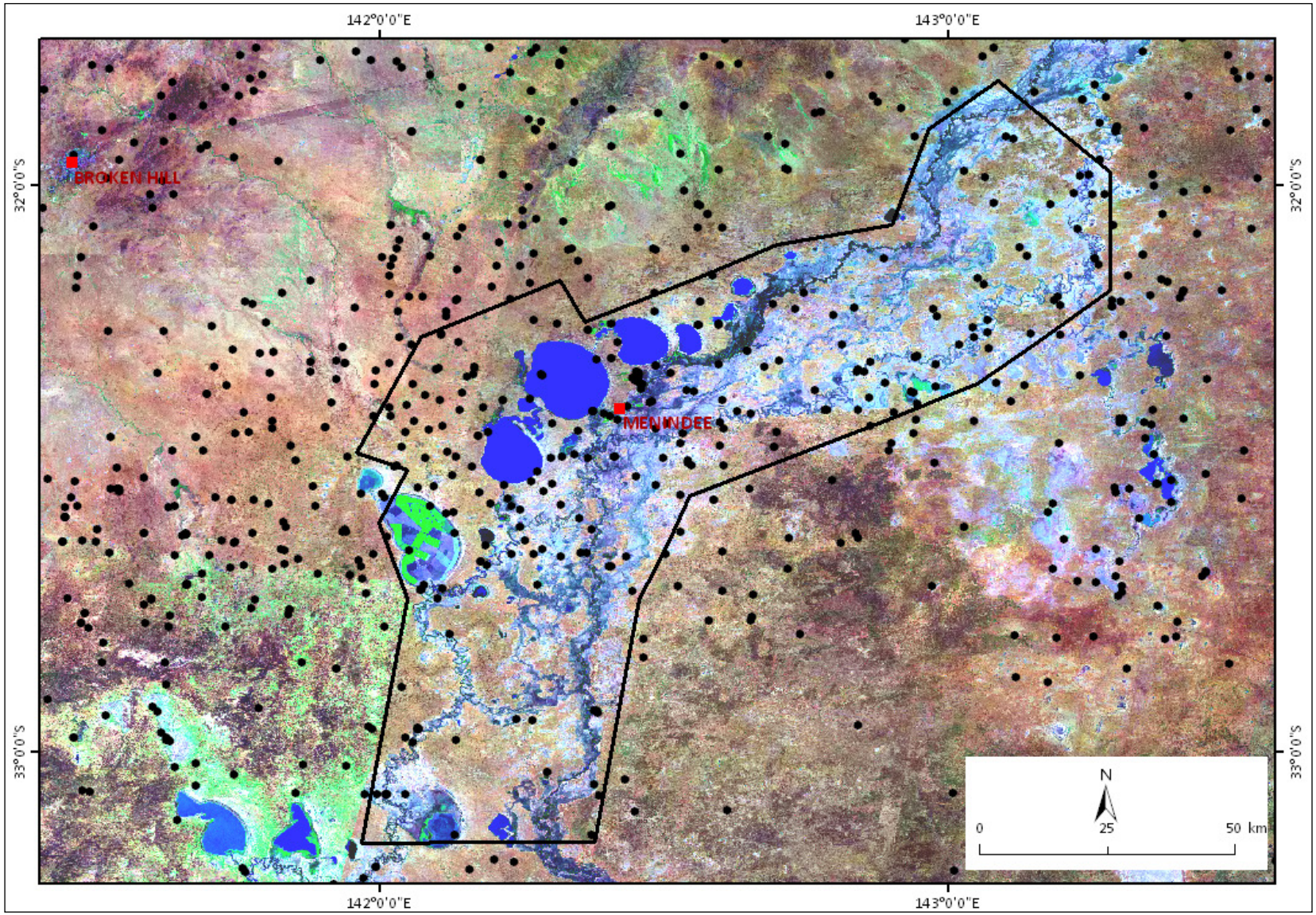



**Figure 4-1.** *Pre-existing boreholes located in or adjacent to the BHMAR project area.*

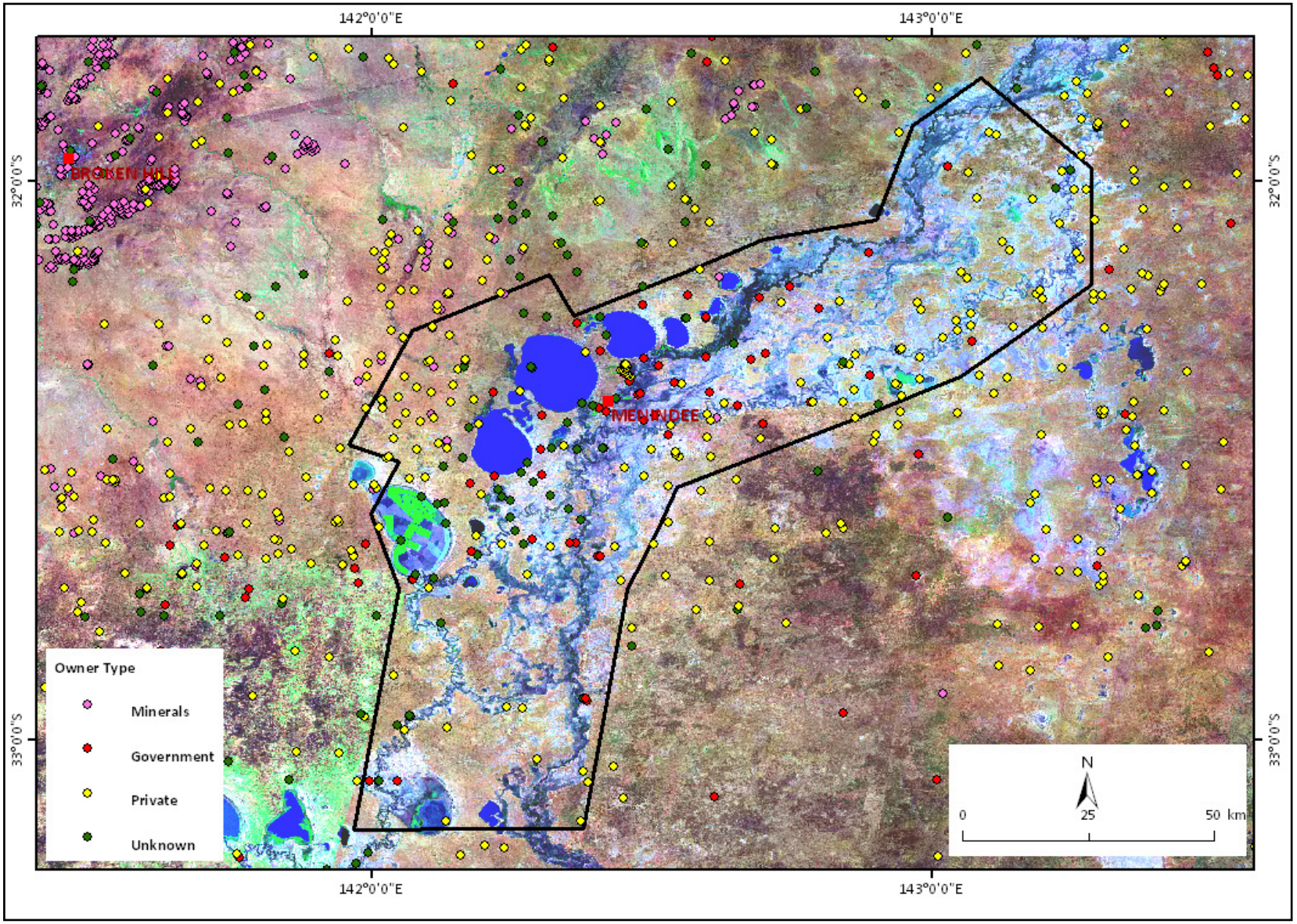



**Figure 4-2.** *Pre-existing boreholes located in or adjacent to the BHMAR project area classified by borehole ownership.*

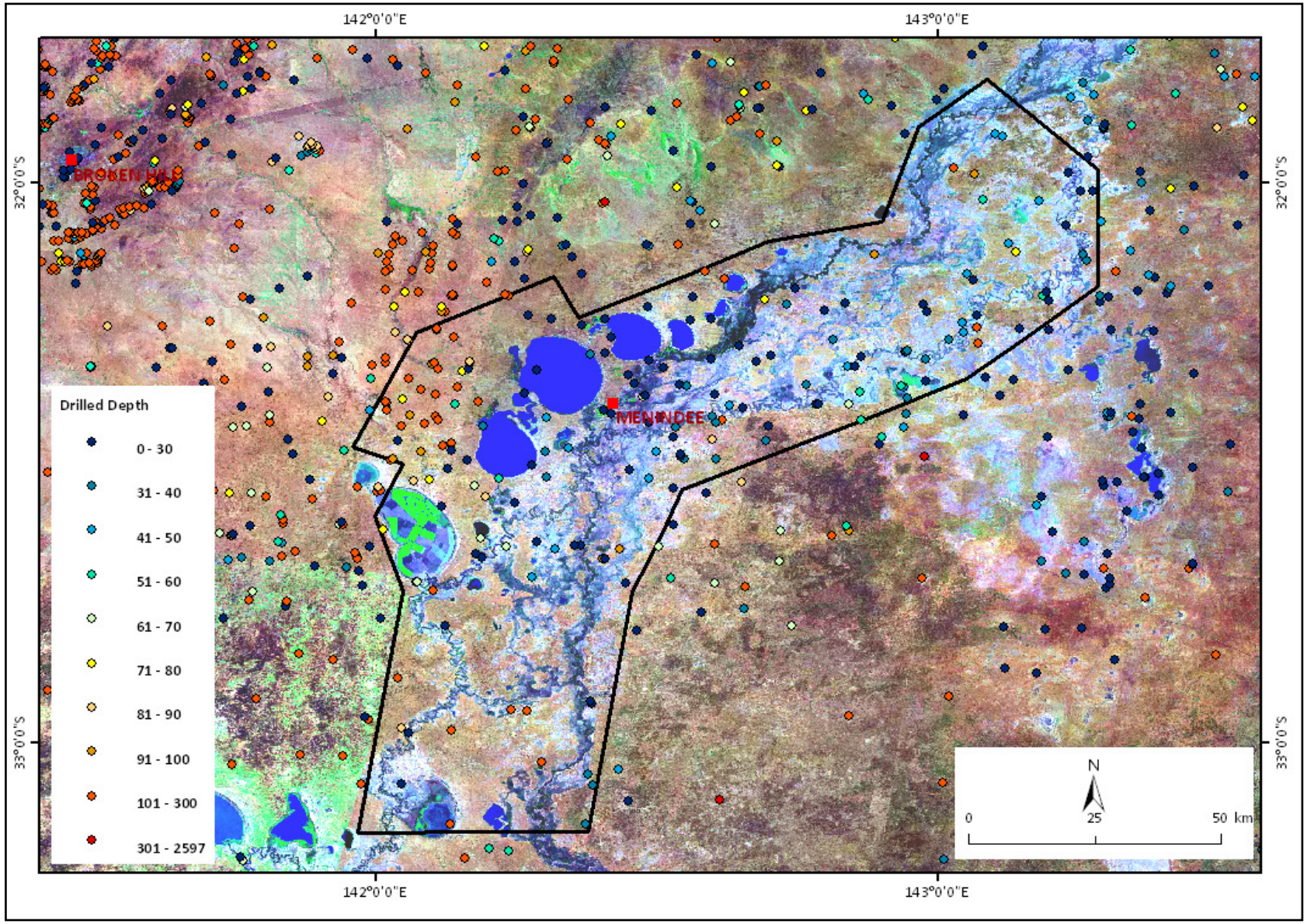



**Figure 4-3.** *The maximum depth of pre-existing boreholes located in or adjacent to the BHMAR project area.*

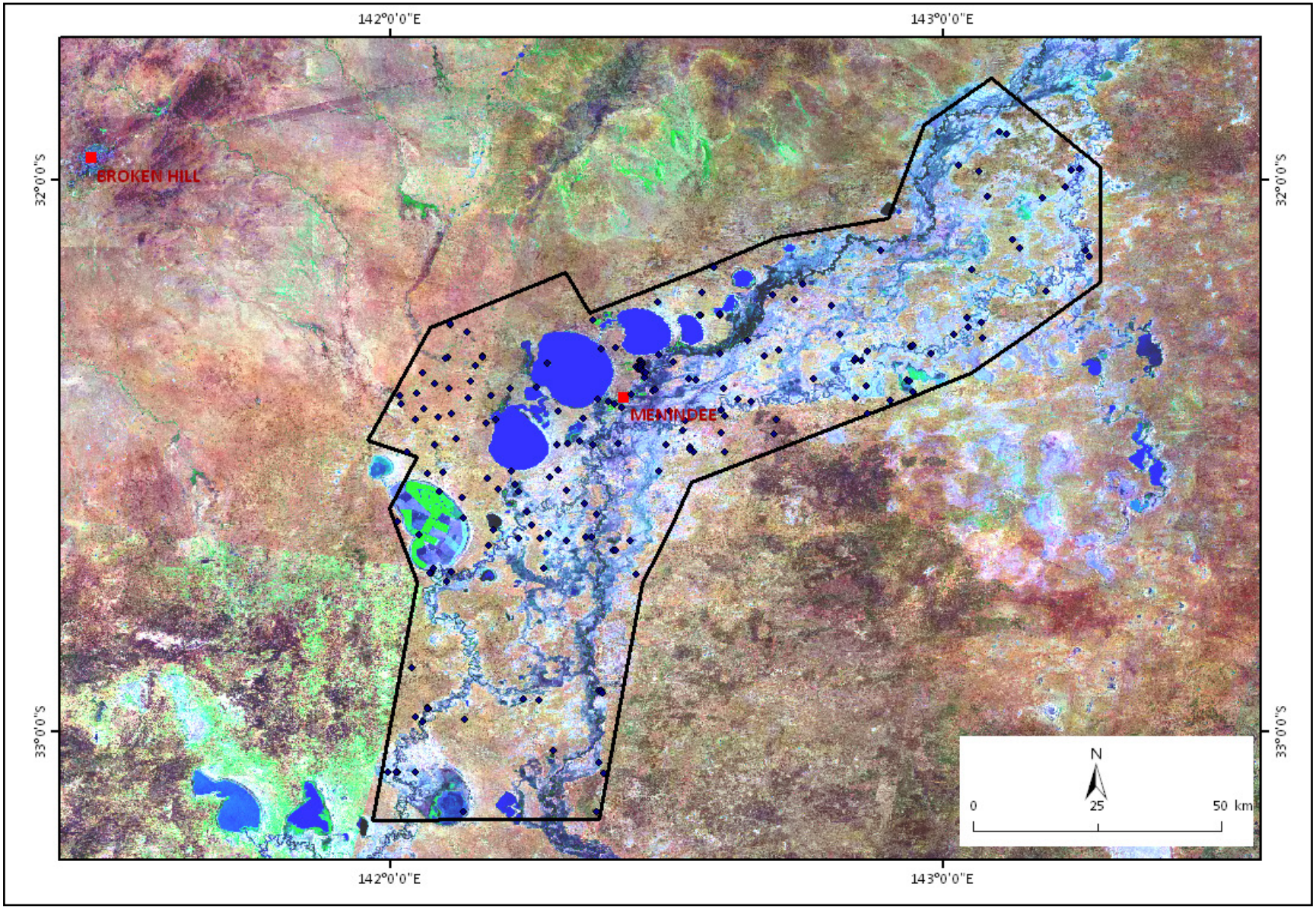



**Figure 4-4.** *Pre-existing boreholes with useable lithological information in the BHMAR project area.*

The manner in which existing boreholes were drilled and completed was critical to the Phase 1 AEM risk assessment exercise and for incorporation in later phases of the project. This is because only boreholes that have PVC casing or are stable unlined holes can be used for downhole electrical induction logging (EM39). The completion status and drilling type (where recorded) of boreholes in the project area are summarised in Table 4-1, with suitable PVC-lined bores in red. Note that the completion status of many holes is not officially recorded in borehole records or databases.

**Table 4-1.** *Combination of completion status and drilling type of boreholes in or adjacent to the BHMAR priority project areas, derived from the project borehole database. The PVC bores (highlighted in red) are the only ones suitable for borehole geophysical logging.*

| Borehole Type | Number of Bores |
|---|---|
| Backfill | 31 |
| Bentonite | 1 |
| Casing Protector | 15 |
| Concrete | 2 |
| Corrugated Galvanised Iron | 1 |
| Crushed Aggregate | 8 |
| Diamond | 336 |
| Drilled Cuttings | 2 |
| Drilled | 1 |
| Fibreglass | 2 |
| Galvanised Steel | 1 |
| Hole | 12 |
| Percussion | 748 |
| **Polyvinyl Chloride (PVC)** | **152** |
| Poured Concrete | 63 |
| Pressure Cemented Casing | 2 |
| Rotary Air Blast Drilling (RAB) | 8 |
| Reverse Circulation Drilling (RC) | 164 |
| Steel | 10 |
| Threaded Steel | 419 |
| Timber | 11 |
| Waterworn/Rounded | 18 |
| Welded Steel | 3 |
| Withdrawn | 82 |
| Unknown | 1200 |

Due to environmental laws in NSW, the mineral exploration holes are back-filled after use, and were therefore not available for subsequent borehole geophysical logging. Geological logs for these mineral exploration holes, usually contained within reports for individual exploration licences, were acquired from NSW Department of Mineral Resources files. Unfortunately, it appears that no geophysical logs for these holes were acquired (at least in the sections of interest), with the exception for limited wireline resistivity logging of the petroleum wells. Geological logs from these mineral industry holes tend to be limited in their descriptions of the stratigraphic intervals of interest, as most effort from the mineral exploration companies was expended on bedrock geology. The exception is for the Mundi Mundi area, where there have been studies of the shallow regolith by researchers from the Cooperative Research Centre for Landscape Environments and Mineral Exploration (CRC LEME) in Geoscience Australia (GA).

Of the large number of boreholes listed as private or of unknown ownership, many have been abandoned or if in operation, are equipped with pumps and so are not ideal for geophysical logging due to the steel equipment fitted and the need to negotiate with land owners to remove pumps for boreholes to be accessed. The latter course of action has been taken only for a few boreholes in areas where there is no other

information (particularly at depth). Most of the boreholes in private ownership have very limited geological descriptions of borehole materials (typically as drillers' logs).

In total, only 152 boreholes have been completed with PVC linings in the broader Broken Hill area. Of these, 64 are owned by the NSW government and/or Country Energy. These agencies have a hydrological monitoring role in the region and the majority of their monitoring bores are PVC-lined. The distribution of these PVC-lined boreholes, and their maximum depth, is shown in Figure 4-5. Overall, most of the boreholes are shallow (<50 m). Of the PVC-line boreholes, 57 within Area 1 (areas 1 and 3 in Lawrie *et al*., 2008), 8 within Area 2, 16 within Area 3, 5 within Area 4, and there are no PVC-lined boreholes in Areas 5 and 6.

The distribution of PVC-lined boreholes for the individual aquifers is also plotted in Figure 4-10. The larger number of boreholes in the shallow aquifers contrasts markedly with the paucity of available boreholes that intercept the deeper aquifers. No diamond core of the aquifer intervals has been preserved, and geological descriptions are highly variable, with most descriptions inadequate for the purposes of a detailed assessment of aquifer properties for managed aquifer recharge (MAR).

Lawrie *et al*. (2008) documented the maximum depths of PVC-lined boreholes within each priority area tabulated by their completion depth in the different aquifers. This tabulation includes all boreholes in available databases, however fieldwork has established that some of these holes have either totally or partially collapsed, and may not be available for borehole logging. An example is borehole EX1 (Country Energy Traverse 2: 0702), which was drilled to depths of 234 m, but was blocked below 150 m. This borehole previously had downhole induction and gamma logged to depths of 185 m (Figure 4-11).

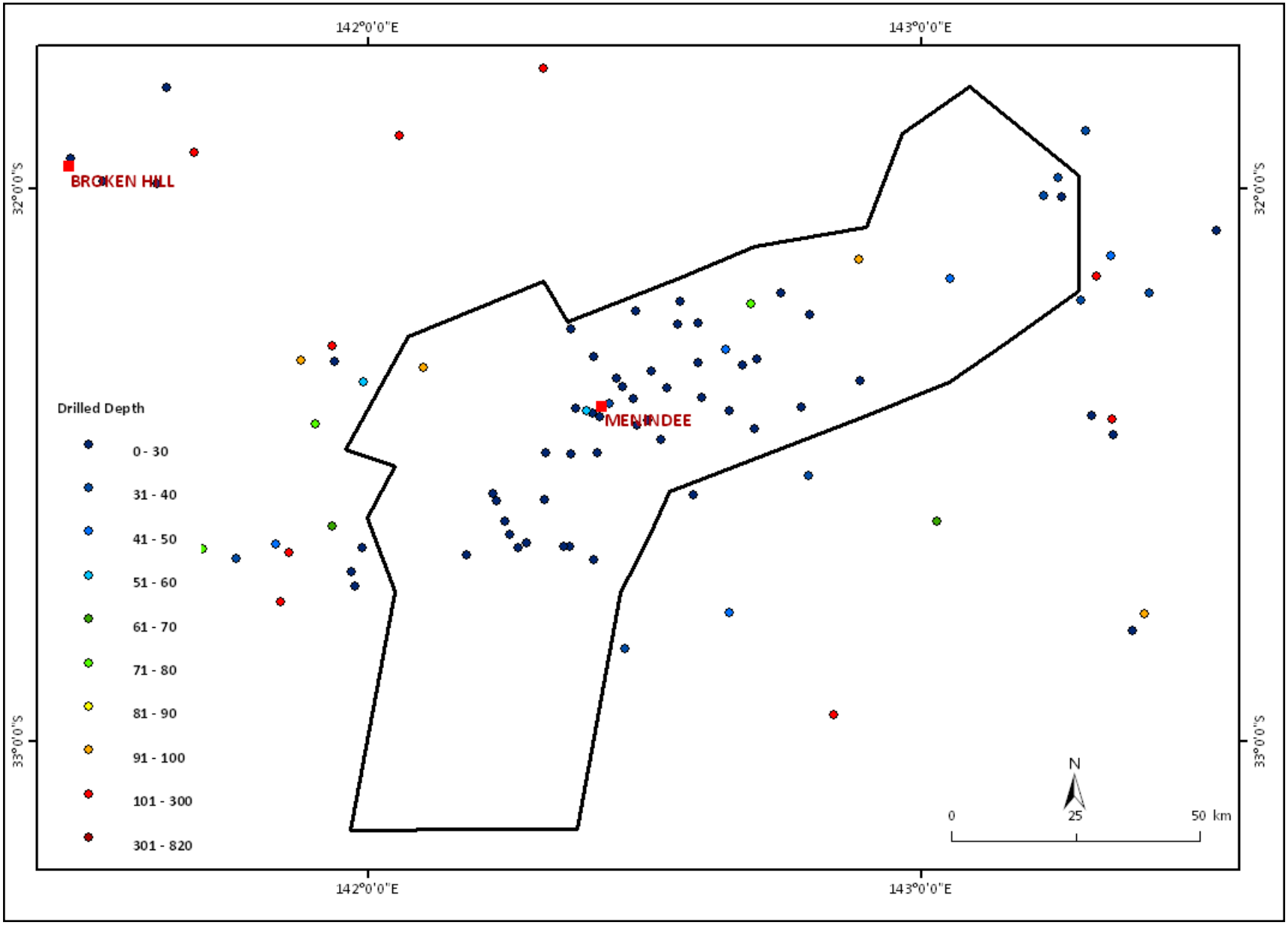



**Figure 4-5.** *Maximum depth of pre-existing PVC-lined boreholes located in the BHMAR project area.*

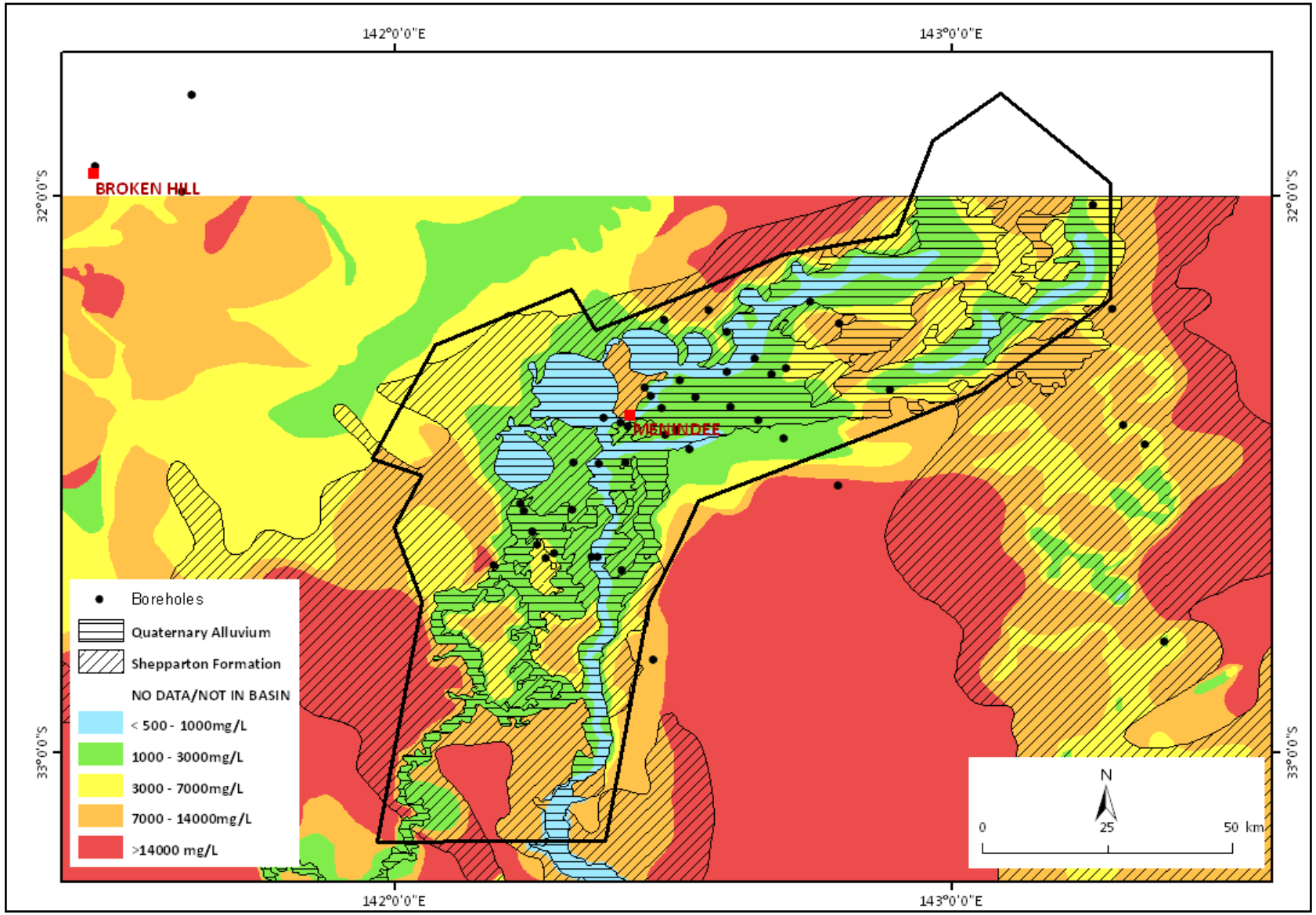



**Figure 4-6.** *Pre-existing PVC-lined boreholes that intercept the shallow aquifers (0-30 m) in the BHMAR project area. Salinity mapping from the Murray Basin Hydrogeological Map Series. As a consequence of the BHMAR Project, the Shepparton Formation has been superseded by the Menindee Formation and Willotia beds for the Lower Darling Valley and hence is not discussed in this report.*

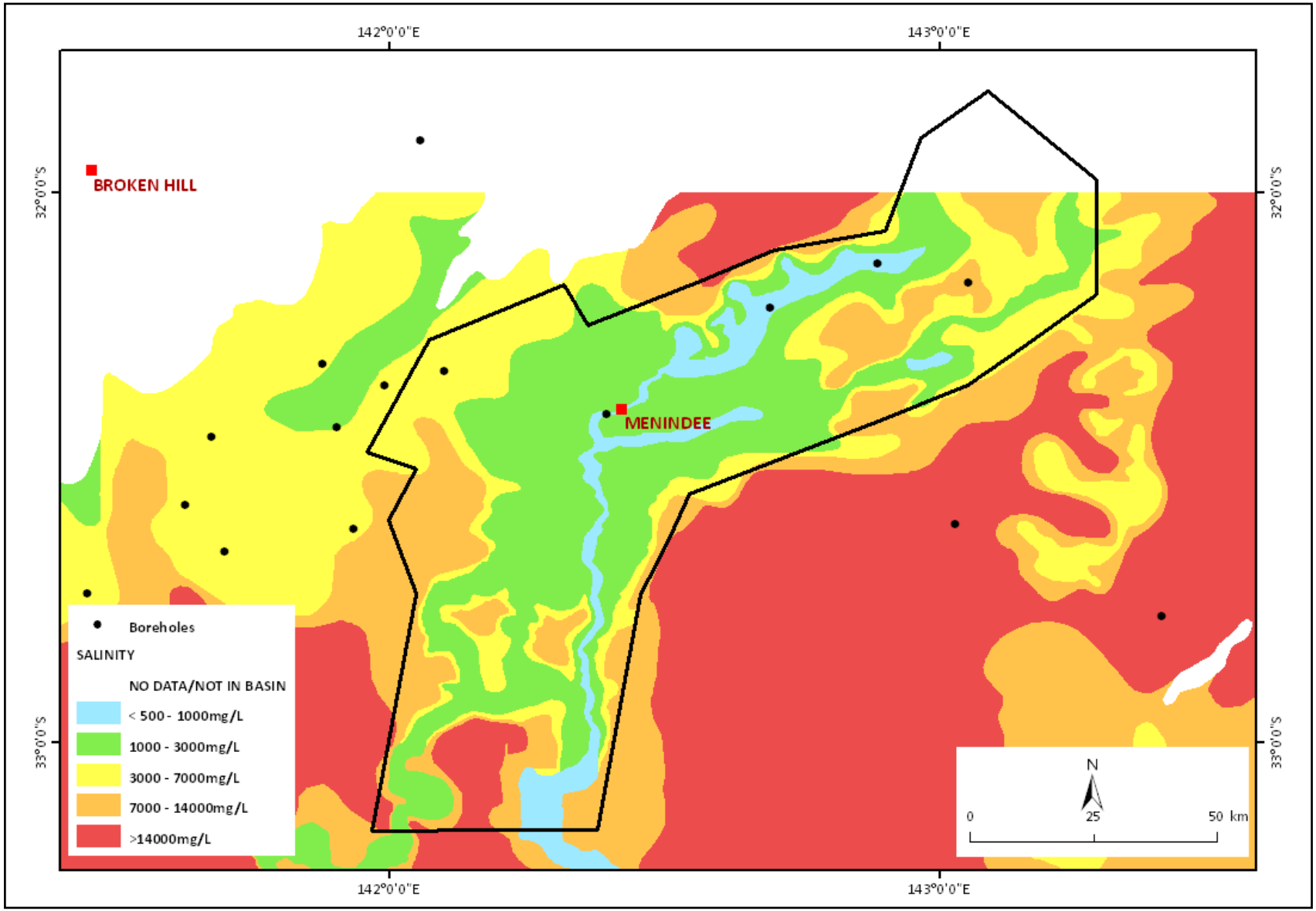



**Figure 4-7.** *Pre-existing PVC-lined boreholes that intercept the Pliocene aquifer (30-100 m) in the BHMAR project area. Salinity mapping from the Murray Basin Hydrogeological Map Series.*

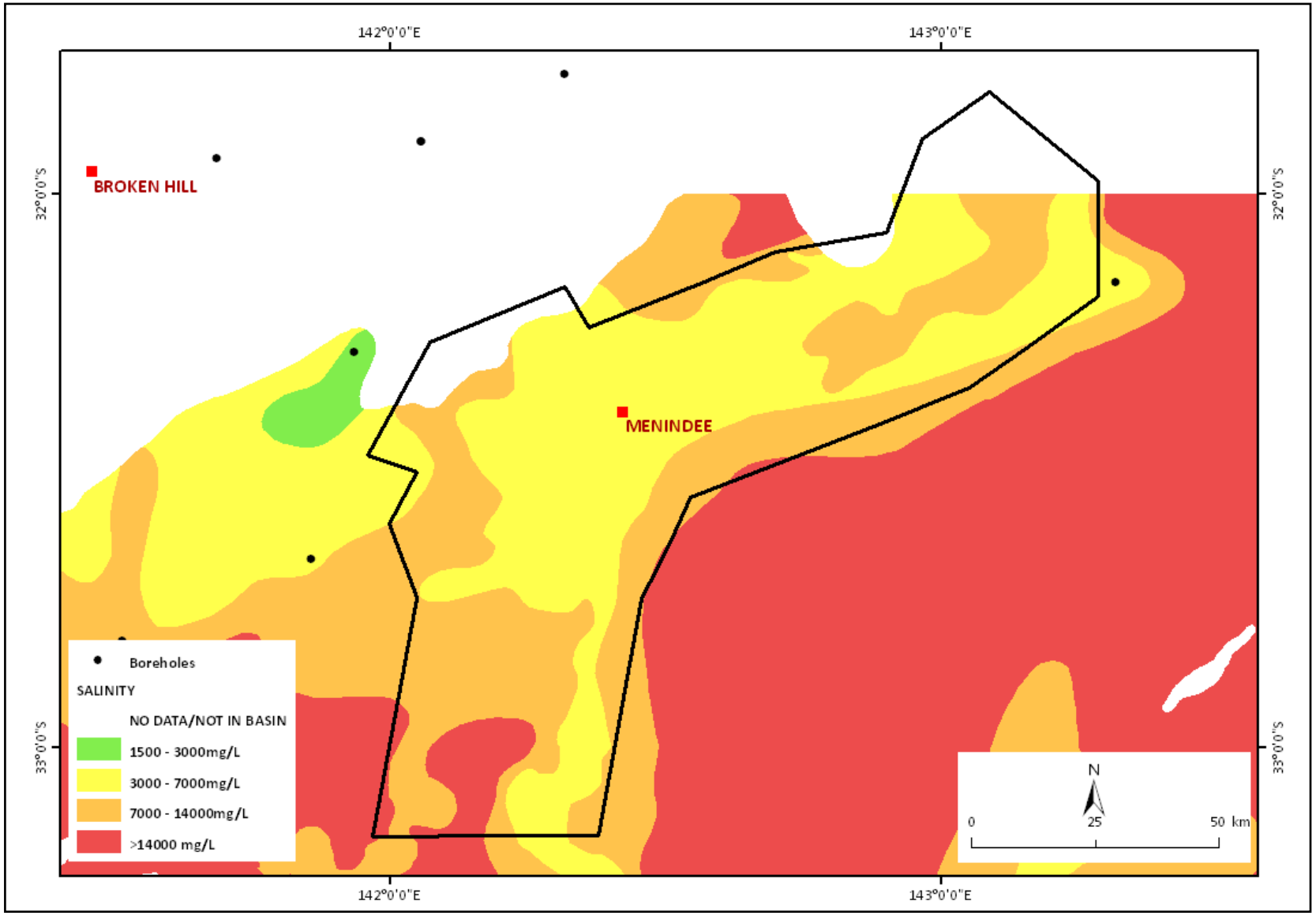



**Figure 4-8.** *Pre-existing PVC-lined boreholes that intercept the upper Renmark Formation aquifer (100-150 m) in the BHMAR project area. Salinity mapping from the Murray Basin Hydrogeological Map Series.*

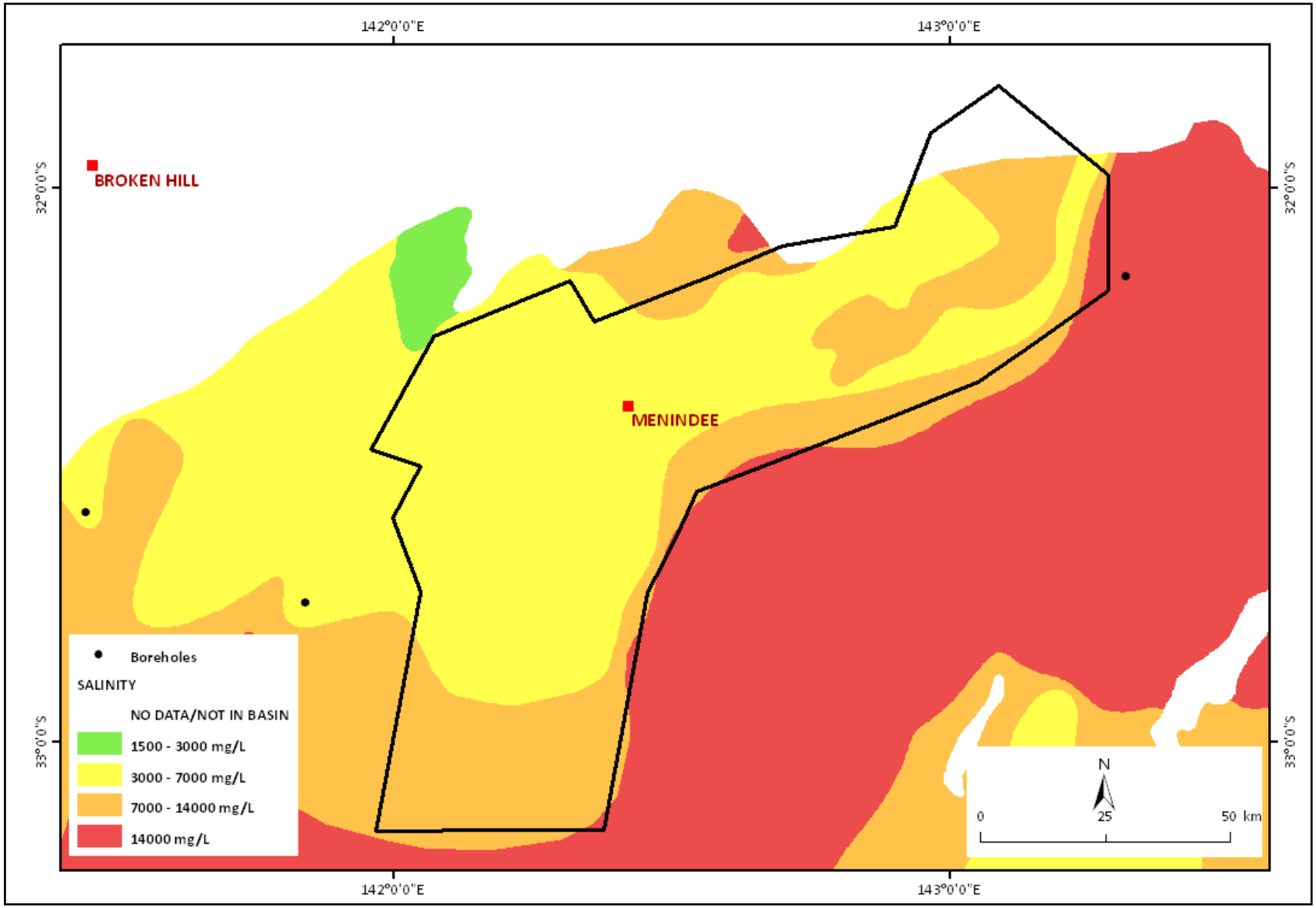



**Figure 4-9.** *Pre-existing PVC-lined boreholes that intercept the middle Renmark Formation aquifer (150-200 m) in the BHMAR project area. Salinity mapping from the Murray Basin Hydrogeological Map Series.*

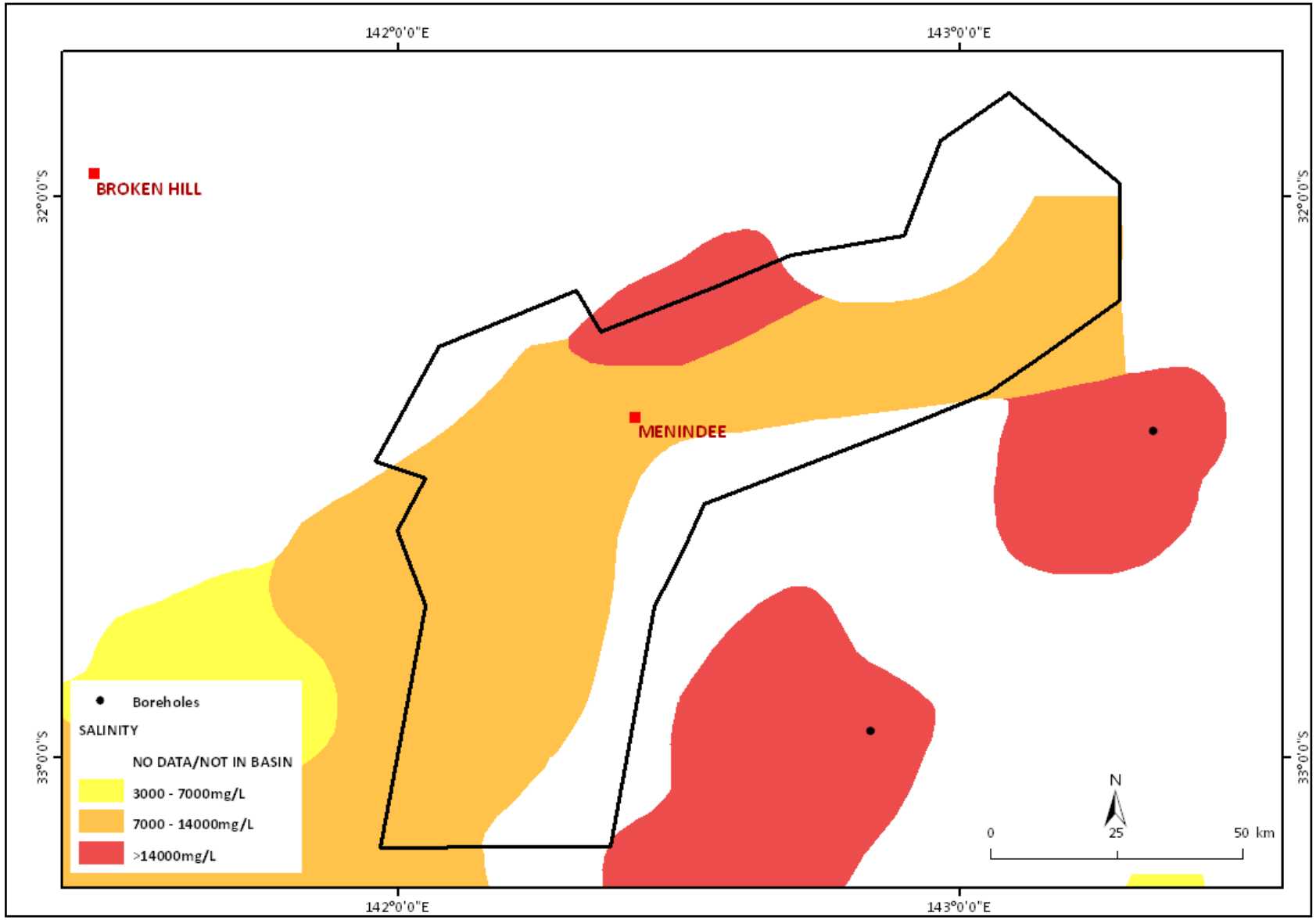



**Figure 4-10.** *Pre-existing PVC-lined boreholes that intercept the lower Renmark Formation aquifer (>200 m) in the BHMAR project area. Salinity mapping from the Murray Basin Hydrogeological Map Series.*

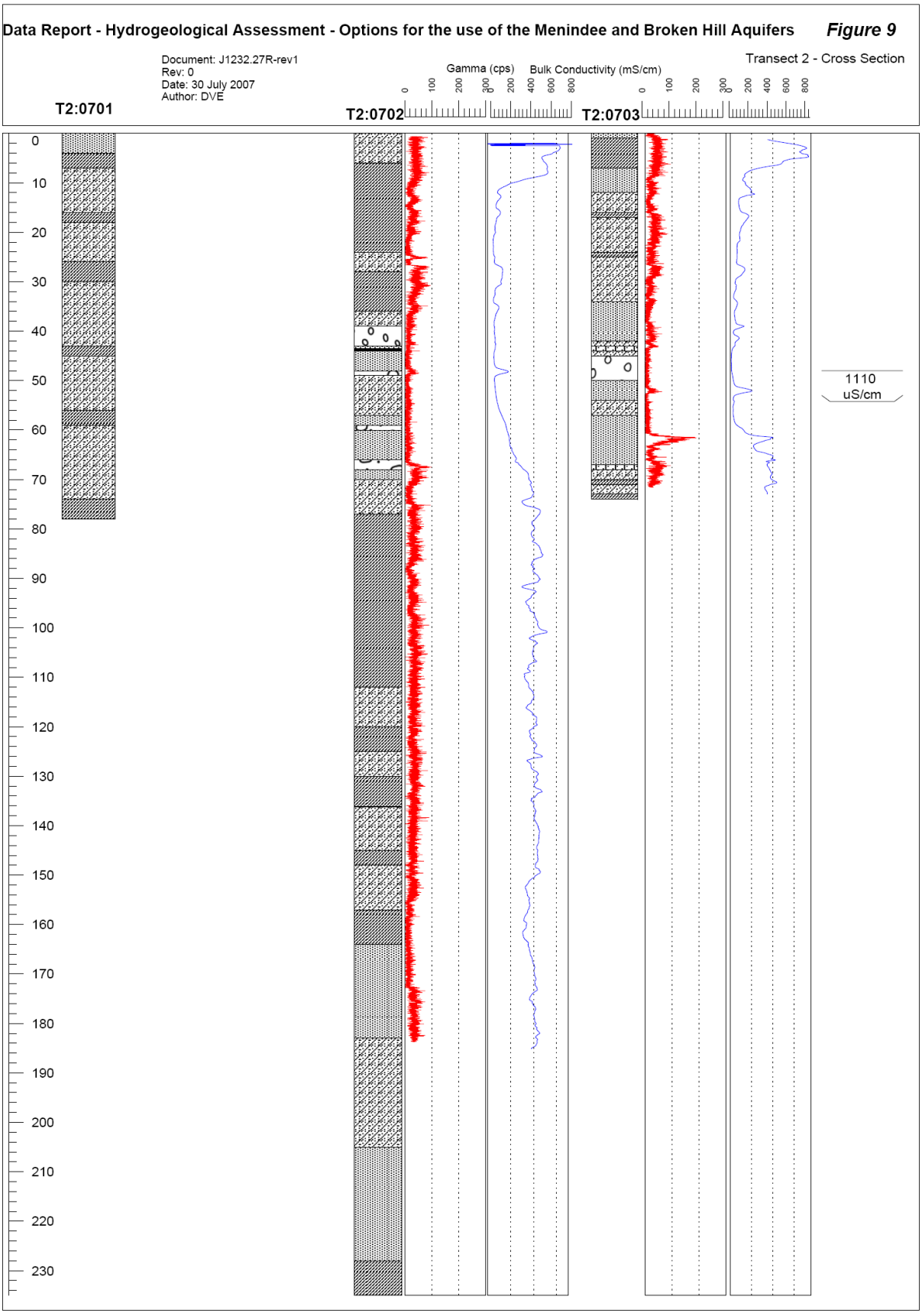



**Figure 4-11.** *Downhole gamma and induction logging of borehole T2:0702 and T2:0703.*

## 4.2 REGIONAL GEOPHYSICS

### 4.2.1 Airborne Magnetic and Gamma Radiometric Data

Airborne magnetic data can used in mapping sedimentary units as well as bedrock and geologic structures, while gamma radiometric surveys, particularly airborne, can be used in mapping surficial soils and geomorphic units, and can potentially help define groundwater recharge and discharge zones. A review of available data for the BHMAR study area shows that while there is coverage over the whole area, there are higher resolution surveys over priority areas 4-6 only (Figure 4-12, Figure 4-13). Publicly available data over the remaining areas is of generally low resolution (400 m line spacing) that has been found to be limited value in mapping soils and geomorphic units in other floodplain landscapes (e.g. the Murray Floodplain; Clarke *et al*., 2007a, b), but may be of use in identifying underlying structures.

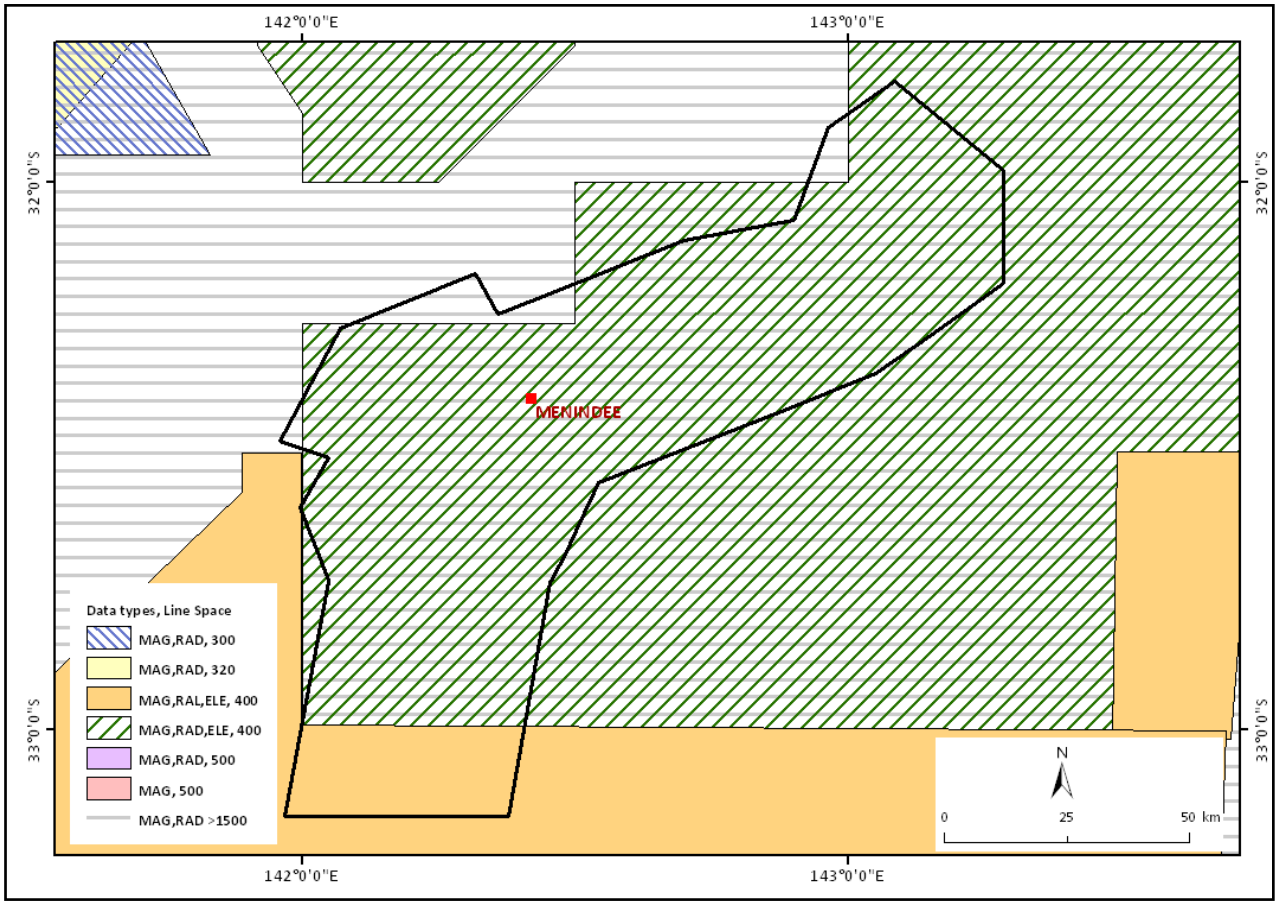



**Figure 4-12.** *Distribution and line-spacing of lower resolution (>300 m line spacing) airborne magnetic (MAG), gamma radiometric (RAD) and elevation (ELE) datasets in the Broken Hill region.*

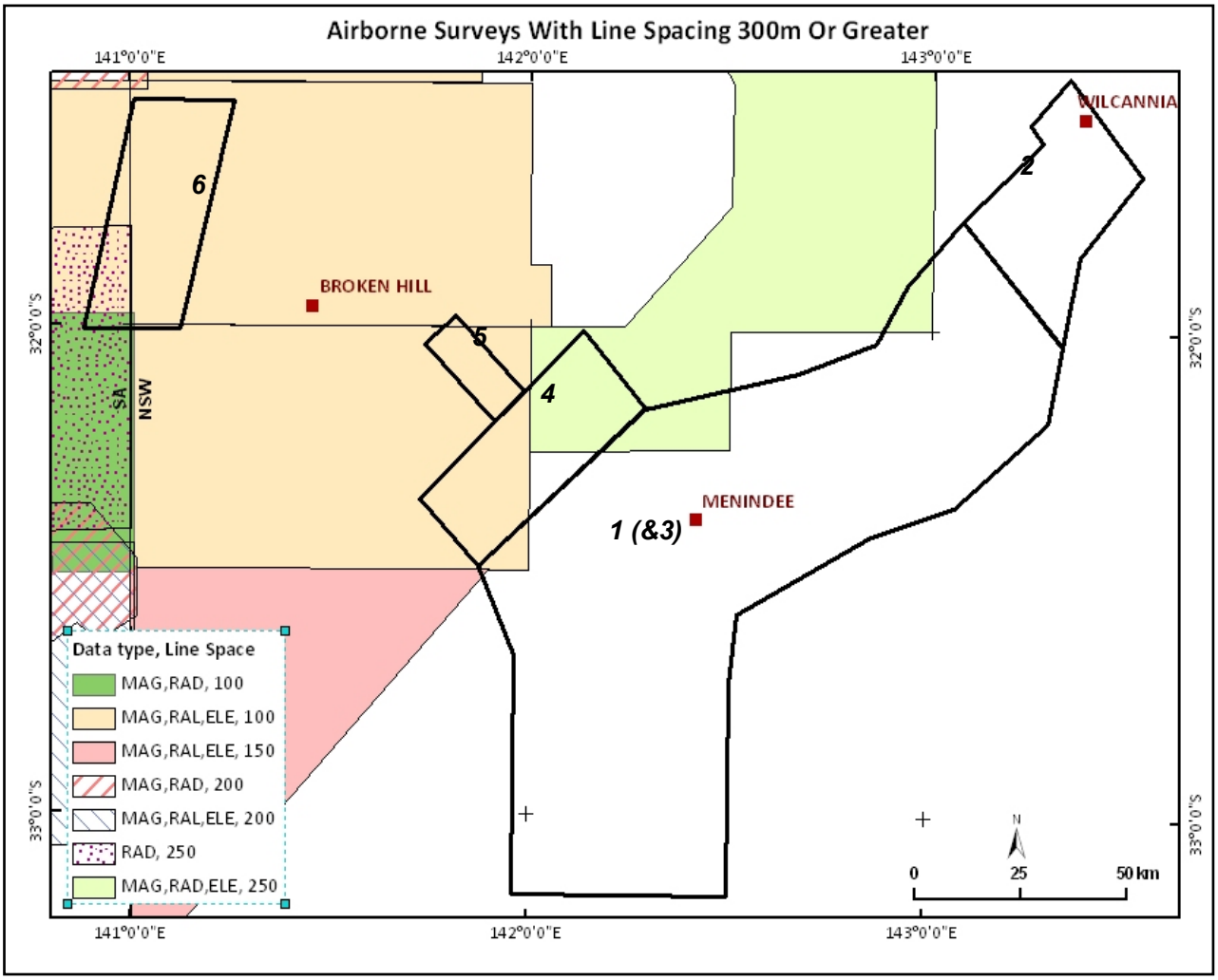



**Figure 4-13.** *Distribution and line-spacing of high resolution (<150 m line spacing) airborne magnetic (MAG), gamma radiometric (RAD) and elevation (ELE) datasets in the Broken Hill region.*

Examples of the airborne magnetics data for the Broken Hill region are shown in Figure 4-14 and Figure 4-15 and gamma radiometric data in Figure 4-16. Considerable near-surface detail is displayed in areas where higher resolution magnetic datasets have been acquired; the data may be of particular use in examining fractured rock aquifers in the study area. In contrast, there is little relevant detail from the near-surface shown in areas 1-3. Elsewhere in the Murray-Darling Basin, airborne magnetic datasets have proven useful in the mapping of hydraulic conductivity variations within Pliocene aquifers, notably the Loxton-Parilla Sands (Lawrie *et al*., 2008). However there are no obvious palaeo-strand line patterns evident in the magnetic data (Figure 4-14, Figure 4-15) nor in the gamma radiometric datasets (Figure 4-16), further suggesting that the Pliocene aquifers are dominantly Calivil Formation.

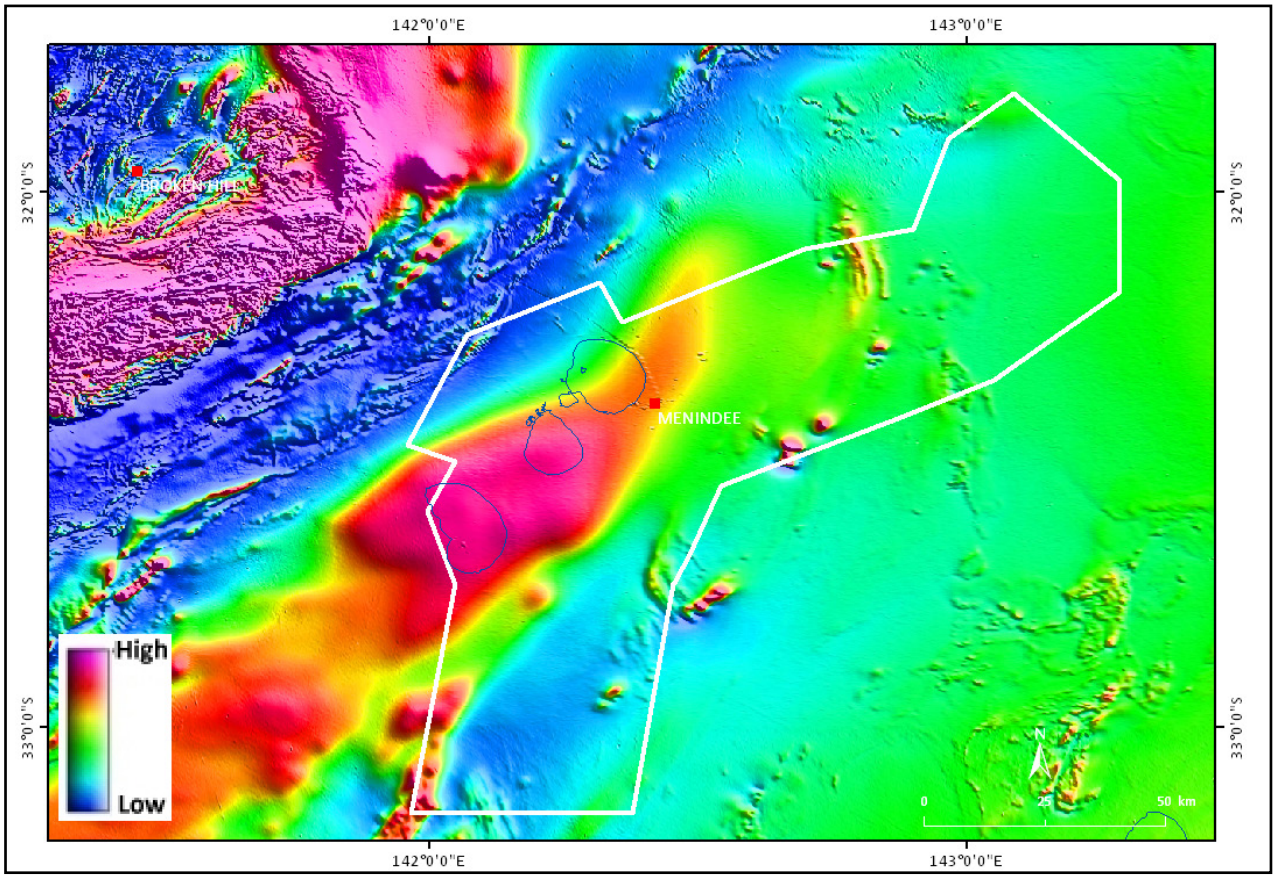



**Figure 4-14.** *Airborne magnetics dataset (stitched) for the Broken Hill area. Data are total magnetic Intensity (RTP).*

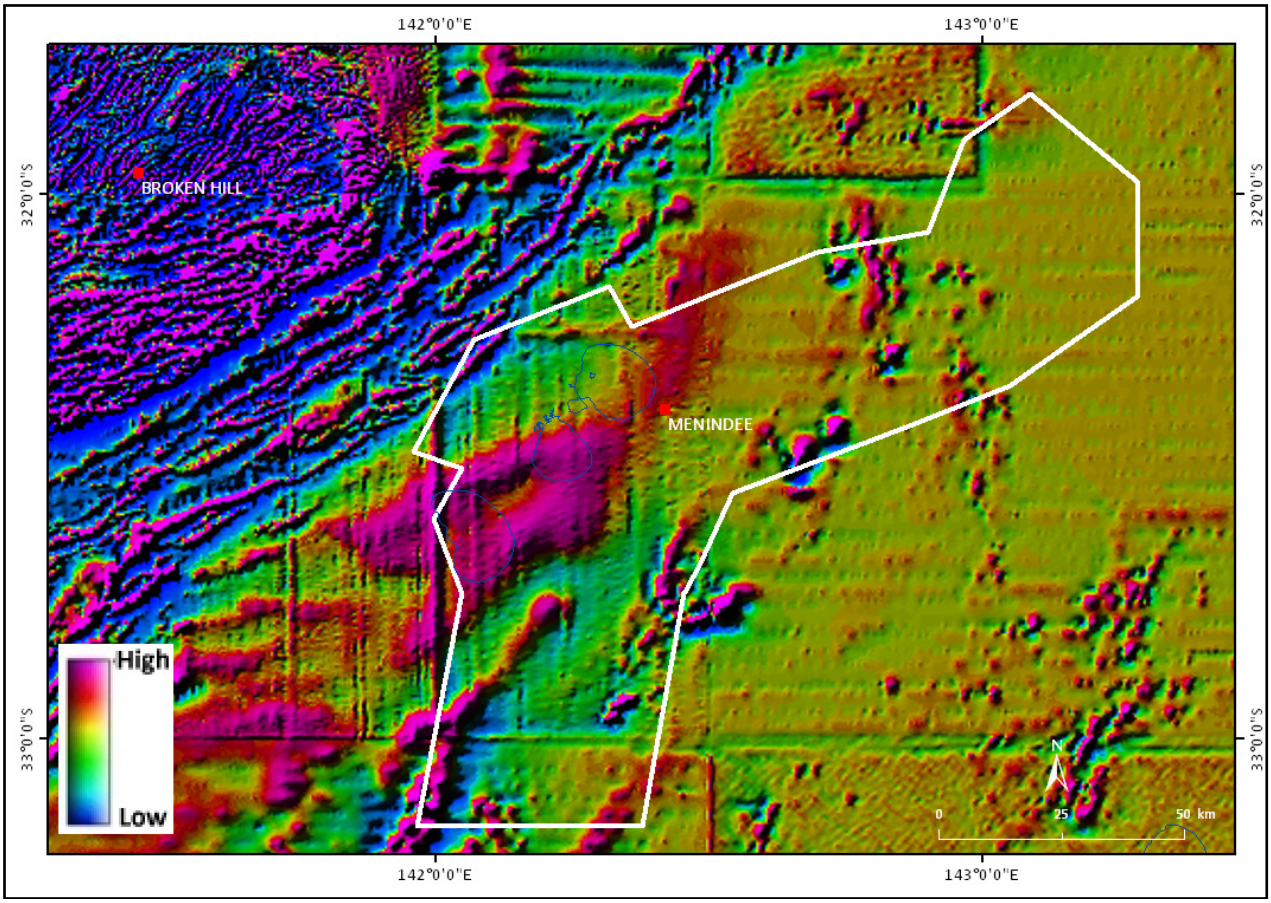



**Figure 4-15.** *Airborne magnetics dataset (stitched) for the Broken Hill area. Data are First Vertical Derivative.*

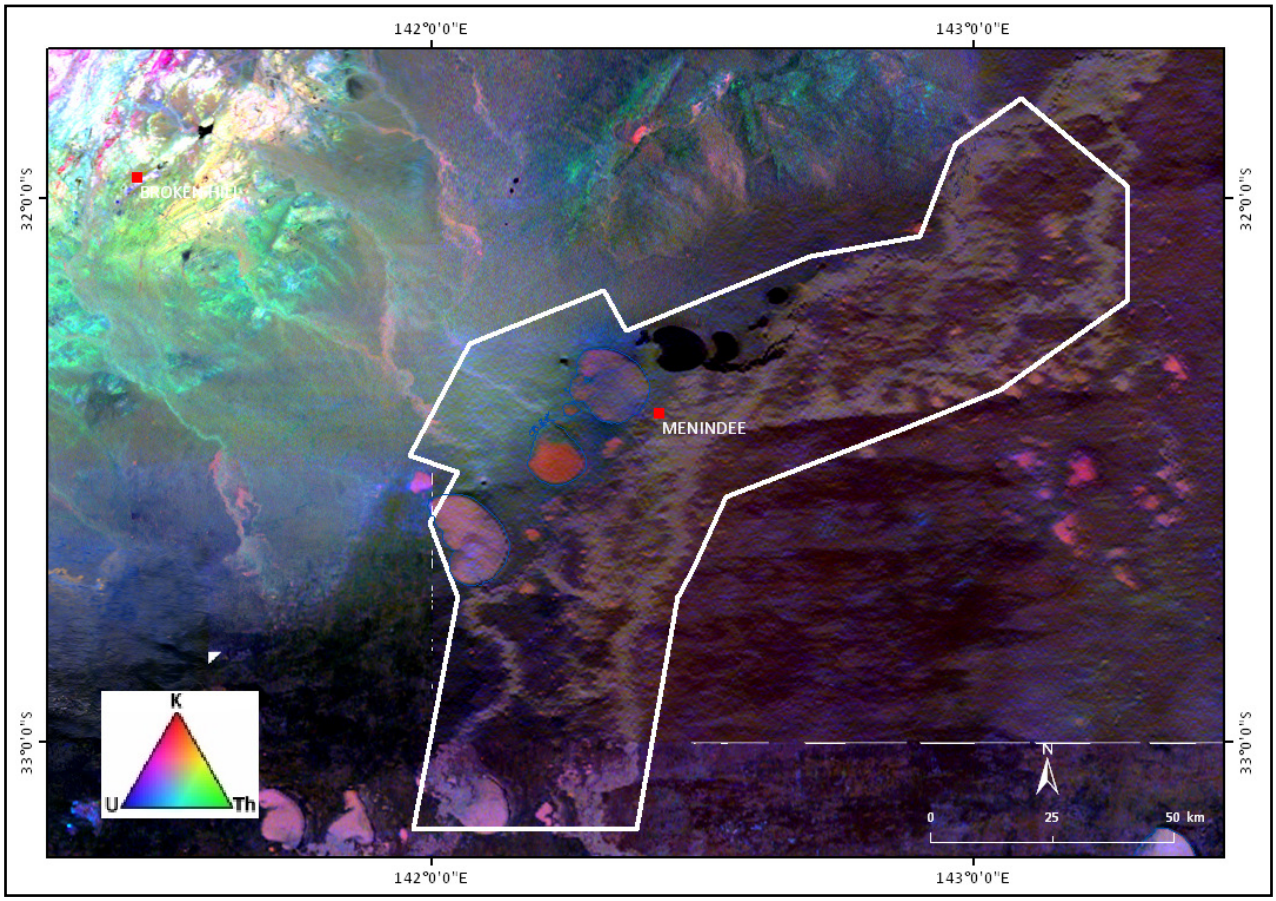



**Figure 4-16.** *A ternary gamma radiometric image for the Broken Hill area. Potassium = red; Uranium = blue; Thorium = green; high total gamma radiation = white; low gamma radiation = black.*

## 4.3 DIGITAL ELEVATION DATA

High resolution LiDAR digital elevation models have proven particularly effective in providing a base for mapping soils, geomorphic units and recharge/discharge areas in floodplain landscapes (Lawrie *et al*., 2009d; Clarke *et al*., 2007a, b). There are no pre-existing LiDAR datasets available for the project areas. As a consequence, the highest resolution pre-existing DEM is the national SRTM dataset (Figure 4-17). Unfortunately, in floodplain environments such as the Murray and Darling systems, the latter are not sufficiently high enough resolution to map the <20 cm elevation differences that typically distinguish the surface soil and geomorphic units (Clarke *et al*., 2007a, b). Hence, acquisition of a LiDAR dataset for the priority project areas was recommended as a priority to provide a base for mapping surface materials and recharge areas and to underpin decisions on MAR options, with the added benefit of useful future application in natural resource management within the region.

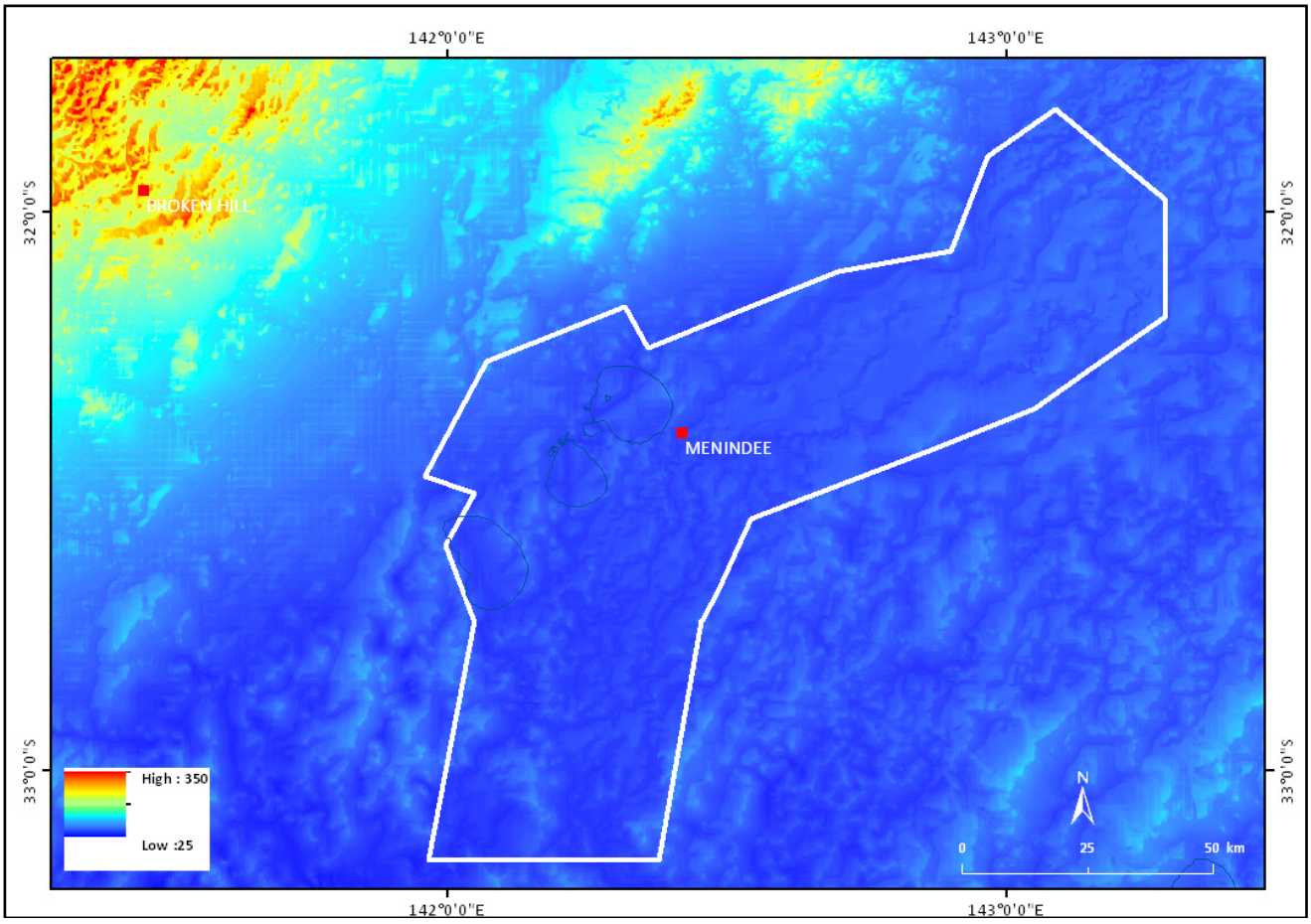



**Figure 4-17.** *SRTM 1 second dataset for the Broken Hill project area, showing elevations above the Australian Height Datum (AHD). Elevations are approximately ± 15 m vertically.*

## 4.4 REMOTELY SENSED SATELLITE DATA

Time-series Landsat data are available for the study area. In the absence of existing flood extent maps, the satellite imagery may be of particular use in contributing to a regional perspective of where floodwaters might flow and accumulate in the floodplain landscape, processes that may be significant to groundwater recharge in the region. Diachi (ALOS) AVNIR2 imagery is also available over most of the project area (Figure 4-18). These datasets may be useful in mapping vegetation, other recharge responses and characteristics, as well as other land surface parameters.

An assessment of MODIS data was that the resolution was too coarse for this study, with many of the riparian zones only 50-200 m in width. Similarly, an assessment of ASTER data found that the data was also of too coarse resolution for integration with finer-scale mapping products.

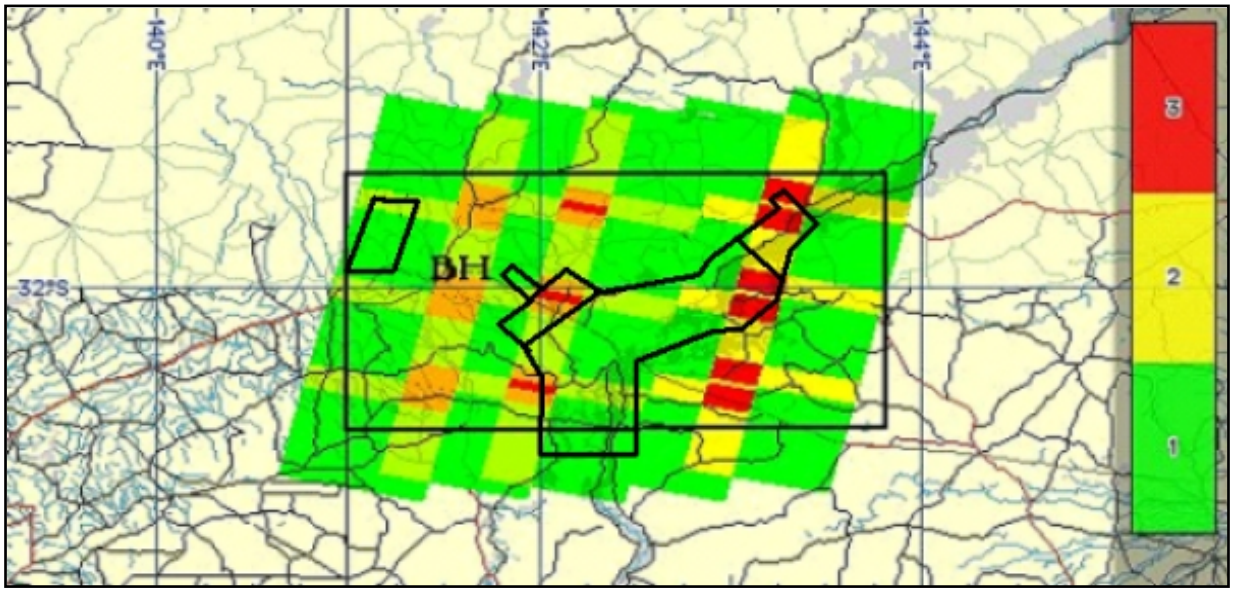



**Figure 4-18.** *ALOS image availability for the Broken Hill area (20 overlapping scenes cover the Broken Hill area of interest). The colours represent the degree of overlap of scenes (green = 1, yellow = 2, red = 3).*

## 4.5 LAND USE AND CADASTRAL MAPPING

The most common land tenure in the region is the Western Lands lease. Land use is primarily grazing, and opportunistic lake bed cropping is common following floods. There do not appear to be any Native Title claims or determinations in the proposed project areas (at end December 2008). However the Menindee Lakes have particular importance for indigenous occupation and there are many sites and artefacts particularly in the lake lunettes. The Kinchega National Park (Figure 4-19) is an area of significant indigenous cultural and environmental value centred on the Menindee Lakes to the south-west of Menindee township.

Maps showing the distribution of historical (pre 1970-2000; Figure 4-20 a-d) and recent (2009-2010; Figure 4-20e) mineral and petroleum exploration licences, show that the Mundi Mundi area has a substantial mineral exploration focus (historically for uranium and silver, and more recently for copper and gold (Figure 4-21). Possible future mining of these resources may result in issues pertaining to claims on shallow groundwater resources in the region. There is also some mineral exploration interest in the Yancowinna Creek and Stephens Creek areas. Exploration interest in the Darling Floodplain is primarily concerned with the much deeper potential for petroleum resources, and is unlikely to impact on groundwater resources being targeted in Murray Geological Basin aquifers.

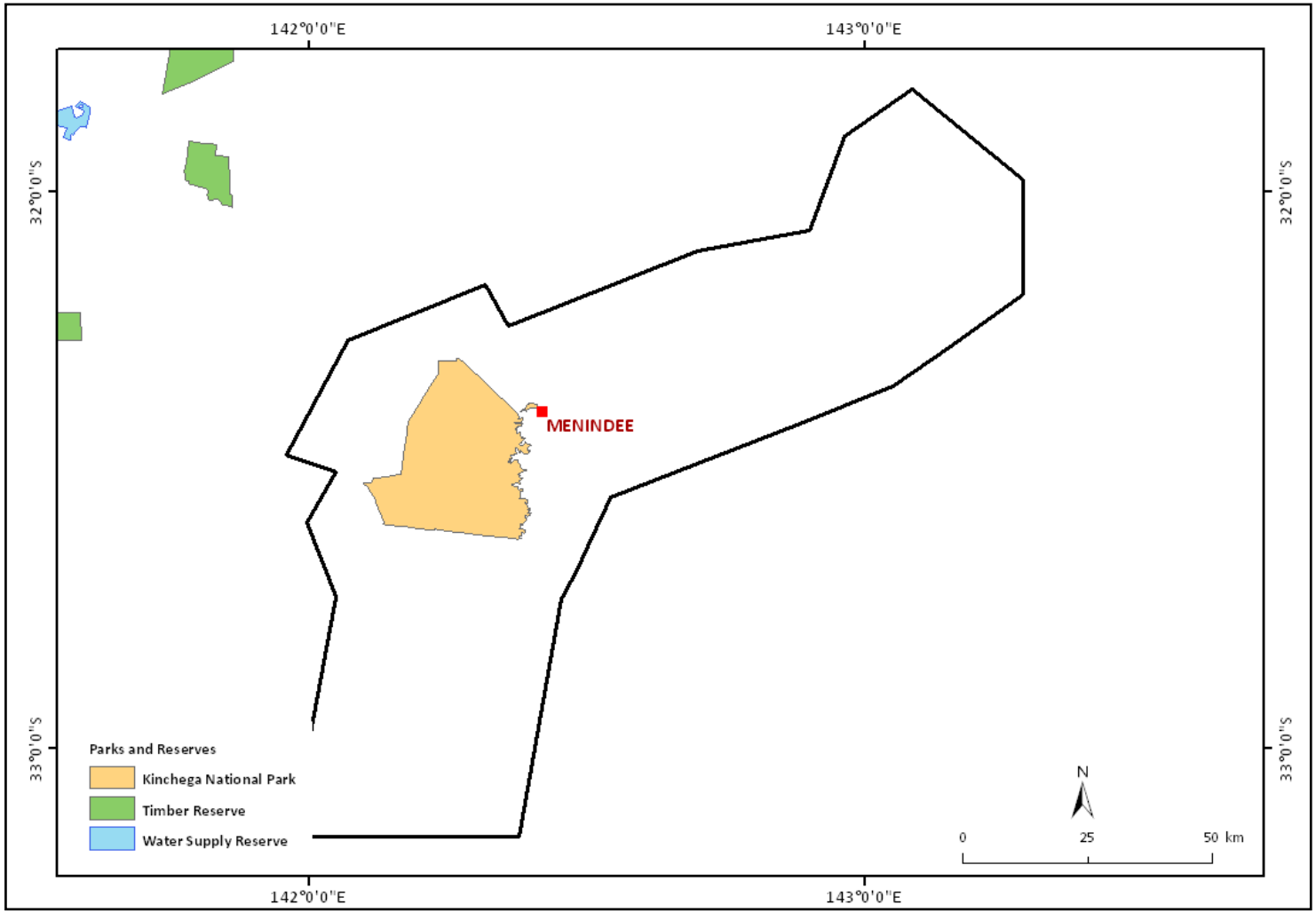



**Figure 4-19.** *Map showing Kinchega National Park, Timber Reserve and Water Supply Reserve Boundaries in the BHMAR project area. Proposed BHMAR study area outlined in thick black. There do not appear to be any Native Title claims or determinations in the proposed project area (at end December 2008). However the lakes have particular importance for indigenous occupation and there are many sites and artefacts particularly in the lake lunettes. The Kinchega National Park is an area of significant cultural and environmental value centred on the Lakes to the SW of Menindee.*

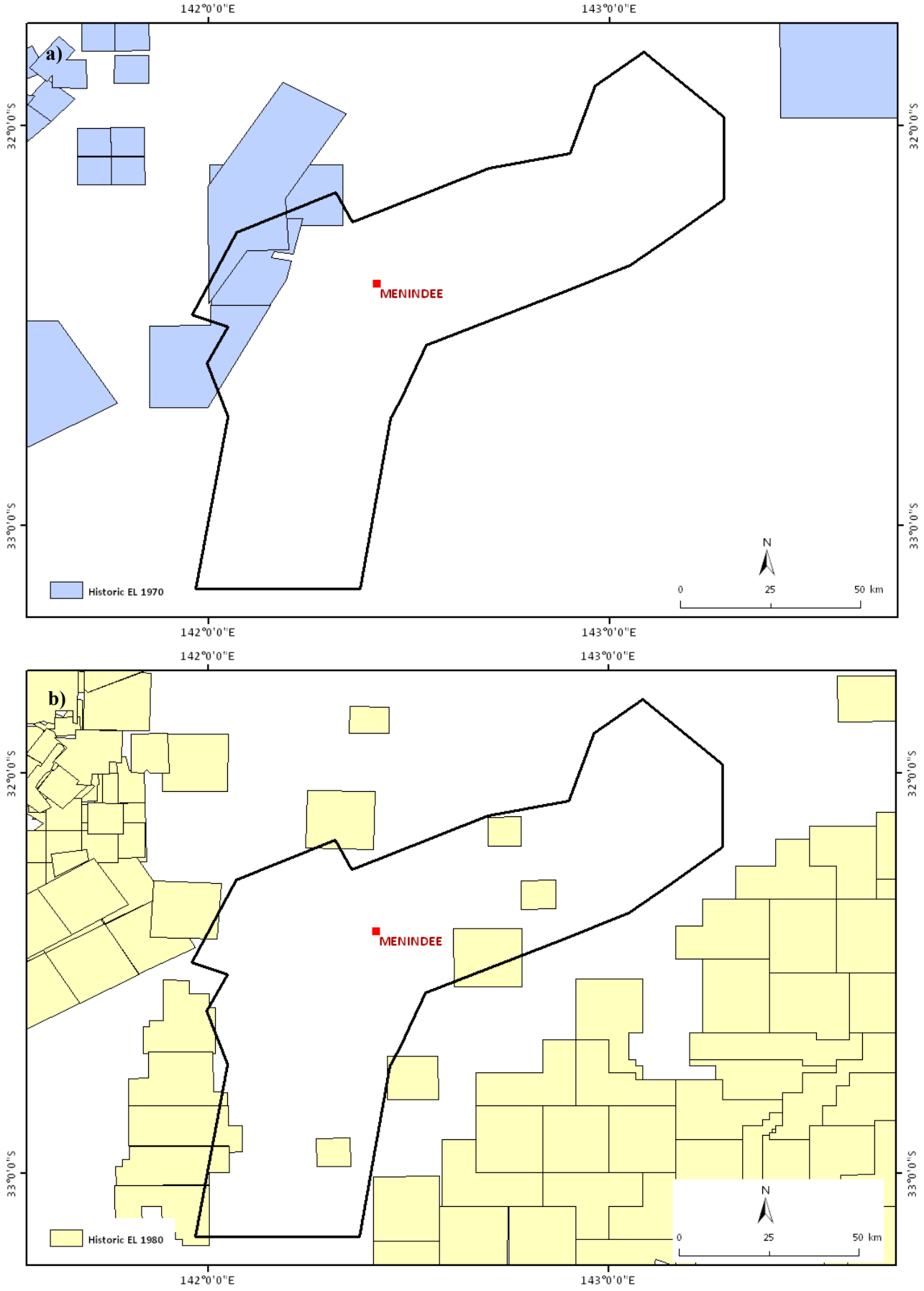



**Figure 4-20.** *Exploration lease areas prior to and during a) 1970 and b) 1980.*

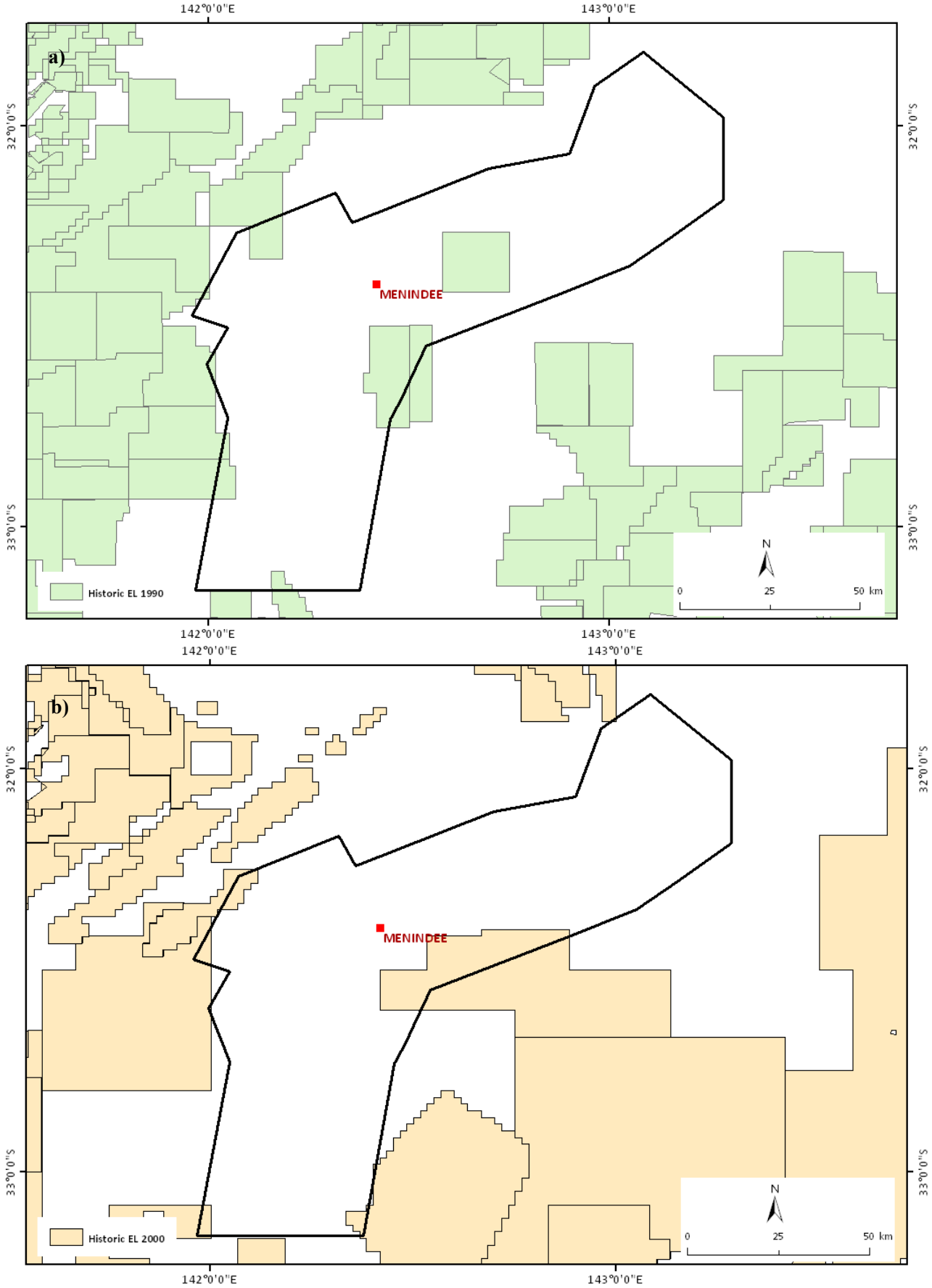



**Figure 4-21.** *Exploration lease areas for a) 1990 and b) 2000.*

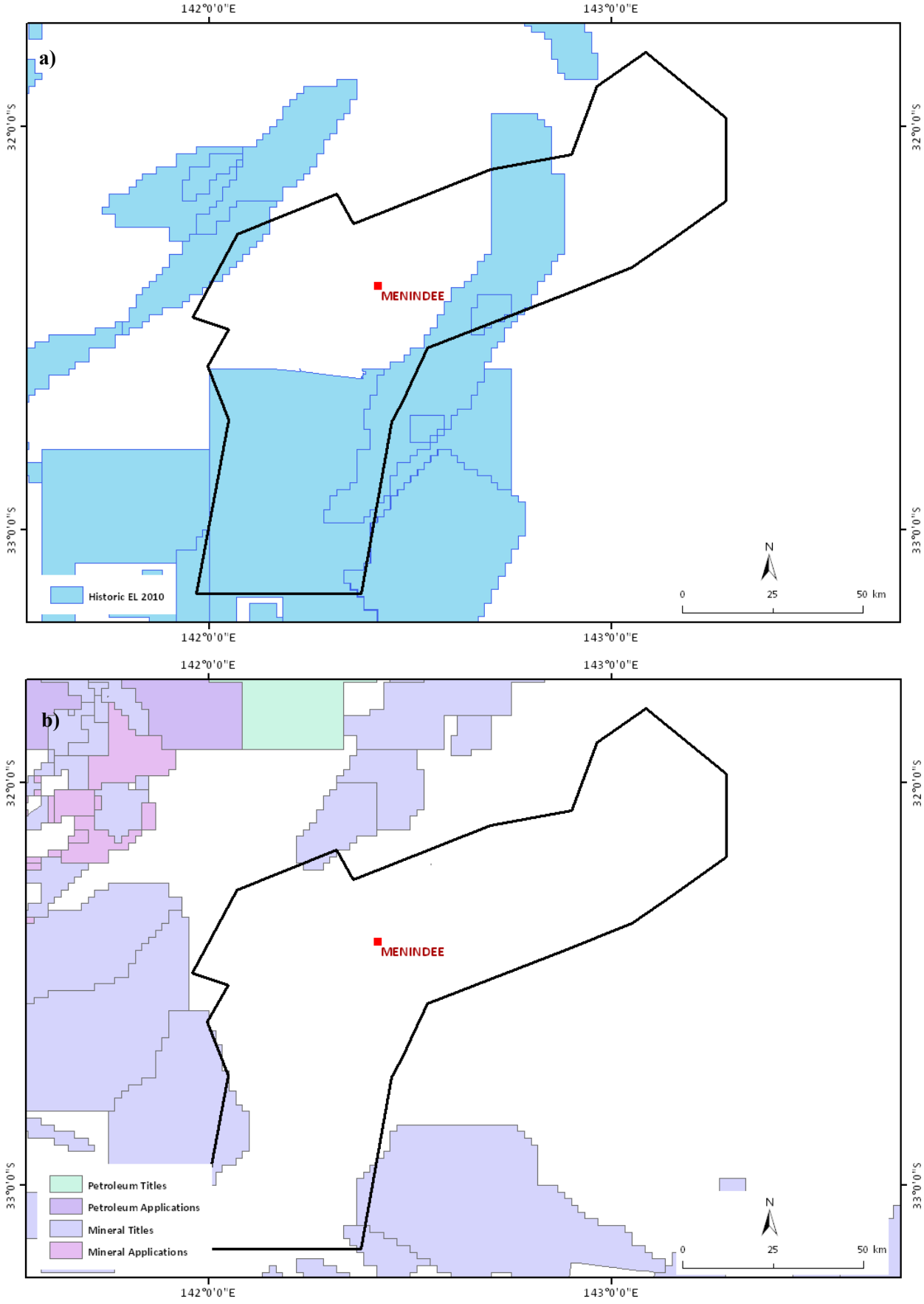



**Figure 4-22.** *Exploration lease areas for a) 2010 and b) current mineral and petroleum exploration titles and applications.*

## 4.6 SUMMARY ASSESSMENT OF PRE-EXISTING DATA

A comprehensive review of pre-existing biophysical (e.g. geological, hydrogeological, hydrogeophysical, hydrogeochemical, landscape, vegetation, cultural and environmental) data relevant to the identification and assessment of potential MAR and groundwater resource targets was carried out in Phase 1 of the BHMAR project (Lawrie *et al*., 2009). This assessment built on existing data compilations (e.g. Lewis *et al*., 2008) and brought together all relevant hydrogeological, geological and geophysical data, including borehole data, from the databases of Geoscience Australia, NSW State Agencies, CSIRO, MDBA, Country Energy, local natural resource management (NRM) and catchment management authorities (CMAs), mineral and energy exploration sources, and landholders.

The review entailed a technical assessment of data, and entry of relevant filtered data in a database linked to the project GIS. This was deemed essential to assist a full technical risk assessment of the data. Relevant pre-existing airborne, ground, in-river and borehole geophysical data (including airborne magnetics, airborne gamma radiometrics, and electromagnetics), remote sensing data (Landsat, ALOS, ASTER, SPOT, SRTM, LiDAR and InSAR data), vegetation structure and condition mapping, and relevant cultural data, were also compiled and assessed for their suitability. The principal findings of the review (Lawrie *et al*., 2009) were:

Borehole geological and geophysical data:

- At first glance, there would appear to be a significant number of pre-existing boreholes in the Broken Hill area. However, Phase 1 investigations found that the vast majority of these bores contained inadequate geological and hydrogeological descriptions and data to assist with the identification and assessment of MAR and/or groundwater resource targets. Most of the bores were not drilled for hydrogeological investigations, hence are not fit for this purpose.
- Greater than 90% of the 3,292 pre-existing bores assessed in the Phase 1 investigations across the 6 potential study areas were shallow bores (<30 m depths). Less than 6% (190 of the 3,292 bores) had useable/reliable lithological data; approximately 0.2% (18 bores) had some lithological data (mainly drillers logs) for the priority Calivil Formation aquifer in the BHMAR study area, and only 6 of these bores contained reliable/useable geological/hydrogeological data.
- Only 152 of the 3,292 bores were recorded as having PVC casing that would enable borehole hydrogeophysical studies to be conducted (e.g. for airborne electromagnetic (AEM) dataset calibration and validation. Only 12 bores with PVC linings were recorded as intersecting the Calivil Formation aquifer in the BHMAR study area. Less than a dozen bores had any borehole geophysical data.
- No core materials for the key aquifer and aquitard intervals existed for the study area, severely limiting assessment of the aquifers and aquitards.

Groundwater and hydrogeological data, maps and models:

- There was sufficient groundwater salinity data from shallow bores and a few deeper bores to state with reasonable certainty that a dilution aureole was developed in proximity to the Darling River and Talyawalka Creek. However, the data density and depth meant that it was not possible to recognise groundwater or MAR targets in the Calivil Formation aquifer using these data.
- There was insufficient major and trace element hydrogeochemical data to carry out MAR risk assessments, or to determine groundwater processes.
- There were pump test data from a couple of bores, and slug tests from half a dozen bores in the study area. However, even these limited data gave some confidence that the Calivil Formation aquifer may have suitable aquifer properties in some locations, although pre-existing data was insufficient to target locations with suitable properties.
- Pre-existing groundwater models for the BHMAR study area were based on a paucity of hydrogeological and geological data, and a limited understanding of groundwater processes including recharge and inter-aquifer leakage. The groundwater models were insufficiently parameterised to assist with the groundwater or MAR assessments.

- Pre-existing regional-scale hydrogeological maps for the study area are superior to the geological maps of the same area. While they are of limited use due to the extrapolation between widely spaced boreholes, there are useful cross-sections as well as salinity-yield distribution plots that assisted with determining the extent of the project area and aided with the design of new data acquisition strategies.
- There were no salinity distribution or hazard maps for the study area.

Geophysical data:

- In addition to very limited borehole geophysical data, one pre-existing ground resistivity survey, and an in-river (and in-lake) reconnaissance resistivity survey were assessed. These data were of limited areal extent and ground penetration and provided limited insights into the stratigraphy and groundwater.
- Regional airborne magnetic and gamma radiometric data over the BHMAR study area is sourced from a patchwork of surveys and specifications. There are no data gaps, however there is no high-resolution data, with the best data being course (400 m +) regional line spacing data in a portion of the study area. There were no AEM data for the project area.
- There are 5 regional seismic reflection surveys and a couple of smaller surveys in and/or bordering the study area. These data were acquired as part of regional studies by Geoscience Australia and the NSW Government, and by the Petroleum sector. While these data generally target deeper crustal structures and basins, they provide some useful information on basement structures in particular.

General geological, tectonic, geomorphic and stratigraphic data

- There were no modern, detailed geomorphic or surface geological maps for the BHMAR study area. Limited investigations around the MLS did however provide some useful insights into the geomorphology of the lakes.
- Geology maps and cross-sections for this area are over 50 years old, and therefore do not take into account more recently acquired data or modern geological interpretations. The existing geological maps are of very limited use.
- The stratigraphy of the area was only understood at a regional scale, with a poor understanding of the Pliocene and younger Murray Basin sediments. In particular, there was only a very cursory understanding of the distribution and characteristics of the aquifers and aquitards of interest in the study area.
- With the exception of the Stokes Range (neotectonics) Fault on the extreme NW boundary of the project area, and some basement faults mapped from seismic, airborne magnetic and regional gravity data, there were no mapped faults in the project area, despite the study area adjacent to the transcontinental Darling River Lineament.

Remote sensing data

- SPOT, ASTER, and time series Landsat data were found to cover the project area adequately.
- The narrowness of riparian and lake-bordering vegetation zones ruled out the use of MODIS data for vegetation condition mapping.

Digital Elevation Models (DEMs):

- It was recognised at the commencement of the project that a high-resolution (<0.5 m vertical resolution, 5-10 m lateral resolution) DEM would be vital for mapping key elements of the surface geomorphology and floodplain hydrology, and for identifying and assessing passive MAR (infiltration) options.
- However, most of the pre-existing DEMs for the study area had insufficient horizontal or vertical resolution to underpin the hydrological and hydrogeological investigations. The highest resolution dataset available was the SRTM dataset, with a vertical resolution of ~10-15 m. Laser DEMs

acquired as part of regional airborne geophysics acquisition programs have a vertical resolution of ± 4 m. There was no suitable time-series InSAR data over the study area, and very few accurately surveyed ground elevation control points.

- There was one small LiDAR survey in the project area (in the vicinity of Lake Wetherell). However, this survey was limited by inadequate reporting of ground control points and data manipulations.
- There were no maps of vegetation structure or condition in the study area.

Land Use, Native Title and Cultural Maps:

- The study area is primarily Western Lands Lease, and is primarily grazing with some local viticulture and opportunistic lake bed cropping (Lake Tandou). The Kinchega National Park is an area of significant indigenous cultural and environmental value.
- There were no native title claims registered over the study area at the time of the project (2008-2012).
- There was a reasonably good regional understanding of the distribution of important Indigenous cultural sites. However, these data did not extent to the local scale, and it was recognised early on in the project that cultural and environmental assessments would have to be carried out at all ground investigation sites.

# 5 LiDAR Data

In the Phase 1 study, a review of available Digital Elevation Model (DEM) data showed that existing datasets were inadequate for mapping floodplain elevations with the accuracy and precision required (Lawrie *et al.,* 2009a). It was recommended that a high resolution LiDAR data be acquired to provide a high resolution topographic base for surface and sub-surface mapping, borehole data comparisons and AEM processing, calibration and interpretation. It was further recommended that specifications of this survey should include vertical resolutions of 15-20 cm. Acquisition of this dataset was viewed as critical for the mapping of surface geomorphology in such a flat landscape, for the mapping and prediction of flood inundation and potential recharge pathways, and for the to the assessment of vegetation health and MAR options (including infiltration).

## 5.1 LIDAR DATA ACQUISITION

Geoscience Australia used an internal LiDAR selection panel convened under the terms of Geoscience Australia's pre-existing Deed of Standing Offer in relation to the acquisition and supply of AEM data to oversee the acquisition of a LiDAR survey for the BHMAR Phase 2 project area. This activity was designed to generate accurate digital terrane (bare earth DTM) and digital surface (earth + vegetation canopy DSM) models. These products are important to provide an accurate topographic base map for the AEM and hydrogeological data including drilling.

The survey was contracted using the Panel's Quotation Request process. The panel was responsible for LiDAR survey design and the drawing up of survey specifications for Quotation Requests and final contracts; established selection criteria for assessment of LiDAR system selection, and provided recommendations on system selection to the project leader and the Department of the Environment; drafted and supervised the drafting of LiDAR survey contracts; oversaw LiDAR data acquisition, Qa/Qc of LiDAR data, and delivery of data and model products for the Phase 2 survey; and were responsible for formal project communications with the LiDAR contractors and for reporting to the project leader on progress against milestones, and for providing early warning to the project leader (and the Department of the Environment) of the need for any significant slips in data acquisition timelines and/or the need for remedial actions.

Upon completion of the tender process, AAMHatch Pty Ltd. was engaged to undertake a LiDAR survey over the BHMAR Phase 2 project area for the purposes of generating accurate bare-earth digital elevation models and digital surface models (DSM) describing vegetation height and density. The total survey covers an area of ~7,856 $km^2$ on the Lower Darling River, downstream from Wilcannia (Figure 5-1). Acquisition was undertaken between June 19$^{th}$ and August 5$^{th}$ 2009 (AAM Hatch, 2009; Table 5-1; Figure 5-2). Dust storm activity significantly reduced visibility (Figure 5-3) and contributed to an extension of the time required for surveying.

A Leica ALS50-II sensor was used for this project. This sensor is capable of detecting multiple returns, with a minimum of 4 potential returns for each outbound laser pulse and can record the intensity of each return. The planned point density for the survey was an average density of 2 points/$m^2$ with actual point spacing average of 0.71 m across the 1032 m wide swath. The maximum cross and long track is 1.27 m and 1.22 m. General capture specifications are shown in Table 5-1. For more details pertaining to the acquisition of the LiDAR, please refer to the AAMHatch Report in Appendix 14 (Lawrie *et al*., 2012f).

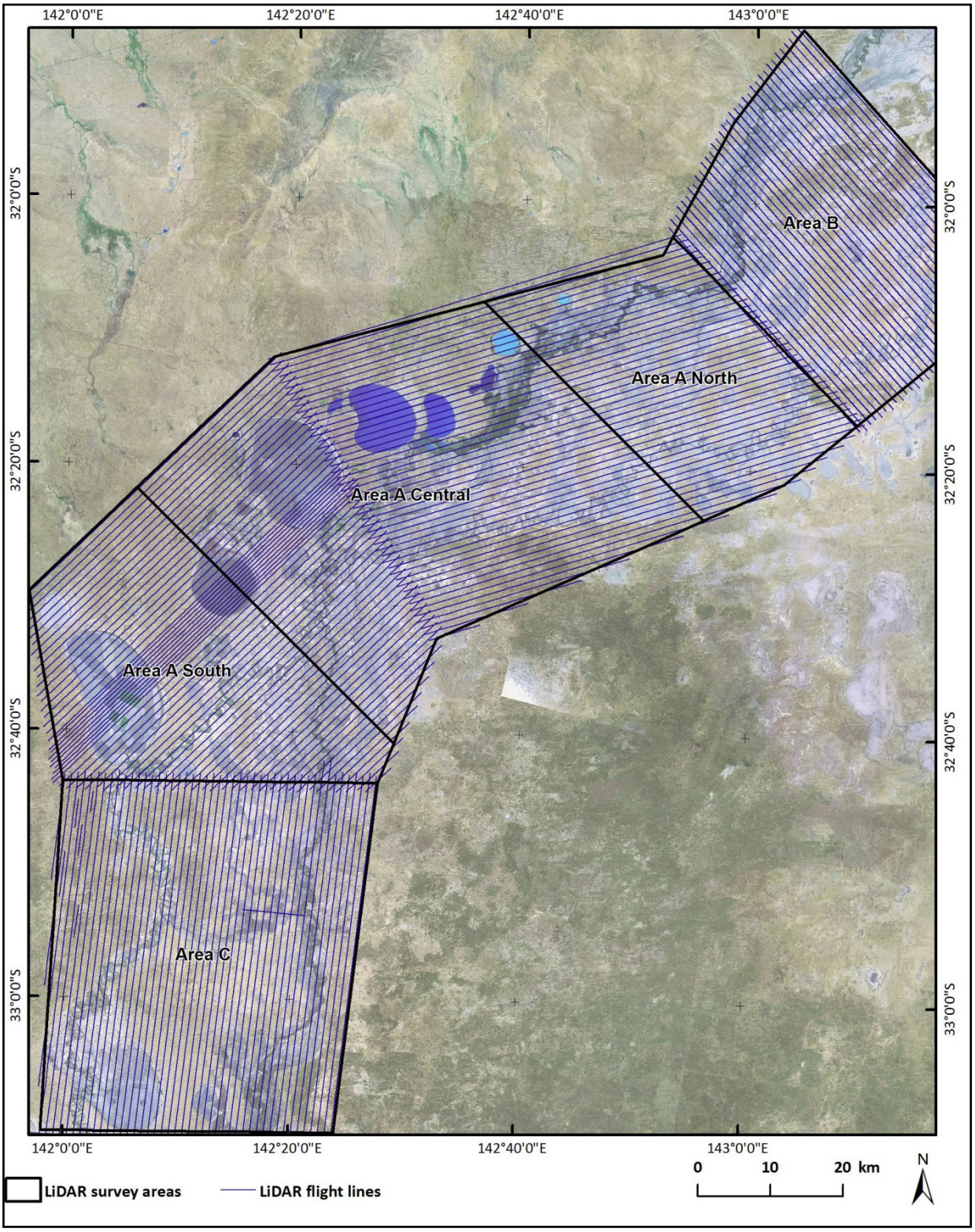



**Figure 5-1.** *LiDAR survey area covering approximately 7856 km$^2$ of the Lower Darling River, downstream of Wilcannia.*

**Table 5-1.** *LiDAR survey data acquisition parameters.*

| **Metadata Elements** | |
|---|---|
| **Characteristic** | **Description** |
| Device Name | Leica ALS50-II S/N 091 |
| IMU Used | Honeywell UIRS S/N 56016277 |
| Acquisition Start Date | 19 June 2009 |
| Acquisition End Date | 05 August 2009 |
| Number of Runs | 208 |
| Number of Cross Runs | 6 |
| Flight Direction | Various Directions |
| Flying Height (AGL) | 1800 m |
| Half Scan Angle | 16 degrees |
| Swath Width | 1032 m |
| Sidelap | 10% |
| Average Point Spacing | 2 pts/$m^2$ |
| Laser Pulse Rate | 127.5kHz |
| Laser Pulse Mode | Multi-pulse |
| Laser, Max Number of Returns per Pulse | Up to Four pulses, $1^{st}$, $2^{nd}$, $3^{rd}$, and $4^{th}$ |
| Laser Intensity | Supplied on all returns |
| Laser footprint size @ nadir, level ground | 0.41 m |
| Grids | 1 m grid cell size Digital Elevation Model (DEM) generated from ± 0.294 m Accuracy (95%) LiDAR |
| Grids | 1 m grid cell size Canopy Elevation Model (CEM) generated from ± 0.294 m Accuracy (95%) LiDAR |
| Grids | 10 m grid cell size Foliage Cover Model (FCM) generated from ± 0.294 m Accuracy (95%) LiDAR |
| Data thinning | Model Key points ±0.15 m RMSE |
| File Format | LAS |
| Horizontal Datum | GDA94 |
| Vertical Datum | AHD using Local Geoid Model Ausgeoid98 |
| Map Projection | MGA Zone 54 |
| Vertical Accuracy Requirement | 0.294 Fundamental Vertical Accuracy, 95% Confidence Level (RMSE*1.96) |
| Horizontal Accuracy Requirement | 0.432 Fundamental Vertical Accuracy, 95% Confidence Level (RMSE*1.7308) |
| System Calibration Certification | Leica Geosystems AG (SN091PII+ Cal Report 080317)17 March 2009 |



**Figure 5-2.** *View of the Menindee Lakes from the AAMHatch survey aircraft.*



**Figure 5-3.** *LiDAR survey grounded at Broken Hill airport due to dust storm activity (image below) which significantly reduced visibility (image above) and contributed to an extension of the time required for surveying.*

A canopy elevation model was produced as one metre ESRI ArcGIS binary grids using ArcGIS with the following methodology (McGaughey, 2007):

- All ground surface derived using natural neighbours interpolation [G] (Floating Point)
- First return vegetation surface derived using natural neighbours interpolation [V1] (Floating Point)
- Height in metres above ground of first vegetation returns [V1] - [G] = [H] (Floating Point)
- Mask of all vegetation ALS returns with 1 m buffer, reclassified to 0 outside mask and NoData inside [M] (Integer)
- Mosaic of canopy height surface and vegetation mask [H] + [M] = CEM (Floating Point)

A foliage cover model has been produced as 10 m ESRI ArcGIS binary grids using ArcGIS with the following methodology:

- Count of all vegetation returns per 10 m cell [V] (Integer)
- Count of total ALS returns per 10 m cell [A] (Integer)
- Proportion of all vegetation to total ALS returns expressed as a percentage ([V] / [A]) * 100 = FCM (Floating Point).

FCM values can be skewed, typically larger, in areas of overlap between flight lines as there will be more returns per $m^2$ simply because two flight lines have covered the same area. Additionally, FCM values can also be skewed because there may be a greater proportion of vegetation returns due to scan angle. Finally, the quality of the vegetation classification used can influence FCM values. This process is used to remove overlap and correctly classify ground returns. In this case, AAMHatch used an algorithm to initially classify ground and then subsequently manually reviewed the data.

## 5.2 CALIBRATION AND DATA PROCESSING

The following section contains extracts from the AAMHatch Final Report which is available in Appendix 14 (Lawrie *et al*., 2012f).

### 5.2.1 Vegetation Capture Issues

An issue raised during the Qa/Qc process was the possibility that vegetation was potentially caught in the ground terrain model. It is not uncommon for surface matter to build up around and under low-lying vegetation, particularly in areas prone to strong winds. Any further removal of suspected vegetation borders on subjectivity and interpretation while having potential to degrade surface accuracy and definition.

After reviewing the issue AAMHatch concluded that all possible vegetation had been removed from the ground surface by utilising a combination of automatic and manual editing/removal of laser strikes not defining the ground surface. The following examples (Figure 5-4, Figure 5-5 and Figure 5-6) illustrate the level of vegetation removal.

### 5.2.2 Gouging or Reduced Terrain around Trees

The Qa/Qc process also identified what appeared to be *'Gouging or reduced terrain around trees'* in the derived LiDAR surface. Two areas were identified and reviewed, specifically targeting the most predominant feature in the terrain. Contours were overlayed on a shaded surface model and compared with the classified LiDAR points. The suspected 'gouging under vegetation' was found to extend well beyond the edge of vegetation/tree canopy (Figure 5-5). *Gouging* occurred in areas open, free from significant vegetation coverage. Profile views were derived over one of the most predominant land features identified. The profile views exhibited no spiking in the ground surface. There appeared to be a natural slope or bank indicating a change in grade of 0.5 m (vertical) over a horizontal distance of 7-10 m.

The review concluded:

- The LiDAR algorithms have not removed or incorrectly recorded laser ranges under vegetation leading to the surface being lower;
- The surface changes shape "dipping" before the vegetation/trees;
- In this case there were no more valid ground strikes to include in the ground surface definition;
- The minor changes in terrain adjacent to vegetation may have been caused by congregation of stock or local wind or water erosion;
- There is no reason to suspect the land feature has been artificially created by the LiDAR;
- All possible vegetation has been removed from the ground surface utilising a combination of automatic and manual editing/removal of laser strikes not defining the ground surface;
- The LiDAR data is an accurate representation of the terrain at the time of the survey.

If vegetation was being modelled, sharp spikes would have been visible in the ground profile. Alternative explanations for the observed features could be attributed to multi-path return, or more likely, artefacts arising from the interpolation process.

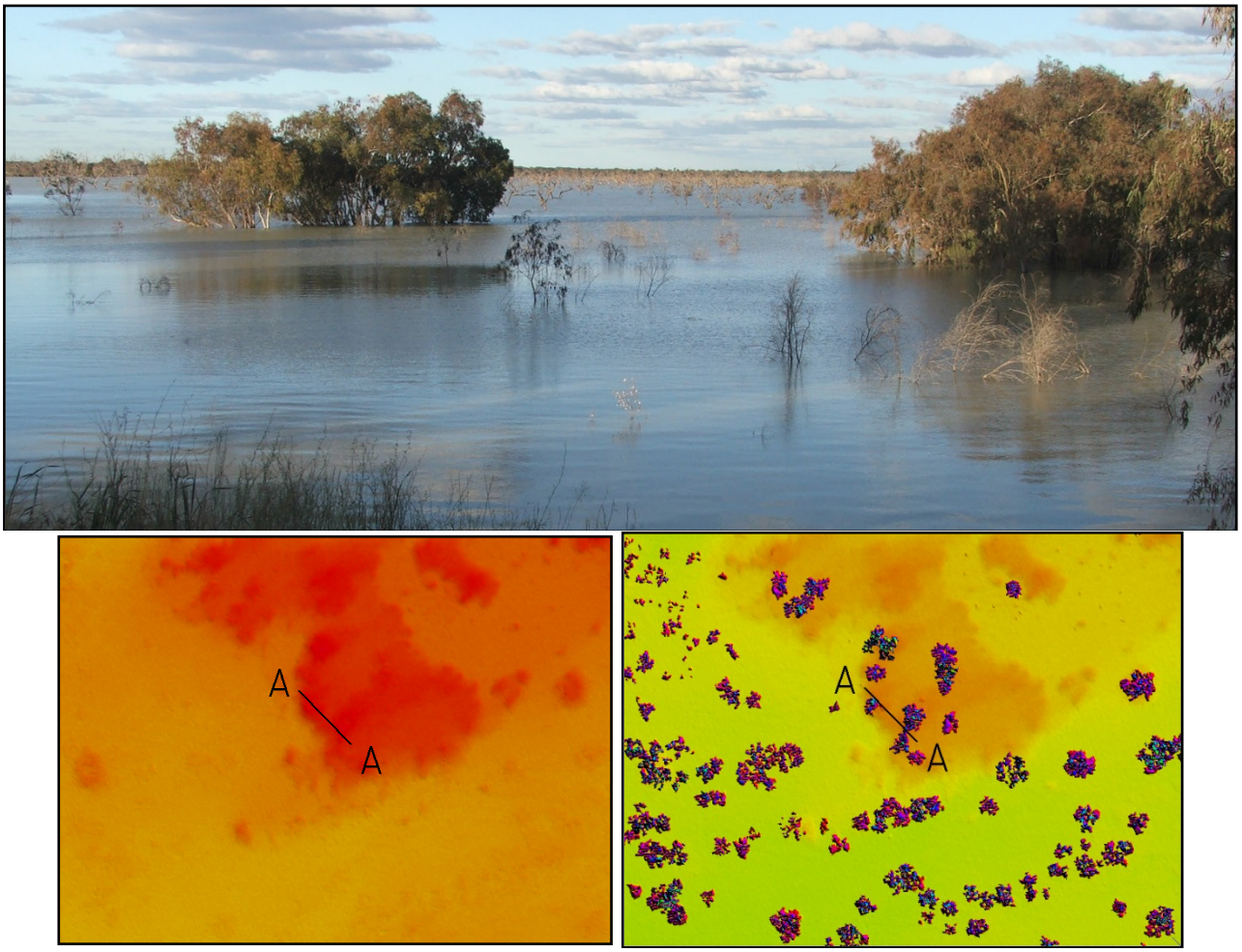



**Figure 5-4.** *Partially submerged vegetation in Lake Wetherell (image above). Figures below show examples of automatic (left) and manual (right) editing/removal of laser strikes not defining the ground surface (i.e. due to vegetation). It is not uncommon for surface matter to build up around and under low-lying vegetation. The figure on the left shows a shaded surface model derived from ground classes, while the figure on the right shows the level of vegetation removal derived from ground and vegetation classes. Any further removal of suspected vegetation borders on subjectivity and interpretation while having potential to degrade surface accuracy and definition (AAMHatch, 2009).*

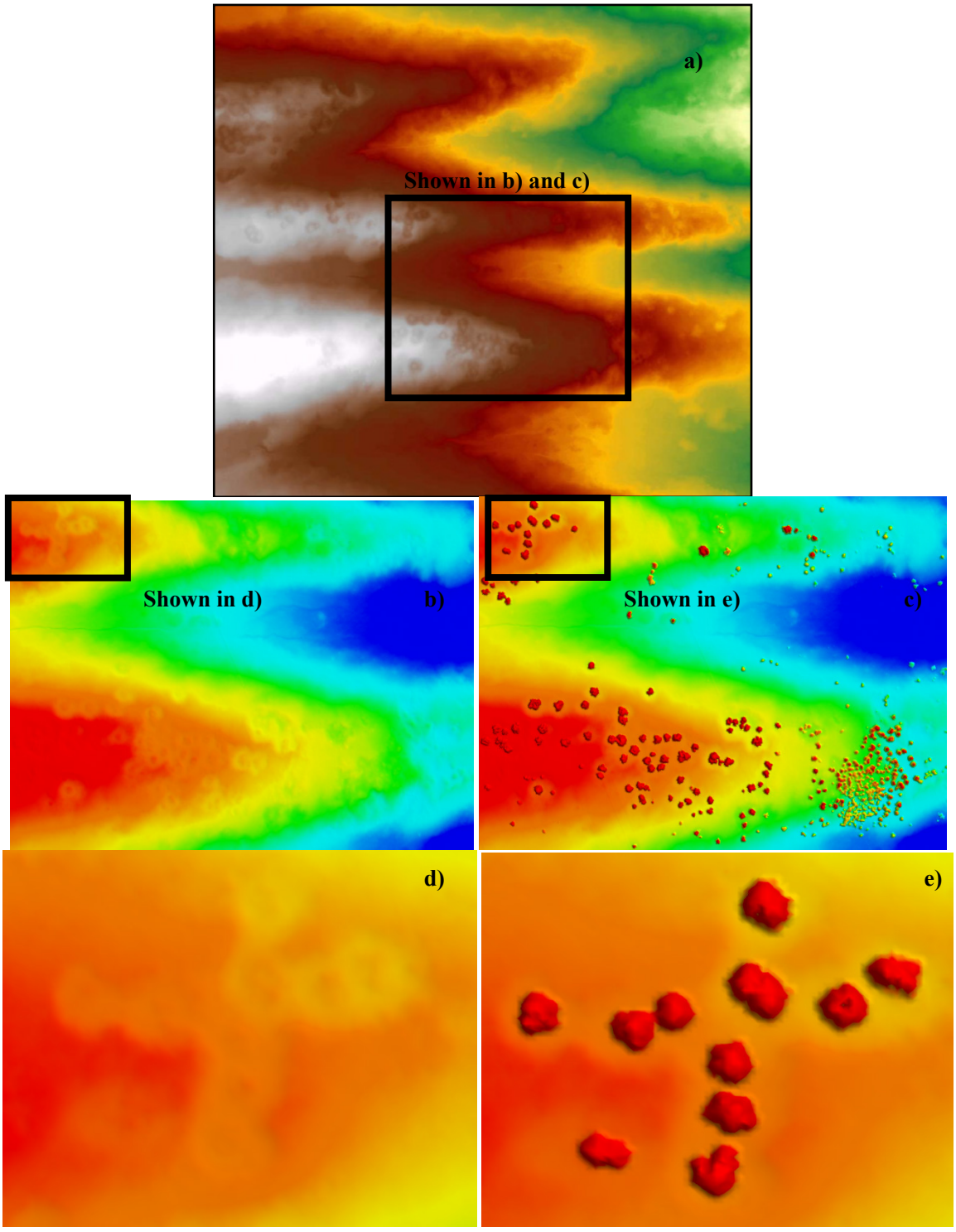



**Figure 5-5.** *LiDAR vegetation removal issues, observed in a) Digital Surface Model (DSM). Comparison between DSM derived from LAS point files included ground classes (b and d – zoomed) and both ground and vegetation classes (c and e – zoomed).*

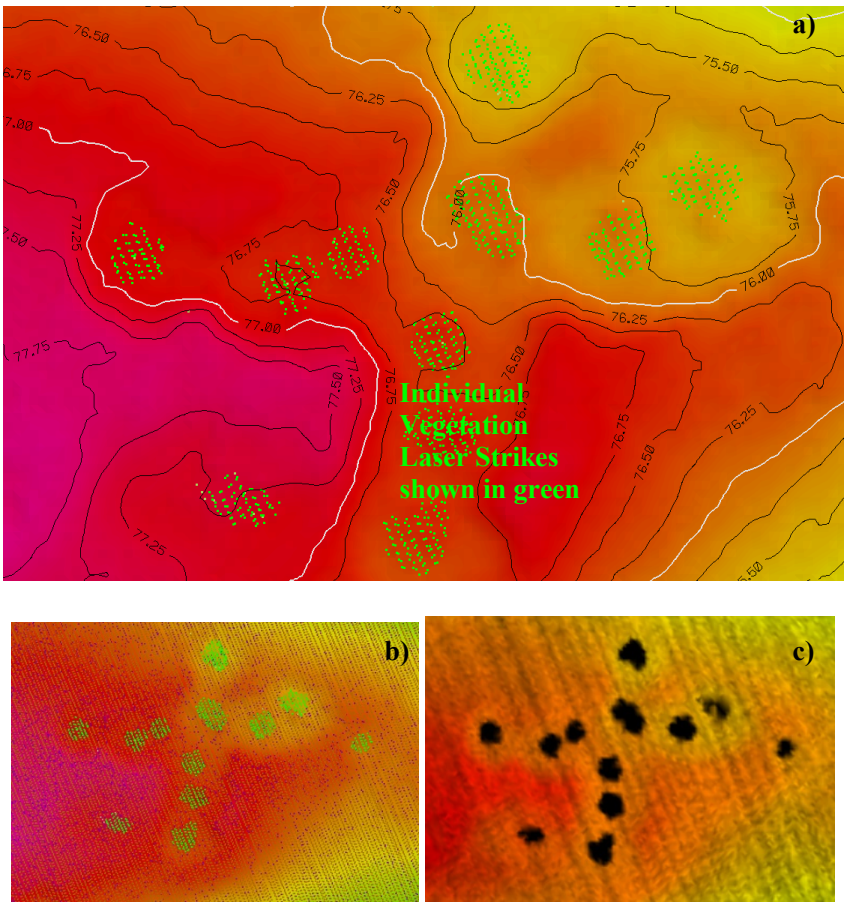



**Figure 5-6.** *Vegetation laser strike removal. Individual vegetation laser strikes are shown as green dots in a) and b) and the final product after removal is shown in c). From AAMHatch (2009).*

### 5.2.3 Classification of Wetland Environments

Wetland areas (Figure 5-7) were noted as areas of special consideration in the LiDAR classification process. Geoscience Australia identified an issue in the definition of the derived LiDAR terrain surface in wetland areas. A review of this issue, carried out by AAMHatch using an example near Lake Wetherell, concluded that these areas present significant complexities for defining a true ground surface because of unreliable LiDAR returns from very turbid surface water. Hopkinson *et al*. (2004) encountered similar affects in the Utikuma Boreal wetland in Alberta, and attributed such underestimation issues to weak laser backscatter from the saturated ground conditions.



**Figure 5-7.** *Wetland environment in the project area showing turbid water in an area with a complex land cover.*

Field checking found that accurate mapping in wetland areas was hindered by a combination of specific issues including:

- Problems posed by the effects of dead (or living vegetation – e.g. trees) protruding from large water bodies;
- Exposed mud and low lying clumping vegetation emerging from the water surface;
- Water interspersed with land having typography of low relief; and
- Areas inundated by turbid water under vegetation.

The image below provides an insight into the complexities of the area in question. The date of the photo is unknown and water levels may be different to when the airborne mission was conducted.

The issues were addressed by:

- Identifying large water bodies and reclassifying as water. Reclassifying vegetation levels above water bodies with fixed water level height,
- Automatic vegetation classification with high parameter settings (0.05 m) to remove low lying vegetation,
- Manual assessment and reclassification of low-lying vegetation emerging from water.

Examples of issues with water body areas (Figure 5-8) and an area of water, vegetation and creek banks (Figure 5-9) before and after the classification corrections were applied. These operations went some way towards resolving the observed inaccuracies but did not eliminate the effects entirely.

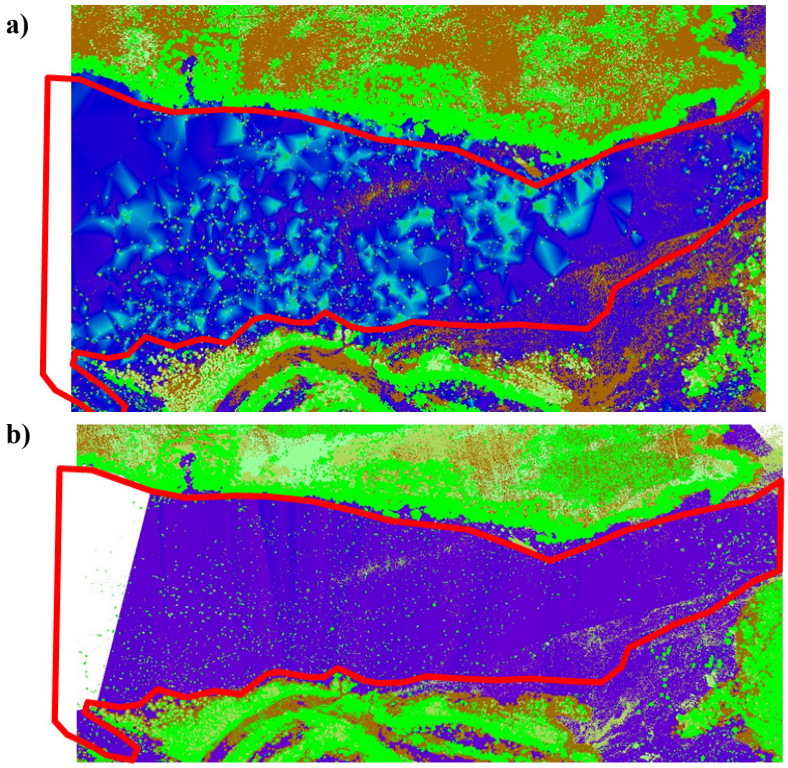



**Figure 5-8.** *LiDAR image showing a) Water body area before classification correction; and b) Water body area after classification correction.*

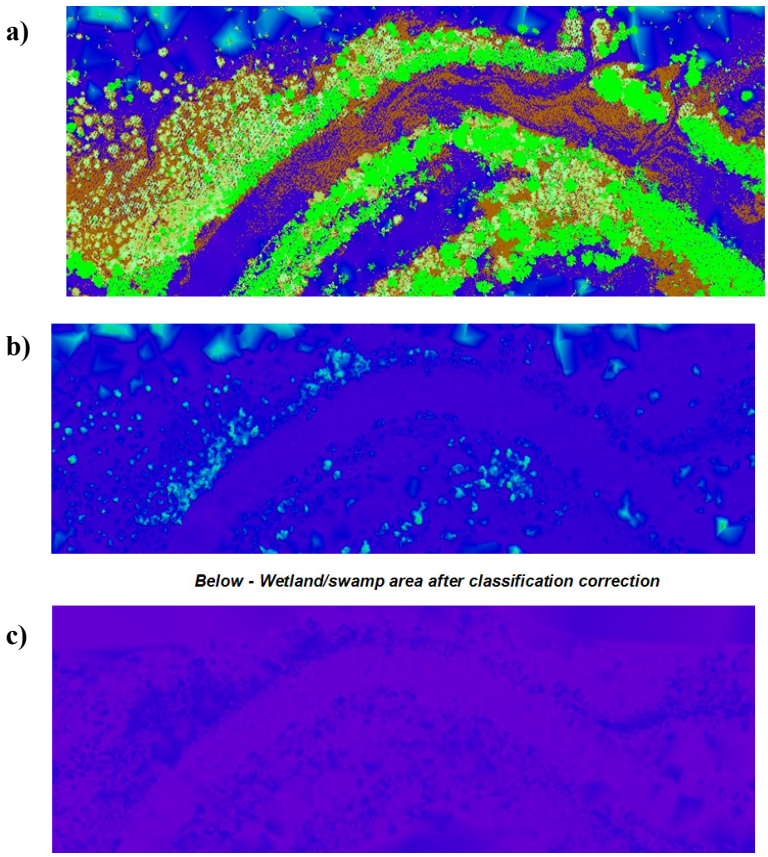



**Figure 5-9.** *LiDAR image showing a) Wetland/swamp area before classification correction; b) Water body area after automatic classification correction; and c) Water body area after manual classification correction. From AAMHatch (2009).*

### 5.2.4 Dataset Merging

In a further attempt to resolve the issues resulting from localised flooding in the Lake Wetherell area at the time of survey (which provided returns from the surface of turbid waters), the LiDAR DEM data provided by AAMHatch was combined with pre-existing Thiess Services Pty Ltd elevation data acquired in November 2001 to March 2002 (Theiss, 2002; see Appendix 14, Lawrie *et al*., 2012f). Bathymetric and aerial laser mapping techniques were used; the number of points generated by the laser was in the order of 17 million data points however, the ground model was decimated to a more manageable density. Thinning was carried out such that points within a 10 m horizontal and 0.100 m vertical radius was averaged (Theiss, 2002).

This data was originally provided as a 15 m grid which takes into account reprojection steps (see Figure 5-10). There are two types of reprojection, horizontal, and vertical. Horizontal reprojections are usually associated with a change in angular measurement unit (decimal degrees to metres) while vertical reprojections are used when changing between spherical models of the Earth (WGS84 uses a simplified ellipsoid while GDA94 uses a gravimetric equipotential surface related to Mean Sea Level).

Horizontal reprojections usually don't have an effect on vertical accuracy since only the X and Y coordinates are re-scaled. An example would be projecting between Australian Geodetic Datum 1966 (AGD66) and Geocentric Datum of Australia (GDA94): in this instance the offset is to the Northeast approximately 200-210 m.

Vertical reprojections can be troublesome; the models used to convert between datums are of lower resolution than LiDAR surveys, so interpolation of the models must occur. Most survey techniques rely on GPS surveys, and all GPS surveys are collected and calculated in decimal degrees using an ellipsoidal datum (WGS84). Most elevation data in Australia has height values that are related to sea level (using one of the Australian Geodetic Datums or geoid models). The process of reprojection from ellipsoid to geoid is a resampling process induces an error of ± 0.05 m (Figure 5-10).

There are two vertical reprojection processes that have been applied to these datasets: projecting from ellipsoidal heights (e.g. WGS84) to geoid heights (e.g. AGD66, AGD84, and GDA94) and projection between geoids (AGD66 to GDA94).

In order to match the spatial resolution of the AAMHatch LiDAR DEM, point and 25 m contour data (used to originally derive the Theiss DEM) were used to resample the Thiess DEM by applying a Topo to Raster bilinear interpolation. The accuracy of the original dataset was reported to be ± 0.18 m (Figure 5-10). The process of resampling a raster to a different resolution is actually an averaging or smoothing process, and vertical error is introduced. Similarly the process of interpolating points and polylines into a raster is an averaging or smoothing process that reduces the fidelity of the dataset by fitting a continuous surface near the input points. These errors can be quantified by comparing the input and output datasets to known elevations or control points, however it is highly localised at areas of high terrain relief such as stream banks and elevated road edges.

The interpolation process added an additional ± 0.03 m as did the resampling from 15 m to 5 m bringing the cumulative RSME up to 0.24 m (Figure 5-10). Where small null values were identified, point and contour data in the vicinity of the null values were interpolated to generate elevation data. For all other areas the conditional statement: *if Thiess DEM < AAMHatch DEM then use Theiss DEM else AAMHatch DEM* was used to selectively retain the lowest elevation value from either the AAMHatch or Theiss DEM as shown in Figure 5-11. This 5 m mosaic DEM was also resampled to 10 m, introducing a further ± 0.03 m error (cumulative RMSE of ± 0.27 m; Figure 5-10).

Two additional elevation datasets were also incorporated into the final compilation DEMs at 5 and 10 m, namely a DEM acquired as part of the Airborne Electromagnetic (AEM) survey, and the Shuttle Radar Topography Mission (SRTM) DEM. The AEM DEM was used to fill a gap between the LiDAR and AEM survey extents. This dataset has a spatial resolution of 60 m and a reported error of ± 4.13 m (Figure 5-10). The SRTM DEM was used to create a 250 m buffer around the BHMAR project extent. This dataset has a spatial resolution of 1 second or 30 m and has a reported error of ± 3.87 m (Figure 5-10; Rodrigues *et al*.,

2006). On comparison with the LiDAR DEM a minimum difference of 3 m was observed. Consequently, the SRTM DEM was uniformly lowered by 3 m to better merge the two datasets.

Both the AEM and SRTM DEMs were firstly resampled to 10 m then to 5 m which, as mentioned previously, incurs an additional ± 0.03 m error at each resampling step (Figure 5-10). The AEM DEM thus has a vertical accuracy of ± 4.19 m and 4.16 m for the 5 and 10 m compilation DEMs respectively. The SRTM DEM similarly has a vertical accuracy of ± 3.93 m and 3.90 m for the 5 and 10 m compilation DEMs respectively (Figure 5-10). While these datasets have a significantly larger error than the LiDAR-derived DEM, they only represent a very small portion of the whole BHMAR study area as shown in Figure 5-12.

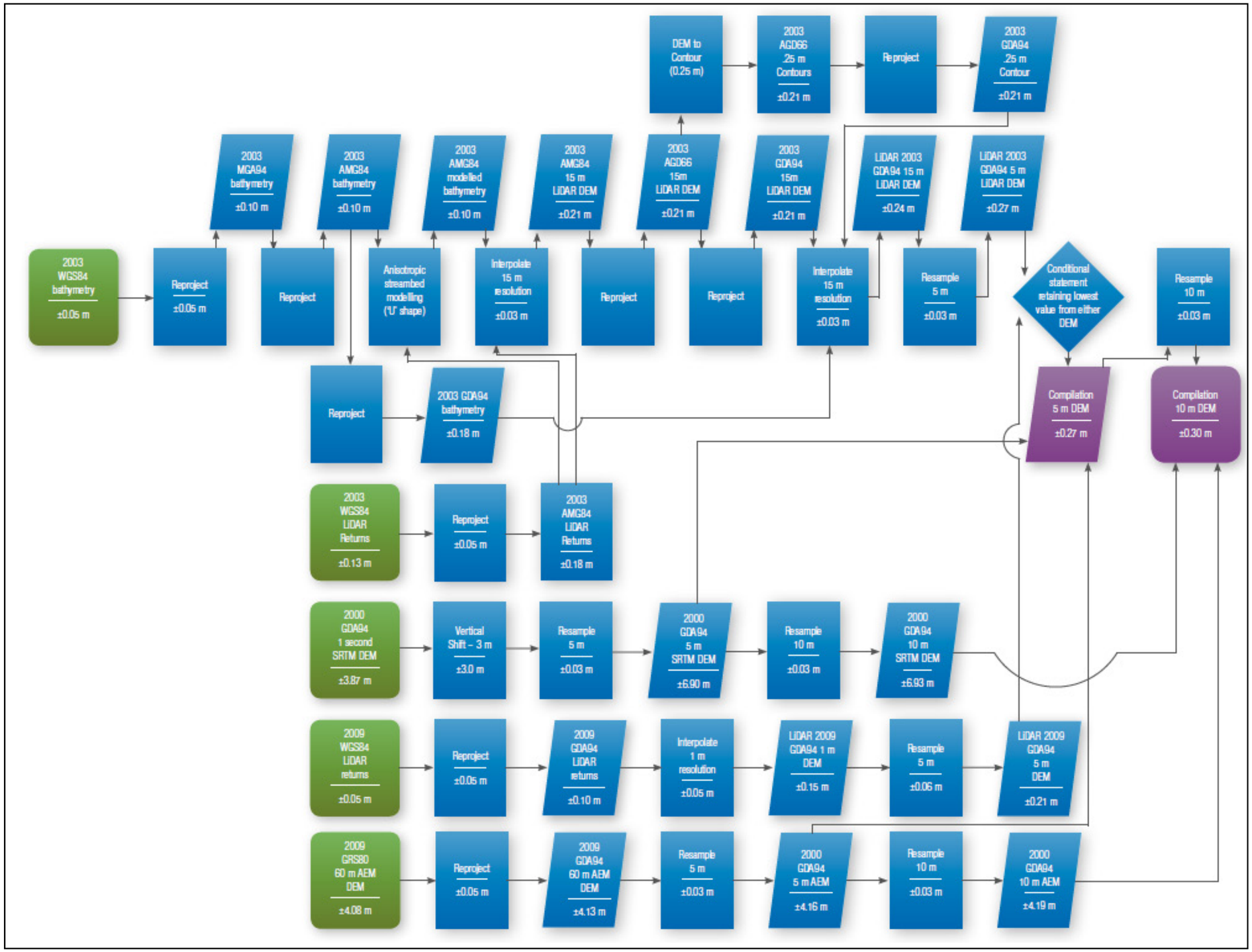



**Figure 5-10.** *Vertical accuracy of base datasets and final compilation surfaces (RMSE or 68%). Green denotes original survey data, blue the various processing steps and purple are final model surfaces.*

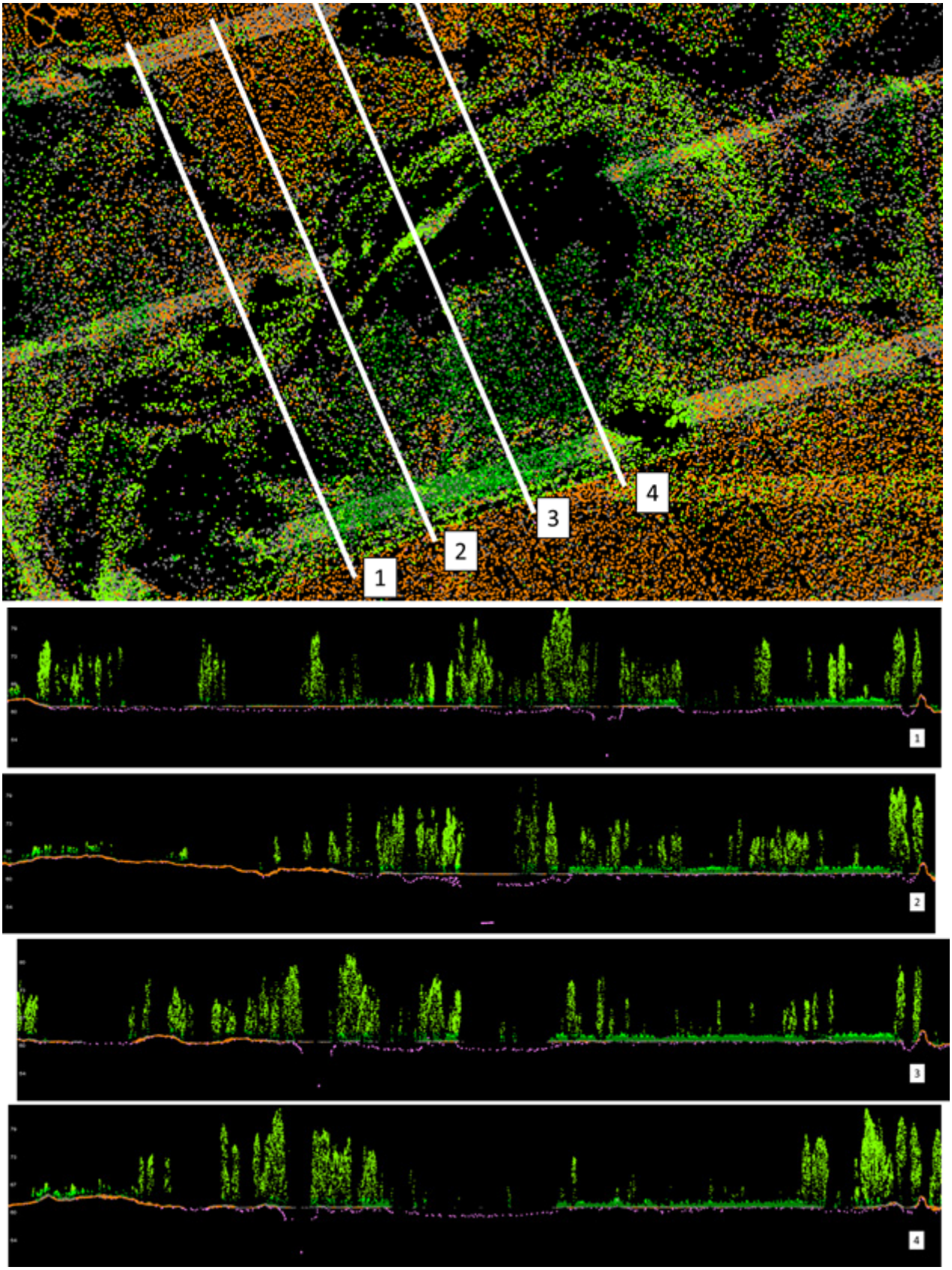



**Figure 5-11.** *Full point clouds from both the Thiess 2003 (pink = ground or bathymetry) and AAMHatch 2009 (green = vegetation; orange = ground) surveys along the Darling River levee. The 2003 survey was able to sense more of the ground (pink dots below orange horizontal line) as the area was not extensively flooded at the time.*

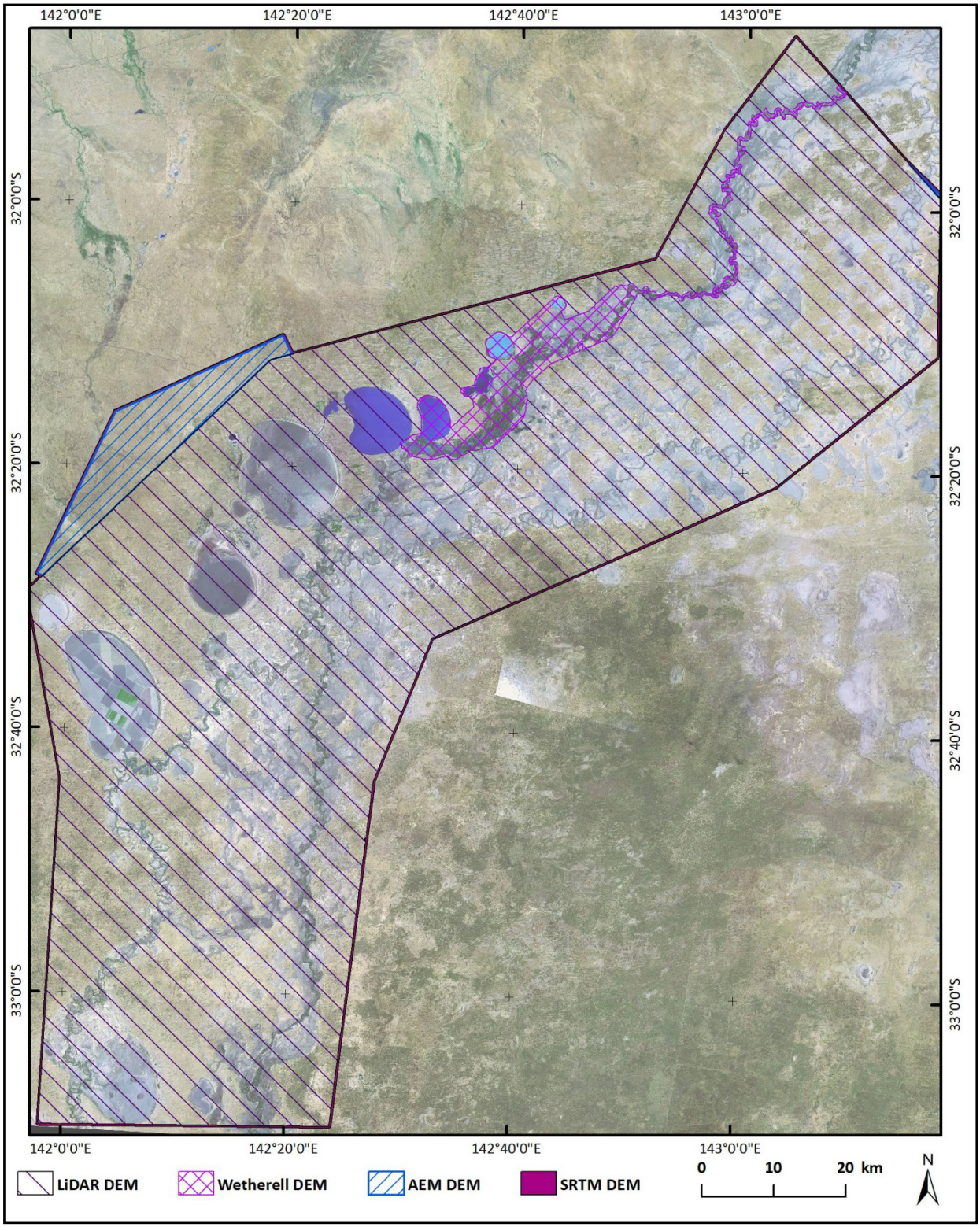



**Figure 5-12.** *Extent and location of the various base datasets.*

### 5.2.5 Assessment of Vertical Accuracy

#### 5.2.5.1 *Introduction*

Several control point datasets were used to assess the vertical accuracy of the DEMs that were used in the creation of both 5 m and 10 m modelling surfaces, and the vertical accuracy of the modelling surfaces themselves. These control point datasets have varying vertical accuracy themselves (Table 5-2). In addition, each input dataset has its own native vertical accuracy measured at the native DEM scale (Table 5-3). Vertical accuracy is calculated by comparing DEM spot elevations to known spot elevations from field surveys, the results of which will be discussed in more detail in this section.

**Table 5-2.** *Control point datasets used to quantify vertical accuracy.*

| Control Point Dataset | Number of measurements | Fundamental Vertical Accuracy |
|---|---|---|
| 250k Spot Heights[1] | 99 | ±5.00 m |
| SCIMS Benchmarks[2] | 74 | ±0.06 m[3] |
| 2009 LiDAR field control points | 1242 | ±0.06 m[3] |
| 2003 LiDAR field control points | 303 | ±0.06 m[3] |
| Borehole collar elevations (2010) | 105 | ±0.06 m[3] |
| Borehole collar elevations (2011) | 32 | ±0.06 m[3] |

Notes: [1] http://www.ga.gov.au/meta/ANZCW0703008969.html

[2] http://www.lpi.nsw.gov.au/surveying/scims_online/class_and_order

[3] RTK GPS vertical uncertainty is highly dependent on observing conditions (e.g. access to open sky, multipath environment, atmospheric conditions and satellite geometry) and the analysis technique used (e.g. single base-station versus network RTK). For a single base-station technique, uncertainties may be larger for measurements conducted >20 km from the reference station (Vollath *et al*., 2002; Feng & Wang, 2008; Wang *et al*., 2010).

**Table 5-3.** *Vertical accuracy for input datasets.*

| Dataset | Native resolution | Vertical Accuracy Source | RMSE | Fundamental Vertical Accuracy |
|---|---|---|---|---|
| 2009 LiDAR survey DEM | 1 m | 1,242 field control points | 0.15 m | 0.294 m |
| 2003 LiDAR survey DEM | 15 m | 303 field control points | 0.13 m | 0.255 m |
| 2011 (AEM) survey DEM | 60 m | 65 250k spot elevations | 4.08 m | 7.997 m |
| 2000 SRTM DEM | 1-second (≈30 m) | 1198 benchmarks | 3.87 m | 7.585 m |

Vertical accuracy can be stated several ways; Root-Mean-Square-Error (RMSE), and Fundamental Vertical Accuracy (FVA). RMSE is the square root of the average of the set of squared differences between dataset coordinate values and coordinate values from an independent source of higher accuracy, when used to describe a normally distributed dataset it represents a range of values that contain 1 σ (sigma) or 1 standard deviation or ≈68% of the population of measurements. FVA is a more rigorous accuracy analysis than RMSE; it is calculated by multiplying RMSE by 1.96. This uncertainty value implies that the true elevation of the point falls within the given range ≈95% of the time.

Both RMSE and FVA are parametric statistics; they rely on a normal or Gaussian distribution confirmed by measuring error population skew ±0.5. When a population is not normally distributed, as LiDAR datasets commonly are, a non-parametric vertical accuracy measurement must be used: a Confidence Level of 95%. The 95% confidence level is similar to FVA in that the interval represents ≈95% of the population, but it is

relatively immune to outliers in the dataset (5% of the population values can be arbitrarily large without changing the calculated output).

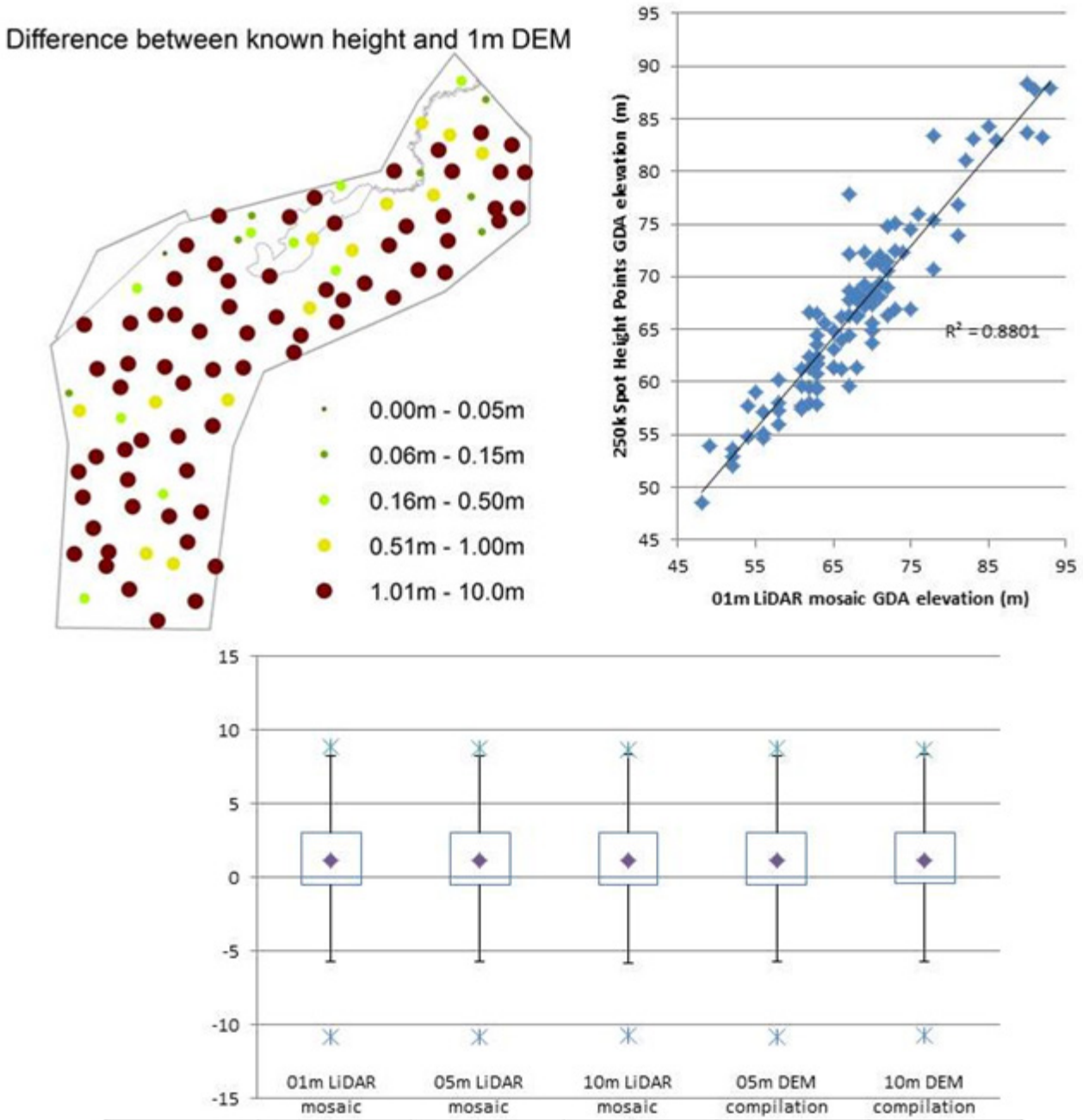
#### 5.2.5.2 *Results*

250k spot heights were used by the original surveyor to validate the radar DEM produced during the capture of the Airborne Electromagnetic (AEM) survey. These control points are of low quality, consisting of integer values, but have been compared to the various DEMs used in this project as seen in Figure 5-13. The dataset has an excellent data distribution across the area of interest but the mean difference between control points and the DEMs is over 1 m and while the error distribution is normal, the FVA is unreasonable for this test.

Survey Control Information Management System (SCIMS) is a dataset maintained by Land and Property Information (LPI) New South Wales. It consists of permanent benchmarks usually associated with infrastructure. Each benchmark has an AHD elevation as well as AHD class and AHD order, 66 of the benchmarks were class L3 (special high-precision surveys) and the remainders were class 1 or 2 (precise trigonometric or GPS heights). The dataset is not well distributed across the study area as seen in Figure 5-14; most data is along a central corridor adjacent to Pooncarie-Menindee Road and Menindee-Wilcannia Road. There are three benchmarks in the 2003 Lake Wetherell survey area, however one is an outlier at 84 m error (mark number 127581).

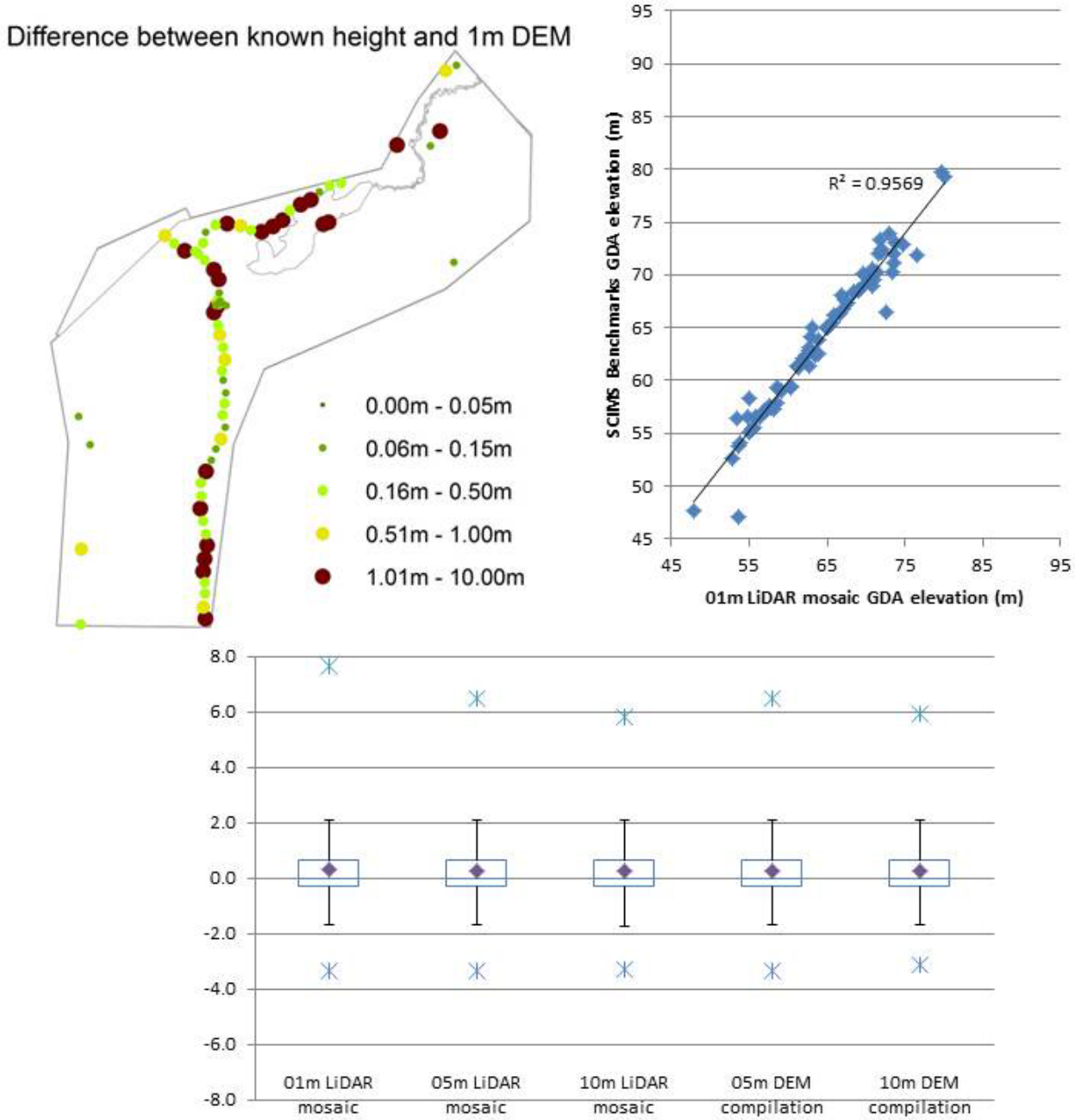
1,242 control points were collected during the 2009 LiDAR survey, and they are from a high quality (centimetre-level) Real Time Kinematic (RTK) GPS survey. These data points are not well distributed as can be seen in Figure 5-15; they follow a similar distribution to the SCIMS benchmarks: along roads and other easy-access areas and only one cluster of 20 data points is within the 2003 Lake Wetherell survey area.

There are 137 boreholes in the study area that were surveyed in September 2010 (105 bores) and September 2011 (32 bores) shown in Figure 5-16. The vertical accuracy of these heights is ~0.02 m. This dataset is in general well distributed across the study area, however only five points correspond with the 2003 Lake Wetherell survey area (concentrated along the southern edge) and were thus insufficient to verify survey accuracy.



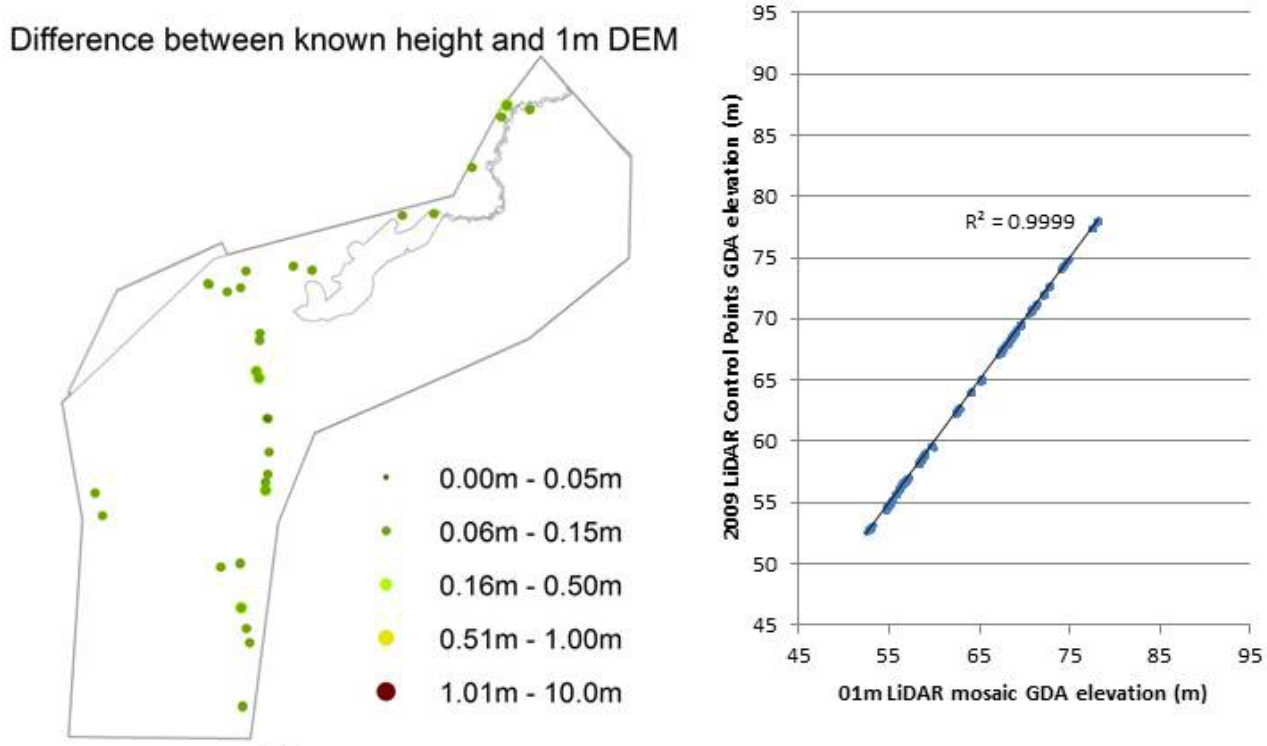

| | 01m LiDAR mosaic | 05m LiDAR mosaic | 10m LiDAR mosaic | 05m DEM compilation | 10m DEM compilation |
|---|---|---|---|---|---|
| Mean | 1.15020 | 1.15117 | 1.15109 | 1.17919 | 1.17935 |
| Skewness | -0.25146 | -0.26076 | -0.24840 | -0.28606 | -0.27633 |
| RMSE | 3.40330 | 3.40222 | 3.39267 | 3.41166 | 3.40422 |
| FVA | 6.67047 | 6.66835 | 6.64963 | 6.68686 | 6.67226 |
| Confidence Level(95.0%) | 0.05904 | 1.05904 | 2.05904 | 3.05904 | 4.05904 |
| count | 99 | 99 | 99 | 99 | 99 |

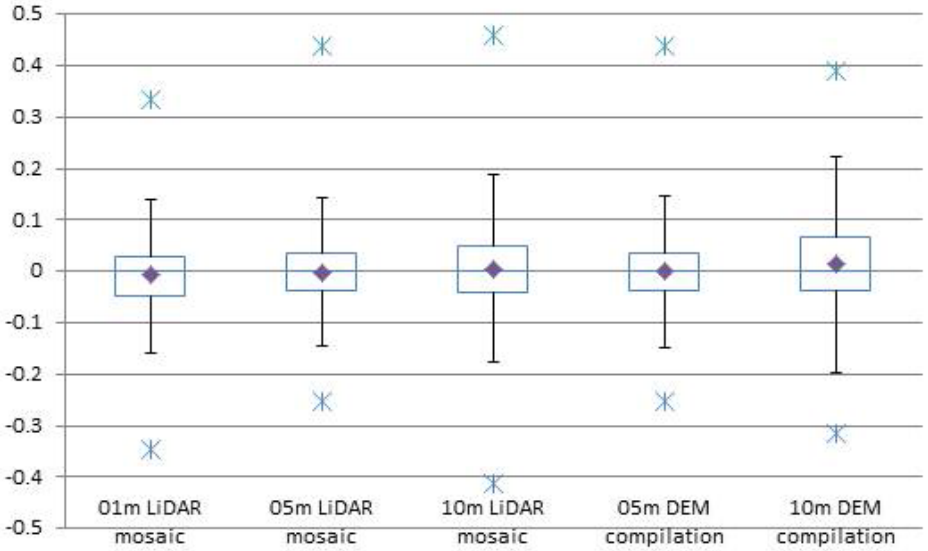
**Figure 5-13.** *Vertical accuracy analysis of DEMs using 1:250,000 spot heights. Box and whisker plots depict five descriptive statistics: minimum and maximum (stars), 25$^{th}$ and 75$^{th}$ percentile plus 1.5 x inter-quartile range (whiskers), 25$^{th}$ and 75$^{th}$ percentile (box extents), and mean (diamond).*




| | 01m LiDAR mosaic | 05m LiDAR mosaic | 10m LiDAR mosaic | 05m DEM compilation | 10m DEM compilation |
|---|---|---|---|---|---|
| Mean | 0.32424 | 0.31244 | 0.28174 | 0.31388 | 0.29971 |
| Skewness | 2.06005 | 1.75203 | 1.37340 | 1.74729 | 1.54034 |
| RMSE | 1.60303 | 1.53247 | 1.42298 | 1.53348 | 1.45081 |
| FVA | 3.14193 | 3.00365 | 2.78903 | 3.00562 | 2.84358 |
| Confidence Level(95.0%) | 0.05904 | 0.05873 | 0.05868 | 0.05873 | 0.05685 |
| count | 74 | 74 | 74 | 74 | 74 |

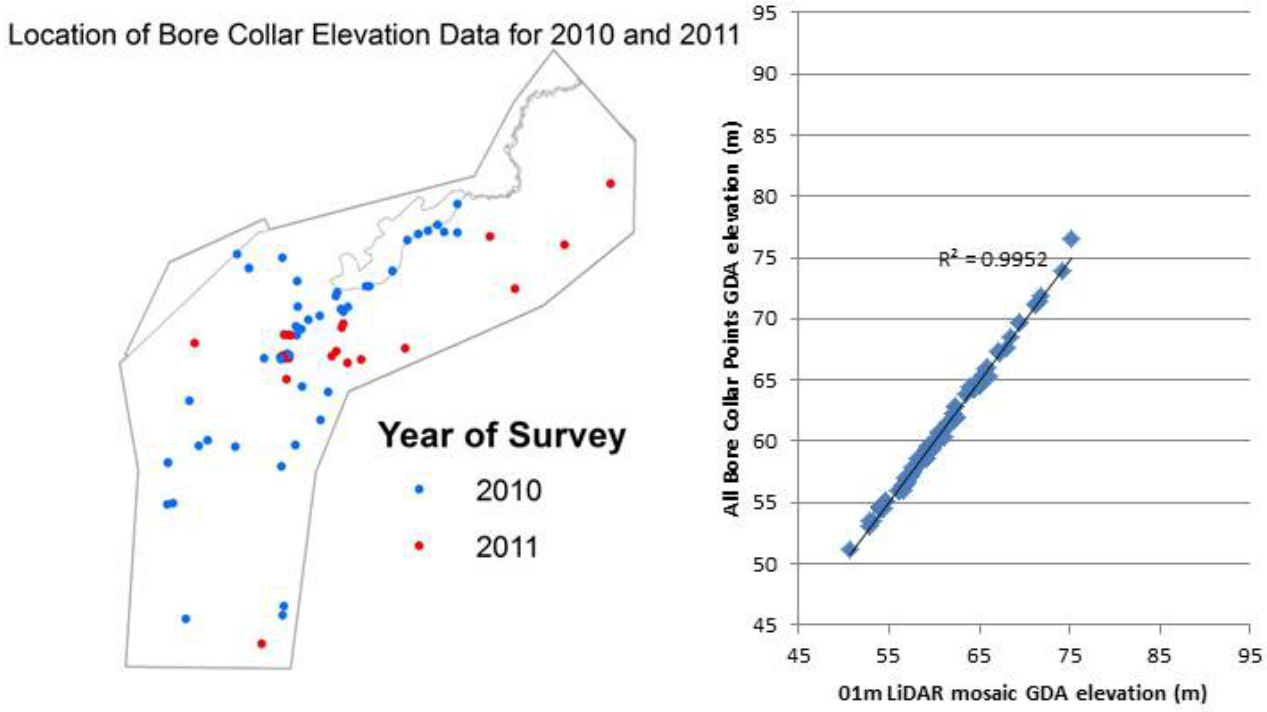
**Figure 5-14.** *Vertical accuracy analysis of DEMs using SCIMS benchmarks.*

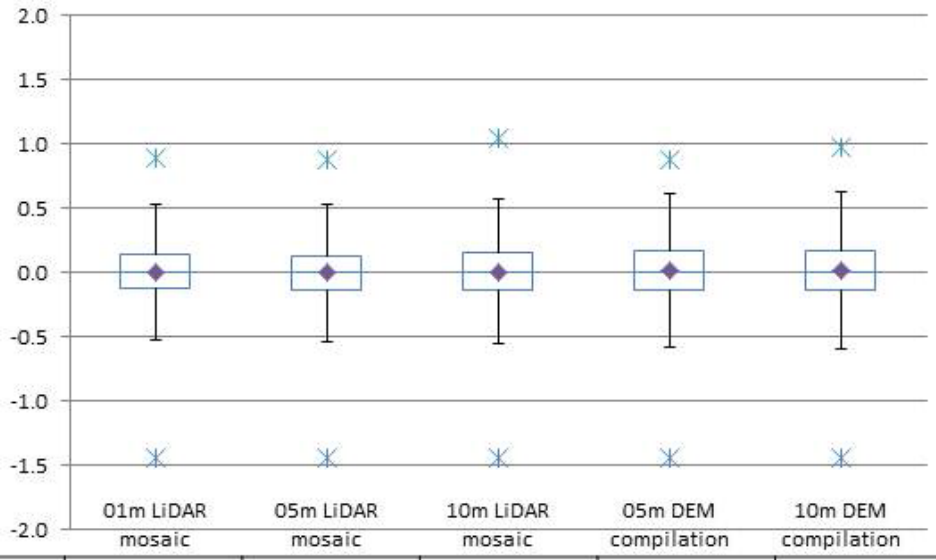



| | 01m LiDAR mosaic | 05m LiDAR mosaic | 10m LiDAR mosaic | 05m DEM compilation | 10m DEM compilation |
|---|---|---|---|---|---|
| Mean | -0.00727 | -0.00088 | 0.00594 | 0.00232 | 0.01351 |
| Skewness | -0.18489 | 0.41759 | 0.19113 | 0.55379 | 0.10534 |
| RMSE | 0.05940 | 0.06602 | 0.08160 | 0.07013 | 0.08385 |
| FVA | 0.11642 | 0.12941 | 0.15994 | 0.13746 | 0.16435 |
| Confidence Level(95.0%) | 0.003283 | 0.003677 | 0.004533 | 0.003904 | 0.004609 |
| count | 1242 | 1242 | 1242 | 1242 | 1242 |

**Figure 5-15.** *Vertical accuracy analysis of DEMs using 2009 LiDAR control points.*




| | 01m LiDAR mosaic | 05m LiDAR mosaic | 10m LiDAR mosaic | 05m DEM compilation | 10m DEM compilation |
|---|---|---|---|---|---|
| Mean | 0.00310 | 0.00240 | 0.00844 | 0.01956 | 0.02010 |
| Skewness | -0.92346 | -0.98840 | -0.81813 | -0.94718 | -0.89514 |
| RMSE | 0.29988 | 0.29835 | 0.30521 | 0.31071 | 0.31144 |
| FVA | 0.58777 | 0.58477 | 0.59821 | 0.60898 | 0.61043 |
| Confidence Level(95.0%) | 0.05904 | 1.05904 | 2.05904 | 3.05904 | 4.05904 |
| count | 137 | 137 | 137 | 137 | 137 |

**Figure 5-16.** *Vertical accuracy analysis of DEMs using all borehole collar elevations.*

From a sub-sample of 46 bores from the central section of the BHMAR project area, 70% were within this error range (Figure 5-17). Six bores were only out by a further 5 cm that could easily be attributed to bore construction changes. The site with the greatest increase in elevation (negative values in Figure 5-17) corresponds with a known recharge site at Lake Menindee (Lawrie *et al.*, 2012c). Similarly, borehole elevation within the ± 15 cm range are not clustered around zero as would be expected, but instead the majority are negative values indicating an overall increase in elevation since the LiDAR was flown.

It is postulated that these changes in elevation may be attributed to floodplain inflation arising from considerable groundwater recharge. Examples of this process have been previously reported due to unusually high-magnitude natural recharge and water table rise in the San Bernardino valley, California (Lu & Danskin, 2001) and due to artificial recharge in the Santa Clara Valley, California (Schmidt & Burgmann, 2003), and the Phoenix area, Arizona (Conway, 2008). In all three instances the observed uplift was of the order of 2 to 4 cm, and occurred after significant land-surface subsidence due to excessive groundwater extraction. While the magnitude of floodplain inflation is similar to the observed clustering of elevation values slightly higher since the acquisition of the LiDAR, significant groundwater extraction has not occurred at this location. Further, the scale of floodplain inflation reported in these studies is considerably less than that observed at the northern edge of Lake Menindee Figure 5-18) which suggests other processes may also be at play. The spatial distribution of these bores is shown in Figure 5-18. Many of the 46 bores used in the analysis are nested and thus appear in the same spatial location.

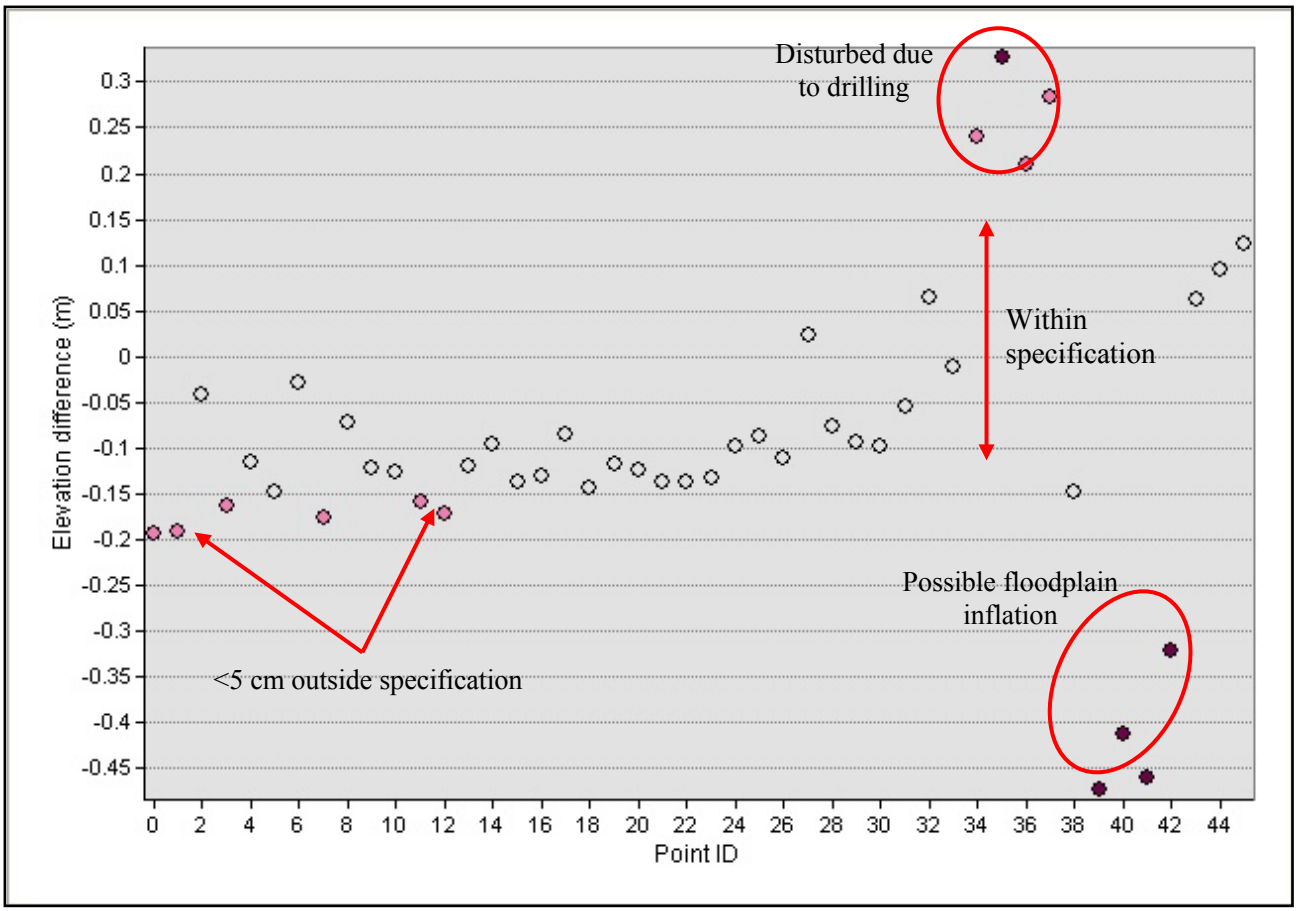



**Figure 5-17.** *Correlation between surveyed elevation and LiDAR DEM elevation. Grey points are within the ± 0.15 m specifications; light pink dots are between ±0.15 and 0.30 m; and dark purple dots are greater than ± 0.30 m. This colour scheme corresponds with Figure 5-18.*

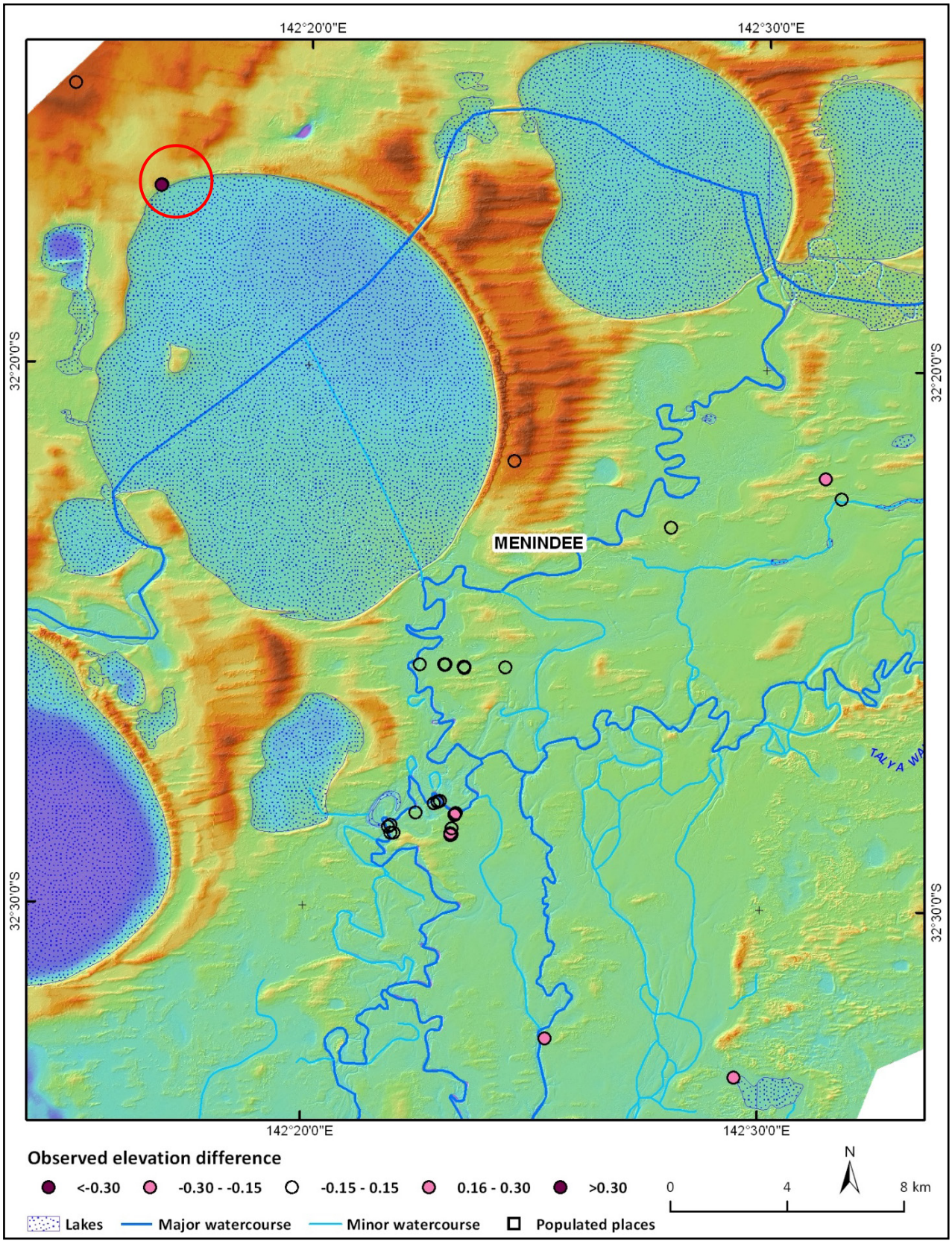
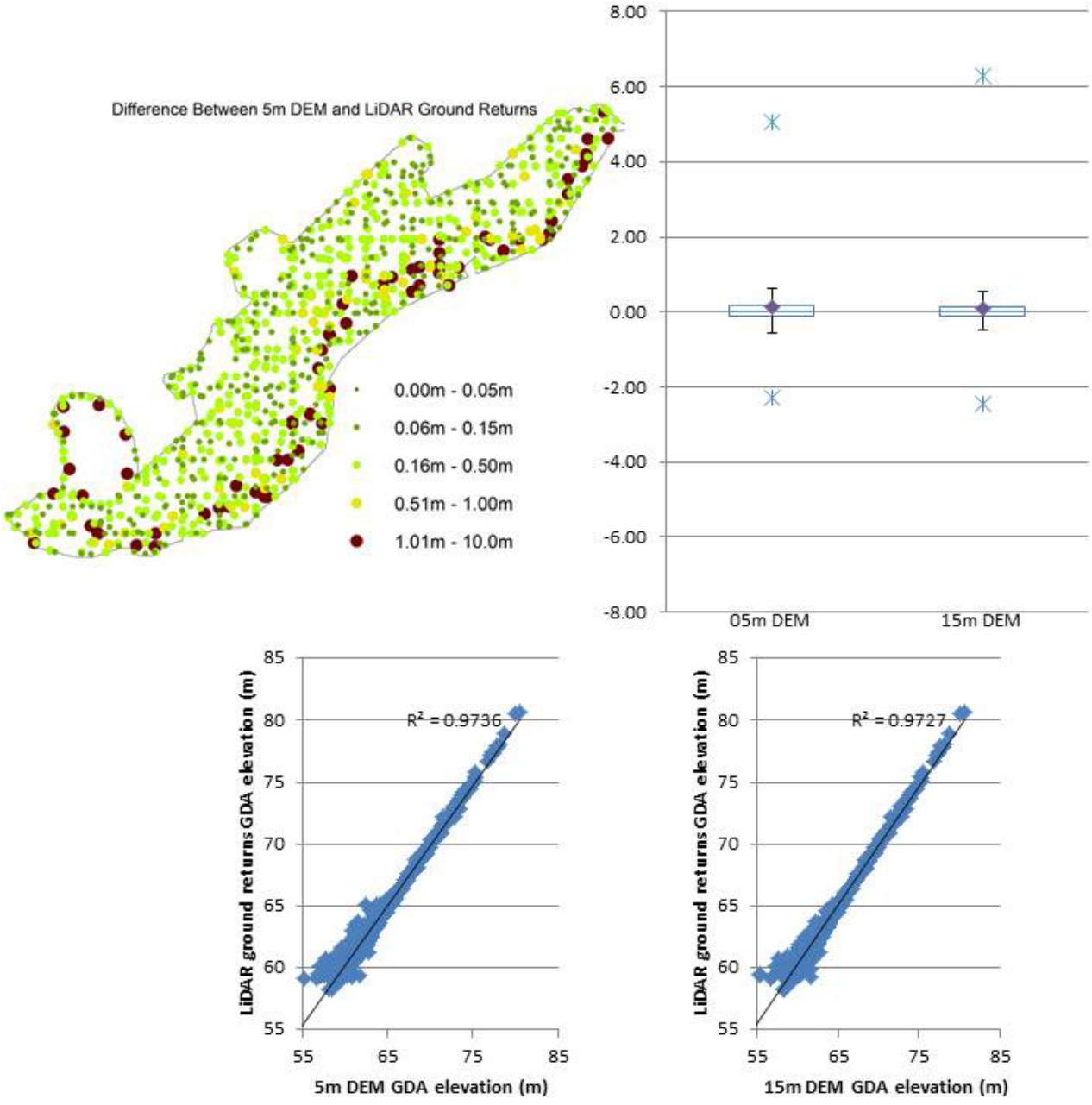



**Figure 5-18.** *Location of surveyed bores used in the analysis of LiDAR DEM accuracy. The red circle denotes the bore with the greatest increase between the LiDAR acquisition in 2009 and bore surveying in 2011, potentially demonstrating floodplain inflation.*

303 control points were collected during the 2003 LiDAR survey at Lake Wetherell, but this control point dataset has been lost. A summary report details their existence and their use in quantifying the vertical error of the 15 m DEM however this data could not be incorporated into the vertical accuracy analysis. Instead, the 5 m and 15 m DEMs created using the Lake Wetherell 15 m DEM, contours, and bathymetry have been compared to a thinned subset of the original LiDAR ground returns in Figure 5-19.




| | 05m Topo to Raster | 15m Topo to Raster |
|---|---|---|
| Mean | 0.01417 | 0.08324 |
| Skewness | -1.03594 | 5.84417 |
| RMSE | 0.32849 | 0.58449 |
| FVA | 0.64385 | 1.14561 |
| Confidence Level(95.0%) | 0.03395 | 0.03454 |
| Count | 1081 | 1081 |

**Figure 5-19.** *Comparison between 5 m, 15 m DEMs and LiDAR ground returns from 2003 Lake Wetherell Survey.*

The LiDAR elevations and the two DEMs are quite coherent but not normally distributed, so FVA is the statistic of importance. This can be interpreted to mean that ~0.03 m vertical accuracy is lost when combining the input datasets into two new smoother DEMs. There is however a spatial component to the vertical accuracy: the DEMs vary from the LiDAR returns much more near the river. This anomaly can be explained by examining the anisotropic streambed modelling that was performed using the bathymetry observations (cited in Theiss, 2002 available in Appendix 14, Lawrie *et al*., 2012f).

#### 5.2.5.3 ***Conclusions***

The final study area DEM has been compiled from many sources with various vertical accuracies ranging from highly-accurate LiDAR surveys to more general SRTM elevation estimates. A general statement about the vertical accuracy of the 5 m and 10 m DEMs can be made by comparison with control points, but the lack of control within the 2003 Lake Wetherell survey area makes this statement misleading. In this case it is worthwhile to consider the vertical accuracy of each input dataset individually.

In addition to a basic vertical accuracy derived from comparison to control points, each input dataset has been transformed through a combination of processes: reprojection, resampling, and interpolation. The quantification of basic vertical accuracy plus error for each transformation process allows for error budgeting. Each transformation process adds error to the vertical accuracy budget.

A careful analysis of Figure 5-10 allows the tracking of vertical error budgets from input datasets (green icons) through to the final outputs (purple icons). Where datasets are combined the higher vertical error is retained except where the dataset is on the periphery of the study area (SRTM and AEM datasets). The 2003 Lake Wetherell LiDAR dataset has many component parts that have been transformed and interpolated several times leading to lower vertical accuracy values than unadulterated LiDAR surveys normally produce (such as the 2009 LiDAR survey in Figure 5-10).

In 2003 the water level at Lake Wetherell was very low, but the elevation survey also had a very low data density, while in 2009 they water level was very high, but the data density was also high. This led to the 2003 survey capturing the streambed very well, however advanced ground-classification algorithms could not be used thus all "last returns" were classified as ground even if it was actually vegetation. In 2009 the deep water obscured much of the stream bed, but the high data density made differentiation of the ground returns much more accurate. Unfortunately, in 2009 only algorithmic ground classification methods were used so the floodwater surface was classified as ground. These two datasets were integrated using the lower of the two to ensure that vegetation was removed from the 2003 dataset, and floodwater (classified as ground) was removed from the 2009 dataset. The trade-off being that the worst vertical accuracy of the two was retained.

When considering the vertical accuracy of the two main data sources, a conservative estimate of the vertical accuracy of the output of the compilation process is ±0.27 m RMSE or ±0.47 m FVA for the 5 m DEM and ±0.30 m RMSE or ±0.52 m FVA for the 10 m DEM. The ICSM (2008) guidelines regarding error reporting led to a general statement of vertical accuracy for the DEMs that read:

*5 m DEM – "Tested 0.52 meters fundamental vertical accuracy at 95 percent confidence level in open terrain using RMSEz x 1.9600" and*

10 m DEM – "*Tested 0.59 meters fundamental vertical accuracy at 95 percent confidence level in open terrain using RMSEz x 1.9600"*

The vertical accuracy of the CEM grid was also reported as ± 0.15 m and FCM was derived from this surface. This was based on three identified land cover classes, surveyed 20 sites, measuring 40 points per land cover class (Figure 5-20). While no additional control points were available to further analysis the vertical accuracy the same principles regarding resampling, reprojecting and interpolation apply. Consequently, it is estimated that the vertical error associated with the CEM is ± 0.18 to account for resampling from 1 m to 5 m.

There are a number of known factors that can influence the likelihood of laser pulse penetration and backscatter as result in increased vertical error including foliage orientation, height, density, and ground surface type. This typically leads to an underestimation of canopy height (e.g. Hopkinson *et al*., 2004; Gareau & Hill, 2003) in some instances as great as 2 m (e.g. Wasser *et al*., 2013).

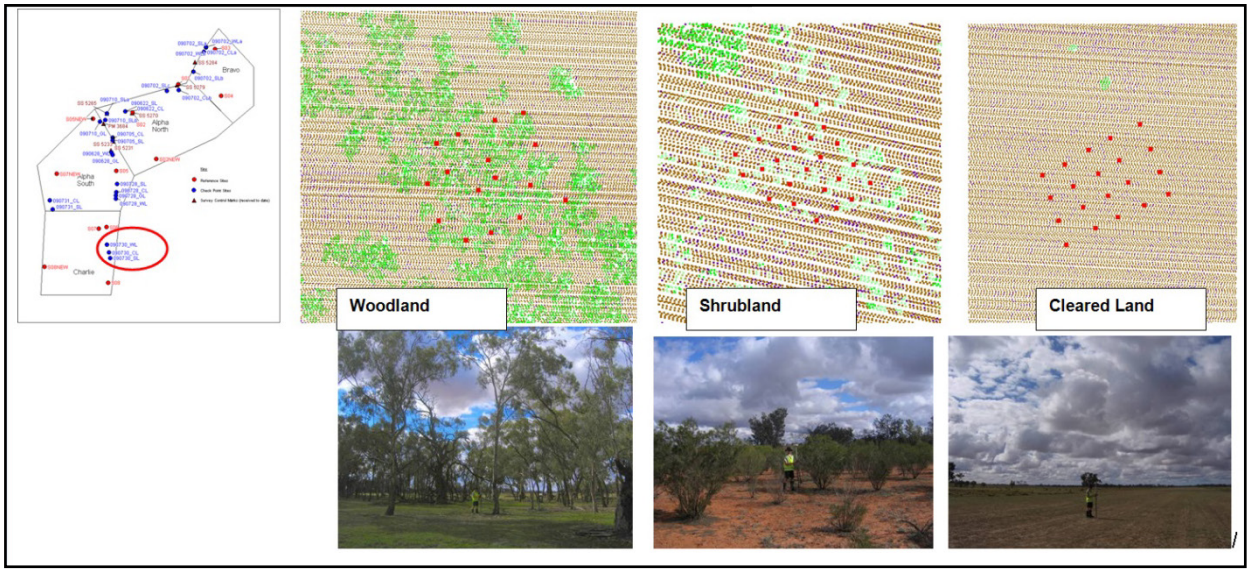



**Figure 5-20.** *Three examples of the diversity of land cover classes encountered in different parts of the project area. More than 20 sites were surveyed (see insert map on left), with 40 points measured per land cover class (see insert map on left). In the images above, the sample distribution sites are shown above a photograph of respective land cover class (e.g. Woodland, Shrubland and Cleared Land).*

## 5.3 UTILITY OF THE HIGH RESOLUTION LIDAR DATASET IN THE BHMAR STUDY AREA

Acquisition of a high-resolution (15-20 cm vertical accuracy) LiDAR dataset has been essential in developing a range of geomorphic, geological and hydrogeological interpretation and planning products. For example, foliage cover, canopy elevation and DEM products generated from the LiDAR data have been used to examine the relationships between vegetation health, landscape position, sedimentary materials and groundwater quality and depth. These data have provided important baseline information for environmental assessments of potential groundwater extraction and MAR impacts on groundwater dependent vegetation. The DEM products have also provided a high-resolution surface datum to hang the sub-surface datasets including AEM, ground geophysical, and borehole data.

In summary, the acquisition of a high resolution LiDAR dataset has enabled:

- Key elements of the floodplain geomorphology to be mapped. The LiDAR dataset has also been critical in guiding the sighting of pits and trenches for validation of the near-surface geomorphic units and in guiding OSL dating sampling strategies;
- Fault scarps to be identified in the landscape. The high resolution of the dataset has also enabled the timing of faulting relative to scroll plain deposition to be ascertained;
- Integration of river bed mapping with surface floodplain mapping;
- Flood inundation modelling to be carried out at a range of scales;
- Assessment of infiltration options for MAR;
- Assessment of the potential impact of groundwater extraction and MAR on groundwater dependent vegetation;

- Cultural heritage and environmental surveys to be carried out with a high degree of spatial accuracy. This was essential for planning all field activities;
- Design of conceptual borefields;
- Planning of surface water engineering works at the MLS.

## 5.4 DEM SUMMARY

In summary, an initial assessment concluded that the BHMAR project required a high resolution DEM with a vertical resolution <0.20 m absolute vertical accuracy for the purposes of aquifer potentiometric mapping, flood modelling, and to map key landscape and geomorphic features across the Darling floodplain. However, this was translated as an absolute vertical accuracy of < 0.2 m (RMSE) or < 0.39 m (FVA - Fundamental Vertical Accuracy) when the contract with the provider was finalised. To avoid confusion in the future, it is recommended that all vertical accuracies should be reported as Fundamental Vertical Accuracy (FVA) representing 95% confidence levels, rather than RMSE values representing 1 sigma or 68% confidence levels. The latter are inadequate for hydrological and hydrogeological applications in most Australian landscape settings. Based largely on the BHMAR project experiences, a number of additional recommendations are made with regard to the acquisition, processing, calibration and validation of remote sensing technologies used for high-resolution elevation surveys.

Based largely on the BHMAR project experiences, a number of additional recommendations are made below with regard to the acquisition, processing, calibration and validation of remote sensing technologies used for high-resolution elevation surveys.

1. The selection of the appropriate elevation survey technology has to be driven by a clear understanding of project requirements. There are a range of satellite and aircraft-mounted systems available, all with different resolution and accuracy capabilities
    a. It is recommended that future projects clearly identify the immediate project requirements, while also paying some heed to the likely future uses of the datasets as part of the project planning phase. Publically-funded datasets should generally anticipate that these datasets will be used for a range of purposes beyond the initial scope, and attempt to adhere to the highest standards in terms of precision, accuracy and metadata description.
    b. For hydrological investigations, it is recommended that particular attention be paid to the vertical accuracy requirements and definitions. In most Australian floodplain landscapes it is recommended that datasets with < 0.2 m vertical accuracies with respect to an application appropriate vertical reference datum, e.g. the national Geoid model, are obtained.
    c. It is recommended that guidelines be drafted providing clear guidance on the resolution capabilities of different systems (precision and accuracy), the limitations of the techniques, and the steps that are required to calibrate these datasets. Such guidelines are required to better inform stakeholders on the potential and limitations of the different technology platforms, and to provide some guidance on the ancillary steps required to ensure the datasets are fit for purpose and adequately calibrated.
2. Complementary techniques. There are a number of elevation mapping techniques that provide different measurements of surface (and sub-surface) datums with geoscience applications. The following recommendations are made:
    a. For hydrological investigations, it is recommended that InSAR techniques be deployed where measurements of temporal variations in land surface heights are required. This includes instances of subsidence and /or ‘floodplain breathing’.
    b. More specifically, it is recommended that inSAR techniques be trialled in the BHMAR study area to assess the degree of floodplain breathing as a consequence of episodic flooding.
    c. It is also recommended that inSAR techniques be trialled in the BHMAR study area to assess the capability of InSAR techniques for mapping watertable fluctuations in unconfined aquifers under Australian landscape conditions.

3. Ground techniques such as Global Navigation Satellite System (GNSS), geodetic levelling, ground based gravity and other geodetic observing techniques might also complement InSAR mapping techniques. To provide reference surfaces for hydrological applications
    a. Currently, the Australian Height Datum (AHD m.s.l.) is used as the reference surface for elevation applications across Australia. While AHD meets the needs of most users, and is used extensively throughout Australia, there must be a recognition within the hydrological community that is not suited for many hydrological applications due to its errors and its definition (m.s.l.) that results in a north–south slope (~1 m) arising as a consequence of sea surface topography. It is therefore recommended that for hydrological applications an appropriate vertical reference datum be adopted. This might be the national Geoid model, which is derived from the national gravity network.
    b. Efforts should be made to capture and archive all elevation surfaces in an ellipsoidal datum, as described in the ICSM LiDAR Acquisition and Tender Templateii, to future proof their use and facilitate their future improvement as the national Geoid model and height datum is improved.
    c. Ellipsoid-geoid transformations are an important source of error in digital elevation modelling applications. In part, this error stems from limitations in the national Geoid model. It is recommended that further observational and modelling efforts be directed toward improvement of the Australian national Geoid model. The contribution of errors associated with the ellipsoid-Geoid transformation in elevation mapping applications is currently poorly understood and also requires additional research.
4. There are a number of recommendations made with respect to the acquisition of airborne LiDAR and derived products. The current ICSM LiDAR Specifications and Tender Template3 should be modified to incorporate learnings from the BHMAR project. These changes include:
    a. Clearly stating the requirement for vertical accuracy in terms of Fundamental Vertical Accuracy (FVA). An FVA of < +/-20cm 95% confidence interval (1.96 x RMSE) is the most appropriate for hydrological modelling in floodplain environments.
    b. Incorporate options for derived products, specifically for hydrological modelling. All derived surfaces should be provided with ellipsoidal and orthometric heights. Orthometric heights should be relative to the AUSGeoid Gravity Model, not the Australian Height Datum 1971 (AHD).
    c. Improved requirements for ground control.
        i. Aircraft trajectories must be computed with reference to local base stations and precise ephemeris data (ITRF), and then subsequently transformed to GDA94.
        ii. Where existing CORS are not within range to ensure fixed ambiguity solutions for trajectories, new base station sites are to be established with permanent marking. The Precise Point Positioning (PPP) technique is not acceptable either as a primary or fall-back solution.
        iii. The GDA94 ellipsoid heights for these sites are to be determined using the AUSPOS Online GPS Processing Service (final orbit product) with a minimum of two 6 hour observations sessions.
        iv. If the setup is a tripod, then it must be reset with a different height between sessions. Refer also to Section 13.4 below for GNSS base station data delivery requirements.
    d. A minimum standard for LiDAR classification of Level 3 ground correction should be stipulated to ensure that all derivative surfaces provide the best possible representation of the ground surface.
    e. A minimum point density of 2 points per square metre is recommended at nadir to improve the chances of obtaining a ground measurement.
    f. There should be a requirement to capture coincident imagery to ensure Level 3 classification is achieved and assist with water masking.

[3] http://www.icsm.gov.au/elevation/LiDAR_Specifications_and_Tender_Template.pdf

# 6 Airborne Electromagnetics (AEM)

## 6.1 USING AEM TO MAP KEY ELEMENTS OF THE HYDROGEOLOGICAL SYSTEM

### 6.1.1 Introduction

Previously, the high cost of investigations, low level of knowledge of risk, and time taken to fill hydrogeological knowledge gaps have been a deterrent to development of MAR options in inland Australia, especially in pioneering projects in new and/or more remote locations. In the BHMAR project, the initial scoping study (Lawrie *et al*., 2008, 2009a) concluded that despite a paucity of relevant hydrogeological data, there was sufficient evidence to suggest there might be relatively fresh groundwater resources stored in aquifers at relatively shallow depths (<100 m) beneath the Darling River floodplain. Furthermore, the scoping study also concluded that the hydrostratigraphy included interbedded aquifers and aquitards that could facilitate the development of MAR options (Lawrie *et al*., 2009a).

To meet the challenge of rapid identification and assessment of potential MAR targets and groundwater resources over a large area (7,541.5 $km^2$) within relatively short timeframes (18 months), it was concluded that the only cost-effective method with the ability to resolve features in this depth range was airborne electromagnetics (AEM) (Lawrie *et al*., 2009a, b).

AEM methods for near-surface hydrogeological investigations have undergone significant improvements in the past 10-15 years (Auken *et al*., 2006; Thompson *et al*., 2007; Macnae, 2007). A wide range of AEM systems and acquisition platforms are available (Allen, 2005; Spies & Woodgate, 2005; Auken *et al*., 2006), and the technology is now recognised as mature, capable of rapidly mapping complex hydrostratigraphy and groundwater quality (salinity) relationships, often providing important broader contextual information on hydrogeological systems (Lawrie *et al*., 2000, 2008, 2009a). The depth of investigation and spatial resolution of these AEM systems varies significantly with system type and also depends on ground conditions (Spies & Woodgate, 2005; Sorensen & Auken, 2004; Munday, 2008). AEM systems also provide a logistical advantage in being able to acquire data systematically over difficult or inaccessible terrane, and areas where ground access is difficult for cultural, heritage or environmental reasons (e.g. Fitterman & Deszcz-Pan, 1998). Borehole and ground EM technologies are also important in providing calibration and validation of AEM inversions (Lawrie *et al*., 2000; Allen, 2005; Spies & Woodgate, 2005).

Internationally, AEM methods have been used successfully to map the hydrogeology and variations in groundwater salinity in a range of geological environments (Siemon *et al*., 2009; Viezzoli *et al*., 2011; Abraham *et al*., 2012). Successful applications include the mapping of seawater intrusion interfaces in both clastic and carbonate aquifer systems (Fitterman & Deszcz-Pan, 1998; D'Ozouville *et al.,* 2008; Supper *et al.,* 2009; Siemon & Steuer, 2011), saline groundwater plumes (Paine, 2003), freshwater-salt water interfaces beneath inland lakes (Martinez & Pitcher, 2008), and surface-groundwater interaction associated with rivers (Paine *et al*., 2009). AEM methods have also been used to map karstic aquifer systems (Doll *et al*., 2000; Smith *et al*., 2003, 2005, 2008) and key elements of the hydrostratigraphy in clastic sedimentary systems (Abraham *et al*., 2011a), and geological framework including faults (Bedrosian *et al*., 2012).

### 6.1.2 Groundwater Salinity and Hydrostratigraphic Mapping in Australia's Salinized Landscapes

In Australia, the application of electromagnetic (EM) methods for hydrogeological investigation is made more complex by the highly salinized nature of many of the landscapes and groundwater systems (George *et al*., 1998; Lawrie *et al*., 2000, 2003a). Many of these landscapes are often deeply and variably weathered, and in many instances, the resulting electrical conductivity distribution does not equate with formation (and/or hydrogeological) boundaries, but instead to a combination of groundwater salinity and formation composition and texture (Lawrie *et al*., 2000, 2003a, 2009). In many instances, the electrical conductivity distribution does not equate with formation (and/or hydrogeological) boundaries, but instead to a

combination of groundwater salinity and formation composition and texture (Lawrie *et al*., 2000, 2003a, 2009). A

However, given a suitable conductivity contrast, AEM methods can be used to map hydrostratigraphic, structural and groundwater elements in the shallow sub-surface in 3-dimensions (Lane *et al*., 2000, 2004; Lawrie *et al*., 2003a, b, 2008, 2010c). The depth of investigations possible with AEM systems depends on the conductivity distribution in the landscape as well as the technology used. In general, greater depth penetration (100 m and more) is achieved using time-domain AEM systems even in salinized landscapes (Roach, 2012; Tan *et al*., 2012), with more limited depth penetration achieved by most multi-frequency helicopter systems (e.g. George *et al.*, 1998; Lawrie *et al*., 2009b).

The Australian Government has funded several major national programs involving AEM for groundwater salinity mapping and management over the past 15 years. The initial program was the National Airborne Geophysics Project (NAGP 1997-1998; George *et al*., 1998, 2000; George & Green, 2000; George & Woodgate, 2002). The NAGP program had mixed success in the utilisation of airborne magnetics, gamma radiometrics and AEM for salinity and groundwater mapping and characterisation (George *et al*., 1998; George & Woodgate, 2002). In part, this was due to the 'developmental' nature of the early AEM systems, and in some examples, to the selection of an inappropriate technology for the specific mapping objective. The relative lack of success in one or two catchments left a perception in some States that AEM technology was not suited for groundwater studies, and its application has remained problematic in some States. This is despite significant successes in comparable landscape settings elsewhere in Australia (Walker *et al*., 2004), and comparative studies of older and new technologies showing the significant advances made in AEM technologies and their application (e.g. Lawrie *et al*., 2010a).

The development of the TEMPEST fixed wing time domain AEM system in the late 1990s (Lane *et al*., 2000), enabled greater depth penetration of salinized landscapes, and provided significant improvement in the ability to resolve hydrostratigraphy and groundwater salinity at shallow depths (Lane *et al*., 2000, 2004). TEMPEST was also successfully used to map fresh groundwater in a buried palaeochannel within an otherwise salinized landscape (George, 1998), while TEMPEST was also used to resolve stratigraphy and groundwater salinity in a number of other small mapping projects (Lane & Pracillo, 2000; Lane *et al*., 2000, 2004). The multi-disciplinary GILMORE Project (1998- 2001; Lawrie *et al*., 2000) also successfully demonstrated the value of using AEM as part of a multi-disciplinary approach to groundwater salinity mapping and hazard assessment, and the importance of drilling, ground and borehole geophysical studies for the calibration, validation and interpretation of AEM surveys.

Subsequently (2001-2008), the Federal government funded the National Action Plan for Salinity and Water Quality (NAPSWQ), with several AEM surveys flown in South Australia under the auspices of the South Australian Salinity Mapping and Management Support Program (SMMSP 2002-2005 e.g. Walker *et al*., 2004). This program demonstrated that AEM could be used cost-effectively to improve salinity management outcomes, with significant input to the assessment and identification of new salinity interception schemes, locating water storage facilities, designing salinity disposal strategies, informing irrigation re-zoning, and in understanding the spatial patterns of salt accumulation in the River Murray floodplain (Lawrie, 2008).

In order to ascertain which technologies should be used (and funded) to map and assess groundwater salinity in Australia, a review of salinity mapping methods was facilitated in 2003-2004 by the Australian Academy of Sciences and the Australian Academy of Technological Sciences and Engineering. This was conducted under the auspices of the Australian Federal Government's Natural Resource Management Ministerial Council. The 2004 Review found that, even with the additional challenges posed by extensive regolith and groundwater salinisation, EM methods are the most appropriate and effective for mapping groundwater and landscape salinisation in the Australian landscape context (Spies & Woodgate, 2005). Moreover, the Review found that AEM is the only *broadacre* technique that can detect and resolve hydrostratigraphy and groundwater quality (salinity) in the sub-surface deeper than the root zone (Spies & Woodgate, 2005).

Following on from the Review, the Federal Government funded the 2005-08 Community Stream Sampling and Salinity Mapping Project (CSS&MP). This program involved the acquisition of significant AEM surveys

to map and assess salinity hazard the Lower Macquarie Catchment (Edwards & McAuley, 2008; Palamara *et al*., 2010), and along a 450 km reach of the Murray River (Lawrie *et al*., 2006, 2008, 2009d).

Significant advances in all aspects of AEM technology selection, survey design, data processing inversion, data interpretation and integration, and product generation have been witnessed as a consequence of these Federally-funded programs (George *et al*., 1998; Lawrie *et al*., 2000, 2006, 2008, 2009d; Walker *et al*., 2004).

### 6.1.3 Use of AEM as Part of Trans-disciplinary Systems Studies of Groundwater Systems in Australia

The multi-disciplinary GILMORE Project demonstrated the value of using AEM as part of a multi-disciplinary approach to groundwater salinity mapping and hazard assessment (Lawrie *et al*., 2000. Subsequently, George *et al*. (2003) identified a number of steps required to ensure that airborne geophysical surveys are used appropriately to map key elements of the hydrostratigraphy and produce cost-effective salinity management outcomes. Previous failures were attributed to an over-emphasis on technology-led approaches to salinity mapping and management, and a lack of clear problem definition and inadequate prior knowledge or subsequent effort taken to understand the functional elements of each landscape. George *et al*. (2003) also emphasised the need to match the appropriate technology to the salinity management issues to be addressed, and articulated a phased methodology to achieve a successful management outcome using airborne geophysics.

Based largely on the lessons articulated by George *et al*. (2003), AEM surveys have increasingly been designed over the past 6 years to address specific land and water management questions within the context of broader natural resource management strategies (Walker *et al*., 2004). Using this approach, a number of AEM surveys have been shown to be cost-effective in addressing salinity and land management issues (Lawrie *et al*., 2003a, b, 2008, 2009a, b, d, 2010a; Walker *et al*., 2004; Munday *et al*., 2007, 2008).

Overall, this approach has played a crucial role in demonstrating the relevance of AEM-based information products for salinity, groundwater and broader land and environmental management (Munday *et al*., 2003a, b; Walker *et al*., 2004; Chamberlain & Wilkinson, 2004; Lawrie, 2006b; Cresswell *et al*., 2007; Munday *et al*., 2007, 2008; Lawrie *et al*., 2009d, 2010a). Successful outcomes from these projects have been attributed not just to advances in science, technology, project design, the calibration and validation of AEM data, and development of customised information products (George *et al*., 2003; Spies & Woodgate, 2005), but also to a high level of consultation between scientists, decision makers and local community groups at all stages in project design, implementation, delivery, knowledge transfer and follow-through (Walker *et al*., 2004).

In Australia, AEM has been used effectively to map hydrostratigraphy, groundwater salinity and the salinity hazard and risk in a number of salinized floodplain environments (Chamberlain and Wilkinson, 2004; Walker *et al*., 2004; Lawrie *et al*., 2008, 2009a, b, 2010a; Munday *et al*.,2006, 2007, 2008; Palamera *et al*., 2010). AEM has also successfully mapped salt water intrusion (Munday *et al*., 2007; Tan *et al*., 2012), and groundwater resources within otherwise salinized landscapes (George *et al*., 1998; Reid *et al*., 2009; Edwards and McAuley 2008; Lawrie *et al*., 2009d; 2012b).

The benefits from AEM surveys are maximised when these technologies are employed within trans-disciplinary, systems-based approaches to the analysis of problems and the development of customised interpretation products (Lawrie *et al*., 2000, 2003a, b, 2009a, b, c, d, 2010a; Spies and Woodgate, 2005). Systems-based approaches incorporate an understanding of landscape evolution and scale, utilise modern investigative approaches to the conceptualisation of aquifer systems, and incorporates data on water, salinity and vegetation dynamics to provide key constraints on aquifer systems (Lawrie *et al*., 2000, 2008, 2009a, 2010a).

Over the past 5 years, a staged approach to survey design combined with forward modelling studies has ensured that appropriate AEM technologies are selected to match the target objectives (Green and Munday,

2004; Lawrie, 2006; Munday *et al*., 2007, 2008; Lawrie *et al*., 2009a, b, 2010a, b, c). In Australian landscape settings AEM-based products have proven effective at providing high resolution baseline data on the spatial distribution of aquifers and aquitards as well as water quality and salt stores in shallow (<120 m) floodplain sediments (Tan *et al*., 2005; Munday *et al*., 2006, 2007; Mullen *et al*., 2007; Lawrie *et al*., 2009a, 2010a, b, c). However, while these datasets and information products address specific gaps in the biophysical knowledge framework, addressing salinity and land management questions usually requires an understanding of underlying biophysical processes and dynamics that often cannot reliably be determined from analysis of spatial patters of conductivity alone (Cresswell *et al*., 2007, Lawrie *et al*., 2010a, b, c).

While increasing sophistication of AEM-derived products (e.g. porosity-corrected lithology products, maps of salt load, salt hazard etc.; Ley-Cooper and McNae, 2007; Tan *et al*., 2009; Lawrie *et al*., 2010a, b, c) has improved their utility and up-take by land and groundwater managers, much of the success of AEM surveys in the past 5 years has come from demonstration of relevance through incorporation of AEM-derived products in regional planning and decision support tools and in groundwater modelling frameworks (Chamberlain & Wilkinson, 2004; Walker *et al*., 2004).

The high resolution (in 2D and 3D) afforded by AEM datasets enables key elements of the hydrogeological system to be mapped and characterised with greater certainty. This has contributed to improved parameterisation of models, and enables more reliable quantitative assessments to be made of the uncertainties and confidence levels in model predictions. It is the adoption of these trans-disciplinary, multi-scale system approaches that underpin the development of more effective salinity and groundwater management strategies, and enable more targeted salinity management actions (Lawrie, 2008; Lawrie *et al*., 2009a).

To date, a large variety of modelling approaches have incorporated AEM-derived products, reflecting the diversity of land management questions tackled. The approaches vary from GIS-based modelling platforms to fully distributed groundwater flow models (Walker *et al*., 2004; Doble *et al*., 2005, 2008; Wang *et al*., 2005; Munday *et al*., 2008; Yan & Howe, 2008; KBR, 2010). The AEM datasets help constrain and parameterise these hydrogeological models (KBR, 2010).

The BHMAR AEM survey has built significantly on the principles, methodologies, experience and products developed for salinity mapping and management in Australia. In particular, the staged approach to technology selection and survey design, and the use of a 4-D systems approach to integrate complex datasets and develop a range of customised information products for use in subsequent hydrogeological and geotechnical modelling was recognised as critical to the likely success of the survey. The process of technology selection, data acquisition, calibration, inversion, validation and generation of derived interpretation products is documented below. The BHMAR survey would appear to be the first use of AEM methods in MAR investigation and assessment.

## 6.2 AEM SYSTEM SELECTION FOR THE BHMAR SURVEY

### 6.2.1 Introduction

Over the past decade, several new airborne electromagnetic (AEM) systems have become available for commercial surveying, and when a new survey involving AEM is planned, one of the crucial choices is to select an appropriate system for the mapping task. A conscious and rational decision-making process is needed to reach a balanced decision that must necessarily be a compromise between many, often conflicting, interests and criteria.

In this study, the choice of an appropriate AEM system for a given task was based on a staged approach utilising:

- A derivative analysis approach to comparing various AEM systems, including forward modelling of system responses, based on geoelectric models derived from ground TEM and borehole induction profiles in the candidate areas (Lawrie *et al*., 2008, 2009a);

- A comparative analysis of candidate systems, consisting of both theoretical considerations and field studies including AEM test lines (Christensen *et al.*, 2009; Lawrie *et al*., 2009b; Christensen & Lawrie, 2012).

### 6.2.2 Step 1: Derivative Analysis Approach Including Ground TEM and Borehole Induction Models and Forward Modelling of System Responses

It has become normal practice for environmental and groundwater studies considering the application of AEM technologies, to undertake an analysis of their suitability to detect a ground response that reflects a given target or suite of targets that have been predefined as being of critical importance (Green & Munday 2004). This process involves forward modelling the ground response for a given AEM system, taking account of their general acquisition characteristics and noise levels. This approach is regarded as integral to reducing the risk associated with the acquisition of AEM data, as it allows us to define whether they are fit for purpose. Specifically, the process of forward modelling provides greater clarity on:

- Their suitability to detect particular targets and
- Whether particular systems are better than others for measuring variability associated with the target(s), i.e. their sensitivities;

When the forward model response is linked to inversion, we are able to better understand what the resolving capabilities of the system might be, particularly in the detection of variations in the vertical conductivity structure. Examples illustrating this approach in Australian conditions are given in Green & Munday 2003, Munday *et al*. (2003a, b), Fitzpatrick & Munday (2006).

Typically, the key features are elements of the hydrostratigraphy such as aquifers and aquitards, groundwater quality etc.

Whilst forward modelling and inverting synthetic data for a ground response will provide some insight into the potential of AEM systems, given particular target characteristics, it is not the only parameter that may determine which system should be employed for any given survey. Other issues to be considered include cost, system availability, and the turnaround time for data delivery. Another important criterion is an analysis of the resolution capability of different AEM systems with regard to the models expected in the survey area and the aims of the investigation (Lawrie *et al*., 2009c; Christensen & Lawrie, 2012).

In the BHMAR project, the first step in the selection process initially followed a derivative analysis approach, involving a forward modelling exercise to determine whether any of the available AEM systems could map such a range of features, and/or narrow down the systems most likely to map these key features (Lawrie *et al*., 2008, 2009a, b). This involved inverting synthetic data for a ground response to provide some insight into the potential of AEM systems, given particular target characteristics and assumed noise levels representative of the systems (Lawrie *et al*., 2009a). Geoelectric models of the candidate areas were derived from ground TEM surveys and borehole induction profiles (Lawrie *et al*., 2008, 2009a).

Phase 1 of the BHMAR study also included an assessment of the likely success of using AEM technologies to map the conceptual MAR and groundwater resource targets (Lawrie *et al*., 2008, 2009a). A risk assessment approach was used to assess the potential for AEM technologies to map the potential aquifer targets and options defined within the Darling Floodplain (Lawrie *et al*., 2009a). The principal geophysical targets were identified as the unconfined aquifers (Coonambidgal Formation, Menindee Formation), the priority target aquifer (Calivil Formation, and Loxton-Parilla Sands), and aquifers in the upper and lower Renmark Group. These targets were paired with the water supply alternative options, principally direct extraction of fresh groundwater, direct extraction of brackish to saline groundwater (as feedstock for desalination plants) or aquifer storage (MAR).

A matrix approach is used in Figure 6-1, based on the two key criteria of:

- Likelihood of technical success – accounting for the probability that the required groundwater resource is likely to be present, discoverable with the available technology, and the water supply alternative can be implemented.
- Likelihood of negative consequences – accounting for the potential and significance of impacts to the water resource, ecosystems and other groundwater users if the option was to be implemented.

In Figure 6-1, the targets considered to have a relatively high probability of technical success combined with relatively low potential of negative consequences, plot in the top right quadrant. Target 5 is the Calivil Formation. All management options were deemed to have a high chance of technical success and a relatively low chance of negative consequences. The Calivil Formation was judged to have a relatively thick aquifer section, to be lithologically distinctive, and sandwiched between hydrologically and electrically contrasting units. The Calivil Formation was therefore assessed as being relatively easy to map, to have a high likelihood of storing water of reasonable quality, and of being recharged by MAR operations. The unit was judged to be only locally connected to the overlying unconfined aquifers, and consequently, the chance of negative effects with respect to impact on these and the modern river channels was judged to be low (Lawrie *et al*., 2009a).

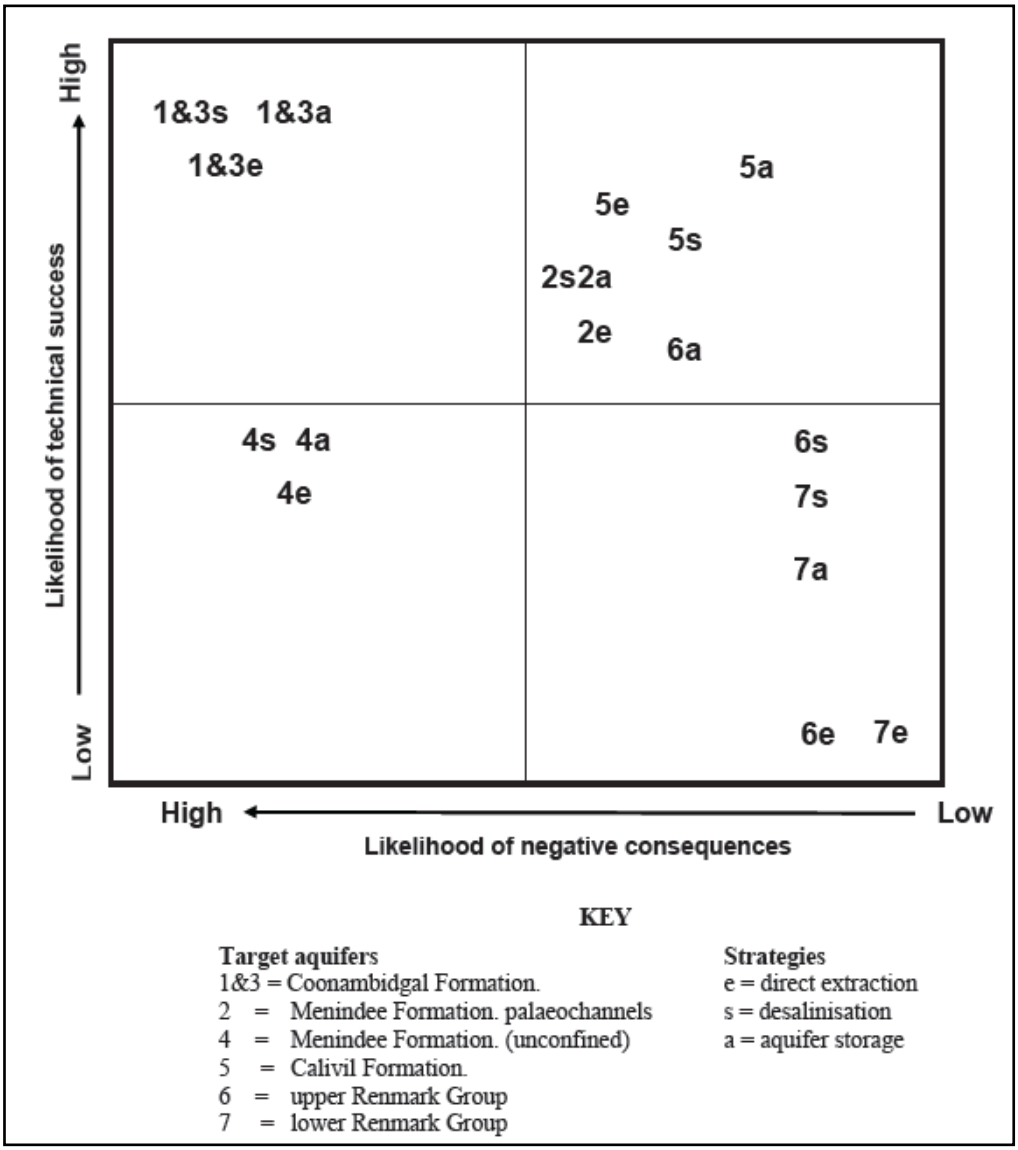



**Figure 6-1.** *Risk plot of aquifer management options expressed as likelihood of technical success against likelihood of negative consequences.*

### 6.2.3 Step 2: Comparative Analysis Utilising Theoretical Considerations and Field Studies Including Test Lines

Though only a part of the full decision-making process, a comparative system analysis with regard to model parameter uncertainty is recommended in a comprehensive selection process of the optimal AEM system for particular survey aims. The model parameter uncertainty of an AEM system depends critically on the achievable signal-to-noise ratio, and the geophysicists involved in the comparative study must use their experience and general insight to evaluate whether the proprietary noise figures supplied by the contractors are reasonable or not.

The most commonly used derivative analysis approach (e.g. Green & Munday, 2004), does not take the parameter correlation into account that is characteristic of the TEM method. Furthermore, the derivative analysis generally overestimates the resolution power of the TEM method - and likely any EM method. The overestimation depends on the model in general and the parameter in question in particular, and there is furthermore no guarantee that the ranking between systems will be the same using the derivative analysis as using the inversion analysis.

In this study, there was a need to detect the MAR and groundwater resource targets with a high degree of confidence. This was necessary to provide quantitative estimates of groundwater and aquifer storage over a very large area of the Darling floodplain, to map key elements of the hydrogeological system that would enable groundwater recharge and flow pathways to be mapped, and to enable MAR targets to be evaluated against rigorous national guidelines for drinking water quality (NRMMC–EPHC–NHMRC, 2008; NHMRC-NRMMC, 2011) and Managed Aquifer Recharge (NRMMC–EPHC–NHMRC, 2009).

In the BHMAR study, it was necessary to select an AEM system with the capability of mapping key functional elements of the hydrogeological system critical to the success in identifying and assessing suitable MAR and groundwater resource targets (Figure 6-2). This necessitated selecting an AEM system capable of mapping heterogeneities in the hydrostratigraphy and hydrogeology, and more specifically, the:

- Thickness and extent of near-surface unconfined aquifers and aquitards that might provide recharge pathways or inhibit surface-groundwater connectivity;
- Thickness, extent and internal textural variability of Pliocene sand aquifers;
- Thickness, extent and internal variability in upper (Blanchetown Clay) and lower (upper Renmark Group) confining aquitards that ‘sandwich’ the Pliocene sand aquifers;
- 3D distribution of groundwater salinity (to help define fresh and brackish groundwater resources);
- Faults that might act as discrete recharge and groundwater flow pathways; and
- Zones of inter-aquifer leakage.

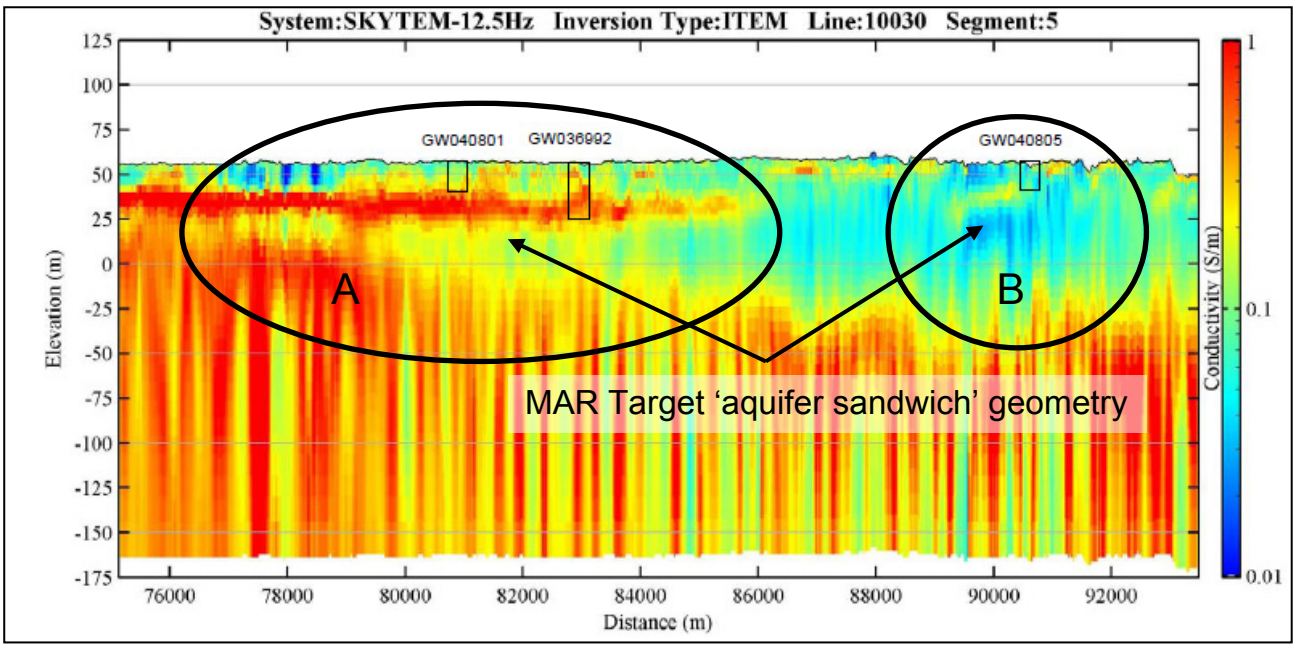



**Figure 6-2.** *Conductivity depth section through two of the MAR targets identified by ground TEM and drilling prior to the test flights. Target A has well developed upper and lower aquitards (conductive layers) with an intervening semi-confined aquifer (more resistive) which in this location is thinning onto a basement high. Target B has fresher groundwater (more resistive) within the target aquifer, associated with leakage from the Darling River.*

A secondary consideration was the ability of the AEM systems to map in situ fresh and brackish groundwater resources.

As the project brief for Phase 2 of the project required recommendations on the presence and suitability of potential MAR sites with an 80% confidence level, and this level of confidence was not obtained in the forward modelling exercise for all of the potential targets, it was decided to acquire test line data through the study area to provide greater certainty in AEM system selection.

In step 2, the following criteria were used to select a suitable AEM system:

Scientific and technical considerations. This involved:

- A 'traditional' derivative analysis approach to comparing various AEM systems, including forward modelling of system responses based on geoelectric models derived from ground TEM and borehole induction profiles in the candidate areas (Lawrie *et al*., 2008, 2009a). Ground and borehole data were obtained specifically for the purposes of this comparison, while new calibration procedures were enacted for the collection of borehole induction log data.
- A comparative analysis of candidate systems, consisting of both theoretical considerations and comparison with ground, borehole EM and AEM test lines (Christensen *et al.*, 2009; Lawrie *et al*., 2009c; Christensen & Lawrie, 2012). Comparative analysis of short-listed systems included:
- Acquisition of AEM test lines for 2 systems (TEMPEST and SkyTEM), short-listed based on the derivative analysis approach. Examples of conductivity depth sections produced from the two systems are shown in Figure 6-3. The SkyTEM identified most of the key elements of the hydrostratigraphy that had been indicated prior to the test flights, and the potential MAR targets identified by ground TEM survey and drilling. The competing system had a greater depth of investigation, however did not adequately resolve the detail of the hydrostratigraphy in the upper 30 m of profile. A range of contractor-supplied inversions and in-house holistic inversions were carried out to assess the potential of each system to map the required elements of the hydrogeological system;

- Fiducial Point (FID point) analysis of test line data utilising conductivity data from 8 individual boreholes on the test lines versus the nearest FID point from each of the 2 systems using contractor supplied inversion products, and in the case of TEMPEST data, some additional inversions carried out by Geoscience Australia staff. The FID point analysis involved comparing conductivity values averaged over 4 m intervals for all 8 boreholes vs. averaged values from nearest FID points for all the inversion products.
- Comparison of existing ground EM and AEM system responses for all the inversion products from both the TEMPEST and SkyTEM systems.
- Specific target analysis. This involved assessment of the ability of each system/inversion method to map each of the 3 primary MAR targets (Primary Pliocene Sands, Secondary Lower Renmark Group Sands, and Tertiary Menindee Formation Sands), utilising all the available inversion products. This involved comparing data from all the inverted test line data (in 20 km line sections) to get an overview perspective on hydrogeological features that need to be mapped.
- Additional hydrogeological data including boreholes close to the test lines were also incorporated into this analysis. System responses for each of the features listed above were tabulated.

Assessment of the ability of the contractor to meet project timing requirements. This included:

- Ability of the contractor to deliver surveys within the specified timeframes– i.e. system availability;
- The demonstrated ability of the contractor to provide field processed data (as inverted conductivity depth sections) under survey conditions, within 48 hrs of acquisition;
- Historical performance of the contractor to provide final data within the required timeframes.

The third issue considered was the cost of the survey (line kilometres) and the impact on the whole project timeframes and budget based on project acquisition timeframes.

The overall relative weighting of these criteria was:

- Ability of the systems to map the potential MAR targets with the required resolution (60%);
- Ability of the contractor to meet the project timelines (30%); and
- Cost of the survey (10%).

After a rigorous assessment process, which included the flying of test lines by two competing systems (Lawrie *et al*., 2009b), the towed SkyTEM time-domain helicopter EM (TDHEM) system (Figure 6-5; Figure 6-6.) operated by Geoforce Pty Ltd. was selected as the successful contractor to carry out the AEM survey of the Broken Hill MAR Phase 2 Project. The survey (31,834 line km) was completed by 2 systems in 9 weeks, well ahead of schedule. iTEM conductivity sections were available within 48 hours of flight line acquisition, enabling rapid targeting of drilling operations.

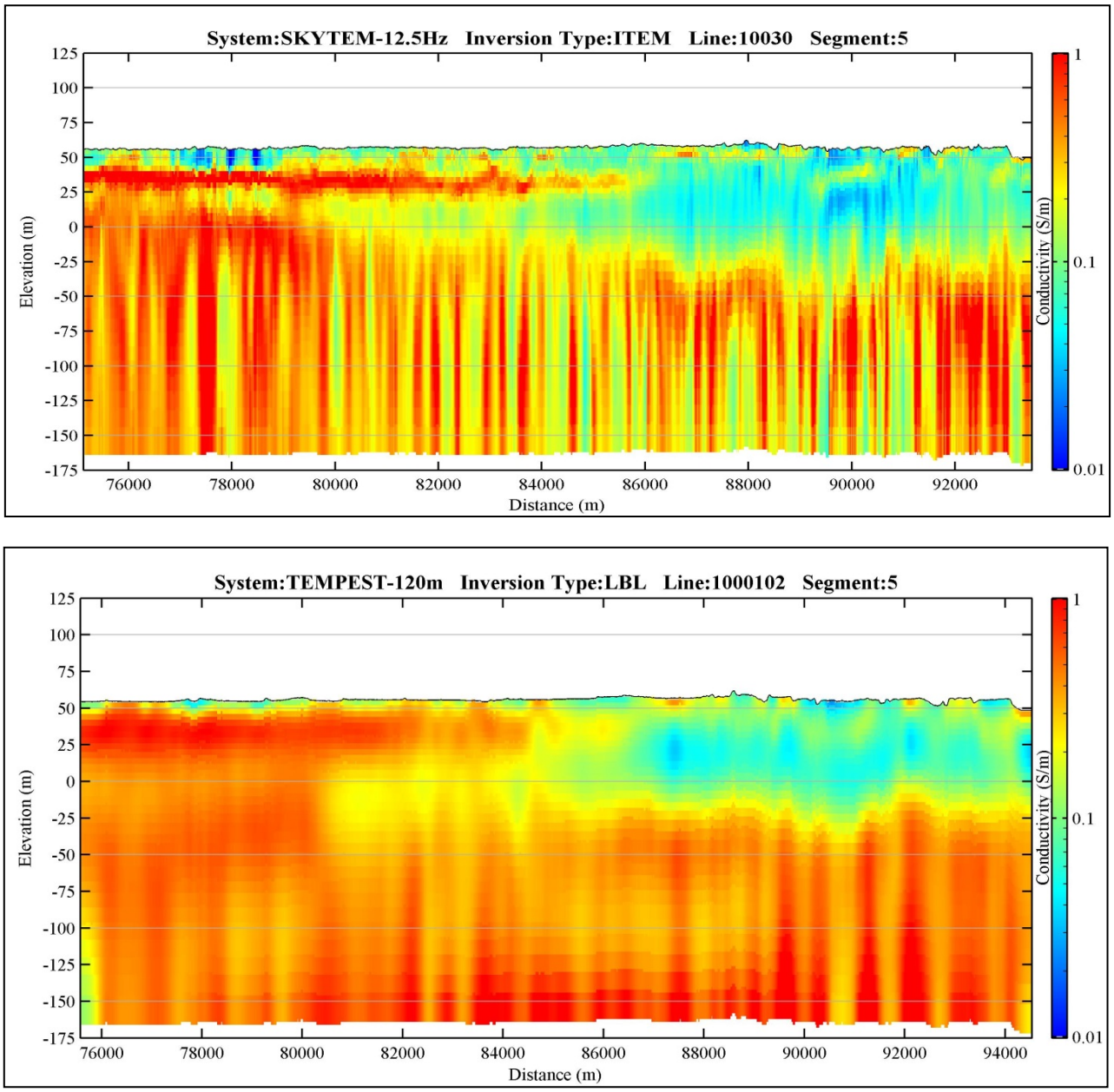



**Figure 6-3.** *Conductivity depth sections from two different AEM systems. System A (SkyTEM, top panel) was able to map most of the key elements of the hydrostratigraphy that had been identified prior to the test flights, and the potential MAR targets identified by ground TEM survey and drilling. System B (bottom panel) had a greater depth of investigation, however did not adequately resolve the detail of the hydrostratigraphy in the upper 30 m of profile. A range of contractor-supplied inversions and in-house holistic inversions were carried out to assess the potential of each system to map the required elements of the hydrogeological system. System A was selected for the BHMAR survey.*

### 6.2.4 Discussion

To illustrate the inversion analysis, we present an excerpt from Christensen & Lawrie (2012).

The data used in the analyses are theoretical data based on forward responses of the representative models to be analysed. After responses are calculated, noise is ascribed according to a noise model based on Geoscience Australia's system definition files. In the forward calculation and inversion analysis, the full system characteristics of the SkyTEM system are taken into account. The TEMPEST system measures the rate of the change of the magnetic field components in receiver coils from a step-like source, but data are deconvolved into 100% duty cycle step responses - and consequently, this is the data type modelled in this comparison.

The 5-layer models in Table 6-1comprise most of the models analysed in Lawrie *et al*. (2009). Model parameters are fixed except for the resistivities of the second and third layers. The resistivity of the second layer varies over a decade from 1 to 10 Ω m while the resistivity of the third layer varies from 0.5 to 50 Ω m, both in 21 steps giving 441 different models. All layer resistivities are quite low except for certain values of the third layer, so it must be expected that depth penetration will be limited. For some of the models, resistivity contrast between neighbouring layers is low, resulting in a poor determination of the layer boundary.

**Table 6-1.** *Parameters of the test models.*

| Layer # | Thickness m | Resistivity Ω m | Lithology |
|---|---|---|---|
| 1 | 10 | 1.6 | Coonambidgal Formation |
| 2 | 15 | 1.0 - 10 | Shepparton Formation, silty sand |
| 3 | 50 | 0.5 - 50 | Calivil Formation sand |
| 4 | 50 | 3 | Upper Renmark Group, silty sand |
| 5 | | 5 | Middle and lower Renmark Group, silty sand |

In Figure 6-4, analyses for the SkyTEM and TEMPEST systems are presented as coloured pixels in templates. Each template shows the relative uncertainty (the square root of the posterior variance of the logarithm of resistivities) of one of the model parameters as a function of the resistivity of the second layer (the abscissa) and the resistivity of the third layer (the ordinate). The colour indicates the relative uncertainty of the model parameter in 6 levels, red being the lowest uncertainty and blue the highest.

For the SkyTEM system, the analyses of the resistivities RHO1, ⋯, RHO5 (cf. Figure 6-4) show that RHO1 is well determined for all models. RHO2 is better determined when layers 2 and 3 are conductive. RHO3 is determined when low, but not when it attains higher values. RHO4 and RHO5 are unresolved. Overall, the analyses show that only the parameters pertaining to the top 2-3 layers can be determined with low to medium uncertainty. The resistivity of the fourth and fifth layers is undetermined. This is mainly due to the low resistivities of the overlying layers and the resulting limited depth penetration.

For the TEMPEST system, the analyses of the resistivities RHO1, ⋯, RHO5 (cf. Figure 6-4) show that RHO1 is reasonably determined for lower values of RHO2 and RHO3, but otherwise poorly determined. RHO5 is reasonably determined for high values of RHO2 and RHO3, but otherwise poorly determined. All other resistivities are by and large undetermined, the exception being the resistivity of the fifth layer for which the relative uncertainty is below 0.5 for the higher values of RHO2 and RHO3. The resistivity of the fifth layer is also the only parameter for which the TEMPEST system shows a somewhat better resolution than the SkyTEM system.

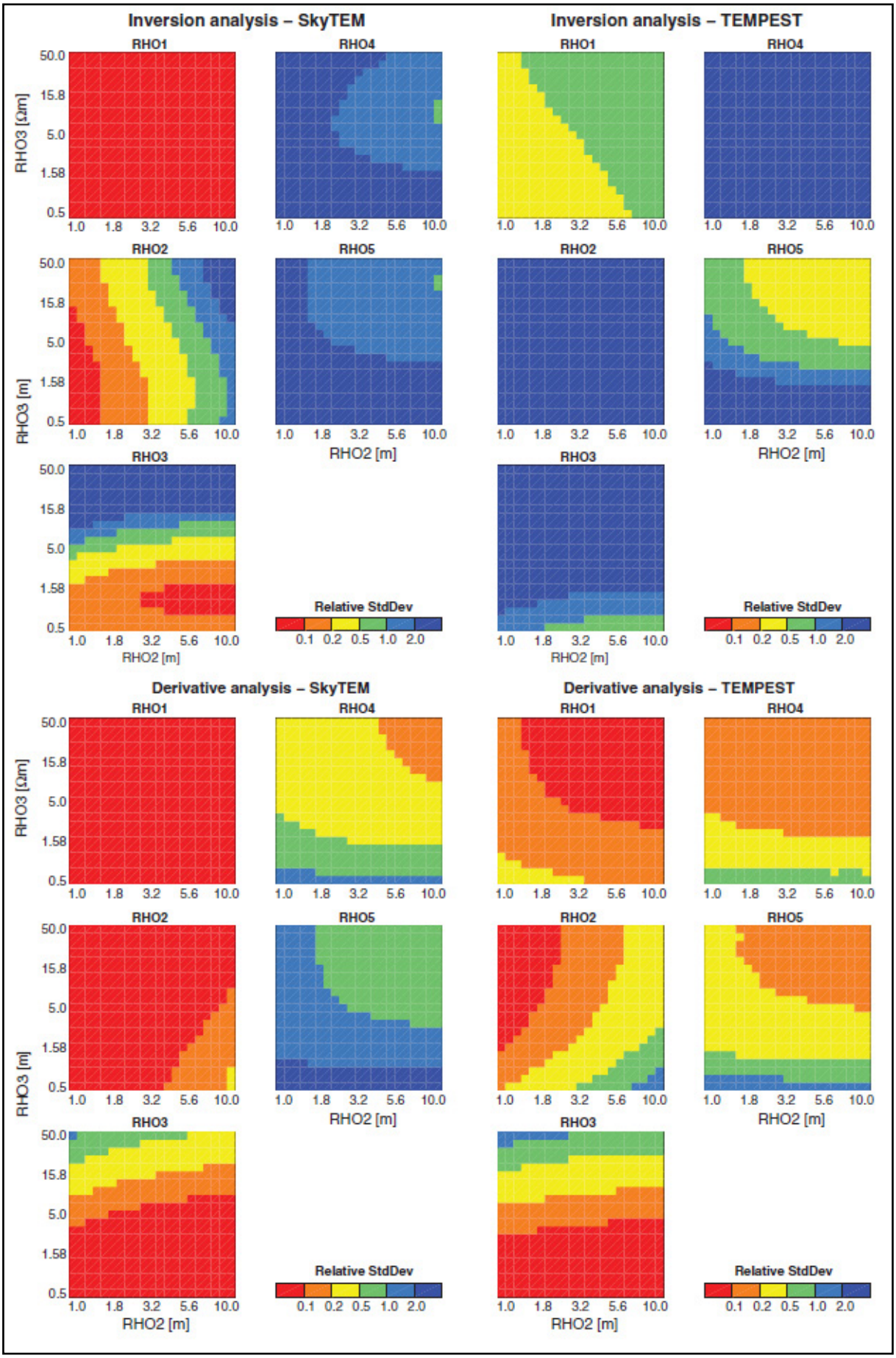



**Figure 6-4.** *Analysis templates for layer resistivities. SkyTEM (left column) and TEMPEST (right column) using the inversion analysis.*

An additional result of using the comparative analysis approach (Lawrie *et al*., 2009b; Christensen & Lawrie, 2012) was that for several of the model parameters of the five-layer conceptual models for the survey area, the derivative analysis gave a different ranking between the SkyTEM and TEMPEST systems than that obtained in the inversion analysis. The use of the derivative analysis method may thus result in a suboptimal choice of AEM system. We do not hesitate to conclude that the inversion analysis is distinctly superior to the derivative analysis and should be used in future work.

Impulse (SkyTEM) and step response (TEMPEST) systems are not equivalent in practice (Christensen & Lawrie, 2012). The near-surface resolution of step response data is inferior to that of impulse response data because, at very early times, the step response does not depend on the surface conductivity while the impulse response is inversely proportional to the surface conductivity. Only at intermediate delay times does the step response reflect the near-surface conductivity and for those delay times, the diffusion depth may be considerably greater than the thickness of the first layer with the consequence that near-surface resolution is lost. Our analysis of the generic TEM system shows that there is a difference between step and impulse systems for the same Tx-Rx geometry. We must therefore emphasise that it is not the extended geometry of the TEMPEST system that causes problems with the near-surface resolution; it is the fact that it - through the applied data processing scheme - provides step and not impulse response data.

In our analyses of the resolution capability of the SkyTEM and TEMPEST systems with regard to the 5-layer models typical for the survey area, the SkyTEM system has the better near-surface resolution and both systems were incapable of mapping layers deeper than ~75 m with any certainty.

## 6.3 SKYTEM TDHEM SYSTEM

The SkyTEM system is a high-resolution helicopter-borne time-domain electromagnetic system. The SkyTEM system was developed for high-resolution groundwater and environmental investigations. It was developed as a rapid alternative to ground-based TEM surveying and has the advantage of delivering much higher data density and spatial area coverage. In Australia, this system has been successfully applied to the mapping of aquifer hydrostratigraphy, salinity and groundwater resources (Reid *et al*., 2009; Lawrie *et al.,* 2009b) and has a demonstrated ability to define both near surface and deep conductivity structure in the Australian landscape context. The spatial resolution of helicopter systems such as SkyTEM returns a weighted average response over lateral distances of ~100 m for near-surface to hundreds of meters at depths of ~100 m.

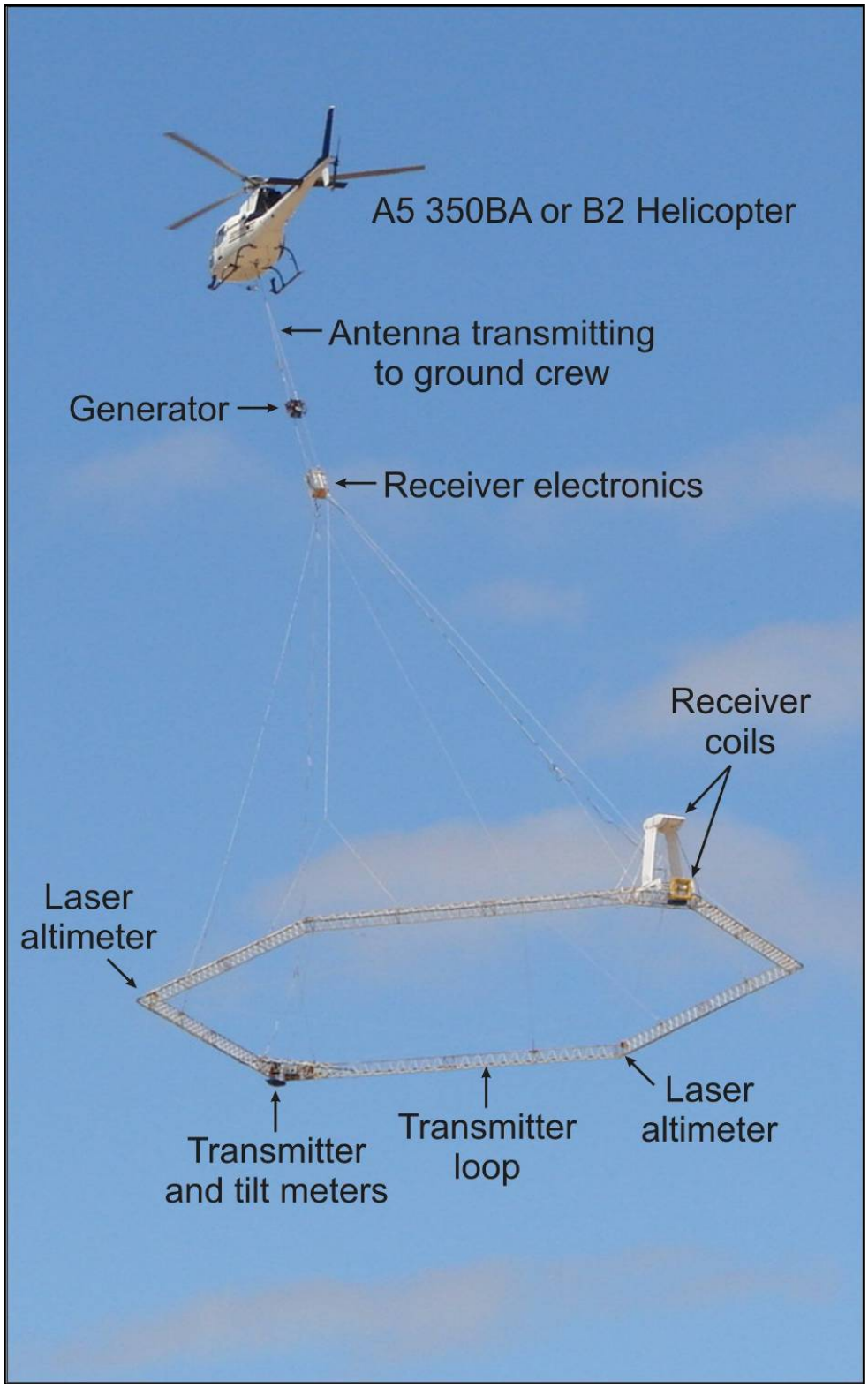



**Figure 6-5.** *The components of the SkyTEM airborne electromagnetic system in flight.*

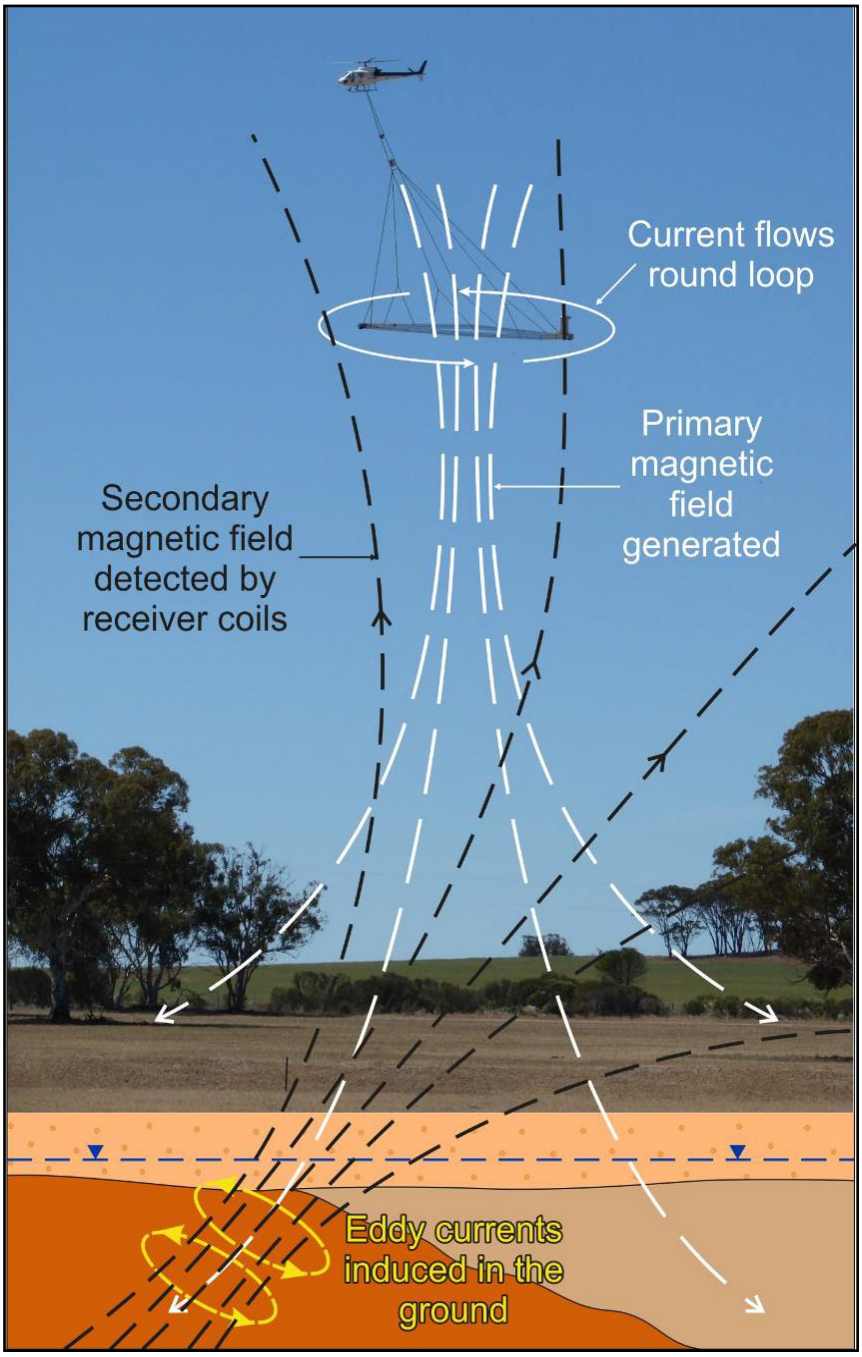



***Figure 6-6.*** *Operating principles of the SkyTEM AEM system.*

The principal features of the SkyTEM system (Figure 6-5; Figure 6-6.) are as follows:

- SkyTEM is a calibrated system designed to give quantitative electromagnetic data across a wide time range, as required for detailed investigations where it is often necessary to be able to distinguish geological units with very slight differences in conductivity. Ancillary data measured by the system includes laser altitude, GPS elevation, transmitter loop attitude, and peak transmitter current for each transient, enabling rigorous quantitative interpretation of the electromagnetic data.
- The instrument is capable of operating in dual moment mode, a unique feature among helicopter-borne TEM systems, combining the high shallow and lateral resolution offered by early time data measured at high base frequency and low current, with the large depth of investigation from later time measurements at low base frequency and high transmitter moment.

- The receiver coils measure both vertical (Z) and horizontal in-line (X) components of the secondary voltage response.
- The receiver coils are placed so as to be null-coupled to the primary field of the transmitter, in order to minimise the self-response of the system. The direct coupling between the transmitter and receiver is very low, and in general no levelling of the electromagnetic data is required. As a consequence data can be processed and inverted in the field, allowing rapid assessment of survey results and planning of infill lines etc. whilst a survey is in progress.
- The low flight height (nominal 30 m) provides high lateral resolution and improved shallow depth resolution. The spatial resolution of helicopter systems such as SkyTEM return a weighted average response over lateral distances of several tens of metres, ranging from ~30-40 m near surface to ~90 m at depths of 100 m.
- Advanced quantitative interpretation programs are available. Fast approximate layered earth interpretation using iTEM can be performed faster than the rate of data acquisition (Christensen *et al*. 2009), enabling very rapid data turnaround. Full nonlinear laterally or spatially constrained inversion can provide improved resolution of layer depths and allows straightforward application of constraints on the conductivity model both laterally and with depth. Incorporation of additional constraints on the inversion, based on geological considerations or additional geophysical data, can be readily performed.

SkyTEM has been deployed in Australia since late 2006, and is operated by Geoforce Pty Ltd under an agreement with SkyTEM Aps, Denmark. Survey objectives in Australia have included groundwater exploration, salinity mapping, contaminated site and tailings dam assessment, and exploration for a range of mineral commodities, including channel iron deposits, palaeochannel and unconformity-hosted uranium, gold, manganese and base metals. In Australia, this system has been successfully applied to the mapping of aquifer hydrostratigraphy, salinity and groundwater resources (Reid *et al*., 2009; Lawrie *et al*., 2009b) and has a demonstrated ability to define both near surface and deep conductivity structure in the Australian landscape context. For an overview of SkyTEM surveys in Australia, see Reid *et al*. (2010).

### 6.3.1 System Configuration

The SkyTEM system has a number of novel design features which distinguish it from other helicopter transient electromagnetic systems. The system is carried as an external sling load, and is independent of the helicopter type (Figure 6-5). A full technical description of the SkyTEM is given by Sorensen & Auken (2004).

A small navigation screen is installed in the helicopter, which receives positional and altitude information via wireless link from GPS antennae and laser altimeters mounted on the transmitter loop frame (Figure 6-5). Other essential operating parameters, such as transmitter current and temperature, battery voltages, pitch and roll of the transmitter loop etc. are also available to the pilot. All navigational and operating parameters can also be received by the ground crew when within radio modem range. The SkyTEM transmitter is powered by a motor generator mounted on the tow cable. Average survey ground speeds are 80–100 km/h. In favourable flying conditions e.g., long flight lines and flat terrain, sustained production rates of 400-500 km/day have been regularly achieved.

The instrument geometry is fixed, with the transmitter loop, receivers and all ancillary instruments rigidly mounted on the transmitter loop frame. For the BHMAR survey, a 314 $m^2$ transmitter loop was used. Ancillary instruments include two independent DGPS receivers, two independent laser altimeters and two sets of independent inclinometers, providing redundancy in the case of instrument failure while the system is airborne. The redundant ancillary data sets are also very useful during quality control of survey data. Each inclinometer set measures the tilt of the frame from horizontal both in and perpendicular to the flight direction. The rigid geometry of the system means that the DGPS position and inclinometer information can be used to determine the exact position of all sensors in three dimensions. Tilt information is used to correct

measured laser altimeter data to the vertical, and can also be used to perform an approximate correction of the EM data for transmitter attitude (Auken *et al*., 2009).

### 6.3.2 Transmitter and Receivers

The transmitter, mounted on a lightweight wooden lattice frame, is a four-turn, 16 x 16 m hexagonal- loop divided into segments for transmitting a low moment pulse from one turn and a high moment from all four turns. The transmitter loop area is 314 $m^2$ (Reid *et al*., 2009). In the SkyTEM system, the receivers are positioned at the rear of the frame, and offset from the transmitter loop in the SkyTEM system (Figure 6-5, Figure 6-6. and Figure 6-7). The weight of the SkyTEM system, accounting frame, electronics and generator, is approximately 350 kg and typical flight speed is 80–100 km/h. It gives a full sounding approximately every 25 m after stacking. The operation altitude is as low as possible, 30–35 m, with variations largely determined by the presence of trees, hills or other cultural features. Good control over altitude is necessary as it prevents false shallow resistive artefacts.




**Figure 6-7.** *SkyTEM acquisition system on the ground at Menindee after a successful day of data acquisition.*

The SkyTEM system has been designed to provide calibrated electromagnetic data over a wide range of delay times (see Table 6-1). The SkyTEM transmitter is capable of operating in several different modes, including a dual transmitter mode as detailed in Sorensen and Auken (2004). The two modes were run during the BHMAR survey. In the Low Moment mode, a low current, high base frequency and fast switch off provides early time data for shallow imaging. In contrast, when in High Moment mode, a higher current and a lower base frequency provide late time data for deeper imaging.

In the dual transmitter mode, the system operates with alternating moments emphasising either shallow mapping or very deep mapping. The Low Moment obtains data at very early times (looking at shallow depths) while the High Moment is capable of obtaining data at deeper penetration depths due to its higher signal to noise ratio at later times. The receiver loop is rigidly mounted at the rear and slightly above the transmitter loop in a near-null position relative to the primary field, thereby minimizing distortions from the transmitter (Figure 6-6). X and Z components of the secondary field are recorded.

In the BHMAR survey, the High Moment (HM) mode used four transmitter turns and a peak current of 100 A, giving a peak moment of 125,600 $Am^2$. Ramp time was 45 μs and the base frequency 25 Hz with a 50%

duty cycle. Gate centre times are between 71 µs and 8.8 ms. The Low Moment (LM) mode uses a single transmitter loop turn and a peak current of 40 A. Base frequency in this mode is 222.2 Hz, with an on-time of 1 ms and off-time of 1.25 ms. Ramp time is typically 8 µs. LM gate centre times range from 14.2 µs to 0.897 ms. Gate delay times for the BHMAR survey are summarized in Table 6-2.

**Table 6-2.** *Gate delay times for High Moment (HM) and Low Moment (LM) modes in microseconds. Gate-open and gate-end are measured relative to the beginning of the turnoff ramp.*

| Gate number | Start | End | Width | Centre | Moment |
|---|---|---|---|---|---|
| **1** | 0.39 | 4 | 3.61 | 2.195 | - |
| **2** | 4.39 | 8 | 3.61 | 6.195 | - |
| **3** | 8.39 | 12 | 3.61 | 10.195 | - |
| **4** | 12.39 | 16 | 3.61 | 14.195 | LM |
| **5** | 16.39 | 20 | 3.61 | 18.195 | LM |
| **6** | 20.39 | 25 | 4.61 | 22.695 | LM |
| **7** | 25.39 | 32 | 6.61 | 28.695 | LM |
| **8** | 32.39 | 40 | 7.61 | 36.195 | LM |
| **9** | 40.39 | 50 | 9.61 | 45.195 | LM |
| **10** | 50.39 | 63 | 12.61 | 56.695 | LM+HM |
| **11** | 63.39 | 79 | 15.61 | 71.195 | LM+HM |
| **12** | 79.39 | 100 | 20.61 | 89.695 | LM+HM |
| **13** | 100.39 | 126 | 25.61 | 113.195 | LM+HM |
| **14** | 126.39 | 158 | 31.61 | 142.195 | LM+HM |
| **15** | 158.39 | 200 | 41.61 | 179.195 | LM+HM |
| **16** | 200.39 | 251 | 50.61 | 225.695 | LM+HM |
| **17** | 251.39 | 316 | 64.61 | 283.695 | LM+HM |
| **18** | 316.39 | 398 | 81.61 | 357.195 | LM+HM |
| **19** | 398.39 | 501 | 102.61 | 449.695 | LM+HM |
| **20** | 501.39 | 631 | 129.61 | 566.195 | LM+HM |
| **21** | 631.39 | 794 | 162.61 | 712.695 | LM+HM |
| **22** | 794.39 | 1000 | 205.61 | 897.195 | LM+HM |
| **23** | 1000.39 | 1259 | 258.61 | 1129.695 | HM |
| **24** | 1259.39 | 1585 | 325.61 | 1422.195 | HM |
| **25** | 1585.39 | 1995 | 409.61 | 1790.195 | HM |
| **26** | 1995.39 | 2512 | 516.61 | 2253.695 | HM |
| **27** | 2512.39 | 3162 | 649.61 | 2837.195 | HM |
| **28** | 3162.39 | 3981 | 818.61 | 3571.695 | HM |
| **29** | 3981.39 | 5012 | 1030.61 | 4496.695 | HM |
| **30** | 5012.39 | 6310 | 1297.61 | 5661.195 | HM |
| **31** | 6310.39 | 7943 | 1632.61 | 7126.695 | HM |
| **32** | 7943.39 | 9999 | 2055.61 | 8971.195 | HM |

Data were sequentially acquired at HM and LM. Noise measurements with the transmitter off were included in the acquisition script; these can provide useful information on background noise levels which may be utilised during inversion of the data. The peak transmitter current was recorded for each transient and is used in data processing and inversion.

The sensors are shielded over-damped coils with an effective area after pre-amplification of 105 $m^2$ and a low-pass cutoff frequency of 450 kHz. Both X and Z-components of dB/dt are measured, with the coils placed in positions at the edge of the transmitter loop where they are approximately null-coupled to the primary field of the transmitter. Detailed aspects of the signal detection scheme are given by Sørensen and Auken (2004). The receiver electronics have a user-selectable low-pass filter to avoid distortion of the early-time response, which is critical for providing reliable shallow information. A value of 300 kHz was used in the BHMAR survey.

An important aspect of the SkyTEM design is that the receiver coils are null-coupled to the primary field of the transmitter. This minimises transmitter bias and means that regular excursions to high altitude to monitor the bias response are not necessary during each flight. In the BHMAR survey, high altitude flights were conducted at the start of the survey to confirm correct operation of the instrument, and at approximately weekly intervals thereafter. The transmitter bias measured at high altitude can be compared with the response measured at survey altitude. Rather than attempt to correct for the bias by subtracting the response measured at high altitude, channels where the bias is >2% of the earth response are not used for subsequent processing and inversion.

### 6.3.3 In-field Data Processing

For surveys where the dual transmitter mode is employed, the LM mode provides unbiased data at the HM channels for which the bias signal is strongest, so there is no loss of information when biased early-time HM channels are excluded. The very small bias signal means that preliminary inversion and presentation of SkyTEM data can be performed without the need for levelling and only a very basic and rapid data processing, and in general data from different flights stitch together seamlessly. The minimal data processing requirements for SkyTEM mean that inversions can be performed on field-processed data immediately after data is dumped from the instrument when the helicopter is grounded to refuel, and the field results are very similar to those from final office-based processing. In the BHMAR survey, data and inversions using the iTEM fast approximate layered-earth inversion code (Christensen, 2002; Christensen *et al*., 2009), were delivered within 48 hours of acquisition.

### 6.3.4 BHMAR AEM Survey Logistics

The survey involved the acquisition of 31,834 line km of data in five main blocks (Figure 6-8) – Area 1 (Central), Area 2 (North), Area 3 broken into areas 3a and 3b (South) and Area 4 (the Sunset Strip extension to the west of Area 1). Two SkyTEM systems (SK1 and SK2) were employed for the survey, and a summary of survey dates and area coverage are shown in Table 6-3. Area 1, centred on the Menindee Lakes, was flown with NW-SE flight lines spaced 200 m apart. Area 2 was flown with NW-SE flight lines spaced 300 m apart. The third block adjoined the core block to the south with lines flown slightly east of north on lines spaced predominantly 300 m apart (Area 3a), with a small area flown with lines spaced 600 m apart (Area 3b). Analysis of initial data led to the survey being extended, with acquisition of a block of survey lines to the northwest of the main survey (Area 4). The flight lines in Area 4 are spaced 250 m to 1 km apart and are approximately 50 km long (Figure 6-8).

The range of flight line numbers within each of the four main survey blocks is given in Table 6-4. In some cases line were repeated for quality-control purposes. A flight line number ending in 0 denotes the first flight on a particular line, and line numbers ending in 1, 2 … denote subsequent flights.

**Table 6-3.** *Sk1 and Sk2 roster and coverage.*

| |
|---|
| SK1 commenced flying on 28th June 2009. |
| SK1 also acquired the Sunset Strip Extension before demobilizing on 4th September 2009. |
| A significant damage to the transmitter loop frame on the 5th July 2009. Damage was repaired during the 6th and 7th July, system recommenced production flying on 8thJuly 2009. (This has some, minor, implications on the modelling of the data) |
| SK2 commenced flying on 3rd July 2009, the northern end of Area 2 on 3rd July 2009. |
| Area 2 was completed on 19th July 2009, after which SK2 relocated to the southern end of Area 1. |
| SK2 relocated to the eastern edge of Area 3 on 4th August 2009, and acquired Areas 3 and 3b (Lines 31250 – 30000) working westwards. |

**Table *6-4.*** *Flight Line naming convention.*

| Area | Start Line | End Line |
|---|---|---|
| Area 1 | 20000 | 25410 |
| Area 2 | 10000 | 11070 |
| Area 3 | 30000 | 31250 |
| Area 4 (extension) | 100000 | 100180 |

The flight number format is the date (yyyymmdd.ff), with the flight number on that day given after the decimal point. Daily flight numbers for system SK1 commence at 01, and those for SK2 commence at 21. For example: 20090702.02 is the second flight for system SK1 on the 2nd July 2009, and 20090724.23 is the third flight for SK2 on 24th July 2009. Survey logistics are summarised in Table 6-5.

In addition to the five main blocks, a series of traverses were flown along the Darling River, Great Darling Anabranch and Talyawalka Creek. The river transects comprise one line along the centreline of each river, with parallel traverses 200 m either side of the centre line. River lines were flown in sections during the course of the survey, using both SK1 and SK2.

The contractor commenced the data acquisition phase of the survey on 26th June 2009 and finished flying on 1 September 2009.The survey took just under ten weeks to complete; which was six weeks ahead of the timing specified in the contract, despite the project area being extended and the addition of the additional hover test calibration experiment (with both SkyTEM systems) (see Section 6.5).

Timing was of the essence with regard to the delivery of data to Geoscience Australia with data from each flight supplied to Geoscience Australia within 48 hours of each successful survey flight. With two helicopter systems used for the majority of the survey, this placed high demands on staff of both the Contractor and Geoscience Australia to ensure that the supply of data was maintained and that no major errors were contained therein. Large airborne electromagnetic surveys such as this – with critical timing constraints – present a logistical challenge, both in field operations, and in subsequent data handling and processing. An excellent flow of communication between Geoscience Australia staff and Geoforce contractors (Figure 6-9) on survey logistics and the Qa/Qc of the dataset contributed to delivery of a high quality dataset ahead of schedule.

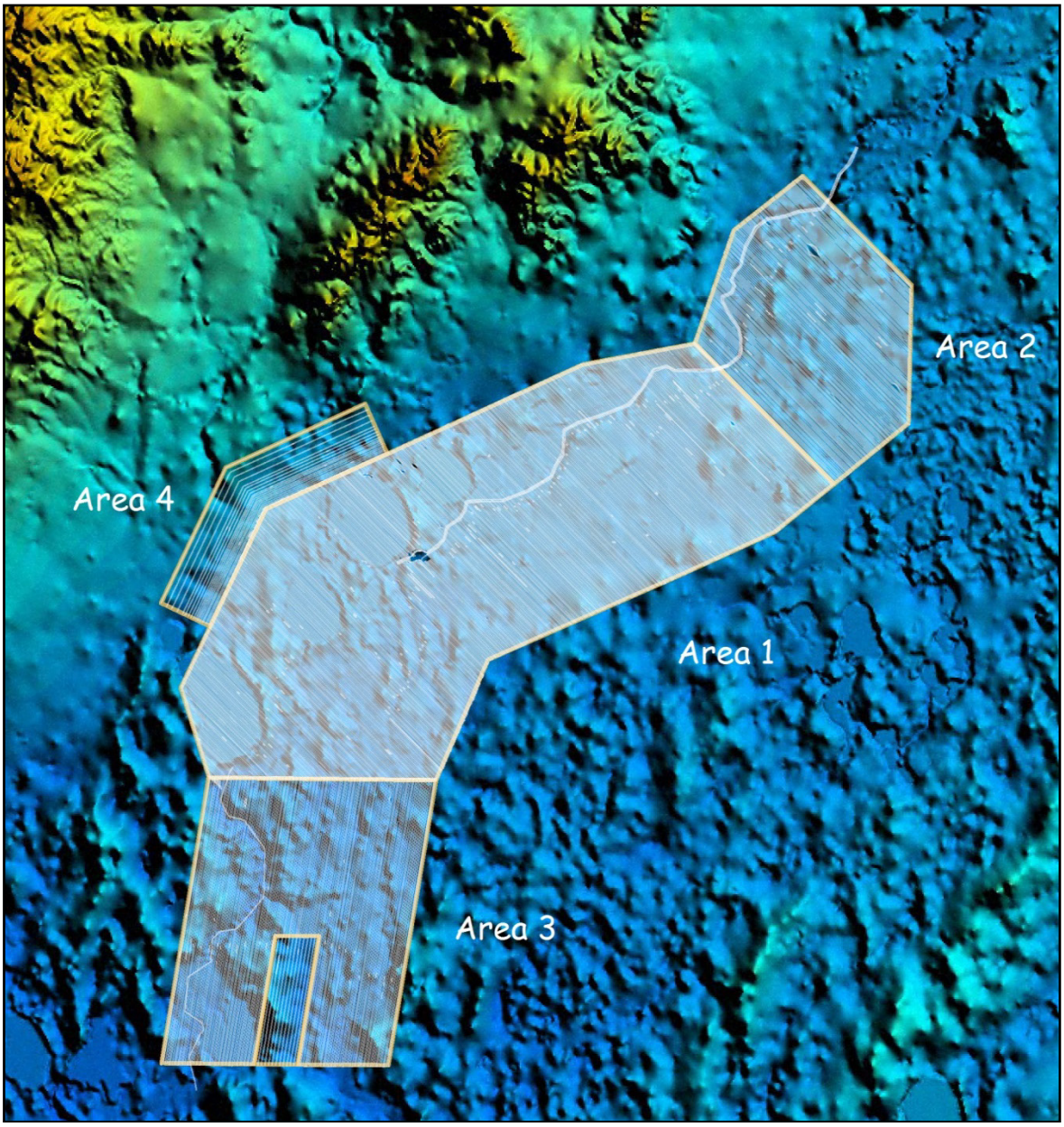



**Figure 6-8.** *Map showing main AEM survey blocks (1-4) and flight line orientations.*

**Table 6-5.** *Summary of SkyTEM survey logistics.*

| | |
|---|---|
| **Survey Company** | Geoforce Pty Ltd |
| **Dates Flown** | 28th June – 3rd September 2009 |
| **Client** | Geoscience Australia |
| **Terrain Clearance** | 30 metres (nominal) |
| **Datasets acquired** | Time-domain EM; Digital Terrain Model |
| **EM System** | SkyTEM (Interleaved Low and High Moment) |
| **Total Line km** | 32,659 km |
| **Helicopter types** | AS350B2, AS350 Super D2 |
| **Navigation** | DGPS |
| **Coordinate System** | MGA54 / GDA94 |



**Figure 6-9.** *SkyTEM field crew with members of the Geoscience Australia BHMAR team at Menindee.*

## 6.4 AEM SYSTEM RESOLUTION AND SENSITIVITY

### 6.4.1 Principle of the TEM Method

The majority of TEM systems consist of a transmitter (Tx) loop and a receiver (Rx) induction coil. The principle of operation is that a current is sent through the Tx loop, and after a while, the on-time, it is turned off very abruptly. While the Tx current is on, it establishes a magnetic field, the primary field, in the surrounding air and the ground, and when the Tx current is turned off, the changing magnetic field induces a current in the ground that moves in circular horizontal paths. Immediately after turnoff, the magnetic field from the currents in the ground, the secondary magnetic field, is equal to the primary magnetic field, but the current is weakened by the electrical resistivity of the ground and dies out. In the process of dissipating, the maximum of the current diffuses downwards and outwards to occupy an increasing volume of the subsurface. At early times, shortly after turnoff, the current will be concentrated in the near-surface part of the subsurface while for late times it will be spread out over a large depth interval. The diffusion is fast at the beginning and becomes slower with time, and the diffusion is slower for a well conducting ground and faster for a more resistive ground, the diffusion speed being proportional to $1/\sqrt{\sigma t}$, where t is the time after turnoff and $\sigma$ is the conductivity.

The changing magnetic field from the dissipating current system in the ground induces an electromotive force in the Rx coil which is measured by the receiver electronics of the TEM equipment as a function of delay time after turnoff. The voltage in the Rx coil can be sampled digitally or integrated over time windows, gates, distributed from early to late times. At early times, when the current is confined to the upper part of the subsurface, the measurements will reflect a weighted average of the conductivity of the near-surface, while at late times, when current has diffused further into the ground, the measurements will reflect an average over a larger depth range. In the inversion of TEM data, these overlapping averages are untangled to produce estimates of the subsurface conductivity as a function of depth.

### 6.4.2 Significance of Transmitter Moment and Turnoff Time

Ambient electromagnetic noise exists anywhere, partly arising from natural sources, e.g. lightning bolts, and partly from man-made sources, e.g. power grid, radio signals, etc. The measured signal in the Rx coil of a TEM system decreases very rapidly with delay time and from a certain delay time, the TEM signal will be of the same order of magnitude as the ambient noise. This is the latest time for which useful measurements can be done and it sets the limit for how far into the ground we can estimate the conductivity. The limit is determined by the ratio between the Tx moment (current times area times number of turns) and the effective

noise, so the larger the Tx moment, or the smaller the effective noise, the better the depth penetration of the system. To maximise the depth penetration it is thus desirable to have a large moment and/or an efficient measuring strategy that reduces the effective noise level.

There is however a drawback to a large Tx moment. The higher the moment, the slower the turnoff of the current, meaning that we can only achieve off-time measurement from a fairly late time and we lose early time measurements that carry information about the near-surface. There is thus an inevitable trade-off between surface resolution and depth penetration. Some TEM systems, like the SkyTEM system, solve this dichotomy by employing two interleaved Tx moments, a small moment where the current can be turned off quickly so that early-time measurements can be taken to give information about the near-surface; and a large moment that will give good depth penetration. The two moments are combined in the inversion of data for a conductivity model.

### 6.4.3 Resolution Limits

In the light of the above considerations, it is clear that the minimal thickness of a top layer that can be resolved by TEM measurements is determined partly by the earliest gate that can be measured and partly by the near-surface conductivity The depth penetration of a certain delay time, t, and subsurface conductivity, $\sigma$, is proportional to $\sqrt{t/\sigma}$, i.e. the shorter the turnoff time and the more conductive the subsurface, the better the resolution of the top layers. Likewise, the resolution at depth is determined by the latest usable gate that is not corrupted by noise.

### 6.4.4 Sensitivity Functions

The resolution of a TEM system can be illustrated by the sensitivity function. A TEM measurement expresses an average over a certain volume of the conductivity. However, not all parts of the subsurface contribute equally to this average. The function that describes the distribution of weights in the subsurface pertaining to a specific data is called a sensitivity function. For any delay time and measurement configuration, it will be a function of the position in three dimensions, and at any point it expresses how the data would change if the conductivity changed at that point.

Where the sensitivity is high, small changes in conductivity will give rise to considerable changes in the data and the conductivity at that point is consequently well determined - and vice versa. If the sensitivity function is concentrated within a small volume, the measured data will have good spatial resolution capabilities because it will express the conductivity in a limited volume - and vice versa. Sensitivity can be both positive and negative as will be clear from the following figures. That means that in the volumes of the subsurface where sensitivity is negative an increase in the conductivity will cause a decrease in the measured data.

In general terms, the spatial resolution of an AEM system varies with the system type; with sample time or frequency; and with ground conductivity (Spies & Woodgate 2005). It is different in the horizontal and vertical direction. Commonly, resolution is considered in terms of the volume of the ground that contributes most of the response for each measurement. The smallest lateral features that can be resolved near surface are around 30-60 m for helicopter systems where good conductivity contrasts are present. These figures increase with depth. Normally the highest resolution is measured along a flight line, with the perpendicular resolution being determined by line spacing. Wide line spacing (>200 m) will limit the definition of conductivity variations both at surface and at depth. These issues should be borne in mind when comparing models of ground conductivity or other products derived from the AEM data to information collected from bore data, or individual soil pits.

To illustrate the 3D sensitivity functions for the step response, Figure 6-10 shows vertical sections through the flight line and Figure 6-11 shows horizontal sections at the ground surface for delay times of 0.1, 1 and 10 ms for the vertical component of the TEM measurements with the SkyTEM system. Each plot has been

normalised with the maximum of the sensitivity function for that particular delay time. The contour lines indicate 80%, 60%, 40%, 20% and 0% contours. Red colours indicate positive sensitivity and blue colours indicate negative sensitivity. Looking at the vertical section through the 3D sensitivity function we see that it is rather simple with a small vertical cylinder of negative sensitivity surrounded by positive sensitivity with almost cylindrical symmetry. The circular character is clearly seen in the plane section. The sensitivity spreads over increasingly larger volumes for later delay times, but notice that the maximum is found at the surface at all times.

There are two types of 1D sensitivity functions. One of them is produced by integrating the 3D sensitivity function from minus infinity to infinity in the two directions of the horizontal plane. This is the vertical sensitivity function illustrating sensitivity as a function of depth. The other is produced by integrating the 3D sensitivity function in the direction perpendicular to the flight direction and from the surface to infinite depth. This is the horizontal sensitivity function illustrating sensitivity as a function of the flight line parameter. In Figure 6-12, vertical and horizontal 1D sensitivity functions for the step response vertical field component are shown for the delay times 0.01, 0.1, 1 and 10 ms for a homogeneous half-space of 5 ohmm (0.2 S/m); the curves are normalised with their maximum absolute value. If we, somewhat arbitrarily, define the depth extent and the horizontal extent to be where the sensitivity functions have decreased to a value of 0.1, we find the values shown in Table 6-6.

The sensitivity functions in Figure 6-10 to Figure 6-12 are derived for specific choices of delay times and half-space conductivity. All length are proportional to $\sqrt{t/\sigma}$, meaning that if the delay time increases with a certain factor or the conductivity decreases with a certain factor, the length scales will be larger by the square root of that factor.

The sensitivity functions shown in Figure 6-10 to Figure 6-12 are for a homogeneous half-space. For a layered earth model they can be different and one must be cautious in using the (to some extent arbitrarily defined) estimates of penetration depth and footprint discussed in the previous sections derived from a homogeneous half-space.

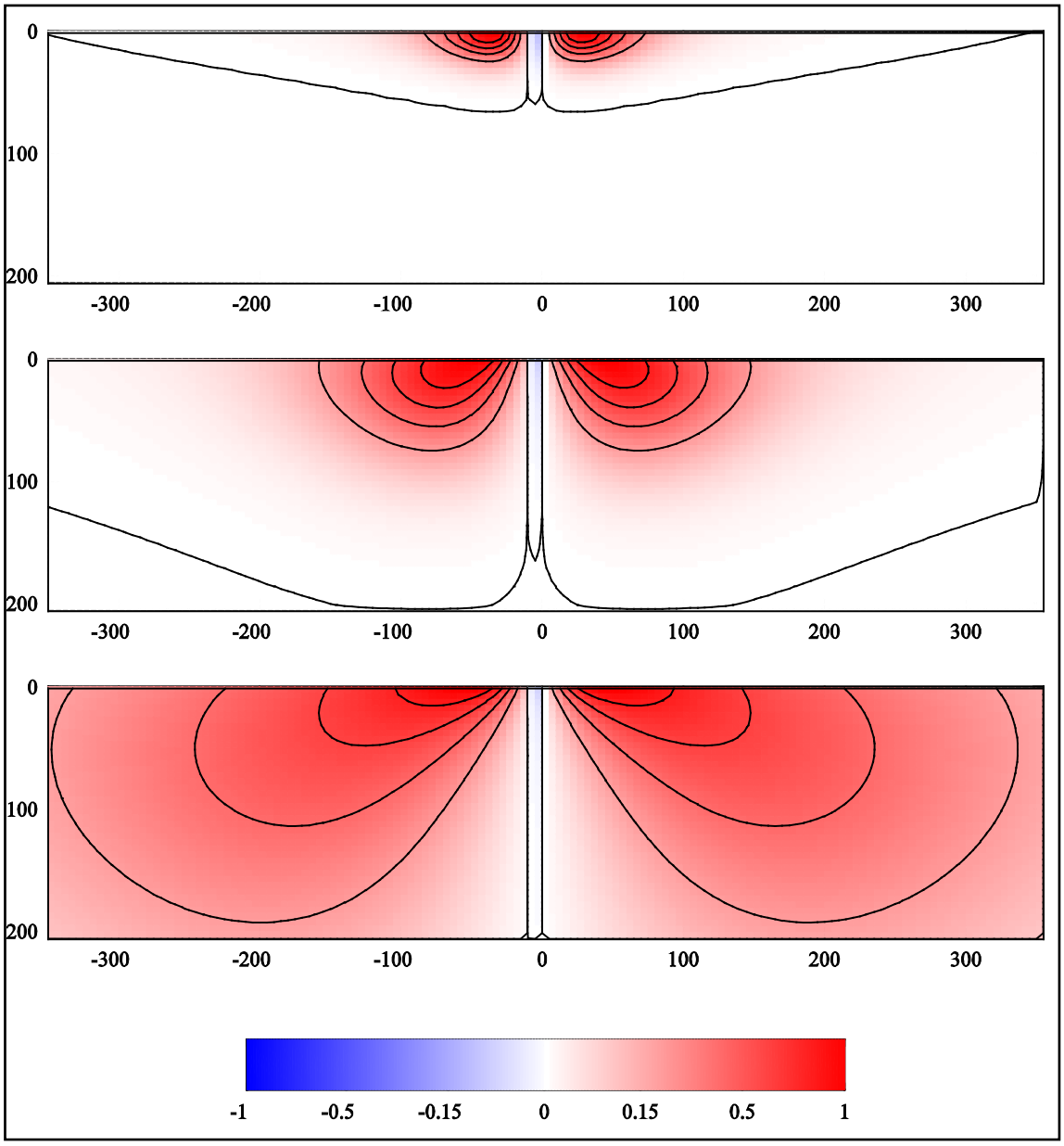



**Figure 6-10.** *Vertical section through the flight line for the normalised 3D step response sensitivity functions for the SkyTEM system at a nominal height of 35 m for a homogeneous half-space of 5 ohmm (0.2 S/m). The delay times for the top, middle and bottom plots are 0.1, 1 and 10 ms, respectively.*

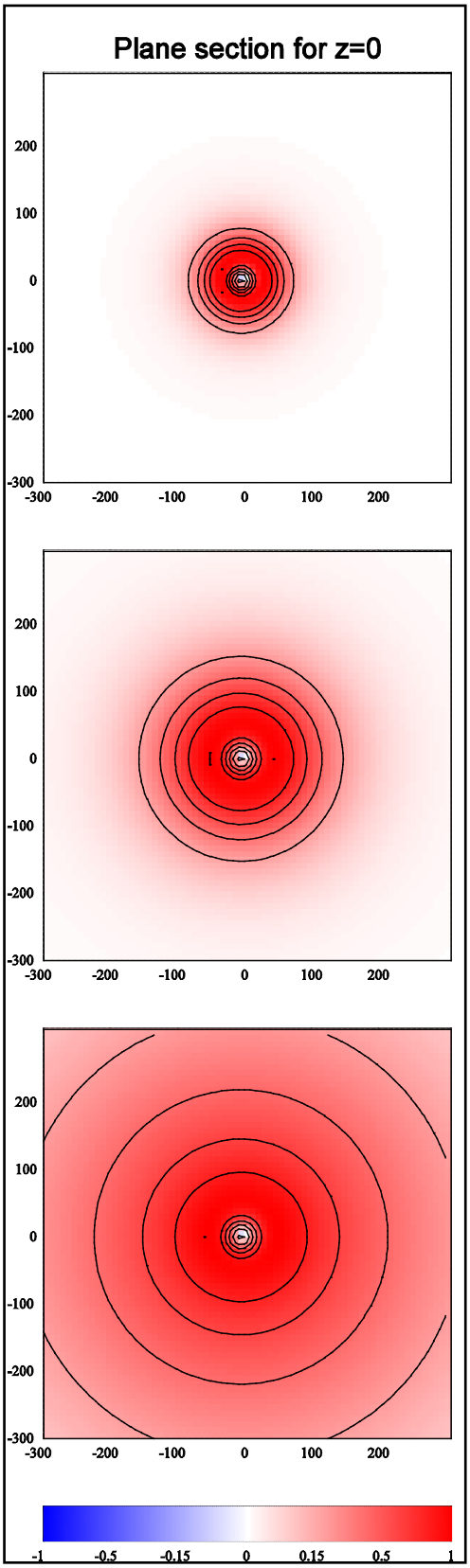



**Figure 6-11.** *Plane section (map view) looking at the surface through the normalised 3D step response sensitivity functions for the SkyTEM system at a nominal height of 35 m for a homogeneous half-space of 5 ohmm (0.2 S/m). The delay times for the top, middle and bottom plots are 0.1, 1 and 10 ms, respectively.*

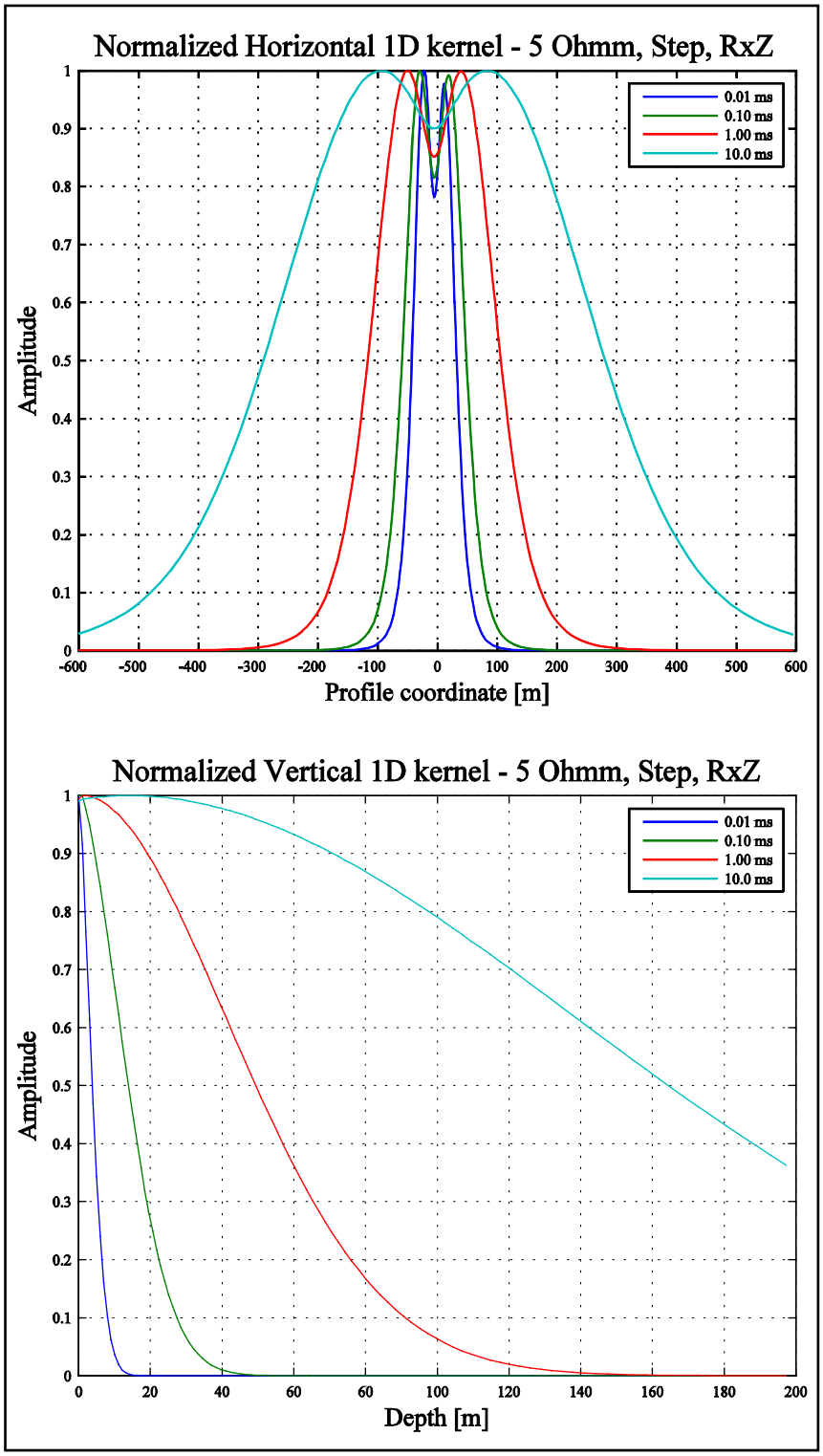



**Figure 6-12.** *Normalised 1D step response sensitivity functions for the SkyTEM system at a nominal height of 35 m for a homogeneous half-space of 5 ohmm.*

**Table 6-6.** *Depth extent and horizontal extent of the 1D step response sensitivity functions for the SkyTEM system at a nominal height of 35 m for a homogeneous half-space of 5 ohmm.*

| Delay time | Vertical extent (m) | Horizontal extent (m) |
|---|---|---|
| 10 µs | 8.5 | 110 |
| 100 µs | 27 | 160 |
| 1 ms | 92 | 346 |
| 10 ms | | 938 |

### 6.4.5 What Depths can be Mapped to with the SkyTEM System?

There are several proposed ways of estimating the depth of penetration of an AEM survey; done both before the survey is flown (in a forward modelling study) and when the AEM data is being inverted to conductivity models (e.g. Spies, 1989; Sattel, 2005). In our case, the depth of investigation for the inversion is an a posteriori estimation based on an analysis of the (Jacobian) sensitivity matrix that was used to calculate the conductivity models at each station (Christensen & Auken, 2012). The columns of the sensitivity matrix are summed and normalised to give an indication of how sensitive the model is to each parameter that enters the calculation. A threshold value is set for the cumulative sensitivity; and the depth at which the cumulative sensitivity drops to less than the threshold value is then determined. This depth is labelled the depth of investigation; and its physical meaning is that the model is no longer sensitive to the data (i.e. that the data is less able to drive the inversion to create a conductivity model that is a reliable reflection of the physical properties of the earth). A practical depth of exploration is not a magnitude that can be stated once and for all for a specific system. The various physical parameters of EM systems such as geometry; transmitter current and waveform, transmitter and receiver sensitivity; accuracy and noise levels, are surely determining qualities, but these must also be adapted to the expected geo-electrical properties of the surveyed ground. All factors come to play when inverting EM data to produce conductivity models, and the DOI is an estimation of how well the model is determined by the data. It is not a 'line of truth' and, in fact, usage of such a term should be avoided.

Forward modelling of the known geo-electric properties of the survey area suggested that the SkyTEM system should credibly resolve depths down to at least 120 m below the surface of the earth except in the more conductive portions of the study area (Lawrie *et al*., 2009c). Analysis of survey results suggests that it has been possible to resolve such depths in the more resistive areas, with shallower penetration (~50 m) in the much more conductive areas, particularly in the south of the area.

### 6.4.6 An Analysis of the Resolution Capability of the AEM Data to Map the Blanchetown Clay

#### 6.4.6.1 *Analysis approach*

In the evaluation of the suitability of the aquifers present in the BHMAR area for artificial recharge, one of the main points to consider is the presence of clays and their ability to establish impermeable boundaries to the aquifer. It is therefore important to analyse just how well the presence and lateral continuity of clay layers can be determined from inversion of AEM data. Often this type of analysis is carried out on a series of theoretical models that span the expected model space and the resolution of layer conductivity and thickness is determined for a large number of models. However, we have chosen a different approach by considering the actual conductivity models identified from the borehole logs of lithology and conductivity. In particular, we analyse how well the Blanchetown Clay layers can be resolved from the inversion of AEM data.

The analysis is carried out by setting up few-layer models with layer boundaries and layer conductivities identified from the logs. For the relevant models, forward responses are calculated for the SkyTEM system in a standard configuration using both the Low and High moments. Once the forward responses are calculated, noise is ascribed to the data using the same noise model as the one outlined in the section on the River Data, Based on the theoretical data, an inversion analysis is performed giving the relative uncertainty of the conductivity of the Blanchetown clay layer, its thickness and the depth to its top. The results are presented in Table 6-3 for all boreholes and Table 6-4 gives the statistics about the analysis.

#### 6.4.6.2 *Results of the analysis*

Out of a total of 78 boreholes from the Phase 2 and Phase 3 drilling campaigns, 16 boreholes were excluded because there was no Blanchetown Clay formation present. Of the remaining 62 boreholes a further 27 boreholes (44 %) were excluded because the conductivity estimates of the model layers resulted in identical conductivities for the Blanchetown Clay and a neighbouring layer, meaning that the Blanchetown Clay could not be resolved at all (see below). The remaining 35 borehole models were analysed as described above.

Boreholes lacking the Blanchetown Clay:

- Phase 2: 16, 28, 33-1, 34, 63
- Phase 3: 33-5, 33-6, 33-7, 33-8, 33-9, 77-3, 77-5, 84-2, 84-3, 84-4, 84-5

Boreholes where the Blanchetown Clay conductivity is identical to a neighbouring layer:

- Phase 2: 17, 18, 21, 22, 23, 35, 41, 57, 64, 71,
- Phase 3: 58-1, 75-7, 79A_2, 79A_5, 79A_6, 79A_10, 79A_12, 80A-2, 80A-6, 80A-7, 80B-2, 83-2. 88-2, 88-6, 88-7, 92-1, 99-1

The results of the analyses are summarised in Table 6-7 and given in detail in Table 6-8, where the relative uncertainties of the conductivity, the layer thickness and the depth to the top of the Blanchetown Clay formation are given. A standard deviation of 0-0.20 indicates a small uncertainty; a standard deviation of 0.20-0.50 indicates a medium uncertainty; a standard deviation of 0.50-1.00 indicates a high uncertainty; and a standard deviation above 1.00 indicates that the parameter is unresolved.

**Table 6-7.** *Distribution of relative uncertainty for the Blanchetown Clay models.*

```
StdDev of Resistivity
---------------------
StdDev 0.00 - 0.20:  5
StdDev 0.20 - 0.50:  6
StdDev 0.50 - 1.00:  5
StdDev 1.00 -     : 19

StdDev of Thickness
-------------------
StdDev 0.00 - 0.20:  2
StdDev 0.20 - 0.50:  1
StdDev 0.50 - 1.00:  4
StdDev 1.00 -     : 28

StdDev of Depth of burial
-------------------------
StdDev 0.00 - 0.20:  5
StdDev 0.20 - 0.50: 10
StdDev 0.50 - 1.00:  7
StdDev 1.00 -     : 13
```

An immediate inspection of Table 6-7 reveals that the model parameters are well determined only for a small fraction of the models. However, it must be remembered that the above analysis indicates how well the parameters are resolved, given the one data set of the particular model. While the analysis of the model parameters is carried out with few-layer models, we also wished to see the result of an inversion with the multi-layer model that was used in the inversion of the entire BHMAR data set. The result of this exercise is seen in Figure 6-13. Though the Blanchetown clay layers come out as poorly resolved in the few-layer analysis, their presence is nevertheless indicated in the multi-layer inversions in Figure 6-13.

To illustrate the first of the above points, the forward modelled theoretical data from the Blanchetown Clay models are inverted with the same 30-layer multi-layer model and the same vertical regularisation that was used in the inversion of the entire BHMAR data set. The noise level is the same as the one used in the analysis. The results are seen in Figure 6-13 where the 35 borehole models that were analysed are plotted with the Blanchetown Clay layer indicated together with the multi-layer inversion models. It is quite clear that most often the Blanchetown Clay formation can be discerned in the multi-layer inversion, especially clearly where the Blanchetown Clay layer is conductive. Naturally, in the situation where the conductivity contrast between the Blanchetown Clay layer and neighbouring layers is small, it is difficult to see the Blanchetown Clay layer. This has been resolved to a certain extent by field validation, expert analysis, and the use of borehole constraints in the final inversions.

**Table 6-8.** *Borehole models and analysis.*

| Borehole ID | Formation sequence | Cond | StdDev | Thk | StdDev | Depth | StdDev |
|---|---|---|---|---|---|---|---|
| 01A-1 | Wo / Wi / B / Ca / R | 800 | 7.16 | 9 | **** | 27 | 3.50 |
| 01B-1 | L / Wi / B / Ca / R | 800 | 1.14 | 25 | **** | 28 | 2.53 |
| 03B-1 | M / B / Ca / R | 700 | 0.57 | 17 | 3.12 | 17 | 0.57 |
| 04-1 | M / B / Ca / R | 300 | 2.74 | 7 | 5.90 | 13 | 0.59 |
| 05 | Wo / B / Ca / R | 900 | 0.05 | 11 | 0.13 | 3 | 0.20 |
| 06 | Wo / Wi / B / Ca / R | 500 | 0.42 | 17 | 3.36 | 15 | 0.51 |
| 14 | M / Wi / B / Ca / R | 300 | **** | 9 | **** | 24 | **** |
| 15 | M / B / Ca / R | 800 | 0.15 | 14 | 0.58 | 12 | 0.11 |
| 19 | Wo / Wi / B / Ca / R | 900 | 6.67 | 5 | **** | 20 | 1.32 |
| 29 | Wo / B / Ca / LP / R | 600 | 0.28 | 7 | 0.65 | 3 | 1.00 |
| 30 | Wo / B / Ca / Ca / R | 900 | 7.33 | 3 | **** | 12 | 2.36 |
| 31 | Wo / B / LP U / LP L / R | 500 | 1.79 | 5 | 4.13 | 3 | 4.89 |
| 36 | Wo / Wi / B / Ca / R | 900 | 0.18 | 18 | 0.55 | 19 | 0.17 |
| 43 | M / B / Ca U / Ca L / R | 800 | 0.24 | 13 | 2.26 | 13 | 0.09 |
| 48 | Wo / M / B / Ca / R | 700 | 0.67 | 10 | 3.86 | 13 | 1.97 |
| 51 | Wo / B / Ca U / Ca L / R | 200 | 2.94 | 9 | **** | 3 | **** |
| 53 | Wo / Wi / B / Ca U / Ca L / R | 700 | 5.37 | 8 | **** | 13 | 7.70 |
| 56 | M / B / Ca / R | 700 | 0.33 | 15 | 6.20 | 14 | 0.76 |
| 61 | M / B / Ca / R | 200 | **** | 5 | **** | 23 | 2.82 |
| 62 | Wo / Wi / B / Ca U / Ca L / R | 300 | **** | 14 | **** | 27 | 5.89 |
| 65 | M / B / Ca / R | 900 | 0.39 | 10 | 1.14 | 13 | 0.24 |
| 66 | Wo / M / B / Ca / R | 800 | 0.26 | 14 | 0.88 | 15 | 0.23 |
| 74 | M / B / Ca / R | 1500 | 0.07 | 11 | 0.16 | 11 | 0.03 |
| 08-1 | M / B / Ca U / Ca L / R | 900 | 0.87 | 9 | **** | 10 | 0.45 |
| 75-1 | M / B / Ca / ? | 400 | 2.86 | 6 | 3.14 | 12 | 0.78 |
| 75-2 | M / B / Ca / ? | 400 | 7.55 | 6 | **** | 12 | 2.35 |
| 75-3 | M / B / Ca / R | 400 | 1.50 | 8 | 5.01 | 12 | 0.39 |
| 75-4 | M / B / Ca / R | 400 | 1.20 | 8 | 3.38 | 12 | 0.34 |
| 75-5 | M / B / Ca / R | 400 | 0.88 | 9 | 3.22 | 11 | 0.38 |
| 75-6 | M / B / Ca / R | 400 | 1.16 | 9 | 4.67 | 11 | 0.24 |
| 75-8 | M / B / Ca / R | 400 | 1.62 | 8 | 5.48 | 12 | 0.34 |
| 77-2 | M / B / Ca / R | 200 | 2.11 | 8 | 3.35 | 12 | 0.38 |
| 88-3 | M / B / Ca / R | 300 | 0.19 | 17 | 0.36 | 11 | 0.34 |
| 88-4 | M / B / Ca / R | 300 | 0.89 | 9 | 1.77 | 12 | 0.80 |
| 88-5 | M / B / Ca / ? | 300 | 2.22 | 6 | 5.02 | 10 | 0.79 |

Co: Coonambidgal
Wo: Woorenin
M: Menindee
Wi: Willotia
B: Blanchetown
Ca: Calivil
LP: Loxton-Parilla
R: Renmark

(U = upper, M = Middle, L = lower)

Cond: Conductivity in [mS/m]
Thk: Thickness in [m]
Depth: Depth to top of Blanchetown Clay layer in [m]
StdDev: Relative uncertainty of the parameter
****: The parameter uncertainty is infinite

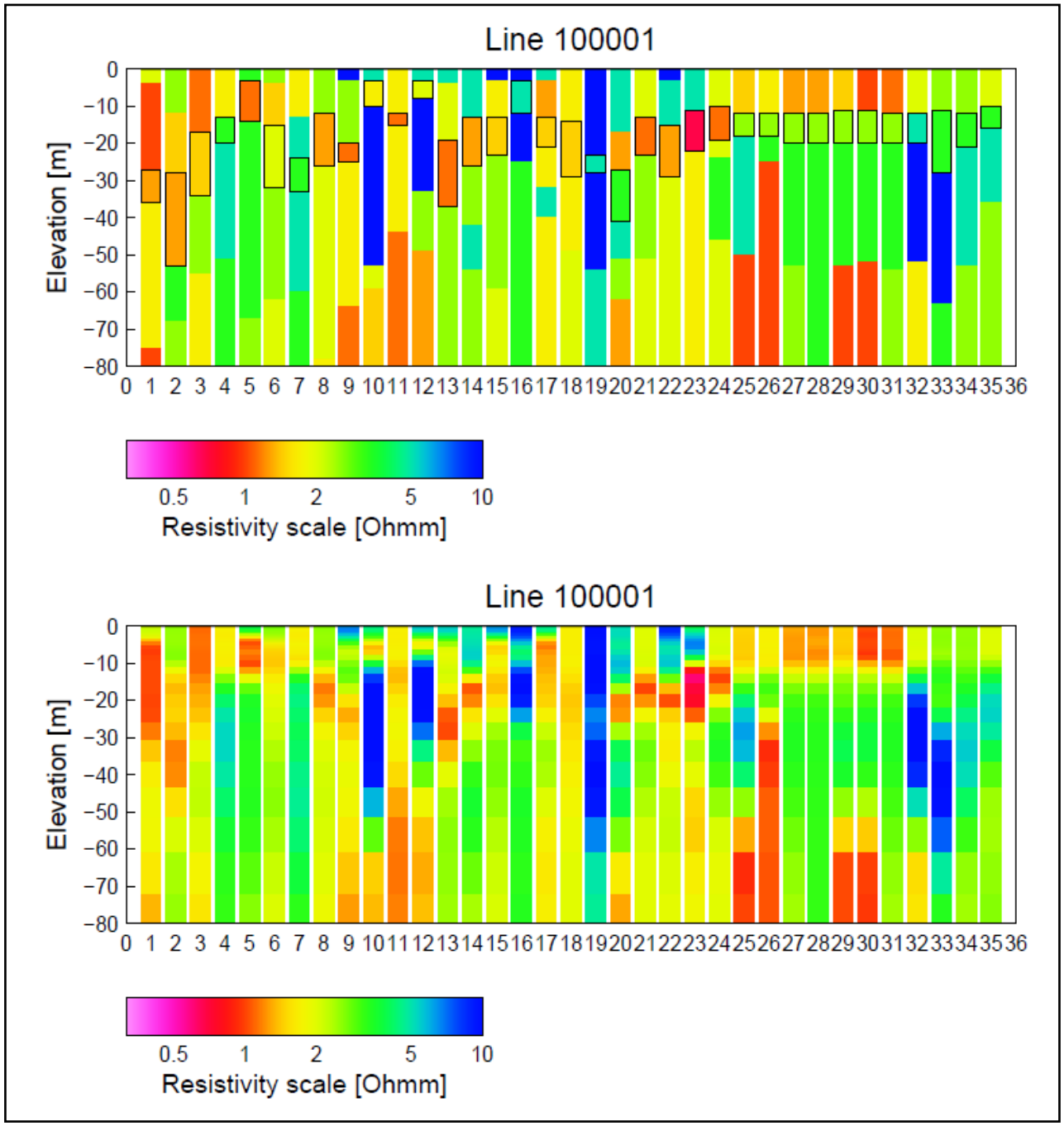



**Figure 6-13.** *Plots of the analysed Blanchetown Clay models. Top: the Blanchetown Clay models as determined from the borehole logs with the Blanchetown Clay layer indicated with a black rectangle; bottom: multi-layer model inversion of the theoretical data from the Blanchetown Clay models.*

## 6.5 SKYTEM SYSTEM CALIBRATION

### 6.5.1 Establishing a Reference Model

Data acquired for the BHMAR survey involved the use of two separate SkyTEM helicopter airborne electromagnetic (AEM) systems (SK1 and SK2) collecting data simultaneously. Initially, data processing and iTEM inversions were carried out separately for each system. Subsequently and prior to carrying out full inversions of the data, an additional calibration of the two SkyTEM systems was carried out in order to ensure data consistency between the two systems. The main objective of the calibration was to determine the optimum time shift and factor shift for the High and Low Moment datasets (Foged & Sorensen, 2010).

To accomplish this, we followed a Danish standard procedure of using a hover test site to calibrate the AEM data. Denmark has established a national EM test-site at Lyngby. This site is recognised as a well-described five-layer earth structure and is used to calibrate any EM equipment used in the Danish National Groundwater Mapping campaign. Any airborne instrument used in the campaign must be able to reproduce the established conductivity model at the calibration site within 5%.

With the aim of setting up a reference site to be used in the BHMAR project, ground-based TEM (WalkTEM) measurements were carried out on the hover spot with an instrument calibrated at the Lyngby (Denmark) test site. The calibration site was located close to Borehole 19 and is called B19 in the following text. Based on the ground calibration measurements we produced a layered earth model that was then defined as the reference model for all subsequent calibration measurements. The SK1 and SK2 systems performed reproducibility tests at the calibration site and were calibrated through an amplitude scaling and a time shift so that conductivity maps and other derived products from the AEM data will connect seamlessly. This was done at the beginning of the survey and not repeated. The contractor assured Geoscience Australia that the SkyTEM system was stable enough that one thorough calibration would suffice.

Nine ground based soundings laid out in a cross with 40 m between adjacent positions were made with a 40 x 40 m transmitter (Tx) loop in a central loop configuration (Figure 6-14). Long stacking times were used to ensure the best possible data quality. The cross shaped layout was chosen to make it possible to detect if large lateral variation in the conductivity structure was present at the site. Apparently, there was no serious lateral variability was detected. We inverted the ground based sounding model using the known system transfer function and fitted the data with a layered model to produce a reference conductivity model.

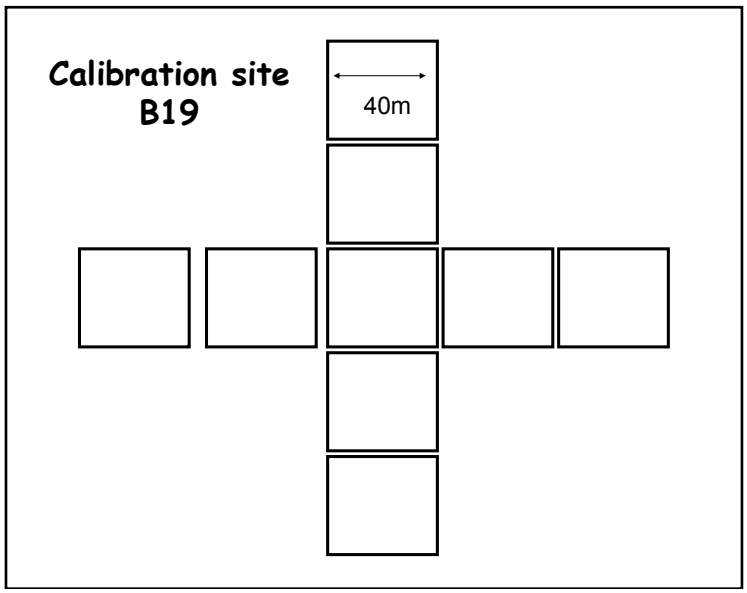



**Figure 6-14.** *Plan view showing layout of ground TEM loops centres around borehole BHMAR19-1.*

### 6.5.2 Airborne Hover Test

The following calibration procedures have been applied:

- Data from the Walk TEM system from the hovering site were processed and inverted to a resistivity model.
- Forward responses from the resistivity model using the SkyTEM transform function were calculated for the different hovering altitudes.

– The forward and the measured SkyTEM responses were compared for each altitude. Common time and factor shifts for the different hovering altitudes were determined based on a minimum difference between the forward response and the calibrated SkyTEM response.

Both AEM systems hovered at the B19 test site at the central position of the cross at four different altitudes: 10, 15, 20 and 30 m, between 2 and 4 minutes at each height to ensure long stacking times and good data quality (Figure 6-15). Days with low wind where selected to performed the hover tests.

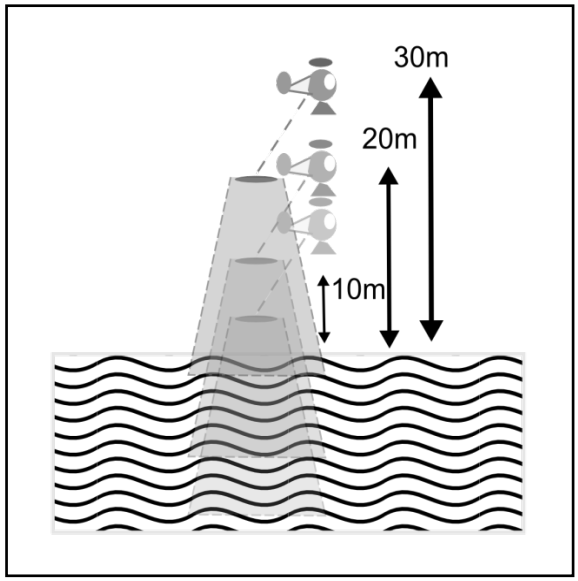



**Figure 6-15.** *Diagrammatic representation of hover test configurations, showing shifts in altitude.*

A relatively large spread of the time shift parameters for each hovering altitude was observed. This might indicate that there was more geological variability at the calibration site than what was apparent in the ground TEM soundings. We have no immediate explanation for this discrepancy. Given that the footprint of the WalkTEM and the SkyTEM systems are most alike at lower altitudes it was decided to use the time shift parameters derived for the hovering altitude of 20 m. Figure 6-16 and Figure 6-17 show the forward data from the ground based resistivity model and from the calibrated SkyTEM system (Foged & Sorensen, 2010).

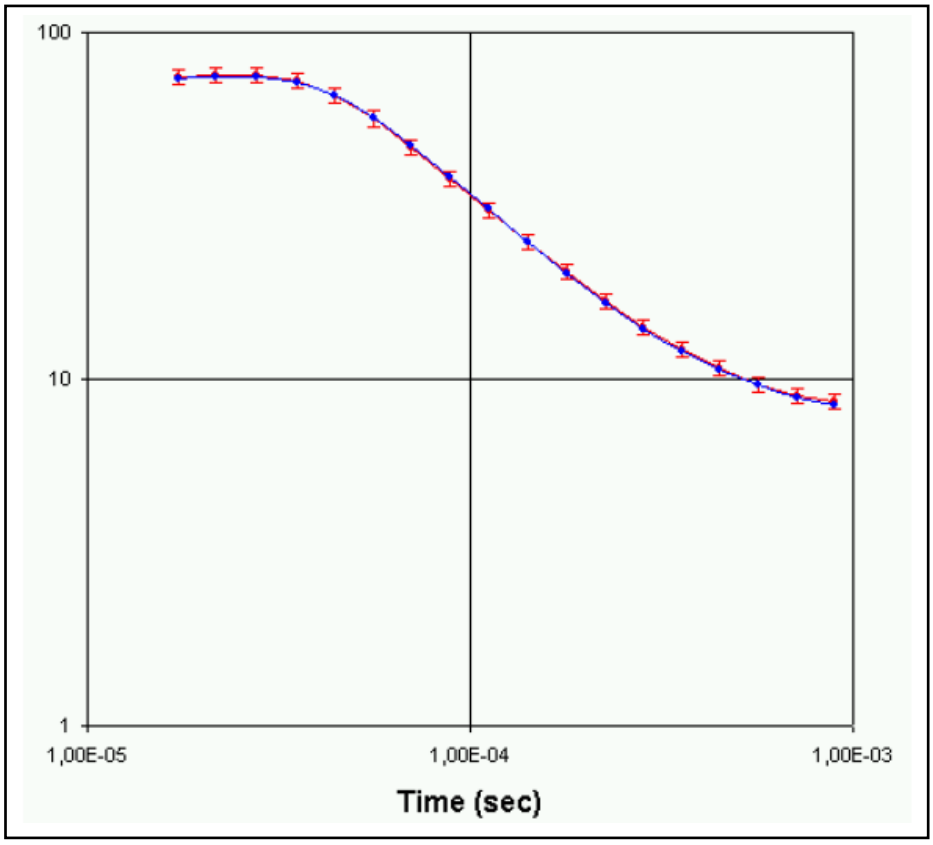



**Figure 6-16.** *Low moment data (rho-a), Forward data (blue) and SkyTEM data (red) after calibration at 19 m above the ground surface.*

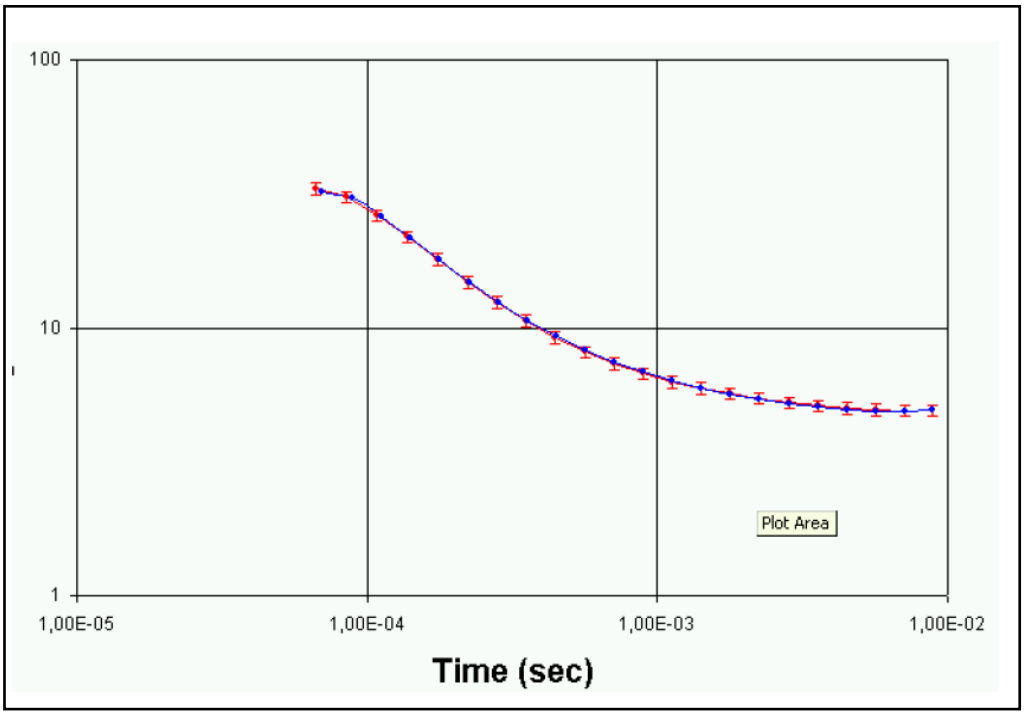



**Figure 6-17.** *High Moment data (rho-a), Forward data (blue) and SkyTEM data (red) after calibration at 19m above the ground surface.*

#### 6.5.2.1 *Re-roping*

The frames of the helicopters need to be in a horizontal position during the calibration measurements to ensure that the vertical magnetic field was measured. The suspension of the frame therefore had to be changed from that of production flight. A few degrees of inclination of the frame is not of great concern because they will be accurately recorded by the inclinometers be accounted for in the subsequent processing, but the more it inclines, the more crosstalk there is between the vertical and the horizontal field.

After the hover test, two perpendicular lines were flown twice in the directions of the cross; the first time at normal production altitude, speed and roping, and the second time at a higher altitude. These short repeat lines were also used to check for lateral conductivity variations.

#### 6.5.2.2 *Hover data processing*

Using the proper system transfer function for the SkyTEM system, the response at each hovering altitude is calculated for the reference conductivity model for both the low and high moment of the data. The measured data are then compared with the response of the reference model. If data differ more than 5% from the reference response, a time shift and an amplitude calibration factor are determined. Experience from other surveys indicates expected time shifts around 0.5-1 microseconds and amplitude factors of 1.05-1.10. The calibration parameters for the two SkyTEM systems were determined to be:

- SK1 Low Moment: Time shift -1 μs and a factor shift of 0.94
- SK1 High Moment: Time shift -4.5 μs and a factor shift of 0.98
- SK2 Low Moment: Time shift -0.6 μs and a factor shift of 0.93
- SK2 High Moment: Time shift -3.0 μs and a factor shift of 0.94

All calibration parameters are in the normal range.

### 6.5.3 SKYTEM Technical Specifications and Data Processing and Inversion

#### 6.5.3.1 *SkyTEM technical specifications*

In order to properly process, reprocess, invert, re-invert and transform raw AEM data to models of conductivity as a function of depth and produce quantitative results, precise knowledge of the instruments transfer function, i.e. the technical characteristics of the system response and electronics is needed. Though it can sometimes be difficult/impossible to get this information from AEM contractors, the SkyTEM system parameters are always fully specified by the contractor; they are seen in Table 6-9 and Table 6-10.

Detailed tables of receiver window start and end times, filters and other specifics from contractor's reports (Reid *et al*., 2009), were incorporated in an earlier report (Lawrie *et al*., 2009b), and are not reported here.

#### 6.5.3.2 *Receiver system gate issues in BHMAR AEM survey*

Two issues were picked up at a late stage in the Qa/Qc of the BHMAR survey. Both issues were significant for data quality and integrity, and resulted in re-processing of the dataset prior to carrying out full inversions of the data at Aarhus University between 22$^{nd}$ January and 12$^{th}$ February 2010. The issues are explained below.

**Table 6-9.** *System transmitter specifications.*

| **EM Transmitter – High Moment** | |
|---|---|
| Transmitter loop area | 314 $m^2$ |
| Number of transmitter loop turns | 4 |
| Peak current (nominal) | 100.0 A |
| Peak moment | 125,600 |
| | A.turn.$m^2$ |
| Tx loop height (nominal) | 30 m |
| **Tx Waveform – High Moment** | |
| Base frequency | 25 Hz |
| Tx duty cycle | 50% |
| Tx waveform | Bipolar |
| Tx on-time | 10 ms |
| Tx off time | 10 ms |
| Average Tx ramp time | 46.39 s (SK1) |
| | 49.03 s (SK2) |
| **EM Transmitter – Low Moment** | |
| Transmitter loop area | 314 $m^2$ |
| Number of transmitter loop turns | 1 |
| Peak current (nominal) | 42 A |
| Peak moment | 13,188 A.turn.$m^2$ |
| Tx loop height (nominal) | 30 m |
| **Tx Waveform – Low Moment** | |
| Base frequency | 222.22 Hz |
| Tx duty cycle | 44.4% |
| Tx waveform | Bipolar |
| Tx on-time | 1 ms |
| Tx off time | 1.25 ms |
| Average Tx ramp time | 9.26 s (SK1) |
| | 9.29 s (SK2) |

**Table 6-10.** *System receiver specifications.*

| **EM Receiver** | |
|---|---|
| EM Sensors | dB/dt coils |
| Rx coil effective area (Z and X) | 31.4 $m^2$ |
| Low pass cut-off frequency for Rx coils | 450 kHz |
| Low pass cut-off frequency for Rx electronics | 300 kHz |
| Front gate (High Moment) | 60 s |
| Front gate (Low Moment) | 10 s |
| **Z-component Rx coil position** | |
| Behind Tx loop centre | 12.62 m |
| Above plane of Tx loop | 2.16 m |
| **X-component Rx coil position** | |
| Behind Tx loop centre | 13.88 m |
| Above plane of Tx loop | 0 m |

Front gates for Low and High Moment measurements were set at 10 microseconds and 60 microseconds, respectively. The effect of the front gate is to exclude any EM signal entering the amplifiers before the front gate has opened. Any gate with a gate-open time earlier than the front gate will be corrupted. The uncertainty of the front gate timing is of the order of 2.5 microseconds (pers. comm., Kurt Sorensen 2009) and the front gate values chosen by Geoforce did not allow for this, being set too close to the gate-open time of the first gate. Analysis by Geoscience Australia and Aarhus University determined that the first usable time gate for

the Low Moment is gate 5 (~18 μs, gate centre time), and the first usable gate for the High Moment is gate 12 (~90 μs, gate centre time), and not 4 and 11 and reported by the contractor. This would not have been discovered without having a calibration site and a reference model for quality control. The implications of processing data using these two gates are shown in Figure 6-18. From the bottom panel in Figure 6-18 it is clear that, as expected, the shallow structures are the ones most affected by the faulty gates.

Analysis of the issue by Geoscience Australia and Aarhus University found that the issue was significant enough to warrant re-processing of the whole dataset. In particular, the early time, near-surface (0-4 m) data was affected. The initial gates were removed from the final data set. Re-processing of the dataset has improved the inversion models for the near surface, although some loss of thin layer resolution in the shallow sub-surface has occurred due to the error by the contractor.

Another issue detected, and reported by Geoforce was that part of the data from area 2 (northern survey area block) has a bias signal problem. The report by Geoforce (Reid *et al*., 2009), specifies that this was due to a problem with two components in the receiver system. As these were replaced on 12th July data collected prior to that date are affected by the bias signal problem (channel 29-32 of the High Moment). Data were re-inverted using channel 12-32 but the late time issue became very pronounced in the inversion results. We then excluded gate 29-32 from the inversions and assigned 10% extra noise to gate 28. The problem affected the deeper parts of the models, while early time data appear unaffected. In Figure 6-19 are plots of the resistivity of layer 14 (77 m to 92 m depth) from the 19 layer inversion.

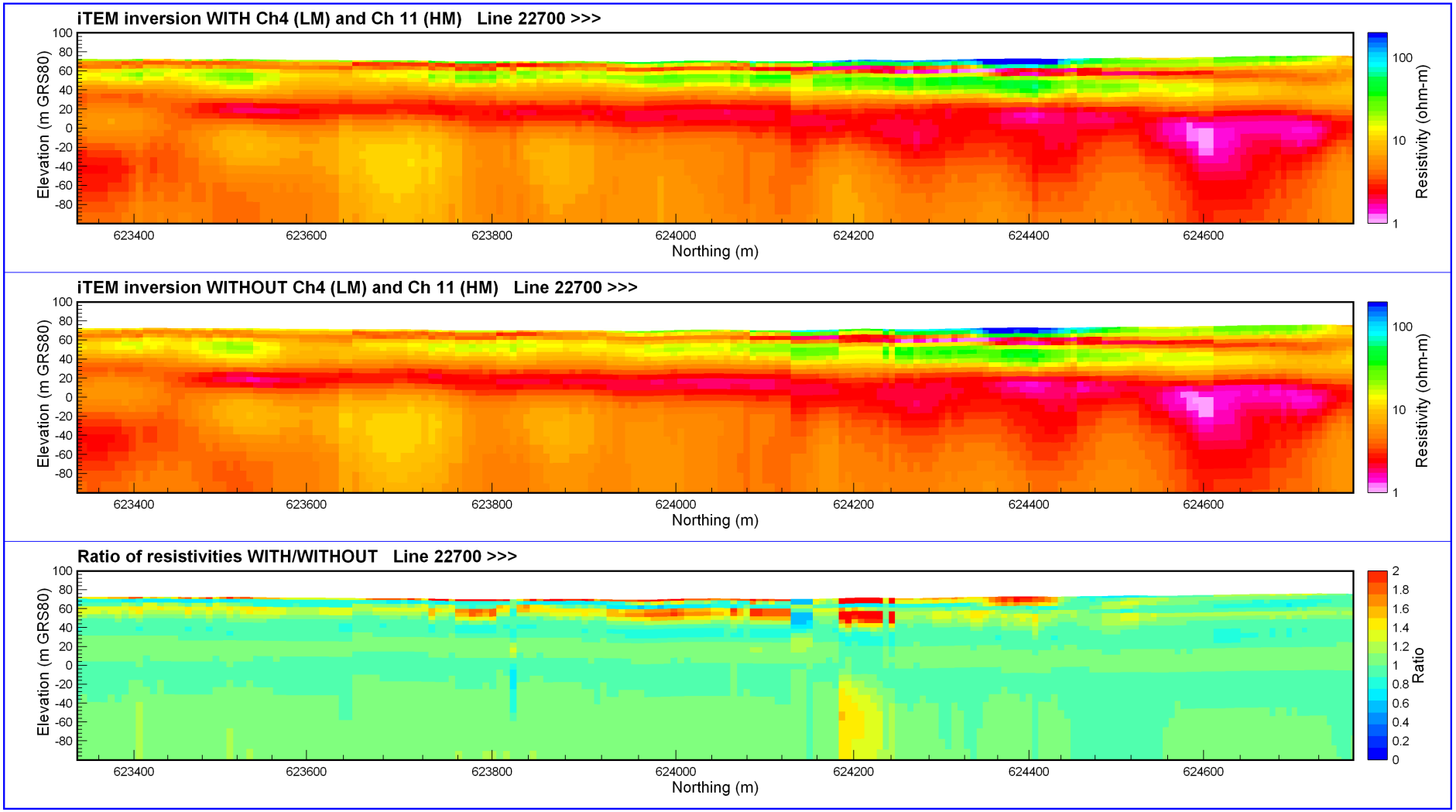



**Figure 6-18.** *iTEM results of processing raw data with and without channels 4 and 11.This is illustrative of the effect of the erroneous frontgate. Top: Inversion with channels 4 (Low Moment) and 11 (High Moment), i.e. as delivered with the Geoforce final report (Reid, 2010). Middle: Without Channels 4 (LM) and 11 (HM). Bottom: Ratio of layer resistivities with/without (i.e. A/B).*

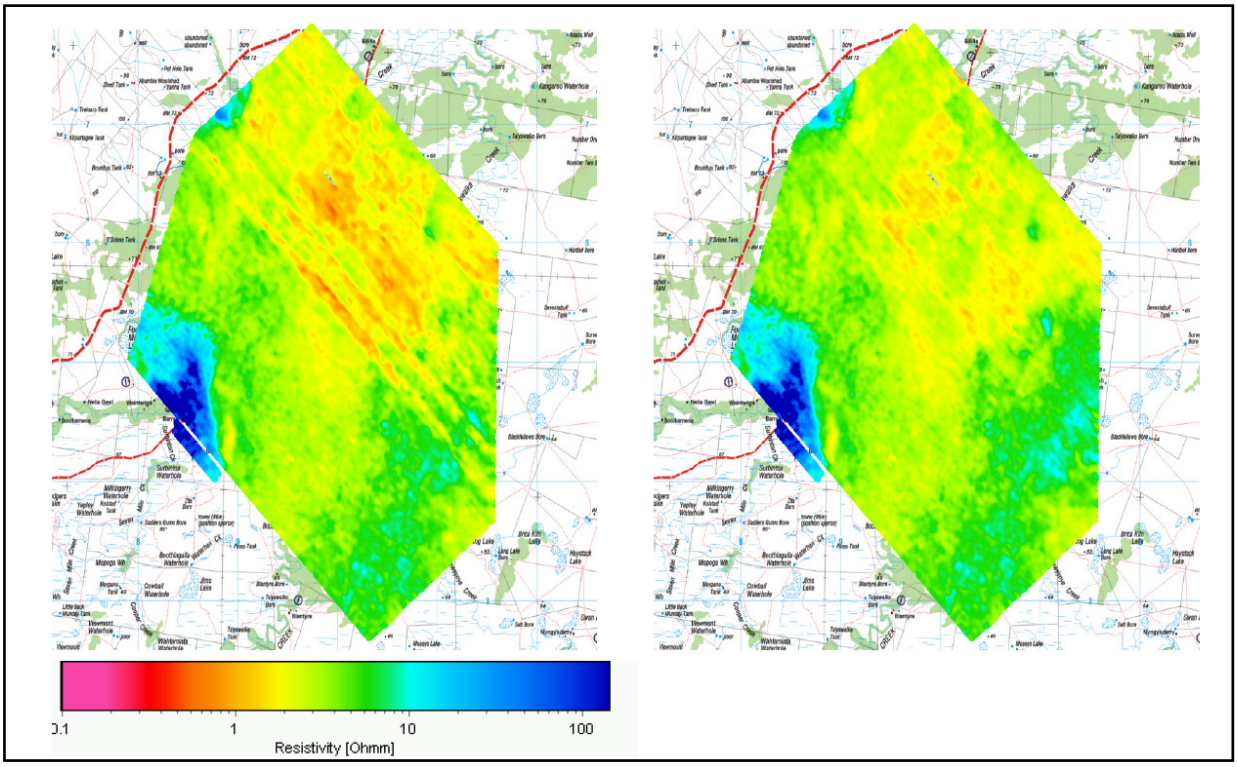



**Figure 6-19.** *Inversion of north section of area 2, with (left) and without (right) bias response on the late time channels.*

### 6.5.4 Processing of River Flight Lines

Three parallel flight lines were acquired flying along the Darling River in order to more directly map surface-groundwater interactions. These lines were centred on the river with two adjacent lines to the left and right with a line spacing of 200 m. In the southernmost part of the BHMAR area (Area 3) the three lines span 60 km of the river. In the southern part of Area1, there are no river flight lines, but from Menindee and toward the NE, traversing Area 1 and Area 2, an additional 120 km of flight lines were flown.
The River Data were not processed as part of the initial processing and inversion carried out by the HydroGeophysics Group at Aarhus University. Data were therefore retrieved from the contractor, GroundProbe (formerly GeoForce) as XYZ oriented ASCII data files with a series of Tx waveform files, one for each of the flight campaigns. An elementary data processing was carried out consisting of identifying the noise level of the two Tx moments and deleting data that were obviously inconsistent with the assumption of a 1D earth or otherwise of no value. The noise model is given by Equation 1:

$$V_{noi} = V_0 \cdot \left( \frac{t}{1\text{ms}} \right)^{-}$$

**Equation 1**

with $V_0 = 2.5\text{x}10^{-12}$ V/Am$^4$ for the Low Moment and $V_0 = 2.5\text{x}10^{-13}$ V/Am$^4$, for the High Moment data, all data scaled with Tx current and both Tx and Rx area. The total relative data uncertainty is then given in Equation 2 as:

$$\Delta d_{rel} = \sqrt{\varepsilon^2 + \left(V_{noi}/V\right)^2}$$

**Equation 2**

for a data value of $V$. The basic relative noise level is set to $\varepsilon = 0.03$.

Data are discarded if they fulfil one of more of the following criteria:

- They are negative.
- They are 10 times smaller than the noise level.
- They produce a positive slope at early times.
- They produce a positive slope at late times.
- The angle between the vectors $\rightarrow P_1P_2$ and $\rightarrow P_2P_3$ for three consecutive points - P1, P2, and P3 - is larger than 90 degrees.
- The slope of the dB/dt data in a log-log plot is smaller than -6 or greater than 2 for two consecutive data points.

After this simple data processing, data are inverted in the same way as all the other data. In the Lateral Parameter Correlation LPC procedure (see Section 6.7.3.11), the River Data are correlated with one another and with the borehole models, but not with models from the other flight lines to avoid inconsistencies due to the fact that the calibration is slightly different for the two data sets. There are a few boreholes in the vicinity of the River Data flight lines, most of them being at least 300 m from a line except for the borehole at (E, N) $\approx$(672000, 6442000) which is situated about 100 m from a flight line. It is therefore anticipated that, the borehole conductivity logs will have no influence on the River Data models, except for the one mentioned above.

## 6.6 BHMAR AEM INVERSIONS

AEM data acquired for exploration or environmental applications are commonly modelled using algorithms such as conductivity depth transform (CDT) or Layered Earth Inversion (LEI) that assume a 1D earth (Sattel, 2005). To date, full 2.5 or 3D inversion of AEM data remains limited, and in many respects unrealistic. For hydrogeological investigations in many Australian basins where the assumption that the subsurface can be represented as a series of horizontal layers holds reasonably well (particularly at the scale of the footprint of most AEM systems), 2.5D or 3D is unnecessary (Sattel, 1998; Lane *et al*., 2000). The 1D model assumption is also legitimate in sub-horizontal, layered sedimentary areas where it produces results that are only slightly distorted by 2D or 3D effects such as might be induced by faults, fractures, or other geological phenomena (Auken *et al*., 2005; Newman *et al*., 1986). Various approximations and transforms are available and fully explained in the literature (e.g. Macnae *et al*., 1998; Christensen, 2002; Sattel, 2005). A schematic representation of the data processing and inversion process is seen in Figure 6-20.

The main presentation products of the AEM data in the BHMAR reports (Lawrie *et al*., 2012 a-e) are the model sections (conductivity-depth sections) and the contoured maps of mean conductivity in depth and elevation intervals (depth-slices). The model sections show a quasi-2D model of the conductivity as a function of depth along the flight lines by concatenating the models found from 1D inversion of each data set. Based on inverted models from the whole survey area, the mean conductivity in depth and elevation intervals can be calculated and shows as colour contoured maps that illustrate the conductivity regime in a certain depth interval. The complete set of these maps makes it possible to acquire a sense of the 3D distribution of conductivity.

In the conductivity depth sections and maps, a linear conductivity scale is used more often in these reports (in preference to a logarithmic scale), as they enable the interpreter to pick out more detail at the lower conductivity end of the scale, where small changes in conductivity have importance for groundwater salinity and recharge mapping and assessment.

Elevation based maps were also used to analyse particular features at depth where the influence of near-surface topography was a complicating factor.

A thorough exposition of the data transformation used in the BHMAR project is given elsewhere (Reid *et al*., 2009; Foged & Sorensen, 2010). Through the BHMAR project period, several inversion products have been produced and used for specific purposes.

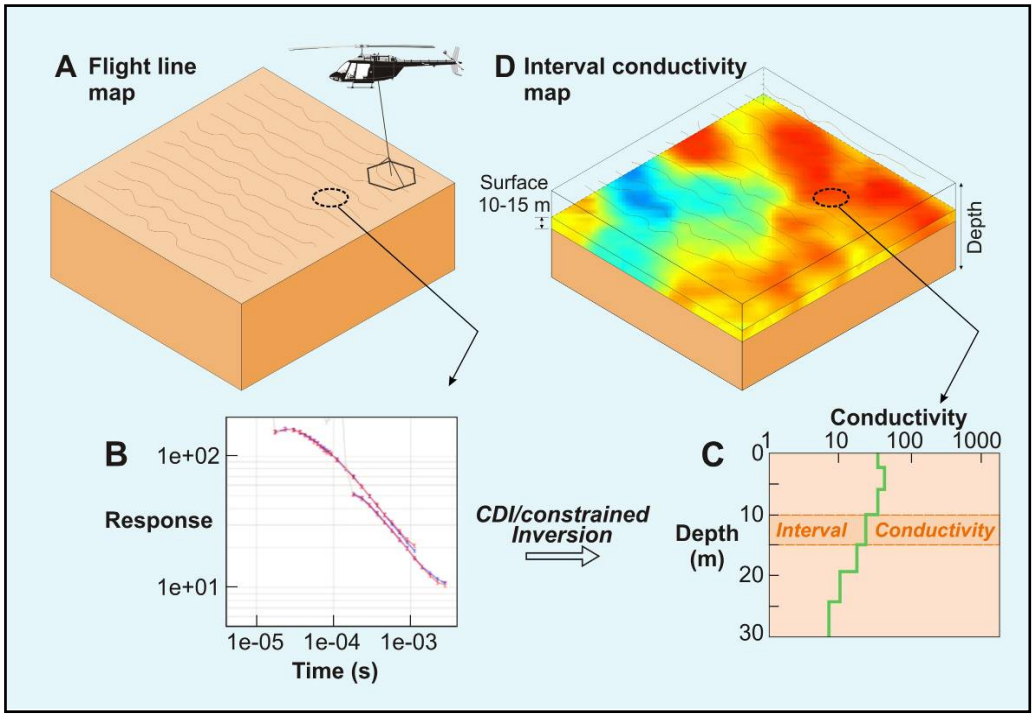



**Figure 6-20.** *Schematic representation of helicopter time domain EM data acquisition and interpretation. a) Data are acquired along parallel flight lines, with inter-leaved high and low transmitter moment; b) Data are processed and binned into soundings at regular intervals along the lines; a plot of apparent resistivity data is show; c) The measured response is used to determine the conductivity as a function of depth by inversion. d) From the inverted models, model sections and maps of mean conductivity in depth or elevation intervals (shown in the figure) can be calculated.*

A number of inversions were carried out for all or part of the survey area. An overview of the inversion products and the role they played in the different phases of the projects is given below.

- Fast Approximate iTEM inversion multi-layer (smooth) models with 35 layers, not laterally constrained (Groundprobe, 2009);
- Initial Spatially Constrained Inversions (SCI) at Geoscience Australia using Aarhus Workbench (WB);
- 5-layer few-layer models and 19-layer multi-layer models using the Laterally/Spatially Constrained Inversions in the Aarhus Workbench at the Aarhus Hydrogeophysics Group (AHG; Fogel & Sorensen, 2010);
- Borehole Spatially Constrained Inversion for GWR1 target area -WB (GA);
- 3D inversion (Wilson *et al*., 2010);
- WAve Number Domain Approximate (WANDA) inversion program (AHG – Christensen, 2012);
- Borehole constrained inversion of GWR1 target area without terrain corrections, and overly regularised and smoothed (Christensen, 2011);
- Full Laterally Spatially Constrained Inversion (parameters obtained from ground surveys) for test area in Jimargil – WB (AHG- Fogel & Sorensen, 2010);
- WAve Number Domain Approximate (WANDA) inversion (Christensen, 2012). This final inversion included borehole constraints and terrain corrections. Numerical models were combined with ground and borehole geological and geophysical data, and information from other inversions, to select the appropriate vertical regularisation and horizontal smoothing.

The various inversions are described in more detail below.

### 6.6.1 Initial Contractor's Inversion

With the data acquisition in 2009 with the SkyTEM system, the contractor (Geoforce, now Groundprobe) delivered data and a preliminary inversion using the approximate inversion program iTEM (Christensen, 2002; Christensen *et al*., 2009) all within 48 hours of acquisition, an unprecedented rapid turnover that was part of the reason for choosing the SkyTEM system in the first place and that was very helpful for the further planning of the project.

The iTEM inversion uses multi-layer (smooth) models with 35 layers. The inversions are done individually on each data set. They serve to verify the quality of the data and are accurate enough to show the conductivity structure of the survey area (Figure 6-21 and Figure 6-22). Inversions were delivered over only 1/3 of the BHMAR area. The plan was that full inversions would be obtained over the entire area using the Aarhus Workbench. The latter inversions were generally thought likely to produce superior inversions when compared to those produced by the fast approximation method.

The iTEM inversions were used successfully to plan the borehole drilling campaign of the first 50 boreholes. In this endeavour, the iTEM inversions proved invaluable, and the geologists selecting targets developed a high level of confidence in the ability of the inversion products to predict conductivity distributions at a regional target scale (Lawrie *et al*., 2010b, c).

#### 6.6.1.1 *Reliability of the iTEM inversion*

Prior to new drilling, pre-existing bores were logged with gamma and induction tools. These data were plotted on the iTEM sections for comparison (Figure 6-21 to Figure 6-23). These comparisons showed that the iTEM inversions were good at predicting the multi-layer conductivity profile; however the depths at which the conductors were predicted could be out by 10 m or more. Subsequently, the multi-layered hydrostratigaphy was confirmed by drilling, with confirmation that predictions of the depths of layer boundaries required improvement. FiD point comparisons with a limited borehole dataset for the priority Jimargil borefield site are presented later in a comparison of 4 inversion products.

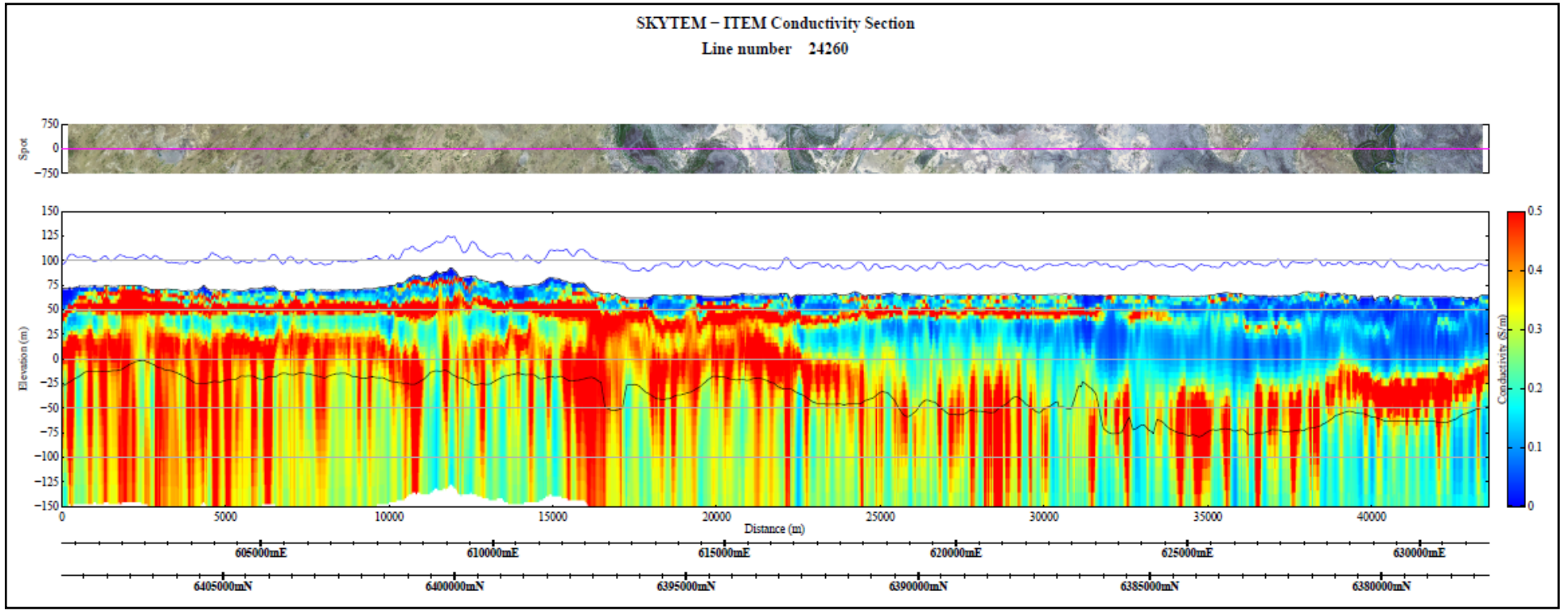



**Figure 6-21.** *An iTEM flight line conductivity depth section showing conductive units in red and resistive units in blue. The multi-layer profile that characterises the near-surface conductivity distribution beneath the Darling floodplain is evident. The semi-continuous upper conductive layer equates generally with the Blanchetown Clay, while the lower conductive unit is the upper Renmark Group sediments. Between these lies the target Pliocene aquifer (Calivil Formation and Loxton-Parilla Sands).The blue curve above the ground surface is the flight height. The black line within the model section is the DOI calculated using the method of Christiansen and Auken.*

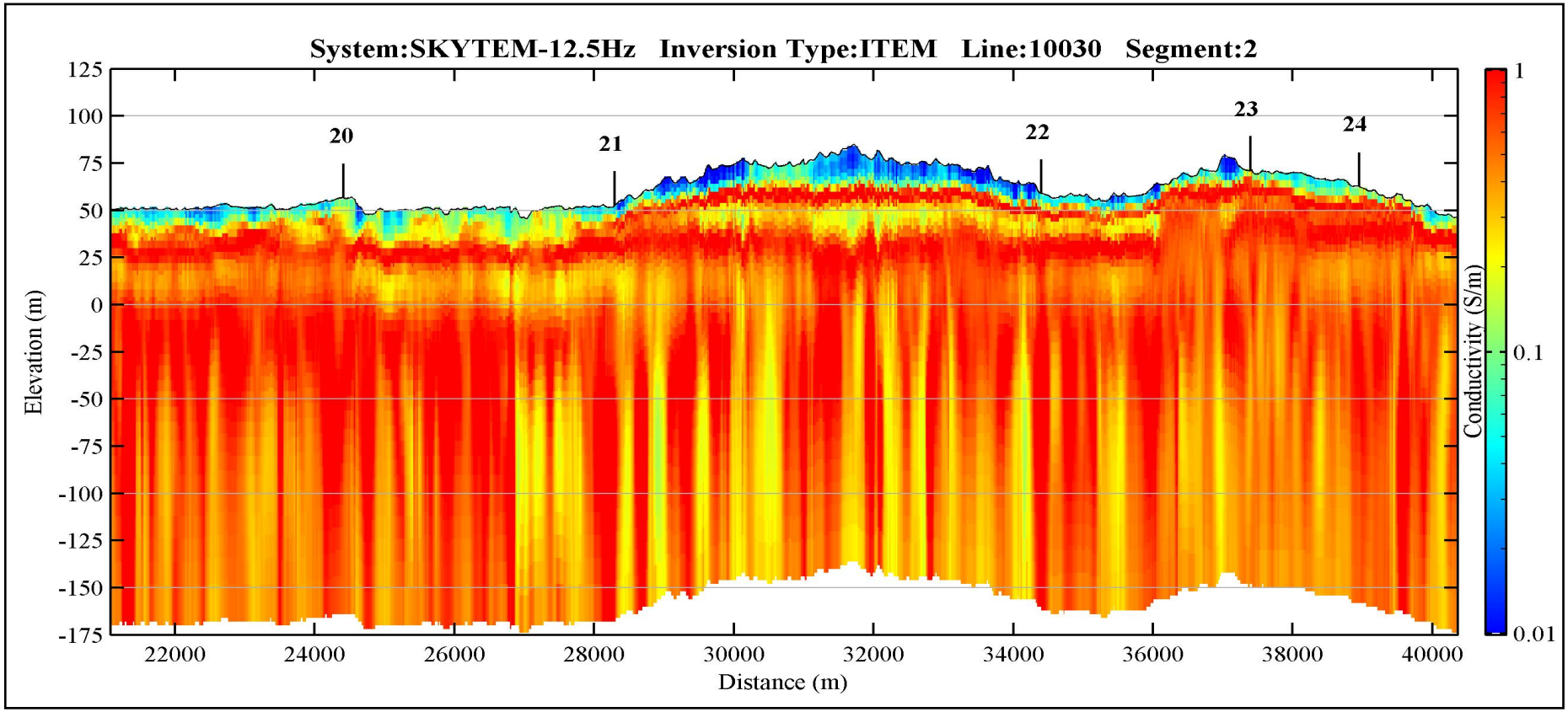



**Figure 6-22.** *An iTEM flight line conductivity depth section showing conductive units in red, near-surface resistive units (sand dunes) in blue and moderately conductive units in yellow and orange. In this area, the conductivities are much higher than in Figure 6-21, as the groundwater is very saline in this area. However, a multi-layer profile is still evident. There is a near-surface conductive unit beneath the dunes, and a second thin continuous layer (Blanchetown Clay), beneath. The lower conductive unit is the upper Renmark Group sediments. Sandwiched between the Blanchetown Clay and Renmark Group sediments is the Loxton-Parilla Sands aquifer, which at this location, contains saline groundwater.*

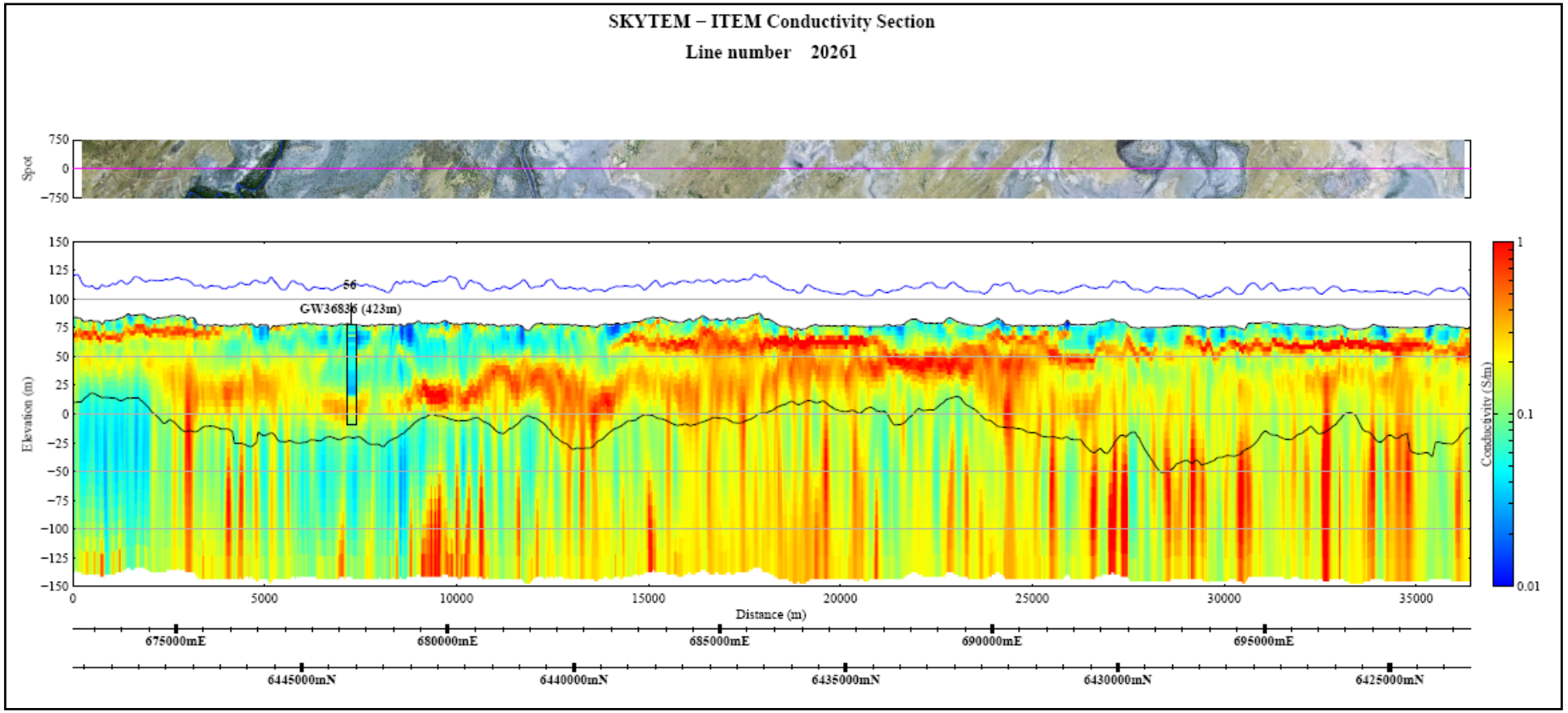



**Figure 6-23.** *An iTEM flight line conductivity depth section showing conductive units in red, near-surface resistive units (sand dunes) in blue and moderately conductive units in yellow and orange. Conductivity data in a pre-existing bore is displayed at the same scale for comparison. The iTEM inversion shows a reasonably good correlation with the borehole induction log data, picking out both the upper conductive layer (Blanchetown Clay) and the lower conductive layer (upper Renmark Group sediments).*

### 6.6.2 Initial Aarhus WorkBench Inversion

At the start of the project, Geoscience Australia had acquired the WorkBench (WB) data processing and inversion program developed by the HydroGeophysics Group at Department of Geosciences, University of Aarhus, Denmark. The comprehensive program system was deemed to be the best offer on the market for the extensive data processing, data inversion and presentation of results that was required for the BHMAR survey. The WB program is capable of performing Laterally Constrained Inversion (LCI) where a group of soundings along a flight line were simultaneously inverted with lateral constraints to ensure horizontal smoothness of the resulting model sections. An option of imposing lateral constraints in the plane (SCI, Spatially Constrained Inversion) had recently been developed and it was the intention to invert the BHMAR data set with this latest option. A module for including the information from borehole conductivity logs as further constraints in the inversion was developed for Geoscience Australia by the HydroGeophysics Group. Eventually, though not including the optional borehole constraints, a WB SCI inversion product was produced.

#### 6.6.2.1 *Reliability of the initial SCI inversion*

The initial SCI inversions had severe shortcomings in terms of providing geologically plausible structures in the top 20 m of the sub-surface (Figure 6-24). This meant that it was difficult to delineate the presence of clays and to distinguish between sand and clay aquifers and aquitards and thereby provide information essential to the hydrogeological models (Lawrie *et al*., 2010b). The reason for this is probably the highly complicated structure of the WB program that was new to the groundwater group geophysicists and the inherent complication of choosing proper inversion constraints facing any inversion project.

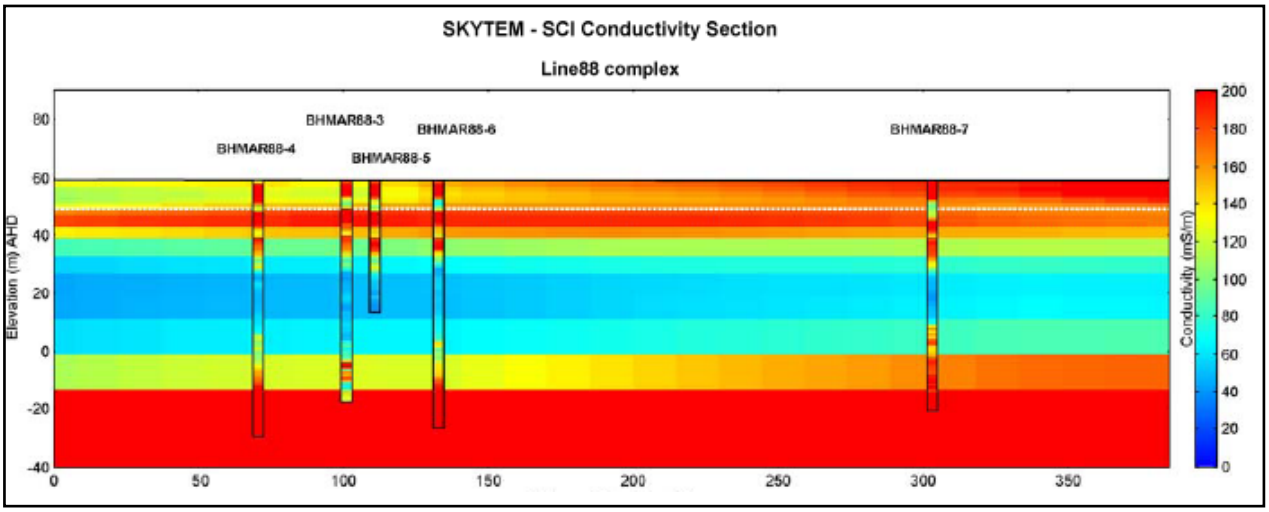



**Figure 6-24.** *SCI conductivity depth section for the BHMAR88 drill site. There is a reasonable correlation with borehole induction logs at depth, but less in the near-surface. This figure also shows the problems of scale, with lateral conductivity variability evident at a local scale, particularly in the near-surface. Ground geophysical methods would be better suited to map that local-scale variability.*

### 6.6.3 LCI WorkBench Inversion (Aarhus University Hydrogeophysics Group)

With the less-than-optimal resolution of the in-house SCI inversion and an approaching deadline in March 2010, it was decided to have the Aarhus University HydroGeophysics Group perform a LCI inversion of the entire BHMAR data set. This was done over a period of a few weeks, and the time constraints did not permit the computationally much heavier SCI inversion.

Subsequently, the whole data set was inverted with full accuracy inversion with 5-layer few-layer models (Figure 6-25) and 19-layer multi-layer models (Figure 6-26) using the Laterally/Spatially Constrained Inversions (LCI and SCI; Auken *et al*., 2005; 2009). The spatially constrained inversion (SCI) is a methodology for inverting the acquired airborne electromagnetic data (which may be of varying spatial density) into conductivity data using a 1D forward solution at each inversion model site. Information from each model migrates horizontally and vertically through spatial constraints applied between nearest neighbouring sites or soundings. SCI produces more complex laterally smoothly-varying output conductivity models that emulate 3D geological variations of sedimentary settings; while at the same time suppressing elongated artefacts that often coincide with survey flight direction. Although each site is inverted for using a 1-dimensional model, the presence of the constraints between model parameters makes each sounding communicate to its neighbours. A more technical description on spatially constrained inversion can be found in Viezzoli *et al.* (2008).

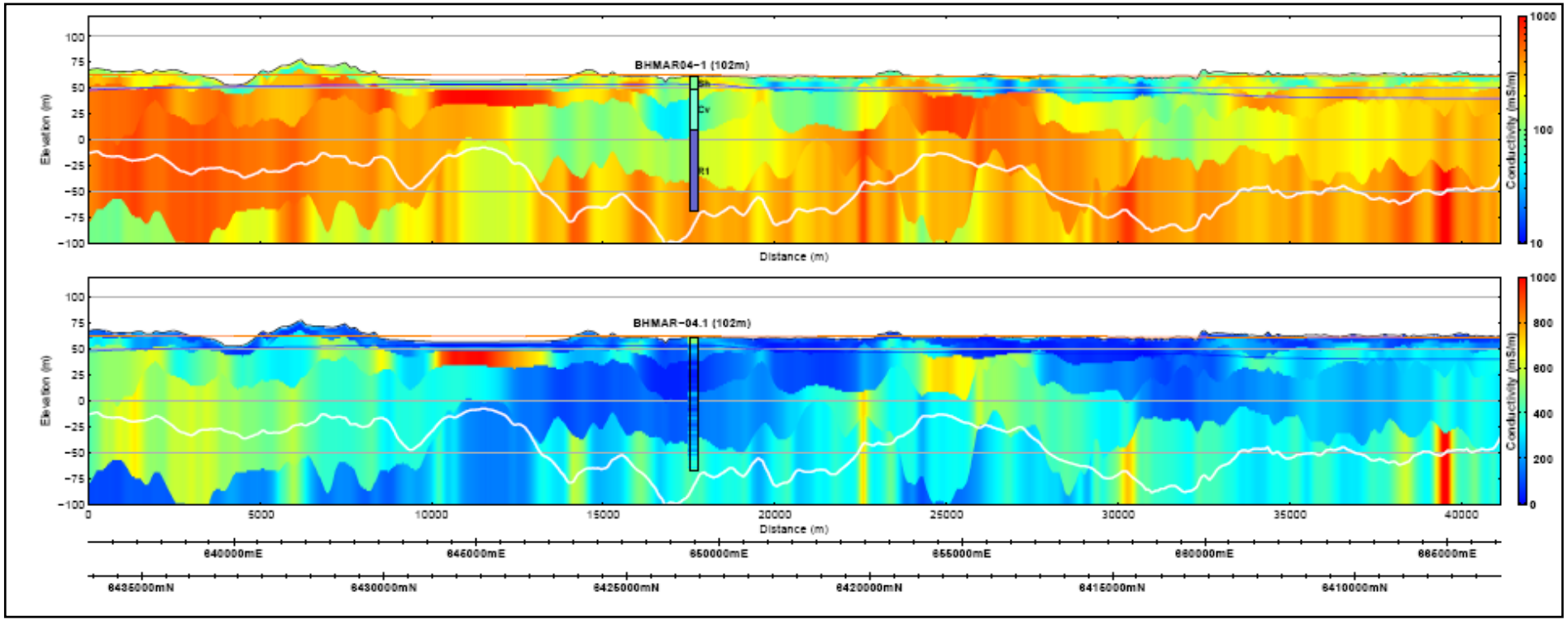



**Figure 6-25.** *LCI 5-layer model sections; colour scales and bore the same as in Figure 6-26. In general, the 5-layer models are too 'blocky' for hydrogeological interpretation in this project. The white lines indicate the DOI.*

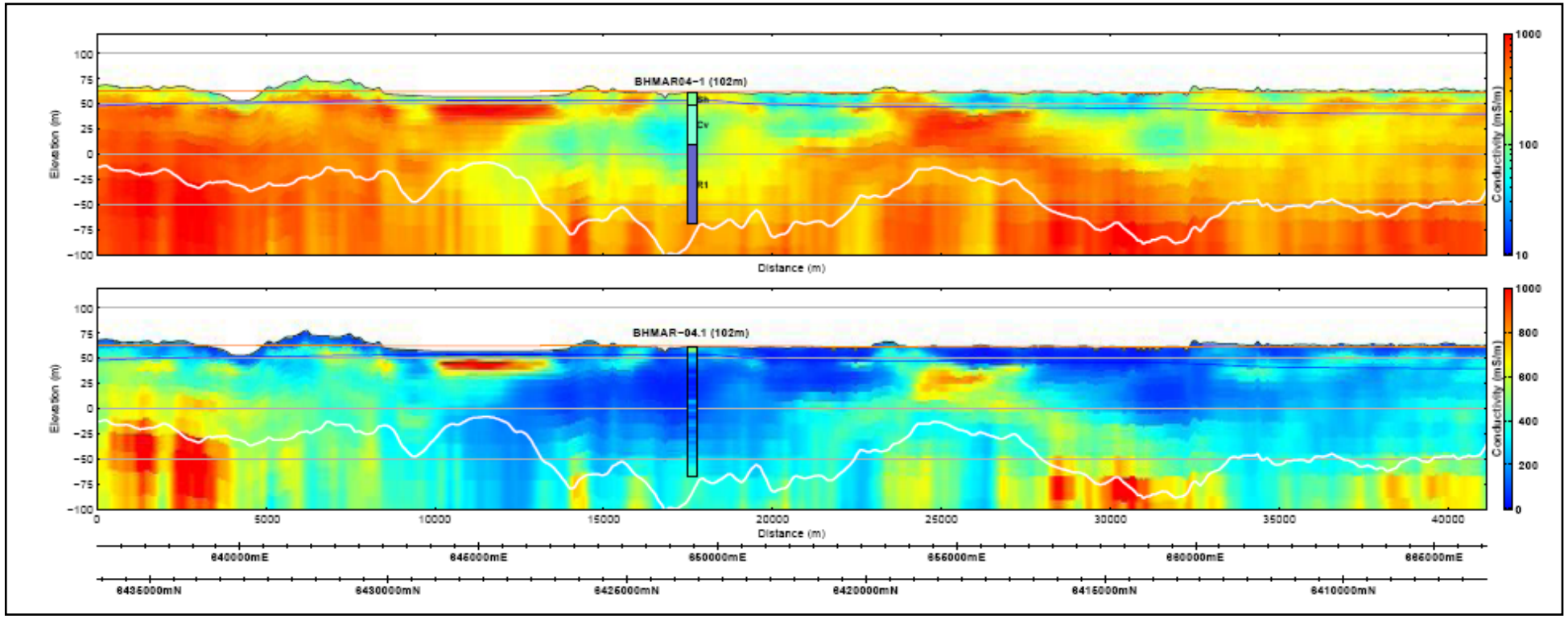



**Figure 6-26.** *LCI 19-layer model section with stratigraphic lithology from boreholes superimposed. In the top section, the conductivity scale is logarithmic, while a linear conductivity scale is used in the bottom panel. Linear stretches are favoured in this report as they enable the interpreter to pick out more detail at the lower conductivity end of the scale, where small changes in conductivity have importance for groundwater salinity mapping and assessment. The white lines indicate the DOI.*

#### 6.6.3.1 *Reliability of the initial 5-layer and 19-layer LCI inversions*

To provide some indication as to whether the conductivity modelled (or inverted) from the SkyTEM data is similar to conductivity measured through borehole logging, we compare the conductivity logs of the boreholes to the conductivity values from various AEM inversion products. Specifically, we analyse the comparison of the conductivities from 19-layer laterally constrained inversion (LCI), 19-layer spatially constrained inversion (SCI) and 19-layer spatially constrained inversion with the addition of borehole conductivity constraints (SCIb).

The analysis is as follows: from the spatially located position of the borehole, we find the layer-conductivity values of the nearest-neighbour inversion model in closest proximity to each borehole (commonly referred to as a fid-point comparison). Each conductivity value from the inversion product represents an average conductivity over a layer that is determined from the parameterisation of the inversion model. Layer thicknesses and depths are shown in Table 6-11. For each borehole, the conductivity values are averaged over the same depth intervals defined by the AEM inversion models. The resulting pairs of data samples are plotted on conductivity vs. conductivity graph, and the data is analysed as a whole. As an example, the conductivity log, its averaged layer values, and the inversion results from various inversion schemes are shown in Figure 6-27. In this example, we see the borehole conductivity log superimposed by the borehole conductivity averaged over the layer thicknesses specified by the inversion model schemes. Examination of Figure 6-27 shows that the inversion layers are different for the LCI and SCI inversions: this has been incorporated in our calculations.

**Table 6-11.** *Thickness and depths of the layers used in the 19-layer inversion models.*

| 19-Layer LCI | | | | | 19-Layer SCI | | | |
|---|---|---|---|---|---|---|---|---|
| **Layer** | **Thickness** | **Depth to top** | **Depth to bottom** | | **Layer** | **Thickness** | **Depth to top** | **Depth to bottom** |
| | **(m)** | **(m)** | **(m)** | | | **(m)** | **(m)** | **(m)** |
| 1 | 2 | 0 | 2 | | 1 | 2 | 0 | 2 |
| 2 | 2.3 | 2 | 4.3 | | 2 | 2.3 | 2 | 4.3 |
| 3 | 2.7 | 4.3 | 7 | | 3 | 2.6 | 4.3 | 6.9 |
| 4 | 3.2 | 7 | 10.2 | | 4 | 2.9 | 6.9 | 9.8 |
| 5 | 3.7 | 10.2 | 13.9 | | 5 | 3.3 | 9.8 | 13.1 |
| 6 | 4.3 | 13.9 | 18.2 | | 6 | 3.8 | 13.1 | 16.9 |
| 7 | 5 | 18.2 | 23.2 | | 7 | 4.3 | 16.9 | 21.2 |
| 8 | 5.9 | 23.2 | 29.1 | | 8 | 4.8 | 21.2 | 26 |
| 9 | 6.9 | 29.1 | 36 | | 9 | 5.5 | 26 | 31.5 |
| 10 | 8 | 36 | 44 | | 10 | 6.3 | 31.5 | 37.8 |
| 11 | 9.3 | 44 | 53.3 | | 11 | 7.1 | 37.8 | 44.9 |
| 12 | 10.9 | 53.3 | 64.2 | | 12 | 8.1 | 44.9 | 53 |
| 13 | 12.7 | 64.2 | 76.9 | | 13 | 9.1 | 53 | 62.1 |
| 14 | 14.8 | 76.9 | 91.7 | | 14 | 10.4 | 62.1 | 72.5 |
| 15 | 17.3 | 91.7 | 109 | | 15 | 11.8 | 72.5 | 84.3 |
| 16 | 20.1 | 109 | 129.1 | | 16 | 13.4 | 84.3 | 97.7 |
| 17 | 23.5 | 129.1 | 152.6 | | 17 | 15.2 | 97.7 | 112.9 |
| 18 | 27.3 | 152.6 | 179.9 | | 18 | 17.254 | 112.9 | 130.154 |
| 19 | ∞ | 179.9 | ∞ | | 19 | ∞ | 130.154 | ∞ |

#### 6.6.3.2 *Consistency of 19-layer LCI with borehole data*

We begin the analysis with a comparison of 19-layer laterally constrained inversion to the conductivity logs of all boreholes logged by Geoscience Australia to date. At the time of the analysis (March 2010) there were

induction logs from 34 boreholes spanning most of the BHMAR project area. This amounts to approximately 460 data pairs over the area. There are fewer data points than the expected value of 646 (34×19) since the borehole conductivity logs were removed from the top 2 m depth intervals (due to effects of steel casing in the boreholes), and not all bores were drilled to 180 m depth. The data pairs of borehole conductivity versus 19-layer LCI inversion models are plotted in the top panel of Figure 6-28.

It is apparent from the figure that there is a general linear trend in the data along a line of slope 1, starting from the origin, implying a good correlation between borehole and inversion models. There are a few spurious points in the data when inversion model conductivities are lower than 300 mS/m. These are generally from shallow layers, where less agreement between inversion and borehole conductivity must be expected due to the poorer resolution of the TEM method for thin, near-surface layers. The red line shown in Figure 6-28 is a linear regression of the AEM inversion regressed to the average borehole conductivity values. In the top left-hand corner of the figure is the result of the regression: $y = 0.873x$, where $y$ is the AEM inversion models and $x$ is the borehole conductivity. Beneath the equation is the coefficient $R$, otherwise known as the Pearson product-moment coefficient of correlation; and $R^2$, which is the coefficient of determination. For this analysis, $R$ is calculated to be $R = 0.867$, and $R^2 = 0.752$. The coefficient of correlation is a measure of the correlation or linear dependence of the variables, while the coefficient of determination is a measure of how well the variance of the regressed fit can be explained by the linear relation. In this case, an $R$ value of 0.867 is an indication of a strong linear relation between borehole and AEM conductivity. The coefficient of determination $R^2 = 0.752$ means that 75% of the variation in the data can be accounted for in terms of random variation about the linear relation $y = 0.873x$.

These results, for all logged boreholes compared to AEM inversion results computed using an LCI inversion, are very good, with a strong correlation between data sets. However, as we will see in Section 6.6.4, we can do better.

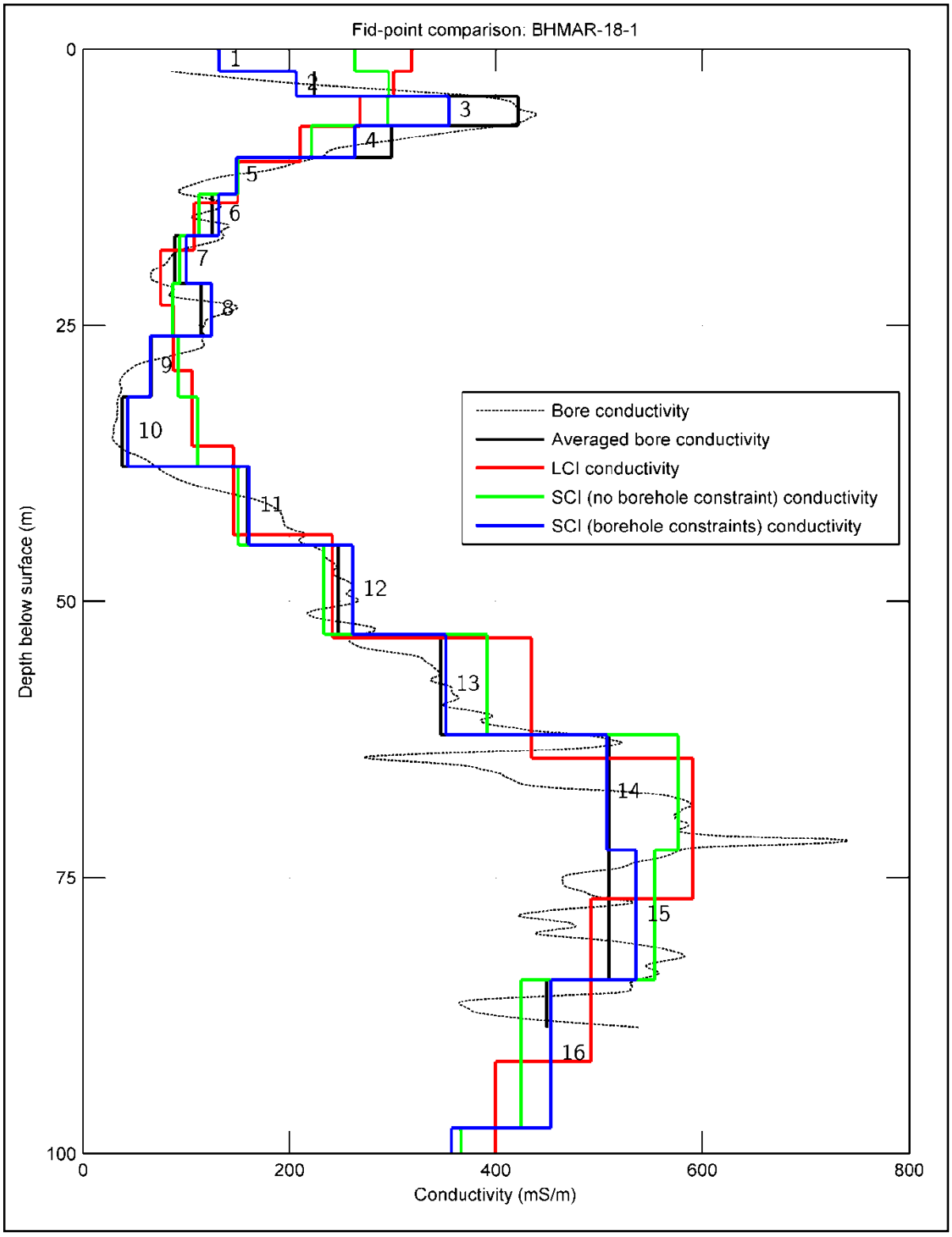



**Figure 6-27.** *Borehole conductivity log for borehole BHMAR18-1. Solid black line shows the borehole conductivity log averaged over the layers specified by the SCI inversion schemes (Table 6-11). Also shown are the inversion model conductivity layers for the nearest neighbouring fiducial point in the following order: LCI (red); SCI without borehole constraints (green); and SCI with borehole constraints (blue). The borehole constrained inversions should improve the fit to near-surface conductivity.*

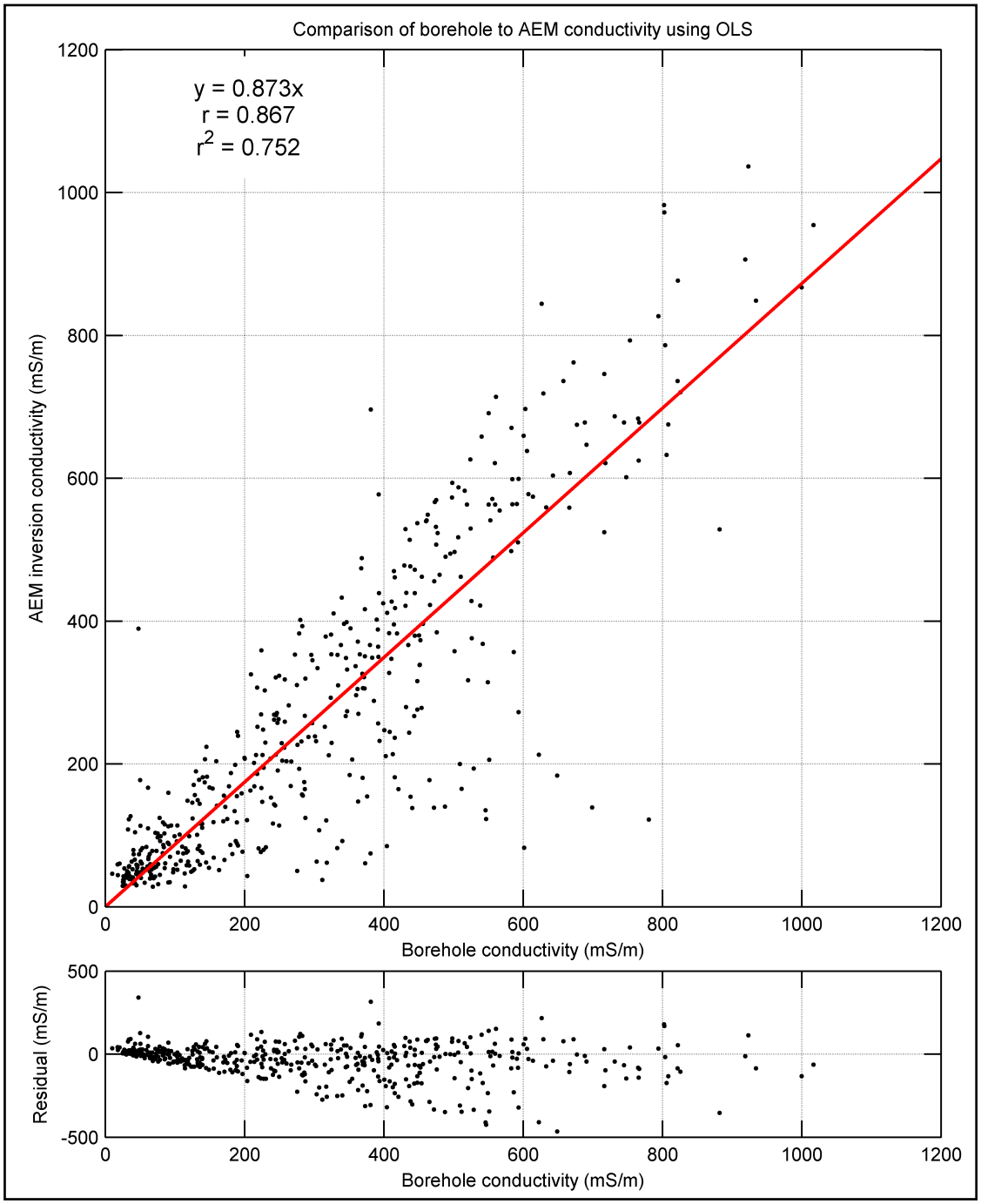



**Figure 6-28.** *Comparison of depth-averaged borehole conductivity to 19-layer AEM inversion conductivities over 34 boreholes located inside the BHMAR survey area. (top panel). Red line shows a linear fit computed using an ordinary least-squares (OLS) linear regression. Bottom panel shows the residual of the observed data from the adjusted data using (red) the OLS linear regression and (black) a straight 1:1 correspondence line.*

### 6.6.3.3 *Discussion*

It has been traditional in reports to compare logged borehole conductivity to AEM inversion models using graphs such as the one shown in the top panel of Figure 6-28. The top panel, which displays all the averaged borehole conductivities paired with their AEM inversion conductivities, shows a strong linear trend in the data along the main diagonal of the graph. It is seen, however, that the line of best fit has a slope of 0.873. It is lower than 1 because the data points in the lower 1/3 of the upper panel draw the regressed line down when calculating the least-squares line of best fit. An analysis of the lower panel of Figure 6-28, which shows the residual of the data (or the vertical separation distance between the observed *y* values and those predicted by the line of fit), indicates that there is a general trend in the data. We see that, for increasing

values of borehole conductivity, the residual tends to increase in a negative direction. This indicates that either the model we have chosen to fit the data with is in error or that we are trying to fit the data in the wrong way.

In using least-squares regression to fit data, there is a general tendency to apply the method with little consideration of the principles underlying the application. In the data shown here, which is an example of the application of ordinary least squares (OLS) linear regression, there are some implicit assumptions made about the data that are fundamentally unfounded and therefore invalidate the results found from an analysis of the data in Figure 6-28.

The first assumption about data and the subsequent regression using OLS is that the *x*-values, or the conductivity measured with the borehole device, are known exactly, i.e. the values of conductivity are known completely without error. As discussed in previously, this is false; and there are several factors that contribute to the error of a single measurement of conductivity with a borehole logging device. However, examination of Figure 6-27 shows a greater problem: variation of the borehole conductivity logs over a layer boundary. Figure 6-28 shows the borehole conductivity, averaged over a finite layer thickness as a single point without any associated variation in its value. But take, for example, layers 10 and 11 in Figure 6-27. Clearly, the variation in the borehole conductivity across layer 10 is much less than that of layer 11, yet this is unaccounted for in Figure 6-28. In subsequent analysis of the data, we have calculated the variation (in terms of a standard deviation of the data) or a measure of spread of the borehole conductivity logs across the layer boundary that is used to calculate its average. In the initial analysis (2010), data points with widely varying conductivity across its layer (such as layer 14, Figure 6-27) will have a larger standard deviation and, hence, lower significance in a regression analysis. This incorrectly down weighs the result in layer 11 because of the larger borehole variability across that layer.

A second assumption using OLS regression is that the variation in data on the *y*-axis is the same for each point. That is, every value of conductivity obtained from inversion of the AEM data has the same amount of error associated with it. This is not a valid assertion to be made about the data obtained from an inversion processed and, in fact, an analysis of variation or goodness of fit from an inversion is made as a routine part of the calculation. Therefore, some layer conductivities in an inversion calculation are better known than others, and the assumption of uniform constant variation of *y*-value (i.e. AEM conductivity) is therefore invalid: different values are known differently well and must be weighted accordingly.

In an effort to incorporate these two significant departures from OLS in our analysis of consistency between AEM inversion products and borehole conductivity logs, we generalise the procedure of regression to include errors of measurement in both borehole and AEM conductivity values. We have derived an inversion method for determining the coefficients in models that we use to attempt to describe the relationship between borehole and AEM inversion data. The generalised method, which we shall call Deming regression (Deming & Birge, 1934), requires a determination of the significance (or weighting) of every data point used in the analysis. The data is then adjusted to fit an assumed model in a least-squares sense.

We have chosen a functional form of:

$$\sigma_a = m\sigma_b$$

**Equation 3**

where $\sigma_a$ is the AEM inverted conductivity, $\sigma_b$ is the borehole conductivity and $m$ is a constant of proportionality. We have made the following assumptions in our model: significance or weight of data is inherited from the data itself (borehole data: calculation of average conductivity for a layer; AEM: from the inversion posterior covariance matrix); the linear regression model is forced through the point (0,0). The second assumption is reasonable since both methods have large undetermined errors as conductivity nears zero.

As a final note on the generalisation of the regression analysis, we have derived a generalisation of the Pearson coefficient of correlation, *r*, that reflects the error in the data:

$$r = \frac{\mathrm{cov}(x_w, y_w)}{\sqrt{\mathrm{cov}(x_w, x_w)\,\mathrm{cov}(y_w, y_w)}}.$$

**Equation 4**

Here, $\mathrm{cov}(x_w,y_w)$ is the covariance between the weighted $x$ and $y$ data, and $\mathrm{cov}(x_w,x_w)$ is the variance of the weighted $x$ data (similar for $y$). We calculate the weighted covariance in the following manner:

$$\mathrm{cov}(x_w, y_w) = \frac{\sum_{i=1} w_{xi} w_{yi} (x_i - \bar{x})(y_i - \bar{y})}{\sum_{i=1} w_{xi} w_{yi}},$$

**Equation 5**

where $x_i$ and $y_i$ are observed data points, $w_{xi}$ and $w_{yi}$ are the weights of the data and $\bar{x}$ and $\bar{y}$ are the weighted means of the observed data, calculated as:

$$x = \frac{\sum_{i=1} w_{xi} x_i}{\sum_{i=1} w_{xi}}.$$

**Equation 6**

The interpretation of the coefficient of correlation is still the same: $r$ is a measure of the linear correlation between two independently measured datasets. Similarly, $R^2$ is a measure of the variance of data once a correlation model is determined. With our new method of analysis, we return to the 19-layer LCI, incorporating error in both borehole and AEM inversion conductivities.

#### 6.6.3.4 *Consistency using 19-layer LCI: Deming regression*

Figure 6-29 is a re-presentation of the conductivity data from Figure 6-28 with the additional feature of a measure of the variance or standard deviation of the data for each pair, represented by horizontal and vertical bars extending from the data point. Wider bar separation is indicative of greater variance in the data. As an example, the variation in both the borehole and conductivity data for the borehole conductivities greater than 800 mS/m are quite large (±100 mS/m for both the borehole and AEM conductivity). Consequently, these data are relatively less significant when calculating a regression analysis.

In all of the programs applied in the BHMAR project, inversion is done on the logarithm of conductivity and consequently the posterior estimates of parameter uncertainty are the absolute uncertainty of log(conductivity). For the comparison, we transform these uncertainties to absolute uncertainties on the conductivity itself by:

$$\Delta\sigma_{abs} = \sigma.\Delta\sigma_{rel}$$

**Equation 7**

For low conductivities, $\Delta\sigma_{rel}$ is large, but σ is small, while for high conductivities, $\Delta\sigma_{rel}$ is small, but σ is large. The absolute uncertainties therefore span a smaller interval than the relative uncertainties, which can be seen in the following figures.

As shown by the text in the upper left-hand corner of Figure 6-29, the linear relationship between the AEM and borehole conductivity is $\sigma_a = 0.926\ \sigma_b$ with an $R$ value of 0.942 and $R^2 = 0.887$. This means that the AEM and borehole conductivity are strongly related, with 88.7% of the residual in the data able to be accounted for through random departure from the linear regression model. These are excellent results; which repeated when we examine the AEM conductivity models generated with spatially constrained inversions.

Some of the vertical uncertainties, particularly at low conductivity, appear as low as around 20 mS/m. This stems from the fact that the AEM inversion and thereby the posterior variances of the model parameters is done in a log space. When this is converted to a linear conductivity space there is less difference between the absolute uncertainties of the low and the high conductivities.

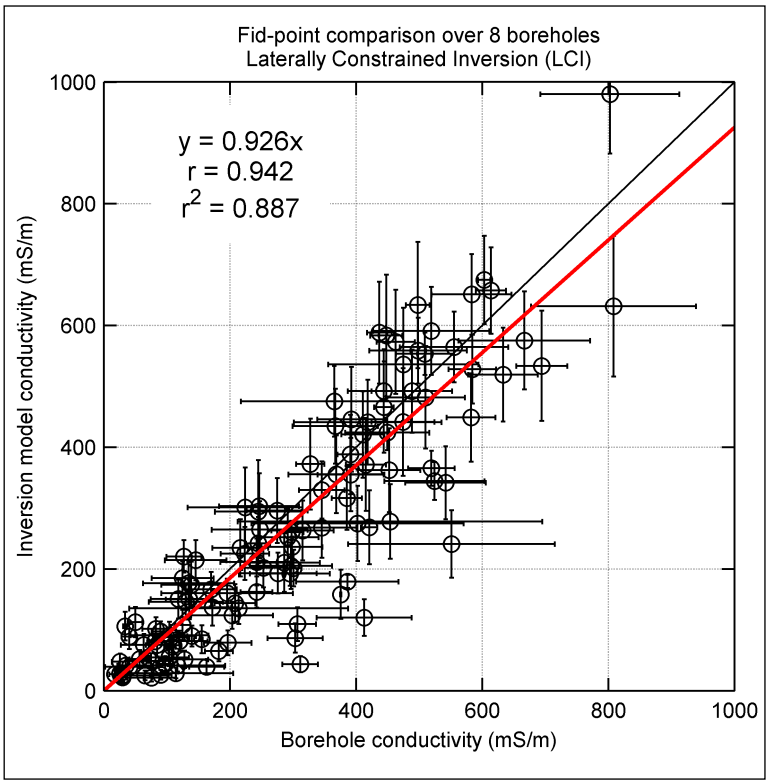



**Figure 6-29.** *Borehole and AEM inversion conductivity data using a laterally constrained inversion (LCI) scheme for 8 boreholes located in the priority area near Menindee. Data are properly represented as points with associated error or variance, indicating significance in the data values. Red line is a linear regression model calculated using a generalised Deming regression that accounts for variation in both x and y variables.*

#### 6.6.3.5 *Consistency using 19-layer SCI: Deming regression*

Figure 6-30 shows the consistency comparison of borehole and AEM inversion conductivity data when the AEM inversion output models are calculated using spatially constrained inversions. In this analysis, we see excellent correlation between AEM and borehole data, with a generalised $R$ value of 0.924 ($R^2$ = 0.855). Further, we see that AEM data is almost directly proportional to borehole conductivity: $\sigma_a = 0.926\ \sigma_b$. Finally, we see that when the SCI inversion is tied to the borehole data through a priori models, we get direct correspondence between AEM and borehole data.

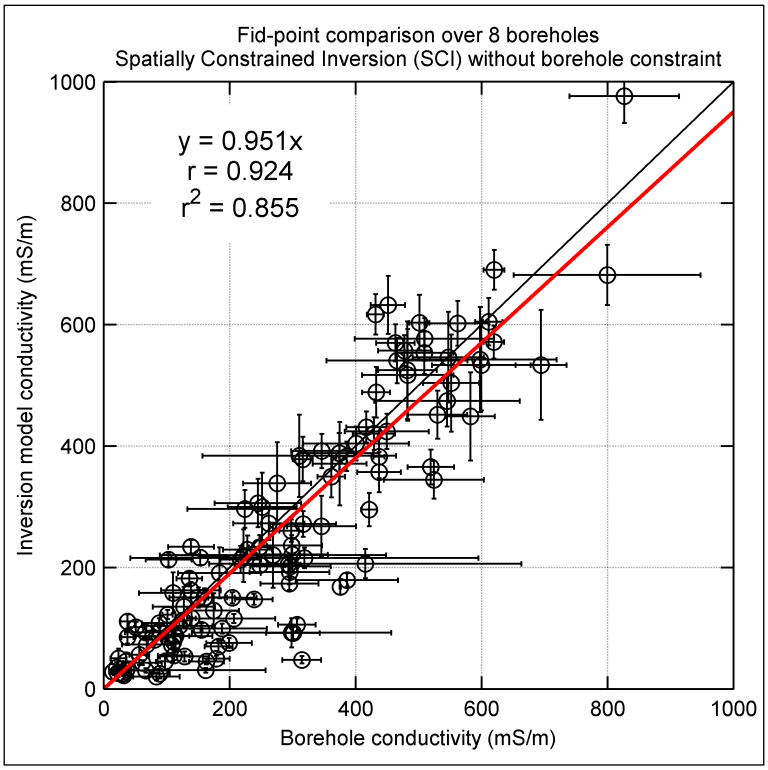



**Figure 6-30.** *Borehole and AEM inversion conductivity data using a spatially constrained inversion (SCI) scheme without borehole constraints for 8 boreholes located in the priority area near Menindee. Red line is a linear regression model calculated using a generalised Deming regression that accounts for variation in both x and y variables. Here, we see that AEM inversions are directly proportional to borehole conductivity.*

#### 6.6.3.6 *Consistency using borehole-constrained 19-layer SCI: Deming regression*

As a final example, we compare borehole data to AEM inversion results when the spatially constrained inversions are further constrained with a priori models that reflect borehole conductivity averaged over the layers used in the inversion. Figure 6-31 shows the consistency between AEM inversions and borehole data for 8 boreholes located in the priority area of the Menindee Lakes. With an $R$ value of 0.951 and an $R^2$ = 0.904, we can say that the borehole conductivity is directly proportional to the AEM data at the borehole sites. Here, $\sigma_a = 0.988\ \sigma_b$, indicating that there is practically a 1:1 correspondence between the data sets, within random variation of the data. This of course is simply an artefact of the use of these bores as a priori data to constrain the inversion. In later inversions, a subset of the borehole conductivity data was not used to constrain the inversion in order to provide a more robust check on the correlations.

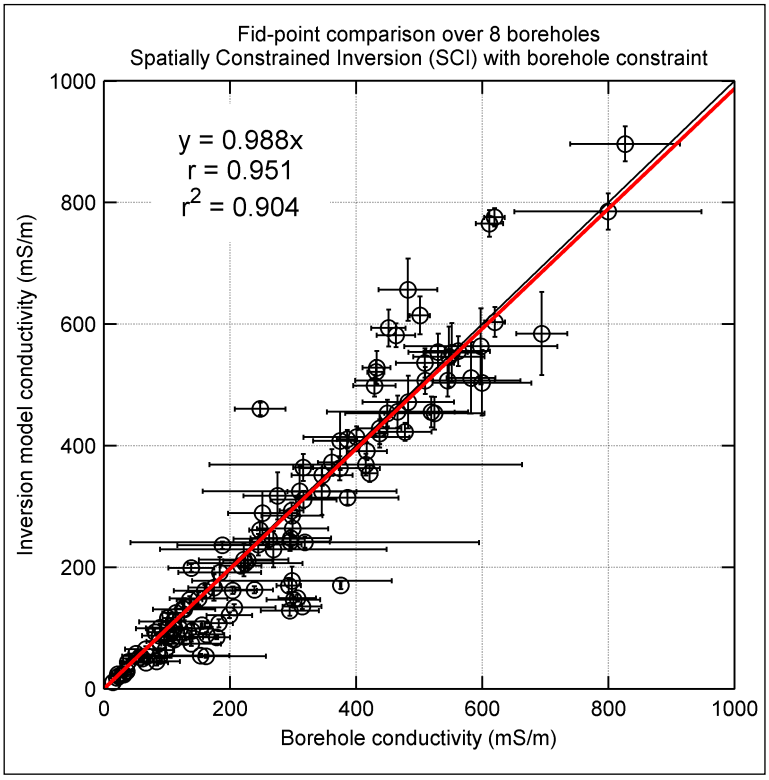



**Figure 6-31.** *Borehole and AEM inversion conductivity data using a spatially constrained inversion (SCI) scheme with borehole constraints for 8 boreholes located in the priority area near Menindee. Red line is a linear model calculated using a generalised Deming regression that accounts for variation in both x and y variables. Here, we see that AEM inversions are exactly proportional to borehole conductivity.*

#### 6.6.3.7 *Discussion and Conclusion*

In this section we have shown that borehole conductivity data, averaged over the layers that are used in the inversion models, agree well with all of the AEM inversion products from the Workbench software. We have applied the traditional method of regression analyses to assess the 'consistency' and 'misfit' between AEM data and borehole data, but the supposition that borehole conductivity values are without error or variance is incorrect, as is the assumption that the errors of the inversion data are the same for all conductivity values. We have therefore suggested a generalisation in the regression analysis and an extension of the Pearson product-moment coefficient of correlation that takes the errors on both data sets into account. The uncertainty of the AEM layer conductivities comes out of the inversion analysis, and as a measure of the uncertainty of the borehole conductivity we have used the variance of the variation over the layers over which it is averaged. Using the generalized approach we have found excellent consistency between borehole conductivity data and the layer conductivities of the different AEM inversion products.

However, the analysis presented in this section was restricted to a comparative analysis of spatially constrained inversions with induction log data for only 8 boreholes in the Menindee priority area. While there is an almost perfect 1:1 correspondence between borehole and inversion conductivity over all layers for these 8 locations, this correlation was reduced when boreholes drilled subsequently were added to the comparison. The initial bores used in the analysis were biased to one particular geological-geoelectrical domain, and the correlations on an individual borehole basis for 80+ bores was reduced in more conductive domains. Furthermore, on closer inspection, while the correlations are overall excellent, in reality, the LCI inversions still failed to resolve the near-surface conductivity distribution adequately.

#### 6.6.3.8 *Further AEM-borehole EM FID point comparisons in the GWR1 target*

As part of an exercise to assess how to further improve the inversions, further AEM-Borehole EM FID point comparisons were carried out in the GWR1 target area late in December 2010. Down-hole induction conductivity logs were recorded with an Auslog induction conductivity meter, operating at 106 khz base frequency and logging at a rate of ~6-8 m/min, sampling at 2.5 cm intervals. 5 boreholes were selected for detailed comparison of down-hole conductivity to AEM inversion and transformation products. The boreholes used were: BHMAR17-1, BHMAR33-1; BHMAR48-1; BHMAR66-1 and BHMAR64-1. These are chosen because they are the logs used to constrain the spatially constrained inversion using borehole constraints (SCI-borehole) that were used to determine drilling prospects in Phase 3 of the project.

Borehole to AEM comparisons were completed on 4 of the inversion products that had been used sequentially in the project, specifically in order of use, the iTEM conductivity-depth approximate inversion (iTEM); laterally constrained inversion (LCI); spatially constrained inversion, without borehole constraints (SCI, an interim product); and spatially constrained inversion, using borehole conductivity constraints (SCI-bore).

The calculation of the comparison of AEM inversion conductivity products to borehole conductivity logs is done by comparing the AEM conductivity for a given layer $i$ ($\sigma_{AEMi}$) to the average borehole conductivity over the same layer ($\sigma_{borei}$). We compute the standard deviation in the borehole conductivity ($s_{borei}$) layer average as a measure of how quickly, or by how much, the borehole conductivity is changing over that averaging layer. A given layer that has a widely varying borehole conductivity log will naturally have a higher variation in the calculation of the standard deviation of the mean conductivity over that layer. Likewise, for every layer of the AEM inversion products, the AEM conductivity estimate for that layer will have a standard deviation ($s_{AEMi}$) that determines how well the inversion algorithm has determined the AEM conductivity for that layer. These standard deviations are thought of as estimates of the surety or variability of the data. Accordingly, we can attribute a level of trust to each data point, for each layer, from both measurements of the conductivity. Comparison of data sets is then a comparison of conductivity points, as measured by the borehole tool and the AEM system, over each layer for each hole. We estimate a goodness of agreement by comparison of the data according to some assumed model, or regression.

One measure of goodness of the fit is given by the calculation of the coefficient of determination, often given the symbol of $R^2$. The coefficient of determination is a measure of the proportion of variability of the data in a set that can be explained by random variation of the data. In other words, $R^2$ determines how well our chosen model can explain any differences between what we expect the data to do (based on our prediction) and what the data actually does. The simplest calculation of $R^2$ is given as $R^2 = 1 - (SS_{err} / SS_{tot})$, whereby $SS_{err}$ is defined as the sum of squares of the residual (or misfit of the relationship) and $SS_{tot}$ is defined as the total sum of squares of the data. If the sum of squares of the residual is zero, then we say that our model has explained every variation in the data in a proportionally linear sense, and the $R^2$ value is 1. If the residual sum of squares is equal to the total sum of squares, then our model does not explain any variability in the data, and the $R^2$ value is 0. We therefore see that $R^2$ is a very basic measure of how well our choice of regression explains any variance in the data. A low value of $R^2$ is not an indication that either data set is invalid; it simply indicates that the model used to explain the variance is a poor choice. In our project, we assume a linear relationship between AEM and borehole conductivity layers: specifically, we expect that for each layer, the AEM conductivity will be exactly proportional to the average borehole conductivity. We can express this as $\sigma_{AEMi} = a \cdot \sigma_{borei}$, where $a$ is the constant of proportionality (which we expect to be 1).

Because we are comparing data sets that were acquired independently of one another, using different tools and techniques and at different times, it is natural to assume that there is variability in the different sets. We can indicate that variability, and provide a measure of it by using the standard deviations of the conductivities that were mentioned earlier. Each data point can then be associated a *weight*, indicating its trustworthiness, by taking the reciprocal of the square of the standard deviation of the data point. For example, if the value of the AEM conductivity at the $i$th layer is estimated to be $\sigma_{AEMi} \pm s_{AEMi}$, then the weight of that data point is given as $w_{AEMi} = 1/ s_{AEMi}$. We see from this relation that values with a low standard deviation will be assigned a greater degree of weight, which is another way of saying that we trust

the data more. Each point of data is assigned its own weight, and these values are taken into consideration when we attempt to describe a relationship between them.

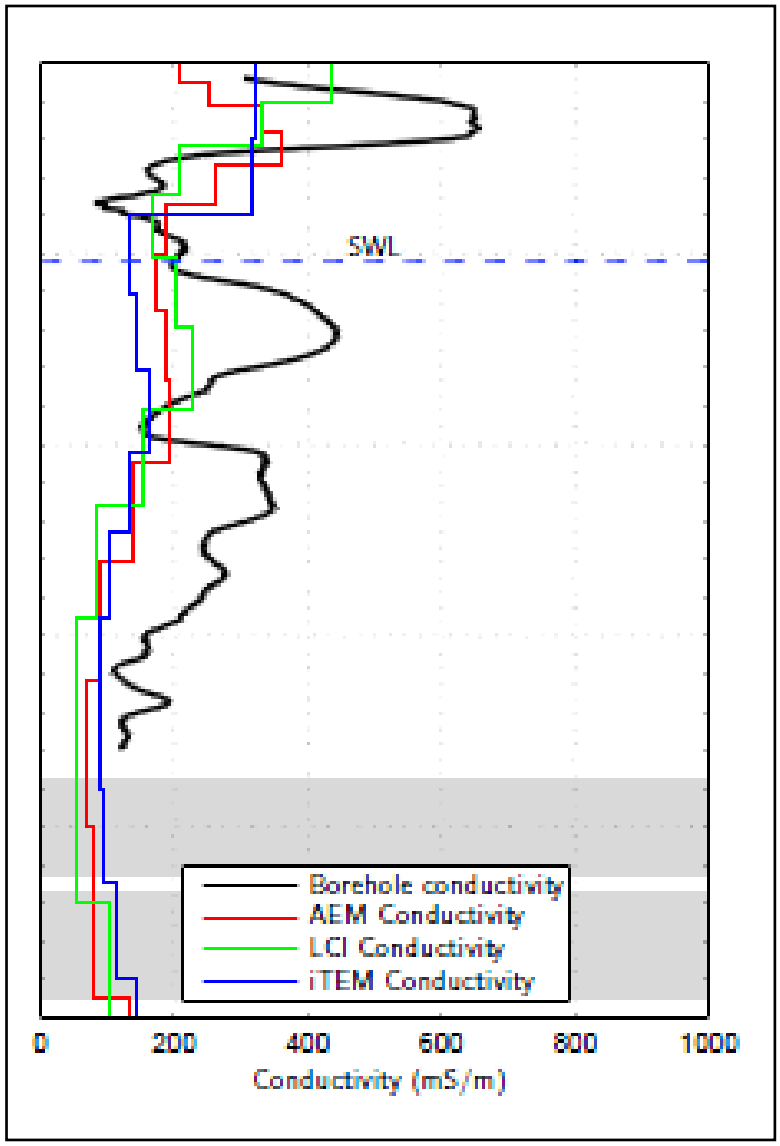



**Figure 6-32.** *Comparison of a borehole conductivity log (black) to various AEM inversion products: borehole and spatially-constrained inversion (SCI-bore) (red); laterally constrained inversion (LCI); and iTEM inversion (blue).*

We begin the analysis with a comparison of a borehole conductivity log (shown with a solid black line in Figure 6-32) to the various AEM inversion products calculated during this project: spatially constrained inversion (red); laterally constrained inversion (LCI); and iTEM inversion (blue). For each inversion product, the average borehole conductivity is calculated over the layer of the inversion technique where the bore log and the inversions overlap. An example for the average borehole-layer calculation for the iTEM inversion is shown in Figure 6-33 (using borehole BHMAR64-1). The borehole conductivity log is shown with a dashed black line, the iTEM inversion is shown in red, and the layer-averaged borehole conductivity is shown with a solid black line. A visual comparison between the two methods indicates similarity on a general trend: both conductivity logs indicate a basic 3-layer conductivity-depth profile: that of a relatively more conductive lake-bed clay overlying the more resistive Calivil Formation, which in turn is overlying the more conductive Renmark Formation.

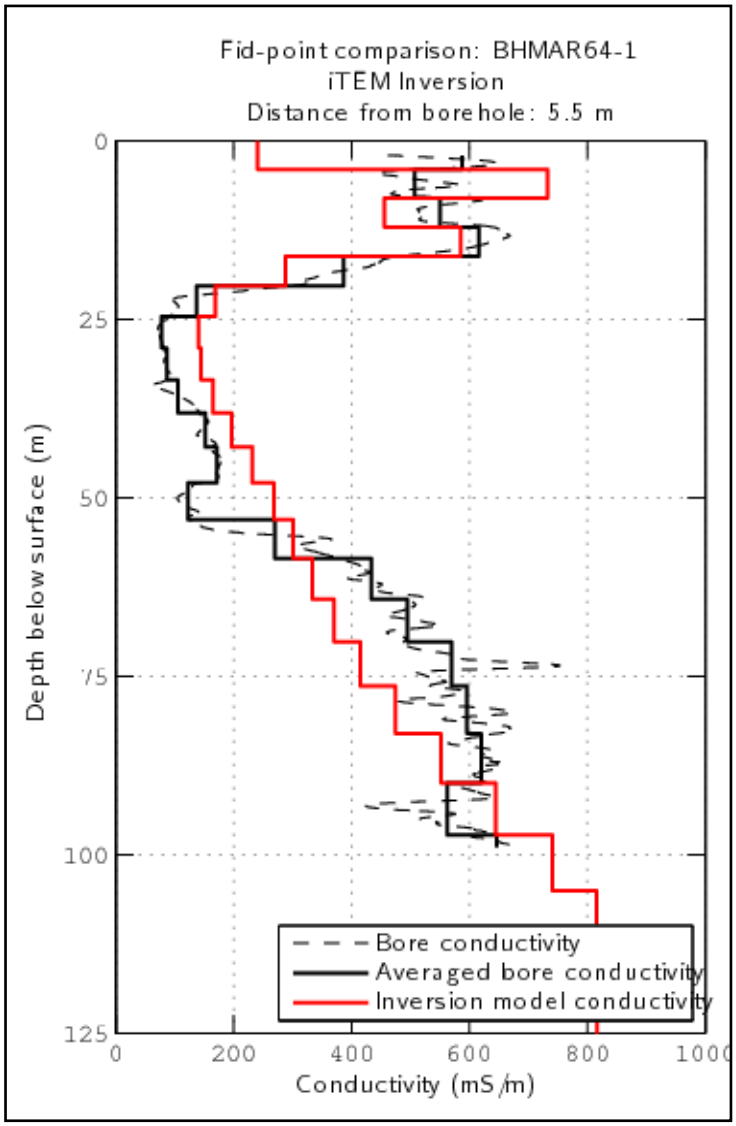



**Figure 6-33.** *Comparison of the iTEM inversion (solid red line) to the borehole conductivity log (dashed black line); and its layer-averaged conductivity values (solid black line) for borehole BHMAR64-1.*

For each layer, a standard deviation is calculated; and these results are compared in Figure 6-34. This comparison shows the relation between iTEM conductivity versus borehole average-layer conductivity for the 20 layers that the two measurements overlap. Each layer is marked with a circle, where the estimated uncertainty (standard deviation) is marked with whiskers in the x- and y-directions. In this case, the linear fit is very close to 1:1, indicating that there is a direct correlation between the iTEM and borehole data. Examination of the data, and the corresponding coefficient of determination, shows that $R^2 = 0.57$. This indicates that the majority of data is accounted for by the relationship chosen, but that there is variability in the data not accounted for by the model. For the lower conductivities, the AEM conductivity seems to be systematically higher than that of the boreholes and vice versa for the higher conductivities. The deviation of this variability from a 1:1 correspondence cannot be addressed at this time.

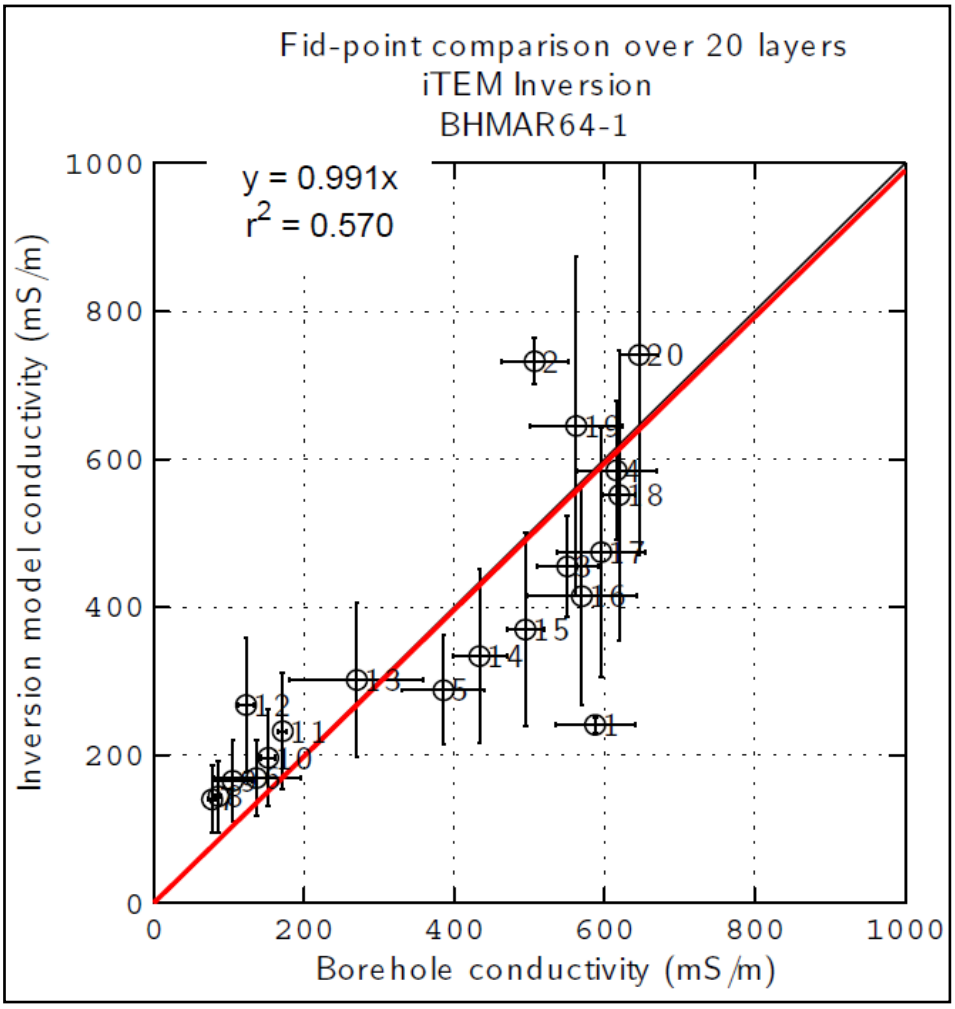



**Figure 6-34.** *Comparison of the iTEM layer conductivities (y-axis) to the layer-averaged conductivities from the borehole logs (x-axis), showing excellent correlation between the two data sets; with a fairly strong indication of correlation through the coefficient of determination ($R^2$) value of 0.57.*

We conducted similar analysis for each of the 5 boreholes indicated previously for each of the 4 inversion products. Four final plots, for all the boreholes considered with each inversion product, are then produced. Figure 6-35 shows the variability of the layer-averaged borehole conductivity for 5 boreholes compared to the nearest-neighbour SCI-bore inversion point for the GWR1 survey area. This figure indicates that in general, the AEM SCI-bore inversion is about 10% lower in estimation for a given layer than the borehole layer-averaged conductivity. That is, if we multiply any AEM layer conductivity by 1.11, we would achieve equivalent borehole layer-average conductivity (most of the time). This relationship is supported with a strong coefficient of determination of 0.845, indicating that most of the variability in the data is accounted for by the model assumed and that there could be a strong relation between the two methods used to obtain conductivity of soils with depth. This strongly encouraging result is a powerful indicator of the level of trustworthiness with which we should imbue the AEM conductivity-depth inversion products.

We have conducted a similar calculation for each of the inversion products for each of the 5 bores (taken individually and as a whole). Each product (except the iTEM) yields an $R^2$ value of greater than 0.7, which is an excellent indication of a directly proportional relation between the borehole logs and the AEM products. A lower $R^2$ value of 0.49 for the iTEM suggests that the differences between iTEM conductivity models and borehole layer-average conductivity cannot be explained by random error alone. However, the general trend of all data sets show that as borehole conductivity increases for a given layer, so too does the AEM conductivity obtained from the inversion. This trending information is further proof of the utility of the AEM system as a valuable tool for groundwater investigation in a regional and whole-of-target sense. We believe that the AEM products are reasonable and justifiable.

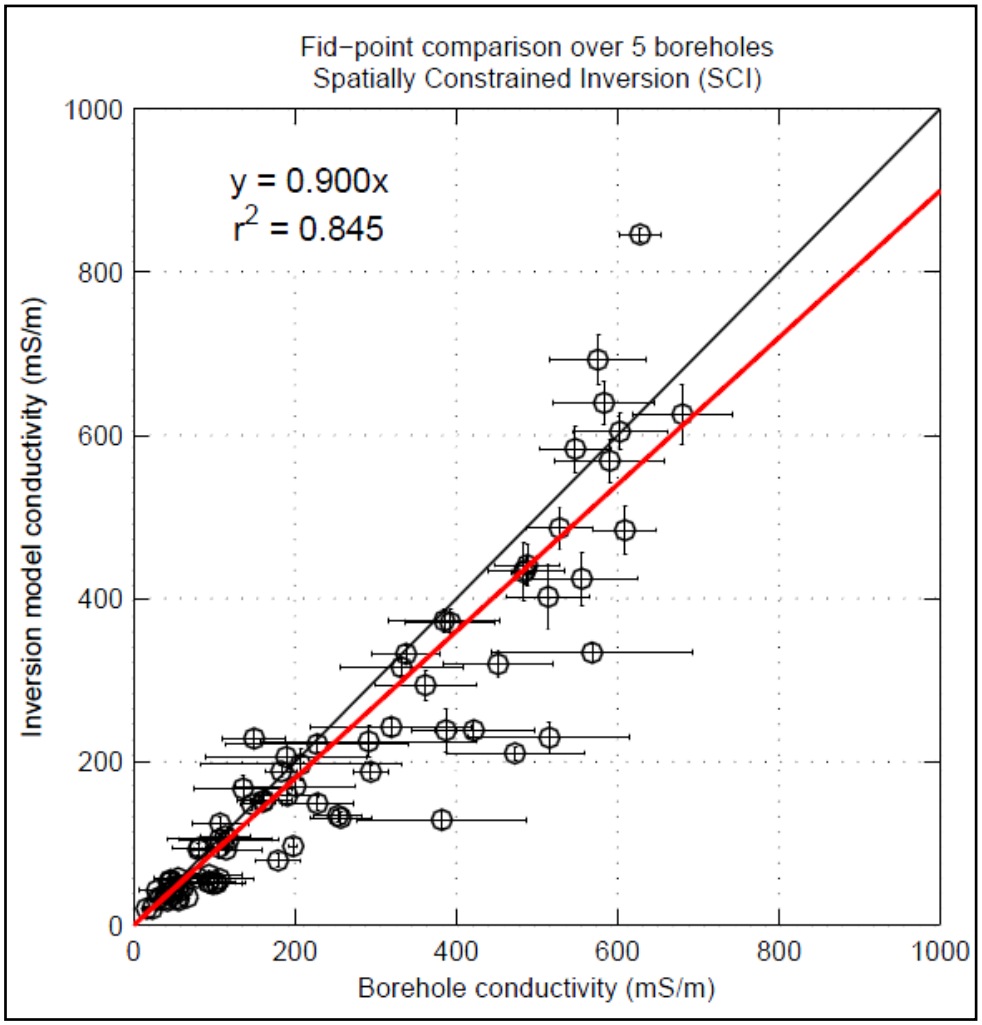



**Figure 6-35.** *Comparison of the layer-averaged borehole conductivity values to the AEM inversion conductivity values from the borehole and spatially-constrained (SCI-bore) inversion product over 5 bores in the survey area of the GWR1 target. Regression indicates that AEM conductivities are 10% lower than borehole conductivities over this area, with an excellent coefficient of determination between the data and the model assumed.*

### 6.6.4 Test Inversion of the GWR Area

The period of November 2010 to March 2011 did not bring much change to the overall inversion products, but it was realized that most of the issues with the top 20 m resolution were connected to a sub-optimal setting of the constraints. With this in mind, new SCI inversion products, limited to the GWR area, were produced in March-April 2011 with the aim of fine-tuning, i.e. reducing, the strength of the constraints to reveal more model details without starting to fit the data errors. The SCI showed marginal improvement in the top 20 m, and was used the interpretation of the priority borefield site (Figure 6-36 and Figure 6-37; Lawrie *et al*., 2011).

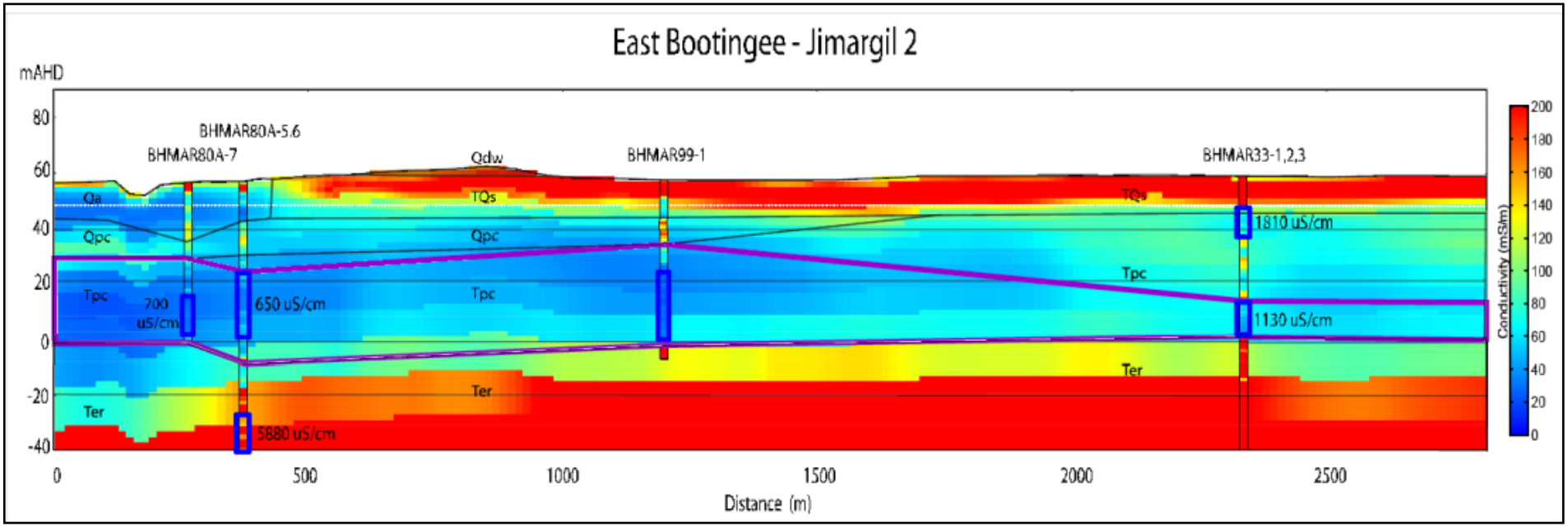



**Figure 6-36.** *LCI conductivity depth section through the Jimargil borefield site. This is a synthetic section extrapolated between flight lines (from Lawrie et al., 2011). The image shows conductivities from the LCI inversion of the AEM data overlain with borehole and salinities of groundwater in screened intervals within the Calivil Formation aquifer. There are problems with this inversion, as the image displays a generally poor correlation between the conductors at depth in the bores and the conductivity sections. The most important conductor (Qpc) appears as a weak conductor in the conductivity section, despite higher conductivities in general in the bores. Interpretations have now been superseded.*

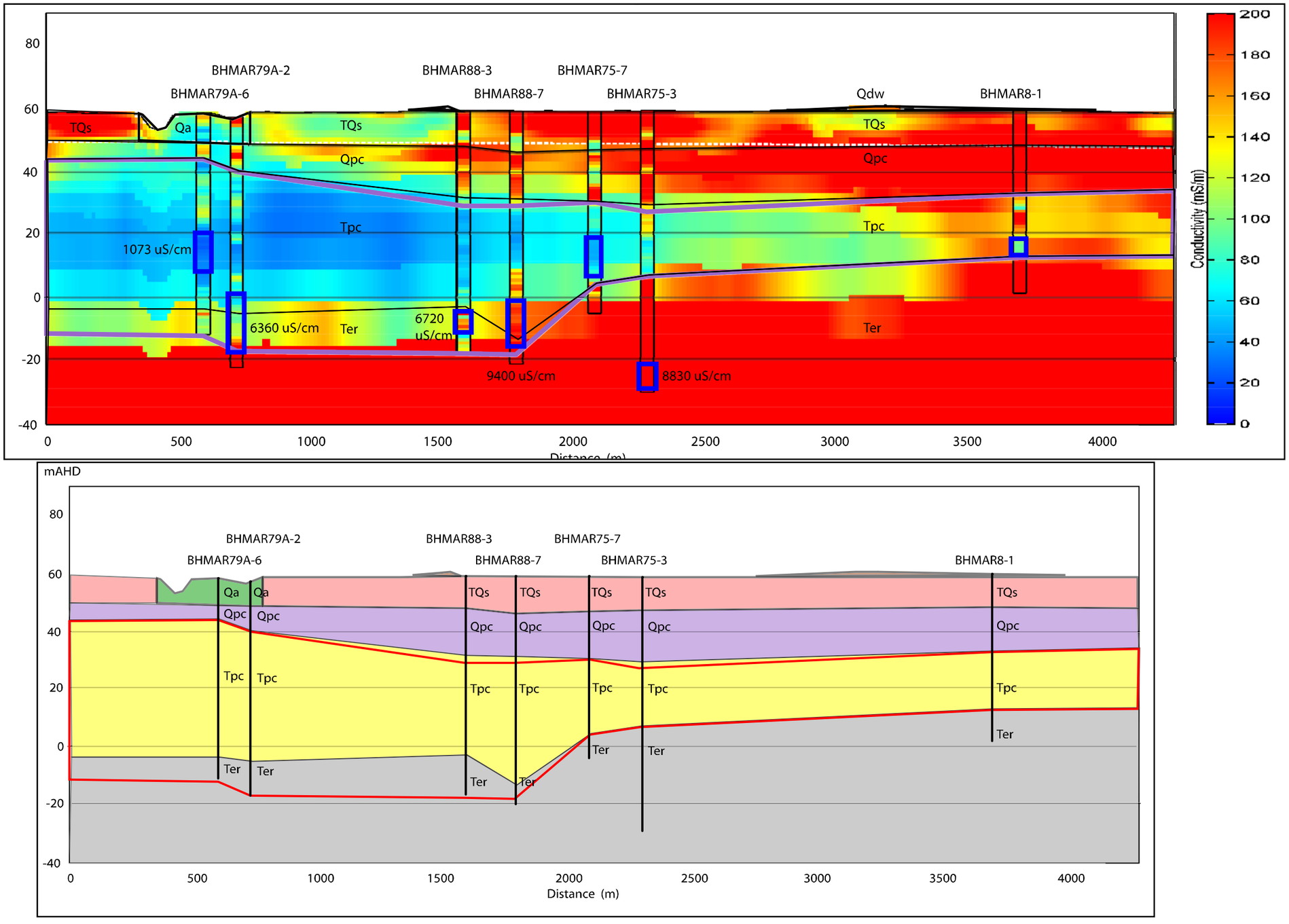



**Figure 6-37.** *East-West cross-sections through the Menindee Common borefield site. From Lawrie et al. (2011). The upper image shows conductivities from AEM data overlain with borehole and salinities of groundwater in screened intervals within the Calivil Formation /Renmark Group aquifer. The lower section shows interpreted lithologies. Tpc is the Calivil Formation, Qpc is the Blanchetown Clay, TQs is the Menindee Formation and Qa is the Coonambidgal Formation. Ter is the Renmark Group. The red line overlays define the productive aquifer boundary in this section. Interpretations have now been superseded.*

### 6.6.5 A 3D Inversion Approach

The option of 3D modelling and inversion has been a topic of considerable interest over many years, but 3D modelling is much more time consuming than 1D inversion with 3D constraints, and only recently has it become an option for major surveys. Geoscience Australia decided to investigate the 3D inversion option (Wilson *et al*., 2010).

However, the results of the 3D inversion did not show the details required for the interpretation, and beyond the initial assessment of its value the product was never used in the further practical interpretation. This can probably be attributed to an incomplete understanding of the complexities of modelling the SkyTEM system response on the part of the 3D inversion contractor.

## 6.7 FINAL (WANDA) INVERSION PRODUCTS

### 6.7.1 Introduction

In parallel with attempts to improve the SCI inversions, an inversion with an updated version of the iTEM program was carried out using the WAve Number Domain Approximate (WANDA) inversion program (Christensen, 2011). This uses a 1D multi-layer model and constraints in 3D to produce a 3D conductivity model. This inversion procedure only takes days to run, enabling the rapid trialling to select the most appropriate vertical and horizontal constraints. This was an essential feature of the inversion code, as it enabled different regularisation settings and lateral parameter correlations to be trialled.

This process of trial and error in these settings, combined with the use of borehole induction log constraints on the inversions greatly assisted with producing a final inversion that best matched the known geology and geoelectric properties derived from ground data. Figure 6-38 and Figure 6-39 show an example of this continued improvement in the inversions. Conductivity depth sections are shown for the same flight line (23421) in the Jimargil borefield area, with (from top to bottom) the original iTEM inversion, the 5-layer LCI and 19-layer LCI, the initial Christensen inversion, and the final WANDA inversion all displayed (and uncertainty plot beneath). In this figure, the layer resolution is improved with the WANDA inversion, with discrete faults observed to off-set the conductive upper aquitard layer (conductive clay layer), as denoted in the gap between the pink dots in Inversion 5. It was not possible to map these fault offsets with confidence in the previous inversions. The ability to map the upper aquitard layer and the faults off-setting this layer, has enabled both of these features to be mapped in a high level of detail (Figure 6-40). The WANDA inversion procedures are described below.

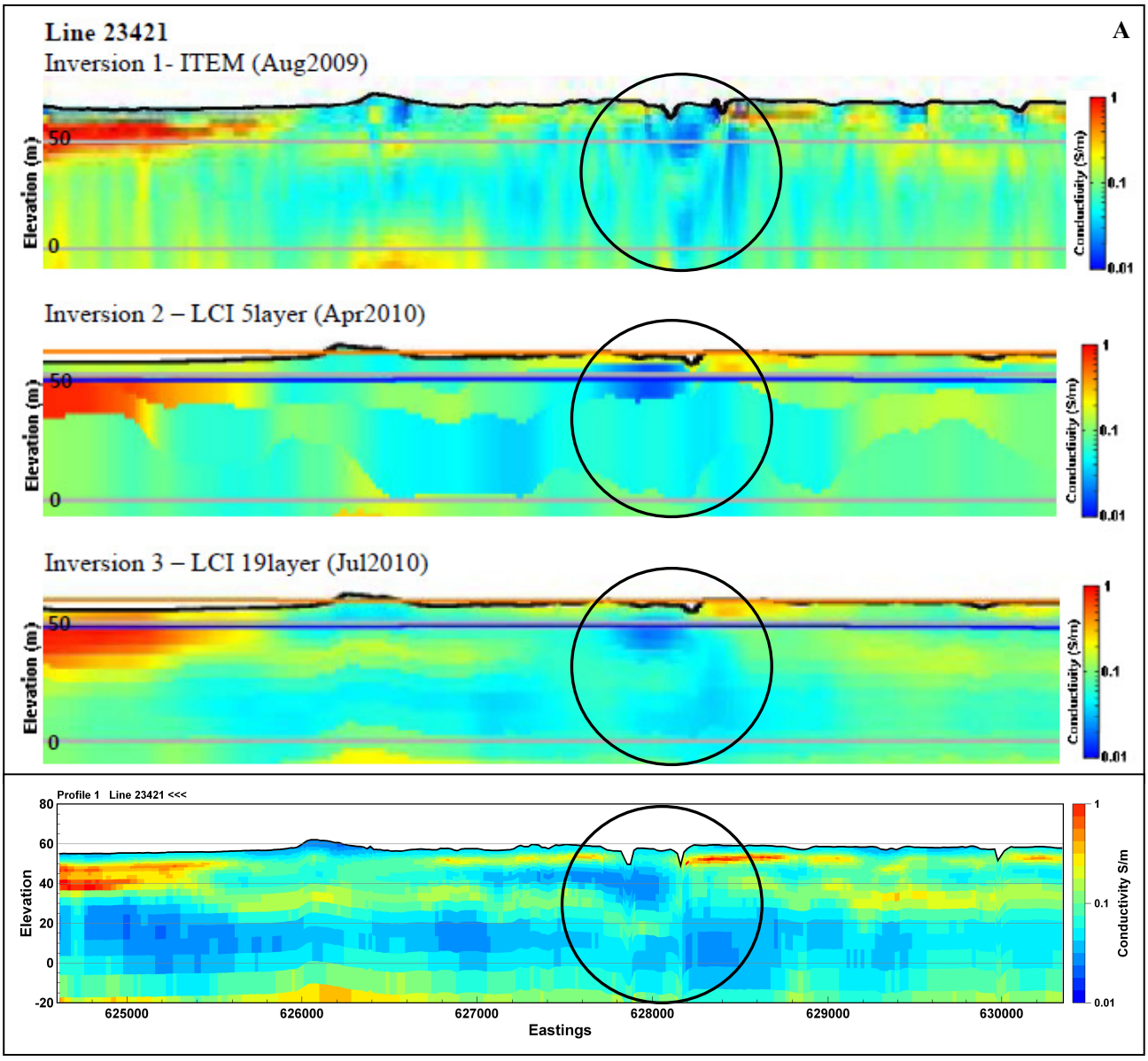



**Figure 6-38.** *Series of conductivity depth sections for one flight line (23421) showing different inversions. These four sections illustrate the improvements in mapping the hydrostratigraphy and faults by optimizing the inversion constraints. The final inversion product (bottom image) clearly shows the offset in conductive layers (clay aquitard) in the middle of the area circled. Previously, there was insufficient confidence in the layer boundary mapping to either identify or map these structures with any degree of confidence.*

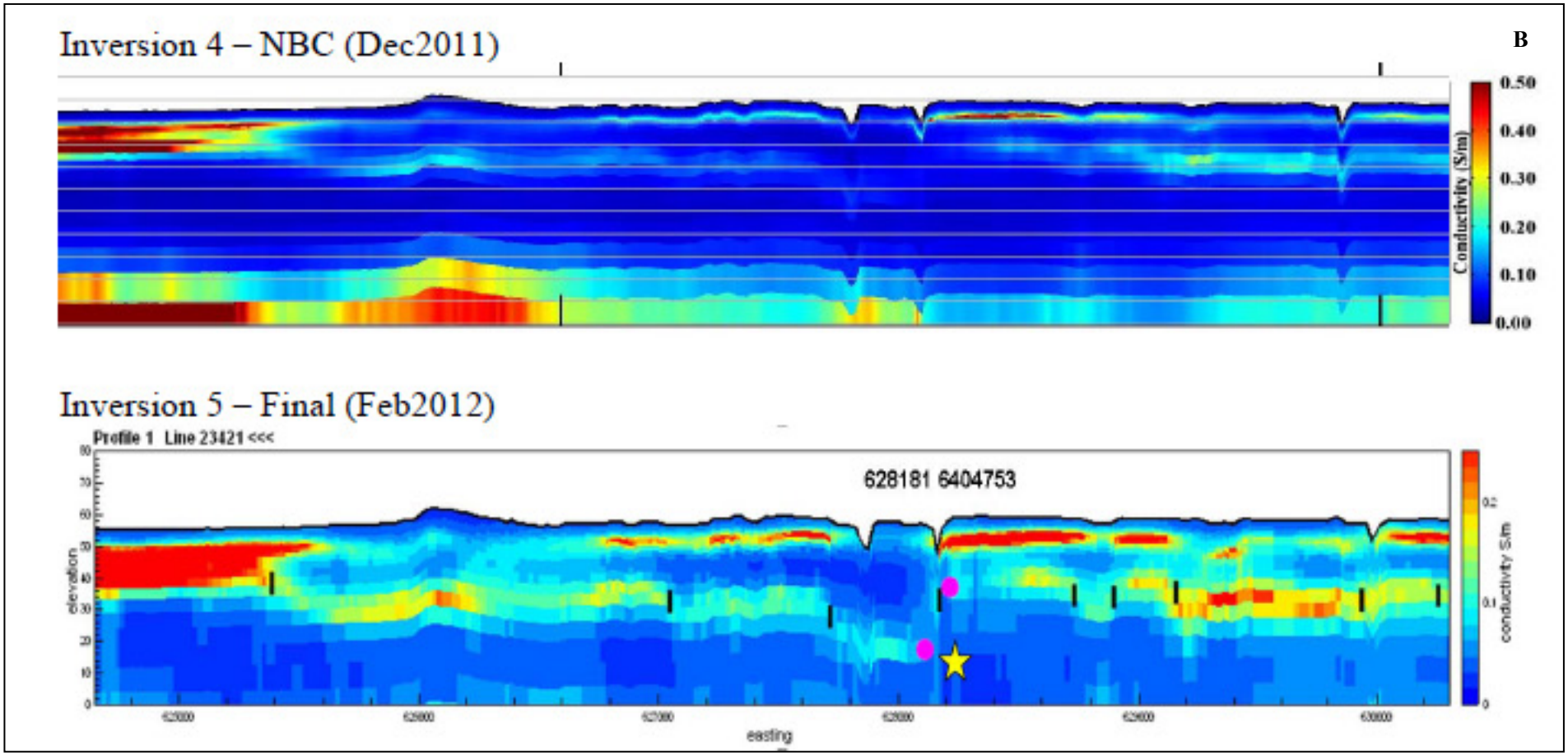



**Figure 6-39.** *Two conductivity depth sections (flight line 23421) produced using the new Wave Number Domain Approximate (WANDA) inversion procedure with a 1D multi-layer model and constraints in 3D. In contrast to Figure 6-38, discrete fault offsets are only evident in this figure. The top image was produced using standard 'tight' regularisation constraints, while the bottom section was produced using 'loose' regularisation settings. Comparison of borehole induction logs with adjacent AEM fiduciary points confirms high confidence levels in the final inversion (bottom section). The bottom image shows the location of a fault offsetting the Blanchetown Clay aquitard (pink dots). Inter-aquifer leakage is facilitated between the overlying unconfined aquifer and the Calivil Formation aquifer (yellow star) at this location.*

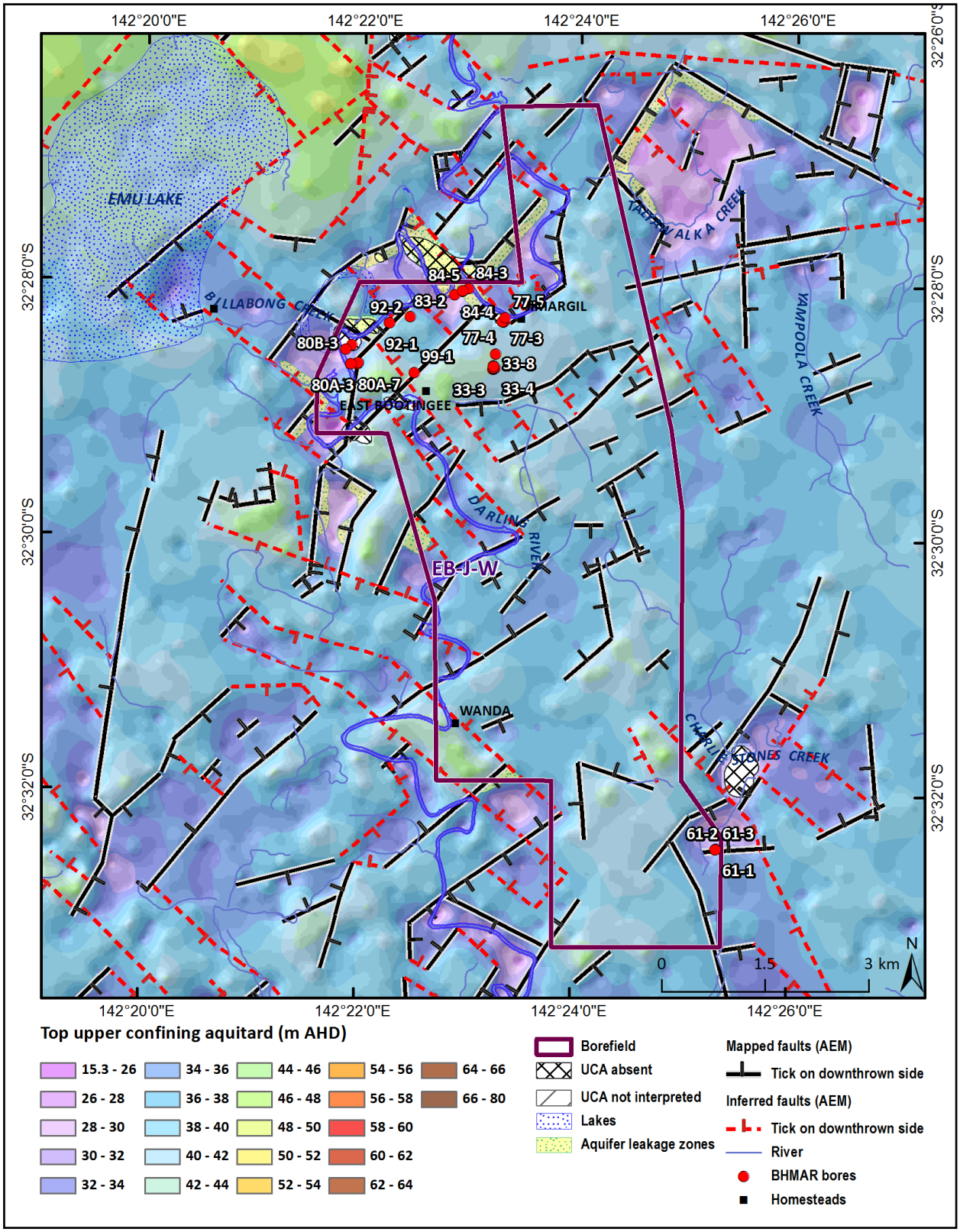



**Figure 6-40.** *Elevation of the top of the upper aquitard in m AHD showing faults in the Jimargil borefield area. Prior to the final WANDA inversion, neither the upper aquitard nor the faults could be mapped with confidence.*

### 6.7.2 Data Post-processing

In October 2011, all SkyTEM data were exported from the WB data base to column oriented, XYZ files in ASCII format. Reformatting programs were made to read the exported data files and write data in a format compatible with the inversion program. The data used in the WANDA inversion are thus exactly the data used in the WB inversion with the same time gates and the same estimates of data uncertainty.

The data exported from the WB come as separate files for the Low Moment (LM) and High Moment (HM) segments, and in the reformatting input files for each moment were created separately. Subsequently the moments were merged by choosing LM as 'principal' or guiding moment, meaning that the data at each LM data position were merged with HM data from the position closest to the LM data. Even though the positions can sometimes be separated by tens of meters, this approach can be justified by considering that the HM data represent current systems of considerably larger extent than a few tens of meters.

In the WANDA inversion of the AEM data, the actual hexagonal transmitter coil is approximated by a circular coil. Considering the shape and the height at which measurements are done, this approximation is excellent. To maintain the zero-coupled position of the z-component receiver coil of the SkyTEM system, the receiver coil is placed at the actual height relative to the transmitter loop, but in the horizontal position where it is zero coupled to the circular loop.

A 15 point piecewise liner waveform that conforms with the calibration measurements carried out during data collection was used. The waveform is found through an inversion process with the calibration measurements as data.

### 6.7.3 Final (WANDA) Inversions: Forward and Inverse Modelling, Correlation and Analysis

#### 6.7.3.1 *Forward mapping*

A generic, approximate forward mapping (Equation 8), was defined in Christensen (2002) and Christensen *et al*. (2009) based on appropriate sensitivity functions in the time/space domain. A different version of the approximate forward mapping is presented here based on the computation of the apparent conductivity in the wavenumber domain. To avoid the tongue-breaking ``wavenumber domain approximate inversion'', it has been given the acronym WANDA (WAve Number Domain Approximate) inversion.

Like the previous version of the approximate inversion, the iTEM program (Christensen, 2002; Christensen *et al*., 2009), the WANDA inversion is based on a fast approximate forward mapping from conductivity as a function of depth to step response for a 1D layered model (Equation 9). This forward mapping consists of two consecutive mappings a mapping from conductivity as a function of depth to apparent conductivity as a function of time (Equation 8), followed by a substitution of the apparent conductivity into a halfspace step response (Equation 10).

The last part of the mapping follows from the definition of apparent conductivity as the conductivity of a halfspace for which the response will be the same as the layered response at the delay time in question. The first mapping (Equation 8), is generic, i.e. it is the same for all transmitter-receiver (Tx-Rx) configurations and field components. In the second mapping (Equation 10), the halfspace response is specific for the configuration and field component in question. However, all halfspace responses need only be calculated once at program start. In the case of airborne systems, a halfspace response must be calculated for a series of transmitter heights with a proper density to allow accurate interpolation.

The WANDA inversion presented here is more accurate than the iTEM inversion and is slower only by a factor of $\approx 2$, meaning that it is 25 times faster than tradition computation methods.

Modelling of the measured instrument response in the time domain is achieved through convolutions of the step response with operators accounting for: (a) repetition, (b) a filter function defining the cut-off of the

receiver coil, (c) a filter function pertaining to the band limitation of the receiver amplifier, (d) the transmitter waveform, and (e) the integration over the gate.

$$\sigma(z) \rightarrow \sigma_a(t)$$

**Equation 8**

$$\sigma(z) \rightarrow B_L^{step}(t)$$

**Equation 9**

$$B_L^{step}(t) = B_{HSP}^{step}(t, \sigma_a(t))$$

**Equation 10**

### 6.7.3.2 *Computational details of the forward mapping*

The vertical magnetic field in the frequency domain for a receiver with polar coordinates $(r,-h)$ from a vertical magnetic dipole transmitter at a height $H$ is given as Equation 11 (Ward & Hohmann, 1987). The first term in the brackets is the primary field, while the second term expresses the secondary field. Assuming the quasi-static approximation to be valid ($u_0 = \lambda$), we have Equation 12.

$$H_z(r,z,\omega) = \frac{m}{4\pi}\int_0^\infty \left[\exp(u_0 h) + \gamma_0 \exp(-u_0 h)\right]\exp(-u_0 H)\frac{\lambda^3}{u_0} J_0(\lambda r) d\lambda$$

**Equation 11**

$$H_z(r,z,\omega) = \frac{m}{4\pi}\int_0^\infty \left[\exp(2\lambda h) + \gamma_0\right]\exp\left[-\lambda(H+h)\right]\lambda^2 J_0(\lambda r) d\lambda$$

**Equation 12**

The kernel function $\gamma_0$ (the reflection coefficient) is obtained through recursion from the bottom of the model, the $N$'th layer, and up:

$$\gamma_n = e^{-2u_n h_n}\frac{\gamma_{n+1} + \psi_{n+1}}{1 + \gamma_{n+1}\psi_{n+1}} \ , \ \gamma_N = 0 \ , h_n = z_n - z_{n-1} \ , \ h_0 = 0$$

**Equation 13**

$$\psi_{n+1} = \frac{u_n/(i\omega\mu_n) - u_{n+1}/(i\omega\mu_{n+1})}{u_n/(i\omega\mu_n) + u_{n+1}/(i\omega\mu_{n+1})} = \frac{u_n - u_{n+1}}{u_n + u_{n+1}} \text{ if all } i\omega\mu_n = i\omega\mu_0$$

**Equation 14**

$$u_n = \sqrt{\lambda^2 + i\omega\mu\sigma_n}$$

**Equation 15**

Expressing the time domain field through an inverse Laplace transform with $s = i\omega$ as the Laplace variable, we have for the step response Equation 16:

$$H_z(r,z,t) = \frac{m}{4\pi}\int_0^\infty \mathsf{L}^{-1}\left\{\frac{1}{s}\left[\exp(2\lambda h) + \gamma_0\right]\right\}\exp\left[-\lambda(H+h)\right]\lambda^2 J_0(\lambda r) d\lambda$$

**Equation 16**

For the homogeneous halfspace, this becomes Equation 17. For a homogeneous halfspace with conductivity $\sigma$, $\gamma_1 = 0$, and $\gamma_0^{HSP}$ becomes Equation 18.

$$H_z(r,z,t)=\frac{m}{4\pi}\int_0^\infty \mathsf{L}^{-1}\left\{\frac{1}{s}\left[\exp(2\lambda h)+\gamma_0^{HSP}\right]\right\}\exp\left[-\lambda(H+h)\right]\lambda^2 J_0(\lambda r)d\lambda$$

**Equation 17**

$$\gamma_0^{HSP}=\psi_{n+1}=\frac{\lambda-u_1}{\lambda+u_1}\Rightarrow 1+\gamma_0^{HSP}=\frac{2\lambda}{\lambda+\sqrt{\lambda^2+\mu\sigma s}}=\frac{2}{1+\sqrt{1+\mu\sigma s/\lambda^2}}$$

**Equation 18**

The apparent conductivity in the time/wavenumber domain for a layered model can then be defined as the conductivity for which the time/wavenumber expression for the homogeneous halfspace is equal to the one for a layered model, i.e. Equation 19 to Equation 21 where the last derivation is chosen for the sake of numerical convenience.

$$\frac{m}{4\pi}\mathsf{L}^{-1}\left\{\frac{1}{s}\left[\exp(2\lambda h)+\gamma_0\right]\right\}\exp\left[-\lambda(H+h)\right]\lambda^2 J_0(\lambda r)$$
$$=\frac{m}{4\pi}\mathsf{L}^{-1}\left\{\frac{1}{s}\left[\exp(2\lambda h)+\gamma_0^{HSP}\right]\right\}\exp\left[-\lambda(H+h)\right]\lambda^2 J_0(\lambda r)\Rightarrow$$

**Equation 19**

$$\mathsf{L}^{-1}\left\{\frac{1}{s}\left[\exp(2\lambda h)+\gamma_0\right]\right\}=\mathsf{L}^{-1}\left\{\frac{1}{s}\left[\exp(2\lambda h)+\gamma_0^{HSP}\right]\right\}\Rightarrow$$

**Equation 20**

$$\mathsf{L}^{-1}\left\{\frac{\gamma_0}{s}\right\}=\mathsf{L}^{-1}\left\{\frac{\gamma_0^{HSP}}{s}\right\}\Leftrightarrow\mathsf{L}^{-1}\left\{\frac{1}{s}\left[1+\gamma_0\right]\right\}=\mathsf{L}^{-1}\left\{\frac{1}{s}\left[1+\gamma_0^{HSP}\right]\right\}$$

**Equation 21**

The inverse Laplace transform of the halfspace expression can be found using Abramowitz & Stegun (1972).

$$\mathsf{H}_z(u)=\mathsf{L}^{-1}\left\{\frac{1}{s}\left[1+\gamma_0^{HSP}\right]\right\}=\mathsf{L}^{-1}\left\{\frac{1}{s}\frac{2}{1+\sqrt{1+\mu\sigma s/\lambda^2}}\right\}$$

**Equation 22**

$$\mathsf{H}_z(u)=\left(1+2u^2\right)\mathrm{erfc}(u)-\frac{2u}{\sqrt{\pi}}\exp\left(-u^2\right),\ u=\lambda\cdot d=\lambda\cdot\sqrt{t/(\mu\sigma)}$$

**Equation 23**

It is seen that $\gamma_0^{HSP}$ is a function of $\left(\mu\sigma s/\lambda^2\right)$ and not of the individual parameters $s$, $\sigma$ and $\lambda$, and, consequently, the time domain expression will be a function of $u=\lambda\cdot d=\lambda\cdot\sqrt{t/(\mu\sigma)}$, where $d$ has the dimension of m and is a measure of diffusion distance. A plot of the function $\mathsf{H}_z(u)$ in Equation 22 is seen in Figure 6-41.

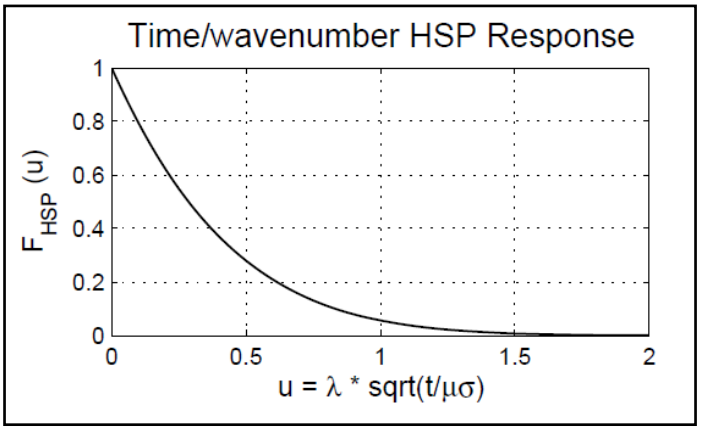



**Figure 6-41.** *Plot of the time/wavenumber domain halfspace response.*

The configuration and field component halfspace responses can now be calculated by substituting $\mathsf{H}_z(u)$ in the integral in Equation 12:

$$H_z(r,z,\omega)=\frac{m}{4\pi}\int_0^\infty \mathsf{H}_z(u)\exp[-\lambda(H+h)]\lambda^2 J_0(\lambda r)d\lambda$$

**Equation 24**

$$H_z(r,z,t)=\frac{m}{4\pi}\int_0^\infty\left[(1+2u^2)\operatorname{erfc}(u)-\frac{2u}{\sqrt{\pi}}\exp(-u^2)\right]\times\exp[-\lambda(H+h)]\lambda^2 J_0(\lambda r)d\lambda$$

**Equation 25**

$$H_z(r,z,t)=\frac{m}{4\pi}\frac{1}{d^3}\int_0^\infty\left[(1+2u^2)\operatorname{erfc}(u)-\frac{2u}{\sqrt{\pi}}\exp(-u^2)\right]\times\exp\left(-u\frac{H+h}{d}\right)u^2 J_0\left(u\frac{r}{d}\right)du$$

**Equation 26**

In the latter formulation, all distance parameters ( $h, H, r$ ) are scaled with the diffusion length $d$ . If the transmitter is an extended circular loop with radius $a$ , and not a magnetic dipole, we have Equation 27.

$$H_z(r,z,t)=\frac{m}{4\pi}\frac{1}{d^3}\int_0^\infty\left[(1+2u^2)\operatorname{erfc}(u)-\frac{2u}{\sqrt{\pi}}\exp(-u^2)\right]\times\exp\left(-u\frac{H+h}{d}\right)u^2\left[\frac{J_1\left(u\frac{a}{d}\right)}{\frac{1}{2}u\frac{a}{d}}\right]J_0\left(u\frac{r}{d}\right)du$$

**Equation 27**

The fact that the halfspace response is analytically given in the wavenumber-time domain means that the time-space expression can be calculated by performing only one transform, the Hankel transform from wavenumber to space. This transform is performed using the Fast Hankel Transform filters by Christensen (1990). This transform can be calculated to essentially any desired accuracy for a time span between nanoseconds and 100s of seconds. This combined with the fact that the approximate apparent conductivity is accurate for very early and the very late times means that layered responses can be calculated very accurately at these times. As mentioned above, the halfspace responses are calculated only once at the beginning of computations and then stored to serve as lookup tables for subsequent computations.

The above derivations concern the step response. Impulse responses can be found by numerical differentiation or by differentiation the kernel function $\mathsf{H}_z(u)$ with respect to time before transformation.

### 6.7.3.3 *Apparent conductivity in the time/wavenumber domain*

From the above it is seen that the procedure for finding the apparent conductivity in the time/wavenumber domain for a delay time, $t$, for any layered model is to recursively compute $\gamma_0$ in the Laplace/wavenumber domain, perform an inverse Laplace transform of $\left\{\frac{1}{s}[1+\gamma_0]\right\}$ and then solve to find the conductivity, $\sigma$, that will make it identical to the halfspace expression. However, the expressions for both the layered model and the halfspace contain the wavenumber, λ, so there is an apparent conductivity for every wavenumber. Our goal is to find an apparent conductivity in the time/wavenumber domain that is as close an approximation as possible to the all-time apparent conductivity for the step response in the time/space domain, so the question is if it is possible to choose a wavenumber so that this goal is achieved. It can be argued that the wavenumber should be the inverse of a typical distance in the space domain, and an obvious choice would then be a wavenumber equal to the inverse of the diffusion distance, i.e. $\lambda_a = 1/d = 1/\sqrt{t/(\mu\sigma)}$ $\lambda_a$ depends on the ratio between the delay time and the conductivity $t/\sigma$, so it remains to choose a conductivity that is proper for the delay time in question. Again, an obvious choice is the apparent conductivity for that delay time: $\sigma_a(t)$. However, the apparent conductivity is the parameter we wish to find, so the procedure becomes iterative.
To sum up, for every delay time, $t$, the procedure is the following:

- Choose an apparent conductivity for that delay time, $\sigma_a$;
- Choose the wavenumber $\lambda = \lambda_a = 1/\sqrt{t/(\mu\sigma_a)}$;
- For that wavenumber, compute $\mathsf{L}^{-1}\left\{\frac{1}{s}[1+\gamma_0]\right\}$ for the layered model;
- Solve the equation $\mathsf{L}^{-1}\left\{\frac{1}{s}[1+\gamma_0]\right\} = \mathsf{H}_z(u)$ to find $u$;
- Find the apparent conductivity, $\sigma_a$, so that $u = \lambda_a \cdot \sqrt{t/(\mu\sigma_a)}$;
- Repeat steps (1) to (5) until $\sigma_a$ does not change.

### 6.7.3.4 *Choosing the initial apparent conductivity*

To reduce the number of iterative steps in the above computation procedure, the initial apparent conductivity must be chosen as close to the final apparent conductivity as possible. This is archived by using the previous method of calculating the apparent conductivity $\sigma(z) \rightarrow \sigma_a(t)$, defined in Christensen (2002) and Christensen *et al*. (2009). This mapping is given by the integral (Equation 28) where $w(\cdot)$ is a weight function that depends on the apparent conductivity. In this way the slower diffusion through good conductors and the faster diffusion through poor conductors is taken into account, i.e. the mapping is model adaptive.

$$\sigma_a(t) = \int_0^\infty \sigma(z) \cdot w(z,t,\sigma_a(t))dz$$

**Equation 28**

For a layered earth model with $N$ layers with conductivities $\sigma_1, \sigma_2, \cdots, \sigma_N$ and upper layer boundaries $z_1, z_2, \cdots, z_N$ ; $z_1 = 0$

$$\sigma_a(t) = \sigma_1 \int_{z_1}^{z_2} w(z,t,\sigma_a(t))dz + \sigma_2 \int_{z_2}^{z_3} w(z,t,\sigma_a(t))dz + \cdots + \sigma_N \int_{z_N}^{\infty} w(z,t,\sigma_a(t))dz$$
$$= \sigma_1[1 - W(z_2)] + \sigma_2[W(z_2) - W(z_3)] + \cdots + \sigma_N[W(z_N)]$$

**Equation 29**

where $W(z,t,\sigma_a(t))$ is the integrated weight function (Equation 30). The integrated weight function is chosen as Equation 31 and the weight function, $w(\cdot)$ is consequently given by Equation 32.

$$W(z,t,\sigma) = \int_z^\infty w(z',t,\sigma)dz'$$

**Equation 30**

$$W(z,t,\sigma) = \text{erfc}(\theta z) \quad , \quad \theta = \sqrt{\frac{\mu\sigma}{ct}}$$

**Equation 31**

$$w(z,t,\sigma) = \frac{2\theta}{\sqrt{\pi}}\exp(-\theta^2 z^2)$$

**Equation 32**

The weight function defined above has continuous derivatives which makes it perform better in the convolutions necessary to model the system response. The parameter $c$ scales the depth extent of the sensitivity function and eventually the depth scaling of the resulting models after inversion. It is chosen to minimise the difference between a series of test models and the approximate inversion results (Christensen, 2002).

#### 6.7.3.5 *Calculating derivatives*

Looking at Equation 29 it is readily seen that the derivatives $\partial\sigma_a/\partial\sigma_i$ are given as Equation 33 and the derivatives of the layered step response are then given as Equation 34.

$$\frac{\partial\sigma_a}{\partial\sigma_i} = W(z_i) - W(z_{i+1})$$

**Equation 33**

$$\frac{\partial B_L^{step}(t)}{\partial\sigma_i} = \frac{\partial B_L^{step}(t)}{\partial\sigma_a}\cdot\frac{\partial\sigma_a}{\partial\sigma_i}$$

**Equation 34**

However, the layered step response is a function of $(t/\sigma)$ and not of $t$ and $\sigma$ independently, so:

$$\frac{\partial B_L^{step}(t)}{\partial\sigma_i} = \frac{t}{\sigma_a}\cdot\frac{\partial B_L^{step}(t)}{\partial t}\cdot\frac{\partial\sigma_a}{\partial\sigma_i}$$

**Equation 35**

and the derivatives are thereby given by the impulse response and the simple derivatives $\partial\sigma_a/\partial\sigma_t$ These approximate derivatives are used in the inversion of the BHMAR AEM data.

#### 6.7.3.6 *Accuracy of the new method*

The accuracy of the WANDA inversion method is determined by the accuracy of the apparent conductivity computation. In Figure 6-42 the accuracy is illustrated by comparing the WANDA step responses with the exact step responses of 2-layer and 3-layer models.

To further verify the WANDA inversion approach, 1,000 random 30-layer models with a top layer thickness of 1 m and a depth to the bottom layer of 500 m were created as realizations of a random stochastic process by multiplying the squareroot of a covariance matrix with a vector of Gaussian distributed random numbers. The covariance matrix of the realizations is based on the same broadband covariance function as the one used in the regularisation of the inversions. Realizations were done in log(conductivity) with a mean of

log(50 mS/m) and a standard deviation of the perturbation of 0.6. This results in models with conductivities reaching well above 1,000 and below 1 mS/m.

The WANDA apparent conductivity response was compared with an accurate computation for all 1,000 models and resulted in a mean error of 1.4 % with a standard deviation of 2.4 %. These numbers should be related to the noise level of the data which is considerably higher.

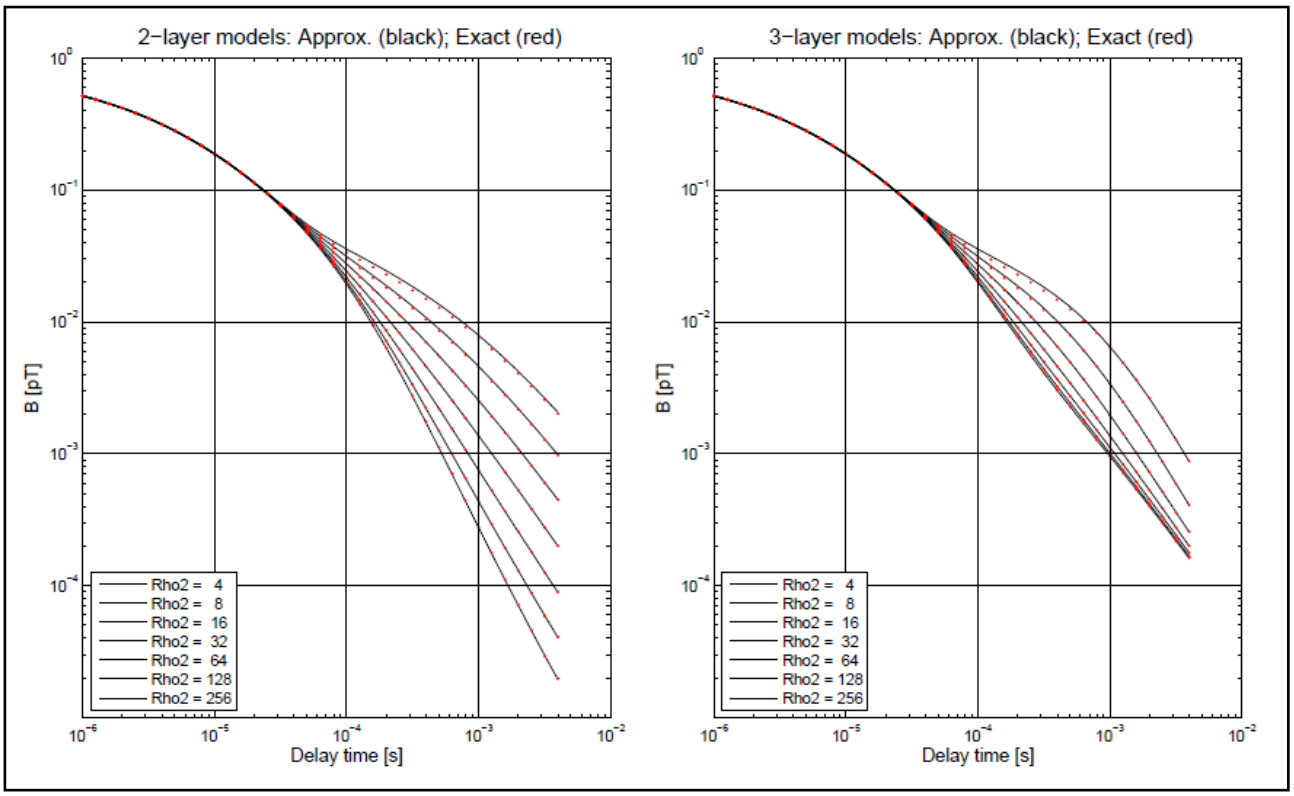



**Figure 6-42.** *Comparison between the WANDA step responses and the exact step responses. The configuration is a central loop system at a height of 30 m with a circular Tx coil with a radius of 10 m. Left: 2-layer ascending and descending curves. Right: maximum and minimum curves. The resistivity of the first layer is 32 Ω m for both 2- and 3-layer models and the resistivity of the bottom layer of the 3-layer models is also 32 Ω m.*

### 6.7.3.7 *Modelling the system response*

Modelling of the measured instrument response in the time domain is achieved through convolutions of the step response with operators accounting for:

- Repetition;
- a filter function defining the cut-off of the receiver coil;
- a filter function pertaining to the band limitation of the receiver amplifier;
- the transmitter waveform; and
- the integration over the gate.

These calculations and how to find the derivatives with respect to model parameters are explained in Christensen (2002) and Christensen *et al*. (2009) and will not be repeated here.

### 6.7.3.8 *Inversion methodology*

There are numerous approaches to the inversion of EM data with a 1D model consisting of horizontal, homogeneous and isotropic layers. The one used in the WANDA inversion method is a well-established iterative damped least squares approach (Menke, 1989). Formally, the model update at the *n*th iteration is given by Equation 36 where $\mathbf{m}$ is the model vector containing the logarithm of the model parameters, $\mathbf{G}$ is the Jacobian matrix containing the derivatives of the data with respect to the model parameters, $T$ is the matrix transpose, $\mathbf{C}_{obs}$ is the data error covariance matrix, $\mathbf{C}_m$ is a model covariance matrix imposing a vertical smoothness constraint on multi-layer models, $\mathbf{d}_{obs}$ is the field data vector, $\mathbf{g}(\mathbf{m}_n)$ is the non-linear forward response vector of the *n*th model, $\mathbf{m}_{prior}$ is the prior model vector, and $1/\sigma_v$. In this study, as is most often the case, the data noise is assumed to be uncorrelated, implying that $\mathbf{C}_{obs}$ is a diagonal matrix.

$$\mathbf{m}_{n+1} = \mathbf{m}_n + \left[ \mathbf{G}_n^T \mathbf{C}_{obs}^{-1} \mathbf{G}_n + \frac{1}{\sigma_v^2} \mathbf{C}_m^{-1} \right] \cdot \left[ \mathbf{G}_n^T \mathbf{C}_{obs}^{-1} (\mathbf{d}_{obs} - \mathbf{g}(\mathbf{m}_n)) + \frac{1}{\sigma_v^2} \mathbf{C}_m^{-1} (\mathbf{m}_{prior} - \mathbf{m}_n) \right]$$

**Equation 36**

The model parameter uncertainty estimate relies on a linear approximation to the posterior covariance matrix, $\mathbf{C}_{est}$ given by Equation 37 where $\mathbf{G}$ is based on the model achieved after the last iteration. The analysis is expressed through the standard deviations of the model parameters obtained as the square root of the diagonal elements of $\mathbf{C}_{est}$ (e.g. Inman *et al.*, 1975).

$$\mathbf{C}_{est} = \left[ \mathbf{G}^T \mathbf{C}_{obs}^{-1} \mathbf{G} + \frac{1}{\sigma_v^2} \mathbf{C}_m^{-1} \right]^{-1}$$

**Equation 37**

### 6.7.3.9 *The multi-layer model*

The model used in the inversion is a multi-layer model, sometimes called a ``smooth'' model, where the subsurface is divided into a large number of layers. In the iterative inversion, the layer boundaries are kept fixed and only the layer conductivities are changed in the inversion. In this study, a 30-layer model is used where the depths to the layer boundaries increase downwards as a hyperbolic sine of the layer number. In this way, the depths to the layer boundaries increase linearly for small depths so that the top layers are all of approximately the same thickness, and the depths to the layer boundaries increase exponentially at large depths so that the thickness of a layer is a factor times the previous one.

In general, the thickness of the top layer and the depth to the lowest layer boundary must be chosen according to the survey aims and the expected depth of investigation for a given system configuration. In this survey, the 30-layer model has a top layer of 0.5 m and the deepest layer boundary is at a depth of 200 m. The asymptotic exponential factor is 1.18, corresponding to 13.6 layers per decade. The initial– and prior - model for the inversion is a homogeneous half-space with a conductivity of 0.1 S/m.

In the inversion with a multi-layer model, constraints are needed to invoke vertical smoothness of the resulting model; otherwise geologically very unlikely models can result from using the over-parameterised multi-layer model. The vertical smoothness is imposed through the model covariance matrix $\mathbf{C}_m$.

### 6.7.3.10 *The model covariance matrix*

We shall adopt a model covariance matrix based on a von Karman covariance function. The general expression for these functions is:

$$\Phi_{\nu,L}(z) = \sigma_\nu{}^2 \frac{2^{1-\nu}}{\Gamma(\nu)} \left( \frac{|z|}{L} \right)^\nu K_\nu \left( \frac{|z|}{L} \right)$$

**Equation 38**

where $K_\nu$ is the modified Bessel function of the second kind and order $\nu$, $\Gamma$ is the gamma function, $L$ is the maximum correlation length accounted for and $\sigma$ controls the amplitude. For $\nu \to 0$, the von Karman function effectively contains all correlation lengths due to the logarithmic singularity of $K_0$. This broadband behaviour ensures superior robustness in the inversion, i.e. model structure on all scales will be permitted if required by the data, and it makes the regularisation imposed by the model covariance matrix insensitive to the discretisation (Serban & Jacobsen, 2001).

The elements of the covariance matrix, $c_{ij}$, pertaining to the correlation between layer *i* and layer *j* are then given by the double integral over the layers:

$$c_{ij} = \int_{z_{i1}}^{z_{i2}} dz \int_{z_{j1}}^{z_{j2}} \Phi_{\nu,L}(|z - z'|) dz'$$

**Equation 39**

where the depths $z_{i1}$ and $z_{i2}$ define the $i'$ th layer and $z_{j1}$ and $z_{j2}$ define the $j'$ th layer.

A good approximation to the von Karman functions that allows rapid calculation and analytical integration over model elements can be achieved by stacking single-scale exponential covariance functions with different correlation lengths (Serban & Jacobsen, 2001):

$$\Phi_{\nu,L_N} \approx \sigma_\nu^2 \sum_{n=0}^{N} C^{n \cdot \nu} \exp\left( - \frac{|z|}{C^n L_N \cdot 0.65} \right)$$

**Equation 40**

$L_N$ is the maximum correlation length represented, $C$ is the factor ($C < 1$) between the correlation lengths, $N$ is the number of stacked single-scale covariance functions and $\sigma_\nu$ is the standard deviation of the correlation. The factor 0.65 in the exponential denominator is an empirical factor that ensures the fit to the von Karman function. The resulting stacked covariance function is essentially free of correlation scale. The lower and upper limits of the correlation lengths are a mathematical convenience and do not influence the correlation properties at the distance scales typically studied.

In this study, the parameters $\nu = 0.1$, $C = 0.1$, $L_N = 10{,}000$ km and $N = 9$ have been used. This means that the covariance function will contain correlation lengths between 6,500 km and 6.5 cm, one per decade. This covers scales of geological variability between the radius of the Earth and small stones; clearly sufficient for the resolution capability of airborne TEM data. Notice that the model covariance matrix only depends on the geometry of the multi-layer model and so it needs to be calculated and inverted only once.

The same broadband covariance matrix is used for the lateral correlation (see Section 6.7.3.11) as for the vertical smoothness. Using the broadband covariance matrix is equivalent to an assumption that the variability of the geology is fractal, and using the same for vertical and horizontal regularisation means that there are no assumptions that the type of variability of conductivity in the vertical and horizontal directions are different, but they can be ascribed different standard deviations, $\sigma_v$ and $\sigma_h$.

The parameter controlling the strength of the regularisation, $\sigma_v$ in Equation 36, Equation 37 and Equation 38 must be given a value that strikes a compromise between smoothness and resolution and it is chosen pragmatically by inspecting the results of different choices. A study was carried out to optimise the choice of $\sigma_v$ and it was found that a value of $\sigma_v = 4$ was appropriate; for details see below. In the inversion of all BHMAR data sets, the same value has been used throughout.

#### 6.7.3.11 *Lateral parameter correlation*

Because of the local character of the data noise in space and time, individual inversion of the sounding data does not ensure lateral continuity of the model sections. However, based on the results of previous investigations in the Broken Hill area, lateral changes in conductivity are expected to be small and it is therefore reasonable to impose continuity by lateral correlation of the models. Techniques for lateral correlation of 1D earth models have been presented in the literature (e.g. Gyulai & Ormos, 1999; Auken & Christiansen, 2004; Brodie & Sambridge, 2006). In this report, we use the Lateral Parameter Correlation (LPC) procedure of Christensen & Tølbøll (2009) for correlating models along the profiles.

The fundamental characteristic of the LPC method is that it separates the inversion from the lateral correlation. A total of three steps are involved in the inversion and lateral correlation of the inversion models:

(1) Individual inversion of every sounding with multi-layer models and vertical smoothness constraints.

(2) Lateral correlation using the LPC method.

(3) A final individual inversion of data identical to step (1), but with the smooth, correlated models as prior models. The variance of the prior is determined in the LPC procedure in step (2).

This makes the method much faster than other methods of lateral correlation relying on a simultaneous inversion of a large number of soundings including lateral constraints in every iterative step. As shown in Christensen & Tølbøll (2009), the LPC method has the desired effect that well determined parameters have more influence on the correlated models than poorly determined parameters.

The LPC method is very flexible in correlating models from different geophysical methods: AEM, ground based resistivity, borehole logs, etc., because it relates only to the models themselves in terms of their location coordinates, their parameter values and their uncertainty. A method of discretisation of the correlation area into smaller, computationally feasible areas while retaining information from all models has been developed and is explained in further detail in Christensen (2012).

For practical purposes, the entire BHMAR data set was divided into 27 subareas to avoid excessively large output files. Area 2 (in the original reference to subareas 1-4 of the BHMAR data set) was divided into 3 subareas, Area 1 into 18 sub-areas, Area 3 into 5 sub-sections and Area 4 is just one subarea. In the lateral correlation of the soundings of one subarea, two adjacent subareas to all sides have been included in the correlation plus the complete set of 92 borehole conductivity log models. This ensures that all soundings and logs that could possibly have an influence on the correlation are included. See also the Section 7 on borehole conductivity logs and data post processing.

#### 6.7.3.12 *Details of the lateral parameter correlation*

Having obtained a model section consisting of individually inverted models, all with the same number of layers, the correlation is carried out on the model parameters, one layer at a time, i.e. first all the resistivities of the first layer, then the resistivities of the second layer, etc. Correlation can be done on layer conductivities or log(resistivities), layer thicknesses and depths to or elevation of layer boundaries, but, evidently, for multi-layer models only on conductivities or log(resistivities). The values of the selected parameter for all models are collected in the parameter vector $\mathbf{p}$. The correlation is formulated as a constrained inversion problem where $\mathbf{p}$ plays the role of the data vector and the model vector that we wish to find, $\mathbf{p}_{cor}$, is a smoother version of $\mathbf{p}$. The forward mapping between $\mathbf{p}$ and $\mathbf{p}_{cor}$ is given by:

$$\mathbf{p} = \mathbf{I}\mathbf{p}_{cor} + \mathbf{e}$$

**Equation 41**

where $\mathbf{I}$ is the identity matrix and $\mathbf{e}$ is the observational error. The smoothing is realised by inverting the above relationship incorporating a model covariance matrix $\mathbf{C}_m$. In the present study, we have used the broadband covariance matrix defined in Equation 41 that is also used for the vertical regularisation of the multi-layer models. With no a priori constraints on $\mathbf{p}_{cor}$ the inversion of (B1) gives as Equation 42.

$$\mathbf{p}_{cor} = \left( \mathbf{I}^T \mathbf{C}_p^{-1} \mathbf{I} + \frac{1}{\sigma_h^2} \mathbf{C}_m^{-1} \right)^{-1} \mathbf{I}^T \mathbf{C}_p^{-1} \mathbf{p} = \left( \mathbf{C}_p^{-1} + \frac{1}{\sigma_h^2} \mathbf{C}_m^{-1} \right)^{-1} \mathbf{C}_p^{-1} \mathbf{p}$$

**Equation 42**

$\mathbf{C}_p$ is a diagonal error covariance matrix of the uncorrelated parameters which are identical to the diagonal elements of the posterior covariance matrix of the individual inversions. The posterior standard deviations of the correlated model parameters are finally estimated as the square root of the diagonal elements of the posterior covariance matrix $\mathbf{C}_{est}$ given as Equation 43.

$$\mathbf{C}_{est} = \left( \mathbf{C}_p^{-1} + \frac{1}{\sigma_h^2} \mathbf{C}_m^{-1} \right)^{-1}$$

**Equation 43**

As mentioned, the inversion problem is solved for each parameter separately. In an earlier version of the program, the model parameter values were correlated one layer at a time. This meant that the correlation would follow the layer and thereby the topography and this could have the effect that the formations in the correlated model sections would appear to follow the topography.

Most often, the adverse effects of this approach would appear for conductive layers; these have a smaller uncertainty than resistive layers and can therefore dominate the correlation and extend their presence along the layer, following the topography.

This can be in accordance with the actual geology, but certainly not always, so a new approach to the correlation was developed. In this approach, for every position along the profile and for every layer, the elevation interval of the layer is projected unto all other model positions, and the parameter is correlated with the average of the parameter values in this elevation interval for all other model positions involved in the correlation. In this way, it is ensured that correlation is truly horizontal.

The average value of the parameter over an elevation interval is calculated as shown in Equation 44 where $\mathbf{f}$ is the vector containing the fraction of the layers coinciding with the elevation interval. The variance of the average is calculated as shown in Equation 45 where $T$ indicates transpose and $\mathbf{C}_{est}^{inv}$ is the posterior covariance matrix of the individual inversions.

$$< p >= \mathbf{f} \cdot \log(\boldsymbol{\rho})$$

**Equation 44**

$$\mathrm{var} < p >= \mathbf{f}^T \mathbf{C}_{est}^{inv} \mathbf{f}$$

**Equation 45**

Once the correlation is done for each layer at a certain position, the process is repeated for the next position. Compared with the former methodology, the latter one is slower by a factor equal to the number of models in a correlation interval (see below). However, it represents a genuine improvement over the previous approach and the increased computation time does not make the problem intractable.

For large data sets the inversion problem may become quite large and the solution thereby time consuming. This is, however, remedied by the method of tiling the plane explained below.

As a consequence of the smoothing involved in the correlation process, the correlated models do not generally fit the data as well as the uncorrelated models. To remedy this, without giving up the smoothness of the correlated models, a subsequent constrained inversion of the data is performed with the correlated values $\mathbf{p}_{cor}$ as a priori model parameters with a diagonal covariance matrix for the prior values defined by the diagonal of $\mathbf{C}_{est}^{cor}$. The residuals after the final inversion are generally somewhat higher than the residuals of the indivdual inversion, but that is to be expected given the constraints imposed on the models.

The lateral parameter correlation method does not depend on data lying on a straight line or being equidistant because the model covariance matrix is based on the actual lateral distance between the models.

#### 6.7.3.13 *Correlation of models from multiple methods*

The LPC method correlates models and so it is of no importance where the models come from, i.e. they can be inversion results from different geophysical methods, e.g. airborne EM, ground resistivity, and borehole logs. All that is required is that the model parameters come with an estimate of their uncertainty. This makes the LPC method quite flexible for correlating all geophysical information within an area. In the entire BHMAR area, models from AEM and borehole conductivity logs have been correlated with one another. The same 30-layer inversion model is used for both AEM and for the borehole models.

#### 6.7.3.14 *Tiling the plane*

The optimal way of correlation is to include all models of the survey in the correlation, but for large surveys, the inversion problem solved in the LPC procedure becomes intractable, both with regard to storage and computation time. Often this problem is circumvented by dividing the survey area into subareas that can be handled within a reasonable time and then correlate all subareas (Viezzoli *et al*., 2008, 2009). Some overlap is needed between the subareas to avoid edge effects, but even if such overlap is implemented, the information from the soundings outside of the area is not included. This means that the long-wavelength behaviour of the correlated parameters will not be able to influence the correlation, though ideally it should.

In this study, a different approach is taken that at the same time ensures that information from all models is included in the correlation and that the inversion problem is of a tractable size. The dilemma can be solved by observing that the correlation effect of parameters at long distances from the central correlation subarea is transferred primarily through averages, i.e. a group of models, binned and averaged into an average model at an average position, will exert their influence on the correlation in much the same way as if they had been included individually. By binning models within subareas of increasing size with distance, it is possible to make all the information in the survey area contribute and still keep the size of the computations involved in the correlation at a reasonable level.

The approach taken here relates to profile-oriented data and defines a line interval in which the models are all included in the correlation individually. For every correlation interval, the subareas over which averages will be made are defined by two sets of orthogonal lines: one defining a constant distance to the correlation line interval and one set perpendicular to them (see Figure 6-43). Within the strip of the plane defined by the two lines passing through the end points of the correlation interval and perpendicular to the line segment, the lines defining constant distance are lines parallel to the correlation interval line segment. Outside of this strip, the equidistance curves will be semicircles with centres at the correlation interval end points. In the strip, the perpendicular lines are perpendicular to the correlation interval line segment and outside of the strip, they are radii passing through the end points of the correlation interval.

The increasing size of the subareas with distance from the correlation interval is implemented by selecting the distance between dividing lines to be the Fibonacci sequence of integer numbers multiplied with a natural

distance unit defined as the average distance between soundings in the correlation interval. In the strip, in the direction parallel to the correlation line, the subareas are further defined as being of a size that is equal to the Fibonacci number of the line closest to the correlation interval. Asymptotically, the Fibonacci sequence represents an exponential increase in distances with a factor equal to the golden rule: $\left(1+\sqrt{5}\right)/2 \approx 1.618$. Because the distance unit is defined locally, the discretisation is capable of adapting to changes in the density of models on a profile line. In the circular regions, the full circle is divided into 14 subsections. This will give the circular areas approximately the same area as the rectangular ones at the same padding level.

Numerical experiments have shown that, even without overlap, models at the edge of the correlation interval will be almost equal to the ones obtained if the whole line was one correlation interval with differences typically smaller than 1-2%. Considering that the models are initial and prior models for a subsequent last inversion, the difference is of no significance.

The tessellation of the plane defined above can be applied in both 1D and 2D correlation. In 1D correlation, only the points on the profile line outside the correlation line interval are averaged in padding cells. In 2D correlation, all points in the plane are included in the averages over the padding cells. All the Broken Hill correlations have been done as 2D correlations.

For practical purposes, the entire BHMAR data set was divided into 27 subareas to avoid excessively large output files. Area 2 (in the original reference to subareas 1-4 of the BHMAR data set) was divided into 3 subareas, Area 1 into 18 subarea, Area 3 into 5 subsections and Area 4 is just one subarea. In the lateral correlation of the soundings of one subarea, two adjacent subareas to all sides have been included in the correlation plus the complete set of 92 borehole conductivity log models. This ensured that all soundings and logs that could possibly have an influence on the correlation were included. See also Section 7 on borehole conductivity logs and data post processing.

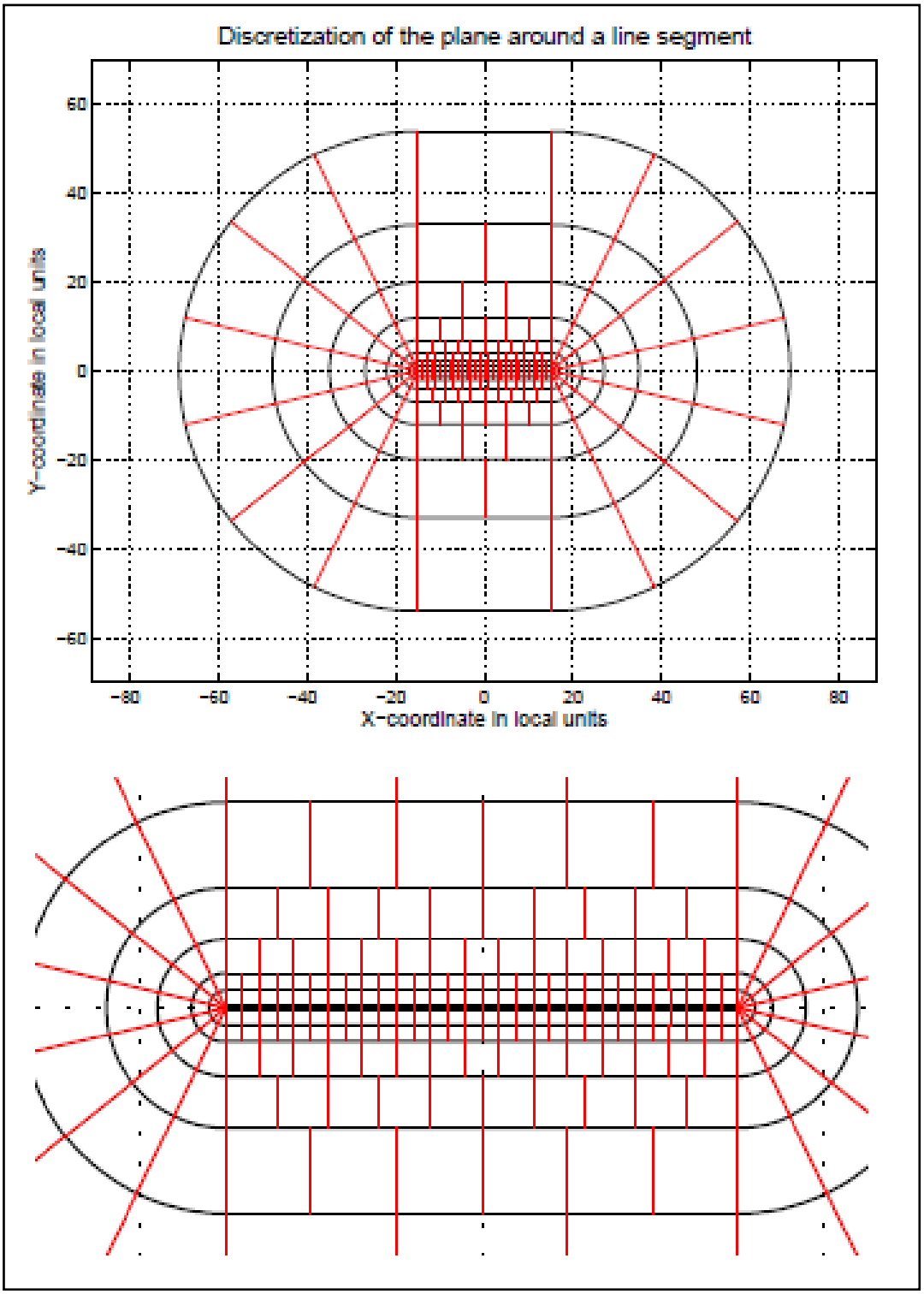



**Figure 6-43.** *The discretisation of the plane around a line segment of length 30 units. The first 8 distance levels are shown (top) with a magnified view of the inner levels (bottom).*

#### 6.7.3.15 *AEM data inversion - choosing the constraints*

One of the primary aims of the re-inversion of the entire BHMAR data set is to improve the resolution of the top 25 m of the subsurface. With this in mind, numerical experiments were conducted to find the optimal choice of vertical and horizontal constraints for selected flight lines in the GWR area, and subsequently the same parameters have been used in the inversion of the entire BHMAR data set. The optimisation effort aimed at finding a setting that was as loose as possible to enhance the conductivity structures that would

emerge in the inversion, while still maintaining stability and avoiding spurious model details resulting from fitting the noise.

In Figure 6-44, StdVer ($\sigma_v$ in Equation 38) and StdHor ($\sigma_h$) refer to standard deviations of the vertical and the horizontal regularisation, respectively; the smaller the number, the tighter the constraint. The figure shows selected model sections among the many combinations tried. In the initial calibration study, the combination of $\sigma_v = 4$ for the vertical and $\sigma_h = 0.6$ for the horizontal constraints were chosen as the best compromise, primarily because it enhances the definition of the second conductive layer. Subsequently, further studies showed that $\sigma_h = 0.7$ was a better choice, and this value has therefore been used throughout.

Choosing the same values of $\sigma_v$ and $\sigma_h$ for the whole survey means that, some parts of the survey could be under-regularised, meaning that model sections might contain characteristics stemming from fitting the data noise; while other parts could be over-regularised, meaning that marginally significant model details might be missing from the model sections. However, experience shows that the broad-band covariance functions used in the vertical and horizontal correlation is stable and robust, so only minor problems with under- and over-regularization are expected.

The selection process for the strengths of the constraints has at its core a pragmatic choice based on experience and discernment and exercised by the interpreter based on an inspection of the consequences of different choices of the constraints for a series of model sections.

#### 6.7.3.16 *Statistical analysis of model properties*

Inversion of an individual data set results in a single final model, and though the final model is the one best fitting the data, it only represents one model among all the equivalent models, i.e. the models that fit the data within the data uncertainty. The off-diagonal elements, the covariances, of the posterior covariance matrix carry information about the coupling between model parameters, i.e. they describe how the other model parameters would change so as to best maintain the ability of the model to fit the data if one parameter is perturbed. This information is what characterises the equivalent models.

A traditional way of sampling the space of equivalent models is to perturb the inversion model and calculate the forward response of the perturbed model (Monte Carlo (MC) methods). The perturbed model is accepted as belonging to the set of equivalent models if the increase in residual is below a certain limit. A different - and much faster approach - to sampling the space of equivalent models consists in multiplying the square root of the posterior covariance matrix with a vector of Gaussian distributed random elements with zero mean and a standard deviation of unity (Tarantola, 1987) to produce a vector of model perturbation that is added to the inversion model. Repeated a large number of times, the models constructed in this way will span the set of equivalent models. Inversion and analysis, and consequently the posterior covariance matrix, refer to the logarithm of the resistivity, so:

$$\Delta\log\mathbf{p} = \sqrt{\mathbf{C}_{est}}\,\mathbf{r}_g \Rightarrow \log\mathbf{p}_{eq} = \log\mathbf{p} + \Delta\log\mathbf{p} \Rightarrow \mathbf{p}_{eq} = \mathbf{p}\cdot\exp\left(\Delta\log\mathbf{p}\right)$$

**Equation 46**

where $\mathbf{p}$ is the parameter vector (the MLM layer resistivities) and $\mathbf{r}_g$ is the Gaussian distributed random vector. Numerical experiments have shown that 1,000 realisations are enough to produce a representative sampling of the set of equivalent models. The covariance matrix is derived under an assumption of linearity, and the set of equivalent models is thus an approximation to the true distribution that could be found in a MC method, but it still contains multidimensional information not contained in the parameter variances.

The idea behind finding statistical estimates of the position of geoelectrical formation boundaries is to analyse the set of equivalent models in terms of whether they fulfil a certain explicit criterion or not. We consider three main types of criteria, namely:

- What is the likelihood that the resistivity of this layer is above (below) a limiting value?

- What is the likelihood that the resistivity of this layer lies in a certain interval?
- What is the likelihood that the resistivity is above (below) a limiting value all the way from the bottom and up (or all the way from the top and down) to the layer boundary?

Questions of the first type will delineate the occurrence of resistivities above (below) a limiting value and thereby identify the vertical and lateral extent of formations that fulfil the criterion when all models of a model section are analysed. Questions of the second type can be viewed as consisting of two criteria of the first type. Questions of the third type will give estimates of the position of layer boundaries between formation with resistivities above (below) the limiting value; it is a cumulative criterion relative to the first type.

For each of the realisations, the layers that fulfil the criterion (analysis of the first type) are counted and the likelihood is then given as the ratio between the number of models fulfilling the criterion and the total number. For criteria of the second type, the likelihood will be the product of the likelihoods of the two composite criteria. If an analysis of the third type is what is needed, the likelihoods of finding the criterion fulfilled, e.g. down to a certain layer boundary counting from above, are found by multiplying the likelihoods that the criterion is fulfilled by all layers down to that boundary, e.g.:

$$P\left(\rho < \rho_{lim} \text{forall} z < z_i\right) = \prod_{j=1}^{i} P\left(\rho_j < \rho_{lim}\right)$$

**Equation 47**

A layer boundary is then defined as the depth where the likelihood is equal to a certain limiting value, in the following (arbitrarily) set to 0.5. See also Christensen (2011; 2012). In Figure 6-45, the three plot frames illustrate the behaviour of the likelihood estimates when the limiting resistivity is varied.

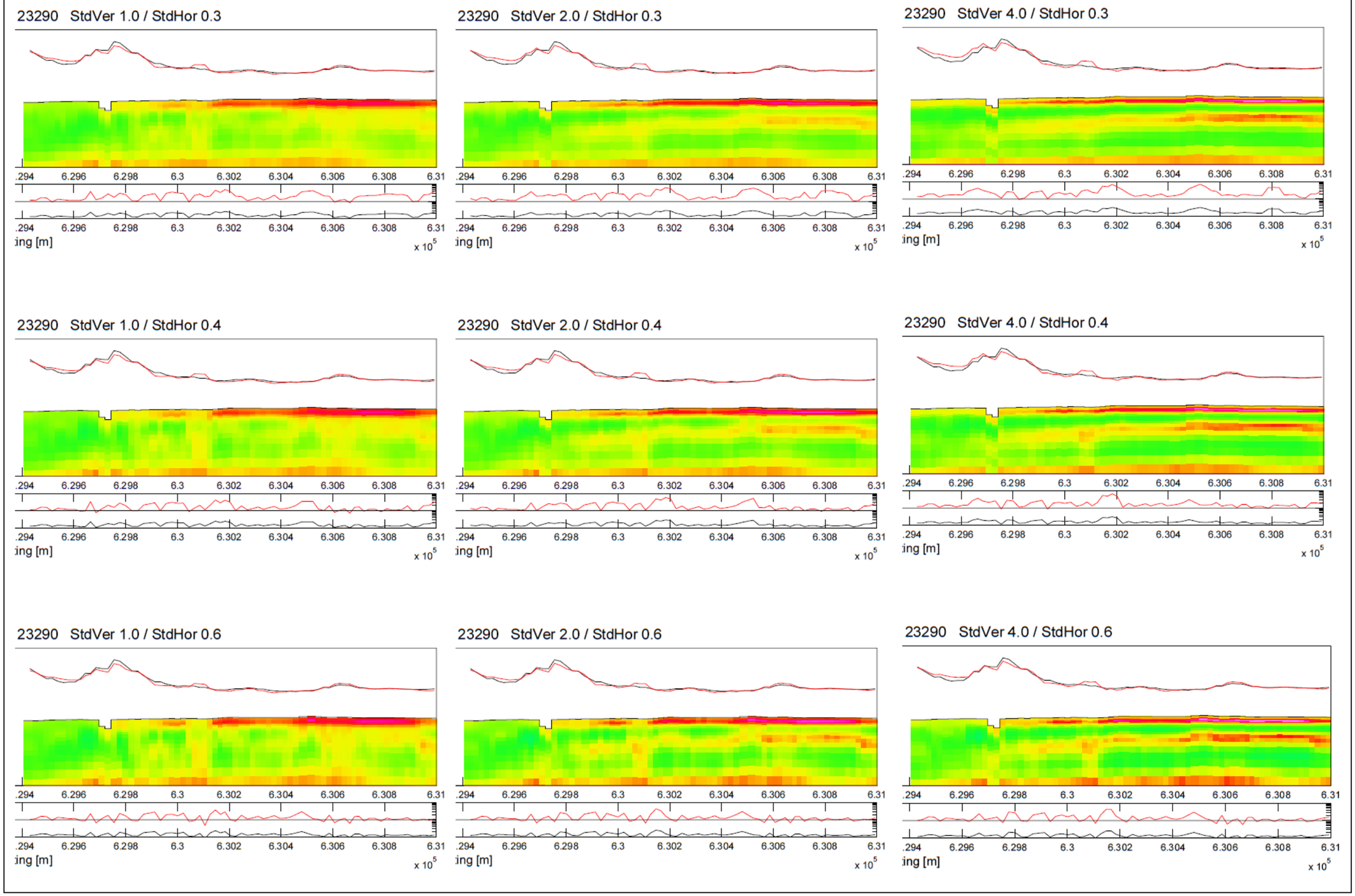



**Figure 6-44.** *Profile Line 23290 from the Jimargil area inverted with different constraints. The titles of the individual plot frames indicate the vertical and the horizontal standard deviation of the constraints.The data residual (red) and the total residual (black) of the different inversion schemes are plotted below the model sections.*

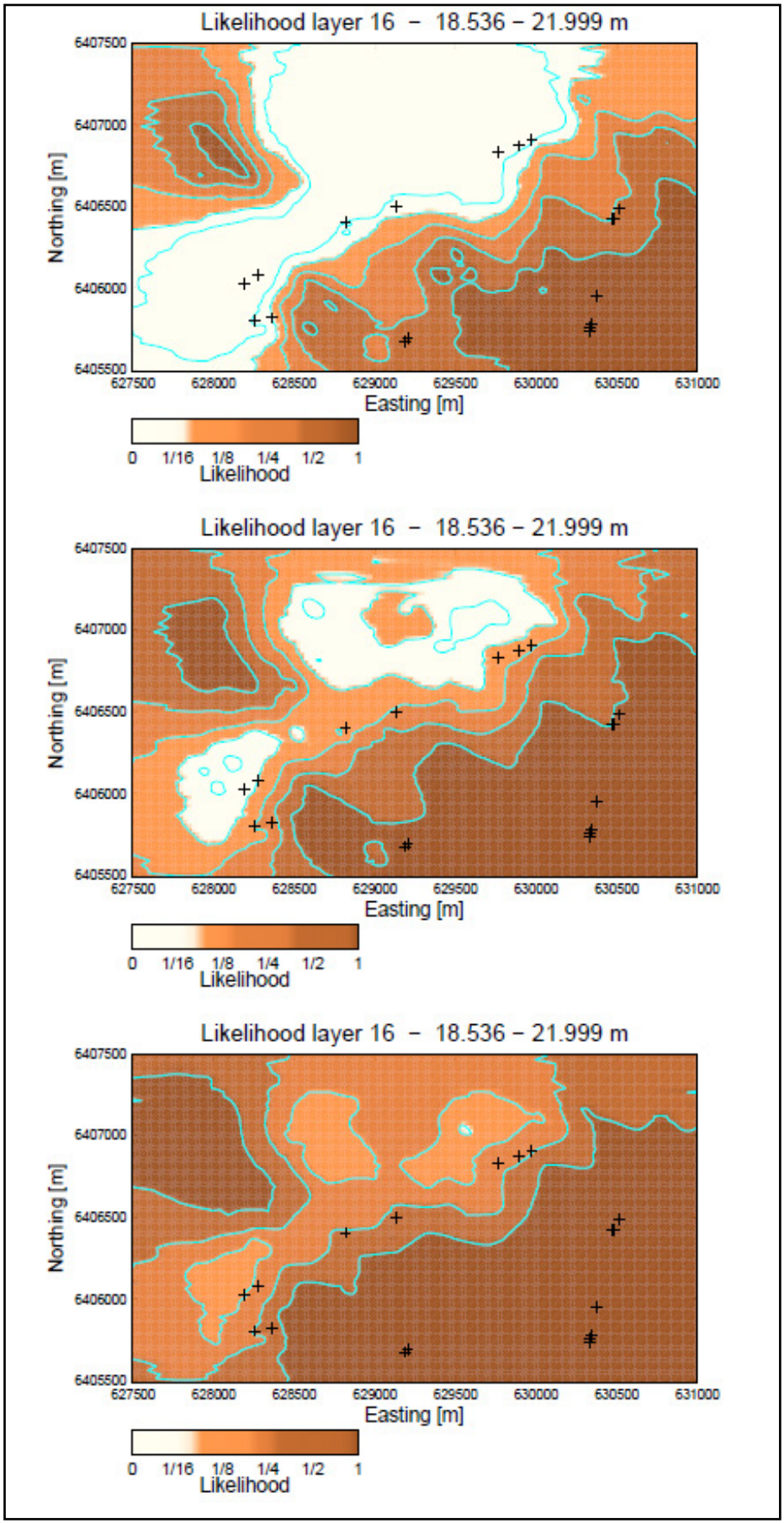



**Figure 6-45.** *Maps from the Jimargil area of the likelihood of the resistivity of the 16th model layer in the depth interval 18.54-22 m being below a limiting value. The maps are based on the inversion including the borehole information. The limiting values for the three maps are, from above: 8, 10 and 12 Ω m. The crosses indicate the borehole positions.*

### 6.7.3.17 *Inversion of borehole conductivity log data*

A total of 94 borehole conductivity logs were made available; some of the boreholes have more than one log in them. The boreholes are very unevenly distributed. There are 20 boreholes in the Menindee Common area, 21 in the Jimargil area, and outside these areas the boreholes are spread out with large distances between them. The positions of the boreholes are shown in Figure 6-45. Two of the logs, BHMAR19-1 and BHMAR80B-2, turned out to have extended depth intervals with missing data, probably discarded because of by iron fittings (scrap?) in the borehole, causing the log tool to go into saturation. These two logs have been discarded from the data set, leaving a total of 92 logs.

In earlier work on the BHMAR data, the conductivity logs were averaged over the multi-layer model used in the AEM inversion. Each layer was ascribed an average conductivity with a standard deviation calculated based on the variability of the conductivity values within the layer. However, in the WANDA inversion product, the conductivity logs have been inverted with the 1D multi-layer model used in the AEM inversion to obtain complete equivalence between the AEM data and the conductivity logs in the way they contribute to the final results. A subroutine for the inversion program capable of inverting the conductivity logs in the low-frequency approximation was developed for this purpose.

The log tool has two coils, a transmitter and a receiver, spaced 0.5 m apart and the operating frequency is 26 kHz. The logs are sampled for every 2.5 cm, meaning that there are around 40 measurements within the vertical extension of the log sensitivity function. There is thus a high degree of over-sampling. The closely spaced log samples are assigned a basic absolute noise level of 10 mS/m and a relative noise level of 5 % (Aaron Davis, personal communication). Because of the high density of the log samples compared with the extent of the sensitivity function, the noise is highly correlated. However, the inversion program used does not support correlated noise, and to compensate for this, the absolute noise level is increased to 40 mS/m and the relative noise increased to 10 %. With these values, the logs were inverted with the same vertical constraint, $\sigma_v = 4$, as the AEM data. The correlation between the log models and the AEM models is done with the logs models from the inversion of the conductivity data with the pertinent parameter error estimates.

In the inversion of the entire BHMAR data set, the borehole conductivity log data have been inverted with the same multi-layer model as the AEM data. This has been done to establish complete equivalence between the way the AEM data and the borehole data contribute to the overall information about the sub-surface conductivity in the lateral parameter correlation procedure (LPC).

In the low-frequency approximation, the induction log response, the apparent conductivity, is a linear function of the formation conductivities as shown in Equation 48 where $S(z)$ is the sensitivity function for the conductivity log.

$$\sigma_a(z) = \int_0^\infty S(z - z')\sigma(z')dz'$$

**Equation 48**

In the low-frequency approximation, for a two-coil system with a coil distance of $L$, $S$ is model independent and is given by Equation 49 where $z = 0$ defines the midpoint between the coils (Moran & Kuntz, 1962). For a layered model with constant conductivities within the layers, the apparent conductivity response is given as Equation 50 and the derivatives used in the Jacobian matrix are easily found as Equation 51.

$$S(z) = \begin{cases} 1/(2L) & \text{for} |z| < \dfrac{L}{2} \\ L/(8z^2) & \text{for} |z| > \dfrac{L}{2} \end{cases}$$

**Equation 49**

$$\sigma_a(z) = \sum_{i=1}^{N} \sigma_i \cdot \int_{z_i}^{z_{i+1}} S(z - z')dz'$$

**Equation 50**

$$\frac{\partial \sigma_a(z)}{\partial \sigma_i} = \int_{z_i}^{z_{i+1}} S(z - z')dz'$$

**Equation 51**

With these formulas, the conductivity log inversion problem is solved in exactly the same way as the AEM problem using the inversion formulation of Equation 36 and Equation 37 resulting in a set of conductivities for each of the model layers and an estimate of their uncertainty.

#### 6.7.3.18 *Estimating the depth of investigation*

Several definition of depth of investigation (DOI) have been presented in the literature. A recent consistent and general approach is that of Christiansen & Auken (2010) who use the derivatives of the final model with regard to the model parameters, squared and summed over all data, to define an integral sensitivity for each model parameter. These number are the ones found in the diagonal of the $\mathbf{G}^T\mathbf{C}_{obs}^{-1}\mathbf{G}$ matrix, see Equation 36. The DOI is then defined by by summing up from bottom to top layers:

$$S(z_i) = \beta_i + \beta_{i+1} + \cdots + \beta_L \quad , \quad \beta_i = \text{diag}\left(\mathbf{G}^T\mathbf{C}_{obs}^{-1}\mathbf{G}\right)_i$$

**Equation 52**

and it is determined as the depth, $z_i$, where the value of $S$ falls below a certain value. This approach to estimating the DOI has been used in the re-inversion of the entire BHMAR data set.

#### 6.7.3.19 *Plots of model and analysis sections*

The results of the inversion are presented as model sections and as maps of mean conductivity in depth and elevation intervals.

In the model section plots, the resistivity/conductivity of the model layers are plotted on a logarithmic/linear scale. The analysis/uncertainty section is constructed in the same way as the model section, but instead of plotting the model parameter, the relative uncertainty of the parameter is plotted. The relative uncertainty is found as the squareroot of the diagonal elements of the posterior covariance matrix:

$$\mathbf{C}_{ana} = \left[ \mathbf{G}^T\mathbf{C}_{obs}^{-1}\mathbf{G} + \frac{1}{\sigma_v^2}\mathbf{C}_m^{-1} \right]^{-1}$$

**Equation 53**

$\mathbf{C}_{ana}$ is based on an analysis of the models after the final inversion and is carried out neglecting the horizontal, but retaining the vertical smoothness constraints, all with a reference value of $\sigma_v = 1$, independent of the actual value of $\sigma_v$ used in the inversion.

#### 6.7.3.20 *Lateral resolution and along-line sampling distance*

After acquisition, all AEM data are subjected to a data processing the primary aim of which is to discard invalid data and to reduce the effective data noise. There are as many ways of doing this as there are AEM contractors, and most often the data processing procedures and principles are considered proprietary information. However, inevitably, all data processing algorithms make use of some sort of stacking, i.e.

mean values are formed along the flight lines for measurements within a certain time/distance interval. This process can be repeated and adapted to the signal level determined by the delay time and the conductivity structure, meaning that late time data, with their poorer signal-to-noise ratio, are often averaged over longer periods (lateral distance) than early time data.

Without going into the details of the initial conditioning of SkyTEM data, the last part of the data processing consists in forming moving averages over time intervals adapted to the signal strength, i.e. the delay time of the gate. The filter width is 1.5 s for early time gates, increasing to 15.3 s for late time gates, corresponding to a distance of 30 m and 300 m respectively. Filtered data are delivered for every 0.5 s corresponding to 10 m interval. It is thus seen that selecting averages for every 30 m is not an under-sampling of the final averages; on the contrary, for late time gates, it is quite a dense sampling. In Figure 6-46 the distribution of the average sounding distance over all BHMAR flight lines is shown. The mean and median is 30 m with a standard deviation of 3.60 m.

From the above considerations, it is clear that one should not confuse the along-line sampling distance with the lateral resolution capability of the data. As long as the along-line sampling density is adequate for the early time data, it will certainly be adequate for the late time data, and the lateral resolution capability will primarily be determined by the effective width of the data processing filters. In the light of this we do not expect to see much difference between the model sections of 30 m and sections with a denser sampling, except that the denser sampling will appear smoother.

To test the above inferences, data from the original data delivery from the contractor with a sampling distance of 13 m were inverted in an area covering the primary area of interest around the Jimargil bore field: Easting interval 627,000-633,000 m, Northing interval 6,403,000-6,410,000 m. In Figure 6-46 the distribution of the average sounding distance in this area is illustrated. The mean and median is 13 m with a standard deviation of 1.50 m. For consistency, this denser data set is compared with the one obtained by selecting every second sounding, i.e. a data set with 26 m sampling distance, very close to the 30 m of the entire BHMAR data set.

In Figure 6-47 model sections for Line 23320 with 13 m and 26 m along-line sampling distances are shown for comparison. Both the 13 m data and 26 m data have been inverted with exactly the same multi-layer model and the same inversion parameters as the ones used for the entire BHMAR data set, in particular the same strengths of the vertical and the horizontal regularization. It is a very attractive, and quite unique, property of the covariance matrices used in the regularization that their effect is discretisation independent (Serban & Jacobsen, 2001). As expected, there are only very minor differences between the two model sections, and there are no obvious differences in the definition of the various formations.

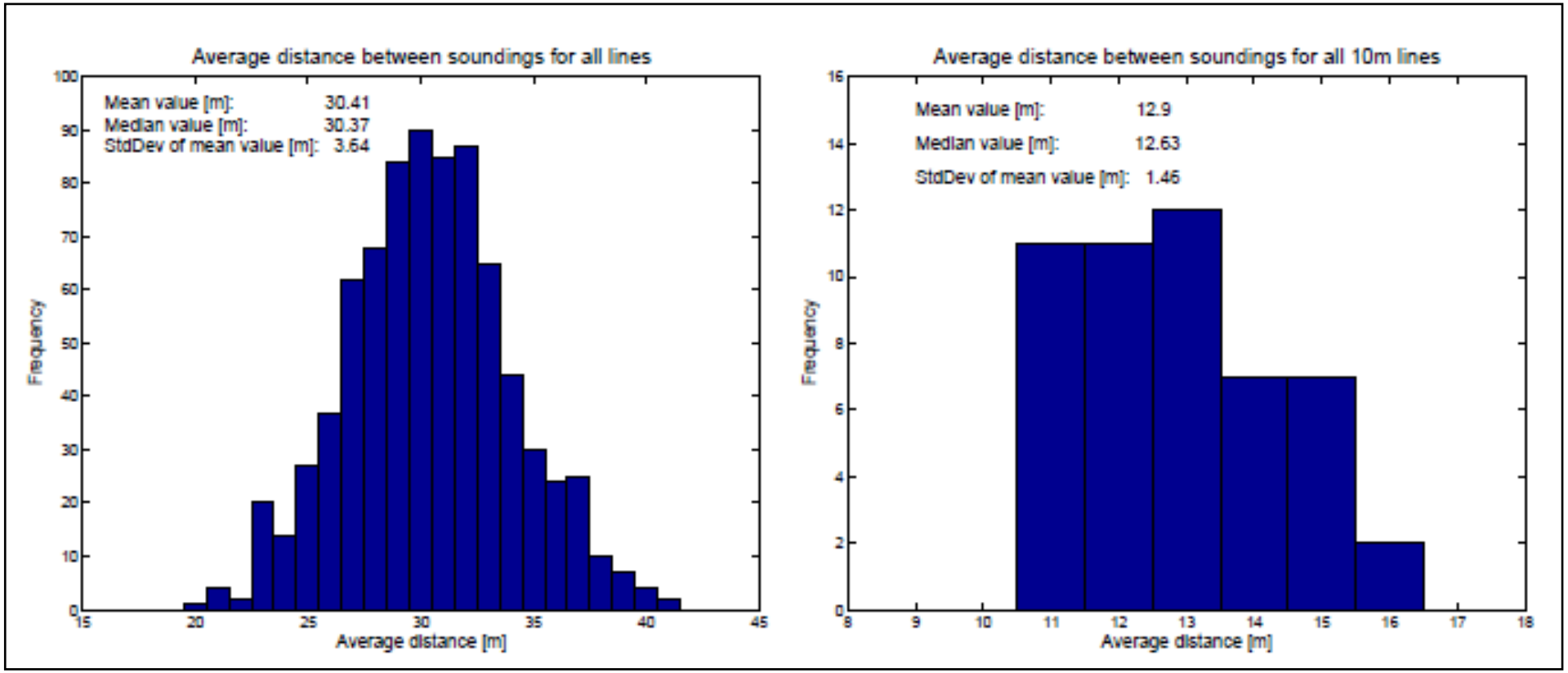



**Figure 6-46.** *Plots of the distribution over all flight lines of the average along-line distance between soundings. Left: for the entire BHMAR data set; right: for the Jimargil subarea with 13 m data spacing.*

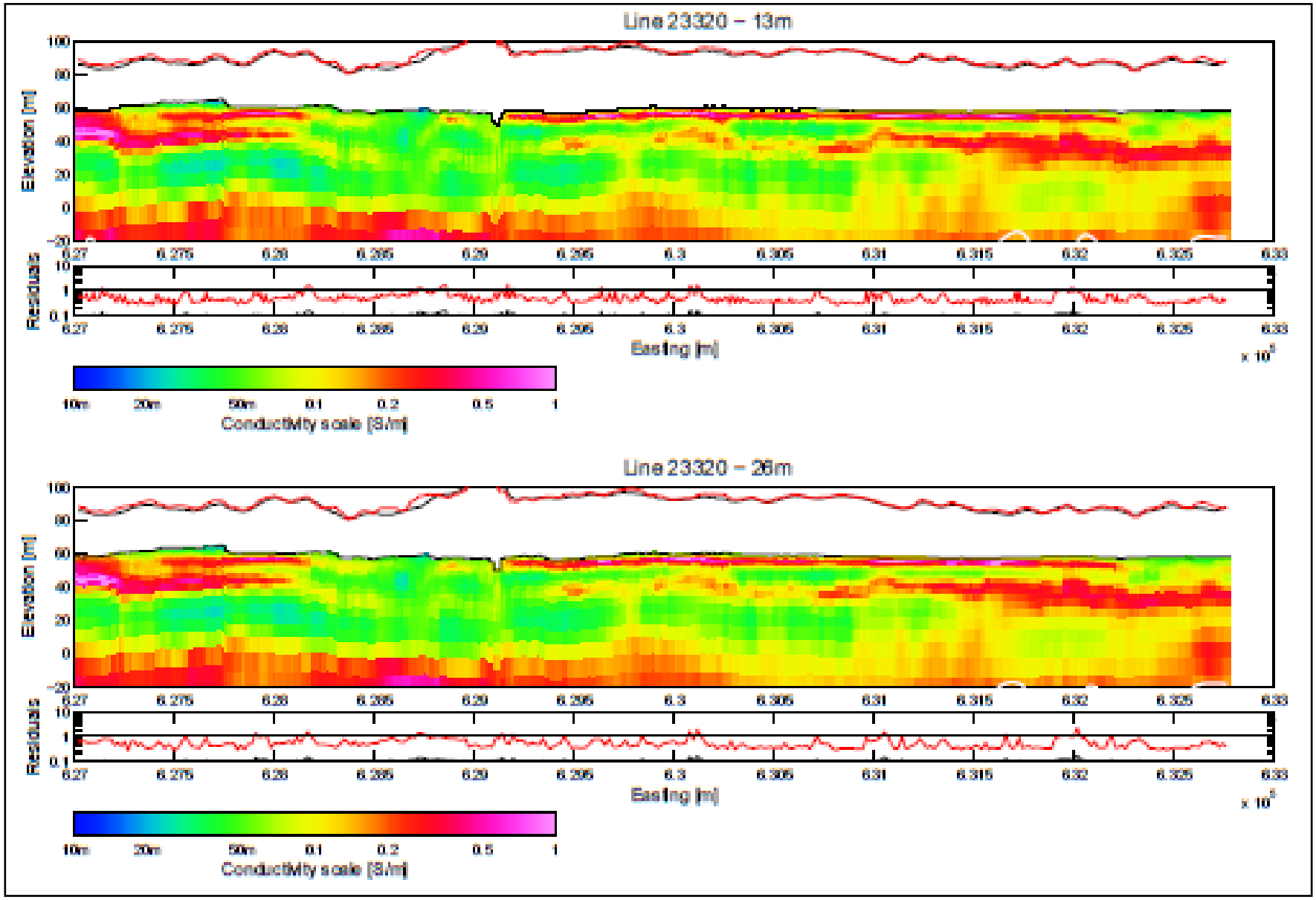



**Figure 6-47.** *Comparison of model sections from the Jimargil area from inversion of the data set with 13 m and 26 m along-line sampling distance, respectively.*

### 6.7.4 An Analysis of the Residuals of the BHMAR Inversion

#### 6.7.4.1 *Statistical distribution of the residuals*

The first statistical measure that we shall consider is the distribution of the normalized residuals:

$$R_i^{dat} = \frac{d_i - r_i}{\Delta d_i}$$

**Equation 54**

for all gates and for the whole survey area. $d_i$ is the data value, $r_i$ is the response value, and $\Delta d_i$ is the data noise. If the noise estimates are reasonable and if the data can be fitted in the 1D inversion, we should expect a value for the mean of the normalised residuals around zero and a standard deviation around 1 or - considering that estimating the noise and constructing a noise model with general validity for the whole survey area is quite challenging – the value should be a small number: ~1-5.The most important issues that might cause the mean to be different from zero and the standard deviation to be larger than one are:

Data processing and calibration might be suboptimal.

- Variations in Tx waveform due to thermal variations during the survey might affect primarily the early gates of the two moments.
- LM and HM data are jointly inverted and any inconsistency between the two moments might cause the standard deviation to increase.
- The actual conductivity structure may deviate from a 1D structure to the extent that the data cannot be fitted in a 1D inversion.

Figure 6-48 shows a histogram of the distribution of the normalized residuals. The mean is indeed close to zero with a value of 0.1, indicating that, overall, the measuring situation and the data processing and calibration have not introduced a bias in the data inconsistent with a 1D inversion. The standard deviation attains a value of 2.4 which is indeed a small number. This shows that, overall, data are consistent with a 1D conductivity model, the noise model is reasonable and the inversion models were able to fit the data.

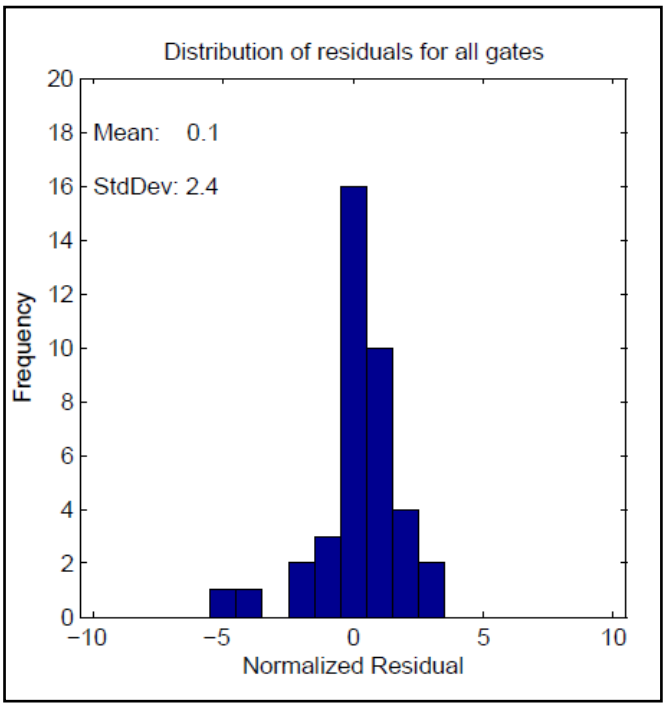



**Figure 6-48.** *Histogram of the distribution of normalized residuals for the whole survey area.*

#### 6.7.4.2 *Statistical distribution of the individual gate residuals*

We shall now look the distribution of the normalised residuals in more detail by considering the distribution separately for each gate. Again, for the same reasons as above, the expectation values for the mean of the normalised residuals and the standard deviation should be zero and one, respectively.

Figure 6-49 shows histograms of the distribution of the normalized residuals for each of the 39 gates. For most of the gates, the mean is close to zero and the standard deviation is a small number. However, certain gates have a slightly skewed distribution of the residuals.

Concerning the LM data, gate 1 and gate 2 have standard deviations of 3.5 and 2.8, respectively. These are the gates that would be most vulnerable to variations in Tx waveform. However, apart from the first couple of gates, the standard deviations are small numbers. The mean is quite close to zero for the gates 1-16, but for gates 17 and 18, the mean values are 1.5 and 2.4 respectively. This might be attributed to the fact that the late LM gates are the ones that will suffer the effect of inconsistencies between the LM and HM gates and/or the fact that the noise is large and more erratic for the late LM gates; it does not necessarily follow a Gaussian distribution.

Concerning the HM data, we see the same effect for the first two gates, 19 and 20, as for the LM: the mean and the standard deviations are elevated relative to the subsequent gates. The early HM gates are the ones most vulnerable to variations in Tx waveform, and they are also the ones that will suffer the effect of inconsistencies between the LM and HM gates. For gates 21-29, the histograms are well-behaved, but for gates 30-37, the distribution is more skewed with higher absolute values of the mean and the standard deviations. These late gates are the ones where the noise increases and become more erratic. The very abrupt change from gate 29 to gate 30 is difficult to explain, but it is primarily gates 30-31 that display anomalous behaviour while the values for gates 32-39 seem more reasonable for late gates.

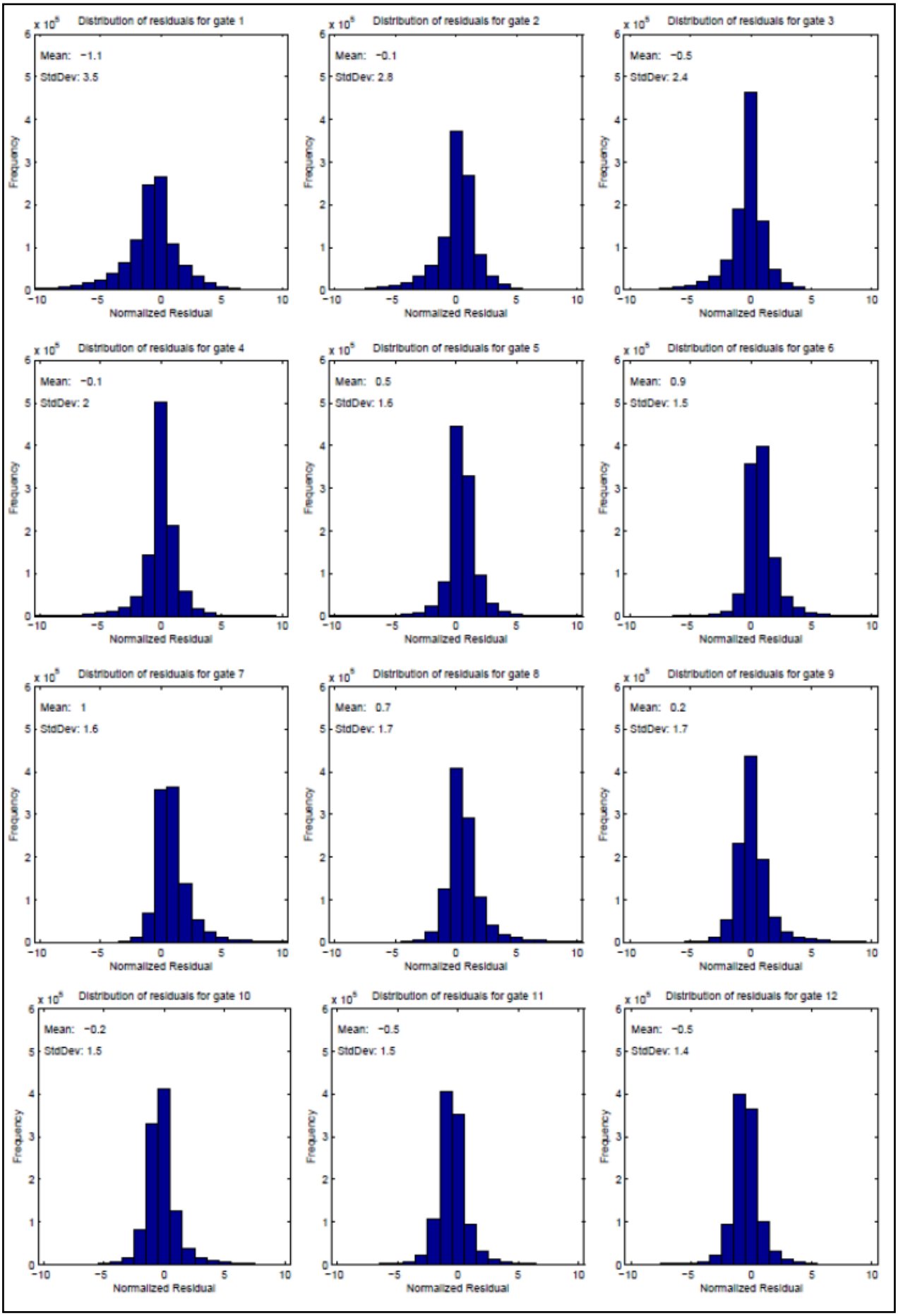



**Figure 6-49.** *Histograms of the distribution of normalized residuals for the 39 gates.*

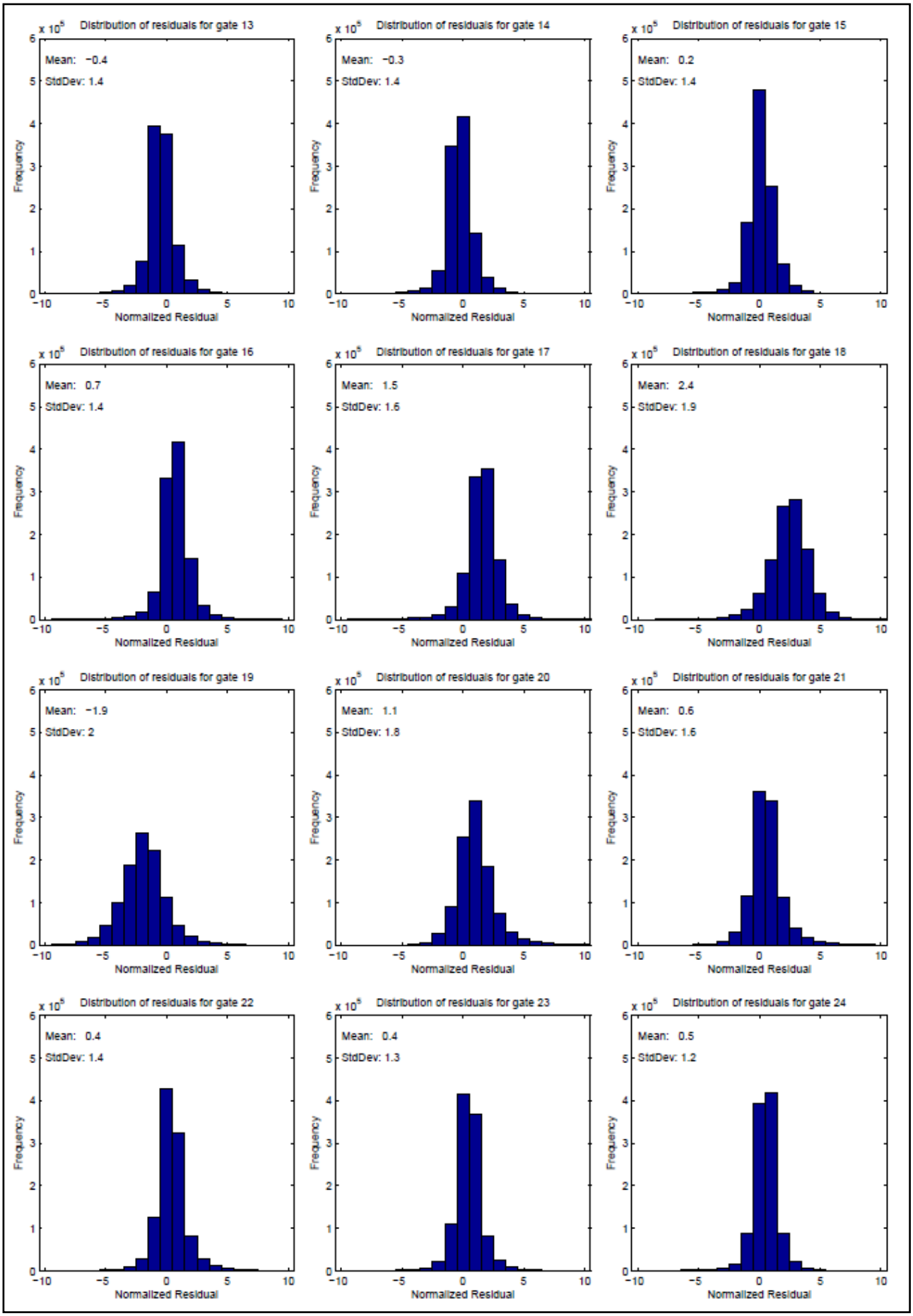



**Figure 6- 49** *continued.*

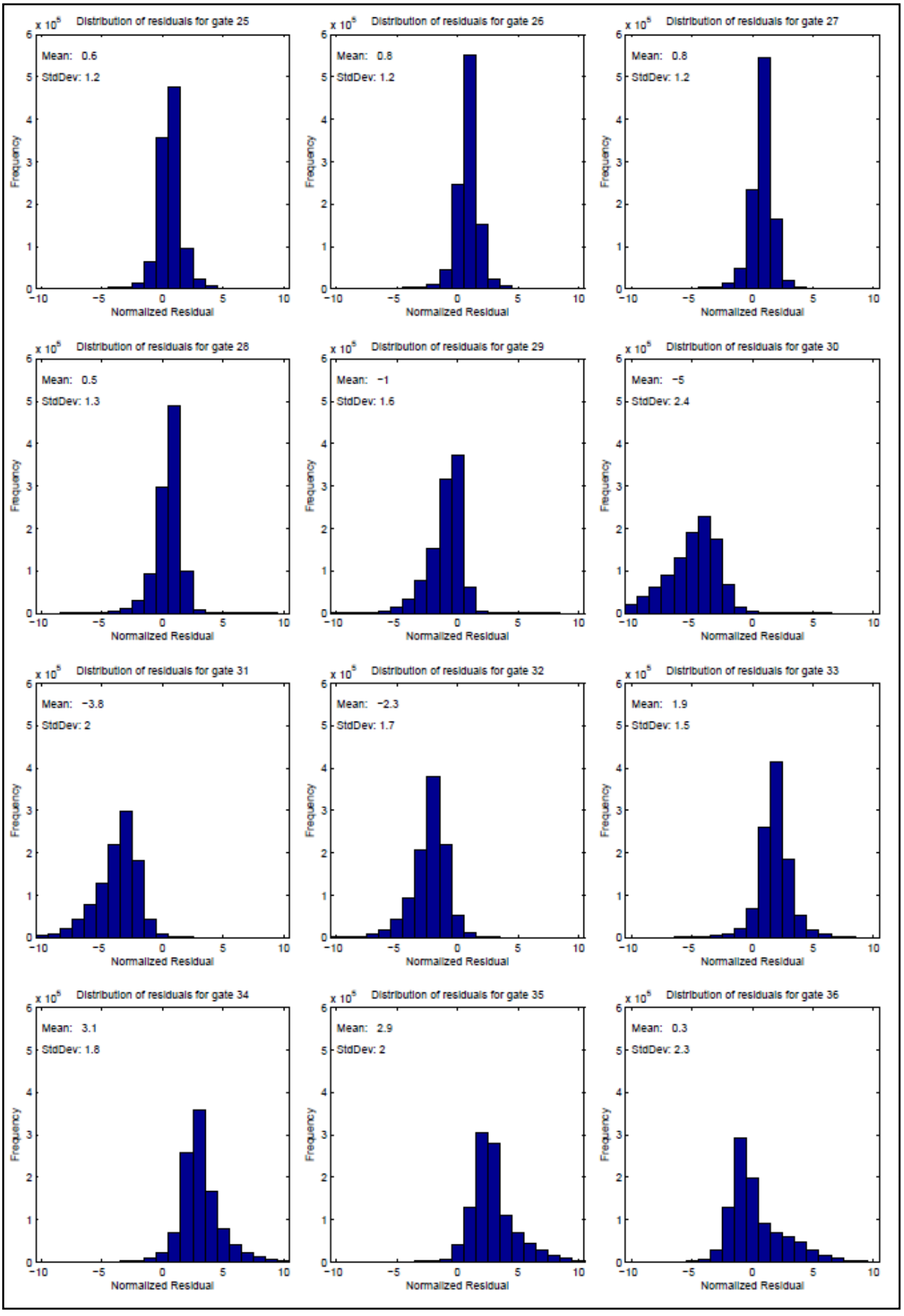



**Figure 6- 49** *continued*

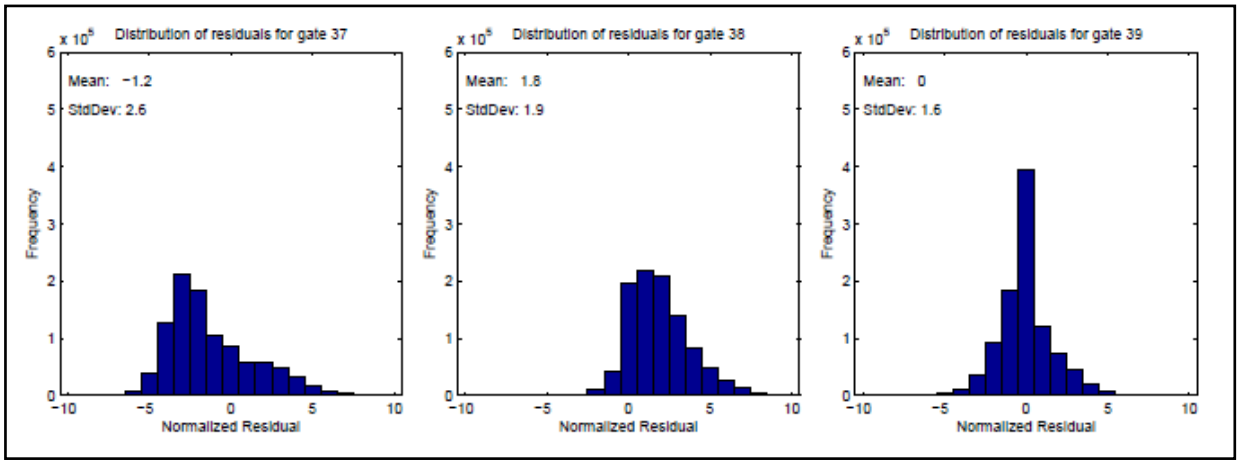



**Figure 6- 49** *continued*

### 6.7.4.3 *Data residual and total residual for the soundings*

In all model sections displaying the results of the inversion, two measures of the goodness of fit to the data are plotted: the data residual and the total residual. These are very basic average measures of the quality of the inversion model: the final model is required to fit the data within the assumed data error while fulfilling the model constraints.

As a measure of the misfit we use the normalized data residual i.e. the squareroot of the average of the sum over all gates of the squares of the difference between the data value, $d_i$, and the response value, $r_i$, normalised with the data noise, $\Delta d_i$:

$$R^{dat} = \sqrt{\frac{1}{N}\sum_{i=1}^{N}\left(\frac{d_i - r_i}{\Delta d_i}\right)^2}$$

**Equation 55**

The total residual is a weighted sum of the normalized data residual and the normlaized residual of the final model relative to the initial (prior) model:

$$R^{tot} = \sqrt{\frac{1}{N+M}\left[\sum_{i=1}^{N}\left(\frac{d_i - r_i}{\Delta d_i}\right)^2 + \sum_{i=1}^{M}\left(\frac{\log\rho_i - \log\rho_i^{prior}}{\Delta\log\rho_i^{prior}}\right)^2\right]}$$

**Equation 56**

The inversion is set to minimize the square of the normalized total residual. For the normalised residuals, a value of 1 indicates that - on average - the model response fits the data within the error ascribed to the data. For the BHMAR survey, most often the total residual acquires a value between 0.1 and 1 indicating successful convergence to a model that fits the data and the constraints. The data residual typically ends on a value of 1-4 which is an acceptable range.

Plots of the topography, the normalised fitting error for the total residual and the fitting error for the data residual for the BHMAR study area are shown in Figure 6-50, Figure 6-51 and Figure 6-52 respectively. In Figure 6-51 and Figure 6-52 centred at (E, N) = (685 km, 6,445 km) there is an area of elliptic shape has a higher residual than the surrounding area. This area is a basement high and therefore quite resistive, meaning that the signal and thereby the signal-to-noise ratio is lower than in the surrounding area. Apparently the noise model has not quite accommodated this effect.

In Figure 6-51 and Figure 6-52, it is seen that the structure of the total residual and the data residual is very much the same. Figure 6-50 displays a topographic map produced to make it possible to see if the patterns in

the residual maps correlate with topography. In general this is not the case, but the arc-shaped feature with a higher residual at the coordinates (E, N) = (610 km, 6,390 km) corresponds to the topographic high marking the NE shore of one of the lakes in the area. The increased residuals can probably be attributed to the navigation manoeuvres necessary to cross the hills bordering the lake.

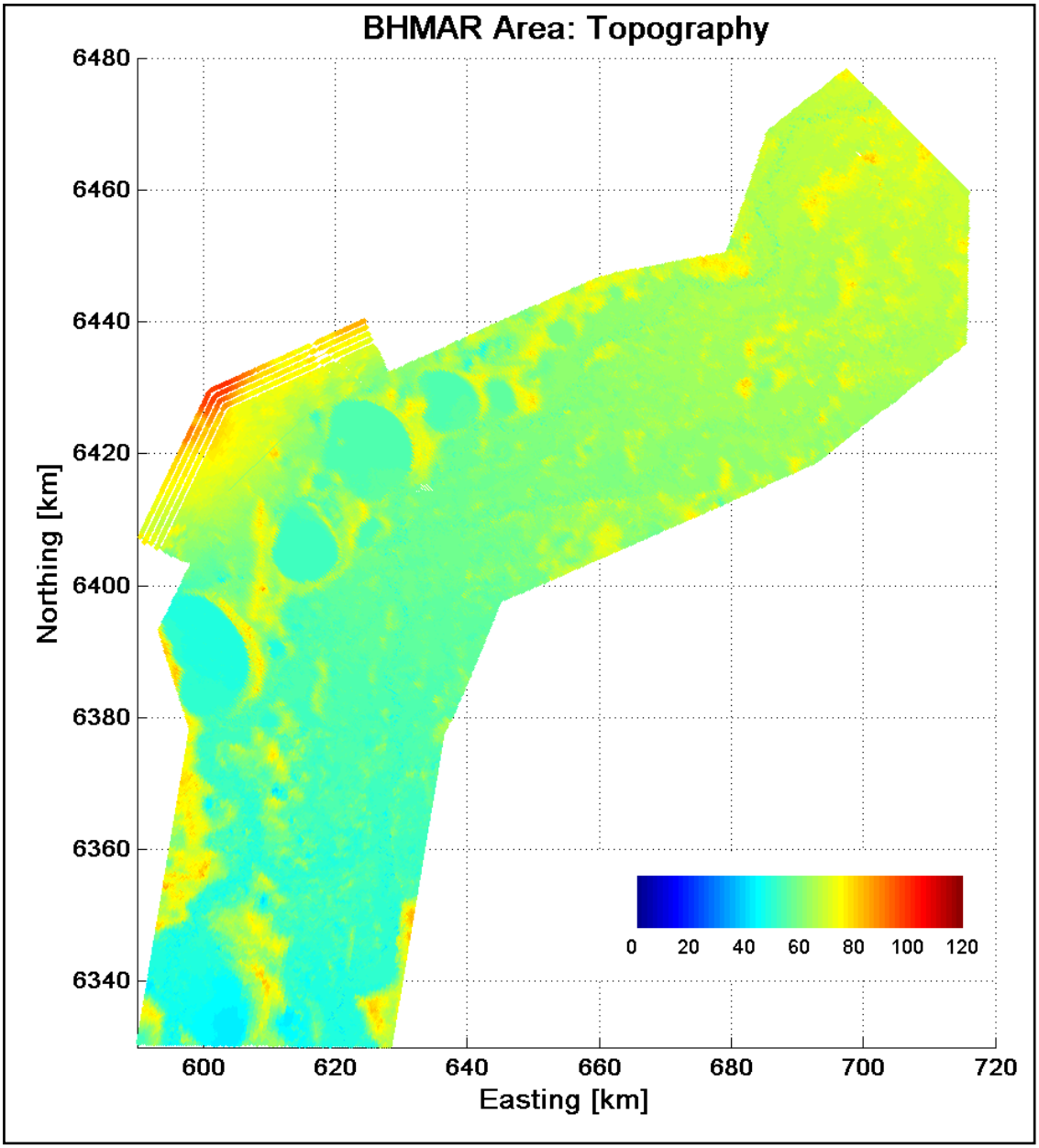



**Figure 6-50.** *Topography for the BHMAR study area.*

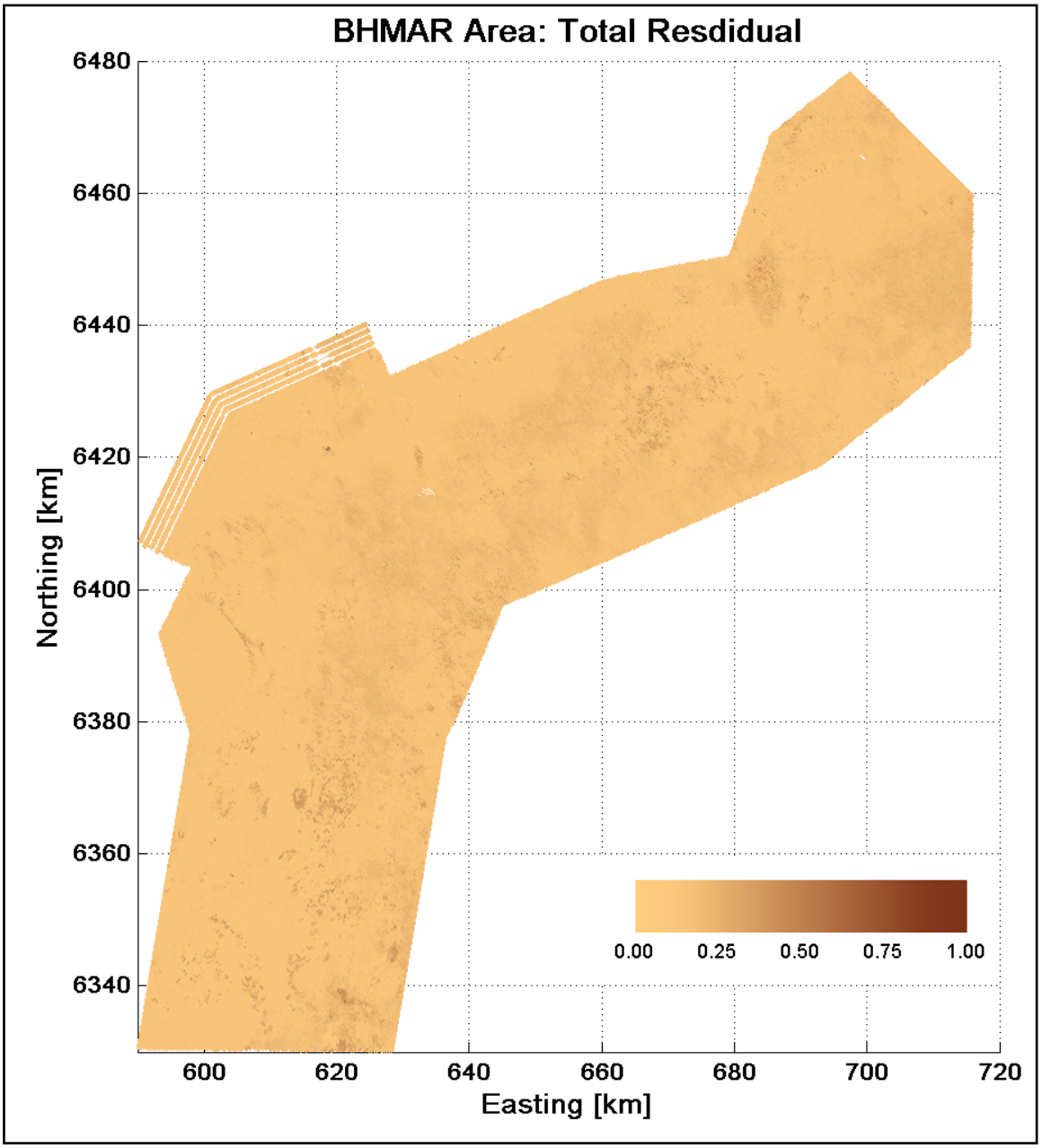



**Figure 6-51.** *Map of fitting error for the total residual for the BHMAR study area.*

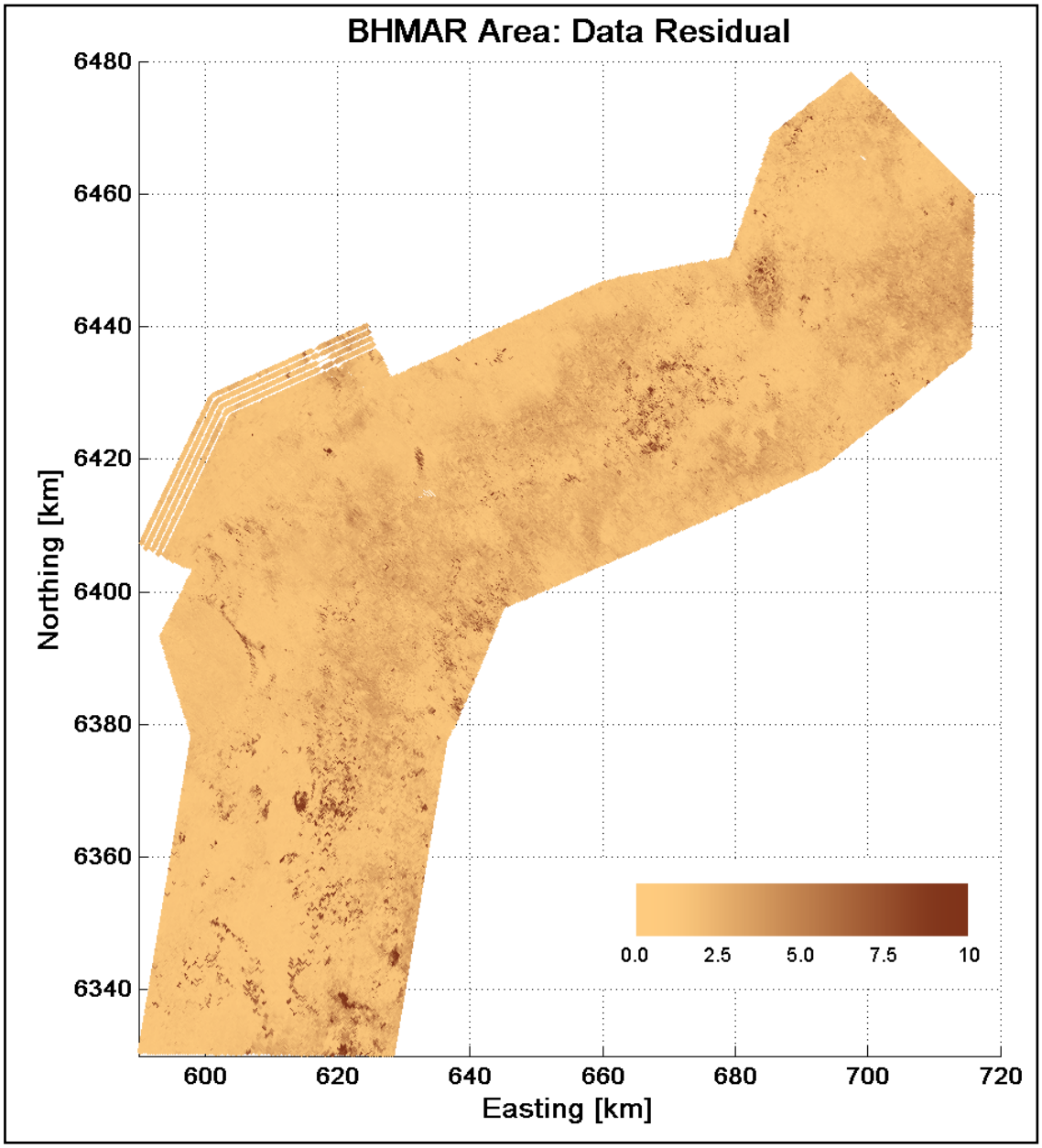



**Figure 6-52.** *Map of fitting error for the data residual for the BHMAR study area.*

### 6.7.4.4 *Data misfits for the individual gates*

To investigate the misfit between data and response for the individual gates, maps of the normalised residuals (Equation 54) have been produced, one for each gate. These will give a more detailed insight into possible inconsistencies between data and response.

When considering the size of the normalised misfits it must be remembered that their values must be compared with the noise levels ascribed to the data through the noise model. For the early gates of both moments, the relative noise has been set to 3% while the noise increases for the later gates to values of 10-50%.

Gates 1-18 (Figure 6-53 to Figure 6-61) are for Low Moment (LM) and gates 19-39 (Figure 6-62 to Figure 6-72) are for High Moment (HM) with gate-open and gate-close times in µs. There is an overlap of 11 gates between the two moments beginning with a gate centred at 90µs and ending with the gate centred at 900 µs.

Gates 36-39 are missing in parts of the north-easternmost blocks. The gate normalised misfits have been plotted for only every 5th sounding, i.e. a total of 200,000 points.

The expected behaviour of the individual misfits for each of the two moments is that they should be fairly similar for the middle range of gates for each moment. In the overall statistics for the gates, we have seen that the early gates of each moment have a slightly higher misfit than the following gates, and we expect to see that reflected in the maps. Concerning the last couple of gates of each moment, the overall statistics showed an increase in the normalised residual. These effects are actually seen in the following plots.

As far as lateral changes in the misfit are concerned, areas with a higher misfit may appear where 3D effects are present. These might appear not only close to conductive anomalies, but are also know to appear where conductive layers terminate abruptly, i.e. at the edges of extended conductive formations. Clearly, the 1D inversion used in the BHMAR survey cannot accommodate abrupt lateral changes in conductivity. Subareas with 3D effects would retain some similarity between the gates and these characteristics are in fact seen in the gate misfit plots where there is a tendency for the overall pattern of highs and lows to be repeated from gate to gate.

#### 6.7.4.5 *Comments on the individual gates*

Concerning the LM data, gate 1, and to a lesser extent gate 2, have slightly higher misfits than the following gates as mentioned above. Apart from that, the gate plots are quite similar until we get to gate 17 and 18, the last two LM gates where the misfit, as expected, increases. From gate 10, the basement high mentioned above becomes visible as an area with higher misfit.

Concerning the HM data, we see the same effect for the first two gates as for the LM: the misfit of gate 19 is higher than for the following gates, and for gate 20 slightly higher. In addition to the issues mentioned above, the fact that LM and HM data are jointly inverted means that a compromise is struck when LM and HM gates are inconsistent, and in this case, the HM gates might be the ones that have suffered a higher misfit. From gate 25, the basement high mentioned above becomes visible as an area with higher misfit. The gate misfits from gate 21 to 28 follow the expected pattern of being quite similar, but at gate 29 the general pattern of low and high misfits seems to become inverted. The gate 30-31 misfits are unexpectedly high and gate 32 somewhat high. No obvious explanation comes to mind for this behaviour. For gate 33 the misfits have the same appearance as the middle gates. Gates 34 and 35 are also quite high, but now we are getting close to the more noise-filled data at the late gates where the misfit is expected to rise.

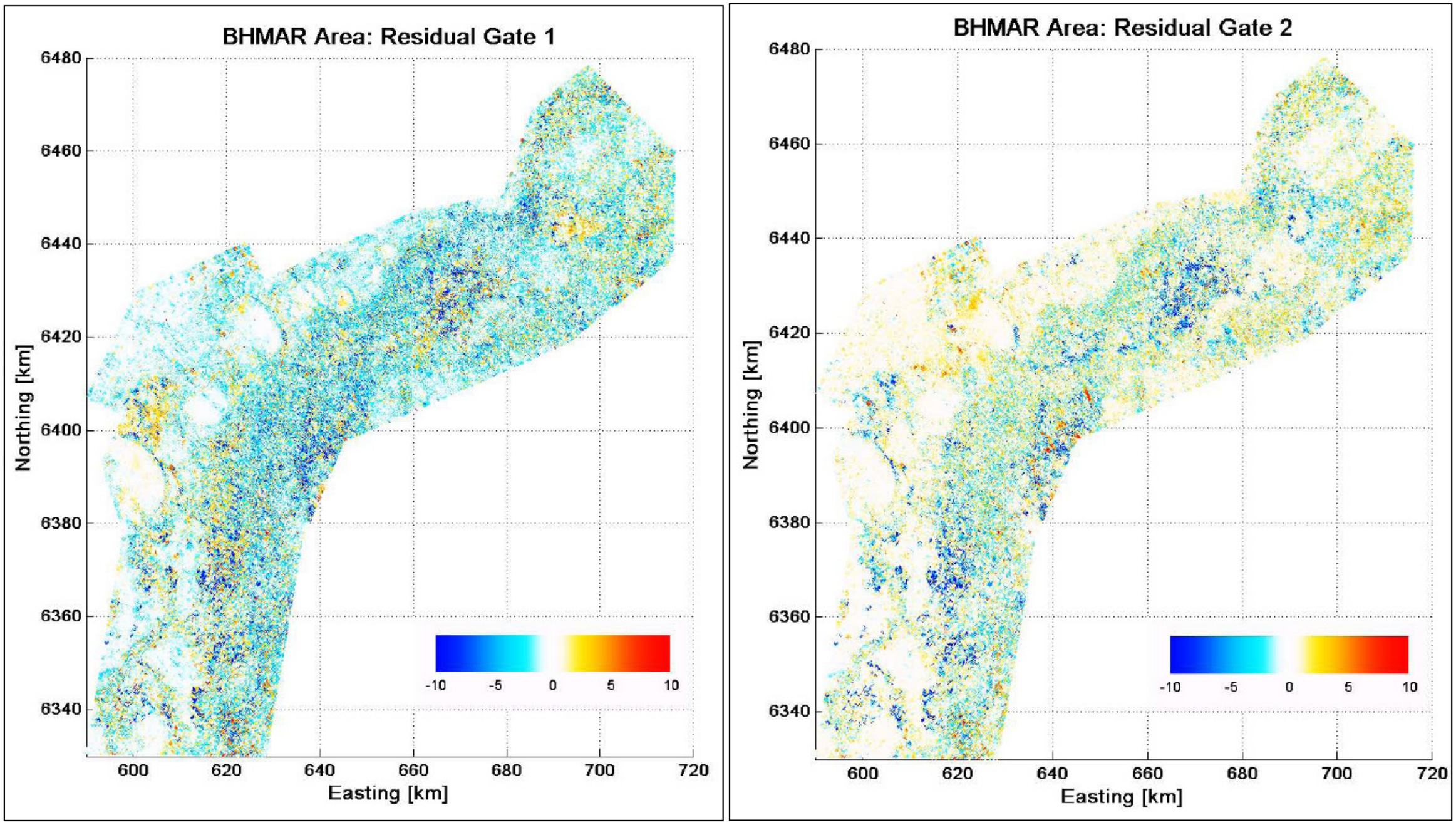
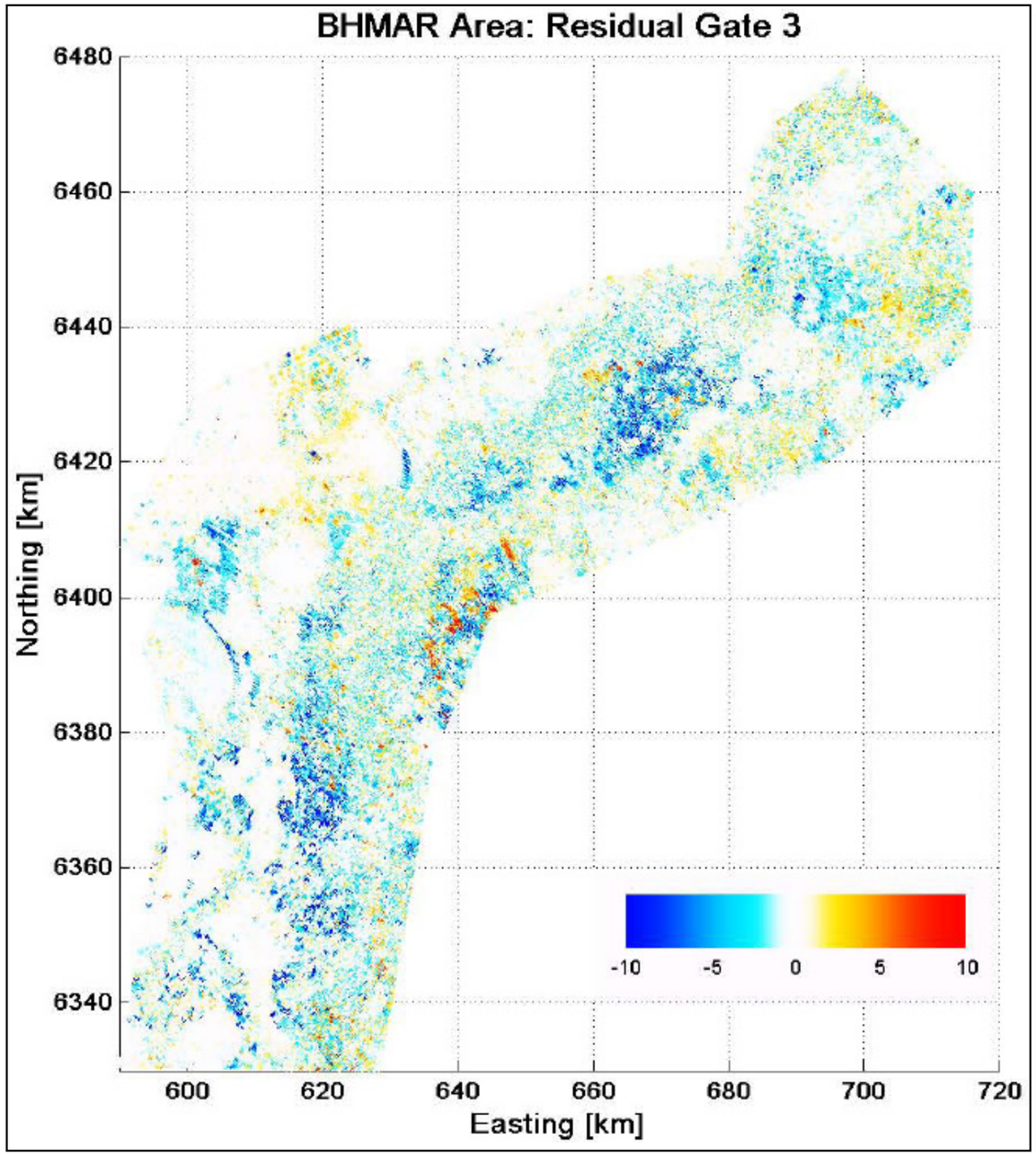



**Figure 6-53.** *Maps of fitting error for the first Low Moment (LM) gate (left) and second LM gate (right) for the BHMAR project area. Problems with the first gate settings were previously identified. The 1st gate image (left) shows a degree of structure reflecting surface topographic effects. There is a low level of misfit associated with the flat lakes, but a poorer level of fit in the adjacent dunes, with higher residuals over narrow banks associated with lake-bordering lunettes that is likely caused by increased pitch and roll as the helicopter climbs to higher elevations over these sharply defined topographic features. There is a good to poor misfit across with some 'speckled' areas of turquoise to red (higher misfit) in the right hand image, indicating a poorer fit in these areas.*



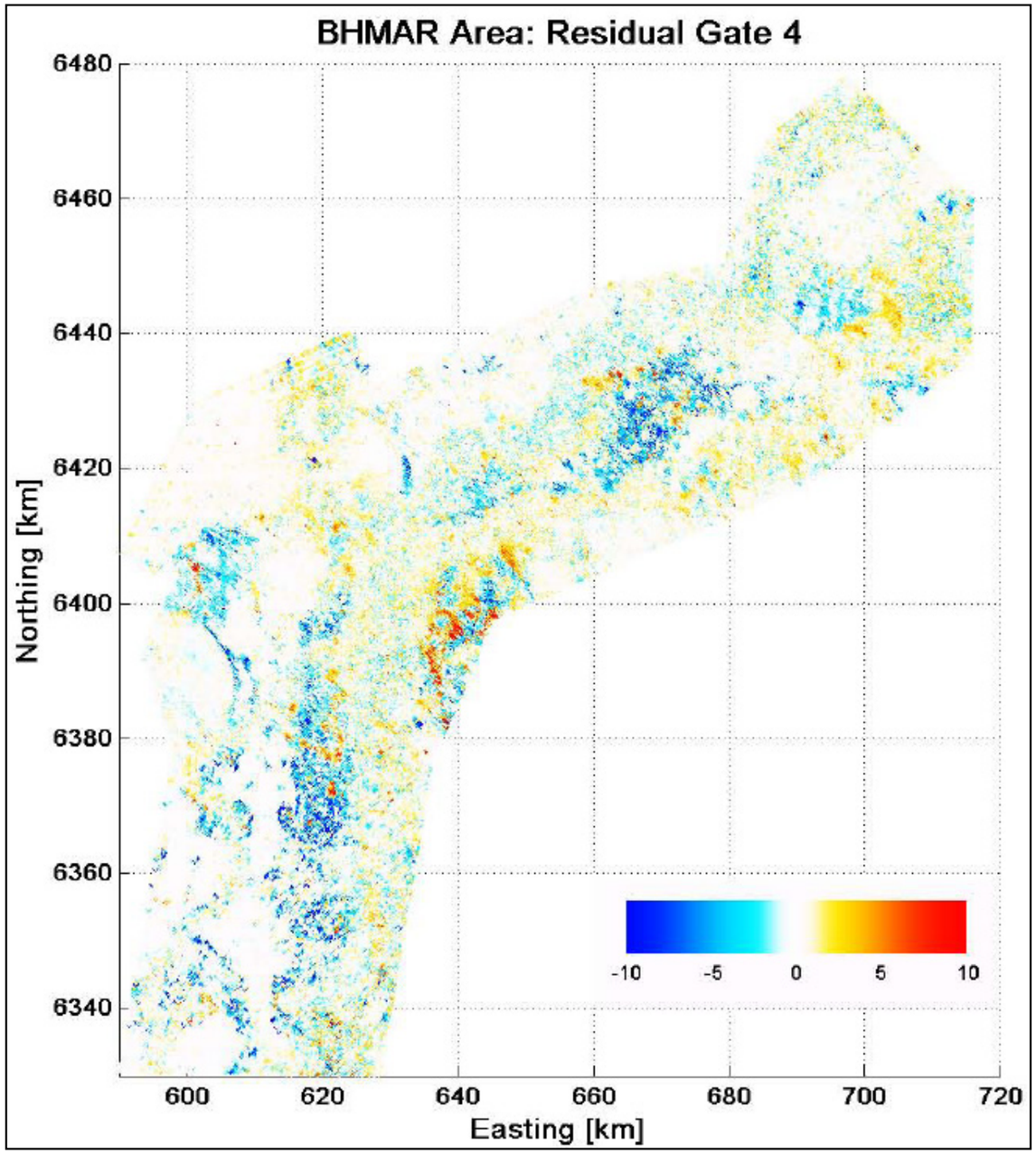




**Figure 6-54.** *Maps of fitting error for the 3rd Low Moment (LM) gate (left) and 4th LM gate (right) for the BHMAR project area. The 3rd gate image (left) shows increasingly good fit compared to the first two gates, with some structure related to topography still remaining around the edges of the lakes. There are some speckled areas of poorer fit in the 'elbow-shaped' area in the east of the area, and the misfit in this area remains through most of the LM gates. In the 4th LM gate (right) the level of misfit is similar to that in the 3rd gate, but with a reduction in the residuals related to topography.*

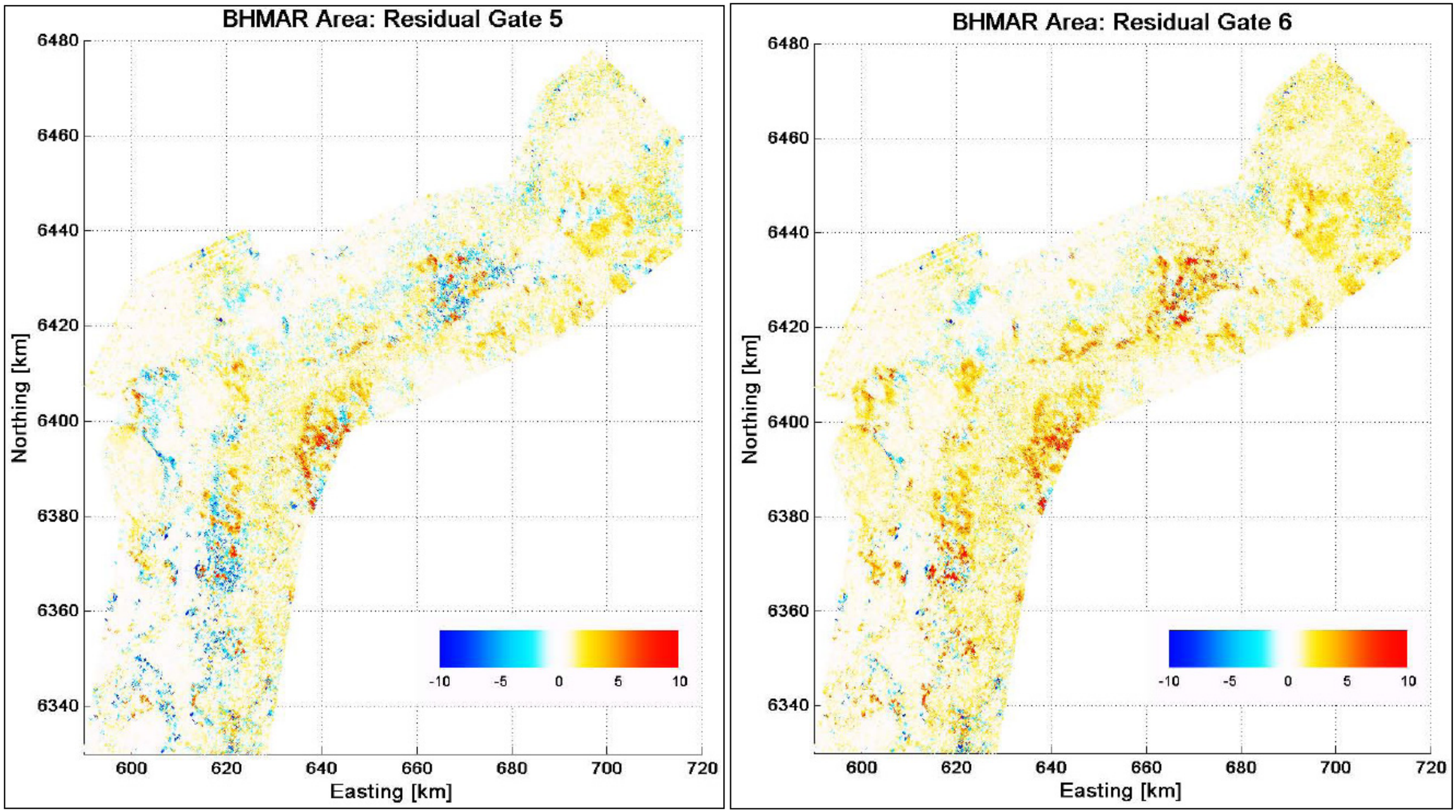



**Figure 6-55.** *Maps of fitting error for the 5th Low Moment (LM) gate (left) and 6th LM gate (right) for the BHMAR project area. The 5th and 6th gate fits are very similar, and generally show a good fit across the area, with the exception the 'elbow-shaped' area in the east of the area, where the misfit is higher, and in a few other higher areas of the landscape. Residuals associated with topography in the 6th gate and later time gates are generally less than in preceding gates.*

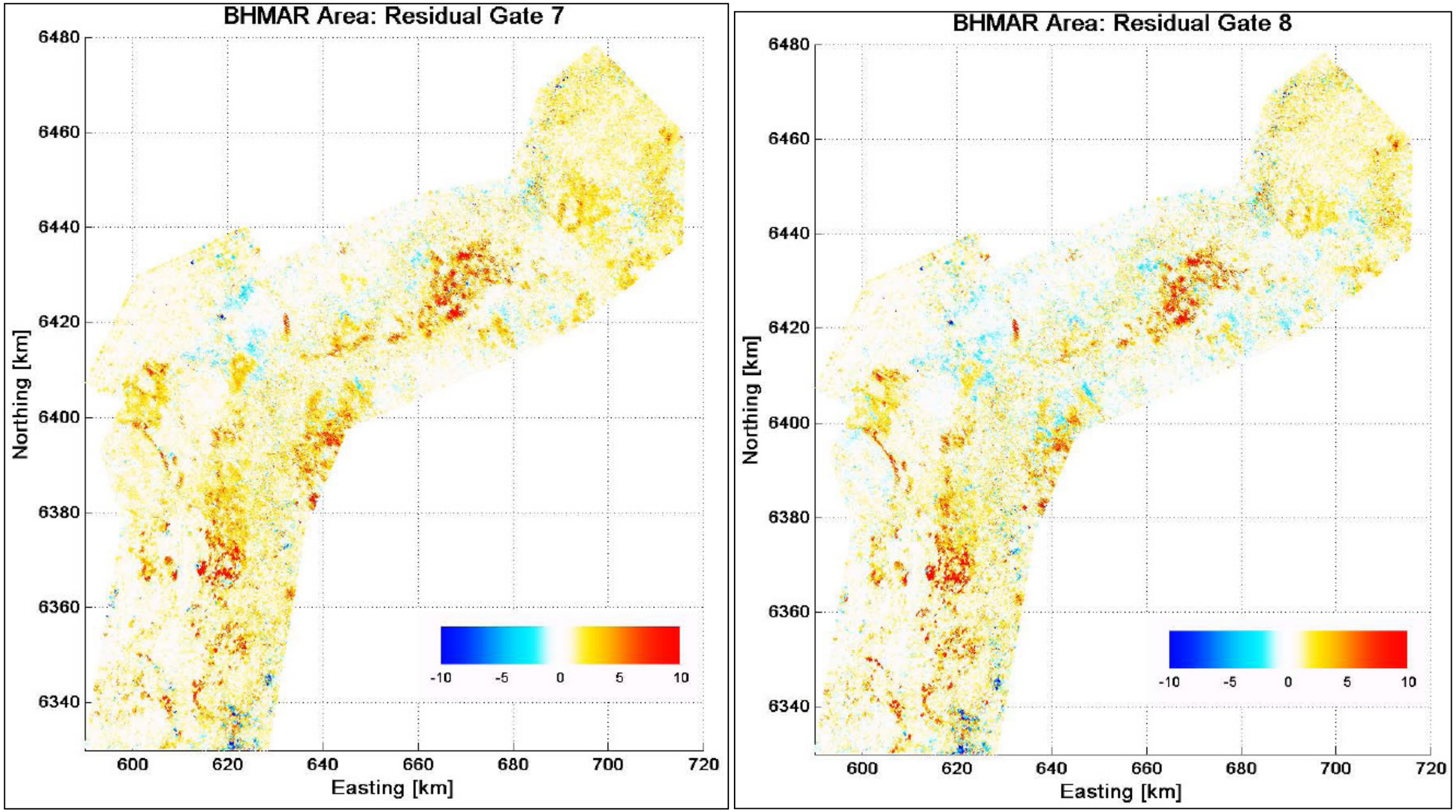



**Figure 6-56.** *Maps of fitting error for the 7th Low Moment (LM) gate (left) and 8th LM gate (right) for the BHMAR project area. The 7th and 8th gate fits are very similar, and generally show a good fit across the area. Exceptions include the 'elbow-shaped' area in the east of the project area, and in a few other higher areas of the landscape.*

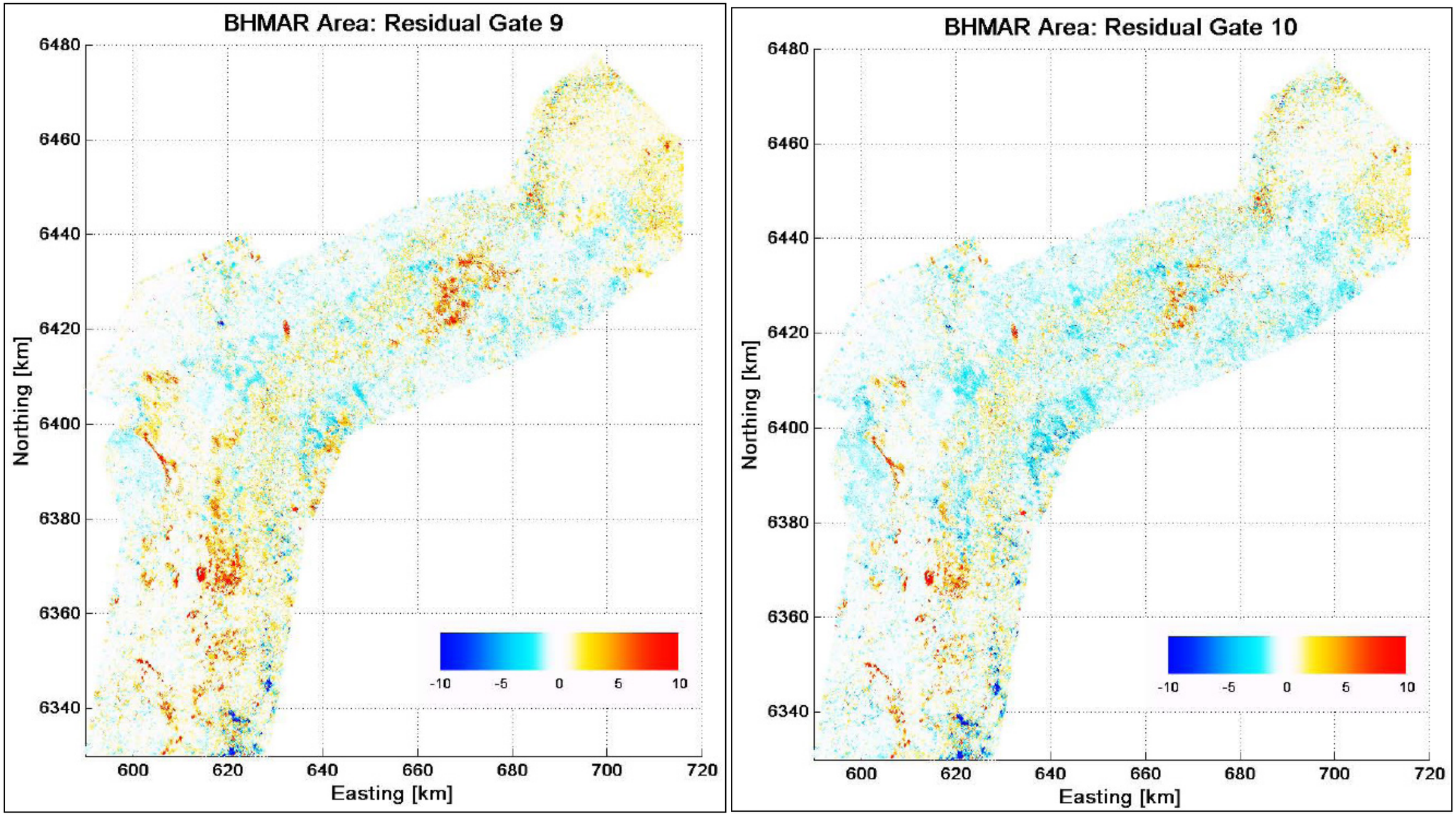



**Figure 6-57.** *Maps of fitting error for the 9th Low Moment (LM) gate (left) and 10th LM gate (right) for the BHMAR project area. The 9th and 10th gate fits are very similar, and generally better than in the preceding gates.*

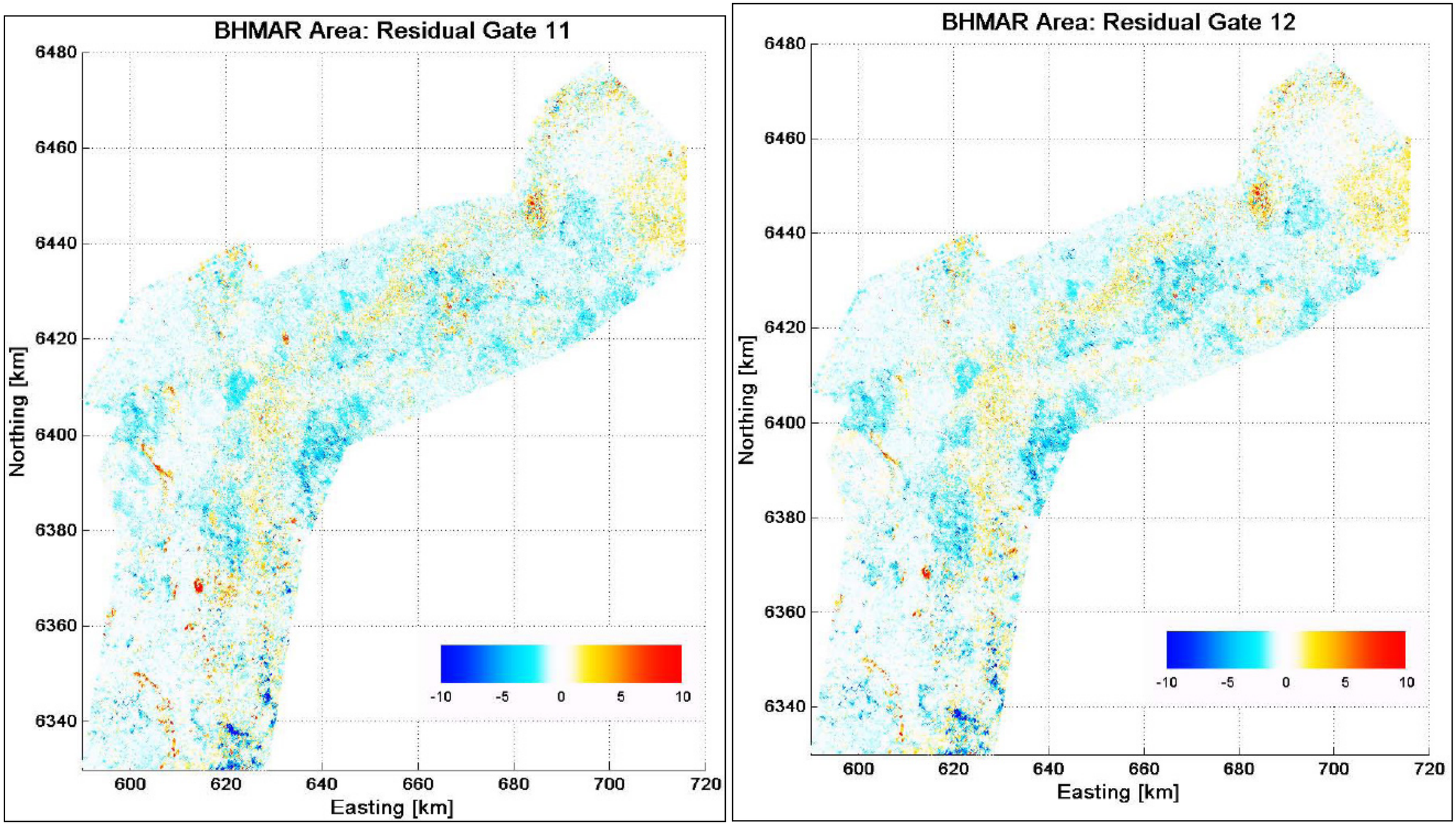



**Figure 6-58.** *Maps of fitting error for the 11th Low Moment (LM) gate (left) and 12th LM gate (right) for the BHMAR project area. The 11th and 12th gate fits are very similar, and generally very good. The greatest misfits are generally with the basement high in the NE of the study area, and the misfits increase with subsequent gates.*

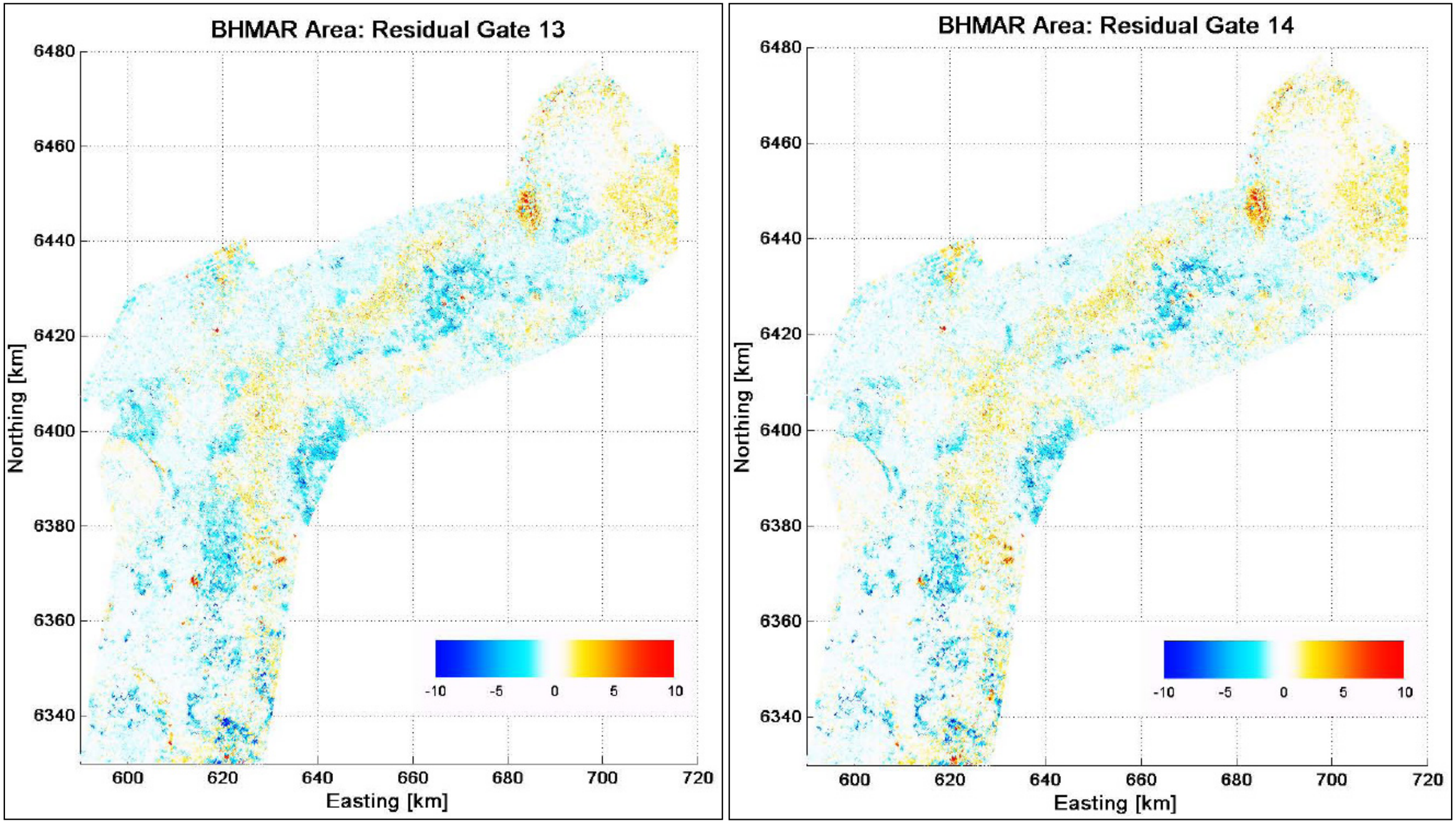



**Figure 6-59.** *Maps of fitting error for the 13th Low Moment (LM) gate (left) and 14th LM gate (right) for the BHMAR project area. The 13th and 14th gate fits are very similar, and generally very good. The greatest misfits are generally with the basement high in the NE of the study area.*

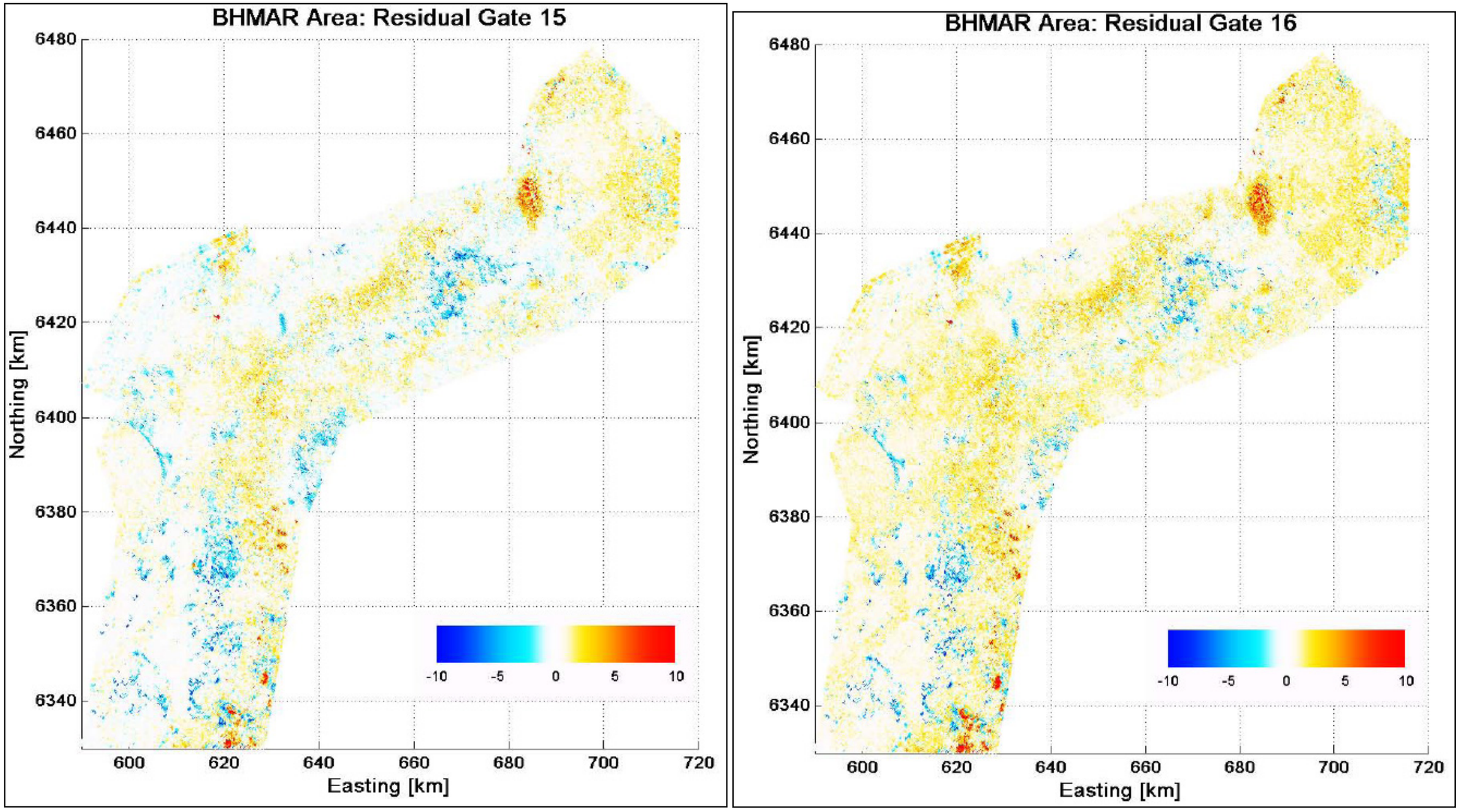



**Figure 6-60.** *Maps of fitting error for the 15th Low Moment (LM) gate (left) and 16th LM gate (right) for the BHMAR project area. The 15th and 16th gate fits are very similar, and generally very good. The greatest misfits are generally with the basement high in the NE of the study area.*

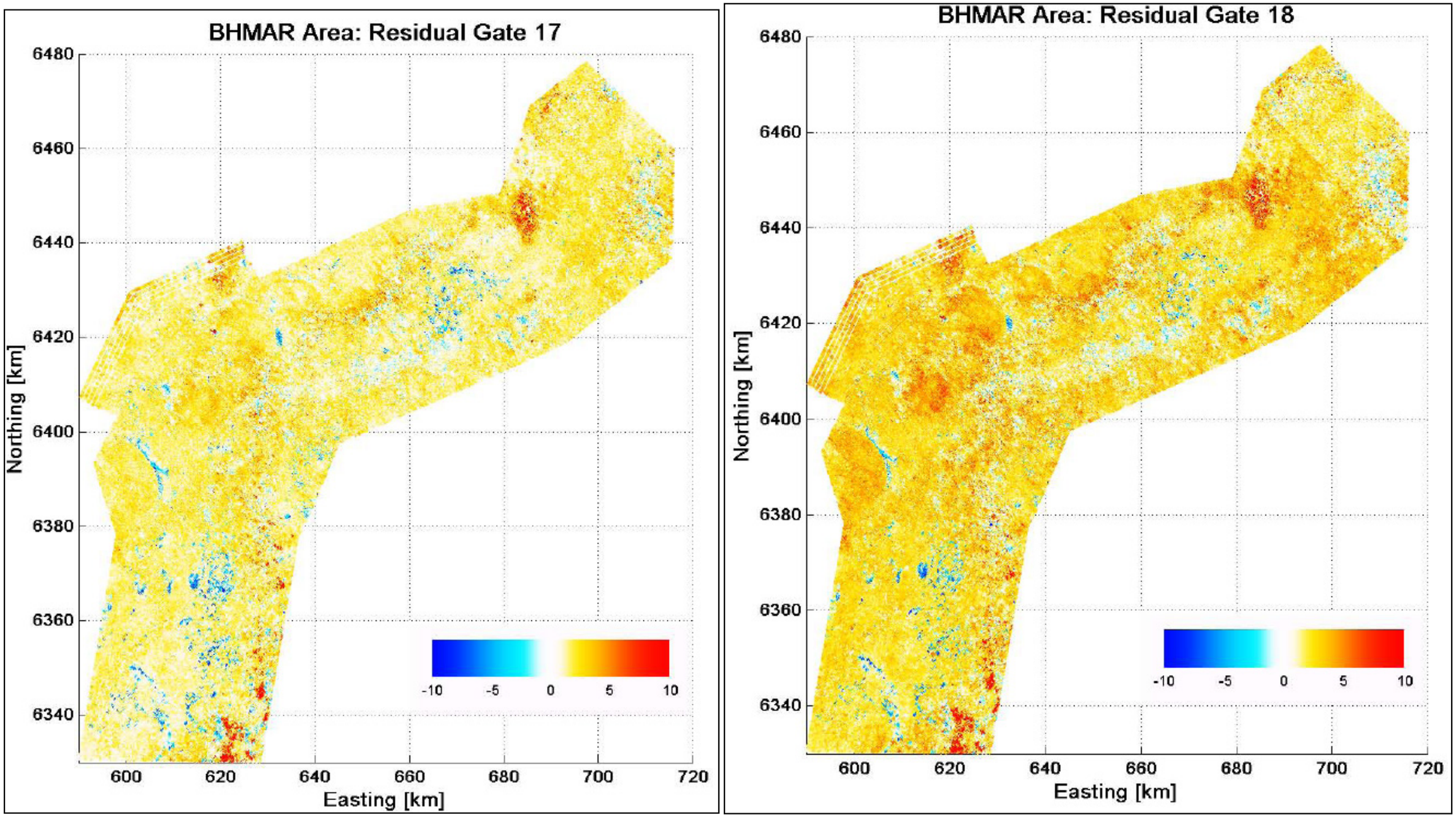



**Figure 6-61.** *Maps of fitting error for the 17th Low Moment (LM) gate (left) and 18th LM gate (right) for the BHMAR project area. The 17th gate fits (left) are generally poorer than for the preceding gates. The greatest misfits are generally with the basement high in the NE of the study area. The misfit observed in the 18th gate (right) is poorer again. The overall level of error in gate 18 indicates that the signal to noise ratio has deteriorated significantly.*

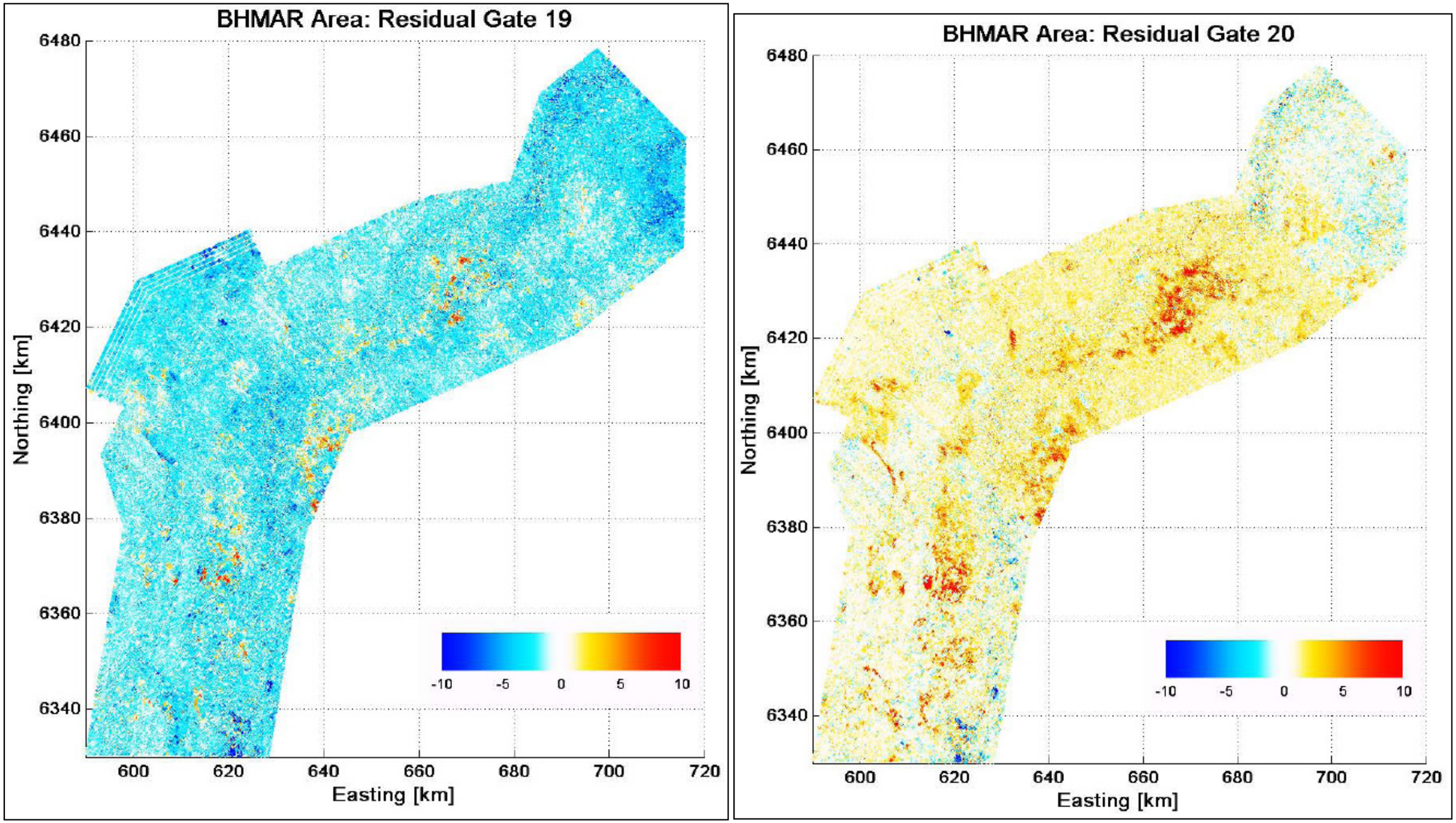



**Figure 6-62.** *Maps of fitting error for the first High Moment (HM) gate (19 – left) and second HM gate (20- right) for the BHMAR project area. The fairly uniform turquoise colours in the initial HM gate (left), indicate ~10% relative fitting error compared with the assigned noise level of 3% (a factor of 3). In the second HM gate (right) the level of misfit is decreased significantly, but with 'speckled' areas of red (higher misfit) in the right hand image present at a few locations reasonably consistently through the dataset, indicating a poor fit in these areas. With joint inversion of the HM and LM, it is more likely that the last gates of the LM and the first gates of the HM are inconsistent, with the integrated levels being too high.*

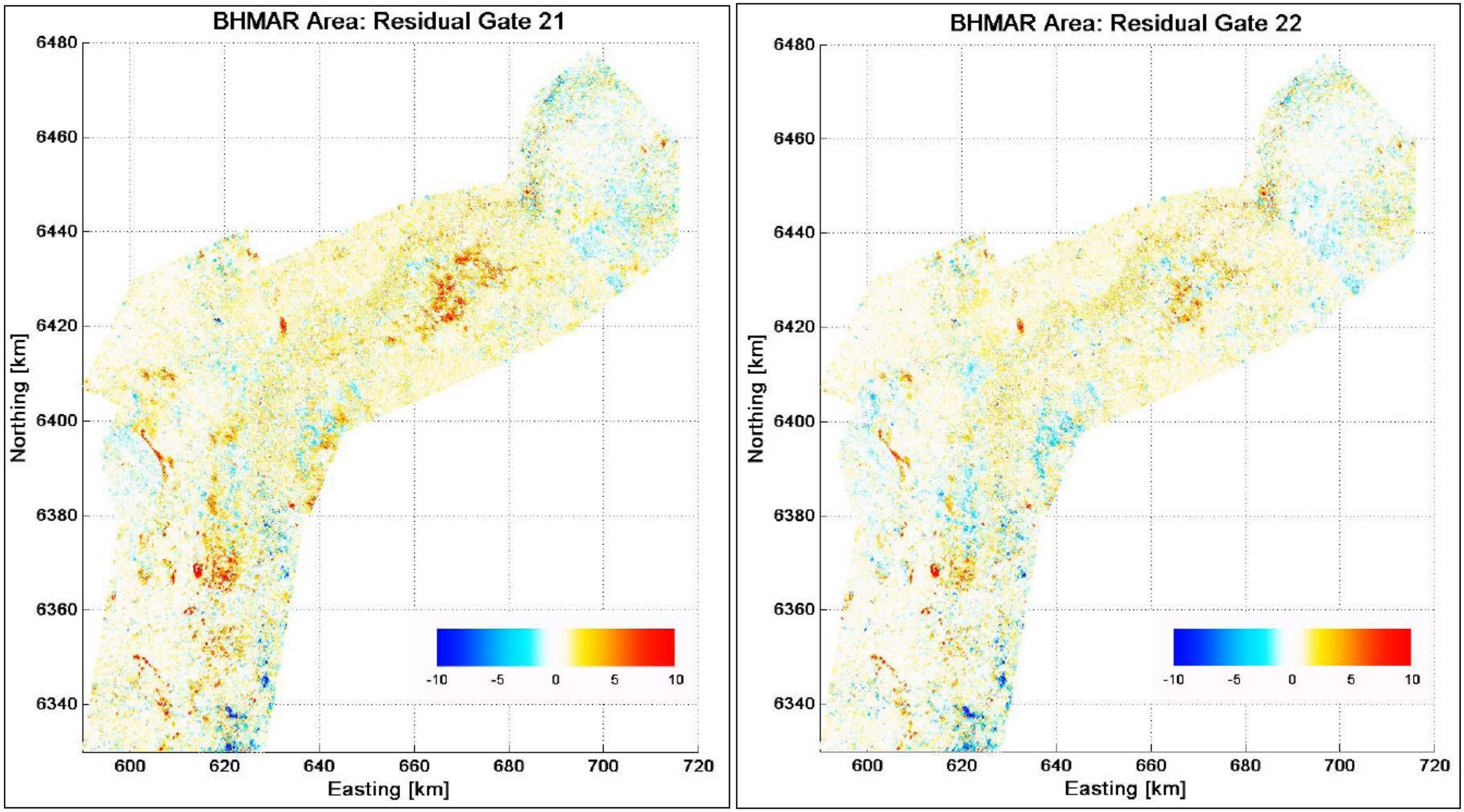



**Figure 6-63.** *Maps of fitting error for the 3rd HM gate (21 – left) and 4th HM gate (22- right) for the BHMAR project area. The levels of misfit have decreased significantly compared with the two initial HM gates, with a low overall level of misfit observed in both gates 21 and 22. There are only a few small 'speckled' areas of red (higher misfit), indicating a poor fit in these areas.*

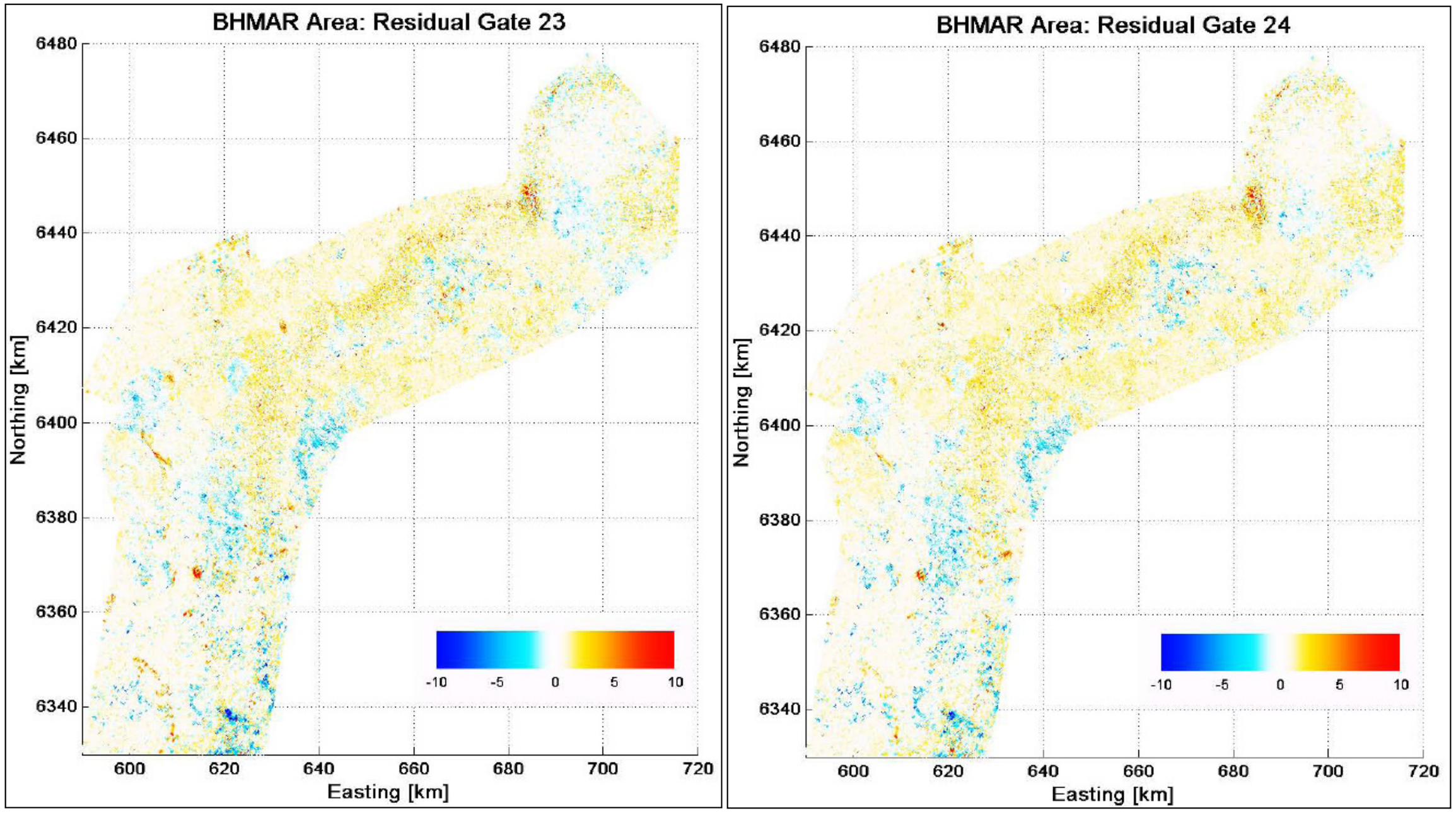



**Figure 6-64.** *Maps of fitting error for the 5th HM gate (23 – left) and 6th HM gate (24- right) for the BHMAR project area. Low levels of misfit are observed in both gates 23 and 24. There are only very few small 'speckled' areas of red (higher misfit), indicating a poor fit in these areas. These areas include an oval area coincident with a basement high feature in the NE of the study area, where higher resistivities in the basement lead to lower signal levels, more noise, and consequently a poorer fit.*

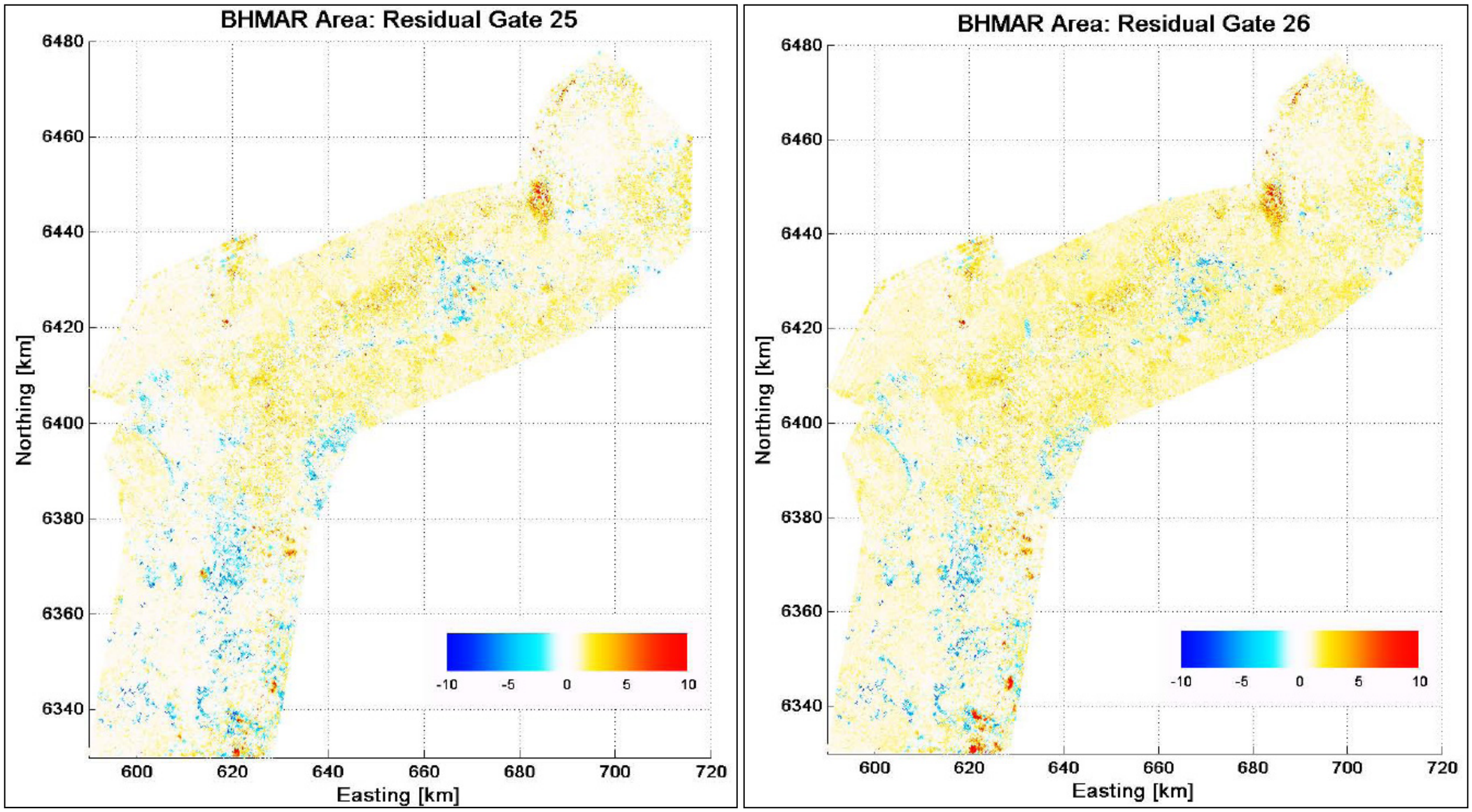
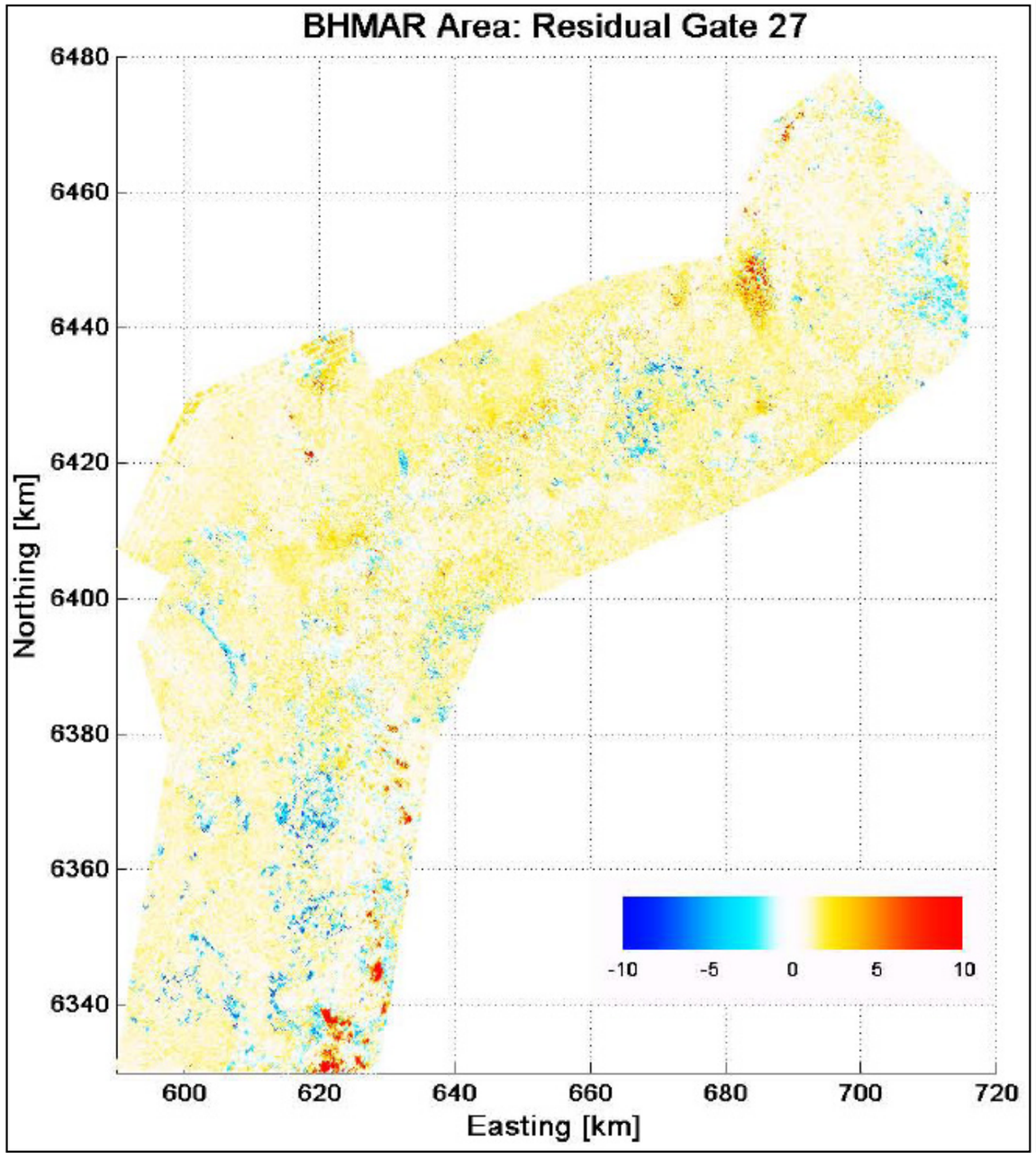



**Figure 6-65.** *Maps of fitting error for the 7th HM gate (25 – left) and 8th HM gate (26- right) for the BHMAR project area. Low levels of misfit are observed in both gates 25 and 26. There are only very few small 'speckled' areas of red (higher misfit), indicating a poor fit in these areas. These areas include the oval area coincident with a basement high feature in the NE of the study area, where higher resistivities in the basement lead to lower signal levels, more noise, and consequently a poorer fit.*



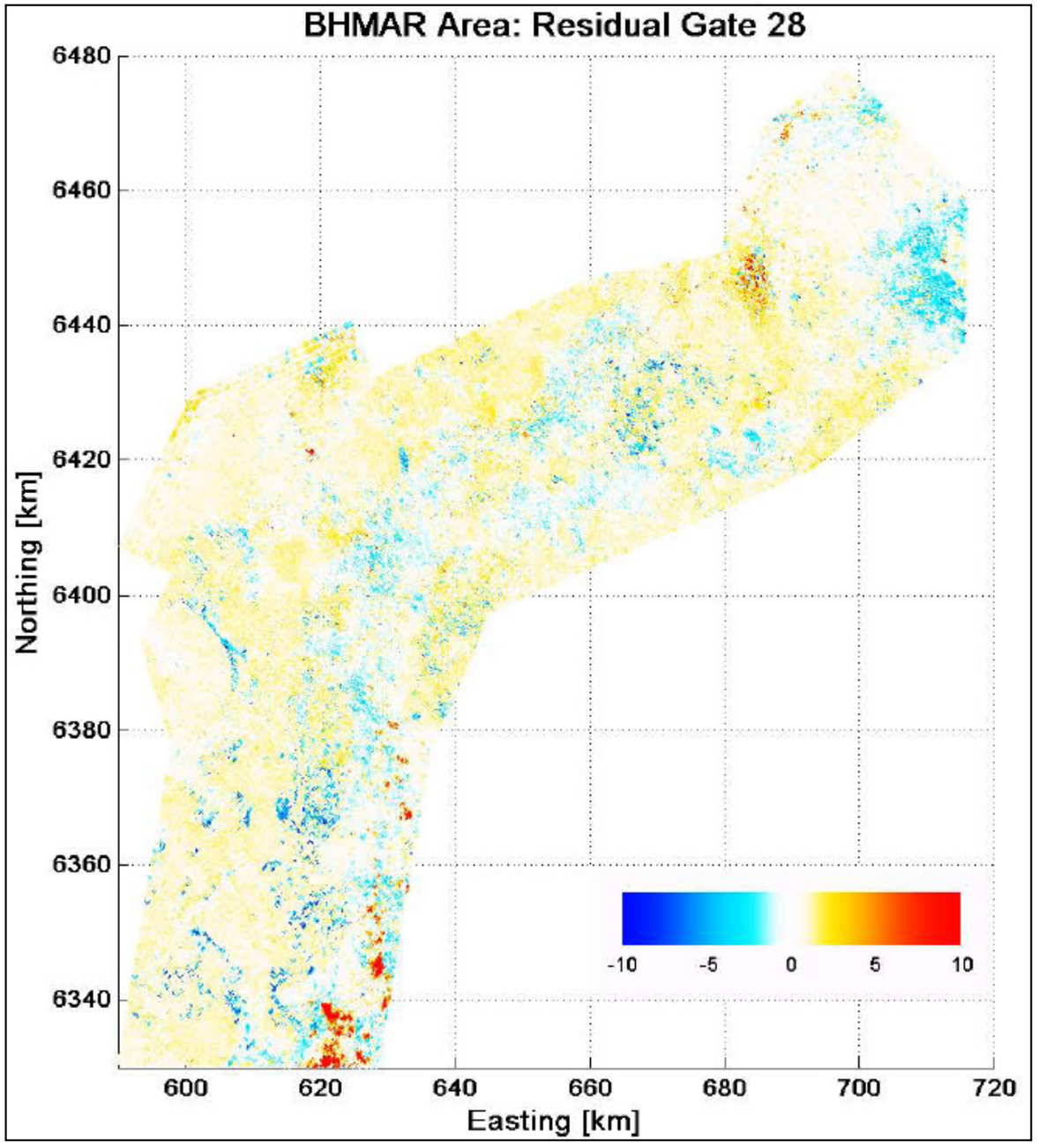




**Figure 6-66.** *Maps of fitting error for the 9th HM gate (27 – left) and 10th HM gate (28- right) for the BHMAR project area. Low levels of misfit are observed in both gates 27 and 28. There are only very few small 'speckled' areas of red (higher misfit), indicating a poor fit in these areas. These areas include the oval area coincident with a basement high feature in the NE of the study area, where higher resistivities in the basement lead to lower signal levels, more noise, and consequently a poorer fit.*

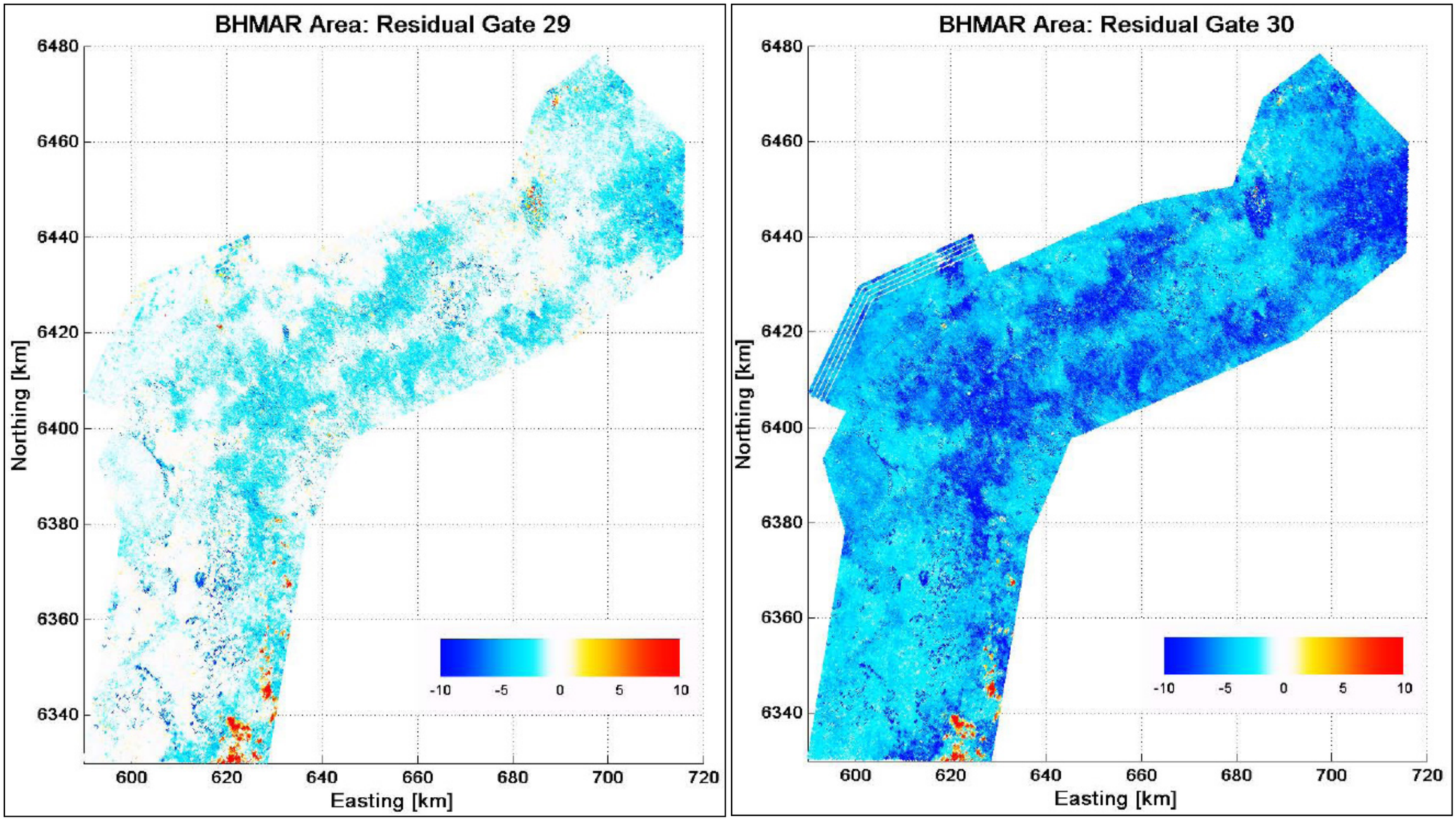



**Figure 6-67.** *Maps of fitting error for the 11th HM gate (29 – left) and 12th HM gate (30- right) for the BHMAR project area. In the 29th gate (left), there are relatively low levels of misfit in significant parts of the area, but with higher misfits associated with areas underlying the major rivers, in contrast to the particularly good fits in the overlying gates. The reason for this is not known. There is also a poor misfit in a triangular area in the extreme NE of the project area. The latter area is an area of significant misfit in the remaining later gates, and is an area where geological interpretation at depth was not possible. Gate 30 is characterised by poor to bad misfits, particularly in the same areas of poor misfit in the earlier gate.*

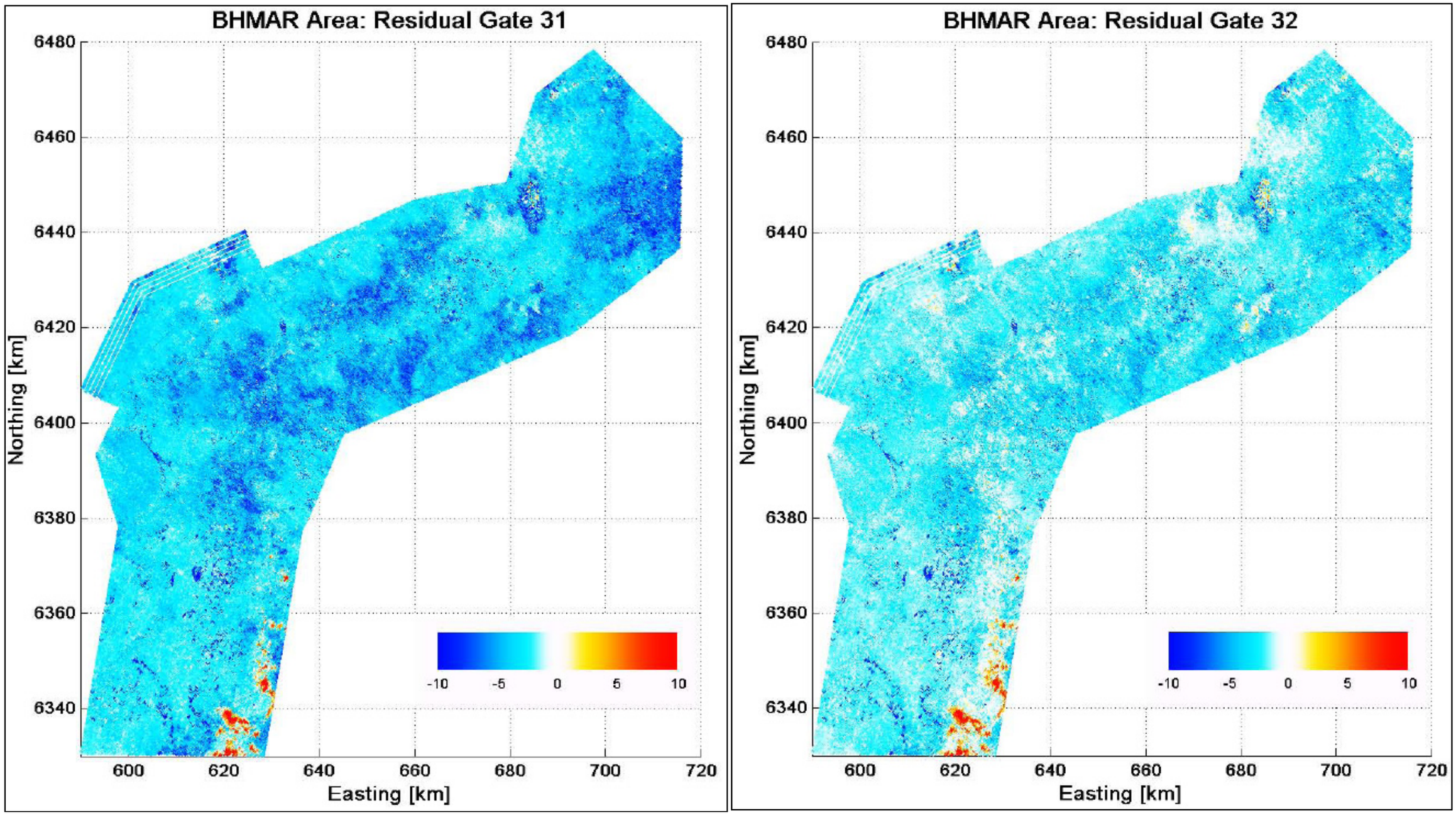



**Figure 6-68.** *Maps of fitting error for the 13th HM gate (31 – left) and 14th HM gate (32- right) for the BHMAR project area. As in the 30th gate, there is a poor to bad misfit across the project area in the 31st gate (left). In the 32nd gate (right), misfits are not as bad as in the 29th and 30th gates, with better fits in the areas coincident with the overlying rivers. The reason for the apparent 'flip' to poor misfits in the 30th and 31st gates is not known. These represent depths below the targets of interest.*

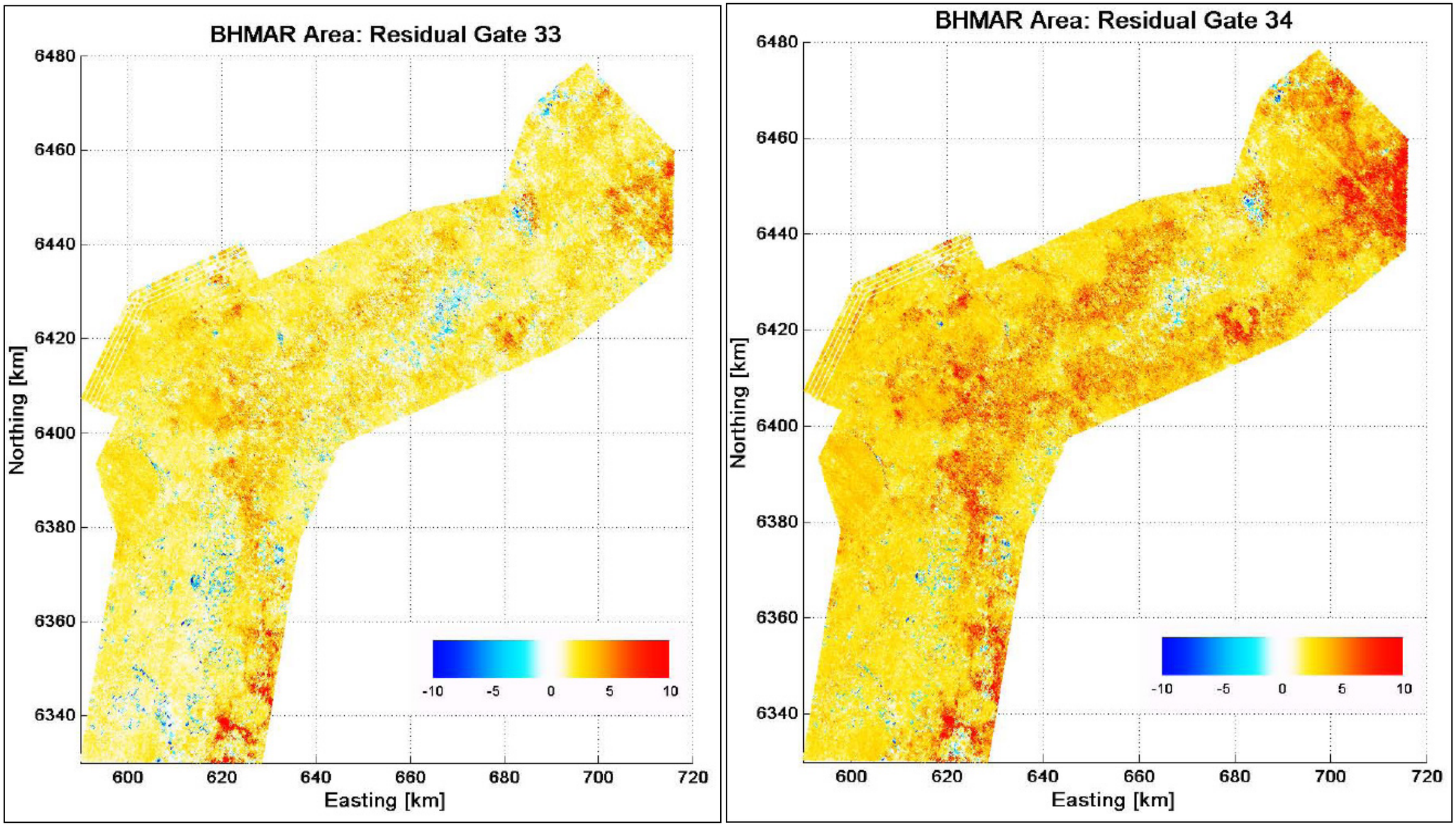



**Figure 6-69.** *Maps of fitting error for the 15th HM gate (33 - left) and 16th HM gate (34- right) for the BHMAR project area. As in the 32nd gate, there is a good- poor misfit across the project area in the 31st gate (left). In the 34th gate (right), misfits are again poor to bad, particularly in the areas coincident with the overlying rivers.*

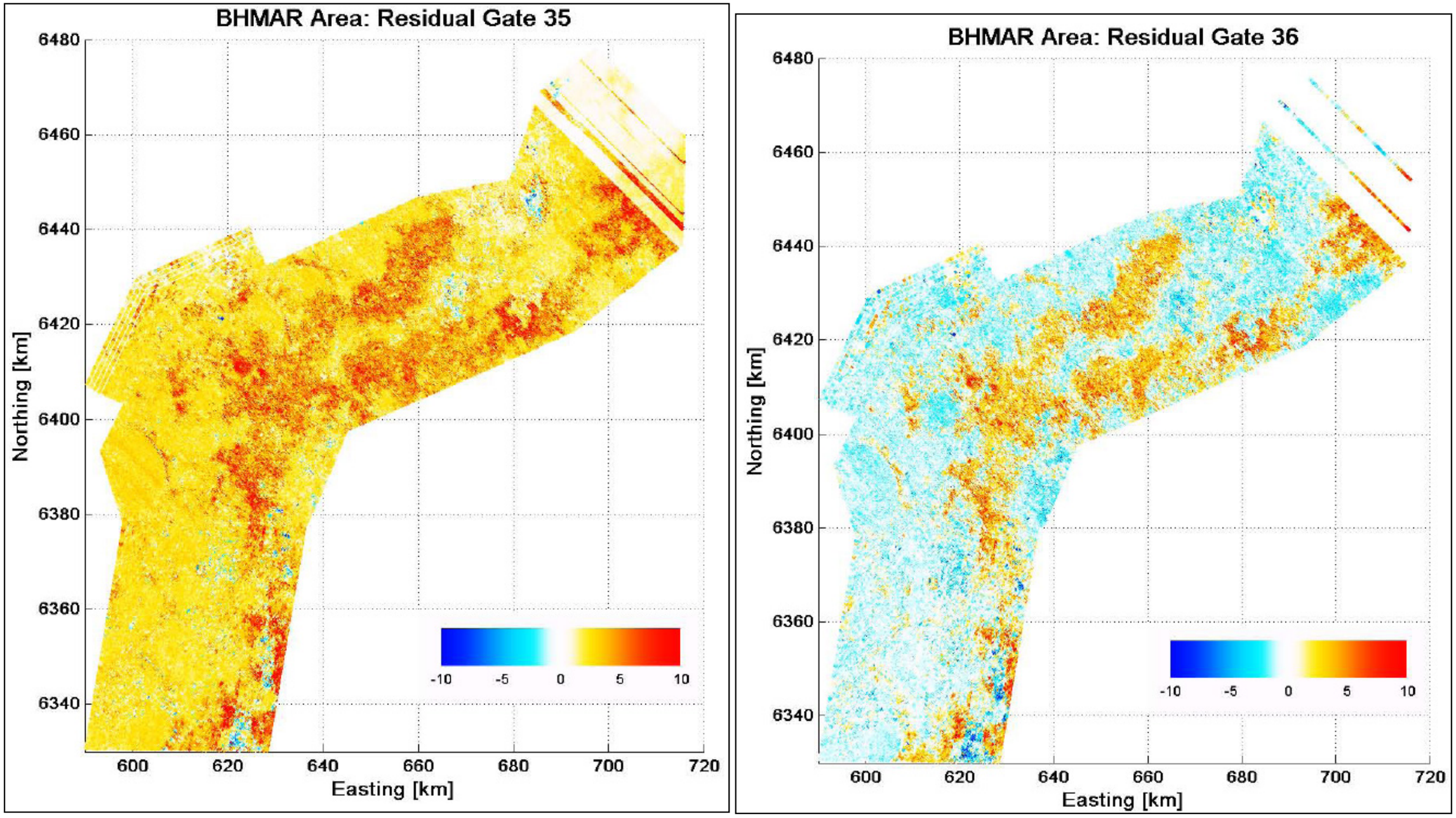



**Figure 6-70.** *Maps of fitting error for the 17th HM gate (35 - left) and 18th HM gate (36- right) for the BHMAR project area. As in the 34th gate, there is a poor to bad misfit across the study area in the 35th gate (left), particularly in the areas coincident with the overlying rivers, and in a triangular area in the NE of the study area. In the 36th gate there is a good to bad misfit across the study area, with poor misfit coincident with the overlying rivers.*

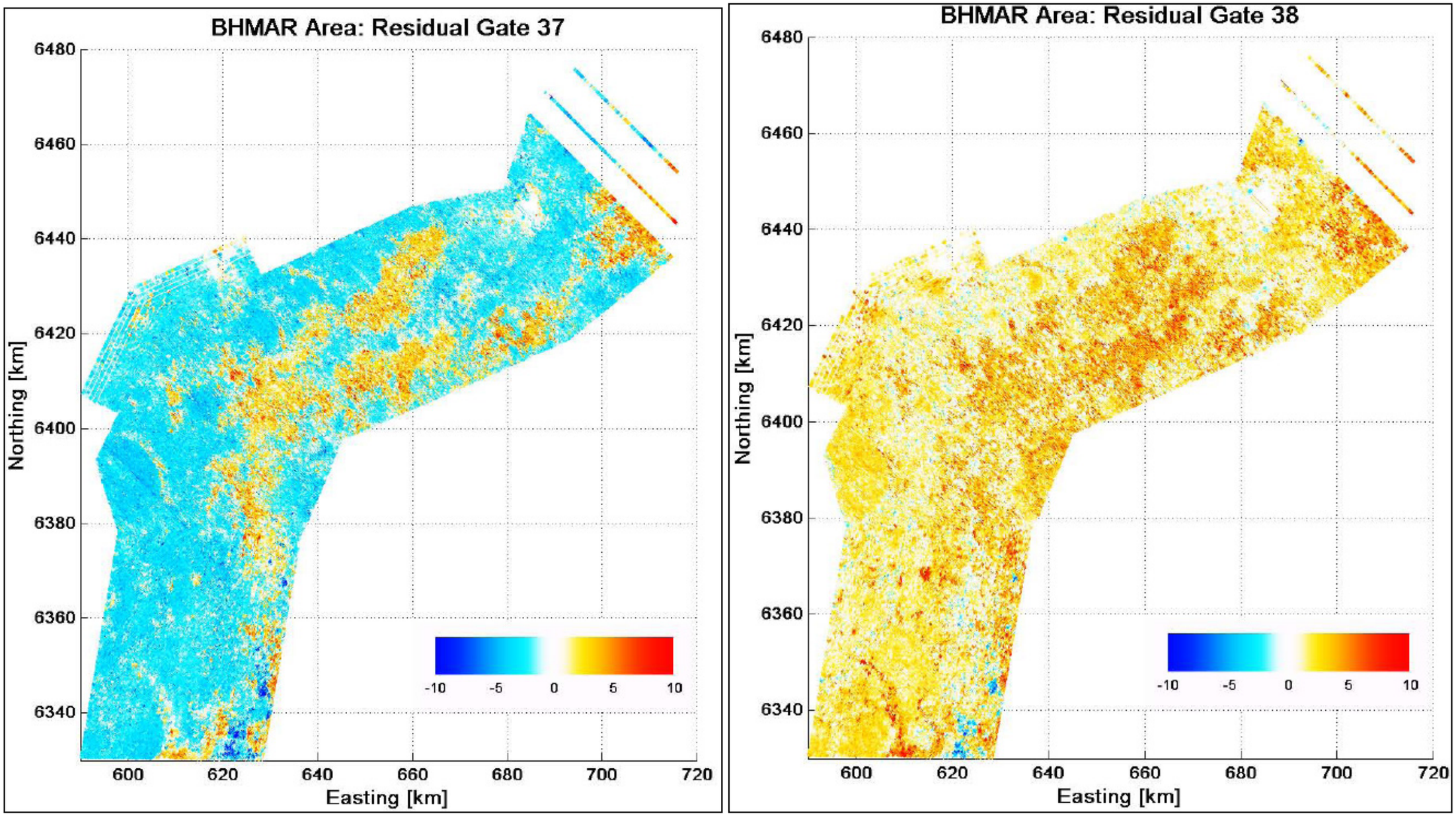



**Figure 6-71.** *Maps of fitting error for the 19th HM gate (37 - left) and 20th HM gate (38- right) for the BHMAR project area. There is a poor to bad misfit across the study area in the 37th gate (left), particularly in the areas coincident with the overlying rivers. The data for the northern area from gate 37 and later timing gates was deemed too poor to include, and was culled by the contractor. In the 38th gate there is a good to bad misfit across the study area, with a particularly bad misfit coincident with the overlying rivers.*

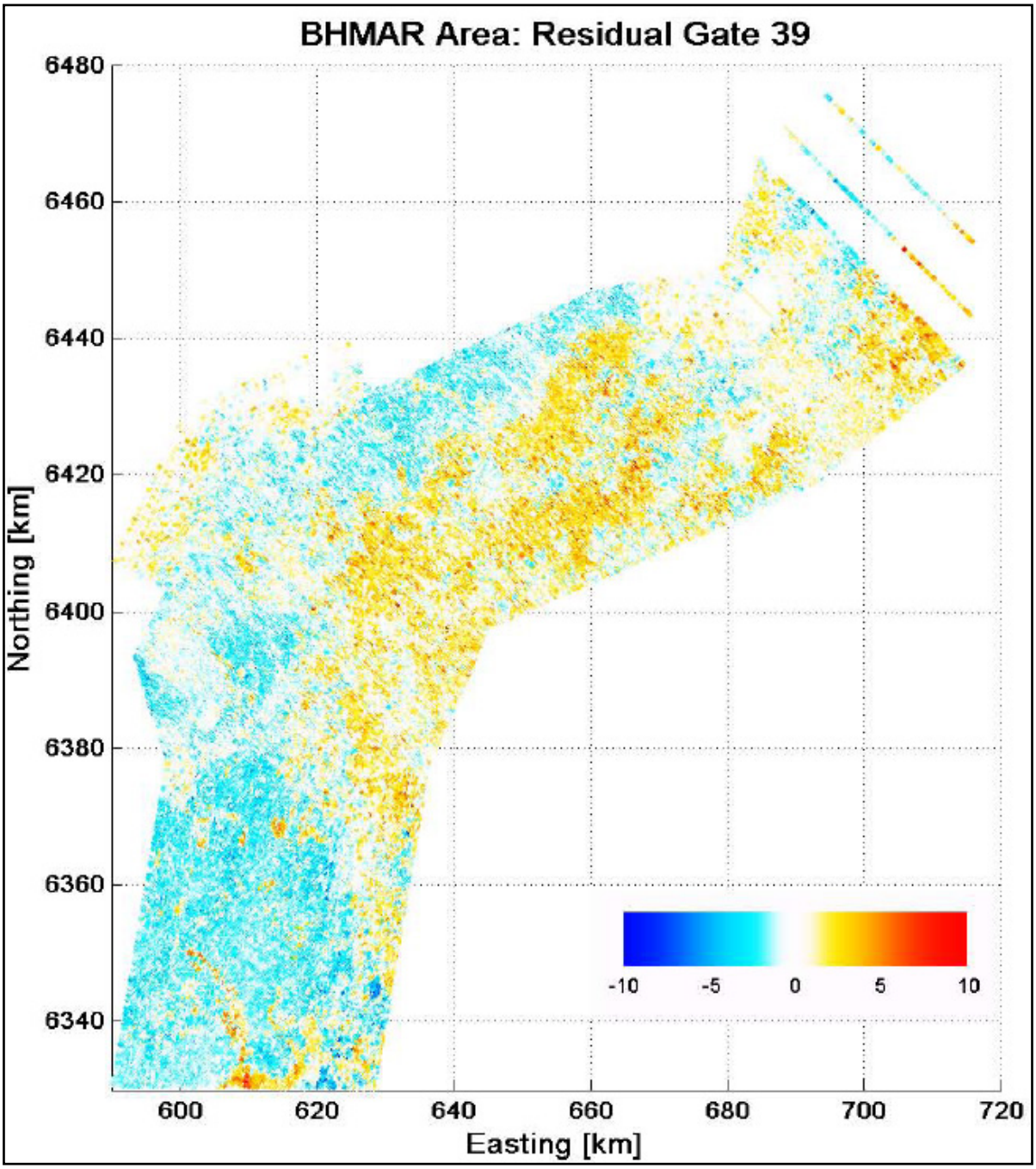



**Figure 6-72.** *Maps of fitting error for the 21st HM gate (39) the BHMAR project area. There is a poor to bad misfit across the study area, particularly in the areas coincident with the overlying rivers. The data for the northern area was deemed too poor to include, and was culled by the contractor.*

#### 6.7.4.6 ***Conclusions***

The histograms over the residuals for the whole survey indicate that, overall, the measuring situation and the data processing and calibration have not introduced a consistent bias in the data incompatible with a 1D inversion. The standard deviation attains a value of 2.4 which is indeed a small number. This shows that, overall, data are consistent with a 1D conductivity model, the noise model is reasonable and the inversion models were able to fit the data.

The histograms for the individual gates show that the mean and the standard deviation is higher for the early and the late gates for each moment, probably due to the effect of varying waveform (early gates), increased noise (late gates) and mutual inconsistencies between the LM and HM data (late LM gates and early HM gates).

The maps of the lateral distribution of the absolute values of the misfits for each gate are in accordance with the results seen in the histograms, but they also show that the occurrence of high and low misfits is quite localised and that the pattern persists between the gates, especially the middle gates on each moment. The fact that the pattern is similar between the gates indicates that 3D effects could be part of the reason for the variation.

A few of the gates, HM gates 30-32, display abnormal behaviour, pointing to inadequacies in the data processing. However, these gates are not the most important ones for mapping the top 40 m of the subsurface - they are focused at greater depth - so their anomalous behaviour does not invalidate the general conclusion that the target depth interval of the BHMAR survey is mapped with consistent well-behaved misfit statistics.

## 6.8 COMPARISON OF BOREHOLE EM DATA WITH THE FINAL INVERSION

### 6.8.1 Introduction

Validation of AEM data inversions is a critical step in determining when a dataset is reliable, and when different inversions approaches are required (Lane *et al.,* 2004). Use of AEM data by a broad range of stakeholders is critically dependent on being able to demonstrate that the inversion products are a good representation of ground conductivity measurements. Of particular importance is being able to quantify how well inversions track changes in ground conductivity with increasing depth.

To validate a suite of inversion products, it has become standard practice in Australia to carry out comparisons of ground conductivity derived from borehole conductivity logging with the nearest AEM Fiduciary Points (Lawrie *et al.,* 2000, 2009c, 2010a, b, c). Whilst borehole data are often cited as 'truth' when it comes to validating the response of an airborne EM system, considerable caution should be exercised when interpreting a comparison of conductivity measurements made with a borehole inductive conductivity tool, against those derived from an AEM system (see Lane *et al*., 2001). Both systems measure an inductive response from the ground; however the systems, data characteristics and sampling volumes are extremely different, and they both contain uncertainty in their measurements. Some of the uncertainties and errors in measurement have been discussed earlier.

Borehole conductivity measurements do not vary in vertical resolution with depth, as both the transmitter loop and receiver coil are present in the tool at the desired depth of measurement. The borehole conductivity tool samples a cylinder with a vertical extent of ~1 meter and a radius of ~1 m as seen in Figure 6-73 where the 2D sensitivity function of the tool is illustrated. Given the small sampling volume, measurements can be subject to the effects of sediment formation changes that arise during and subsequent to drilling.

Other factors that affect borehole conductivity measurements are: porosity of soil; water salinity (current channelling); mineralogy; rock alteration etc. The consequences of groundwater of varying quality entering the hole from different levels in the hole are unknown (Lane *et al*., 2000). Added to these issues is the matter relating to the calibration accuracy of the logging tool which is also generally unknown, contrary to a commonly held understanding. Temperature variation of the borehole sonde causes varying conductivity measurements due to the widening and shortening of the separation distance between the transmitter and receiver coils (which are positively and directly coupled).

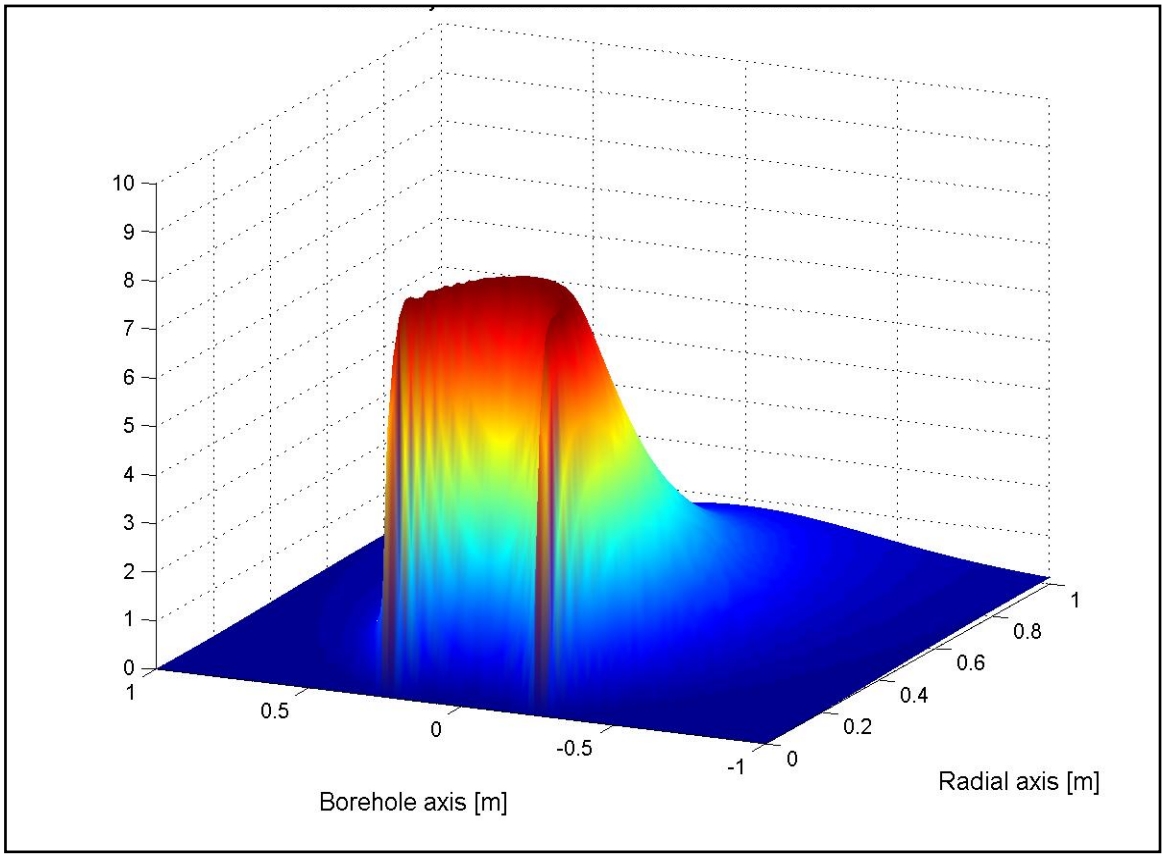



**Figure 6-73.** *2D sensitivity function of the borehole conductivity tool. The tool samples a cylinder with a vertical extent of ~1 m and a radius of ~1 m.*

SkyTEM measurements are made with transmitter loop and receiver coils positioned about 30 m above the ground. As a consequence, the vertical resolution of conductivity diminishes with depth. Ground response, measured as a function of delay time, results in an increased sampling volume at later times (Lane *et al*., 2000). If we make the simplification of the near-surface footprint (indicative of the resolution of an AEM system, a definition provided by Liu & Becker (1990)), the footprint of the SkyTEM system could be estimated as a multiple of the "scale" of the system, where scale is the function of the transmitter loop ground clearance (~30 m). The scale multiple is between 1 and 4, depending on the receiver coil component and the amount of the ground response that originates from within the footprint. For the SkyTEM system, this is between ~30 m and 120 m. It is evident that a more rigorous definition of the sampling volume needs to be determined and, while this is discussed in Section 6.4.4, we need to arrive at a result that is physically sound in order to proceed with a borehole-conductivity to AEM inversion-conductivity comparison. This is the subject of further analysis.

In an ideal situation, ground conductivity from a series of closely spaced bores sampling the entire footprint of the SkyTEM system should be combined prior to a comparison with the modelled conductivity from the airborne dataset. This ensures that local variations in conductivity defined by borehole logs are incorporated into a weighted or averaged ground response, thereby forming a more valid basis for comparison with the airborne data. Realistically these data are rarely available and, therefore, a comparison between the two is, at best, indicative rather than definitive. For this reason, we encourage the use of the terms ‘consistency’, ‘inconsistency’ and ‘misfit’ when comparing AEM inversion results to borehole conductivity.

An added issue to consider is that the inversion procedure used to derive a model of ground conductivity from the SkyTEM dataset assumes that conductivity structures are horizontally layered within the ground; and that the conductivity value defined for each discrete depth layer accounts for average ground conductivity across or through that particular depth interval. Furthermore, as mentioned above, the conductivity log has the same sensitivity at all depths and will therefore be able to indicate rather thin layers at depth whereas the models arising from inversion of the SkyTEM data will not due to the broadening of the

sensitivity function with depth. With SkyTEM, the along-line sampling intervals differ for the High and Low Moments respectively and, although the sampling interval along flight lines is relatively close (<20 m), this adds an additional limit to the horizontal spatial resolution of the system.

### 6.8.2 Comparing Borehole Conductivity Logs and Final AEM Inversion Results

Traditionally, the misfit between borehole conductivity logs and AEM inversion models has been expressed through the so-called 'FID point comparison'. In this approach, the borehole conductivity log is compared with the model conductivities obtained from inversion of AEM data from the location closest to the borehole (Lawrie *et al*., 2000, 2006, 2008, 2009a-d, 2010a-c; Lane *et al*., 2000).

In modern inversion practices, the information from the borehole conductivity logs is included as constraints in the inversion of the AEM data. The borehole logs represent valuable information that, naturally, should be included in the inversion to obtain the best possible models. The borehole log information will spread to the adjacent models through the lateral correlation of the inversion, and experience from this project shows that, with the lateral correlation strengths used in the final inversion, the borehole information affects the inversion models within a radius of 50-300 m from the borehole. It follows that the misfit between the borehole log and the closest AEM inversion model will become smaller when borehole information is used in the inversion than if it is not, and the comparison between borehole conductivities and AEM inversion model conductivities must be seen in that perspective.

In the following sections, the AEM inversion models are compared with borehole conductivity logs that were not included in the inversion, thus establishing an independent test.

There are several issues that need be acknowledged in connection with using this method to assess possible inconsistencies between borehole conductivity logs and the models resulting from AEM inversion. The basic problem with the comparison is the huge scale difference between the volume occupied by the sensitivity of the log tool and the corresponding volume for the sensitivity function of an airborne TEM measurement. At early delay times for the AEM data, the ratio between the log volume and the AEM volume is of the order of 1:10,000 while for late times, the ratio is of the order of 1:10,000,000 The scale issue is a long and complicated discussion worth a research effort of its own, and this is not the place to go into details. However, it must be kept in mind that in a comparison between conductivity values coming from geophysical methods with such disparate sensitivity distributions, there will potentially be many cases of apparent, but false, inconsistency between the borehole conductivity and the AEM conductivity, and likewise there will be many cases of apparent, but false, consistency.

Another issue worth mentioning is that the AEM inversion models are found through inversion, they are *models* found by assuming a 1D conductivity distribution, while the conductivity logs are *data* indicating an *apparent* conductivity. A more consistent approach to the comparison would be to avoid comparing numbers from model space and data space, and instead make a comparison in the model space for both methods (ModMod) or in the data space (DatDat) for both models.

The ModMod comparison can be achieved by inverting the conductivity log data with the same 1D multi-layer model as the one used in the AEM inversion and then perform the comparison between layer conductivities. The DatDat comparison can be carried out by first inverting the conductivity log data to obtain a 1D model and then forward calculating the response of that model for an AEM system and compare with the actually measured data at the FID point position.

In the following sections - for all boreholes in the BHMAR survey - we shall pursue both of the two self-consistent approaches by comparing models with models and data with data and express the difference between the borehole and AEM parameters taking their uncertainty into account.

We shall express the misfits through a normalized least squares residual, i.e. the sum of the squares of the differences between the two parameters to be compared divided by the variance of the difference; this sum is

then divided by the number of terms to give an average value, and finally the square root is taken to deliver a result that reflects the difference and not the square. By dividing each term with the variance of the difference, the difference is weighted according to how much we can trust each of the terms. This ensures that the value of the residual carries a reasonable significance in expressing the overall, mean difference between the two parameters to be compared: a difference is considered more serious if the uncertainties are small and less serious if the uncertainties are large. The normalised residual thus measures the difference in units of the uncertainty on the parameters. If the normalised residual has a value of unity, it means that on average the expected difference between the parameters is of the same order of magnitude as the uncertainty on the parameters, i.e. statistically they are the same.

#### 6.8.2.1 *ModMod comparison*

To find a borehole model, the apparent conductivity data were inverted with the same 30-layer model as the AEM data using the low-frequency approximation for the borehole log tool defined in Section 6.7.3.17, and with the inversion comes an estimate of the uncertainty of the layer conductivities (the variance).

For the ModMod comparison, the residual is defined as:

$$R_{ModMod} = \sqrt{\frac{1}{L}\sum_{i=1}^{L} \frac{\left(\sigma_i^{aem} - \sigma_i^{log}\right)^2}{\mathrm{var}\left(\sigma_i^{aem}\right) + \mathrm{var}\left(\sigma_i^{log}\right)}}$$

**Equation 57**

where L is the number of layers, $\sigma_i^{log}$ and $\sigma_i^{aem}$ are the conductivity of the $i$'th layer of the borehole and AEM models, respectively; var $\left(\sigma_i^{log}\right)$ and var $\left(\sigma_i^{aem}\right)$ are the corresponding variances, respectively. The variance of the difference: $\left(\sigma_i^{aem} - \sigma_i^{log}\right)$, is the sum of the variances of the two terms: var $\left(\sigma_i^{aem} - \sigma_i^{log}\right) =$ var $\left(\sigma_i^{aem}\right) +$ var $\left(\sigma_i^{log}\right)$ because $\sigma_i^{aem}$ and $\sigma_i^{log}$ are uncorrelated.

#### 6.8.2.2 *DatDat comparison*

To be able to carry out a comparison in the data space, we need to compute the forward response of a borehole model. First, the log conductivity data were inverted to find a model, and to ensure that all borehole conductivity variation was accounted for, we used a 101-layer model. We then computed the AEM forward response, i.e. the data that would be measured by the AEM system, if the subsurface had the conductivity structure of the borehole model. In this forward response calculation, we used the same height and the same number of data as in the AEM model closest to the borehole.

In the same way as before, for the DatDat comparison, the residual is defined as:

$$R_{DatDat} = \sqrt{\frac{1}{M}\sum_{i=1}^{M} \frac{\left(V_i^{aem} - V_i^{log}\right)^2}{\mathrm{var}\left(V_i^{aem}\right) + \mathrm{var}\left(V_i^{log}\right)}}$$

**Equation 58**

where $M$ is the number of data, $V_i^{log}$ and $V_i^{aem}$ are the AEM response of the borehole models and the measured AEM data, respectively; var $\left(V_i^{log}\right)$ and var $\left(V_i^{aem}\right)$ are the corresponding variances, respectively.

Again, the sum of the variances is the variance of the difference $\left(V_i^{aem} - V_i^{log}\right)$ because the two terms are uncorrelated. The variance of the measured AEM data comes out of the noise estimates performed as part of the data processing, but the variance of the model response of the borehole model needs a little explanation.

The measured log conductivity data comes with an uncertainty which is estimated in the below equation and when inverting the borehole data with a 1D model, this uncertainty propagates to the model so that the layer

conductivities are associated with an uncertainty. An estimate of this uncertainty comes out of the inversion process through the posterior covariance matrix, $C_{est}$ (see Section 6.6). In the same way, when using this model to calculate the AEM forwards response, the uncertainty of the layer conductivities propagate to the calculated response. The uncertainty on the forward response can be estimated by the following expression:

$$\mathbf{C}_{pred} = \mathbf{J} \cdot \mathbf{C}_{est} \cdot \mathbf{J}^T$$

**Equation 59**

where J is the Jacobian matrix containing the derivatives of the data with respect to the layer conductivities for the borehole model, JT is the transpose of J, and Cest is the posterior covariance matrix of the inversion of the borehole data. The resulting matrix, Cpred, is the covariance matrix of the uncertainty of the forward response containing the terms var $\left(V_i^{log}\right)$ in the diagonal.

#### 6.8.2.3 *Results of the ModMod and DatDat comparisons for the final inversions*

To illustrate the comparisons, plots have been made for all 92 boreholes depicting the three comparisons defined above. The ModMod and the DatDat comparisons are shown in two different plots. Here, only a few examples will be shown, but in Appendix 4 (Apps *et al.*, 2012c) all 92 plots pertaining to the boreholes in the BHMAR area are shown for both the ModMod and the DatDat comparisons.

Figure 6-74 and Figure 6-75 show plots of the ModMod and the DatDat comparisons for borehole BHMAR33-7. An explanation of the plot is given in the figure caption. For the BHMAR33-7 there is a very high degree of consistency in the FID point comparison. Figure 6-76 and Figure 6-77 are plots of the ModMod and the DatDat comparisons for borehole BHMAR03B-1 where there is more inconsistency in the FID point comparison. The AEM model does register the high conductivity layers seen in the log at 5 m and 18 m, but they are both placed deeper in the AEM model. Notice also that the uncertainty of the borehole model conductivities is very high at the surface. This is caused by the fact that there are no conductivity log samples above 2.5 m depth, meaning that the uncertainty on the borehole model conductivities becomes very high, determined primarily by the regularization of the borehole data inversion. This characteristic is seen in several of the borehole models. The fact that the near-surface layers of the borehole model are determined primarily by the regularization and thereby the background model also accounts for the differences seen for early gates in the DatDat comparison.

To investigate whether there is a correlation between the residuals of the ModMod comparisons and the distance between the borehole and the AEM model - a larger distance might be connected with a larger misfit - the residuals have been plotted as a function of the distance between the borehole and the closest AEM model. Figure 6-78 shows the result. An immediate inspection shows that there is a very weak correlation between the FID distance and the residuals.

Likewise, to see if the ModMod residuals are correlated with the data residuals of the AEM inversion - a large degree of discrepancy might be caused by a poor data set - a similar plot is shown in Figure 6-78. Again, an immediate inspection shows that the correlation is weak. A similar investigation to see if the DatDat residuals were correlated with the data residuals of the AEM inversion gave the result that there was no correlation (plot not shown).

The distributions of the ModMod and the DatDat residuals for all boreholes are illustrated in the histograms of Figure 6-81, Figure 6-80 and Figure 6-81. For the ModMod residuals, the mean is 1.8 with a standard deviation of 0.7 and a maximum value of 5. The mean of the DatDat residuals is 6.3 with a standard deviation of 4.7

The fact that the ModMod residuals are of the order of 1 shows that, overall, there is good consistency between the borehole models and the AEM models. The DatDat residuals are somewhat higher, but the mean value of 6.3 must be compared with the mean value of the data residual in the AEM inversion which is 2.9, meaning that they are of the same order of magnitude, so, overall, there is a good consistency between the

measured data and the predicted data from the borehole models. It is worth noticing that using a 30-layer model instead of the 101 layer model to calculate the AEM forward response gave almost identical results (not shown here). All residuals and their mean, standard deviation and median values are listed in Table 6-12.

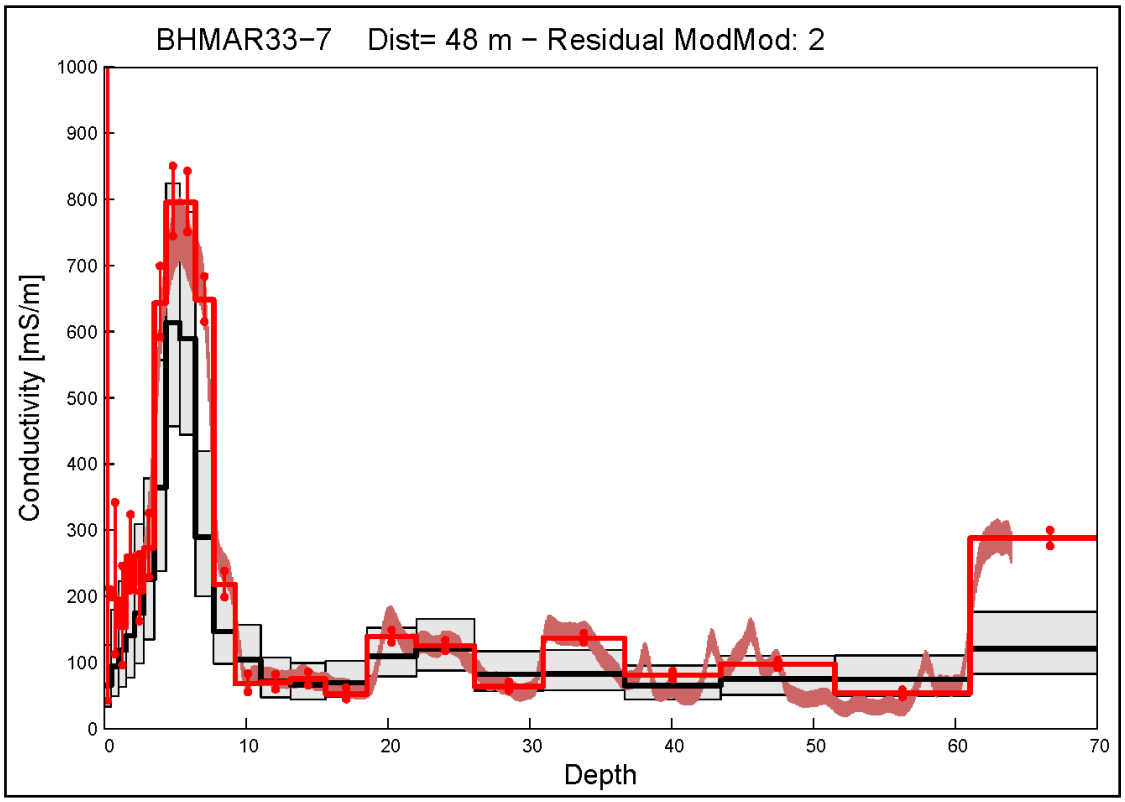



**Figure 6-74.** *ModMod comparison for BHMAR33-7. Borehole conductivity plotted in dark red as vertical line segments indicating the uncertainty. The 30-layer AEM model closest to the borehole is plotted in black with layer conductivity uncertainties indicated by the grey bars. The 30-layer borehole inversion model is plotted in red with layer conductivity uncertainties indicated by the red error bars. The distance between borehole and AEM model is given in the plot title together with the ModMod residual.*

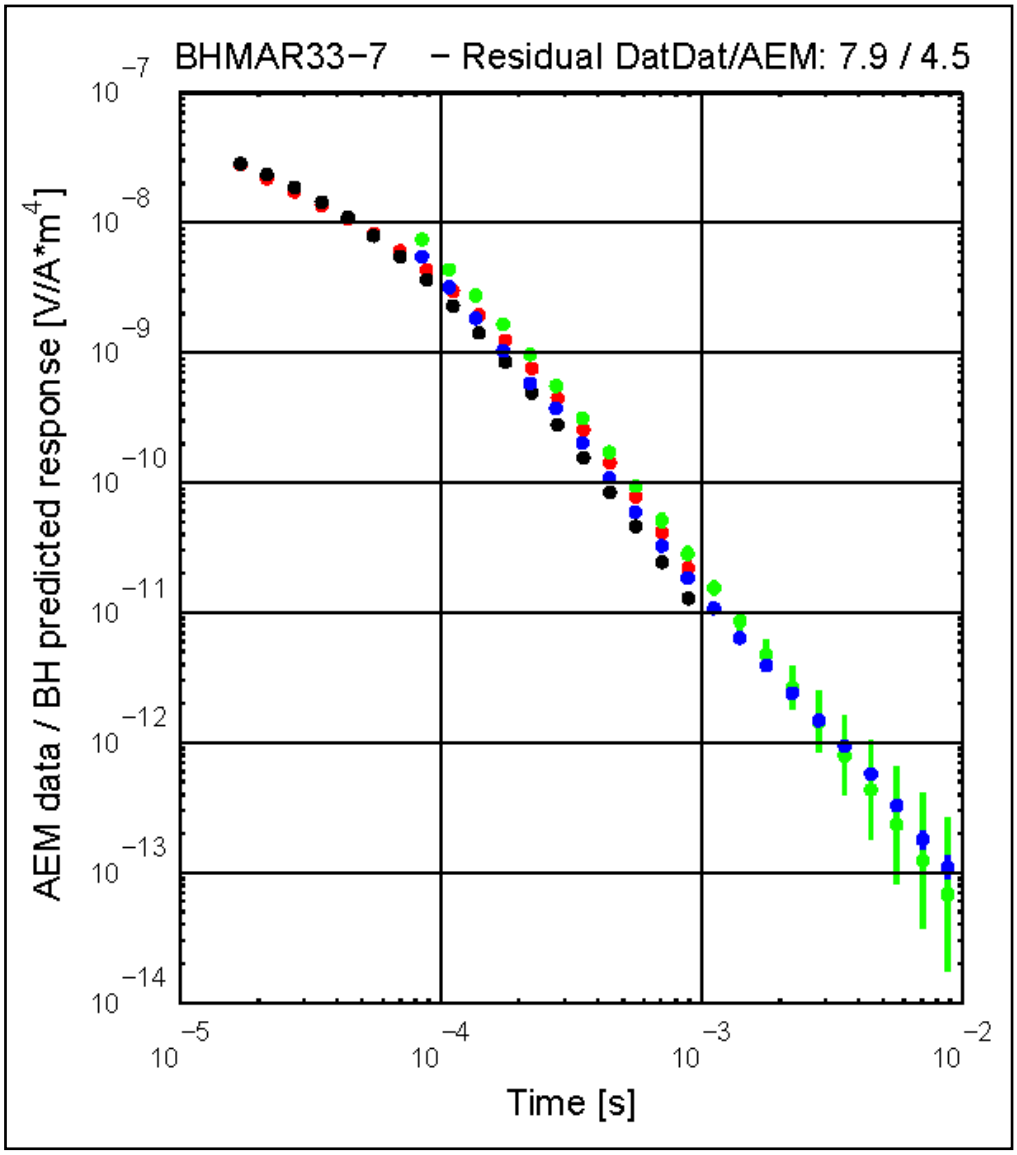



**Figure 6-75.** *DatDat comparison for BHMAR33-7. AEM data are plotted in black (Low Moment) and blue (High Moment) while borehole response is plotted in red (Low Moment) and green (High Moment). Error bars indicate the uncertainty of the data and response. The DatDat residual is given in the title together with the data residual of the AEM inversion for comparison.*

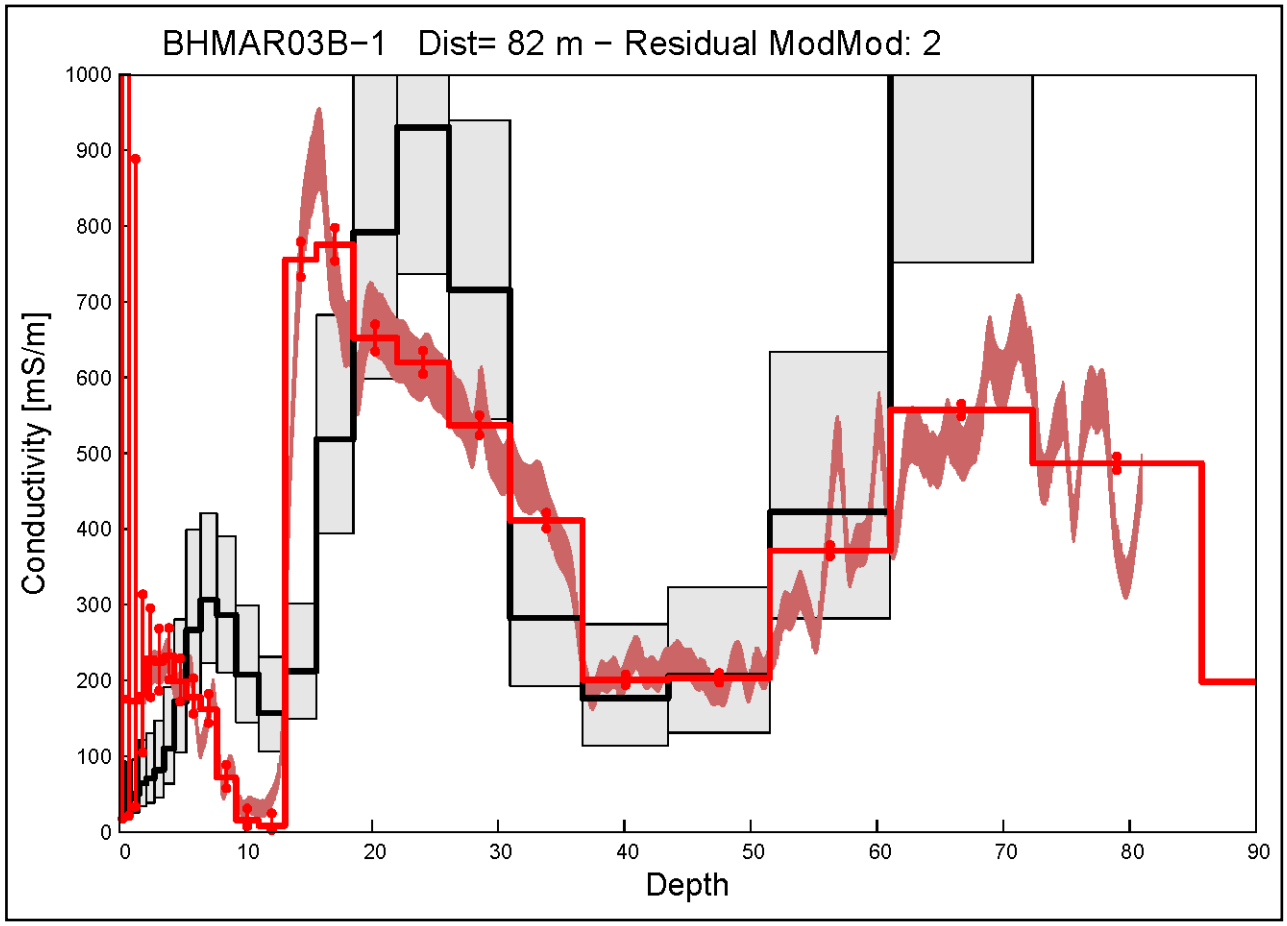



**Figure 6-76.** *ModMod comparison plot for BHMAR03B-1 borehole. Borehole conductivity plotted in dark red as vertical line segments indicating the uncertainty. The 30-layer AEM model closest to the borehole is plotted in black with layer conductivity uncertainties indicated by the grey bars. The 30-layer borehole inversion model is plotted in red with layer conductivity uncertainties indicated by the red error bars. The distance between borehole and AEM model is given in the plot title together with the ModMod residual.*

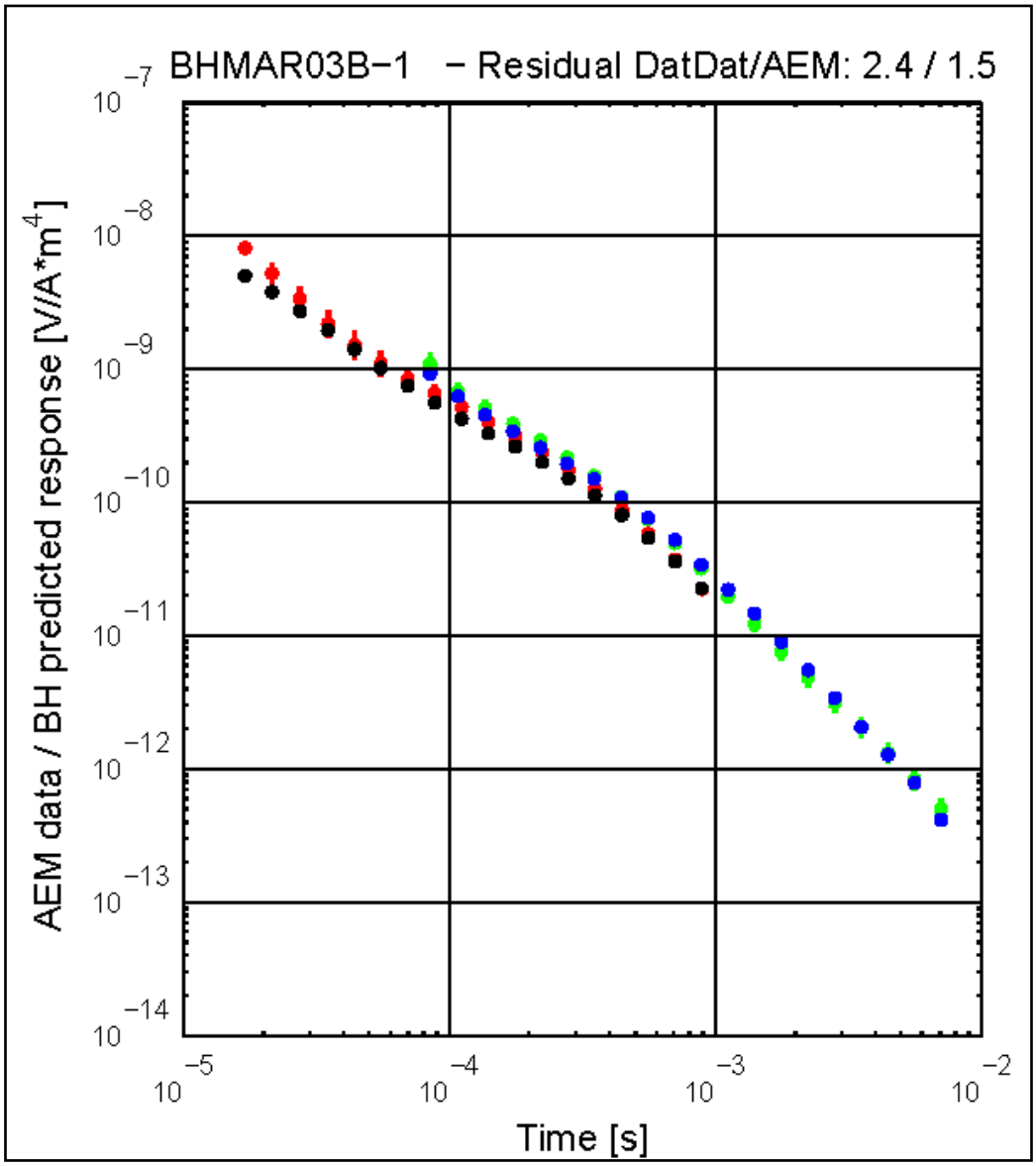



**Figure 6-77.** *DatDat comparison plot for the BHMAR03B-1 borehole. AEM data are plotted in black (Low Moment) and blue (High Moment) while borehole response is plotted in red (Low Moment) and green (High Moment). Error bars indicate the uncertainty of the data and response. The DatDat residual is given in the title together with the data residual of the AEM inversion for comparison.*

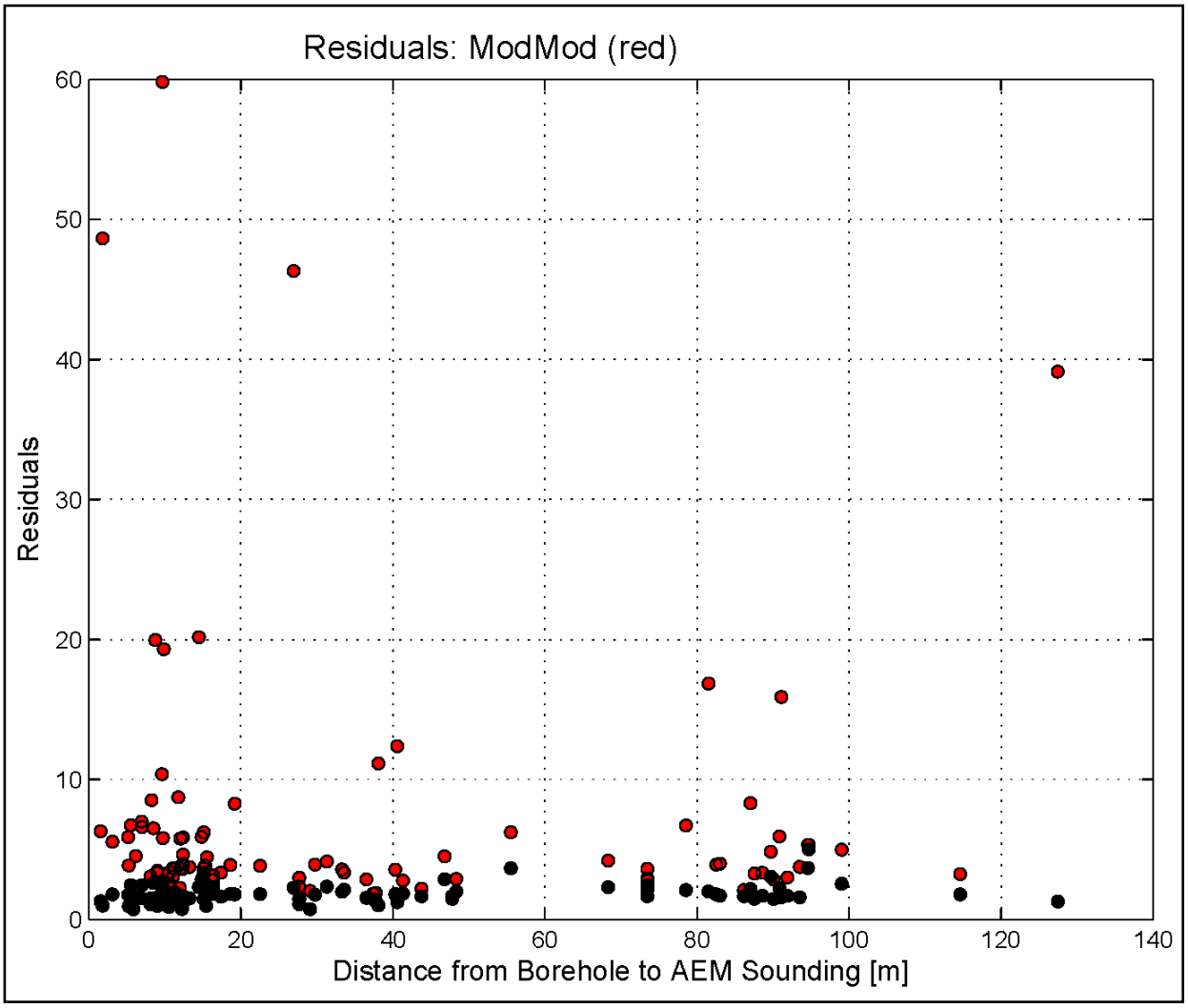



**Figure 6-78.** *ModMod residuals as a function of the distance between the borehole and the closest AEM sounding. It is seen that there is really no correlation between the two parameters.*

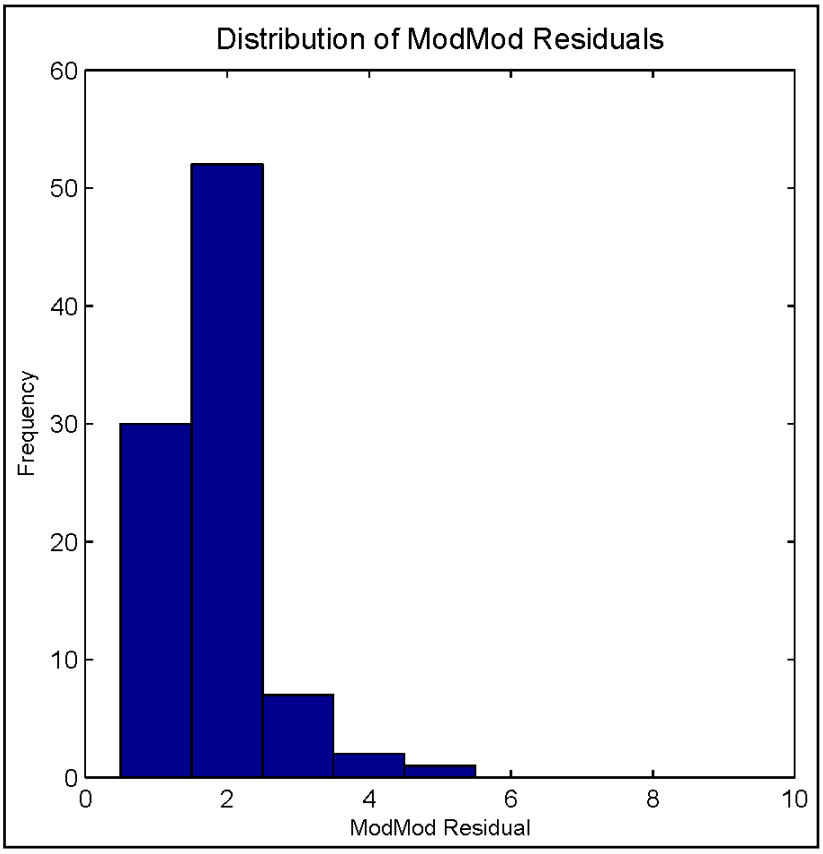



**Figure 6-79**. *Histogram showing the distribution of the ModMod residuals listed in Table 6-12.*

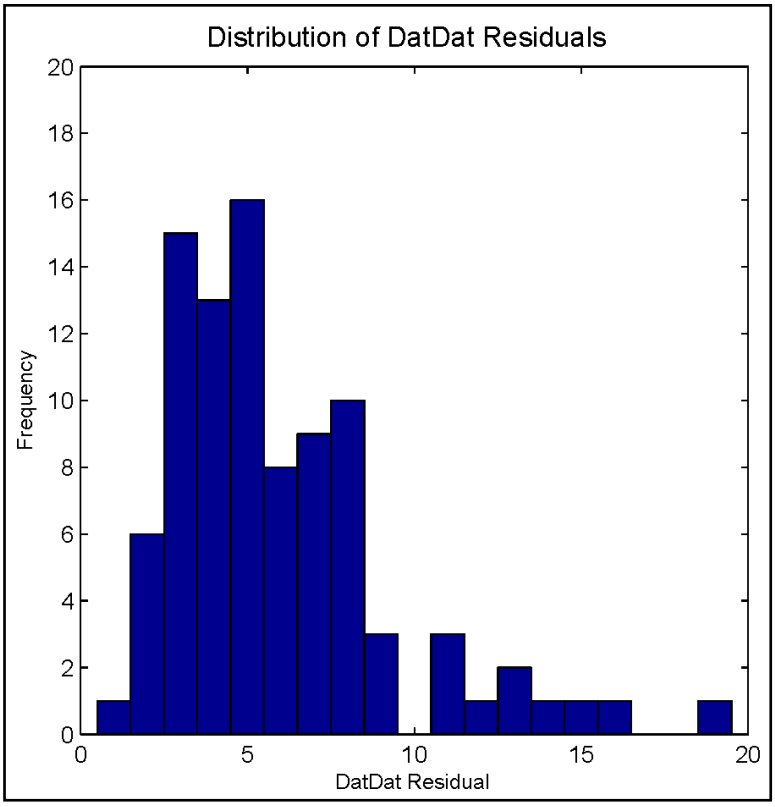



**Figure 6-80**. *Histogram showing the distribution of the DatDat residuals listed in Table 6-12.*

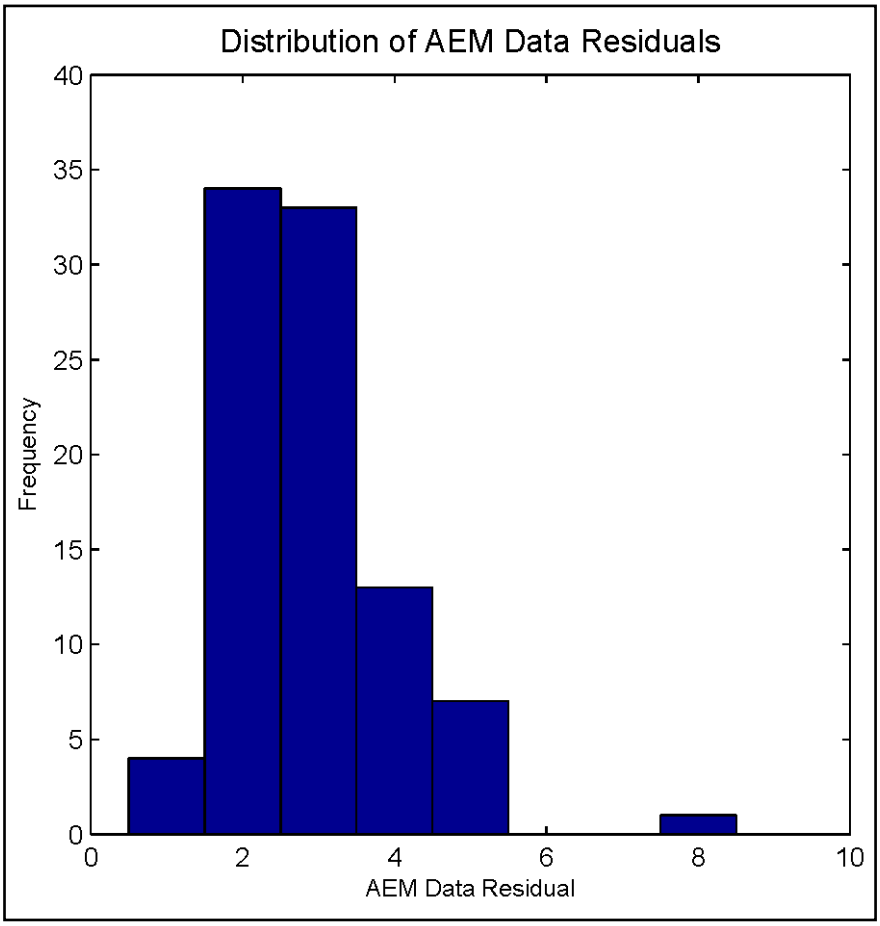



**Figure 6-81**. *Histogram showing the distribution of the data residuals of the AEM inversion listed in Table 6-12.*

**Table 6-12.** *ModMod and DatDat residuals for all 92 boreholes together with the data residual of the AEM inversion. The stars indicate residuals above a certain limiting value which is 3 for the ModMod residuals, 10 for the DatDat residuals, and 5 for the AEM data residuals.*

| Phase 2 boreholes | | | | |
|---|---|---|---|---|
| **Label** | **Dist** | **ModMod** | **DatDat** | **AEM ResDat** |
| **BHMAR01A-1** | 127 | 1.3 | 5 | 1.518 |
| **BHMAR01B-1** | 41 | 1.2 | 3.5 | 1.722 |
| **BHMAR03B-1** | 82 | 2 | 2.4 | 1.51 |
| **BHMAR03B-2** | 79 | 2.1 | 1.8 | 1.51 |
| **BHMAR04-1** | 94 | 1.6 | 5.1 | 2.674 |
| **BHMAR04-2** | 90 | 1.5 | 5.3 | 2.674 |
| **BHMAR05-1** | 91 | 2.2 | 3.7 | 3.659 |
| **BHMAR05-2** | 87 | 2.2 | 3.2 | 3.659 |
| **BHMAR06-1** | 91 | 1.6 | 5 | 2.288 |
| **BHMAR14-1** | 13 | 1.5 | 3.2 | 3.622 |
| **BHMAR15-1** | 27 | 2.3 | 5.9 | 2.435 |
| **BHMAR16-1** | 99 | 2.5 | 6.1 | 5.078* |
| **BHMAR17-1** | 11 | 1.8 | 5.1 | 3.165 |
| **BHMAR17-2** | 17 | 1.6 | 3.7 | 3.165 |
| **BHMAR18-1** | 12 | 0.8 | 2.8 | 1.862 |
| **BHMAR18-2** | 6 | 0.7 | 2.7 | 1.862 |
| **BHMAR19-2** | 9 | 2.6 | 5.3 | 8.187* |

| | | | | |
|---|---|---|---|---|
| **BHMAR21-1** | 90 | 3.1* | 15.4* | 4.501 |
| **BHMAR21-3** | 95 | 3.7* | 18.8* | 4.501 |
| **BHMAR22-1** | 38 | 1 | 3.7 | 1.672 |
| **BHMAR23-1** | 31 | 2.3 | 8.9 | 1.936 |
| **BHMAR23-2** | 30 | 1.8 | 7.1 | 1.936 |
| **BHMAR28-1** | 7 | 1.5 | 4.7 | 1.262 |
| **BHMAR29-1** | 12 | 1.4 | 6.9 | 2.615 |
| **BHMAR30-1** | 2 | 1 | 7.9 | 1.172 |
| **BHMAR31-1** | 9 | 1 | 3.4 | 2.098 |
| **BHMAR33-1** | 10 | 2.5 | 8.4 | 4.917 |
| **BHMAR33-4** | 40 | 1.8 | 6.4 | 4.917 |
| **BHMAR34-1** | 8 | 1.1 | 5.8 | 2.162 |
| **BHMAR34-3** | 37 | 1.5 | 3.6 | 2.162 |
| **BHMAR35-1** | 115 | 1.8 | 4.9 | 2.622 |
| **BHMAR36-1** | 14 | 2.3 | 1.1 | 1.696 |
| **BHMAR41-1** | 7 | 2.4 | 4.4 | 2.787 |
| **BHMAR43-1** | 5 | 1.8 | 2.5 | 1.666 |
| **BHMAR43-2** | 3 | 1.8 | 2.5 | 1.666 |
| **BHMAR48-1** | 15 | 2.9 | 5.9 | 2.428 |
| **BHMAR51-1** | 83 | 1.7 | 3.3 | 3.208 |
| **BHMAR53-1** | 10 | 1.3 | 4.7 | 2.149 |
| **BHMAR56-1** | 9 | 1.1 | 3.1 | 1.783 |
| **BHMAR57-1** | 10 | 2 | 1.7 | 1.898 |
| **BHMAR61-1** | 47 | 2.9 | 3.6 | 2.587 |
| **BHMAR61-2** | 44 | 1.7 | 3.3 | 2.587 |
| **BHMAR61-3** | 48 | 1.7 | 2.9 | 2.587 |
| **BHMAR63-1** | 11 | 1.9 | 5.2 | 3.851 |
| **BHMAR64-1** | 10 | 1.2 | 2.6 | 3.009 |
| **BHMAR64-2** | 6 | 1.5 | 3 | 3.009 |
| **BHMAR65-1** | 12 | 1.4 | 6.2 | 2.473 |
| **BHMAR66-1** | 12 | 1.7 | 3.5 | 1.402 |
| **BHMAR71-1** | 5 | 1 | 2.8 | 2.918 |
| **BHMAR74-1** | 8 | 1.5 | 4.3 | 1.659 |

| **Phase 3 Boreholes** | | | | |
|---|---|---|---|---|
| **Label** | **Dist** | **ModMod** | **DatDat** | **AEM ResDat** |
| **BHMAR08-1** | 19 | 1.8 | 5.5 | 2.74 |
| **BHMAR33-5** | 15 | 3.4* | 13.7* | 5.394* |
| **BHMAR33-7** | 48 | 2 | 7.9 | 4.456 |
| **BHMAR33-8** | 11 | 1.9 | 7.4 | 2.331 |
| **BHMAR33-9** | 34 | 2.1 | 8.4 | 5.394* |
| **BHMAR58-1** | 56 | 3.6* | 8.1 | 2.517 |
| **BHMAR62-1** | 6 | 2.5 | 3.4 | 3.158 |
| **BHMAR75-1** | 12 | 1.7 | 4.3 | 3.668 |
| **BHMAR75-2** | 12 | 1.1 | 2.3 | 3.668 |
| **BHMAR75-3** | 12 | 1.6 | 6.9 | 3.668 |
| **BHMAR75-4** | 15 | 1.4 | 5.3 | 2.818 |

| | | | | |
|---|---|---|---|---|
| **BHMAR75-5** | 9 | 1.6 | 6.2 | 3.668 |
| **BHMAR75-6** | 15 | 1.9 | 10.7* | 3.698 |
| **BHMAR75-7** | 83 | 1.8 | 7.9 | 3.178 |
| **BHMAR75-8** | 16 | 2 | 8.6 | 3.698 |
| **BHMAR77-2** | 2 | 1.3 | 9.1 | 4.394 |
| **BHMAR77-4** | 11 | 0.9 | 2.6 | 4.394 |
| **BHMAR77-5** | 68 | 2.3 | 15.8* | 2.05 |
| **BHMAR79A-2** | 15 | 1 | 6.8 | 2.363 |
| **BHMAR79A-5** | 38 | 1.3 | 4.5 | 1.988 |
| **BHMAR79A-6** | 86 | 1.7 | 4.5 | 1.841 |
| **BHMAR79A-10** | 37 | 1.4 | 7.8 | 1.988 |
| **BHMAR79A-12** | 41 | 1.8 | 11.2* | 2.341 |
| **BHMAR80A-2** | 73 | 2.4 | 12.8* | 3.261 |
| **BHMAR80A-3** | 16 | 1.8 | 5.4 | 3.031 |
| **BHMAR80A-4** | 73 | 1.7 | 3.7 | 3.261 |
| **BHMAR80A-6** | 73 | 2.1 | 12.2* | 3.261 |
| **BHMAR80A-7** | 16 | 2.3 | 12.8* | 3.031 |
| **BHMAR80B-3** | 89 | 1.7 | 4.3 | 2.78 |
| **BHMAR83-2** | 95 | 5.0* | 37.9* | 2.712 |
| **BHMAR84-3** | 19 | 1.8 | 7.3 | 2.202 |
| **BHMAR84-4** | 23 | 1.8 | 7.6 | 2.132 |
| **BHMAR84-5** | 92 | 1.7 | 5 | 9.550* |
| **BHMAR88-2** | 11 | 1.1 | 7.1 | 2.899 |
| **BHMAR88-3** | 11 | 1.4 | 7.8 | 2.899 |
| **BHMAR88-4** | 29 | 0.7 | 7.2 | 3.449 |
| **BHMAR88-5** | 12 | 1.4 | 5.1 | 3.449 |
| **BHMAR88-6** | 11 | 0.9 | 7.7 | 3.449 |
| **BHMAR88-7** | 88 | 1.5 | 4.8 | 3.023 |
| **BHMAR92-1** | 28 | 1.5 | 6.5 | 2.191 |
| **BHMAR92-2** | 28 | 1.1 | 4.8 | 2.191 |
| **BHMAR99-1** | 33 | 2 | 11.3* | 2.532 |

**STATISTICAL PARAMETERS**

| LABEL | ModMod | DatDat | AEM ResDat |
|---|---|---|---|
| **MEAN** | 1.8 | 6.3 | 2.9 |
| **STDDEV** | 0.7 | 4.7 | 1.3 |
| **MEDIAN** | 1.7 | 5.15 | 2.7 |

Dist:The distance between the borehole and the nearest AEM sounding in m.

ModMod:The ModMod normalised residual.

DatDat: The DatDat normalised residual.

AEM_ResDat: The normalised data residual of the AEM inversion.

#### 6.8.2.4 *Estimating a functional relationship in the ModMod comparison*

Figure 6-82 and Figure 6-83 show cross-plots of the values of the layer conductivities of the borehole models and the AEM models in a log-log plot with the pertinent error bars. The plotted values lie close to the straight line indicating identity between them - as should be expected from the fact that the values of the average residuals are all small numbers.

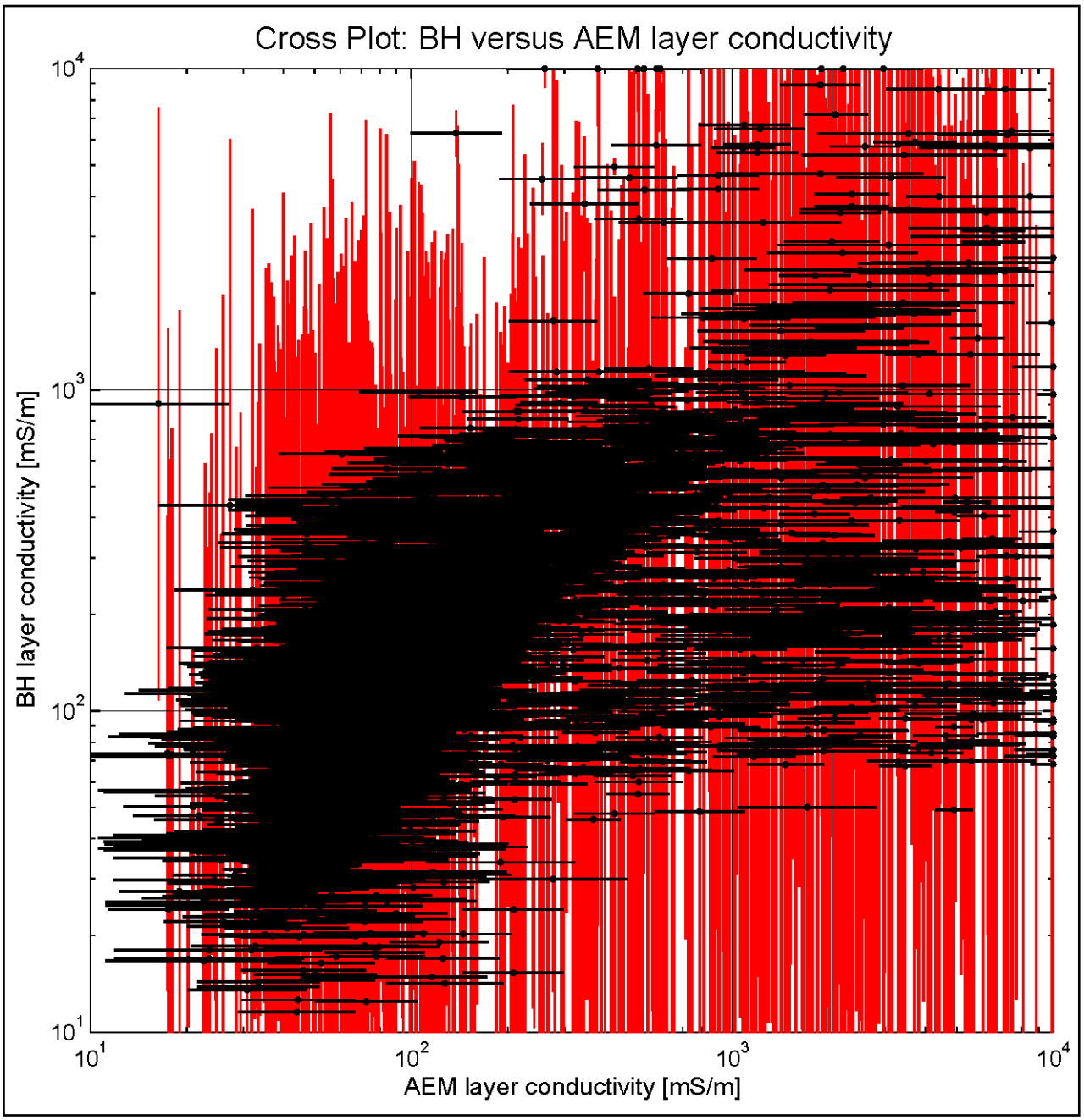



**Figure 6-82.** *Cross plot on a logarithmic scale of the AEM model conductivity as a function of the borehole model conductivity. In the log-log plot, the uncertainties of both parameters are indicated by error bars.*

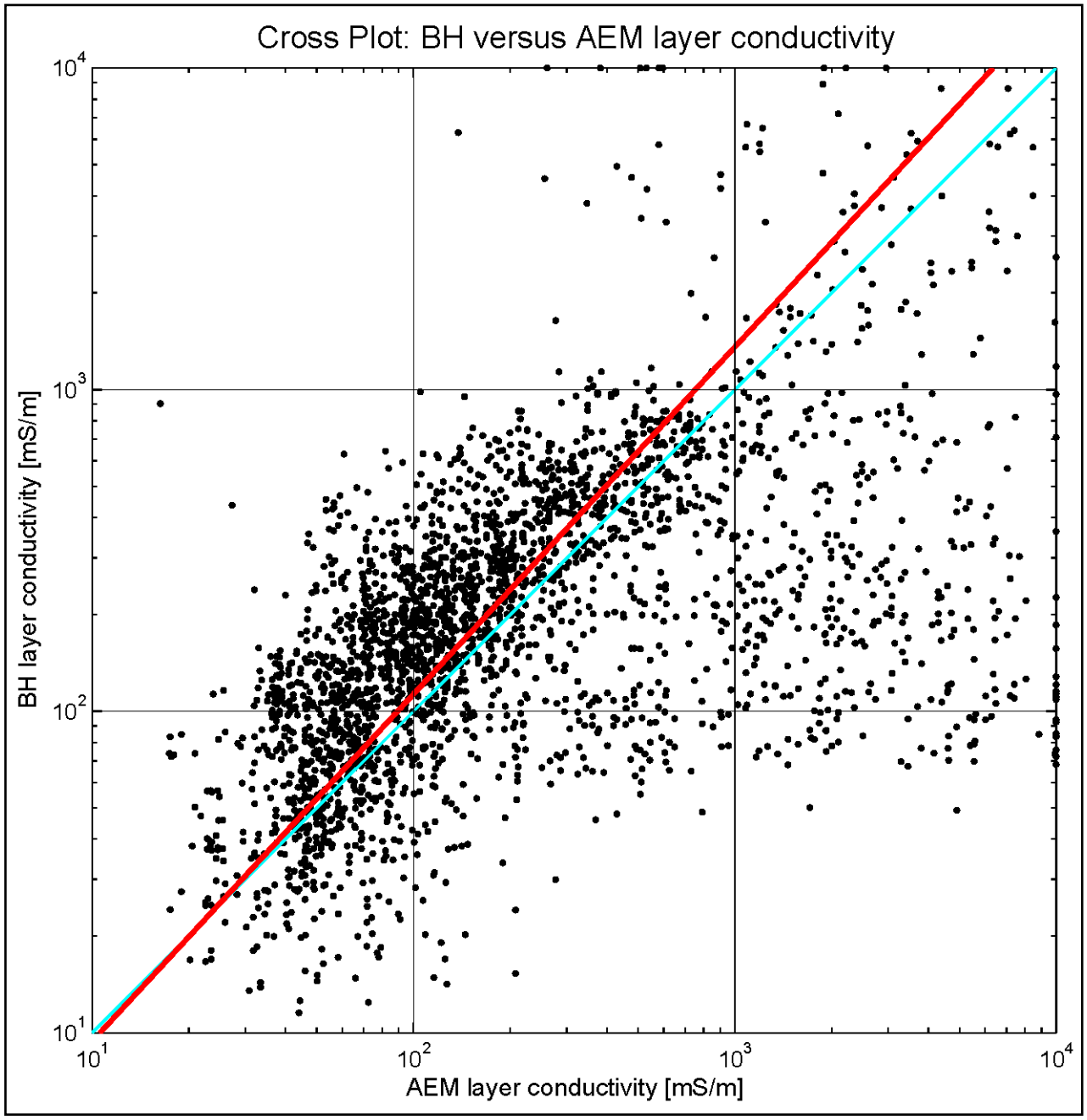



**Figure 6-83.** *Cross plot on a logarithmic scale of the AEM model conductivity as a function of the borehole model conductivity. The identity mapping is shown with a thin cyan line while the least squares linear fit, taking uncertainties on both parameters into account, is indicated with a thicker red line. The error bars have been omitted for clarity.*

A linear regression in log scale has been performed to find a functional relationship between the two conductivities. In the regression analysis, the uncertainties on both borehole layer conductivities and AEM layer conductivities have been taken into account, i.e. we have found the parameters *a* and *b* that minimize the residual:

$$R_{err}^{ModMod} = \sqrt{\frac{1}{L}\sum_{i=1}^{L}\frac{\left[\log\sigma_i^{log} - \left(a\cdot\log\sigma_i^{aem} + b\right)\right]^2}{\mathrm{var}\left(\log\sigma_i^{log}\right) + a^2\cdot\mathrm{var}\left(\log\sigma_i^{aem}\right)}}$$

**Equation 60**

The regression has been carried out using the MATLAB script York_fit.m (©Travis Wiens, 2010) that is freely available on the MathWorks web site (York *et al*., 2004). The parameters minimising the residual and their uncertainties were found to be: $a = 1.0793 \pm 0.0114$ and $b = -0.2425 \pm 0.061$ so that:

$$\log\sigma_{log} = a \cdot \log\sigma_{aem} + b = 1.0793 \cdot \sigma_{aem} - 0.2425 \quad \Rightarrow$$

**Equation 61**

$$\sigma_{log} = e^{b} \cdot (\sigma_{aem})^{a} = 0.7847 \cdot (\sigma_{aem})^{1.0793}$$

**Equation 62**

with a residual of $R_{err}^{ModMod} = 1.34$.

In the plot including the error bars it is seen that a great portion of especially the $\sigma_{log}$ values have very high uncertainties. This is caused by the limited depth extent of the borehole conductivity logs which naturally makes the layer conductivities of the borehole model completely uncertain for layers above and below the depth extent of the log.

In Figure 6-83, a thin cyan line indicates the identity line between σaem and σlog while the regression line taking the uncertainties into account is indicated by a thicker red line. It is seen that the residual is of the order of unity, indicating that the fit is good, and the functional relationship is close to the identity mapping. Closer inspection reveals that when layer conductivities are in the middle range of 40-400 mS/m, there is a tendency for σlog to be higher than σaem. This could be an expression of the fact that in the depth range where conductivity log data are present, the depth resolution of AEM data is poorer than the depth resolution of the conductivity log data, and in the regularised inversion with vertical smoothness constraints, the AEM models will therefore be more smooth, meaning that the amplitudes of the AEM layer conductivities will be smaller than that of the borehole layer conductivities. It is also seen that for the very high layer conductivities above 1,000 mS/m, σaem is clearly higher than σlog. This could be caused by the fact that the depth penetration of the AEM data is generally below the depth extent of the borehole conductivity logs and the AEM model will therefore pick up the very conductive deeper parts of the subsurface while the borehole models will not.

To test the robustness of the method of estimating the regression line, the above analysis has been repeated including only the borehole model layers for which the relative uncertainty of the conductivity is less than 0.2, i.e. only the layers where there were actually conductivity log data. The plots are seen in Figure 6-84 and Figure 6-85, and the regression parameters are:

$$\log\sigma_{log} = a \cdot \log\sigma_{aem} + b = 1.0344 \cdot \sigma_{aem} + 0.0084 \quad \Rightarrow$$

**Equation 63**

$$\sigma_{log} = e^{b} \cdot (\sigma_{aem})^{a} = 1.0084 \cdot (\sigma_{aem})^{1.0344}$$

**Equation 64**

with a residual of $R_{err}^{ModMod} = 1.6371$. This is no dramatic change from the case of including all layer conductivity values, but gives a clearer picture of the relationship, and the methodology must be considered reliable and robust.

In the case when uncertainty is neglected, the correlation coefficient, $R^2$, traditionally used in linear regressions, is given by:

$$R^2 = 1 - \frac{SS_{err}}{SS_{tot}} = 1 - \frac{\sum (y_i - f_i)^2}{\sum (y_i - -y)^2} = 1 - \frac{\sum [y_i - (ax_i - b)]^2}{\sum (y_i - -y)^2}$$

**Equation 65**

where $SS_{err}$ is the unnormalised residual defined above and $SS_{tot}$ is the total variability of the data and -$y$ is the mean value of $y$. In the case where uncertainty on $x$ both $y$ and is taken into account, we must derive a generalisation of the above formula. The residual term is already defined in Equation 60 so, in the same way, we need to normalise the expression for the total variability with the variance. It is easy to prove that the covariance between $y_i$ and -$y$:

$$\mathrm{var}(y_i - -y) = \mathrm{var}\, y_i + \mathrm{var} - y = \mathrm{var}\, y_i + 1/\sum_{i=1}^{N} \frac{1}{\mathrm{var}\, y_i}$$

**Equation 66**

The correlation coefficient will therefore be given by:

$$R^2 = 1 - \frac{\sum \frac{[y_i - (ax_i - b)]^2}{\mathrm{var} y_i + a^2 \cdot \mathrm{var} x_i}}{\sum \frac{(y_i - -y)^2}{\mathrm{var} y_i + 1/\sum (1/\mathrm{var}\, y_i)}}$$

**Equation 67**

Using this formula we find for the ModMod comparison: $R^2 = 0.98347$. If we use the formula with the unweighted sums, we find $R^2 = 0.99712$.

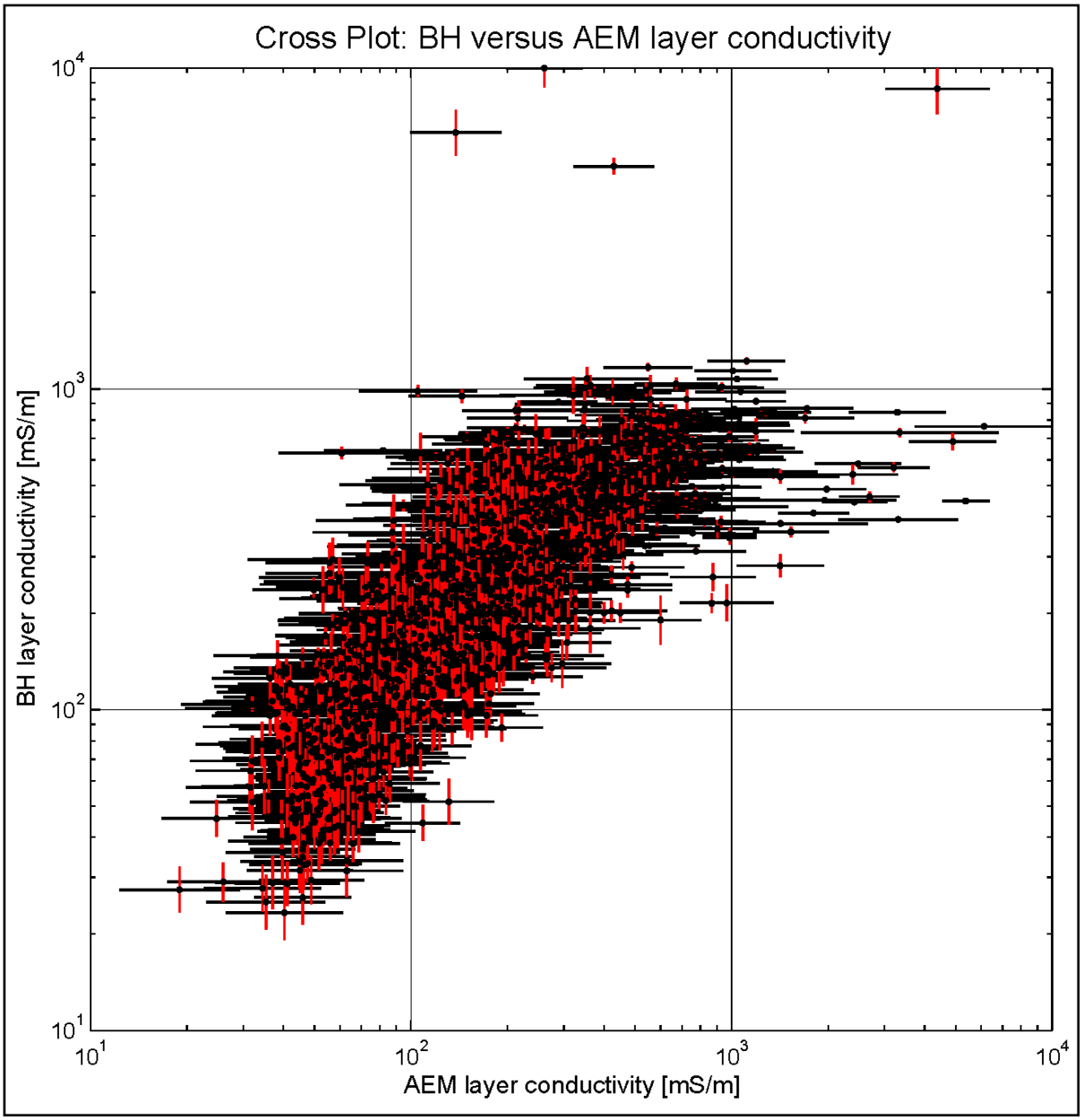



**Figure 6-84.** *Cross plot on a logarithmic scale of the AEM model conductivity as a function of the borehole model conductivity. Only the borehole model layers for which the relative uncertainty of the conductivity is less than 0.2 are included. In the log-log plot, the uncertainties of both parameters are indicated by error bars.*

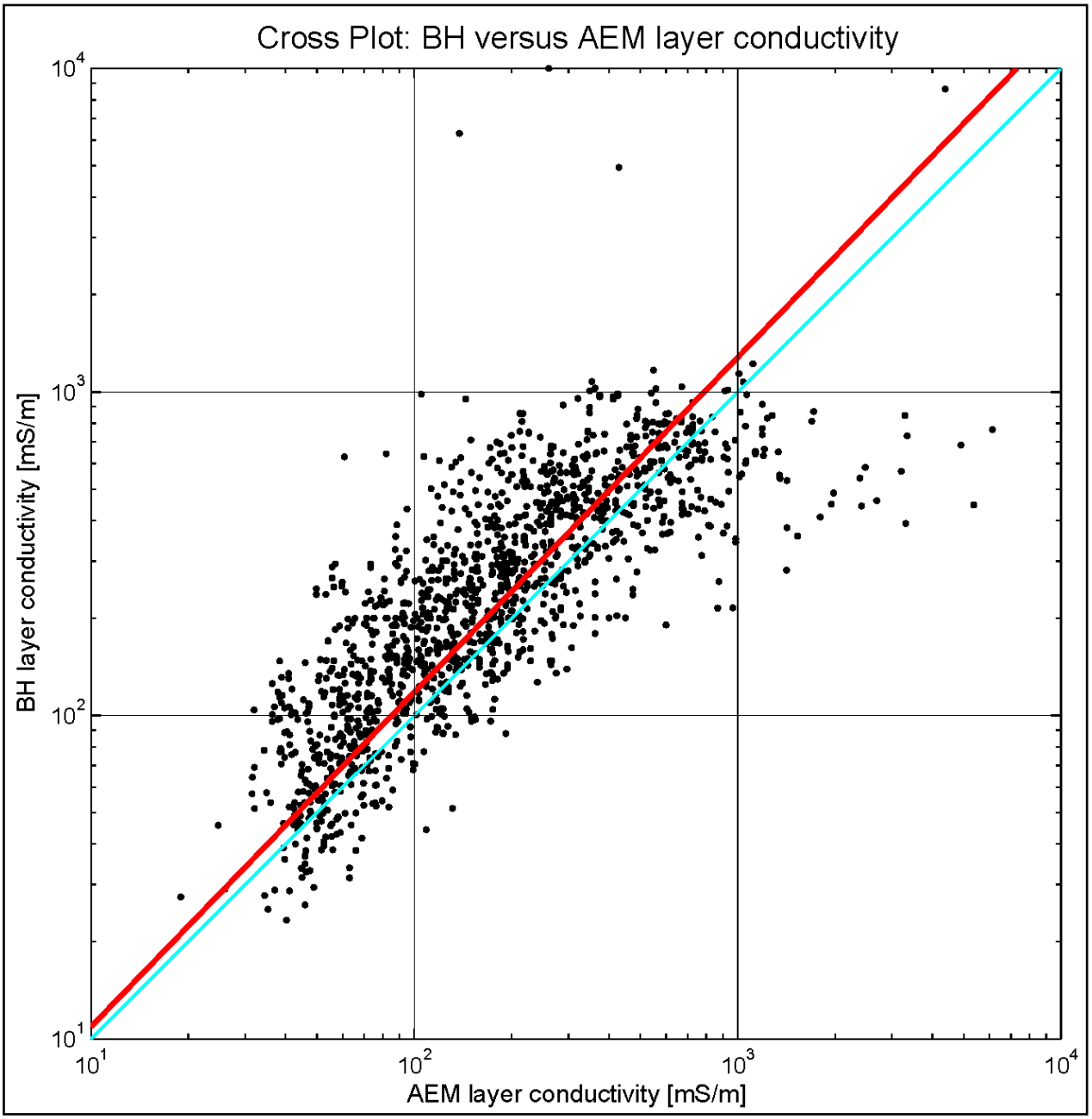



**Figure 6-85.** *Cross plot on a logarithmic scale of the AEM model conductivity as a function of the borehole model conductivity. Only the borehole model layers for which the relative uncertainty of the conductivity is less than 0.2 are included. The identity mapping is shown with a thin cyan line while the least squares linear fit, taking uncertainties on both parameters into account, is indicated with a thicker red line. The error bars have been omitted for clarity.*

#### 6.8.2.5 *Estimating a functional relationship in the DatDat comparison*

Figure 6-86 and Figure 6-87 shows a cross-plot of the values of the measured AEM data and the data predicted from the borehole models in a log-log plot with the pertinent error bars. It is clear that the plotted values lie close to the straight line indicating identity between them; as should be expected from the fact that the values of the average residuals are all small numbers.

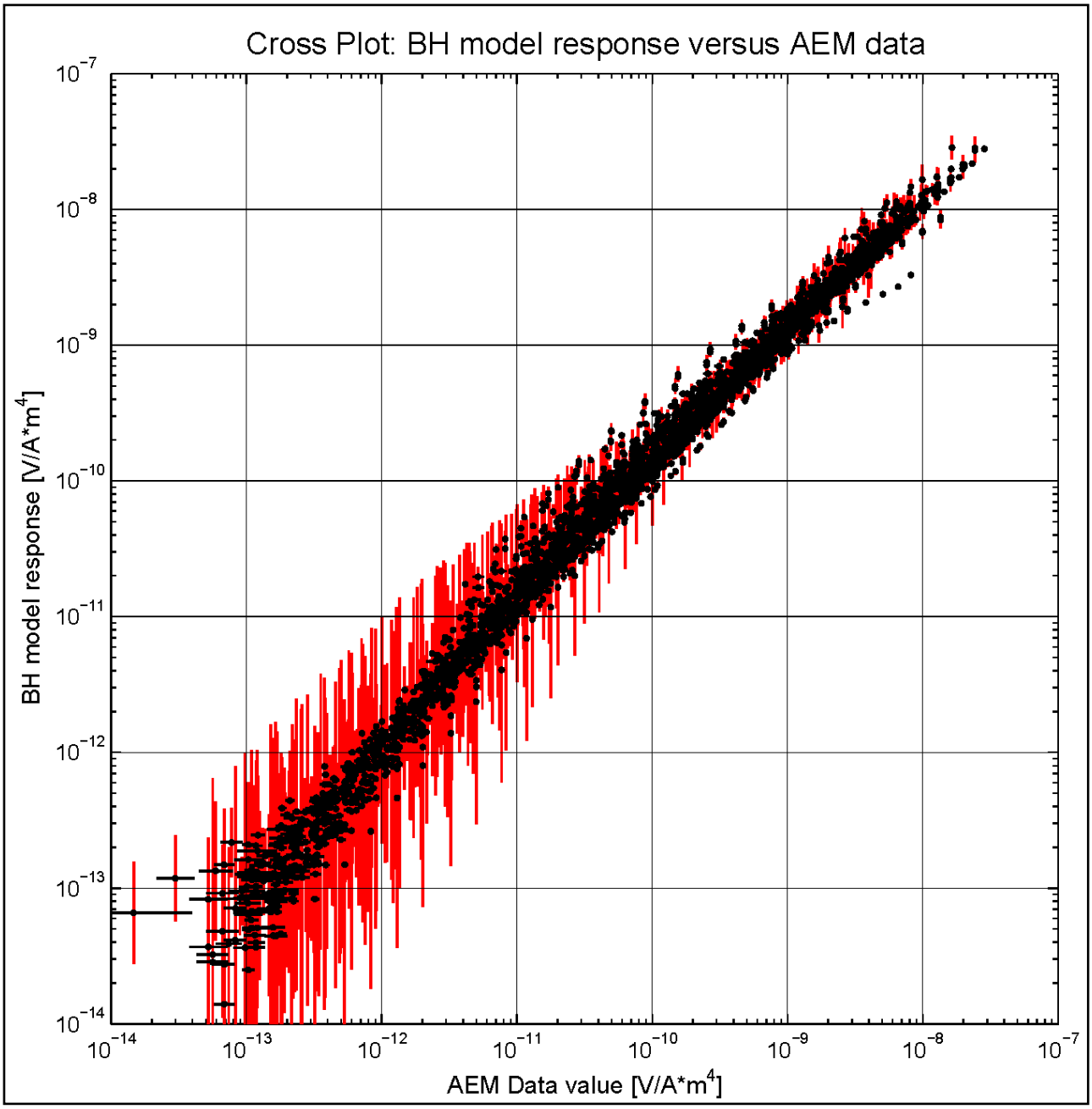



**Figure 6-86.** *Cross plot on a logarithmic scale of the AEM conductivity as a function of the borehole conductivity. In the log-log plot, the uncertainties of both parameters are indicated by error bars.*

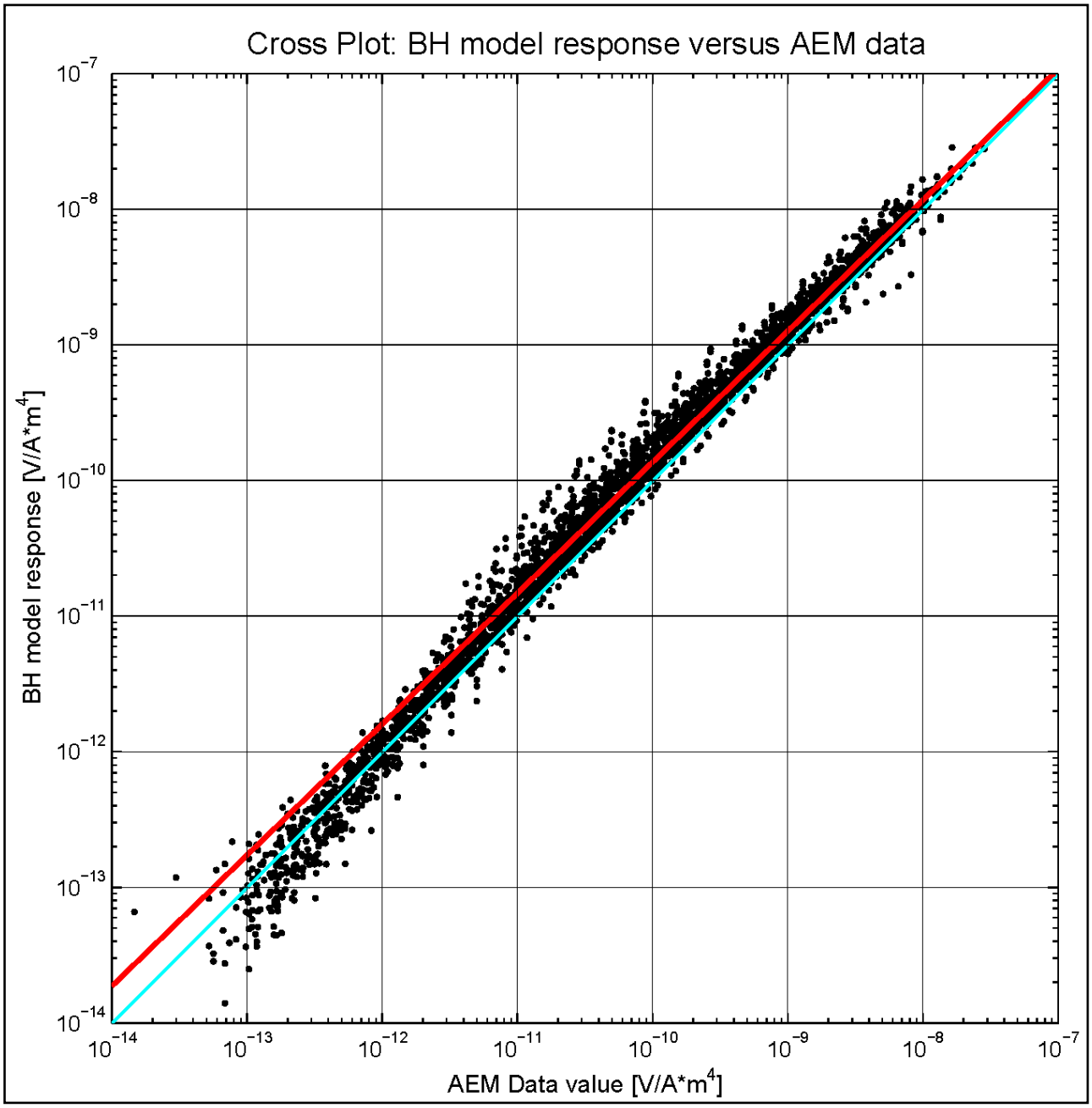



**Figure 6-87.** *Cross plot on a logarithmic scale of the AEM conductivity as a function of the borehole conductivity. The identity mapping is shown with a thin cyan line while the least squares linear fit, taking uncertainties on both parameters into account, is indicated with a thicker red line. The error bars have been omitted for clarity.*

In the same way as for the ModMod comparison, a linear regression in log scale has been performed to find a functional relationship between the AEM data and the forward response of the borehole models. In the regression analysis, the uncertainties on both parameters have been taken into account, i.e. we have found the parameters *a* and *b* that minimize the residual:

$$R_{err}^{DatDat} = \sqrt{\frac{1}{M}\sum_{i=1}^{M}\frac{\left[\log V_i^{log} - \left(a \cdot V_i^{aem} + b\right)\right]^2}{\mathrm{var}\left(\log V_i^{log}\right) + a^2 \cdot \mathrm{var}\left(\log V_i^{aem}\right)}}$$

**Equation 68**

The optimum parameters of the functional relationship and their uncertainties were found to be: $a = 0.966 \pm 0.00071$ and $b = -0.471 \pm 0.0151$ so that:

$$\log V_{log} = a \cdot \log V_{aem} + b = 0.966 \cdot V_{aem} - 0.471 \quad \Rightarrow$$

**Equation 69**

$$V_{log} = e^{b} \cdot (V_{aem})^{a} = 0.6243 \cdot (V_{aem})^{0.966}$$

**Equation 70**

with a residual of $R_{err}^{DatDat} = 3.1$. Using the same formula as for the ModMod comparison, we find for the DatDat comparison $R^2 = 0.99064$. If we use the formula with the unweighted sums, we find $R^2 = 0.99986$.

In Figure 6-87, a thin cyan line indicates the identity line between Vaem and Vlog while the regression line taking the uncertainties into account is indicated by a thicker red line. It is seen that the residual is of the order of unity, indicating that the fit is good, and the functional relationship is close to the identity mapping. Closer inspection reveals that when data values are high, corresponding to early times (upper right corner of the plot) the relation is very close to the identity mapping; for intermediate values, corresponding to intermediate times, the borehole response seems generally higher than the AEM data, while at small amplitudes, corresponding to late times (lower left corner of the plot), the borehole response is lower. This is obviously a reflection in the data space of the observation concerning the ModMod comparison made in the Section 6.8.2.1 that for layer conductivities in the middle range, the borehole values seem higher than the AEM values.

## 6.8.3 A Comparison with Pre-existing Borehole Induction Log Data

### 6.8.3.1 *Results of the ModMod and DatDat comparisons*

As an additional and independent test, comparisons were made for 11 boreholes in the BHMAR area drilled and logged prior to the BHMAR survey. All analysis procedures were the same as for the BHMAR boreholes, so only a summary is included here.

To illustrate the comparisons, plots have been made for all 11 boreholes depicting the two comparisons defined above. Here, we shall show two examples, but in Appendix 4 (Apps *et al*., 2012c) all 11 plots pertaining to the old boreholes are shown for both the ModMod and the DatDat comparisons.

Figure 6-88 and Figure 6-89 show plots of the ModMod and the DatDat comparisons for borehole GW36812. An explanation of the plot is given in the figure caption of Figure 6-83. For the GW36812 there is a very high degree of consistency in the FID point comparison.

In Figure 6-90 and Figure 6-91 are plots of the ModMod and the DatDat comparisons for borehole GW36891 where there is more inconsistency in the FID point comparison. The AEM model does register the high conductivity layers seen in the log at 10 m though it is placed somewhat deeper, but the AEM model indicates higher conductivity below a depth of 100 m. However, the ModMod residual is still quite small because of the high uncertainties of the AEM layer conductivities below 100 m. Like for the BHMAR boreholes, the ModMod residuals are uncorrelated with the distance between the borehole and the AEM sounding and with the AEM inversion residual (no plots shown).

The fact that the ModMod residuals are of the order of 1 shows that, overall, there is good consistency between the borehole models and the AEM models. The DatDat residuals are somewhat higher, but the mean value of 4.5 must be compared with the mean value of the data residual in the AEM inversion which is 2.1, meaning that they are of the same order of magnitude, so, overall, there is a good consistency between the measured data and the predicted data from the borehole models. The analysis for the 11 old boreholes was done with a 30-layer model. All residuals and their mean, standard deviation and median values are listed in Table 6-13.

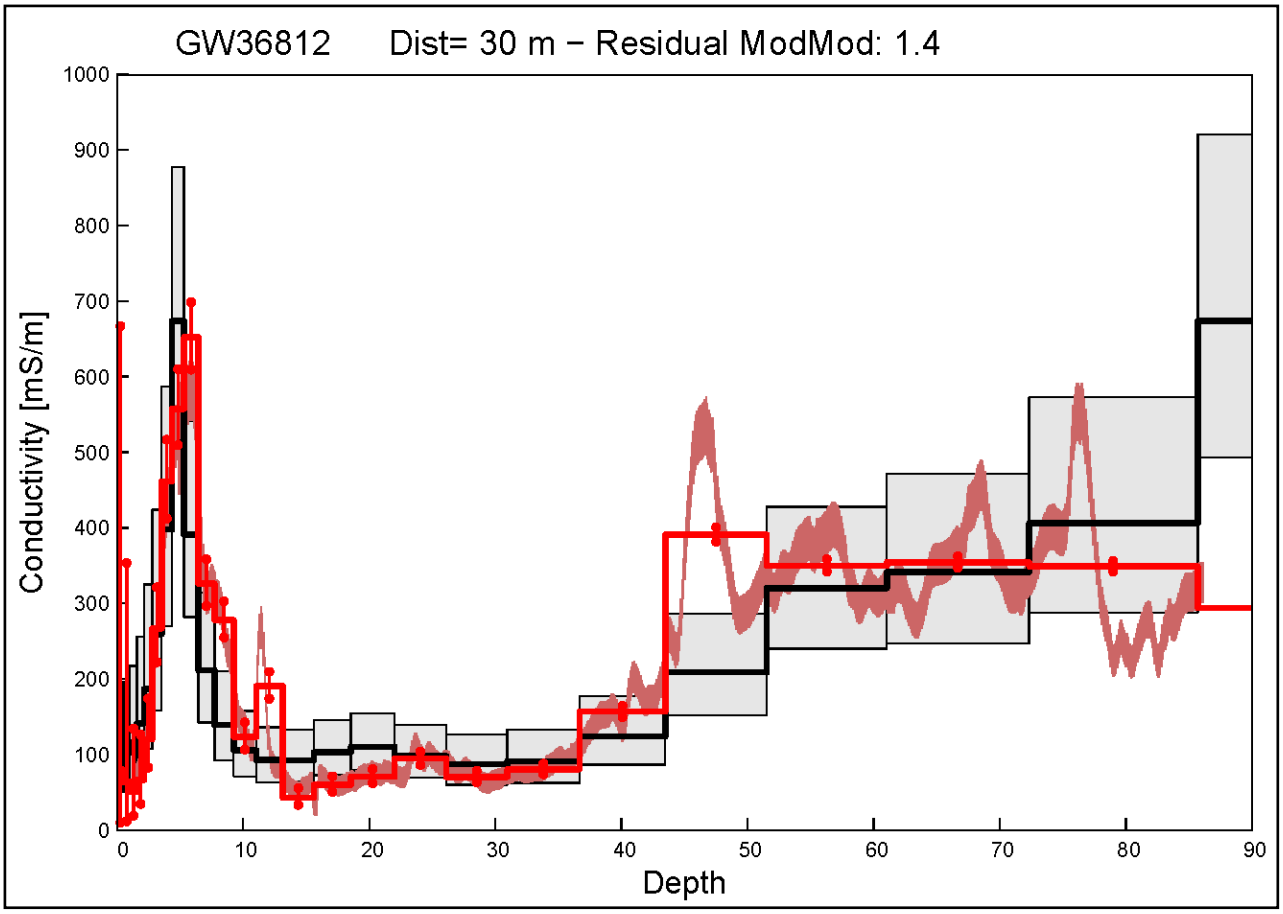



**Figure 6-88.** *ModMod comparison plot for the GW36812 borehole. Borehole conductivity plotted in dark red as vertical line segments indicating the uncertainty. The 30-layer AEM model closest to the borehole is plotted in black with layer conductivity uncertainties indicated by the grey bars. The 30-layer borehole inversion model is plotted in red with layer conductivity uncertainties indicated by the red error bars. The distance between borehole and AEM model is given in the plot title together with the residuals.*

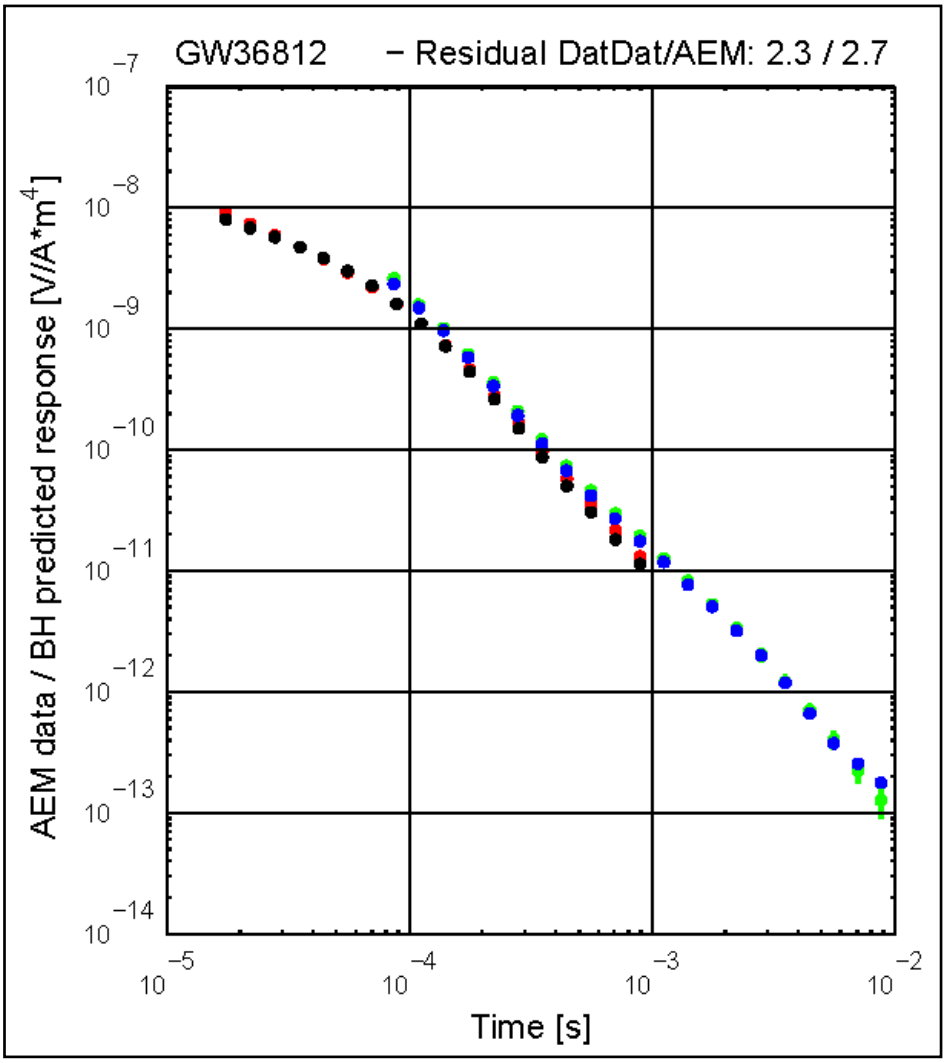



**Figure 6-89.** *ModMod comparison plot for the GW36812 borehole. AEM data are plotted in black (Low Moment) and blue (High Moment) while borehole response is plotted in red (Low Moment) and green (High Moment). Error bars indicate the uncertainty of the data and response. The DatDat residual is given in the title together with the data residual of the AEM inversion for comparison.*

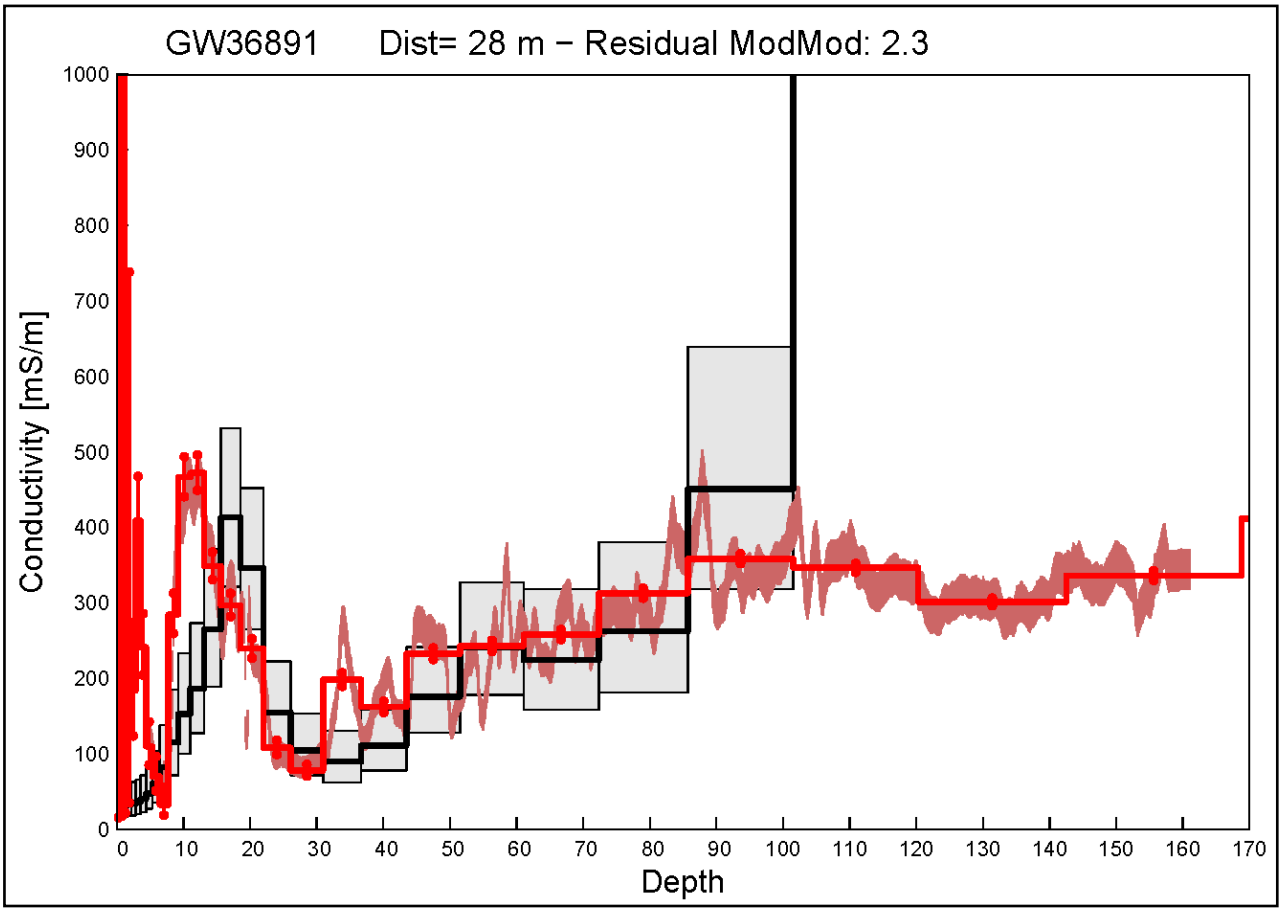



**Figure 6-90.** *ModMod comparison plot for the GW36891 borehole. Borehole conductivity plotted in dark red as vertical line segments indicating the uncertainty. The 30-layer AEM model closest to the borehole is plotted in black with layer conductivity uncertainties indicated by the grey bars. The 30-layer borehole inversion model is plotted in red with layer conductivity uncertainties indicated by the red error bars. The distance between borehole and AEM model is given in the plot title together with the residuals.*

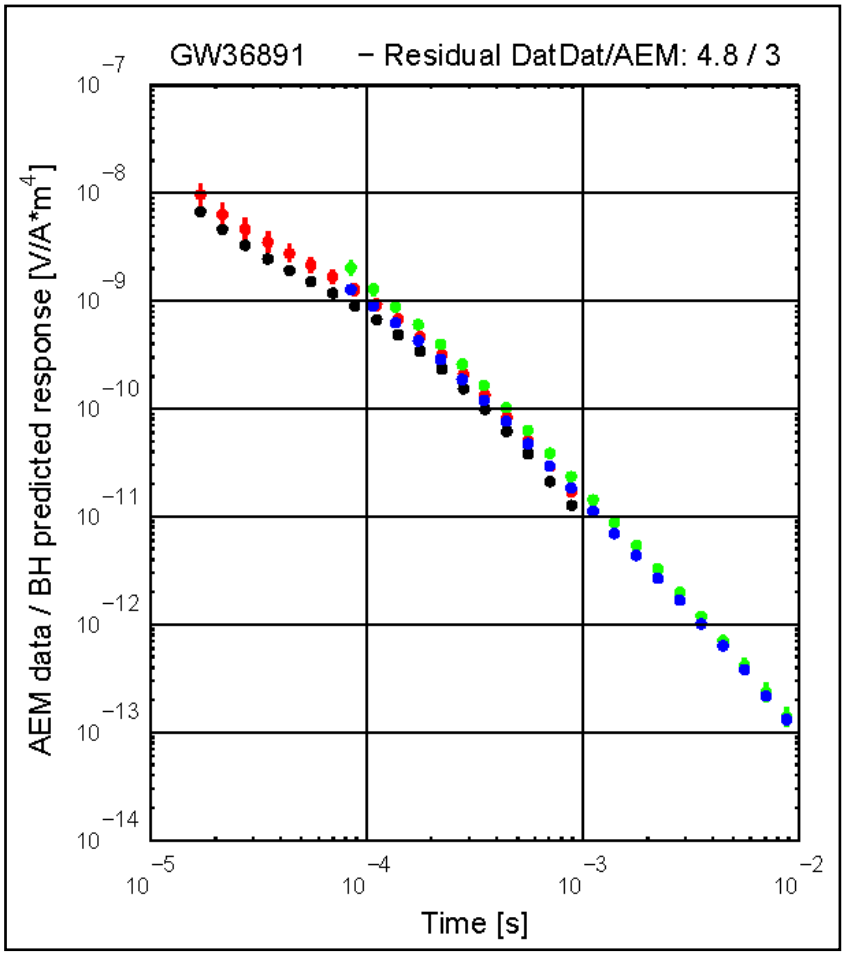



**Figure 6-91.** *DatDat comparison plot for the GW36891 borehole. AEM data are plotted in black (Low Moment) and blue (High Moment) while borehole response is plotted in red (Low Moment) and green (High Moment). Error bars indicate the uncertainty of the data and response. The DatDat residual is given in the title together with the data residual of the AEM inversion for comparison.*

**Table 6-13.** *ModMod and DatDat residuals for all 11 pre-existing boreholes together with the data residual of the AEM inversion.*

| LABEL | Dist | ModMod | DatDat | AEM ResDat |
|---|---|---|---|---|
| **GW36807** | 73 | 1.5 | 2.6 | 1.3 |
| **GW36812** | 30 | 1.4 | 2.3 | 2.7 |
| **GW36815** | 82 | 2.4 | 1.3 | 1.7 |
| **GW36836** | 49 | 2 | 1.9 | 2.4 |
| **GW36837** | 63 | 1.9 | 3.5 | 3 |
| **GW36838** | 146 | 2.2 | 7.9 | 2 |
| **GW36891** | 28 | 2.3 | 4.8 | 3 |
| **GW87790** | 60 | 1 | 2.2 | 1.4 |
| **GW878001** | 58 | 1.3 | 4.5 | 1.7 |
| **GW87801** | 38 | 1.4 | 5.3 | 1.6 |
| **EX1** | 100 | 2.2 | 13.1 | 2.8 |

**Statistical Parameters**

| LABEL | Mod Mod | Dat Dat | AEM_Res Dat |
|---|---|---|---|
| **Mean** | 1.8 | 4.5 | 2.1 |
| **StdDev** | 0.5 | 3.3 | 0.6 |
| **Median** | 1.9 | 3.5 | 2.1 |

Dist: The distance between the borehole and the nearest AEM sounding in m.

ModMod: The ModMod normalised residual.

DatDat: The DatDat normalised residual.

AEM ResDat: The normalised data residual of the AEM inversion.

#### 6.8.3.2 *Estimating a functional relationship in the ModMod comparison*

Figure 6-92 and Figure 6-93 shows a cross-plot of the values of the layer conductivities of the borehole models and the AEM models in a log-log plot with the pertinent error bars. It is clear that the plotted values lie close to the straight line indicating identity between them - as should be expected from the fact that the values of the average residuals are all small numbers.

The parameters minimising the residual in the below equation and their uncertainties were found to be: $a$=0.9803±0.0283 and $b$= -0.3657±0.1736 so that:

$$\log\sigma_{log} = a \cdot \log\sigma_{aem} + b = 0.9803 \cdot \sigma_{aem} - 0.3657 \quad \Rightarrow$$

**Equation 71**

$$\sigma_{log} = e^{b} \cdot (\sigma_{aem})^{a} = 0.6937 \cdot (\sigma_{aem})^{0.9803}$$

**Equation 72**

with a residual of $R_{err}^{ModMod} = 2.2$. The correlation coefficient for the ModMod comparison is $R^2$ = 0.94765. If we use the formula with the unweighted sums, we find: $R^2$ = 0.99204.

In the plot including the error bars it is seen that a great portion of especially the σlog values have very high uncertainties. This is caused by the limited depth extent of the borehole conductivity logs which naturally makes the layer conductivities of the borehole model completely uncertain for layers above and below the depth extent of the log.

In Figure 6-93, a thin cyan line indicates the identity line between $\sigma_{aem}$ and $\sigma_{log}$ while the regression line taking the uncertainties into account is indicated by a thicker red line. It is seen that the residual is of the order of unity, indicating that the fit is good, and the functional relationship is close to the identity mapping.

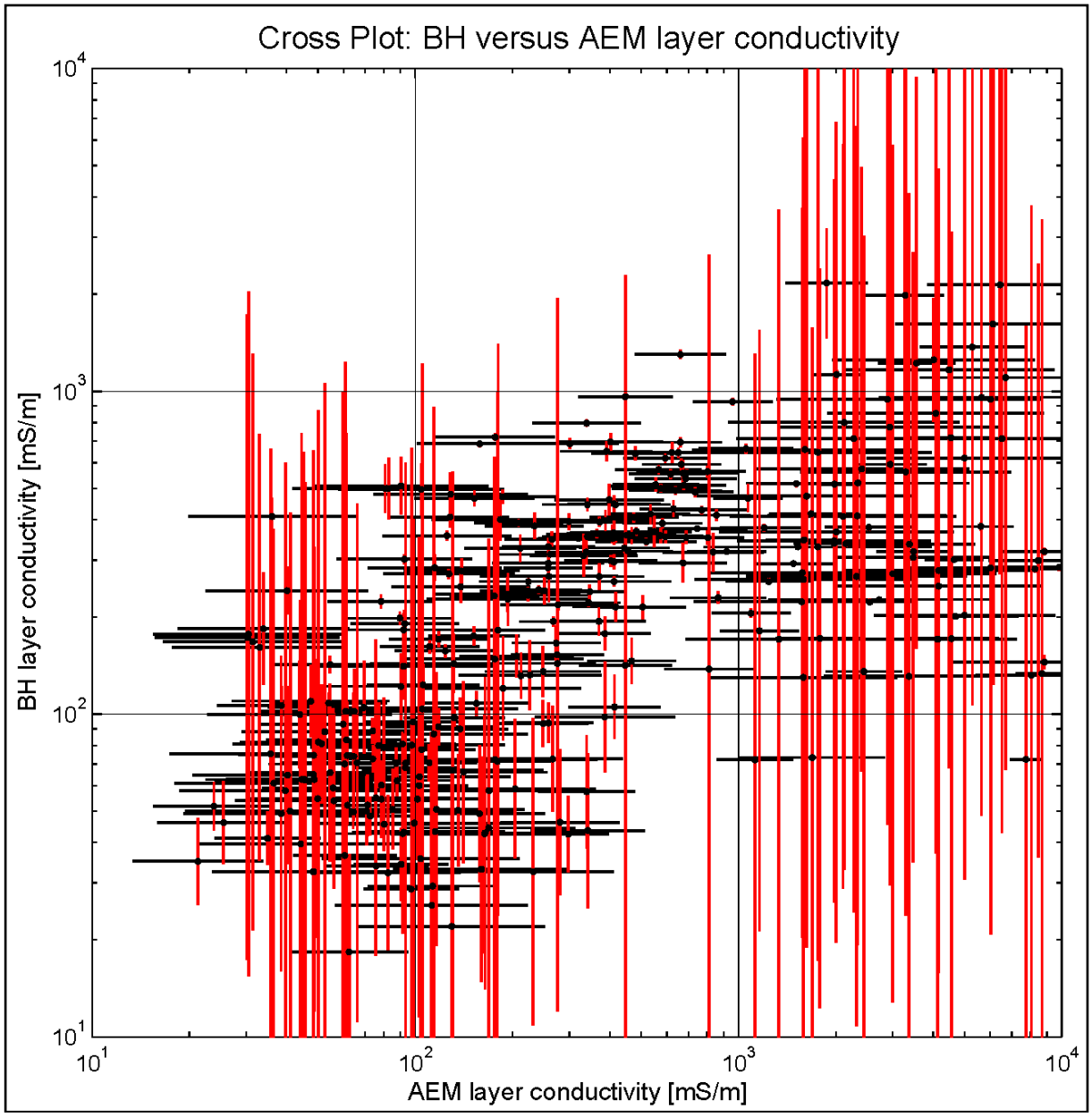



**Figure 6-92.** *Cross plot on a logarithmic scale of the AEM model conductivity as a function of the borehole model conductivity. In the log-log plot, the uncertainties of both parameters are indicated by error bars.*

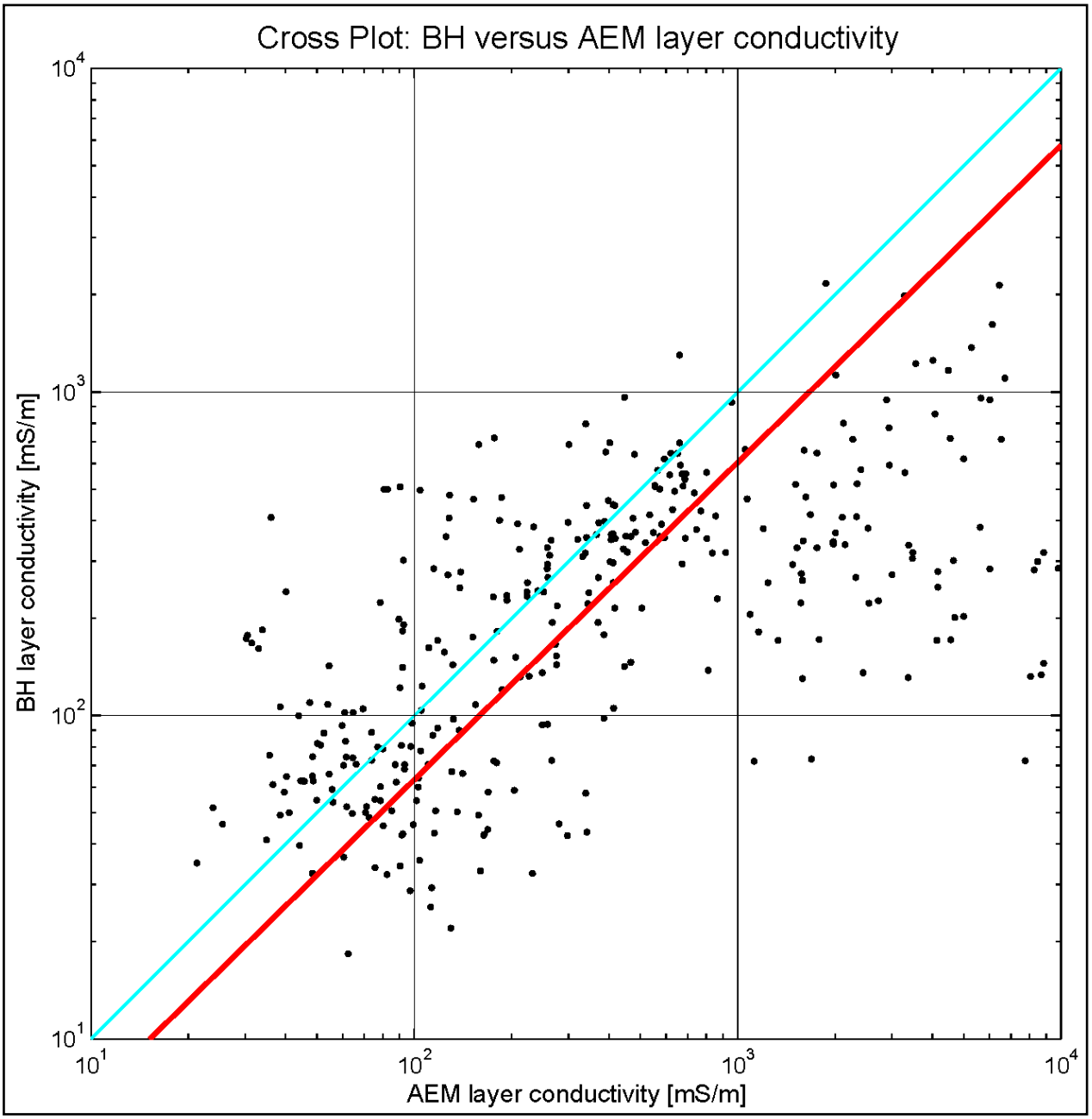



**Figure 6-93.** *Cross plot on a logarithmic scale of the AEM model conductivity as a function of the borehole model conductivity. The identity mapping is shown with a thin cyan line while the least squares linear fit, taking uncertainties on both parameters into account, is indicated with a thicker red line. The error bars have been omitted for clarity.*

#### 6.8.3.3 *Estimating a functional relationship in the DatDat comparison*

Figure 6-94 and Figure 6-95 shows cross-plots of the values of the measured AEM data and the data predicted from the borehole models in a log-log plot with the pertinent error bars. It is clear that the plotted values lie close to the straight line indicating identity between them, as should be expected from the fact that the values of the average residuals are all small numbers.

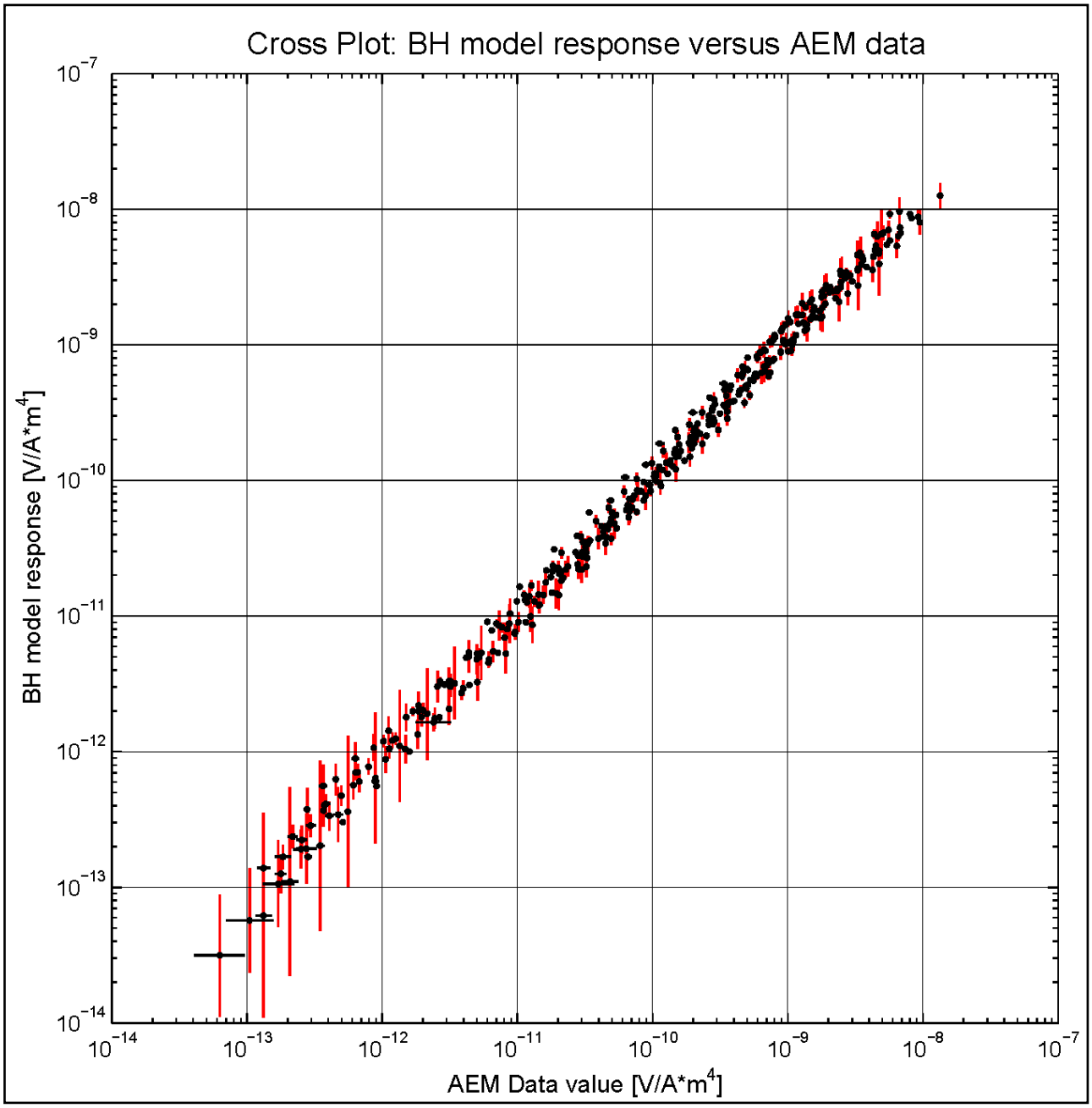



**Figure 6-94.** *Cross plot on a logarithmic scale of the AEM conductivity as a function of the borehole conductivity. In the log-log plot, the uncertainties of both parameters are indicated by error bars.*

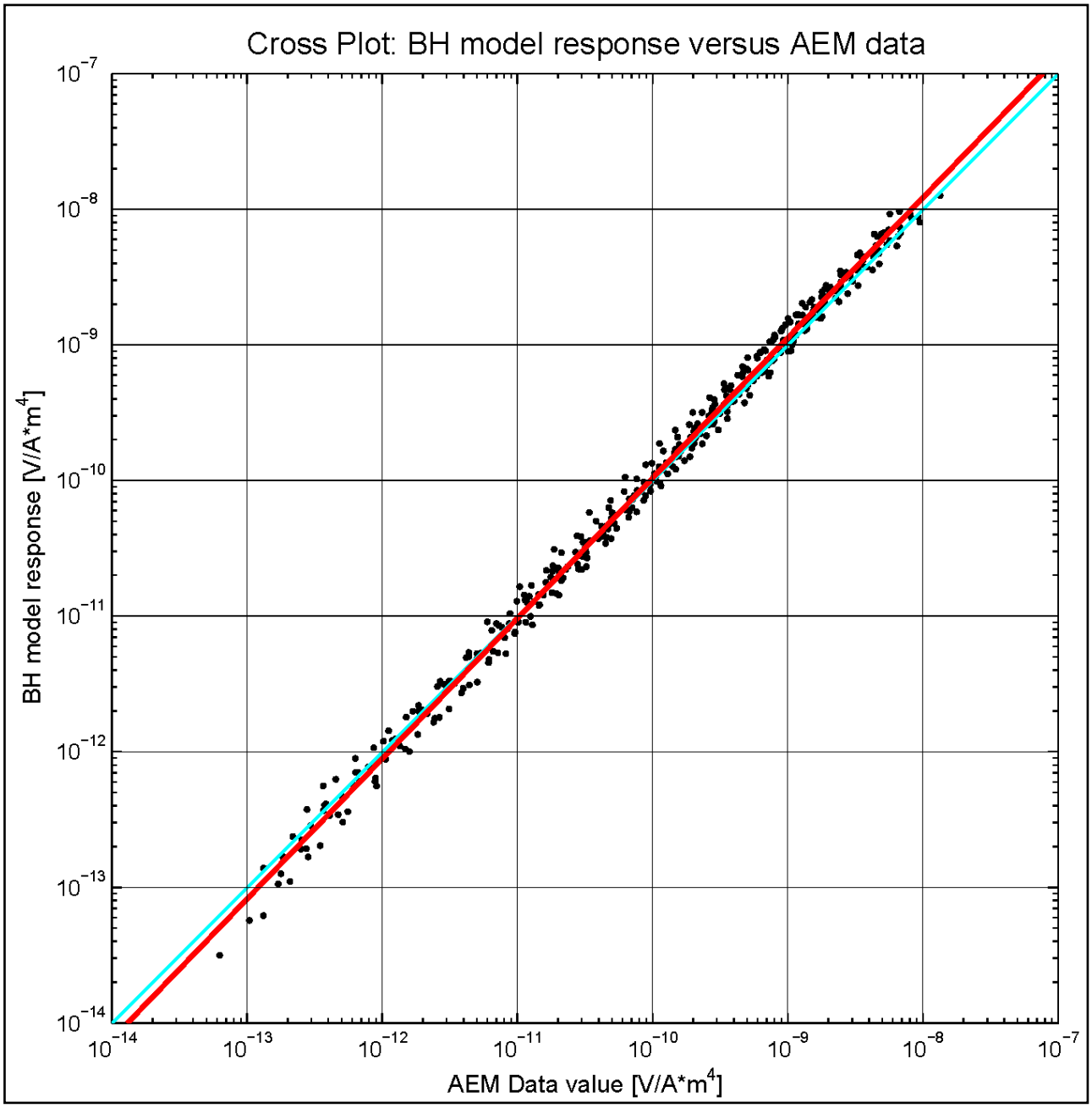



**Figure 6-95.** *Cross plot on a logarithmic scale of the AEM conductivity as a function of the borehole conductivity. The identity mapping is shown with a thin cyan line while the least squares linear fit, taking uncertainties on both parameters into account, is indicated with a thicker red line. The error bars have been omitted for clarity.*

The optimum parameters of the functional relationship and their uncertainties were found to be: $a$=1.0344±0.0015 and $b$=0.8322±0.0331 so that:

$$\log V_{log} = a \cdot \log V_{aem} + b = 1.0344 \cdot V_{aem} + 0.8322 \quad \Rightarrow$$

**Equation 73**

$$V_{log} = e^{b} \cdot \left(V_{aem}\right)^{a} = 2.2984 \cdot \left(V_{aem}\right)^{1.0344}$$

**Equation 74**

with a residual of $R_{err}^{DatDat} = 2.8$. The correlation coefficient for the DatDat comparison is $R^2 = 0.99841$. If we use the formula with the unweighted sums, we find: $R^2 = 0.99999$.

In Figure 6-95, a thin cyan line indicates the identity line between $V_{aem}$ and $V_{log}$ while the regression line taking the uncertainties into account is indicated by a thicker red line. It is seen that the residual is of the order of unity, indicating that the fit is good, and the functional relationship is close to the identity mapping.

## 6.9 TRANS-DIMENSIONAL MARKOV CHAIN MONTE CARLO UNCERTAINTY ANALYSIS

To gain an insight into the uncertainty of the AEM derived conductivity models we have performed Bayesian inference via a reversible jump Markov Chain Monte Carlo (RJ-McMC) inversion of nine selected AEM data sets. The selected data sets were the nearest AEM data sets to nine geologically representative borehole sites for which downhole conductivity logs were available.

As part of the RJ-McMC inversion, a large ensemble of models that fit the data to within the estimated noise levels are generated. The ensemble is generated in such a fashion that the statistical distribution of the models in the ensemble asymptotically converges to the true posterior likelihood distribution of model parameters, given the prior model parameters and the observed data. Thus by analysing the statistical properties of the ensemble we gain insights into the uncertainty and non-uniqueness of the inversion results. Thorough descriptions of the technique are provided in Malinverno (2002), Bodin and Sambridge (2009), Bodin *et al.* (2009) and Minsley (2011). The algorithm used for this particular work is described by Brodie and Sambridge (2012).

The nine AEM data sets used in the RJ-McMC inversion were selected from the same SkyTEM data set as was used in the inversion of the complete BHMAR survey area. Also the same noise level estimates were assigned to the data. However in the RJ-McMC inversion we did not invert for the transmitter loop height and we did not include any constraints from the downhole conductivity log data. The 18 Low Moment and 21 High Moment SkyTEM data were inverted together at each site, but each of the nine data sets was inverted separately.

Sixteen independent Markov chains were sampled in parallel in the inversion of each data set. In each chain 200,000 samples were acquired. Models were accumulated into the posterior probability and change-point histograms after the burn-in period of 10,000 samples. Therefore a total of 3.04 million (190,000 x 16) samples were acquired after the burn-in period. The data were fitted to around the expected misfit level of 39 (18+21 data) within the 10,000 sample burn-in period. We did not carry out any specific tests to signify if the Markov Chains had converged to the true posterior distribution or not.

A minimum of 1 and maximum of 10 layers were allowed in the models. The model was parameterised in linear-depth and base ten logarithmic-conductivity units. The model bounds were 0-200 m in depth and 0.001-5 S/m in conductivity. For the storage of the posterior histograms the model space was discretized into 200 depth-cells and 100 conductivity-cells.

We used uniform prior probability distributions for the model parameters. The proposal distributions standard deviations were set to 0.5 logarithmic decades for the conductivity value change proposition, and 1.0 decade for the birth-death conductivity value change proposition, and 4 m for the nucleus move proposition.

Figure 6-96 shows a summary of the RJ-McMC inversion of the AEM data set nearest to borehole BHMAR08-1. Above the top left panel details of the locations of the bore and the AEM data set are given along with the distance between borehole and the location of the AEM data. The top left panel shows the progression of the data misfit for each of the 16 Markov Chains in a different colour. The vertical red line shows the end of the burn-in period (10,000 samples) and the horizontal line shows the expected data misfit for the assigned noise levels. The bottom left panel shows a histogram of the number of layers in the acceptable models, indicating in this case that at least four layers are required to explain the data.

The centre panel shows the model domain down to 120 m depth with the nearest downhole conductivity log (magenta) and the 30 layer inversion model (green) produced by the gradient based inversion algorithm applied to the whole BHMAR data set (BHMAR-AEM). Also plotted on the centre panel in shades of copper is the 2D posterior probability density histogram. The darker shades of copper indicate zones of higher likelihood and white indicates a likelihood bellow 0.05. The solid blue trace shows the $50^{th}$ percentile conductivity value for each depth cell, in other words, the conductivity at which 50% of the models have a lower conductivity for each depth. The $10^{th}$ and $90^{th}$ percentile models are plotted as dashed blue traces. The width of the copper coloured areas, or similarly, the spread between the $10^{th}$ and $90^{th}$ percentile models gives an indication of the model uncertainty (smaller spread indicates lower uncertainty).

The far right panel shows the 1D change-point histogram. Both the copper shading and the red trace show the same information just in different forms, which is the probability of a layer interface occurring at that depth. The width of the peaks indicates the uncertainty of the layer interfaces. In this example it shows a well resolved interface at around 10 m depth and a less well resolved interface at around 20 m depth.

Overall, for the example in Figure 6-96, the borehole conductivity log and the AEM inversion model lie around the centre of the McMC likelihood interval, but there are exceptions. In the depth interval from 0 to 20 m, the McMC likelihood indicates that just two layers are sufficient to account for the AEM data. The borehole conductivity log, with its much higher ability to distinguish local conductivity changes, shows considerably more structure. Some of this structure is reflected in the AEM inversion model, most likely because the conductivity structure of the borehole log was used as prior information in the AEM inversion. At depths below 80-100 m, the AEM inversion model shows higher conductivities than seem likely from the McMC analysis, but at this depth we are getting close to the limits of depth penetration for the AEM data.

It is worth noticing the asymmetric character of the $10^{th}$ and $90^{th}$ percentile traces relative to the $50^{th}$ percentile contour in Figure 6-96, clearly seen between 10 m and 20 m depth. The low-conductivity contour has much larger excursions away from the $50^{th}$ percentile line than the high-conductivity contour, indicating a well-known characteristic of inductive EM methods: the sensitivity to low conductivities is much smaller than the sensitivity to high conductivities, or, with other words, the high conductivities are associated with a smaller uncertainty than the low conductivities. This appears clearly in the McMC analysis, but cannot be seen in a traditional linearised posterior covariance analysis of AEM inversion. The RJ-McMC inversion plots of the other 8 sites are contained in Appendix 4 (Apps *et al*., 2012c).

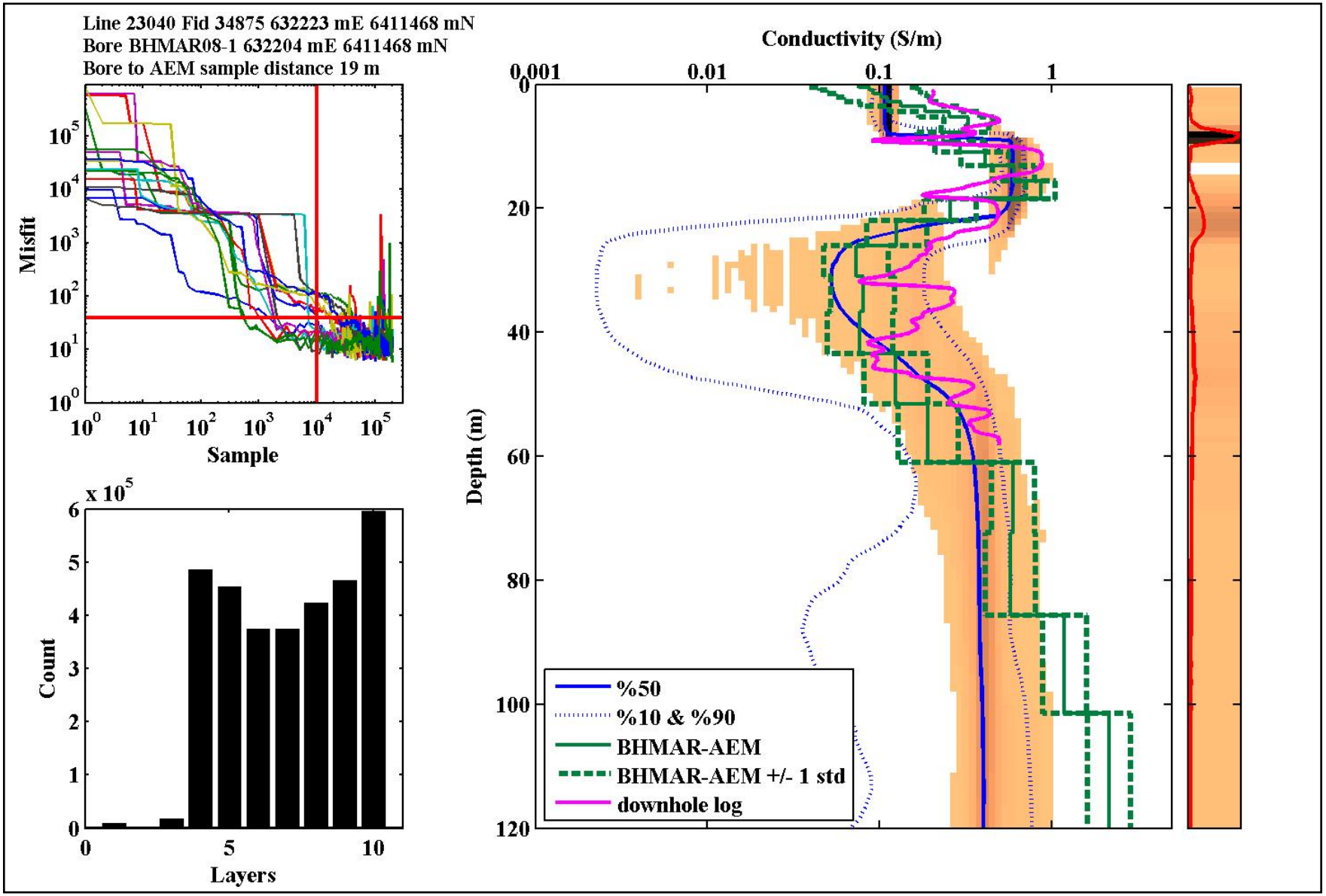



**Figure 6-96.** *Summary of the RJ-McMC inversion of the AEM data set nearest to borehole BHMAR08-1 The plots are described in more detail in the text.*

## 6.10 RE-GRIDDING THE BHMAR INVERSION RESULTS USING INCREASINGLY SPARSE DATA

### 6.10.1 Background

The re-gridding exercise is designed to provide the information necessary to assess whether the original line spacing of 200 m was necessary for the purpose of the BHMAR project. It also serves as a guide for future decisions concerning line spacing in AEM surveys that take the size of the geological features under consideration into account.

The resolution that can be obtained in an AEM survey deteriorates with increasing line spacing, thus the decision on line spacing is a very important one. On the one hand, the data have to be dense enough to provide the resolution necessary for the aim of the survey and, on the other hand, to minimize the cost of the survey, line spacing should not be excessively larger than what is necessary. It must be remembered, however, that the issue of cost is more complicated than just being inversely proportional to the line spacing. Mobilisation cost, availability, time savings with long lines in large surveys etc. are all play a role for the final cost.

### 6.10.2 The Re-gridding Experiment

In the BHMAR survey line spacing varies over the survey area, but within Area 2 it is consistently 200 m, so we have chosen to limit our re-gridding investigation to Area 2. Grids were made based on all AEM lines, every 3$^{rd}$ line, every 5$^{th}$ line, every 10$^{th}$ line and every 25$^{th}$ line, corresponding to a line distance of 200 m, 600 m, 1 km, 2 km and 5 km, respectively. The spacing between grid points along lines is 40 m in both directions. Area 2 is limited by the polygon with vertex coordinates in the table below, and only points within this polygon have been rendered in the plot frames (Table 6-14).

**Table 6-14.** *Vertex coordinates used in the re-gridding experiment.*

| Easting m | Northing m |
|---|---|
| 702782 | 6426884 |
| 679492 | 6450174 |
| 660817 | 6446714 |
| 607720 | 6422694 |
| 593561 | 6393111 |
| 598236 | 6378176 |
| 598229 | 6378133 |
| 636218 | 6377748 |
| 644914 | 6397720 |
| 677095 | 6411817 |
| 692912 | 6418921 |
| 702782 | 6426884 |

The flight direction in Area 2 is not consistently alternating, partly because some of the lines consist of several sub-lines, so we have not taken the flight direction into account in the choice of the sparse line gridding. We do not consider this to be problematic because the SkyTEM system is not particularly sensitive to flight direction, especially after the standard data corrections. The line spacing, the number of lines and the number of data points within Area 2 for the five data sets are given in Table 6-15 below.

**Table 6-15.** *Parameters used in the re-gridding experiment.*

| | Line spacing | Number of lines | Number of data points |
|---|---|---|---|
| **Every line** | 200 m | 734 | 700,279 |
| **Every 3rd line** | 600 m | 242 | 233,657 |
| **Every 5th line** | 1 km | 152 | 140,703 |
| **Every 10th line** | 2 km | 84 | 70,498 |
| **Every 25th line** | 5 km | 32 | 29,063 |
| **Every 50th line** | 10 km | 17 | 14,984 |

The number of grid points in the area for all the plots is 2,595,670. The grid points have been found using the Natural Neighbour (NN) interpolation and the Lateral Parameter Correlation (LPC) methods and the rendering is carried out by plotting a square with side lengths 40 m for every grid point centred around the grid point and coloured according to its value. All plot map linear conductivity and are rendered in a linear colour scale in conductivity spanning the interval of 0 - 0.5 S/m. The plots show the layer conductivity of each of the 30 layers of the model used in the inversion of the BHMAR data.

The plot window for all plots is Easting 590000 E and 705,000 E (115 km) and Northing 6375000 N and 6455000 N (80 km). The plots have been rendered unto an A4 page in landscape format and the plotting area has the physical dimensions of 23 cm (Easting) times 16 cm (Northing), i.e. 5 km per centimetre. With a grid density of 40 m in both directions, this means that there are 125 pixels per square centimetre and actual physical reproductions should have a resolution that is capable of offering this resolution.

The inversion results used in the re-gridding investigation have been obtained through a laterally correlated inversion. This means that, in principle, all sounding have influenced all other soundings, so even when only a fraction of the lines are used for the plots, the selected lines contain information about the neighbouring lines that have been excluded. A consistent approach to eliminate this issue would be to invert the whole BHMAR data set, but only using the lines that are included in the re-gridding, i.e. a separate inversion would have to be done for the every 3rd line case, the every 5th line case, etc. However, this would be a major computational task and for that reason we have not followed that route. It must therefore be understood that the details seen in the plots based on a more sparse line selection are overly optimistic, in particular for the every 3rd line case and less so for the every 5th line case and the cases with even more sparse data.

On the following pages, the plots for the 5 different data densities are show for layers 11 and 22 of the models using two different interpolation methods (Figure 6-99 to Figure 6-110). The plots show in general terms that first order, regional conductivity patterns are consistently observed from 200 m to 10 km line spacing. However, second and third order features are progressively lost as conductivity boundaries are smoothed and finer-scale features within broader anomalies are lost. More detailed analysis of these plots, and the implications for mapping MAR targets and groundwater resources respectively, is to be found in Lawrie *et al*. ( 2012c and d).

#### 6.10.2.1 *Natural Neighbour (NN) Interpolation*

The Natural Neighbour (NN) interpolation method is based on a Delaunay triangulation of the data points, i.e. the locations of the AEM data sets along the flight lines. A Delaunay triangulation for a set of points in a plane is a triangulation such that no point is inside the circumcircle of any triangle. Delaunay triangulations maximize the minimum angle of all the angles of the triangles in the triangulation; they tend to avoid skinny triangles. The triangulation is named after Boris Delaunay (Delaunay, 1934)

The Delaunay triangulation in turn defines a tessellation of the plane consisting of the Voronoi cells (Sibson, 1981). Each Voronoi cell is centred on one of the data points and its edges are defined by connecting the centres of the circumcircles of the Delaunay triangles to which the point belongs.

In this way, the edges are defined by the lines connecting the centres of the circumcircles of the Delaunay triangulation. See Figure 6-97 and Figure 6-98.

The value of the interpolated point is found by adding its position to the data positions and updating the Delaunay triangulation to find the Voronoi cell of the interpolation point. The interpolated value is then given as a weighted sum of the values of the data points in the Voronoi cells it overlaps; the weight factors are given as the overlap normalized with the area of the Voronoi cell of the interpolation point. Interpolation is done in linear conductivity.

The NN interpolation has some desirable properties. Being completely defined by the geometry of the original data points, it is without configuration parameters, so it is not possible to choose the wrong configuration parameter. The surface defined by the NN interpolation is overall continuous and once differentiable and passes through the original data points (Li & Götze, 1999).

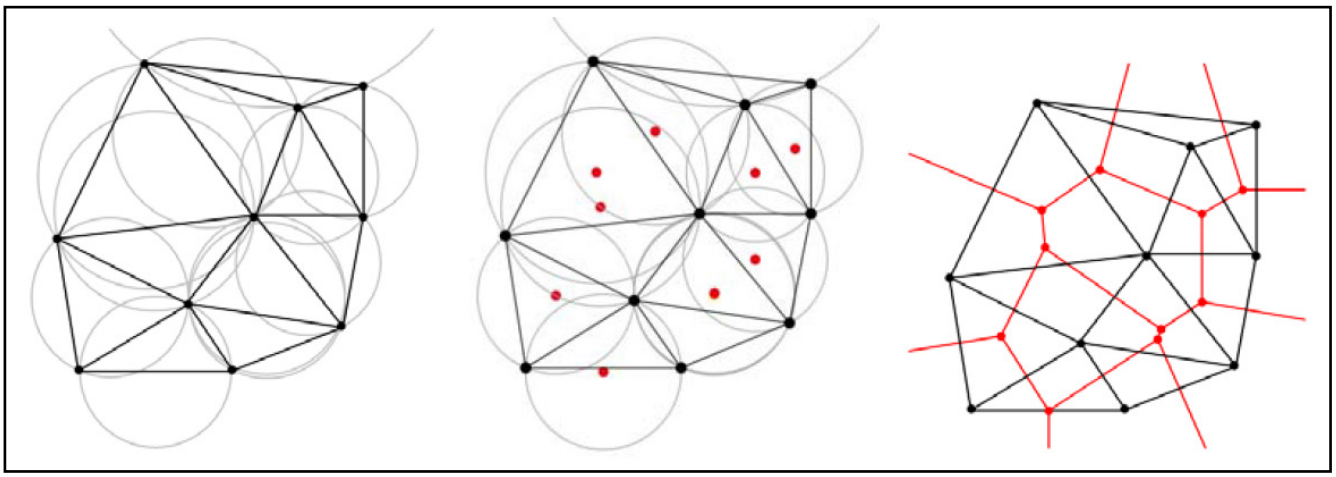


**Figure 6-97.** *Delaunay triangulation Left: The Delaunay triangulation with all the circumcircles. Middle: centres of circumscribed circles are indicated. Right: Connecting the centres of the circumcircles produces the Voronoi diagram (in red).*

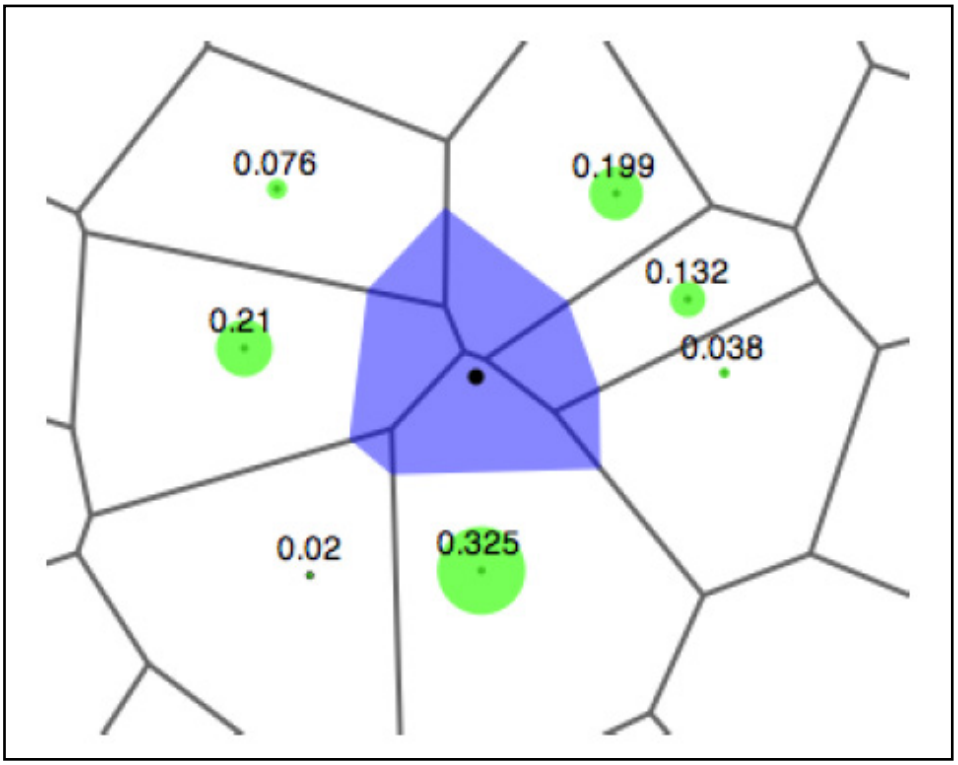



**Figure 6-98.** *Overlapping areas between the Voronoi cell of the interpolation point and the neighbouring Voronoi cells.*

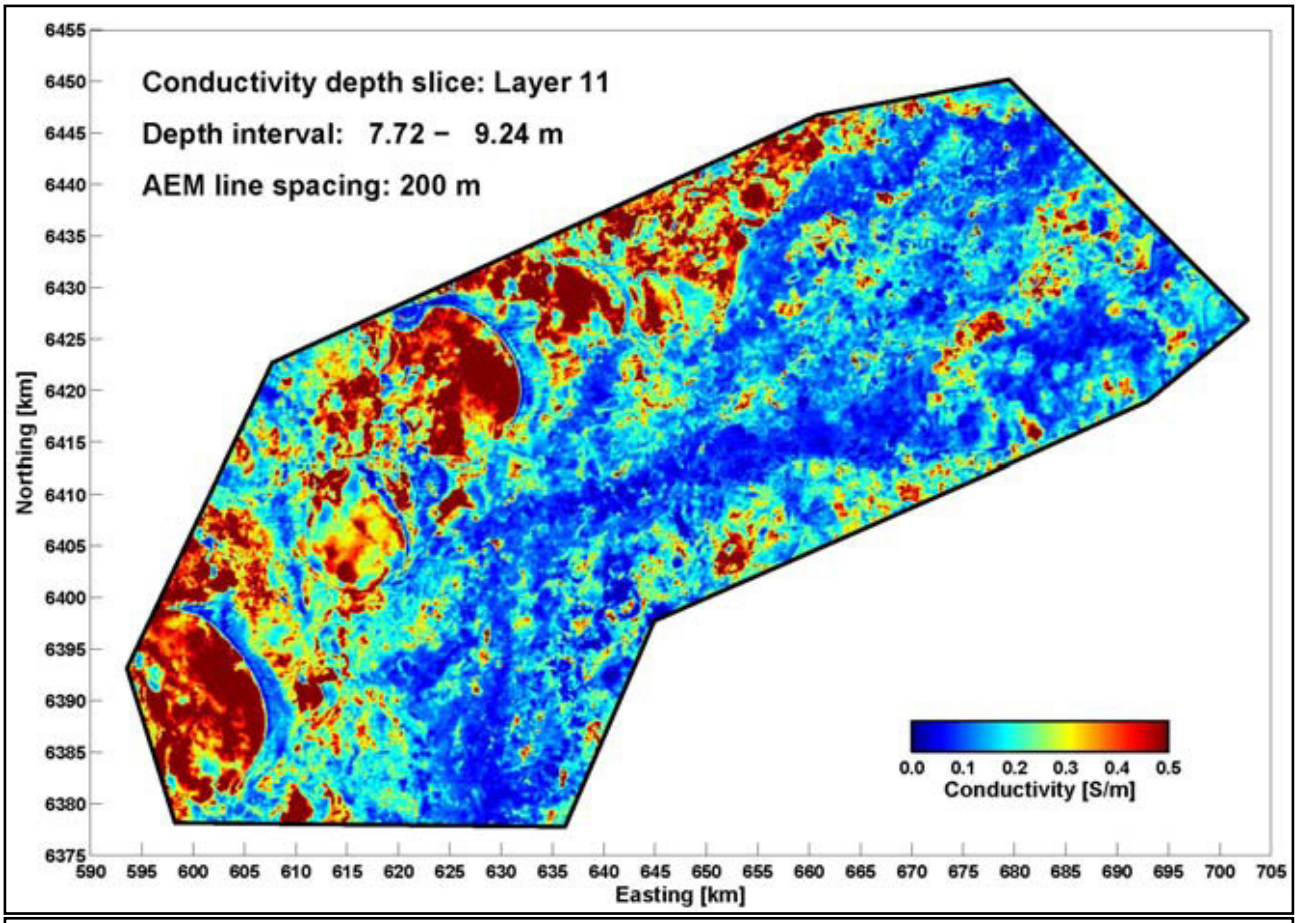
#### 6.10.2.2 *Interpolation using the Lateral Parameter Correlation (LPC) Method*

To investigate the significance of the interpolation method, in addition to the NN method, we have used the Lateral Parameter Correlation (LPC) method. This methodology was used for the lateral correlation in the inversion of the BHMAR AEM data (Christensen and Tølbøll, 2009), but it equally well offers itself as a means to interpolate regularly grid points from a set of irregularly spaced data. The main characteristic of the method is that the interpolated value is found from a weighting of all data points taking the uncertainty of the data point into account. In this respect it resembles kriging, but there is no selection of data points; all data points are included. Optionally, a smoothing of user-defined strength can be introduced in the interpolation.

The LPC interpolation was carried out on the logarithm of conductivity with a very slight smoothing, but the results of the interpolation are plotted in linear conductivity in the same way as for the NN interpolation. Results for layers 11 and 22 are shown in Figure 6-99 to Figure 6-104.

#### 6.10.2.3 *Comparing the NN and LPC Interpolation Results*

For the plots with a dense data base, 200 m to 1 km line spacing, there is no difference between the NN and the LPC interpolations, but for the more sparse data bases, there is a visible difference between the results. The NN interpolation by its nature seeks to connect values on one line with the neighbouring lines to produce a more connected plot, while the LPC interpolation is more isotropic in the weighting of data points and the result is more unconnected structures. This illustrates that the degree of connectedness of structures in maps produced from sparse data sets is mainly determined by the choice of interpolation method, and this should be kept in mind when assessing the optimal line spacing. Results for layers 11 and 22 are shown in Figure 6-105 to Figure 6-110.



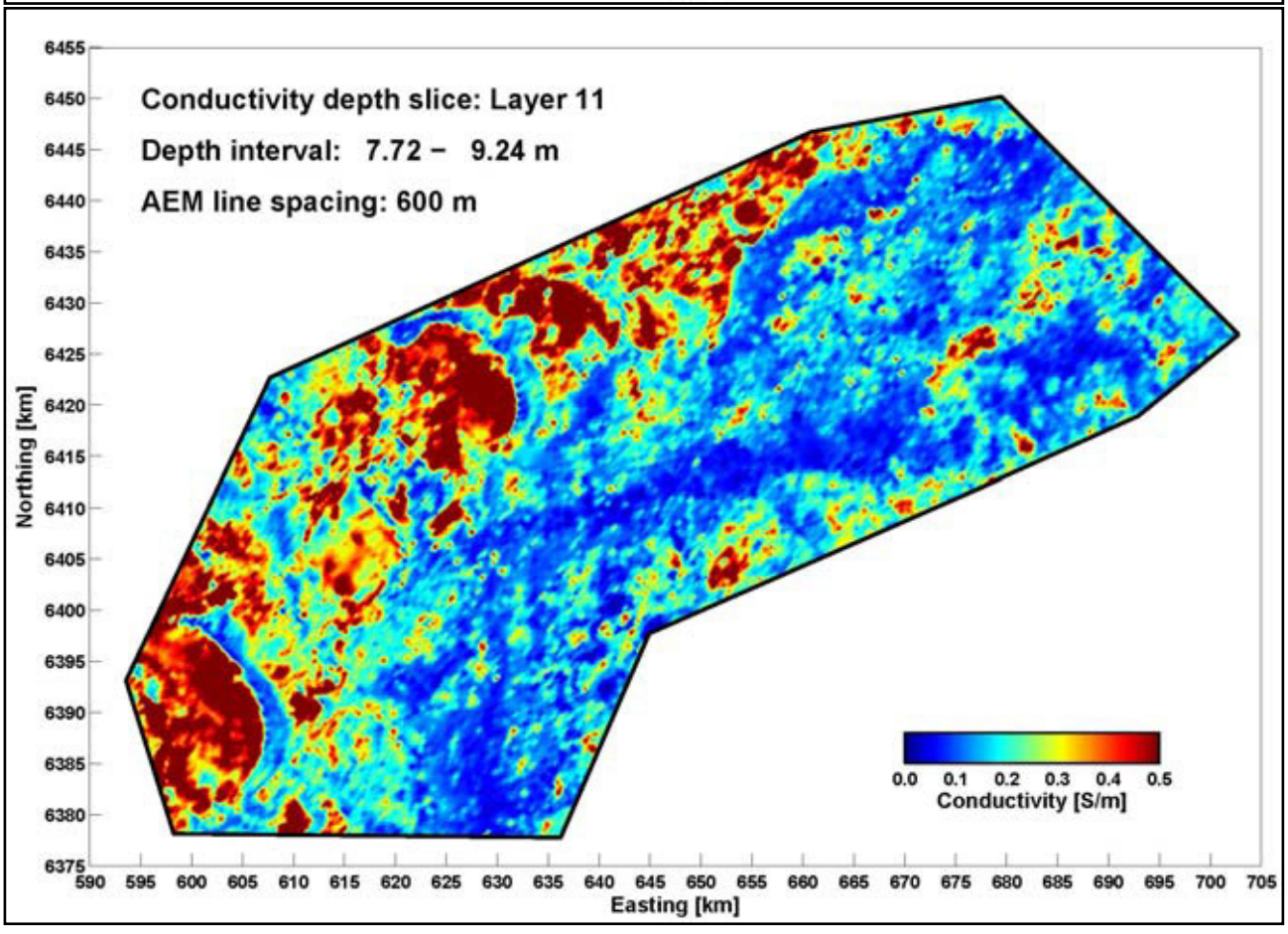




**Figure 6-99.** *Maps of results from 200 m and 600 m line spacings using NN interpolation in layer 11 (7.22-9.24 m).*

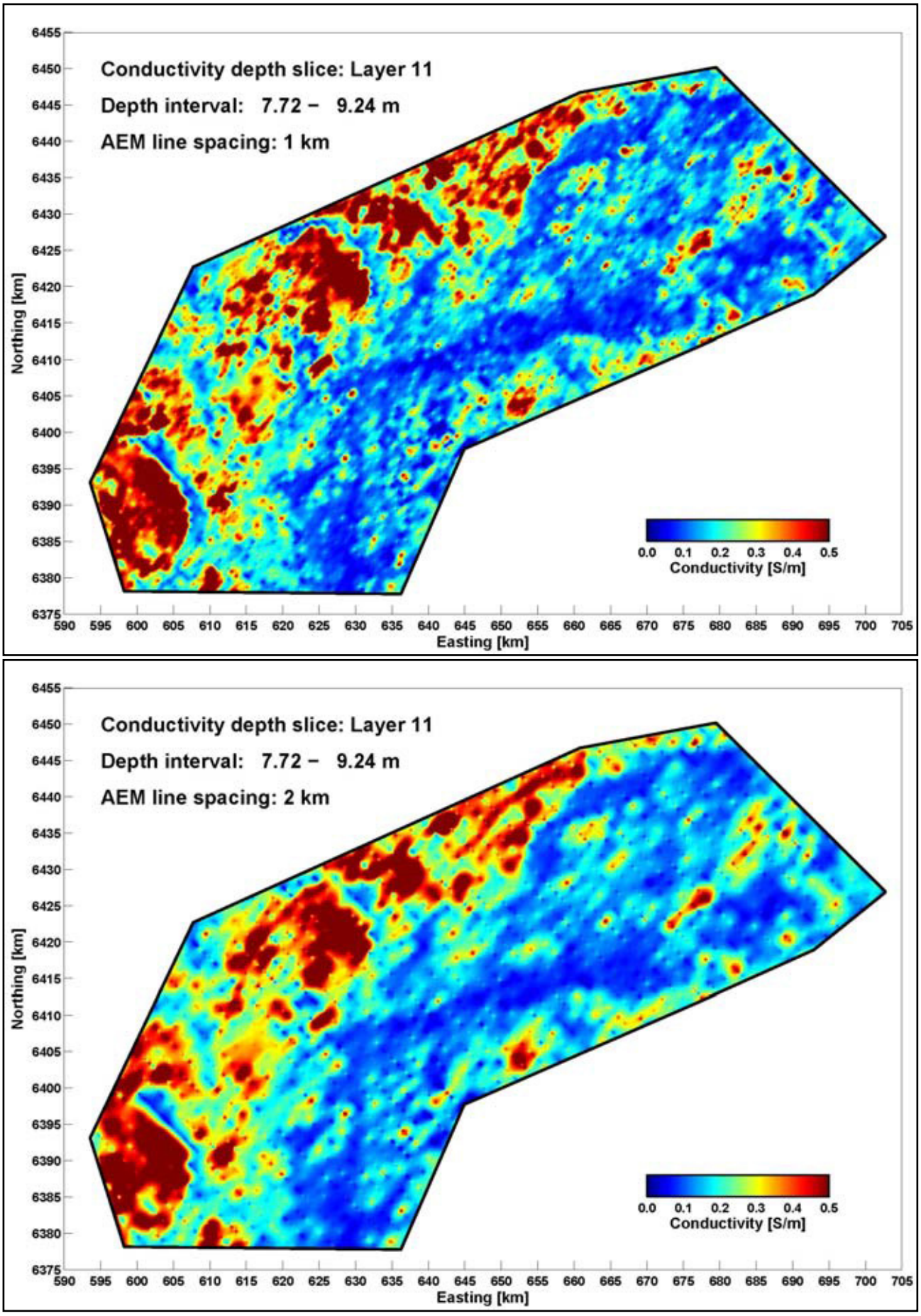



**Figure 6-100.** *Maps of results from 1 km and 2 km line spacings using NN interpolation in layer 11 (7.22-9.24 m).*

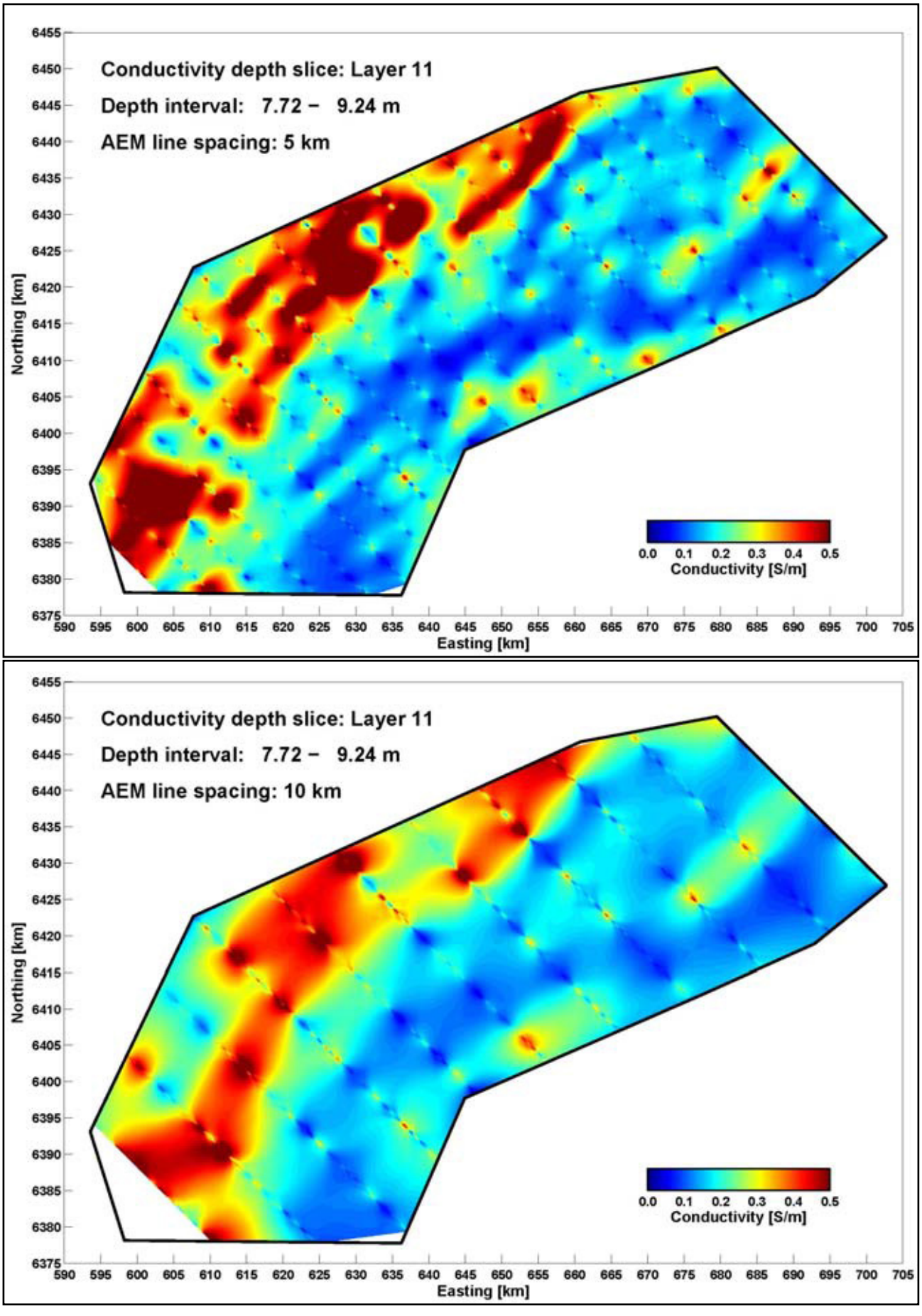



**Figure 6-101.** *Maps of results from 5 km and10 km line spacings using NN interpolation in layer 11 (7.22-9.24 m).*

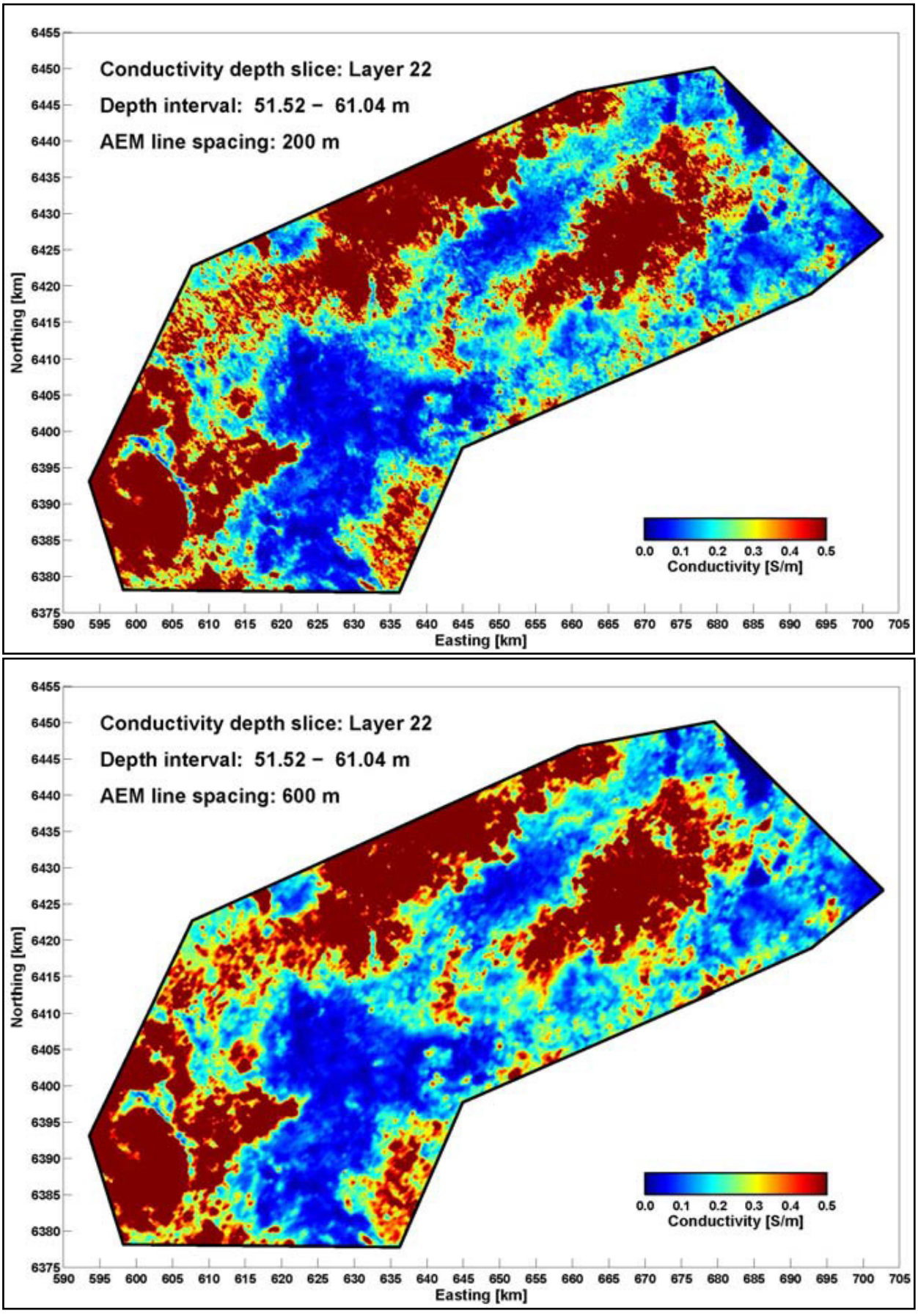



**Figure 6-102.** *Maps of results from 200 m and 600 m line spacings using NN interpolation in layer 22 (51.52-61.04 m).*

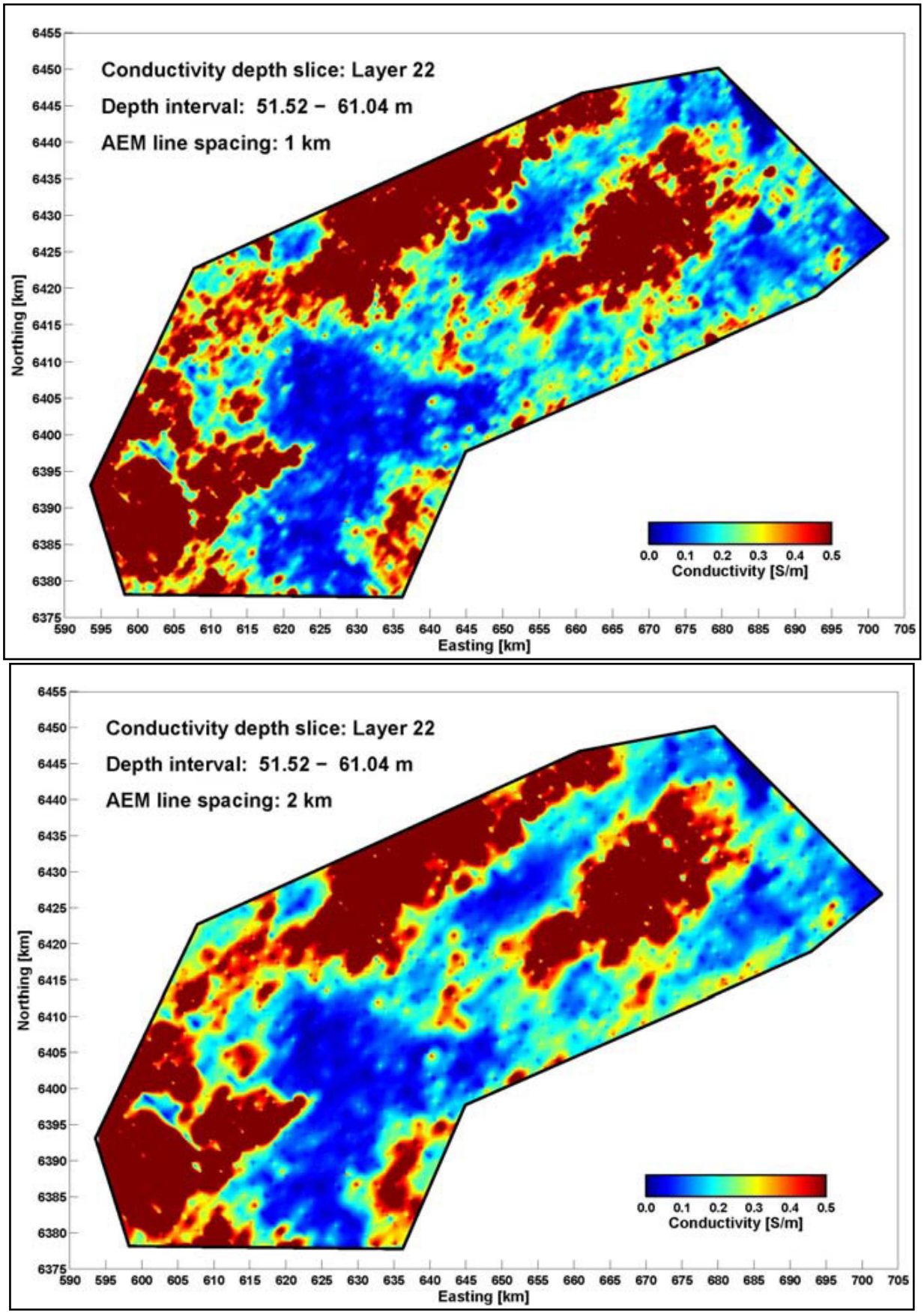



**Figure 6-103.** *Maps of results from 1 km and 2 km line spacings using NN interpolation in layer 22 (51.52-61.04 m).*

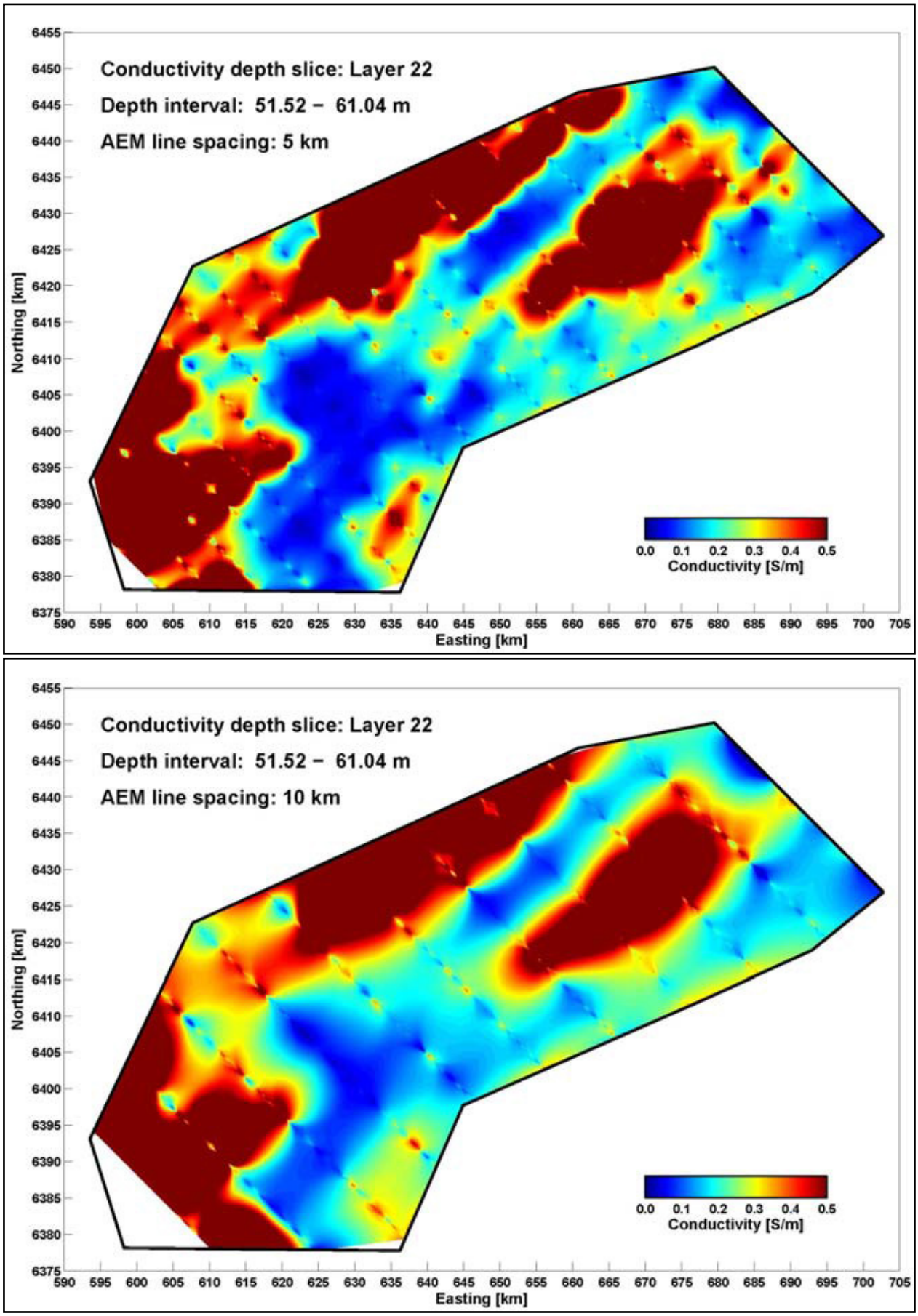



**Figure 6-104.** *Maps of results from 5 km and10 km line spacings using NN interpolation in layer 22 (51.52-61.04 m).*

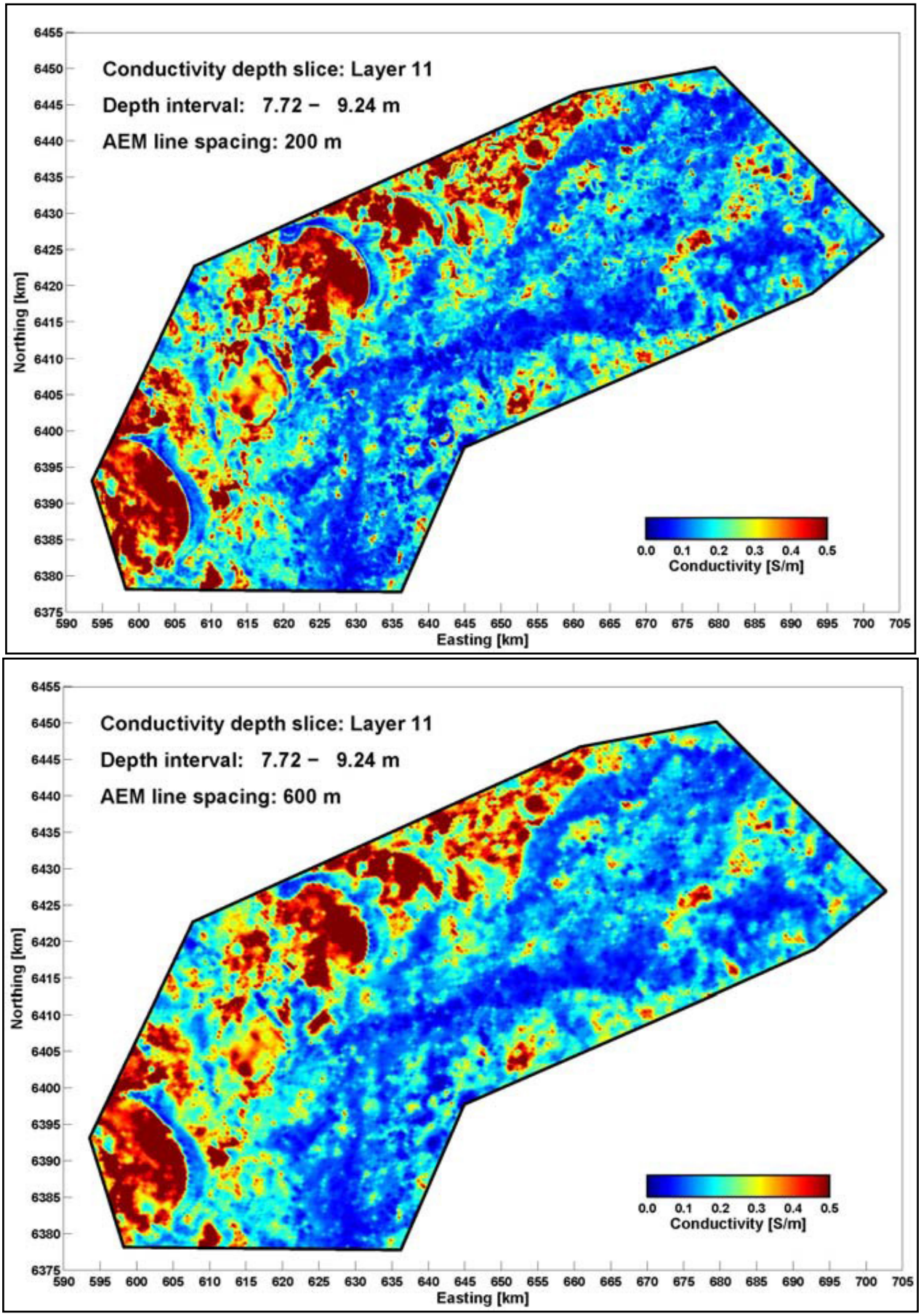



**Figure 6-105.** *Maps of results from 200 m and 600 m line spacings using LPC interpolation in layer 11 (7.22-9.24 m).*

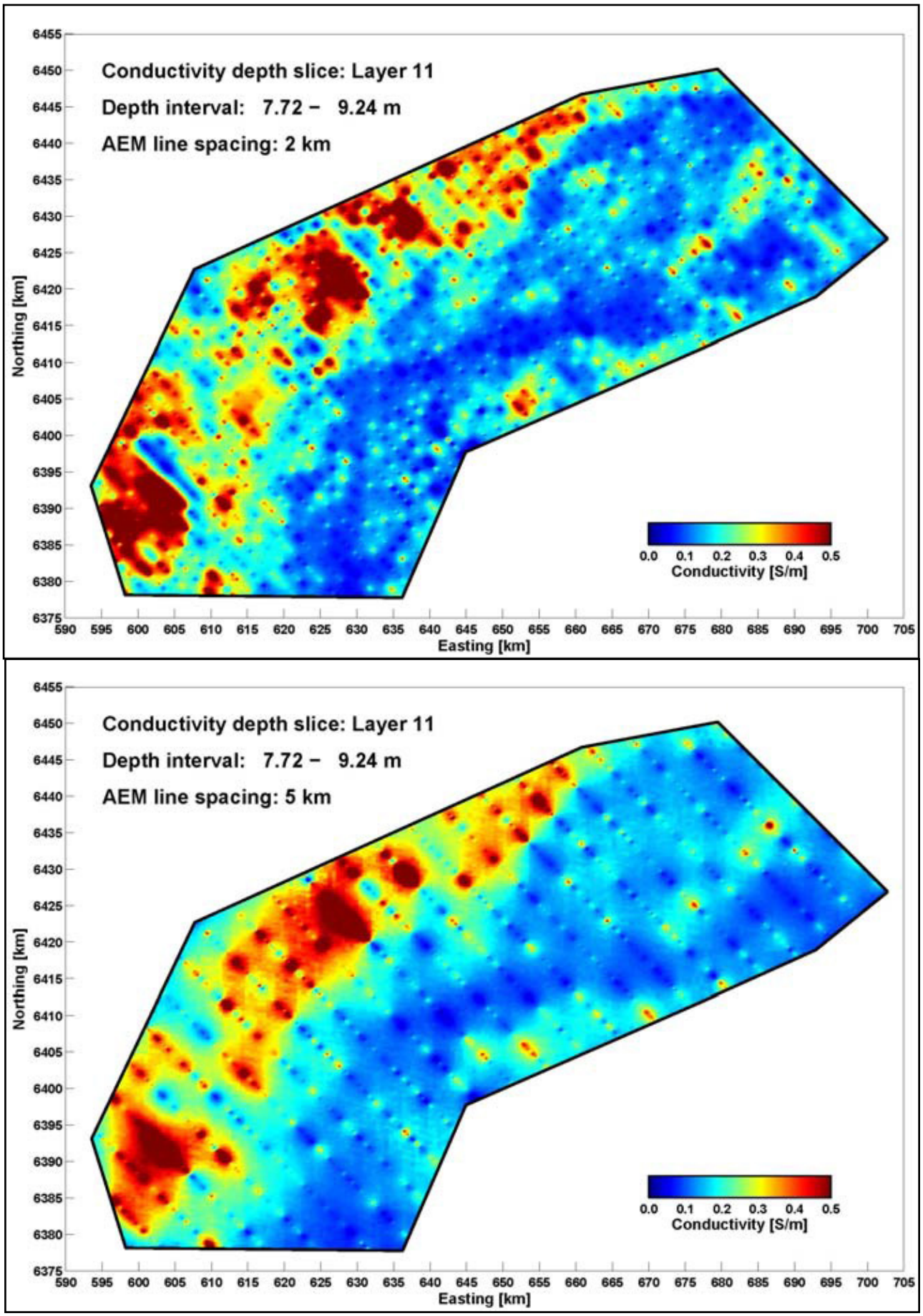
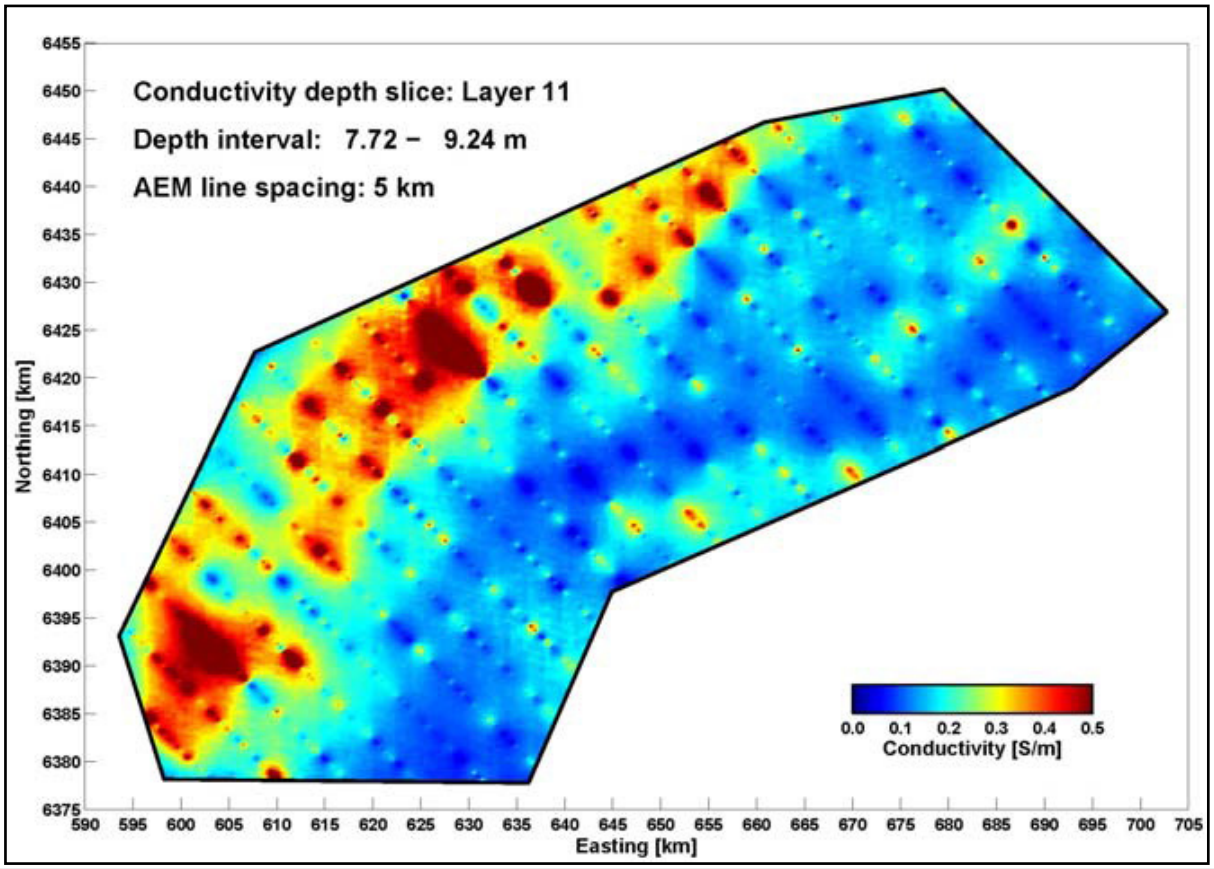



**Figure 6-106.** *Maps of results from 1 km and 2 km line spacings using LPC interpolation in layer 11 (7.22-9.24 m).*



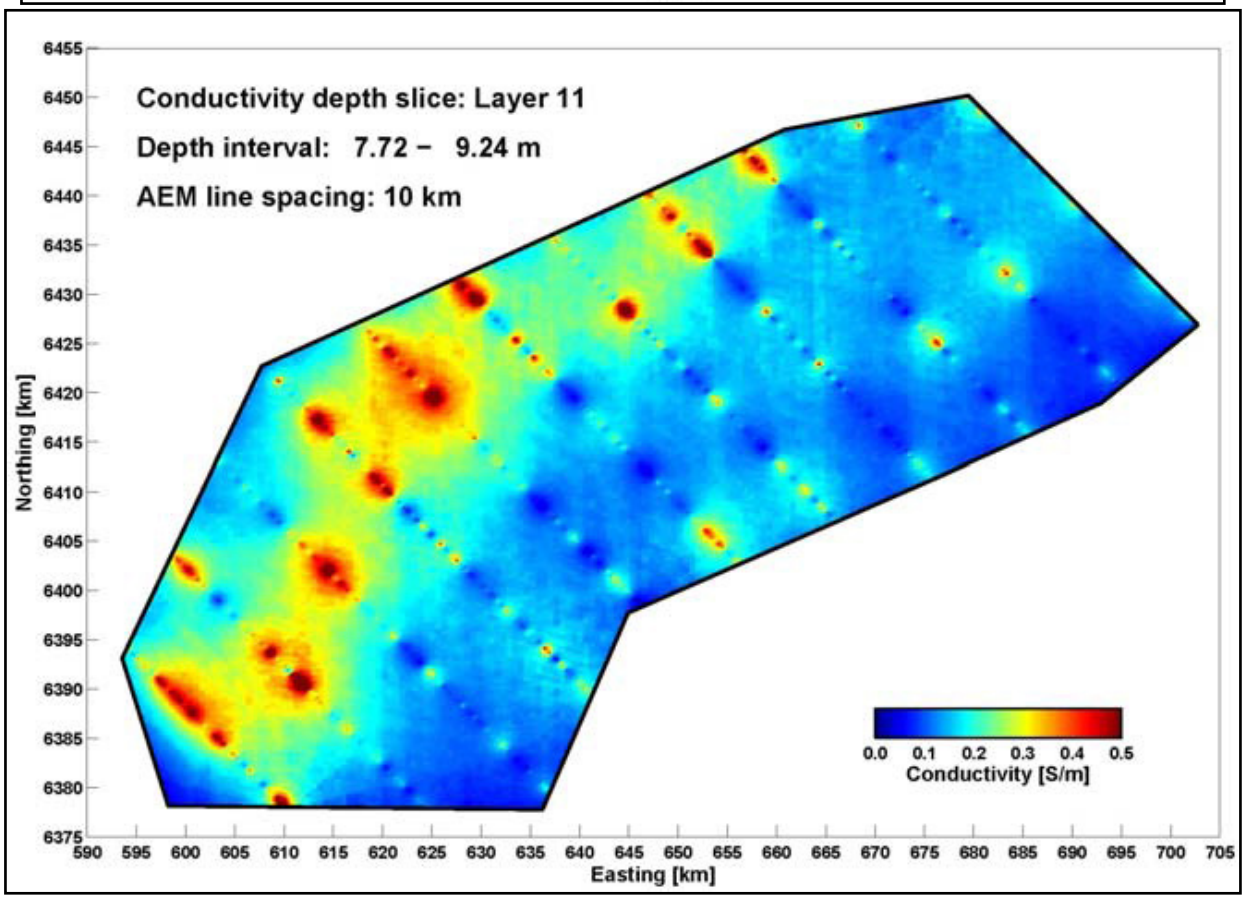




**Figure 6-107.** *Maps of results from5 km and 10 km line spacings using LPC interpolation in layer 11 (7.22-9.24 m).*

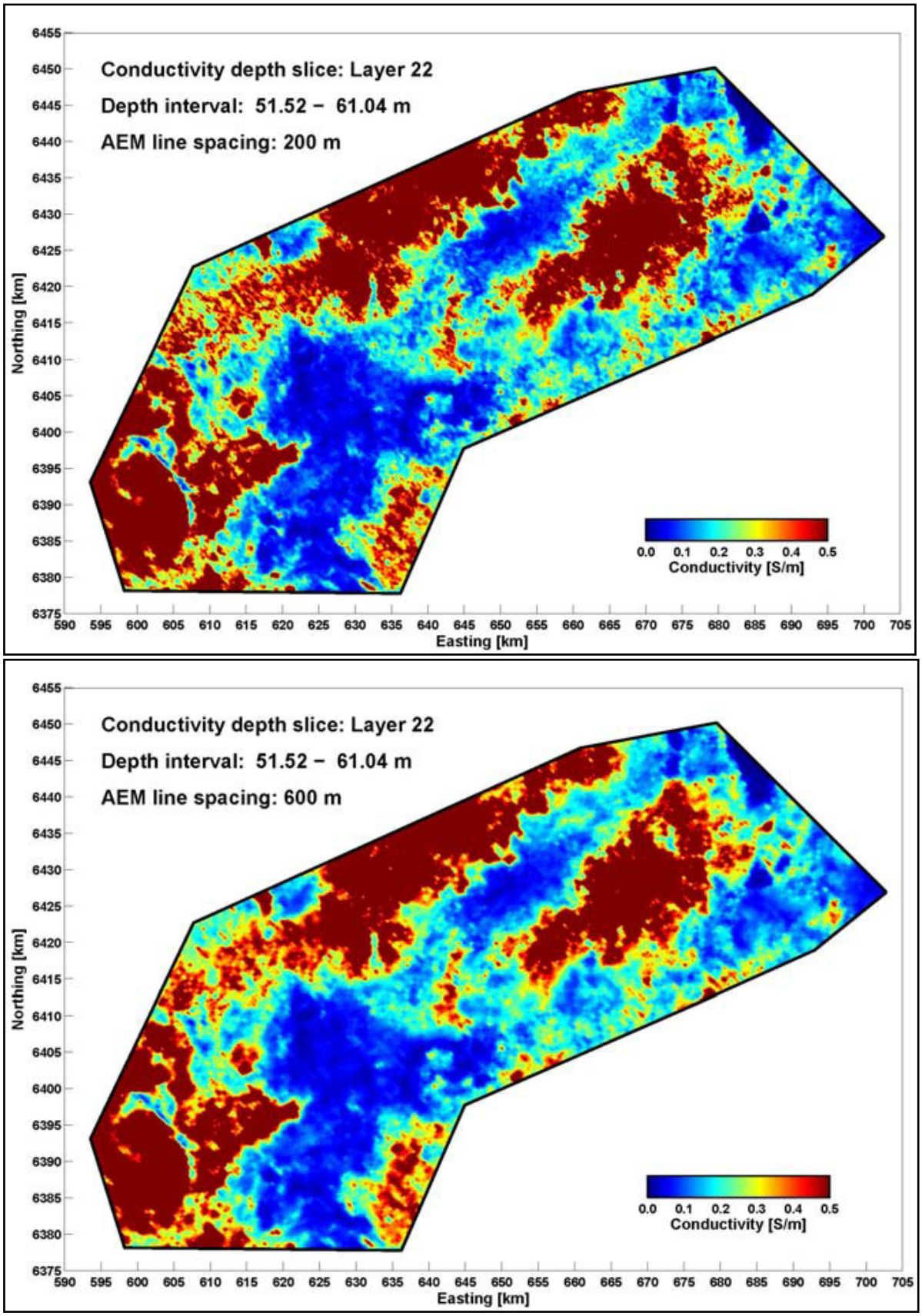



**Figure 6-108.** *Maps of results from 200 m and 600 m line spacings using LPC interpolation in layer 22 (51.52-61.04 m).*

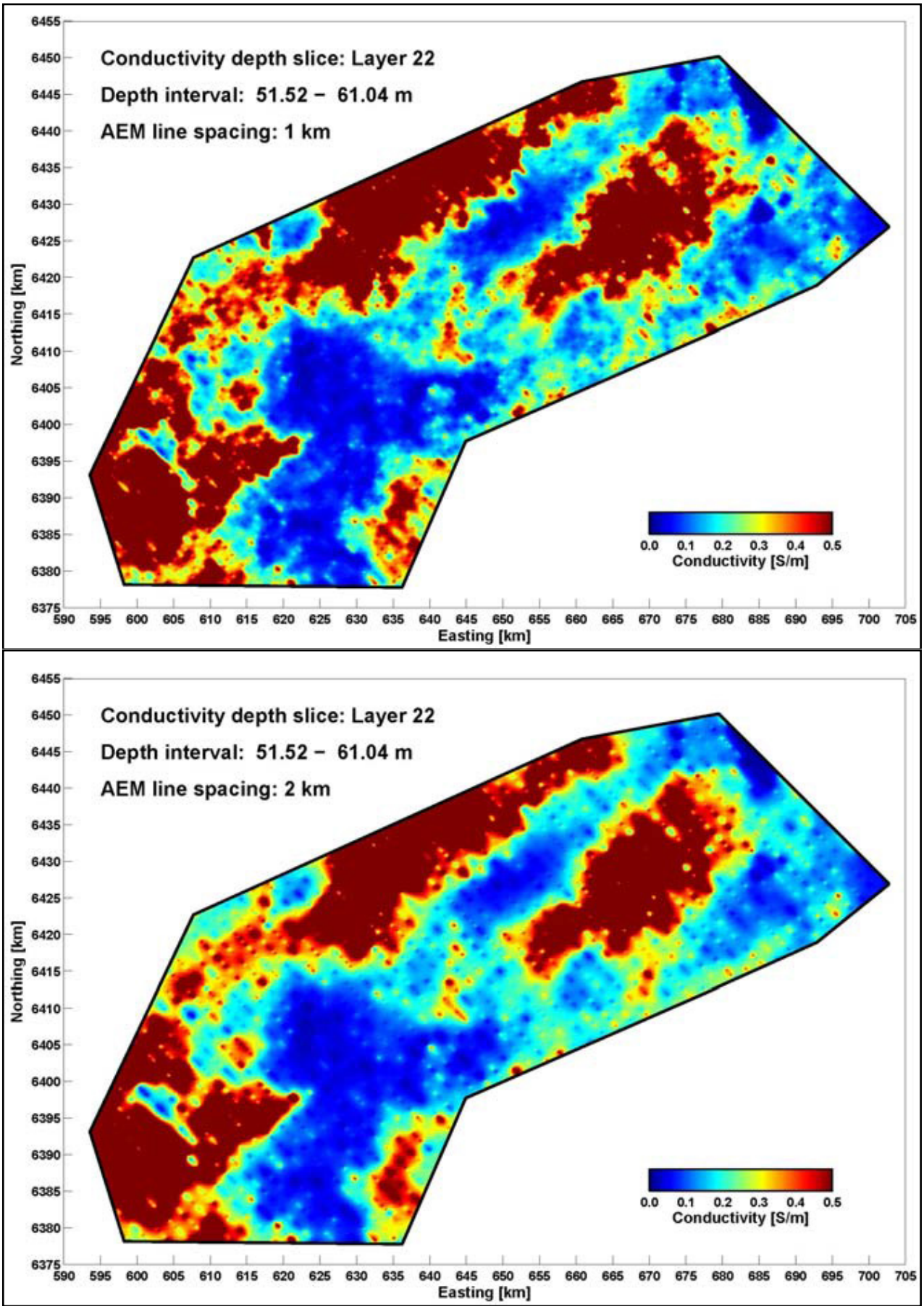



**Figure 6-109.** *Maps of results from 1 km and 2 km line spacings using LPC interpolation in layer 22 (51.52-61.04 m).*

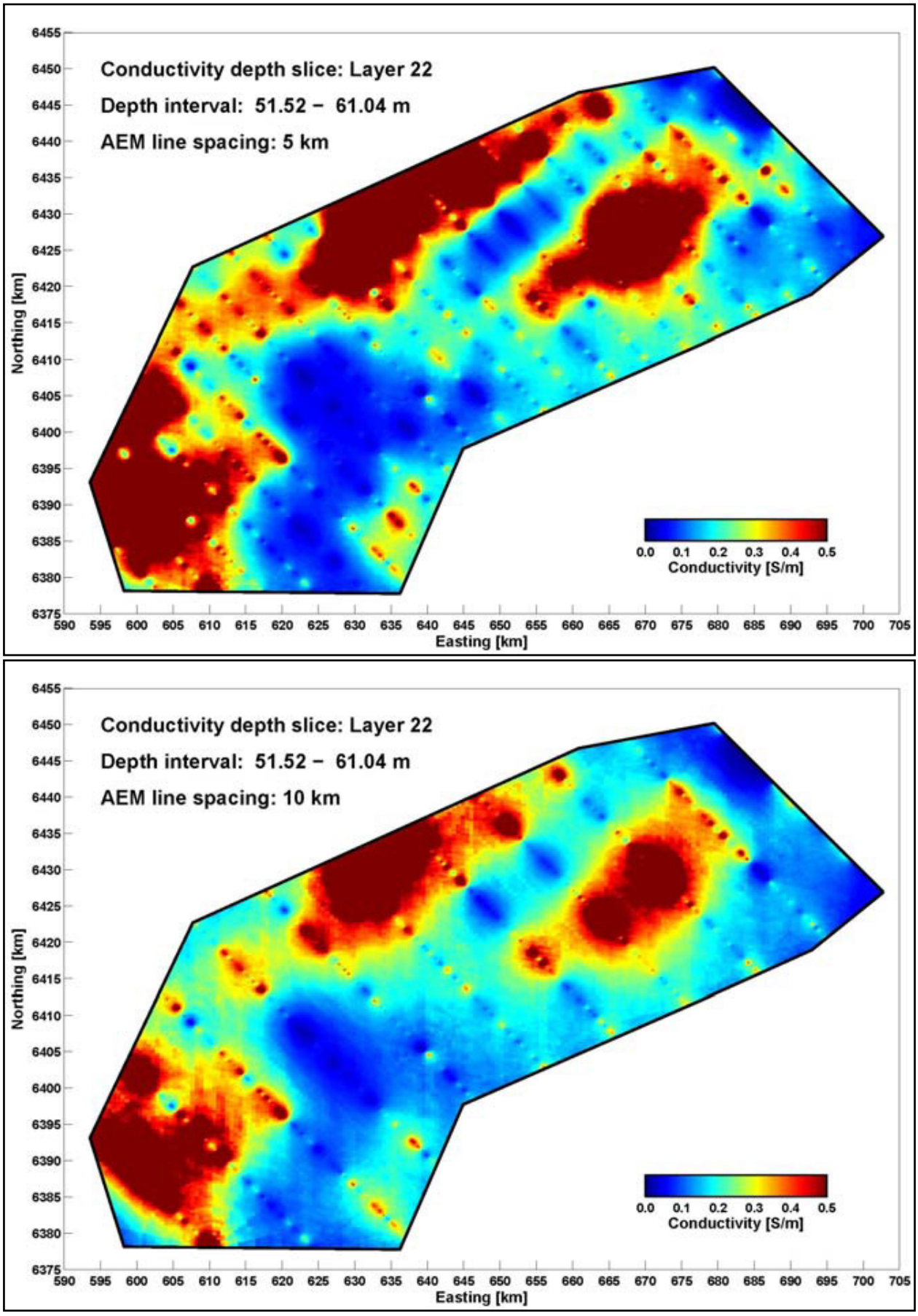



**Figure 6-110.** *Maps of results from 5 km and 10 km line spacings using LPC interpolation in layer 22 (51.52-61.04 m).*

## 6.11 SUMMARY

The BHMAR study has reinforced the experience over the past 15 years that high-resolution AEM data is required to map key functional elements of the hydrogeological system in the near-surface (top 100 m) in the Australian landscape context. To produce robust, high-resolution conductivity models, a rigorous approach is required to AEM technology selection, survey design and data acquisition, as well as data processing and inversion (Lawrie *et al*., 2009b; Christensen & Lawrie, 2012).

More specifically, optimisation of AEM data requires careful consideration of AEM system suitability, calibration, validation and inversion methods. The choice of an appropriate AEM system for a given task should be based on a comparative analysis of candidate systems, consisting of both theoretical considerations and field studies including test lines over representative hydrostratigraphic targets (Christensen & Lawrie, 2012).

In this study there have been a number of important innovations in this study. Development of the WANDA inversion code was critical to the overall success of the project. This inversion procedure only takes days to run, enabling the rapid trialling to select the most appropriate vertical and horizontal constraints. Previously, full inversions of the BHMAR dataset took weeks/months to run, providing limited opportunity to adjust the inversion parameters. Initial unconstrained inversions did not produce conductivity distributions that matched well to borehole conductivities.

Selection of the most appropriate inversion parameters for the WANDA approximate constrained inversions was facilitated by a trans-disciplinary research method. Participation of all research team members in formulating hydrogeological conceptual models led to a loosening of the regularization constraints in the WANDA inversion. In modern laterally-correlated inversion of AEM data, the usefulness of the resulting inversion models depends critically on an optimal choice of the vertical and horizontal regularization of the inversion. Set the constraints too tight, and the resulting models will become overly smooth and potential resolution is lost. Set the constraints too loose and spurious model details will appear that have no bearing on the hydrogeology. There are several approaches to an automatic choice of the regularization level in AEM inversion based predominantly on obtaining a certain pre-defined data misfit with the smoothest possible model.

In this study we used a pragmatic approach to optimizing the constraints by an iterative procedure involving all available geological, hydrogeological, geochemical, hydraulic and morphological data and understanding. In this approach, in a process of both confirming and negating established interpretations and underlying assumptions, the inversion results are judged by their ability to support a coherent conceptual model based on all available information.

A trans-disciplinary approach is dependent on integrating a team of scientists, where all facets of data and interpretation are considered and questioned in a trans-disciplinary analysis of the hydrogeological system. Necessary elements for this approach to succeed are the experience and professional insights of the scientists involved and a willingness and ability of scientists from diverse areas to establish a dialogue that will question and refine the inversion constraints and the quality of the final hydrogeological conceptual model.

This approach has been essential to the identification and assessment of MAR and groundwater extraction options in the Broken Hill Managed Aquifer Recharge project. The resultant improved 3D conductivity model revealed details of the hydrostratigraphy and neotectonics. Prior to the mapping of near-surface hydrostratigraphy and structural features, it had not been possible to explain apparently contradictory data, nor develop a plausible hydrogeological conceptual model.

Also of importance in this study has been the development of a unique lateral correlation procedure that correlates strictly horizontally. Another important contribution has been the development of new FID point-borehole correlation procedures in the DAT/DAT and MOD/MOD space. The use of Bayesian inference via a reversible jump Markov Chain Monte Carlo (RJ-McMC) inversion for selected AEM data sets provided useful (quantitative) insights into the robustness of inversion models,. Overall, the AEM inversion models and the borehole conductivity logs are consistent with the likelihood distribution derived in the RJ-McMC analysis. It is anticipated that this approach will be developed further.

In summary, a rigorous approach to AEM technology selection, processing and inversion has been important in the project, while of equal importance has been a pragmatic approach to optimizing the inversion constraints. This was achieved in a trans-disciplinary team environment, using an iterative procedure involving all available geological, hydrogeological, geochemical, hydraulic and morphological data and understanding. In this approach, in a process of both confirming and negating established interpretations and underlying assumptions, the inversion results are judged both by comparisons with other hydrogeophysical constraints at the borehole scale, but also by their ability to support a coherent conceptual model based on all available biophysical information. It is our understanding that this is the first use of AEM as part of trans-disciplinary mapping and assessment of MAR targets.

# 7 Borehole Geophysics

Three campaigns (Phase 1, Phase 2 and Phase 3a) of downhole induction conductivity and gamma logging were carried out. All borehole logging data are contained in Appendix 3 (Apps *et al*., 2012f) and displayed graphically in Appendix 1 (Halas *et al*., 2012a).

## 7.1 INDUCTION CONDUCTIVITY LOGGING

The goal was to measure, as accurately as possible, the electrical conductivity of the earth materials penetrated by the borehole. The equipment used, rented from Auslog Pty Ltd, is an A034 induction conductivity logging tool. It has the advantage over galvanic resistivity logging tools that it does not require physical contact with the earth material whose conductivity is measured. The borehole tool, called a sonde, is lowered into a borehole by a winch mechanism with an odometer device that is capable of measuring its depth. The Auslog sonde contains three coils: a transmitter, a receiver and a focussing coil, operating at a base frequency of 106 kHz. Table 7-1, below, displays the physical and operating specifications of the A034 induction conductivity tool used. Borehole geophysical logs for all surveyed bores are contained in Appendix 3 (Apps *et al*., 2012f).

**Table 7-1.** *Physical and operational characteristics of the Auslog Pty Ltd A034 induction conductivity tool.*

| **Tool Parameters** | **A034** |
|---|---|
| Diameter | 38 mm |
| Length | 1400 mm |
| Weight | 5 kg |
| Max. Working Temperature | 70°C |
| Max. Working Pressure | 10 MPa |
| Min. no. of Conductors (incl. armour) | 2 |
| Supply Voltage Range | 20 - 45 VDC |
| **Measuring Parameters** | |
| Sensor | 3-coil system |
| Inter-coil Spacing | 50 cm |
| Operating Frequency | ~106 kHz |
| Conductivity Range | 1 - 3000 mS/m |
| Noise Level | <0.5 mS/m |
| Accuracy | <100 mS/m (5% F.S.)<br>100 - 1000 mS/m (3% F.S.)<br>1000 – 3000 mS/m (10% F.S.) |
| Communication | 0 - 20000 cps |

The magnetic field produced by the currents in the transmitter coil, the primary field, induces currents in the ground moving in circles around the transmitter coil. These eddy currents in turn produce a secondary magnetic field which then induces a voltage in the receiver coil that has an in-phase and an out-of-phase (or quadrature) component. Using a voltage-to-frequency converter, the out-of-phase component is converted to a counts-per-second reading which is then transformed into apparent conductivity values. There are several basic assumptions in this model that must be taken into consideration:

- The conductivity is computed assuming the tool to operate in the low-frequency range of the electromagnetic induction method;
- The conductivity is computed assuming the tool is situated in a homogeneous full-space;
- The tool is calibrated.

Violation of these ideal assumptions will affect the reliability of the borehole measurement and will be discussed below.

Re (1): In the low frequency approximation, the out-of-phase part of the measured voltage is linearly related to the conductivity. It is valid if the conductivity of the ground is lower than a certain threshold and if the conductivity becomes too high, in practical terms higher than 1000 mS/m, the log will underestimate the true conductivity.

Re (2): This condition is clearly not valid in practice; actually, it is the very variation of conductivity down the hole, reflecting the changing stratigraphy, we wish to measure with the tool. However, a number of circumstances can jeopardise the reliability of the conductivity estimate.

Like any other electromagnetic instrument, the induction log measures an average of the conductivity, an apparent conductivity, within a certain volume weighted according to the sensitivity function of the tool. The sonde used in our campaign, is a two-coil system with a coil separation of 0.5 m and the sensitivity lies mainly within a vertical cylinder with a height of ~2 m and a diameter of ~1 m. When the tool is situated at a depth of less than ~2 m, part of the sensitivity is above ground, and the zero conductivity of the air becomes part of the average conductivity measured by the tool, meaning that the conductivity becomes lower than the conductivity of the near-surface earth material. This effect can be corrected for using a sensitivity analysis of the borehole device, but we have elected to remove induction conductivity data from at least the first 2 m from every log.

When the tool is underground by the required amount, it will measure an average of the conductivity of the surrounding formations and the conductivity of the borehole. If air filled, the zero conductivity of the borehole will lower the measured apparent conductivity and if the borehole is filled with very conductive fluid, the apparent conductivity will be increased.

Likewise, the presence of metallic objects will seriously influence the measurement and, because of their extremely high conductivity, the measurements will be completely corrupted. Consequently, the borehole device must be operated well away from any metal objects such as fences, cars, sheds, sheet metal, etc. Metal objects left in boreholes, such as metal casing or drill rods, destroy valid conductivity readings. This can be seen very clearly in the conductivity log for borehole BHMAR-19-1, where drillers left 10 m of drill rod and a drill head in the hole. In the conductivity logs for this report, measurements corrupted by metal objects have been removed.

Re 3): A reliable measurement is of course only achievable if the tool is well calibrated. In particular, if there is an offset on the tool readings, all apparent conductivity will be shifted by the offset value. If positive, the apparent conductivity cannot go below the offset value and low conductivities will be obscured by the offset.

An effect of this occurs when earth conductivity is very low. The approximation of linear correlation between conductivity and tool counts is no longer valid, resulting in an overestimation of conductivity values. Consequently, the measured values of low and high conductivity have an error associated with them and must be treated with caution. This is a calibration issue and is caused by a positive offset in the base level of tool counts (referred to as a bias level).

The calibration issue will be discussed in detail in a Section 7.1.2.

### 7.1.1 Logging Procedures

Conductivity measurements of boreholes were conducted following a strict operation procedure which was devised specifically for this campaign by Geoscience Australia after consideration of previous borehole logging programs. To ensure data quality and consistency, we chose a calibration borehole for repeat measurements that is fairly deep, has an interesting range of conductivity values; yet was also closely located to the base of the logging crew.

For the beginning of the campaign, we logged the repeat hole once per day at the beginning of the day's logging. Holes were chosen based on a priority of location, but also to minimise logistics and travel times. The conductivity sonde was lowered and raised at average speeds of 6-8 m/minute, with a spatial measurement frequency of one measurement every 25 mm. Downhole measurements were compared to uphole measurements to ensure repeatability of the conductivity measurement. Conductivity records were made using the Auslog Pty Ltd proprietary software module called WellVision. Our procedure was as follows:

- Arrive at borehole site and choose a location for setup. Locate the vehicle a few metres away from the bore Figure 7-1.
- Setup by arranging winch, releasing spindle brake on the winch, connecting batteries, booting computer, tool preparation, pulley preparation etc.
- Open up the field notes file for bore. Each well requires a separate file, even if it is part of a nest at one site. Record all field circumstances.
- Start the WellVision program, choose the borehole or create a new borehole. Creating a new site will require a little extra time: but put the easting and northing in the hole information.
- Attach the tool to the winch and select the tool from the menu in the WellVision program.
- Place the conductivity tool into the bore and run it down to the water level, bringing the tool to groundwater temperature. This is accomplished by running the sonde down and up about 30 m below the water table at a rate of 10 m/min. For bores shallower than 30 m the tool was dropped down to about 3 m from the bottom to cool in standing water for approximately 10-20 minutes. This is not necessary when moving from one bore to another in a nest: the tool should be cool by the completion of the first hole.
- Position the tool so that the end of the spring is level with the top of the bore casing. Calculate the proper depth setting by subtracting the measurement point of the sonde from the average height of the casing above ground level.
- Start the run in WellVision. Select depth measurements, and set the depth collection to be 25 mm. Choose travel direction of tool.
- Set the depth in the WellVision program to be equal to the calculated depth from step 7.
- Begin the run, start the winch. Run winch at speeds of approximately 6 m/min.
- While waiting, prepare for next run, and fill out the logging notes. Keep near the panic stop button: the tool can get stuck and the cable will tangle.
- Once tool has reached bottom, stop the winch, stop the record.
- Set up a new run for logging up the hole.
- Set the depth for the tool on this new up-logging run. Use the depth that the program has recorded for the end of the previous downhole log. If the tool has hit bottom of the well and some extra cable spooled out, note this in the field notes file.
- Exercise extreme caution as the tool approaches the surface, keeping a finger on the trigger of the emergency stop. Slow the winch down as sonde approaches surface level.
- Log the next bore if you are at a nested site, and repeat the instructions up to this point.

– Once finished with the induction logging for the site, execute a calibration procedure.

### 7.1.2 Calibration

We have devised instructions for calibration of the induction conductivity logging tool that were followed by all borehole loggers. This method offers an extension of previous calibration methods in that it uses a suite of calibration experiments to derive a statistically robust transfer function between measured voltage and conductivity (under the assumptions listed previously in the discussion of the borehole induction conductivity sonde). Our calibration method is divided into a software section and a procedural section.

#### 7.1.2.1 *Software*

In the WellVision program, go to *Acquire\Tool Setup\ToolCalibration*. A panel will appear that has a sidebar and 3 tabs. This is the calibration panel for the instrument. On the bottom of the sidebar (to the left), there are 3 radio buttons that you can select for the calibration procedure. For a new calibration, select *New Calibration* and click the large button *Create a new calibration entry*. You will be able to edit the 3 tabs on the right-hand side of the panel. Click on the button *Clear all*. On the right-hand side, enter the value of the calibration coil (the jig value), whether it is 0, 200, 500 or 700 mS/m. Change the sample rate to 0.1 s, the delay to 1 s (it won't accept any lower) and the sample count to 512. When you have set up the tool for the measurement, click on the button *Acquire point*.

#### 7.1.2.2 *Procedure*

Calibration of the induction tool must take place after the tool has been used to log the well. We have noticed a temperature-dependent variability in the conductivity values of a single borehole, so it is imperative that the tool is at or near the temperature it was while logging. The tool was calibrated at every site; following this procedure:

– Calibration must be done after logging (down and up run).
– Unwind the tool a distance of ~15 m from the vehicle, having one person holding the tool and keeping tension on the cable. Ensure, as best as possible, that you are not near metal. The handler must not wear metal including watches, jewellery, steel-cap shoes, etc.
– Go into the WellVision Acquire\Tool Setup\ToolCalibration and start a new calibration.
– Enter jig value of 0 mS/m. Hold the tool as levelly and as stably as possible at shoulder height.
– Change the sample rate to 0.1 s, the delay to 1 s and the sample count to 512. When you have set up the tool for the measurement, click on the button acquire point.
– After measurement, place the 200 mS/m coil on the tool so that the centre of the coil coincides with the red dot on the tool. Keep the tool at shoulder height. Be consistent with how you place the coils on the tool (for instance, letters facing cable).
  Enter jig value of 200 mS/m in the WellVision software.
– Reset measurement parameters for the acquisition sample. When you have set up the tool for the measurement, click on the button acquire point.
– Place the 500 mS/m coil on the tool so that the centre of the coil coincides with the red dot on the tool. Keep the tool at shoulder height Figure 7-2. Be consistent with how you place the coils on the tool (for instance, letters facing cable).
– Enter jig value of 500 mS/m.
– Reset measurement parameters for the acquisition sample. When you have set up the tool for the measurement, click on the button acquire point.

- Place the 200 mS/m and the 500 mS/m coils on the tool so that each coil straddles the red dot on the tool. Keep the tool at shoulder height. Be consistent with how you place the coils on the tool (for instance, letters facing cable).
- Enter jig value of 700 mS/m.
- Reset measurement parameters for the acquisition sample. When you have set up the tool for the measurement, click on the button acquire point.
- Write the calibration settings to a .csv format, with the name of the file being 'InductionCalibratedyyyymmddHHMM.csv'}, where yyyymmddHHMM are the numerics for year (yyyy), month (mm), day of month (dd), hours (HH) and minutes (MM).
- Use standard format for the csv file that and record all values that are recorded for each jig value: count; sample count (should always be 512); minimum count; maximum count; standard deviation and variance of measurement. There are 6 values recorded for each jig value.
- Save the csv file in the Calibrations folder.
- Wheel the tool in and proceed to the next site.



**Figure 7-1**. *Photograph of borehole logging set-up in the field.*



**Figure 7-2**. *Calibration ring position on the induction conductivity tool during a calibration experiment.*

#### 7.1.2.3 ***Results***

Figure 7-3 shows the counts per second (i.e. secondary voltage) measured versus calibration jig value for every calibration experiment recorded during the entire borehole logging campaign. This resulted in a total of 58 experiments, conducted at random locations at random times of the working day by at least 3 different operators. The total number of days covered in the calibration experiments is about 100 days. As is to be expected, the spread or variation in voltage increases with increasing jig value: a feature that is common in these types of measurements. Rather than using an individual look-up table that yields conductivity from counts per second, we have found a functional form for the data that expresses jig values as a function of counts or voltage. This method was chosen in order to arrive at a calibration scheme that can be applied to every conductivity measurement. To be able to fit the calibration data and to attempt to account for the low-conductivity departure from linearity in the relation between voltage and conductivity, we have chosen the functional form of :

$$\sigma = ax^b + c,$$

**Equation 75**

where $\sigma$ is conductivity, $x$ is the measured voltage, recorded in counts per second, and $a$, $b$ and $c$ are parameters determined from the data in a least-squares sense. We solve for the parameters $a$, $b$ and $c$ using a Levenberg-Marquardt algorithm. This provides us with a smoothly-varying function that has well-defined confidence limits for the conductivity ranges that we are interested in for this campaign. The functional form of the calibration equation is shown in Figure 7-4, and it accounts for 99.97% of the variability in the data ($R^2$= 0.9997). However, despite these advances in calibration and logging procedures we still have not implemented a calibration scheme that directly relates secondary voltage to soil conductivity. So far, we have proven that what we can measure with this particular borehole tool is self-consistent, repeatable, and non-varying over a time span of 100 days. We have not, as of yet, determined a method of determining conductivity independently of the calibration coil rings (which are constructed individually for each tool, possess different self-inductances and can potentially get mixed up when tools return to the parent company).

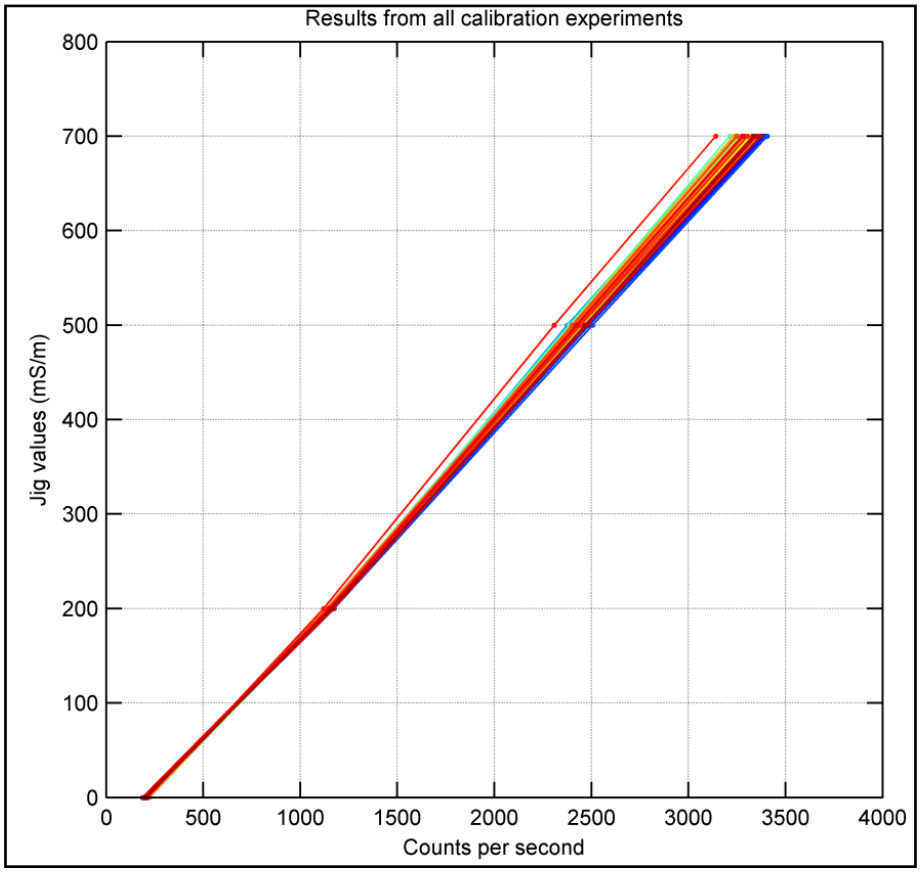



**Figure 7-3.** *Counts per second (i.e. secondary voltage) versus calibration ring jig value for every calibration experiment undertaken during the entire borehole logging campaign.*

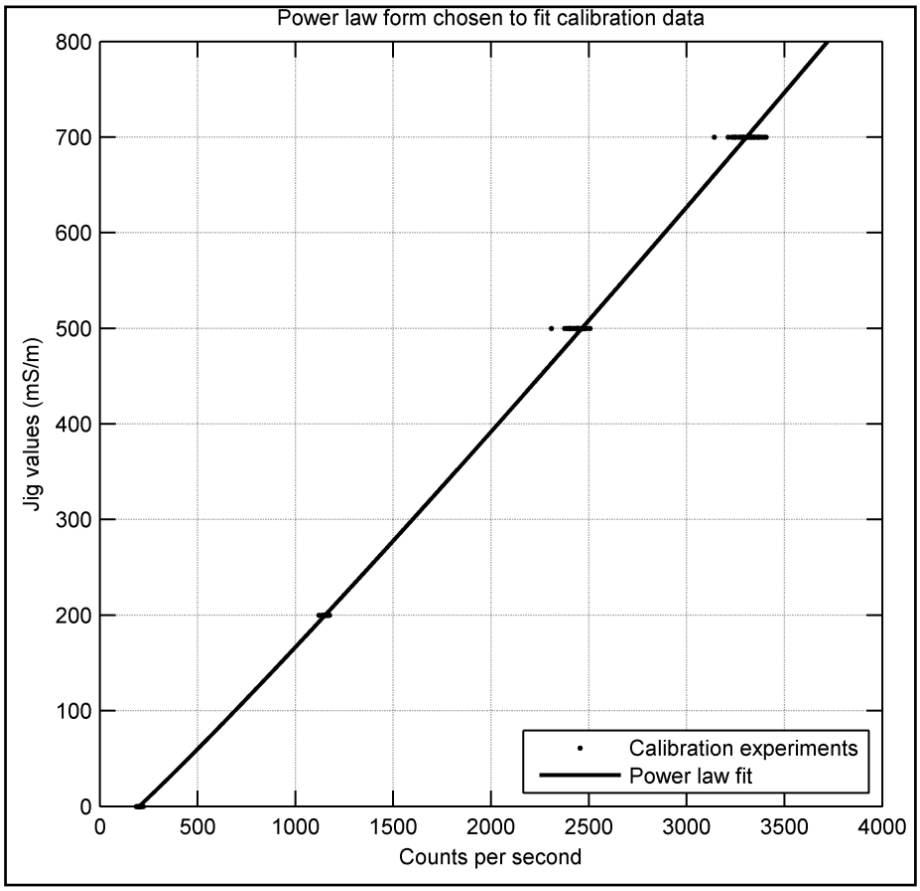



**Figure 7-4.** *Results of a functional fit to the calibration data using a form of* $\sigma = ax^b+c$.

### 7.1.3 Processing

After recording the down- and uphole log of all boreholes, the raw voltage data was exported using a common format for well logging data (LAS format). Raw voltage data, recorded as counts per second, were converted to conductivity using our calibration formula. Every bore log was examined for repeatability on the down- and uplog, and the results compared using a maximum correlation method to determine depth with anomaly. Signals recognised as metal objects, cable slack, noise variations and near-surface effects were removed from the processed data sets. The resulting finalised data was then written back to LAS format and stored in our archives. These data are used in the conductivity logs presented in this report and are also used for the fid-point correlations discussed in Section 6.6.

## 7.2 NATURAL GAMMA LOGGING

Gamma logging is a radioactive technique measuring naturally occurring gamma radiation emitted from rocks around the borehole. Gamma radiation is classified as very high-frequency radiation that arises due to the natural radioactive decay of various elements in the soil structure. The most significant naturally occurring sources of gamma radiation are potassium-40 (K-40) and the daughter products of the uranium- and thorium-decay processes (U and Th, respectively).

In sedimentary rock sequences, relatively high natural gamma counts are recorded in shales and clay bearing rocks, as they include weathering products of potassium feldspar and mica and tend to concentrate uranium and thorium by ion absorption and exchange. In contrast, low gamma counts are typically recorded for clean sandstones and limestones. However, many regolith clays are leached and do not contain substantial amounts of potassium. Therefore, this interpretation is not always applicable for regolith units (Chopra *et al.*, 2002).

The gamma measuring sonde used in this campaign was the A631 natural gamma tool, rented from Auslog Pty Ltd. It operates using a solid sodium-iodide (NaI) scintillation crystal of 25.4×76.2 mm which records the total radiation count. More complex gamma tools use a spectrometer capable of differentiating between K, Th and U sources. The physical and operational characteristics of the A631 gamma tool are shown in Table 7-2. It is uncertain at this time whether or not the gamma tool was calibrated by Auslog Pty Ltd before being sent for use by Geoscience Australia.

**Table 7-2.** *The physical and operational characteristics of the A631 gamma tool.*

| Model | A631 Natural Gamma Tool |
|---|---|
| Diameter | 43 mm |
| Length | 1130 mm |
| Weight | 4.0 kg |
| Pressure Rating | 21000 kPa |
| Temp Rating | 0 - 70°C |
| Power | 30 VDC |
| Detector Type | Scintillation Crystal |
| Crystal | NaI(Ti) |
| Size | 25.4 mm × 76.2 mm |

As stated earlier, all borehole logging data is presented in Appendix 1 (Halas *et al*., 2012a). Each page of the borehole logging data contains the information for an individual well. On each page is a series of plots that show well-construction, stratigraphy, basic lithology, natural gamma and induction electrical conductivity. On the last panel is shown the downhole electrical conductivity (measured with the A034 sonde) compared to the nearest-neighbour electrical conductivity model produced by the AEM borehole and spatially-constrained inversion (SCI-bore). These plots offer at-a-glance information of relevant borehole data, allowing us to compare the lithological information to the measured gamma and conductivity products.

## 7.3 NUCLEAR MAGNETIC RESONANCE (NMR) LOGGING

### 7.3.1 Why NMR Logging in the BHMAR Area?

The accuracy of hydrogeological frameworks and the predictive accuracy of the groundwater-flow models built from those frameworks depend upon the quality and quantity of hydrologic and geologic data available for the aquifer in the modelled area. Borehole logs often are used in conjunction with regional bedrock topography, outcrop observations, and other ancillary information to build hydrogeological frameworks in a manner that best reflects the understanding of the scale and geometry of the studied aquifer. Given the heterogeneity and size of certain aquifers, the availability of reliable geologic data often is relatively sparse. Lack of reliable geologic data is a significant limitation to groundwater-flow model results and one of the common sources of model error (Konikow & Bredehoeft, 1992). Quantitative estimates of hydraulic properties, such as hydraulic conductivity and specific yield, are typically assigned from lithological descriptions of test holes based on the published laboratory derived values (Johnson, 1967). Typically, limited in groundwater applications is the extensive use of expensive and time consuming laboratory measurements of cores which can be biased by sampling and the difficulty of making measurements on unconsolidated materials.

Historically, the only means of obtaining additional detailed, quantitative information on an aquifer system is through installation of observation wells and performing aquifer tests. The drilling of additional boreholes, installation of observation wells and performing aquifer tests is both time-consuming and expensive. Aquifer tests are unique in design and interpretation from site to site and lead themselves to be influenced by the position of the screened intervals. Furthermore, in many environments, it is becoming increasingly difficult to obtain environmental clearances for disposing of the produced waters. Given the heterogeneity and size of the aquifer system in the BHMAR area, an improved, more cost-effective approach was needed to provide quantitative estimates of aquifer properties. Nuclear Magnetic Resonance (NMR) can provide a direct measurement of the presence of water in the pore space of aquifer materials. Detection and direct measurement is possible due to the nuclear magnetization of the hydrogen (protons) in the water. These measurements are the basis of the familiar MRI (magnetic resonance imaging) in medical applications. NMR has been widely used in logging applications within the petroleum industry for the past 30 years. Recently, developments of systems specifically designed for application in the groundwater community have allowed the NMR logging technologies to be applied in groundwater studies (Knight *et al*., 2012, Dlubac *et al*., 2011, Walsh *et al*., 2010). One of the big benefits of the use if NMR logging is that measurements are made throughout the borehole and are not limited to the areas of the interpreted screened interval for the aquifer tests. Another benefit is the fine scale of the measurements typical on the order of 0.5 meters between measurements. In an aquifer as heterogeneity as the ones in the BHMAR area the benefit of the NMR logging can be a much more quantitative view of the scale at which that heterogeneity occurs.

### 7.3.2 NMR Background

Geophysical methods where developed to provide a way of imaging the earth. Geophysics exploited the link between physical properties, which can be measured with geophysical instruments, and geological or hydrogeological features of interest. The problem typically is the complexity of the link between the physical properties and the features of the geology and hydrogeology. For example, electrical methods cannot discriminate between the presence of conductive groundwater and the presence of conductive material such as clays or metallic mineralization. However, Nuclear Magnetic Resonance (NMR) can provide a more direct measurement to the presence of water in the pore space of geological materials. NMR logging has become a frequent data source for lithology-independent porosity, fluid typing, and pore system analysis in oil and gas wells (Kenyon *et al*., 1995; Alvarado *et al*., 2003).

The first borehole NMR geophysical instruments were developed in the 1960's (Brown & Gamson, 1960). Over the past several decades, advancements in these instruments have resulted in NMR being considered a proven technology for acquiring high quality measurements of hydrogen-rich materials. However like other borehole logging technologies, borehole NMR is limited to only sampling the formation immediately around the annulus of the borehole.

Three characteristic relaxation times are distinguished in NMR: the effective transverse relaxation time $T_2$*, the transverse relaxation time $T_2$, and the longitudinal relaxation time $T_1$. The magnitude of each of these parameters can depend on the static field strength (Godefroy *et al*., 2001). The most important parameter measured in NMR logging, and of specific interest for hydrogeological applications, is the measurement of the NMR transversal relaxation time constant, $T_2$, which represents the time it takes the transverse component of the nuclear spins associated with the hydrogen nuclei to return to equilibrium after perturbation by an external electromagnetic pulse. The parameter $T_2$ is well-known to be sensitive to the geometry of the water-filled pore space and can be related to the hydraulic conductivity (Cohen & Mendelson, 1982).

Another parameter that can be measured in NMR logging is the longitudinal relaxation time constant, $T_1$, which describes the time required for the longitudinal component of the nuclear spins associated with the hydrogen nuclei to return to equilibrium after perturbation by an external electromagnetic pulse. $T_1$ is controlled by the degree of proton alignment, and different fluids have different $T_1$ relaxation times (Coates *et al*., 1999). The petroleum industry uses $T_1$ to help differentiate oil and gas from water.

$T_2$* is the final parameter measured in NMR logging. It describes the transverse component of decay towards its equilibrium values of zero recorded at the receiver as the free induction decay (FID). The FID is a transient oscillating voltage and in many porous rocks it can be characterised by a single decay time $T_2$* (Chen *et al*., 2005). However $T_2$* is extremely sensitive to magnetic materials and can be biased by these inhomogeneities in the background magnetic field. This is why a $T_2$ measurement scheme is typically employed.

### 7.3.3 Borehole NMR Measurements

Borehole measurements of the NMR response of water in a porous geological material are described, by (Dunn *et al.,* 2002). In the presence of a static magnetic field (*B0*), the nuclear spins associated with the hydrogen nuclei of the water molecules align, producing a net magnetic moment in the direction of *B0*. This results in a macroscopic magnetization, defined as the net magnetic moment per unit volume. The spins precess about the background field at the Larmor frequency *f*, related to *B0* as follows:

$$f = \frac{\gamma}{2\pi}|B_0|$$

**Equation 76**

where $\gamma$ is the gyromagnetic ratio of hydrogen, equal to 0.2675 rad/(nT·s).

The NMR measurement involves applying an external electromagnetic pulse, oscillating at the Larmor frequency and perpendicular to *B0*, which tips the spins into a plane transverse to *B0*. Precession of the spins in the transverse plane generates a detectable signal that decays over time as the spins relax to their equilibrium position. The initial signal amplitude, just after the applied pulse, is directly proportional to the total amount of water sampled by the NMR measurement. The measured change in signal amplitude over time, referred to as the NMR decay-curve, contains information about the porous material saturated with water (Figure 7-5).

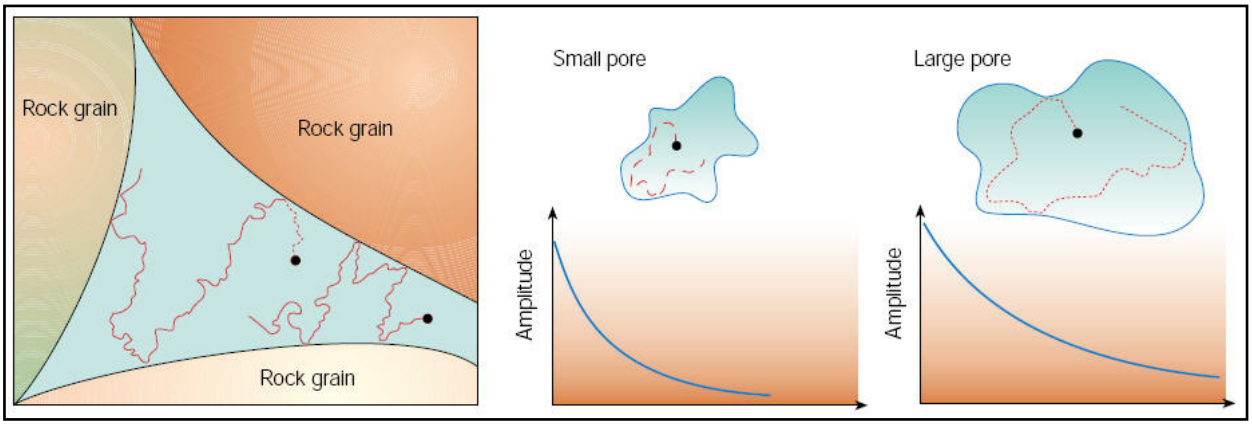



**Figure 7-5.** *Speed of relaxation which depends on how often protons collide with grains, governed by the surface to volume (S/V) ratio. Collisions are less frequent in large pores as they have a smaller S/V ratio. The result is a large $T_2$ decay time. Similarly, small pores have a large S/V ratio and a short relaxation time $T_2$ (Vista Clara, 2011).*

The acquisition of borehole NMR measurements involves lowering an instrument into a borehole to obtain the NMR decay-curve at sub-meter intervals over the depth of the borehole. In this study we used the Vista Clara Javelin system (Vista Clara, 2011). One or more permanent magnets, mounted in the instruments, provide the static magnetic field with field strength on the order of ~0.005 T to 0.02 T, and a corresponding Larmor frequency of ~250 kHz to 1 MHz. A transmitter in the tool generates a radio-frequency magnetic field to excite the spins and detect the NMR signal.

The standard borehole NMR $T_2$ measurement uses a Carr-Purcell-Meiboom-Gill (CPMG) pulse sequence (Carr & Purcell, 1954; Meiboom & Gill, 1958), designed to eliminate the influence of static inhomogeneous magnetic fields (Figure 7-6). The fundamental of the CPMG pulse sequence is the NMR echo, which is formed by successive Radio Frequency (RF) pulses that have specified echo spacing after the initial tipping pulse. Under the condition of fast diffusion, where the diffusion of the hydrogen nuclei within the pore space is not the rate-controlling step in the relaxation process, the borehole NMR response of water in a single pore can be described as single exponential decay of the measured transverse magnetization signal $A$ as a function of time $t$:

$$A(t) = A_o e^{-t/T2}$$

**Equation 77**

where $A0$ is the initial magnetization signal at t=0, and $T_2$ is the transverse relaxation time. The corresponding relaxation rate $T_2^{-1}$ is given by the following expression (Brownstein & Tarr, 1979; Cohen & Mendelson, 1982):

$$T_2^{-1} = T_{2B}^{-1} + \rho_2 S/V$$

**Equation 78**

where $T_{2B}$ is the relaxation time of the bulk fluid, $S/V$ is the surface-area-to-volume ratio of the pore, and $\rho_2$ is the surface relaxivity, a property describing the capacity of the surface of the pore space to enhance relaxation. The term $\rho_2 S/V$, called the surface relaxation rate, typically dominates the measured $T_2$ relaxation time. Equation 78 assumes that the use of the CPMG pulse sequence effectively eliminates a third possible form of relaxation, referred to as diffusion relaxation, which occurs when the hydrogen nuclei diffuse in the presence of an inhomogeneous magnetic field.

In a porous medium such as an aquifer, water is held in many pores with different pore sizes; thus the decay curve can be multi-exponential in form, resulting in a distribution of relaxation times (Figure 7-7). This distribution is commonly represented by the mean log $T_2$ value, $T_{2ML}$, which is considered representative of the mean pore size (Kenyon *et al*., 1988). The link between $T_2$ and the geometry of the pore space has led to

the use of borehole NMR $T_2$ measurements for estimating the properties of petroleum reservoirs such as pore-size distribution, irreducible saturation, and permeability (Seevers, 1966; Kenyon *et al*., 1988; Straley *et al*., 1995). In order to obtain estimates of permeability, measured NMR relaxation times have been used in the Kozeny-Carmen expression (Carman, 1956) along with empirically determined constants (Seevers, 1966; Kenyon *et al*., 1988).

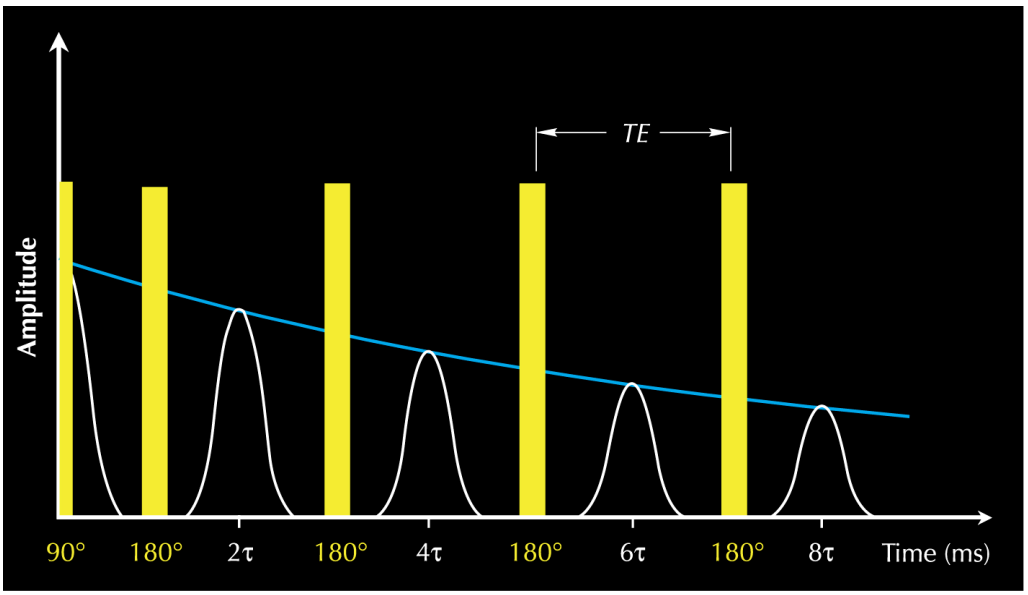



**Figure 7-6.** *CPMG pulse sequence used to generate a spin-echo train. CPMG pulse consists of a 90° pulse followed by a sequence of 180° pulses. Spin echoes of decreasing amplitude follow the 180° pulses. TE is the inter-echo spacing τ is time of the 90° pulse (modified from Coates et al., 1999).*

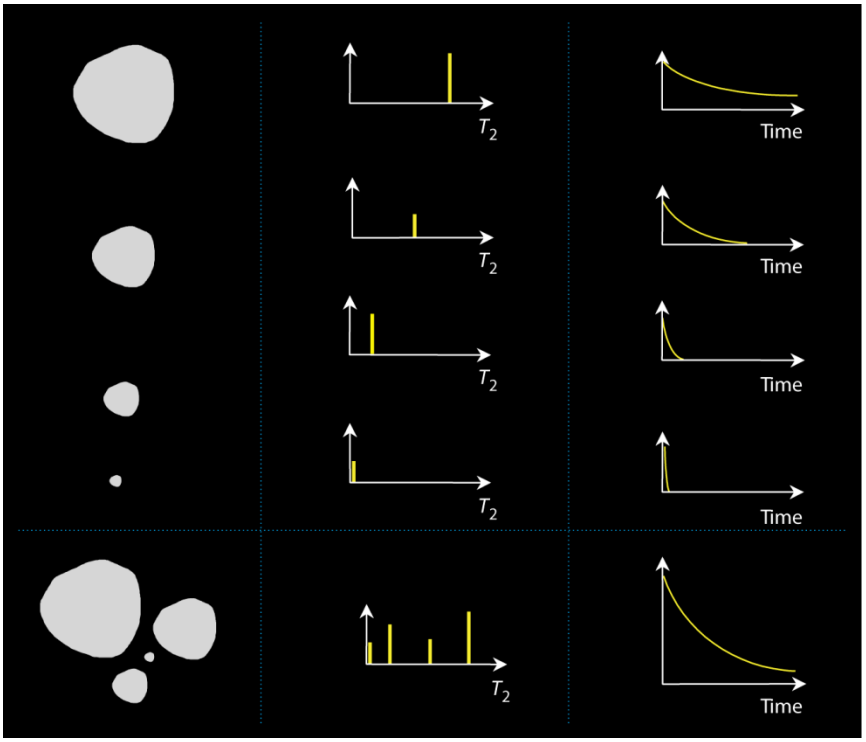



**Figure 7-7.** *Diagram of the impact of 100% water saturated pores on $T_2$. A single large pore (Upper left) with a single $T_2$ value (upper centre), and its spin-echo train exhibiting a single-exponential decay (upper right). Multiple pores (bottom left) have multiple $T_2$ values (bottom centre), and their composite spin-echo train with multi-exponential decay (bottom right). (Modified from Coates et al., 1999).*

### 7.3.4 NMR Field Acquisition Method

#### 7.3.4.1 *NMR equipment*

The Vista Clara Inc., Javelin tool was developed to fill a specific need for NMR borehole technology suitable for groundwater investigations (Walsh *et al*., 2010). This involved reducing the size of the probe and decreasing the cost and logistics required to field a system. Recent studies in Central Nebraska, USA have indicated that the Javelin compares well with traditional petroleum industry NMR tools, and allows collection of NMR data shallower then large petroleum industry NMR tools (Knight *et al*., 2012).

The Javelin logging system consists of probe, cable, tripod, winch, surface control unit, reference coil, and laptop (Figure 7-8). The probe is 8.9 cm in diameter and is 2.1 m in length. The Javelin tool samples a thin cylindrical shell with a thickness of ~2 mm and a length of ~50 cm, located a radial distance of ~19 cm from the centre of the tool (Vista Clara, 2011). The selection of the tool diameter and the depth of investigation are critical to ensure a measurement of the formation is obtained. In boreholes that were over drilled and subsequently cased and the annular space filled with another material (i.e. bentonite or sand-pack) and the will impact the measurement if the investigated shell is within the annulus of the borehole. Additional, if the hole is very rugose and there have been many washouts the measurements can also be negatively impacted. As the NMR tool measures a zone close to the annulus any disturbance or changing of the material may cause variations in the NMR measurements, this may include development for aquifer testing, compaction due to drilling and the introduction of drilling mud into the formations due to drilling.

Prior to the 2013 acquisition program, Vista Clara calibrated the probe in a water tank in a shielded room. The calibration is a linear process that sets the received voltage to a value when the tool is in 100% water. The calibration was provided with the Javelin upon shipment. To check the calibration in the field the field crew conducted experiments where the tool was submerged in a tank of water. While the data is noisy due to the tool being exposed to the eclectic fields above the surface of the earth the results indicated that the 290 kHz and the 245 kHz frequencies were recording 100% water ± 3%. With the 245 kHz on the lower end of an average of 97% water and the 290-kHz on the higher end with 103% water. When both frequencies were processed together the average was typically 100% water. Figure 7-9 is a screen capture of the combined 245 and 290-kHz processed data. Results from the water tank experiment indicated that the calibration was correct and that the tools response could be used to compare with the results of the 2011 BHMAR borehole NMR dataset.



**Figure 7-8.** *Vista Clara Javelin NMR logging system consisting of a probe, cable, winch, surface control unit, reference coil and laptop (from Vista Clara, 2011).*

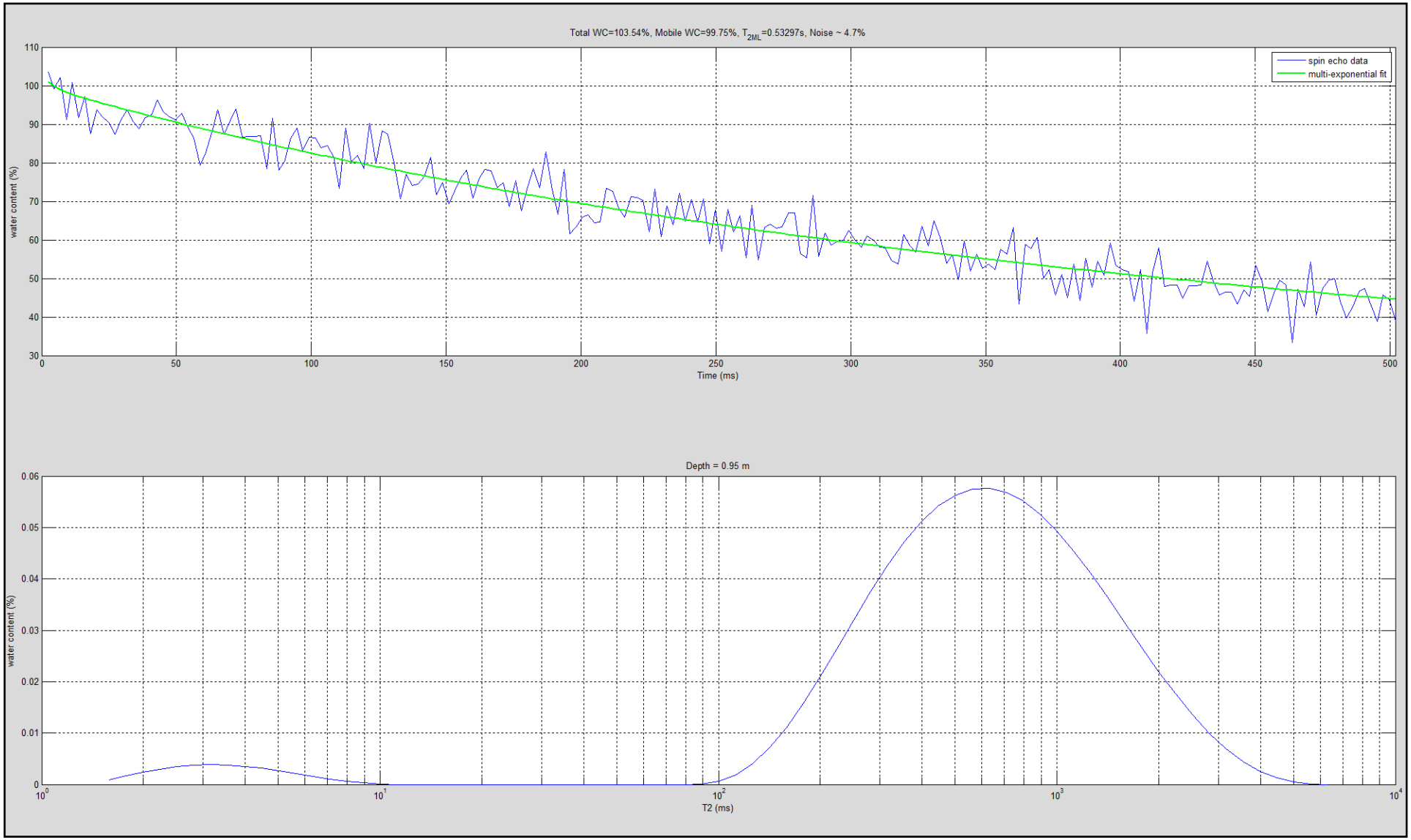



**Figure 7-9.** *Field NMR water tank experiment. This was conducted with the tool submerged in a tank of water and operated at 245 and 290 kHz. The upper plot is the CMPG decays and multi-exponential fit. The lower plot is the $T_2$ distribution. A regularization factor of 30 was used in the processing.*

7.3.4.2 ***NMR log acquisition***

*2011 NMR Acquisition Program*

From August 26 to October 9, 2011 NMR borehole data were acquired using the Javelin slim-hole logging system in 26 BHMAR sonic cored boreholes and three BHMAR mud rotary boreholes (Table 7-3). The NMR measurement interval was every 0.5 m from surface to depths of ~70 m. The generator, laptop, reference coil, surface control unit, winch and tripod were arranged on the surface near the borehole. One important feature of the Javelin system is the use of a remote reference coil. This reference coil allows the removal of environmental noise form the NMR measurements increasing signal to noise and allowing the system to be deployed in many "high noise" environments while also reducing the number of stacks required to collect quality data (Walsh *et al*., 2010). The probe was centralised over the well and the centre of the magnet is positioned at 1 m below natural ground surface. The after each measurement cycle the probe was lowered every half metre collecting measurements down the borehole length. Details of the instrument, setup, logging procedure and safety are described in Vista Clara (2011).

**Table *7-3.*** *NMR borehole data acquired in 2011 using the Javelin logging system for the BHMAR project including borehole, drilling method, logged interval, and data logged.*

| Borehole | Drilling method | NMR logged interval (meters) | Date logged |
|---|---|---|---|
| BHMAR3B-1 | Sonic coring | 2-60 | Sep 26, 2011 |
| BHMAR04-1 | Sonic coring | 2-70 | Sep 24, 2011 |
| BHMAR08-1 | Sonic coring | 1-59 | Aug 29, 2011 |
| BHMAR16-1 | Sonic coring | 2-60 | Sep 27, 2011 |
| BHMAR21-1 | Sonic coring | 2-80 | Sep 13, 2011 |
| BHMAR23-1 | Sonic coring | 2-95 | Sep 16, 2011 |
| BHMAR29-1 | Sonic coring | 2-60 | Sep 23, 2011 |
| BHMAR31-1 | Sonic coring | 2-60 | Sep 22, 2011 |
| BHMAR33-1 | Sonic coring | 2-64 | Aug 31, 2011 |
| BHMAR33-8 | Sonic coring | 14-53.5 | Sep 30, 2011 |
| BHMAR34-1 | Sonic coring | 2-60 | Sep 21, 2011 |
| BHMAR35-1 | Sonic coring | 2-54 | Sep 17, 2011 |
| BHMAR36-1 | Sonic coring | 15-85 | Oct 1, 2011 |
| BHMAR58-1 | Sonic coring | 2-75 | Sep 18, 2011 |
| BHMAR61-1 | Sonic coring | 2-70 | Sep 20, 2011 |
| BHMAR62-1 | Mud rotary | 15-65 | Sep 29, 2011 |
| BHMAR63-1 | Mud rotary | 5-45 | Oct 3, 2011 |
| BHMAR66-1 | Sonic coring | 17-62 | Oct 4, 2011 |
| BHMAR75-3 | Mud rotary | 1-89.5 | Aug 26, 2011 |
| BHMAR75-5 | Sonic coring | 2-52.5 | Sep 19, 2011 |
| BHMAR77-2 | Sonic coring | 2-65 | Oct 9, 2011 |
| BHMAR79A-6 | Sonic coring | 2-71 | Sep 15, 2011 |
| BHMAR80A-2 | Sonic coring | 2-65 | Sep 4, 2011 |
| BHMAR80B-2 | Sonic coring | 2-72 | Sep 6, 2011 |
| BHMAR83-2 | Sonic coring | 2-65 | Sep 9,2011 |
| BHMAR84-2 | Sonic coring | 2-59 | Sep 9, 2011 |
| BHMAR88-3 | Sonic coring | 2-71 | Sep 11, 2011 |
| BHMAR92-1 | Sonic coring | 2-70 | Sep 7, 2011 |
| BHMAR99-1 | Sonic coring | 2-63 | Sep 2, 2011 |

Prior to data acquisition, several acquisition settings need to be specified by the operator. NMR acquisition settings include probe ID, cable ID, operating mode, frequency, recovery time, echo train, echo spacing, number of averages, and probe quality factor, plus the typical depth settings required in any log. Details on these setting can be found in Vista Clara (2011). The acquisition settings in the BHMAR project NMR logging program are summarised in Table 7-4. Recovery time is a critical setting that controls the amount time between successive CPMG measurement scans. It should be set to a value longer than the NMR

longitudinal relaxation time $T_1$, which describes the time required for the longitudinal component of the decay recover to equilibrium following a single measurement (Figure 7-10). Using too short a value for the recovery time will lead to underestimation of water content and biasing results towards short $T_2$ decay times. Using to long of a recovery time will increase the acquisition time required to collect a complete NMR log of a borehole. In order to determine the appropriate recovery time for the BHMAR study several tests were made in many BHMAR boreholes to verify that recovery time was correctly set prior to completing a full NMR log while minimizing the recovery time setting to reduce the acquisition time. Field tests were also conducted to determine the number of averages that were required to obtain stable data. For these tests the Javelin was lowered to a set depth and was run with different averaging over several acquisition cycles. The tool was not moved during the acquisition of multiple measurement cycles and each cycle could be compared to determine if noise was causing instability in the NMR measurements. Several averaging values were evaluated with a value of 100 providing the most stable results while optimizing acquisition speed. For the BHMAR study the average hole took ~ 12 hours to log with the selected acquisition parameters.

**Table 7-4.** *Operator settings of the BHMAR project NMR logging program.*

| Operator setting | Value used in BHMAR logging |
|---|---|
| Probe ID | JP250G |
| Cable ID | 142 m |
| Operating mode | 245 kHz |
| Frequency | 253.703 kHz |
| Recovery time | 4-5* s |
| Echo train | 70 µs |
| Echo Spacing | 2.25 ms |
| Number of averages | 100 |
| Probe quality Factor | ~53 |

Note: Five second was used to log BHMAR 21-1, BHMAR 31-1, BHMAR 80A-2, and BHMAR 99-1.

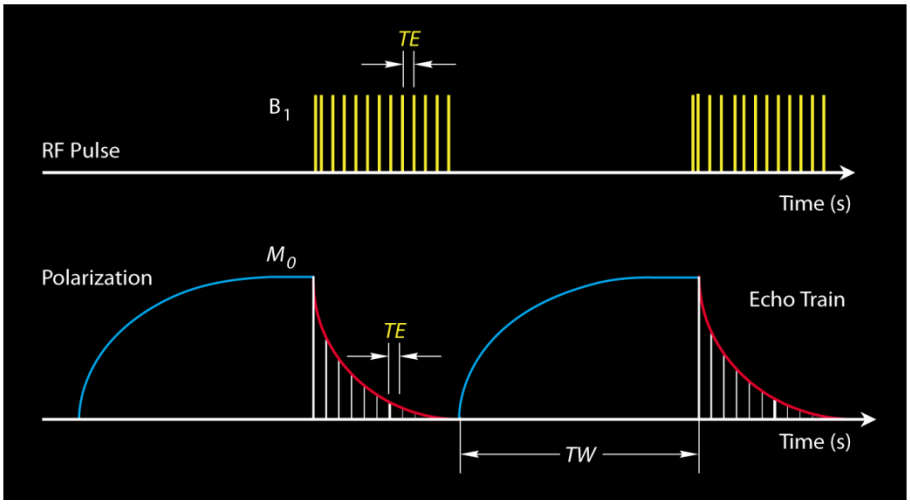



**Figure 7-10.** *NMR measurement timing diagram (top) CPMG pulse at the echo spacing TE sequences (yellow); and, (bottom) polarization longitudinal relaxation $T_1$ curves (blue) at the recovery time TW and the spin-echo-train (red) (modified from Coates et al., 1999).*

*2013 NMR Acquisition Program*

This 2013 NMR data acquisition study was instigated by technical review comments made by the USGS. The reviewers pointed to the low values for effective porosity and groundwater resource volumes as inconsistent with previously published results and contemporary understanding of the hydrogeological system. This prompted a laboratory analysis of many gravimetric samples from BHMAR sonic cores and analysis of selected Lexan-encapsulated cores for total and effective porosity. 10 bores were logged using the improved Javelin system at inter-echo spacing of mainly 0.0015 seconds and 0.00225 seconds for three bores (Table 7-5).

Initial indications were that NMR results underestimated both total and effective porosity. This provided a problem for the calculation of the groundwater resource volumes as the NMR was specifically used to sample the heterogeneous areas within the BHMAR study area. Through dialog with experts in the use of NMR, manufactures of NMR instruments, and academic researchers it was determined that the errors could be caused by a calibration error in the NMR instrument or by strong magnetic effects.

In order to address these concerns and assess the accuracy of the NMR data, an additional field program was undertaken in April 2013. This included re-logging key boreholes, collecting data at multiple frequencies and logging additional holes that had corresponding Lexan-encapsulated core. The purpose of the study was to determine if the NMR data was constant between years and to identify any calibration or magnetic effect that could be observed. If a calibration offset was determined and the data form 2011 and 2013 were consistent, an exhaustive analysis of the NMR data compared with the laboratory measurements of total porosity and effective porosity would be conducted.

**Table 7-5.** *NMR data acquired in April 2013 using the Javelin logging system for the BHMAR project. Borehole, inter-echo spacing, and logged interval are shown.*

| Borehole | Inter-echo Spacing (seconds) | NMR logged From (m) | NMR logged To (m) |
|---|---|---|---|
| BHMAR88-3 | 0.00150 | 10 | 71 |
| BHMAR66-1 | 0.00150 | 16 | 71 |
| BHMAR79A-6 | 0.00150 | 8.5 | 70.5 |
| BHMAR92-1 | 0.00150 | 9.5 | 76 |
| BHMAR3B-1 | 0.00150 | 12.5 | 73 |
| BHMAR77-2 | 0.00150 | 10.5 | 64 |
| BHMAR80A-2 | 0.00150 | 8 | 64 |
| BHMAR33-9 | 0.00150 and 0.00225 | 3 | 62 |
| BHMAR75-8 | 0.00150 and 0.00225 | 3 | 54 |
| BHMAR99-1 | 0.00150 and 0.00225 | 24 | 61 |

#### 7.3.4.3 ***NMR log processing***

*2011 NMR Processing*

After completion of the NMR log the Javelin data files were processed using the Javelin Log Processing program (Vista Clara, 2011). The log processing program is used to extract the spin echo signals, filtering and scale the echo signals, conduct the noise cancellation, remove impulse noise, and produce a data set that is input in to an interpretation program. The scaling of the echo signals is done through a calibration factor that is determined at the factory. The factor is determined by submersing the sonde into a 100% water bath and measuring the amplitude of the response at the tool operating frequency (Vista Clara, 2011). The linear calibration is simply the conversion: X nanovolts (nV) is equal to 100% water. This calibration value is used in the processing to scale the echo signals to the water content. The response of the tool is also verified with respect to the conductivity of water with no significant impact until the conductivity of the water is greater than 1 S/m (Vista Clara, 2011). To begin the processing of the NMR signals we first look at the CPMG decay (echo-time decays) curves. Figure 7-11 is an example CPMG decay curves versus depth for an entire log. The amplitude of the CPMG decay curve can be fit by a sum of decaying exponentials, each with a different decay constant. The collection of all the decay constants forms the $T_2$ distribution. In water-saturated rocks, the decay curve associated with a single pore will be a single exponential with a decay constant proportional to pore size. Thus, small pores have small $T_2$ values and large pores have large $T_2$ values (Brownstein & Tarr, 1979; Kenyon, 1992). An example of the multi-exponential fit to the time series CPMG decay curve and inversion result for a $T_2$ distribution at a single depth measurement are shown in Figure 7-11.

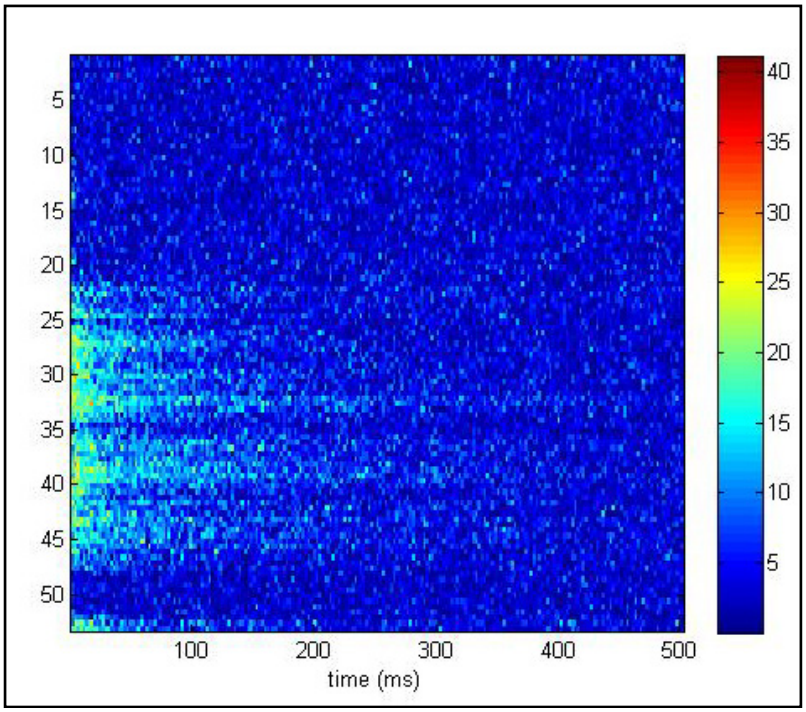



**Figure 7-11.** *CPMG decay curves versus depth for an entire log, shown as a colour map. The decay in amplitude from red at left (early time) to blue right (late time) reflects the CPMG relative amplitude (Vista Clara, 2011).*

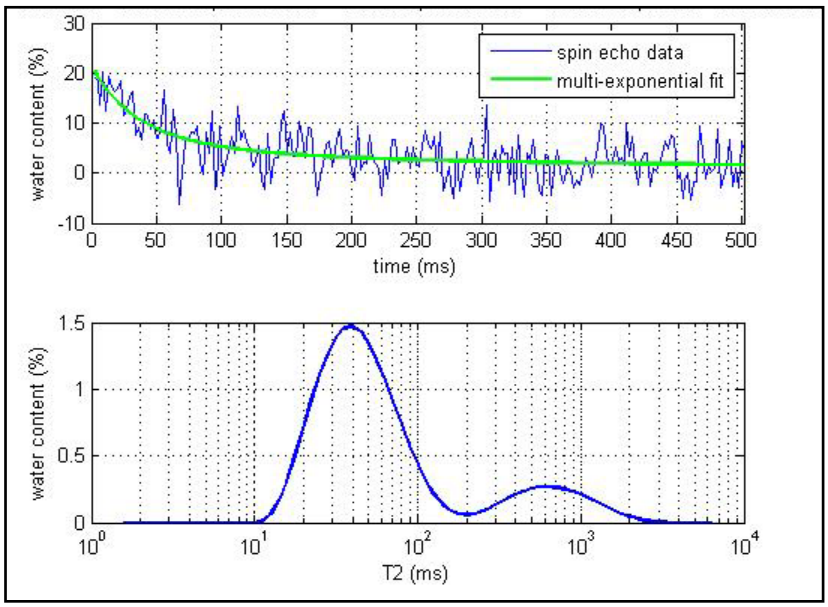



**Figure 7-12.** *Multi-exponential fit window of the time series CPMG decay curve and multi-exponential inversion result. The top panel shows the time series CPMG decay curve scaled to water content. The lower panel shows the $T_2$ distribution based on a multi-exponential fit to the decay curve (Vista Clara, 2011).*

2013 NMR Processing

Several changes have been implemented in the Vista Clara Javelin system between September 2011 and April 2013 (Walsh *et al*., 2010). Two of the changes that are important for processing of the data include: recording of two frequencies including 245,000 Hz (245 kHz) and 290,000 Hz (290 kHz) data sequentially; and the shortening of the inter-echo spacing to 0.0015 seconds (1.5 ms). There have been other hardware enhancements to the system that have no impact on the processing of the data (Vista Clara, personal communication April 30, 2013).

Vista Clara's interpretation software "Interpret Javelin Log version 1.1.0a" implements the above enhancements to the Javelin system within the current version of the software. The software takes the field processed Javelin files and implements an inversion of the Carr-Purcell-Meiboom-Gill (CPMG) pulse sequence (Carr & Purcell, 1954; Meiboom & Gill, 1958), decays to solve for a $T_2$ distribution (with user input for Vertical Depth "# Depth Intervals" and Regularization Factor). The derivation of the $T_2$ distribution allows the software to calculate total water, mobile water, capillary bound-water, and clay bound-water (based on user inputs for $T_2$ cutoffs), and hydraulic conductivity based on three formulations: Schlumberger-Doll Research Equation; the Sum of Squares Equation, and the Timur-Coates Equation (with user inputs for calibration coefficients and formula exponents). Details are explained in Vista Clara's software documentation manual (Vista Clara, 2013). The software outputs two ASCII text files, one with the $T_2$ distributions values and a second file with the calculated total water, mobile water, capillary water, bound water and the hydraulic conductive ($K$) from the three formulations included in the software. Table 7-6 summarizes the user input used in the processing of the BHMAR 2013 Javelin data.

**Table 7-6.** *User input parameters for the Interpret Javelin Log version 1.1.0a software.*

| User Input parameter | Values Used by XRI in processing the 2013 Javelin data |
|---|---|
| Vertical Averaging (# Depth Intervals) | 1 (equal to 0.5 m for this study) |
| Regularization Factor | 30 |
| K Estimators: C_SDR and N_SDR | Not Used |
| K Estimators: C_SOE | Not Used |
| K Estimators: C_TC and N_TC | Not Used |
| $T_2$ cutoff: Clay Bound (ms) | 3 |
| $T_2$ cutoff: Capillary Bound (ms) | 33 |

For the 2013 NMR data, noise was an observable dominant feature in the near surface data, i.e. 0-15 m depths. Through pertinent discussion with the field crew and Vista Clara it was determined that the source of the noise was radiated noise from the electrical generator used to power the system. Average noise on the data within the first 25 m was typically on the order of ~8% while deeper data exhibited an average noise characteristic of ~ 4%. Beginning with the logs collected on April 23, 2013 the generator was placed in a metal container that provided some shielding of the radiated noise from the generator. This resulted in bringing the average noise down to 6% in the upper 25 meters and ~3% in the lower sections. An additional line-conditioner system was placed in line with the generator on April 29, 2013 that brought the average noise figures down to ~5% in the upper 25 meters and ~2.5% in the lower sections. As a comparison the average noise figures from the 2011 data were ~ 3% for the entire dataset. It is important to note that the noise is not just caused by the generator, as low signal approaches the ambient noise floor, signal to noise goes down leading to potential impacts in the derived $T_2$ distributions and the calculated aquifer properties. An additional technique that can be used to reduce noise is to average over a larger depth interval. Several runs were completed on selected logs to determine if the averages were preserving the short $T_2$ distributions. For example, if the short decays are preserved and they are continuous over several depths, they are most likely to be signal rather than artefacts. When the data was examined without cross checking with data across the depth intervals, these short decays may appear to be noise. This was used as a basis for selecting the regularization that was used in the 2013 BHMAR borehole NMR dataset. A 1.5 or a 2.0 depth resolution was not an option for the BHMAR area. Thus, the full depth resolution 0.5 m data was used in the interpretations after the regularization was selected.

In some of the early logs from the 2013 BHMAR borehole NMR data, the field crew and Vista Clara noted some data that included decays around 3 sec. This is not feasible in a porous media and thus was identified by the staff of Vista Clara as receiver coil ringing when the coil became hot while running the 1.5 ms inter-echo spacing in the unsaturated zone (personal communication Vista Clara 2013). To avoid this problem the logs where run while moving the tool up from the bottom of the hole. This allowed the tool to be cooled in the saturated zone and water filled borehole. Not collecting logs in the unsaturated zone resulting in no

impact to the database as the derived aquifer property values assume 100% saturation. All data that contained the ringing was removed from the database prior to interpretation.

#### 7.3.4.4 *Selection of regularization factor used in the CPMG decay curve inversion for deriving a $T_2$ distribution*

The critical parameter for processing is the regularization factor that is used in the inversion of the CPMG decays to derive the $T_2$ distribution. A balance exists between over smoothing by using a high regularization factor and allowing noise into the inversion using too low a regularization factor. One large disadvantage that the software has is that only one regularization factor can be used for the complete inversion run. Within a log the noise changes from the top to the bottom of the hole and from within fine-grain and coarse-grain sediments. Hence too large a regularization factor in a fine-grained section can smooth out the short decays effectively blinding the inversion to the signal. Vice versa, using too low a regularization can allow the introduction of noise into the signal and adding decays that do not exist. High signal areas such as coarse-grained sediments, typical need low regularization as the decays are well defined. For the 2013 BHMAR borehole NMR data a series of inversions were run resulting in an optimized value of 30 being selected. This is also the default setting recommended by Vista Clara.

The processing of the CPMG decay curve data requires the selection of a regularization factor to be entered in to the Javelin Processing software. In order to determine an appropriate regularization factor the CPMG decay curve data need to be examined for noise and an evaluation of the impact of the regularization factor needs to be completed. It is important to note that the Vista Clara Javelin software utilizes a constant regularization factor for the complete NMR log. This process could be improved by allowing the software to select an appropriate regularization factor based on the noise in the data. This will need to be relegated to future work at this point as no software is in place to complete this processing.

As the NMR system passes through a zone that contains little water there is low signal strength, or no signal if there is an absence of water. When the water is contained in small pores the $T_2$ decay will be fast and may not be well resolved by the system due to the short decay times, as any decays shorter than the inter echo spacing will not be observable. Noisy data requires stronger regularization to suppress the impact of noise on the calculation of the $T_2$ distributions. Note the short decay curve in Figure 7-13a due to the small pores in the silt layer, and the high noise in most of the decay curve. Whereas in Figure 7-13b, the signal stays higher for longer with lower noise compared with Figure 7-13A. Using the current software a middle ground needs to be reached where the regularization suppresses the noise and the shape of the $T_2$ distributions is preserved.

To evaluate the best regularization factor for the BHMAR project, the regularization factor was manually set at (1, 3, 5, 10, 20 and 100) in the processing software for the NMR log of BHMAR58-1. Three sections of the BHMAR58-1 log were examined including: 32 m mud of the Blanchetown, 38 m muddy sand/fine to medium sand of the upper Calivil Formation, and 67 medium sand of the Calivil Formation). Examination of the changes in the $T_2$ distribution can provide insight into the impact of the regularization (Figure 7-14). The regularization factor's impact on the shape of the $T_2$ distribution is apparent with the increase in the factor; the distributions are reduced in magnitude and are smoothed. Examining the $T_2$ distribution is useful, but the impact on the calculation of the free-water, bound-water, and $T_{2ML}$ (using a $T_2$ cut-off of 33 ms discussed later) needs to be assessed. Figure 7-15 is a plot of the NMR derived free-water, bound-water and $T_{2ML}$ for the three zones in BHMAR58-1. With the regularization set too low, the inversion tends to fit the noise, and therefore the inversion fit in the $T_2$ distribution translates to high-frequency noise in the curves of free-water, bound-water and $T_{2ML}$. When the regularization is set too high the details are lost in the $T_2$ distributions and in the curves of free-water, bound-water and $T_{2ML}$.

From the understanding of the noise that is apparent in Figure 7-13, the obvious impacts of over regularization at factor values of 20 and 100 in Figure 7-14, and the minimal impact of the regularization on the free-water (Figure 7-15) a regulation of five was selected for processing the data from the BHMAR NMR dataset. This is a compromise selection in order to minimize the impact of the noise but also allowing the fundamental shape of the cures to be preserved.

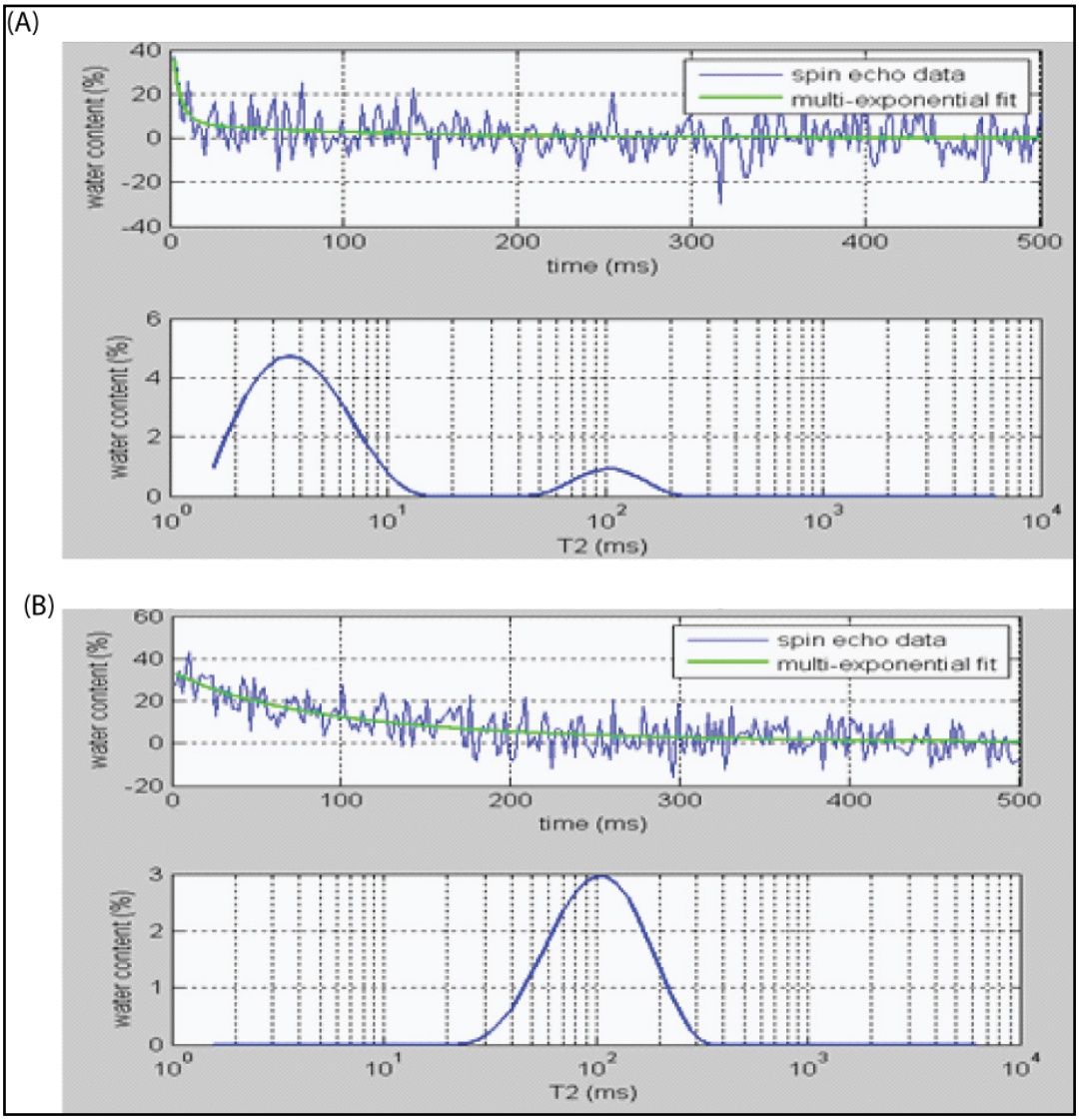



**Figure 7-13.** *(A) Top, CPMG decay curve (spin echo) data (blue) with the multi-exponential fit (green), and bottom the resulting $T_2$ distribution for a fine grained silt layer, and (B) Top, CPMG decay curve (spin echo) data (blue) with the multi-exponential fit (green), and bottom the resulting $T_2$ distribution for a coarse grained sand layer.*

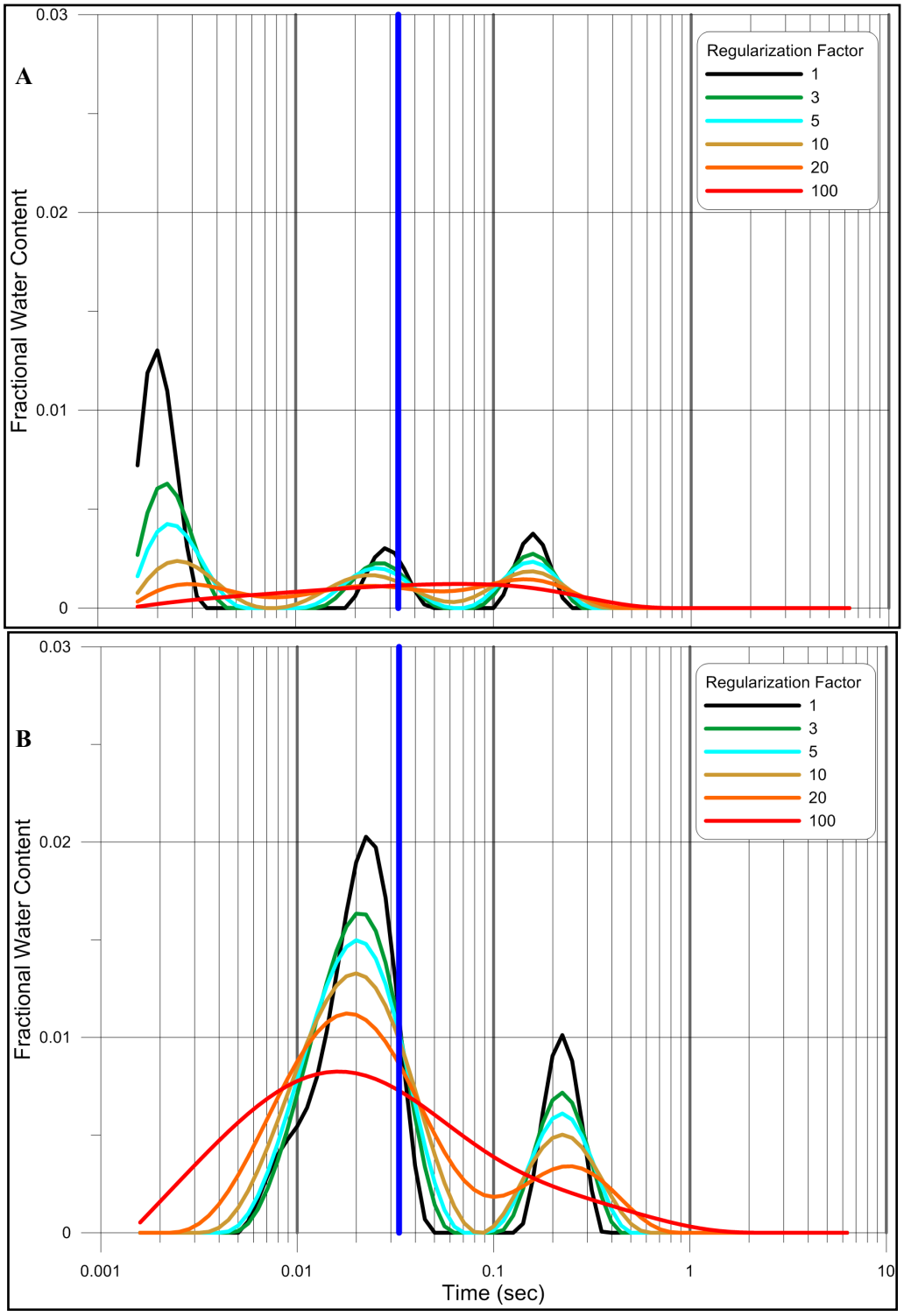



**Figure 7-14.** *$T_2$ distributions in BHMAR58-1 with the regulation factor varied (A) 32 m depth within the muds of the Blanchetown Clay, (B) 38 m depth within the sandy mud/fine sand in the upper Calivil Formation, and (C) 67 m depth within the medium sand of the Calivil Formation. $T_2$ cut-off of 0.033 seconds.*

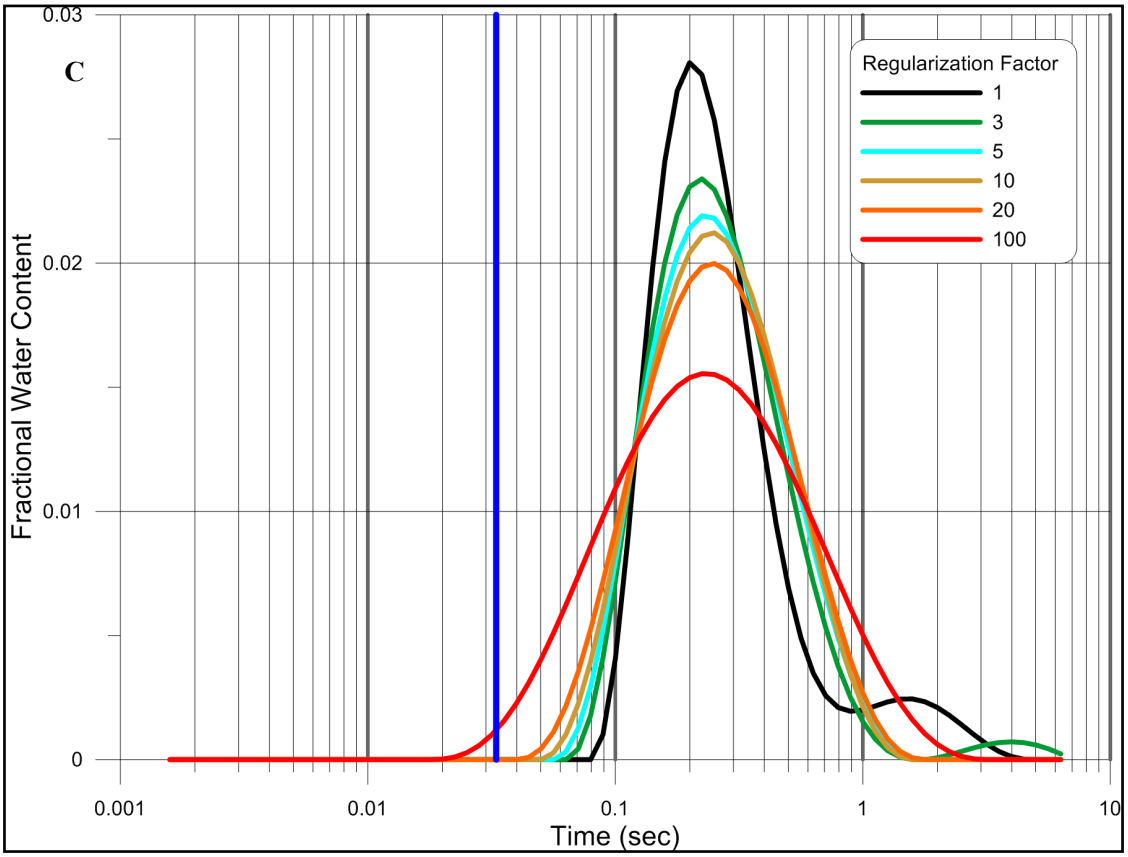



**Figure 7-14 cont.** *$T_2$ Distributions in BHMAR58-1 with the regulation factor varied (A) 32 m depth within the muds of the Blanchetown Clay, (B) 38 m depth within the sandy mud/fine sand in the upper Calivil Formation, and (C) 67 m depth within the medium sand of the Calivil Formation. $T_2$ cut-off of 0.033 seconds.*

The current (April 2013) version of the Javelin system allows for sequential frequency collection at 245 and 290 kHz. The "Interpret Javelin Log version 1.1.0a" software allows dual frequency data to be processed together. This is a powerful technique to reduce noise in the data and allow for improved sampling of the formation. One frequency samples a thin cylindrical shell around the borehole that is controlled by the gradient of the magnetic field created by the magnetics within the tool. At a specific distance the Larmor frequency is at the specified frequency of the measurement. Thus the 245 kHz measurements can penetrate deeper than the 290 kHz measurements. This allows an approximately ~1 cm thick shell ~19 cm from the centre of the tool (Vista Clara, 2013). The dual frequency can also be used to assess the impact of drilling fluid invasion of the on the borehole wall. Separate processing of the frequencies indicated that there was minimal impact of the drilling fluids on selected sections of the borehole. However, what was observed is some variability in the sediments within the averaging shell. This can be expected as if a larger grain is sitting within the shell at one frequency it may not be located within the shell of the next frequency. Therefore, the bulk effect should be to average the response over the 0.5 logging increment.

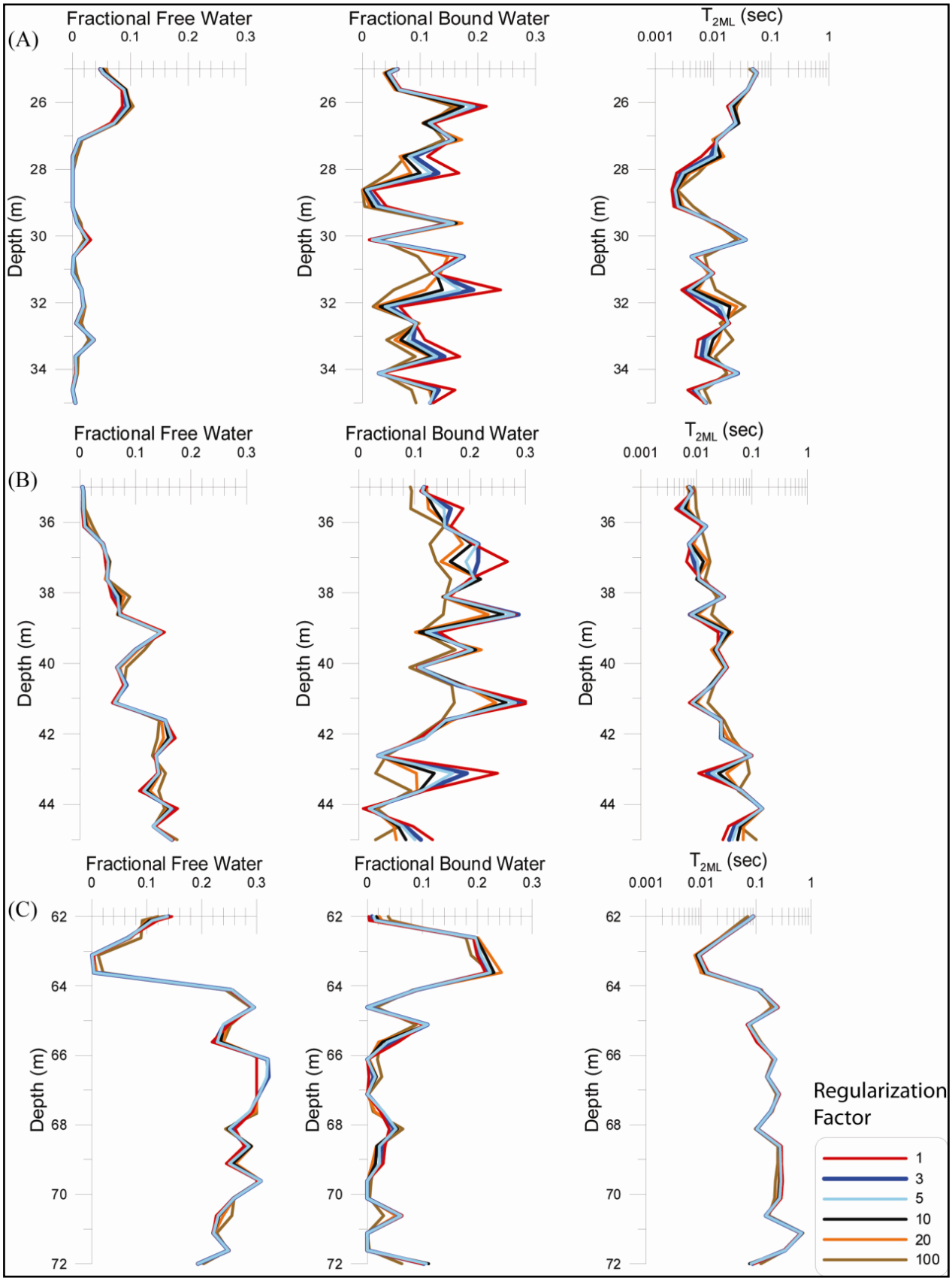



**Figure 7-15.** *BHMAR58-1 logging with the regulation factor varied (A) 25 to 35 m depth within the muds of the Blanchetown Clay, (B) 35 to 45 m depth within the muds, sandy mud, and fine sand in the upper Calivil Formation, and (C) 62 to 72 m depth within the medium sand of the Calivil Formation.*

### 7.3.4.5 *Calculating free-water and bound-water from $T_2$ distributions*

The next steps in processing involve converting the $T_2$ distributions into logs of bound-water, free-water and total water or total porosity. Down the log at every measurement depth the resulting $T_2$ distribution represents the distribution of pore sizes at that depth with every $T_2$ value corresponding to a pore size (Coates *et al*., 1999). The area under the $T_2$ distribution curve is equal to the initial amplitude of the decay and can be directly related to saturated porosity. This porosity and pore-size information from NMR measurements can be used to estimate both the hydraulic conductivity and the potentially effective porosity. Coates *et al*. (1999) uses the term 'free-fluid index' to represent the effective porosity. We use the term ‘free-water’ to represent the water-saturated effective porosity.

The estimate of free-water is based on the assumption that the moveable water is contained in large pores, and the bound-water is contained in small pores or is locked up as clay-bound-water. To estimate free-water, a $T_2$ value selected which corresponds to the point above which the water can be removed or drained from the larger pores (Figure 7-16, Figure 7-17). This $T_2$ value is called the $T_2$ cut-off (Coates *et al*., 1997; Timure, 1969). Coates *et al*. (1997) showed that $T_2$ cut-off values of 33 ms are appropriate for sandstones. The 33 ms $T_2$ cut-off is widely accepted as the standard for sandstone environments (Song, 2010). To improve this estimate a rigorous laboratory program would need to be performed on core samples to determine specifically the value for $T_2$ cut-off value for each lithological unit (Coates *et al*., 1999; Chen *et al.*, 1998). A $T_2$ cut-off value of 33 ms was used throughout the BHMAR study to calculate free and bound-water. Logs estimating bound, free, and total water can be then produced for all the logs within the BHMAR area.

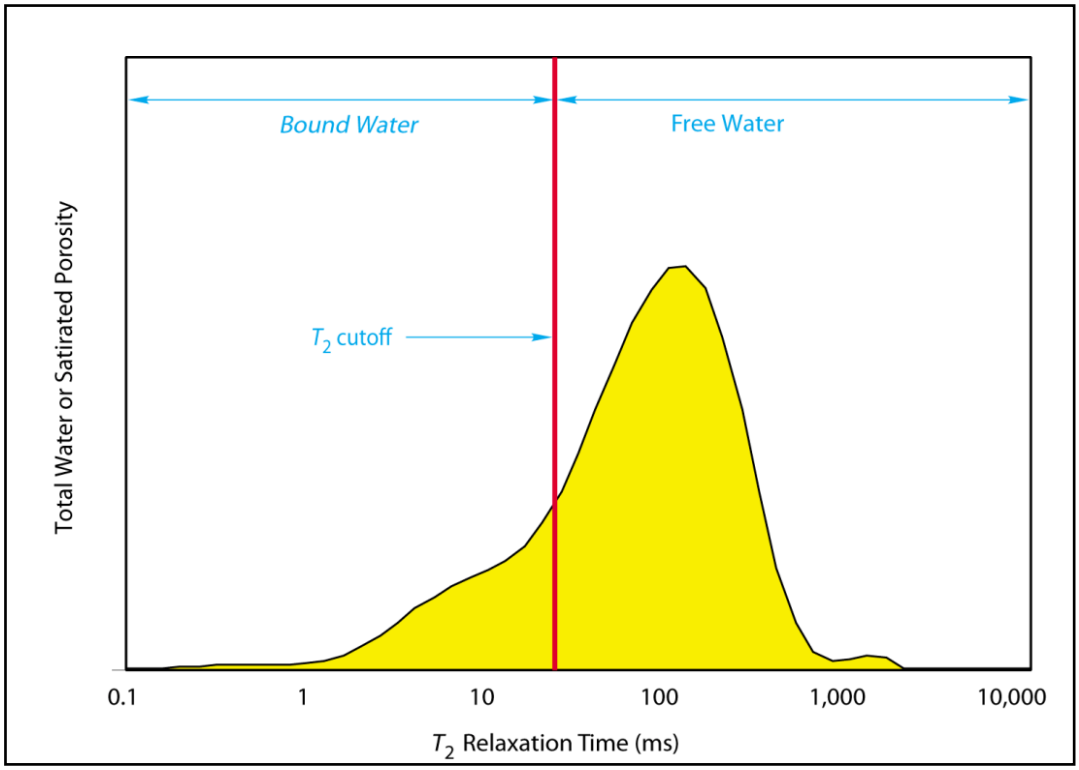



**Figure 7-16.** *The $T_2$ distribution composed of free and bound-water in a saturated aquifer. Because pore size is the primary controlling factor in establishing the amount of fluid that can movable, and because the $T_2$ spectrum is related to pore-size distribution, a fixed $T_2$ cut-off value relates to a pore size at and below which water will not move or is irreducible (modified from Coates et al., 1999).*

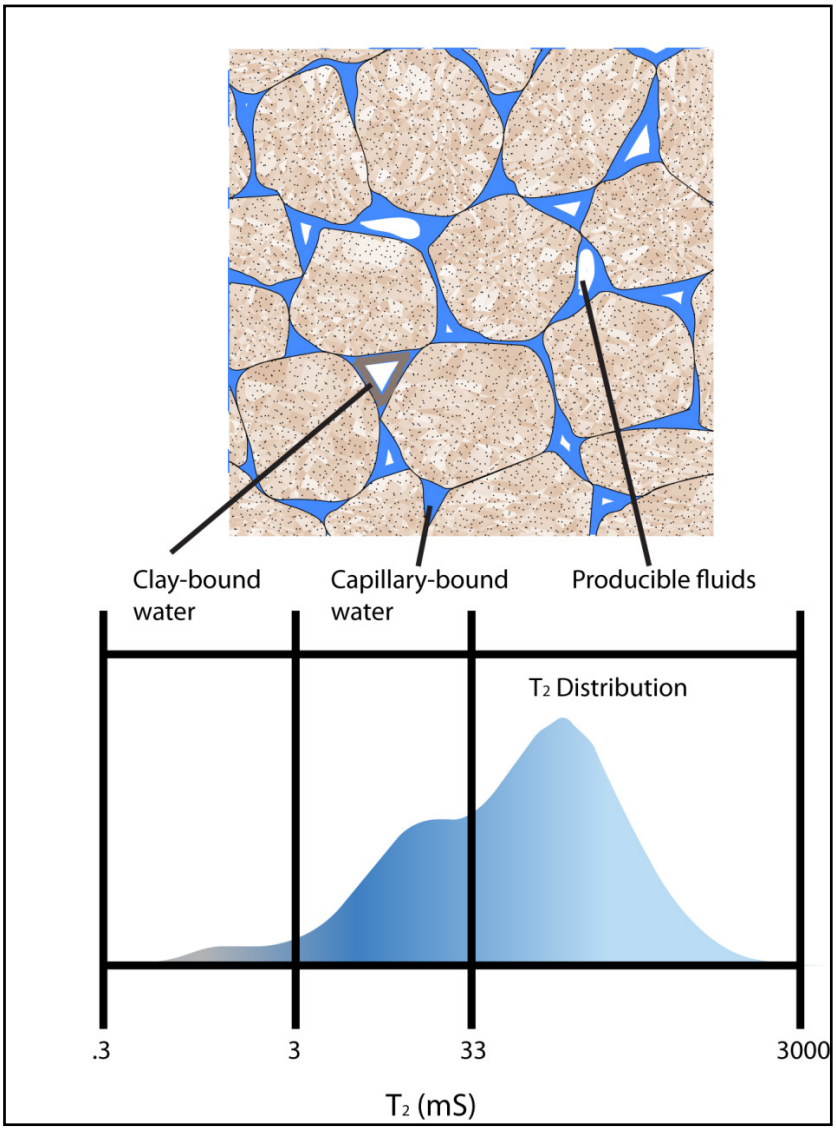



**Figure 7-17.** *Location of the water in the pores influencing the $T_2$ distribution. Producible fluids include free-water (white), in the larger pores. Free-water contributes to the longer $T_2$ time components. Capillary-bound-water (dark blue) is held against sand grains by surface tension and cannot be produced. Clay-bound-water (gray) is also non-producible. Shorter $T_2$ time components are from irreducible water that is closely bound to grain surfaces (Modified from Allan et al., 2000).*

#### 7.3.4.6 ***Discussion on the impact of changing the $T_2$ cut-off by 10%***

To evaluate the sensitivity of the $T_2$ cut-off, the $T_2$ cut-off was changed by 10% on either side of the standard published 33 ms for sandstone from 30 to 36 ms. Note that the total water will not change as the total calibrated area under the $T_2$ curve is equal to the total water. BHMAR58-1 was selected to analyse the impact of the $T_2$ cut-off. Figure 7-18 is a plot of the total water and bound-water calculated with 30, 33 and 36 ms. The test exhibits that the sensitivity of the $T_2$ cut-off within 10% of the accepted value of 33 ms is very small. In the worst case the values in the saturated aquifer within the Calivil Formation show only a range of fractional effective porosity or free-water of 0.18 to 0.22.

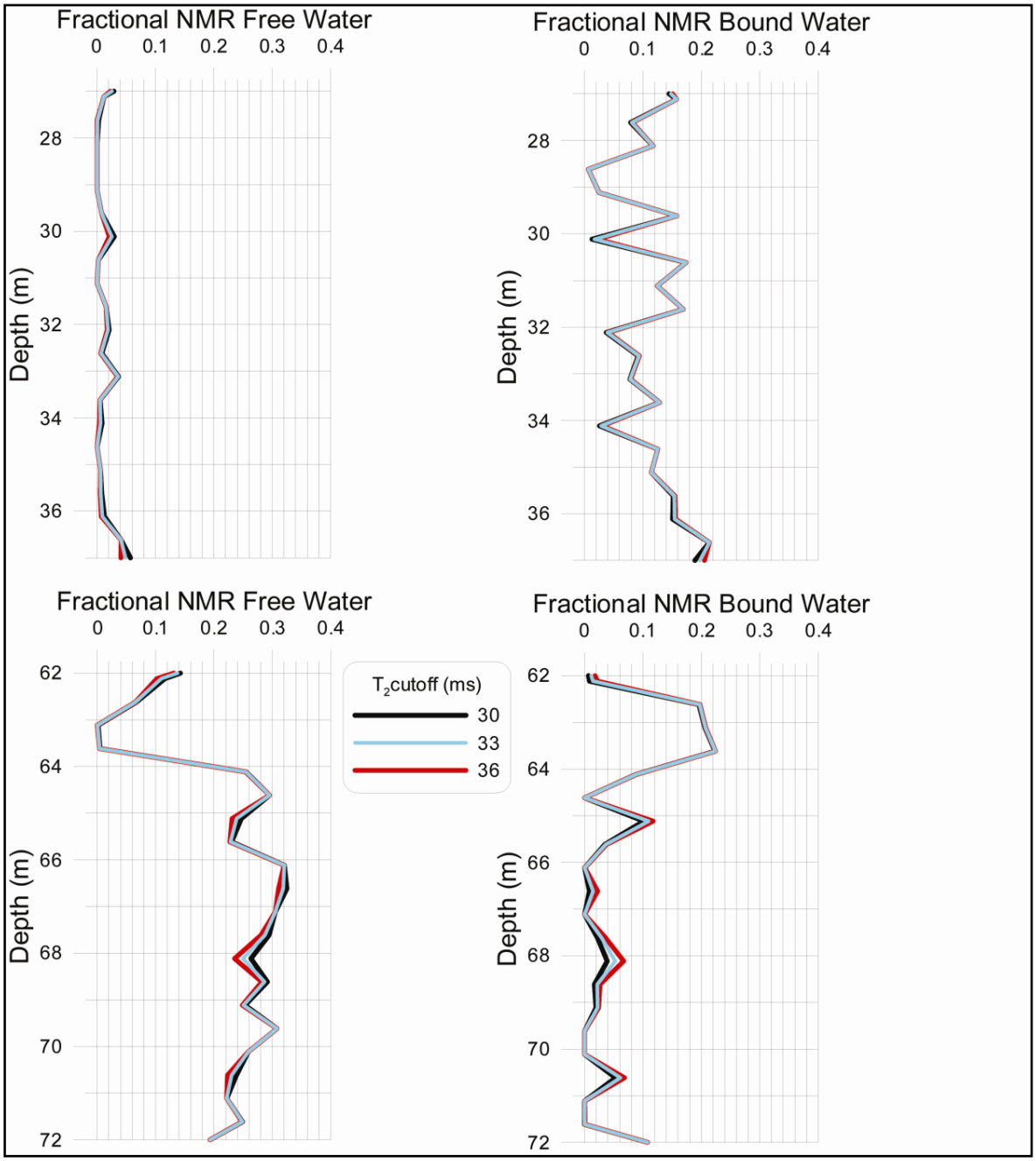



**Figure 7-18.** *Fractional NMR free-water (left) and fractional bound-water (right) for two depth intervals in BHMAR58-1. Plots illustrate the variations in values using a $T_2$ cut-off that is 10% on either side of the 33 ms used throughout the study.*

### 7.3.4.7 *Comparison of 2011 and 2013 Borehole NMR Data*

The 2011 borehole NMR data was compared to the 2013 borehole NMR data by using a depth by depth comparison. One of the first observations made of the BHMAR99-1 was an obvious +1.0 meter offset between the 2011 and 2013 data based in the shape of the curves (Figure 7-19). An inspection of BHMAR80A-2 also suggested a +1.0 offset between the 2011 and the 2013 data. At that point an examination of the depth offset in the 2011 data was conducted and it was determined that there was a +1.0 offset in several of the borehole collected in 2011. The data that were corrected for the incorrect offset included: BHMAR08-1, BHMAR33-1, BHMAR75-3, BHMAR80A-2, and BHMAR99-1.

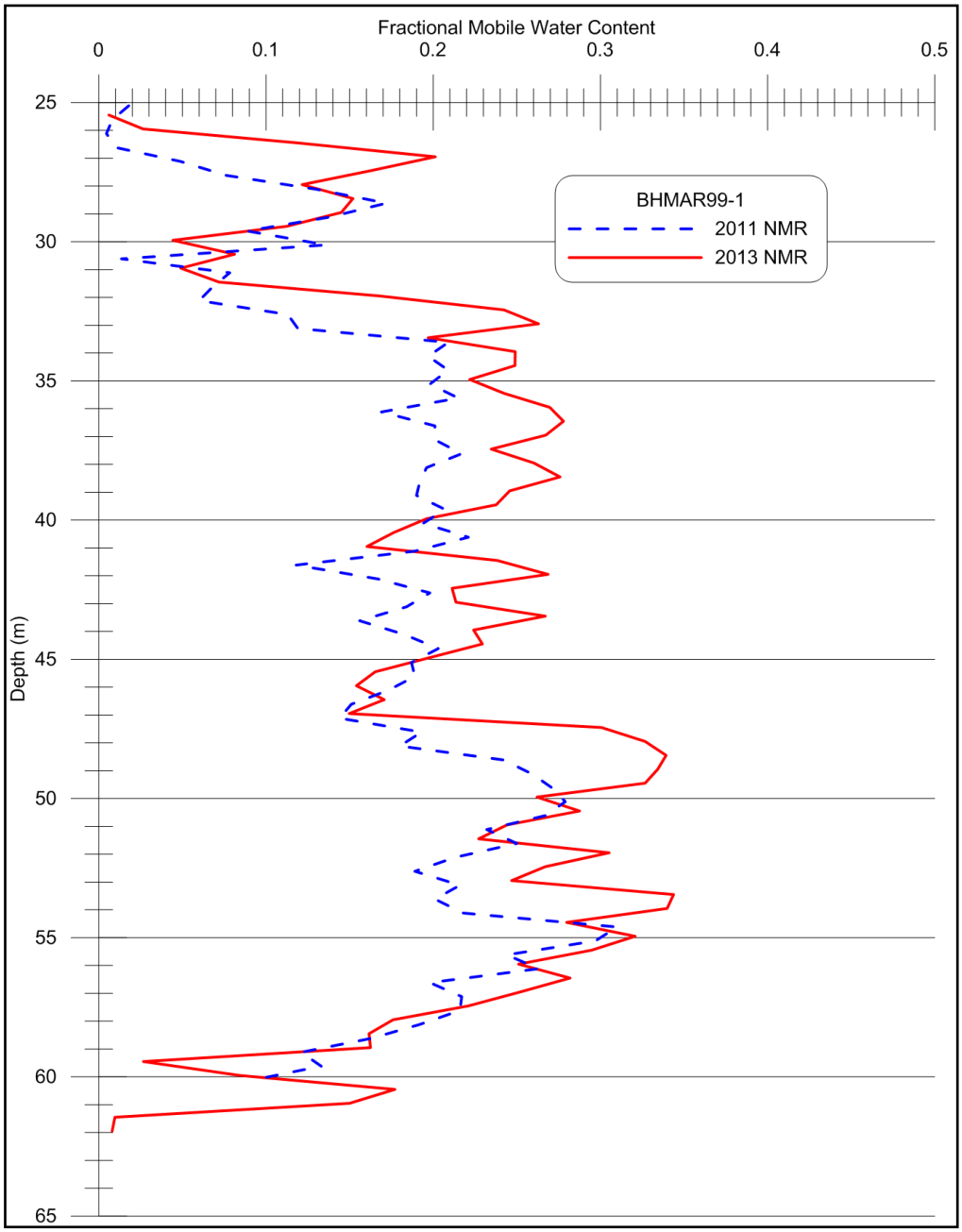



**Figure 7-19.** *BHMAR99-1 2011 (blue dashed line) and 2013 (red solid line) mobile water plots with depth. A depth and magnitude offset is observed between the two datasets.*

Examining section of the data shown in Figure 7-19, it is apparent there is an offset in the magnitude of the curves between 2013 and 2011. This could be caused by a set of systematic problems including but not limited: to 1) calibration errors in 2011 or 2013; 2) a different $T_2$ cutoff used in the calculation of the mobile water; 3) differences in processing; 4) changes in the Javelin settings; or 5) geological changes within the borehole. In assessing the cause, the following points were noted:

- The possible cause is calibration in 2011 as 2013 data were checked in the field by conducting a tank test in 100% water.
- The same $T_2$ cutoff was used for both data sets so that is not the issue.
- The data were reprocessed using the same version of software and settings and the results were the same.

- The data sets with the inter-echo spacing and frequency were identical and the same amplitude offset was observed.
- There was no geological, chemical, or hydrogeological reason for a chance in the borehole conditions that would allow an increase in the mobile water.

The calibration error in the 2011 data was determined to be the cause of the amplitude offset. To verify that conclusion a few boreholes would need to be examined. BHMAR80A-2 and BHMAR77-2 were also examined for amplitude offset in the total, mobile and bound water. Similar offsets were observed in each of the boreholes. Assuming that the error is solely an issue in calibration the solution should be a linear bias to all the water content data. To determine the offset a segments of the total water NMR log through coarse-grained sediments were selected from BHMAR99-1, BHMAR80A-2, and BHMAR77-2. This was done to remove any issue related to noise from short $T_2$ decays and the total water was used as it will not be impacted by the $T_2$ cutoff selection. A simple ratio was calculated and a scale factor was applied to provide the best fit between the 2013 data and the 2011 data times a scale factor. It was determined that the best-fit scale factor was x 1.20 (Table 7-7).

**Table 7-7.** *Scaling factor applied to 2011 NMR data to make it comparable to 2013 data.*

| Borehole | Scaling Factor (x2011) |
|---|---|
| BHMAR99-1 | 1.21 |
| BHMAR80A-2 | 1.18 |
| BHMAR77-2 | 1.2 |

After applying the scaling factor to the 2011 total water, mobile water and bound water a more consistent correlation of the 2011 and 2013 data was achieved (Figure 7-20 and Figure 7-21). With any of these point-by-point comparisons it is important to note that noise changes over time and there are always differences in measurement depths. In Figure 7-20 to Figure 7-22 there are areas in the curves that are over corrected in the 2013 data and areas that are under corrected in the 2013 data. This is consequence of a best-fit calculated for the scaling factor. At this point Vista Clara was contacted as to why there would be a calibration offset in the 2011 data. They indicated that after the system left the Vista Clara for Australia in 2011 it was repackaged in a different housing prior to the logging at BHMAR. While they indicated that this would not necessitate a recalibration of the Javelin, a recalibration was not conducted after the repackaging and could be the source of the observed offset (personal communication Vista Clara, 2013). To test the scaling offset is consistent BHMAR92-1 was tested independently from the three holes to confirm the observed offset. The comparison between BHMAR92-1 from 2013 with the corrected 2011 was also successful. At this point the corrections were applied to all of the total water, mobile water, and bound water data from 2011.

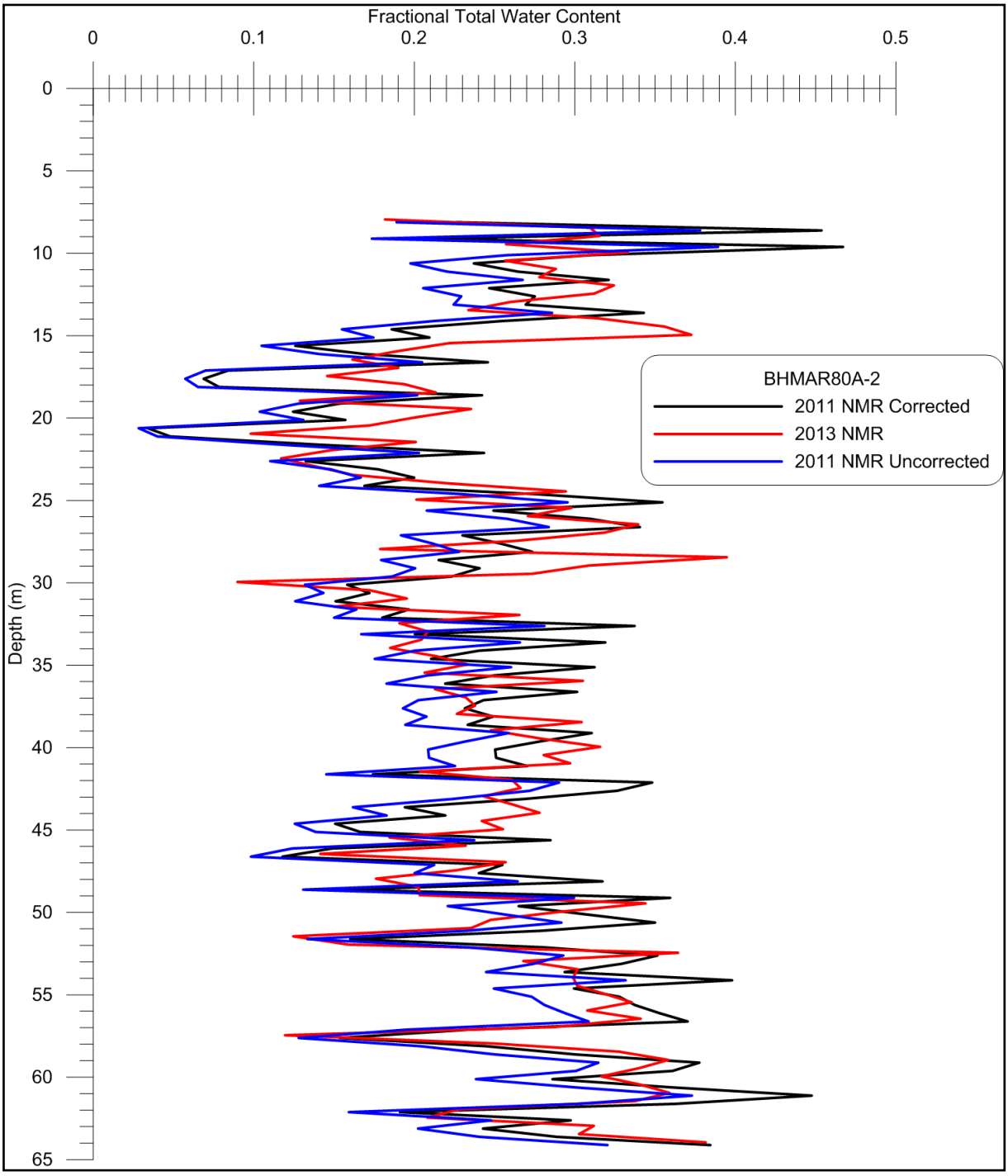



**Figure 7-20.** *Comparison between corrected 2012 total water (black line), 2013 total water (red line) and uncorrected 2011 total water (blue line) for BHMAR80A-2.*

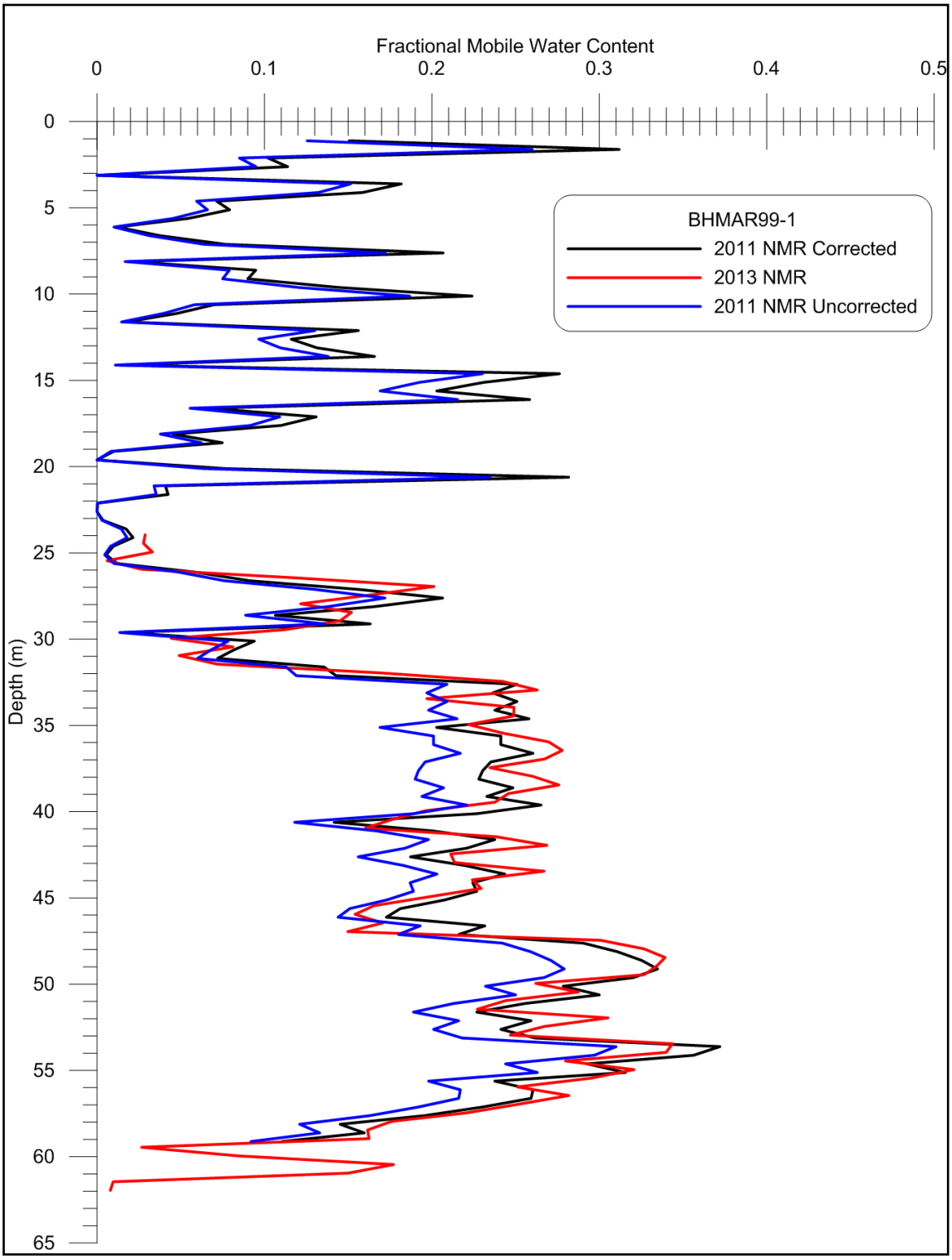



**Figure 7-21.** *Comparison between corrected 2011 mobile water (black line), 2013 mobile water (red line) and uncorrected 2011 mobile water (blue line) for BHMAR99-1.*

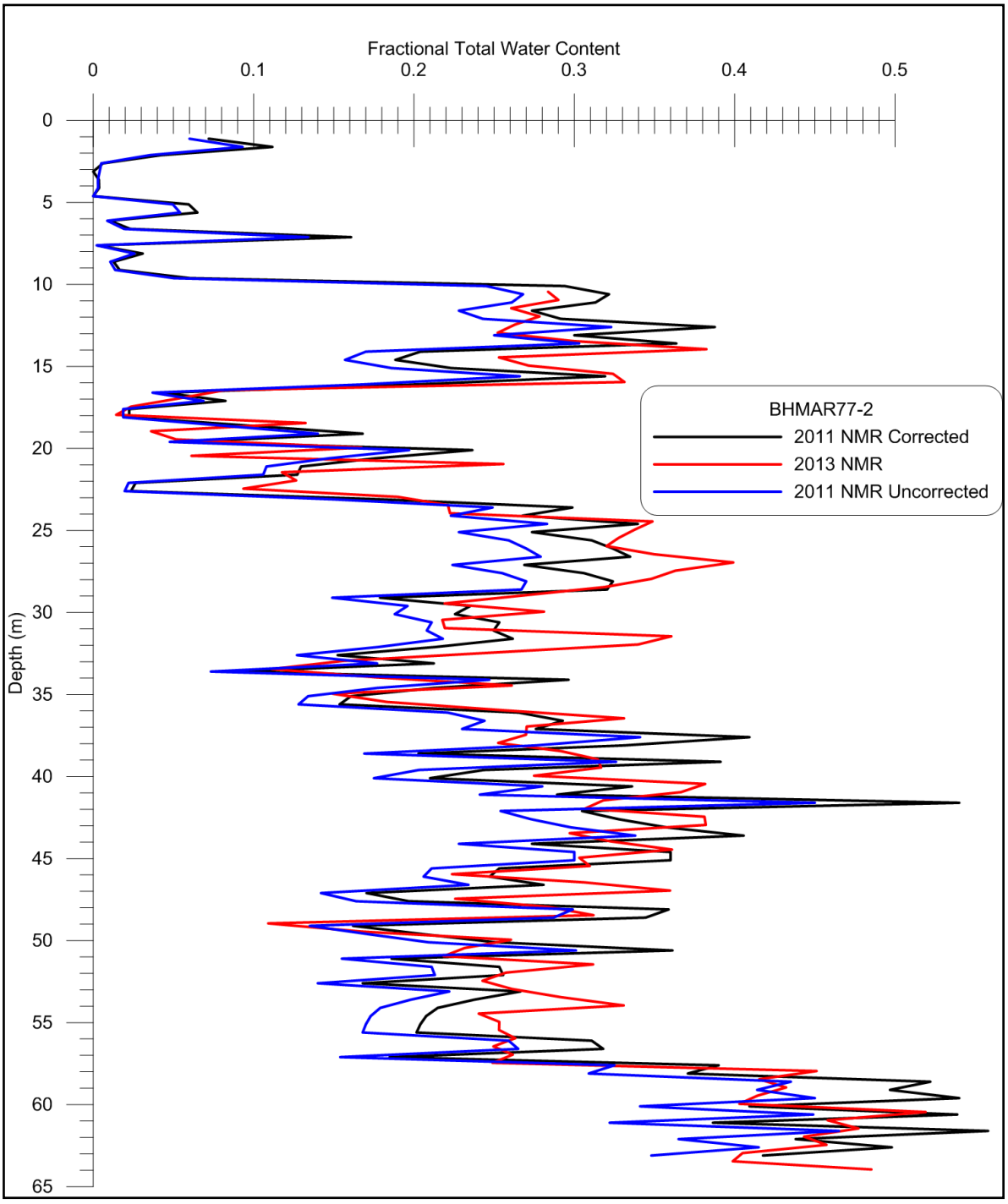



**Figure 7-22.** *Comparison between corrected 2011 total water (black line), 2013 total water (red line) and uncorrected 2011 total water (blue line) for BHMAR77-2.*

### 7.3.5 NMR Derived Hydraulic Conductivity

NMR properties of aquifers are dependent on porosity, pore size, pore-fluid properties and mineralogy. NMR estimates of hydraulic conductivity are based on theoretical models that show that hydraulic conductivity increases with both increasing porosity and increasing pore size. There are two basic types of hydraulic conductivity models that have been developed. The free-fluid or Timure-Coates model and the average $T_2$ or Schlumberger-Doll Research Equation (SDR) model (Timure, 1969; Kenyon *et al.,* 1988; Coates *et al*., 1997). The Timure-Coates formulation relies on the relationship of free-water/bound-water. This relationship can become unstable when bound-water is very low for example dry clays detected in the BHMAR Project area. For this reason the SDR Equation was utilized in the BHMAR study.

For the BHMAR study, the SDR Equation (Equation 79) was used to estimate hydraulic conductivity $K_{SDR}$ where $\varphi$ is the NMR total porosity, $m$ is related to the cementation (an exponent of 2 was used in the BHMAR study), $T_{2ML}$ is the logarithmic mean of the $T_2$ distributions, and $C$ is a formation coefficient that depends on the formation type and is related to tortuosity.

$$K_{SDR} = C\,\varphi^2\,(T_{2ML})^2$$

**Equation 79**

Variations in $C$ have been found with different lithology, so a lithologically based $C$ should be determinable if lithology is known. The petroleum industry has spent many resources on the determination of a proper $C$ (Straley *et al*., 1995; Kleinberg *et al.,* 2003; Kenyon *et al*., 1995; Alvarado *et al*., 2003; Daigle & Dugan, 2009). However, even within a formation of uniform lithology, variations in mineralogy, cementation, and magnetic coatings content will affect hydraulic conductivity, and this will not be accounted for with a constant value of $C$.

Prior to the calculation of the NMR derived hydraulic conductivity for the BHMAR data the NMR borehole data were classified into five hydraulic classes. This was done by classifying the NMR data per acquisition interval using the sonic core logs lithological descriptions, laboratory grain size distribution, the electrical induction logs, the natural gamma borehole logs, hyperspectral logs, and mineralogical analysis (as described in Section 11).

Based on permeameter tests (as described in other sections of this report) on selected core samples (Table 7-8), an average hydraulic conductivity $K_{ave}$ was assigned to each of the hydraulic class. Using the SDR Equation, $C$ was calculated from the $K_{ave}$ for each hydraulic class. The average $C$ value $C_{ave}$ for each hydraulic texture class was then calculated and is assumed to represent the overall $C$ for each of the hydraulic classes (Table 7-9).

**Table 7-8.** *Permeameter results from preserved sonic core samples.*

| Borehole | Depth (m) | Hydraulic class | K min (m/d) | K ave (m/d) | K max (m/d) |
|---|---|---|---|---|---|
| **BHMAR8-1** | 11.25 | Mud | $3.46 \times 10^{-6}$ | $4.32 \times 10^{-6}$ | $6.91 \times 10^{-6}$ |
| **BHMAR8-1** | 12.25 | Mud | | $8.64 \times 10^{-8}$ | |
| **BHMAR8-1** | 20 | Mud | $8.64 \times 10^{-8}$ | $8.64 \times 10^{-7}$ | |
| **BHMAR8-1** | 23.5 | Mud | | $8.64 \times 10^{-8}$ | |
| **BHMAR33-9** | 17 | Coarse to very coarse sand | 0.864 | 0.864 | 0.864 |
| **BHMAR 33-9** | 20.5 | Mud | | $8.64 \times 10^{-8}$ | |
| **BHMAR 33-9** | 29 | Fine sand | 0.432 | 0.518 | 0.518 |
| **BHMAR 33-9** | 32.7 | Mud | $3.46 \times 10^{-6}$ | $4.32 \times 10^{-6}$ | $5.18 \times 10^{-6}$ |
| **BHMAR 33-9** | 40.5 | Coarse to very coarse sand | 0.0605 | 0.0691 | 0.0691 |
| **BHMAR 33-9** | 50 | Coarse to very coarse sand | $4.32 \times 10^{-5}$ | $8.64 \times 10^{-5}$ | $8.64 \times 10^{-2}$ |
| **BHMAR 33-9** | 55 | Coarse to very coarse sand | >0.864 | | |
| **BHMAR 75-8** | 25 | Mud | | $8.64 \times 10^{-8}$ | |
| **BHMAR 75-8** | 33 | Medium sand | $7.78 \times 10^{-5}$ | $8.64 \times 10^{-5}$ | $8.64 \times 10^{-5}$ |
| **BHMAR 75-8** | 38.5 | Silty very fine sand | | $1.73 \times 10^{-5}$ | |
| **BHMAR 75-8** | 43 | Coarse to very coarse sand | 0.0864 | 0.173 | 0.173 |
| **BHMAR 75-8** | 49.5 | Coarse to very coarse sand | 0.778 | 0.864 | 0.864 |
| **BHMAR 80B-2** | 15.25 | Mud | $1.73 \times 10^{-6}$ | $5.18 \times 10^{-6}$ | $7.78 \times 10^{-6}$ |
| **BHMAR 80B-2** | 17.3 | Mud | $8.64 \times 10^{-6}$ | $8.64 \times 10^{-6}$ | $1.73 \times 10^{-5}$ |
| **BHMAR 80B-2** | 19.75 | Mud | $8.64 \times 10^{-7}$ | $7.78 \times 10^{-6}$ | $8.64 \times 10^{-6}$ |

Note: Laboratory results were reported in m/s and have been converted to m/day.

**Table 7-9.** *Initial $K_{ave}$ and $C_{ave}$ values for the hydraulic texture classes.*

| Hydraulic texture class | $K_{ave}$ (m/d) | $C_{ave}$ |
|---|---|---|
| Mud | $1 \times 10^{-6}$ | 20 |
| Silty very fine sand | $1 \times 10^{-5}$ | 300 |
| Fine sand | 0.1 | 66000 |
| Medium sand | 0.5 | 67000 |
| Coarse to very coarse sand | 3 | 46000 |

In selected zones of the BHMAR boreholes aquifer parameters were derived with both pumping and slug tests. From the slug test interval a $K_{slug}$ and a transmissivity $T_{slug}$ were derived using the pumping tests as an independent check (see Sections 13.2 and 13.3). These results can be used as a control to check the $C_{ave}$ values derived from the permeameter tests as applied to the SDR Equation (Nielsen *et al*., 2011; Abraham *et al*., 2011b; Dlubac *et al*., 2011). Table 7-10 summarizes the zones where aquifer tests were completed and if the slug test were coincident (in the same borehole) or adjacent (within 3 m) of the NMR log. The mud rotary boreholes were removed from the data set due to the concern that the mud invasion was at the same depth as the sensitivity zone of the Javelin used in the BHMAR study. Further discussion on the impact of drilling can be found below.

**Table 7-10.** *BHMAR boreholes and NMR data location either coincident or adjacent to slug test location and the slug test results summarized for the zone that test results overlap with NMR logs.*

| Borehole | NMR log location | Slug test interval (m) | KSlug (m/day) | TSlug ($m^2$/day) |
|---|---|---|---|---|
| **BHMAR03B-2** | Coincident | 37-55 | 20 | 369 |
| **BHMAR04-1** | Coincident | 90-102 | 5.5 | 66 |
| **BHMAR04-3** | Adjacent | 8-14 | 7.5 | 45 |
| **BHMAR08-1** | Coincident | 42-46 | 17 | 65 |
| **BHMAR16-1** | Coincident | 12-52 | 2.9 | 118 |
| **BHMAR21-1** | Coincident | 20-74 | 2.6 | 140 |
| **BHMAR21-2** | Adjacent | 10.5-13.5 | 9.3 | 30 |
| **BHMAR21-3** | Adjacent | 32-56 | 1.8 | 44 |
| **BHMAR23-2** | Adjacent | 29-47 | 0.62 | 11 |
| **BHMAR23-3** | Adjacent | 13-24 | 32 | 343 |
| **BHMAR29-1** | Coincident | 17-53 | 7.7 | 277 |
| **BHMAR31-1** | Coincident | 11-51 | 5.4 | 217 |
| **BHMAR33-8** | Coincident | 46-52 | 4.6 | 27 |
| **BHMAR34-1** | Coincident | 27-51 | 10.4 | 250 |
| **BHMAR35-1** | Coincident | 16-46 | 0.6 | 18 |
| **BHMAR58-1** | Coincident | 63-69 | 6.7 | 40 |
| **BHMAR61-3** | Adjacent | 33-39 | 1 | 10 |
| **BHMAR66-1** | Coincident | 30-60 | 6.8 | 203 |
| **BHMAR75-5** | Coincident | 40-52 | 51 | 609 |
| **BHMAR77-2** | Coincident | 47-55 | 26 | 211 |
| **BHMAR79A-6** | Coincident | 38-50 | 26 | 317 |
| **BHMAR80A-2** | Coincident | 35-53 | 21 | 372 |
| **BHMAR80B-2** | Coincident | 53-65 | 14 | 168 |
| **BHMAR84-2** | Coincident | 45-51 | 0.39 | 2.4 |
| **BHMAR88-3** | Coincident | 65-71 | 2 | 12 |
| **BHMAR92-1** | Coincident | 32-62 | 7.6 | 229 |
| **BHMAR99-1** | Coincident | 33-57 | 11.6 | 278 |

To validate $C_{ave}$ (Table 7-9), the $T_{slug}$ results were compared to the $T_{SDR}$ results. The $T_{SDR}$ was calculated by taking the sum of the $K_{NMR}$ over the screen interval of the slug test:

$$T_{SDR} = \frac{B}{n}\sum_{i=1}^{n} C_i \phi_i^2 T_{2,i}^2$$

**Equation 80**

or

$$T_{SDR} = \frac{B}{n}\sum_{i=1}^{n} K_{SDR,i}$$

**Equation 81**

where $B$ is the thickness of the screen interval and n is the NMR logged interval. Initially, $T_{SDR}$ versus $T_{slug}$ were plotted against each other using a constant $C$ value of 46,000 (Figure 7-23). There is substantial scatter in the plot. A likely cause of this scatter may be the difference in lithology and not breaking down the solution of $C$ by hydraulic classes as noted above. The next step was to use $C_{ave}$ values from the permeameter measurements (Table 7-8) and solve for a linear least squares fit for each of the hydraulic classes. Figure 7-24, a plot of $T_{SDR}$ versus $T_{slug}$ after applying the $C_{ave}$, indicates that a majority of the data are within one order of magnitude from the 1:1 relation line for $T$. However, three data points are still outside the one order of magnitude bounds of Figure 7-24.

This may be due to the fact that the slug test zones or screened intervals are biased toward good aquifer materials (i.e. coarse to very-coarse sand). However, the $C_{ave}$ of the mud and silty very-fine sand are constrained by the permeameter tests, and are under-represented in the lithology within the slug test screened intervals. This is again due to the fact that the screens were placed over the aquifers interpreted from the in-field lithology logging during drilling. Thus, the $C_{ave}$ of the mud, silty very fine sand, and the coarse to very coarse sand classes remained unchanged after the initial determination of $C_{ave}$ for those hydraulic classes using the permeameter results. Within the 26 boreholes, seven boreholes have relatively thick sequence of fine and medium sand. These seven bores were evaluated by linearly varying the $K_{ave}$ and deriving the $C_{ave}$. The $K_{SDR}$ and $T_{SDR}$ of the 26 boreholes were recalculated and $T_{SDR}$ and $T_{Slug}$ were revaluated. The final $K_{ave}$ and $C_{ave}$ (Table 7-11) were selected when the error was minimised (Figure 7-25) for $T_{SDR}$ within or close to, one order of magnitude to the $T_{Slug}$ (Figure 7-25). Overall the $T_{SDR}$ and $T_{Slug}$ in compare well considering the accuracy of estimating $T$ from slug tests (Black, 2010).

With the determination of the $C_{ave}$ for each of the hydraulic classes $K_{SDR}$ can be calculated for the NMR logs throughout the BHMAR study area. This provides a vertical log of the $K_{SDR}$ over each of the NMR logged intervals within the BHMAR. It is important to note the self-consistency that exists within the calibration of the $C$ values for the SDR equation. The initial $C$ values were determined from the permeameter testing, then the $C$ values were adjusted based on measurement bias to match the slug test results for the same intervals within the BHMAR boreholes.

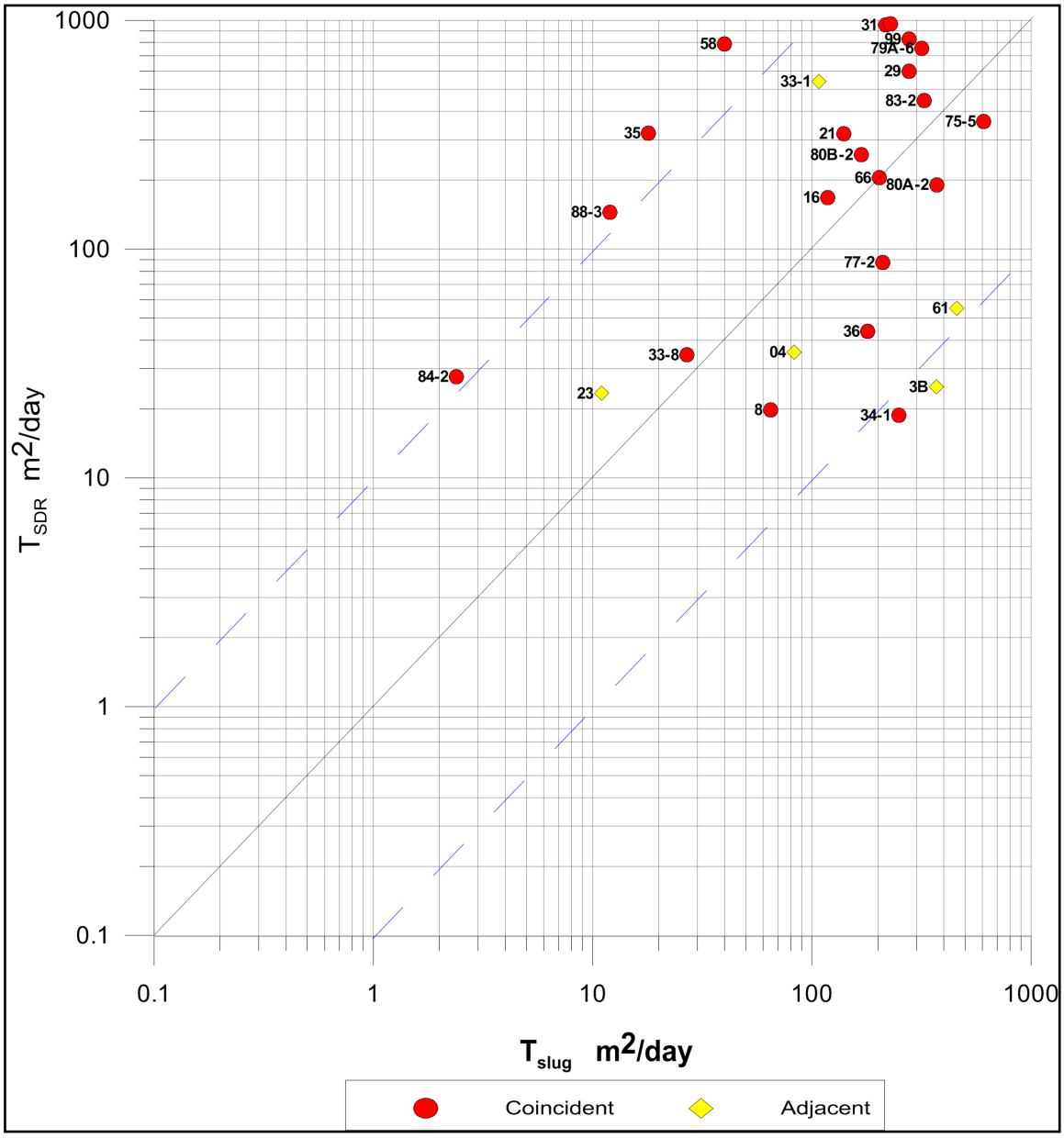



**Figure 7-23.** *Calculated transmissivity ($T_{SDR}$) based on a single C = 46,000 versus transmissivity from the slug tests ($T_{Slug}$).*

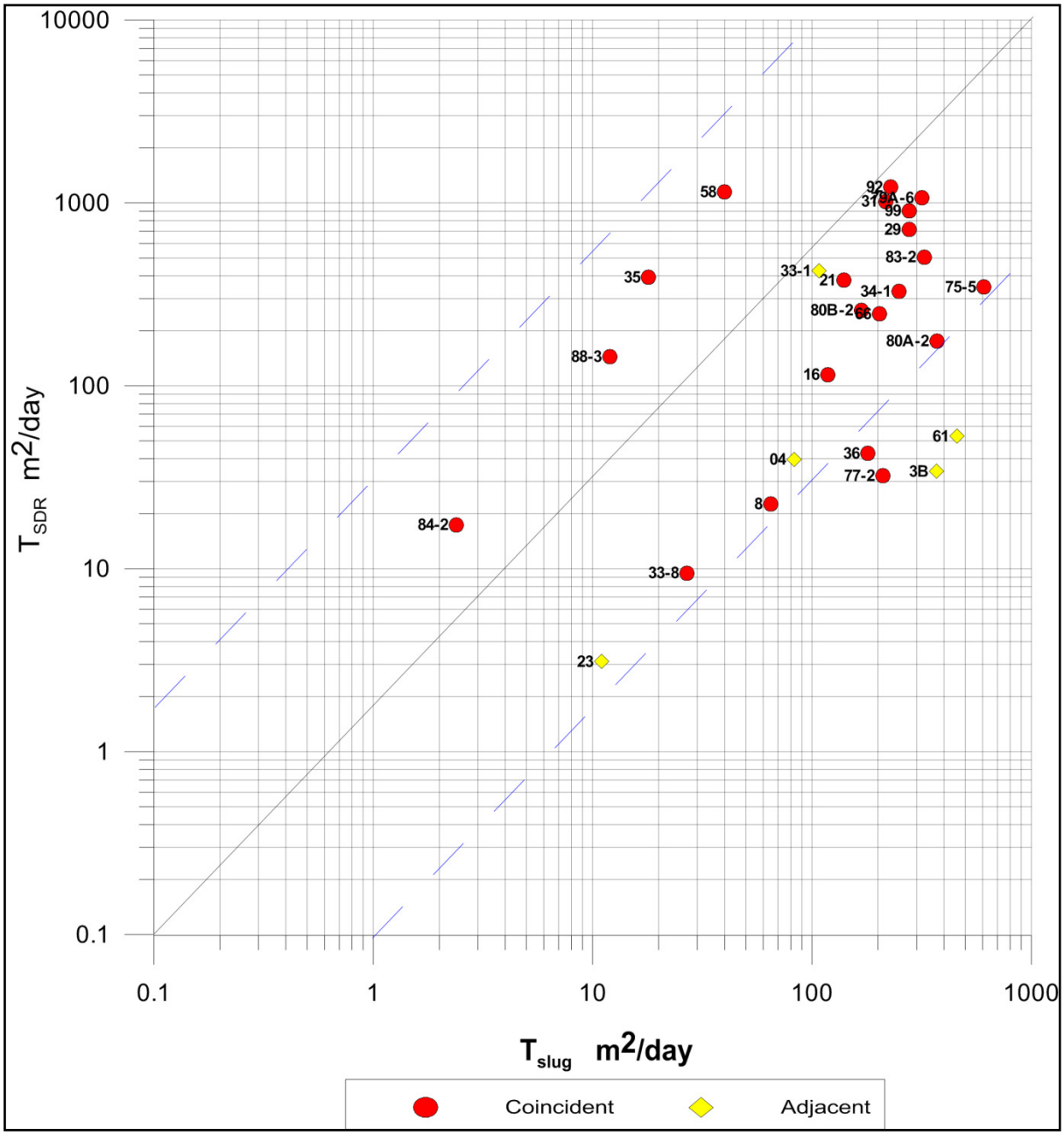



**Figure 7-24.** *Calculated transmissivity ($T_{SDR}$) based on the initial hydraulic classes C values from the permeameter tests versus transmissivity from the slug tests ($T_{Slug}$).*

**Table 7-11.** *Final $K_{ave}$ and $C_{ave}$ values for the hydraulic texture classes.*

| Hydraulic texture class | $K_{ave}$ (m/d) | $C_{ave}$ |
|---|---|---|
| Mud | 1 x $10^{-6}$ | 20 |
| Silty very fine sand | 1 x $10^{-5}$ | 300 |
| Fine sand | 0.03 | 19000 |
| Medium sand | 0.15 | 20000 |
| Coarse to very coarse sand | 3 | 46000 |

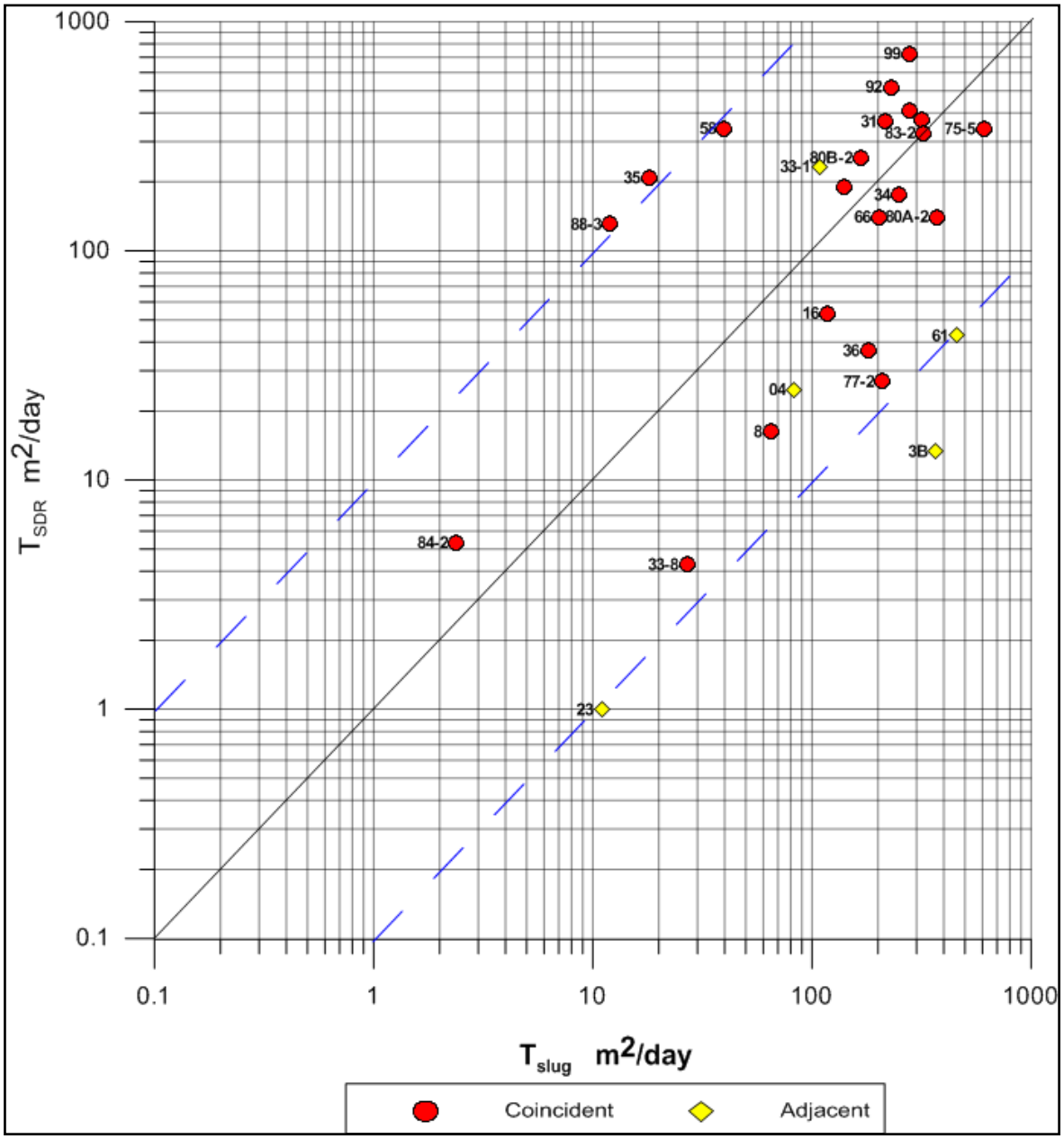



**Figure 7-25.** *Calculated transmissivity ($T_{SDR}$) based on the final hydraulic classes NMR derived $C_{ave}$ values, versus transmissivity from the slug tests ($T_{Slug}$).*

### 7.3.5.1 *Possible causes of variations in NMR versus slug test results and errors in water content calculations*

One question that arises with the inspection of Figure 7-25 is, why is there a range in the NMR derived $T_{SDR}$ values versus the slug test derived $T_{Slug}$? These differences could arise from several factors or a combination of several of these factors: system noise, magnetic susceptibility changes, clay mineralogy, pore coupling, drilling disturbances, development of aquifer test zones, and slug test uncertainties, and to what extent does error impact the calculation of water contents.

### 7.3.5.2 *System noise*

Errors in the measurement of the NMR log can be translated to errors in the $T_2$ distributions. As illustrated above when the regularization is set too low, data noise and spikes can have an influence on the measurements. In cases of low signal strength these errors can be compounded. The Javelin system is

designed to minimize these errors with the use of the reference coil and removal of impulse noise. However, some of these problems do get through the processing. Obvious noise spikes are removed from the logs. These are areas were the $T_{2ML}$ are on the order of 3-7 seconds and are physically unrealizable, especially in areas where there is very low free-water content. In a few zones of the vadose zone of the BHMAR, these data spikes were removed from the data set. There is still the possibility that some system noise will be introduced into the NMR measurement. These problems are minimised through averaging and through regularization. As pointed out above, static tests were conducted in the BHMAR area to determine the best averaging to use. Tests were also conducted with the Javelin sonde placed in a plastic barrel filled with water. The Javelin was run with settings that would mimic the data collection with the exception of the recovery time which was set to 10 seconds to avoid any interference. Also it is important to note that the system was exposed to more noise on the surface than what is sensed in the borehole. The earth acts like a shield and attenuates some of the ambient noise. The results of the multiple measurements in the water filled barrel produced a standard deviation of 1.7% for the water content and a standard deviation of 8.5 ms for the $T_{2ML.}$ A simular test was done with the plastic barrel filled with saturated sand. The results of the multiple measurements in the saturated sand filled barrel produced a standard deviation of 5.8% for the water content and a standard deviation of 13.0 ms for $T_{2ML}$.

Noise in the NMR signal can translate to errors in the determination of the water content and the $T_{2ML}$ value used in the calculation of the $K_{SDR.}$ However, these errors are no greater than 6.0% as determined from the barrel tests. As with all data the results need to be looked at with a critical eye toward the hydrogeological realistic nature of the derived results. The results presented here have been processed to minimize the impacts of noise but most certainly there are still noise induced impacts throughout the dataset.

#### 7.3.5.3 *Magnetic susceptibility*

Impacts of magnetic susceptibility have long been noted in NMR measurements. The CMPG pulse was designed to minimise the impacts of the inhomogeneous magnetic field. However, many workers have shown that there are still important effects on NMR from magnetically susceptible grains and grain coatings (Bergman *et al*., 1995; Keating & Knight, 2007; Keating & Knight, 2008; Keating *et al.*, 2008; Grunewald & Knight, 2009; Grunewald & Knight 2011; Daigle & Dugan, 2011). Magnetic susceptibility variations can cause the shape of the $T_2$ distributions to shift in time. This can be then manifested in the $T_{2ML}$ value that is used in the calculation of the $K_{SDR}$. A much more complete analysis on the impacts of the magnetic susceptibility can be found in the above references.

To test for the variation in magnetic susceptibility in the BHMAR area two segments of the core from BHMAR80A-2 (0 to 13.4 m) and BHMAR99-1 (23 to 65 m) were tested. BHMAR80A-2 and BHMAR99-1 were selected based on their separation on the $T_{SDR}$ versus $T_{Slug}$ cross plot (Figure 7-25). A Fugro GMS2 magnetic susceptibility meter was used to collect the readings. The meter has a sensitivity of 10-5 SI units and a range up to 10 SI units. The results of the magnetic susceptibility tests are summarized in Table 7-12. There is an indication that there are magnetic susceptible minerals within the boreholes in the BHMAR area and the variation is quite significant. Without a more extensive magnetic susceptibility program it would be difficult to say anything more than there may be variations in the magnetic susceptibility throughout the area. These data however, do not provide a geological reason for the variations.

**Table 7-12.** *Magnetic susceptibility readings summary for BHMAR80A-2 and BHMAR99-1.*

| Borehole | BHMAR80A-2 | BHMAR99-1 |
|---|---|---|
| Mean ($10^{-5}$ SI) | 315 | 773 |
| Median ($10^{-5}$ SI) | 140 | 573 |
| Standard Deviation ($10^{-5}$ SI) | 403 | 751 |
| Minimum ($10^{-5}$ SI) | 1 | 1 |
| Maximum ($10^{-5}$ SI) | 1534 | 5356 |
| Number of Readings | 34 | 143 |

Iron coatings can have an influence on the $T_2$ distributions. Keating & Knight (2009) found that the $T_2$ distributions were different for the different iron oxides. However, they indicated that further research is required to determine what mechanism is causing this behavior. Keating & Knight (2007) indicated that the addition of magnetite to the quartz sand resulted in internal gradients and a led to a decrease in the $T_2$ distributions. They also conclusively showed that the NMR relaxation rate of water-saturated sand is affected by both the presence and the mineralogical form of iron, and that the dominant effect of ferrihydrite, goethite, hematite, lepidocrocite, and magnetite was to decrease $T_2$ which is dependent on ($S/V$)

The presence of iron oxides on the surface will generally cause the decay times to shorten. The iron plays into the decay rate because of the surface relaxation rate in Equation 77, were $\rho_2 S/V$ the surface relaxation rate, is primarily a function of the grain mineralogy and increase in magnitude with more iron. The iron coatings would shorten the decay times, but would unlikely to decrease the amplitude of the signal and under estimate the water content.

XRD and Hylogging work at BHMAR has indicated that there is iron present throughout much of the BHMAR study areas (XRD and Hylogger described in Sections 11.5.4 and 11.5.6 respectively). Haematite is restricted to the Calivil and Renmark Formations, although goethite is ubiquitous, regardless of the presence or absence of organic matter. Specifically, abundant iron coatings have been observed in the Calivil. However, without a much denser spatial sampling of the area the extent of the changes in the iron abundance and coatings cannot be used to subdivide the NMR data into a unique hydro-iron unit as was done with the hydraulic unit for the calculation of specific $C$ values for the SDR equation. Thus, these magnetic minerals and iron coating may be causing some of the variation in Figure 7-25.

#### 7.3.5.4 *Clay mineralogy*

Previous work has shown that the mineralogy of the grains that make up the rock have an impact on the NMR responses. The existence of iron-rich clays and the nonquartz grains in clastics affect the surface relaxivity and the internal field inhomogeneity (Chen *et al*., 2011). The overall impact is to decrease the $T_2$ distribution in time, and lower the $T_{2ML}$ values. In the examination of Figure 7-23 of the simple single $C$ value it was determined that there were a couple groups of boreholes in the BHMAR area that exhibit different behavior and may indicate that a unique $C$ value was required in the SDR equation.

In the examination of the cores from the BHMAR area some general conclusions can be made about the clay mineralogy. The Coonambidgal Formation appears to be dominated by smectitic clays, whereas older fine-grained units are dominated by kaolinite. The Blanchetown and Calivil Formations are primarily not distinct mineralogically, but only in relatively abundance of different minerals. The sands in the Calivil Formation contain either smectitic or kaolinitic clays.

In order to assess the potential impact of clays hyperspectral data from the BHMAR project area was collected using the Hylogger system (see Section 11.5.6) to characterize several core intervals (Table 7-13). The aim of this was to provide additional information on mineralogy to that obtained from XRD analysis of specific sample intervals. Of particular importance to the project was the need to better quantify the distribution of iron-bearing phases and clays, in both the Calivil Formation and Blanchetown Clay, because of the influence of these clays on the hydraulic properties of the units and on geophysical values derived from the NMR logging.

**Table 7-13.** *Core intervals selected for Hylogging.*

| Hole | BHMAR 23-1 | BHMAR 33-6 | BHMAR 75-5 | BHMAR 80A-2 |
|---|---|---|---|---|
| Interval(s) | 93.1-95.0 m | 8.6-64.5 m | 16.1-27.66 m; 55.4-57.6 m | 13.6-53.0 m |
| Scanned length | 1.9 m | 55.9 m | 11.56 m; 2.2 m | 39.4 m |
| Reason selected | Possible Paleozoic (or palaeochannel) | Section through aquifer | Conductive Blanchetown and part of main aquifer Contact with Renmark | Resistive Blanchetown and section through aquifer |

An apparent correlation between the NMR $T_{SDR}$ values and the mineralogy of screen intervals from Hylogger in holes BHMAR36-6 and BHMAR75-5, with BHMAR36-6 corresponding to smectites in the screened aquifer interval, BHMAR75-5 corresponding to kaolinite in the screened aquifer interval. Time constrains precluded testing the cores with the Hylogger system however clay mineralogy identified with the PIMA hyperspectral system could be used to determine variability of clay mineralogy.

The summary PIMA results on a hole-by-hole basis are shown in Table 7-14. Of 15 holes eight had dominant clay mineralogy as predicted, one did not, and six had equivocal results - either equal amounts of both clay species or only a single meaning result for the whole.

The differences in the behaviour of the NMR responses in the screened intervals indicate that a more detailed approach to determine the *C* maybe required. The complicating process is that in main aquifer of the BHMAR area is that the Calivil Formation has both types of clays present. Changes in the clay mineralogy cannot be used to subdivide the NMR data into a unique hydro-clay unit as was done with the hydraulic unit for the calculation of specific *C* values for the SDR equation. This is due to the mixture of clays in the aquifers and a lack of understanding of the causes of the mixtures of clays. There a clear correlation with the impact of the clay on the NMR results, but decoupling that from the logs where we do not have detailed clay mineralogy would be difficult. A much more detailed analysis of the cores would need to be required to determine the extent of the impacts of the clay. Thus, these clay minerals may be causing some of the variation in Figure 7-25 by decreasing the bulk $T_2$ distributions in some of the aquifer zones.

**Table 7-14.** *Summary PIMA results.*

| Hole | From | To | Length | No. samples | Predicted dominant clay | Success |
|---|---|---|---|---|---|---|
| 08-1 | 41 | 46 | 5 | 2 | Kaolinite | No |
| 16-1 | 12 | 52 | 40 | 16 | Kaolinite | Yes |
| 29-1 | 17 | 53 | 36 | 11 | Kaolinite | Yes |
| 33-8 | 46 | 52 | 6 | 2 | Smectite | Yes |
| 34-1 | 27 | 51 | 24 | 13 | Kaolinite | Yes |
| 35-1 | 16 | 46 | 30 | 10 | Smectite | Yes |
| 58-1 | 62 | 69 | 7 | 3 | Smectite | Equivocal |
| 66-1 | 30 | 60 | 30 | 8 | Kaolinite | Yes |
| 75-5 | 40 | 52 | 12 | 7 | Kaolinite | Yes |
| 77-2 | 46 | 55 | 9 | 4 | Kaolinite | Equivocal |
| 79A-6 | 38 | 50 | 12 | 4 | Kaolinite | Yes |
| 80A-2 | 36 | 52 | 16 | 10 | Kaolinite | Equivocal |
| 88-3 | 65 | 71 | 6 | 2 | Smectite | Equivocal |
| 92-1 | 32 | 62 | 30 | 11 | Smectite | Equivocal |
| 99-1 | 33 | 57 | 24 | 8 | Smectite | Yes |

#### 7.3.5.5 ***Pore size interaction***

Recent worked has illustrated that when pore coupling (well-connected pores), is strong, the relaxation time distribution misrepresents the underlying bimodal pore-size distribution of micropores and macropores (Grunewald & Knight 2011; Grunewald & Knight, 2009). They showed that the bimodal relaxation-time distribution becomes merged and the relative amplitude of the peaks fails to reflect the true macropore and micropore volume in the $T_2$ distribution.

Typical interpretations assume a model of isolated pores with a single diffusion. The models assume that each pore combines independently to the total NMR signal with a characteristic relaxation time corresponding to $\rho_2 S/V$. The problem with this simplified model is when the pores are sufficiently connected

that the diffusion proton can readily move through multiple pores during a NMR measurement. This can lead to misinterpretations of the pore structure.

Grunewald & Knight (2009) also showed that a reduction in the pore coupling was observed with increasing iron content. They attributed this to a decrease in the distance protons are able to diffuse before relaxing. The conclusion of this work demonstrated that surface geochemistry is an important factor determining the degree to which pore coupling occurs.

In the BHMAR area there is evidence that there is pore sorting in some of the lithologic units. When the median grain size is plotted against the mode and they do not fall on a straight line it indicates pore sorting of the sediments (Figure 7-26). This can indicate that there may be several pore sizes within a lithology unit.

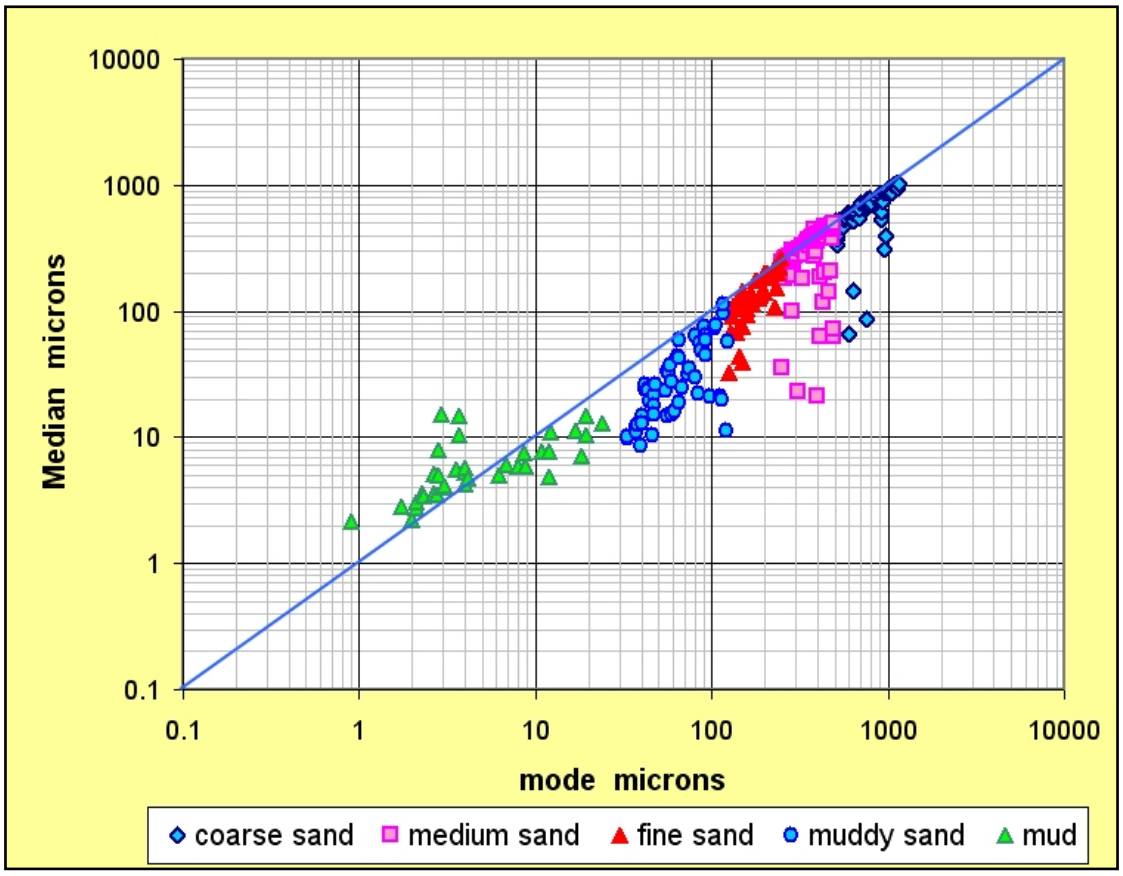



**Figure 7-26.** *Plot of the median versus the mode for the grain size analyses from the BHMAR study. Note that some of the values are not on the 1:1 line (blue) indicating skewed distribution and poor sorting.*

To properly analyse for pore-coupling in the BHMAR laboratory tests would need to be conducted on samples of the formations. The impact of this is that the $T_2$ distributions may be shifted down in time and the amplitudes may be deceased. This effect may also lead to the scatter that is observed in Figure 7-25.

#### 7.3.5.6 *Borehole construction*

Boreholes are constructed by either removing material by drilling, or by compressing material by a direct push probe. There are many methods of drilling from augers to air reverse rotary. In the BHMAR study two methods were used to drill the boreholes including mud rotary and sonic drilling (discussed in Section 10). In mud rotary mud is used to lubricate, cool, and flush the materials from the bit that grinds the materials as it is pushed into the earth. A consequence of mud rotary drilling is that mud is injected into the formation

(invasion zone). A rugose hole is also typically generated when drilling in unconsolidated materials where the fine grained zones are relatively round and the coarse areas display washouts. The skill of the driller and the mud program dictate the quality of the borehole. Sonic drilling is much less disturbing to the materials around the borehole as the main drill stem is vibrated into the earth and the material in the drill stem is flushed away with the drilling fluid virtual not contacting the formations. Some mud is typically used during the vibration of the drill stem into the earth but only when necessary in flowing-sands. When the casing is placed the formation the annulus is filled with a sand/gravel pack, bentonite seal, or cement grout (see well construction details in Appendix 12, Apps & Gibson, 2012).

The consequence of the drilling is that the natural system is disturbed and the act of drilling the borehole has changed the surrounding formations. This is a fact of drilling a borehole and is ubiquitous. The point is to minimize these impacts or correct for them. The logging industry has developed many robust methods for correcting for rugose holes and for correcting for mud invasion.

NMR logs are sensitive to a shell around the borehole annulus. The sensitive zone was ~19 cm from the center of the hole with the Javelin used in the BHMAR study. If diameter of the hole is at or greater than the diameter of the sensitive zone, the NMR will not be detecting the formation. If the casing is off center it may cause the NMR shell to sample some of the annular material. Depending on the composition of that material it may cause the NMR readings to be higher or lower than the actual formation. The best way to deal with this problem is to use sonic drilling or in the case of the mud rotary to conduct a caliper log of the borehole to detect zones that washouts have occurred.

For the BHMAR study the sonic drilling holes were drilled to a diameter of 17.8 cm. and in some cases mud is used in limited quantities. The casing was PVC with a diameter of 9 cm. The mud rotary annulus was on the order of 17.8 cm but no calipers logs were conducted. As noted above the mud rotary data were excluded from the BHMAR dataset analyzed for hydraulic conductivity, as washouts can have adverse impacts on the measurements (Knight *et al*., 2012).

To date no correction factors have been developed for the Javelin tool as in many of the petroleum logging applications. In the petroleum industry a suit of logs are run and multi-depth induction sensors are used to determine the depth of which mud invasion has occurred and the NMR shell is adjusted or multiple NMR shells are used to overcome the washout and mud invasion effects. There is a limit to what can be done as with any system if it is not detecting the formation it cannot provide any information about it.

The impact of the drilling may be the introduction of mud into the formation within the sensitive zone of the NMR causing a net decrease in the total water, free-water, and $K_{SDR}$ values. There could also be an increase in the bound-water values with the introduction of mud. As noted above, the casing could also be off center in the annuals casing the values to be impacted by the annular materials. Without additional measurements of the depth of mud invasion and the deviation in the casing it is difficult to quantify if any of these effects impact the estimations of free-water or effective porosity and the $K_{SDR.}$ Thus, the borehole construction effects could also be leading to the scatter that we observe in Figure 7-25.

#### 7.3.5.7 *Development of aquifer test zones*

For an appropriate designed aquifer test the accepted procedure is to install a screen over the interpreted aquifer interval and the annulus of the area of the screen is filled with sand ore the formation is allowed to collapse on the screen. Typically above and below the screen a bentonite plug is installed to prevent leakage around the screen. Prior to aquifer testing the aquifer test zone is developed (Moench, 1985; Moench, 1997) this involves pumping the test zone flushing the areas of fines in order to establish a good hydraulic connection between the borehole and the formation (see Section 10.4 on the construction of the boreholes and development). This causes problems for the NMR as the NMR is sensitive to the area immediately surrounding the borehole. If the NMR log is conducted after the development of the aquifer test zone the flushing of the fines could be reflected as an increase in the $T_2$ distributions and an increase in the total and free-water content and a decrease in the bound-water. Simular, impacts have been observed at test site in Kansas, USA (Walsh, 2012).

In the BHMAR study the NMR logs were conducted after the screened intervals had been developed. As stated above the zone of investigation of the Javelin used in this study was ~19 cm from the centre of the borehole. The bores were drilled at a diameter of 17.8 cm, and a 9 cm diameter screen was installed. For some of the areas in the BHMAR area there may be some impacts of increased estimates of $K_{SDR}$, total water and total free-water, while bound-water could be decreased.

To asses this impact the NMR logging would need to have been completed before and after test zone development. This was not done in this study. However, in this study there were five slug test zones that were located in adjacent boreholes that would not have been impacted by the aquifer test zone development. These data were including in the analysis of the $K_{SDR}$ values. Again these impacts may also be contribution to the scatter that is observed in Figure 7-25.

#### 7.3.5.8 *Slug test errors*

As noted above and explained in the (Section) there are errors and uncertainties associated this type of measurement of the aquifer properties. As with any measurement there are assumptions inherent uncertainties. Some of these issues have been identified by Black (2010) were in mixed permeability zones (e.g. screens across interbedded sediments) the errors can be in terms of orders of magnitude, whereas errors due to faulty procedures do not exceed factors of 2 or 3 times the determined value.

The slug tests were critical for the calibration of the $C$ values used in the SDR equation. It is believed that the slug tests do give good representation of the aquifer properties in the BHMAR area and compare well with the pumping tests conducted (see Sections 13.2 and 13.3). However, there are errors and uncertainties in these measurements and those will be translated to scatter in the $T_{SDR}$ and $T_{Slug}$ cross plot in Figure 7-25.

#### 7.3.5.9 *Permeameter test errors*

Elsewhere in this report, the errors and analysis of the permeameter tests conducted on the cores from the BHMAR. Those values were used to set the initial values on the $C_{ave}$ for the SDR equation. It is important to note that the permeameter results represent a much smaller scale measurement then the NMR and the slug tests. The Permeameter tests were conducted on 10 cm long cores, the NMR readings were measured over 50 cm, and the slug tests were over multiple meters. The petroleum industry deals with these scale variation by conducting many laboratory tests. This is typically infeasible in many groundwater studies and is made even more difficult dealing with unconsolidated sediments. These scale differences will inherently add scatter into the estimates of hydraulic conductivity that is reflected in Figure 7-25.

### 7.3.6 NMR Logs of Total-, Free- and Bound-water, and Hydraulic Conductivity

Using the 33 ms $T_2$ cut-off and the resulting calculation of the bound, free, and total water allows for a detail examination of the characteristics of the water filled porosity within the BHMAR area. This measurement of water and pore geometries is difficult and/or impossible with any other geophysical tool. Caution needs to be exercised in detailed examination of these logs to be certain that the measurements have accrued within the saturated portion of the aquifer. The assumptions built into the calculation of the total water and $K$ assume that the system contains only water and that system is fully saturated.

Coupling in the data from the permeameter results with the empirical relationships derived from the NMR $T_2$ distributions also allows calculation of a $K$ at the resolution of the NMR measurements (0.5 m). Further confidence is then gained in the verification of the NMR derived $T_{SDR}$ versus the $T_{Slug}$ results. This would only occur if the $C_{ave}$ values were correctly determined. However, as with other empirical measurements errors occur do to a mismatch between the measurement scale and the calibration scale. The petroleum industry has faced this issue for decades with the use of these empirical relationships. They have reduced the problems of scale by charactering producing aquifers with a multitude of laboratory measurements. In many groundwater studies this is not financial possible. The final note is that the $K_{SDR}$ values are based on published and accepted physical relationships between $T_2$ distributions and permeability. These values are calibrated with laboratory measurements of area specific materials. The resulting calculations of $T_{SDR}$ over the same intervals of a much different scale measurements of the slug tests produce consistent verified values for $T$.

Figure 7-27 is an example of BHMAR58-1 with the bound-water, free-water and the $K_{SDR}$ plotted. Correlation can be observed were the bound-water increased the $K_{SDR}$ deceases. These zones correspond with aquitards. Inversely, where the free-water increases and the $K_{SDR}$ increases indicates the presence of an aquifer.

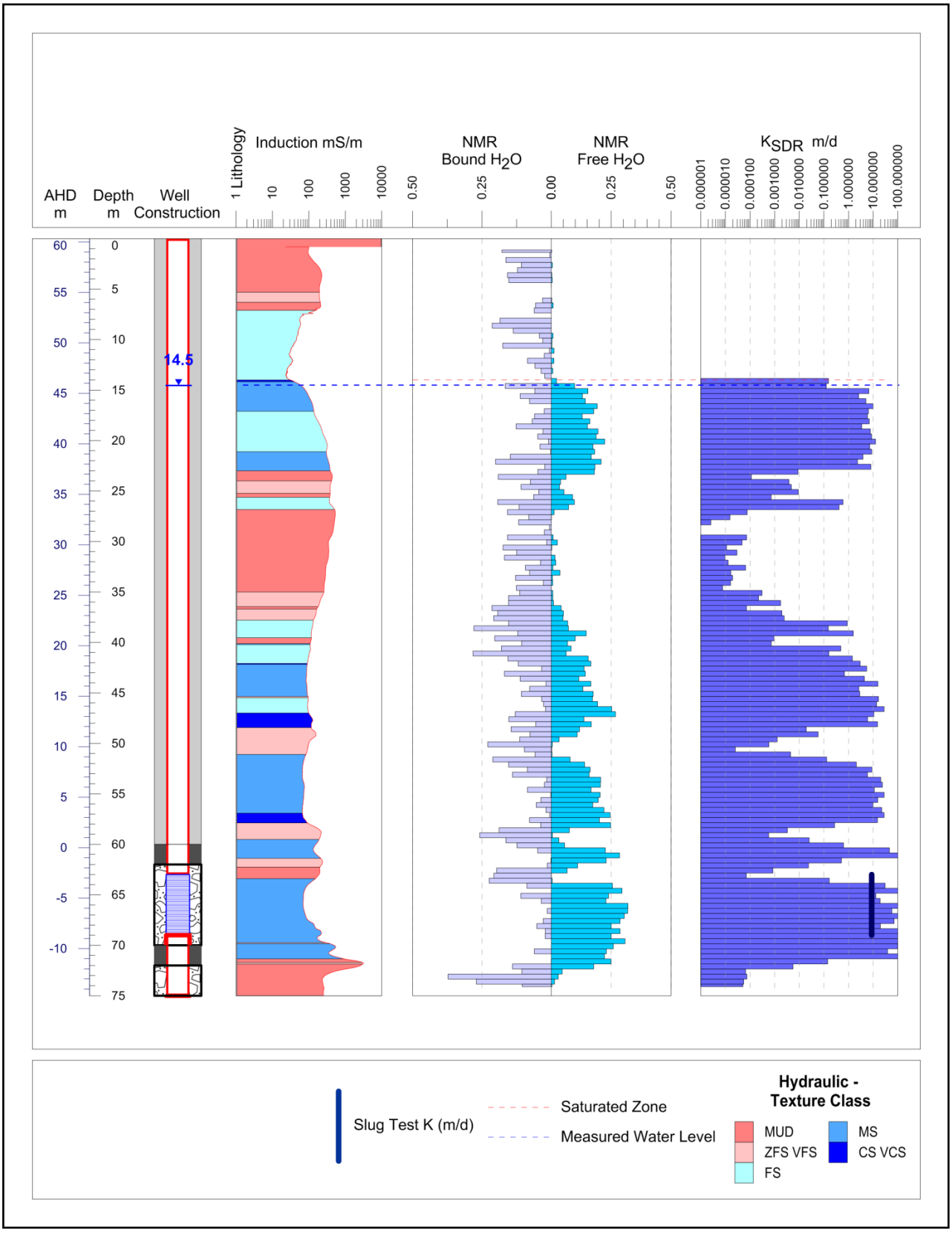



**Figure 7-27.** *Downhole plots of bound-water, free-water and the $K_{SDR}$ for BHMAR58-1, water table indicated by dashed line.*

### 7.3.7 Recommendations for Future NMR Applications

The obvious difference in using NMR to determine hydrogeological properties in the groundwater field versus the petroleum industry is the lack of financial resources. This has delayed the application of the technology several decades. This is changing with the new instruments that have been developed by Vista Clara and by the application of petroleum systems by petroleum service companies (Knight *et al*., 2012; Walsh, 2012). What is still needed is further analysis of the NMR responses in unconsolidated sediments to develop the background on the application of these tools to the unconsolidated material that make up many of the aquifers around the world. Stanford and Rutgers Universities are leaders in the research into NMR properties of unconsolidated materials for groundwater application. However, much more work needs to be done to develop the library of data that will allow groundwater investigators to fully take advantage of the elegance of NMR measurements. This includes laboratory procedures to measure the NMR on core samples. It is only through the laboratory analysis that many of the effects noted that can cause variations in the NMR signals can be clearly identified.

Careful preparation of boreholes and the logging of the boreholes prior to aquifer test zone development need to be addressed at the beginning. NMR logging needs to be more than an add-on at the end of a study, but a critical part of the program from the beginning. This doesn't mean that the measurement of NMR logs in wells that were not optimally drilled is not useful, but rather suggested that to minimize the impacts of well construction and development on the results boreholes should be designed for NMR logging to be successful.

The scale of the aquifer tests need also to be looked at in a manner that is closer to what the NMR is providing. A zone of a screen needs to be selected for an aquifer tests. This automatically biases the aquifer test to the aquifer test zone and provides a bulk measurement over that zone. One manner in which that can be changed is to complete the wells with continues screens over an aquifer and log the well with a borehole flow-meter (Paillet, 2000). Work in Central Nebraska has shown that the use of borehole-flow meters to calibrate NMR measurements are extremely useful and provide better scaling of the *C* values in the hydraulic conductivity equations (Dlubac *et al*., 2013; Irons *et al*., 2012).

Further work is required on the way the *C* values are calculated for the specific units. Methods of inversion should be evaluated to examine the relationships between the lithological units and the calibration data (i.e. slug tests, pumping test, permeameter tests, and flow meter tests). Each measurement has its own uncertainty and by combining those measurements into an inversion may allow those uncertainties to be used in a numerically rigorous way to solve for a best fit *C* value function. In addition to the inversion of many parameters together it is also important to examine the impacts of the summation of the NMR zones over the aquifer test interval.

While hydraulic conductivity can be computed in a variety of ways, Tartakovsky *et al.* (2000) showed that the bounds of effective transmissivity are given when computed with the harmonic and arithmetic means of the hydraulic conductivities. In the BHMAR study the transmissivity was calculated by sampling summing the transmissivity for each of the NMR measurement intervals and then comparing that to the Slug test transmissivity values. While, this has provided a valuable product more investigation is required to verify that this is a stable approach. NMR logging has a bright future in the groundwater community can provide a unique measurement that up to now has not been available.

# 8 Ground Geophysics

AEM is best suited for mapping at regional rather than borefield scales, hence the approach adopted was to acquire an AEM dataset with a high resolution (mostly 200 m line-spacing in key areas), and to acquire ground (and borehole) geophysical data in more localised areas to assess the ability of the AEM system to map local-scale heterogeneity in the hydrogeological system.

Geoscience Australia engaged the services of Zonge Engineering to carry out a Dipole-Dipole Induced Polarisation (DDIP), Offset Pole-Dipole (3DIP) survey of the Project area, over a period concordant with aquifer pump and injection testing. The aim of the survey was to use the resistivity/IP technique to discriminate between clay and brackish to saline groundwater to depths up to 70 metres below surface over an area of approximately 500 x 2500 metres. The survey should also provide sufficient resolution to produce a map of the confining clay layer, and holes in this clay layer. All resistivity and IP inversion data are contained in Appendix 10 (Apps *et al*., 2012d).

## 8.1 TIME SERIES MONITORING OF AQUIFER PUMP TESTS

Ground resistivity surveys were initially designed with the intention of monitoring potential groundwater quality and volume changes during injection of surface water into the Calivil Formation aquifer at a depth of 40-50 m below surface over a period of several weeks. The initial plan was to monitor any changes (e.g. through displacement and/or mixing of the two water types) upon injection of river water or water from the overlying unconfined aquifer into the Calivil Formation aquifer. The river water has a lower electrical conductivity (EC of <300 EC compared with ~1000 EC in the aquifer at this site), so it was anticipated that changes in water quality would be imaged through a temporal resistivity survey.

Two sites were selected (Menindee Common and Jimargil), and cultural and environmental heritage clearances obtained. However, laboratory clogging experiments showed that it was likely that clogging of the Calivil Formation aquifer would most likely occur if untreated river water was used in the injection test, and plans modified. Insufficient water was found in the nearby unconfined aquifer at both locations, so plans for the injection test were abandoned.

However, the observation network was constructed at the Jimargil and Menindee sites to monitor short-duration (7-day) groundwater pump tests, with disposal of groundwater in the nearby Darling River. Gaining permission necessitated modelling of the potential downstream impacts on water quality. Unfortunately, it was not possible to gain permissions from regulatory authorities for a longer term pump test from the Calivil Formation aquifer at Site BHMAR33, due to downstream impacts of disposing of ~12)) TDS groundwater into the river for the requested 3 month test. It was not possible to gain permissions for disposal of the groundwater from the aquifer at the Menindee site, so the resistivity monitoring array was not commissioned at that site.

The location of the observation network surrounding the bore used for the pump test at the Jimargil site (Sites BHMAR33) is shown in Figure 8-1. Four dipole-dipole lines, arranged in a cross-hatch pattern in 2 cardinal directions as designed by Geoscience Australia, were placed surrounding injection well. The electrodes were spaced 25 m apart on each line and operated in a dipole-dipole resistivity sounding. At Site 33, four survey lines, each of 375 metres length, were laid, with 2 lines at right angles to the first. The 375 m lines have 16 electrodes each; and these will stay in place for the duration of the experiment. Measurements were taken with pole-pole or pole-dipole injection of current from each of the 16 electrodes in both cardinal directions. Initial results from the survey are provided in Figure 8-2.

At site 33, the ground resistivity data mapped a conductive clay-rich unit overlying a more resistive (Calivil Formation) aquifer. The results of the pump test showed no measureable change in the groundwater salinities, or resistivities, in the monitored aquifer zone after 6 days of groundwater pumping. The results were not overly informative, as it was expected that any saline groundwater ingress from the underlying or adjacent formations would only be observed after longer duration (3 month or longer) pump tests.




**Figure 8-1.** *Google Earth image of BHMAR33 ground resistivity survey lines.*

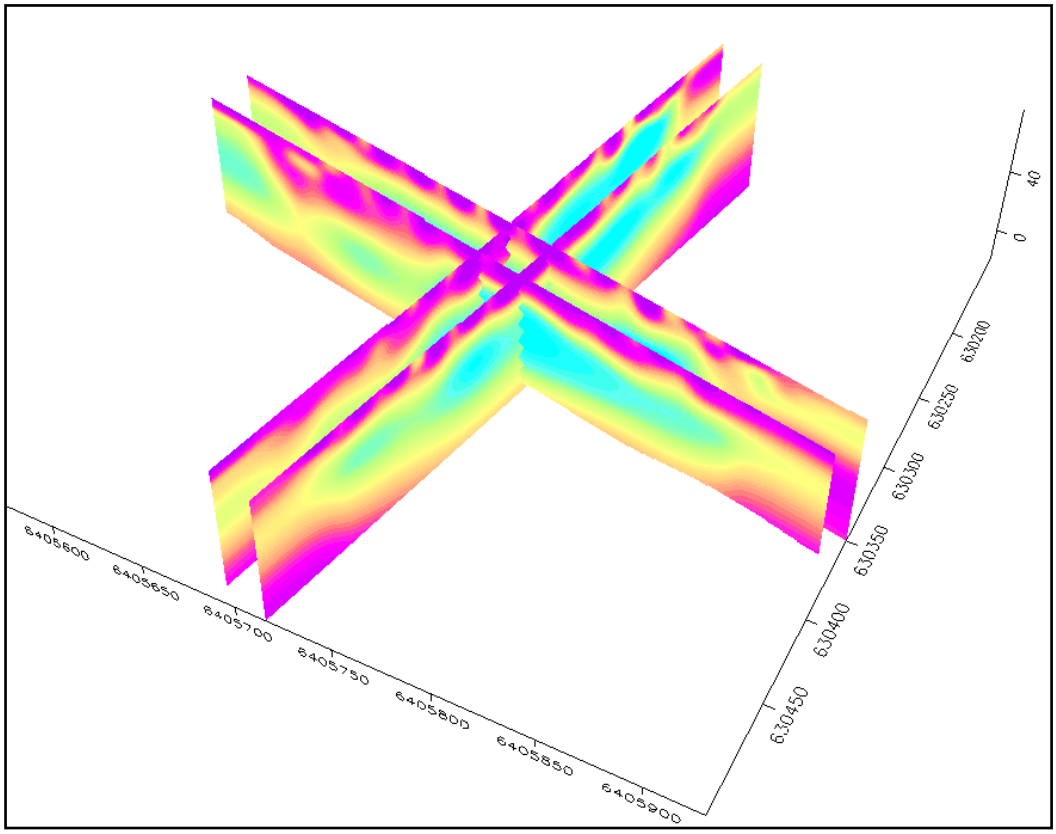



**Figure 8-2.** *Oblique 3D view showing the baseline data (pre-pump test) from the resistivity survey at the BHMAR33 site. The purple colours indicate conductive ground (clays) while the blue colours are resistive areas coincident with the Calivil Formation aquifer. It was anticipated that daily surveys would pick up time-series changes in water quality (salinity) within the aquifer, particularly over a planned month-long injection test.*

## 8.2 GROUND RESISTIVITY AND INDUCED POLARISATION SURVEYS

### 8.2.1 Menindee Common

The aim of this survey was to test the effectiveness of discrimination between clay and saline water to depths up to 70 m below surface at sufficient resolution to map a clay aquitard layer estimated to be between 10 to 40 metres below surface. The Blanchetown Clay layer, estimated to be between surface layer down to 40 metres below surface, was thought to be absent in a number of 'holes' in which areas of Blanchetown clay are replaced with more sandy soils. These soils are believed to have similar electrical conductivity to Blanchetown Clay, thereby limiting their detectability by the EM techniques. Induced polarisation, whereby areas of the ground are electrically charged, potentially allow discrimination between chargeable clays and non-chargeable sandy materials.

Survey planning aimed at detecting 'holes' on the order of several tens to hundreds of metres in the Blanchetown Clay layer. Accordingly, an east-west oriented swath of north-south oriented lines with 25 metre electrode spacing (which provides spatial resolution along-line on the order of ~50 m). Test lines are approximately 2.5 km long. Figure 8-3 shows the location of the survey lines, and Figure 8-4 is an image showing comparison of the ground results with the SCI inversion of the AEM data for the same section line. Note that the final WANDA inversion results were not available at the time this comparison was carried out.




**Figure 8-3.** *Google Earth image of the Menindee Common resistivity survey.*

Ground resistivity and induced polarisation multi-plots, such as that shown in Figure 8-4, display some of the results of the geophysical inversions provided by the contractor (Zonge Engineering) for Geoscience Australia. In the top panel of Figure 8-4 we see the inversion result from the ground-based geophysical survey. The second panel displays the corresponding borehole and spatially-constrained inversion models obtained from the inversion of the AEM SkyTEM data. The third panel shows the ground-based chargeability inversion results provided by Zonge Engineering, whilst the last panel shows the resistivity sensitivity of the ground-based geophysics inversion. In Appendix 10b (Apps *et al*., 2012d), there are additionally resistivity and chargeability multi-plots of the ground-based geophysics inversion results. These multi-plot pages have panels displaying inverted resistivity, data and apparent resistivity, as well as inverted chargeability.

Inversion models provided by Zonge Engineering were obtained using the Zonge Engineering proprietary software TS2DIP. TS2DIP attempts to simultaneously minimise the error between observed and calculated data, the difference between background and inversion model parameters, and the roughness of the inversion model. Ground resistivity and chargeability are simultaneously inverted for during a single iteration. Products such as sensitivity, resolution width and depth of investigation are by-products or parameter-estimation products that assist the interpreter in assessing the utility of the inversion products. Graphs of model sensitivity display how well parameters are estimated by the inversion. Areas of high sensitivity might be resolved by the observed data, while low sensitivities mean that the parameter will be more poorly resolved. According to the TS2DIP manual, 2% sensitivity roughly contours the maximum depth of investigation for the data surveyed. Correspondingly, the white lines on the ground-based geophysics multi-plots are the contours for the 2% line of the on-version sensitivity.

Zonge Engineering provided another parameter that measures the depth of investigation in the inversion results. The panels labelled 'Conductivity Depth of Investigation' follow the investigation described by Oldenburg & Li (1999). The values of the depth of investigation parameter range between 0 (whereby the data dominates the inversion process over the model parameters), and 1, which indicates that the reference model for the inversion dominates the inversion process. In other words, a value of 1 indicates that the data does not have enough information to change the model parameters and the model is considered to be model-driven. The panel displaying 'Resolution Width' is a depth-section that indicates the minimum-sized geological structure that may be realistically identified by the inversion process per pixel. This is discussed in the paper by Alumbaugh & Newman (2000).

A summary inspection of the inversion results from Line 26N (Appendix 10) shows that the resolution width of the inversion increases with depth. Resolution performance is best at the surface near the electrodes, and ranges from metres (near-surface) to about 80 m at a depth of 80 m, indicating that the existence of 'holes' in the Blanchetown Clay should be detectable, presuming that they are not just conductivity variability within the clay. The sections for both ground-based and airborne conductivity models are presented on a logarithmic scale ranging from 10 mS/m to 500 mS/m. This scale was chosen because it allows us to easily determine differences in the resistivity inversion models since galvanic resistivity surveys are more sensitive to ratios in resistivity/conductivity. Additionally, conductivity and lithology logs for nearby boreholes are included on the panels of the ground-based and AEM conductivity plots.

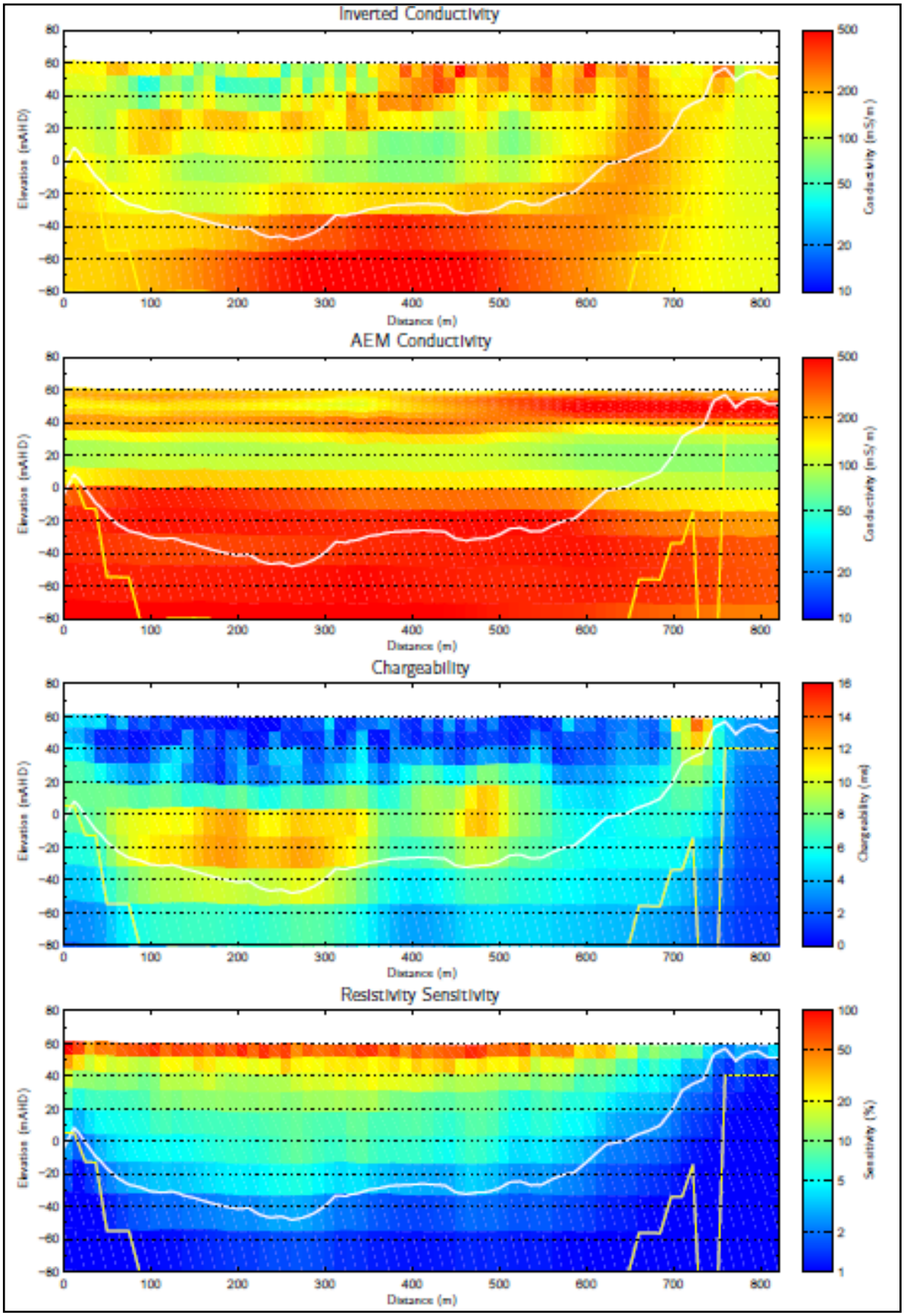



**Figure 8-4.** *IP and Resistivity Inversions compared with AEM conductivity data for survey line 1700N. The top image is inverted conductivity of the ground survey, the 2nd image from top is AEM conductivity, the 2nd image from bottom is Chargeability (from the ground survey data) and the lower image is Sensitivity of the Resistivity survey. The data show that the ground resistivity data are able to resolve differences in Clay layer thickness and variability more effectively than the AEM data. The white line represents the calculated depth of investigation limit.*

### 8.2.2 Jimargil-East Bootingee

The survey at the Jimargil-East Bootingee site consisted of six DC/IP profiles, located in the close proximity of the Darling River. The lines were measured by Zonge Australia, with an electrode spacing of 10 meters and a dipole-dipole array. Furthermore, seven induction and gamma logs were measured in the survey site. Figure 8-5 shows the mutual location of the lines and induction logs. The spacing of electrodes was tightened following analysis of the Menindee Common surveys by Niels Christensen. Unfortunately, the presence of sensitive cultural heritage sites and fence lines necessitated some of the survey lines terminating within 50 m of borehole sites located near the ends of survey lines. This limited the utility of the borehole data for survey calibration and validation.

The resistivity and IP data were collected using the same equipment as earlier surveys. Initial inversions were provided by Zonge, but were later inverted by Aarhus University. The results are discussed below.




**Figure 8-5.** *Overview map of the collected IP and resistivity data at Jimargil. The DC/IP profiles are shown as yellow lines and the induction/gamma logs as red circles. In total 6 lines were measured with a line length ranging from 420 to 1380 m.*

## 8.3 AARHUS UNIVERSITY INVERSIONS OF THE GROUND GEOPHYSICAL DATA AT JIMARGIL

In the project framework, a collaboration between Geoscience Australia and Aarhus University was established, in order to process and invert the direct current (DC) and induced polarization (IP) data acquired along six lines in the nearby of Darling river, in order to obtain a detailed description of clay layers that are important for the regional hydrological model. The material in this section is extracted from a report by Pedersen & Fiandaca (2011).

### 8.3.1 Time Domain Induced Polarization

Time domain induced polarization (TDIP or IP) consists of measuring a voltage decay resulting from an exciting current pulse in the subsoil. Immediately after the current is turned on, a potential, $V_i$, raises across

the potential electrodes. After a charge-up effect, the primary voltage, $V_{DC}$, is measured for the computation of the DC resistivity just before the current is turned off.

When the current is turned off, the voltage drops to a secondary level, $V_s$, and then decays with time during the relaxation period. This decay curve is characteristic of the medium (in terms of initial magnitude, slope and relaxation time), and represents the target of time domain induced polarization (Figure 8-6).

Because of inductive coupling occurring after the current shut-off, a time gap or induced polarization delay is applied before performing the measurements. The signal decay is usually integrated over *n* time windows or gates for the computation of the chargeability M. The integral chargeability is defined as:

$$M(t) = \frac{1}{V_{DC}\left[t_{i+1} - t_i\right]} \int_{t_i}^{t_{i+1}} V_{ip}\, dt$$

**Equation 82**

where $V_{DC}$ [V] is the potential used for calculating the DC resistivity, $V_{ip}$ is the intrinsic or secondary potential [mV] that can be seen as the transient response resulting from the ground polarization after the current is shut-off. The $t_i$ and $t_{i+1}$are the open and close times for the gate over which the signal is integrated.

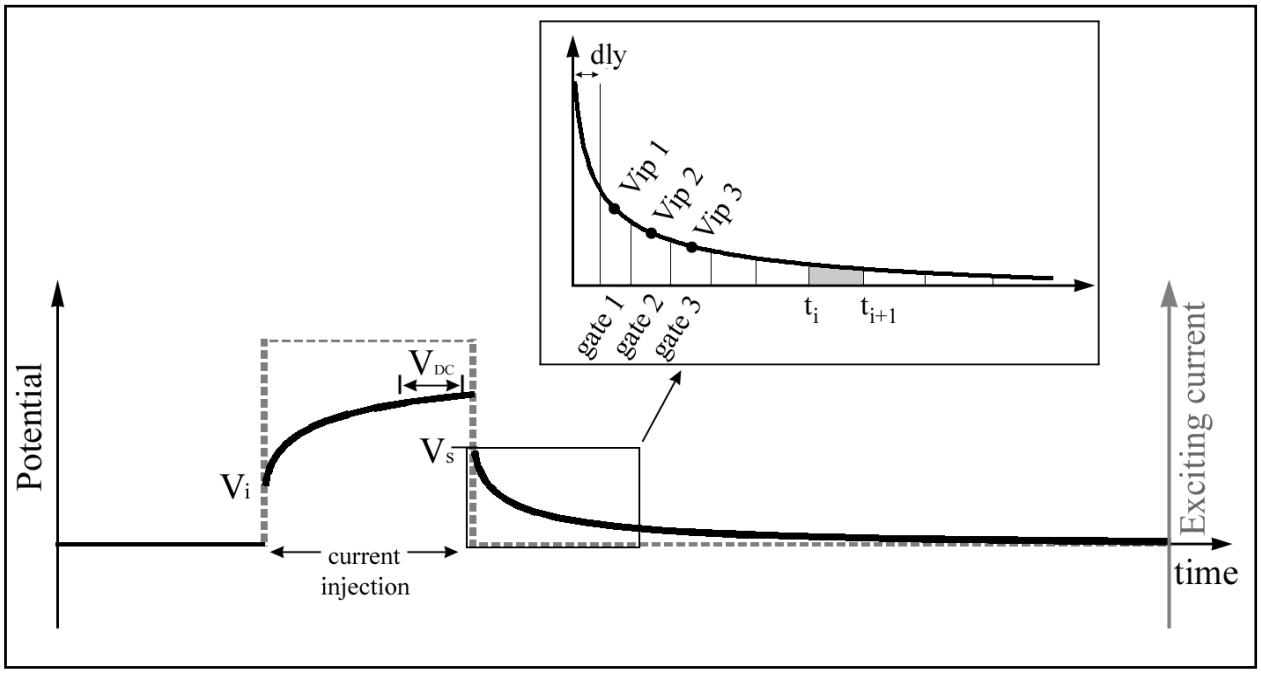



**Figure 8-6.** *Basic principles of time domain DC/IP acquisition. $V_{DC}$ is the direct current voltage used for calculating the DC resistivity. $V_{ip}$ is the secondary voltage used for calculating the chargeability between the open time $t_i$ and close time $t_{i+1}$ of the acquisition gates.*

The induced polarization method has been used increasingly in environmental investigations because IP measurements are very sensitive to the low frequency capacitive properties of rocks and soils (Chen *et al.*, 2008). These properties are associated with diffusion-controlled polarization processes that occur at the mineral-fluid interface (Slater & Lesmes, 2002). Usually, DC resistivity and IP are used jointly in order to discriminate between materials displaying an identical signature in resistivity (e.g., brine and clay). Slater and Glaser (2003) showed from the results of crosshole electrical imaging performed on sandy sediments, that high-resolution IP measurements might be used to make a lithological description, allowing a differentiation between silt/clay and sands of different grain size. Kemna *et al*. (2004) used the IP method in crosshole surveys in order to make a lithological characterization and to detect hydrocarbons.

In this report the induced polarization phenomenon is treated in terms of the Cole-Cole model (Cole & Cole, 1941, Pelton *et al.*, 1978), that has been widely applied in the inversion of both TDIP data (e.g. in Yuval and Oldenburg, 1997 and Hönig and Tezkan, 2007, Fiandaca *et al.*, 2012) and spectral induced polarization (SIP) data (e.g. in Yoshioka and Zhdanov, 2005; Loke *et al.*, 2006; Ghorbani *et al.*, 2007; Chen *et al.*, 2008).

In the Cole-Cole model the frequency-dependent complex resistivity of the soil $\zeta$ is expressed in terms of four parameters:

$$\zeta(\omega) = \varrho\left[1 - m_0\left(1 - \frac{1}{1+(i\omega\tau)^C}\right)\right]$$

**Equation 83**

where $\rho$ is the DC resistivity, $m_0$ is the intrinsic chargeability, $\tau$ is the time constant and $C$ is the frequency exponent; $\omega$ and $i$ are the angular frequency and the imaginary unit, respectively.

The intrinsic chargeability $m_0$ describes the magnitude of the IP phenomenon, being the value of the IP decay just after the current turn off. The time constant $\tau$ increases with increasing mineral grain size and differences in $\tau$ are thus indicative of differences in mineral texture. The frequency dependence is associated with the particle size distribution, so differences in the frequency dependence constant $C$ are indicative of differences in mineral structure (e.g. Slater & Glaser, 2003).

### 8.3.2 Survey and Data Processing

The data processing was carried out with the Aarhus Workbench program package, which has been developed at Aarhus University by the HydroGeophysics Group.

In the processing procedure all bad data points are removed. Bad data points can be caused by several factors, but the most common are simply poor contact between the electrodes and the ground. Other typical causes are couplings or instrument errors.

#### 8.3.2.1 *DC processing*

When processing the DC resistivity data, the data from the lines are inspected manually and all the data points with an erratic appearance are removed. An example showing Line six and which data points that are typically removed are presented in Figure 8-7. The data are plotted for each focus depth (corresponding to the different coloured lines in Figure 8-7), whereby the poorer data points are identified and removed.

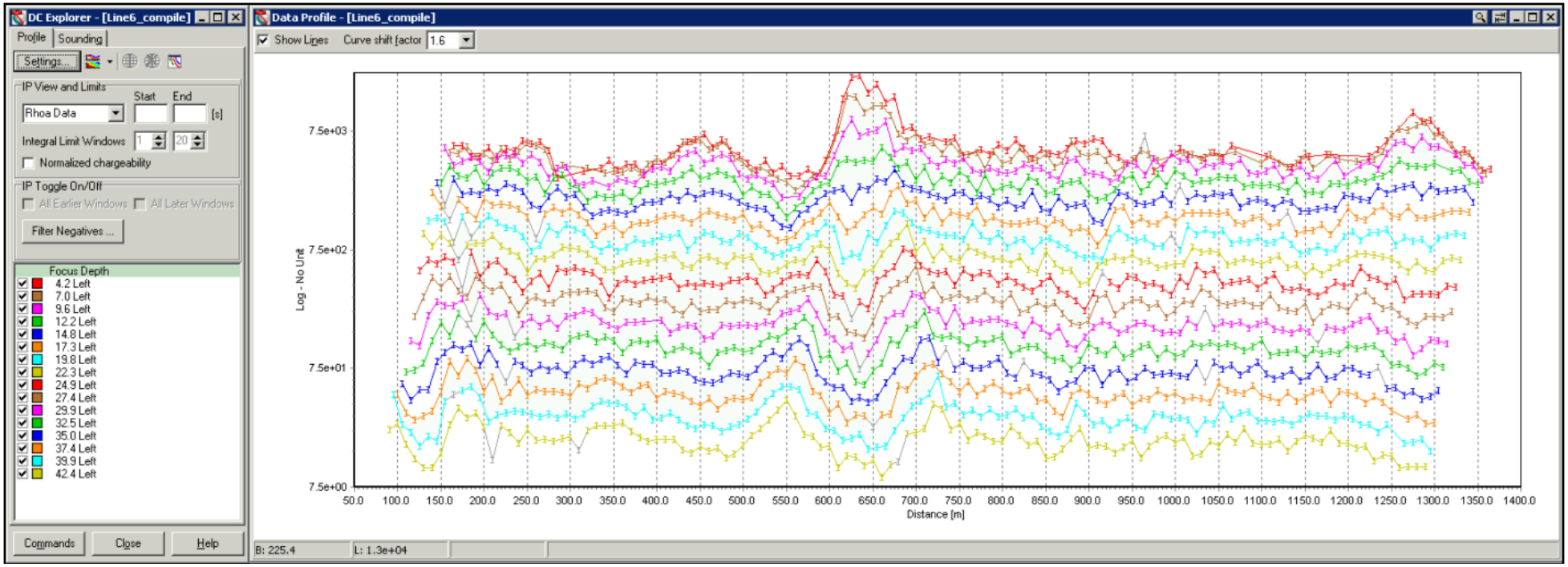



**Figure 8-7.** *Resistivity data for Line 6 showing removal of bad data points caused by noise or poor electrode contact. These stand out as data points with a "jiggered" appearance and are removed. The removed points are grey.*

Afterwards the entire data profile is looked at as individual Vertical Electrical Sounding (VES) curves. An example of a sounding curve is shown on Figure 8-8. Here outlying data-points are removed, so the walkthrough of all soundings curve serves as a control on the previous processing. Unfortunately, no explanation of the error assignment was provided by the contractors.

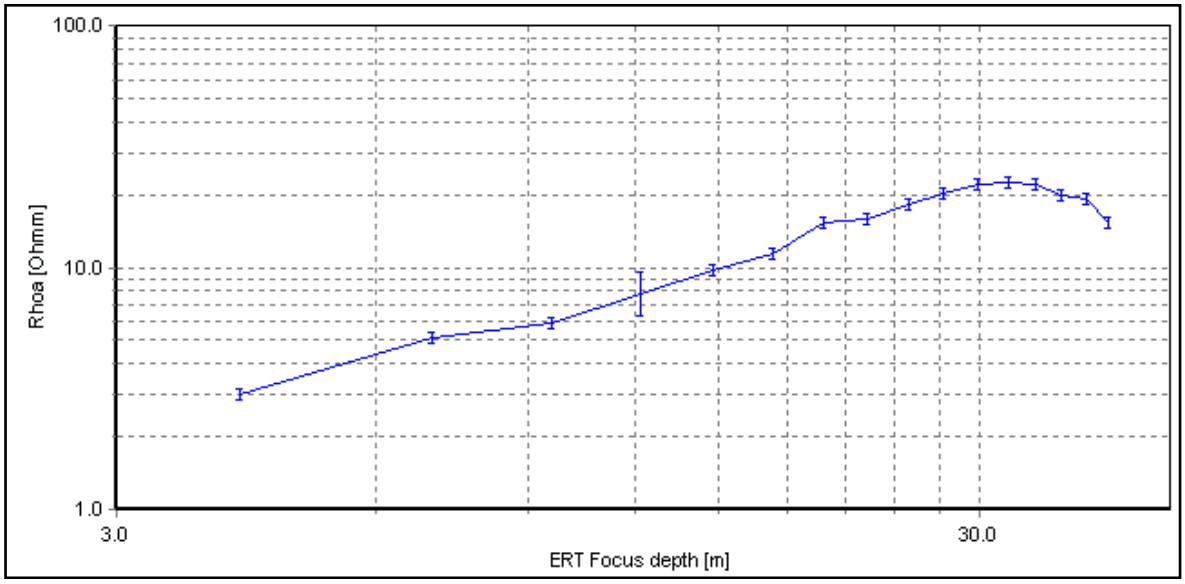



**Figure 8-8.** *Example vertical electrical sounding (VES) curve from Line 6. The VES is from a profile distance of 315 m.*

#### 8.3.2.2 *IP processing*

In the processing of the induced polarization data, all the induced polarization decay curves are evaluated one by one, which means manual inspection of a total of 6225 decay curves. Bad induced polarization data points are defined as induced polarization decay curves where negative chargeability values or positive increasing values are present. Furthermore, a decay curve that goes up and down periodically due to a periodic source of an unknown origin are classified as bad data points and deleted in the processing procedure.

Figure 8-9a shows a proper decay curve, where the chargeability values slowly decrease with increasing time, until they reach a steady value. Figure 8-9b shows a decay curve with oscillating chargeability values, which are removed before the inversion. Figure 8-9c shows a decay curve with negative chargeability values. The negative chargeability values can be caused by galvanic couplings, and hence the decay curve is likewise removed before the inversion.

In general, the data quality is very good for all lines in terms of both DC and IP data, and the signal-to-noise ratio is good down to about 45 meters focus depth (a fraction of the electrode spacing determined by the contractors). This was also evident in the processing, where less than 1% of the data had to be removed.

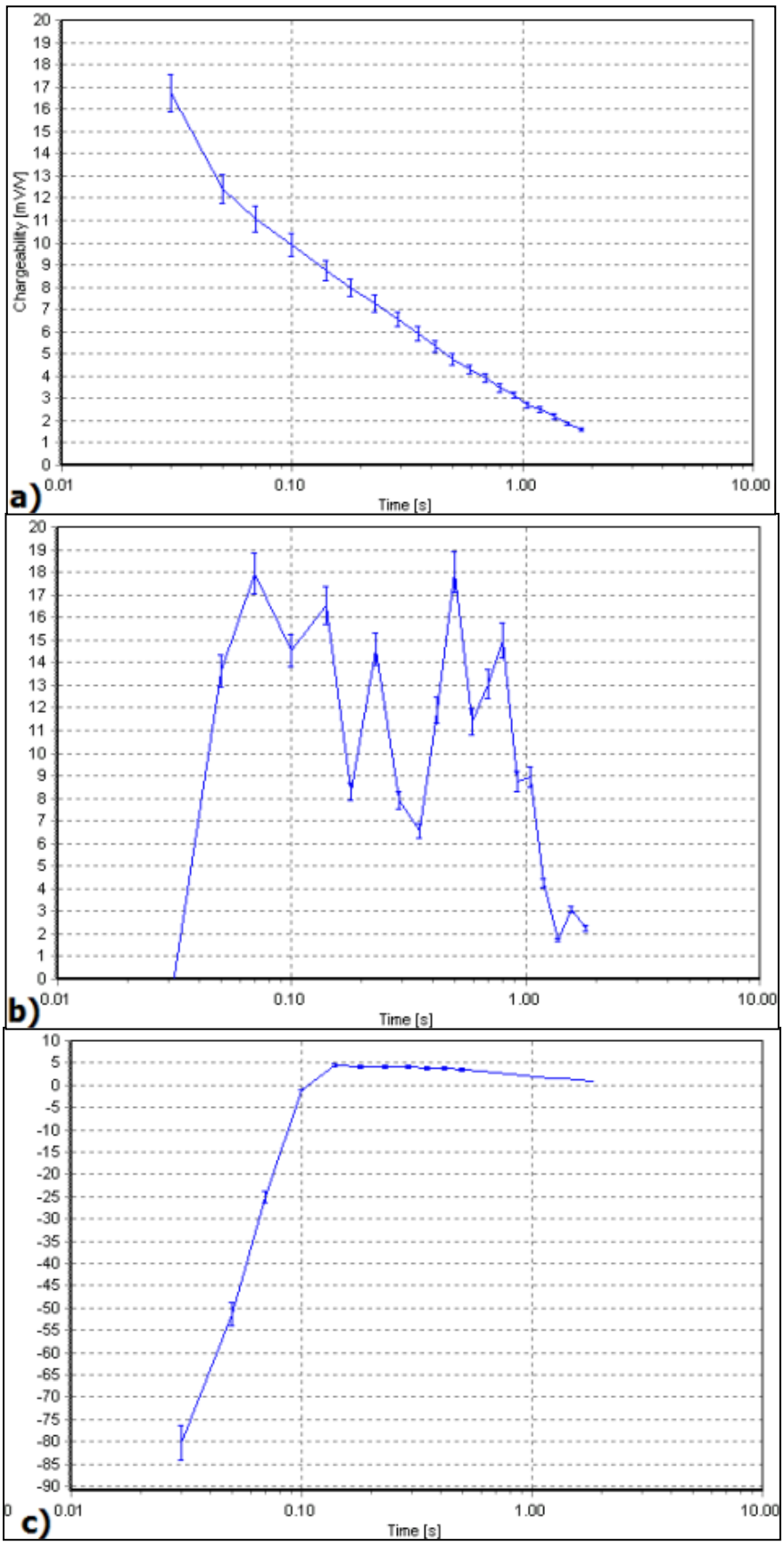



**Figure 8-9.** *Examples of IP decay curves from Line 6. a) A good decay curve with positive decreasing chargeability values. b) A bad decay curve with oscillating chargeability values. c) A bad IP decay curve with negative chargeability values possibly due to capacitive couplings.*

### 8.3.3 Inversion

The data has been inverted with the em1Dinv inversion code developed by the HydroGeophysics Group, Aarhus University.

The code uses a new implementation of the 1D-LCI algorithm for TDIP data (Fiandaca *et al.,* 2012), where the time domain forward response is computed for a layered medium via a Hankel transform of the frequency-domain kernel. In the code the complex resistivity of the layers is described in terms of the Cole-Cole model (Pelton *et al.*, 1978). The inversion is carried out with the 1D-LCI implementation (Auken *et al.,* 2005), to retrieve the four Cole-Cole parameters ($\rho$, $m_0$, $\tau$ and $C$), for each layer. Where ρ is the resistivity, $m_0$ the magnitude of the chargeability at t=0 and describes the polarization magnitude, $\tau$ is a constant which characterizes the decay length and $C$ is a constant that controls the frequency dependence.

The code uses the full IP decay curve to assess the spectral content of the IP phenomenon, allowing for a detailed description of the sub-soil. Furthermore, it implements full waveform modeling by taking into account the number of stacks used during the measurement procedure as well as the pulse duration for the charge up effect. If the waveform modeling is ignored the final $m_0$ magnitude is strongly underestimated (up to several hundred percent (Fiandaca *et al.,* 2012)).

The advantage of the new code is that it uses the entire IP decay curve, resulting in a better understanding of the polarization phenomena and in the end a more detailed description of the soil.

#### 8.3.3.1 *Laterally constrained inversion*

With the 1D Laterally Constrained Inversion (1D-LCI) methodology (Auken *et al.*, 2005), neighbour one-dimensional models are connected laterally, by requiring correlation between neighbouring parameters, e.g. the chargeability and depth (Figure 8-10). Constraining neighbouring models can be considered reasonable if the geology is assumed to have slow lateral variations, which often is the case in a sedimentary environment (although not always in a fluvial environment), and the LCI methodology can thus be considered as a priori information on the geological variability in the measurement area.

The principle behind the LCI methodology is shown in Figure 8-10. Here the specific parameters i.e. the chargeability and depth between neighbour models are bound together, resulting in laterally smooth model sections with sharp layer boundaries.

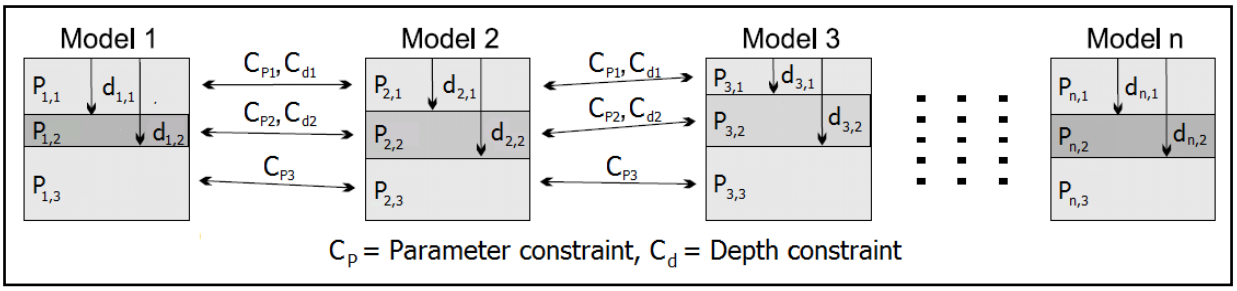



**Figure 8-10.** *Laterally constrained inversion (LCI) methodology. Neighboring models are connected laterally by requiring correlation between neighbouring parameters. The parameters are the resistivity, chargeability, time constant, frequency dependency and depth to the layer boundary for the respective layers in the different models.*

The LCI methodology gives a better estimation of the poorly to completely unresolved models, allowing the migration of information through the constraints. Furthermore, by using the lateral constraints, erratic, geologically improbably models are avoided.

#### 8.3.3.2 *Depth of investigation*

The Depth Of Investigation (DOI) method, which has been developed at Aarhus University by the HydroGeophysics Group and is fully integrated in the em1Dinv inversion algorithm, calculates the depth of investigation of the inversion as a function of the actual inverted model, the measured data and their uncertainties. The methodology is based on a recalculated sensitivity (Jacobian) matrix of the final model. A priori information, model constraints or other information added to the system are not considered. The DOI calculation only takes into account the number of data points, and the data uncertainty. Thus, the DOI is purely data driven.

Always two numbers are presented for the DOI – an upper and a lower number. As a guideline the layers above DOI upper are well founded in data. Between DOI upper and DOI lower the model is not as strong in the data, and below DOI lower the model is very weak in the data, and interpreting these parts of the model should be done with caution.

To show the methodology, an example with a Transient Electromagnetic (TEM) setup is used. Assuming a simple 3-layer model, the sensitivity function can be plotted versus depth (left image in Figure 8-11). The sensitivity function comes directly from the recalculated sensitivity matrix (Jacobian). As expected, the sensitivity to the second layer is low since the TEM method has poor resolution of resistive layers, whereas there are high sensitivities to the first and the third layer. If the sensitivities are summed up from deep to shallow, the right side image in Figure 8-11 emerges. This plot shows the total sensitivity in a given depth and downwards. Next, a threshold value that indicates the minimum amount of sensitivity needed for indicative information is set. In the example in Figure 8-11 a threshold value of 5% of the cumulated sensitivity was settled upon giving a DOI of approximately 180 m. The setting of the threshold value was very much a question of tuning based on experience and comparing different models with different methods.

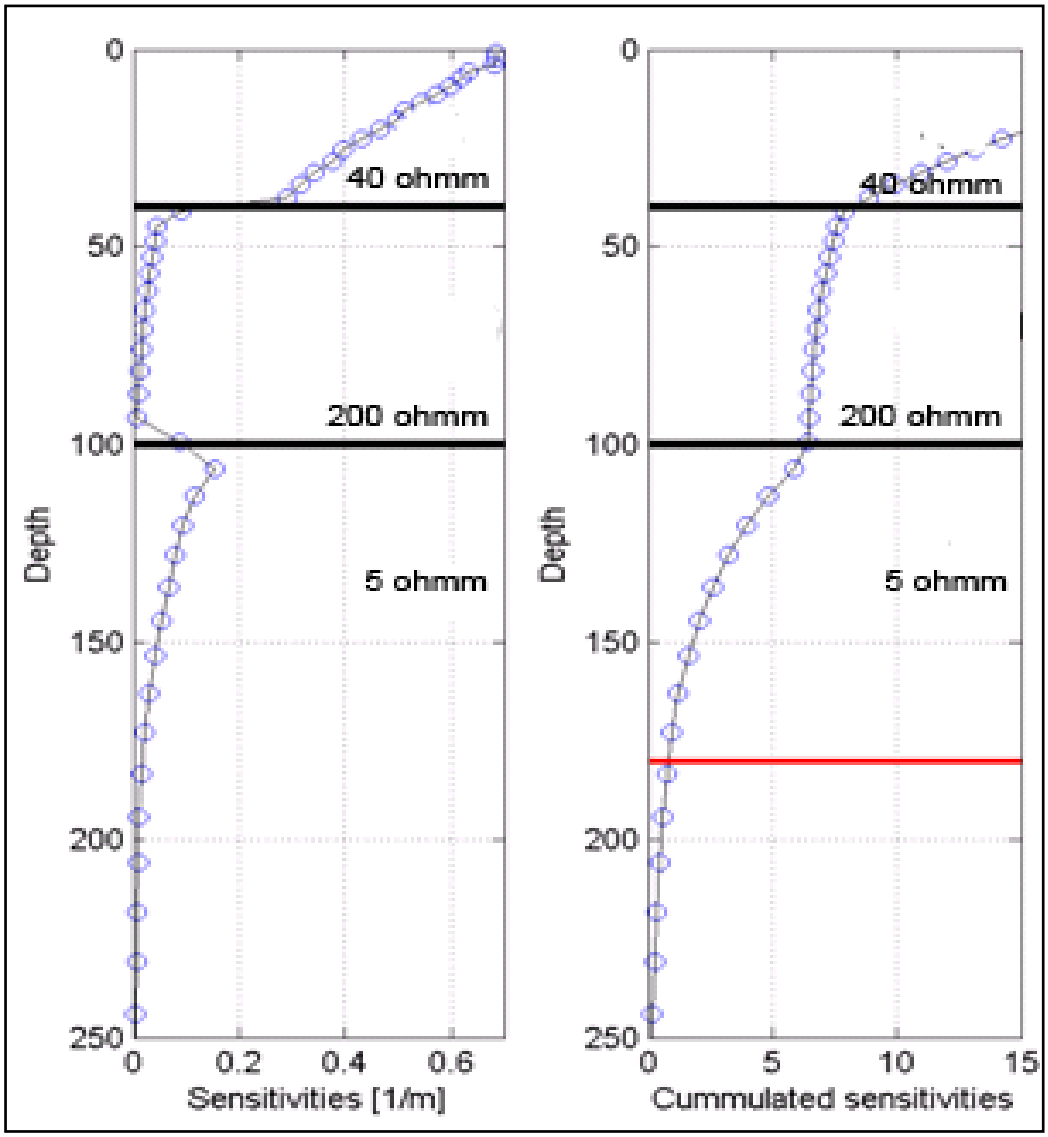



**Figure 8-11.** *Sensitivities calculated for a re-discretized version of the model indicated by the black lines; resistivities of layers are written on the plot. The left plot is the sensitivity function itself. The right plot shows the cumulated sensitivities. The red line indicates the DOI given by the threshold value.*

In this example the model was sub-discretized into many layers to support the visual understanding of the concept. In fact, it is not necessary to sub-discretize a model with few layers into more than maybe 12-15 layers to obtain a reasonably precise DOI - e.g. within 3-5 m for the examples in Figure 8-11.

The DOI for DC/IP inversions is computed as described for the TEM data for each 1D sounding (taking into account both DC and IP data) and each inversion parameter (i.e. $\rho$, $m_0$, $\tau$ and $C$). The main difference between the TEM and DC/IP application of the DOI is due to the array design of the DC/IP soundings. In fact at the edges of the profiles, the 1D soundings extracted from the DC/IP profiles contain a different number of data. In particular for the Dipole-Dipole array acquired in the site, at the edges of the profiles two different situations happen. At one edge the maximum dipole order decreases from 15 to 1. At the other edge the minimum dipole order increases from 1 to 15. While the first situation is well supported by the DOI, that shows a decreased depth of investigation at the corresponding edge of the profile, the second situation may result in misleading interpretations. In fact when the minimum dipole order increases from 1 to 15 when approaching the edge of the profile, the resolution of the investigation strongly decreases in the top part of the inversion.

The DOI alone does not allow recognizing profile areas where the information is missing in the top part. For this reason the inversion interpretation has to be guided also by the uncertainty analysis of the inverted

parameters, calculated as described in the following paragraph. Figure 8-13 shows the chargeability section for line 6, with the upper and lower DOI shown as faded grey bars (with upper and lower thresholds equal to 5% and 2% respectively). In the south-eastern part of the line 6, there is a shallower DOI, since there are no data with high pseudo-depth (maximum dipole order decreasing from 15 to 1). In the north-western part the DOI does not decrease, but the top part of the model is not resolved because of the lack of data with shallow pseudo-depth (minimum dipole order increasing from 1 to 15).

#### 8.3.3.3 *Uncertainty analysis*

On all the inversion results the uncertainty analysis on the parameters was computed through the covariance of the estimated error for linear mapping Cest described by Tarantola & Valette (1982). Because the model parameters are represented as logarithms, the analysis gives a standard deviation factor (STDF) for the ith parameter mi defined by Equation 84.

$$STDF(mi) = \exp(\sqrt{(Cest(i,i))})$$

**Equation 84**

Hence, under lognormal assumption, and assuming parameter correlations are not significant, it is 68% likely that the $i^{th}$ model parameter mi falls in the interval $mi/STDF(mi) < mi < mi \cdot STDF(mi)$ while the DOI does not depend on the prior information and on the vertical/lateral constraints, the uncertainty analysis presented in this report takes into account the constraints. For this reason in the areas where the values of the inversion parameters are constraints-driven the maximum STDF depends on the constraints values. Figure 8-13 shows the $m_0$ inversion section of line 6 shaded by both the DOI and the uncertainty analysis (with STDF > 1.25).The DOI and uncertainty analysis shading agrees well in the entire profile except at the north-western edge, where the uncertainty analysis clarifies the constraints-driven inversion part.

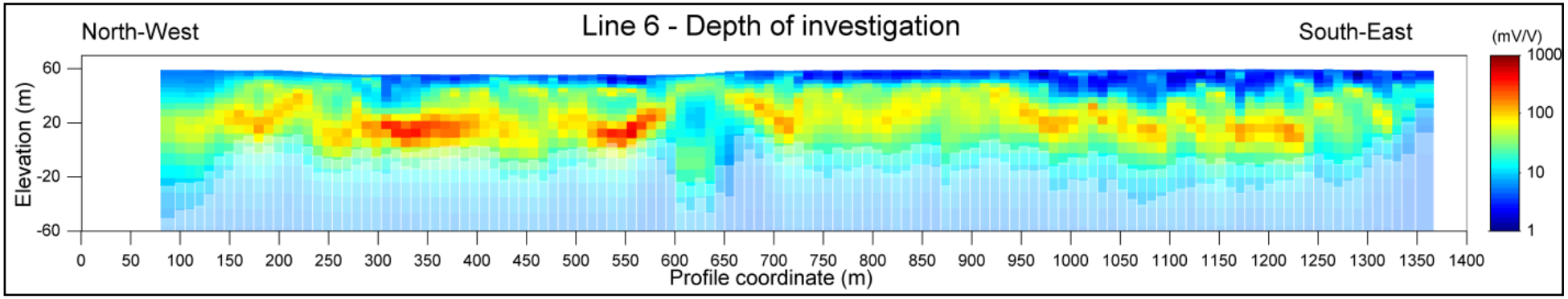



**Figure 8-12.** *Chargeability ($m_0$) section for Line 6. The upper and lower DOI is shown as faded grey bars.*

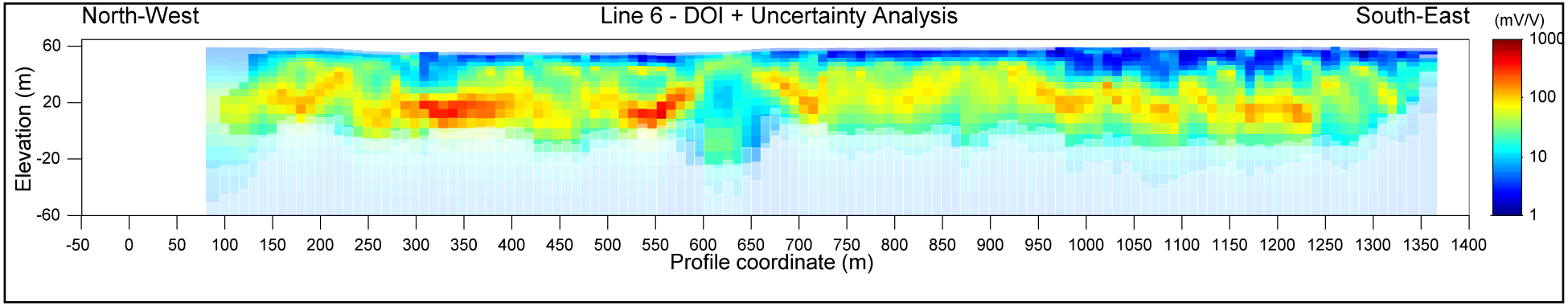



**Figure 8-13.** *Chargeability ($m_0$) section for line 6. Section shaded by both DOI and uncertainty analysis. The sections show significant lateral variability.*

#### 8.3.3.4 *Technical specifications of the Inversion and quality check*

Table 8-1 shows the inversion settings used for the smooth many-layers inversion. The inversion settings summarized in Table 8-1 have been used for all the lines.

**Table 8-1.** *Inversion settings for LCI smooth setup.*

| | | |
|---|---|---|
| **Starting model** | Number of layers | 21 |
| | Depth to first layer | 0.8 m |
| | Depth to last layer | 130 m |
| | Increasing thickness factor | 1.1 |
| | Resistivity $\rho$ | average $\rho_{apparent}$ $\Omega$m |
| | Intrinsic chargeability $m_0$ | 5 mV/V |
| | Time constant $\tau$ | 1 s |
| | Frequency exponent C | 1 [dim-less] |
| **Vertical/horizontal constraints** | Constraint on $\rho$ [factor] | 2.0/1.2 |
| | Constraint on $m_0$ [factor] | 2.0/1.2 |
| | Constraint on $\tau$ [factor] | 2.0/1.2 |
| | Constraint on C [factor] | 2.0/1.2 |
| | Constraint on thickness | Fixed thicknesses |
| | Constraint on depth | Fixed Depths |
| **DOI settings** | Number of layers | 25 |
| | First depth | 0.8 m |
| | Last depth | 300 m |
| | Relative high threshold | 5% |
| | Relative low threshold | 2% |

After the inversion the individual DC sounding curves and induced polarization decay curves are manually inspected to ensure that the data are correctly fitted along the entire profiles. Figure 8-14 shows an example of a DC sounding curve (left in the figure) and the corresponding induced polarization decay curves (on the right) For each quadrupole there is an DC measurement and a corresponding induced polarization decay curve. The 1D approximation of the forward response implies the impossibility of fitting the DC data within the data error when significant 2D variations are present. For instance this happens when different quadrupoles at the same pseudo-depth exhibit values that differ more than the data errors. In this case the forward data resulting from the inversion represent an average of the field data, also driven by the lateral constraints along the profile. This effect is higher for the DC data, compared to the IP data. For this reason the residual for the DC soundings represents mainly a 1D misfit, as compared to the induced polarization data fit.

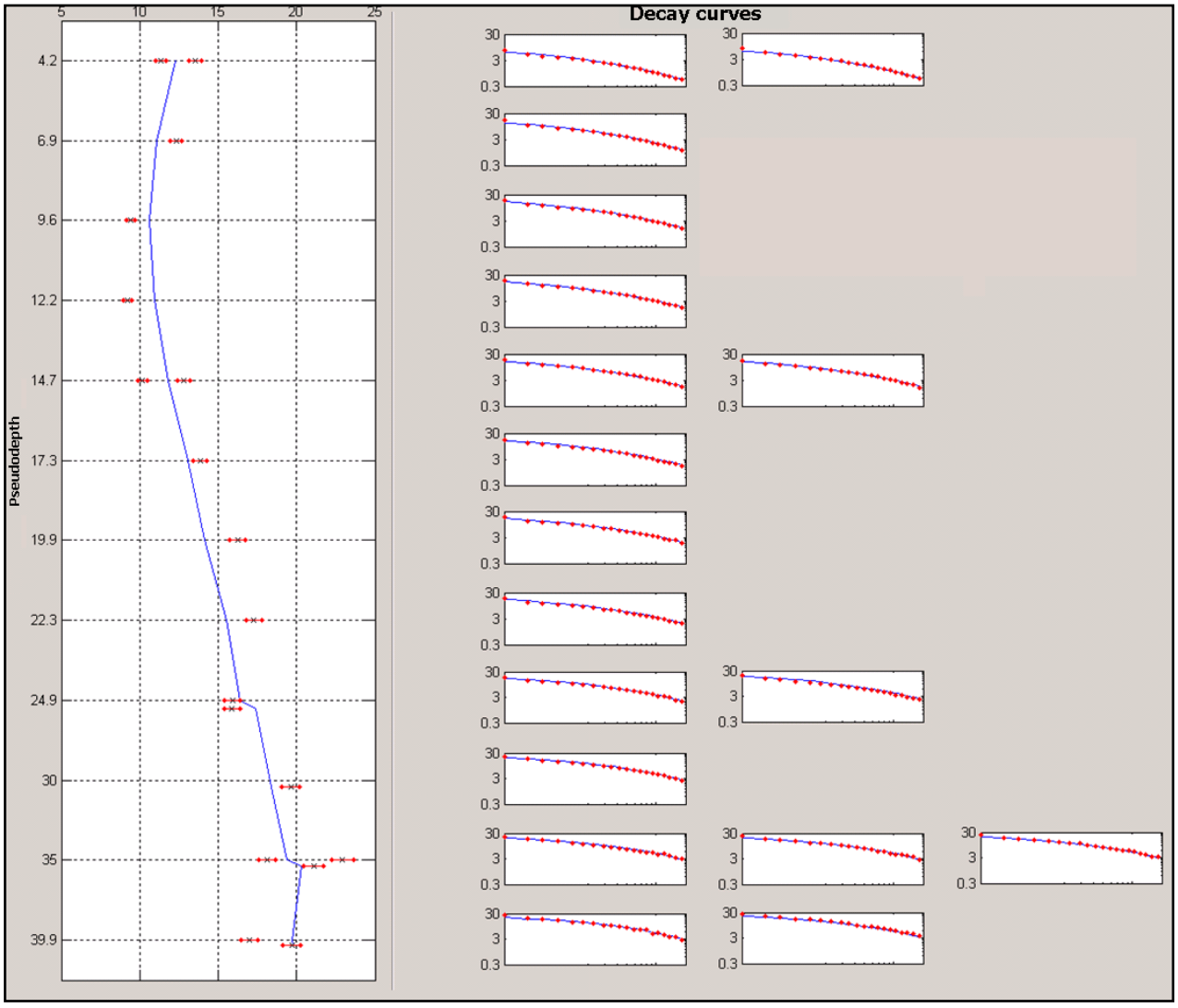



**Figure 8-14.** *Example DC sounding curve and IP decay curves. Left: DC sounding curve. The data-points are plotted as red dots with error bars, and the actual fit as a blue line. Right: Induced polarization decay curves. The measured induced polarization data-points are shown as red dots with error bars, and the datafit as a blue line.*

## 8.3.4 Results

### 8.3.4.1 *DC/IP results*

All the DC/IP lines have been inverted with the algorithm and the settings presented in the former paragraphs, the inversion parameters being the four Cole-Cole parameters ($\rho$, $m_0$, $\tau$ and $C$). In order to facilitate the comparison with the Geoscience Australia AEM survey, in the following figures the resistivity plots are presented in terms of electrical conductivity $\sigma=1/\rho$, instead of resistivity $\rho$.

Figure 8-15 presents the inversion of line 8, with one section for each inversion parameter. The high and low DOI are indicated in the plots by shading with semi-transparent rectangles the poorly resolved model areas. All the inversion sections show pseudo-layered models, but with significant lateral variability of the parameter values, especially in the conductivity section (Figure 8-15a) and the $m_0$ section (Figure 8-15b).

The conductivity section (Figure 8-15a) presents a highly conductive (conductivity above 0.3 S/m) shallow (up to 10 m deep) layer and a conductive (conductivity above 0.1 S/m) deep (elevation below 20 m) patchy layer, at the limit of the depth of investigation. The conductivity in the area between the shallow and the deep conductive layers decreases significantly, and large lateral variations are present.

The $m_0$ section (Figure 8-15b) presents two layers with high $m_0$ values ($m_0$ above 50 mV/V), but again with large lateral heterogeneity. The elevation of the shallower chargeable layer is not compatible with the shallow conductive layer of the σ section, while the deep chargeable layer is in agreement with the deep conductive one. Based on our experience the non-compatibility between the depths of the shallow conductive layer and the shallow chargeable layer is not explainable in terms of model-equivalence and/or lack of resolution, because of the shallowness of the layers. In fact the DC/IP algorithm used for inverting the data has proven its capability of retrieving the correct depth of shallow chargeable anomalies both in synthetic studies (Fiandaca *et al*., 2012) and field studies with borehole verification (Gazoty *et al*., 2012). The absence of a high-$m_0$ layer corresponding to the shallow high-σ layer can be explained by two reasons, probably both affecting the result. First of all the high conductivity damps the magnitude of the IP decay, as shown in Slater & Glaser (2003). Secondly the τ value in the top part of the line is small, indicating fast decays that could be below the limit of detectability with the used time range in the IP acquisition. The low IP response in the clays may be due to low moisture contents and/or small quantities of fresh groundwater in the pores in the clay in this area. The clays are also quite compacted in this area.

The τ section (Figure 8-15c) shows increasing values of τ with depth, above 2 seconds at elevations below 5 m. The elevations of the deep high-$m_0$ layer and the deep high-τ layer are slightly different, but this difference could be due to model-equivalence. In fact the contribution to the forward response of the top part of the deep chargeable layer, where τ exhibits low values, is small when compared to the high-τ bottom part. Consequently the bottom part of the deep chargeable layer (where both $m_0$ and τ are well resolved – see Pedersen & Fiandaca, 2011), is less affected by model-equivalence than the top part (where τ is not well resolved). Nevertheless, the discrepancy in elevation of the high-$m_0$ and high-τ sections could be due also to the soil complexity, considering that the gamma logs close to the line 8 present thin layers with moderate cps in the top part of the high-$m_0$ deep layer. In any case, the high-τ values of the deeper high-$m_0$ layer indicate varying soil texture, when compared to the shallow high-$m_0$ layer.

Also the C section shows layered anomalies (Figure 8-15d), with a good spatial correlation between the high-$m_0$ layers and the high-C layers.

The lateral variations in the high-$m_0$ layers are spatially correlated with the lateral variations of conductivity: high $m_0$ values correspond to low σ values. This correlation can be explained introducing the concept of normalized chargeability. Several studies in the laboratory showed that the better parameter for soil discrimination and clay detection with IP is the chargeability normalized by the resistivity of the soil, instead of the chargeability alone (Slater & Lesmes, 2002). The normalized chargeability in fact is less influenced by the conductivity of the water contained in the soil and allows the discrimination of lithotypes in presence of variation of the fluid and ion content.

For this reason all the inverted lines are presented in the following in terms of conductivity σ and normalized integral chargeability <m>σ. The normalized integral chargeability section has been computed from the inversion parameters in two steps. The integral chargeability <m> is calculated by computing the average chargeability in the acquisition time range for each inversion layer of each 1D model. This average depends on the values of the three Cole-Cole parameters $m_0$, $\tau$ and $C$ and weights more the layers with high-τ values. It has to be noted that using the integral chargeability after inversion is not equivalent to the direct inversion of the integral chargeability. In fact it is possible to include the waveform effect in the forward response computation only by describing the time characteristic of the decays (in terms of $\tau$ and $C$). We chose to use the <m> values in the normalized chargeability plots to take into account both $m_0$ and $\tau$ sections, considering that these parameters do not show anomaly patterns perfectly correlated in depth. The second step in the <m>σ computation is the multiplication of the integral chargeability <m> by the conductivity σ obtained in the inversion process.

All the inversions of the DC/IP lines contained in Appendix 10 (Apps *et al*., 2012d) are displayed in terms of conductivity σ and normalized integral chargeability. <m>σ. The sections are shaded by both DOI and uncertainty analysis (high DOI threshold = 5%; low DOI threshold = 2%; uncertainty analysis STDF threshold = 1.25). Considering that the <m>σ values are not direct inversion parameters, the lower DOI values and higher STDF values of the four parameters have been used for the plot shading. Induction logs and gamma logs are superposed on the conductivity and normalized chargeability sections respectively. The

same x and z scale has been used for all the lines, to facilitate the comparison. Finally, the inversion models with all the four Cole-Cole parameters and the corresponding uncertainty analysis (Pedersen & Fiandaca, 2011) are shown in Appendix 10 (Apps *et al*., 2012d).

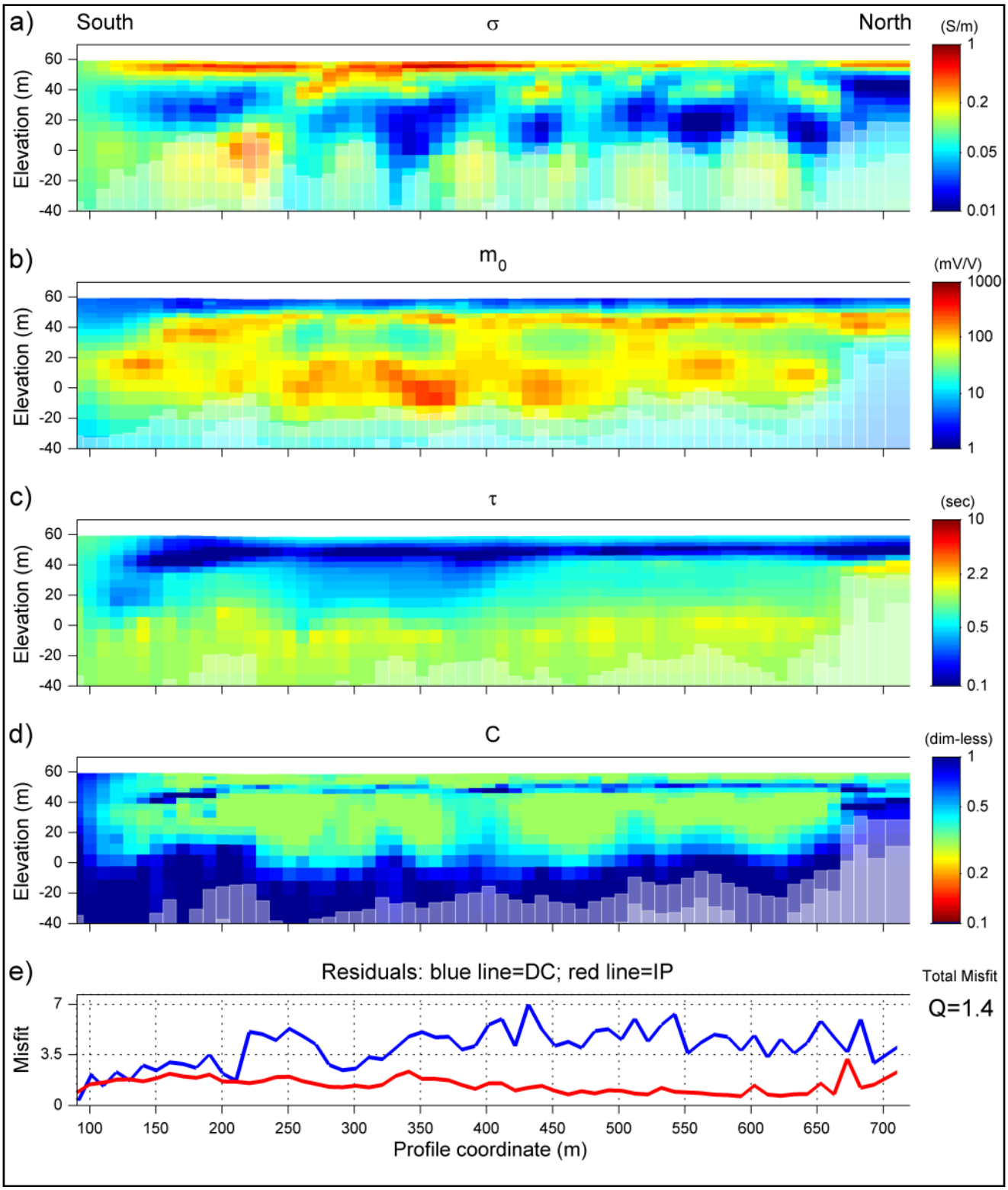



**Figure 8-15.** *Sections for Line 8. a) Conductivity section b) Chargeability section c) Time constant section d) Frequency dependency section e) Misfit plot for DC and IP data.*

Summarizing the results of all the inversions, four main characteristics can be recognized:

- A conductive shallow (depth < 10 m) layer is present in all the lines in good agreement with the induction logs, but with significant lateral variations in line 4, line 1 and line 2. A corresponding layer is not clearly shown in the <m>σ sections, even if the normalized chargeability shows often increased values in correspondence of the conductive layer. The gamma logs show really high values in the depth range of this layer.
- A chargeable layer, approximately at elevations comprised between 50 m and 30 m, is present in all the lines except line 2. A corresponding layer is not clearly shown in the conductivity sections, even if spatial correlations are present in some profiles. In the same depth range the logs show increased gamma and conductivity values.
- A deep chargeable layer, with elevation below 20 m, is present in line 8 and partially in line 6, at the limit of the depth of investigation. The other lines show chargeable anomalies at the same depth, but the layering is less evident or not present at all. The σ sections show patchy conductive anomalies at corresponding depth. The logs show high gamma and conductivity values at elevations close to 0 m.
- All the inversions show high lateral heterogeneity, especially when approaching the river (line 1 and line 2; northern part of line 3 and line 4).

As clearly shown by the uncertainty analysis, a quantitative comparison between inversion results and log information is often difficult because of the position of the boreholes, too close to the edges of the profiles. Considering these limitations, the comparison is definitively satisfactory.

### 8.3.5 AEM, Induction and Gamma Log Comparison

The inverted DC/ IP lines have been thoroughly compared with the airborne electromagnetic (AEM) profiles measured in the survey area. Figure 8-16 shows the location of the DC/IP lines and the crossing AEM profiles. In Figure 8-16 the AEM profiles are shown as red lines with the individual soundings as black dots on top, and the DC/IP lines as yellow lines with the individual soundings as black dots on top. As seen in Figure 8-16, none of the AEM profiles is located at the same location of any DC/IP lines, which makes a direct comparison difficult even though at a few locations the profiles cross each other.

In order to compare the lines it was decided to use DC/IP lines and AEM profiles that are aligned parallel, instead of comparing interpolated profiles from the AEM grid, since the interpolation will strongly influence the comparison.

When comparing ground geophysical inversion results with borehole logs, it must be remembered that the borehole log – both conductivity and gamma logs – have a sensitivity volume that it orders of magnitude smaller than that of the ground geophysical measurements. There is therefore ample possibility of seeing discrepancies between borehole and ground geophysical results, and the comparisons in the following sections must be seen in this light.

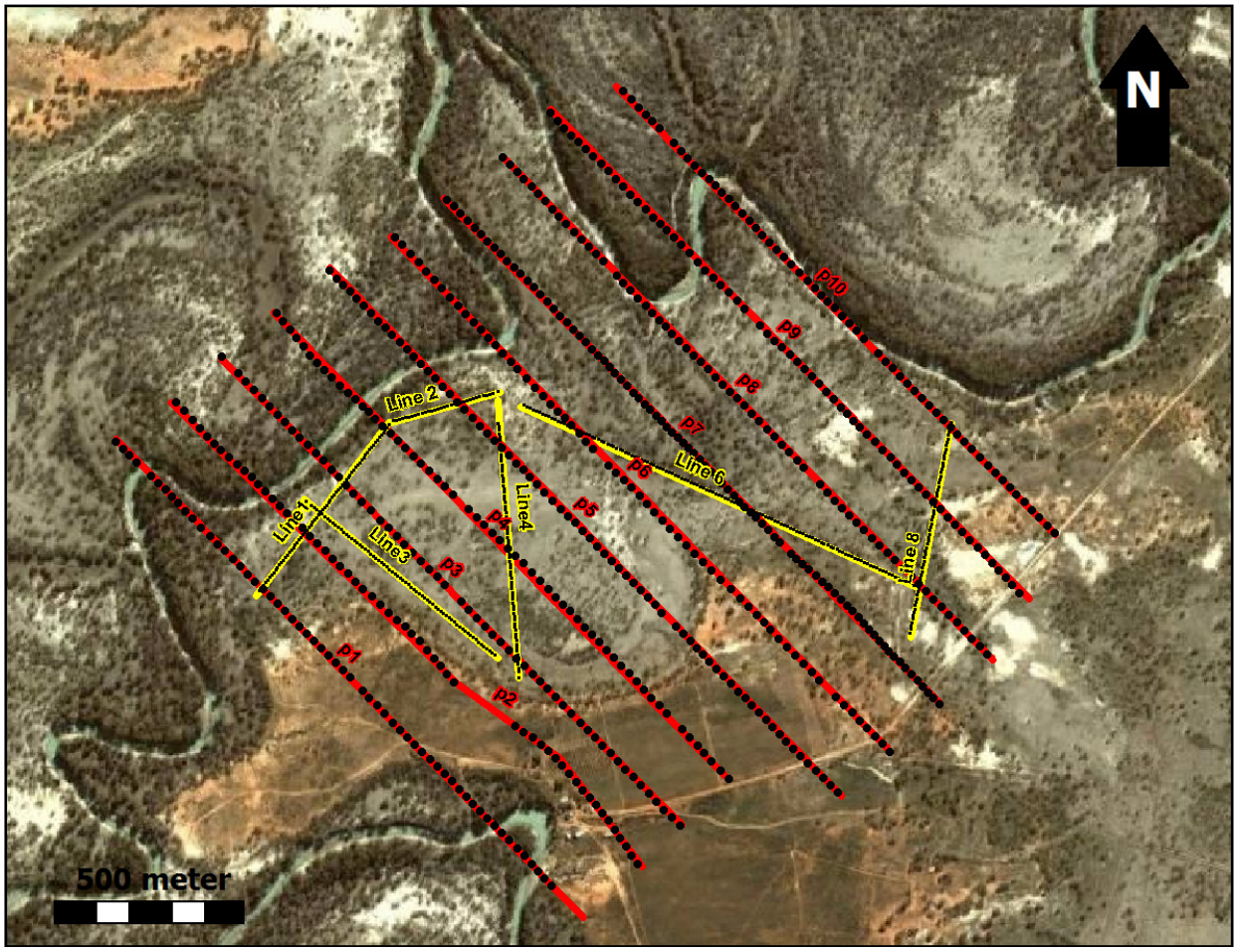



**Figure 8-16.** *Map showing AEM profiles and DC/IP lines. The DC/IP lines are shown as yellow lines and the individual soundings as black dots. The AEM profiles are shown as red dots with the individual soundings plotted as black dots.*

The following text will focus on DC/IP line 3 and profile 2 and 3 from the initial Christensen (2011) AEM inversions. It is important to note that a distance of 70 m exists between profiles hence they do not overlap completely. Figure 8-17 shows a comparison of the conductivity and normalized integral chargeability sections of DC/IP line 3 and AEM profile 2 and profile 3. Judging from Figure 8-17 there are four key-points that should be noticed:

- There are clear lateral variations in the DC/IP line, especially in elevation from 40 to 0 meters.
- Very small lateral variations are present in the Geoscience Australia AEM inversions - the characteristic of the AEM sections looks very smooth.
- The conductivity at elevations between 30 and 0 m is lower in the DC line, as compared to the Geoscience Australia AEM profiles, but the same layer is seen in both DC and AEM sections.
- Generally the same layers are seen in both conductivity model sections, except for the conductive layer with elevation between 50 m and 30 m, clearly present only in the AEM inversions and picked up in the 99-1 induction log. A chargeable layer is present in the <m>σ section of line 3, with depths that in some places agree with the high cps layer of the 99-1 gamma log and in some places not.

At first glance, the initial Christensen (2011) AEM inversions appear to have tight lateral constraints, since both the models from profile 2 and 3 show a pancake structure in the entire survey area. The survey area is a fluvial landscape, hence the geological sequence is highly influenced by the Darling River that cuts the banks and puts in place different kind of deposits in the area. One would thus not expect a homogeneous pancake structure in the area, and this might be driven by the lateral constraints in the AEM inversion.

The lower conductivity in an elevation of 30-0 m in the model for line 3, as compared to the Geoscience Australia AEM profiles can be explained by the higher sensitivity of the DC method towards less conductive layers. Whereas the transient electromagnetic method has high sensitivity and resolution of good conductors, the method are to a strong degree affected by high resistivity equivalence, and hence the conductivity of less conductive less will be poorly determined.

For the same reasons the conductive layer at elevations between 50 m and 30 m clearly evident only in the AEM inversions could be less resolvable in the DC line, but the layer is resolved in the chargeability section.

To clarify if the lateral variations in the Geoscience Australia inversions are smoothed out by the lateral constraints and/or by the approximation in the forward response, a spatially constrained inversion (SCI) was run for the collected AEM data in the entire DC/IP survey area. The Aarhus Workbench settings for the smooth SCI inversion are shown in Table 8-2.

**Table 8-2.** *Inversion settings for smooth SCI setup.*

| Item | | Value |
|---|---|---|
| **Software** | Aarhus Workbench version | 3.3 |
| **SCI cells** | Approximate cell size [number of models] | 75 |
| | Number of layers | 19 |
| | Starting resistivities [Ωm] | 30 |
| | Thickness of first layer [m] | 1.5 |
| | Depth to last layer [m] | 150 |
| | Thickness distribution of layers | 1.1 |
| | Horizontal constraints of resistivities [factor] | 3.0 |
| | Vertical constraints of resistivities [factor] | 5.0 |
| | Reference distance [m] | 30 |
| **SCI constraints/ Prior constraints** | Prior thickness | Fixed |
| | Prior resistivities | None |
| | Prior on flight altitude [m] | 3.0 |
| | Lateral constraints on flight altitude [factor] | 1.3 |
| | Minimum number of gates per moment | 7 |

Figure 8-17 shows the Geoscience Australia AEM inversion results for profile 2 and 3, and the DC/IP line 3. Notice that exactly the same dataset and soundings have been used for the SCI AEM and Geoscience Australia AEM inversion. The SCI inversion has loose vertical and horizontal constraints, and compared with the Geoscience Australia AEM inversion results, the lateral variations are much more evident in the survey area. The lateral variations seen in the DC/IP lines are also seen in the AEM inversions.

The lateral variations are also evident in the induction logs, which is clear when comparing all the induction logs that line 8 crosses. Even though the line is only 700 m long, there are strong lateral variations in the induction logs. Finally a consideration on the conductive layer always present in the Geoscience Australia AEM inversions at elevations comprised between 50 m and 30 m is needed. This layer is often present also in the SCI inversions, with much higher lateral variations. But sometimes the layer is not shown at all in the SCI inversions in disagreement with the induction logs that indicate its presence. The continuous presence of this conductive layer in the Geoscience Australia AEM inversions might be driven by the joint inversion of induction logs data together with tight lateral constraints, instead of driven by the AEM data.

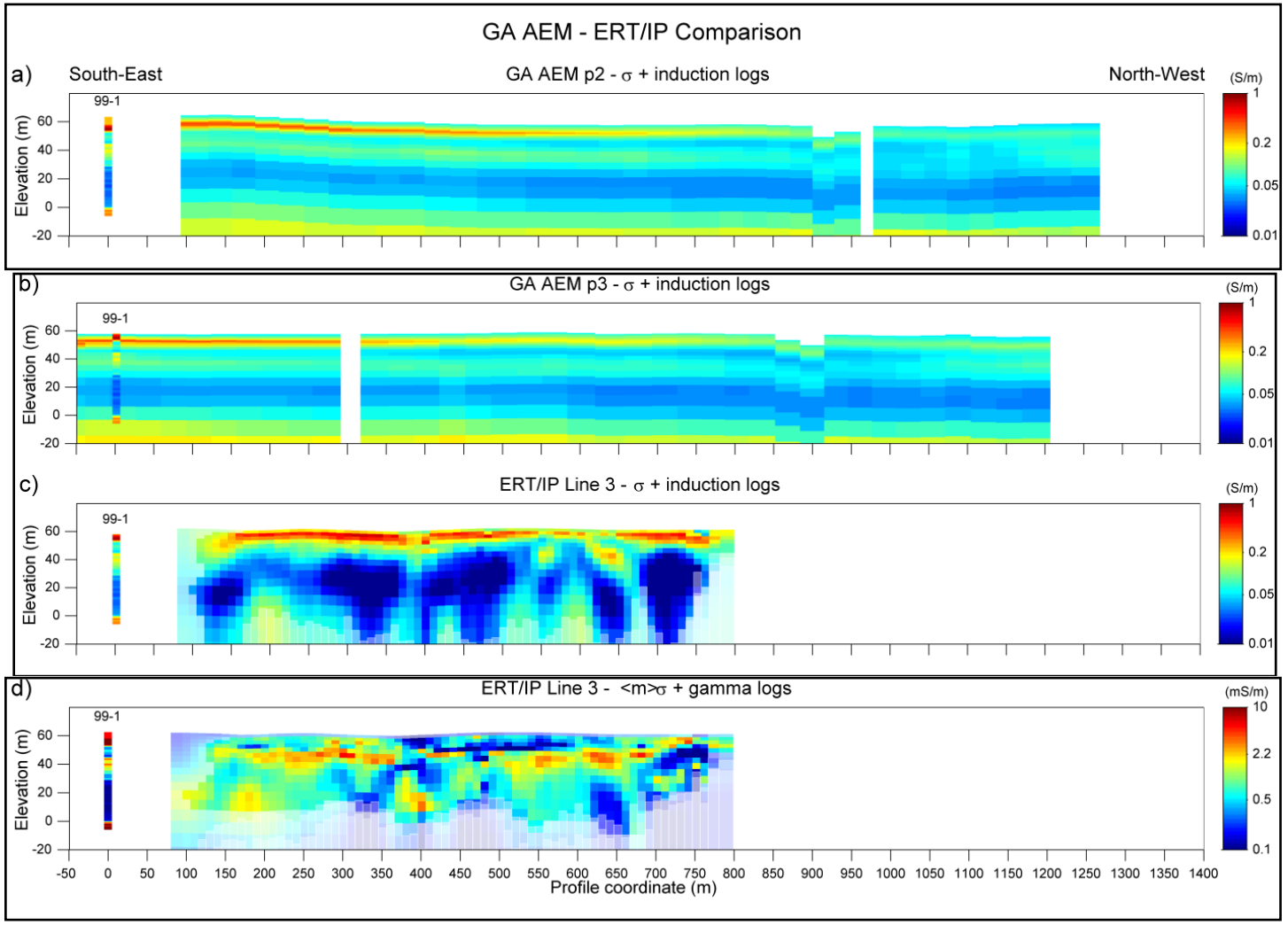



**Figure 8-17.** *Comparison between AEM inversions provided by Geoscience Australia and DC/IP line 3. a) Geoscience Australia AEM profile 2; b) Geoscience Australia AEM profile 3; c) DC/IP line 3, σ section; and d) DC/IP line 3, <m>σ section; with borehole gamma logs plotted in the model sections.*

It is difficult to make a direct comparison between the DC/IP lines and the induction/gamma logs, since almost all the logs are located at the edge of the profiles. But for line 8 there is an induction/gamma log in the center of the profile, where also the AEM profile 8 intersects the line. Figure 8-18 shows the comparison among the inverted conductivity for the induction log 33-8, for the closer Geoscience Australia AEM and SCI AEM models of p8, and for closer DC model of line 8. It should be noted that for the Geoscience Australia AEM inversion, the induction log and AEM data are jointly inverted. All inversions see clearly the near-surface conductive layer in 0-10 m depth but, as expected, both the Geoscience Australia and SCI AEM inversions resolve better the conductive layer in 10-20 m depth. The DC/IP inversion and the Geoscience Australia AEM inversion are the ones closest to the resistive area in 20-30 m depth while the SCI inversion indicates high conductivities. The conductive layer in 30-40 m depth is not clearly indicated by any of the inversions, while the rise in conductivity at 40-50 m depth is reflected only in the DC/IP inversion which, however, stays at high conductivities where the log clearly decreases to lower values at a depth of 45 m. However, his depth range is really below the DOI of the DC/IP inversion.

Figure 8-19 shows the comparison between the normalized integral chargeability and the gamma log 33-8, in the DC/IP sounding where line 8 crosses the log 33-8. As can be seen there are evident differences between the DC/IP sounding and the gamma log in the top 10 m while the – on average – slow rise of the gamma count in the depth interval 10-45 m is reflected in an average increase in the normalized integral chargeability. The DC/IP inversion indicates a rise in chargeability below 45 m, but much of this interval is below the DOI if the DC/IP inversion.

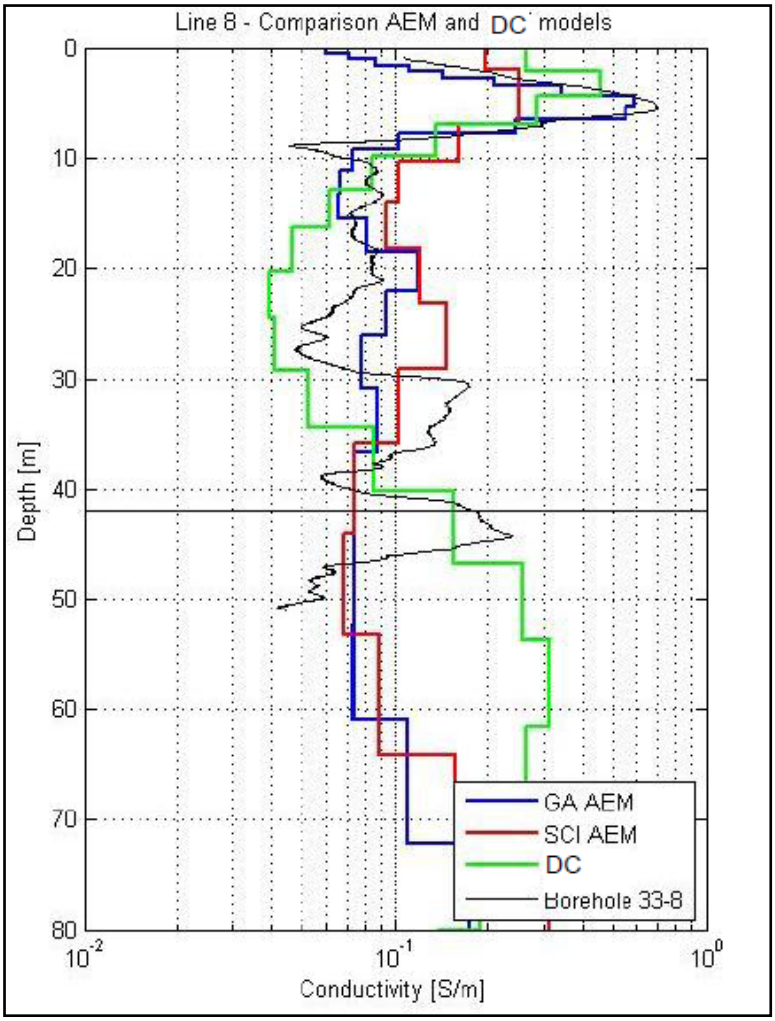



**Figure 8-18.** *Comparison between the inverted conductivity for Geoscience Australia (initial Christensen) AEM, SCI AEM, DC and the induction log BHMAR33-8, where line 8 and profile 8 cross the log. The black line marks the DOI for the DC sounding.*

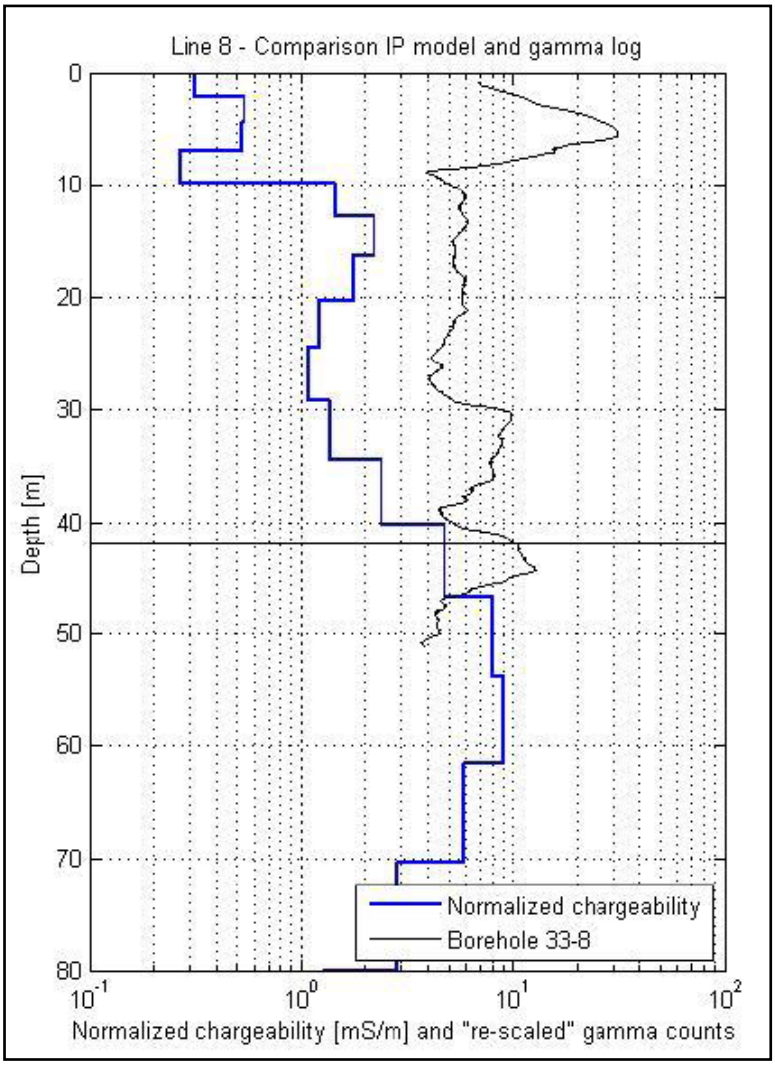



**Figure 8-19.** *Comparison between the normalized integral chargeability and the gamma log BHMAR33-8 in the sounding where line 8 crosses the log BHMAR33-8. The gamma log cps values have been divided by 100 to facilitate the comparison on the same scale. The black line marks the DOI for the IP sounding.*

### 8.3.6 Geological Comparison

In the following a comparison between the ground-based IP results and the geological description in the Jimargil area is made. The geological description of the Jimargil area provided by Geoscience Australia is explained in Lawrie *et al*. (2012c), and furthermore the geology along the individual lines is summarized.

From the geology description of the Jimargil area it is worth nothing that it is a geological and hydrological complex area, which will influence not only the measured conductivity, but also the IP signal. The strong variability in saturation within individual layers, and the fact that there are differences in groundwater salinity will influence the geophysical results. Furthermore the alternation of several layers with medium/high clay content gives serious problems of resolution in discriminating the different geological layers present in the site.

Figure 8-20 and Figure 8-21 show the IP lines together with the geological description of the boreholes plotted on top. The grey line between the boreholes shows a simple linear interpolation of the extent of the Blanchetown Clay between neighbouring boreholes.

For line 1 (Figure 8-20a) the Blanchetown Clay is seen as a layer with a normalized chargeability of 1-5 mS/m, in an elevation of 32-45 m. In many places there is also a signal below and above the Blanchetown Clay, which most likely corresponds to the clay-rich top of the Calivil Formation. However, there are also

chargeability highs above the Blanchetown clay interval indicated by the simple linear interpolation between the boreholes and chargeability lows such as the ones between a profile distance of 400 to 450 meters and 550 to 600 meters.

Line 2 (Figure 8-20b) present and image of considerable lateral variations in the conductivity, and it is difficult to see a consistent correspondence between the interpolated Blanchetown Clay interval and the IP section.

Line 3 (Figure 8-21a) presents a better correspondence between the extrapolated depth interval of the Blanchetown Clay and the chargeability than what was seen in Figure 8-20, but the chargeable layer seems to become more shallow toward NW.

The Blanchetown Clay is clearly seen at line 4 (Figure 8-21b) as a layer with a high normalized chargeability of above 1 mS/m, but it also reveals that the layer is most likely situated at a greater depth, and hence a simple linear interpolation between boreholes does not work here. In the interval 250-350 m the chargeable formation seems to lie above the extrapolated Blanchetown Clay depth interval. The thickness of the Blanchetown Clay is known to vary a lot in the area, due to undulating palaeo-topography and post-depositional erosion.

### 8.3.7 Discussion and Conclusions

The geophysical model obtained by the inversion of the DC/IP data for the Jimargil area shows, with lateral variations in the site, three layers well matching in depth with the high conductivity/gamma counts layers found in the borehole logs. In particular the layer at elevations comprised between 50 m and 30 m is clearly shown in the major part of the normalized integral chargeability sections, while it is not well depicted by the corresponding conductivity sections, probably because of the lack of resolution of the DC method for this thin conductive layer, and because of the variability in conductivity of the layer resulting from highly variable pore fluid compositions (400-20,000 EC), and variability in clay type.

The DC/IP and the AEM inversions show a common general trend between the conductivity sections, even if the conductive layer between 50 m and 30 m in elevation is much better resolved by the AEM inversions and the resistive area below the conductive layer is more contrasted in the DC/IP sections. These differences are reasonably due to the different sensitivities of the two methods to the conductive and the resistive anomalies, respectively.

A second and significant difference between the DC/IP conductivity models and the initial Christensen AEM conductivity models is in the lateral variability of the models, much more pronounced in the DC/IP inversions. A SCI inversion of the AEM data without approximations in the 1D forward response and with loose vertical and lateral constraints was performed to investigate the cause of the different lateral variability of the DC/IP and AEM conductivity profiles. The DC/IP and SCI models show a much more similar lateral heterogeneity, indicating that the difference with the Geoscience Australia AEM models might depend on the inversion settings and/or on the forward algorithm. The analysis in this chapter was incentive to reconsider the vertical and lateral regularization of the final AEM inversion (Christensen, 2012).

The comparison between the borehole description and the IP lines showed some agreement with the geology in the area, but the correspondence between the chargeability highs and the Blanchetown Clay varies significantly over the area.

Overall, the resistivity and IP surveys deliver a more detailed resolution of the conductivity structure that can be provided by airborne geophysical methods. With their better resolution, the resistivity and IP survey demonstrated a very high degree of complexity of the geological setting where they were carried out, but were nevertheless able to outline - sometimes exclusively through the IP response - the presence of clays in the depth range of 10-30 m. In similar geological regimes in the BHMAR area, i.e. in the fluvial plain

environment, the same degree of complexity must be expected, a fact that has been taken into account in the overall (hydro)geological interpretation of the BHMAR area.

### 8.3.8 Recommendations and Future Work

For future surveys with depth of investigation up to 30-40 m it could be useful to use multi-electrode systems, in order to decrease the acquisition time. Multi-electrode systems consist of a number of electrodes, typically 40-100, which are connected to the ground along a line with the same distance between the electrodes. The electrodes are through cables connected to an instrument which is placed central in the configuration and controls the switching unit, current waveform, potential measurement etc. In comparison with traditional soundings methods, the multi-electrode systems are faster to be set up in the field and allow acquiring arrays different from the dipole-dipole in a time-effective manner. Using arrays different from the dipole-dipole it is possible to reduce the stack size of the measurements without decreasing the signal-to-noise ratio. This results in a faster acquisition.

With regards to survey design, it would be useful to have the induction and gamma logs located closer to the centre of the lines where possible. It was not possible to do this in this area because of logistic constraints. A helping tool for selecting the mutual position of lines and logs is the plot of the quadrupole sequence selected for the survey in a pseudo-section. The edges of the lines, where the data coverage in the pseudo-section is incomplete, should be avoided for comparing lines with logs and crossing lines. The comparison of crossing lines is also recommended, as well as the comparison with logs, because it confirms inter-line consistency, which gives a quick idea of the inversion algorithm is working correctly. Finally, if a comparison is planned with other geophysical methods, it would be easier to compare the results acquiring coincident lines, which was also not possible here due to logistic constraints.

Future work should also examine the potential effects on the IP results of significant iron cementation in parts of the Calivil Formation aquifer, while further assessment of the water content and solutes in the Blanchetown Clay is also recommended to guide interpretation of any future ground geophysical surveys.

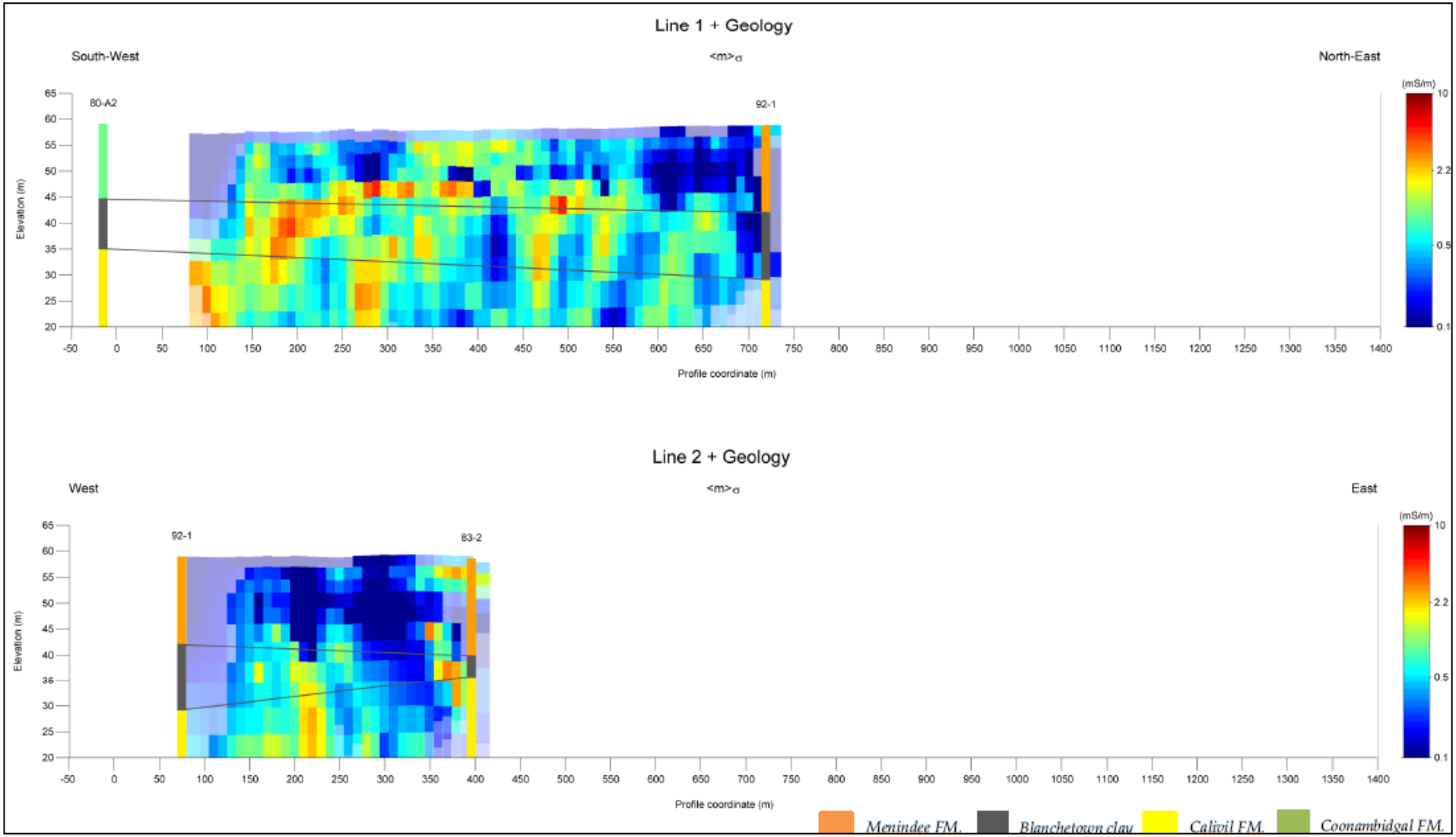



**Figure 8-20.** *IP sections for Lines 1 and 2. Top image is Line 1- IP section with focus on the upper 50 m and boreholes plotted on top. Bottom image is Line 2- IP section with focus on the upper 50 m and boreholes plotted on top.*

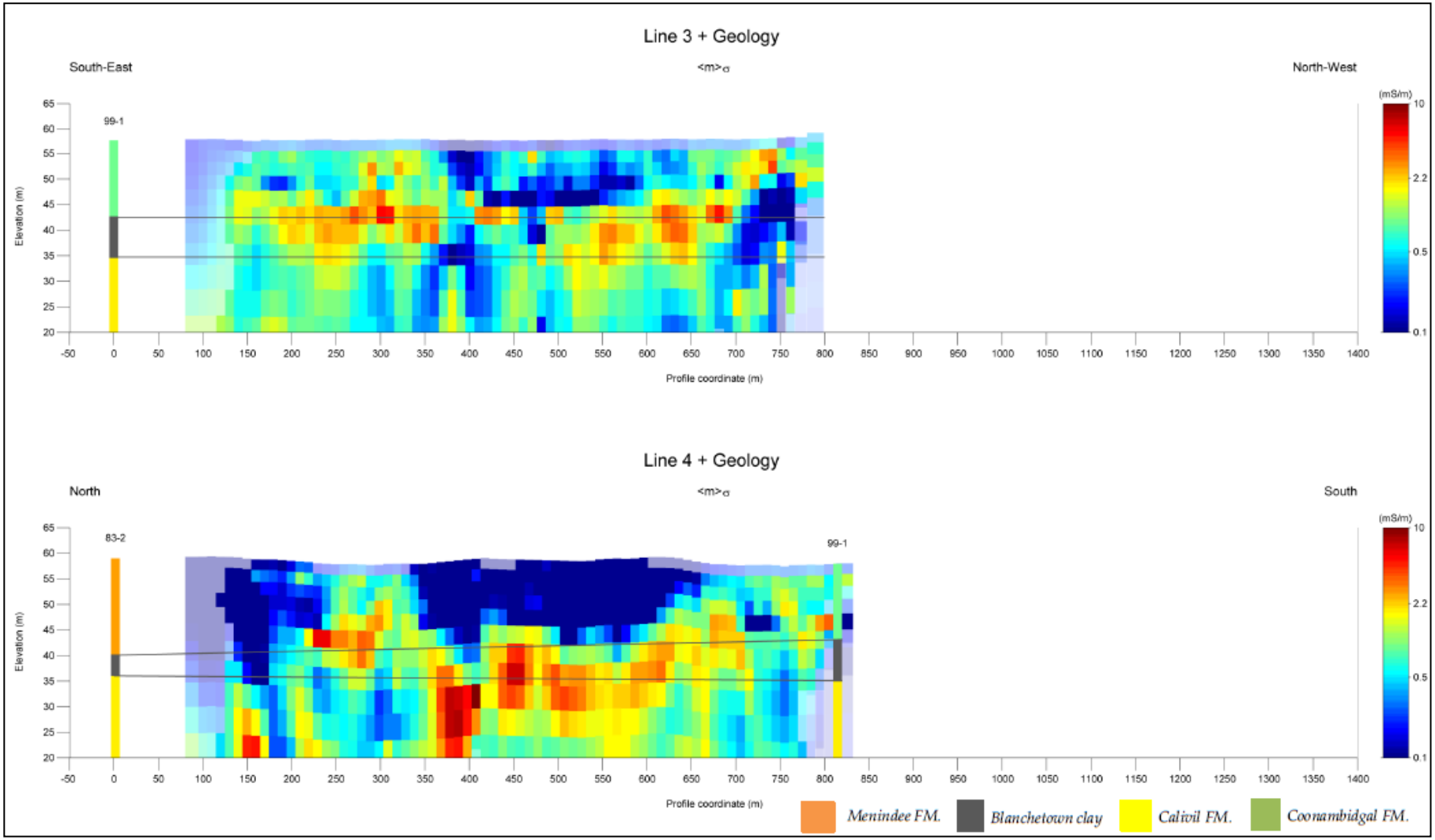



**Figure 8-21.** *IP sections for Lines 3 and 4. Top image is Line 3- IP section with focus on the upper 50 and boreholes plotted on top. Bottom image is Line 4- IP section with focus on the upper 50 m and boreholes plotted on top.*

# 9 In-River Geophysical Surveys and Sediment Sampling

## 9.1 PROJECT REQUIREMENTS AND SURVEY OPTIONS

### 9.1.1 Background

An understanding of the hydraulic connection between the Darling River and the alluvial aquifers in the target area is critically important for:

- Assessing bank filtration and basin infiltration options associated with a managed aquifer recharge scheme;
- Defining the magnitude of groundwater recharge, and thereby establishing sustainable extraction rates.

Existing datasets were reviewed, and found to be of poor quality, so to achieve the desired outcomes, new in-river surveying was required to:

- Map surface-groundwater connectivity, specifically the preferred leakage points from the river base to the underlying aquifers; and
- Determine the nature and extent of the sediments at the base of the river.

Investigations to date (from drilling, geophysics, and hydrogeochemistry of bore water samples), combined with local information about river flows, suggest there is significant leakage of the river to underlying aquifers (both the shallow Coonambidgal/Menindee and underlying Calivil Formation). However, the nature and dynamics of river leakage in the target area appear to result from a complex interplay between the geometry of the aquifers, the depth of incision of the river, the composition and thickness of the river bed sediments, and the river-flow conditions

The current conceptual understanding is that groundwater recharge occurs at points along the river where the river is deeply incised into a pre-existing sediment profile and/or where there are sandy substrates beneath the river. In both instances, recharge is likely to occur only in reaches of the river where underlying aquitards (such as the Blanchetown Clay) are limited or non-existent. These become focused zones of river leakage (and consequently aquifer recharge zones). In-river surveying was required to confirm this conceptual model and to achieve the objectives outlined above. Without this information, it would have been difficult to provide the site-specific information required to properly assess the MAR options in the target area, or properly assess the groundwater resource and environmental impacts of potential groundwater extraction. In-river survey data is contained in Appendix 10 (Apps *et al*., 2012d).

### 9.1.2 Technologies for In-river Surveys

#### 9.1.2.1 *Single-beam echo sounder*

Initial single beam echo sounder surveys were conducted to map a single profile of river depths down the centre of the river. The initial echo-sounding survey allowed specific reaches to be targeted for more detailed investigation. This included sub-bottom profiling to understand the nature of underlying sediments and recharge ‘holes’.

The system works by periodically sending a single cone shaped discrete sonar pulse to the riverbed beneath the vessel then recording the reflected sound. As the vessel moves forward, the repeated echo sounder pulses (pings) produces a single point echo recording of the riverbed. The system records the reflection time to measure water depth. The operating frequency is 200 kHz. GPS navigation points were also inserted into the data record. The survey route was about 20 km along the Darling River within the project area.

#### 9.1.2.2 *Multibeam echo sounder*

The multibeam echo sounder system maps the riverbed by periodically sending a sonar pulse in a fan shaped swath beneath the vessel then recording the reflected sound. As the vessel moves forward, the repeated echo sounder pulses (pings) a strip of the riverbed. The system records the reflection time to measure water depth. A spatial representation of the morphology of the riverbed can be determined by conducting adjacent lines over the area of investigation with some overlap in the swath to achieve 100% spatial coverage. In addition, the reflection strength of the signal can be used to gain some insight into the texture and composition of the riverbed. The multibeam data was used to identify areas where physical sampling would take place. Generally, sampling occurred so as to cover representative riverbed environments. The Multibeam survey is discussed in more detail in Section 9.2.

#### 9.1.2.3 *Sub-bottom profiler*

An Edgetech sub-bottom profiler (SBP) SB216S was also used, which operates at frequencies of 1 to 16 kHz. This is a shallow penetration sonar system which sends an acoustic pulse to the riverbed every 0.5 s, and records acoustic information from the riverbed surface and shallow sub-bottom sediments. These pulses are then reflected off the riverbed and shallow sub-surface sediments and recorded on board the vessel. The energy from the sub-bottom profiler is concentrated in a relatively narrow beam and the maximum source level is about 216 dB at 1 m.

#### 9.1.2.4 *Grab sampling*

The grab collects a sample of the riverbed using a set of closable jaws. The jaws close and collect the sample after being triggered when the grab contacts the riverbed. The grab collects 1 L of material and is suitable for sampling only unconsolidated material (i.e. muds and sands).

#### 9.1.2.5 *Pole corer*

The pole corer comprises of a 76 mm clear polycarbonate tube which is hand pushed into the river/lake bed to a maximum depth of 1.5 m. The tube has a valve attached to the end which is closed when the tube reaches the end of its sampling depth. The closed valve enables a vacuum to be held above the sample which holds the sample in the tube as it is removed from the river/lake bed. This sampling method enables field verification of the surface sediment with the sample available for laboratory analysis.

## 9.2 MULTIBEAM SONAR RIVERBED MAPPING

### 9.2.1 Introduction

A multibeam echo sounder river bed mapping survey was undertaken (mid-December, 2011) for the BHMAR Project for the purpose of elucidating the relationship of the Darling River to the adjacent aquifers. The survey area is as shown in Figure 9-1. The surveyed river section is approximately 22 km of river immediately south of Weir 32, which is 6 km south by southwest of Menindee township on the Darling River.

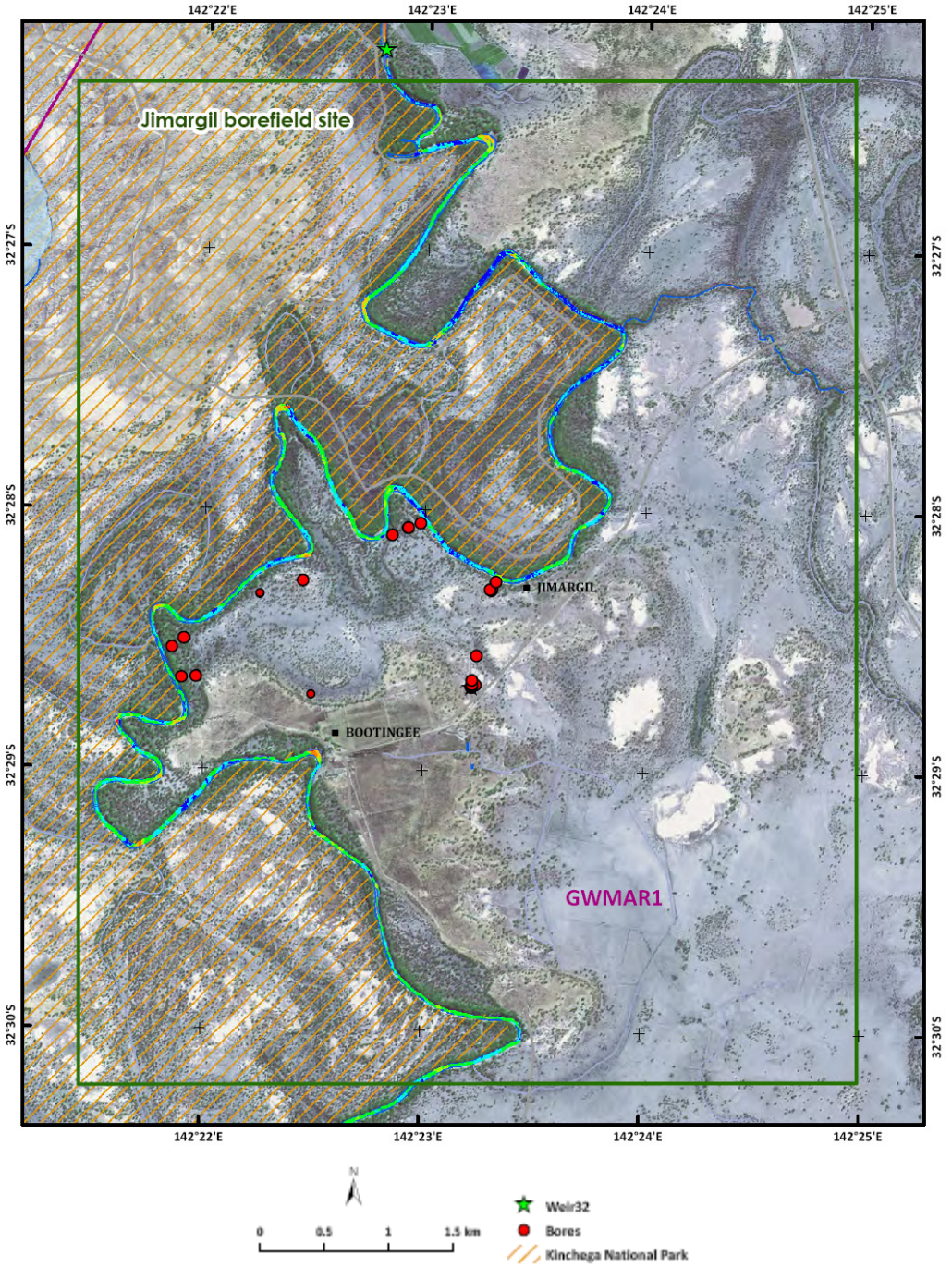



**Figure 9-1.** *Extent of in-river survey. Blue to green to orange colour range along river represents river depths from shallow (<2 m) to deep (>5 m).*

The survey was carried out in mid-December as this period corresponded with adequate river water flows due to releases from the Menindee Lakes system. The flows enabled the river to be navigable and of suitable depth for a multibeam sonar survey. The timeframe during which the survey could occur was also dictated by the availability of the essential survey resources such as the survey vessel, relevant positioning equipment and consultant, and the Geoscience Australia survey staff.

During the survey period water was released from the Menindee lakes water storage system to enhance environmental flows and to create room in the system for flood waters progressing down the Darling River. Over the three survey days 15$^{th}$ to the 17$^{th}$ of December, the river flow at Weir 32 Menindee rose from 6500 ML to 8500 ML per day, yielding a change in river height at Weir 32 of 2.6 to 3.1 m over the course of the survey. The weir was completely submerged by these flow rates.

The river section was completely sounded over the three survey days producing accurate detail of the river bed. For the majority of the river bed survey, the horizontal and vertical accuracies were within target (less than ± 0.15 m). However two hours of survey data (northern stretch, southern side of the river) exhibits positional and height discrepancies of up to 1.5 m due to too few Global Navigation Satellite System (GNSS) satellites in continuous view at the time. The river bed morphology in this period is however correct.

## 9.2.2 Methodology

### 9.2.2.1 *The Multibeam Echo Sounder System (MBES)*

The Kongsberg EM3002S multibeam bathymetric echo sounding system used for this survey utilises a sonar head with multiple transducers to sound the sea/river bed. The system is capable of determining depths in shallow water with resolution of 1 cm, positional accuracy better than 10 cm and the sea/river bed sounded at a spacing of better than 30 cm.

The MBES is capable of attaining multiple soundings of the river bed per ping of sound by using two arrays of sound transducers. One array of transducers generate a ping of sound that ensonifies the river floor as a narrow swathe the returning echoes from the swathe of sound are measured by another array of transducers to form multiple beams of detection.

The amplitude and phase of the recorded echoes in each beam enable the range and angle of the echo (being the depth and position) in each beam to be mathematically resolved. With additional mathematical processing, more than one depth may be resolved per beam. In the case of the Kongsberg EM3002 sonar head, 160 beams are generated and up to 254 soundings per swathe may be resolved.

The processing electronics of the MBES determine the range and angle of the echoes from the sonar head. To resolve the echoes as an accurate location and depth, the multibeam system includes a highly accurate motion referencing positioning system and sound velocimetry. This enables the orientation and position of the sonar head to be determined when the ping was transmitted and received, thus a location and depth resolved. To complete the accurate determination of the echo location, the sound velocity profile of the river water column and at the sonar head surface to water interface was determined, to calculate the echo sound ray path due to refraction.

### 9.2.2.2 *Survey design issues*

MBES hydrographic surveys are most commonly undertaken in a marine environment where the survey environment is often relatively simple compared to inland rivers. With marine surveys, the MBES motion referencing positioning system has a clear view of the sky and thus obtains accurate positioning and a survey can be planned in a manner ensuring that the sonar heads will not run into submerged objects. A MBES marine survey is a set of depths corrected to a measured and predictable tide, relative to a vertical datum being the Mean Sea Level (MSL) or the Lowest Astronomical Tide (LAT) at a designated location.

A river bed, such as the Darling River is a very restricted environment: a survey can only be conducted when there is adequate depth of water such as during water storage releases or flood events. The river surface height is variable due to increasing water flows, restrictions in the river and the slope of the river downhill. River height is not easily measured or predictable across the survey area. It is also a difficult environment to obtain accurate positioning as the river is relatively narrow, in a gully and is enclosed by overhanging trees thus restricting a clear view of the sky and GNSS satellites (Figure 9-2).




**Figure 9-2.** *Trees overhanging the river the cause of GNSS satellite reception difficulties.*

There is also the risk of encountering submerged fallen trees in the river which can damage the sonar head. As it was not possible to sound the unknown ground from known ground or deeper waters to determine locations of submerged objects, an appropriate mounting system was designed to protect the sonar head. This is described in more detail Section 9.2.2.3.

In addressing the variable and unpredictable river level height the survey was set up more akin to a land survey, were the river bed was not determined as a depth but as an elevation off the WGS84 ellipsoid. The river bed elevation was derived from the height of the sonar head above the ellipsoid, which was only achieved by very accurate GNSS positioning. The elevation of the sounded points were derived by computing an irregular GPS tide in the CARIS bathymetry processing software using the accurately determined GPS heights of the sonar head.

To attain accurate positioning a Real Time Kinematic (RTK) solution was considered. The RTK set-up requires specific equipment and additional time to establish adequate radio masts and repeaters. This is necessary to deal with the unknown loss of radio signal being delivered horizontally over ridges, through trees and into a gully. Therefore an Applanix POSMV 320 motion referencing and positioning system with L1/L2 receivers was utilised. This allowed the full motion and positioning data to be post processed using Applanix POSPac software, yielding a Post Processed Kinematic (PPK) solution. The data was post processed against an installed GPS base station adjacent to the surveyed river section.

Post-processing of positioning data was used to resolve errors associated with GNSS satellite slips and insufficient number of visible satellites. As part of survey planning, GNSS satellite plots were generated. The plots indicated that the number of clearly observable satellites, being those overhead whilst on the river, were less during the latter part of the survey day. Unfortunately, due to restrictions as to where it was possible to launch the vessel into the river, it was not possible to avoid surveying in the latter part of the day. Post-processing positional data acquired in the afternoons of day one and three yielded correct and accurate positions. However as mentioned previously, 2 hours of acquired data on the afternoon of the second day contained unresolvable positioning errors; the error in the horizontal and the vertical being up to 1.5 m. Though the positioning was erroneous, the motion data was good thus the generated images of the river bed morphology during this period are correct.

For relatively accurate real-time positioning during the survey, a C-Nav real-time wide area RTCM GNSS correction signal was supplied to the Applanix motion referencing system to deliver reasonable real-time positioning whilst on survey as a basic quality check.

#### 9.2.2.3 ***Survey equipment and software***

The survey vessel (Figure 9-3) used was a 5.3 m open aluminium boat with a single 4 stroke 60 Hp outboard motor which generated little vibration and no resonations though the vessel structure. The vessel was a very stable platform due to the weight and hull structure. Survey speed was predominately below 4.5 knots ground speed.

The multibeam echo sounder was a single head Kongsberg EM 3002S system rotated to port at 30 degrees up from horizontal. The system has a sounding frequency of 300 kHz and the sounding system is roll and pitch stabilised. The system was controlled and data acquired using Kongsberg's Seafloor Information Software. The system was run in the high density equidistant mode, thus 254 soundings were determined per ping and the system attempted to maintain equal spacing between soundings.

The motion referencing and positioning system was an Applanix PosMV 320 system with BD 950 GNSS receivers with L1/L2 enabled, dual GNSS antenna and a high precision inertial motion unit (IMU) coupled to an auxiliary high precision C-Nav 2050R differentially corrected GPS unit receiving a satellite broadcast wide area correction signal.

The sonar system mounting (Figure 9-4, Figure 9-5) was purpose-built over the aft post mount system and was designed to be rapidly installed on a 5 m vessel with an outboard motor. The IMU was rigidly fixed to the sonar head via the post. The post was hinged; the hinge angle was maintained by adjustable struts fitted with shear pins. A shear pin system was used for the safety of the sonar heads, in the event that the sonar head bumped into a submersed object, the pins would shear and the head would hinge up and out of the water. The sonar head was also fitted with an aluminium plate encompassing the forward side of the head for protection against collisions with submerged objects such as fallen trees.



**Figure 9-3.** *The survey vessel underway.*




**Figure 9-4.** *Survey vessel setup demonstrating locations of the Inertial Measurement Unit (a), the Multibeam sonar head (b), the sound velocimeter(c).*

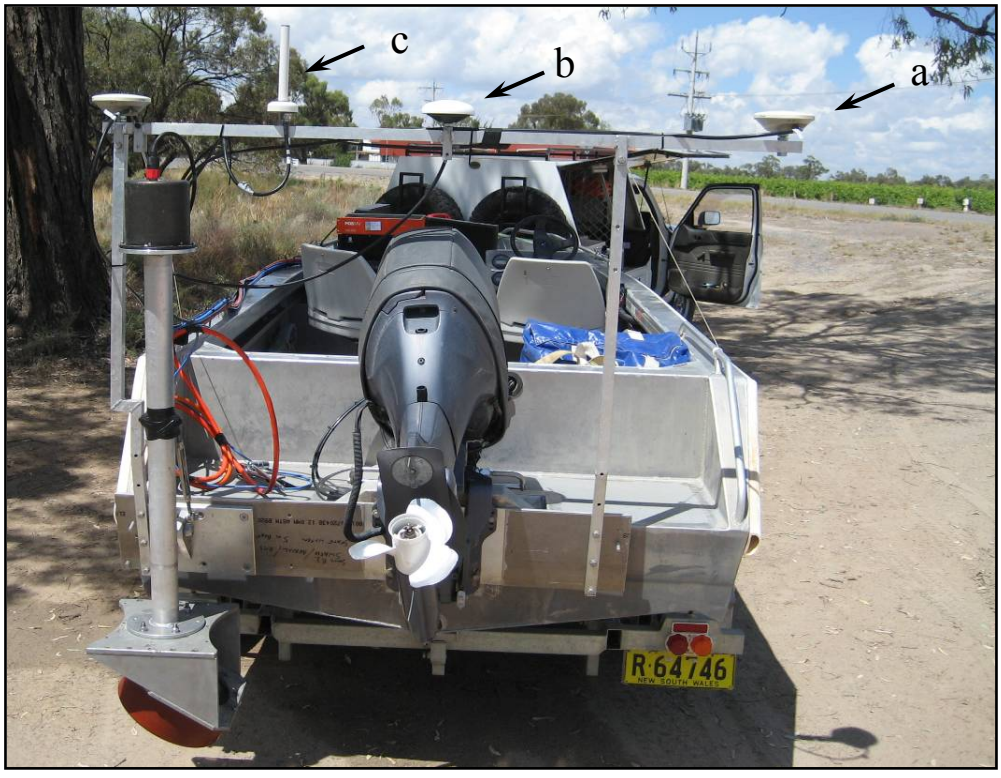



**Figure 9-5.** *Survey vessel setup demonstrating locations of Applanix GPS antenna (a), C-Nav GPS Antenna (b), hi gain C-Nav DGPS correction signal antenna(c).*

The sonar head mount and the IMU post were accurately machined thus the system offsets were known at the commencement of the survey. Thus post-patch test, only a 0.3 degree roll offset needed to be applied in processing. All the MBES control, acquisition and processing electronics were mounted on the raised deck in the forward section of the vessel (Figure 9-6).

The sound velocities in the water at the sonar head were measured using a Valeport mini sound velocity sensor. The sound velocity over the first two days of the survey remained steady at 1489 to 1490 m/s; on the third day the value was fixed in the acquisition software at 1490 m/s due to interference with stable velocity readings by vegetation detritus in the water column. As the river was shallow and well mixed due to high flows, the sound velocity profile for the river was set as 'constant' down the water column at 1490 m/s.

The Positioning and motion referencing data was post-processed using Applanix POSPac MMS software to generate Single Best Estimates of Trajectory (SBET) files which were applied in the bathymetric processing software.

A GPS base station (Figure 9-7) was used as a reference for post-processing vessel positioning and the motion referencing data. The base station was a Leica AT504 GNSS antenna with a choke ring coupled to a Leica GRX1200 receiver logger. GPS base station data was processed online using the Geoscience Australia website AUSPOS online GPS processing service. The base station was installed 300 m south of Bootingee Homestead and 200 m east of the river. All points surveyed on the river were within 6 km of the base station.

The bathymetry processing software for merging and processing the acquired positioning, orientation and sonar data was CARIS HIPS version 7.1.0

Further details of the equipment, the installation, data processing and validation are presented in the Post Processing and Analysis of Position and Orientation Data Report Darling River Bed Multibeam Sonar Survey December 2011 and the MBES Installation and Technical Notes (Appendix 10, Apps *et al*., 2012d).




**Figure 9-6.** *Survey system electronics setup on the vessel, the real-time display in the centre.*

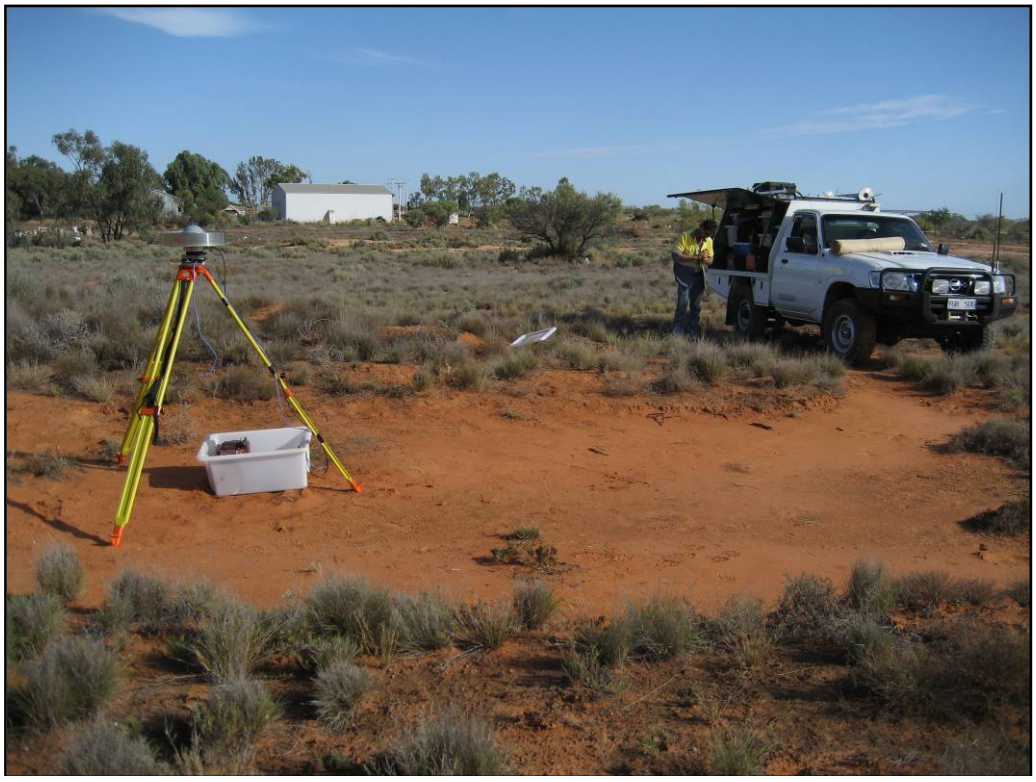


**Figure 9-7.** *GPS base station, protective fencing removed, 300 m south of Bootingee Homestead.*

#### 9.2.2.4 *Time format for acquired data*

All data was recorded in Universal Time Co-ordinated (UTC) as obtained from the GPS. The survey days were the 15th to the 17th of December 2011 being Julian days 349, 350, 351.

#### 9.2.2.5 *Horizontal and vertical datums*

All data was acquired and processed to the WGS84 ellipsoid geodetic datum. The elevations were reduced to the reference height (GRS80 ellipsoid height) of the GPS base station as attained from the AUSPOS GPS processing report. The height of the station was 72.282 m above the ellipsoid and the derived AHD (AUSGEOID09) height for the station was 61.840 m however the determined elevations were corrected by (minus) 0.101 m after an error in the calculation of the GNSS base station antenna height was realised.

#### 9.2.2.6 *Horizontal and vertical accuracies and resolution*

Horizontal and vertical accuracies for a valid echo were better than 10 cm following the application of post-processed motion and positioning data, provided the positioning system had the minimum number of clearly observable GNSS satellites in view at the time of data acquisition.

Vertical resolution was 1 cm and dependant on the nature of the surface the sound is being reflected from. For example with muds the ping may penetrate the surface prior to being reflected.

Horizontal resolution was dependant on the range from the sonar head and the rate of progress of the survey vessel. For this survey the horizontal resolution overall was better than 30 cm and the horizontal resolution for the bulk of the soundings was better than 15 cm.

Non valid echoes are those that do not logically fit the morphology of the base surface and may be a result of the MBES processing artefacts or strong secondary echoes. The non-valid echoes are readily seen when manually inspecting the soundings and the bulk are removed during the processing of the data.

#### 9.2.2.7 *Surveying the river bed*

On arrival at Menindee the GPS base station was initially established 300 m south of the Bootingee homestead, and the GPS station was within 6 km of all points surveyed on the river The early installation allowed 24 hours of acquired data to be processed prior to the commencement of the survey, establishing a reference height and position for post-processing of the MBES motion and positioning data.

Following installation of the GPS station, various river banks sites were inspected for ease of access to the river and launching the boat. The dirt ramp to the river adjacent to Bootingee Homestead was selected as the only safe and reliable point to launch the vessel with the MBES installed.

The river was also assessed for navigational safety, with a particular focus on areas of restricted flow or accumulated debris. On inspection, it was found that the increased volume of water within the river channel associated with river releases created a relatively safe uniform, smooth, stable flow rate of ~3 knots without any white water turbulence.

Each survey day the MBES was re-installed on the vessel. The MBES mechanical mounts were rigidly fixed and the GPS antennas were able to remain installed between survey days, thus the system did not require patch tests and calibration each day. A patch test is a surveyed set of lines over ground that is flat in one area and in the other area possesses a sharp slope. The lines surveyed over this ground in a distinct pattern enable the system to be corrected for small angle offsets between the IMU and the sonar head.

For the river survey the multibeam sonar head was installed looking up 30 degrees to port and the runtime parameters for angular distribution of the swathe were predominately set to 33 degrees to starboard and 94 degrees to port. This allowed the ground beneath the vessel and up to the waterline on the port side of the vessel to be surveyed. This covers slightly more half of the river bed when surveyed in one pass, therefore to survey the river the vessel only needed to progress out along the river in one continuous direction and return by the end of the day to completely survey a section of the river. Occasional extra passes were required where the river bed morphology created sounding difficulties.

On December 14$^{th}$, the vessel became available at midday, the mounts and system were installed aboard the vessel and the set-up was trialled on the river behind Menindee township.

On the first survey day (15$^{th}$ December) the Applanix PosMV motion referencing GPS Azimuth Measurement Subsystem (GAMS) required calibration in an area of clearly observable GNSS satellites whilst undertaking manoeuvres to generate distinct changes in direction and motion. Due to the restrictions in doing this on the river, the system was calibrated by towing the boat on the trailer around open ground with the motion referencing and positioning system fully installed.

The shorter southern section of the river was surveyed and processed on the first day, along with the patch tests and other system calibrations. On Day Two, the river bed was surveyed correctly on the journey to Weir 32 however on the return journey it was noted sections of the coverage were not as coherent with due to the real-time positioning data losing accuracy. Failing light prevented further data acquisition was not possible on Day Two. Surveying commenced on Day Three, with an attempt to cover ground that was not surveyed adequately the previous day. Unfortunately the full stretch of river bed requiring re-surveying was not completed before poor weather caused a halt to data acquisition. The final day of surveying also had to be abandoned due to inaccessibility to the launching site.

### 9.2.3 Data Processing

The MBES data files were imported into the CARIS bathymetry processing software. The imported data was corrected for a 0.3 degree roll offset, then loaded with the POSPac derived SBETs and a GPS tide was computed for the data from the SBET positioning. The GPS tide also contained the GPS base station antenna height correction of minus 0.101 m. The computing of the GPS tide corrected the elevation of the river bed soundings for the variations in water height due to increasing flow, restrictions and the slope of the river and shifts the soundings from depth to elevation off the ellipsoid.

The imported data was then merged with the loaded SBETs and the computed GPS tide, and a 0.1 m resolution base surface generated. The data was then manually inspected and cleaned of the bulk of erroneous soundings, enhancing river bed morphology features.

Due to the nature of the river bed soundings and the MBES artefact soundings, the routine mathematical filters available in CARIS proved to be unsuccessful in rejecting erroneous soundings, retaining valid soundings and maintaining the detail observable in the base surface. Therefore the filters were not used.

The processed sounding data was then exported as the products outlined below.

#### 9.2.3.1 *Validation of the elevation of the surveyed and processed soundings*

In order to validate the determined river bed elevations, the GPS base station (Figure 9-7) with the accurate ellipsoid height was optically dumpy levelled to the waterline on the river (Figure 9-8) on the afternoon of the 17th of December. Two points on the river bed were selected from the data acquired immediately prior to levelling, one point near to below the echo sounder and the other point at the outer edge of the swathe of soundings. The depth of the waterline and the height from the waterline to the GPS station was added. The difference between these elevations the GPS station elevation was 0.041 m, well within the required accuracy limits.



**Figure 9-8.** *Optical dumpy levelling of the river waterline to the GPS base station to validate the processed river bed bathymetry heights.*

### 9.2.4 Processed Data Products and Formats

Finalised survey data sets were compiled as:

- X,Y,Z ASCII points files; longitude, latitude and elevation data at 0.1 m spacings.
- The metric map co-ordinate files are WGS84 co-ordinates projected as UTM54S and at 0.1 metre spacings.
- The GeoTIFF images were bounded by WGS84 geographical co-ordinates and projected as UTM54S. The images were generated from a 0.1 m resolution surface.
- Google Earth kmz files were derived from the WGS84 and unprojected GeoTIFFs.

## 9.3 RESULTS

### 9.3.1 Single Beam Echo Sounder Data

Preliminary results from some of the raw data files from the single beam echo sounder data are shown in Figure 9-9. The data appear to successfully map variations in river bed topology- mapping 'cod holes' in the river bed at bends in the river where scouring is likely to be at a maximum. These 'holes' are up to 6 m in depth below the thalweg of the river. This is a potentially important observation, as the river bed is already ~10 m below the floodplain surface, and depths of ~16 m below the current floodplain surface indicate that the holes are developed within the top of the Calivil Formation aquifer. These may be point recharge zones. This supports anecdotal evidence from local landholders who informed the team that many of these holes never dry up (e.g. Figure 9-10), and when floodwaters do come down the Darling, the river can be 'held up' for quite a few hours while floodwaters 'disappear' into these holes.

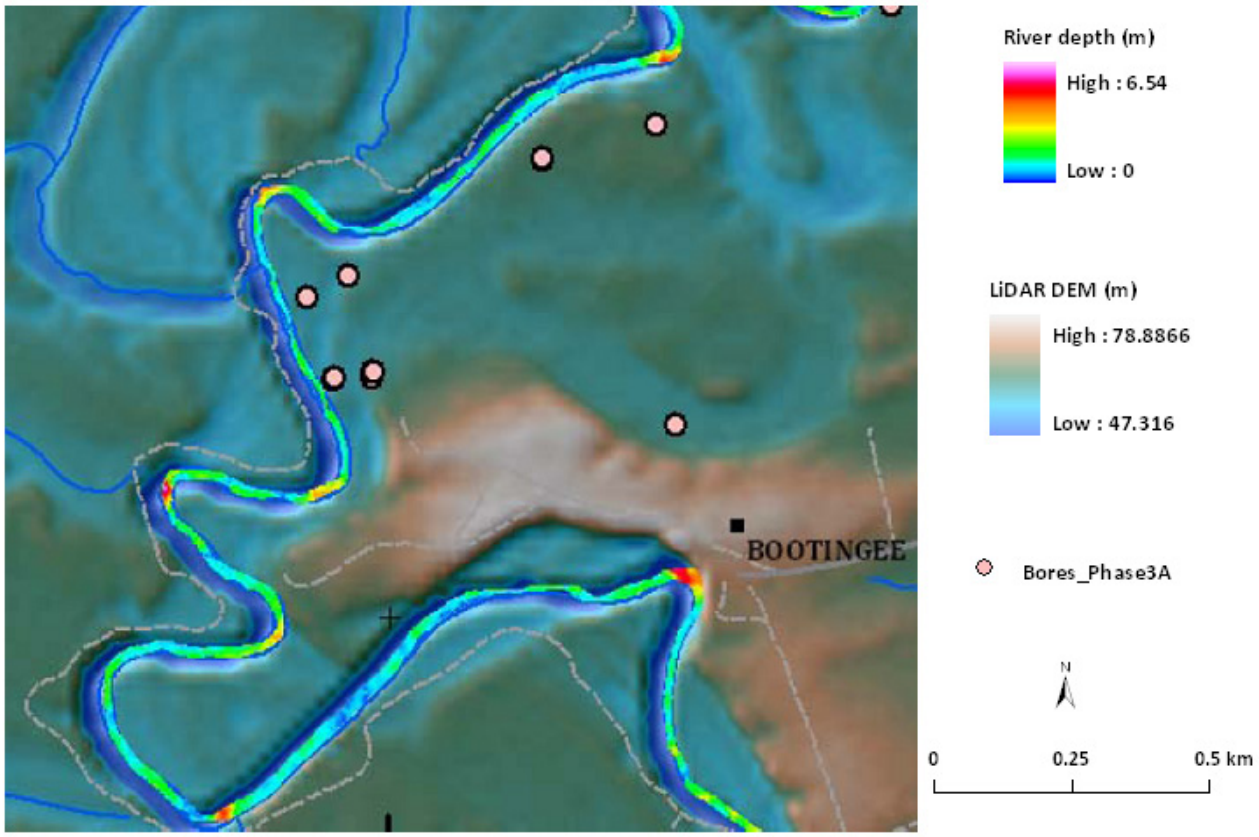



**Figure 9-9.** *In-river survey single beam echo sounder data draped over the LiDAR dataset. The red areas are 'holes' in the river bed up to 6 m below the river bed surface.*

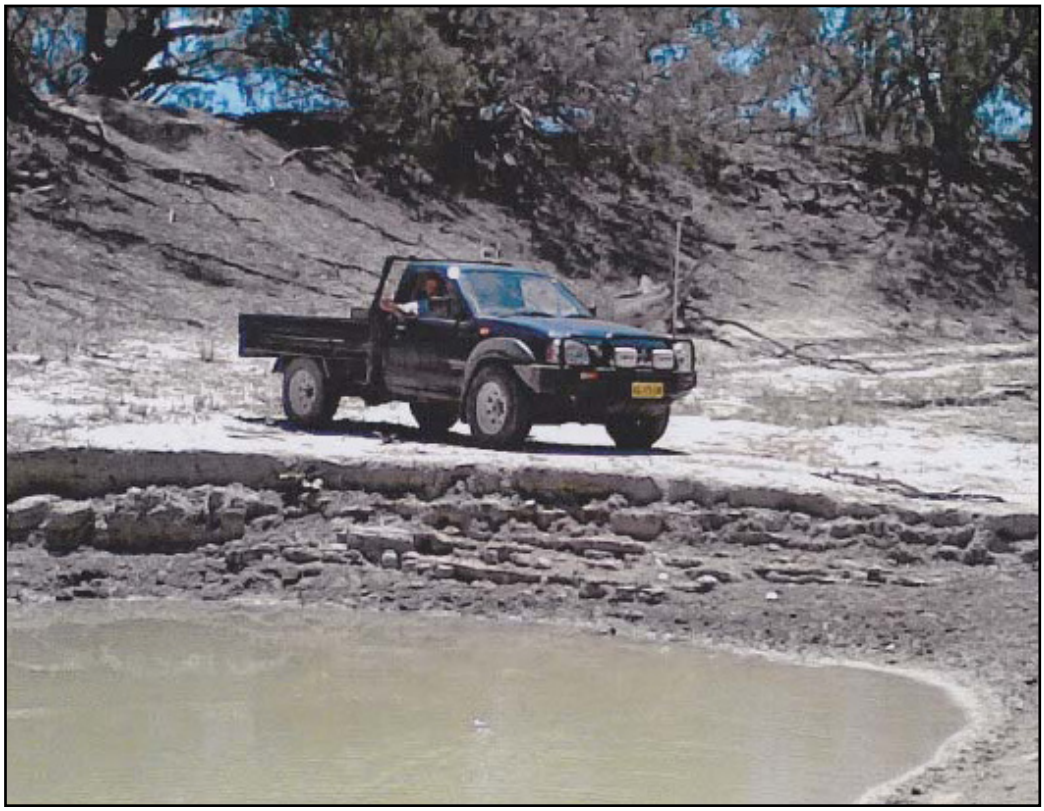


**Figure 9-10.** *Photograph of the Darling River bed in drought. The pool in the foreground is a perennial waterhole. The vehicle is on a calcrete layer in the middle of the river. Photograph courtesy of Stewart Oates, Jimargil.*

## 9.4 MULTIBEAM ECHO SOUNDER DATA

The multibeam survey showed that the river bed at the time of survey was marked by a strong bar and riffle morphology, with deeper scoured reaches alternating with shallow reaches marked by sand bars composed of transverse, oblique, parabolic and crescentic simple and compound sand waves. Rippled surfaces of bedforms show up as zones of strong backscatter in sonar imagery, interpreted as being from a veneer of coarse sediment (Figure 9-11 and Figure 9-12). Sandwaves are frequently exposed on the river bed when water levels are low (Figure 9-13).

River bed sampling by corer and grab showed that the depositional reaches were composed mostly of fine to medium sand, with minor coarse sand. A biogenic component, consisting both of comminuted mollusc debris and small woody fragments (twigs, leaves and seed cases), was common (Figure 9-14).

Erosional reaches are characterised by hard bottoms composed of calcreted sediments and thin lags of small woody debris (twigs, leaves, small branches, and seed cases), coarse shell fragments (mostly unioid bivalves, with minor gastropods), quartz gravel, and calcrete clasts.

Twenty nine large depressions ranging in depth below the rest of the river bed of 5 to 11 m were present in the survey area. Of these, 23 occurred on medium to sharp bends. Since there were 26 bends in the survey area, most bends had such depressions. Of the remaining six depressions, five occurred on straight reaches and one is associated with Weir 32. These features are 10-40 m wide and 50 -120 m long. The largest of these depressions are associated with widening of the river channel (Figure 9-15). Tree debris are largely absent from these deep depressions, which sampling showed are lined with a hard clay, probably the Blanchetown Clay. At least one depression was cut through a basal calcrete, visible in photographs when the river was low (Figure 9-10) and also in the sonar imagery (Figure 9-16). Tree debris are largely absent from these deep depressions, which when sampled in a number of locations are lined with a hard clay with minor fine woody debris and coarse sand. Their usual location at sharp bends indicates that they most likely formed and then kept open by river scour. Active sand waves upstream and downstream of the depressions shows that sand migrates through them, presumably during floods. The presence of a depression immediately

downstream of Weir 32 (completed in 1958) shows that these features can form quite quickly, within a few decades.

Elsewhere in the survey area tree debris proved to be rare (Figure 9-17). This is attributed to a combination of factors, including relative limited tree fall, due to the relative sparse gallery forest when compared to the extensive *Eucalyptus camaldulensis* riverine forests along the Murray, and partial de-snagging of the river to aid navigation in the early 20$^{th}$ century.

This survey has a number of implications for the sedimentary dynamics and channel bottom morphology of the Darling River, the architecture of palaeochannels, and connectivity between the river and the aquifer.

The thin and patchy nature of the sediment cover of the bed of the Darling River in the survey area, and its relatively high biogenic content for a river sediment, suggests that this reach of the river is starved of sand-sized sediment. Sand sources are unclear, but may be derived largely from reworking of the older Menindee Formation and Willotia beds. The presently fixed nature of the Darling channel (Thoms & Sheldon, 2000) means that relatively little new sand-sized sediment is being generated through bed erosion.

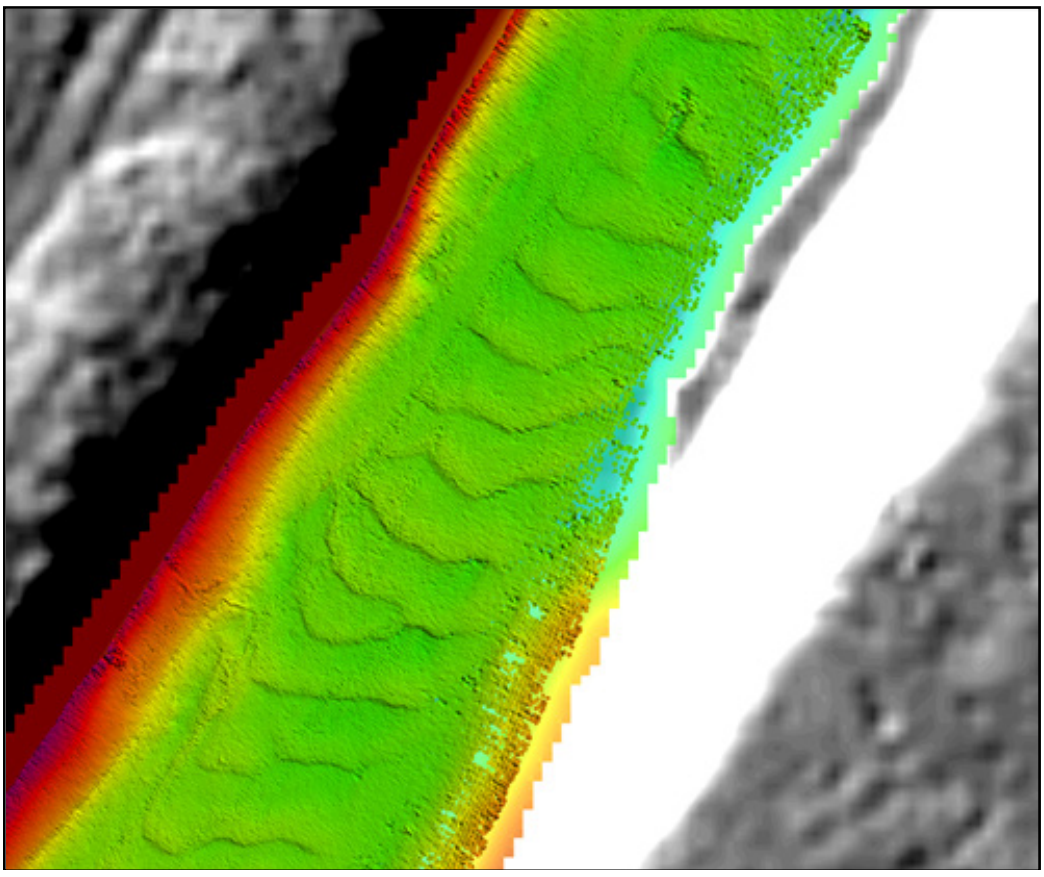


**Figure 9-11.** *Example of transverse sand waves in bed of Darling River mapped by multibeam echo sounder survey.*

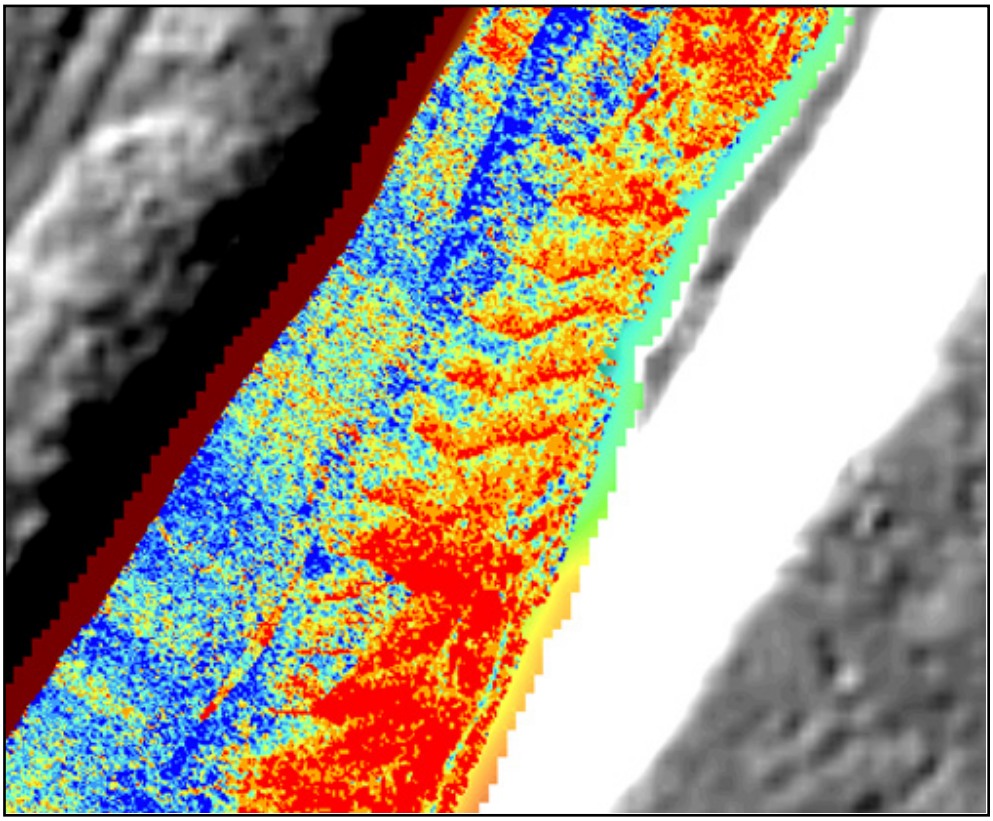


**Figure 9-12.** *Multibeam backscatter image of transverse sand waves in bed of Darling River (same location as Figure 9-11) showing higher backscatter (red) towards sand wave crests, suggesting concentration of coarser sediment. Mismatch between left and right sides of river are due to mismatch between different survey runs.*



**Figure 9-13.** *Sand waves exposed by lower water levels along bed of Darling River, East Bootingee.*




**Figure 9-14.** *Coarse lag of calcrete fragments and woody debris at sediment site 7.*

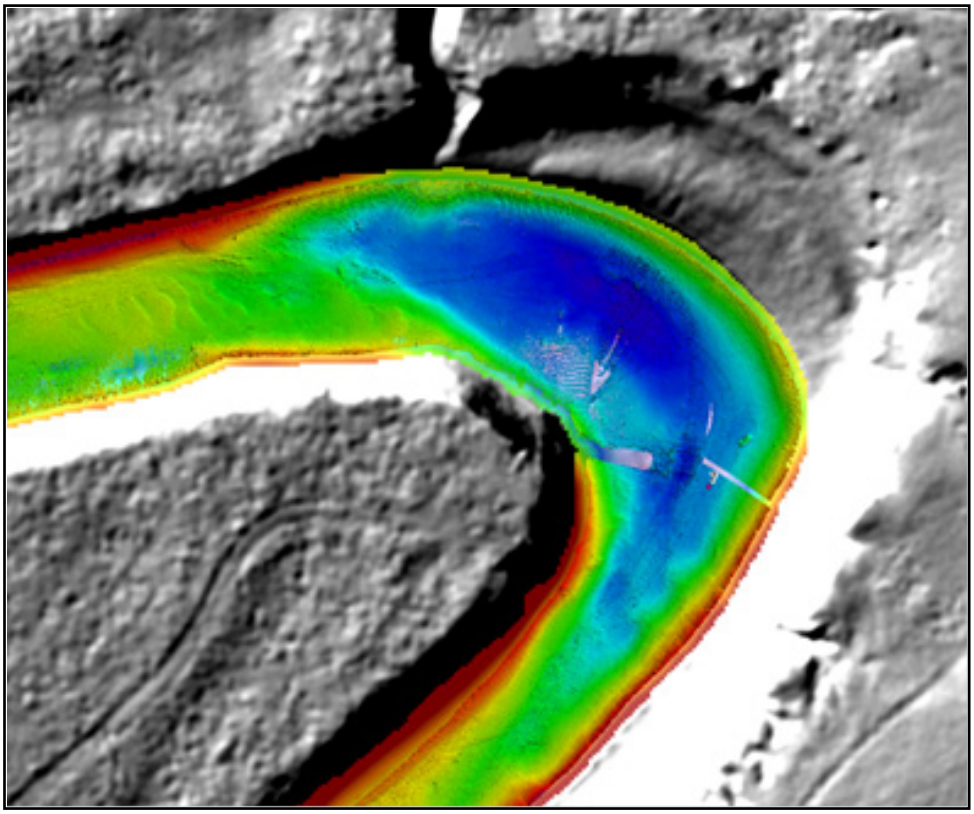


**Figure 9-15.** *Multibeam image of large river bed depression on sharp bend in the river at Appin Station and distinct channel widening. Sand waves occur both up (left) and down (bottom) stream of the depression.*

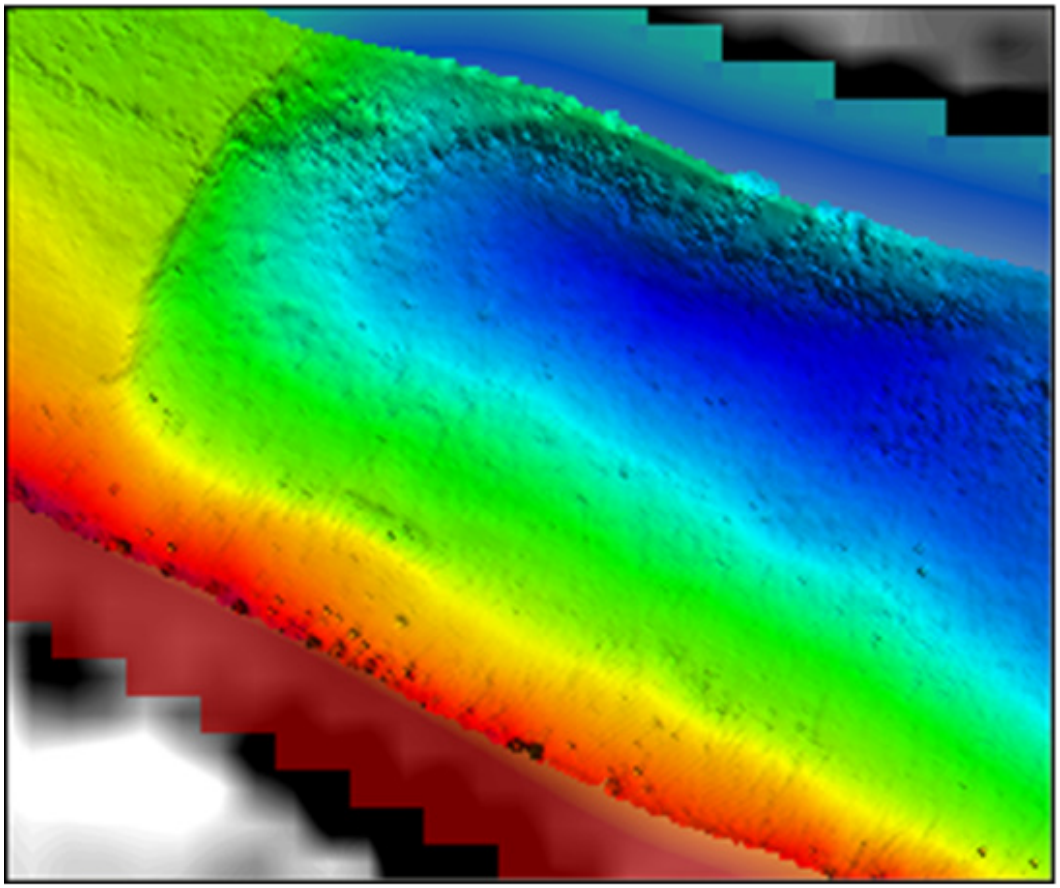


**Figure 9-16.** *Multibeam image of river bed depression on Jimargil Station with distinct upstream lip formed by erosion through a calcrete layer on the bed of the Darling River. Figure 9-10 is a photograph at this site during drought conditions.*

The Darling River is currently a fixed channel that has been migrating in the geologically recent past (Thoms & Sheldon 2000). or the reason of fluvial dynamics it seems likely that large river bed depressions would be scoured during periods of lateral migration and therefore it is considered that the present depressions have developed since the channel became fixed. As already noted, the presence of a scour depression downstream of Weir 32 suggests that these depressions can form quickly.

Given that river bed depressions occur mostly (79%) on river bends and most (88%) of medium to sharp bends have such depressions, we consider it likely that most large bends in the project area, especially those with channel widening, are likely to have such depressions. They are likely to be a common feature of the Darling River in this reach.

It is considered likely that each palaeochannel of the Darling River evident in the older Coonambidgal, Menindee and Willotia phases has, similar to the modern channel, evolved from an actively migrating to a fixed channel. It is therefore likely that the final palaeochannel positions formed in these phases likewise formed channel bed depressions prior to their abandonment.

Channel bed depressions up to 11 m deep are potential zones for river water to enter the semi-confined aquifers where the Blanchetown Clay is thin or absent. This has not happened in the channel bed survey area where all holes occur in areas of thick Blanchetown Clay. However elsewhere along the Darling River it may be significant.

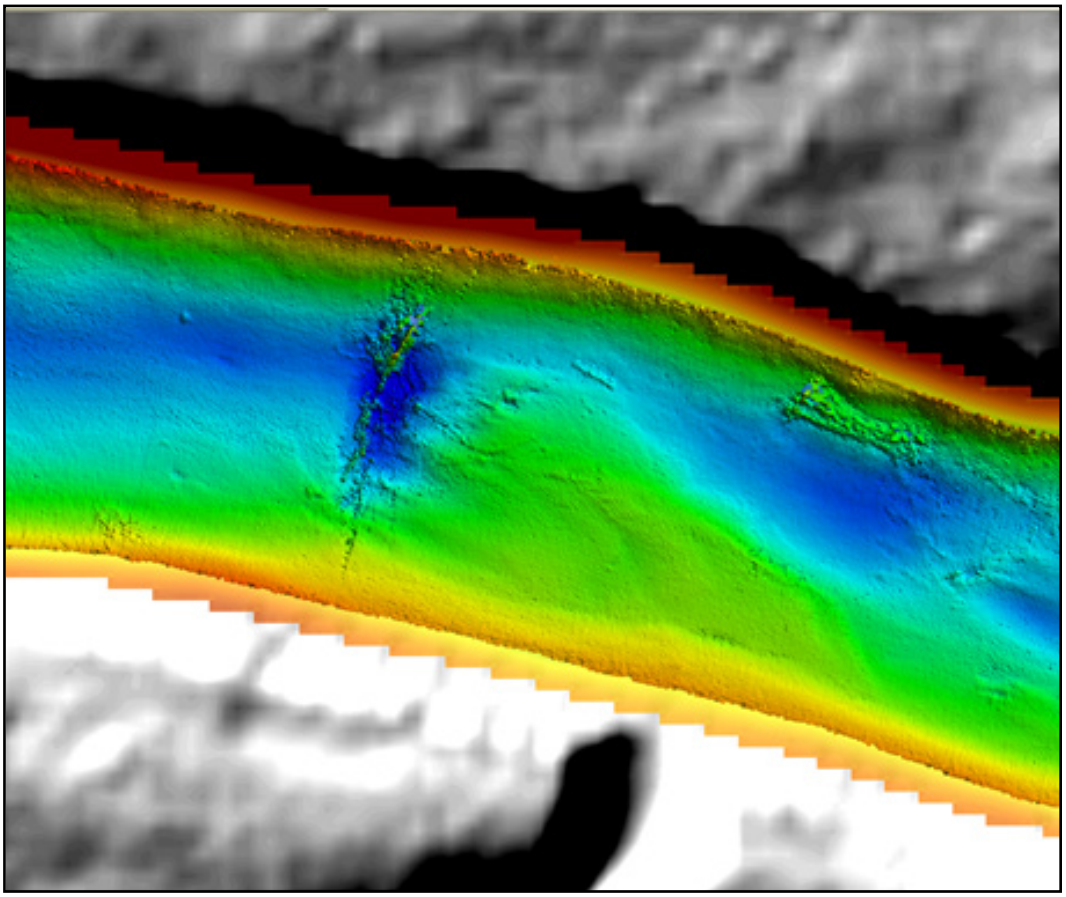


**Figure 9-17.** *Multibeam image of large woody debris formed by fallen trees in bed of Darling River. The tree that has fallen across the river has extensive scour associated with it, and a downstream sand bar. The tree that has fallen parallel to the bank has had little influence on river bed erosion and sedimentation.*

# 10 Drilling Program

## 10.1 DRILLING PHASES

A drilling program, targeted using airborne electromagnetics (AEM) data and informed by a knowledge of landscape evolution and sedimentology, was carried out to confirm the presence of essential hydrostratigraphic elements (aquifer and confining aquitards) for MAR viability. Two areas were selected as representative of potential borefield sites within the priority target. The aims of the drilling program were to:

- Provide new boreholes for geophysical logging for AEM calibration and validation;
- Define the hydrostratigraphy profiles;
- Obtain geological samples for laboratory analysis;
- Carry out aquifer hydraulic testing; and
- Construct groundwater monitoring bores.

The drilling was put out to tender, and Boart Longyear Pty Ltd were engaged to undertake the drilling program using a combination of rotary mud (Section 10.2) and sonic (Section 10.3) drilling techniques. Drilling occurred during both Phase 2 and Phase 3a of the project and all drilling data gathered over the course of the project is contained in the accompanying appendices. Borehole geological, geophysical and hydrogeochemical data is displayed in Appendix 1 (Halas *et al*., 2012a), photographs of the core are displayed in Appendix 2 (Spulak *et al*., 2012), and drilling construction, location and remediation reports are in Appendix 12 (Apps & Gibson, 2012).

106 bores were drilled, including 47 rotary mud and 59 sonic bores, two of which were drilled using polycarbonate tubes to encapsulate the core to reduce post sampling chemical changes to the core from exposure to oxygen. These cores are commonly referred to in this suite of reports as Lexan or Lexan-lined cores. Sonic coring was selected as the main drilling technology due to its unsurpassed ability to successfully core difficult geological materials with minimal sample loss and contamination, and the ability to construct piezometers without the hole caving in before insertion of PVC casing. The issue of contamination is discussed in more detail in Section 11.2.1.

Core recovery was excellent (~99.6%) for both phases of drilling. Such recovery is unprecedented in drilling the Calivil Formation and Renmark Group where previous attempts had resulted in 30% recovery at best. The recovery of core materials using the sonic drilling technique provided an opportunity to directly sample and analyse aquifer material (such as grain size distribution, palynology to assign geological age, pore water chemistry, permeameter measurements, and mineralogical analysis using X-ray diffraction and fluorescence) with minimal contamination. This provided a more detailed understanding of the variability in aquifer and aquitard architecture (lithology, stratigraphy, and oxidation profiles) over scales as small as 1 cm.

## 10.2 ROTARY MUD DRILLING

A standard mud rotary drill rig was used for drilling holes for geophysical logging and stratigraphic interpretation, and for well development (Figure 10-1). Cuttings samples were collected every metre using a wire strainer in the drilling mud. Cutting samples were described in the field, and packed for shipping to Canberra. This drill technique suffers from many disadvantages compared with sonic, but is cheaper and quicker. Samples do not necessarily reflect the geological materials being drilled, due to the possibility of contamination from cave-ins, the time lag for circulation of drill mud, and the inability of the wire strainer to collect fine cuttings entrained in the drilling mud. In addition, there were problems at some sites with holes collapsing after the drill stem was withdrawn, making it impossible to install piezometer casing to the full depth of the hole. This usually meant a change had to be made to the length of sump, rather than changes to the screened interval. Examples include BHMAR21-3, 56-1, 65-1 and 80A-6. There is also potential that drilling mud invasion, particularly in the more permeable horizons, can unduly influence downhole geophysical logging (such as induction or gamma) and the subsequent interpretation or analysis of this logging.



**Figure 10-1.** *Rotary rig engaged in well development.*

## 10.3 SONIC DRILLING

The sonic drill technique (Figure 10-2 to Figure 10-4) uses audible frequency vibration rather than rotation to advance a core drill bit and steel casing. Its principal advantages over traditional rotary coring techniques are that it returns almost 100% core recovery in unconsolidated materials, particularly sands and gravels, and can provide core largely uncontaminated by drilling fluid. A core barrel (normally 6 m for our drilling) is attached to a pipe string attached to a vibration head on the drill mast, and penetrates earth materials by displacement of soft sediment, or fracturing of brittle rock. No water was used during the drilling of sonic core in our program, although it can be used to cool the drill bit and core during drilling of dry materials. The core barrel penetrates the strata through the combination of vibration and slow rotation.

When the core barrel is full, it is brought to the surface by withdrawing the drill pipes. The steel casing system prevents the hole from caving in or binding on the drill stem. The core is extruded from the core barrel by vibration and hydraulic pressure into plastic sleeving which is sealed at one end, in “sausages” of approximately 1 m lengths (Figure 10-4 and Figure 10-5). The use of hydraulic pressure to help extrude core often resulted in contamination of the uppermost part of the core with locally sourced surface water used for this purpose; this is discussed in more detail in Section 11.2.1.

After withdrawal of the core barrel and extrusion of the core, steel casing (which has an annular hard face bit) is driven down to the bottom of the cored interval. At shallow depths in some holes, a large diameter core barrel was used to remove the annulus of sediment between the inside of the casing and the hole left by the core barrel, but at deeper depths this was removed by circulating water (and at times drilling mud) at low flow rates whilst advancing the casing. The fluid carrying entrained drilled material returned to the surface outside the casing in a narrow annulus kept open by hydraulic pressure. Thus although it was considered there was minimal contamination of core by water used in the drilling process, there was the possibility of contamination of surrounding aquifers by the fluid used during advancing of casing. In virtually all cases this was river water derived directly from the Darling River, or indirectly via the Menindee water treatment plant.



**Figure 10-2.** *Sonic drilling rig in operating mode during a hot summer's day on the Darling Floodplain.*



**Figure 10-3.** *The sonic drilling rig operated 24 hrs per day with 2 crews.*



**Figure 10-4.** *Sonic drilling rig, with vibration head on the mast and drill rod attached. Top of casing and drill stem in ground is visible beneath the work platform. Core "sausages" are slid down the corrugated metal chute on the right.*



**Figure 10-5.** *Ross S. Brodie and Elder from the Indigenous community examine drillcore.*

In all but one core run (where the entire core was lost) it was considered that the entire drilled distance was preserved in the core barrel. However, the length preserved in the "sausages" differed slightly, mainly due to expansion of core (e.g. due to release of pressure, opening of micro- and macro-fractures, expansion of clays, repacking of sand grains etc) or settling of loose sand to completely fill the plastic tubing, which is of larger diameter than the core.

Immediately after extrusion the "sausages" were labelled and a brief field description made by examination of the material accessible in the open ends of the "sausages" and by looking and feeling through the plastic film. Occasionally incisions were made through the film to aid interpretation. The "sausages" were then sealed by tying off the open end, and any holes in the film sealed with duct tape to prevent fluid loss. They were then packed in metal core trays and placed in a refrigerated van (2-4º C) at the drill site. Cores were relayed to a large refrigerated truck used to freight them to Canberra, or if it was absent on a trip, to a cool room at a Menindee table grape processing facility for cool storage until return of the truck.

During Phase 3 an encapsulated sampling technique was also trialled. This involved a split 1.5 m core barrel containing a sample tube composed of polycarbonate (trade name Lexan). Once 1.5 m had been drilled the core was retrieved, the ends of the Lexan tube sealed and purged with argon gas to reduce oxidation and other post-drilling reactions that could influence rock and pore fluid chemistry. Spot measurements of electrical conductivity and redox potential were taken by drilling holes in the Lexan and inserting probes. The probe holes and those used for the gas purge were immediately sealed using silicone. The core was then refrigerated along with the other samples. This technique reduces post-sampling chemical changes to the core from exposure to oxygen.

Sonic drilling generally proceeded smoothly, but at times there were problems. These included failure of the vibration head (spares were carried, and could be fitted relatively quickly), fracture of metal pipes through metal fatigue (particularly casing), and jammed casing due to binding/caving of sediment. Three diameters of casing were available (nominally 175, 200 and 225 mm), and in the case of fractured or jammed casing, the casing string was over-drilled with the next available size, and the smaller diameter casing withdrawn by use of a fishing tool (if necessary). However, in two holes, remnants of steel casing were abandoned in the hole (BHMAR19-1 at approx. 12-22 m and BHMAR80B-2 10-14 m). The presence of this casing resulted in spurious conductivity logs over these intervals.

The pre-inserted casing was particularly advantageous for the construction of piezometers, as the PVC piezometer casing and screen could be lowered into the hole inside the steel casing. The latter was then progressively withdrawn as the combination of gravel pack, bentonite and cement were then poured around the PVC to fill the annulus space. This prevented any cave-ins prior to the PVC being put in place, or bridging by collapse of the hole against the PVC. Some shallow piezometers were drilled with the sonic rig, but water was used to assist drilling, and samples not retained.

Sonic drilling is far more costly than the more traditional techniques. The justification for using such a relatively expensive drilling technique is the vastly superior data it obtains. The superior data return manifests itself in five main areas:

- High resolution geological logging (x100 non-core methods);
- Greatly improved facies interpretation (14 of the 19 fluvial facies recognised by Miall (1996) can be recognised from sonic drilling, compared with 4 from rotary mud);
- High resolution in-core measurements (x100 non-core methods);
- High resolution sampling (x10 non-core methods); and
- Uncontaminated pore water in core.

### 10.3.1 Benefits of Using Sonic Core

The sonic drilling technique resulted in almost 100% core recovery. However in some examples resistant lithologies such as indurated beds and hard clays were fractured, and mobile sands were partly fluidised, causing some liquefaction textures along contacts. Despite this, even in the most easily disturbed material such as gravels and sands, bedding features as small as 1 cm across could be distinguished, and mm-scale laminations in fine grained sands, silts and clays were also observed. This greatly facilitates interpretation of the sedimentary facies and depositional environments which can have a profound influence on the geometry and connectivity of the hydrogeological units.

Miall (1996), in a benchmark compilation of fluvial sedimentology and architecture, recognised 19 key fluvial facies in outcrop (Table 10-1). These facies allow the significance of specific lithologies to be identified, for example, whether a gravel unit is part of a major channel sequence and thus more likely to have a high water yield, or whether it is more likely to be just a local coarsening of an otherwise fine-grained succession (Figure 10-6a). Likewise, a detailed understanding of facies allowed the distinction between fine-grained units within a floodplain deposit and thus a more widespread aquitard, or simply a localised channel plug of only minor significance.

The number of distinguishable facies decreases when they are reconstructed from subsurface information (Figure 10-6b), because of the decrease in information available. In contrast with the 19 facies distinguishable in outcrop, only 14 can be identified from the sonic cores. This is still sufficient to identify all the major facies and only precludes a few more detailed subdivisions in bedform type and channel morphology. In contrast, only four facies were observed from rotary or percussion samples, allowing only the most basic logging and facies interpretation (Table 10-1, Figure 10-6). Additionally because core depths are measured precisely with the sonic technique, the thickness and depths of geological units can be determined to cm scale accuracy.

While sonic drilling produces some disturbance to the sample, conventional rotary techniques homogenise the sample over the sampling interval (typically 1 m). While this is adequate for characterising thick formations, it does amalgamate interbedded units or polymict lithologies. In a mud rotary hole an interval may appear to be made up of muddy sand, whereas sonic core revealed for example interbedded clean sands and thin muds, or mud clasts in clean sand, or indeed homogeneous muddy sand. Each of these lithologies would have distinctly different hydrologic properties, information about which would be lost in mud rotary drilling. In the same way, unless contacts between units fall exactly at the sample interval, two different units will be homogenised, for example a clean sand over clay will become a clayey sand or sandy clay. Mud rotary techniques also introduce sample bias because of the complex process by which the drilled material is brought to the surface. Lastly, mud rotary techniques have a built-in time lag between the depth at which a unit is encountered and the depth at which that material is brought to the surface. This is illustrated by the one metre offset in depth between the base of the main gravel unit in BHMAR 75-3 in the lithological and gamma logs (Figure 10-7). Taken together with the homogenisation of samples and contacts this means that the thicknesses and depths of geological units is known at best to the nearest metre, with deeper holes the inaccuracy can increase to several metres.

**Table 10-1.** *Facies differentiation from different drilling technologies. Facies classified after Miall (1996).*

| Outcrop (19 facies) | | | | Sonic drilling (14 facies) | | | | Rotary mud (4 facies) | | | |
|---|---|---|---|---|---|---|---|---|---|---|---|
| **Facies code** | **Facies** | **Structures** | **Interpretation** | **Facies code** | **Facies** | **Structures** | **Interpretation** | **Facies code** | **Facies** | **Structures** | **Interp** |
| Gmm | Matrix-supported massive gravel | Weak grading | High strength plastic debris flow | Gm | Matrix-supported massive gravel | Ungraded | High strength plastic debris flow | | | | |
| Gmg | Matrix supported gravel | Inverse to normal grading | Low strength pseudo-plastic debris flow | Gmg | Matrix supported gravel | Graded | Low strength pseudo-plastic debris flow | | | | |
| Gci | Clast supported gravel | Inverse grading | Clastic rich high or low strength debris flow | Gci | Clast supported gravel | Inverse grading | Clastic rich high or low strength debris flow | | | | |
| Gcm | Clast supported massive gravel | None | Pseudo-plastic debris flow (initial bedload, turbulent flow | Gcm | Clast supported massive gravel | None | Pseudo-plastic debris flow (initial bedload, turbulent flow) | | | | |
| Gh | Clast supported crudely bedded gravel | Horizontal bedding, imbrication | Longitudinal deposits, lags, sieve deposits | Gh | Clast supported crudely bedded gravel | None | Horizontal bedding, imbrication | | | | Debris flows, high velocity flows, or bedload |
| Gt | Stratified gravel | Trough cross beds | Minor channel fills | (Gx) | Stratified gravel | None | Channel fills and transverse bedforms | G | Gravel | None | |
| Gp | Stratified gravel | Planar cross beds | Transverse bedforms | | | | | | | | |
| St | Fgr-Cgr sand, may be pebbly | Trough cross beds | Sinuous crested and linguoid dunes | (Sb) | Fgr-Cgr sand, may be pebbly | Bedded | Channel, channel bar deposits | | | | |
| Sp | Fgr-Cgr sand, may be pebbly | Planar cross beds | Transverse and linguoid dunes | | | | | | | | |
| Sr | Fgr-Cgr sand | Ripple cross-lamination | Ripples (lower flow regime) | (Slm) | Fgr-Cgr sand, may be pebbly | Laminated | Channel bar crevasse splay deposits | | | | |
| Sh | Fgr-Cgr sand, may be pebbly | Horizontal lamination | Plane bed flow (critical flow) | | | | | | | | |
| Sl | Fgr-Cgr sand, may be pebbly | Low angle cross beds | Scour fills, washed out dunes, anti dunes | (Sm) | Fgr-Cgr sand, may be pebbly | Massive | Gravity flow deposits | S | Sand | None | Channel, channel bar, gravity flow deposits |
| Ss | Fgr-Cgr sand, may be pebbly | Broad shallow scours | Scour fill | | | | | | | | |
| Sm | Fine to coarse sand | Massive or faint lamination | Sediment gravity flow deposits | | | | | | | | |
| Fl | Sand, silt, mud | Fine lamination, very small ripples | Overbank, abandoned channel or waning flood deposits | Fl | Sand, silt, mud | Fine lamination, very small ripples | Overbank, abandoned channel or waning flood deposits | F | Silt, clay | None | Overbank, backswamp, or abandoned channel |

| Outcrop (19 facies) | | | | Sonic drilling (14 facies) | | | | Rotary mud (4 facies) | | | |
|---|---|---|---|---|---|---|---|---|---|---|---|
| **Facies code** | **Facies** | **Structures** | **Interpretation** | **Facies code** | **Facies** | **Structures** | **Interpretation** | **Facies code** | **Facies** | **Structures** | **Interp** |
| Fm | Mud, silt | Massive, desiccation cracks | Backswamp or abandoned channel deposits | Fm | Mud, silt | Massive, desiccation cracks | Backswamp or abandoned channel deposits | | | | deposits |
| Fr | Mud, silt | Massive, roots, bioturbation | Root bed, incipient soil | Fr | Mud, silt | Massive, roots, bioturbation | Root bed, incipient soil | | | | |
| C | Coal, carbonaceous mud | Plant material, mud films | Vegetated swamp deposits | C | Coal, carbonaceous mud | Plant material, mud films | Vegetated swamp deposits | C | Coal, carbonaceous mud | Plant material | Vegetated swamp deposits |
| P | Palaeosol carbonate | Pedogenic nodules, induration | Soils with chemical precipitation | P | Palaeosol carbonate | Pedogenic nodules, induration | Soils with chemical precipitation | | | | |

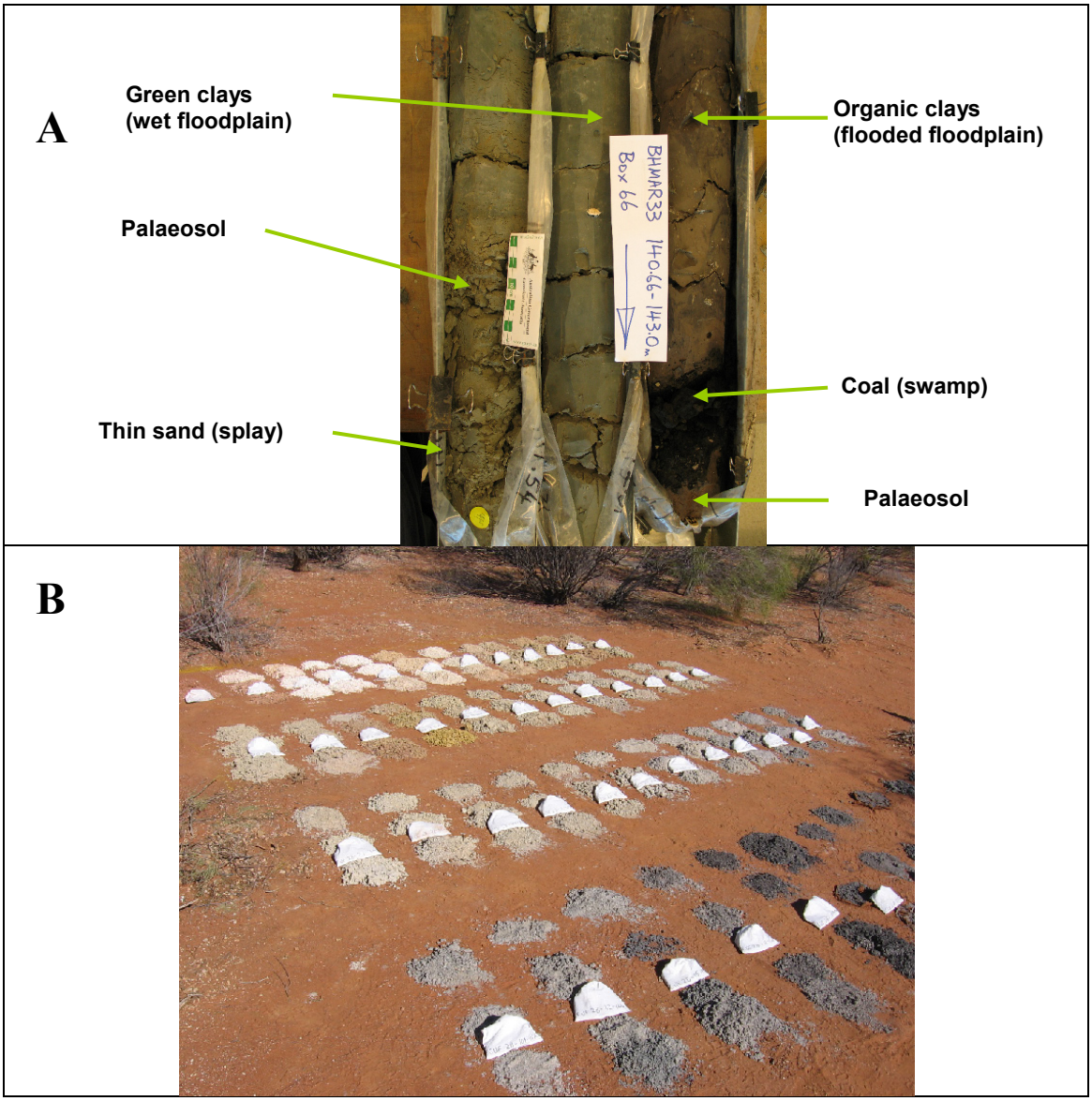



**Figure 10-6.** *Visual comparisons of materials and geological detail obtained using the sonic drilling technique and rotary mud drilling. A) sonic core, showing range of different facies visible in ~3 m interval of Renmark Group. B) Rotary drilling samples from a Murchison (WA) palaeovalley showing poor differentiation of samples (photo by S. Lewis). Little can be determined from these samples other than the aggregate grainsize and composition over the sample interval and colour.*

A real-world example of this is the comparison between the lithologic logs for rotary mud hole BHMAR75-3 and sonic hole BHMAR75-5 (summarised in Figure 10-7 and Table 10-2) drilled 10 m apart. In BHMAR75-3 Figure 10-7) 23 different lithological units were described in the field from the surface to the base of the Calivil Formation. In BHMAR75-5 (Figure 10-7) 43 different units were logged for the same interval. Multiple entries of the same lithology refer to minor differences in such as colour and induration too subtle to be captured by the summary log.

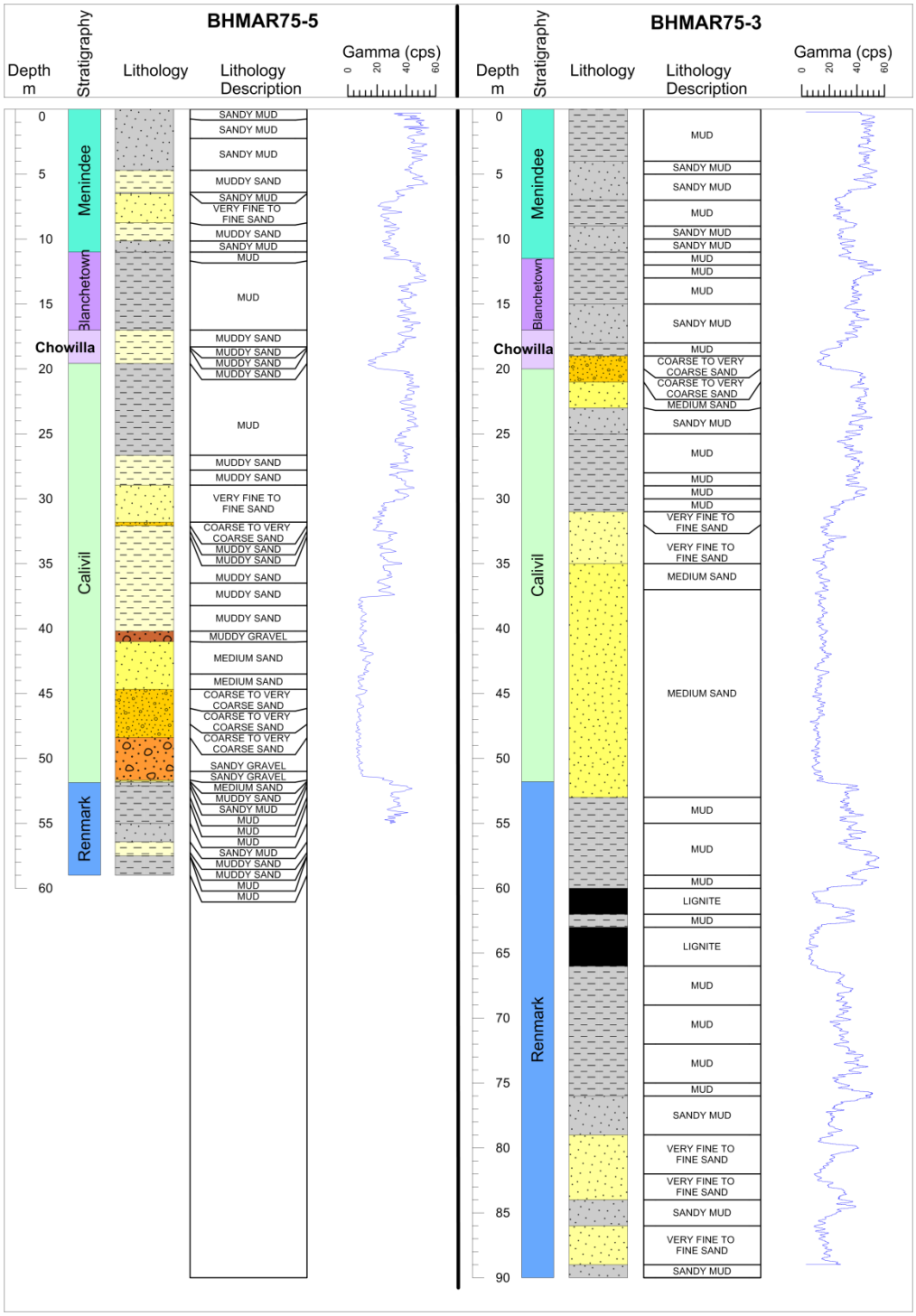



**Figure 10-7.** *Comparisons of geological detail obtained from rotary mud drilling versus the sonic drilling technique at adjacent bores at site BHMAR75. The data on the right (stratigraphy, lithology and borehole gamma log) are from a rotary mud hole (BHMAR75-3) while the data on the left are from a sonic hole (BHMAR75-5). The two holes are 10 m apart, with BHMAR75-5 10 m west of BMHAR75-3. Comparison reveals that interpretations based on the rotary mud technique combined with interpretation of the gamma log pick the broader stratigraphic units and some of the detail within the finer-grained units quite well, but that the differences in grain size within the sand aquifer cannot be picked and the percentage of sand in finer grained materials is also underestimated. By comparison, a high level of detail on aquifer stratigraphy is obtained from the sonic core, allowing optimisation of screen design and pump (and injection) tests. The sonic technique also provides other key textural data (e.g. reductomorphic features) and samples for pore fluid analysis not possibly obtained from the rotary mud technique.*

Importantly, within the main aquifer zone only one lithological unit is recognised in the rotary mud hole compared with 4 in the sonic hole. In terms of resolution and characterisation of geological units, core collection techniques such as sonic drilling allow the potential for cm-scale or better resolution of bedding, lithology, and contacts, depending on the drilling conditions. This can result in data quality improvements (perhaps 100 times more precision and accuracy than mud rotary techniques) and comparable resolution of the geological data with the down-hole geophysical measurements (~10 cm).

**Table 10-2.** *Comparison in data quality between specific sonic and rotary mud holes.*

| **Hole** | **BHMAR 75-3** | **BHMAR 75-5** |
|---|---|---|
| **Method** | Mud rotary | Sonic core |
| **Depth to base Calivil** | 51.8 m | 51.87 m |
| **Recognised lithological units to base Calivil** | 22 | 33 |
| **Thickness of main aquifer zone** | 17 m | 12 m |
| **Number lithological units in main aquifer zone** | 1 | 4 |

## 10.4 BORE CONSTRUCTION

Piezometers were installed following Australian guidelines (LWBC, 2003) Most piezometers were constructed using threaded class 8 or 12 heavy duty 80 mm PVC pipe. Many holes were drilled much deeper than the required screened interval, and a sump was constructed consisting of un-slotted casing with an end cap, followed by the screen (slotted PVC pipe with welded flanged joints), and then by threaded casing to the surface. Plastic centralisers were installed over the screened interval. The sump was backfilled with gravel to a depth of 3 m below the screen which was overlain by 2 m of bentonite (as chips) and then gravel to a thickness of 1 m above the screen. Another 2 m of bentonite was added and then cement grout was added up to the surface. When the screen was placed at the bottom of the piezometer, a 1 m sump was constructed from non-slotted casing. Gravel pack was introduced to 1 m above the screen, then 2 m of bentonite, then cement grout to the surface. All piezometers were protected by a locked galvanised steel casing which emplaced in a cement block at the surface. Piezometer nests were constructed by installing two or three holes approximately 2-3 metres apart in a line as per the construction details in Lawrie *et al*. (2010c).

# 11 Sonic Core Logging, Sampling and Analysis

## 11.1 CORE DESCRIPTION AND SAMPLING

Sonic drill core materials were wrapped in polythene sleeves immediately upon extrusion at the drill site. The core were visually logged through the sleeves and immediately refrigerated on-site in a small refrigerated van. Every evening the core were transferred from the drillsite in the refrigerated van to a cold store facility near Menindee, with core then transferred weekly to Canberra using a large refrigerated truck. In Canberra, the core was stored in pallets in a cold store facility off-site at Hume. The cores were stored in cool rooms at 4$^{o}$C, and transferred on an as-needs basis from the cold store facility to a refrigerated container on-site at GA.

The cores were processed as follows:

- Preparation - The trays were laid out on the bench in sequence and the lengths of the cores were measured and compared to the depths measured in the field during each run (i.e. 1.5 m, 3 m, or 6 m). The start and end depths of each core section were determined and the depths were labelled on the plastic sleeves. The sleeves were then slit (Figure 11-1) and pegged back to reveal the core. Generally there was a 2-5 mm thick rind of smeared material along the outer layer of the core. This rind was scraped or pared away to reveal the primary material and reduce the potential for contamination of samples.
- Description – The cores were photographed (Appendix 2, Spulak *et al*., 2012) and fully described including textures, colour (Munsell soil codes, see Munsell Color 2000), mineralogy, sedimentary structures and where evident facies boundaries.
- Initial measurements – A series of measurements were taken at specific intervals including mechanical strength or hardness, bulk electrical conductivity (EC), pH and oxidation potential. The frequency at which measurements were taken allowed for much more accurate comparison between the point and geophysical datasets.
- Sampling - Representative core samples were taken at approximately 3 m intervals for later analysis of gravimetric moisture contents, bulk density, grain size (using laser diffraction and sieve methods), pore fluid chemistry, bulk geochemistry, mineral identification and quantification, and palynology. The latter two analyses were carried out on a limited number of samples. Because the sonic core was largely intact, samples could be collected every 10 cm if required, allowing much more frequent analysis of chemical properties, age, and other derived parameters. While some of these analyses (specifically whole rock XRF and XRD, palynology, grainsize) could be applied to rotary or percussion samples, the samples would at best be collected from 1 m composites. In the case of samples collected by the mud rotary technique, samples were further compromised by drilling muds and from intervals higher in the stratigraphy. The pore fluid extract data simply could not be obtained using techniques other than sonic core drilling.
- During the sampling phase, up to two portions were typically taken from the same 10 cm interval (Figure 11-2). One for physical properties including grainsize, moisture content, bulk density, X-Ray Diffraction (XRD), X-Ray Fluorescence (XRF) and Inductively Coupled Plasma Mass Spectroscopy (ICP-MS). A second was taken for pore fluid extraction.

Full geological logs are available in Appendix 1 (Halas *et al.*, 2012a), core photographs are to be found in Appendix 2 (Spulak *et al*., 2012).




**Figure 11-1.** *Photograph of sonic core prepared for sampling.*

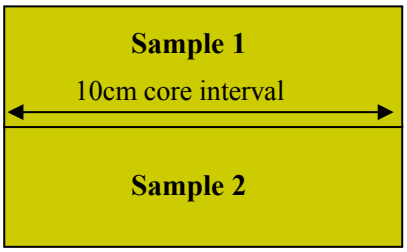



**Figure 11-2.** *Sonic core sampling approach, collecting two samples of equivalent material from the same 10 cm core interval.*

## 11.2 PORE FLUID ANALYSIS

### 11.2.1 Potential Contamination

While sonic core drilling minimises contamination of the sample pore fluids through isolating the sample from drilling fluids, minor contamination can occur when water is used to assist the extrusion of the core, as discussed in Section 10.3. Typical sonic core runs were 6 m in length. Injection of water led to the top 30-50 cm being much sloppier than the normal core. These zones were examined for lithology but where never sampled for pore fluid analysis. As a precaution samples were generally not taken from the top 50 cm of the core, even when contamination was not visible, and never taken from visibly contaminated zones. Two figures illustration the degree of visible contamination that can sometimes be seen at the start of a core run. Figure 11-3 shows the effect in clay rich sediments and Figure 11-4 in sandy sediments. Figure 11-5 shows how samples are taken well below the top of the run even when there is no visible sign of contamination.

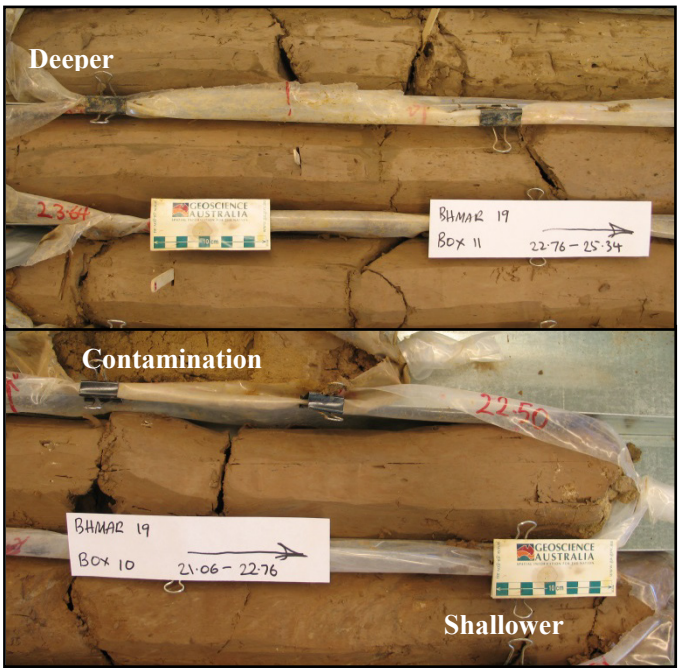



**Figure 11-3.** *Contaminated zone in BHMAR19 sonic core, showing sloppy texture in clay-rich sediments from drilling water affecting the uppermost core in the run. Effected zone is 36 cm in length. Note the contrast between the appearance of the contaminated section with respect to core at shallower and greater depth of contaminated run.*




**Figure 11-4.** *Contaminated zone in BHMAR08 sonic core, showing slightly sloppy texture in sandy sediments from water in uppermost core in 6 m run. Effected zone is ~80 cm in length. Note the contrast between the appearance of the contaminated section with respect to core at shallower and greater depth of contaminated run.*




**Figure 11-5.** *Sample point (yellow spot) at least 60 cm below top of sonic core run at 47 m in BHMAR58, even though there is no visible sign of contamination by fluid injection.*

By avoiding sampling of visibly contaminated zones and generally not sampling within 0.5 m of the top of the core, the likelihood of pore fluid contamination was minimises. A further check for the presence of contamination of pore fluids by drilling water can be obtained by comparing the salinity of the uppermost sample in a core run against that in samples above and below. Because the drilling water used was low salinity river or mains water, this would produce an unusually low salinity value in the core, if present.

The salinity of pore fluids sampled from 43 sonic cores was assessed. Six bores had examples of potential pore fluid contamination as shown in Figure 11-6. Of all the pore fluids sampled, only 0.6% was identified as being potentially contaminated. Consequently, the issue of contamination of pore fluids by drilling water is considered to be very minor.

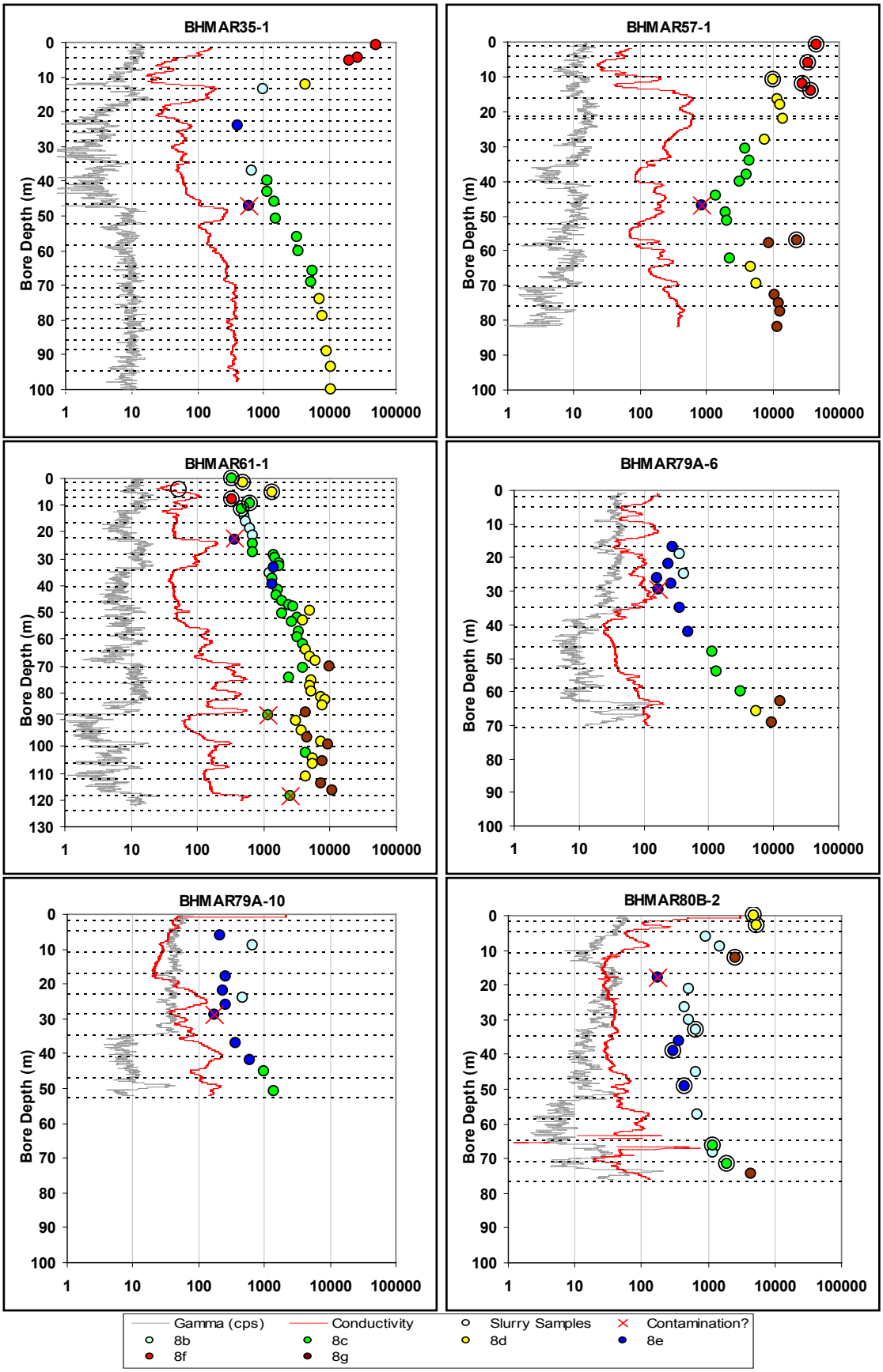



**Figure 11-6.** *Six borehole plots representing the only sonic cores where pore fluid contamination may be observed. Dashed horizontal lines represent the start of a new core run. Potential contamination (shown with a red cross) is interpreted wherever a pore fluid salinity value is notably fresher than measurements above and/or below and is <50 cm below a new core run. Pore fluids, extracted using the slurry paste method are denoted by a white halo. Less confidence is attributed to these values. Pore fluid classification (8b-8g) is of no importance in this analysis.*

### 11.2.2 Extraction

Three different techniques for extracting pore-water from core material were used in this study – high pressure core pressing, slurry method and saturation paste. The extraction method used depends on the moisture content of the core and the texture of the core material. The pressing method described in Section 11.2.2.1 is the preferred method, however if the core did not yield an adequate volume of sample (Table 11-1) an alternative method was required. When the BHMAR drilling campaign started in October 2009, there was no laboratory protocol for measuring the salinity of materials that were too dry to yield fluid using the hydraulic press method. Thus, a slurry method was improvised. In late 2010, the Geoscience Australia laboratory was equipped with the apparatus for saturation paste extract method which is the standard procedure used in pedology (see Rayment & Lyons, 2010, Sonneveld *et al*., 1990).

The saturation paste method (on 200 g portions) is applicable to the vast majority of the collected samples. On occasions where there was significant (>70%) coarse materials (>4 mm) such as gravels, more sample was required to obtain the minimum volume of pore-water. This usually relates to the uppermost 10 m of the profile and/or to coarse sandy samples which, although moist, do not compress sufficiently to drive out the water. Additionally, some heavy clays retained water when pressed and therefore did not yield sufficient volume. The minimum volume of pore-water required for full analysis changed dependant on the EC (total dissolved solids) of the sample. Table 11-1 proves a summary of the volumes required in relation to EC ranges.

**Table 11-1.** *Volume of pore-water required as a function of electrical conductivity (EC).*

| Electrical Conductivity approx. µS/cm | Minimum Volume of Sample mL |
|---|---|
| <1000 | 13.0 |
| 1000 – 3,500 | 10.5 |
| 3,500 – 5,000 | 7.5 |
| 5,000 – 10,000 | 5.5 |
| 10,000 – 20,000 | 4.5 |
| >20,000 | 4.0 |

#### 11.2.2.1 *Hydraulic Core Pressing Method*

The goal of the hydraulic core pressing method was to collect sufficient volume of pore water to enable a complete suite of analyses to be carried out on the sample. The volume required by the hydrogeochemistry laboratory varied depending on the electrical conductivity (EC) of the sample. The EC is an indication of the total ionic strength, or saltiness of the sample. Low EC solutions are analysed directly (with no dilution), therefore more sample was required than for the higher EC samples which were diluted prior to analysis.

Table 11-1 summarises the minimum volumes required for particular EC ranges. Larger volumes are preferred, particularly of the lower EC samples as this allows for repeat analyses. The approximate EC value is determined after about 3 mL of pore fluid has been extracted. Samples with high moisture content yield enough fluid over a short period of pressing, however samples with low moisture content have to be left in the presses for up to 12 hours and yield low volumes of fluid. This method was developed in-house by the Bureau of Rural Science (BRS) and Geoscience Australia, and has not been published, so is given in full below.

*Methods*
Assemble press unit as follows:

- Place steel filter disc then two GF/C filters into the base of the unit
- Place the rubber ring in the groove on top of the base unit
- Fit sleeve over the base unit
- Turn over, put bolts into holes and tighten evenly
- Load approx. 60 g to 100 g of sample into assembled press unit from the 220 mL collection vial and tamp down firmly with the slug and hammer
- Place a plastic stopper disc over the loaded sample
- Place press unit under hydraulic ram
- Bring pressure up slowly to 1,500 psi; do not force it as this can break the paper filter.
- Attach a 10 mL syringe to the outlet in the base
- Bring pressure slowly up to 2,500 psi
- Leave for about 10 minutes, then check the syringe for any air bubbles that may have been extruded along with the fluid; if there is a significant amount of air in the syringe, remove it from the base, carefully depress plunger to remove air by holding it vertically, and re-attach it to the base.
- Bring the pressure up to 5,000 psi as marked on gauges
- Check on press and ram over time, bringing the pressure back up to 5,000 psi (the pressure drops as fluid is extruded)
- When approximately 3 mL fluid has been extruded carefully rinse the EC probe and place it in the sample. At this stage there is no need to calibrate the meter as you are just obtaining an estimate of the EC which is used as a guide for the final fluid volume required. See the details of volumes required vs. EC values listed in Table 11-1 above.
- When enough fluid has been extruded, pull plunger on syringe back slightly while releasing the hydraulic ram pressure
- Remove syringe from unit, attach 0.45µm syringe filter and filter fluid into 30 mL vial
- Once the total volume of sample required is accumulated in the sample vial measure pH and Eh1
- It is important to measure pH as soon after extraction as possible as changes in pH can occur with absorption or degassing of $CO_2$.
- Eh is a measure of the oxidising/reducing potential of the sample and also changes during storage, therefore it is measured in sequence with pH. It is roughly inversely related to pH (i.e. lower pH samples tend to have higher Eh values).
- An accurate EC with calibration of the meter is determined once the whole batch of samples has been extracted
- All results are recorded on the working sheet.

Ensure that the presses are thoroughly cleaned after each use.

- Turn press upside down and remove screws
- Pull base out of sleeve – if it doesn't come out easily the sleeve may need to be gently tapped using the copper head of the hammer until it slides off
- Throw any sample in base into the bin, make sure the steel filter disc is retained
- Place steel tube on wooden square on the floor, balance the press unit sleeve over the tube ensuring that the plastic disc is facing up

- Place steel slug into sleeve and force it down with the hammer until the sample & the plastic disc come out
- Throw out sample
- Put press unit sleeve, base, filter disc and plastic disc into sink filled with very hot water
- Clean using scourer
- Place clean, wet unit components on drying rack
- Use pressurised air to dry components – warn other people in the near vicinity that you will be using the air line
- Use a pipe cleaner to remove any sample that has filled fluid port.

#### 11.2.2.2 *Slurry Paste Method*

This method was developed in-house by BRS/GA and no external documentation exists. The method entails adding a known amount of ultra-pure water to oven-dried sample, rewetting and mixing the sample in ultrasonic bath followed by hydraulic pressing. Samples weighed 100 grams and water volumes were 50 ml. As a method it is considered to give only an approximate value of TDS because of cation exchange processing going on during wetting and drying. However, salinity results from this 'slurry' method were found to be comparable to those subjected to hydraulic press only, and useful for providing indicative salt contents for dry samples. The method was used until the Saturation Paste Extraction method was proven to give superior results.

#### 11.2.2.3 *Saturation Paste Extraction Method*

For core samples that were too dry and did not yield sufficient amounts of pore fluid, the saturation paste extraction method was used. This process involves the addition of pure water to bring the sample up to a known, reproducible moisture tension. Fluid was then extracted using pore pressers. This method has been taken from the accepted standard method for saturation pastes (method 2D1, Rayment & Lyons, 2010) and so not described in detail. Numerous researches have compared the ionic concentrations determined in sediment fluids (pressed samples), to those obtained with saturation pastes. Sonneveld *et al*. (1990) found that concentrations in soil solutions correlated reasonably closely with those of saturation pastes.

### 11.2.3 Compatibility Between Different Extraction Methods

Core profiles often have sediment processed by more than one method, therefore it was important to elucidate the comparability or disparity amongst the three methods, namely the hydraulic press, slurry and saturation extract. An experiment was undertaken to investigate this and to establish the mineral solubility, element mobility and water-rock interactions when sediments of different textures and compositions are subjected to varying physical conditions.

The few results that were conducted as part of the laboratory's Qa/Qc procedure indicate some trends between the slurry method and hydraulic press methods only. Elements that are highly soluble (e.g. Na, Cl) showed no significant difference between the methods. Divalent cations (e.g. Ca, Mg) decreases in the slurry method possibly associated with their re-absorption onto the clay surfaces. Silica abundance increases in the slurry method, likely a result from the calculation of 'in-situ' concentrations when the dilution factor was used.

Four sets of experiment were conducted with individual procedures designed for the saturation extract, slurry, hydraulic press methods and a reference (Table 11-2).

**Table 11-2.** *Procedures and analyses for the saturation extract, slurry, hydraulic press and reference methods.*

| Saturation Extract | Slurry | Hydraulic Press only | Reference |
|---|---|---|---|
| Oven dry at 45°C, water content measured | Oven dry at 105°C, water content measured | Hydraulic press | Oven dry at 105°C |
| Known amount of water added | Known amount of water added | Fluid undergoes hydrochemical analysis | Tungsten-carbide milling |
| Leave overnight, sample wet up from capillary rise | Mixing and homogenising in ultrasonic bath | Sediment residue undergoes oven dry at 105°C | Inorganic chemical analysis |
| Hydraulic press | Hydraulic press | Tungsten-carbide milling | |
| Fluid undergoes hydrochemical analysis | Fluid undergoes hydrochemical analysis | Inorganic chemical analysis | |
| Sediment residue undergoes oven dry at 105°C | Sediment residue undergoes oven dry at 105°C | | |
| Tungsten-carbide milling | Tungsten-carbide milling | | |
| Inorganic chemical analysis | Inorganic chemical analysis | | |

## 11.3 PHYSICAL PROPERTIES

A total of 4876 sediment samples were analysed for physical properties including grainsize, bulk density and moisture content.

### 11.3.1 Grainsize Analysis

Two different methods were used to obtain grainsize data – laser and sieve. Both methods have strengths and weaknesses as discussed below.

#### 11.3.1.1 *Malvern laser particle size analyser*

Laser diffraction is used to measure the volume weighted percentage of particles in a sample. Primarily designed for use by the paint manufacturing, pharmaceutical and food industries, at Geoscience Australia the machine is mainly used for analysis of marine sediment, estuarine sediment and regolith samples.

The high precision of the laser technique and the numerous detectable texture classes results in high quality data especially in the < 63 µm range (i.e. clay and silt). However, there is a limitation in the laser technique due to the construction of the instrument, prevents it from analysing coarser (i.e. >1.7 mm in diameter) sediments. These coarse size fractions are commonly present in sediments of various environmental settings, and the lack of data from this instrument implies that an alternative method needs to be sought.

#### 11.3.1.2 *Wet sieving grainsize analysis*

Traditionally, sedimentary and soil textures have been quantified using the settling or sieving technique. Sieving is a robust technique, and the textural classes that can be delineated are only limited by the range of sieves available. It is well adapted to provide results based on the Wentworth scale, but is not very likely to provide further information within each class fraction, especially clay.

Wet Sieving grainsize analysis was also used to determine the percentages of the mud, sand and gravel fractions of a sediment sample. This was done by splitting the sample into the separate fractions, using a wet

sieving method, and then determining the percentages of these fractions by weight. Two sieves were used in the analyses, 2 mm and 63 μm.

#### 11.3.1.3 *Compatibility of results*

Laser grainsize analysis is particularly good at measuring particles in the finer end of the scale, while sieving is better at measuring grainsize of larger particles. Thus merging the two sets of results appear to be a logical choice to utilise the strengths of both methods. However, the units of measurement and the way particles are measured differ, causing a number of issues.

The sieve technique gives results in weight and is dependent on the smallest dimension of the individual particle so as to pass through or be retained by the square mesh. The laser technique measures the volume and is dependent on the assumption of particle sphericity and its effects on diffracting the laser beam. The amount of materials used for sieving usually involves tens of grams whereas the laser technique utilises only one to two grams. The latter becomes an issue of representation of the population. Sample duplicates or quadruplets are needed to improve the representativeness.

To date, results from several studies carried out to compare the sieve and the laser diffraction techniques support the compatibility of both techniques. However, these studies were based on splitting homogenised samples and subjecting the materials to the laser and sieve method concurrently. Sediments used were well to moderately well-sorted which facilitated the delineation of an outlier in the results.

An internal analysis of the compatibility between different grainsize analysis results obtained for the BHMAR Project core was carried out. Separate sieved fractions were re-analysed using the laser instrument to aid direct comparison between sieved and laser diffraction results. Laser diffraction analysis was also conducted on the whole sample for further comparison. A range of sediments from well sorted mud, fine, medium or coarse sand to poorly sorted mud and sand were also analysed.

To merge the sieve results in weight% and the laser diffraction results in volume% particle density had to be determined. To achieve this, the sieved and weighed coarse textured materials (i.e. coarse to very coarse sand and granules) were placed in a water filled measuring cylinder to determine the volume displaced. The calculated density is expected to be similar to that of quartz (i.e. 2.65 g/cm$^3$). The simplified procedures are summarised in Table 11-3.

**Table 11-3.** *Procedures for comparing the sieve and laser diffraction techniques.*

| Experiment | Reference |
|---|---|
| Homogenised sample passed through a set of sieves based on Wentworth's scale; clay, silt, very fine sand, fine sand, medium sand, coarse sand, very coarse sand, and granule/pebble. | Homogenised sample passed through a set of sieves based on Wentworth's scale: mud, sand, granule/pebble. Each fraction (dry) is weighed. |
| Particles retain on each sieve are dried and weighed | Analyse sample using the laser diffraction technique. Top cut of 1.7 mm to be used. |
| Each size fraction is analysed using laser diffraction technique | |
| Very coarse sand and granule fractions are placed in water filled measuring cylinder to determine the volume displaced and calculate the density. For coarse textured samples, the abundant very coarse sand and granule should be measured separately. Omit this step for fine textured samples. | |

#### 11.3.1.4 *Textural analysis of fine-grained samples*

There is an apparent overabundance of non clay-sized material in the laser textural results of many fine-grained sediment samples from the BHMAR Project, especially in Blanchetown Clay. The Blanchetown Clay was deposited in a large lake and fine-grained lacustrine sediments well away from shorelines would be expected to contain abundant clay-sized material. Some Blanchetown Clay determinations were very

obviously wrong, for example wet sieving results for BHMAR 22-1 samples at 19.2 and 23.2 m depth indicated 19 and 56% gravel respectively. Laboratory core logging describes the clay at these levels as dry and crumbly, indicating the presence of hard clay aggregates that have not been broken down by the laser grainsize dispersion process, and have been incorrectly measured as gravel in the textural analyses. Other similar examples also occur. This led to conjecture that there was a significant problem with post-depositional aggregates in these samples which the standard Geoscience Australia Sedimentology Laboratory sample pre-treatment regime had not disaggregated.

There are three possible sources of post-depositional aggregates in the Darling Valley fine-grained sediments:

- Since deposition of the Blanchetown Clay ceased sometime between ~0.6 and ~1 Ma (Bowler, 1980; An *et al*., 1986; Bowler *et al*., 2006, McLaren *et al*., 2009) it has been buried by approximately 20 m or more of younger sediment and is likely to have been alternatively wet and dry during Quaternary climatic cycles. Some levels of the Blanchetown Clay have been found to currently have very low moisture content. The combination of burial, compaction and drying will undoubtedly result in the production of larger aggregates of clay-sized material. Clay-rich facies of older underlying stratigraphic units (Calivil Formation and Renmark Group) will have experienced greater burial and compaction but are less likely to have dried.
- Cementation of fine-grained sediments by secondary minerals associated with pedogenic (soil-forming) and early diagenetic processes can form aggregates which resist dispersion. Soil carbonate nodules are probably the most important of these materials but gypsum, iron, manganese, organic and siliceous cementation may also occur.
- The pore-water salinities of many of the BHMAR project sediments are high, especially in fine-grained sediments and away from the modern stream-channel flush zones. Within the Blanchetown Clay unit, pore-water salinities range from fresh to very saline (TDS <100 to > 35000 mg/L). The anions in saline pore waters, particularly $Cl^-$ and $SO_4^{2-}$, will be incorporated into the suspension during the Laboratory Dispersion Protocol (LDP) process and may be responsible for flocculation – therefore producing aggregates in the measurement suspension. Previous experience with playa and salt-lake sediments has demonstrated the necessity to remove all soluble salts from the sediment prior to textural analyses.

*Pretreatment and Dispersion of Samples*

The Geoscience Australia Sedimentology Laboratory uses a Malvern Instruments Mastersizer 2000 (Ver. 5.53) laser grainsize analyser to measure an approximately 1 gm sample dispersed in water using a protocol referred to here as the LDP:

- Initial drying after sub-sampling.
- Addition of water and $H_2O_2$, for at least overnight and up to a few days, to remove organics and assist sample breakdown.
- Ultrasonic treatment.
- Chemical dispersant is not added unless evidence during measurement suggests that the sample is not disaggregating.

For measurement in the laser grainsize instrument the subsample is placed in a beaker that contains a litre of water that cycles through the system via an impellor, which is assumed to also assist in breaking the sample down and maintaining dispersion. Sample disaggregation and dispersion is observed in real time as the sample cycles through the system. Repeated ultra-sonic treatment is applied until no further change is seen. Three repeat sample measurement runs are made to assess sample dispersion stability.

From the clear evidence, detailed above, that clay aggregates resistant to the minimalist LDP regime occur in Blanchetown Clay samples a more intensive pre-treatment regime was designed to overcome these problems. This more robust dispersion regime included washing to remove soluble salts, a more vigorous agitation regime to breakdown aggregates and introduced a dispersing agent to keep particles in suspension and to

prevent flocculation. This regime was based on sample treatment protocols used in the past by John Magee for size analysis of playa and salt-lake samples and is referred to as the Magee Dispersion Protocol (MDP):

- Washing the salts from the sediment by agitation (by paddle stirrer) in de-ionised water, then centrifuging and pouring off supernatant liquid. This step may require repetition.
- Sample placed in 600 ml de-ionised water with dispersant (5 ml 5% NaOH plus 10 ml of 10% Sodium Tri-poly-phosphate).
- Ultrasonic disaggregation
- Agitation for 30+ minutes by an electric paddle stirrer.

In most cases for the playa/salt-lake sediments, this regime resulted in disruption of clay aggregates and continuous dispersion for at least 24 hours in a standard 1150 ml settling tube.

*Initial Experiment to Test Laser Grainsize Results*

Following discussions with the Geoscience Australia Sediment Laboratory a number of Blanchetown Clay and Renmark Formation samples known to be clay-rich were resubmitted for laser textural analyses using the MDP for sample dispersion. The comparison between the initial analyses of these samples using the LDP and the repeat analyses using the MDP showed some unexpected results. Eight of these comparisons are shown in Figure 11-7 and Figure 11-8. All samples showed an increased volume of clay-sized material evident as either a slight shift of the smallest measured grainsize towards the finer particle-size range and/or, more significantly, a shift of the finer-grained modal peak from around 3-4 μm to about 0.75 μm. These changes were as expected following the use of a more rigorous dispersion regime with removal of salts, stronger agitation and addition of a chemical dispersant agent. However, the results also showed a significant increase in the sand fraction, evident as an increase in the amplitude of the sand-sized mode (BHMAR 36-1, 33.5 m; BHMAR 35-1, 14 m; BHMAR 31-1, 3 m), or a coarsening of the distribution range (BHMAR 33-1, 22.1 m and 176.9 m; BHMAR 57-1, 18 m; BHMAR 21-1, 15 m). Only BHMAR 14-1, 26.22 m does not show one of these characteristics but even it shows production of a significant new modal peak around 70 μm in the sand range.

As there was no conceivable way that the revised dispersion protocol could actually create sand grains it was concluded that drying of the samples between the initial and repeat analyses had resulted in the formation of grain aggregates, which even the more rigorous MDP dispersion process was unable to disaggregate. The initial samples were analysed with close to their original moisture content.

*Second Experiment to Test Laser Grainsize Results*

The initial experimental results had demonstrated that the more rigorous dispersant process has broken down some small aggregates (<10 μm) into constituent particles of <1 μm but had not resolved the question of larger sand-sized clay or mud aggregates. Accordingly, a more comprehensive investigation of dispersant regimes was undertaken using new samples from core material. Sonic core BHMAR 75-8 was obtained in Lexan polycarbonate core-tube liners sealed and stored at 4º C in the field immediately after retrieval, thereby allowing minimal sample drying prior to sub-sampling and submission to the Geoscience Australia Sedimentology lab for laser grainsize analysis

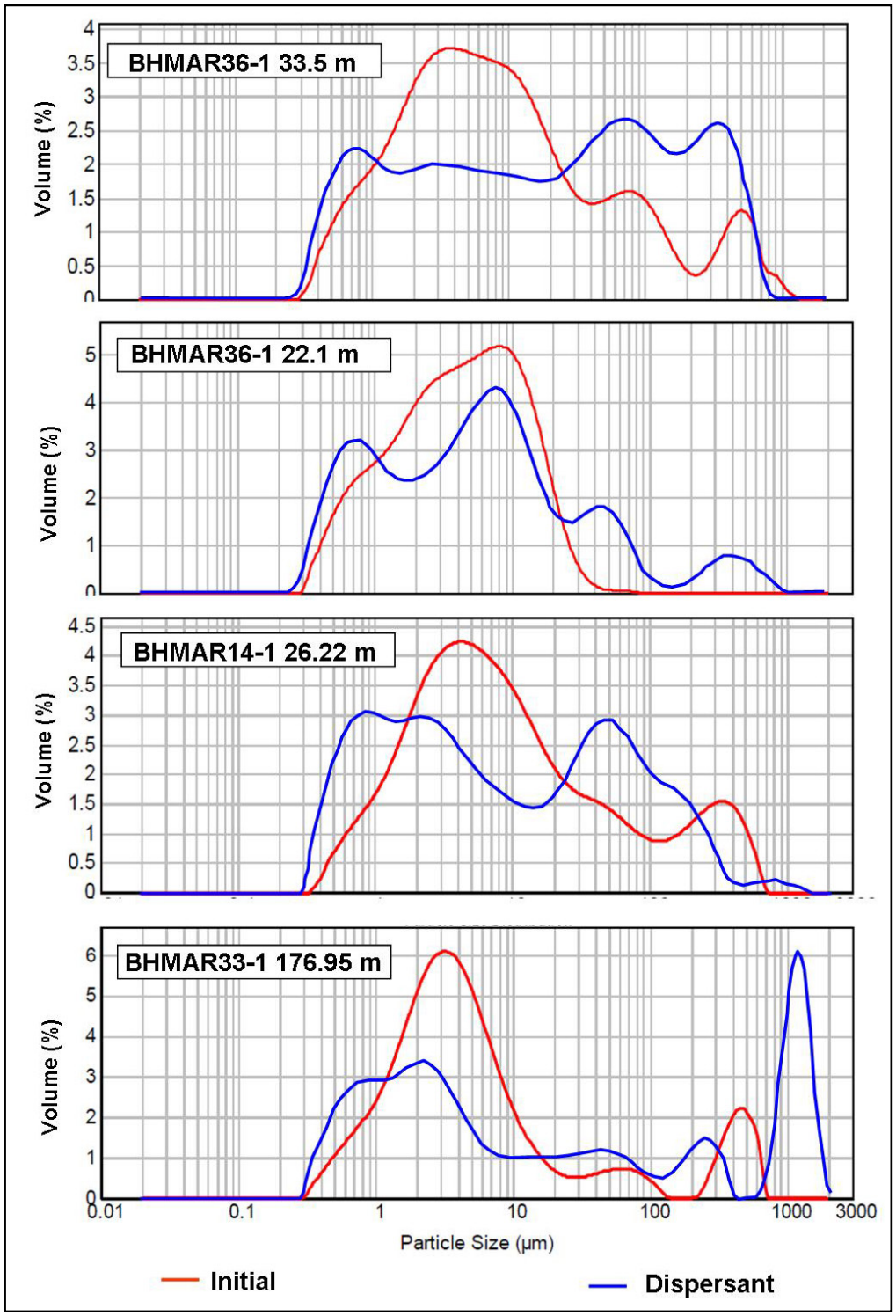



*Figure 11-7. Comparison between original laser textural analysis results using the Laboratory Dispersion Protocol (red) and the Magee Dispersion Protocol (blue).*

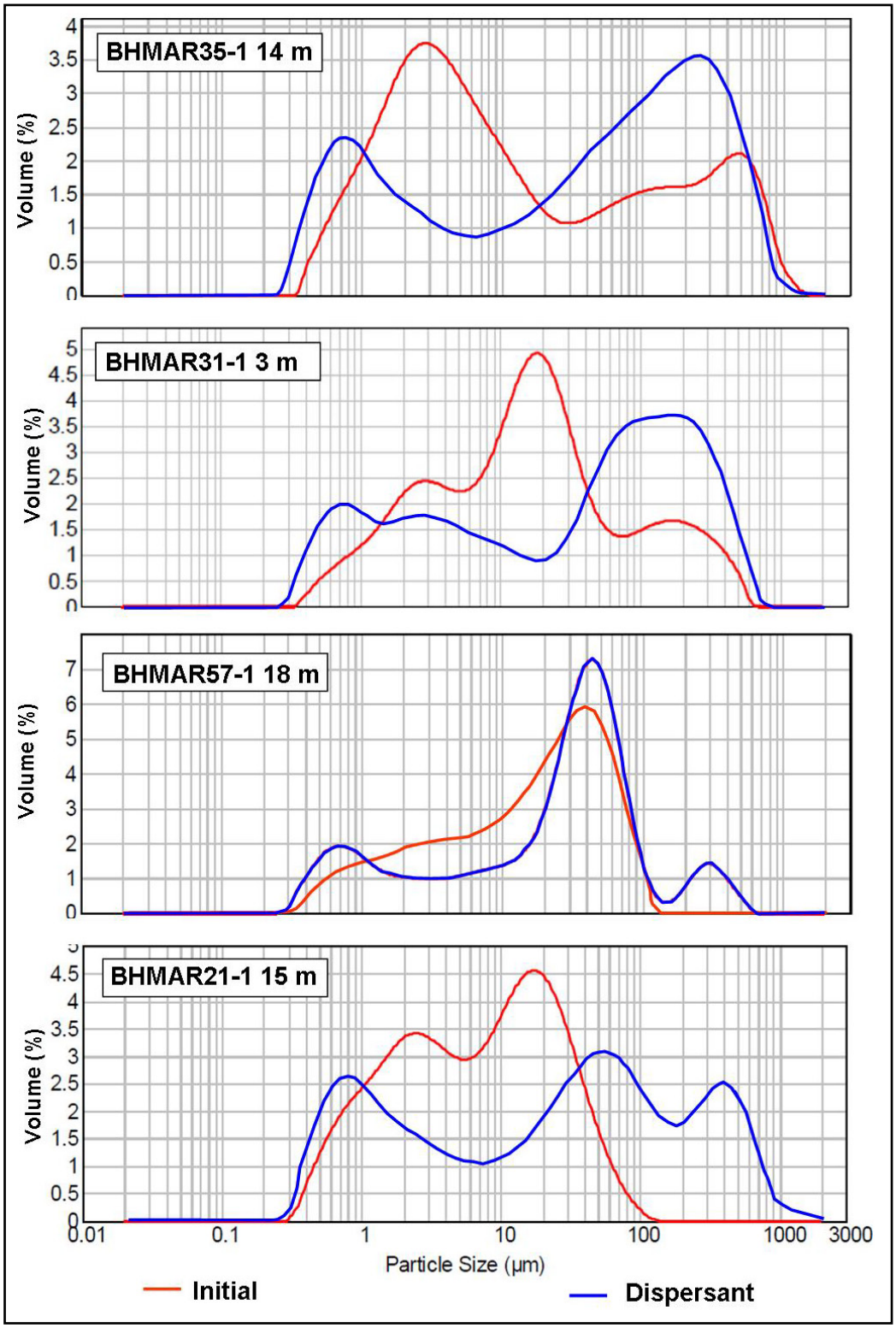



**Figure 11-8.** *Comparison between original laser textural analysis results using the Laboratory Dispersion Protocol (red) and the Magee Dispersion Protocol (blue).*

Two samples from Core BHMAR 75-8 (at 12.4-12.5 m and 15.5-15.6 m) with different natural moisture contents were chosen and submitted to the laboratory for preparation and analysis according to the scheme illustrated in Figure 11-9. This experiment was designed to test the following aspects of laser grainsize analyses:

- The difference between the LDP and MDP dispersion protocols.
- The effect of treatment with dilute acid (10% HCl) to remove secondary carbonate cementation, which neither dispersion protocol can disrupt. Secondary carbonate nodules have been logged in BHMAR core samples in the Blanchetown Clay.
- The repeatability of laser grainsize analyses by doing 5 repetitions of all samples analysed. The laser instrument methodology necessarily uses small samples and problems of obtaining representative samples are likely to be greater when particle size increases and the number of particles is lower.
- The nature of the sand-sized grains was analysed by wet sieving and retaining a >63 µm fraction for microscopic examination.
- The mineralogy of each sample was determined by quantitative bulk XRD analysis. This allows an independent assessment of likely grainsize by quantifying clay mineral abundance (likely to form most clay-sized particles) versus quartz (+ minor feldspar) which are likely to form any non clay-aggregate silt- and sand-sized grains.

The original moisture contents of the samples were 2.45% for BHMAR 75-8 12.4-12-5 and 24.9% for BHMAR 75-8 15.5-15.6. The results of the laser analyses are shown in Figure 11-10 (BHMAR 75-8 12.4-12-5) and Figure 11-11 (BHMAR 75-8 15.5-15.6). The percentage of clay minerals, quartz, feldspar and calcite as determined by quantitative XRD analysis are presented in Table 11-4.

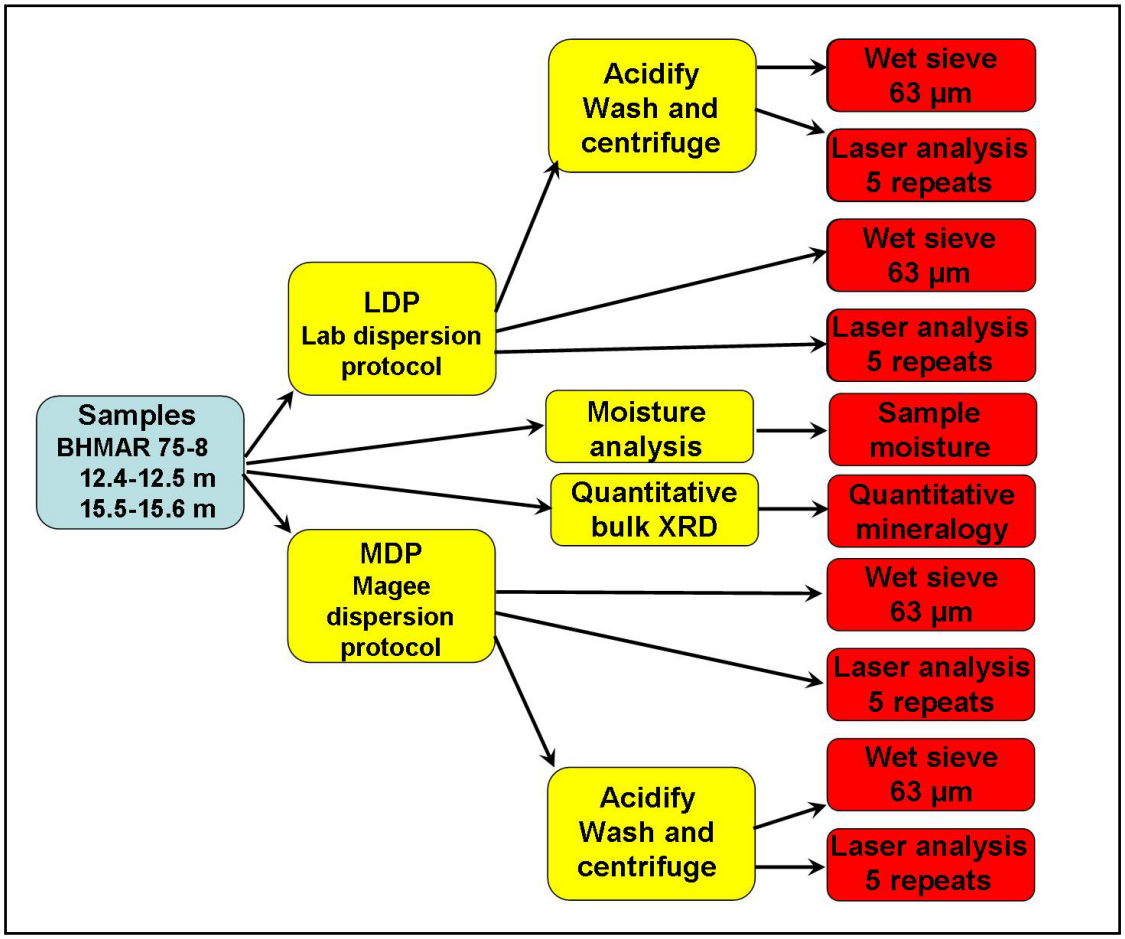



**Figure 11-9**. *Workflow diagram for second experiment, investigating the BHMAR sample laser grainsize analysis.*

**Table 11-4.** *Mineralogy percentages for BHMAR75-8 samples 12.4-12.5 and 15.5-15.6 m determined by quantitative XRD analysis.*

| Sample: BHMAR 75-8 | Kaolinite % | Smectite % | Mica % | Total clay% | Quartz % | Feldspar % | Calcite % |
|---|---|---|---|---|---|---|---|
| 12.4-12.5 m | 34.6 | 23 | 3.3 | 60.9 | 20.8 | 6.9 | 11.4 |
| 15.5-15.6 m | 24.1 | 25.8 | 9.8 | 59.7 | 35.3 | 3.4 | 1.6 |

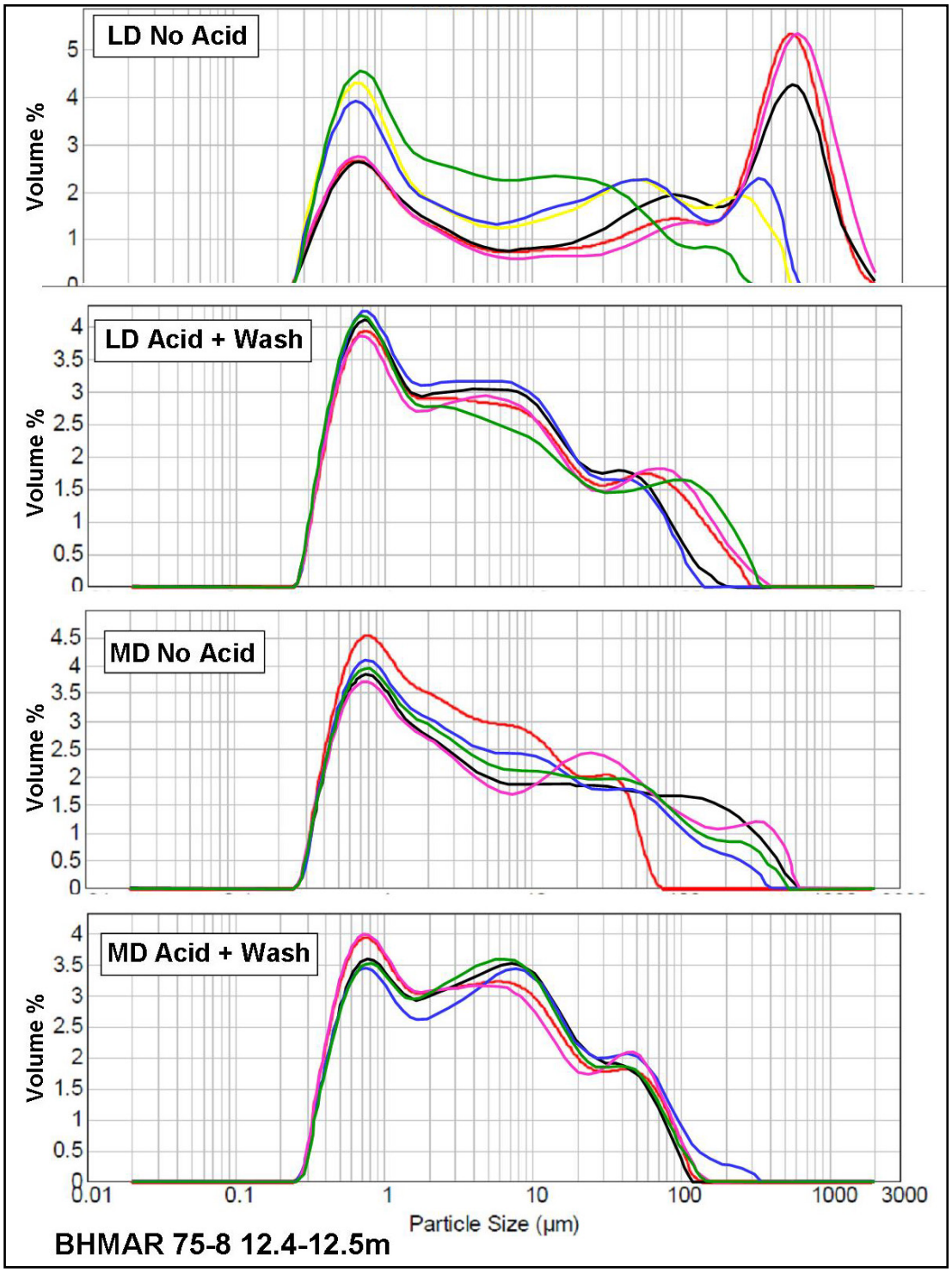



**Figure 11-10.** *Laser grainsize analysis for BHMAR75-8, 12.4-12.5 m. The inset boxes indicate the dispersion regime for each sub-sample and the different coloured curves represent analyses. Note the Y-axis scales vary.*

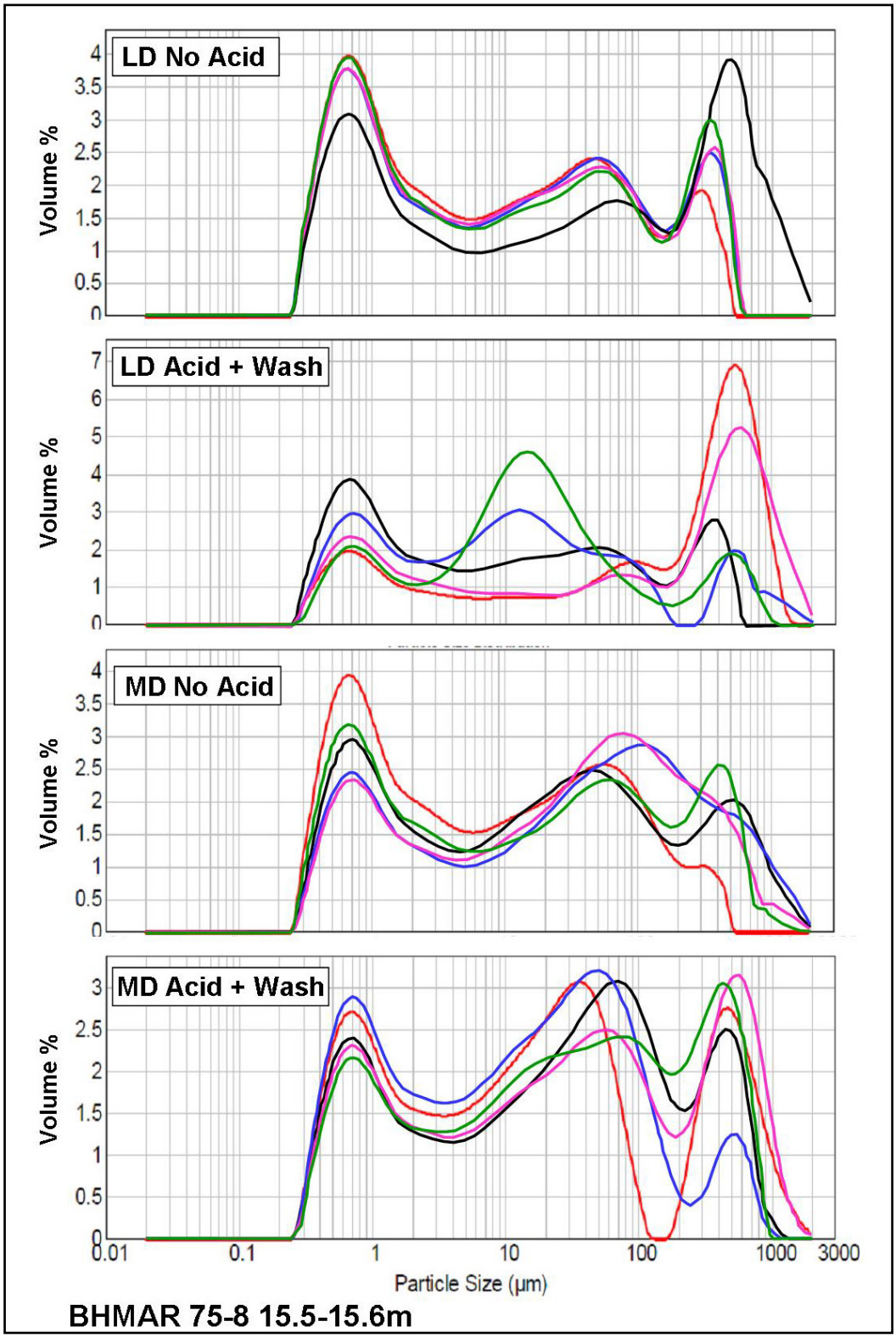



**Figure 11-11.** *Laser grainsize analysis for BHMAR75-8, 15.5-15.6 m. The inset boxes indicate the dispersion regime for each sub-sample and the different coloured curves represent analyses. Note the Y-axis scales vary.*

Sample BHMAR 75-8, 12.4-12.5 m is relatively dry (2.45% moisture content) and it contains about 60% clay mineral content (Table 11-4) a combination suggesting a high probability of the occurrence of clay or mud aggregates due to drying. Additionally, the relatively high abundance of calcite (11.4%, Table 11-4) in this sample strongly suggests the presence of secondary carbonate soil nodules which are also highly likely to cement clay and silt grains into sand-sized or larger particles. The relatively high proportion of quartz and feldspar (27.7%, Table 11-4) suggests the likelihood that significant amounts of primary depositional silt- and/or sand-sized grains will be present. The laser grainsize results (Figure 11-10) support these conclusions. All four dispersion techniques demonstrate the presence of abundant clay with a modal peak around 0.7-0.8 μm but the standard LDP dispersion (upper panel in Figure 11-10) also has abundant sand with a modal peak of around 600 μm, in the coarse-sand range. The addition of acid treatment to the LDP dispersion and the more robust MDP dispersion regime (middle panels in Figure 11-10) both eliminate the coarse-sand component leaving a fine-medium sand 'tail' in the distribution, with the MDP slightly less effective in this process. This provides strong evidence that coarse sand-sized mud aggregates are present in the sample that are resistant to the standard LDP dispersion, and the likelihood that secondary carbonate cementation plays a significant role in this process. The combination of acid treatment and the MDP dispersion (lower panel, Figure 11-10), which provides the strongest dispersion regime, results in the virtual elimination of all sand particles coarser than 150 μm and the creation of a broad silt peak with a modal value around 6-7 μm in the fine-silt range. In conclusion, this sample consists of abundant clay with a modal peak around 0.7-0.8 μm and significant quartz and feldspar particles in the silt to very fine sand range. Hand-lens examination of the >63 μm wet sieve fraction demonstrated the reality of a very fine sand quartz-dominant component. Based on a comparison of the mineral percentages and the MDP plus acid particle-size distribution, it is likely that there are silt-sized clay aggregates that even this most rigorous pre-treatment and dispersion regime has not disaggregated.

The wide variation between six repeat analyses of the LDP dispersion of BHMAR 75-8 12.4-12.5 m, which contains abundant sand-sized particles in the medium to very coarse sand range, demonstrates the difficulties of obtaining small representative samples of coarser-grained particles. The non-depositional processes (drying and secondary-carbonate cementation), which have produced these sand-sized particles, probably also plays a role by resulting in less systematic grain-size distributions. The more robust pre-treatment and dispersion regimes which eliminated the coarser fraction and broke up non-depositional aggregates resulted in more consistent results in repeat analyses. This is particularly true for the MDP plus acid dispersion regime for which the five repeats show very consistent results.

Sample BHMAR 75-8 15.5-15.6 m is wet (24.9% moisture content, probably saturated) and also contains about 60% clay mineral content (Table 11-4) but is probably unlikely to contain abundant clay or mud aggregates due to its water saturation. Additionally, the relatively low abundance of calcite (1.6%, Table 11-4) in this sample suggests minimal development of secondary carbonate soil nodules cementing clay and silt grains into sand-sized or larger particles. The higher proportion of quartz and feldspar (38.7%, Table 11-4) than in the 12.4-12.5 m sample suggests a stronger likelihood that significant amounts of primary depositional silt- and/or sand-sized grains will be present. The laser grainsize results (Figure 11-11) support these conclusions. All four dispersion techniques demonstrate the presence of abundant clay with a modal peak around 0.7-0.8 μm but they all also have abundant sand with modal peaks around 300-500 μm, in the medium-sand range. Between these clay and medium sand modes there is some variability in the particle-size distribution and location of modal peaks in the silt to fine-sand range but little systematic variation between different dispersion regimes. This indicates that the sample contains minimal post-depositional aggregates of mud- and clay-sized particles. In conclusion, this sample is a medium sandy mud with abundant clay with a modal peak around 0.7-0.8 μm and significant quartz and feldspar particles in both the silt and medium sand ranges. Hand-lens examination of the >63 μm wet sieve fraction demonstrated the reality of an abundant medium-sand quartz-dominant component.

All dispersion regimes for BHMAR75-8 15.5-15.6 m show a wide variation between repeat analyses due to the abundant sand-sized particles and the difficulties of obtaining small representative samples of sediment with significant coarser-grained particles. The increased variability in the more robust pre-treatment and dispersion regimes (lower three panels, Figure 11-11) suggests that some grain aggregates may have been disaggregated but the actual particle size distributions do not specifically support this interpretation.

*Implications for BHMAR Project Laser Grainsize Analyses*

The results of these investigations have clear implications for the interpretation of and confidence in laser grain-size analyses conducted for the BHMAR Project.

- Mud- and clay-sized sediments are highly likely to contain sand-sized or larger mud- and clay-particle aggregates if they have been dried (either naturally of in the laboratory) or contain secondary carbonate (or other) cementation. Air drying is sufficient to produce aggregates and it should be noted that the same process turns wet mud into adobe bricks.
- The standard minimal dispersion regime used in the Geoscience Australia Sedimentology Laboratory does not disaggregate these secondary particles.
- However, the standard dispersion regime does successfully determine the correct modal grainsize of the clay-fraction of samples that contain significant sand-sized clay- and mud-aggregates.
- Stronger pre-treatment regimes (including acid) and dispersion protocols can more effectively disaggregate these secondary particles but must necessarily add to laboratory time and therefore costs.
- In future, stronger pre-treatment (including acid) and dispersion regimes should be used for mud- and clay-rich samples which are dry or are known to have dried in the past and/or contain secondary cementation. Moisture analyses and quantitative XRD mineralogy determinations can help inform the decision to select samples requiring these processes.

Sand-sized sediments have issues with repeatability of results, due to the difficulty of obtaining representative samples because of the small sample requirements of the measuring instrument. This constraint is likely to increase with coarser textured samples.

*Broader Implications – Processing Samples from other Areas*

- Representative samples should be tested prior to routine analyses to determine the most appropriate disaggregation method for a batch of samples;
- Routine treatment with HCl where carbonate cementation is possible;
- Establish methodologies for dealing with non-carbonate cementation; and
- Develop sample splitting methods to ensure statistically representative sub-sampling.

### 11.3.2 Moisture Content

Gravimetric water content is a measure of the amount of water contained within a particular sample through the measurement of the wet and dry sample mass. It is defined as being the mass of the water contained within the sample divided by the mass of the sample dry. For the purposes of this study the moisture content was then expressed as a percentage of the sample using Equation 85.

$$\theta g = \text{gravimetric moisture} = \frac{\text{mass of wet sample (g)} - \text{mass of dry sample (g)}}{\text{mass of dry sample (g)}} \times 100$$

**Equation 85**

### 11.3.3 Bulk Density Determination

The bulk density of a sample is defined as the ratio between its dry mass and the bulk volume of the dry sample and is measured in g/cm$^3$. It is determined by Equation 86.

$\rho b = Mass/Volume$.

**Equation 86**

Density determination is often determined using the Archimedes Principle that states that any object immersed in a fluid, is buoyed up by a force that is equal to the weight of the fluid displaced by the object. The weight of the fluid displaced is directly proportional to the volume of displaced fluid and therefore the volume of the object submerged.

The sample, typically 5-10 grams, was oven-dried at 40$^o$C for 24 hours. A fragment of the dried sample would be coated with beeswax and weighed with a Metter Toledo XS64 density measuring analytical balance. This balance enables measurement of the sample first in air and then in an integral water bath.

## 11.4 PALYNOLOGY

Palynology is the study of pollen, spores, dinoflagellates, and other microscopic palynomorphs. Ninety three (93) sonic core samples from twenty two (22) drillholes were submitted for dating and interpretation of depositional environment. As different species were abundant at different types and under different climatic conditions, the identification of pollen and spores can be used to provide approximate ages and depositional environment for the sediments in which the samples were contained.

All samples were processed for fossil pollen and spores (miospores) and algal cysts (dinoflagellates) by the PalSed Laboratory at Geoscience Australia, using standard techniques of oxidation and filtration through 5 and 10 micron sieve cloth (see Traverse, 1988). Yields of kerogen, miospore and algal cysts varied from negligible to excellent; the preservation of miospores and dinocysts in the more productive samples was uniformly good.

Confidence ratings vary from very low to high depending on yield, the presence or absence of age-diagnostic fossil species (morphospecies) and the extent to which the in situ microfloral assemblages (microfloras) had been diluted by downhole caved younger material or reworked older material. For example, a number of microfloras were wholly dominated by reworked Jurassic (BHMAR35-1) or Permian taxa (BHMAR21-1).

Most of the samples submitted for palynostratigraphic analysis yielded some organic matter although much of this was in the form of colloidal-size fines, or plant detritus in which the cellular structure has been destroyed by natural oxidative processes (opaques, semi-opaques). Preservation of fossil pollen, spores and algal cysts was much more sporadic, with most drillholes yielding only dateable 1-3 samples. In some instances, highly productive samples were located within a metre of palynologically barren samples. Sediments accumulating in cut-off channels/backswamps or marine-influenced depositional environments usually preserved abundant, very diverse microfloras.

Dateable microfloras range in age from Plio-Pleistocene (*Tubulifloridites pleistocenicus* Zone) to Oligocene-late Early Miocene (*Proteacidites tuberculatus* Equivalent Zone), with a strong bias towards the Pliocene (*Monotocidites galeatus* and earlier *Tubulifloridites pleistocenicus* Zones) and late Early to Middle Miocene (*Canthiumidites bellus* Equivalent Zone). The age breakdowns allow the samples to be correlated with late Miocene-Pliocene Calivil Formation, Oligocene-Middle Miocene Renmark (non-marine), Geera Clay Equivalent (paralic), and Geera Clay (marginal marine) Formations with a moderate to high degree of confidence.

With very few exceptions, the lithostratigraphic correlations based on palynostratigraphic evidence agree with correlations based on lithostratigraphic evidence. One unexpected result was the occurrence of pollen

closely resembling those produced mangroves, including the Grey Mangrove (*Avicennia marina*) and unidentified members of the Rhizophoraceae. One Rhizophoraceae specimen in the Calivil Formation implies mangroves survived in the Menindee Lakes area as recently as the Early Pliocene. A second unexpected result was the presence of Jurassic microfloras, given that strata of this age have not been recorded in infrabasins underlying the Tertiary Murray Basin. The Jurassic microfloras and those dominated by reworked Permo-Triassic miospores and algae potentially act as sediment tracers, which in turn may assist in reconstructing the tectonic history of region.

## 11.5 ROCK CHEMISTRY AND MINERALOGY

### 11.5.1 Preparation

A total of 1,852 sonic core samples were analysed for rock chemistry and mineralogy. There are four types of samples that required processing – clay, clay, silt and sand mixture, sand, and pebbles. Each sample type requires different preparation.

**Clay –** during the drying process the wet clays will turn into hard, difficult to work with, material. The clays must therefore be broken up to allow the sample to pass through the riffle splitter without blocking the unit. The current method requires the sample to be placed in several heavy duty plastic bags and pulverized using a hammer. The pulverized material is then passed through a sieve and collected in a bucket. This may need to be performed several times to allow the entire sample to pass through the sieve.

**Clay, silt and sand mixture** – these samples may be partly friable. Samples can be passed through a sieve to collect all the hard clay material. The hard clay material can then be processed as above.

**Sand** – these samples can be directly riffle split from their drying trays.

**Pebbly** – pebbles can be broken up using a hammer or crushed using the Boyd Crusher.

Samples were run through the riffle splitter three times to homogenise the sample before taking the final splits. Samples were then milled using the Tungsten Carbine unit. A number of samples were previously milled in steel mills which resulted in contamination of the samples. When XRF and ICP-MS analysis was carried out these samples recorded elevated metal levels. The milling protocol was consequently changed to Tungsten Carbine and samples were re-milled and re-analysed.

### 11.5.2 XRF

#### 11.5.2.1 *Introduction*

X-Ray flourescence (XRF) is an analytical technique which uses the interaction of x-rays with a target material to determine its elemental composition (i.e. the range of oxides present and their proportion).

The routinely determined major oxides are $SiO_2$, $TiO_2$, $Al_2O_3$, $Fe_2O_3$, MnO, MgO, CaO, $Na_2O$, $K_2O$, $P_2O_5$ and $SO_3$. BaO, $Cr_2O_3$, NiO, CuO, ZnO, $Rb_2O$, SrO and $ZrO_2$ can be run as a supplementary to these. Detection limits of some of these oxides are shown in Table 11-5.

Four programs are available for major oxide determinations:

- 12:22 MAJORS. Designed for silicate rock samples;
- 57:43 MAJORS. This program was devised to handle samples that are difficult to fuse with the 12:22 flux. Trace elements Sc, V, Cr, Ni, Cu, Zn, Ba and Cl are determined on these fusions for sediment and other samples that may contain significant NaCl;

- Fe Stone MAJORS. This is a variation of the 12:22 majors. The count rate from the Fe K alpha line is filtered to bring it within counter limits; and
- SULPHIDES. This is another variation of the 12:22 method. The spectrometer parameters are set to allow for high Fe, Zn, and Cu count rates. Pb M alpha is used to ensure infinite thickness. Fe, Mn, Ba, Cr, Ni, Cu, Zn, Pb and S are determined as elements rather than oxides.

**Table 11-5.** *XRF major oxides.*

| Analyte | Detection Limit |
|---|---|
| $SiO_2$ | 0.006% |
| $TiO_2$ | 0.002% |
| $Al_2O_3$ | 0.001% |
| $Fe_2O_3$ | 0.002% |
| MnO | 0.001% |
| MgO | 0.004% |
| CaO | 0.002% |
| $Na_2O$ | 0.004% |
| $K_2O$ | 0.002% |
| $P_2O_5$ | 0.001% |
| $SO_3$ | 0.001% |
| MLO1 | 0.001% |

The trace elements Sc, V, Cr, Ni, Cu, Zn, As, Rb, Sr, Zr, Ba and F are routinely determined to complement those determined by the labs ICP-MS. The determinations are carried on a powder pellet. Detection limits for these trace elements are shown in Table 11-7.

Three programs have been developed for the determination of these elements:

- TRACES. This program is for routine silicate samples;
- Fe Stone TRACES. The Fe K alpha count rate is filtered to bring it within counter limits. Alpha coefficients for high Fe content samples are also significantly different from the TRACES program; and
- Carbonate TRACES. Used for carbonate samples with significantly different alpha coefficients than routine silicate samples.

**Table 11-6.** *Titrimetry.*

| Analyte | Detection Limit |
|---|---|
| FeO | 0.01% |

**Table 11-7.** *XRF trace detection limits (ppm).*

| As | Ba | Ce | Co | Cr | Cs | Cu | F | La | Mo | Nb | Nd |
|---|---|---|---|---|---|---|---|---|---|---|---|
| 2 | 8 | 10 | 2 | 2 | 8 | 1 | 50 | 6 | 1 | 1 | 10 |
| **Ni** | **Pb** | **Rb** | **Sc** | **Sr** | **Th** | **U** | **V** | **W** | **Y** | **Zn** | **Zr** |
| 1 | 2 | 1 | 2 | 1 | 2 | 2 | 2 | 3 | 1 | 1 | 1 |

#### 11.5.2.2 ***Methods***

The XRF used is a Philips PW2404 4 kW sequential spectrometer using a ruthenium (Rh) tube. It is used to determine the major elements present in samples and a range of the routinely more abundant trace elements to complement those analysed on the ICP-MS. The instrument is calibrated using a range of USGS and SARM (S. African Ref. Material) international standards. The method used is a variation of Norrish & Hutton (1969). No heavy absorber is added to the flux in this procedure.

Depending on the type of sample presented, Geoscience Australia's laboratory used one of three Lithium Borate fluxes. These are:

- 12:22 Flux. 12 parts Lithium Tetraborate and 22 parts Lithium Metaborate, used for 'normal' rocks.
- 57:43 Flux. 57% Lithium Tetraborate and 43% Lithium Metaborate which is used for carbonates.
- LM100. Lithium Metaborate, used for rocks with >75% $SiO_2$ content.

Glass fusions are prepared by accurately weighing approximately 0.80 g sample and 4.80 g of the selected flux into a Pt95%/Au5% crucible. 0.5 ml of a 20% $LiNO_3$ solution is added and the mixture sintered at 400 C for 10 minutes to oxidise any sulphide present. A pellet of blended cellulose and $NH_4I$ is added and the crucible is then transferred to a Bradway rocking furnace and heated at 1100ºC (12:22 and 57:43 fluxes), or 1000ºC (LM 100 flux) for a further 10 minutes. The molten mix is then poured into a preheated mould and cooled in an air stream. It is now ready for measurement using the appropriate 'Majors Program'.

The XRF is used to determine trace elements Zr, Sr, Rb, Zn, Cu, Ni, Cr, V, Sc and Ba on powder pellets. An extended program that adds in analyses for As, Ce, Co, Cs, La, Mo, Nb, Nd, Pb, Th, U, W and Y can be used if ICP-MS analyses are not required. Powder pellets are prepared by mixing 15 g of sample with 1.5 ml of a 7% PVA solution. The mixture is pressed to 2 ton per square inch and the resulting pellet air dried for 24 hours prior to measuring. The XRF analysis method used is a variation of Norrish & Chappell (1977).

## 11.5.3 ICP-MS

### 11.5.3.1 *Introduction*

Inductively coupled plasma-mass spectrometry (ICP-MS) is an analytical technique used for elemental determinations. ICP-MS combines a high temperature ICP source with a mass spectrometer. The ICP source converts the atoms of the elements in the sample to ions. These ions are then separated and detected by the mass spectrometer. ICP-MS has many advantages over other elemental analysis techniques such as atomic absorption and optical emission spectrometry. This includes equal or better detection limits, higher throughput and the ability to handle both simple and complex matrices with a minimum of matrix interferences.

### 11.5.3.2 *Methods*

The laboratory's ICP-MS is an AGILENT 4500Ce. It is used to determine a range of trace elements to complement those analysed on the XRF. The instrument is calibrated using synthetic standards. The calibrations obtained are verified against a range of USGS and SARM (S. African Ref. Material) and other international standards. Australian Soil and Plant Analysis Council (ASPAC) standards are also used.

In the Minerals and Geohazards laboratory samples are introduced to the ICP-MS as a mildly acidic aqueous solution containing approximately 100 ppm dissolved solids by way of a nebuliser which aspirates the sample with high velocity argon, forming a fine aerosol or mist. The aerosol then passes into a spray chamber where larger drops are removed via a drain. This process is necessary to produce droplets small enough to be vaporised in the plasma torch. Typically, only 2% of the original must pass through the spray chamber.

Trace elements routinely determined by the ICP-MS are Be, V, Cr, Ni, Cu, Zn, Ga, Ge, As, Rb, Sr, Y, Zr, Nb, Mo, Ag, Cd, Sn, Sb, Cs, Ba, La, Ce, Pr, Nd, Sm, Eu, Tb, Gd, Dy, Ho, Er, Yb, Lu, Hf, Ta, Pb, Bi, Th and U. Detection limits are shown in Table 11-8. The analytical method used divides the analytes above into four groups. The counts obtained from each analyte are ratioed against an isotope introduced to the solution as an internal standard. Inter element interference factors are determined using a range of single element solutions.

**Table 11-8.** *Detection limits of ICP-MS trace element analysis.*

| Analyte | Detection Limit | Analyte | Detection Limit |
|---|---|---|---|
| Ag | 0.01 ppm | Mo | 0.01 ppm |
| Be | 0.05 ppm | Nb | 0.04 ppm |
| Bi | 0.01 ppm | Nd | 0.01 ppm |
| Cd | 0.05 ppm | Pb | 0.5 ppm |
| Ce | 0.02 ppm | Pr | 0.01 ppm |
| Cs | 0.01 ppm | Sb | 0.01 ppm |
| Dy | 0.01 ppm | Sm | 0.01 ppm |
| Er | 0.01 ppm | Sn | 0.01 ppm |
| Eu | 0.50 ppm | Ta | 0.06 ppm |
| Ga | 0.1 ppm | Tb | 0.01 ppm |
| Gd | 0.01 ppm | Th | 0.01 ppm |
| Ge | 0.02 ppm | Tl | 0.01 ppm |
| Hf | 0.01 ppm | Tm | 0.01 ppm |
| Ho | 0.01 ppm | U | 0.07 ppm |
| La | 0.02 ppm | Y | 0.22 ppm |
| Lu | 0.01 ppm | Yb | 0.01 ppm |

## 11.5.4 XRD

### 11.5.4.1 *Introduction*

X-ray diffraction (XRD) is a versatile, non-destructive technique that reveals detailed information about the chemical composition and crystallographic structure of natural materials. Based on the principle of X-ray diffraction, a wealth of structural, physical and chemical information about the material investigated can be obtained.

### 11.5.4.2 *Methods*

X-ray diffraction was carried out with SIEMENS D501 and D5005 Bragg-Brentano diffractometers, each equipped with a graphite monochromator and scintillation detector, using CuKα radiation and CoKα radiation, respectively. The scan range for bulk samples was 2 to 70° 2-theta for Cu radiation, and 4 to 84 ° 2-theta for Co radiation, at a step width of 0.02°, and a scan speed of 1° and 2° per minute, respectively. Samples were milled in ethanol with a McCrone micronizing mill, dried, spiked with 20 wt% corundum and suspended on a side-packed sample holder.

Clay separation was performed by the settling method, and samples prepared according to the Millipore Filter Transfer Method (Moore and Reynolds, 1997). Clay samples were analysed after Mg-saturation (scan range 2-42° 2theta, step width 0.02°, scan speed 1°/min), saturation with ethylene glycol (2-32°, 0.02°, 1°/min), and heating to 350°C (2-28°, 0.02°, 1°/min) and to 550°C (2-28°, 0.02°, 1°/min).

The results were interpreted using the SIEMENS software package Diffracplus Eva 10 (2003) for identification, and Siroquant V3 for quantification.

## 11.5.5 Hyperspectral Studies of Core Materials

Hyperspectral methods collect large amounts of data over narrow spectral bands within a continuous spectral range (Chang, 2003). Mineral information is extracted from the data via interpretive software. Hyperspectral instruments can be used to study either individual samples, or continuous scanning of core, or from satellites or aircraft (Kuosmanen *et al.,* 2005). These methods allow the rapid acquisition of mineral data with a minimum of sample preparation.

Hyperspectal data is collected in a number of broad spectral bands, including the visible to near-infrared (VNIR), short wavelength infrared (SWIR), and thermal infrared (TIR) bands. The actual wavelengths detected varies from instrument to instrument, but VNIR is typically between 400 and 1400 nanometers (nm), SWIR 1.4 and 3 micrometres (μm) (1400 and 3000 nm), and TIR 8–15 μm.

A caveat to all hyperspectral mineral detections is that they are reported as abundances of minerals detected, not of total abundance. So, for example, since quartz cannot be detected by PIMA, a scan with this instrument might report a sample as containing 50% kaolinite, 40% nontronite, and 10% gypsum, even though it is 90% quartz.

Most studies to date have used Hylogger for the capturing of data in support of mineral exploration (Tappert *et al.,* 2011, Mauger and Huntington, 2005). Its use in published groundwater exploration prior to this study has been nil. Unlike Hylogger, PIMA has been extensively used in the study of groundwater related mineralogy, for example in connection with salinity (e.g. Dehaan and Taylor, 2003) or hydrothermal systems (Yang *et al.,* 2000).

### 11.5.6 HyLogger

#### 11.5.6.1 *Introduction*

The HyLogger instrument was developed by CSIRO to provide hyperspectral data on spectral properties to determine mineral composition. It is described by them as a prototype system of integrated hardware and software that facilitate the rapid collection of high density spectral reflectance measurements and continuous high-resolution colour imagery of drill core/chips/powders. HyLogging is non-destructive and the core/chips are measured in their original trays. The robotically controlled procedure, coupled with the largely automated processing software, *The Spectral Geologist (TSG) - Core*, enables the identification of a suite of minerals by their diagnostic spectral absorption features displayed in the Visible-to-Near-Infrared (VNIR) to Short-Wave-Infrared (SWIR) regions and the Thermal Infrared (TIR) region of the electromagnetic spectrum (CSIRO, undated). The system is ideal for the mapping of hydrated minerals, iron oxides, sulphates, carbonates and, less reliably, tectosilicates and organics. Since mineral identification by TSG is automated, matches must be taken with care.

#### 11.5.6.2 *Methods and analysis*

The system used by this study is that operated by the Geological Survey of South Australia in their Glenside Core Library. The selected cores were scraped flat and air-dried for at least 72 hours before being shipped. On arrival in Adelaide the core trays underwent further preparation, trimming excess PVC sleeving, inserting of black cardboard to mask reflections from the galvanised iron of the core trays, and inserting wooden blocks with precise depth intervals. Further air-drying for 72 hours ensured the samples were dry enough for scanning.

We initially acquired hyperspectral data from the BHMAR project area using the Hylogger system to characterise several core intervals (Table 11-9). The aim of this was to provide additional information on mineralogy to that obtained from XRD analysis of specific sample intervals. Of particular importance to the project was the need to better quantify the distribution of iron-bearing phases and clays, in both the Calivil Formation and Blanchetown Clay, because of the influence of these clays on the hydraulic properties of the units and on geophysical values derived from then, especially the NMR logging.

**Table 11-9.** *Core intervals selected for Hylogging.*

| Hole | BHMAR 23-1 | BHMAR 33-6 | BHMAR 75-5 | BHMAR 80A-2 |
|---|---|---|---|---|
| **Interval(s)** | 93.1-95.0 m | 8.6-64.5 m | 16.1-27.66 m<br>55.4-57.6 m | 13.6-53.0 m |
| **Scanned length** | 1.9 m | 55.9 m | 11.56 m<br>2.2 m | 39.4 m |
| **Reason selected** | Possible Paleozoic (or palaeochannel) | Section through aquifer | Conductive Blanchetown and part of main aquifer<br>Contact with Renmark | Resistive Blanchetown and section through aquifer |

An apparent correlation between the Kernel Function of NHMR-derived hydraulic conductivity data and the mineralogy of screen intervals from Hylogger in holes BHMAR 36-6 and BHMAR 75-5 was noted (see below), with Kernel Functions (*C* values) of 6,200 corresponding with predominantly smectites in the screened aquifer interval, and *C* values of 46,000 corresponding with kaolinite in the screened aquifer interval.

This made it possible to predict the dominant clay in the screened aquifer intervals in the remaining NMR-logged holes (Table 11-10). Time constrains precluded testing this prediction using Hylogger, however we deemed that determinations of clay mineralogy in the archived lab samples from these holes using the PIMA hyperspectral tool would be an adequate test.

**Table 11-10.** *Clay mineralogy in bores predicted from Kernel Function.*

| Hole | From | To | Screen Length | C value (Kernel Function) | Predicted dominant clay |
|---|---|---|---|---|---|
| 08-1 | 41 | 46 | 5 | 46,000 | Kaolinite |
| 16-1 | 12 | 52 | 40 | 46,000 | Kaolinite |
| 29-1 | 17 | 53 | 36 | 46,000 | Kaolinite |
| 34-1 | 27 | 51 | 24 | 46,000 | Kaolinite |
| 35-1 | 16 | 46 | 30 | 6,200 | Smectite |
| 58-1 | 62 | 69 | 7 | 6,200 | Smectite |
| 66-1 | 30 | 60 | 30 | 46,000 | Kaolinite |
| 75-5 | 40 | 52 | 12 | 46,000 | Kaolinite |
| 77-2 | 46 | 55 | 9 | 46,000 | Kaolinite |
| 79A-6 | 38 | 50 | 12 | 46,000 | Kaolinite |
| 88-3 | 65 | 71 | 6 | 6,200 | Smectite |
| 92-1 | 32 | 62 | 30 | 6,200 | Smectite |
| 99-1 | 33 | 57 | 24 | 6,200 | Smectite |

TSG does not return mineral percentage estimates but displays relative abundance. For most holes relative abundances of kaolin and smectite (generated by TSA (The Spectral Assistant – were given the smectite being the sum of all smectitic phases, such as montmorillonite and nontronite). In BHMAR 23 a smectite index is used rather than relative abundance because TSA was unable to deliver relative abundance even though mixing between kaolin and smectite can be seen in the spectra. For goethite and hematite a CSIRO-derived scalar was used to determine the position of the key absorption feature. Samples are more hematitic towards the shorter wavelengths and goethitic towards the longer wavelengths.

## 11.5.7 PIMA

### 11.5.7.1 *Introduction*

The Portable Infrared Mineral Analyser (PIMA) is an instrument which uses Short Wavelength Infrared Light (SWIR) in the range of 1300 to 2500 nm to illuminate a sample. Certain wavelengths of light within this range are absorbed due to the bending and stretching of molecular bonds. These absorptions appear as troughs or negative peaks below the spectrum's baseline, which represents 100% reflectance. The wavelength and shape of the peaks are unique to certain minerals and therefore enable mineral identification. The features within the SWIR range in most cases do not represent the fundamental vibrations of bonds but rather overtones and combination tones.

The type of bonds which display absorption features within the PIMA range include mineral groups such as sulphates, hydroxylated silicates, carbonates, phyllosilicates and ammonium-bearing minerals. Many of these absorptions are due to hydroxyl bonds which make it a particularly good tool for analysing different clays such as kaolinite and smectite and for identifying varying compositions of chlorites, biotites and sericites.

*Absorption effects*

A major absorption in the SWIR range is that of bound/interlayered water which is present in smectite clays. This water is not "free" or "wet" water but is actually part of the mineral structure. Free water does have a unique absorption that appears as a very deep and rounded feature and is present in wet samples or due to a fluid inclusion. For this reason all samples must be dry before sampling.

Many of the minerals have absorption features at the same wavelength, which overprint one another, making the identification of minerals particularly hard in some mixtures. Minerals such as muscovite and illite have very similar spectra that are only separated by minor absorption shapes which themselves are often overprinted. For this reason the minerals identified in this data set are only ones that have absorptions in the PIMA range and can be clearly recognised in the mixed spectrum.

The spectra may contain varying degrees of noise that ranges from occasional spikes, which do not affect the spectrum drastically, to complete destruction of the spectrum which prevents any minerals being identified or information extracted. This type of noise is caused by dark and opaque minerals such as pyrite and magnetite. Samples that have a particularly high magnetic susceptibility commonly have very intense noise.

### 11.5.7.2 *Methods and analysis*

The instrument used to analyse the borehole samples was the Integrated Spectronics Pty. Ltd. Portable Infrared Spectrometer (PIMA) II. This instrument readily identifies minerals associated with hydrous alteration, including sulphate, carbonates, opal, clays and micas (Thompson *et al*., 1999). Unlike Hylogger, PIMA is unable to differentiate non-hydrated iron oxides or detect iron oxides and organics. Spectral resolution of the PIMA is 6-10 nm. Data was interpreted using the PIMA SP/RAP Acquisition Module ©98 Version 2.2. Spectra were matched against an electronic library in the software. Matches therefore should be taken with care. The samples in this study were run using the PIMA II owned and operated by Geoscience Australia.

Small subsets – about a spoonful – were taken of the remnant archived samples from the screened interval depths of sonic bores holes that were logged with the NMR (Table 11-11). These samples were air dried in small plastic dishes (sample bottle caps) an oven set at 30 degrees for periods of 46 to 72 hours before being scanned by the PIMA. The samples were placed in a glass petri dish for scanning. Although BHMAR 80A-2 had already been scanned with the Hylogger, samples for PIMA analysis were also taken for comparison.

**Table 11-11.** *Samples selected for PIMA analysis.*

| Hole | From | To | Screen Length | Number of samples |
|---|---|---|---|---|
| 08-1 | 41 | 46 | 5 | 2 |
| 16-1 | 12 | 52 | 40 | 16 |
| 29-1 | 17 | 53 | 36 | 11 |
| 33-8 | 46 | 52 | 6 | 2 |
| 34-1 | 27 | 51 | 24 | 13 |
| 35-1 | 16 | 46 | 30 | 10 |
| 58-1 | 62 | 69 | 7 | 3 |
| 66-1 | 30 | 60 | 30 | 8 |
| 75-5 | 40 | 52 | 12 | 7 |
| 77-2 | 46 | 55 | 9 | 4 |
| 79A-6 | 38 | 50 | 12 | 4 |
| 80A-2 | 36 | 52 | 16 | 10 |
| 88-3 | 65 | 71 | 6 | 2 |
| 92-1 | 32 | 62 | 30 | 11 |
| 99-1 | 33 | 57 | 24 | 8 |

## 11.6 MAR CLOGGING POTENTIAL (CSIRO)

The success of a proposed Broken Hill Managed Aquifer Recharge scheme strongly relies on defining appropriate design and operational parameters in order to maintain high rates of recharge over the long term. Understanding the factors that control infiltration basin clogging or well clogging during Aquifer Storage and Recovery (ASR) and cause recharge rates to decline is essential to achieving this goal. CSIRO was commissioned by Geoscience Australia to define the water quality criteria and hence minimum pre-treatment requirements necessary to store Darling River Water at an acceptable scale within defined aquifers.

Studies were performed in the laboratory to determine the potential for near-well clogging for the proposed Broken Hill ASR and infiltration sites (see Section 9 of Lawrie *et al*., 2012c). Samples of the target Calivil Formation aquifer and Coonambidgal Formation material from the BHMAR33 bore were packed into separate columns to evaluate clogging potential for ASR and infiltration basins respectively.

Four types of water were studied for the ASR case, including untreated Darling River water, bank filtration treated Darling River water; Menindee town water and Menindee town water treated by granular activated carbon filtration.

All columns were allowed to equilibrate with recirculating groundwater for 24 hours prior to testing of recharge water. Hydraulic heads and basic influent water quality data were recorded, and samples were analysed for a range of physico-chemical parameters. At the end of the studies the columns were sectioned and an index of microbial growth was analysed along the length of the column.

Declines in hydraulic conductivity from a mean of 2.17 m/d occurred within all columns of Calivil Formation sands over the 37 days of the experiment. The GAC treated town water gave an 8% decline in hydraulic conductivity over the 16 cm length of columns, which was significantly lower than the decline observed in the other source waters with mean declines of 26-29%. Over the first 3 cm of column length, where most clogging occurred in each column, the mean hydraulic conductivity declined by 10% for GAC treated town water compared with 40 to 50% for the other source waters. The penetration of the zone of reduced permeability was least for GAC treated town water (<8 cm) compared with other source waters, notably untreated river water (>13 cm). Although the turbidity and membrane filtration index were two to three orders of magnitude higher for untreated river water than all other sources, the differences in clogging rates were surprisingly small. Nutrient concentrations (C, N and P) varied over a much smaller range (less than one order of magnitude) with GAC treated town water having the lowest concentrations. Evidence from polysaccharide concentrations and bacterial numbers in columns when they were dissected and analysed at the end of the experiment confirmed that biological growth was the dominant form of clogging. This was evident by the non-linear decrease in hydraulic conductivity, the accumulation of DNA and polysaccharides

at the inlet (indicators of biofilm) and the observation of fine colloidal material trapped in the biofilm (for the Darling River waters). Further chemical clogging through precipitation of minerals was found not to occur within the laboratory columns, and dispersion of clay was also found to be negligible.

In relating these column results to the field situation of a MAR trial, care should be taken to account for the differences between water quality available for the trial and formation characteristics at the trial site in relation to those that were used in the column study. The results demonstrate that of the four water types tested only one (GAC treated town water) is likely to be viable for ASR over the longer term for an operational site. Use of the other waters that resulted in significant clogging over 5 weeks in columns is not advised.

Even so, there is still a slight risk of chronic clogging over the longer term, but as with other ASR sites it is expected that this would be manageable by backflushing of the ASR well to remove any accumulated particulate material from time to time (NRMMC-EPHC–NHMRC, 2009). This purging would be governed by monitoring to keep track of changes in near-well hydraulic conductivity at each injection well as is standard practice. It is possible that other possibly cheaper types of treatment could be substituted, for example by reliance on chlorination for management of near-well biological clogging. However these have risks that would need to be assessed in tests with longer columns and in field trials using the GAC treated town water as a reference source for side by side evaluation if treatment costs suggest such measures warrant consideration. Monitoring of water quality, notably nutrients and turbidity in injectant is also warranted as verification of treatment performance and to allow mass balances to be calculated for the ASR wells.

The infiltration experiment shows that more permeable media than those that were sampled are needed if infiltration basins are likely to be effective. An initial hydraulic conductivity of at least 1 m/d is recommended in order to achieve desirable hydraulic loading rates of 30 to 50 m/year with only infrequent basin maintenance.

These risks in proceeding with a pilot trial should be manageable to within acceptable limits by ensuring:

- That the quality of the source water from the Darling River is improved by pre-treatment prior to injection. Pre-treatment should involve conventional coagulation/flocculation to achieve low particulate levels and granular activated carbon (biofiltration) to remove DBOC. Average values of water quality parameters for GAC treated town water used in the experiment provide an indicative target for injectant quality, assuming that column material is representative of future ASR wells (i.e. turbidity < 0.6 NTU, MFI < 2 $s/L^2$, DOC< 5 mg/L, BDOC < 0.2 mg/L, total N < 0.2 mg/, total P < 0.5 mg/L). Consideration should be given to disinfection of the water to allow residual disinfectant to keep the well face clean, and possible relaxation of some of these targets, recognising that this approach would require validation before adoption.
- The turbidity, pH, conductivity, nutrients and oxygen status of the injectant as well as the injection rates and pressures should be carefully monitored during the trial to evaluate the operational performance and to enable fine-tuning in subsequent phases of project development.
- Additional parameters should also be evaluated in the injectant and at observation wells directly influenced by breakthrough of recharge water. Parameters would include total and dissolved iron and manganese, electrical conductivity, pH, redox potential, dissolved oxygen, total dissolved-gas pressure, temperature, major ions, nitrogen species (nitrate, ammonium and total Kjeldahl Nitrogen), phosphorus (total and soluble reactive P) and dissolved organic carbon and biodegradable dissolved organic carbon.

For the full CSIRO report, refer to Appendix 11 (Apps & Lawrie, 2012).

## 11.7 LABORATORY HYDRAULIC CONDUCTIVITY TESTS

Hydraulic conductivity of 19 core samples, 11 aquitard samples and 8 aquifer samples was completed by the Water Research Laboratory at the University of New South Wales using a desktop falling head methods (for aquifers) and centrifuge permeameter (for aquitards).

Groundwater studies often assume that hydraulic conductivity (K) is equivalent to the intrinsic permeability of geological material, since there is little variation in fluid density and viscosity in shallow groundwater systems (van der Kamp, 2001). In subsequent discussion the terms permeability and hydraulic conductivity, K (dimensions L/T) are used interchangeably. Low permeability material is defined by Neuzil (1986) as K $<10^{-8}$ m/s, although permeabilities much lower than this have been estimated for formations in the study area (e.g. $10^{-16}$ m/s). It was found that permeability commonly varies over 3 orders of magnitude for similar porosity (Neuzil, 1994). The natural variability of hydraulic conductivity within apparently homogeneous geological media is large. On this basis, it is reasonable to report permeability measurements to the nearest order of magnitude. Laboratory techniques, however, may be able to report a more precise value to a tenth of an order of magnitude (or two significant figures). Natural permeability variability, both within a core sample, and between core samples from adjacent depths are likely to be more variable than plausible laboratory measurement precision.

### 11.7.1 Preparation

#### 11.7.1.1 *Physical characterization of the core*

AS 1289.2.1.1 sets out the method for laboratory determination of the moisture content of a soil as a percentage of its dry mass, using a standard oven. The moisture content (w) of the soil as a percentage of the dry mass can be calculated from Equation 87.

$$\omega = \frac{m_b - m_c}{m_c - m_a} \times 100$$

**Equation 87**

Where $w$ is moisture content of soil, in percent; $m_b$ is mass of container and wet soil, in grams; $m_c$ is mass of container and dry soil, in grams; and $m_a$ is mass of container, in grams.

A pocket penetrometer was used to provide an indication of sediment stiffness. A penetrometer measures the resistance in pushing a rod into the core sediment surface and is a measure of the unconfined compressive strength (UCS - typically in units of kg/cm$^2$).

#### 11.7.1.2 *Preparation of influent water*

Influent water was synthesised to approximately the pore fluid at the depth of core collection. Using water quality data, total ionic strength and major ion ratios (chloride, sulfate, sodium and calcium) were calculated for target solutions. Analytical grade reagents were prepared with Milli-Q pure water to target concentrations and the pH adjusted if necessary with concentrated nitric acid. EC and pH values of prepared solutions were measured with calibrated water quality meters.

Five different types (A-E) of influent water were prepared for the 19 cores to be tested.

#### 11.7.1.3 *Setting core in test liners*

Cores were set in liners for both benchtop and centrifuge permeameter testing (Figure 11-12). If the cores were within Lexan drill liners, these were left undisturbed and included in the resin set. A temporary blank

base, covered in silicon grease, was used to ensure that the base of the core was at a distance suitable to fit geotextile filter cloth and drainage plate for testing. Two-pack resin (Megapoxy 240) was mixed according to manufacturer instructions and poured into the annulus between the core and the liner and allowed to cure over at least 24 hours. Core lengths were generally 100 mm for falling head permeameter and 50-100 mm for centrifuge permeameter testing.

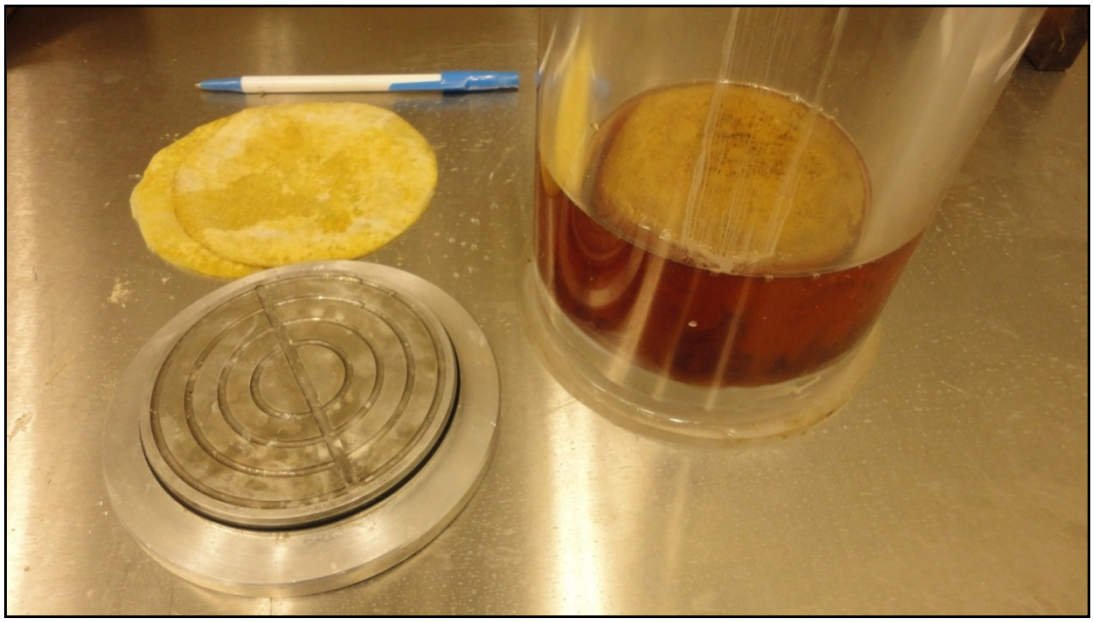


**Figure 11-12.** *Resin setting of core.*

## 11.7.2 Analysis

### 11.7.2.1 *Benchtop*

"Aquifer" cores were tested using benchtop methods suitable for sands and silts. Confirmation of method suitability was based on manual inspection of sediment on opening of each core.

Direct determination of permeability in the laboratory using a device called a falling head permeameter (Figure 11-13) following AS 1289.6.7.2-2001. WRL designed and fabricated acrylic permeameter cells were used, including filter plates and air vents. Cores were tested 'bottom up' to allow air to escape and flow. Core dimensions were typically 100 mm length by 85-90 mm diameter, set in resin.

Glass burettes of varying internal diameters (<10-35 mm) were available to complete testing within approximately 5 minutes or longer time periods (maximum of ~ 15 hours), depending on the hydraulic conductivity. The base of the burette tape (to nearest mm) was positioned 300 mm from the base of the core, and the head measurements corrected relative to the influent outflow height. Cores were permitted to 'saturate' prior to testing, and each core tested twice or three times.

Hydraulic conductivity calculations for the falling head permeameter test were based on Equation 88.

$$K = \frac{2.3 a_s h}{(6 \times 10^4) \times At} \times \log_{10}\left[\frac{h_i}{h_f}\right]$$

**Equation 88**

Where $K$ is coefficient of permeability at test temperature (m/second); $a_s$ is cross-sectional area of standpipe ($mm^2$); $h$ is thickness of specimen (mm); $A$ is cross-sectional area of specimen ($mm^2$); $t$ is time interval for measurement (minutes); $h_i$ is initial height in the standpipe (mm); and $h_f$ is final height in the standpipe after time interval $t$ (mm).



**Figure 11-13.** *Benchtop falling head permeameter.*

### 11.7.2.2 ***Centrifuge permeameter***

Cores received labelled as "aquitards" were tested using centrifuge permeameter methods suitable for low permeability silts and clays. Confirmation of method suitability was based on manual inspection of sediment on opening of each core.

The centrifuge permeameter (Figure 11-14) located at WRL is a new facility of the National Centre for Groundwater Research and Training (NCGRT) to characterize aquitards. The permeability of low permeability drill core from clayey sediment and shale (up to ~500 g) is tested under accelerated gravity in a Broadbent G-18 geotechnical centrifuge (2 m diameter). Steady- state flow equilibrium is achieved faster at accelerated gravity than for other laboratory testing, and in- situ stresses can be applied to drill core collected from <100 m depth.

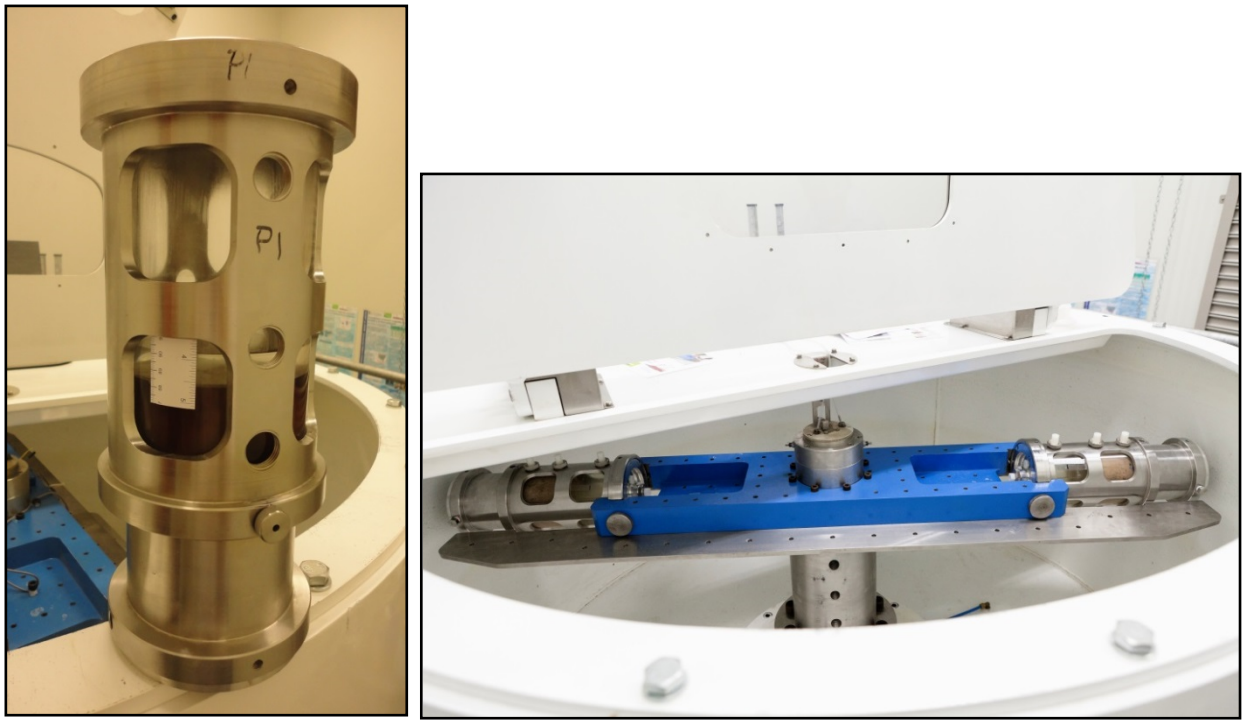



**Figure 11-14.** *Photographs of the centrifuge permeameter.*

The NCGRT Centrifuge permeameter testing used a method adapted from ASTM D6527-2000. Duplicate core samples of 65-100 mm diameter and 50 to 100 mm length were required for simultaneous testing at either end of the beam. Samples were resin sealed in acrylic liners. Influent for testing (at least 2 litres per core) was provided from a similar depth to the core sample. Alternatively, synthesized water or deionized water was used in some cases, although this adversely affected the permeability. Depending on depth and consolidation state of the sample, the standard centrifuge steady-state flow method is suitable to test permeabilities in the range of $10^{-6}$ to $10^{-12}$ m/s.

For these tests, cores of 80-95 mm diameter and 50-100 mm length were set in resin and placed on a geotextile cloth and on top of a drainage plate, and sealed within the permeameter 'cage'. An influent head of 10-50 mm was ponded on the sample, and effluent was collected in a reservoir below the cores. Two core samples were balanced to the nearest 1 g and tested simultaneously at either end of the centrifuge beam, with manual measurements of head and effluent volume (to the nearest 0.01 g) during brief centrifuge stops. The centrifuge permeameter was operated at 10 g-force for 10 minutes, 20 g-force for 30 minutes and 100 g-force for the duration of the test, or 150 g-force for some very low hydraulic conductivity cores.

Total centrifuge run was approximately 2 days for each set of two samples, given the very low hydraulic conductivity (total of 6 centrifuge runs, NCGRT Tests 7-12).

Hydraulic conductivity calculations for the centrifuge permeameter were based Equation 89.

$$K = \frac{Q}{A} \times \frac{0.253}{\rho_w r(\omega)^2}$$

**Equation 89**

Where $K$ is hydraulic conductivity (m/second); $Q$ is fluid flux (mL/hour); ω is angular velocity (RPM); $\rho$ is sample flow area ($cm^2$); $r$ is radial distance (cm); and $\rho_W$ is fluid density ($g/cm^3$). Centrifugal acceleration (a) is equal to the scaling factor (N), or G-max, multiplied by g-level (a = N x g). Centrifugal acceleration, or N, at any point within the centrifuge core is calculated as follows:

$$a = \omega^2 r$$

**Equation 90**

Where $a$ is the centrifugal acceleration (m/s$^2$), ω is the angular velocity (radian/second), $r$ is the radius from the axis of rotation (m). The angular velocity is related to *RPM* (revolutions per minute) as follows:

$$\omega = 2\Pi \times RPM / 60$$

**Equation 91**

Substituting this equation into the preceding equation and dividing by $g$ gives this final equation 91 to determine the $N$ scale (or *G-max*) for a given *RPM* and radius $r$:

$$N = 0.001122 \times (RPM)^2 \times r$$

**Equation 92**

## 11.8 TOTAL AND EFFECTIVE POROSITY

Total and effective porosity measurements were undertaken on representative samples of the aquifer units. This data was used in a correlation with the borehole NMR data, to assess the potential for the NMR free water as a surrogate for effective porosity. The emphasis was on the Calivil Formation semi-confined aquifer but sampling also included the overlying unconfined Menindee Formation. Sampling was across a variety of textures, ranging from stiff clay to gravel, with the aim of characterising effective porosity across the textural classes.

Porosity measurements were carried out on intact core specimens obtained using the sonic coring technique. Lexan PVC lining of 1.5 m length was inserted into the core barrel during drilling and the sediment core was extruded from the barrel together with the lexan lining. The cores were immediately capped on both ends and sealed to prevent escape of water and to minimise the exposure to the atmosphere. This procedure reduced the opportunity for the sediment sample volume to shrink or expand, hence altering its porosity.

The lexan core samples were collected from two sites, BHMAR33-9 and BHMAR75-8. At each site, there is a stratigraphic bore located within 30 m (BHMAR33-8 and BHMAR75-5, respectively) from which the stratigraphy and textural logging was used to plan the lexan-encapsulated coring and the subsequent sampling strategy. The required core length for the porosity analysis is 15cm. A total of 25 samples were obtained to provide a range of representative textures (Table 11-12).

Depending on the sample medium, different disciplines (e.g. agriculture, geotechnical, petroleum) use different approaches to determine porosity. To obtain a comparison of these methods, three laboratories were chosen to carry out a suite of analyses. These include Core Laboratories Australia in Perth, Soil Water Solutions in Adelaide and University of New South Wales Department of Petroleum Engineering in Sydney. The three methods chosen were the helium injection, kerosene saturation and matric potential methods.

### 11.8.1 Helium Injection Method

For this procedure, the lexan core samples were freeze dried using dry ice and a known volume of core plugs were subsequently obtained by drilling with compressed air. These core plugs were encapsulated in a nickel sleeve with stainless steel end screens. The sample was injected with helium at 800 psi. The volume of helium injected divided by the total volume of core plug is used to derive the total porosity in percent.

**Table 11-12.** *Samples of lexan-encapsulated sonic core for measurement of total and effective porosity.*

| Borehole | Depth m | Stratigraphy | Texture | Texture Class |
|---|---|---|---|---|
| **BHMAR33-9** | 3.48 | Menindee Formation | Medium sand | 4 |
| **BHMAR33-9** | 15.20 | Menindee Formation | Fine sand | 3 |
| **BHMAR33-9** | 17.25 | Menindee Formation | Medium sand | 4 |
| **BHMAR33-9** | 28.46 | Calivil Formation | Fine sand | 3 |
| **BHMAR33-9** | 29.30 | Calivil Formation | Fine sand | 3 |
| **BHMAR33-9** | 38.95 | Calivil Formation | Muddy sand | 2 |
| **BHMAR33-9** | 50.15 | Calivil Formation | Gravelly sand | 5 |
| **BHMAR33-9** | 50.85 | Calivil Formation | Coarse sand | 5 |
| **BHMAR33-9** | 56.45 | Calivil Formation | Gravelly sand | 5 |
| **BHMAR75-8** | 20.55 | Calivil Formation | Mud | 1 |
| **BHMAR75-8** | 26.75 | Calivil Formation | Mud | 1 |
| **BHMAR75-8** | 30.20 | Calivil Formation | Fine sand | 3 |
| **BHMAR75-8** | 30.75 | Calivil Formation | Muddy sand | 2 |
| **BHMAR75-8** | 31.45 | Calivil Formation | Muddy sand | 2 |
| **BHMAR75-8** | 33.00 | Calivil Formation | Medium sand | 4 |
| **BHMAR75-8** | 40.80 | Calivil Formation | Gravelly sand | 5 |
| **BHMAR75-8** | 42.65 | Calivil Formation | Gravelly sand | 5 |
| **BHMAR75-8** | 44.15 | Calivil Formation | Gravelly sand | 5 |
| **BHMAR75-8** | 45.65 | Calivil Formation | Gravelly sand | 5 |
| **BHMAR75-8** | 46.35 | Calivil Formation | Medium sand | 4 |
| **BHMAR75-8** | 47.17 | Calivil Formation | Coarse sand | 5 |
| **BHMAR75-8** | 47.87 | Calivil Formation | Coarse sand | 5 |
| **BHMAR75-8** | 50.15 | Calivil Formation | Gravel | 5 |
| **BHMAR75-8** | 51.65 | Calivil Formation | Gravel | 5 |
| **BHMAR75-8** | 52.35 | Calivil Formation | Medium sand | 4 |

### 11.8.2 Kerosene Saturation Method

Sediment sample plugs were taken from the lexan cores and encapsulated using sieve screen and Teflon tape. The samples were oven dried at 60$^{o}$C until there was no loss in weight between two consecutive measurements. The samples were then placed in a dessicator and a vacuum applied at 10 kPa for 24 hours. Kerosene was released into the dessicator to saturate the sample and the weight of the fully saturated sample measured. From the known volume of the core plugs, density of the kerosene, and the difference between dry and wet weights, the total pore volume was determined.

### 11.8.3 Matric Potential Method

The lexan core samples were fitted at one end using cloth and sealed on the other end with a casing attached to a flexible tube. The core, with the cloth end facing down, was fully immersed into a water bath using rain water. A 8 kPa suction was applied via the flexible tube and the core was let to stand for 24 hours to allow full saturation.

The fully saturated core was removed from the water bath and weighed and this is reported as the water retained at 0.1 kPa. The core was immediately placed onto a porous ceramic plate (cloth end facing down) with a 0.5 kPa suction applied to the plate. The core was weighed again after 12 hours and placed backed onto the ceramic plate. This process was repeated with increasing suction applied at 5 kPa, 10 kPa, 70 kPa and 200 kPa. The core would shrink to some extent and the volume of the shrunken core measured and the bulk density calculated. Assuming a particle density of 2.65 g/cm$^3$, the total porosity was calculated using the equation 1 – (bulk density/particle density). Three samples containing a high proportion of iron coated gravel or carbonate cement were measured separately to determine the actual particle density. These measured particle densities, up to 3 g/cm$^3$, were used to derive the total porosity for these particular samples.

To determine the partial porosity at various matric potentials, the weight of water loss were determined by subtracting the total porosity by the volume of water still remaining in the core. The water retention curves (Figure 11-15 and Figure 11-16) show an inflexion point at 10 kPa, which suggests that the water loss at this matric potential best represents the effective porosity.

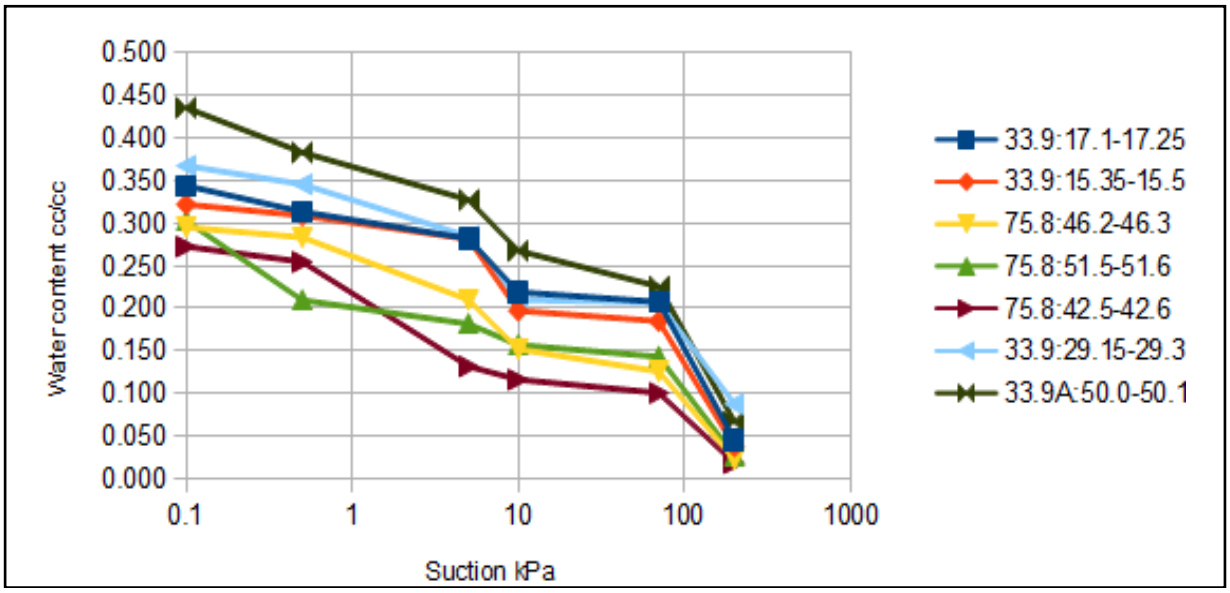



**Figure 11-15.** *Water retention graph for fine textured samples, which include silty sand and fine sand.*

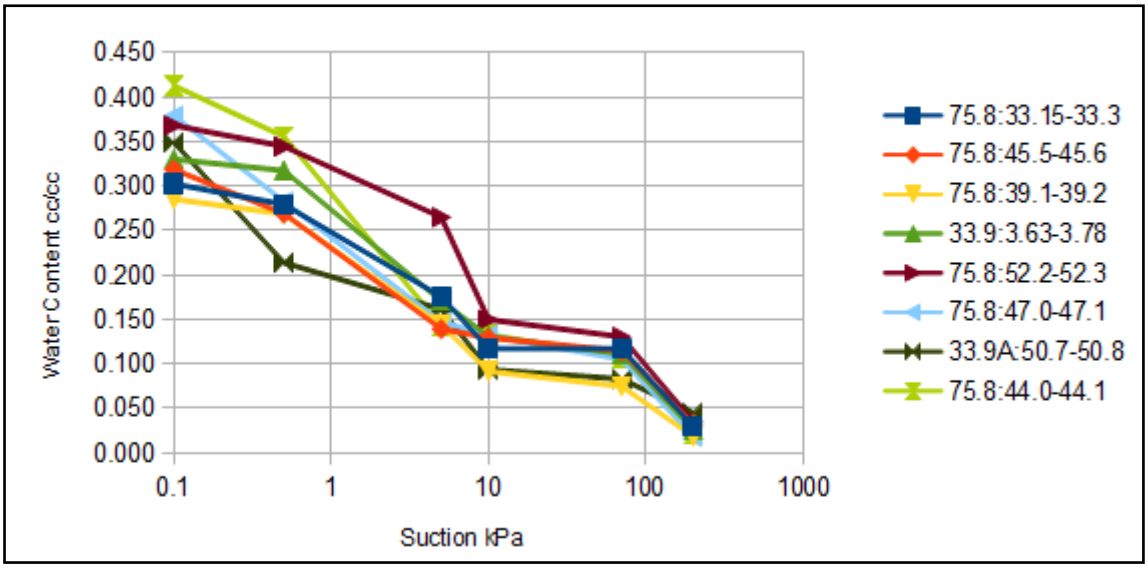



**Figure 11-16.** *Water retention graph for medium- to coarse-textured sand samples.*

### 11.8.4 Results

The total porosity values from the three methods are summarised in Table 11-13. The porosities at specific matric potentials are summarised in Table 11-14. These data were used to compare with the NMR data to derive a surrogate for effective porosity (refer to Section 17.13). The water loss at 10 kPa and 70 kPa is comparable to the mobile water, whereas the water loss at 200 kPa and the total porosity are more comparable to the total water detected by the NMR system.

**Table 11-13.** *Total porosity of selected lexan core samples using three different methods.*

| Borehole | Depth (m) | Texture | Texture Class | Helium Injection Porosity vol% | Matric Potential Porosity vol% | Kerosene Saturation Porosity vol% |
|---|---|---|---|---|---|---|
| BHMAR33-9 | 3.48 | Medium sand | 4 | 38.7 | 36 | |
| BHMAR33-9 | 15.20 | Fine sand | 3 | 38.2 | 36 | 40.9 |
| BHMAR33-9 | 17.25 | Medium sand | 4 | 39.3 | 37 | |
| BHMAR33-9 | 28.46 | Fine sand | 3 | 39.0 | 38 | |
| BHMAR33-9 | 29.30 | Fine sand | 3 | 43.4 | 38 | |
| BHMAR33-9 | 38.95 | Muddy sand | 2 | 38.1 | 34 | 44.9 |
| BHMAR33-9 | 50.15 | Gravelly sand | 5 | NA | 38 | 46.7 |
| BHMAR33-9 | 50.85 | Coarse sand | 5 | 33.4 | 38 | |
| BHMAR33-9 | 56.45 | Gravelly sand | 5 | 35.5 | 31 | 31.4 |
| BHMAR75-8 | 20.55 | Mud | 1 | 41.9 | 40 | 45.3 |
| BHMAR75-8 | 26.75 | Mud | 1 | 36.2 | 47 | 26.9 |
| BHMAR75-8 | 30.20 | Fine sand | 3 | 40.0 | 40 | |
| BHMAR75-8 | 30.75 | Muddy sand | 2 | 39.5 | 41 | |
| BHMAR75-8 | 31.45 | Muddy sand | 2 | 41.4 | 41 | |
| BHMAR75-8 | 33.00 | Medium sand | 4 | 40.3 | 35 | 47 |
| BHMAR75-8 | 40.80 | Gravelly sand | 5 | 34.9 | 21 | |
| BHMAR75-8 | 42.65 | Gravelly sand | 5 | 41.3 | 29 | 44.2 |
| BHMAR75-8 | 44.15 | Gravelly sand | 5 | 36.4 | 48 | 39.7 |
| BHMAR75-8 | 45.65 | Gravelly sand | 5 | 36.9 | 35 | |
| BHMAR75-8 | 46.35 | Medium sand | 4 | 34.6 | 27 | |
| BHMAR75-8 | 47.17 | Coarse sand | 5 | 35.4 | 37 | |
| BHMAR75-8 | 47.87 | Coarse sand | 5 | 30.9 | 25 | |
| BHMAR75-8 | 50.15 | Gravel | 5 | 39.1 | 27 | 36.3 |
| BHMAR75-8 | 51.65 | Gravel | 5 | 33.3 | 31 | |
| BHMAR75-8 | 52.35 | Medium sand | 4 | 37.9 | 49 | |

**Table 11-14.** *Partial porosity at specific matric potentials for selected lexan core samples.*

| Borehole | Depth (m) | Porosity vol ratio At 0.1 kPa | Porosity vol ratio At 0.5 kPa | Porosity vol ratio At 5 kPa | Porosity vol ratio At 10 kPa | Porosity vol ratio At 70 kPa | Porosity vol ratio At 200 kPa |
|---|---|---|---|---|---|---|---|
| BHMAR33-9 | 3.48 | 0.03 | 0.05 | 0.19 | 0.23 | 0.25 | 0.34 |
| BHMAR33-9 | 15.20 | 0.03 | 0.05 | 0.08 | 0.16 | 0.17 | 0.32 |
| BHMAR33-9 | 17.25 | 0.03 | 0.06 | 0.09 | 0.16 | 0.17 | 0.33 |
| BHMAR33-9 | 28.46 | 0.01 | 0.02 | 0.07 | 0.11 | 0.14 | 0.31 |
| BHMAR33-9 | 29.30 | 0.01 | 0.03 | 0.09 | 0.17 | 0.17 | 0.29 |
| BHMAR33-9 | 38.95 | 0.06 | 0.04 | 0.05 | 0.10 | 0.10 | 0.29 |
| BHMAR33-9 | 50.15 | 0.05 | 0.05 | 0.11 | 0.17 | 0.21 | 0.37 |
| BHMAR33-9 | 50.85 | 0.03 | 0.16 | 0.22 | 0.28 | 0.29 | 0.33 |
| BHMAR33-9 | 56.45 | 0.05 | 0.04 | 0.06 | 0.07 | 0.10 | 0.27 |
| BHMAR75-8 | 20.55 | 0.07 | NA | NA | NA | NA | 0.03 |
| BHMAR75-8 | 26.75 | 0.01 | NA | NA | NA | NA | 0.11 |
| BHMAR75-8 | 30.20 | 0.09 | 0.06 | 0.08 | 0.11 | 0.15 | 0.30 |
| BHMAR75-8 | 30.75 | 0.02 | 0.01 | 0.02 | 0.04 | 0.06 | 0.22 |
| BHMAR75-8 | 31.45 | 0.05 | 0.07 | 0.18 | 0.24 | 0.24 | 0.32 |
| BHMAR75-8 | 33.00 | 0.06 | 0.08 | 0.20 | 0.25 | 0.27 | 0.33 |
| BHMAR75-8 | 40.80 | 0.07 | 0.00 | 0.01 | 0.02 | 0.03 | 0.11 |
| BHMAR75-8 | 42.65 | 0.01 | 0.03 | 0.15 | 0.17 | 0.19 | 0.27 |
| BHMAR75-8 | 44.15 | 0.07 | 0.12 | 0.34 | 0.35 | 0.37 | 0.46 |
| BHMAR75-8 | 45.65 | 0.03 | 0.08 | 0.21 | 0.22 | 0.24 | 0.32 |
| BHMAR75-8 | 46.35 | 0.03 | 0.01 | 0.09 | 0.14 | 0.17 | 0.27 |
| BHMAR75-8 | 47.17 | 0.01 | 0.10 | 0.23 | 0.25 | 0.27 | 0.36 |
| BHMAR75-8 | 47.87 | 0.00 | 0.02 | 0.10 | 0.11 | 0.22 | 0.24 |
| BHMAR75-8 | 50.15 | 0.16 | 0.21 | 0.23 | 0.25 | 0.25 | 0.33 |
| BHMAR75-8 | 51.65 | 0.00 | 0.10 | 0.12 | 0.15 | 0.16 | 0.28 |
| BHMAR75-8 | 52.35 | 0.12 | 0.14 | 0.22 | 0.34 | 0.36 | 0.45 |

# 12 Sampling and Analysis of Near-Surface Units

## 12.1 FIELD SAMPLING

In order to understand the evolution of the Darling River valley sequence and to relate the landscape units to subsurface aquifer recharge, the landform mapping elements were examined by description and sampling of stratigraphic sections in key landforms, laboratory analysis of sediment samples and dating samples. Stratigraphic sections provided by tractor-excavated pits and hand auger holes have been used in most parts of the landscape, which lack any natural exposure of the sediments. Tractor-excavated pits and cliff sections are preferred as they provide three-dimensional exposure of the sediment architecture to enable description and sampling for laboratory and OSL dating analyses. Auger holes provide additional vertical stratigraphic information and also samples for some laboratory and OSL dating analyses.

### 12.1.1 Natural Exposures

A number of natural river-cut cliff exposures were examined. These were scraped clean on the cliff face and extended at the base by step excavation using a spade. Access for description and sampling was by ladder where necessary.

### 12.1.2 Tractor Excavated Pits

Trenches were dug using a large Doosan DL300 17.3 tonne wheel loader with a ~3 $m^3$ bucket (Figure 12-1). The operator excavated a hole by scraping a thin layer while driving forwards to form a downward-sloping ramp then backing out and emptying the bucket onto piles adjacent to the pit. The dimensions of the resultant holes were 2.9 m wide, ~3.5 m deep, and about 25 m long with vertical sides allowing description and sampling after cleaning by hand with a spade. The dimensions of the holes, the coherent nature of the sediments and the ramp profile of the long dimension all ensured a high level of safety in entering and sampling the pits. Holes were backfilled by replacing the earth from the piles with the bucket and driving over the fill to cause some compaction.

### 12.1.3 Hand-auger Holes

Holes were hand augered using the Dormer system (Figure 12-2) with both sand and soil auger heads (dependant on sediment type) and aluminium pipe extension rods. A sampler head and steel hammering anvil were attached to the rods to enable steel OSL dating sample tubes to be hammered into the sediment down the hole. The equipment is light and efficient and up to 6.5 m depth was attained. Some overbank mud sediments were too hard for hand-auger penetration.



**Figure 12-1.** *Wheel loader excavating trench DR03 on the Darling River scroll plain.*

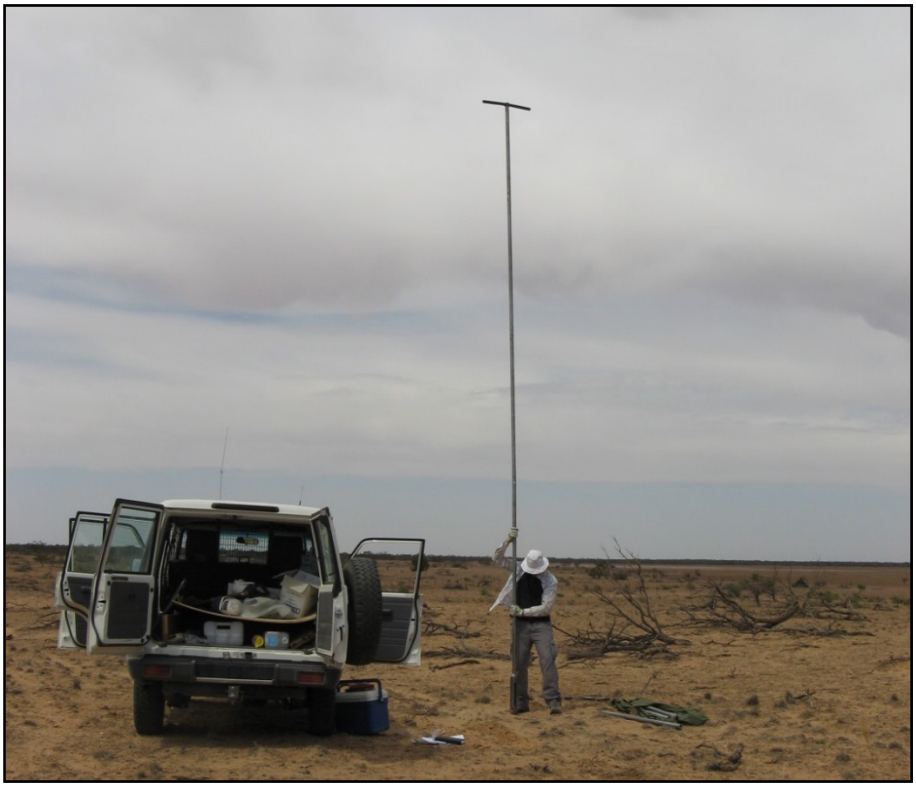


**Figure 12-2.** *Hand augering on dunes at the eastern margin of the Three Mile Creek floodplain.*

## 12.2 QUATERNARY FLUVIAL-UNIT GEOCHRONOLOGY

### 12.2.1 OSL Dating

The Quaternary fluvial units can be mostly separated on the basis of cross-cutting relationships and also by surface morphology because scroll-plain traces become incrementally obscured through time by continued deposition of overbank mud. However, a numeric chronology for the units is very useful to:

- Confirm the relative chronology;
- Allow elucidation of the landscape history; and
- Inform about recharge processes and rates in combination with groundwater chemistry and groundwater age dating.

Prior to this study there were no numeric age determinations from any Quaternary fluvial units in the Menindee area, with a small suite of conventional radiocarbon dates from about 250 km upstream near Tilpa from the late 1970s providing the only numeric chronology. In the Menindee area, some radiocarbon and luminescence dates have been obtained from the lunettes of Lakes Menindee, Cawndilla and Tandou and a number of archaeological features on the fluvial landscape surface, particularly shell middens, have been radiocarbon dated. However, none of these dates provide a useful numeric chronology for the Quaternary fluvial units.

This study has mainly utilised Optically-Stimulated Luminescence (OSL) dating of fluvial quartz sand grains (19 dates) supplemented by four radiocarbon dates from a piece of wood, which was fortuitously recovered in a sonic drill core, to provide the first numeric chronology for Quaternary fluvial units in the Menindee area.

Luminescence dating is a Quaternary dating technique developed over the past few decades with a potential age-range that usually extends back some hundreds of thousands of years from close to the present. Luminescence dating depends on environmental radioactivity but is not a direct radiometric technique like radiocarbon and uranium-series dating, whereby the known half-life of the radioactive isotope is combined with measurements of the parent and daughter atoms to calculate the age. Rather it depends on measuring incrementally derived radiation damage in crystalline minerals. Different atoms form lattice arrangements in natural mineral crystals such as quartz and feldspar. Natural environmental radiation, due to a combination of trace quantities of radioactive elements such as thorium, uranium and potassium as well as cosmic radiation can cause relocation of electrons within a crystal lattice thereby storing energy. The energy traps are usually present due to imperfections and atomic substitutions within the crystal lattice. Luminescence, or the emission of light, occurs when that stored energy is released and the amount of energy released is directly proportional to both the strength of the radiation dose and the time that the dose has been received by the crystal lattice. The stored energy in the crystal can be zeroed or bleached and thereby released as light or luminescence, by shining visible light on it (OSL or optically-stimulated luminescence), by heating (TL or thermo-luminescence) or by infra-red radiation (IRSL or infra-red stimulated luminescence).

In Australian depositional systems there are abundant quartz sand grains highly amenable to OSL-dating. The OSL clock is reset to zero during deposition by wind or water when a quartz grain is exposed to visible sunlight and all the previously stored energy is released. OSL is particularly useful for dating sedimentary processes because only a few seconds of exposure to sunlight will re-set the energy level in quartz grains to zero. For most fluvial and aeolian sediments this will occur during the last active depositional phase they have experienced. After post-depositional burial and removal from light exposure, the crystal lattice of the quartz grain again begins to accumulate stored energy. For OSL dating, a light-proof tube is used to sample quartz-rich sediment and safe-light conditions are used to refine a purified quartz-grain sample of specific size. A laser light stimulates the grains and photomultipliers quantify the luminescence emitted by the grains thereby measuring the amount of stored energy in the quartz (the palaeodose). By applying known laboratory radiation doses to the sample its ability to capture and store energy is calibrated. The time elapsed since its last zeroing or bleaching (exposure to sunlight during deposition) can be calculated by comparing the palaeodose measurement with the measured dose response and the environmental dose which the sample received in its field position. The field dose is calculated from laboratory measurements of the uranium,

thorium and potassium abundance of the total sediment sample. The field dose can also be measured in the field by use of a gamma spectrometer, but this was not done for the BHMAR Project samples, because of a lack of access to these high-cost instruments. The latitude, longitude, altitude and burial depth of the sample are used to calculate the cosmic radiation dose (Prescott and Hutton, 1994). Water held in the sample attenuates the effectiveness of radiation penetration and impact and a correction factor is applied according to the measured moisture content.

#### 12.2.1.1 *Sampling methodology, preparation and measurement*

OSL samples were obtained by three different methods in different sampling environments:

**Tractor-pit samples –** As mentioned in Section 12.1, a large wheel loader excavated a ramped hole approximately 25-30 metres long, 2.9 metres wide and up to 3.5-4 m deep. The vertical sides of the pit at the deepest point were cleaned with a shovel by hand, logged and sampled using a step ladder for access as required. OSL Samples were obtained in the side wall section by hammering in 4 cm diameter 10 cm long stainless steel tubes, which were removed and sealed with plastic end caps. A polythene zip-lock bag, filled by enlarging the OSL sample tube hole, was obtained as an additional loose sample for dose-rate analyses. In the laboratory, 2 cm of sediment from each end of the tube, which would have been briefly exposed to light during sampling, was discarded and used for moisture content analyses and dose rate analyses.

**Hand auger-hole samples -** Using Dormer hand augers with aluminium extension rods and a combination of sand-auger heads and Jarrett soil-auger heads the stratigraphic and sampling hole was deepened in 10-20 cm auger bites depending on the sediment hardness. The stratigraphy was logged and an OSL sample taken when at least 30-40 cm of suitable clean sands at an appropriate depth was encountered. The sample tubes (65 mm diameter) contained 20 cm of empty space when screwed onto the sampler head, which was attached to the auger extensions and lowered down the hole until the tube rests on the bottom.

A solid steel anvil was attached to the top of the extension rods and the sample was hammered into the sand at the bottom of the hole with a small sledge hammer. Because of some cm-scale uncertainty about the down-hole depth measurement and how much loose sediment may lie on the bottom of the hole, hammering ceased when penetration stopped (usually after a measured drive of 15-18 cm). The sample was then pulled out and the bottom end was capped with a black plastic external end cap as soon as possible. The sample tube was detached from the sampler head and capped with a red internal end cap, which filled the empty part of the tube previously occupied by the sampler head (Figure 12-3). The sediment sample at both ends of the tube was only briefly exposed to sunlight in this process.

The auger hole was then reamed out with the auger head to the same level that the bottom of the OSL sample tube had penetrated and that auger sample discarded as it was normally contaminated by abrasion of the outside of the sample tube by the quartz sediment. A 5-10 cm sample of new clean sediment was then augered and retained in a plastic bag to be used for chemical analyses, if required.

In the OSL laboratory, a portion of the quartz sand was removed from each end the tube (2 cm at the bottom and 5 cm at the top) and discarded, due to light contamination at the time of sampling. The extra sediment at the top of the sample tube (formerly the bottom of the auger hole) was discarded due to the potential for sample contamination in the bottom of the hole due to the augering process. The discarded sample-tube end material was used for in-situ moisture analysis and/or radioisotope analyses for dose-rate determination. In four of the samples retrieved by this method (TAN01/3, TAN01/5, CUTH01/1 and LAR01/1) some field difficulties occurred with incomplete filling of the sample tube. In all cases variations of the sub-sampling protocol in the OSL laboratory for these samples ensured that good quality sub-samples were obtained and measured.

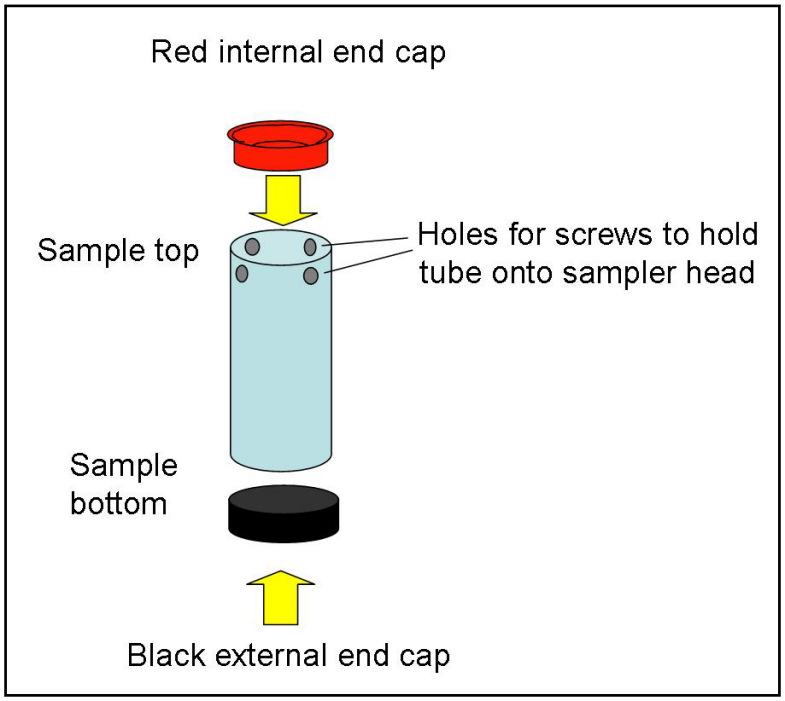



**Figure 12-3.** *Hand-auger OSL sample tubes and end cups.*

**Sonic-core samples -** BHMAR Project cored holes were drilled by Boart Longyear using the sonic drilling method discussed in Section 10.3. This relatively new drilling technique provides core by using sonic vibration to penetrate the sediment with minimal rotation and contamination of the core by drilling fluids. Normally the sonic cores are extruded from core barrels into polythene sausages then placed in core trays. An option with the sonic technique is to have 1.5 m lengths of 80 mm diameter Lexan polycarbonate tubing inside the core barrel and the core retained within that tube. This preserves the structure of unconsolidated sands and the tubes can be sealed to prevent oxidation of sediments and pore fluids etc. This method was adapted by painting the outside of the normally clear tubes black prior to use and by wrapping the whole core length in thick black polythene after removal from the drill rig. Two 1.5 m sections of drillhole BHMAR 75-8 were collected in this fashion to obtain samples for OSL dating. This was only partially successful in limiting light exposure, as substantial amounts of the black paint tended to scrape off as the tube was vibrated through the sands. An additional issue was that some heating of the Lexan occurred during the coring process, which was particularly evident in dry clay-rich material. This issue is not believed to have been significant for the wet sands sampled for OSL.

Examination of the ends of the 1.5 m Lexan core tubes at the time of drilling indicated the presence of clean moist fine sands ideal for OSL dating and the surrounding closely spaced drillholes and the geophysical logs of the BHMAR 75-8 borehole, indicated no major changes of lithology within at least 50 vertical cm of each sub-sample. The two 1.5 m Lexan tube lengths sampled this way for OSL were sub-sampled by cutting out a 15 cm section 30 cm from one end of the core length as indicated in the left-hand side of Figure 12-4. The ends of these sub samples were wrapped with bubble wrap and taped then capped with over-sized light-proof hard PVC end caps securely taped in place. Each tube was then wrapped in thick black polythene then placed in light-proof photographic bags and placed in a box with a lid. This was done under OSL safe-light conditions after which the samples were sent to the OSL laboratory in Adelaide for further sub-sampling, refinement and OSL dating.

During sub-sampling in the OSL laboratory (right-hand side of Figure 12-4) only 1 cm of each end was discarded because the ends of these samples have minimal light-exposure risk. However, there is considerable light exposure risk for the outer annulus of the sample via the clear tube walls being partially stripped of black paint during the process of initial recovery from the drilling operation and wrapping; drilling was done in strong daylight. A 40 mm diameter tube (yellow in Figure 12-4) was pressed into the centre of the sample, after removal of one of the 1 cm end zones and only that inner core was used for OSL

measurements leaving behind a 20 mm wide annulus of potentially light-affected material. The outer annulus and the 1 cm ends were combined to provide material for dose rate and moisture determinations. The efficacy, of this sub-sampling process in eliminating light contamination is demonstrated by the old age, at saturation level, determined for this sample.

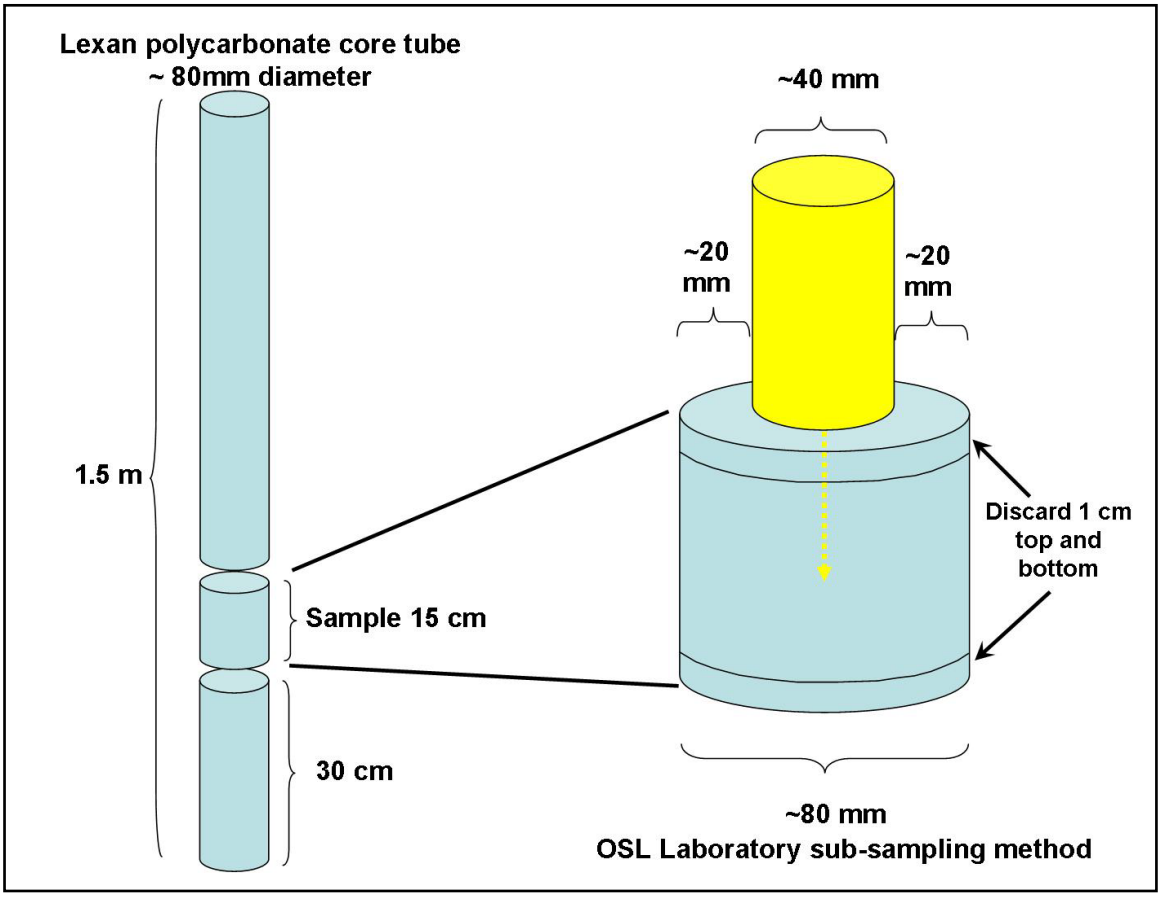



**Figure 12-4.** *Sonic drilling Lexan tube OSL sample and sub-sampling protocol.*

#### 12.2.1.2 *OSL laboratory sample preparation and measurement*

Under subdued red safelight in the laboratory, the portion of each sample not exposed to light during collection and transport, was prepared for OSL dating using a standard procedure designed to isolate grains of pure quartz. A 10% solution of HCl (hydrochloric acid) was used to digest carbonates, followed by treatment with NaOH (sodium hydroxide) solution to break up clay aggregates and remove any organic material. Grains in the 125–250 µm range were selected by sieving and then etched for 40 minutes in 40% HF (hydrofluoric acid) to remove feldspar and other non-quartz material, and to etch the outer 9 µm of the quartz grains, which eliminates the alpha particle contribution to the irradiation of the grains. The remaining quartz was then washed in warm 10% HCl to remove fluorides, and heavy minerals separated in a non-toxic heavy liquid (2.67 gm/cc lithium heteropolytungstate). The remaining quartz concentrate was re-sieved to separate the 125–180 µm fraction (appropriate for small aliquot measurements) and the 180–212 µm and 212-250 µm fractions (appropriate for single grain measurements). All of the samples yielded an adequate quantity of quartz grains in the selected size ranges.

Luminescence measurements were carried out in the School of Chemistry and Physics, University of Adelaide using a RisÓ TL/OSLDA-20 reader. Radiation was applied using a $^{90}Sr/^{90}Y$ β-source. Luminescence was stimulated using a green laser beam (wavelength 532 nm) for single grains. Emitted luminescence was detected using an EMI 9235QB photomultiplier and Hoya U340 filter. A pilot study run on one single grain disc indicated all samples had enough grains with measurable luminescence required for

dating and estimation of the dose values to be used in the measurement protocol. The disks were measured using the SAR (Single Aliquot Regeneration) protocol devised by Murray and Wintle (2000) and details of the measurement protocols and the analysis and interpretation of the sample responses are contained in the report from the laboratory in Appendix 7 (Apps *et al*., 2012e).

Materials from the discarded light-contaminated portions of the sample were used for environmental dose rate measurement. ICPMS (Inductively Coupled Plasma Mass Spectroscopy) analyses of Uranium (U), thorium (Th) and ICPAES (Inductively Coupled Plasma Atomic Emission Spectrometry) of potassium (K) determinations were carried out by Genalysis Laboratories, Perth. TSAC (thick source alpha counting) measurements of U and Th were undertaken in the OSL laboratory and XRF (X-Ray Fluorescence spectroscopy) measurement of K by CSIRO Urrbrae Laboratories, Adelaide. The water content of the material was measured by weighing, drying overnight at 125ºC, and re-weighing. The water content was calculated as% of dry weight. Variations in the water content during the depositional history of the sample will affect the age determination. An increase of 1% in water content may result in an increase of 0.5% to 1% in the calculated age. Most of the samples had a high water content (up to 22.6% in the case of BHMAR 75-8/2), which significantly affected the calculated dose rate. The cosmic-ray contribution was obtained using the published relationship between cosmic ray penetration, depth, altitude and latitude (Prescott & Hutton, 1994). Nuclide concentrations, water content and cosmic contribution values are shown in Table 12-1.

The environmental dose rates were calculated from the above information using the "AGE99" program of Grün (2009). For each sample a mean dose rate to be used in the age calculation was determined by averaging two separate dose rate calculations. Firstly, from the average K values combined with the ICPMS values for U and Th, and, secondly, the dose rate from the average K values combined with the TSAC values for U and Th. The error for the mean dose rates is the standard deviation of the two values, or the average of the individual errors, whichever is greater.

#### 12.2.1.3 ***Luminescence samples dated***

Table 12-1 provides details of the 19 samples submitted for OSL dating, including sample numbers, fluvial phase dated, sample type, location and depth below surface. The samples were obtained from a variety of Darling Valley Quaternary fluvial phases including eleven from the Coonambidgal Formation - four from the Darling River scroll-plain phase, five from the anabranch scroll-plain phase and two from the relict scroll-plain phase. Six samples are from various phases of the Menindee Formation, one from a flood-plain bar on the Menindee Formation and one from a lateral-valley equivalent of the Menindee Formation.

**Table 12-1.** *Details of nineteen OSL-dated samples.*

| Lab Code | Field code | Fluvial phase | Sample type | Easting | Northing | Depth (cm) |
|---|---|---|---|---|---|---|
| AdBL 10016 | DR01/05 | Darling R scroll plain | T-E Pit | 637630 | 6417688 | 200 |
| AdBL 10017 | DR01/10 | Darling R scroll plain | T-E Pit | 637630 | 6417688 | 334 |
| AdGL 11091 | DR01A/1 | Darling R scroll plain | Hand auger | 637424 | 6417600 | 280-300 |
| AdGL 11092 | CHW01/1 | Darling R scroll plain | Hand auger | 620640 | 6336406 | 200-214 |
| AdBL 10013 | TAL02/6 | Anabranch scroll plain, Talyawalka | T-E Pit | 641507 | 6410736 | 237 |
| AdBL 10014 | TAL03/6 | Anabranch scroll plain, Talyawalka | T-E Pit | 641724 | 6410458 | 200 |
| AdBL 10012 | TAL04/9 | Anabranch scroll plain, Talyawalka | T-E Pit | 641848 | 6410195 | 319 |
| AdGL 11095 | TAN01/1 | Anabranch scroll plain, Coonalhugga | Hand auger | 622732 | 6379787 | 205-220 |
| AdGL 11097 | CUTH01/1 | Anabranch scroll plain, Great Darling Anabranch | Hand auger | 597498 | 6348646 | 520-532 |
| AdGL 11096 | TAN01/5 | Relict scroll plain, Coonalhugga | Hand auger | 622732 | 6379787 | 450-465 |
| AdGL 11098 | LAR01/1 | Relict scroll plain, Talyawalka | Hand auger | 676353 | 6414981 | 390-407 |
| AdBL 10018 | DRO2/8 | Menindee Formation | T-E Pit | 637455 | 6417542 | 345 |
| AdBL 10019 | DRO3/9 | Menindee Formation | T-E Pit | 637564 | 6417057 | 405 |
| AdBL 10011 | DRO6/6 | Menindee Formation | Hand auger | 637788 | 6417057 | 270-280 |
| AdGL 11093 | CHW02/1 | Menindee Formation | Hand auger | 622077 | 6336297 | 230-248 |
| AdGL 11094 | CHW02/3 | Menindee Formation | Hand auger | 622077 | 6336297 | 350-367 |
| AdGL 11099 | BHMAR 75-8/2 | Menindee Formation | Sonic core | 630780 | 6411483 | 980-995 |
| AdBL 10015 | 3MC06/10 | Flood plain bar on Menindee Formation | T-E Pit | 644153 | 6414823 | 300 |
| AdBL 10020 | MN01/8 | Lateral valley fluvial sands | Hand auger | 621548 | 6427523 | 460-478 |

T-E Pit = Tractor-Excavated Pit

### 12.2.2 Sediment Radiocarbon Dating

While radiocarbon dating operates over a relatively short time period (~40,000 to present) when compared to geological time, it is one of the most commonly used tools for dating Quaternary sediments, since its discovery in the early 1950s.

There are three natural isotopes of carbon that occur on Earth:

- Stable carbon-12 comprises 99%;
- Stable carbon-13 comprises 1%; and
- Radioactive carbon-14 comprises only trace amounts (0.0000000001%) of the carbon in the atmosphere and is produced continually in the upper atmosphere by a reaction between cosmic radiation and atmospheric nitrogen.

The rate of atmospheric radiocarbon production can vary in the long term as the cosmic-ray flux varies. However, at shorter timescales it forms an equilibrium ratio in the atmosphere with the much more abundant carbon-12, according to the balance between carbon-14 production and radioactive decay of carbon-14 into nitrogen-14. This atmospheric equilibrium ratio is reflected in a living plant as it removes carbon from the atmosphere by photosynthesis, and converts it into woody tissue. The same equilibrium ratio is passed on through the food chain and also by other chemical processes in the carbon cycle involving atmospheric carbon, though many processes may involve some isotopic fractionation.

In wood samples, the carbon-14 of the plant tissue begins to decay to nitrogen-14 without being replenished by atmospheric carbon-14 when the plant dies. As this process continues, the ratio of carbon-14 to carbon-12 is reduced at a rate dependant on the carbon-14 radioactive half-life. Wood samples can therefore be dated by measuring the relative abundance of carbon-14 and carbon-12. Similarly, radiocarbon dating can be applied to other plant materials, animal material, charcoal, carbon contained in calcium carbonate minerals such as coral and shells or organic or inorganic carbon dissolved in groundwater.

However, in addition to radioactive decay of carbon-14 to nitrogen-14, other factors can influence the atmospheric equilibrium ratio of carbon-14 to carbon-12 over timescales of hundreds to thousands of years. These include processes associated with the carbon cycle, the cosmic-ray flux and human activities:

- The Earth's carbon cycle involves the movement of carbon between reservoirs in the hydrosphere, the biosphere, the lithosphere and the atmosphere in both organic and inorganic (carbonate) sub-systems. On long time scales, carbon reservoirs can change due to sequestration of carbon from the organic sub-cycle as coal and gas and from the inorganic sub-cycle as carbonate rocks formed by reefs or shell and test accumulations. On shorter time scales, the isotopic equilibrium of atmospheric reservoir is buffered by the large reservoir of carbon dioxide dissolved in the ocean and the slow process of interaction between the carbon stores in the atmosphere and the ocean.
- The production rate of carbon-14 in the atmosphere is moderated by the strength of the Earth's magnetic field, which controls the strength of cosmic radiation.
- Human activity has also impacted the carbon isotopic balance of the atmosphere by the release of carbon with different isotopic signatures into the atmosphere through land clearing since the Neolithic and the burning of fossil fuels since the Industrial Revolution. The atmospheric atomic bomb tests during the 1950s and 1960s almost doubled the natural abundance of Carbon-14 in the atmosphere.

Calibration of radiocarbon dates to counteract uncertainty due to variations in the carbon isotopic ratio of the atmosphere requires dating a series of samples by both radiocarbon and another dating technique not subject to the same uncertainties. Dendrochronology, or tree-ring counting, provides calibration back to about 12,500 years from individual tree rings of known calendar age which are radiocarbon dated. The dendrochronology calibration record is currently being extended back in time by radiocarbon dating and dendrochronology of fossil wood preserved in bogs, swamps and fluvial sediments. Calibration is extended beyond the dendrochronology record, over the whole range of radiocarbon dating back to about 55,000 years, by cross-dating speleothems and marine corals by both radiocarbon and uranium-series dating.

By convention, radiocarbon laboratories always report dates in the form 4470 ± 45 years BP, where the years are uncalibrated radiocarbon years before present (1950) and calculated using the original Libby-determined half-life of 5568 years. For comparison with other dating techniques which provide ages in calendar years the radiocarbon age is calibrated for variations in the C-14 production rate as detailed above and for the more recently determined radiocarbon half-life of 5730 ± 30 years. There are a number of Internet sites where online calibration can be done and dates for this study were calibrated using OxCal 4.1 (Bronk Ramsay, 2009) using the Southern Hemisphere calibration data in McCormac *et al*. (2004).

After initial discovery of the technique, the abundance of carbon-14 atoms in a dating sample was determined by direct counting by photomultipliers of beta radiation, emitted during radioactive decay, that were converted to pulses of light in a liquid scintillometer. When carbon-14 abundance is very low, in old samples, this technique requires large sample sizes and long counting times and results in high measurement uncertainty. Many of these measurement difficulties have been overcome by the development of accelerator mass spectrometry (AMS) for radiocarbon dating. Mass spectrometry separates atoms according to their different masses with acceleration of the atoms to high speed occurring in an AMS system. The efficiency of C-14 abundance measurement by AMS has reduced the required sample size by a factor of about 1000 and the required measurement time by a factor of about 100. It has also greatly reduced the measurement uncertainty. These measurement efficiency improvements in theory can allow a detection limit of about 0.037% of the already very low original carbon-14 abundance (0.0000000001% of atmospheric carbon), which could theoretically enable age determinations to 10.5 half- lives, or about 60 000 years ago. However,

the practical limit for reliable dating is around 40 000 years because when the abundance of carbon-14 in samples becomes very low it is virtually impossible to ensure prevention of sample contamination with younger carbon containing elevated carbon-14 levels. Such contamination can be derived from the field condition of the sample or be absorbed by the sample during processing or measurement.

#### 12.2.2.1 *Sample location, preparation and measurement*

The sonic-core drill site BHMAR79A-2 is located close to the outer margin of the Coonambidgal Formation Darling River scroll plain at 57.06 m AHD on Menindee Common downstream of Menindee. During laboratory logging of the split core, relatively large (>5 cm scale) black fragments of apparent wood were recorded in the core in the basal scroll-plain sand at 8.7 m (Figure 12-5) and 8.9 m depth where the base of the Coonambidgal Formation was at 9.1 m. These samples were extracted from the core and the one from 8.7 m (48.36 AHD) was found to be a larger sample which formed a single solid mass. It seemed evident from visual and hand-lens examination that the sample had originally been wood, though it was uncertain whether it was now degraded wood blackened by absorption of humic compounds or whether it had been burnt and consisted of charcoal also probably containing post-depositional humic material.

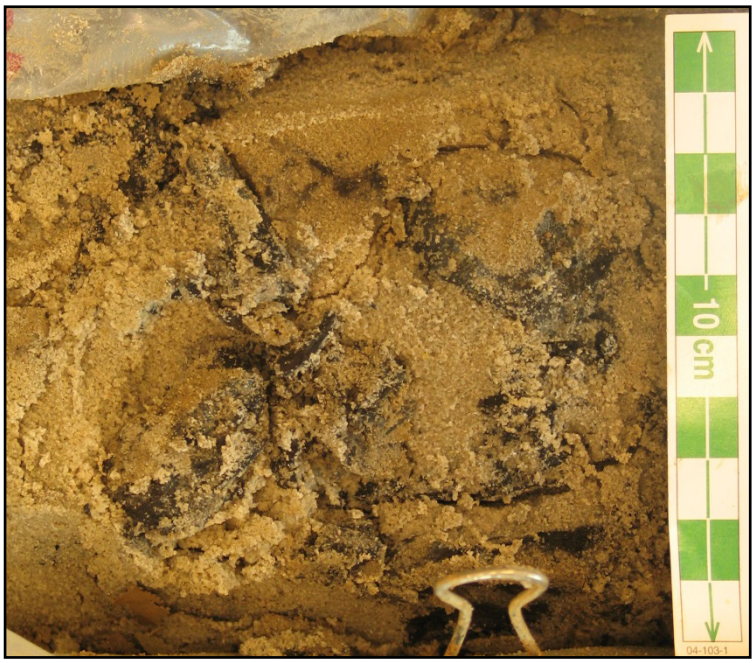



**Figure 12-5.** *Blackened wood sample in fluvial sand at 8.7 m depth in sonic core BHMAR 79A-2.*

Dr Richard Gillespie, radiocarbon geochemistry consultant, was engaged to assess the sample and if possible prepare a cellulose extract for AMS radiocarbon dating. Cellulose is a strong crystalline polysaccharide long-chain non-branched polymer that is resistant to hydrolysis and is present in plant cell walls. Dr Gillespie's initial investigation demonstrated that the sample was definitely wood and, despite the black colouration, that it had never been burnt. He then applied the following method for cellulose extraction that he has developed (Gillespie *et al.*, 2008; Stevenson *et al.*, 2010):

- Sample soaked overnight in alkaline hypochlorite at room temp
- Sample treated with chlorite in pH1-3 HCl for 2 hrs at 70-80°C
- Sample treated with 0.5 M HCl at 70-80°C
- Treatment for 1-2 hrs in alkaline hypochlorite at room temp
- Treatment with hot chlorite in pH1-3 HCl for 2 hrs at 70-80°C

Multiple washes with demineralised water were carried out between all steps and of the final cellulose sample before AMS target production. This produced a white sample of cellulose which Dr Gillespie assessed to be a good quality sample for dating, very likely to give the correct sample age if well within the range of the technique, i.e. in the Holocene as expected. The cellulose sample was submitted to the ANU (Australian National University) bench-top AMS radiocarbon facility at RSES (Research School of Earth Sciences) where a target was prepared from the cellulose for AMS measurement

Because of the age, size and nature of the sample it was ideal for inclusion, with Geoscience Australia approval, in an Australian Institute of Nuclear Science and Engineering (AINSE)-funded project of Dr Gillespie's which was investigating the efficacy of various pre-treatment regimes in removing organic contamination of wood and charcoal samples. Accordingly, four additional samples with varying pre-treatment regimes were prepared for dating at the Australian Nuclear Science and Technology Organisation (ANSTO) AMS radiocarbon facility:

- Untreated black wood sample
- An extract of holocellulose (a mixture of cellulose and hemicellulose, which is a group of polysaccharides with short-chain branched polymer molecules also present in plant cell walls, that are amorphous, lack strength and are more easily hydrolysed by comparison with cellulose)
- A sample with acid-base-acid (ABA) treatment, the standard methodology used by most laboratories to remove organic contamination
- A sample with acid-base + wet chemical oxidation (ABOX) treatment, a more rigorous pre-treatment regime (Bird *et al*., 1999, 2002; Turney *et al*., 2001a, 2001b).

These samples were sent to the ANSTO AMS radiocarbon dating laboratory for target production and dating. For unknown reasons target preparation at ANSTO failed for the ABA sample and it was not able to be dated.

# 13 Hydraulic Testing

## 13.1 AIR LIFT TESTS

Following construction, the BHMAR monitoring bores were developed by air lift using a compressor, and either a polythene or galvanised iron pipe. Development was undertaken by incrementally lowering the pipe down to the base of the screen. Progress was monitored in terms of discoloration and sand content of the air-lifted groundwater, and by the regular measurement of flow rate, electrical conductivity and pH. Development was finalised when the groundwater was visually clear of suspended material and the field water quality parameters stabilised to reflect ambient groundwater conditions. The water level in the bore was measured both before and after development. The data collected during development provided an initial indicator of bore yield as well as groundwater quality and is summarised in Table 13-1.

**Table 13-1.** *Summary of air-lift development of project monitoring bores.*

| Hole | Screened Aquifer | Screened Interval Depths (m) | Date Developed | Initial SWL (TOC) | Airlift EC (µS/cm) | Airlift pH | Airlift Temp (ºC) | Airlift Rate (L/s) |
|---|---|---|---|---|---|---|---|---|
| BHMAR01A- | Calivil | 47-79 | 12/02/2010 | - | >20000 | 7.8 | 23.2 | 2.3 |
| BHMAR01B- | Calivil | 56-63 | 8/12/2009 | 35.60 | 10820 | 8.2 | 22.7 | 1 |
| BHMAR03B- | Upper | 65-71 | 1/12/2009 | 12.59 | 19190 | 7.8 | 13.8 | >4 |
| BHMAR03B- | Calivil | 37-55 | 2/12/2009 | 12.60 | 11050 | 7.9 | 22.2 | 2 |
| BHMAR04-1 | Upper | 90-102 | 5/12/2009 | 17.68 | 4760 | 8.1 | 22.7 | 3 |
| BHMAR04-2 | Calivil | 34-52 | 3/12/2009 | 7.49 | 758 | 8.2 | 21.9 | 3 |
| BHMAR04-3 | Menindee | 8-14 | 3/12/2009 | 7.28 | 7590 | 8.1 | 21.2 | 1 |
| BHMAR05-1 | Upper | 94.5-100.5 | 5/12/2009 | 22.77 | - | - | - | <0.1 |
| BHMAR05-2 | Calivil | 28-40 | 3/12/2009 | 18.25 | 1414 | 8.7 | 23.9 | 1 |
| BHMAR06-1 | Calivil | 30-60 | 4/12/2009 | 17.20 | 7830 | 8.6 | 24.0 | 1 |
| BHMAR08-1 | Calivil | 42-46 | 10/09/2010 | 11.3 | 4290 | | | - |
| BHMAR14-1 | Calivil | 41-59 | 3/12/2009 | 13.28 | 3010 | 8.3 | 23.1 | 1.5 |
| BHMAR15-1 | Calivil | 53-79 | 22/01/2010 | 19.00 | 13170 | 8.4 | 24.0 | 0.4 |
| BHMAR16-1 | Calivil | 12-52 | 28/01/2010 | 20.15 | 862 | 8.5 | 22.8 | 1.7 |
| BHMAR17-1 | Calivil | 54-72 | 1/12/2009 | 15.30 | 3110 | 8.1 | 21.0 | 3 |
| BHMAR17-2 | Calivil | 22.5-34.5 | 1/12/2009 | 14.88 | 3110 | 8.6 | 20.4 | >1 |
| BHMAR18-1 | Upper | 63-69 | 6/12/2009 | 4.95 | 22880 | 7.2 | 23.8 | 3 |
| BHMAR18-2 | Calivil | 25-52 | 12/12/2009 | 5.37 | 3190 | 7.8 | 20.7 | 2 |
| BHMAR19-1 | Calivil | 45-60 | 9/12/2009 | 20.28 | 6700 | 8.1 | 23.0 | 3 |
| BHMAR19-2 | Willotia | 16-22 | 31/03/2010 | 20.31 | 3370 | 8.7 | 25.9 | <.002 |
| BHMAR21-1 | Calivil/Upper Renmark | 20-74 | 9/12/2009 | 11.71 | 497 | 7.7 | 22.8 | 2 |
| BHMAR21-2 | Menindee | 10.5-13.5 | 9/12/2009 | 10.61 | 474 | 8.3 | 22.9 | 0.3 |
| BHMAR21-3 | Calivil | 32-56 | 8/05/2010 | - | 440 | | | 20 |
| BHMAR22-1 | Calivil | 30-56 | 6/12/2009 | 5.35 | 25110 | 7.3 | 19.5 | 7 |
| BHMAR23-1 | Palaeozoic | 81-105 | 17/12/2009 | 22.16 | 5000 | 7.9 | 28.2 | 3.5 |
| BHMAR23-2 | Calivil | 29-47 | 24/01/2010 | 14.90 | 1035 | 8.3 | 22.0 | 1.1 |
| BHMAR23-3 | Menindee | 13-24 | 29/03/2010 | 13.40 | 571 | 8.3 | 21.9 | 2 |
| BHMAR23-4 | Menindee | 19-25 | 13/05/2010 | 14.2 | 500 | 8.4 | 21.4 | 4 |
| BHMAR28-1 | Calivil/Loxton -Parilla | 15-50 | 16/12/2009 | 12.51 | 21700 | 7.2 | 26.8 | 1 |
| BHMAR29-1 | Calivil | 17-53 | 16/12/2009 | 14.05 | 2570 | 7.6 | | 29.2 |
| BHMAR30-1 | Calivil | 37-75 | 18/12/09? | 17.43 | >26000 | 8.4 | 24.4 | 0.35 |
| BHMAR31-1 | Loxton-Parilla | 11-51 | 16/04/2010 | 12.80 | 6230 | 8.1 | 23.2 | 3 |
| BHMAR33-1 | Lower | 182-206 | 18/04/2010 | 19.00 | 1268 | 8.0 | 25.7 | 3 |

| | | | | | | | | |
|---|---|---|---|---|---|---|---|---|
| BHMAR33-2 | Calivil | 48-59 | 28/03/2010 | 11.3 | 1131 | 8.2 | 25.4 | 3 |
| BHMAR33-3 | Menindee | 14-23 | 28/03/2010 | 8.2 | 1807 | 7.7 | 24.6 | >1 |
| BHMAR33-4 | Calivil | 48-58 | 1/05/2010 | 6.72 | 1200 | 8.1 | 21.3 | 25 |
| BHMAR33-5 | Calivil | 48-59 | 16/09/2010 | 11.41 | 1214 | | | 25 |
| BHMAR33-6 | Calivil | 47-58 | 17/08/2010 | 10.95 | 1162 | 8.0 | - | 4 |
| BHMAR33-7 | Calivil | 48-57 | 18/08/2010 | 10.85 | 1200 | 7.9 | - | 5 |
| BHMAR33-8 | Calivil | 46-52 | 17/08/2010 | 11.55 | 1102 | 8.0 | - | 2.9 |
| BHMAR33-9 | Calivil | 50-56 | | 11.22 | 1174 | | | 5 |
| BHMAR34-1 | Calivil | 27-51 | 18/12/2009 | 8.41 | 623 | 7.8 | 22.8 | 2 |
| BHMAR34-2 | Menindee | 8-20 | 23/01/2010 | 8.80 | 1058 | 8.3 | 23.0 | 0.5 |
| BHMAR34-3 | Calivil | 28-42.5 | 24/04/2010 | 8.94 | 746 | 8.5 | 21.6 | 5 |
| BHMAR35-1 | Calivil | 16-46 | 17/04/2010 | 21.50 | 1160 | 8.5 | 21.2 | 2.5 |
| BHMAR36-1 | Calivil | 38-82 | 10/12/2009 | 18.68 | 11940 | 7.8 | 24.0 | 3 |
| BHMAR41-1 | Calivil | 36-60 | 2/12/2009 | 14.05 | 14000 | 7.6 | 21.9 | 2 |
| BHMAR43-1 | Upper | 59-65 | 6/12/2009 | 6.52 | - | - | - | - |
| BHMAR43-2 | Calivil | 28.5-40.5 | 4/12/2009 | 14.98 | 7020 | 8.3 | 23.3 | 3 |
| BHMAR48-1 | Calivil | 35.5-58.5 | 13/12/2009 | 14.69 | 5790 | 7.9 | 23.9 | 3 |
| BHMAR51-1 | Calivil | 16-25 | 27/01/2010 | 14.10 | 1164 | 7.5 | 30.8 | <0.03 |
| BHMAR53-1 | Calivil | 30-40 | 13/05/2010 | - | 8700 | | | 0.03 |
| BHMAR56-1 | Calivil | 43-49 | 12/12/2009 | 14.30 | >25000 | 7.7 | 22.2 | 2 |
| BHMAR57-1 | Calivil/Upper Renmark | 34.5-82.5 | 13/12/2009 | 16.90 | 7335 | 7.6 | 24.9 | 3 |
| BHMAR58-1 | Calivil | 63-69 | 26/10/2010 | 14.53 | 1854 | 8.2 | 23.0 | 3.3 |
| BHMAR61-1 | Upper | 86-116 | 16/12/2009 | 16.75 | 3990 | 8.2 | 24.2 | 3.5 |
| BHMAR61-2 | Calivil | 36-66 | 17/12/2009 | 14.27 | 1777 | 8.1 | 26.2 | 4 |
| BHMAR61-3 | Menindee | 12.5-22.5 | 17/12/2009 | 14.56 | 690 | 8.1 | 24.8 | 1 |
| BHMAR62-1 | Calivil | 44-60 | 7/12/2009 | 24.31 | 16870 | 7.9 | 23.9 | 3 |
| BHMAR63-1 | Calivil | 33-39 | 24/01/2010 | 25.00 | 2650 | 8.3 | 24.1 | 0.8 |
| BHMAR64-1 | Upper | 82-98 | 7/12/2009 | 9.28 | 26100 | 7.2 | 22.0 | 3 |
| BHMAR64-2 | Calivil | 20-55 | 11/12/2009 | 8.68 | 5720 | 7.6 | 18.4 | 5 |
| BHMAR65-1 | Calivil | 32-56 | 2/12/2009 | 12.45 | 13060 | 7.8 | 19.6 | 3 |
| BHMAR66-1 | Calivil | 30-60 | 2/12/2009 | 15.27 | 18840 | 7.2 | 23.1 | 3.5 |
| BHMAR74-1 | Calivil | 33-68 | 13/02/2010 | 15.50 | >20000 | 7.8 | 23.5 | 3.3 |
| BHMAR75-1 | Calivil | 37.5-42.5; 43.5-45; 45- | 22/10/2010 | - | 1810 | 8.3 | 22.2 | >5 |
| BHMAR75-3 | Renmark | 82-88 | 19/09/2010 | 10.76 | 8840 | 7.6 | 22.8 | 2.5 |
| BHMAR75-4 | Calivil | 41-53 | 19/09/2010 | 10.58 | 1981 | 8.1 | 22.0 | >5 |
| BHMAR75-5 | Calivil | 40-52 | 3/09/2010 | 10.17 | 1825 | 8.0 | 22.1 | 6 |
| BHMAR75-6 | Calivil | 41-53 | 21/09/2010 | 10.57 | 1803 | 8.1 | 22.0 | >5 |
| BHMAR77-2 | Calivil | 47-55 | | - | 810 | 8.4 | 20.0 | 2 |
| BHMAR77-3 | Menindee | 11-16 | 14-15/8/10 | 5.75 | 1345 | 8.5 | 18.2 | 0.06 |
| BHMAR77-4 | Menindee | 11-15 | | 11.07 | 1391 | 8.5 | 18.1 | 0.1 |
| BHMAR77-5 | Calivil | 46-56 | 18/08/2010 | 12.75 | 964 | 8.1 | - | 5 |
| BHMAR79A- | Renmark | 65-77 | 21/09/2010 | 7.84 | 6360 | 7.7 | 21.7 | >5 |
| BHMAR79A- | Calivil | 18-24 | | 7.58 | | | | 2 |
| BHMAR79A- | Calivil | 38-50 | 8/10/2010 | 8.91 | 1073 | 7.8 | 20.7 | 8 |
| BHMAR79A- | Calivil | 35-48 | 7/10/2010 | 7.84 | 957 | 7.7 | 20.7 | 5 |
| BHMAR79A- | Calivil | 41-48 | 7/10/2010 | 6.36 | | | | 4 |
| BHMAR80A- | Calivil | 35-53 | 24/08/2010 | 8.03 | 495 | 8.1 | - | >5 |
| BHMAR80A- | Coonambidgal | 11-17 | 25/08/2010 | 6.81 | 578 | 8.2 | 20.4 | 0.4 |
| BHMAR80A- | Coonambidgal | 10-14 | 4/10/2010 | 7.80 | 495 | 8.1 | 21.8 | 0.6 |

| | | | | | | | | |
|---|---|---|---|---|---|---|---|---|
| BHMAR80A-5 | Calivil | 35-45; 48.5-50.5; 53.5- | 3/10/2010 | 7.45 | 653 | 7.9 | 21.5 | 42 |
| BHMAR80A- | Renmark | 84-102 | 4/10/2010 | 8.93 | 5880 | 7.8 | 22.3 | 4 |
| BHMAR80A- | Calivil | 42-54 | 2/10/2010 | 8.30 | 696 | 7.8 | 21.0 | 6.7 |
| BHMAR80B- | Calivil | 53-65 | 4/09/2010 | 8.77 | | | | |
| BHMAR80B- | Coonambidgal | 11-16 | 2/09/2010 | 8.34 | 724 | 8.1 | 20.7 | 0.16 |
| BHMAR83-2 | Calivil | 48-63 | 2/09/2010 | 14.55 | 1190 | 7.9 | 21.9 | 4.5 |
| BHMAR84-2 | Calivil | 45-51 | 24/08/2010 | 9.09 | 2510 | 8.4 | 21.0 | 0.9 |
| BHMAR84-3 | Menindee | 10-23 | 23/08/2010 | 9.21 | 401 | 8.2 | 21.0 | 0.6 |
| BHMAR84-4 | Menindee | 12-23 | 23/08/2010 | 8.32 | 416 | 8.2 | 20.2 | 0.8 |
| BHMAR84-5 | Menindee | 10-23 | 24/08/2010 | 8.40 | 1334 | 8.1 | 20.6 | 1.1 |
| BHMAR88-2 | Calivil | 43-55 | 20/09/2010 | 10.48 | 2050 | 8.1 | 22.1 | >5 |
| BHMAR88-3 | Upper | 65-71 | 2/10/2010 | 10.30 | 6720 | 7.6 | 23.0 | 4 |
| BHMAR88-4 | Calivil | 43-55; 79-85 | 22/09/2010 | 9.32 | 1591 | 8.4 | 22.1 | 0.7 |
| BHMAR88-5 | Calivil | 35-41 | 3/10/2010 | 10.07 | 1452 | 8.0 | 22.5 | 5 |
| BHMAR88-6 | Calivil | 38-50; 82-88 | 2/10/2010 | 10.09 | 3230 | 8.0 | 22.6 | 6 |
| BHMAR88-7 | Calivil | 60-76 | 1/10/2010 | 10.02 | 9400 | 7.6 | 22.8 | 5 |
| BHMAR92-1 | Calivil | 32-62 | 4/10/2010 | 10.16 | 846 | 7.7 | 21.3 | 6.7 |
| BHMAR99-1 | Calivil | 33-57 | | 10.07 | | | | 5 |

Notes: Depths to top and base of screened interval measured relative to ground surface.

SWL (TOC) is the standing water level in the borehole prior to test measured relative to the top of bore casing.

Airlift EC is the groundwater electrical conductivity (µS/cm) measured at completion of air lift.

Groundwater pH, temperature and airlift rate also measured at final stages of air lift.

## 13.2 SLUG TESTING

A slug test is a simple routine to estimate hydraulic parameters of the screened aquifer. A 'slug' is rapidly lowered into the borehole water column to create an instantaneous displacement (rise) in water level. The rate of recovery is monitored, with the time taken to return to initial water level conditions a function of aquifer transmissivity within the screened interval.

A slug test was undertaken for all BHMAR monitoring bores. Solid cylindrical slugs of various lengths were constructed using 62 mm OD PVC pipe, to fit within the bore casing. The pipe was partially filled with sand to overcome buoyancy, and the ends sealed with machine tapered plastic plugs. The largest slug of about 1.5 m length was designed to create a 1 m displacement of groundwater within the 80 mm-cased monitoring bore. The field procedure was modified from that developed by Butler *et al*. (2007) and involved:

- Taking an initial measurement of the groundwater level from the top of the bore casing protector (or other reference) using an electronic water level meter.

- Installing a pressure transducer data logger (Diver DI-702 10-m) at a depth of about 4-5 m below the standing water level. This ensured that the logger was clear of any physical contact with the slug downhole. The logger was connected to a laptop by a direct data cable allowing regular downloading of data during the test (Figure 13-1). This was important in deciding when the groundwater level had stabilised to pre-test conditions. The cable was firmly secured to the casing protector to prevent extraneous movement of the logger. A half-second time interval was used for data logging, considering the need to capture critical water level changes 5-10 seconds after the slug was introduced (or removed).
- Starting with the 0.5 m length slug, measuring out the water level depth reading, from the base of the slug and along the connecting rope, and temporarily marking this length on the rope (using plastic tape). This identified during the test when the base of the slug was just above the water level

downhole. A similar marker representing the slug length along the rope from this marker was temporarily fixed on the rope and used to check downhole that the slug was completely immersed following lowering. In this way, there was a guide in terms of the downhole position of the slug relative to the groundwater level during the test. The end of the rope was tied to something secure to avoid losing the slug down the hole.

- After stable readings of pre-test conditions had been made, lowering the slug downhole so that the base was just above (~10-30 cm) the standing water level. Smooth movement of the rope and slug was facilitated by a pulley fitted over the bore opening (Figure 13-1). Whilst still holding the rope, it was then tied off and secured, allowing for the slug length as the drop distance. The slug was then allowed to quickly but smoothly drop into the water column to commence the falling head test, where water displacement by the slug caused a rapid water level rise. This lowering only needed to be slightly greater than the slug length with the rope tied off to secure the slug in this lowered position.
- By updating the laptop data from the logger, recovery of the water level back to static conditions could be monitored. When this had occurred, the slug could be quickly and smoothly pulled back up to its previous position with its base just above the static water level. This induced a downward displacement and commencement of a rising head test.

This cycle of releasing and retrieving the slug to provide a falling head and rising head test was repeated at least three times. This results in a total of six slug response curves that could be compared and evaluated. If there were problems with the data recovered, such as significant noise, then additional tests were made.

The entire procedure was repeated using the 1.5 m slug, to test assumptions used in slug test solutions. Figure 13-2 shows the results of a typical test showing three repetitions of the combination of falling head and rising head tests. Figure 13-3 showing an oscillatory response that is indicative of high hydraulic conductivity for the screened aquifer section.



**Figure 13-1.** *Slug testing of project bores using pulley attachment and pressure transducer with direct data cable for downloading of groundwater level data during the test.*

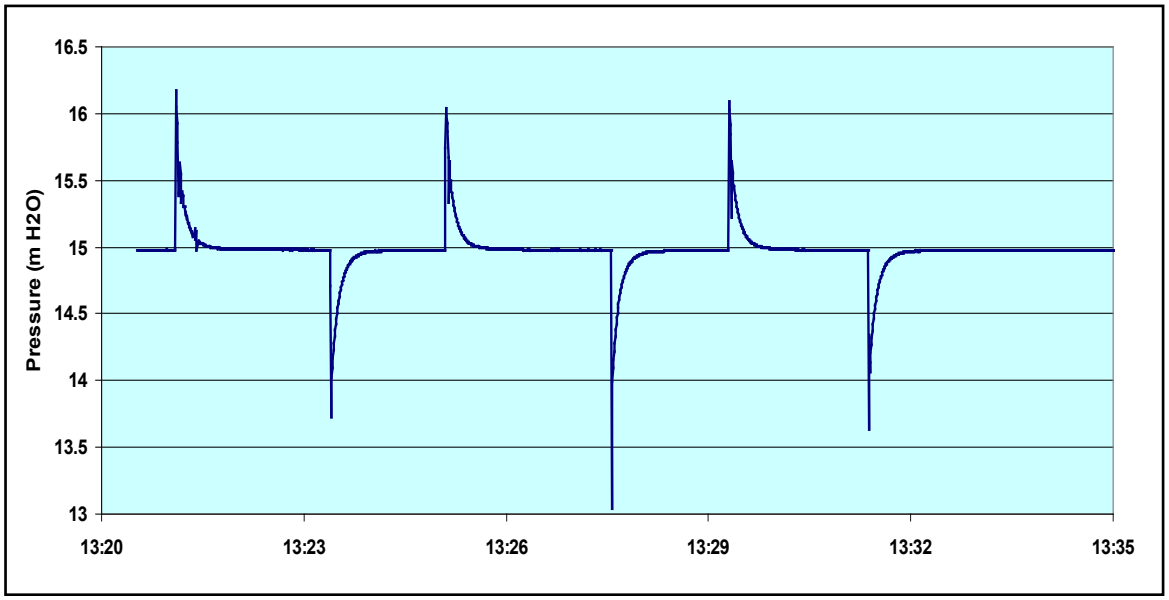



**Figure 13-2.** *Typical data logger response during a series of falling head and rising head slug tests.*

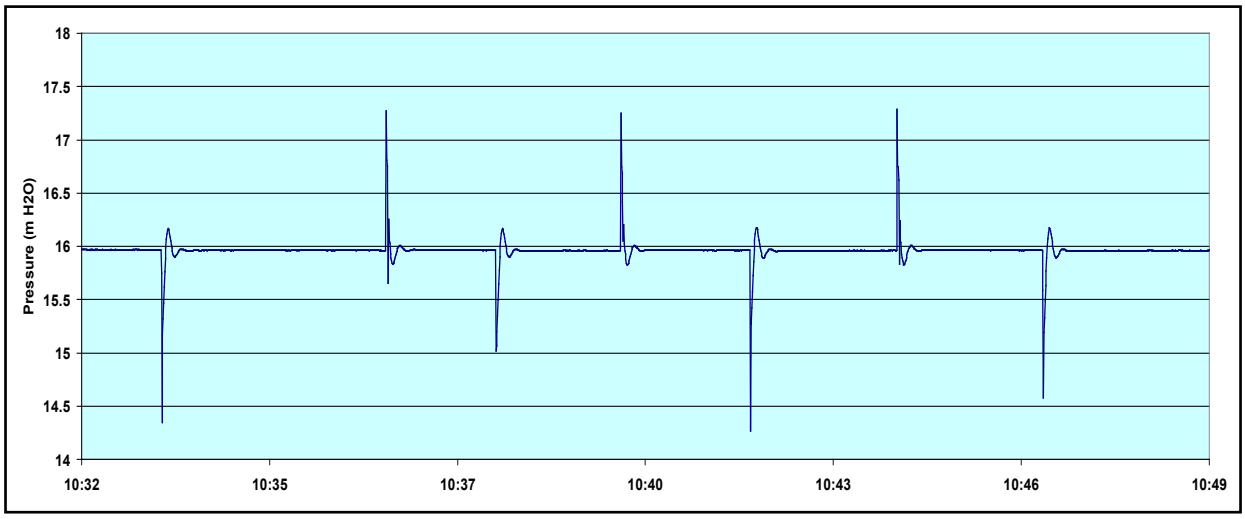



**Figure 13-3.** *Oscillatory water level response during a series of falling head and rising head slug test, indicative of high hydraulic conductivity.*

Butler *et al*. (2007) was used as a guide to interpretation of the slug test monitoring data. A minimum of four of the best water level recovery curves for the borehole were visually selected from the monitoring. By plotting these curves in terms of the head deviation from static (i.e. for each reading, the difference with the pre-test pressure reading) and the time since the test began, these recovery curves could be directly compared. The recovery curves were also normalized, by dividing the head deviation with the theoretical displacement calculated by the dimensions of the slug and the bore casing. On this basis, the recovery curve with the best quality data (e.g. lowest data noise) and which best represented the groundwater response in the borehole was selected for analysis.

AQTESOLV was used to apply slug test solutions to the selected recovery curve, to derive estimates of hydraulic conductivity, transmissivity and storativity. Butler (1998) and Butler *et al*. (2007) provide guidance in terms of logical workflows to select a solution with the most appropriate assumptions. This selection was based on factors such as aquifer confinement, penetration of the screen into the aquifer, the plausibility of derived storativity values, and the comparison between theoretical and actual initial displacement.

Table 13-2 summarises the results of the slug test analysis. The variation in the solution applied reflects the process described above. Unconfined aquifers tended to be analysed using the Bouwer & Rice (1976) or Hvorslev (1951) solutions, and confined aquifers using the Cooper *et al*. (1967) or Hyder *et al*. (1994) solutions, with the latter also referred to as the KGS model in Table 13-2. In some bores, an oscillatory water level response was recorded. This is caused by inertial effects in the well and is a reflection of relatively high hydraulic conductivities. In these cases (termed 'underdamped' responses), the McElwee & Zenner (1998) nonlinear solution was applied.

**Table 13-2.** *Summary of slug test interpretations for BHMAR project bores.*

| Hole Name | Screened Aquifer | Aquifer Saturated Interval | Aquifer Type | Test Solution | Hydraulic Conductivity (m/d) | Trans-missivity ($m^2$/d) | Storativity | Slug Test Conf. |
|---|---|---|---|---|---|---|---|---|
| BHMAR01A-1 | Calivil | 36-79 | confined | KGS | 4.8 | 155 | 1.E-05 | |
| BHMAR01B-1 | Calivil | 53-68 | confined | KGS | 5.5 | 39 | 5.E-02 | |
| BHMAR03B-1 | Upper Renmark | 61-71 | confined | KGS (skin) | 8 | 51 | 6.E-05 | L |
| BHMAR03B-2 | Calivil | 34-55 | confined | Butler | 20 | 369 | - | M |
| BHMAR04-1 | Upper Renmark | 90-101 | confined | KGS | 5.5 | 66 | 1.E-04 | H |
| BHMAR04-2 | Calivil | 34-52 | confined | Cooper *et al.* | 4.6 | 83 | 4.E-04 | |
| BHMAR04-3 | Menindee | 9-13 | unconfined | Bouwer-Rice | 7.5 | 45 | - | L |
| BHMAR04-4 | Calivil | 20-51 | confined | Cooper *et al.* | 4.5 | 32 | 7.E-03 | |
| BHMAR05-1 | Upper Renmark | 94.5-100.5 | confined | Hvorslev | 0.05 | 0.3 | - | |
| BHMAR05-2 | Calivil | 28-40 | confined | Cooper *et al.* | 2.4 | 28 | 4.E-02 | |
| BHMAR06-1 | Calivil | 32-62 | confined | Hvorslev | 0.05 | 1.4 | - | |
| BHMAR08-1 | Calivil | 19-47 | confined | KGS | 17 | 65 | 4.E-03 | M |
| BHMAR14-1 | Calivil | 41-59 | confined | Cooper *et al.* | 0.4 | 8 | 2.E-02 | |
| BHMAR15-1 | Calivil | 33-78 | confined | KGS | 0.06 | 1.5 | 5.E-03 | |
| BHMAR16-1 | Calivil | 19-50 | confined | KGS | 2.9 | 118 | 9.E-03 | M |
| BHMAR17-1 | Calivil | 54-72 | confined | KGS | 7.8 | 141 | 1.E-05 | |
| BHMAR17-2 | Calivil | 22.5-34.5 | confined | Cooper *et al.* | 0.35 | 4 | 1.E-01 | |
| BHMAR18-1 | Upper Renmark | 55.5-70.5 | confined | Cooper *et al.* | 1.9 | 11 | 7.E-04 | |
| BHMAR18-2 | Calivil | 20.5-52 | confined | Cooper *et al.* | 1.9 | 51 | 7.E-05 | |
| BHMAR19-1 | Calivil | 45-64 | confined | Cooper *et al.* | 5.7 | 85 | 1.E-06 | |
| BHMAR19-2 | Willotia | 2-19.5 | unconfined | Bouwer-Rice | 0.7 | 4.2 | - | |
| BHMAR21-1 | Calivil/ Renmark | 20-74 | confined | KGS | 2.6 | 140 | 5.E-05 | M |
| BHMAR21-2 | Menindee | 10.5-13.5 | unconfined | Bouwer-Rice | 9.3 | 30 | - | M |
| BHMAR21-3 | Calivil | 20-58 | confined | KGS | 1.8 | 44 | 1.E-04 | M |
| BHMAR22-1 | Calivil | 24.6-58.5 | confined | Butler | 19 | 487 | - | |
| BHMAR23-1 | Palaeozoic | 81-105 | confined | KGS | 5.6 | 134 | 4.E-05 | M |
| BHMAR23-2 | Calivil | 31-45 | confined | Cooper *et al.* | 0.62 | 11 | 4.E-03 | H |
| BHMAR23-3 | Menindee | 8.5-23.5 | unconfined | Springer-Gelhar | 32 | 343 | - | M |
| BHMAR23-4 | Menindee | 8.5-23.5 | unconfined | KGS | 11 | 63 | 6.E-04 | |
| BHMAR28-1 | Calivil/Loxton-Parilla | 14-55 | confined | KGS | 0.5 | 17 | 2.E-03 | |
| BHMAR29-1 | Calivil | 13-59 | confined | KGS | 7.7 | 277 | 5.E-05 | M |
| BHMAR30-1 | Calivil | 35-75 | confined | Hvorslev | 0.05 | 2 | - | |
| BHMAR31-1 | Loxton-Parilla | 13-49 | unconfined | KGS | 5.4 | 217 | 1.E-03 | H |
| BHMAR33-1 | Lower Renmark | 182-222? | confined | Butler | 4.5 | 108 | - | M |

| | | | | | | | | |
|---|---|---|---|---|---|---|---|---|
| BHMAR33-2 | Calivil | 36-59 | confined | Butler | 22 | 238 | - | |
| BHMAR33-3 | Menindee | 13-23 | confined | KGS | 21 | 624 | 1.E-04 | |
| BHMAR33-4 | Calivil | | confined | Bouwer-Rice | 69 | 688 | - | |
| BHMAR33-5 | Calivil | | confined | KGS | 57 | 624 | 1.E-05 | |
| BHMAR33-6 | Calivil | 35-58 | confined | Butler | 18 | 198 | - | |
| BHMAR33-7 | Calivil | 34-60 | confined | Butler | 25 | 230 | - | |
| BHMAR33-8 | Calivil | 47-52 | confined | KGS | 4.6 | 27 | 8.E-04 | H |
| BHMAR33-9 | Calivil | 49-58 | confined | KGS | 12.2 | 73 | 9.E-05 | |
| BHMAR34-1 | Calivil | 27-51 | confined | KGS | 10.4 | 250 | 1.E-05 | M |
| BHMAR34-2 | Menindee | 8-20 | unconfined | Hvorslev | 0.9 | 11 | - | |
| BHMAR34-3 | Calivil | 27-51 | confined | KGS | 0.07 | 1 | 3.E-03 | |
| BHMAR35-1 | Calivil | 17-47 | unconfined | Hvorslev | 0.6 | 18 | - | M |
| BHMAR36-1 | Calivil | 38-82 | confined | Butler | 4.1 | 180 | - | H |
| BHMAR41-1 | Calivil | 60-66 | confined | KGS | 0.8 | 19 | 7.E-04 | |
| BHMAR43-1 | Upper Renmark | 59-63 | confined | - | - | - | - | |
| BHMAR43-2 | Calivil | 26-54 | confined | KGS | 1.3 | 16 | 7.E-03 | |
| BHMAR48-1 | Calivil | 34.5-59 | confined | KGS | 4.3 | 101 | - | |
| BHMAR51-1 | Calivil | 15-26 | unconfined | - | - | - | - | |
| BHMAR53-1 | Calivil | 33-40 | confined | KGS | 0.3 | 3.7 | 6.E-02 | |
| BHMAR56-1 | Calivil | 29-49 | confined | KGS | 0.2 | 2.5 | - | |
| BHMAR57-1 | Calivil/Upper Renmark | 29-59 | confined | Butler | 5.5 | 264 | - | |
| BHMAR58-1 | Calivil | 35-71 | confined | KGS | 6.7 | 40 | 1.E-03 | L |
| BHMAR61-1 | Upper Renmark | 86-118 | confined | McElwee-Zenner | 10 | 300 | - | H |
| BHMAR61-2 | Calivil | 34-66 | confined | McElwee-Zenner | 15 | 459 | - | |
| BHMAR61-3 | Menindee | 12.5-22.5 | unconfined | Bouwer-Rice | 1 | 10 | - | M |
| BHMAR62-1 | Calivil | 44-60 | confined | Cooper *et al.* | 11 | 170 | - | L |
| BHMAR63-1 | Calivil | 33-39 | confined | KGS | 28 | 167 | 8.E-03 | M |
| BHMAR64-1 | Upper Renmark | 82-98 | confined | McElwee-Zenner | 7.9 | 128 | - | |
| BHMAR64-2 | Calivil | 20-55 | confined | McElwee-Zenner | 6.2 | 218 | - | |
| BHMAR65-1 | Calivil | 32-55 | confined | KGS | 7 | 168 | 8.E-03 | |
| BHMAR66-1 | Calivil | 29-61 | confined | Butler | 6.8 | 203 | - | M |
| BHMAR74-1 | Calivil | 32.5-70.5 | confined | KGS | 4.6 | 161 | 1.E-02 | |
| BHMAR75-1 | Calivil | 20-52 | confined | Butler | 15 | 176 | - | |
| BHMAR75-2 | Calivil | 18-53? | unconfined | KGS | 1.3 | 6.6 | 1.E-01 | |
| BHMAR75-3 | Renmark | 79-89 | confined | KGS | 1.7 | 10 | 4.E-03 | M |
| BHMAR75-4 | Calivil | 20-53 | confined | Butler | 35 | 424 | - | |
| BHMAR75-5 | Calivil | 27-52 | confined | Butler | 51 | 609 | - | M |
| BHMAR75-6 | Calivil | 19-54 | confined | Butler | 31 | 374 | - | |

| | | | | | | | | |
|---|---|---|---|---|---|---|---|---|
| BHMAR75-7 | Calivil | 20-55 | confined | Butler | 35 | 420 | - | |
| BHMAR75-8 | Calivil | 20-52 | confined | Butler | 28 | 112 | - | |
| BHMAR77-2 | Calivil | 22-56 | confined | Butler | 26 | 211 | - | H |
| BHMAR77-3 | Menindee | 10-15 | unconfined | Bouwer-Rice | 0.44 | 2 | - | |
| BHMAR77-4 | Menindee | 10-15 | unconfined | Bouwer-Rice | 1.7 | 7 | - | |
| BHMAR77-5 | Calivil | 44-57 | confined | Butler | 18 | 184 | - | |
| BHMAR79A-2 | Renmark | 64-77 | confined | Butler | 45 | 546 | - | |
| BHMAR79A-5 | Calivil | 16-24 | confined | KGS | 1.3 | 8 | 4.E-02 | |
| BHMAR79A-6 | Calivil | 28-63 | confined | Butler | 26 | 317 | - | H |
| BHMAR79A-10 | Calivil | 30-62 | confined | Butler | 42 | 540 | - | |
| BHMAR79A-12 | Calivil | 40-60 | confined | Butler | 23 | 164 | - | |
| BHMAR80A-2 | Calivil | 24-62 | confined | Butler | 21 | 372 | - | M |
| BHMAR80A-3 | Coonambidgal | 5.5-18 | unconfined | Bouwer-Rice | 1 | 6 | - | |
| BHMAR80A-4 | Coonambidgal | 5.5-14 | unconfined | Bouwer-Rice | 5.9 | 35 | - | |
| BHMAR80A-5 | Calivil | 24-62 | confined | Butler | 137 | 1850 | - | |
| BHMAR80A-6 | Renmark | 84-102 | confined | KGS | 2.7 | 49 | 1.E-02 | |
| BHMAR80A-7 | Calivil | 27-62 | confined | Butler | 25 | 306 | - | |
| BHMAR80B-2 | Calivil | 21-67 | confined | Butler | 14 | 168 | - | H |
| BHMAR80B-3 | Coonambidgal | 6-16 | unconfined | Bouwer-Rice | 1.6 | 8 | - | |
| BHMAR83-2 | Calivil | 23-61 | confined | Butler | 22 | 325 | - | M |
| BHMAR84-2 | Calivil | 20-52 | confined | KGS | 0.39 | 2.4 | 9.E-02 | L |
| BHMAR84-3 | Menindee | 8-22 | unconfined | Bouwer-Rice | 0.4 | 4 | - | |
| BHMAR84-4 | Menindee | 7-19 | unconfined | Bouwer-Rice | 0.4 | 4 | - | |
| BHMAR84-5 | Menindee | 7-14 | unconfined | Bouwer-Rice | 2 | 27 | - | |
| BHMAR88-2 | Calivil | 30-61 | confined | Bouwer-Rice | 0.1 | 1 | - | |
| BHMAR88-3 | Upper Renmark | 59-89 | confined | KGS | 2 | 12 | 9.E-03 | L |
| BHMAR88-4 | Calivil | 67?-85 | confined | Bouwer-Rice | 1.7 | 31 | - | |
| BHMAR88-5 | Calivil | 35-55 | confined | KGS | 16.5 | 99 | 2.E-03 | |
| BHMAR88-6 | Calivil | 32-88 | confined | Butler | 25 | 450 | - | |
| BHMAR88-7 | Calivil | 57-77 | confined | KGS | 5.9 | 94 | 2.E-04 | |
| BHMAR92-1 | Calivil | 33-63 | confined | Butler | 7.6 | 229 | - | L |
| BHMAR92-2 | Menindee | 8-16 | unconfined | Bouwer-Rice | 0.2 | 0.8 | - | |
| BHMAR99-1 | Calivil | 23-59 | confined | Butler | 11.6 | 278 | - | H |

## 13.3 PUMP TESTS

Two pump tests of production bores were undertaken within the Jimargil target as part of Phase 3a of the BHMAR project. The objectives of the pump tests were to:

- Quantify the hydraulic properties (transmissivity and storage coefficient) of the Calivil Formation target aquifer.
- Investigate the level of confinement of the target aquifer, with respect to overlying clay units within the upper Calivil and Menindee Formation sequences.
- Investigate the potential of downward leakage from shallow aquifers, particularly sand sequences within the upper Calivil, Menindee or Coonambidgal Formations.
- Monitor any potential watertable drawdown in shallow bores located near the Darling River.

In September 2010, a 7-day pump test was undertaken at the BHMAR33 site. Figure 13-4 shows the location of the pumped bore BHMAR33-5 as well as associated infrastructure such as monitoring bores and temporary pipeline. In October 2010, a 7-day pump test of the BHMAR80A-5 production bore nearer to the Darling River (Figure 13-5) was curtailed to five days due to the imminent threat of flooding of the site.

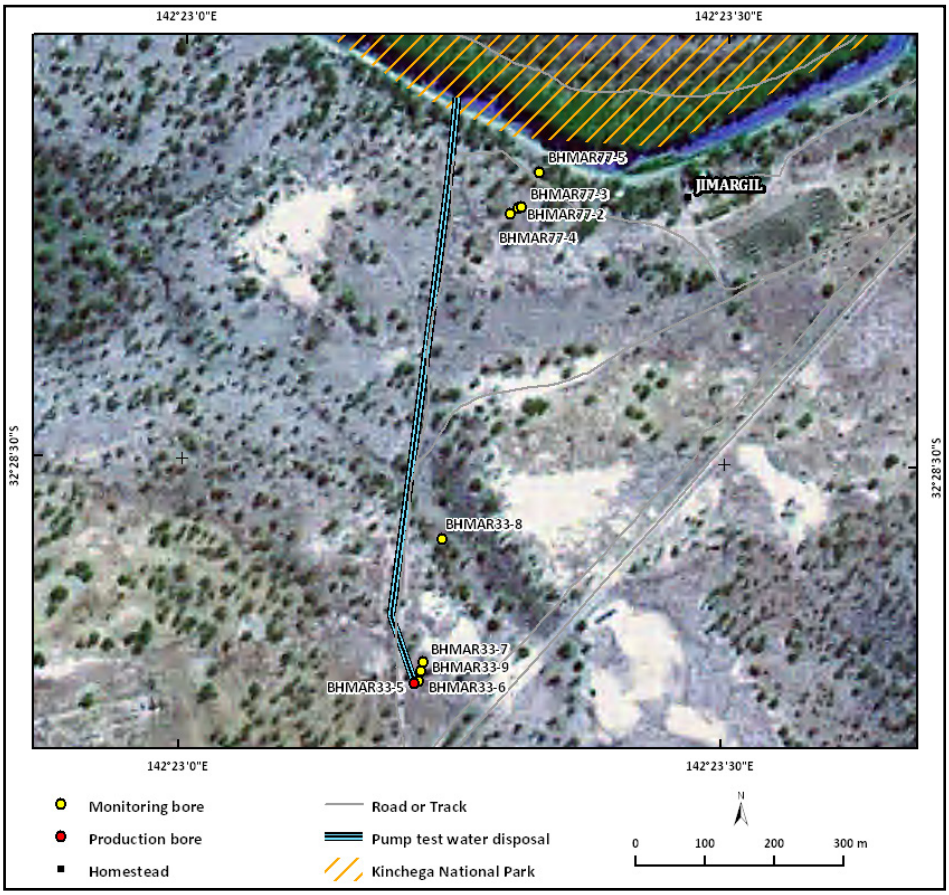



**Figure 13-4.** *Map showing the infrastructure associated with the BHMAR33-5 aquifer test, including the pump test bore and associated monitoring bores at sites 33 and 77, and the route of the temporary flexible pipeline to the river.*

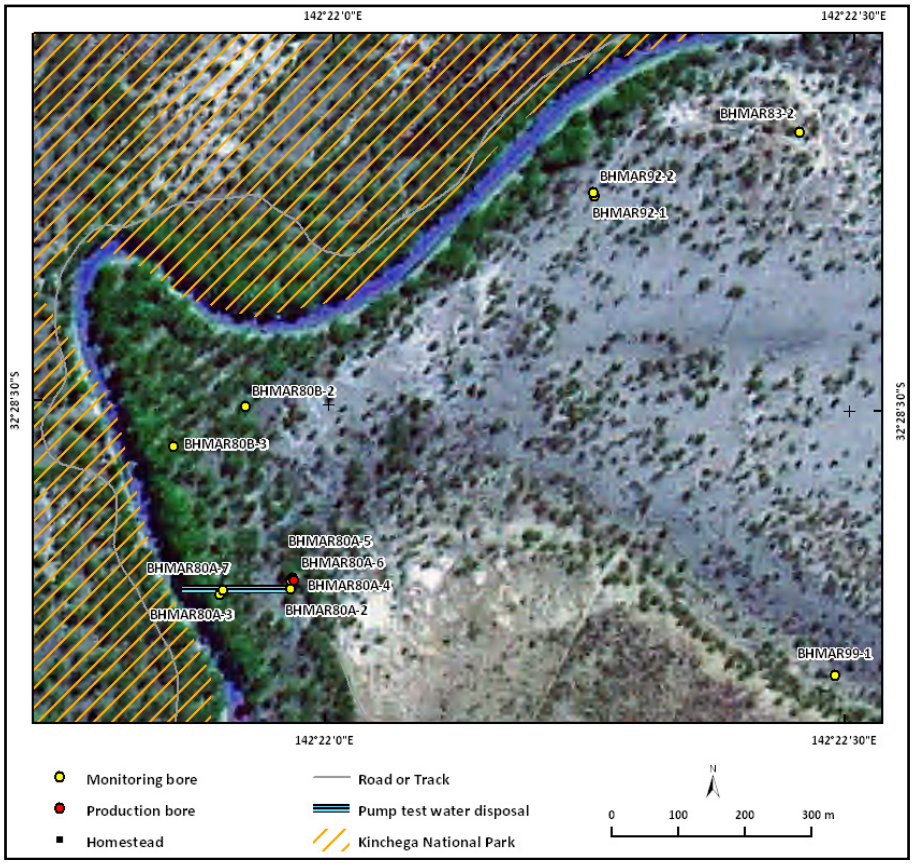



**Figure 13-5.** *Map showing the location and infrastructure associated with the aquifer test of the BHMAR80A-5 project bore, including the pumping and monitoring bores, and the route of the temporary flexible pipeline to the river.*

Pump test operations were undertaken by the Impax Group, with on-site supervision and additional monitoring undertaken by Geoscience Australia staff. The pump tests were designed as three phases of operation:

- An initial step drawdown test involving a minimum of 3 x 2 hourly stages, with the pumping rate of each subsequent stage significantly higher than the last. Given initial air lift testing during development, and the anticipated injection rate, pumping rates of 10, 15 and 25 L/s were proposed, with each subsequent actual pumping rate dependent on results of the previous stage.
- A single rate pump test for 7 days, with continual pumping at a constant flow rate as defined by the step drawdown test.
- A recovery phase of up to 7 days or until equilibrium of groundwater levels was achieved.

The pump test data for BHMAR33-5 and BHMAR80A-5 are summarised in Appendix 6 (Somerville *et al*., 2012).

### 13.3.1 Pumping Bores

The appropriate design and construction of bores for pump and injection tests is a vital step in assessment of aquifer hydraulic properties. In order to more fully assess the hydraulic properties of the Calivil Formation aquifer, a review of bore construction methods was carried out by Geoscience Australia with input from CSIRO, Impax, Environmental Strategies and Boart Longyear, to assess whether the Phase 2 BHMAR33-4 bore was suitable for a comprehensive range of pump and injection tests. This review concluded that there was a high likelihood of screen clogging or failure over longer duration and higher flow injection testing, and a decision was made to adopt a more robust production bore design for aquifer stress testing. Consequently, a decision was made to customise the screens for proposed pump and injection test bores. Due to time constraints, screen design had to be based on on-site sieve analysis rather than laboratory derived full range grain size analyses. Whilst this may result in small reductions in bore efficiencies, limitations imposed by the borehole diameter and available pumps are thought to be a more significant factor.

#### 13.3.1.1 *BHMAR33-5 Pumping Bore*

The project bore BHMAR33-5 was the pumping bore for the initial step drawdown, constant rate and recovery test in September 2010. Borehole construction is summarised in Table 13-3 and involved:

- A target aquifer depth interval 48-59 m from natural ground surface into lower Calivil Formation sands and gravels
- Drilling of a 14” hole by a mud rotary rig
- Use of polymer muds rather than bentonite to facilitate development and reduce clogging potential
- Class 18 PVC 200 mm belled casing, with centralisers along casing and screen every 6 m
- An 11 m length type 316 stainless steel wedge wired screen over the 48-59 m interval. Aperture of 1 mm slot, with 8 inch (203 mm) pipe size
- A 1 m length type 316 stainless steel blank as sump below screen (59-60 m)
- A 1-2 mm graded artificial gravel pack, installed to 2 m above top of screen (46-60 m)
- A pitot tube installed in the annulus to 53 m mid-screen depth (25 mm conduit with slotted interval to allow installation of Diver logger). However, this tube became blocked during construction and could not be used during the pump test.
- A 2 m annulus interval of hydrated bentonite pellets above the gravel pack (44-46 m)
- Cement grout above bentonite to surface, using a ‘tremie’ pipe (0-44 m).

Figure 13-6 shows the construction of the BHMAR33-5 test bore with respect to the site hydrogeology.

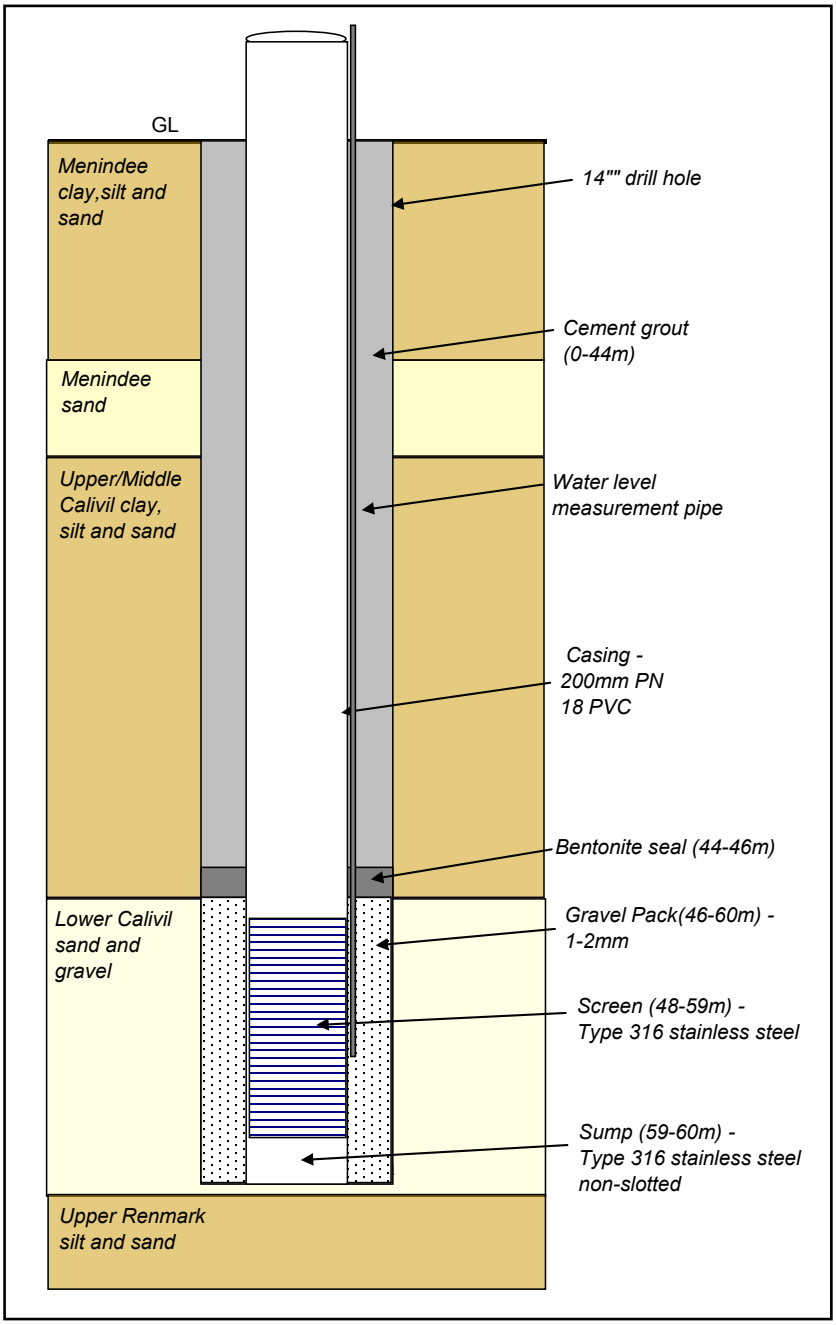



**Figure 13-6.** *Construction details of the BHMAR33-5 aquifer test bore.*

**Table 13-3.** *Construction summary for BHMAR33-5 aquifer test bore.*

| **Casing** – Class 18 PVC 200 mm belled casing | | |
|---|---|---|
| **Depth Interval (m)** | **Length (m)** | |
| +1-48 | 49 m | Allow 1-m above ground |
| **Well Screen** – type 316 stainless steel, nominal 8 inch pipe size | | |
| **Depth Interval (m)** | **Length (m)** | **Slot/Aperture (mm)** |
| 48-59 | 11 m | 1 mm |
| 59-60 | 1 m | Zero slot (sump) |
| **Gravel Pack/Grout** | | |
| **Depth Interval (m)** | **Length (m)** | **Specification** |
| 0-44 | 44 m | Cement grout |
| 44-46 | 2 m | Hydrated bentonite pellets |
| 46-60 | 14 m | 1-2 mm gravel pack |

#### 13.3.1.2 *BHMAR80A-5 Pumping Bore*

The project bore BHMAR80A-5 was the pumping bore for the second test in October 2010. The construction of the bore is summarised in Table 13-4 and included:

- A target aquifer depth interval of 35-55 m from natural ground surface into lower Calivil Formation sands and gravels.
- Drilling of a 14" hole by a mud rotary rig.
- Class 18 PVC 200 mm belled casing, with centralisers along casing and screen every 6 m.
- Various type 316 stainless steel wedge wired screened intervals over the 35-56.5 m zone. Aperture of 1 or 3 mm slot depending on interval grainsize sieve analysis, with 8 inch (203 mm) pipe size. Multiple screened intervals were used instead of a single 35-56 m screen, to isolate finer grained sections previously identified by the nearby sonic drilling and confirmed by the sieve analyses.
- Various type 316 stainless steel blanks between screened intervals as well as a 1 m length sump.
- A combination of 1-2 mm or 3-5 mm graded artificial gravel pack, depending on the interval grainsize sieve analysis.
- A pitot tube installed in the annulus to 35 m depth (38 mm conduit with slots at bottom 3 m and open at base).
- A 2 m annulus interval of hydrated bentonite pellets above the gravel pack (44-46 m).
- Cement grout above bentonite to surface, using a tremie pipe (0-44 m).

Figure 13-7 shows the construction of the BHMAR80A-5 bore with respect to the site hydrogeology.

**Table 13-4.** *Construction summary of BHMAR 80A-5 aquifer test bore.*

| **Casing** – Class 18 PVC 200 mm belled casing | | |
|---|---|---|
| **Interval (m)** | **Length (m)** | |
| +1-35 | 36 m | Allow 1-m above ground |
| **Well Screen** – type 316 stainless steel, nominal 8 inch pipe size | | |
| **Interval (m)** | **Length (m)** | **Slot/Aperture (mm)** |
| 35-45 | 10 m | 3 mm |
| 45-48.5 | 3.5 m | Zero slot (no screen) |
| 48.5-50.5 | 2 m | 1 mm |
| 50.5-53.5 | 3 m | Zero slot (no screen) |
| 53.5-55.5 | 2 m | 1 mm |
| 55.5-56.5 | 1 m | Zero slot (sump) |
| **Gravel Pack/Grout** | | |
| **Interval (m)** | **Length (m)** | **Specification** |
| 0-31 | 31 m | Cement grout |
| 31-33 | 2 m | Hydrated bentonite pellets |
| 33-46 | 13 m | 3-5 mm gravel pack |
| 46-56.5 | 4 m | 1-2 mm gravel pack |

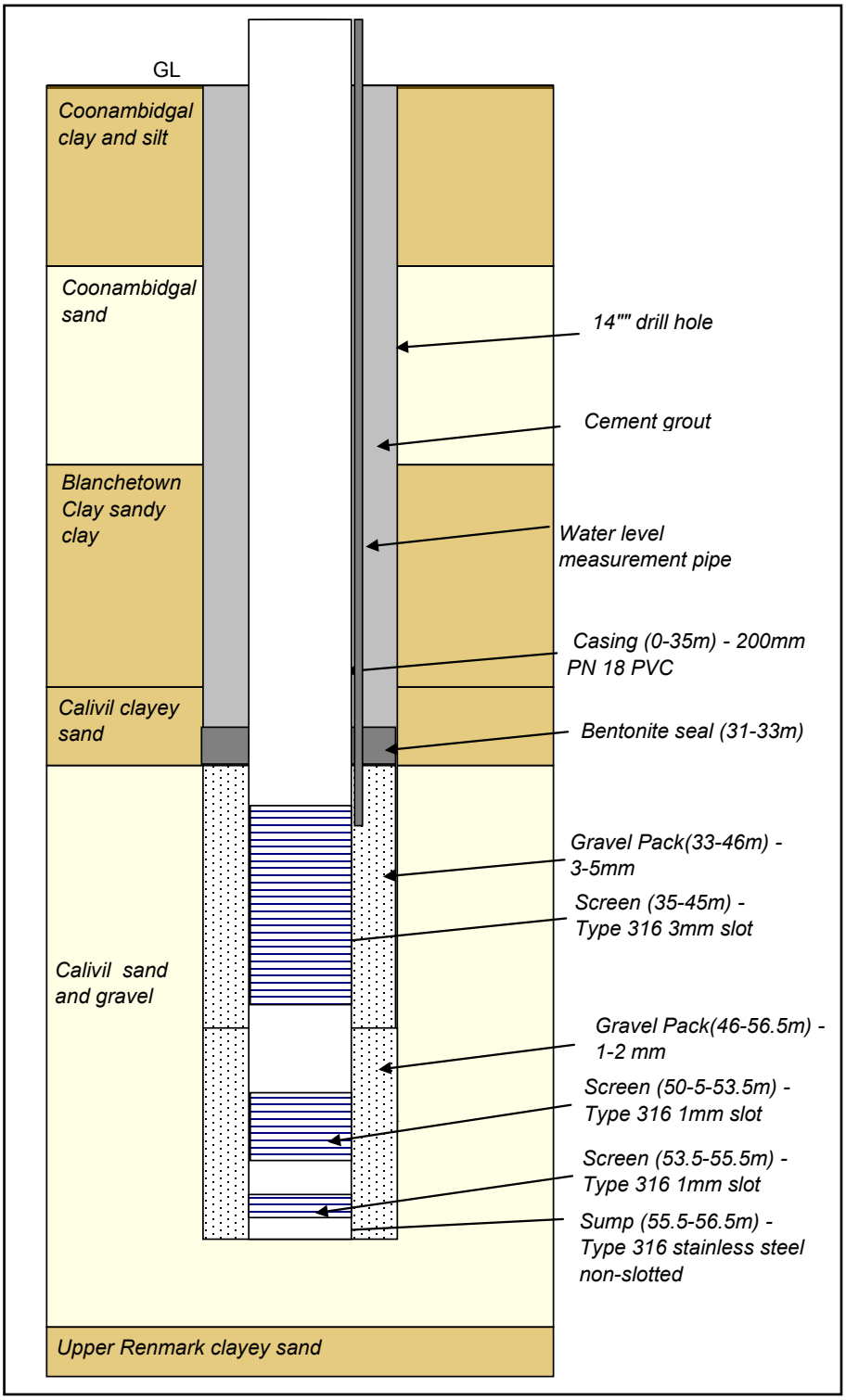



**Figure 13-7.** *Construction details of the BHMAR80A-5 aquifer test bore.*

### 13.3.2 Pumping and Pipeline Infrastructure

The pump test equipment used in the tests is summarised in Table 13-5. By way of example, Figure 13-8 shows the pumping equipment assembled at the BHMAR33-5 bore site.

A submersible pump unit was used to deliver up to 28 L/s from the 200 mm diameter bore (Figure 13-9). The groundwater was pumped through a combination of 110 mm polythene pipe and 150 mm lay-flat pipe where it was discharged through a diffuser into the river. As a requirement of the test, discharge had to be delivered

at least 300 m away from the bore head to ensure no local recharge, so in-river discharge was the preferred option. For the BHMAR33-5 test, the pipeline distance was about 900 m. The location of the temporary pipeline for this test is shown on Figure 13-4, following a corridor of already disturbed ground parallel to the boundary fence between Jimargil and East Bootingee stations adjacent to a fenceline track.

As the BHMAR80A-5 bore is closer to the Darling River, the pipeline distance for this test was only about 160 m (Figure 13-5).

Surveys determined that there was no cultural impediment to deploying these temporary pipelines. The pipe was laid on the ground and required no excavation or ground disturbance. The route avoided all perennial shrubs and trees and required no clearing or disturbance of vegetation. A specially designed poly-spinner towed behind a 4WD vehicle was used to lay and retrieve the poly pipe where appropriate. For the BHMAR80A-5 test, the pipeline was manually laid and recovered.

Where the pipeline route met the river there was a steep bank extending down about 8-10 m between the floodplain and the river level (Figure 13-10). The bank had no vegetation or cultural heritage materials which would have been impacted by the pipeline. Pump-test water disposal occurred directly into the river which eliminated any possibility of bank erosion.

**Table 13-5.** *Specification of equipment used for BHMAR33-5 and 80A-5 aquifer tests.*

| **PUMP UNIT ( Duty 65M3H @ 75 M Head )** |
|---|
| Franklin FPS-70-8 ST Submersible Turbine DI Pump End |
| Franklin 18.5KW 304 Water Well Submersible motor |
| M 80 mm Flexibore Hose 48 |
| 80 mm Stainless Steel Couplings |
| Nylon Cable Straps 100 |
| 100 mm x 80 mm Stainless Steel Bush |
| 200 mm Galvanised Bore Cap |
| Installation Roller |
| Set Lifting Clamps |
| Break Off Plug Fitted |
| **DISCHARGE FITTINGS** |
| 100 mm Gear Operated Butterfly Valve |
| 100 mm Toro Flow Meter |
| 10 mm Poly Butt Weld Flanges |
| 110 mm Poly Butt Weld Elbows |
| Sets 100 mm Gaskets, Bolts and Nuts |
| **DISCHARGE DIFFUSER** |
| Floating Diffuser as detailed in Figure 13-11 and Figure 13-12 |
| **PIPELINE** |
| M 110 mm PN12 Poly Pipe 900 m<br>150 mm Lay-Flat Pipe 900 m |
| 110 mm Poly Joiners |
| **SWITCBOARD and GENSET** |
| Zenner VFD Switchboard with low level probe, pressure switches and safety controls |
| Weiley Control Box |
| Cummins 43 KVA Genset with engine protection system |

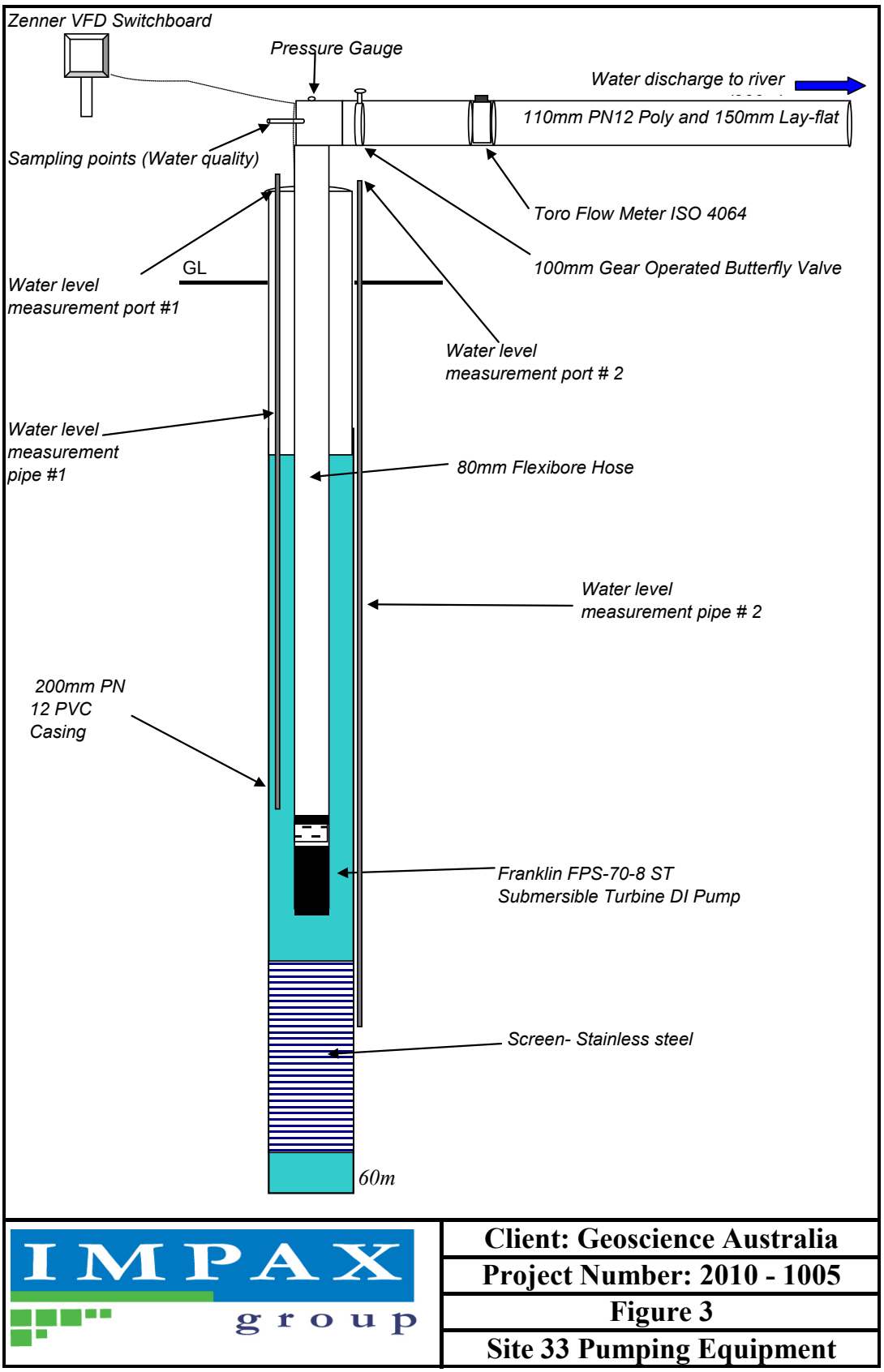



**Figure 13-8.** *Pumping equipment used for the BHMAR33-5 aquifer test.*



**Figure 13-9.** *Photograph showing Geoscience Australia staff and contractors at the headworks of the BHMAR33-5 production bore during aquifer testing.*



**Figure 13-10.** *Photograph showing groundwater discharge into the river via the diffuser array at Jimargil during the BHMAR33-5 aquifer test. Note the low flow conditions at the time (September 2010).*

### 13.3.3 Pump Test Discharge

A stringent approvals process was followed to ensure that the pump tests and groundwater disposal met with the approval of the regulatory and responsible agencies.

Figure 13-11 and Figure 13-12 are diagrams of the diffuser that was used to discharge groundwater into the river in a manner to avoid erosion. A 1 m x 1 m floating platform was constructed using a wooden base with foam floats secured underneath. A 3 m length of 150 mm PVC screen was used as the diffuser. The floating platform was located in the middle of the river, and was tethered on either side of the bank to ensure it remained securely in mid-stream. One flexible length of poly pipe was run from the discharge diffuser float back to the bank, and provided sufficient flexibility to cope with changes in the height of the river over the course of the test.

Water was discharged directly from the diffuser PVC screen into the middle of the river, with minimal surface water disturbance thereby avoiding bank erosion on either side of the river in the vicinity of the diffuser. Floating baffles were installed on either side of the river to absorb any increase in surface water movement and protect the river banks from erosion. No equipment or materials was installed in such a way that would obstruct the free passage of floodwater flowing in, to or from the river at the site.

The diffuser and its placement were designed to discharge groundwater at the centre of the river channel at shallow water depth (<0.5 m) in order to avoid plumes of discharge water hugging the shore and impacting adversely on biologically important areas.

Reflective tape was attached to the tether ropes and a flashlight beacon and other markers were installed on top of the floating platform. Temporary warning signs were also placed both upstream and downstream of the diffuser location, in locations visible to boating traffic.

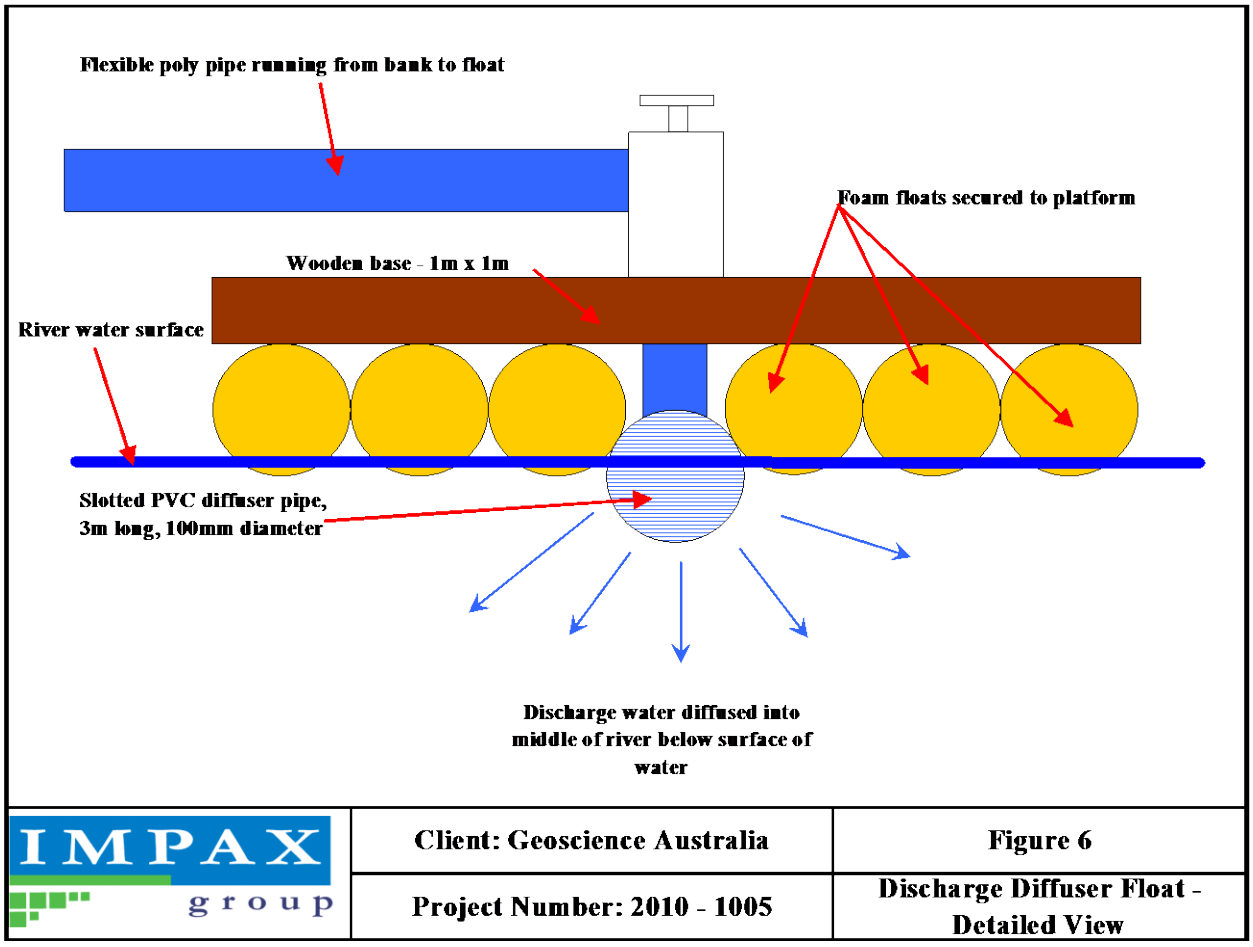



**Figure 13-11.** *Cross section design view of floating diffuser platform used to discharge aquifer test groundwater.*

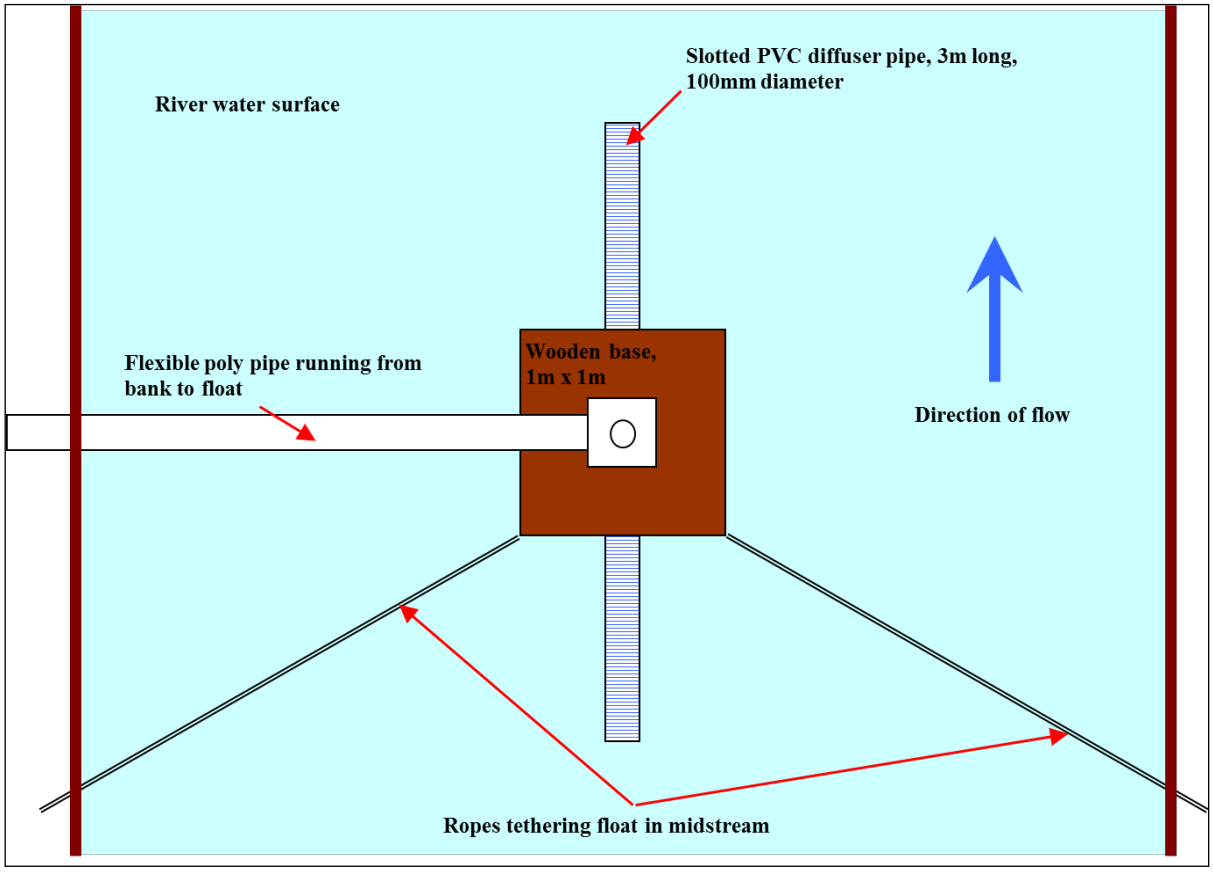



**Figure 13-12.** *Overhead design view of floating diffuser platform used to discharge aquifer test groundwater.*

### 13.3.4 Groundwater Level Monitoring

For this pump test, groundwater level responses were measured in the pumped Calivil Formation aquifer, as well as both shallow (Menindee and Coonambidgal Formation ) and deeper (Renmark Group) aquifers. Pressure transducers were installed in monitoring bores distributed around the pump test bore to record water-level fluctuations at various distances from the pumped bore, and also in different aquifers. Water levels were also manually measured at scheduled time steps during the tests. Table 13-6 provides details on the groundwater monitoring network established in the vicinity of the pumped bores. Loggers were also installed in the water column of the pumping bore, as well as within the pitot tube in the gravel pack to evaluate borehole efficiency. At the request of neighbouring landholders, data loggers were installed temporarily in private stock and domestic supply bores, to monitor groundwater conditions further away from the test site. Standing water level data is contained in Appendix 6 (Somerville *et al*., 2012).

**Table 13-6.** *Summary of project monitoring bores used for the BHMAR33-5 and BHMAR80A-5 aquifer tests.*

| **BHMAR33-5 Pump Test** | | | |
|---|---|---|---|
| **Borehole** | **Aquifer** | **Distance from BHMAR33-5 bore** | **Screened Interval (m) below ground surface** |
| 33-5 | Calivil | 0 | 48-59 |
| 33-1 | Lower Renmark | 9 | 182-206 |
| 33-2 | Calivil | 9 | 48-59 |
| 33-3 | Menindee | 9 | 14-23 |
| 33-4 | Calivil | 35 | 48-58 |
| 33-6 | Calivil | 10 | 47-58 |
| 33-7 | Calivil | 41 | 48-57 |
| 33-8 | Calivil | 208 | 46-52 |
| 77-2 | Calivil | 682 | 47-55 |
| 77-3 | Menindee | 695 | 11-16 |
| 77-4 | Menindee | 687 | 11-15 |
| 77-5 | Calivil | 765 | 46-56 |
| | | | |
| **BHMAR80A-5 Pump Test** | | | |
| **Borehole** | **Aquifer** | **Distance from BHMAR80A-5 bore** | **Screened Interval (m) below ground surface** |
| 80A-5 | Calivil | 0 | 35-55.5 |
| 80A-2 | Calivil | 5 | 35-53 |
| 80A-3 | Coonambidgal | 110 | 11-17 |
| 80A-4 | Coonambidgal | 5 | 10-14 |
| 80A-6 | Renmark | 5 | 84-102 |
| 80A-7 | Calivil | 110 | 42-54 |
| 80B-2 | Calivil | 270 | 53-65 |
| 80B-3 | Coonambidgal | 270 | 11-16 |
| 92-1 | Calivil | 740 | 32-62 |
| 83-2 | Calivil | 1000 | 48-63 |
| 84-2 | Calivil | 1830 | 45-53 |
| 84-3 | Coonambidgal | 1920 | 10-23 |
| 33-3 | Menindee | 1950 | 14-23 |
| 33-2 | Calivil | 1950 | 48-59 |
| 33-1 | Lower Renmark | 1950 | 181-206 |
| 33-8 | Calivil | 2000 | 46-52 |
| 77-3 | Menindee | 2200 | 11-16 |
| 77-5 | Calivil | 2230 | 46-56 |

### 13.3.5 Pumped Flow Monitoring

Monitoring of groundwater discharge is a necessary requirement for pump test analysis. A 100 mm magnetic flow meter was installed at the pumped bore headworks, of the type manufactured by ABB with specifications approved by the NSW Office of Water. The pumping rate was manually recorded during the pump test, rather than any digital logging.

#### 13.3.5.1 *Groundwater Quality Monitoring*

To comply with licence conditions, the electrical conductivity (EC) of the groundwater discharge was measured every six hours. This was undertaken from a sampling point at the headworks (Figure 13-9). The test was designed so that disposal of groundwater to the Darling River was to stop if the groundwater salinity exceeded 2000 µS/cm. However, this threshold was not exceeded during either of the pump tests.

As part of the hydrochemical assessment of the target aquifer, Geoscience Australia staff also undertook additional monitoring and sampling of the groundwater discharge as follows:

- Field water quality measurements on a 6-hourly basis that were additional to the EC monitoring including pH, temperature, Eh, dissolved oxygen, alkalinity, ferrous iron, total iron, sulfide and turbidity
- Sampling of initial (Day 1) and final (Day 7) groundwater discharge for major ions, trace metals, nutrients, organic carbon, chlorofluorocarbons, radon, stable isotopes and radiocarbon
- A daily sample (Day 2-6) of the groundwater discharge for major cations, major anions, total metals and dissolved metals.

#### 13.3.5.2 *River Flow and Water Quality Monitoring*

Comprehensive in-river monitoring was conducted as part of the pump tests including:

- Hydrographic surveys of river flow using the current meter flow gauging method conducted both upstream and downstream of the discharge diffuser. Surveys were mainly from a boat, however they were also conducted by wading across the river when the water level was low and it was safe to do so. A current meter was used to obtain accurate soundings and velocities at given distances and depths across the selected section. Hydrographic surveys were completed using The Impax Group Technical Operating Procedure No: 70020 – Hydrographic Current Meter Gaugings
- Monitoring of river electrical conductivity both upstream and downstream of the discharge diffuser using a portable EC meter. This was conducted at the same time as the water flow surveying using The Impax Group Technical Operating Procedure No: 70020 – Hydrographic Current Meter Gauging. A separate cross section of the river giving the EC profile was recorded, generally using the gauging method, however instead of recording water flow soundings, water quality (EC) measurements was instead recorded. Final calculations for each cross section were then obtained by multiplying the average conductivity by the average velocity by the area of each section. The calculations were summed for each section and by dividing the summed calculations by the total flow, the average stream conductivity was determined.
- Staff gauge installation as any height data collected at hydrographic stations must be relative to a datum. An automatic level was used to establish gauge, orifice and/or probe levels by connection to the station bench mark. Staff gauge installation and levelling was conducted in accordance with The Impax Group Technical Operating Procedure No: 70063 – Hydrographic Levelling of Staff Gauges.

# 14 Water Sampling and Analysis

A comprehensive program of water sampling and hydrochemical analysis was carried out to assess water quality criteria and understand hydrological processes. Sampling included that of cumulative rainfall, surface water (river, lake storages and treated water supply) and groundwater from selected existing bores and from the monitoring bores constructed by the BHMAR project. In addition, the pore fluids extracted from the sonic core were also submitted for hydrochemical analysis. Sample collection, preservation and transport were undertaken by GA, as well as measurement of field parameters and major ion analyses. Specific water analyses were contracted to external laboratories, such as for trace elements, stable isotopes (deuterium and oxygen-18), nutrients, organic carbon (TOC and DOC), radon, chlorofluorocarbon and radiocarbon. Overall, 184 groundwaters from 104 bores, 1144 pore fluids from 49 cored holes, 56 surface waters from 26 sites, 10 rainfall samples from the Menindee site were sampled and analysed. The hydrochemical analyses undertaken in the water sampling program are summarised in Table 14-1.

**Table 14-1.** *Hydrochemical analysis suite used in BHMAR water sampling program.*

| Suite | Lab | Samples | Analytes and limit of reporting (LOR) in mg/L | Methods |
|---|---|---|---|---|
| Field water quality | Field | groundwater<br>surface water | electrical conductivity EC, pH, redox Eh, dissolved oxygen DO, temperature, turbidity | Field meters and sensors, daily calibration using standard solutions |
| Field alkalinity | Field | groundwater<br>surface water | total alkalinity | Hach digital titrator |
| Specific ions | Field | groundwater | ferrous iron $Fe^{2+}$, total iron Fe, sulfide $S^{2-}$ | Hach spectrophotometer |
| Major cations | Geoscience Australia Canberra | groundwater<br>surface water<br>rainfall<br>pore fluid | Calcium (0.1), potassium (0.5), magnesium (0.1), sodium (0.1), sulphur (0.3), silica (0.1), aluminium (0.02), boron (0.01), barium (0.005), copper (0.025), iron (0.02), lithium (0.02), manganese (0.005), strontium (0.01), zinc (0.02) | Inductively coupled plasma atomic emission spectroscopy ICP-OES |
| Major anions | Geoscience Australia Canberra | groundwater<br>surface water<br>rainfall<br>pore fluid | total alkalinity (10), lab EC, lab pH, fluoride (0.5), chloride (2), bromide (0.05), nitrate (0.1), sulfate (0.5) | Auto-titrator<br>Lab EC-pH meter<br>Ion chromatograph |
| Total metals | ALS Sydney | groundwater<br>surface water<br>selected pore fluid | *Note 1* | Inductively coupled plasma mass spectrometry ICP-MS |
| Dissolved metals | ALS Sydney | groundwater<br>surface water<br>selected pore fluid | *Note 1* | Inductively coupled plasma mass spectrometry ICP-MS |
| Total nutrients | ALS Canberra | groundwater<br>surface water | total nitrogen (0.05), total phosphorous (0.05) | APHA 2005, Part 4500-P J, Part 4500-P G |
| Dissolved nutrients | ALS Canberra | groundwater<br>surface water | Ammonia (0.01), nitrate (0.01), nitrite (0.01), orthophosphate (0.01), oxidised nitrogen (0.01) | APHA 2005, Part 4500-NH3 H, Part 4500-NO3-I |
| Organic carbon | ALS Canberra | groundwater<br>surface water | Total organic carbon TOC (1), dissolved organic carbon DOC (1) | APHA 2005, Part 5310B |
| Biodegradable dissolved organic | Australian Water Quality Centre | selected surface water | biodegradable dissolved organic carbon BDOC (0.2) | APHA 2005, Part 5310B Bacterial inoculum and aeration |

| | | | | |
|---|---|---|---|---|
| carbon | Adelaide | | | |
| Pesticide Screen | National Measurement Institute Sydney | selected surface water | NR47 Screen *Note 2*<br>Phenoxy-acid Herbicides Screen *Note 3*<br>NR51 Screen *Note 4* | Gas chromatography mass spectrometry<br>GC-MS |
| Suspended solids | Geoscience Australia Canberra | selected surface water | Total suspended solids and particle size distribution | Laser particle size analyser |
| Chlorofluoro-carbons | CSIRO Adelaide | groundwater | CFC-11, CFC-12 concentration (5 pg/kg) and apparent age (yrs) | Purge and trap gas chromatography |
| Radon | CSIRO Adelaide | groundwater surface water | radon (0.005 Bq/L) | Liquid scintillation counter |
| Stable isotopes of water | Rafter GNS New Zealand | groundwater surface water rainfall selected pore fluids | deuterium $\delta^2H$ (1 ‰), oxygen-18 $\delta^{18}O$ (0.1 ‰) | Automated equilibration system<br>Stable isotope gas ratio mass spectrometer |
| Radiocarbon | Rafter GNS New Zealand | groundwater selected surface water (C-13) | carbon-13 $\delta^{13}C$, carbon-14 $\delta^{14}C$,% modern C, radiocarbon age | Accelerator mass spectrometry AMS |
| Strontium isotopes | Australian National University Canberra | selected groundwater selected surface water | $^{87}Sr/^{86}Sr$ | Thermal ionization mass spectrometry TIMS |

Notes: Total and dissolved metals include aluminium (0.01), dysprosium (0.001), silver (0.001), arsenic (0.001), bismuth (0.001), erbium (0.001), boron (0.05), europium (0.001), strontium (0.001), barium (0.001), gadolinium (0.001), titanium (0.01), beryllium (0.001), gallium (0.001), cadmium (0.0001), hafnium (0.01), tellurium (0.005), cobalt (0.001), holmium (0.001), uranium (0.001), caesium (0.001), chromium (0.001), indium (0.001), copper (0.001), lanthanum (0.001), rubidium (0.001), lithium (0.001), lutetium (0.001), thorium (0.001), cerium (0.001), manganese (0.001), neodymium (0.001), molybdenum (0.001), praseodymium (0.001), nickel (0.001), samarium (0.001), lead (0.001), terbium (0.001), antimony (0.001), thulium (0.001), selenium (0.01), ytterbium (0.001), tin (0.001), yttrium (0.001), thallium (0.001), zirconium (0.005), vanadium (0.01), zinc (0.005), iron (0.05).

NR47 Pesticide screen for *Organochlorine pesticides* (HCB, Heptachlor, Heptachlor epoxide, Aldrin, gamma-BHC (Lindane), alpha-BHC, beta-BHC, delta-BHC, trans-Chlordane, cis-Chlordane, Oxychlordane, Dieldrin, p,p-DDE, p,p-DDD, p,p-DDT, Endrin, Endrin aldehyde, Endrin ketone, alpha-Endosulfan, beta-Endosulfan, Endosulfan sulfate, Methoxychlor, Dicofol), *Organophosphate Pesticides* (Dichlorvos, Demeton-S-methyl, Diazinon, Dimethoate, Chlorpyrifos, Chlorpyrifos methyl, Malathion, Fenthion, Ethion, Fenitrothion, Chlorfenvinphos (E), Chlorfenvinphos (Z), Parathion (ethyl), Parathion methyl, Pirimiphos methyl, Pirimiphos ethyl, Azinphos methyl, Azinphos ethyl, Bromophos ethyl, Carbophenothion, Coumaphos, Dioxathion, Fenamiphos, Fenchlorphos, Formothion, Methacrifos, Methidathion, Mevinphos, Phorate, Phosalone, Profenophos, Prothiofos, Thiometon, Triazophos), *Synthetic Pyrethroids* (Bifenthrin, Bioresmethrin, Cyfluthrin, Cyhalothrin, Cypermethrin, Deltamethrin, Fenvalerate, Flumethrin, Permethrin (cis and trans), Phenothrin), *Fungicides* (Bupirimate, Chlorothalonil, Cyprodinil, Dichlofluanid, Dicloran, Difenoconazole, Dimethomorph,, Diphenylamine, Fenarimol, Flusilazole, Hexaconazole, Iprodione, Imazalil, Metalaxyl, Penconazole, o-Phenylphenol, Prochloraz, Procymidone, Propiconazole I, Propiconazole II, Pyrimethanil, Tebuconazole, Vinclozolin *Carbamates* (Carbaryl, Fenoxycarb, Pirimicarb) *Herbicides* (Atrazine, Diuron, Linuron, Simazine, Hexazinone, Metolachlor, Molinate, Oxtfluorfen, Pendimethalin, Trifluralin) *Miscellaneous* (Buprofezin, Methoprene, Piperonyl Butoxide, Propargite, Tebufenpyrad, Tetradifon) – limit of reporting of 0.1 ug/L.

Phenoxy-acid herbicides screen for Dicamba, MCPA, Dichlorprop, 2,4-D, 2,4,5-T, 2,4,5-TP, 2,4-DB, MCPP, Trichlopyr – limit of reporting of 1 ug/L.

NR51 Screen for Acephate, Aldicarb, Bensulfuron methyl, Bromacil, Carbaryl, Carbendazim, Carbofuran, Carbofuran-3-hydroxy, Chlortoluron, Cyanazine, Diuron, Endothal, Fipronil, Imazalil, Imazethapyr, Imidacloprid, Isoproturon, Linuron, Metalaxyl, Methamidophos, Methomyl, Metolachlor, Metsulfuron methyl, Monocrotophos, Omethoate, Oxamyl (Thixamyl), Pirimicarb, Propazine, Pyriproxyfen, Sethoxydim, Tebuconazole, Tebuthiuron, Temephos, Terbuthylazine, Thiabendazole, Thiodicarb, Triadimefon, Vamidothion – limit of reporting of 5 ug/L.

The program also included a QA/QC sampling and analysis component. This involved processing of deionised water samples used to check for potential contamination, such as field blanks using the same procedures as a normal sample (such as filtering and acidification) to test contamination introduced by field procedures, acid blanks to test any contaminants in the acid and blanks prepared in the laboratory beforehand and transported with the samples, to test for environmental contamination. Field duplicates, nominally one per 20 samples, were also taken. This was an extra sample taken at the field site using the same field procedures to test the analytical precision of the lab. Spiked duplicates where known amounts of a number of elements of interest were added to the sample were also used. Details about the QA/QC process are provided in Section 14.4.

As indicated by Table 14-1, the analysis suite is comprehensive and includes standard analyses for assessing suitability for water use (such as major cations, major anions, dissolved metals, dissolved nutrients) as well as analyses used to help understand groundwater processes (including tracers such as chlorofluorocarbons (CFCs), stable isotopes and radiocarbon). The levels of reporting (LOR) relating to analytes are also presented in Table 14-1. The sampling requirements vary across this analytical suite and Table 14-2 summarises these requirements in terms of the sample bottle, field treatments and storage.

**Table 14-2.** *Sampling requirements for hydrochemical analysis suite.*

| Analysis | Container | Field treatment | Storage | Storage life |
|---|---|---|---|---|
| Major cations | HDPE, 50 mL (or 125 mL) acid rinsed and capped | Filter: 0.45 µm. Acidify: $HNO_3$ to 2 vol.% | Refrigerate | 1 year |
| Major anions | HDPE, 125 mL | Filter: 0.45 µm | Refrigerate | 1 year |
| Total metals | PE, 125 mL supplied by lab | Acidify: $HNO_3$ | Refrigerate | 6 months |
| Dissolved metals | PE, 125 mL supplied by lab | Filter: 0.45 µm. Acidify: $HNO_3$ | Refrigerate | 6 months |
| Total nutrients | PET, 50 mL supplied by lab | No treatment | Refrigerate | 7 days |
| Dissolved nutrients | Plastic vial, 15 mL supplied by lab | Filter: 0.45 µm | Freeze; leave <1 mL air gap | 14 days |
| Total Organic Carbon | Amber glass, 30 mL, acid rinsed and baked; Teflon/Al-lined cap. supplied by lab | No treatment | Refrigerate | 7 days |
| Dissolved Organic Carbon | Amber glass, 30 mL, acid rinsed and baked; Teflon/Al-lined cap. supplied by lab | Filter: 0.45 µm | Refrigerate | 7 days |
| Biodegradable Dissolved Organic Carbon | 1 L glass bottle supplied by lab lab | no air gap no treatment | Refrigerate | Deliver within 24 hours (on ice). |
| Pesticide Screen | 1L amber glass bottle Bottles, eskies, ice bricks all supplied by lab | No treatment | Refrigerate Dark | 7 days Samples to NMI within 4 days |
| Suspended Solids | 10-L sample container | No treatment | Refrigerate | 1 month |
| Chlorofluorocarbons | 3 of glass, 125 mL; screw top metal lid supplied by lab | Sample into bottle submerged in stainless steel drum to minimise air contamination. Use nylon tubing | Tighten lids with pliers; keep out of light. Refrigerate. | 7 days, |
| Radon | PET, 1.25 L soft drink bottles | Specialised sampling | | 2-3 days |

| | | | | |
|---|---|---|---|---|
| | Pre-weighed glass vial with scintillant supplied by lab | procedure | | |
| Stable Isotope | Glass, 28 mL McCartney; screw top metal lid | No filter | Strictly no headspace. Refrigerate | 1 year |
| Radiocarbon | 1L amber glass, bottle, teflon-lined cap; larger vol. if pH <6 and/or low EC. | No treatment Fill bottle submerged in metal bucket | Strictly no headspace. Refrigerate | |
| Strontium isotopes | HDPE 125 mL acid rinsed and capped | Filter 0.45 µm Acidify: $HNO_3$ | Refrigerate | 1 month |

Some of these sampling procedures were very specific. For example, the groundwater radon samples were taken using the PET method (CSIRO, 2011) where the samples were collected in 1.25L PET soft drink bottles. A mineral oil scintillant (21 mL) from a pre-weighed and labelled low diffusion PET vial was added to the sample, before mixing by inverting the sample bottle every 2 seconds for 4 minutes to transfer the radon to the scintillant. The bottle was left to stand to allow the scintillant to settle to the top. The oil phase was returned to the vial by squeezing the bottle and pushing the oil through a custom glass nozzle (Figure 14-1). The vial was capped, labelled and despatched to the laboratory within 2-3 days of sampling.

The hydrochemistry analyses are reported in Appendix 6 (Somerville *et al*., 2012), with bore locations and details summarised in Appendix 12 (Apps & Gibson, 2012). Pore fluid and saturation extract data are reported in Appendix 6 (Somerville *et al*., 2012).



**Figure 14-1.** *Radon sampling procedure involving extracting an oil-scintillant from the PET bottle after slowly shaking the water/oil mixture (CSIRO, 2011).*

## 14.1 GROUNDWATER SAMPLING

Following construction, the BHMAR monitoring bores were developed by air lift using a compressor. Electrical conductivity and pH were monitored and a groundwater sample for major ion analysis (Figure 13-1) was also collected towards the end of development. This provided a preliminary guide to groundwater quality for the screened aquifer. More detailed sampling of the monitoring bores occurred at least 3 weeks after air lift development to allow groundwater conditions to stabilise and equilibrate. For many bores, the intervening period between development and sampling spanned several months, due to postponement of the field program due to flooding in 2010-11. Re-sampling of selected bores after flooding allowed the opportunity to investigate any hydrochemical response. A Bennett low-flow pump was used for the groundwater sampling program, the pump and associated equipment is shown in Figure 14-2. The basic principle is to pump at a sufficiently low rate to minimise drawdown, with lateral groundwater movement through the well screen avoiding disturbance of stagnant water in the casing above and below the pump intake. The method has the advantages of:

- Mitigating the need to purge at least three well volumes from the well casing before sampling, therefore reducing the pumping time required. This can also simplify disposal of pumped groundwater, particularly for saline (or potentially contaminated) aquifers;
- The opportunity to take multiple samples down the screened interval, to help characterise hydrochemical variation with depth. This allowed confirmation of salinity stratification in some of the monitoring bores in the study area. In contrast, the sample from conventional purged pumping is an aggregate for the entire well screen interval;
- Minimising the disturbance of any sediment collected in the bore sump, reducing sample turbidity and therefore reducing filtering effort and the hydrochemical effects of fine particulates;
- A pumping depth capacity of 300 m, allowance for continuous flows and a readily adjustable flow rate. This enabled sampling of the 206 m deep bore monitoring the Lower Renmark aquifer at the Jimargil borefield target;
- Relatively simple and robust mechanics using compressed air as the motive force, rather than electricity (and associated electronics).

The standard workflow associated with the collection of the groundwater samples is summarised in Figure 14-3 and involved the following steps:

- Notifying the relevant landholder of the visit to the project site. This was also an opportunity to check road conditions and any other issues related to site access (such as livestock movements).
- Recording of basic information about the borehole and its surroundings, focussing on any site rehabilitation or bore maintenance that may be required. A standard Project Site Details form was designed to document this information in the field.
- Measuring the groundwater level relative to the top of the borehole protector (or other reference) using an electronic dipper. If a logger was installed in the borehole this was first removed and carefully stowed after a data download. A Borehole Measurements form was used to document the borehole details, the water level measurement (including the reference used) and the logger details.
- Calibrating the field chemistry equipment used during groundwater sampling. The standard suite of field chemistry parameters were electrical conductivity (EC), pH, temperature, redox (Eh) and dissolved oxygen (DO). The sensors were checked for calibration at each site and a Field Calibration Record form was used to keep a log of the calibration undertaken during the sampling trip. For EC, a 718 ± 29 µS/cm QC standard was used as a check, with standard EC solutions used for calibration. The reading for a pH 8.15 ± 0.05 seawater QC standard was taken and then calibration if necessary using pH 4 and 7 solutions. The Eh and temperature reading for a Zobell's solution was used as a check for redox. The DO sensor was calibrated using air for saturated DO and sodium sulfite solution for zero DO.
- Installing and operating the Bennett low-flow pump. The pump intake was lowered by winch to a set depth within the well screen, and flow regulated to a recommended 0.5 L/min (Puls and Barcelona,

1996). A flow cell was set up to house the field chemistry sensors, with a separate sampling line used so that samples did not have to be taken through the flow cell, to avoid potential KCl contamination from the pH sensor. At certain bores, samples were taken from multiple depths. In this situation the shallowest sample was taken first and the pump then lowered, to minimise disturbance of the well column.

- Recording of EC, pH, Eh, temperature and DO of pumped flow through the flow cell arrangement, nominally every 5 minutes. Also regular monitoring of the flow rate, by filling a beaker or graduated cylinder of known volume (0.5 or 1 L) and recording the fill time. The groundwater level was also measured to check that drawdown during low-flow pumping was within 0.1 m (Puls and Barcelona, 1996). In some cases, a data logger (Diver DI702 10 m) was temporarily installed at a depth of 5-7 m below the groundwater level, with a direct data cable used to monitor the groundwater level response to low-flow pumping. Also any observations about the pumped flow, such as changes in the colour, clarity, any precipitates, tannin, degassing or odour (such as sulfide, organic, contaminant) were noted. A Water Sampling Field Measurements form was used to keep a record of the time-series of field chemistry, flow rates, pump pressure, water levels and observations. Sampling commenced when field chemistry stabilised. EC and DO tended to be the most reliable indicators, with the criteria of 3 consecutive 5-minute readings within ±3% for EC and ±0.3 mg/L for DO used. The criteria for the other parameters were ±0.1 pH, ±10 mV Eh and ±0.2 °C temperature.
- Measuring field alkalinity, ferrous iron ($Fe^{2+}$), total iron ($Fe_{tot}$), sulfide ($S^{2-}$) and turbidity once the field parameters had stabilised. Alkalinity was measured using a digital titrator with sulfuric acid (1.6N or 0.16N) down to pH 4.3 (methyl orange). A seawater total alkalinity standard (114 ±4 mg/L $CaCO_3$) was used as a QC check. A Hach field spectrophotometer was used to measure $Fe^{2+}$, $Fe_{tot}$, $S^{2-}$ and turbidity. All these measurements were nominally undertaken in triplicate with the results recorded on a *Water Sample Details* form (see Appendix 6, Somerville *et al*., 2012).
- Collecting, preserving and storing groundwater samples based on analytical requirements (Table 14-2). Filtering of small volumes was done by syringe with 0.45µm filter cartridges, combined with GSC pre-filters where required. For large volume or turbid samples, either a glass Erlenmeyer flask system or plastic filtration kit was used. Any sample acidification used reagent-grade nitric acid. The *Water Sample Details* form was used to record information about the water samples taken from the borehole.
- Cleaning and maintenance of sampling equipment, using procedures recommended for each piece (such as use of distilled water or acid wash). Reinstalling of any loggers, packing equipment and samples, securing and locking of bores and clean-up of the site.
- Despatch of samples to relevant labs located in Australia and New Zealand (Table 14-1). A *Chain of Custody (COC)* form accompanied each sample batch to the laboratory. Some laboratories had their own COC template and submission requirements, if not, a project COC form was used.




**Figure 14-2.** *Photographs showing groundwater sampling in progress (top left and bottom). The Bennett low-flow pump is pictured in the top right image.*

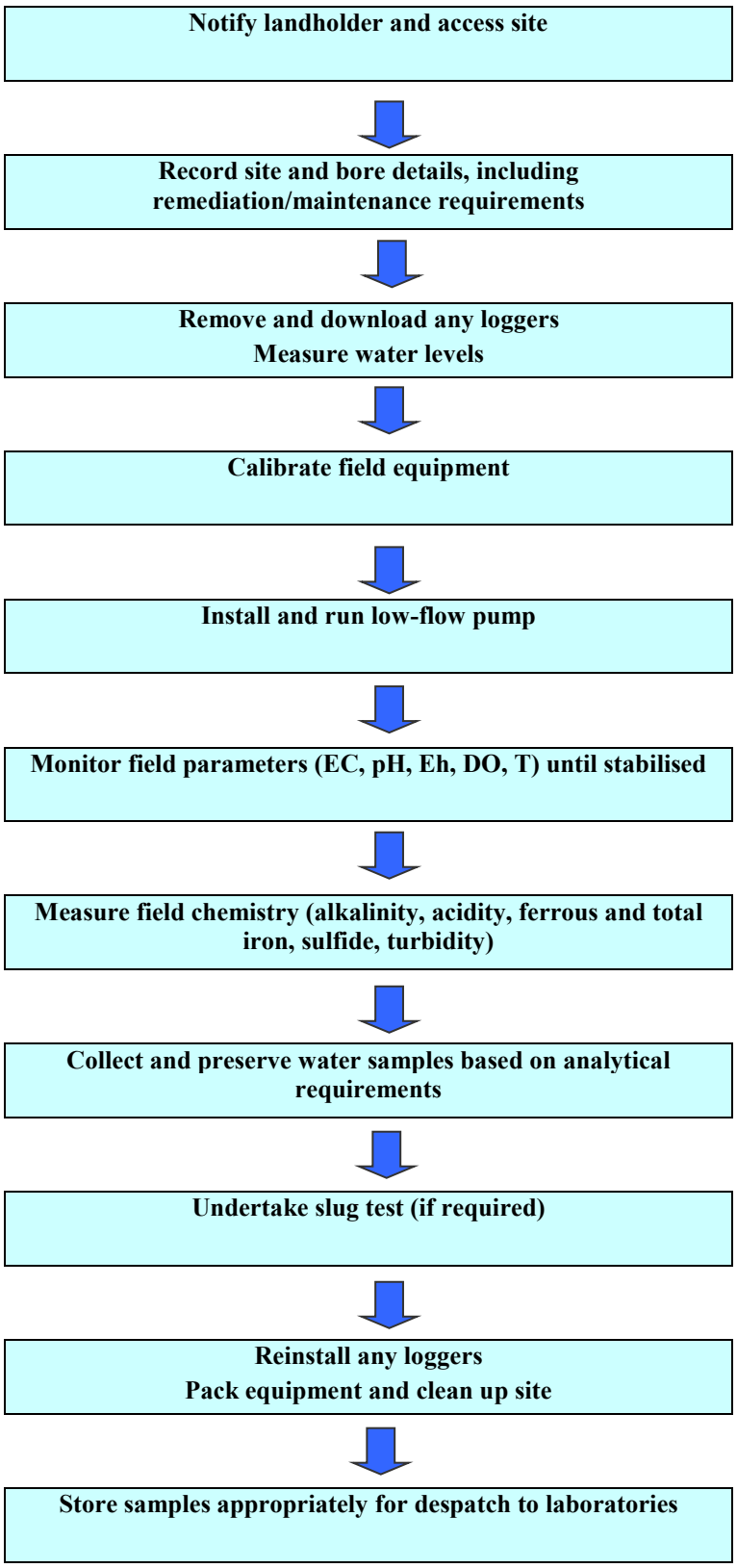



**Figure 14-3.** *General workflow for the collection of groundwater samples.*

## 14.2 SURFACE WATER AND RAINFALL SAMPLING

Surface water sampling focussed on sites along the Darling River and the Menindee Lakes Storages, with the multiple objectives of (1) assessing suitability for drinking water quality, (2) identifying potential issues for use as source water for any proposed MAR scheme and (3) helping to understand important groundwater processes such as recharge via river or lake leakage. Wherever possible, the sampling sites corresponded with the existing water quality monitoring network to add value to the historic data record. These sites are listed in Table 14-3. The project team also coordinated with regional NSW State Water staff on their scheduled surface water sampling runs. Water samples were either collected from near-shore or further into the water storages via boat, nominally at a water depth of ~0.5 m. Turbidity, electrical conductivity, pH, temperature and dissolved oxygen of these samples were measured in the field, using the same equipment and procedures documented above for groundwater sampling. Samples were taken and preserved for analysis of major cations and anions, trace metals, nutrients, organic carbon, stable isotopes and radon (Table 14-1). At some sites, additional samples were taken for more specialised analysis (Table 14-1), such as:

- A pesticide screen, testing for the presence for a range of organochlorine, organophosphate, synthetic pyrethroid, fungicide, carbamate and other pesticides;
- biodegradable dissolved organic carbon (BDOC) for the assessment of source water potential for microbiological clogging; and
- Laser measurement of particle size distribution of suspended solids. The suspended solids are subsequently filtered for chemical and mineralogical analysis by XRF/XRD. This data was used to assess mechanical clogging potential of MAR source water.

**Table 14-3.** *NSW State Water surface water monitoring sites sampled by BHMAR project.*

| Site No | Location | Easting | Northing |
|---|---|---|---|
| 42510001 | Darling River @ Bararoo | 684476 | 6445486 |
| 42510002 | Darling River @ Viewmont | 666231 | 6439256 |
| 42510003 | 3 Mile Creek | 651771 | 6424502 |
| 42510004 | Lake Wetherell | 641491 | 6424850 |
| 42510008 | Lake Tandure | 644675 | 6426994 |
| 42510037 | Copi Hollow | 630461 | 6429060 |
| 42510010 | Lake Pamamaroo | 634786 | 6430529 |
| 42510009 | Pamamaroo Inlet | 641365 | 6425304 |
| 42510013 | Pamamaroo Outlet | 640985 | 6424952 |
| 425 012 | Darling River @ Weir 32 | 629739 | 6410343 |
| 42510057 | Darling River @ Menindee BHWB | 634715 | 6415302 |

A bulk deposition rainfall collector was established for the duration of the project at the NSW State Water Menindee depot. A series of cumulative monthly rainfall samples were obtained for major ion and stable isotope analysis. The data was used to help interpret the surface water and groundwater chemistry, and to assess groundwater recharge magnitude and dynamics.

The rainfall collector was of simple design constructed from HDPE, PVC and stainless steel components (Figure 14-4). A HDPE funnel was attached to a 2 L HDPE sample bottle using a standard electrical gland nut fitting. The bottle and funnel was retained in a holder suspended from a 150 mm PVC screw cap. This was in turn lowered into the housing made up of a length of 150 mm stormwater pipe with an end cap to form the base. The 150 mm screw cap was screwed into the corresponding threaded coupling on the housing to secure the unit. The housing was attached with hose clamps to a steel post driven into the ground.

Before installation, the sample collection bottle was thoroughly cleaned and rinsed with distilled water. Paraffin oil (100 mL) was placed in the bottle before deployment to minimise evaporation of the sample. The sample bottle was simply replaced on a regular basis, and subsamples decanted and filtered for laboratory analysis.

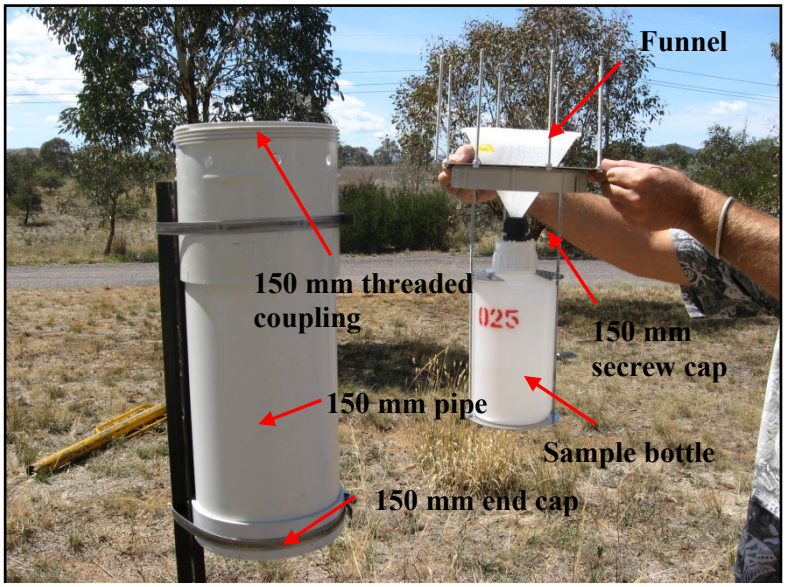



**Figure 14-4.** *Photograph of components of the cumulative rainfall collector used for BHMAR project.*

## 14.3 PORE FLUID SAMPLING

The sonic coring provided the opportunity to extract pore fluids for hydrochemical analysis. The procedures used to extract pore fluids from specific depth samples down the cored profile are documented in Section 11.2. Electrical conductivity, pH and Eh were measured for these pore fluids in the Geoscience Australia laboratory, before routine major cation and anion analysis (Table 14-1). A subset of these pore fluids (47 samples) were also despatched to an external laboratory for the dissolved metals analysis suite (Table 14-1).

Due to the sampling and extraction of these samples under aerobic conditions, these pore fluids do not reflect ambient groundwater hydrochemistry. The oxidised nature of these samples is confirmed by high Eh readings, typically exceeding 300 mV, and this would be reflected particularly in changes in redox sensitive species (such as iron) and the potential for post-extraction metal mobilisation. However, the major cation and anion pore fluid analyses were still useful in characterising hydrogeological processes, particularly investigating the relationship between surface water and groundwater dynamics. The pore fluids also provided some indicators in terms of risks associated with redox processes associated with potential MAR operations, such as the injection of oxygenated source water into the Calivil Formation target aquifer.

## 14.4 QUALITY CONTROL PROCEDURES

### 14.4.1 Internal QA/QC

All samples are submitted for processing and analysis through the Geoscience Australia laboratories laboratory submissions (Lab Subs) system. Each sample and its unique sample identification number are checked for correctness prior to commencement of any laboratory work. All samples are stored refrigerated at 4ºC. All instrumentation was maintained in good working order and serviced at a frequency relevant to its usage and complexity.

#### 14.4.1.1 *Duplicates, repeatability and calibration*

During the core pressing process (see Section 11) a duplicate sample was collected as a check on the precision of the procedure from core processing through to analysis. Acceptable precision on values that are well above the limit of reporting is ± 5%. The same solution was analysed twice within each analytical run,

and with a short time delay in order to assess both the method bias and precision of the analyses. Acceptable precision on values that are well above the limit of reporting is ± 5%. All analytical instruments were calibrated at the start of the analytical run and drift monitors were analysed at regular intervals to ensure that accuracy of the data is maintained. Wherever possible a sample independent of the calibration solutions is analysed at the beginning of the analytical run and immediately after calibration to verify the accuracy of the results.

#### 14.4.1.2 *Pre-release checks of complete datasets*

Where all major and minor cations and anions were determined, an ionic balance was calculated. This was an expression of the percentage difference between the sum of the anions and cations (meq/L) and should be between ±5%, except where the electrical conductivity was low, in which case ±10% is acceptable.

An estimate of the total dissolved solids (TDS) component of the sample was calculated from the sum of the ions analysed. The TDS:EC ratio then allowed a semi-quantitative check on the analysed electrical conductivity (EC). There was no single conversion from EC to TDS as the sample ratio is dependent on the sample composition; however for NaCl waters the ratio was approximately 0.5, for KCl waters, 0.55, for $Na_2SO_4$ waters 1 and for a general fresh water mixture was between 0.65 and 0.85. The S: $SO_4$ ratio was a check on the analysis of sulphur by ICP-OES and $SO_4$ by Ion Chromatography (IC). In oxidised water the S measured on the ICP-OES was assumed to be $SO_4$ and therefore provides a comparison for analysis by two different methods. If data is accurate the ratio is expected to be within ±5%.

### 14.4.2 ALS QA/QC

The analytical procedures used to measure dissolved metal concentrations were developed from established internationally recognized procedures such as those published by the USEPA, APHA, AS and NEPM. Where moisture determination was performed, results were reported on a dry weight basis. In cases where "less than" results were reported as higher than the detection limit, possible explanations include primary sample extract/digestate dilution and/or insufficient sample for analysis. Where the detection limit of a reported result differs from standard detection limit, this may be due to high moisture content, insufficient sample (reduced weight employed) or matrix interference.

Three QA/QC methods were used by ALS laboratories: laboratory duplicates, method blanks, laboratory control spikes and matrix spikes.

#### 14.4.2.1 *Laboratory Duplicates*

The quality control term Laboratory Duplicate refers to a randomly selected intra-laboratory split. Laboratory duplicates provide information regarding method precision and sample heterogeneity. The permitted ranges for the Relative Percent Deviation (RPD) of Laboratory Duplicates are specified in ALS Method QWI-EN/38 and are dependent on the magnitude of results in comparison to the level of reporting.

*Groundwater results*

The RPD was calculated as the percent difference between the duplicate results and the original sample. For example, a sample with concentration of dissolved metals at 100 mg/l with concentration of duplicate at 105 mg/l give a RPD of 5%. Likewise, a duplicate result of 95 mg/l also gives a RPD of 5%. The RPD between original and duplicate groundwater samples ranges from 0-8.2%. Results less than three times the detection limit are not included due to the high level of inherent error with small changes in low concentrations. 10 out of 49 analyses have a RPD greater than 5%. The mean RPD for all groundwater samples with a concentration equal or greater than 3 times the detection limit is 2.5% and the median is 1.4%.This is within the ± 5% acceptable precision range. Figure 14-5 compares the original and duplicate groundwater samples.

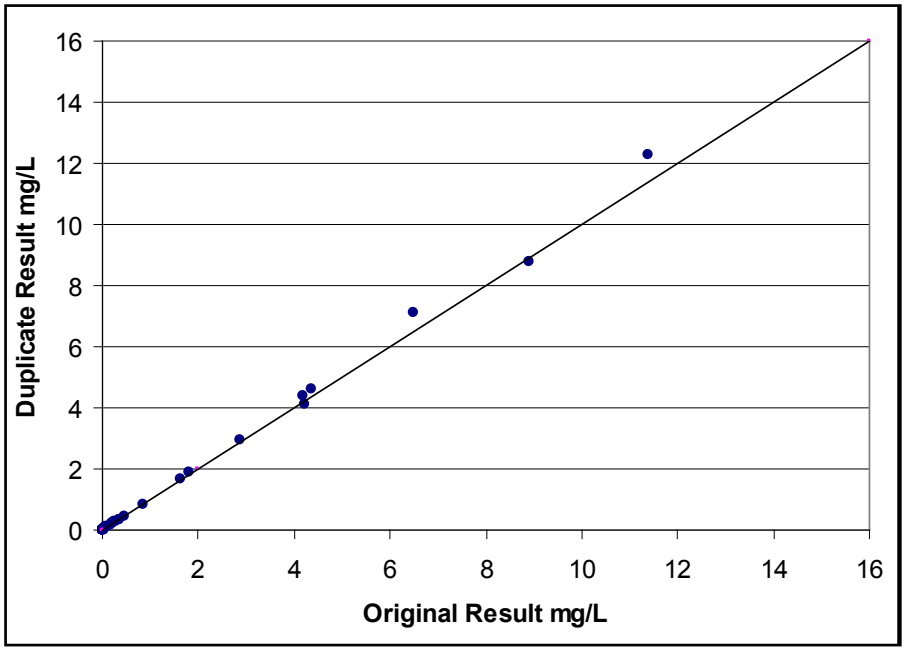



**Figure 14-5.** *Graph showing the original and duplicate results for dissolved metals in all groundwater samples. The black line represents the line y=x to illustrate the closeness of fit between original and duplicate lab results.*

*Pore Fluid results*

The RPD between original and duplicate pore fluid samples ranges from 0-62.6%. The high RPD is attributed to a single sample which concentration is very low (2.2 mg/l). As a result, a duplicate of 3.25 mg/l gives 60% deviation. Again, results less than three times the detection limit were not included due to the high level of inherent error with small changes in low concentrations. The mean RPD for all pore fluid samples is 4.2% and the median is 0.0%. Out of 436 samples there are 12 with a precision beyond the acceptable ±5% while 97.2% of analyses are within the acceptable precision range. Figure 14-6 compares the original and duplicate pore fluid samples.

### 14.4.2.2 *Method Blank and Laboratory Control Spike*

The quality control term Method/Laboratory Blank refers to an analyte free matrix to which all reagents are added in the same volumes or proportions as used in standard sample preparation. The purpose of this QC parameter is to monitor potential laboratory contamination. The quality control term Laboratory Control Sample (LCS) refers to a certified reference material, or a known interference free matrix spiked with target analytes. The purpose of this QC parameter is to monitor method precision and accuracy independent of sample matrix. Dynamic Recovery Limits are based on statistical evaluation of processed LCS.

### 14.4.2.3 *Method Blank and Laboratory Control Spike result*

The method blank reports show that all elements are below detection limit while the LCS method yielded spike recovery percentages between 70-116%. This means that at 70% recovery, the test result is 30% less than actual spike concentration whereas 116% recovery indicates that result is 16% higher than actual. 12 out of 150 analyses failed the QA/QC standards of 30% and were beyond the acceptable recovery limits; 92% of all Laboratory control spike analyses yielded satisfactory results.

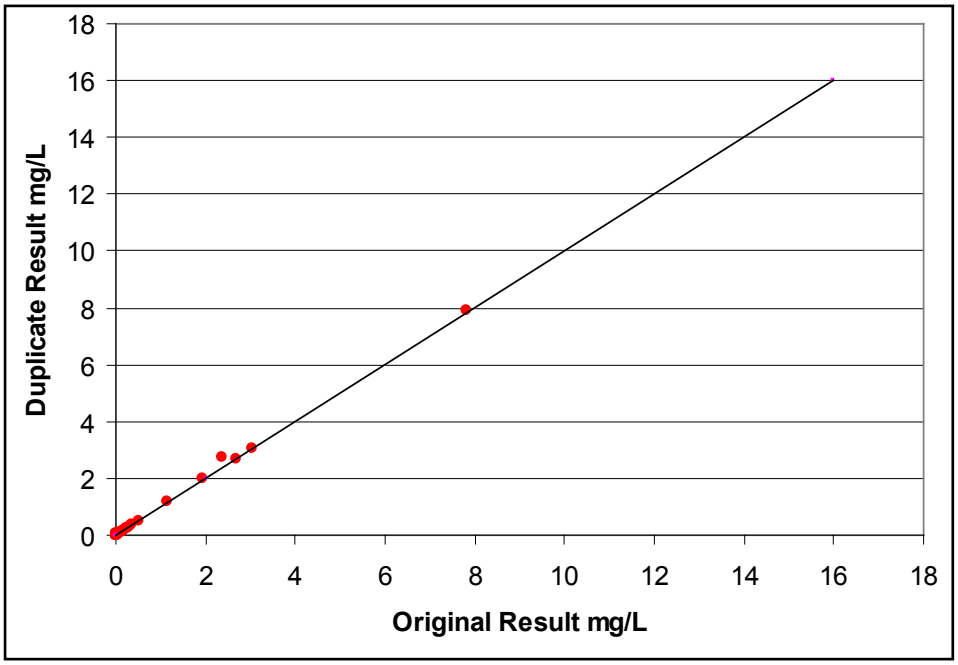



**Figure 14-6.** *Graph showing the original and duplicate results for dissolved metals in pore fluid samples. The black line represents the line y=x to illustrate the closeness of fit between original and duplicate lab results.*

#### 14.4.2.4 ***Matrix Spike***

The quality control term Matrix Spike (MS) refers to an intra-laboratory split sample spiked with a representative set of target analytes. The purpose of this QC parameter is to monitor potential matrix effects on analyte recoveries. Static Recovery Limits as per laboratory Data Quality Objectives (DQOs). Ideal recovery ranges stated may be waived in the event of sample matrix interference

*Matrix spike result*

The Matrix spike reports show that the spike recovery percentage for dissolved metals in all samples ranges between 84.7% and 109%. In this case 84.7% means that the recovery is 15.3% lower than the actual spike concentration whereas 109% means that the recovery is 9% higher than actual. The accepted recovery limit is 30%, i.e. 70-130%; no matrix spike results failed the QA/QC standards.

## 14.5 HYDROCHEMICAL DATA PROCESSING AND ANALYSIS

Upon receipt from the laboratories, the analytical data was compiled into Excel spreadsheets for processing, charting and analysis. Figure 14-7 provides an overview of the data quality of the groundwater, surface water and rainfall analytical results in terms of the charge balance associated with the major ions. This shows that most of the samples fit within the criteria of having the error in the charge balance within 5%. The charge balance error for the remainder mainly relate to analyses being incomplete. A similar plot for the pore fluid major ion analyses shows a greater range in the charge balance error, although again the bulk of the samples fit within the 5% threshold (Figure 14-8). Errors in the pore fluid samples relate to incomplete analyses and small sample volumes.

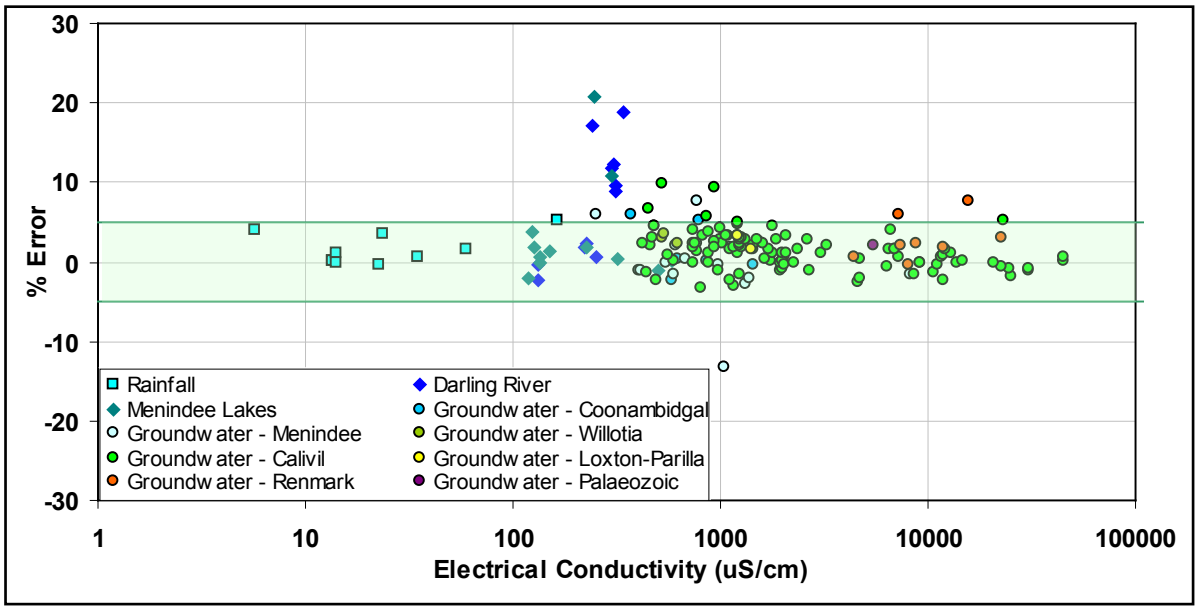



**Figure 14-7.** *Charge balance for BHMAR major ion analyses of surface water, rainfall and groundwater samples.*

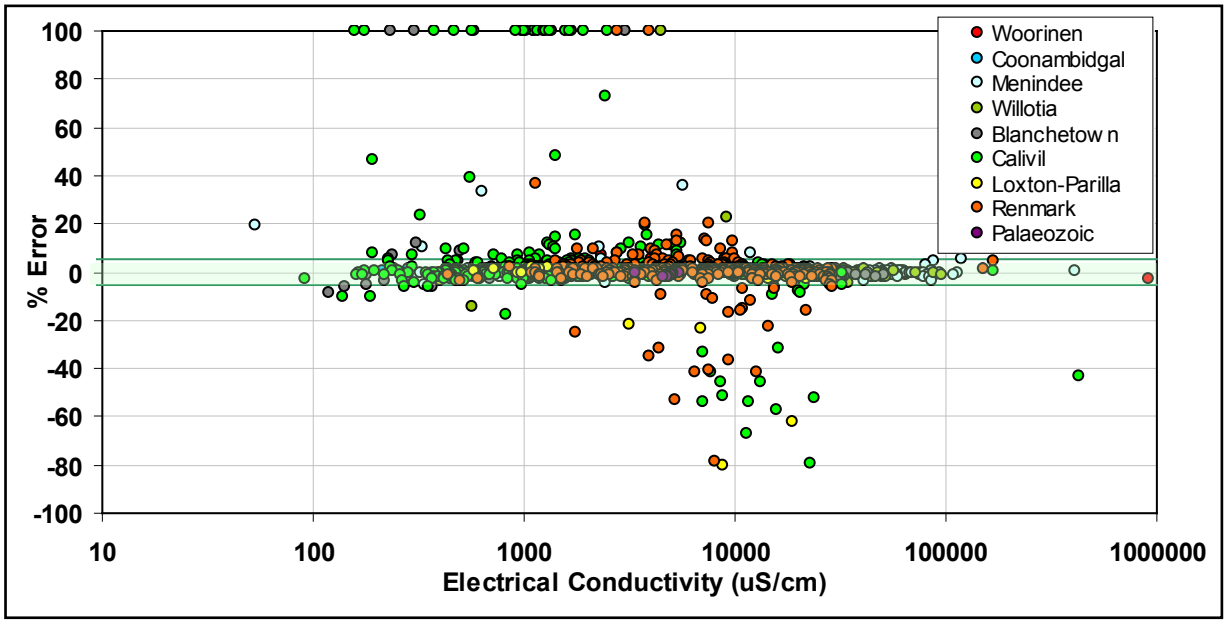



***Figure 14-8.*** *Charge balance for BHMAR major ion analyses of pore fluid samples.*

The hydrochemical data collected by the project was combined with the available historical water quality data record. This was principally monitoring of major ions and nutrients for key sites on the Darling River and the Menindee Lakes Storages undertaken by NSW State Water and NSW Office of Water. Interpretation of the hydrochemical data was restricted to the data within the 5% error margin for charge balance between major cations and anions.

Excel was used to generate:

- A comprehensive range of scatter plots comparing analytes (including combinations and ratios) in raw concentration format (such as mg/L), or as milliequivalents or millimoles. This provided useful insights into processes such as surface water- groundwater interaction, mineral reactions and redox processes.
- A matrix table to present for each monitoring bore the number of incidences that groundwater samples exceeded the Australian Drinking Water Guidelines 2011 (ADWG, 2011). This covered health, aesthetic or operational thresholds relating to 31 water quality criteria. Similar exceedance matrix tables were generated for the pore fluid and surface water sample results.
- Correlation matrices to assess relationships between analytes. Relationships with a relatively positive ($R^2 > 0.5$) or negative correlation ($R^2 < -0.5$) were targeted for generation of scatter plots between analytes. A correlation matrix was generated using the combined surface water, rainfall and groundwater samples as one population, and a separate correlation matrix was generated using the pore fluid data.
- Box and whisker style plots summarising the data distribution for various groupings of hydrochemical analyses.
- Downhole plots of the pore fluid data, including co-plotting of other downhole datasets such as gamma and induction logging.
- Classification of the redox condition of each groundwater sample using the measured dissolved oxygen, nitrate, manganese, iron, sulfate and sulfide concentrations. This was based on the classification schema and Excel worksheet developed by Jurgens *et al*. (2009).

The data was also imported into an Aquachem 2010.1 database for additional data processing and analysis. By using Aquachem, a range of more specialised plots such as Durov, Piper, Wilcox or Schoeller plots could be generated. Aquachem also provides an interface to PHREEQC (Parkhurst & Appelo, 1999), a USGS computer program for performing various low-temperature aqueous geochemical calculations. This was used to undertake speciation and saturation-index calculations. Aquachem was also used to calculate bicarbonate and carbonate concentrations from the total alkalinity and pH measurements as well as other parameters like water type, hardness, ionic strength, ryznar stability index, langelier saturation index, sodium adsorption ratio and magnesium hazard.

### 14.5.1 Fuzzy-k Means Cluster Analysis

A particular aspect of the hydrochemical data analysis was the application of fuzzy-k means cluster analysis. As stated by Güler & Thyne (2004), fuzzy logic analysis is a "multivalued logic that allows intermediate values to be defined between conventional evaluations like yes/no, true/false, black/white, 0/1, etc." Unlike statistical techniques such as probability, fuzziness analyses deals with degrees and is nonstatistical. The result is the clustering of the samples into a defined number of groups (or classes), with each sample assigned an index (0-1) in terms of how well it belongs to each of these classes. It is these indices that describe the fuzziness of how well samples are assigned to classes.

The hydrochemistry data was analysed in this way with limited manipulation in order to not introduce any bias into the process. Analytes and samples were included for fuzzy-k means analysis if at least 70% of the

samples had data i.e. the analysis was carried out and there was a measured value. Samples or analytes with a large proportion of null values were not included as the fuzzy-k analysis would simply define a null data cluster of samples of no hydrogeological significance.

The combined pore fluid, groundwater, surface water and rainfall samples with sufficient data for cluster analysis consisted of a population of 1669 samples across 25 analytes (B, Ba, Br, Ca, Cl, $CO_3$, EC, Eh, F, $HCO_3$, K, Total Alkalinity, Mg, Mn, Na, $NO_3$, lab pH, $SiO_2$, $SO_4$, Sr, Field Alkalinity, Ionic Strength, Sum Anions, Sum Cations and Sum All Ions). While fuzzy-k analysis can be done on any data, the range of values in the samples across all of the analytes is nearly 6 orders of magnitude which could result in smaller values being swamped. In order to decrease the apparent spread of values, the log of each value was calculated and used in the fuzzy analysis.

The fuzzy-k analysis was done using the program FuzME [4] developed by the Australian Centre for Precision Agriculture at Sydney University. In order to determine the optimal number of classes to group the data, multiple runs were carried out under the settings shown in Figure 14-9.

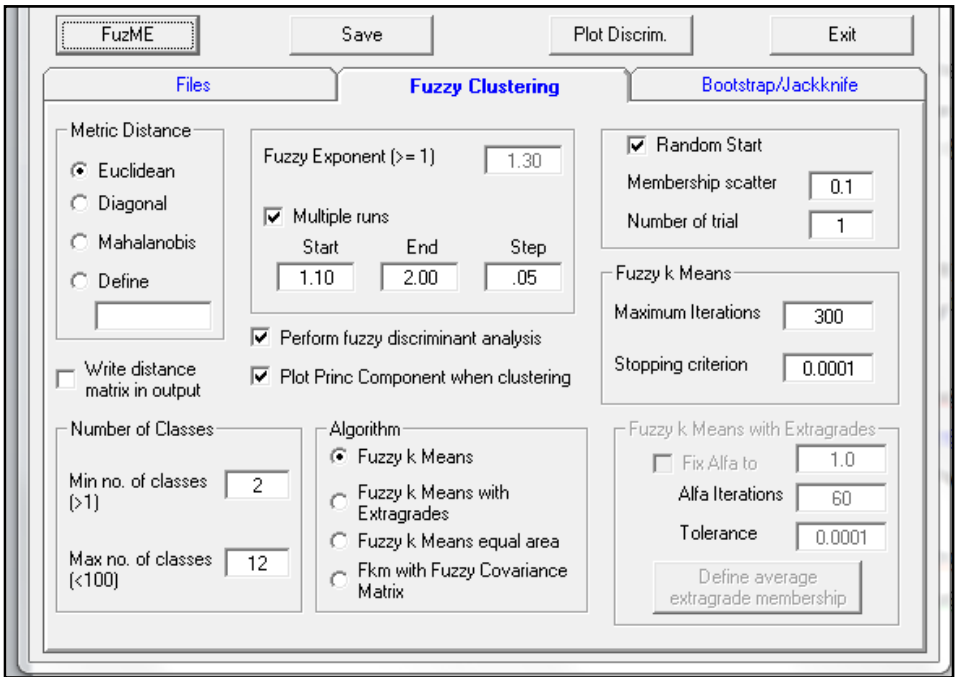



***Figure 14-9.*** *Interface of the FuzME software used for fuzzy k-means cluster analysis.*

The goal of the multiple runs was to choose a clustering scenario that was neither too definitive (non-fuzzy) nor too vague (fuzzy). As part of its analysis, FuzME produces the cluster validation functions FPI and MPE, where a FPI value of 1 is fuzzy and a zero FPI is non-fuzzy. In this study, a FPI of about 0.25 was chosen as ideal.

A workable range of clustering (2-12 classes) for a fuzzy exponent of 1.35 was found to contain the desired FPI range of 0.25 (Figure 14-10). The ideal number of classes for plotting and further analysis was then chosen by selecting the number of classes with the relatively ideal FPI (closest to 0.25) which would be useful for hydrochemical analysis, such as investigating the relationships between the groundwater samples with the river and lake samples.

[4] http://www.usyd.edu.au/agriculture/acpa/software/fuzme.shtml

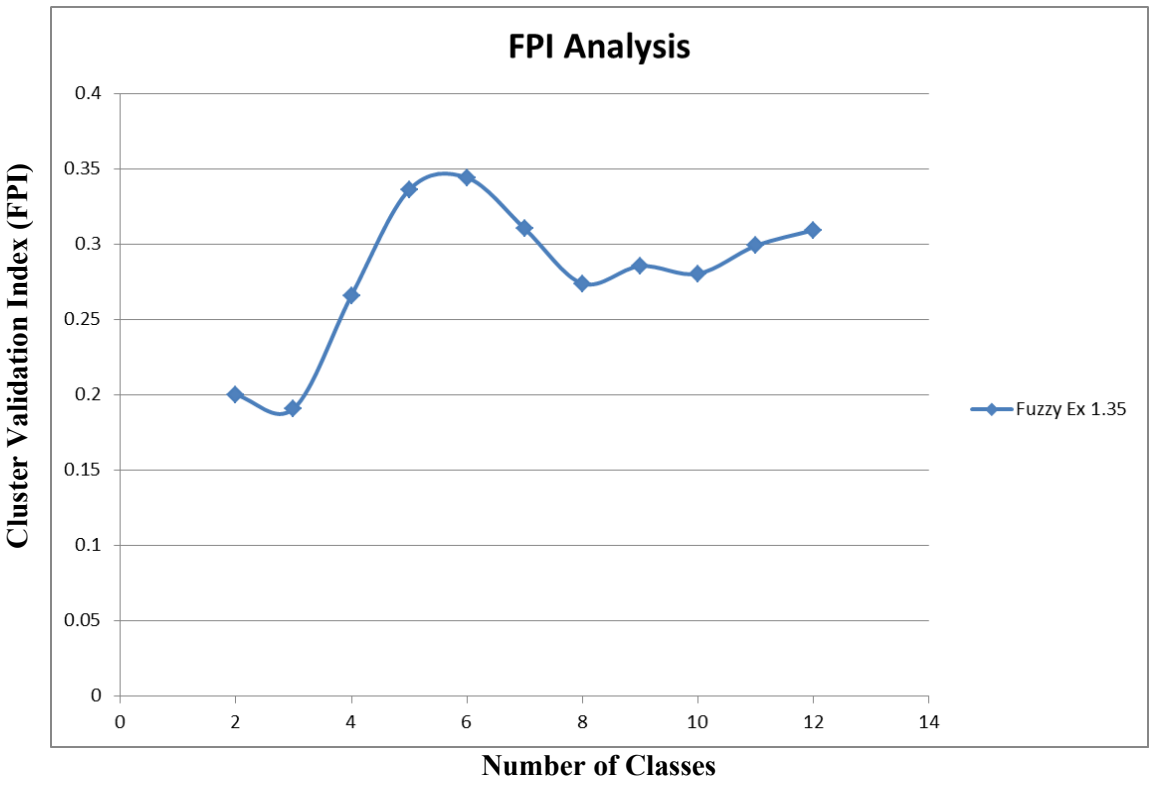



**Figure 14-10.** *Plot of the cluster validation index FPI with the number of resulting data clusters (or classes), using a fuzzy exponent of 1.35.*

Clustering the data into four classes would meet the criteria of a FPI of about 0.25 (Figure 14-10) but this option is not ideal as it does not subdivide the data sufficiently to provide any hydrogeological insight. Eight or ten classes represent category minimums with FPI towards 0.25 (Figure 14-10) and on this basis, the fuzzy analysis was undertaken to group the sample data into eight classes.

## 14.6 GEOCHEMICAL MODELLING (CSIRO)

A geochemical evaluation was undertaken to identify detrimental effects, such as clogging by mineral precipitation and other reactions, on the quality of recovered water from potential MAR activities in the project area (Vanderzalm *et al*., 2012). The source water used in MAR is typically of different composition than the ambient groundwater and is unlikely to be in equilibrium with the aquifer minerals. For example, fresh and oxygenated stormwater and treated wastewater have been successfully stored in brackish, anoxic, limestone aquifers for recovery as irrigation supply (Herczeg *et al*., 2004; Vanderzalm *et al*., 2006). Geochemical reactions may occur between the source water and the ambient groundwater or the mineral phases within the target storage zone. These reactions include redox, cation exchange and mineral equilibrium processes and provide water treatment (Dillon *et al*., 2008b) but can also lead to deleterious changes in water quality between injection and recovery (e.g. arsenic or iron) or loss of aquifer permeability (e.g. chemical precipitation, clay swelling). It is necessary to understand the potential for geochemical reactions to determine the necessary measures to manage their impact on the success of the proposed MAR scheme.

The PHREEQC code (Parkhurst & Appelo, 1999) was used to examine:

- aqueous speciation and mineral saturation indices of groundwater and surface water with the SOLUTION keyword;

- reactions and product water quality expected as a result of mixing between the source water from the Darling River and the mineral phases present in the Calivil Formation aquifer at bore BHMAR33-2 using the EQUILIBRIUM PHASES and EXCHANGE subroutines;
- mixing between the Darling River source water and the ambient groundwater in the Calivil Formation aquifer at bore BHMAR33-2 using the MIX subroutine;
- mixing between the groundwater from the storage zone with that in the overlying Menindee Formation aquifer at BHMAR33-2 using the MIX subroutine;
- aeration of the overlying Menindee Formation aquifer at BHMAR33-2 using the EQUILIBRIUM PHASES subroutine;
- reactions and product water quality expected as a result of mixing between source water from a near-river Calivil Formation bore (BHMAR80A-5) and the mineral phases present in the Calivil Formation aquifer at a proposed injection test bore (BHMAR33-2) using the EQUILIBRIUM PHASES subroutine;
- mixing between the near-river Calivil Formation bore (BHMAR80A-5) source water and the ambient groundwater in the Calivil Formation aquifer at a proposed injection test bore (BHMAR33-2) using the MIX subroutine.

The microbiological influence on hydrochemical processes, such as redox reactions, was not able to be incorporated in this analysis. If any reactions could render recovered water unsuitable for drinking, recommendations were made regarding possible treatment to either (a) prevent excessive formation of the element or mineral, and (b) remove the undesirable element from the recovered water supply, and (c) recommend which approach is preferred, or what further measurements would be required to define the most robust, sustainable and efficient treatment process.

### 14.6.1 Sediment Chemistry

The sediment chemistry from borehole core BHMAR33-4 was utilised, consisting of major elemental analysis by X-ray Fluorescence and trace metal and metalloid analysis by acid digestion and quantification by ICP-MS (Section 11.5.3). The analysis of sediment geochemistry was focused on discrete intervals as follows:

- Menindee Formation 14-23 m, the screened interval of BHMAR33-3 observation bore;
- Calivil Formation target aquifer 48-58 m, the target interval for MAR and screened interval of BHMAR33-2 observation bore;
- Lower Renmark Group 182-206 m, the screened interval of BHMAR33-1 observation bore.

A target interval 'composite' sample was prepared from eighteen sub-samples taken at 0.5 m intervals between 48.5-56 m for use in the laboratory column study at CSIRO Waite Laboratories. This composite was amalgamated, dried at 45ºC and sieved to remove sediments greater than 2 mm (Page *et al*., 2010).

Three samples of Coonambidgal Formation were available to evaluate the potential for MAR by infiltration and reactions between the source water and the sediment at the base of the infiltration pit. The first sample of sediment from the Coonambidgal Formation was collected from a hand dug pit to ~0.2 m on 29/7/10 and returned to the CSIRO Waite Laboratories for use in the laboratory column study and geochemical analysis. Subsequently, in August 2010, two samples deemed to be more representative of the material at the base of an infiltration pit were provided from bank filtration bore BHMAR80A-2 at depths of 17.24 and 17.84 m respectively. For the purpose of this report, these three samples will be referred to as Coonambidgal A, B and C respectively. While the infiltration methodology was not pursued in the field investigations the results of analyses on these Coonambidgal Formation sediments will be reported for information purposes.

Four sediment samples; the composite Calivil Formation material, the fine fraction (<50 μm) of the composite Calivil Formation material, Coonambidgal A and Coonambidgal B/C (combined), were analysed

for trace metal, metalloid and nutrient concentrations, cation exchange capacity, exchangeable cations, carbonate and clay mineralogy at the CSIRO Waite Laboratories. Sediment analysis methods, including acid digestion and quantification by ICP spectroscopy, mid infrared spectroscopy (MIR), X-ray Diffraction (XRD) are described in detail in Page *et al*. (2010).

The sediment geochemistry was later revised with 160 additional core samples from the Calivil Formation aquifer at the Jimargil and East Bootingee sites (Appendix 6, Somerville *et al*., 2012). The use of core material from a number of bores within these two site areas improved the understanding of spatial variability in the geochemistry of the Calivil Formation aquifer rather than being specific to a particular site, or ASR bore, as with the initial assessment.

### 14.6.2 Groundwater Chemistry

The water quality data used in the geochemical modelling were 37 groundwater samples from Calivil Formation screened aquifer intervals in the Jimargil borefield target area, as well as representative Coonambidgal and Menindee Formation groundwaters in the same area (Vanderzalm *et al*., 2012). The use of ambient groundwater quality data from several bores within the target area improved the understanding of spatial variability in the geochemistry of the Calivil Formation aquifer rather than being specific to a particular site, or ASR bore, as with the initial assessment.

The ambient groundwater samples used were sampled from between 19 and 59 m below ground surface, with a median depth of 51 m. Pumped groundwater was sampled after physico-chemical water quality parameters had stabilised. Water samples analysed by Geoscience Australia for soluble metal and metalloid concentrations were filtered in the field. However samples transported to ALS for analysis of total and soluble metals and metalloids were not filtered in the field, following advice from the laboratory. Therefore some loss of soluble to insoluble species may have occurred prior to analysis at ALS. Iron data is presented in a number of ways; as Fe-soluble based on field filtered samples and also as Fe(2) and Fe-total, both analysed in the field.

The following relationship was used to convert Eh (V SHE) to pe values:

pe =Eh/0.059 at 25ºC (Appelo & Postma, 1999).

The cation-anion charge balance was within 5% for all samples used, aside from the BH80A-2 Calivil Formation groundwater sample at 7%.

### 14.6.3 Source Water Chemistry

The following source waters for MAR were used:

- Darling River- 6 samples from Weir 32 sampled by Geoscience Australia (Appendix 6, Somerville *et al*., 2012). Soluble concentrations were used, where available, to represent the Darling River source water following treatment to remove particulates.
- Bank filtrate from the Coonambidgal and Calivil Formations – 3 samples; BHMAR84-5 (31/8/2010) and the Wanda house bore (6/7/2010) from the Coonambidgal Formation and BHMAR80A-2 (1/9/2010) from the Calivil Formation.

### 14.6.4 Geochemical Modelling

It is important to initially understand the chemical compositions of the individual end-member water samples, and then examine the potential for geochemical reactions to occur and impact on water quality or aquifer permeability. A summary of each of the simulations and the model subroutine implemented in PHREEQC (Parkhurst & Appelo 1999) v 2.17.0 is shown in Table 14-4. Where a number of sample dates were available for one location, one date was selected, based on the quality of input data, to represent the location for use in the reaction scenarios as indicated in Table 14-4.

**Table 14-4.** *Model simulations and the subroutines implemented in PHREEQC.*

| Simulation | Details | PHREEQC subroutine |
|---|---|---|
| 1 | Calculate speciation and saturation indices | SOLUTION |
| 2 | Calculate exchanger composition in equilibrum with solution | EXCHANGE |
| 3 | Equilibrate Darling River source water sampled at Weir 32 with mineral phases in Calivil Formation aquifer in bore BHMAR33-2 | EQUILIBRIUM_PHASES |
| 4 | Equilibrate Darling River source water sampled at Weir 32 with exchanger composition in Calivil Formation aquifer in bore BHMAR33-2 | EXCHANGE |
| 5 | Equilibrate Calivil Formation bank filtrate (BHMAR80A-2) with mineral phases in Calivil Formation aquifer in bore BHMAR33-2 | EQUILIBRIUM_PHASES |
| 6 | Equilibrate Calivil Formation bank filtrate (BHMAR80A-2) source water with exchanger composition in Calivil Formation aquifer in bore BHMAR33-2 | EXCHANGE |
| 7 | Mix Darling River source water (Weir 32, 15/2/2010) and ambient groundwater in the Calivil Formation aquifer at bore BHMAR33-2 | MIX |
| 8 | Mix Calivil Formation bank filtrate source water (BHMAR80A-2) and ambient groundwater in the Calivil Formation aquifer at bore BHMAR33-2 | MIX |
| 9 | Mix groundwater from the ASR storage zone (BHMAR33-2) with overlying groundwater in the Menindee Formation (BHMAR33-3) | MIX |
| 10 | Aerate groundwater in the overlying Menindee Formation (BHMAR33-3) | EQUILIBRIUM_PHASES |

Chloride was set to achieve charge balance in all simulations.

Simulations representing a reaction in the aquifer were undertaken at a pe fixed to an appropriate value for that aquifer as follows: Calivil Formation pe fixed at 2; Menindee Formation pe fixed at 2. Uncertainty in this estimate, due to the small number of measurements available, will influence the outcome of the simulations. If pe is not fixed, redox equilibrium is reached and this results in values that are unrealistic for the aquifer.

Revised simulations (numbers 1, 2, 3, 4, 7) used a pe fixed at 3 for the Calivil Formation aquifer, based on the median of the extended monitoring data set (Vanderzalm *et al*., 2012; Appendix C). In addition to BHMAR33-2, BHMAR80A-5 was assessed as the Calivil Formation aquifer end-member in simulations 1, 2 and 7. BHMAR80A-5 is a preferred target for MAR within the GWR1 target area based on recent hydrogeological assessment.

It is acknowledged that measurements of Eh, used to calculate pe, are prone to error due to lack of equilibrium between redox couples within the sample and also due to technical issues with reliability of electrodes as discussed in Appelo & Postma (1999). Using available redox couples; O(-2)/O(0), Fe(2)/Fe(3), S(-2)/S(6) or the presence or absence of indicative redox species indicates multiple or mixed redox

conditions within the Calivil Formation storage zone. Of these redox pairs, the redox state indicated by the Fe(2)/Fe(3) redox couple is closest to that estimated from the measured Eh. As the fate of iron is important in this investigation it was deemed reasonable to adopt redox conditions estimated from measured Eh values within simulations. Saturation indices of mineral phases in storage zone were used to examine source water propensity for reaction. Saturation indices 0±2 considered as those influencing the water sample. A positive saturation index indicates a solution is super-saturated with respect to the mineral phase and will tend toward equilibrium through precipitation of that mineral. Conversely a negative saturation index indicates the solution is sub-saturated and may lead to dissolution of the mineral phase.

### 14.6.5 Statistical Analysis

Microsoft Office Excel 2003 and Sigmaplot for Windows v11.0 (Systat Software 2008) were used for statistical analysis of the data. Spearman Rank Order Correlation was used to examine the relationship between major and minor elements within the BHMAR33 core samples.

The geochemistry of the aquifer sediment, ambient groundwater and potential MAR source water is described in Vanderzalm *et al*. (2012). A summary of potential mixing and reactions and possible impacts on water quality and clogging processes is also provided.

# 15 Hydrographic Monitoring and Analysis

## 15.1 GROUNDWATER LEVEL AND TEMPERATURE MONITORING

A groundwater level and temperature monitoring network has been established in the project area with the objectives of:

- Helping determine the dominant groundwater recharge processes, either by rainfall infiltration, direct and continuous river leakage, overbank floodplain inundation or altered in-river conditions during high flows;
- Attributing changes in groundwater head to recharge processes rather than hydraulic loading;
- Comparing groundwater levels prior to and after the onset of flooding of the Darling River and associated refilling of the Menindee Lakes Storages in 2010;
- Defining the nature and extent of surface water-aquifer connectivity and to estimate the rate of recharge to the aquifers;
- Providing insights into the magnitude of flows in the Darling River that are required to replenish aquifer storage;
- Quantifying any changes in water chemistry and salinity with a unit change in groundwater water level in response to flooding; and
- Maintaining loggers at nested piezometer sites so that groundwater levels and trends in the various aquifers (notably the Coonambidgal, Menindee and Calivil Formations) can be compared. This is important in understanding vertical hydraulic gradients and the potential for inter-aquifer leakage.

Standing water level and temperature data are summarised in Appendix 6 (Somerville *et al.*, 2012).

### 15.1.1 Data Collection

CeraDiver pressure transducer loggers were installed in a selection of project bores, to monitor groundwater levels through time. At certain sites, installation of Diver CTD loggers has enabled combined monitoring of groundwater level, electrical conductivity and temperature. The focus of monitoring is along the floodplain corridors of the Darling River and Talyawalka Creek, as well as other areas such as identified areas of subsurface leakage from Lake Menindee. Hobo TidbiT temperature loggers were also temporarily installed (from 18$^{th}$-27$^{th}$ August 2012) in selected bores within the GWR1 target to check against existing temperature data obtained from the Diver CTD loggers. Water temperate was measured every 30 minutes to an accuracy of 0.2°C. Barometric loggers have also been installed at selected sites to enable atmospheric correction of the pressure transducer data. The current status of the monitoring network is summarised in Table 15-1 and the locations of the monitoring sites are plotted in Figure 15-1.

**Table 15-1.** *Status of groundwater level monitoring in the BHMAR project area. Red text denotes bores where Hobo temperature loggers were temporarily installed.*

| Hole Name | Easting | Northing | Screened Aquifer | Screened Interval (m) | Logger ID | Logger Type | Date From | Date To |
|---|---|---|---|---|---|---|---|---|
| BHMAR04-1 | 649392 | 6423554 | Upper Renmark | 90-102 | G0539 | DI702-20m | 23/01/10 | Current |
| BHMAR04-2 | 649393 | 6423552 | Calivil | 34-52 | G0537 | DI702-20m | 23/01/10 | Current |
| BHMAR04-3 | 649391 | 6423558 | Menindee | 8-14 | J1347 | DI701-10m | 23/01/10 | Current |
| BHMAR05-1 | 662290 | 6436398 | Upper Renmark | 94.5-100.5 | G0529 | DI702-20m | 23/01/10 | 16/07/11 |
| BHMAR05-2 | 662287 | 6436397 | Calivil | 28-40 | G1966 | DI702-20m | 23/01/10 | 14/08/11 |
| BHMAR06-1 | 667109 | 6438656 | Calivil | 30-60 | G1983 | DI702-20m | 23/10/10 | 5/08/10 |
| BHMAR06-1 | 667109 | 6438656 | Calivil | 30-60 | D8845 | BARO DI500 | 23/01/10 | Current |
| BHMAR14-1 | 671927 | 6443886 | Calivil | 41-59 | G1955 | DI702-20m | 27/01/10 | 16/08/11 |
| BHMAR16-1 | 686211 | 6422954 | Calivil | 12-52 | D1261 | CTD - 10m | 19/03/10 | Current |
| BHMAR17-1 | 637881 | 6416245 | Calivil | 54-72 | H1838 | DI702-10m | 23/01/10 | 26/08/11 |
| BHMAR17-1 | 637881 | 6416245 | Calivil | 54-72 | F4442 | BARO DI500 | 23/01/10 | 26/08/11 |
| BHMAR17-2 | 637879 | 6416243 | Calivil | 22.5-34.5 | G4545 | DI702-20m | 23/01/10 | 27/06/11 |
| BHMAR18-2 | 628659 | 6426047 | Calivil | 25-52 | G1947 | DI702-20m | 14/02/10 | Current |
| BHMAR21-1 | 628458 | 6379095 | Calivil/Upper Renmark | 20-74 | 87829 | CTD-10m | 26/01/10 | Current |
| BHMAR21-2 | 628457 | 6379092 | Menindee | 10.5-13.5 | G1944 | DI702-20m | 26/01/10 | Current |
| BHMAR23-1 | 620437 | 6428004 | Palaeozoic | 81-105 | G4450 | DI702-10m | 25/09/11 | Current |
| BHMAR23-2 | 620439 | 6428002 | Calivil | 29-47 | G1980 | DI702-20m | 15/02/10 | Current |
| BHMAR23-3 | 620441 | 6428000 | Menindee | 13-24 | H1838 | DI702-10m | 17/02/12 | Current |
| BHMAR29-1 | 629101 | 6344552 | Calivil | 17-53 | G1957 | DI702-20m | 5/05/10 | Current |
| BHMAR31-1 | 623613 | 6335284 | Loxton-Parilla | 11-51 | G1946 | DI702-20m | 6/05/10 | Current |
| BHMAR31-1 | 623613 | 6335284 | Loxton-Parilla | 11-51 | F4442 | BARO DI500 | 4/09/11 | Current |
| BHMAR33-1 | 630325 | 6405732 | Lower Renmark | 182-206 | G0529 | DI701-20m | 24/10/10 | Current |
| BHMAR33-1 | 630325 | 6405732 | Lower Renmark | 182-206 | F4423 | BARO DI500 | 27/08/11 | Current |
| BHMAR33-2 | 630329 | 6405730 | Calivil | 48-59 | G4518 | DI702-20m | 2/04/10 | Current |
| BHMAR33-3 | 630322 | 6405735 | Menindee | 14-23 | J1325 | DI701-10m | 2/10/10 | Current |
| BHMAR33-8 | 630364 | 6405954 | Calivil | 46-52 | J1347 | DI701-10m | 2/10/10 | 29/06/11 |
| BHMAR34-1 | 655910 | 6427345 | Calivil | 27-51 | G1972 | DI702-20m | 27/01/10 | Current |
| BHMAR34-2 | 655912 | 6427348 | Menindee | 8-20 | 87748 | CTD-10m | 27/01/10 | Current |
| BHMAR35-1 | 709828 | 6448866 | Calivil | 16-46 | G1955 | DI702-20m | 1/05/10 | Current |
| BHMAR48-1 | 640033 | 6397431 | Calivil | 35.5-58.5 | J1288 | DI701-10m | 17/08/10 | Current |
| BHMAR57-1 | 648160 | 6405440 | Calivil/Upper Renmark | 34.5-82.5 | G4472 | DI701-10m | 17/08/10 | 1/08/11 |
| BHMAR61-1 | 633543 | 6398759 | Upper Renmark | 86-116 | J1345 | DI701-10m | 4/05/10 | Current |
| BHMAR61-2 | 633544 | 6398760 | Calivil | 36-66 | J1341 | DI701-10m | 23/01/10 | Current |
| BHMAR61-3 | 633541 | 6398758 | Menindee | 12.5-22.5 | J1292 | DI701-10m | 24/10/10 | Current |
| BHMAR75-2 | 630807 | 6411478 | Calivil | 18-23 | J0818 | DI701-10m | 1/08/11 | Current |
| BHMAR75-3 | 630807 | 6411480 | Renmark | 82-88 | H1818 | DI701-10m | 16/02/12 | Current |
| BHMAR75-5 | 630801 | 6411481 | Calivil | 40-52 | J1276 | DI701-10m | 24/10/10 | Current |
| BHMAR77-2 | 630471 | 6406417 | Calivil | 47-55 | G7562 | DI701-10m | 15/02/12 | Current |
| BHMAR77-3 | 630476 | 6406430 | Menindee | 11-16 | C7430 | DI701-10m | 28/08/10 | Current |
| BHMAR77-5 | 630503 | 6406480 | Calivil | 46-56 | J1276 | DI701-10m | 24/10/10 | 28/08/11 |
| BHMAR79A-2 | 629268 | 6411571 | Renmark | 65-77 | J1295 | DI701-10m | 21/10/10 | Current |
| BHMAR79A-5 | 629269 | 6411540 | Calivil | 18-24 | J1338 | DI701-10m | 21/10/10 | Current |
| BHMAR79A-6 | 629144 | 6411598 | Calivil | 38-50 | G1975 | DI701-10m | 24/10/10 | 4/06/11 |
| BHMAR80A-2 | 628363 | 6405816 | Calivil | 35-53 | G4518 | DI702-20m | 24/10/10 | 27/08/11 |

| | | | | | | | | |
|---|---|---|---|---|---|---|---|---|
| BHMAR80A-3 | 628261 | 6405810 | Coonambidgal | 11-17 | J1259 | DI701-10m | 1/10/10 | 2/07/11 |
| BHMAR80A-6 | 628370 | 6405822 | Renmark | 84-102 | H1818 | DI701-10m | 24/10/10 | 27/08/11 |
| BHMAR80A-7 | 628264 | 6405812 | Calivil | 42-54 | C3302 | DI702-20m | 3/10/10 | 2/07/11 |
| BHMAR80B-2 | 628278 | 6406088 | Calivil | 53-65 | G7562 | DI701-10m | 24/10/10 | 27/08/11 |
| BHMAR80B-3 | 628193 | 6406025 | Coonambidgal | 11-16 | J0818 | DI701-10m | 24/10/10 | 28/08/11 |
| BHMAR84-2 | 629879 | 6406865 | Calivil | 45-51 | J1273 | DI701-10m | 24/10/10 | Current |
| BHMAR84-3 | 629969 | 6406898 | Menindee | 10-23 | J1297 | DI701-10m | 24/10/10 | 27/08/11 |
| BHMAR84-4 | 629766 | 6406814 | Menindee | 12-23 | H1848 | DI701-10m | 24/10/10 | Current |
| BHMAR88-3 | 630119 | 6411570 | Upper Renmark | 65-71 | D1261 | CTD - 10m | 24/10/10 | Current |
| BHMAR88-5 | 630138 | 6411567 | Calivil | 35-41 | G7430 | DI701-10m | 24/10/10 | 28/08/11 |
| BHMAR92-1 | 628823 | 6406401 | Calivil | 32-62 | G7511 | DI701-10m | 5/10/10 | Current |
| BHMAR92-2 | 628827 | 6406406 | Menindee | 12-16 | G1966 | DI702-20m | 21/10/10 | Current |
| BHMAR99-1 | 629188 | 6405687 | Calivil | 33-57 | G4499 | DI701-10m | 21/10/10 | Current |

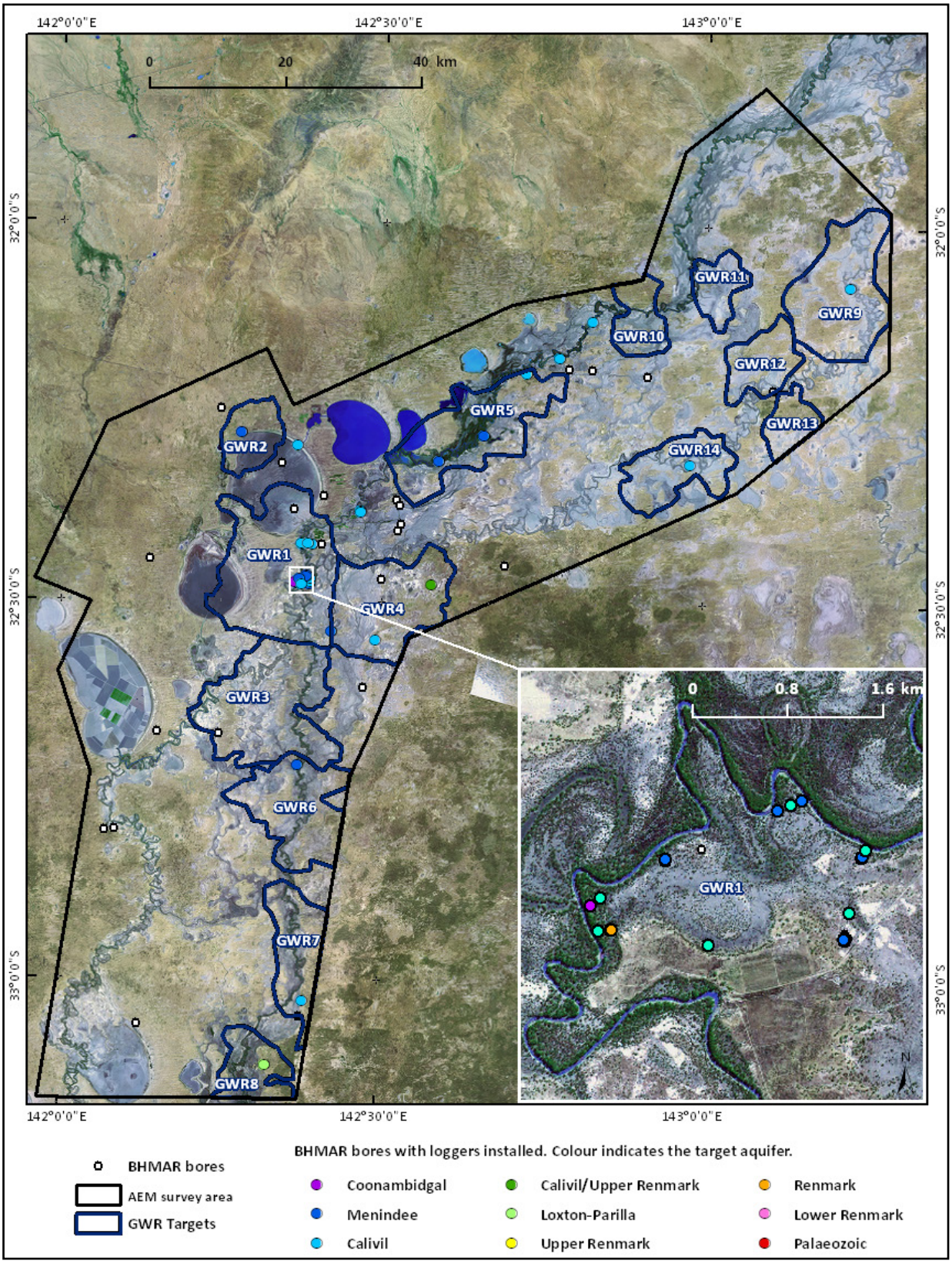



**Figure 15-1.** *Location of groundwater level monitoring network in the BHMAR project area.*

Installation of the loggers is relatively simple, involving attaching the logger to a wire cable which is in turn secured to the bore cap. The length of the cable was measured to determine the position of the logger down the hole. The loggers were initially set to take a reading every 15 minutes, but this was later changed to hourly readings. Data from the loggers were downloaded nominally every 3 months, but the flooding in late 2010 meant access to many of the sites was restricted over a 6 month period. Data downloads involved connecting the logger to a USB reading unit and using the Diver-Office software to manage communication. The data was saved both within the Diver project database as well as exported and archived as CSV files.

During each site visit, the groundwater level was measured relative to the top of the casing protector (or similar reference) using an electronic dipper. The height to the top of the casing protector (and any other measurement reference points) relative to the natural ground surface was measured. Using the survey data of the borehole infrastructure (Section 10.4), the elevation (m AHD) of the reference points and the related groundwater level measurements could be derived. This was used to convert the logger readings of the pressure of the water column above the logger, to the more meaningful elevation (m AHD) of the groundwater level. The measurements and observations for the site visit were recorded on a project Borehole Measurements form.

### 15.1.2 Data Processing and Interpretation

As well as data storage in the Diver-Office project database, an Excel spreadsheet was created for each of the monitoring bores. The processing of the Diver logger data included the following:

- Details of each site visit such as manual groundwater level measurements and other observations were recorded in the spreadsheet. The elevation (m AHD) of these groundwater levels were calculated using the survey data.
- Obviously spurious data in the logger output, such as atmospheric pressure readings recorded when the logger was removed from the bore for downloading of data, were removed from the logging record.
- Water level, EC and temperature logger data was typically resampled to a consistent hourly interval using an Excel function. This enabled direct comparison of data between bores and also facilitated data processing.
- The raw pressure data from the logger was translated to a time series of the elevation (m AHD) of the groundwater level, using the manual level measurements as control. This conversion had to take into account factors such as modifications to the cable length which changed the downhole position of the logger as well as changes to the reference point used for the manual level measurements (such as part removal of bore casing or installation of a casing protector).
- Adjustments for barometric pressure were undertaken using the BETCO (Barometric and Earth Tide Response Correction) software package (BETCO, 2005). BETCO removes fluctuations in the groundwater levels due to barometric pressure and Earth tides. The software adjusts water level measurements according to the barometric measurements collected at equal intervals and time, by applying a multiple regression technique. The input data is either a CSV file or Excel spreadsheet consisting of observed water levels and barometric pressures in consistent units (either head or pressure) and the measurement date and time. The output is a matrix of adjusted water-level measurements versus time in either CSV or Excel format.
- The corrected data for a monitoring bore was plotted with data from other bores or the historic record of river gauge heights or lake levels.

A barometric pressure recording logger was installed at site BHMAR06-1 (for the period January 2010 to December 2011) and another at BHMAR17-1 (February 2010 to August 2011). A linear regression was applied to the combined barometric pressure data from the two sites, yielding a regression coefficient ($R^2$) of ~0.97. Given this result, the data record from site BHMAR06-1 was used as the proxy record of barometric pressure for the overall study area for the period January 2010 to December 2011. Following an audit of the

network in November 2011, barometric loggers are currently being maintained at sites BHMAR06 to the north, BHMAR33 at the Jimargil target borefield area and BHMAR31 to the south (Figure 15-1).

The manual groundwater level measurements provided a control for assessing the accuracy of the derived time-series of groundwater elevations. A confidence level was assigned based on the closeness of the match in terms of High (< 0.05 m variance), Moderate (0.05 - 0.1 m variance) or Low (> 0.1 m variance). Possible reasons for a low confidence outcome include faulty logger operation, drift in the logger data, failure to properly re-install the logger after a data download, or inaccuracies in the elevation calculations for the reference points used for the manual measurements.

The groundwater time series data was compared against existing surface water hydrographic monitoring. Time series data of surface water levels in the Darling River at Weir 32, Lake Menindee and Lake Wetherell were provided by New South Wales State Water. The surface water and lake levels data is for the period May 2010 to December 2011 which covered the flood event and refilling of the lake storages. The water level in the Darling River at Weir 32 was at a minimum of 1.59 m on 14/10/2010, rising to a peak of 7.16 m on 10/03/2011, followed by another peak of 6.88 m on 03/04/2011 after which time the river level declined until the onset of high flow conditions in early 2012. The onset of the rise in surface water levels was used as a baseline to estimate the lag and the rate of rise of groundwater in the aquifers (Table 15-2).

The change in the water level (RWL) in each bore over time was estimated as the difference in metres between the starting RWL and final RWL over the monitoring period. The magnitude of the change in groundwater height (ΔRWL in metres) was used to infer the possible connectivity of surface water and groundwater in conjunction with the stratigraphic data. The peak groundwater height in each bore was measured in order to compare the lag time response of the peak in the groundwater at each bore to the peak in surface waters as discussed above. This was done by estimating the change in water level (ΔRWL) divided by the difference in days between the start date and final monitoring date for each bore to give the rate of rise in groundwater in m/day (Table 15-2).

**Table 15-2.** *Analysis of time lags and hydrographic responses in BHMAR project bores.*

| Hole Name | Aquifer | Screened Interval | No. of days: Start to End | ΔRWL: Start to End (m) | Peak RWL | Peak: No. of days | ΔRWL (m): Start to Peak | Recharge Source | Confidence |
|---|---|---|---|---|---|---|---|---|---|
| 84-3 | Coonambidgal | 10-23 | 307 | 0.84 | 55.04 | 162 | 5.43 | Weir 32 | MOD |
| 84-4 | Coonambidgal | 12-23 | 341 | 0.78 | 51.96 | 162 | 2.74 | Weir 32 | MOD |
| 04-3 | Menindee | 8-14 | 571 | 1.70 | 56.64 | 571 | 1.71 | Weir 32 | HIGH |
| 33-3 | Menindee | 14-23 | 407 | 0.34 | 48.59 | 358 | 0.38 | Weir 32 | HIGH |
| 77-3 | Menindee | 11-16 | 307 | 0.69 | 49.48 | 182 | 1.17 | Weir 32 | MOD |
| 92-2 | Menindee | 12-16 | 773 | 1.32 | 50.55 | 203 | 1.67 | Weir 32 | MOD |
| 34-2 | Menindee | 8-20 | 680 | 0.56 | 54.50 | 680 | 0.56 | Weir 32 | MOD |
| 21-2 | Menindee | 10.5-23.5 | 677 | 1.51 | 45.63 | 595 | 1.51 | Weir 32 | MOD |
| 61-3 | Menindee | 12.5-22.5 | 642 | 0.42 | 45.35 | 486 | 0.74 | Charlie Stones | MOD |
| 35-1 | Calivil | 16-46 | 576 | -0.04 | 46.63 | 44 | 0.03 | Talyawalka | LOW |
| 16-1 | Calivil | 12.52 | 626 | 0.05 | 43.80 | 106 | 0.07 | Talyawalka | MOD |
| 14-1 | Calivil | 41-59 | 566 | 0.11 | 53.32 | 309 | 0.56 | Lake Wetherell | MOD |
| 06-1 | Calivil | 30-60 | 194 | 0.10 | 51.63 | 46 | 0.20 | Lake Wetherell | MOD |
| 05-2 | Calivil | 28-40 | 568 | 0.24 | 54.14 | 535 | 0.29 | Lake Wetherell | HIGH |
| 34-1 | Calivil | 27-51 | 680 | 0.95 | 54.93 | 676 | 0.98 | Lake Wetherell | MOD |
| 04-2 | Calivil | 34-52 | 575 | 1.16 | 55.92 | 575 | 1.17 | Lake Wetherell | MOD |

| | | | | | | | | | |
|---|---|---|---|---|---|---|---|---|---|
| 17-1 | Calivil | 54-72 | 580 | 0.80 | 48.84 | 379 | 1.20 | Lake Wetherell | MOD |
| 17-2 | Calivil | 22.5-34.5 | 521 | 0.58 | 48.59 | 379 | 0.86 | Lake Wetherell | HIGH |
| 57-1 | Calivil/Upper Renmark | 34.5-82.5 | 349 | 0.16 | 43.29 | 336 | 0.32 | Talyawalka | HIGH |
| 23-2 | Calivil | 29-47 | 407 | 4.01 | 56.94 | 407 | 4.01 | Lake Menindee | HIGH |
| 75-2 | Chowilla/Upper Calivil | 18-23 | 407 | 0.16 | 49.28 | 203 | 0.16 | Weir 32 | MOD |
| 75-5 | Calivil | 40-52 | 369 | -0.18 | 50.61 | 320 | 0.20 | Weir 32 | HIGH |
| 88-5 | Calivil | 35-41 | 307 | 0.69 | 50.39 | 302 | 0.75 | Weir 32 | LOW |
| 33-8 | Calivil | 46-52 | 249 | 1.31 | 49.14 | 141 | 1.36 | Weir 32 | MOD |
| 92-1 | Calivil | 32-62 | 407 | 0.66 | 49.55 | 358 | 0.75 | Weir 32 | MOD |
| 80A-7 | Calivil | 42-54 | 251 | 0.58 | 49.32 | 247 | 0.68 | Weir 32 | MOD |
| 80A-2 | Calivil | 35-53 | 773 | 0.82 | 50.10 | 358 | 0.86 | Weir 32 | LOW |
| 80B-2 | Calivil | 53-65 | 307 | 0.64 | 50.12 | 162 | 0.74 | Weir 32 | HIGH |
| 61-2 | Calivil | 36-66 | 568 | 0.27 | 45.22 | 385 | 0.37 | Charlie Stones | MOD |
| 29-1 | Calivil | 17-53 | 506 | -0.25 | 40.59 | 174 | 0.77 | Weir 32 | LOW |
| 21-1 | Calivil/Upper Renmark | 20-74 | 676 | 0.49 | 43.67 | 580 | 0.49 | Weir 32 | MOD |
| 31-1 | Loxton-Parilla | 11-51 | 573 | 0.04 | 40.26 | 478 | 0.21 | Weir 32 | HIGH |
| 05-1 | Upper Renmark | 94.5-100.5 | 265 | 0.16 | 46.51 | 161 | 0.35 | Lake Wetherell | LOW |
| 04-1 | Upper Renmark | 90-102 | 575 | 0.68 | 45.43 | 434 | 0.74 | Lake Wetherell | HIGH |
| 79A-2 | Upper Renmark | 65-77 | 407 | 0.82 | 50.10 | 358 | 0.86 | Weir 32 | MOD |
| 33-1 | Lower Renmark | 182-206 | 407 | 0.16 | 40.84 | 162 | 0.38 | Weir 32 | HIGH |
| 88-3 | Upper Renmark | 65-71 | 379 | 0.51 | 49.97 | 357 | 0.77 | Weir 32 | MOD |
| 80A-6 | Upper Renmark | 84-102 | 307 | 0.64 | 48.70 | 161 | 0.76 | Weir 32 | LOW |
| 61-1 | Upper Renmark | 86-116 | 578 | 0.23 | 42.54 | 335 | 0.47 | Weir 32 | HIGH |

## 15.2 POTENTIOMETRIC SURFACES

Regional watertable mapping from Brodie (1994) and Kellett (1994) was updated, based on the sonic drilling program. The depth to watertable could be interpreted from the changes in saturation of the sonic core with depth. This was supplemented by the direct measurements from the shallow monitoring bores constructed by the BHMAR project into the unconfined Coonambidgal and Menindee Formation aquifers. This data was combined with historical groundwater level data available from the NSW Office of Water groundwater databases. Using the surveyed borehole elevations, the watertable depth measurements could be converted to watertable elevations (m AHD). Where survey data was not available, the elevation of the bore was derived by sampling the regional LiDAR gridded data at the borehole location. The elevation contours of the watertable surface from Brodie (1994) and Kellett (1994) were used as a base and edited within ArcMap using the new project data and the historic NSW data. The AEM depth slices were also used as a guide, particularly where shallow resistive zones were inferred to be related to enhanced recharge and watertable mounding. Based on the borehole monitoring, the watertable surface was interpreted to be representative for December 2011. A grid of the watertable elevation was generated from these updated contours using the Arc Topo to Raster function. This grid was then subtracted from the LiDAR surface elevation grid, to derive a regional grid of the depth to watertable.

A similar process was undertaken to compile contours and a grid of the elevation of the Calivil Formation potentiometric surface for December 2011. Editing of the Brodie (1994) and Kellett (1994) mapping within ArcMap was guided by the NSW historic data, the project water level measurements and the relevant AEM depth slices for the Calivil Formation. The resulting grid was subtracted from the watertable elevation grid, to derive a grid of the vertical head difference between the shallow and Calivil Formation aquifers. This was

a useful guide, as it highlighted misinterpretation of contours in the areas with no borehole control. An iterative process of adjusting the contours, generating the relevant grids and comparing the difference between the grids resulted in greater confidence in the interpretation of these potentiometric surfaces.

The influence of density contrasts between aquifers, mainly due to groundwater salinity differences, was assessed by converting the measured groundwater levels to equivalent freshwater heads. This used Equation 93.

$$h_{f,i} = \frac{\rho_i}{\rho_f} - \frac{\rho_i - \rho_f}{\rho_f} Z_i$$

**Equation 93**

where $h_{f,i}$ is the freshwater head, $h_i$ is the measured water level relative to $Z_i$, the mean elevation of the well screen, $\rho_f$ is the fresh water density and $\rho_i$ is the groundwater density around the screen.

## 15.3 GROUNDWATER MODELLING (CSIRO)

Two simple conceptual groundwater flow and solute transport models were used to assess the potential viability of the Calivil Formation storage zone within the Jimargil target area (Miotlinksi *et al*., 2010). There was no attempt to reproduce the spatial heterogeneity of the Calivil Formation aquifer and confining layers, nor the nature of the connection to the surface water system, as to do so would require considerably more information than was available at the time of the modelling. However the conceptual models represent conditions encountered for the two boreholes (BHMAR33-1 and BHMAR80A-5) where hydraulic information was available from pump tests (refer Section 13.3).

FEFLOW software was used to represent axisymmetric conditions at sites BHMAR33 and 80A making use of stratigraphic information and results of the pumping tests of about 1 week duration. At the bore BHMAR33-5, the pumping test interpretation that best fits the data shows that the Calivil Formation aquifer is transmissive (T=300 $m^2$/d; S=1.33x10-3; ne=0.25; b=22.5 m; EC=1250 µS/cm), and leaky (semi-confined) and at this site the overlying unconfined Menindee Formation aquifer is more brackish (EC=1540 µS/cm). Whereas at the bore BHMAR80A-5, the Calivil Formation aquifer was more transmissive, fresher (T=900 $m^2$/d; S=5.7x10-4; ne=0.25; b=29 m; EC=500 µS/cm) and behaved as fully confined. Table 15-3 and Figure 15-2 summarise the input parameters used in the FEFLOW models used to characterise these two sites.

For each model two scenarios were considered. These consisted of two years of continuous injection of fresh source water (EC=250 µS/cm) followed by storage for a year then recovery for two years at the same rate as injection. Rates were set at 25 L/s and 50 L/s representing a total storage and recovery per well of 1.58 GL and 3.15 GL respectively.

At these two sites, the models predicted head and salinity with respect to radius from an ASR well in the Calivil Formation aquifer (and the superficial aquifer for the semi-confined case) at the end of injection and at the end of recovery. The salinity of water recovered during the two years of recovery was also calculated. The modelling of the two sites was performed independently, that is neglecting interference between wells, but allows the level of hydraulic interference for multiple ASR wells in close proximity to be estimated by superposition. The modelling is regarded as conceptual rather than simulating actual conditions because it does not take account of heterogeneity across the Jimargil target area, including that evident within the Calivil Formation aquifer and in the confining layers by comparison between the two sites.

It is noted that this modelling was carried out prior to the final inversions and revisions to the hydrostratigraphy and structural model for the Jimargil borefield area.

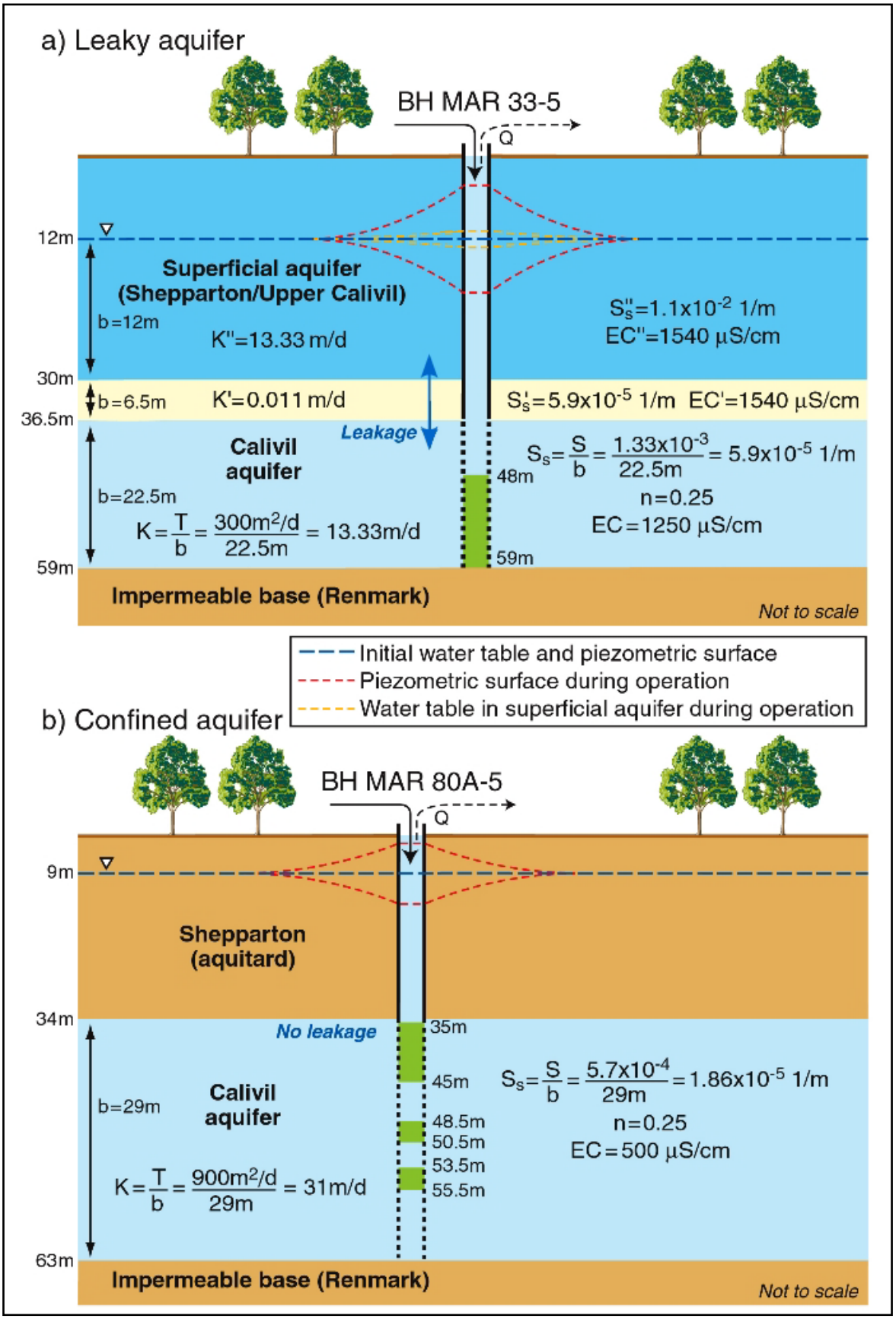



**Figure 15-2.** *Input parameters used for FEFLOW modelling of ASR scenarios at sites BHMAR 33 and 80A (Miotlinski et al., 2010).*

**Table 15-3.** *Parameters of the numerical model of ASR system – a leaky and a confined aquifer.*

| Parameters | Leaky aquifer | Confined aquifer |
|---|---|---|
| Dimensions | 2D vertical axisymmetric<br>x, y = 10000 m × 59 m | 2D vertical axisymmetric<br>x, y = 10000 m × 29 m |
| Unsteady flow | 1825 days in total | 1825 days in total |
| Flow initials | h (0, r) = 0 m | h (0, r) = 0 m |
| **Flow boundaries:** | | |
| Well pumping rate and lengths | $q_1=Q_1/2\pi$ = 2160 $m^3/d$ (25 L/s)<br>$q_2=Q_2/2\pi$ = 4320 $m^3/d$ (50 L/s)<br>Injection $Q_i$: 0-730 d<br>Storage (Q = 0 $m^3/d$): 730-1095 d<br>Recovery $Q_r$: 1095-1825 d | $q_1=Q_1/2\pi$ = 2160 $m^3/d$ (25 L/s)<br>$q_2=Q_2/2\pi$ = 4320 $m^3/d$ (50 L/s)<br>Injection $Q_i$: 0-730 d<br>Storage (Q = 0 $m^3/d$): 730-1095 d<br>Recovery $Q_r$: 1095-1825 d |
| Specified head at the outer boundary | H(t, 10000 m) = 0 m | H(t, 10000 m) = 0 m |
| **Flow materials:** | | |
| Conductivity*/transmissivity of aquifers: | $T_C$ = 300 $m^2/d$ for Calivil Formation which corresponds to: K = 13.33 m/d for well permeability deposits (Lower Calivil and Shepparton/Upper Calivil sandy layer)<br>K' = 1.1 $\times 10^{-2}$ m/d for a confining layer, which corresponds to the leakage coefficient of 1.7 $\times$ $10^{-3}$ $d^{-1}$ | $T_C$ = 900 $m^2/d$ for Calivil Formation which corresponds to: K = 31 m/d |
| Thickness of beds | b = 22.5 m (Calivil Formation)<br>b' = 6.5 m (overlying aquitard)<br>b" = 18 m (overlying aquifer) | b = 29 m (Calivil) |
| Storage coefficient (confined)<br><br>Specific yield (unconfined) | S = 5.9 $\times$ $10^{-5}$ $m^{-1}$ (Calivil Formation and overlying aquitard)<br><br>Sy = 0.2 (overlying aquifer) | S = 1.86 $\times$ $10^{-5}$ $m^{-1}$ (Calivil Formation aquifer) |
| Anisotropy factor | A = 1 | A = 1 |
| **Unsteady transport** | | |
| Transport initials | c (0, r) = 1250 µS/cm in Calivil Formation<br>c' and c" (0, r) = 1540 µS/cm in overlying layers | c (0, r) = 500 µS/cm in Calivil Formation |
| Transport boundaries: | | |
| Constant concentration at the injection point | $c(t, 0) = c_0$ = 250 µS/cm | $c(t, 0) = c_0$ = 250 µS/cm |
| Transport materials | | |
| Porosity | $\varepsilon$ = 0.25 | $\varepsilon$ = 0.25 |
| Molecular diffusivity | $D_d = 10^{-9}$ $m^2/s$ | $D_d = 10^{-9}$ $m^2/s$ |
| Longitudinal, transverse dispersivity | $\beta_L$ = 5 m, $\beta_T$ = 0.5 m | $\beta_L$ = 5 m, $\beta_T$ = 0.5 m |
| FEM | Finite element quadrilateral mesh | Finite element quadrilateral mesh |
| Time stepping regime | Automatic step control (AB/TR)*<br>$t_0$ = 0.001 d | Automatic step control (AB/TR)*<br>$t_0$ = 0.001 d |
| Solver | PCG* | PCG* |

Notes: * see FEFLOW Reference Manual (Diersch 2002) for detail

# 16 Recharge Studies

## 16.1 BACKGROUND

Significant volumes of fresh groundwater have been identified in aquifer targets along the Darling and Talyawalka floodplains in the BHMAR study area (Lawrie *et al.,* 2012d). Long-term extraction of these resources is predicated on reducing to acceptable limits any potential negative impacts such as groundwater level decline, saline water ingress or reduced ecosystem health. As well as groundwater storage, this requires an understanding of aquifer replenishment. This section details the various methods employed in the BHMAR Project to estimate recharge and discusses some of the limitations of these approaches.

## 16.2 ESTIMATING GROUNDWATER RESOURES IN DATA-POOR AREAS PROJECT

Recently, a suite of tools for estimating groundwater recharge (and discharge) anywhere across Australia has been released (Leaney *et al*., 2011). The premise of the tool suite was to provide a nationally consistent approach to groundwater recharge (and discharge) estimation for data poor areas. The authors stressed that where the value of the groundwater resource necessitates field based studies, the tool should not be used in lieu of more detailed investigations. Leaney *et al.* (2011) go on to say that only direct (rainfall-driven) downward water movement to the watertable is addressed in their study and leakage from watercourses has not been considered. The three methods applied in their study (Method of Last Resort, Percentage Clay, and Chloride Mass Balance) therefore cannot be applied to confined systems, and do not account for recharge from rivers or lateral groundwater flow. This is particularly important for the BHMAR Project area as it has been established that river leakage brought about but high (flood) river flows is the primary mechanism for groundwater recharge.

### 16.2.1 Method of Last Resort (MOLR)

*"The MOLR is the most widely applicable [groundwater recharge estimation] method and uses the relationship observed between deep drainage and rainfall for different soil orders (as defined by the Australian Soil Classification) and vegetation cover. As the inputs are all national-scale digital datasets, the MOLR has been produced as a nationally consistent spatial coverage. This method has a high degree of uncertainty as the correlations only explain about 60% of the variance in recharge measurements across Australia; uncertainty in the groundwater recharge estimated using these relationships is generally considerably greater than an order of magnitude (Crosbie et al., 2010)."* Leaney *et al*. (2011).

The Crosbie *et al.* (2010) MOLR spatial coverage does not cover the BHMAR study area. There was evidently a lack of field data to develop a relationship in the BHMAR study area. Consequently the MOLR cannot be used to calculate vertical recharge in the project area. This method also only provides an estimate of potential recharge to the watertable and thus could not be applied to the semi-confined (Calivil Formation) aquifer.

### 16.2.2 Percentage Clay Method

The percentage clay method is based on a log-linear relationship first established by Kennett-Smith *et al*. (1994) between deep drainage under cropped land and the percentage clay content of surface soils (approximately the top 2 m). This relationship was found to include a third variable – rainfall (Wohling *et al*., 2011).

As was the case with MOLR, this method only provides an estimate of potential recharge to the watertable and thus could not be applied to the semi-confined (Calivil Formation) aquifer. Furthermore, Leaney *et al*.

(2011) recommend it only be used if the clay content in the top 2 m has been measured in the field. If actual measurements have been obtained, recharge estimates have a slightly lower uncertainty than the MOLR (Leaney *et al.*, 2011). Pre-existing percentage clay measurements are not publically available for this particular region. However, as part of the BHMAR Project, a series of sonic boreholes were drilled across the study area. Samples were taken throughout the fully-recovered core and analysed for a suite of parameters including physical properties such as grain size. Unfortunately as was the case with the MOLR, the relationships derived from field based studies could not be extrapolated to the low rainfall conditions experienced in the study area which is another limitation of this approach.

### 16.2.3 Chloride Mass Balance Method

The Groundwater Chloride Mass Balance (GCMB) is the most common method used to estimate steady-state recharge in Australia, due to its ease of use and minimal data requirements (Crosbie *et al.,* 2010). *"…it is very simple conceptually and the analytical costs are comparatively cheap. The method is valid because chloride in pore water is excluded by evaporation and transpiration leaving it to concentrate in the unsaturated zone, and eventually reach the groundwater via advection. It is a method for estimating net groundwater recharge because chloride can continue to be concentrated in the saturated zone if vegetation is exploiting this source of water."* Leaney *et al*. (2011).

There are some limitations of this method; GCMB can only be calculated if the groundwater at the screen depth is at a steady state. If vegetation clearing has occurred, a period of time must elapse before a new steady state is reached; this period of time varies with rainfall rates and hydraulic properties of the soil/regolith between the surface and the bore screen. There are other assumptions inherent in this methodology discussed by Leaney *et al*. (2011). For example, the chloride in groundwater is assumed to originate from precipitation. If there are other subsurface sources of chloride beside precipitation, such as halite deposits or marine-sourced formation waters, then the calculated recharge rates would be erroneously low. The bromide/chloride ratio of groundwater can be used to investigate the potential influence of halite dissolution in groundwater evolution (Davis *et al*., 1998; Wood, 1999; Kloppman *et al.,* 2001). The deeper, more saline groundwaters in the study area have a Br/Cl ratio slightly lower than for conventional seawater, suggesting some influence of halite dissolution (Lawrie *et al.,* 2012b). As river recharge is concluded to be the dominant recharge process, the starting chloride concentration would be greater than that modelled for precipitation. In which case, recharge rates would have been underestimated.

The GCMB method was employed using pre-existing data, namely chloride in rainfall, average rainfall amount and soil classes (available via MapConnect[1]) and groundwater chloride data (available from NSW Office of Water). Equation 94 was used where $R$ is the long term recharge rate (m/d), $D$ is the chloride deposition rate (kg/m$^2$/d) and $C_g$ is the concentration of chloride in the groundwater (kg/m$^3$).The chloride deposition rate ($D$) is the combination of the average chloride concentration (kg/m$^3$) in rainfall and the average rainfall rate (m/d):

$$R = \frac{D}{C_g}$$

**Equation 94**

Groundwater recharge rates derived from this method (using existing groundwater chloride measurements) ranged from 0.1 to 7.3 mm/yr in the BHMAR study area with an average direct groundwater recharge rate (n= 30; taken at differing rainfall and soil classes) of 1.2 mm/yr. As part of the BHMAR Project, a series of sonic boreholes were drilled across the study area. Samples were taken throughout the fully-recovered core and analysed for a suite of parameters including pore fluid chloride concentrations. When applied to the GCMB method, this data provided a downhole profile of estimated recharge rates and can be related back to direct versus lateral recharge processes. While groundwater recharge based on these fully-recovered cores

[1] http://ga.gov.au/topographic-mapping/mapconnect.html

ranged from 0.1 to 37 mm/yr, the average direct groundwater recharge rate calculated from 706 pore fluid samples was 1.8 mm/yr (see Appendix 8, Apps *et al*., 2012a). The downhole variability in the recharge estimates associated with different hydrostratigraphic units suggests that the groundwater recharge regime is more complex than simply direct recharge from precipitation that assumes a disconnection between surface water and groundwater. If the dominant recharge mechanism is by river leakage, then the underlying assumptions of the chloride mass balance method do not hold and the derived recharge statistics are not valid.

## 16.3 WATERTABLE FLUCTUATION METHOD

The watertable fluctuation (WTF) method is a simple approach to estimating recharge using groundwater level data (Healy & Cook, 2002). The approach has a long history of application in groundwater resource studies (Meinzer, 1923; White, 1932; Rasmussen & Andreasen, 1959).The assumption is made that any rises in groundwater levels in an unconfined aquifer are due to percolating waters reaching the watertable. On this basis, Equation 95 was used to estimate the recharge rate ($R$) where $S_y$ is the specific yield of the unconfined aquifer, $\Delta h$ is the rise (m) in the elevation of the groundwater level and $\Delta t$ is the duration (d) of the recharge event:

$$R = Sy\frac{\Delta h}{\Delta t}$$

**Equation 95**

Recharge is equated to the volume of water stored in the incremental volume of aquifer defined by the watertable rise. This assumes that other components of the water budget such as baseflow, pumping, inter-aquifer leakage or evapotranspiration are effectively zero during the time of recharge. The method is independent of the actual mechanism of recharge, whether it is piston flow though the unsaturated zone, via preferential pathways such as fractures, or from leakage of surface water features.

There are limitations to its application (Healy & Cook, 2002). The method is only applied to unconfined aquifers and works better for shallow dynamic systems where the watertable response is rapid and strong. It becomes difficult to reconcile groundwater fluctuations with recharge episodes for aquifers with deep watertables due to the time lag associated with downward infiltration through the unsaturated zone. Constant rates of recharge cannot be distinguished as the method relies on the short-term response to rainfall or flood events. Other mechanisms for watertable fluctuations need to be recognised, including diurnal evapotranspiration cycles, ocean tides and transmission of changes to atmospheric pressure. The method only estimates recharge at the site of the bore, so may be representative for only a small area of the catchment.

As indicated in Equation 95, a reliable estimate of specific yield is required to quantify recharge. This is typically defined as the volume of water that an unconfined aquifer releases from storage per unit surface area of aquifer per unit decline in the watertable (Freeze & Cherry, 1979). In the context of recharge calculations, this relates to the volume of water added to the aquifer per unit rise in the watertable. In the absence of direct measurements for the Coonambidgal Formation, Menindee Formation and Willotia beds aquifers, a nominal specific yield range of 0.05-0.10 was used in the calculations. This uncertainty in aquifer specific yield represents the greatest uncertainty in the resulting recharge estimates using this method.

Results for the bores in the shallow unconfined aquifer are summarised in Table 16-1. The event recharge along the Darling River corridor for the 2010-11 flood event period varies by at least an order of magnitude (19-543 mm) but is significant compared to recharge estimates based on diffuse rainfall (<1 mm/yr). The 2010-11 flood event represents a groundwater recharge volume of 19-543 megalitres (ML) per kilometre square of aquifer receiving recharge along the river corridor during this event. In the north near Lake Wetherell (BHMAR34-2) the average daily recharge during the 2010-11 flood event was ~0.06 mm/d; in the Jimargil-East Bootingee area (BHMAR77-3, BHMAR84-4, BHMAR92-2 and BHMAR33-3) the average daily recharge ranged from 0.07 to 1.3 mm/d; and further south at Tandou (BHMAR21-2) recharge was ~0.2

mm/d. At the northwest margin of Lake Menindee (BHMAR23-2) recharge from lake leakage was ~0.7 mm/d, equating to ~300 ML per kilometre square of aquifer over the 2010-11 flood event period.

**Table 16-1.** *Recharge estimates for unconfined aquifers based on watertable fluctuation method.*

| BHMAR | Aquifer | Screened Interval | Location | ΔRWL (m): Start to PEAK | Peak: days | Event Recharge (mm) | Event Daily Recharge (mm/d) | Recharge Source | Conf. |
|---|---|---|---|---|---|---|---|---|---|
| 84-3 | Coonambidgal | 10-23 | East Bootingee | 5.43 | 162 | 272-543 | 1.7-3.4 | Darling | MOD |
| 84-4 | Coonambidgal | 12-23 | East Bootingee | 2.74 | 162 | 137-274 | 0.9-1.7 | Darling | MOD |
| 04-3 | Menindee | 8-14 | Lake Wetherell | 1.71 | 571 | 86-171 | 0.1-0.3 | Wetherell | HIGH |
| 77-3 | Menindee | 11-16 | Jimargil | 1.17 | 182 | 59-117 | 0.3-0.6 | Darling | MOD |
| 33-3 | Menindee | 14-23 | Jimargil | 0.38 | 358 | 19-38 | 0.05-0.1 | Darling | HIGH |
| 92-2 | Menindee | 12-16 | East Bootingee | 1.67 | 203 | 83-167 | 0.4-0.8 | Darling | MOD |
| 34-2 | Menindee | 8-20 | Lake Wetherell | 0.56 | 680 | 28-56 | 0.04-0.08 | Wetherell | MOD |
| 21-2 | Menindee | 10.5-23.5 | Tandou | 1.51 | 595 | 76-151 | 0.13-0.25 | Darling | MOD |
| 61-3 | Menindee | 12.5-22.5 | Wanda | 0.74 | 486 | 37-74 | 0.08-0.15 | Charlie Stones Ck | MOD |
| 23-2 | Menindee/ Calivil | 29-47 | Lake Menindee | 4.01 | 407 | 200-401 | 0.5-1.0 | Menindee | HIGH |

## 16.4 GROUNDWATER MOUNDING MODEL

Hantush (1967) developed analytical equations to estimate steady state groundwater mounding associated with uniform percolation. Bouwer (2002) applied these in the context of artificial recharge investigations to estimate infiltration from long strip basins using Equation 96:

$$H_c - H_n = \frac{iW}{2T}\left(\frac{W}{4} + L_n\right)$$

**Equation 96**

where $H_c$ is the height of the groundwater mound in the centre of the recharge area, $H_n$ is the height at the watertable at a control site away from the recharge area, $W$ is the width of the recharge area, $L_n$ is the distance between the edge of the recharge area and the control site, $T$ is the aquifer transmissivity and $i$ is the average infiltration rate (Figure 16-1).

The steady state equation assumes that the recharge feature (mound) has a length of at least five times the width ($W$). On this basis, the equation was used to estimate the infiltration rate from the Darling River, based on the geometry of the resulting watertable mound. Table 16-2 summarises the application of this equation using selected bores at Jimargil-East Bootingeee as control sites.

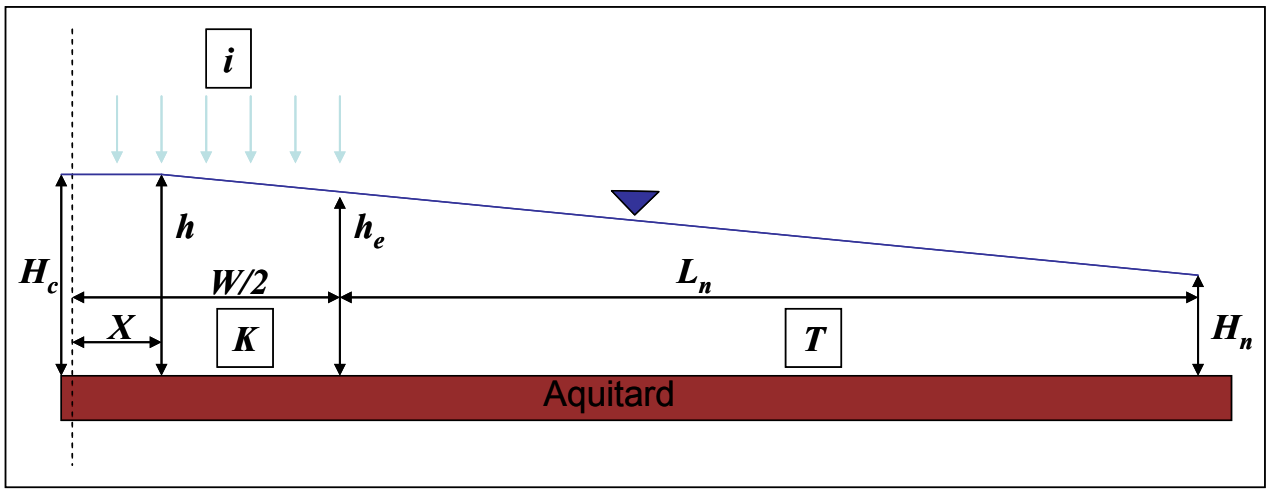



**Figure 16-1.** Section showing geometry and parameters for calculating the groundwater mound below a long infiltration area (strip) of width W (from Bouwer, 2002).

**Table 16-2.** *Summary of estimates of infiltration rates using Bouwer (2002) groundwater mounding equation.*

| Parameter | Value | Rationale |
|---|---|---|
| **Control Site BHMAR 80A-3** | | |
| $H_c$ | 8.1 | Aquifer base (42.4 m AHD) from 80A-2 log and RWL (50.4 m AHD) interpolated from measured RWL at 80A-4 |
| $H_n$ | 7.9 | Aquifer base (42.4 m AHD) from 80A-2 log and measured RWL (50.3 m AHD) at 80A-4 |
| W | 80 | Width (m) of Darling River bank full |
| T | 4.8 | Sum of NMR T values for saturated part of watertable aquifer in 80A-2 |
| $L_n$ | 125 | Distance from river edge to 80A-2 |
| **Infiltration (mm/d)** | **0.17** | |
| **Infiltration (mm/yr)** | **60** | |
| **Control Site BHMAR99-2** | | |
| $H_c$ | 7.4 | Aquifer base (43 m AHD) from 99-1 log and RWL (50.4 m AHD) interpolated from measured RWL at 80A-4 |
| $H_n$ | 6.5 | Aquifer base (43 m AHD) from 99-1 log and RWL (49.5 m AHD) interpolated from December 2011 watertable contours |
| W | 80 | Width (m) of Darling River bank full |
| T | 13.1 | Sum of NMR T values for saturated part of watertable aquifer in 99-1 |
| $L_n$ | 1005 | Distance from river edge to 99-1 |
| **Infiltration (mm/d)** | **0.29** | |
| **Infiltration (mm/yr)** | **105** | |
| **Control Site BHMAR92-2** | | |
| $H_c$ | 8.3 | Aquifer base (42 m AHD) from 92-1 log and RWL (50.3) interpolated from measured RWL from 92-2 |
| $H_n$ | 8.2 | Aquifer base (42 m AHD) from 92-1 log and measured RWL (50.2 m AHD) from 92-2 |
| W | 80 | Width of Darling River bank full |
| T | 10 | NMR T values for saturated part of watertable aquifer in 92-1 |
| $L_n$ | 85 | Distance from river edge to 92-1 |
| **Infiltration (mm/d)** | **0.24** | |
| **Infiltration (mm/yr)** | **87** | |

## 16.5 FLOOD FREQUENCY ANALYSIS

Hydrographic and hydrochemical analysis concluded that groundwater recharge is dominated by river leakage associated with high-flow events (Lawrie *et al*., 2012b). Not only does the recharge during high streamflow events need to be quantified, but also an understanding of the duration and frequency of these flow events. Such an analysis was undertaken using the historic stream gauging record for the Darling River at Weir 32 (425012) by:

- Checking for any gaps in the data record which spans about 38 years (1974-2012). Such gaps were minor (<1% of the record) and were filled by linear interpolation between the existing bounding data.
- Defining a streamflow event as a continuous record of daily streamflows that exceeded a defined threshold (e.g. 10,000 ML/d). Statistics were collected such as the event duration, total and maximum event streamflow for events where flow exceeded the particular flow threshold.
- Repeating the compilation of these event statistics using different flow thresholds.

Table 16-3 summarises these streamflow event statistics. The number of events decreased as the magnitude of the threshold increased (Figure 16-2a). This is also the case for the proportion of the historic record that had recorded daily streamflows exceeding the threshold (Figure 16-2b). About 16% of the record had streamflows exceeding 10,000 ML/d whilst about 4% had streamflows exceeding 25,000 ML/d.

These statistics are needed to derive a long-term recharge average, considering that the recharge associated with episodic high-flow events is interspersed with relatively long periods of zero recharge under low to average river flow conditions. This requires an understanding of what constitutes a reasonable streamflow threshold where recharge by river leakage becomes significant. Hydrographs of near-river monitoring bores screened in the Calivil Formation aquifer show a response to high flows before the onset of overbank conditions. For the Weir 32 site, responses to streamflows on the order of 8-10,000 ML/d were observed, below the gauge level corresponding to overbank flow of about 19,000 ML/d. In terms of duration, these streamflows represent about 16-18% of the overall historic record (Table 16-3). This would mean that active recharge to the groundwater system would only occur for about 17% of the time. On this basis, the recharge rate associated with the episodic high streamflows would need to be multiplied by this factor (0.17) to derive a long term average recharge rate. This analysis supports the need to maintain a hydrographic network in the study area, to monitor the groundwater response to streamflow events of varying magnitude.

**Table 16-3.** *Summary of events exceeding flow thresholds for the Darling River at Weir 32 gauge record.*

| Flow Threshold (ML/d) | Total Days | Proportion of Record | Number of events | Minimum Duration | Maximum Duration | Average Duration |
|---|---|---|---|---|---|---|
| 5000 | 3216 | 0.23 | 38 | 3 | 360 | 85 |
| 8000 | 2573 | 0.18 | 29 | 5 | 355 | 89 |
| 10000 | 2171 | 0.16 | 22 | 2 | 342 | 99 |
| 15000 | 1728 | 0.12 | 20 | 9 | 212 | 86 |
| 19000 | 1136 | 0.08 | 18 | 7 | 181 | 63 |
| 25000 | 604 | 0.04 | 9 | 1 | 110 | 67 |

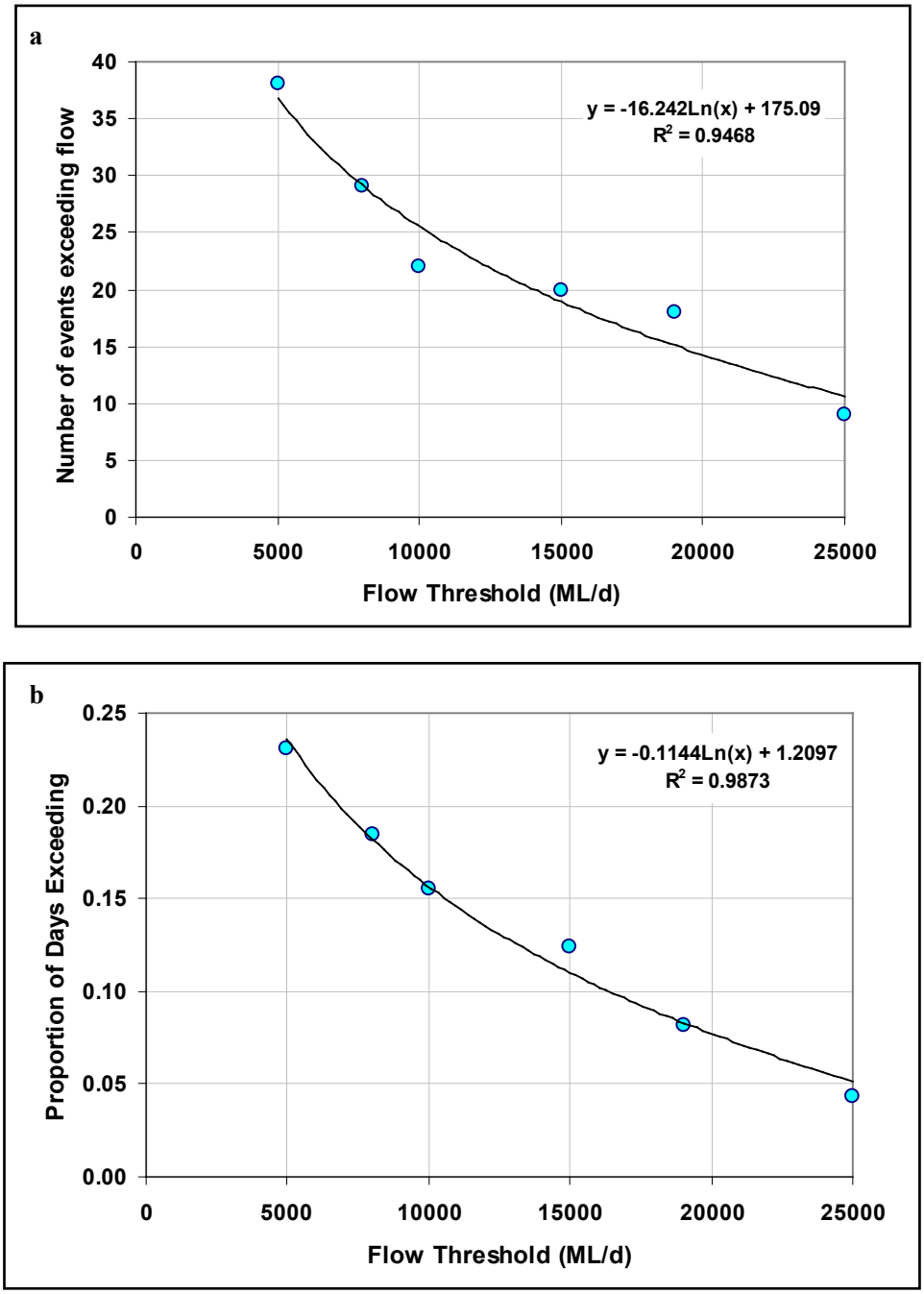



**Figure 16-2.** Number and proportion of streamflow events exceeding streamflow thresholds for Darling River at Weir 32.

## 16.6 RADIOCARBON DEPTH MODELS

The depth profile of radiocarbon ($^{14}C$) concentrations in groundwater can be used to estimate a steady state recharge rate (Vogel 1966, Walker & Cook, 1991). Equation 97 relates the $^{14}C$ depth profile in the absence of diffusion:

$$C = C_0\left(\frac{H}{H-z}\right)e^{-\lambda H\theta / R}$$

**Equation 97**

Where $C_0$ is the initial $^{14}C$ groundwater concentration at the watertable, $C$ is the $^{14}C$ concentration at depth $z$ below the watertable, $H$ is the depth to aquifer base, $\lambda$ is the $^{14}C$ radioactive decay constant (1/8270 $yr^{-1}$), $\theta$ is aquifer porosity and $R$ is the recharge rate. Equation 97 considers uniform recharge for an unconfined aquifer with constant thickness and porosity and with uniform horizontal velocity with depth.

Solving for recharge (R), Equation 97 becomes:

$$R = \frac{-\lambda H\theta}{\ln(CH-z)-\ln(C_0H)}$$

**Equation 98**

However, the assumptions inherent in this equation are invalid for the Calivil Formation target aquifer, being semi-confined rather than unconfined. Based on Cook & Bohlke (2000), the equivalent equation for a semi-confined aquifer with constant thickness in the confined part is:

$$C = C_0e^{-\lambda(z\theta / R + xH\theta / Rw)}$$

**Equation 99**

Which equates to:

$$R = \frac{-\lambda\theta(z+wH/x)}{\ln(C)-\ln(C_0)}$$

**Equation 100**

Where $H$ is the constant aquifer thickness, $C$ is the $^{14}C$ concentration at depth $z$ from the top of the aquifer, $w$ is the width of the recharge area and $x$ is the horizontal distance between the site and the edge of the recharge source.

Table 16-4 summarises the results of applying the unconfined recharge model (Equation 98) to the Coonambidgal and Menindee Formation radiocarbon samples, and the confined recharge model (Equation 100) to the Calivil Formation radiocarbon samples. For the Coonambidgal Formation samples, the initial $C_0$ concentration was set at 115 pMC which is the maximum recorded for these shallow bores. As the equivalent for the confined model represents the $^{14}C$ input at the top of the Calivil Formation aquifer, a range defined by the minimum (101 pMC) and the maximum (115 pMC) for the shallow aquifer samples were used in the confined model calculations. This is the reason why the radiocarbon recharge estimates for the Calivil Formation is reported as a range.

**Table 16-4.** *Summary of radiocarbon recharge estimates for selected Jimargil-East Bootingee bores.*

| | | | Unconfined Model | | Confined Model | |
|---|---|---|---|---|---|---|
| **BHMAR** | **Aquifer** | **Screened Interval** | **R (mm/d)** | **R (mm/yr)** | **R (mm/d)** | **R (mm/yr)** |
| 80A-3 | Coonambidgal | 11-17 | .02 | 6 | N/A | N/A |
| 80A-4 | Coonambidgal | 10-14 | .03 | 10 | N/A | N/A |
| 80B-3 | Coonambidgal | 11-16 | .02 | 7 | N/A | N/A |
| 84-3 | Coonambidgal | 10-23 | .01 | 5 | N/A | N/A |
| 84-4 | Coonambidgal | 12-23 | .01 | 5 | N/A | N/A |
| 84-5 | Coonambidgal | 10-23 | .02 | 8 | N/A | N/A |
| 77-3 | Menindee | 11-16 | .02 | 8 | N/A | N/A |
| 77-4 | Menindee | 11-15 | .03 | 10 | N/A | N/A |
| 92-2 | Menindee | 12-16 | .05 | 19 | N/A | N/A |
| 77-2 | Calivil | 47-55 | N/A | N/A | .01-.02 | 5-6 |
| 77-5 | Calivil | 46-56 | N/A | N/A | .07-0.10 | 27-35 |
| 80A-2 | Calivil | 35-53 | N/A | N/A | .02-.03 | 7-13 |
| 80A-5 | Calivil | 35-55.5 | N/A | N/A | | |
| 80A-7 | Calivil | 42-54 | N/A | N/A | .05-.09 | 18-35 |
| 80B-2 | Calivil | 53-65 | N/A | N/A | .016-.024 | 6-9 |
| 83-2 | Calivil | 48-63 | N/A | N/A | .01-.013 | 4-5 |
| 84-2 | Calivil | 45-51 | N/A | N/A | .004-.005 | 1.6-1.7 |
| 92-1 | Calivil | 32-62 | N/A | N/A | .01-.02 | 5-8 |

## 16.7 RECOMMENDATIONS

There are many different methods for estimating groundwater recharge. Some of these provide estimates of potential recharge or deep drainage, which is the flux below the root zone that has the potential to reach the watertable over varying periods of time. Other methods focus on groundwater responses where recharge accessions have actually reached the watertable. In general, these methods relate to the unconfined aquifer and cannot be extrapolated to estimating groundwater recharge to confined or semi-confined aquifers. This requires an understanding of the geometry and structure of the hydrostratigraphy, including the aquitards overlying (semi)confined aquifers.

It is important to understand the assumptions inherent in any recharge estimation method and the implications of these on method suitability. This is important to ensure that the recharge method is appropriate to the conceptual model developed for the groundwater system. For example, the groundwater chloride mass balance method assumes that the chloride in groundwater originates from rainfall, with no other subsurface chloride sources. It also assumes that surface water leakage to the aquifer is absent. With river/lake leakage interpreted as the dominant recharge mechanism, these assumptions are not met so the derived potential recharge estimates are not valid.

Recharge to the Calivil Formation is dominated by episodic leakage during high river flows and via structurally controlled disruptions to the regional overlying aquitards. This results in significant variations in recharge rates in both space and time, resulting in significant challenges in terms of extrapolating point-based recharge estimates. Relatively simple approaches have been applied to extrapolating estimates of rainfall-induced recharge across the landscape. For example, mapping of controlling factors such as vegetation, topography, land use and soil/regolith textures can be used to characterise the spatial variability of diffuse recharge. However, it is difficult to use similar approaches for structurally controlled episodic river leakage where recharge is focussed in specific areas and specific times. It is recommended that a transient groundwater flow model be constructed and calibrated to the hydrographic responses to a series of flood events.

# 17 Data Integration and Mapped Products

## 17.1 FLOOD INUNDATION MAPPING

### 17.1.1 Introduction

In the Darling floodplain environment, floods are highly likely to play a significant role in determining the location and effectiveness of recharge events by:

- Raising the hydraulic head in aquifers;
- By eroding fine grained sediment plugs from river channels and holes; and
- By extending the water/sediment contact zone from the channels to the floodplains.

Lawrie *et al*. (2012b) discusses the hydrogeological conceptual model and recharge mechanisms for the study site, including the importance of flood events for recharge to the Calivil Formation aquifer. Modelling of the approximate extent of floods is also important from a borefield design point of view.

Flood extent mapping can be undertaken in a variety of ways, ranging from simple fill models reliant on elevation data (e.g. Wang *et al*., 2002 ); more complex numerical 1D or 2D models (e.g. Horritt *et al*., 2006; Cook & Merwade, 2009); or remote sensing approaches utilising radar (e.g. Henry *et al*., 2006) or multispectral imagery (e.g. Islam *et al*., 2010). The first two can be used to report both historical events and predict future scenarios while the later (remote sensing approaches) are only capable of reporting on previous events; they are also useful in validating the methodology of the first two approaches.

The fundamental difference between and simple fill models and 1D/2D numerical models (e.g. hydraulic models), is that where a simple fill model uses a single known or estimated water level to produce a corresponding flood inundation extent, numerical models account for and model the complex movement of water across the landscape in generating water levels and flood extents (de Moel *et al*., 2009). Numerical models are however data intensive and somewhat subjective, being affected by input data, type of model and description of the river geometry in the model (Cook & Merwade, 2009). Data requirements can include, for example cross-sectional and/or continuous surface topographic information, friction parameters, flow rates and boundary conditions (Cook & Merwade, 2009). This type of information was not available within the project study area, thus precluding a similar approach from being utilised.

The two key data inputs for a simple fill model are water level (either modelled or measured) with a digital elevation model (DEM). The spatial resolutions and vertical accuracy of space-borne DEMs are not typically fine enough to represent small structures such as narrow channels connecting main rivers and floodplains that are critical to developing accurate flood extents (Wilson *et al*., 2007). These limitations are overcome with the use of a high resolution LiDAR DEM. Such a dataset was acquired for the project study area; the specifications of which are discussed in Section 5. Both space-borne and airborne (e.g. LiDAR) DEMs suffer from random noise caused by operating platform manoeuvre errors and the effects of thermal pollution on sensors (Rodriguez *et al*., 2006), and are unable to penetrate water bodies such as rivers or lakes. These issues and the processing undertaken to account for them in the LiDAR DEM, are also discussed in Section 5. In addition to the DEM, a river gauging station provided adequate water level input data to produce flood inundation extents, both historic and predictive, using a simple fill model. Wang *et al*. (2002) similarly used river gauge readings to inundate the DEM in densely vegetated areas in place of an otherwise remotely sensed methodology. The authors go on to outline the limitations of this approach:

- Better suited to low relief terrain;
- Inability to map inundation areas at higher elevations; and
- Restricted to an area within a ‘reasonable’ distance from the river gauge station; the distance being influenced by the amount of topographic variation.

As the study area exhibits a 20 m difference in floodplain elevation over the length of the river, a slightly more sophisticated approach was used in this study. This is discussed in more detail, along with the application and limitations of the LiDAR-derived flood inundation extent mapping, in Section 17.1.2.

Finally while a remote sensing approach is not predictive, it provides a point of truth to validate or calibrate other methods against, or if processed in a certain way, can be used to map historic inundation independently of any other method. Henry *et al*. (2006) investigated the best approach to mapping floods using Advanced Synthetic Aperture Radar (ASAR) in a case study of the Elbe River, while Islam *et al*. (2010) utilised freely available MODIS imagery to assess the inundation and recession patterns of 2004 and 2007 flooding in Bangladesh. A comprehensive set of Landsat 5 TM satellite imagery was acquired for the purpose of assessing vegetation condition (Section 17.2). As this imagery was already available for the project study area, it was used in preference to other datasets. Landsat has greater spatial resolution than MODIS (30 m versus 250 m); and is cheaper and requires less pre- and post-processing than SAR. The main advantage of using radar imagery is its ability to penetrate cloud and vegetation canopy cover. Several authors have successfully utilised SAR to map flooded areas (e.g. Hess *et al*., 1995; Wang, 2004).

There are a number of methods used to identify surface water from spectral imagery such as Landsat, for example Wang *et al*. (2002) used a simple two-band (TM4+TM7) combination and thresholds; Hui *et al*. (2008) used the Normalised Difference Water Index (NDWI), available; and Hudson & Colditz (2003) used Principal Component (PC) analysis and image classification. Application and limitations are also discussed.

## 17.1.2 LiDAR-derived Potential Flood Extents

### 17.1.2.1 *Methodology*

*Levelling the DEM*

A Digital Elevation Model (DEM) was derived from a 1 m resolution LiDAR raster dataset. Processing applied to this dataset is discussed in Section 5. As concluded by Wang *et al*. (2002), the topography within the area of interest needs to be largely flat-lying for a simple fill inundation model to be effective. The BHMAR project area exhibits as much a 20 m difference in the elevation between the upper and lower reaches of the Darling River (Figure 17-1). Relative changes in elevation between for example the river channel, floodplain and dunes are confounded by the regional tilt in the floodplain. To account for this the LiDAR surface needed to be 'levelled' which would adjust these landscape features to a common reference point and allow for a simple fill inundation model to be run.

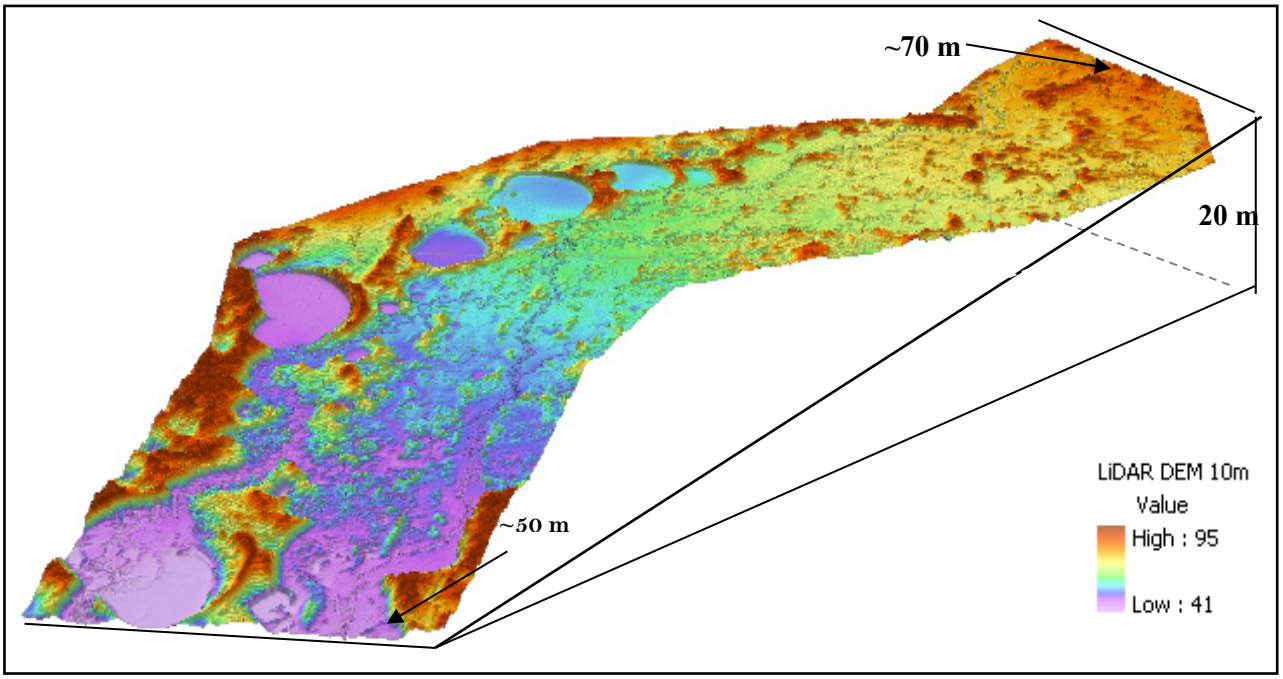



**Figure 17-1.** *LiDAR DEM surface showing a 20 m difference between the upper and lower reaches of the Darling River within the study area.*

As the elevation of the Darling River channel varied over the study area, and thus was not the lowest lying feature in the landscape, it could was not easily identified. Instead, a drop raster was created (using ArcGIS©) to identify the flattest areas, or areas with minimal continuing change along a flow path (i.e. lakes and river channels). The blue areas in Figure 17-2 represent landforms with minimal elevation change. Those identified as corresponding with the Darling River channel were used to generate a floodplain trend surface (Figure 17-3) where river channel elevations were equal. This trend surface was then subtracted from the LiDAR DEM to generate a levelled DEM. Figure 17-4 shows a comparison between the original DEM and the levelled DEM. Note how geomorphic features are difficult are to identify in the original DEM as they are masked by the overall stepwise change in floodplain elevation from upstream to downstream (Figure 17-4a). These geomorphic features become much more apparent in the levelled DEM (Figure 17-4b).

*Flooding the surface*

The levelled DEM was then adjusted to the zero gauge height at the Darling River gauging station (Site 425012; the only gauge station in the study area), upstream of Weir 32 which is equivalent to 51.825 m AHD. However at the time of LiDAR acquisition, the spatial location of this gauge was inundated therefore the water surface, rather than the river channel was mapped. The river level as recorded by the gauge at this time was approximately 1 m therefore an additional metre was factored into the adjustment of the LiDAR. River-level readings from historical and current events can be extracted from the NSW Office of Water real time river data website1. Flood extent and flood depth could then be derived by elevation slicing up to any chosen river level.

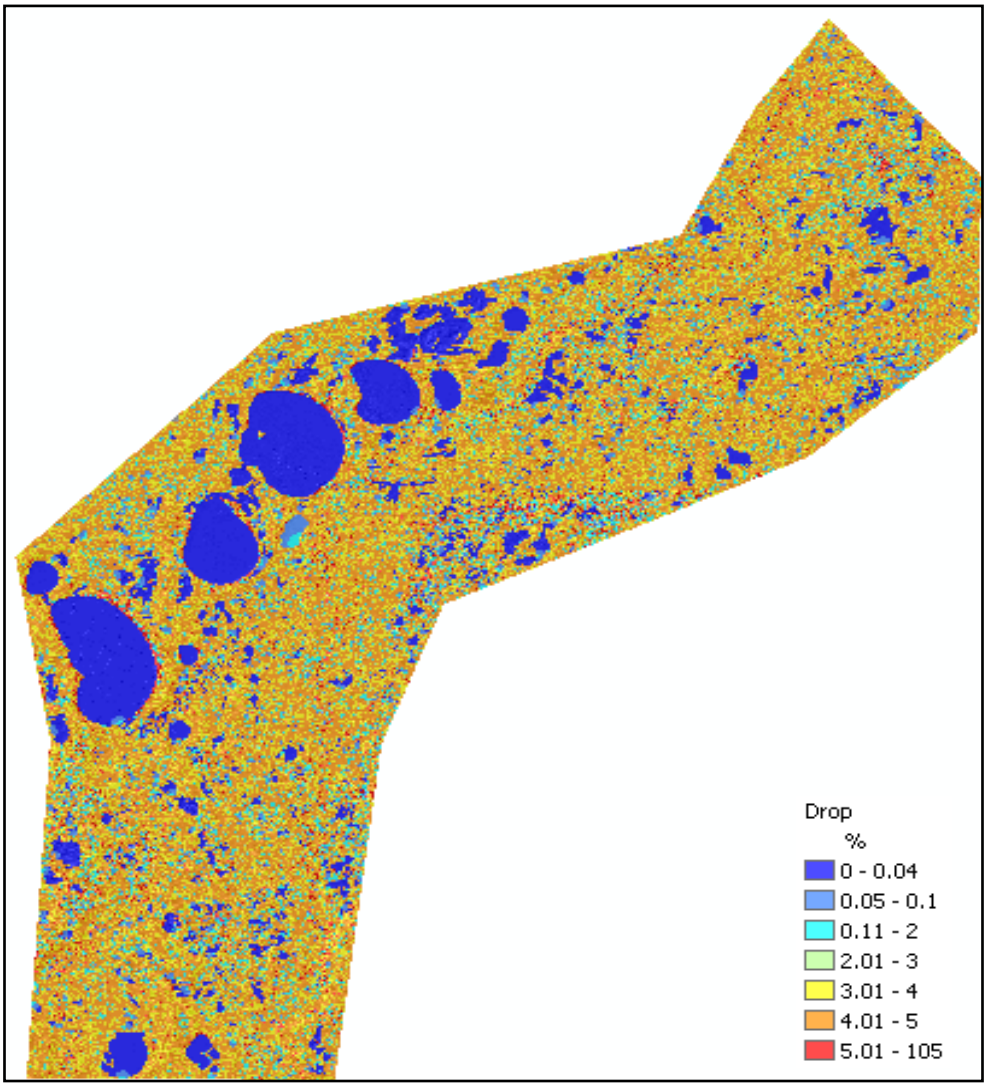



**Figure 17-2.** *Elevation drop grid highlighting flat areas or areas with minimal continuing change along a flow path (blue).*

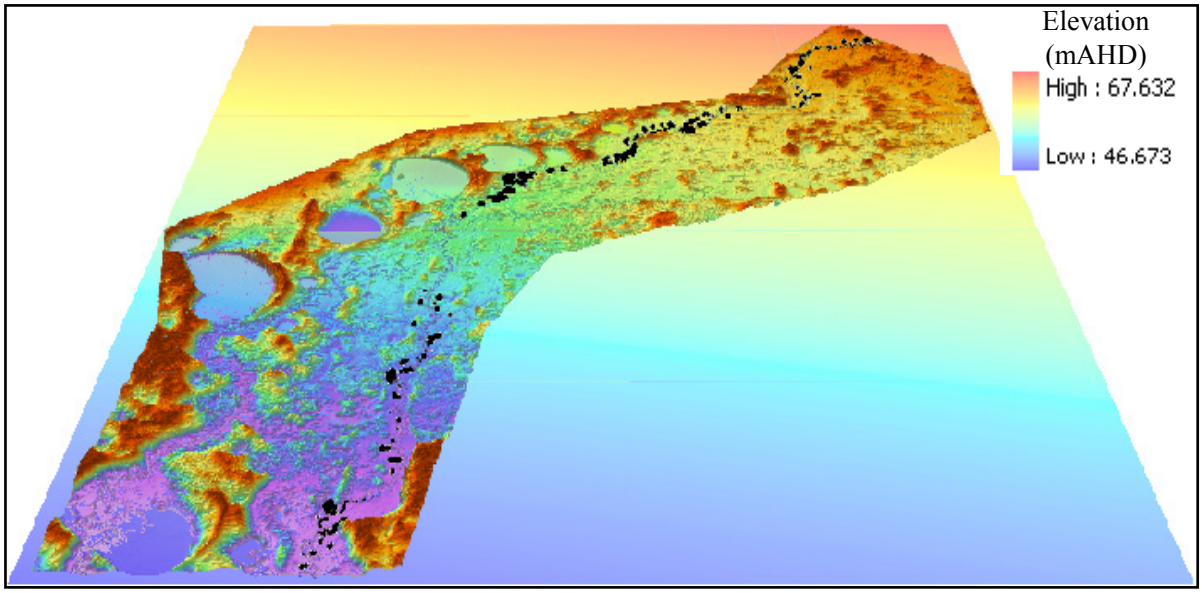



**Figure 17-3.** *Floodplain trend surface overlain by original DEM and flat areas or areas with minimal continuing change identified in the drop grid.*

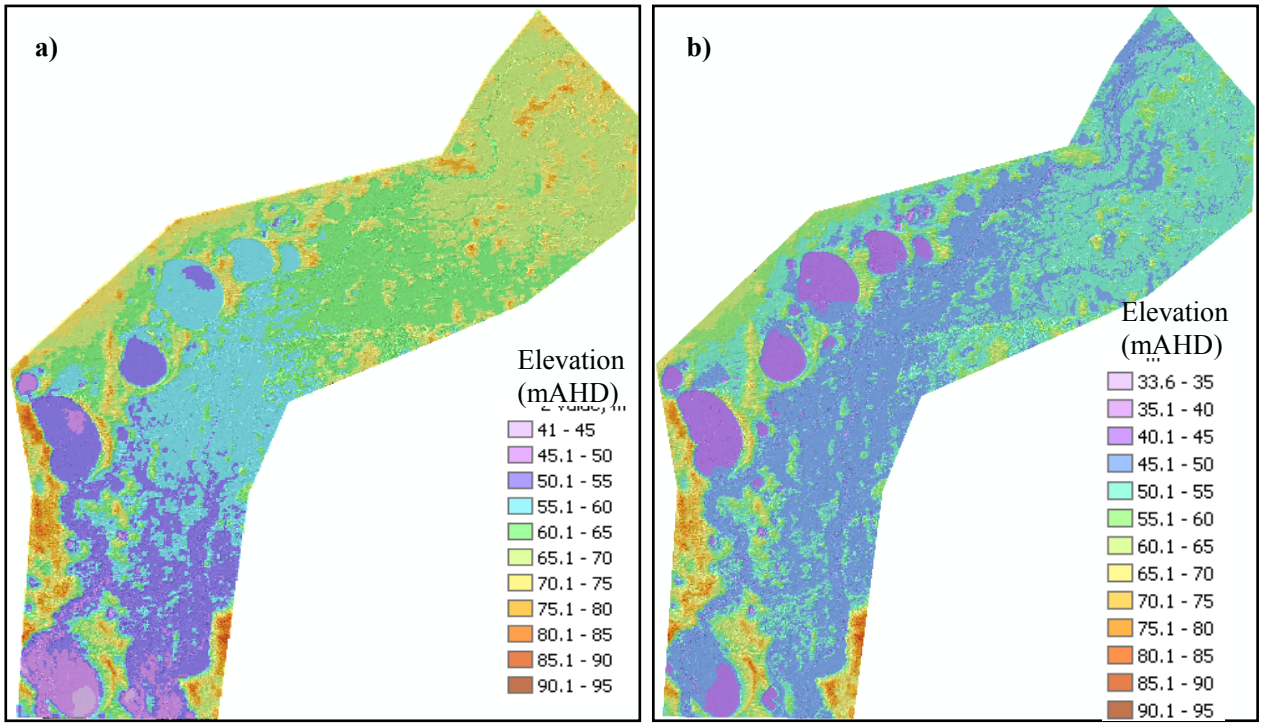



**Figure 17-4.** *Comparison between a) the original DEM and b) the levelled DEM. Note the difference between the AEM elevation slices.*

### 17.1.2.2 ***Validation***

The LiDAR-derived flood surfaces were validated by both qualitative and quantitatively. A qualitative comparison was made with Landsat TM 5 satellite images from the 1990, 2010 and 2011 floods as well as photographs of inundation from the 2010 and 2011 flood events. A quantitative comparison was made between three Landsat TM 5 scenes in 1990 and associated LiDAR-derived flood extents. Table 17-1 indicates the various Landsat scenes used in the validation process and the associated modelled flood level. Two Landsat scenes were required to cover the full study area as shown in Figure 17-5.

*Qualitative Assessment*

The predictive flood modelling was visually comparing to Landsat colour composite images (Bands 742) which presents vegetation in familiar green tones and helps discriminate moisture content in both vegetation and soil. Landsat dates were matched with recorded water level at a river gauge station (Site 425012) for that date. River level data was extracted from the NSW water real-time river data website[1]. River levels vary from 4.3 m depth, which is close to the point at which overbank flow initiates, to 7.0 m which is equivalent to considerable floodplain inundation.

Figure 17-6, Figure 17-7, Figure 17-8 and Figure 17-9 show the LiDAR predictive flood modelling and the actual flood record from Landsat images for four dates listed in Table 17-1. Visually there appears to be a very high correspondence in all four validation examples. Qualitative validation was also possible from photographs: 1) taken at known points along the Darling River as it was beginning to spill over the river channel in October 2010; and 2) taken from an aerial reconnaissance survey at the peak of flooding in March 2011. Dates associated with these photographs were matched to the water level at the river gauge station compared to the predictive flood modelling for that water level (Figure 17-10, Figure 17-11 and Figure 17-12).

[1] http://waterinfo.nsw.gov.au/water.shtml?ppbm=SURFACE_WATER&rs&3&rskm_url

**Table 17-1.** *Satellite images used to validate LiDAR-derived flood extents. The associated river level is also indicated, as is the type of analysis undertaken.*

| Date | River Level (m) | Analysis |
|---|---|---|
| 8/05/1990 | 6.1 | Qualitative; Quantitative |
| 25/06/1990 | 6.5 | Quantitative |
| 29/09/1990 | 6.9 | Qualitative; Quantitative |
| 2/12/1990 | 4.3 | Qualitative |
| 25/10/2010 | 5.18 | Qualitative |
| 28/10/2010 | 5.6 | Qualitative |
| 15/03/2011 | 7 | Qualitative |
| 16/03/2011 | 6.8 | Qualitative |

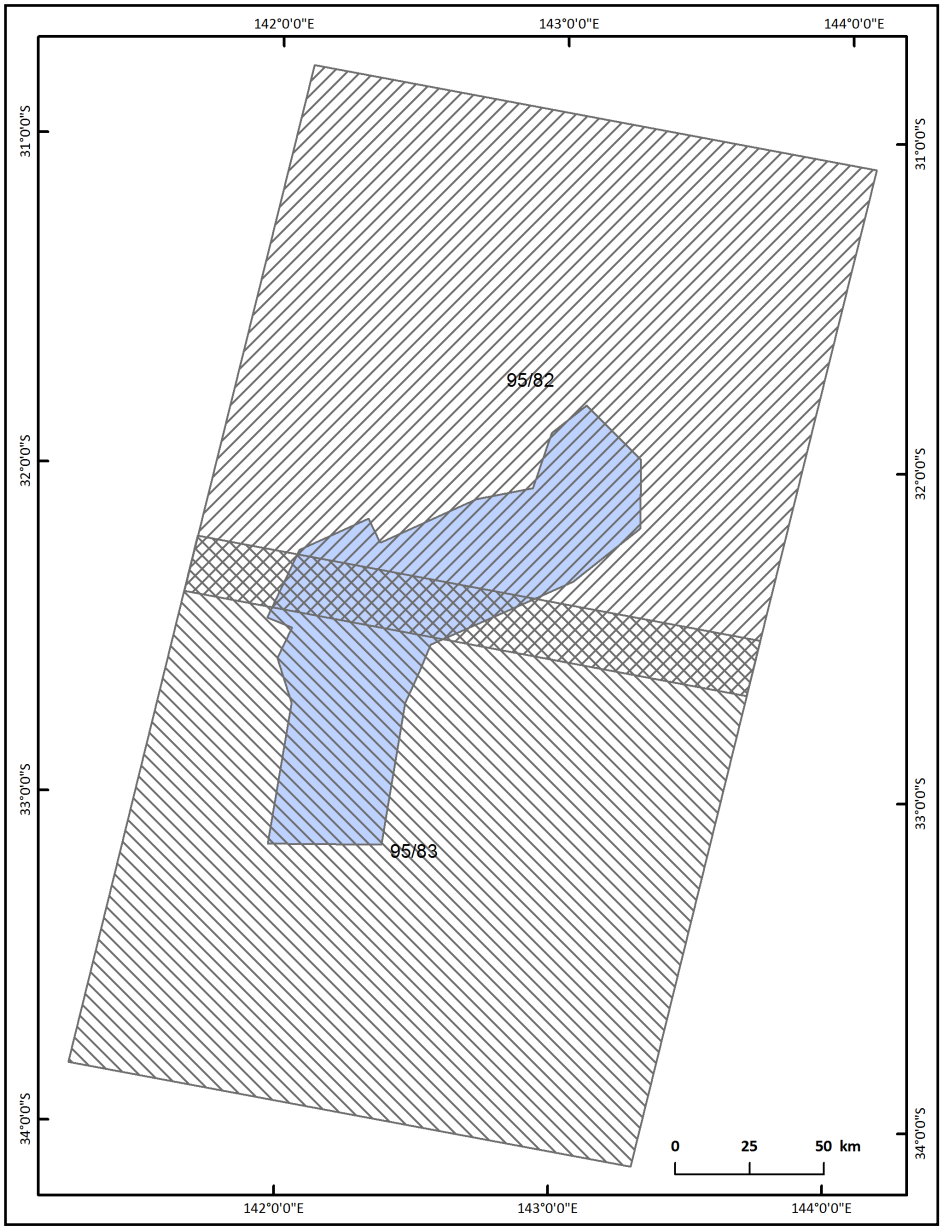



***Figure 17-5.*** *Location and extent of Landsat scenes 95/82 and 95/83.*

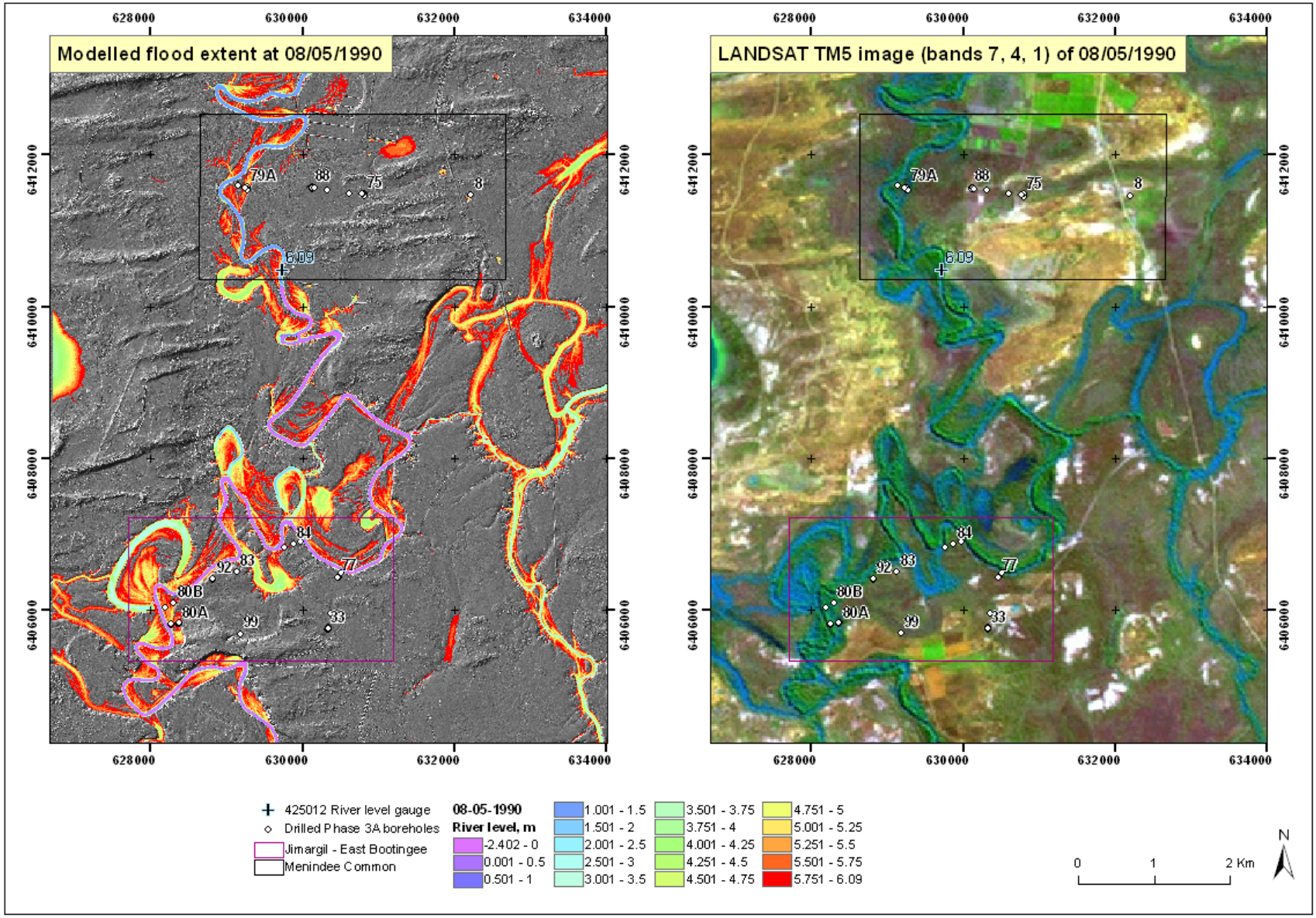



**Figure 17-6.** *Modelled flood extent (left) and Landsat image (right) showing area flooded on 8th May 1990, river level at 6.0 m at Site 425012 gauging station upstream of Weir 32. Boxes denote the borefields at Menindee Common (north) and Jimargil (south).*

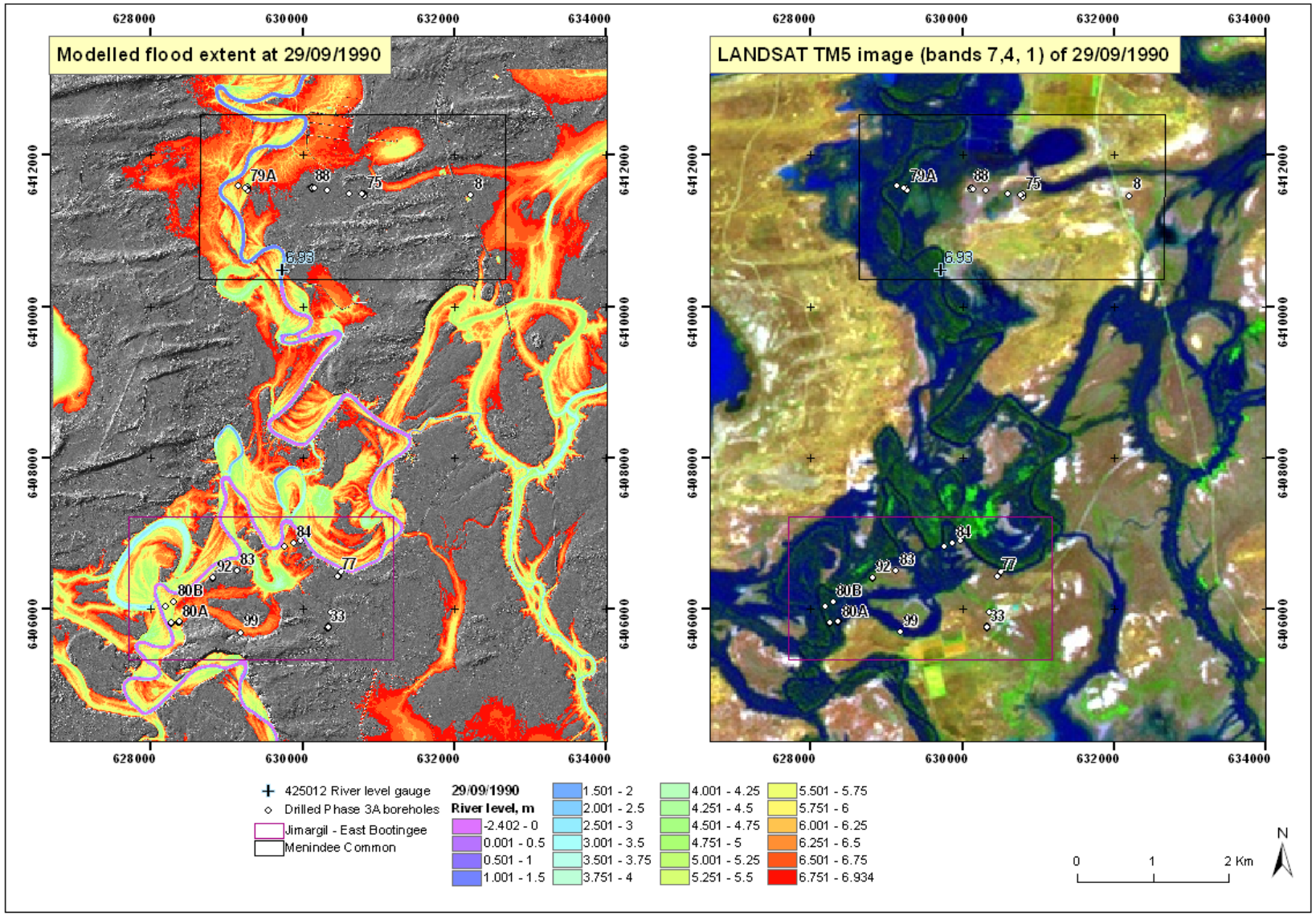



**Figure 17-7.** *Modelled flood extent (left) and Landsat image (right) showing area flooded on 29th September 1990, with the river level at 6.0 m at Site 425012 gauging station upstream of Weir 32. Boxes denote the borefields at Menindee Common (north) and Jimargil (south). Menindee Common is shown in greater detail in Figure 17-10 and Figure 17-11.*

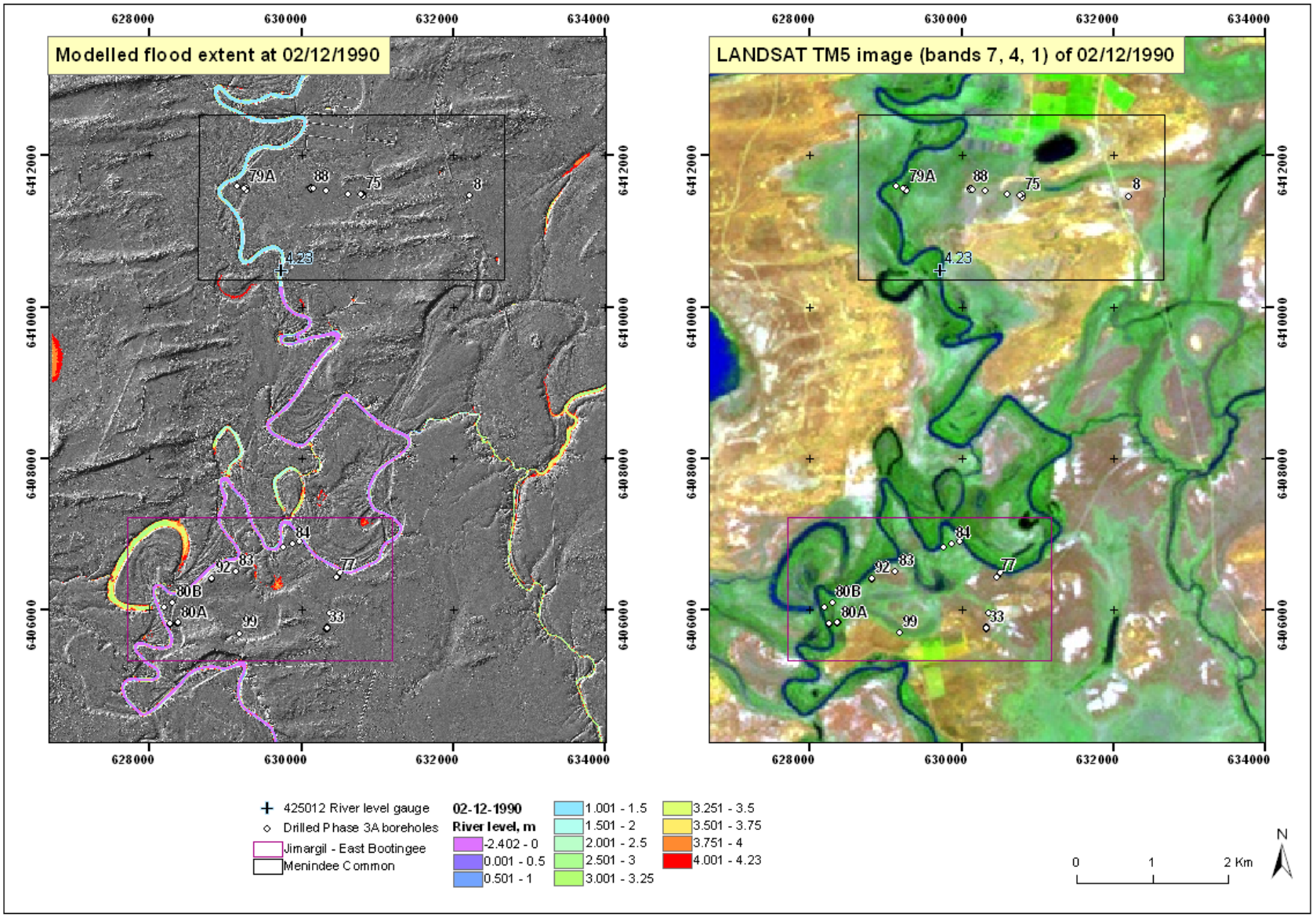



**Figure 17-8.** *Modelled flood extent (left) and Landsat image (right) showing area flooded on 2nd December 1990, river level at 4.3 m at Site 425012 gauging station upstream of Weir 32. The box relates to the extent shown in Figure 17-10 and Figure 17-11. Boxes denote the borefields at Menindee Common (north) and Jimargil (south).*

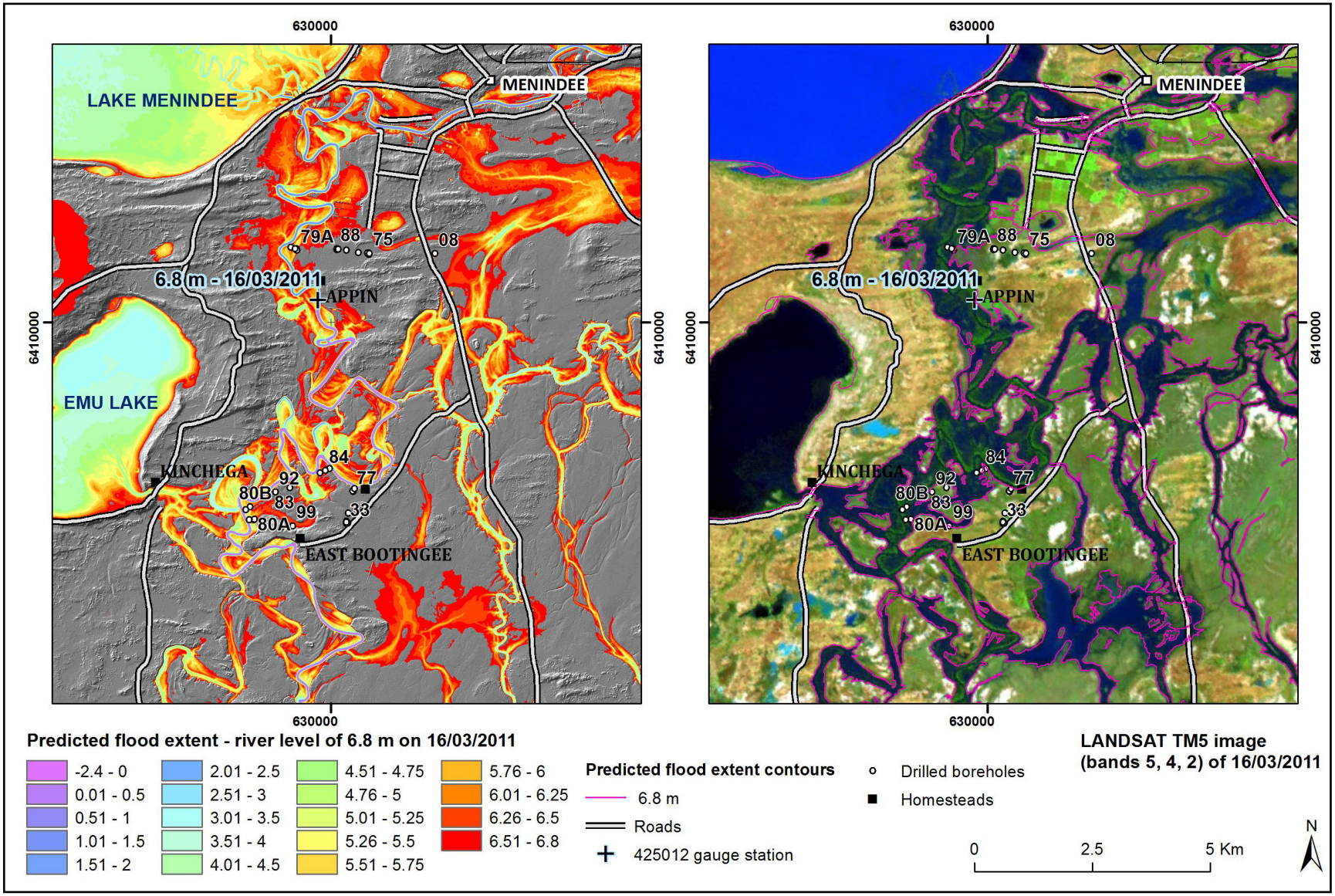



**Figure 17-9.** *Modelled flood extent (left) and Landsat image (right) showing area flooded on the 16th March 2011, with 6.8 m river level at Site 425012 gauging station upstream of Weir 32. The modelled flood extent is indicated as a pink outline in on the Landsat image.*

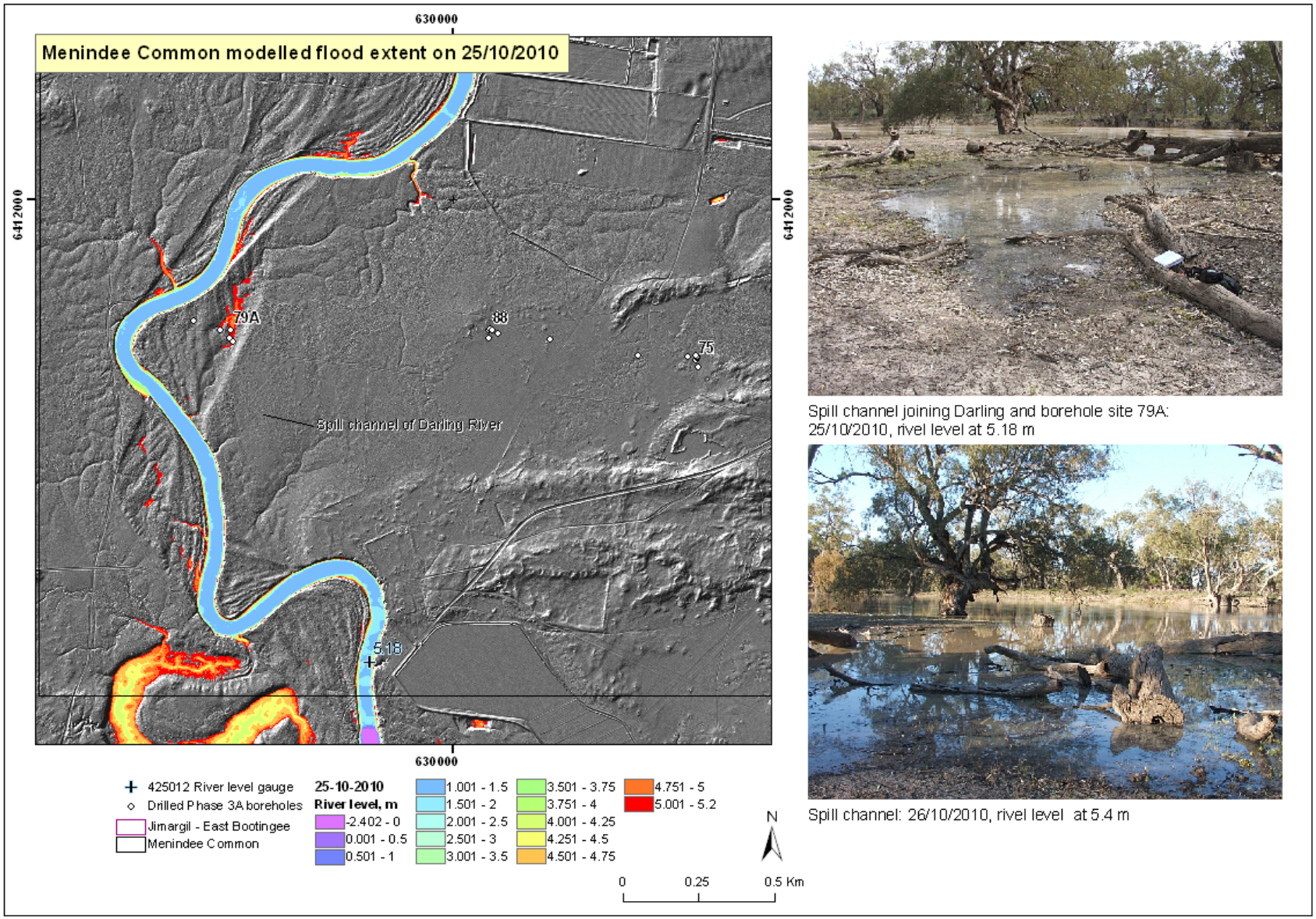



**Figure 17-10.** *Modelled flood extent at a river level of 5.18 m at Site 425012 gauging station upstream of Weir 32 recorded on 25th October 2010 (left) compared to on-ground photographs of inundation (right).*

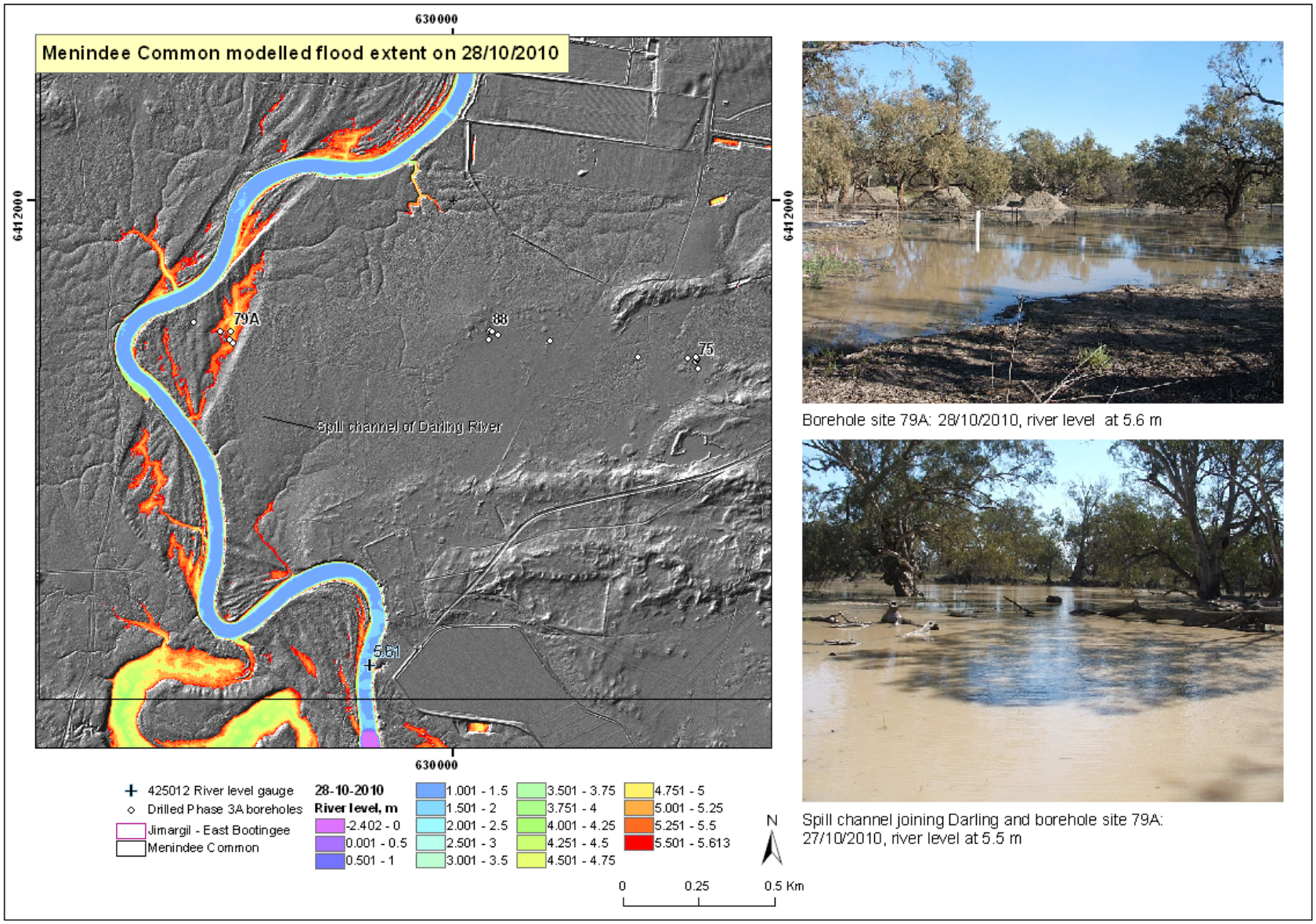



**Figure 17-11.** *Modelled flood extent at a river level of 5.6 m recorded at Site 425012 gauging station upstream of Weir 32 on 28th October 2010 (left) compared to on-ground photographs of inundation (right) at Menindee Common borehole site BHMAR79A.*

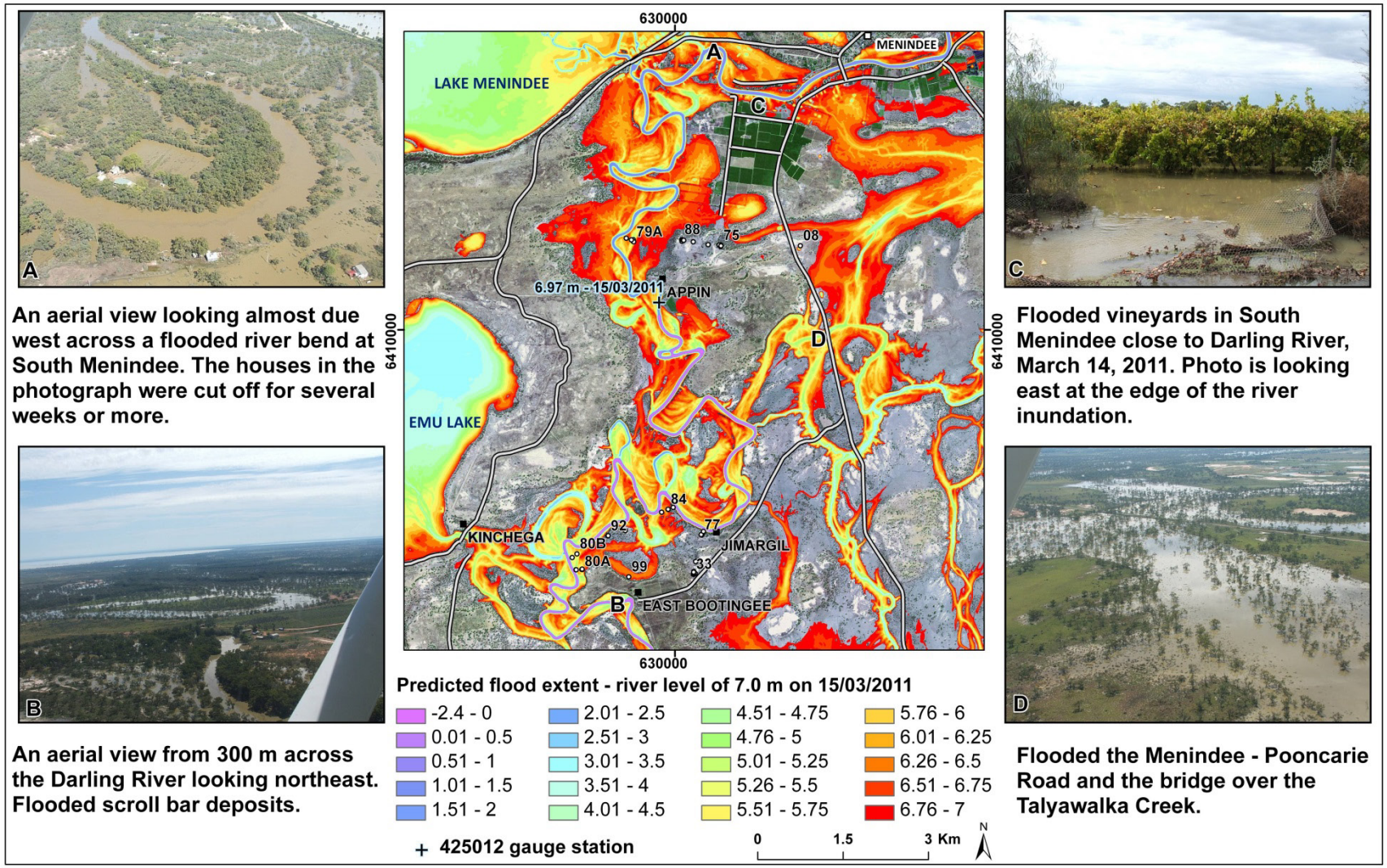



**Figure 17-12.** *Validation of modelled flood extent on the 15th March 2011, with a 7 m recorded river level (at Site 425012). Associated ground and aerial photographs are denoted.*

*Quantitative Assessment*

To complement the qualitative assessment, a quantitative comparison was made between mapped water in three Landsat TM 5 scenes as the corresponding LiDAR-derived flood extents. Water bodies were extracted from the Landsat scenes using version 8 of the water body extraction code. The water body extraction algorithm is described in Lymburner *et al*. (2008). The algorithm outputs three classes: open water, water-bare soil mixture and water-vegetation mixture. All three classes were combined for the purposes of the comparison as the LiDAR-derived flood extent does not discriminate between flooded trees and open water. The Landsat flood extent surface was resampled to the same grid size (5 m) as the LiDAR flood extent. Water information was then extracted from both datasets for each cell. This information was then compared, with four classes being identified: flooded/flooded match, non-flooded/non-flooded match, over-estimation of modelled flood extent, and under-estimation of modelled flood extent. This process was undertaken for three different dates and associated river level heights in 1990. Table 17-2 shows the percentage of the central area being validated that corresponded to the different classes for each. This is also shown spatially in Figure 17-13, Figure 17-14 and Figure 17-15.

***Table 17-2.*** *Results of a quantitative analysis of the LiDAR-derived modelled flood extents.*

| | **08/05/1990; 6.1 m** | **25/06/1990; 6.5 m** | **29/09/1990; 6.9 m** |
|---|---|---|---|
| **Comparison class** | **%** | **%** | **%** |
| Non-flooded areas match | 79.11 | 69.27 | 72.59 |
| Over-estimation of predicted flooded areas | 3.67 | 3.36 | 7.08 |
| Flooded areas match | 15.19 | 18.70 | 19.44 |
| Under-estimation of predicted flooded areas | 2.03 | 8.62 | 0.89 |

The observed match (flooded/flooded and non-flooded/non-flooded) between the two datasets ranges from 88-94% of the landscape. There are a number of possible explanations for this variability. This variability can be attributed to the location of the flood front with respect to river gauge point. For example, after a flood front has moved through, flood waters may still linger in low-lying areas of the landscape which would be inconsistent with predicted flood extent modelling.

Furthermore it is important to note that the central area of interest includes a number of regulated lakes. Water levels in these lakes can be quite disassociated with recorded river levels. For example, in Figure 17-14 there is considerable under-estimation evident in the Lake Wetherell area. This suggests that water was artificially held at quite high levels within this storage lake at the time the Landsat imagery was acquired; this cannot be accounted for in the simple bath-tub fill flood modelling. A similar observation is made at Lake Speculation and Spectacle Lakes, which are connected to Lake Menindee and Lake Cawndilla respectively; both of which are also regulated. Table 17-3 shows recorded lake levels corresponding to the various Landsat images. Note the relatively high water levels at Lake Wetherell in April.

**Table 17-3.** *Recorded water levels at Lakes Wetherell, Menindee and Cawndilla. No regulation exists between Lakes Menindee and Cawndilla hence water levels are the same within both lakes.*

| **Lake** | **08/05/1990; 6.1 m** | **25/06/1990; 6.5 m** | **29/09/1990; 6.9 m** |
|---|---|---|---|
| Lake Wetherell | 60.801 | 62.082 | 60.528 |
| Lakes Menindee & Cawndilla | 58.49 | 59.98 | 60.43 |

Over-estimation of the predicted flood extent is typically observed in areas outside the floodplain as observed in Figure 17-15. As the flood extent is effectively generated as a slice through the landscape at a particular elevation it is not surprising that low-lying areas beyond the floodplain are also being identified. These areas are easily identified as they are disconnected to the river. The accuracy of the modelled flood extent surfaces could be improved by developing an automated process for removing these areas.

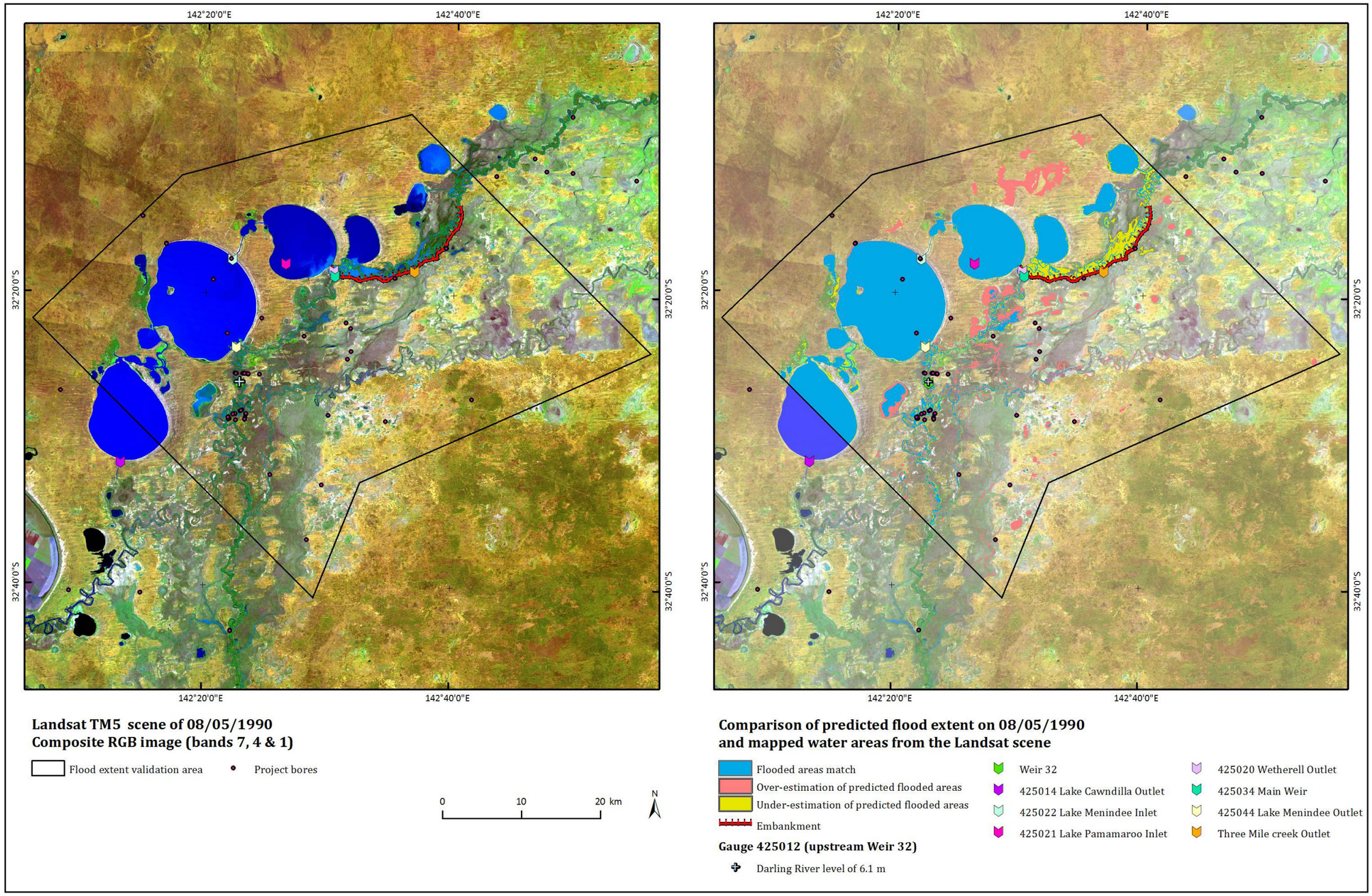



**Figure 17-13.** *Quantitative comparison between Landsat and LiDAR-derived flood extents on 8th April, 1990. Left: Landsat (bands 741) imagery (left) and right: results of comparison.*

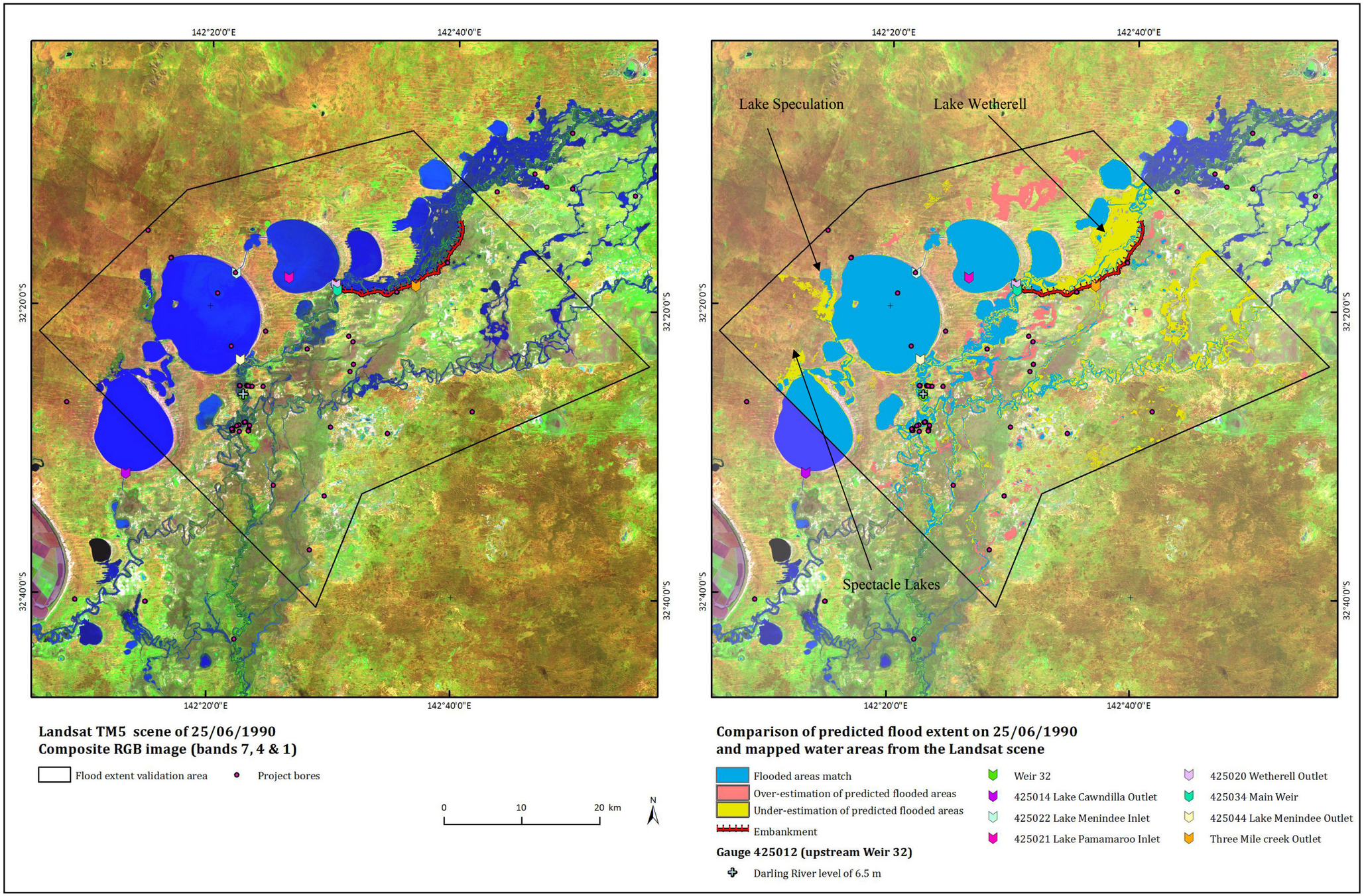



**Figure 17-14.** *Quantitative comparison between Landsat and LiDAR-derived flood extents on 25th June, 1990. Left: Landsat (bands 741) imagery (left) and right: results of comparison.*

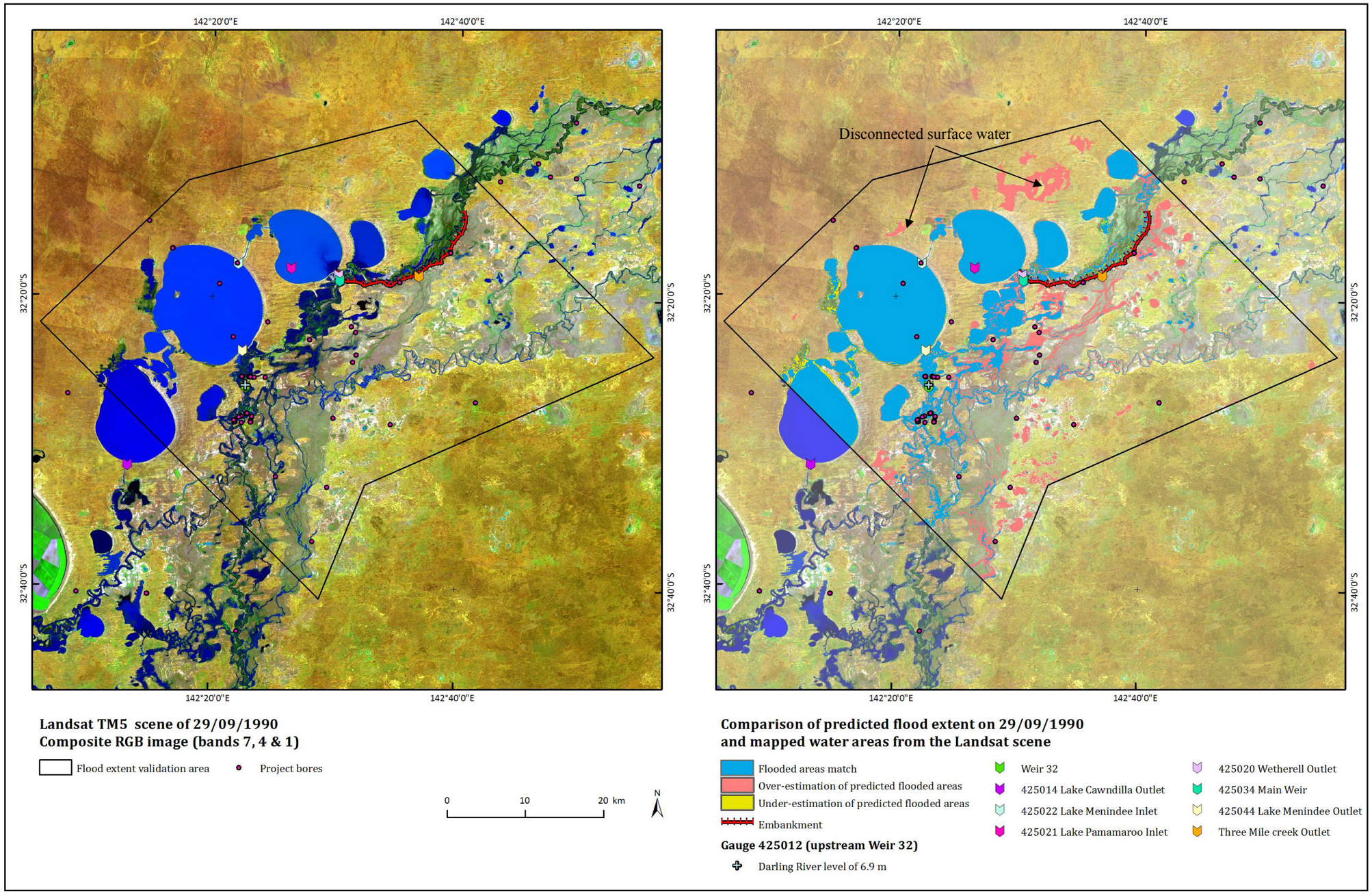



**Figure 17-15.** *Quantitative comparison between Landsat and LiDAR-derived flood extents on 29th September, 1990. Left: Landsat (bands 741) imagery (left) and right: results of comparison.*

#### 17.1.2.3 *Limitations*

This flood inundation modelling only shows the theoretical extent of inundation due to river-level rise based only on elevation and does not take into account flow pathways and impediments to flow or loss of water due to evaporation, soil wetting, and leakage via faults or surface cracks. This may lead to an overestimation however results of the quantitative validation suggest this only affects a small percentage of the landscape. However modelling the impact of flooding in and around the Menindee Lakes is problematic as the lakes are regulated and do not necessarily fill under natural flood conditions.

The accuracy of flood modelling decreases with distance from the river gauge station. Validation of the methodology in the central section of the project area indicates good accuracy. More broadly, there appears to be under-estimation in the north, particularly in relation to Talyawalka Creek; and over-estimation in the south, along both the Darling River and the Darling Anabranch (Figure 17-16). In these areas, flood extent can instead be gained from the Landsat water classification.

There are also limitations with utilising Landsat imagery for flood modelling. Landsat has a repeat cycle of approximately every 16 days, and is affected by cloud cover – both of which limit the number of suitable scenes for analysis. As a consequence of this, Landsat images are not always available for key flood events. Landsat also has a spatial resolution of 30 m as opposed to the LiDAR DEM using in this study (5 m spatial resolution). This causes issues with mixed pixel responses, for example when a single pixel is in reality both wet and dry. The water body extraction algorithm can only essentially assign wet or not wet. Finally, the ability of Landsat to detect surface water can be affected by dense canopy cover (Wang *et al*., 2002). Only the Darling River channel is associated with anything other than open forest hence this is unlikely to affect the analysis considerably. These products are also unable to provide any information about the depth of water inundating any surface which is a strength of the LiDAR products.

#### 17.1.2.4 *Recommendations*

The accuracy of the modelled flood extent surfaces could be improved by developing an automated process for removing areas disconnected from the river. Alternative methods for example, generating continuous surface flow networks (e.g. Poppenga *et al*., 2010) in discretized stretches of the river, could also be trialled in the northern and southern portions of the BHMAR Project area to reduce over- and under-estimation. Hydrodynamic modelling could also be developed, utilising the extensive data obtained over the course of the BHMAR Project.

#### 17.1.2.5 *Application*

Operationalisation of a groundwater extraction or MAR scheme will require installation of new infrastructure including bores, pumps, treatment plant(s), pipelines etc., some of which will necessarily be located on the floodplain and may be subject to flood inundation. Consequently, the LiDAR predictive flood modelling could be used to assist with engineering design work in the central, priority areas, e.g. Jimargil and Lake Menindee proposed borefields. Beyond this central area, confidence in the accuracy of modelling diminishes. Landsat-derived flood extents were used for the northern and southern sections to provide an indication of flood extent during previous events (i.e. 1990 flood). This was useful for assessing whether flood waters previously came into contact with mapped faults (and therefore may again in the future), facilitating groundwater recharge. The Landsat products were also used to assess when and roughly how often water was held in the various lakes.

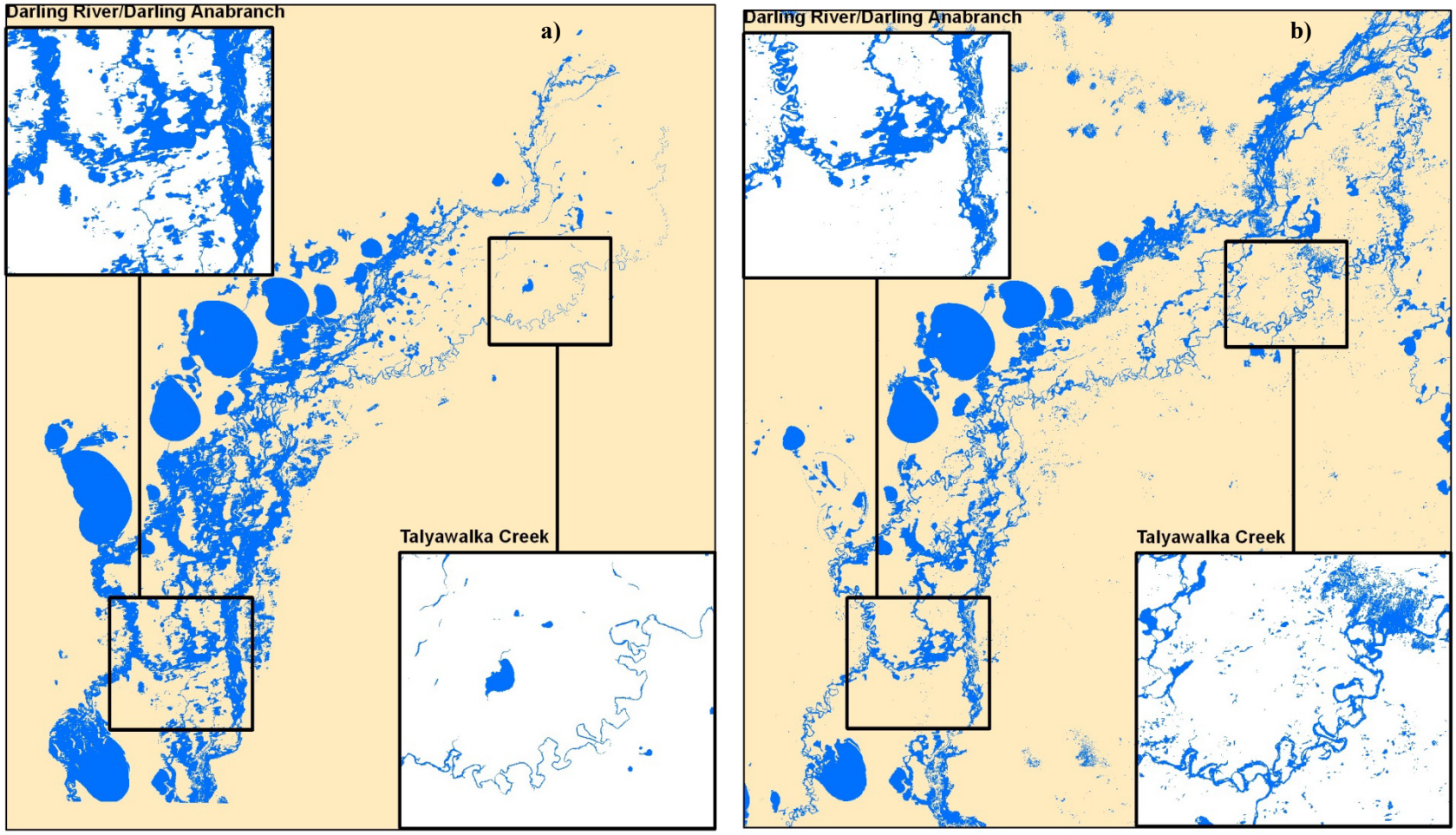



**Figure 17-16.** *Comparison between the a) LiDAR-derived and b) Landsat-derived flood extent for the 1990 event. The LiDAR image used a water level of 7.4 m which corresponded to the highest recorded level for 1990 (on 25 July) and the Landsat image incorporated 9 scenes spread relatively evenly over the course of the year. The basis for the Landsat-derived flood extent is discussed in Section 17.2.3.4.*

## 17.2 VEGETATION HEALTH AND GROUNDWATER DEPENDENCE MAPPING

### 17.2.1 Introduction

The Broken Hill Managed Aquifer Recharge (BHMAR) Project was tasked with assessing whether a sustainable groundwater resource extraction approach, including Managed Aquifer Recharge (MAR) is a feasible option for securing Broken Hill's water supply in times of drought, instead of using surface water stored in the Menindee Lakes. Under NSW legislation, any changes to the management of the lakes must consider environmental, social and economic issues. The health and condition of iconic native Australian riparian and floodplain vegetation, principally River Red Gums and Black Box, is consequently an important consideration.

Ideally a thorough investigation of vegetation dynamics would involve detailed plot scale vegetation surveys, visual assessment techniques such as crown size, crown density, epicormic growth and dead branches (e.g. Eldridge *et al*., 1993; MDBC, 2003; Doody &Overton, 2009) and ecophysiological studies (e.g. Doody *et al*., 2009). However due to the time constraints inherent in this project, this was not possible. Instead a GIS/remote sensing approach was developed to identify relative changes in vegetation health both spatially and temporally, with minimal field validation.

As field studies are often both labour intensive and time consuming, a number of authors have used minimal field study data to calibrate or validate a more remotely sensed approach (e.g. Fuller *et al*., 1997; Wagenseil & Samimi, 2007; Cunningham *et al*., 2009). Landsat reflective bands and Normalised Difference Vegetation Index (NDVI) were used in conjunction with other environmental predictor variables to successfully map River Red Gum health along the Murray River (Cunningham *et al*., 2007; 2009). While percentage canopy cover is routinely used to assess tree health (e.g. Doody *et al*., 2009), it can also be obtained from LiDAR Foliage Projected Cover (FPC) and in conjunction with LiDAR Canopy DEM (CEM) data, to provide high-resolution vegetation structure mapping.

Two different remotely sensed datasets were used in the vegetation assessment, namely LiDAR and Landsat series of satellites (5 and 7). The Landsat series satellites were combined to provide over 150 observations of the study area between 1987 and 2011. Canopy Digital Elevation Model (CEM) and Foliage Projected Cover (FPC) data generated from LiDAR were combined to generate a Vegetation Structure dataset. This was used to characterize the spatial and temporal behaviour of woody vegetation within the study area. The multi-temporal dynamics of the woody vegetation canopy were then compared to the availability of different water sources i.e. groundwater, river water, rainfall, flooding. An excellent match was observed between the Landsat derived vegetation structural classes and those mapped using the high resolution LiDAR.

This section will provide details about the three input datasets, specifically acquisition, basic processing, advanced processing, validation and derived products, and other datasets used in the integrative interpretation process.

### 17.2.2 Acquisition, Basic Processing and Existing Datasets

#### 17.2.2.1 *Field sampling*

Two separate vegetation sampling and observation field trips were undertaken in May 2010 and August 2011. A total of 213 sites were visited, the distribution of which is shown in Figure 17-18. At each site, twigs, small branches, burrs and seed pods were sampled from different vegetation species, including trees, shrubs and grasses. Site photos were also taken, recording vegetation structure and landform. Soil samples were also taken at each site and are discussed in more detail in Section 12.1. The structural information obtained during these trips was used to validate the LiDAR derived vegetation structural mapping discussed in Section 17.2.3.1. The detailed site records are available in Appendix 3 (Apps *et al*., 2012f).

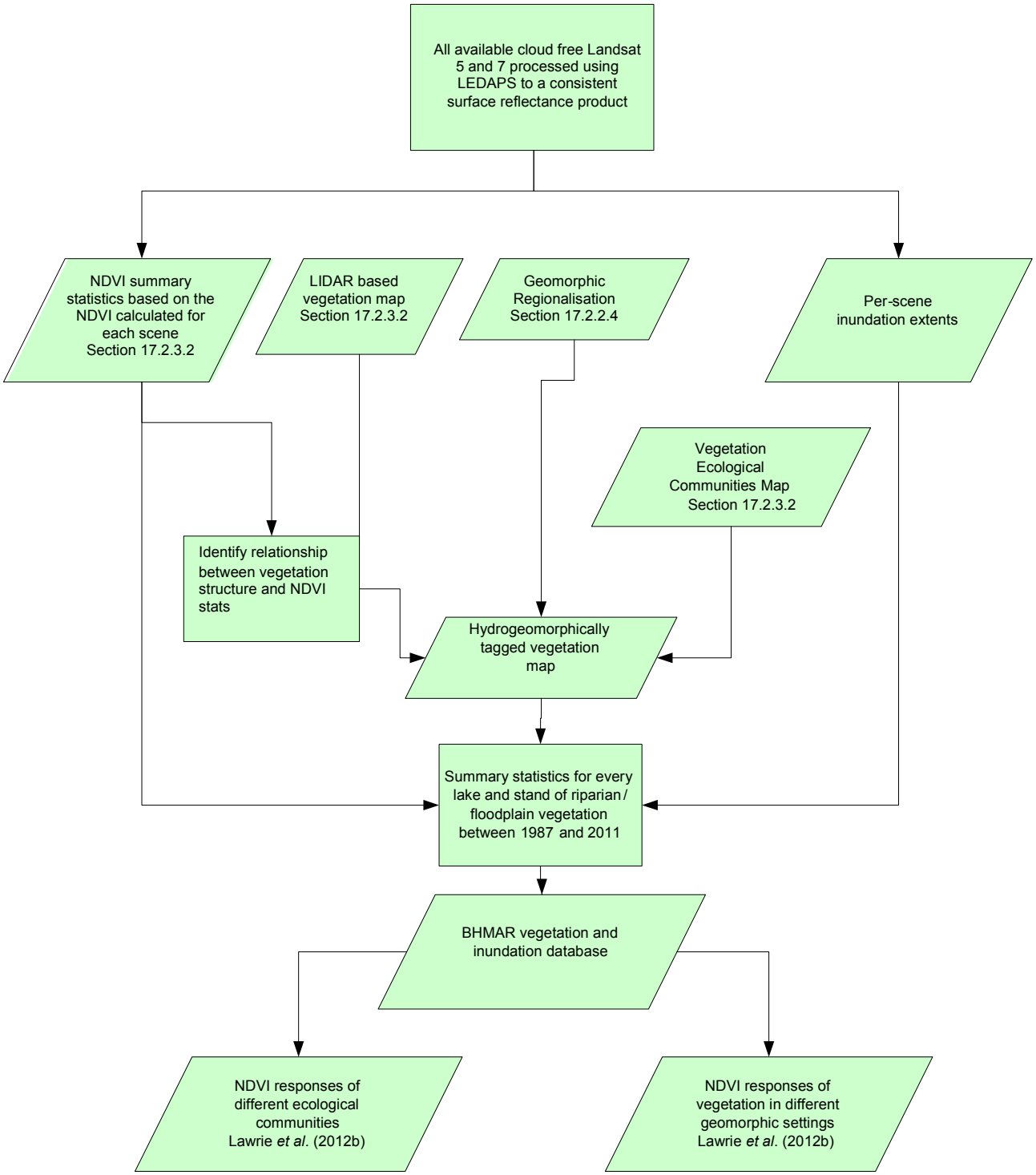



**Figure 17-17.** *Flow chart describing the workflow for analysing the remote sensing data.*

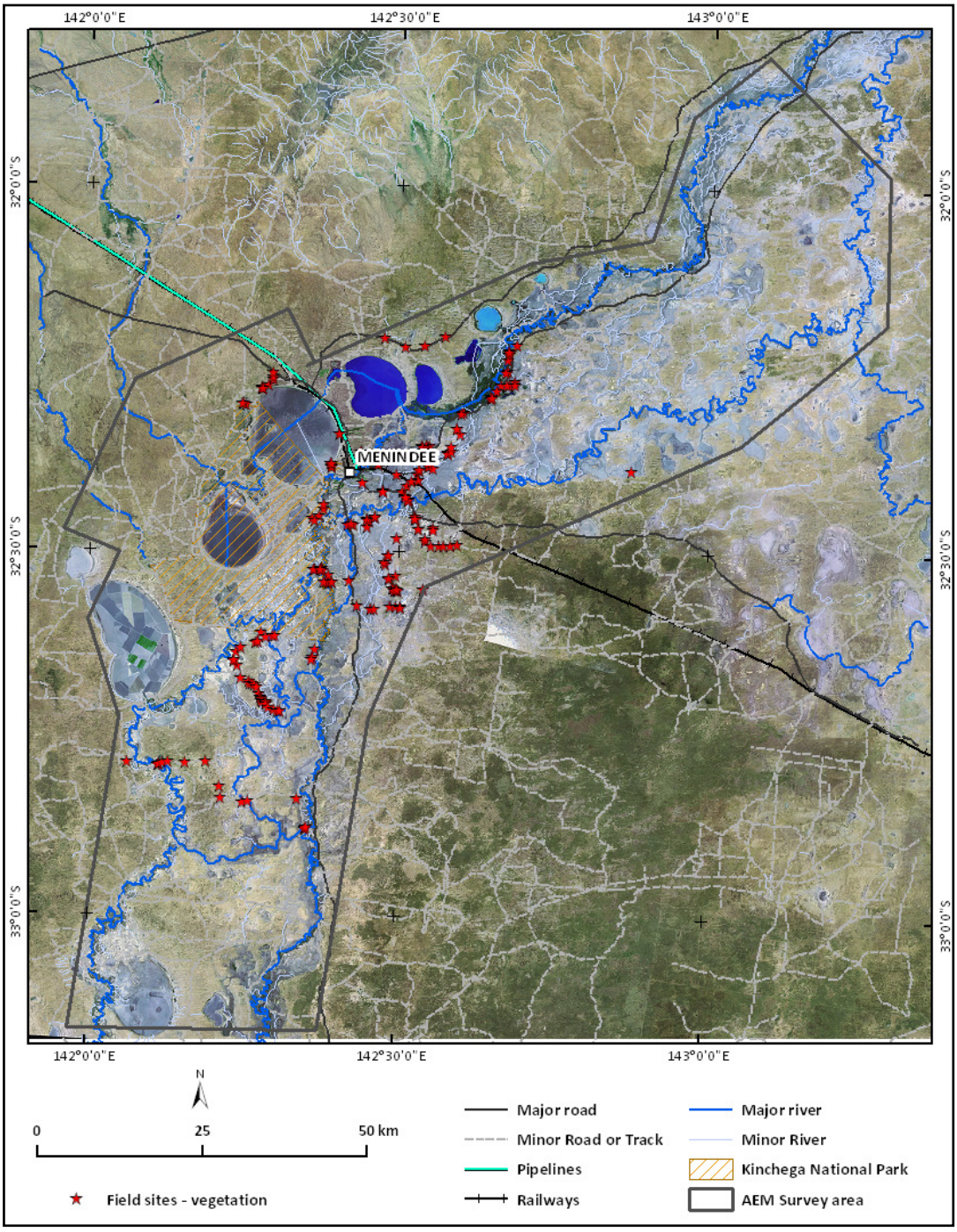



**Figure 17-18.** *Location of vegetation field sites within the BHMAR study area.*

### 17.2.2.2 ***LiDAR***

High resolution LiDAR imagery was acquired by AAMHatch Pty Ltd. for the study site between June and September 2009, which included Digital Elevation Model (DEM), Canopy Digital Elevation Model (CEM) and Foliage Cover Model (FCM) surfaces. The DEM, CEM and FCM have spatial resolutions of 5 m, 1 m and 10 m respectively. The total survey covers an area of ~7,856 km$^2$ on the Lower Darling River, downstream from Wilcannia. Acquisition was undertaken between June 19$^{th}$ and August 5$^{th}$ 2009. A Leica ALS50-II sensor was used for this project. This sensor is capable of detecting multiple returns, with a minimum of four potential returns for each outbound laser pulse and can record the intensity of each return. The planned point density for the survey was an average density of two points per m² with actual point spacing average of 0.71 m across the 1032 m wide swath. The maximum cross and long track is 1.27 m and 1.22 m. The vertical accuracy is ± 0.15 m and the horizontal accuracy is ± 0.25 m. For more details pertaining to the acquisition of the LiDAR, refer to Section 5 or Appendix 14 (Lawrie *et al*., 2012f). This

data was provided as a 1 m grid that was re-sampled to 5 m using a bilinear interpolation. General capture specifications are shown in Table 17-4.

**Table 17-4.** *LiDAR survey data acquisition parameters as reported by AAMHatch Pty Ltd.*

| **Metadata Elements** | |
|---|---|
| **Characteristic** | **Description** |
| Device Name | Leica ALS50-II S/N 091 |
| IMU Used | Honeywell UIRS S/N 56016277 |
| Acquisition Start Date | 19 June 2009 |
| Acquisition End Date | 05 August 2009 |
| Number of Runs | 208 |
| Number of Cross Runs | 6 |
| Flight Direction | Various Directions |
| Flying Height (AGL) | 1800 m |
| Half Scan Angle | 16 degrees |
| Swath Width | 1032 m |
| Sidelap | 10% |
| Average Point Spacing | 2 pts/$m^2$ |
| Laser Pulse Rate | 127.5kHz |
| Laser Pulse Mode | Multi-pulse |
| Laser, Max Number of Returns per Pulse | Up to Four pulses, $1^{st}$, $2^{nd}$, $3^{rd}$, and $4^{th}$ |
| Laser Intensity | Supplied on all returns |
| Laser footprint size @ nadir, level ground | 0.41 m |
| Grids | 1 m grid cell size Digital Elevation Model (DEM) generated from ± 0.294 m Accuracy (95%) LiDAR |
| Grids | 1 m grid cell size Canopy Elevation Model (CEM) generated from ± 0.294 m Accuracy (95%) LiDAR |
| Grids | 10 m grid cell size Foliage Cover Model (FCM) generated from ± 0.294 m Accuracy (95%) LiDAR |
| Data thinning | Model Key points ±0.15 m RMSE |
| File Format | LAS |
| Horizontal Datum | GDA94 |
| Vertical Datum | AHD using Local Geoid Model Ausgeoid98 |
| Map Projection | MGA Zone 54 |
| Vertical Accuracy Requirement | 0.294 Fundamental Vertical Accuracy, 95% Confidence Level (RMSE*1.96) |
| Horizontal Accuracy Requirement | 0.432 Fundamental Vertical Accuracy, 95% Confidence Level (RMSE*1.7308) |
| System Calibration Certification | Leica Geosystems AG (SN091PII+ Cal Report 080317)17 March 2009 |

CEM derived from LiDAR provides exact height values (Figure 17-19) at 1 m horizontal resolution. The CEM was produced as 1 m ESRI ArcGIS binary grids using ArcGIS with the following methodology:

- All ground surface derived using natural neighbours interpolation [G] (Floating Point)
- First return vegetation surface derived using natural neighbours interpolation [V1] (Floating Point)
- Height in metres above ground of first vegetation returns [V1] - [G] = [H] (Floating Point)
- Mask of all vegetation ALS returns with 1 m buffer, reclassified to 0 outside mask and NoData inside [M] (Integer)
- Mosaic of canopy height surface and vegetation mask [H] + [M] = CEM (Floating Point)

FCM derived from LiDAR provides a percentage foliage cover for each 10 m cell. The FCM was produced as 10 m ESRI ArcGIS binary grids using ArcGIS with the following methodology:

- Count of all vegetation returns per 10 m cell [V] (Integer)
- Count of total Airborne Laser Scanning (ALS) returns per 10 m cell [A] (Integer)
- Proportion of all vegetation to total ALS returns expressed as a percentage ([V] / [A]) * 100 = FCM (Floating Point; McGaughey, 2007).
- Foliage cover is defined for each stratum as 'the proportion of the ground, which would be shaded if sunshine came from directly overhead' and includes branches and leaves (Figure 17-19).

The provider reports vertical accuracy of ± 0.15 m for the CEM based on comparison with 473 surveyed field sites. Much greater error is however observed in the Lake Wetherell area due to weak laser backscatter from the saturated ground conditions. A similar observation was made by Hopkinson *et al*. (2004). An assessment of the vertical accuracy of the DEM surface is discussed in Section 17.1.2.1). It is estimated the CEM has a vertical accuracy of ± 0.18 m.

A number of factors can influence the likelihood of laser pulse penetration and backscatter including foliage orientation, height, density, and ground surface type. This typically leads to an underestimation of canopy height (e.g. Hopkinson *et al*., 2004; Gaveau & Hill, 2003) in some instances as great as 2 m (e.g. Wasser *et al*., 2013). Regardless of this systematic bias, authors typically report a reasonable match ($R^2$ >0.9) between LiDAR canopy height and field measurements (e.g. Cartus *et al*., 2012; Hopkinson *et al*., 2004).

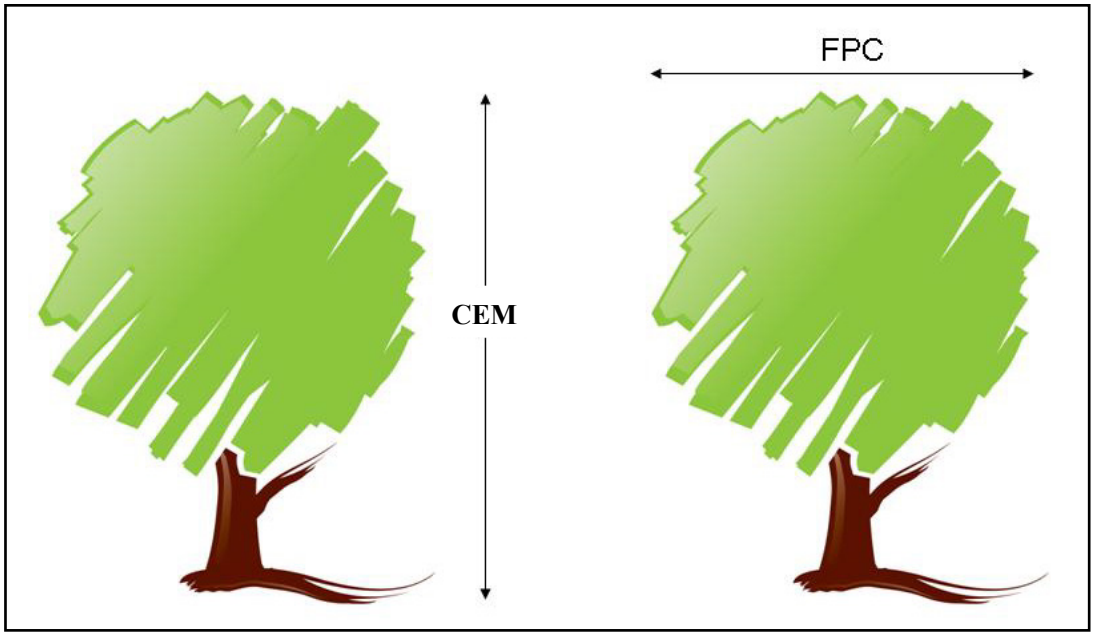



**Figure 17-19.** *FPC and CEM measurements.*

CEM and FPC were used in the generation of a high-resolution vegetation structural map as discussed in Section 17.2.3.1 in conjunction with field validation (Section 17.2.2.1).

### 17.2.2.3 ***Landsat***

Landsat 5 satellite was launched into a repetitive, circular, sun-synchronous, near-polar orbit at an altitude of 705 km. Each orbit takes approximately 99 minutes and just over 14.5 orbits occur each day. This results in a 16-day repeat cycle. The Landsat 5 thematic mapper (TM) was launched in 1982 and ceased operation in 2011, consequently almost 30 years-worth of TM imagery has been archived. Landsat TM measures six bands of radiation in the visible and infrared (IR) range of the electromagnetic spectrum (EMS) at a spatial resolution of 30 m, and a single band in the thermal range with a spatial resolution of 120 m. Table 17-5 summarises the number of Landsat scenes from each year acquired for the project. All Landsat scenes were pre-processed using LPGS version 11.4.0 and radiometrically corrected using LEDAPS version 1.0.4.

**Table 17-5.** *Number of Landsat scenes acquired for each year. Note some years have very few suitable available scenes which influences the degree of confidence in the derived results.*

| Year | Row 82 | Row 83 |
|---|---|---|
| 1987 | 2 | 2 |
| 1988 | 7 | 10 |
| 1989 | 7 | 9 |
| 1990 | 9 | 9 |
| 1991 | 5 | 3 |
| 1992 | 7 | 7 |
| 1993 | 9 | 10 |
| 1994 | 10 | 6 |
| 1995 | 8 | 5 |
| 1996 | 7 | 5 |
| 1997 | 10 | 8 |
| 1998 | 4 | 1 |
| 1999 | 3 | 1 |
| 2000 | 7 | 7 |
| 2001 | 5 | 7 |
| 2002 | 12 | 12 |
| 2003 | 2 | 7 |
| 2004 | 9 | 10 |
| 2005 | 5 | 8 |
| 2006 | 7 | 5 |
| 2007 | 8 | 6 |
| 2008 | 3 | 3 |
| 2009 | 7 | 6 |
| 2010 | 2 | 1 |
| 2011 | 3 | 2 |
| Total | 158 | 150 |

#### 17.2.2.4 ***Geomorphic Regionalisation***

The study area was divided into a series of sub-regions or populations (Figure 17-20), in order to compare Landsat reflectance signatures of similar vegetation communities. This included identifying the floodplain, riparian channel, lake-fringing vegetation, lake inundation zones and other more specific areas of interest.

Existing landform (geomorphic) mapping was used to identify the floodplain and riparian zones. As part of the BHMAR Project, a landform map of the whole study area was compiled at approximately 1:80,000 for a usable scale of 1:100,000. For more details about the landform mapping refer to Section 17.4.1of this report. Both the floodplain and riparian zone are subject to different water regimes (low flow, bank full and overbank flow) depending on their location in the system. Consequently, these features were separated into river and creek reaches. Historic lake level data was used to generate the lake extents (Full Supply Level - FSL) of Menindee, Cawndilla, Pamamaroo, Wetherell and Tandure using the 5 m LiDAR DEM. Similarly, the 2010/11 maximum extent and the historic maximum extent were generated. For all other lakes, the fringing vegetation was manually digitised from a SPOT image; specific areas of interest were likewise generated.

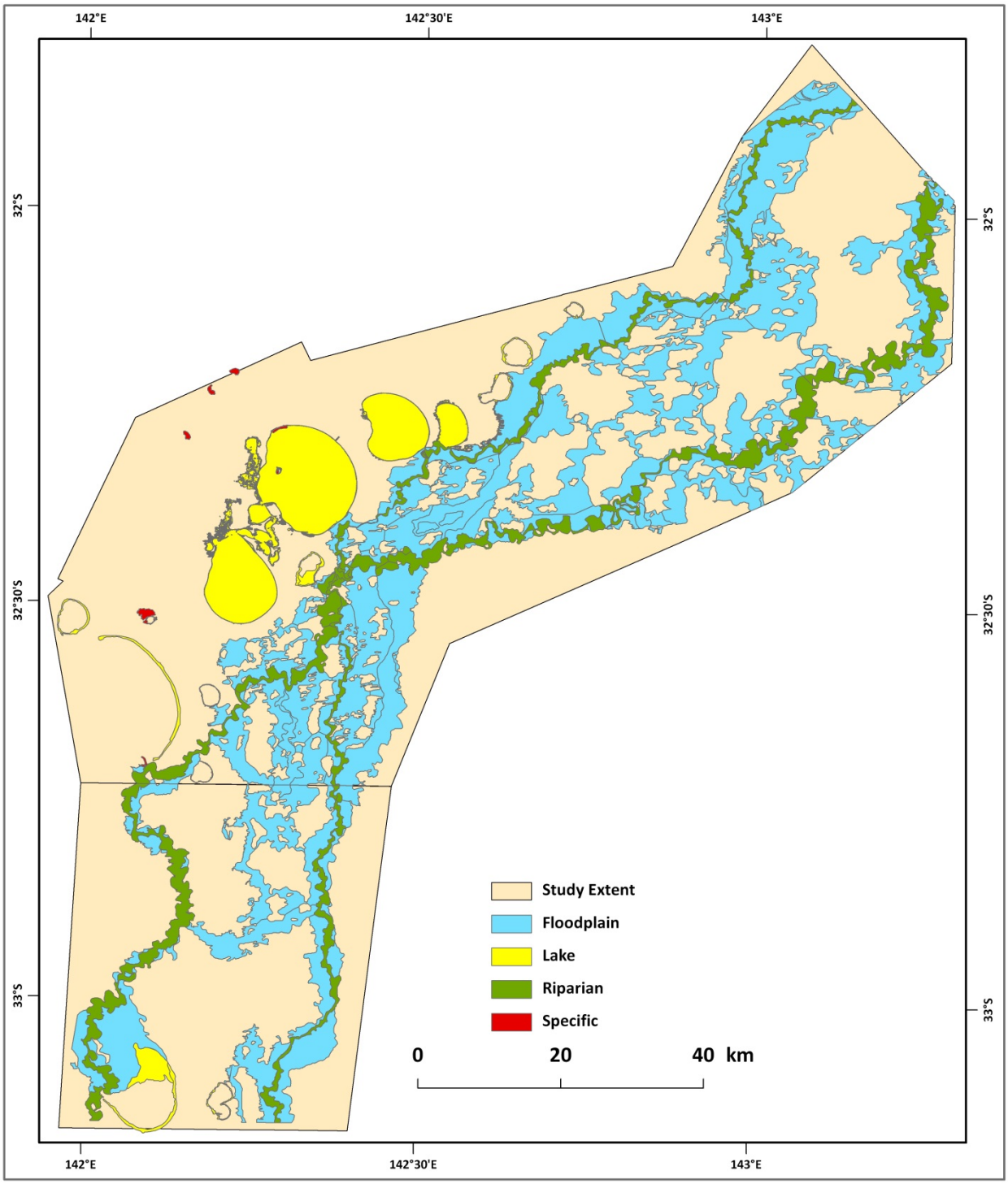



**Figure 17-20.** *Geomorphic-based regionalisation.*

### 17.2.3 Advanced Processing and Derived Products

#### 17.2.3.1 *LiDAR-derived Vegetation Structure*

High resolution LiDAR imagery was acquired for the study site including Digital Elevation Model (DEM), Canopy Digital Elevation Model (CEM) and Foliage Cover Model (FCM) surfaces (see Section17.2.2.2). These values were then grouped into 11 height ranges and associated growth forms, (sub-) stratum codes and descriptions, and structural formation classes using ESCAVI (2003) and Walker & Hopkins (1990). For example, a CEM value of 15.5 m would result in that cell being classified as height class 7 which relates to either mid-range tree or tall mallee tree. FCM derived from LiDAR provides a percentage foliage cover for each 10 m cell. Foliage cover is defined for each stratum as 'the proportion of the ground, which would be shaded if sunshine came from directly overhead' and includes branches and leaves. This percentage foliage cover information was then converted to 14 foliage cover classes with corresponding cover code information (e.g. open, sparse, etc).

11 CEM and 14 FCM derived classes were then combined to generate a series of (sub-) stratum/ (sub-) form structural classes based on ESCAVI (2003) as shown in Figure 17-21 and Figure 17-22 respectively. The 17 stratum structural classes can be grouped into Upper, Mid and Lower classes (Figure 17-21), whereas the sub-stratum structural classes can be further divided into Upper-1, -2 and -3; Mid-1, -2 and -3; and Lower-1, -2 and -3 (Figure 17-22). A similar application of LiDAR derived canopy structure characteristics has previously been used to detect and monitor change/disturbance to forest communities (Peterson & Nelson, 2009). The dataset was also visually matched against other pre-existing vegetation mapping (Ritman, 1995; Taylor-Wood *et al*., 2002) with good results.

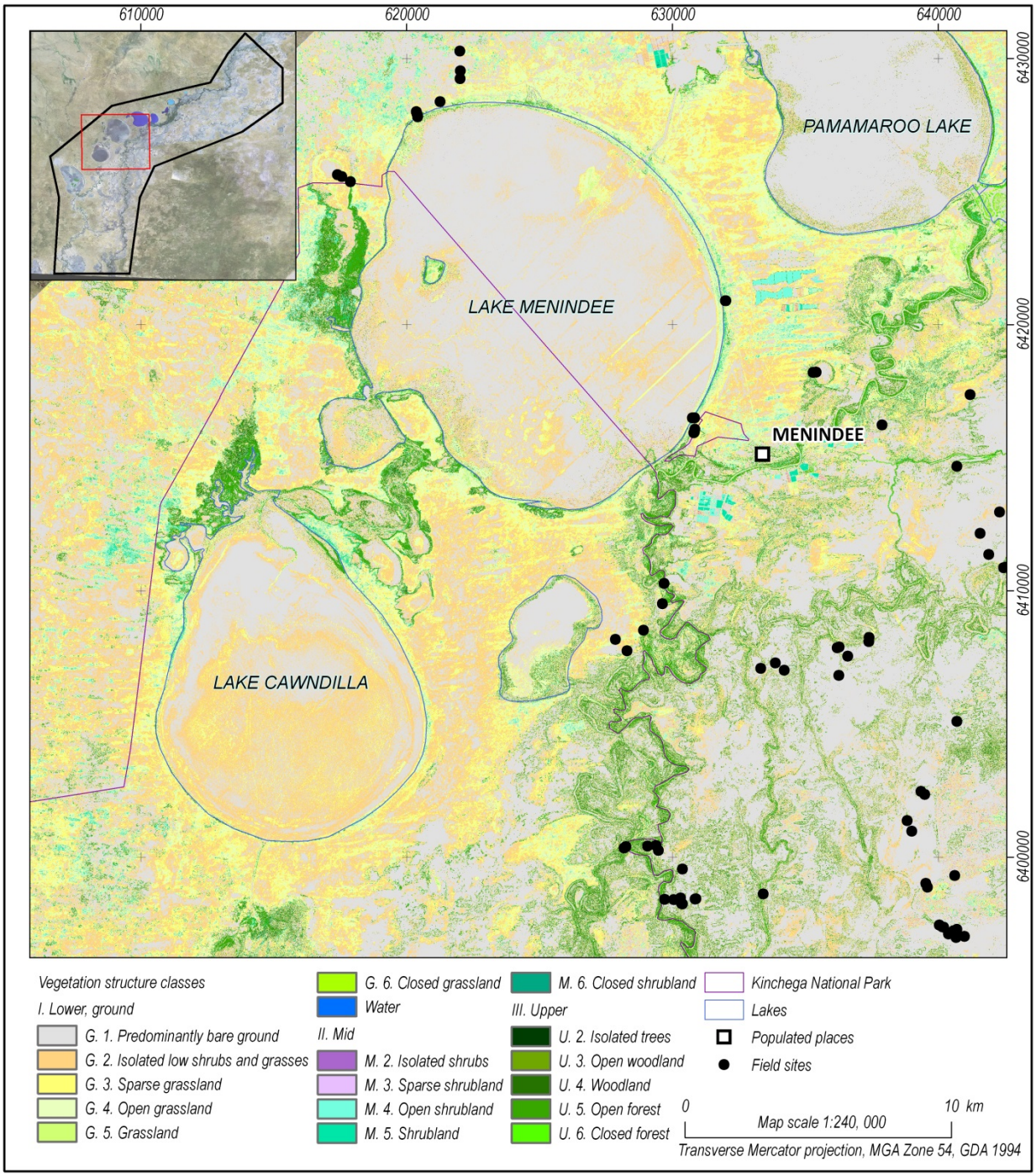



**Figure 17-21.** *Unique stratum structural classes identified in the central study area. Note the location of Lake Cawndilla which is shown in Figure 17-22.*

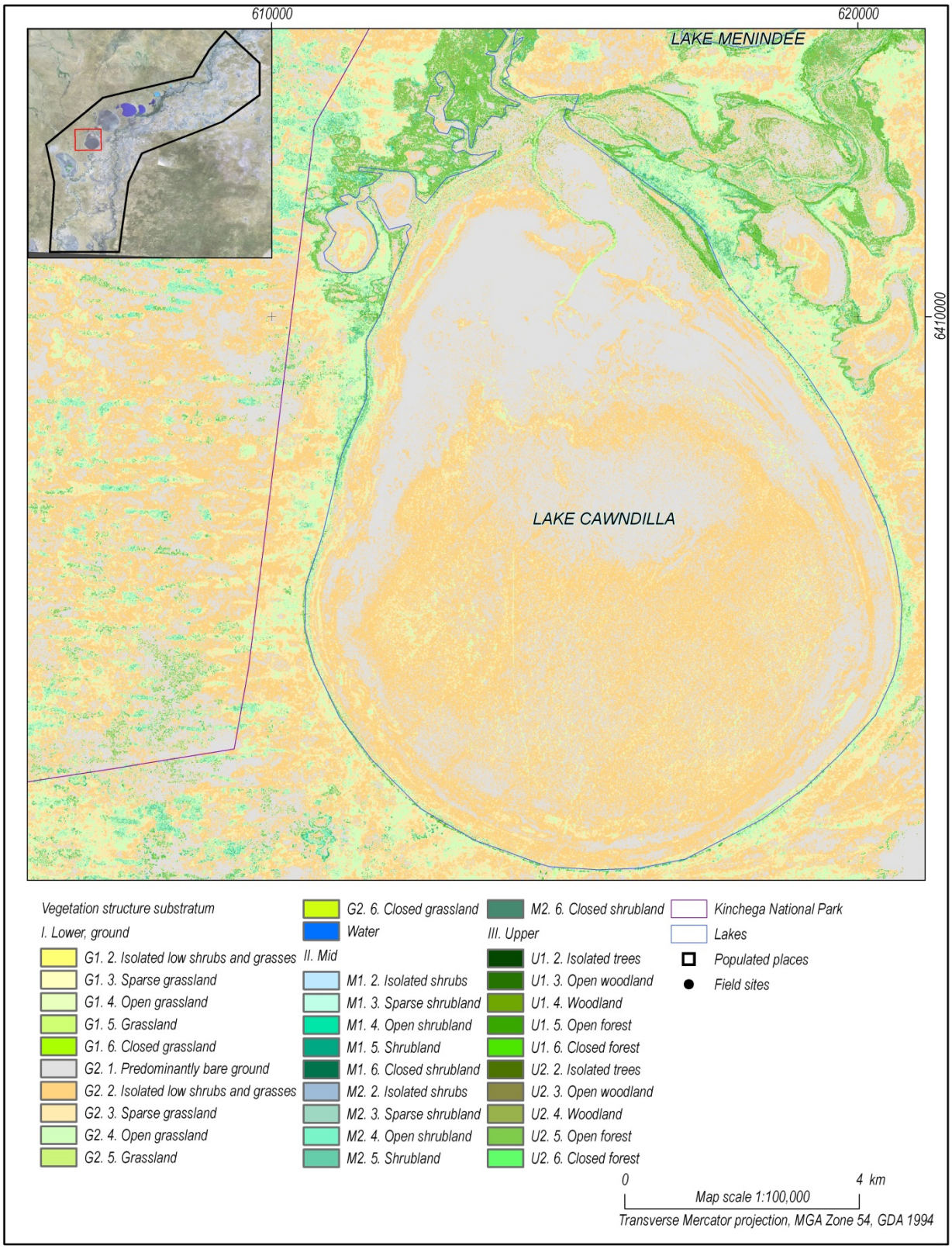



**Figure 17-22.** *Unique sub-stratum structural classes for Lake Cawndilla.*

*Validation*

Biophysical attributes were observed in the field with the purpose of validating the LiDAR vegetation structural mapping. Two separate vegetation sampling and observation trips were undertaken in May 2010 and August 2011 (see Figure 17-23) both of which occurred quite some time after the acquisition of the LiDAR (June-August 2009).

139 sites were visited in May 2010; at each site, twigs, small branches, burrs and seed pods were sampled from different vegetation species, including trees, shrubs and grasses. Site photos were also taken, recording vegetation structure and landform. 74 sites were visited in August 2011 as part of a soil sampling program. Site photos were taken and in some cases general observations regarding the vegetation were recorded.

For consistency between the two field observation datasets, sites with suitably indicative photos were classified into relevant LiDAR vegetation structural classes using the information provided in Table 17-6. As there was no consistency with which the photos were taken (i.e. standing on the coordinate point looking north, east, south and west), the vegetation classification was compared to LiDAR cells in a 3x3 grid matrix. If the corresponding LiDAR cell matched the photo then it was considered to be a 'good' match. If any of the surrounding cells matched the field photo then it was a 'moderate' match and if no match was evident then it was considered to be a 'poor' match. In examples where the field photo was assigned multiple vegetation structural classes, all had to be present within the 3x3 grid matrix in order to be classified as a good match.

***Table 17-6.*** *Vegetation structural classes and associated CEM and FPC ranges.*

| Vegetation structure | Storey | FPC range | CEM range |
|---|---|---|---|
| Water | Ground | 0 | 0 |
| Predominantly bare ground | Ground | 0% | 0 |
| Isolated low shrubs and grasses | Ground | <5% | <1 m |
| Sparse grasslands | Ground | 5-10% | <1 m |
| Open grasslands | Ground | 10-30% | <1 m |
| Grasslands | Ground | 30-70% | <1 m |
| Closed grasslands | Ground | 70-100% | <1 m |
| Isolated shrubs | Mid | <5% | 1-3 m |
| Sparse shrubland | Mid | 5-10% | 1-3 m |
| Open shrubland | Mid | 10-30% | 1-3 m |
| Shrubland | Mid | 30-70% | 1-3 m |
| Closed shrubland | Mid | 70-100% | 1-3 m |
| Isolated trees | Upper | <5% | >3 m |
| Open woodland | Upper | 5-10% | >3 m |
| Woodland | Upper | 10-30% | >3 m |
| Open forest | Upper | 30-70% | >3 m |
| Closed forest | Upper | 70-100% | >3 m |

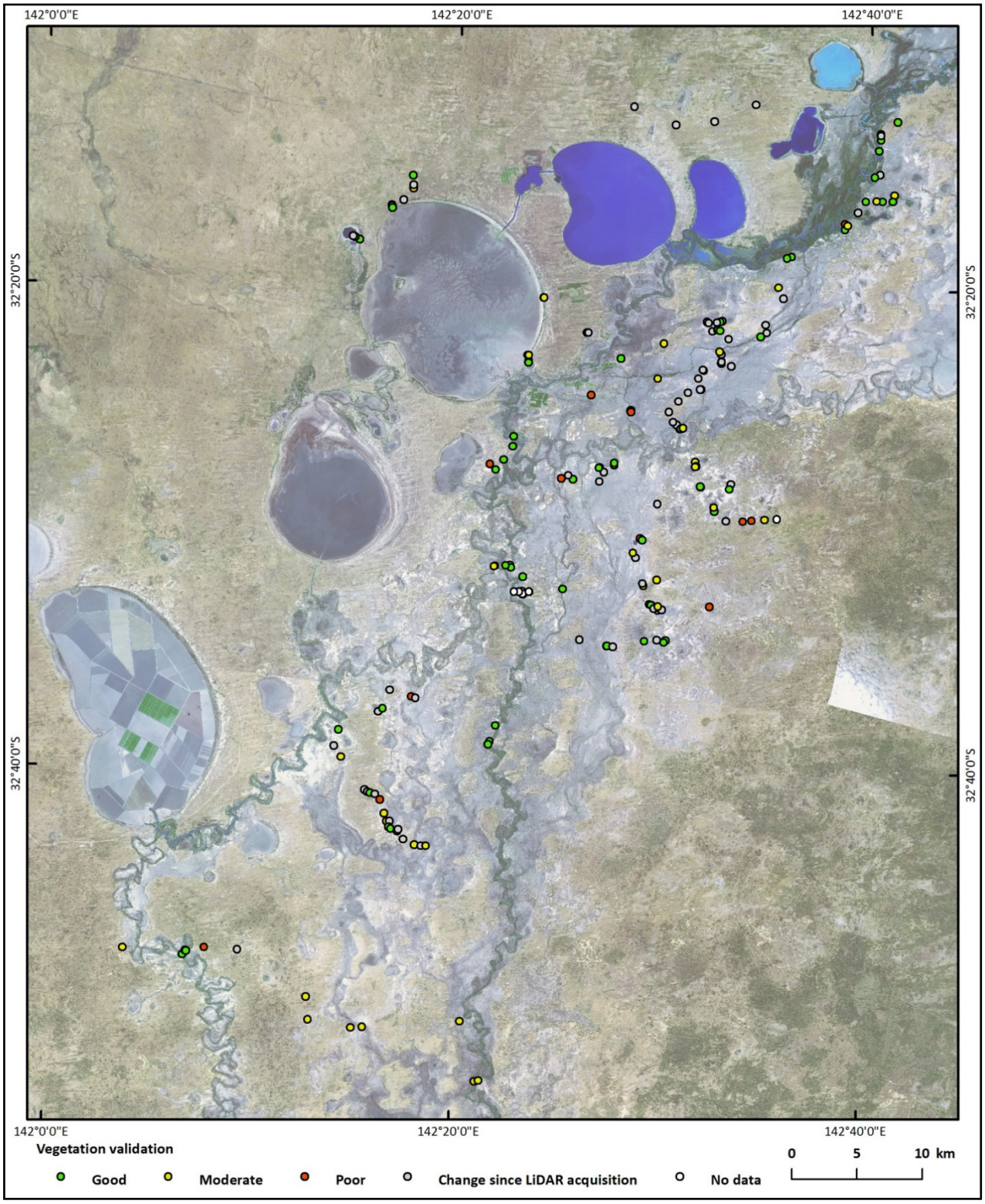



**Figure 17-23.** *Location of vegetation field sites and comparison with LiDAR vegetation structural mapping.*

Extensive flooding and localised rainfall occurred between the acquisition of the LiDAR and the field observations in May 2010, which had implications for ground cover observations. Over 43 sites were noted as having a more extensive ground cover in the field than was mapped in 2009. While it is likely that these sites were in fact a good match with that mapped by the LiDAR, the sites were not included in the comparison. Nine sites also had insufficient photographic data to make an assessment. Of the remaining 87 field sites, 61% were considered a good match (n=53), 29% a moderate match (n=29) and 10% a poor match (n=9) as shown in Figure 17-23. Comparison between the LiDAR vegetation mapping and the August 2011

field observations reduced poorer results (good: 35%; moderate: 49%; poor: 16%; 50% of sites excluded from analysis). This can largely be attributed to the long period of time between the acquisition of the LiDAR and the field trip. Furthermore, the landscape was subjected to very different climatic conditions at these times: end of a severe drought versus breaking of the drought and extensive rainfall and prolonged flooding. Consequently, field observations made in August 2011 could not be used to validate the LiDAR vegetation mapping.

*Limitations and uncertainty*

The reported vertical accuracy of the CEM (1 m) is ±0.15 m however after a number of processing steps, the final estimated vertical accuracy is ±0.18 m. Additional information about vertical accuracy assessment of the LiDAR DEM and CEM can be found in Section 5.2.5.

Some field data were collected with the (dual) purpose of validating the LiDAR vegetation structural mapping however there were a number of limitations with this dataset. Field sites were typically selected based on surface material sampling requirements hence many of the sites were located on bare ground. This reduced the ability of the field data to fully validate all vegetation structural classes. Biophysical attributes recorded in the field were not systematically collection or easily comparable with the vegetation structure hence only a qualitative comparison could be achieved using field photos. These photos were taken approximately one and two years after the LiDAR was originally flown and after the drought had broken. This has implications for ground/canopy cover observations and to a lesser extent vegetation height. For example, with the sudden availability of large volumes of water, ground cover in particular flourished rapidly where bare ground previously dominated. Where this was observed, sites were not included in the validation statistics. It is however likely that these sites were in fact a good match with that mapped by the LiDAR. In the case of the later field trip (August 2011) too much time had passed and vegetation changed too substantially to use this data for validation purposes. The May 2010 data however suggested a 90% good to moderate match with the vegetation mapping.

The vegetation structural classification was derived from LiDAR data acquired towards the end of a severe drought; acquisition occurred between June 19th and August 5th 2009. Had the LiDAR been acquired towards the end of a wet period, canopy information for the same vegetation community would have been quite different. This may result in an underestimation of canopy density. Similarly, only this dataset represents vegetation structure at one point in time. It does not provide an understanding of how changes in hydrologic regimes alter observed biophysical parameters.

#### 17.2.3.2 ***Landsat-derived Vegetation Mapping***

*Using NDVI to map vegetation characteristics*

Vegetation indices, namely Landsat Normalised Difference Vegetation Index (NDVI) are effective measures of vegetation features on the Earth's surface through the use of different band combinations. The response of vegetation to the electromagnetic spectrum is influenced by factors such as difference in chlorophyll content, nutrient levels, water content and underlying soil characteristics (Zhao *et al*., 2009). NDVI uses the radiances or reflectance from a red channel (~0.66 μm) and a near-infrared channel (NIR) (~0.86 μm) to display vegetation in terms of greenness; the NDVI formula is given in Equation 101. The red channel (Landsat 5 Thematic Mapper (TM) Band 3) is located in the strong chlorophyll absorption region, while the NIR channel (Landsat 5 Thematic Mapper (TM) Band 4) is located in the high reflectance plateau of vegetation canopies (Gao, 1996). Chlorophyll in plant leaves strongly absorbs visible light for use in photosynthesis while the cell structure of the leaves strongly reflects near-infrared light. NDVI ranges from -1 to 1; NDVI values are close to zero in the absence of green leaves.

$$NDVI = (NIR - RED) / (NIR + RED)$$

**Equation 101**

*NDVI* is a widely used indicator of vegetation condition including productivity, biomass, health and vigour (e.g. Scanlon *et al*., 2002; Tweed *et al*., 2007; Quinonez-Pinon *et al*., 2007; Cunningham *et al*., 2009: Akumu *et al*., 2010). While NDVI can partly eliminate effects of the solar zenith angle, sensor's observing angle, and atmospheric conditions (Kaufman & Tanre, 1992) it is sensitive to both atmospheric aerosols (Holben, 1986) and soil background (Lillesaeter, 1982), and prone to oversaturation (Huete, 1985).

*NDVI summary statistics*

The NDVI values for a pixel will fluctuate throughout a year as a function of the type of vegetation (if any) present at that location in combination with the amount of water available to the vegetation. Several papers have recently investigated the relationship between vegetation and rainfall (e.g. Omuto, 2011). Areas that receive steady year round supply of water are typically evergreen, whereas areas that receive varying amounts of water throughout the year will fluctuate in response to the available water. This assumes that the vegetation is not energy limited at any point during the year which is a reasonable assumption within this study area.

Different types of vegetation respond differently to water availability. Grasses in particular tend to respond rapidly to the availability of water, resulting in a characteristic 'flush' of green following a rainfall event or a flood pulse. Trees typically respond more slowly to available water. A previous study (Fuller *et al*., 1997) has found that the tree layer appears to be a relatively important component of NDVI during the dry season when the field layer is largely senescent, accounting for 20-40% of the satellite signal, with maximum contribution occurring at the end of the dry season. However in the inverse the tree layer appears to have minimal effect on landscape-scale NDVI when both layers were photosynthetically active. Multi-temporal NDVI analysis can be used to optimise the discrimination of rain-green/ephemeral vegetation versus ever-green vegetation by focusing on the driest time of the year when rain-green vegetation is senescent or absent. This concept is illustrated in Figure 17-24. Note that during wetter periods the difference between the two curves is reduced, whereas during drier periods when the curves are at local minima the difference is much larger. It is interesting to note that during the drought periods of the early 2000s successive dry years sees a decrease in greenness in the open forest, to the point where the dry season minimum values have dropped much lower than they did during the 1990's.

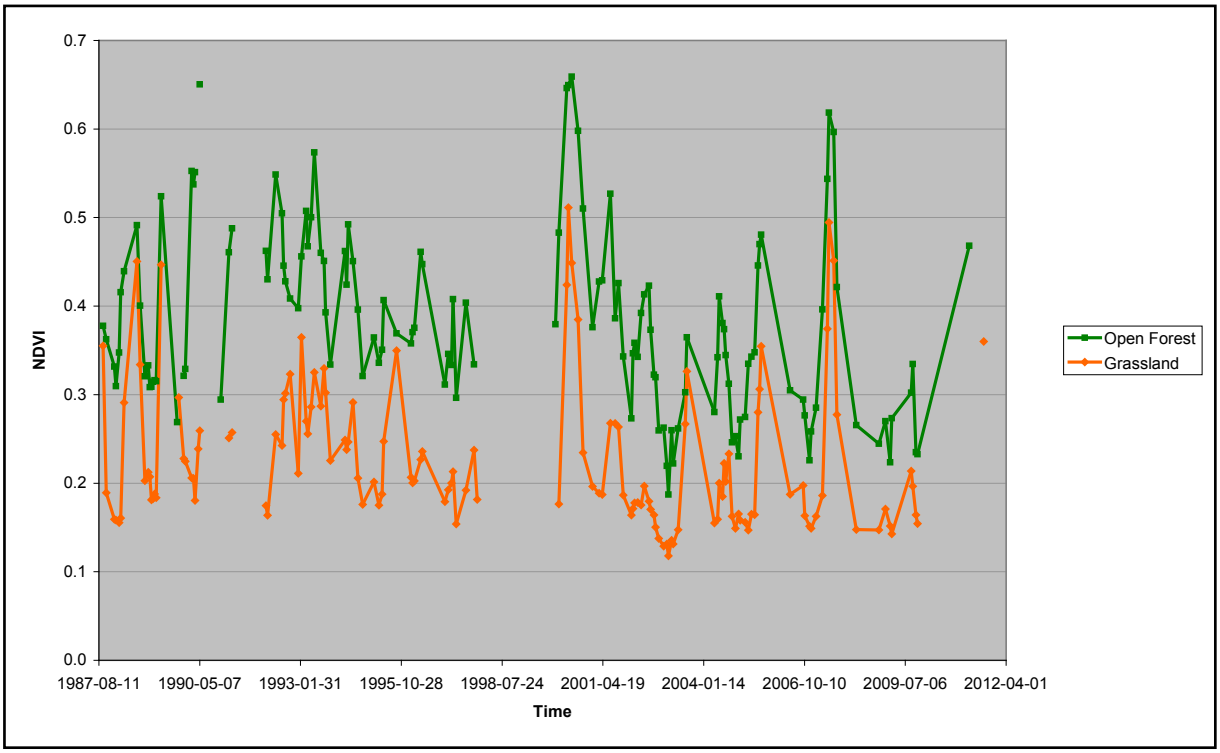



**Figure 17-24.** *NDVI time series for typical grassland and forest pixels.*

In northern parts of Australia that have a distinct 'dry season', picking Landsat scenes to discriminate rain-green and ever-green vegetation can be achieved by focusing on a fairly narrow range of dates towards the end of the dry season (Armston *et al*., 2009). In the study area, the combination of episodic rainfall events and floodplain inundation events necessitate the use of a statistical rather than seasonal approach.

This statistical approach entails calculating the NDVI for all cloud free scenes within a particular year and then placing them into a data stack. The stack is then used to calculate the maximum, minimum, mean and standard deviation for the NDVI values for each pixel within that year (Figure 17-25). The result is four bands that show the annual maximum, minimum, average and standard deviation in NDVI values. The annual minimum NDVI values are analogous to 'dry season' NDVI values and provide the best opportunity to discriminate ephemeral/rain-green vegetation from evergreen vegetation and have been used to generate drought specific time series Landsat dataset. Note how the annual minimum NDVI values in Figure 17-25 show the least amount of variability, effectively minimising the influence of rainfall on vegetation.

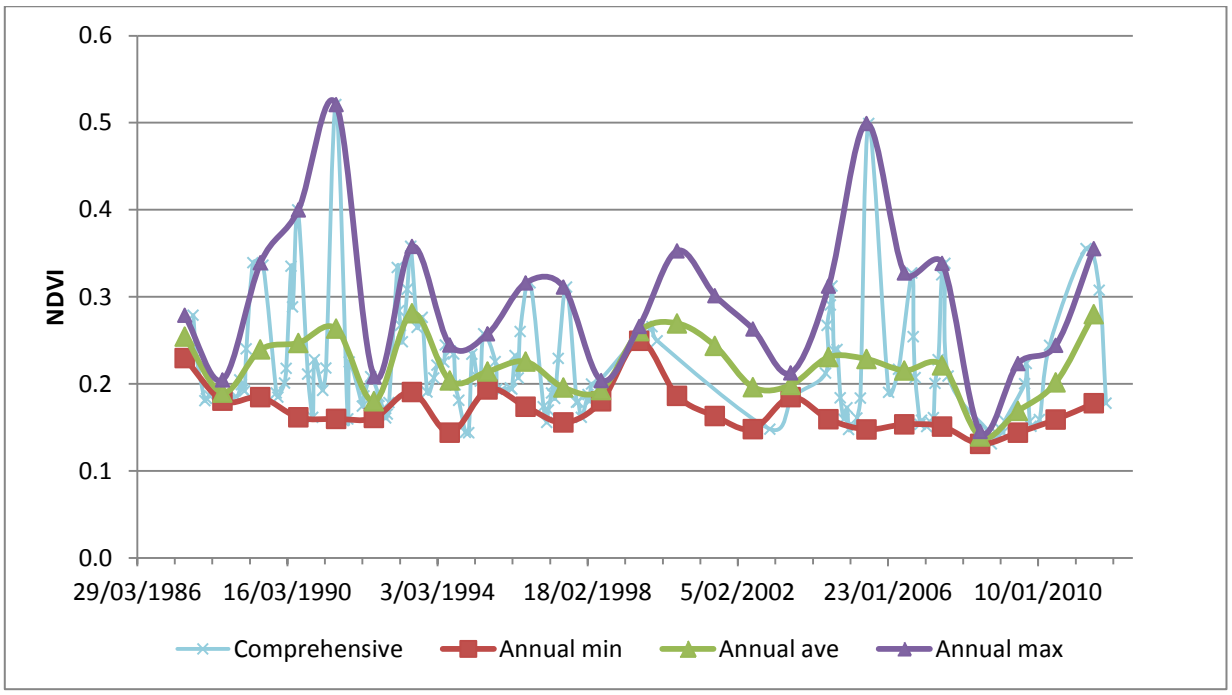



**Figure 17-25.** *Annual NDVI statistics (minimum, maximum and average) compared with individual 'comprehensive' average NDVI values for each scene. This data relates to a single vegetation community. There are thousands of similar communities that statistics have been calculated for.*

*Vegetation structural classification*

As mentioned, the study area was divided into a series of sub-regions or populations based according to the Hierarchy Level 1:

- Floodplain,
- Lake,
- Riparian
- Local Groundwater Expression
- Surrounding landscape

Each sub-region was further divided into the following vegetation structural/land cover classes (Hierarchy Level 2; Figure 17-26):

- Closed Forest
- Open Forest
- Woodland
- Open Woodland
- Shrubs and Grasses
- Water bodies
- Palustrine Wetlands7

This allowed NDVI time series statistics to be calculated for each Hierarchy Level 2 sub-region or averaged across different level 2 or level 1 sub-region. Based on annual minimum NDVI values, the same classification approach, as used for the LiDAR derived vegetation structure, was mapped at a Landsat scale.

[7] The wetland areas represent the large areas of lignum located in Lake Wetherell near the entrance to Lake Bijijie they don't include areas that behave like wetlands for short periods of time following flood events *i.e.* ephemeral wetlands

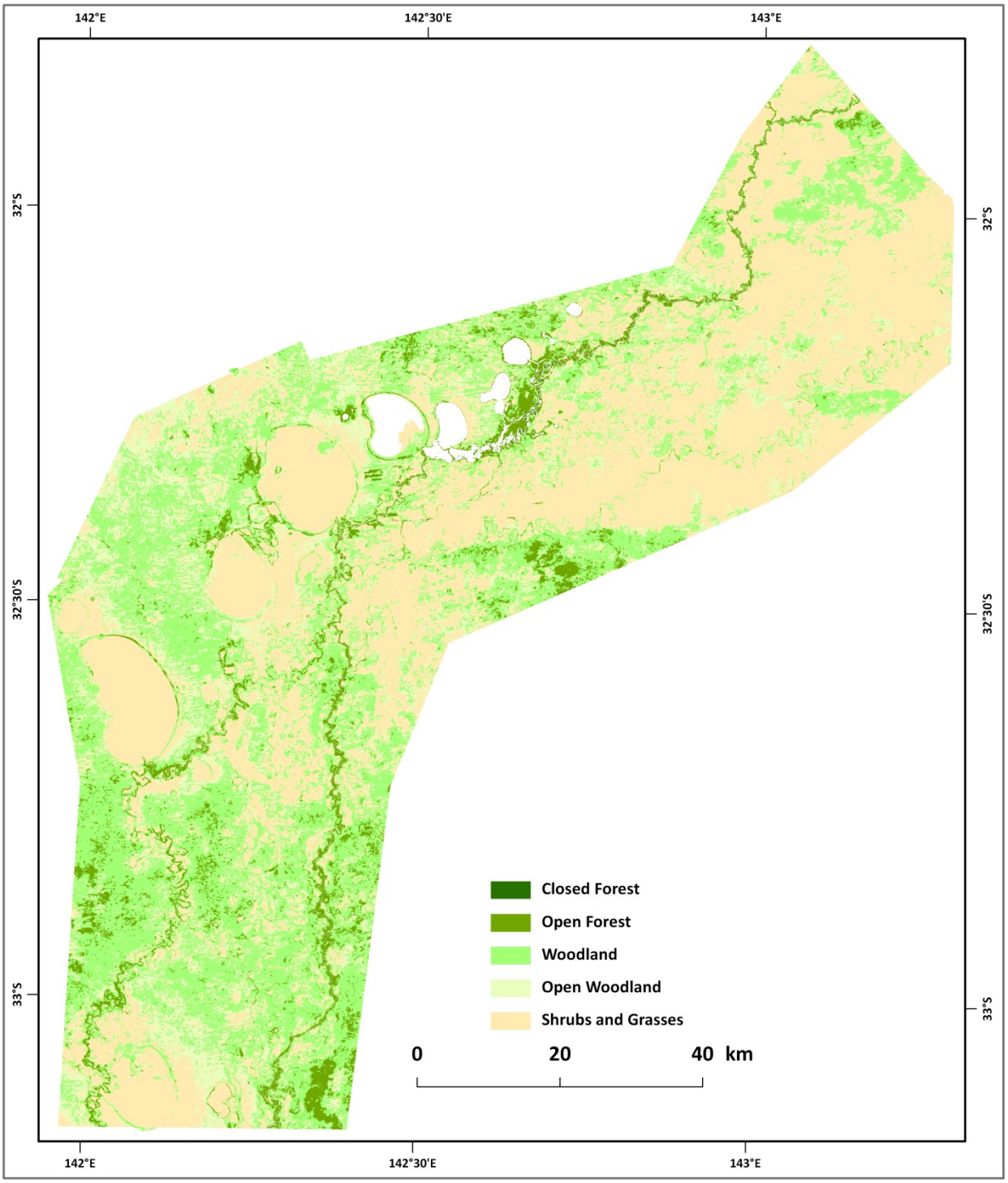



**Figure 17-26.** *Distribution of vegetation structural/land cover classes (Hierarchy Level 2).*

An image segmentation approach (Figure 17-27) in eCognition 8 ™ was used to separate different stands of trees based on their annual minimum NDVI values. 2009 was selected as the year of interest as it corresponded with the acquisition of the LiDAR data. This meant that a relationship could be established between the LiDAR derived vegetation structural information and the annual minimum NDVI values. The LiDAR is a classified raster, which meant that it was possible to calculate the statistical characteristics of the NDVI raster for each class of the LIDAR raster.

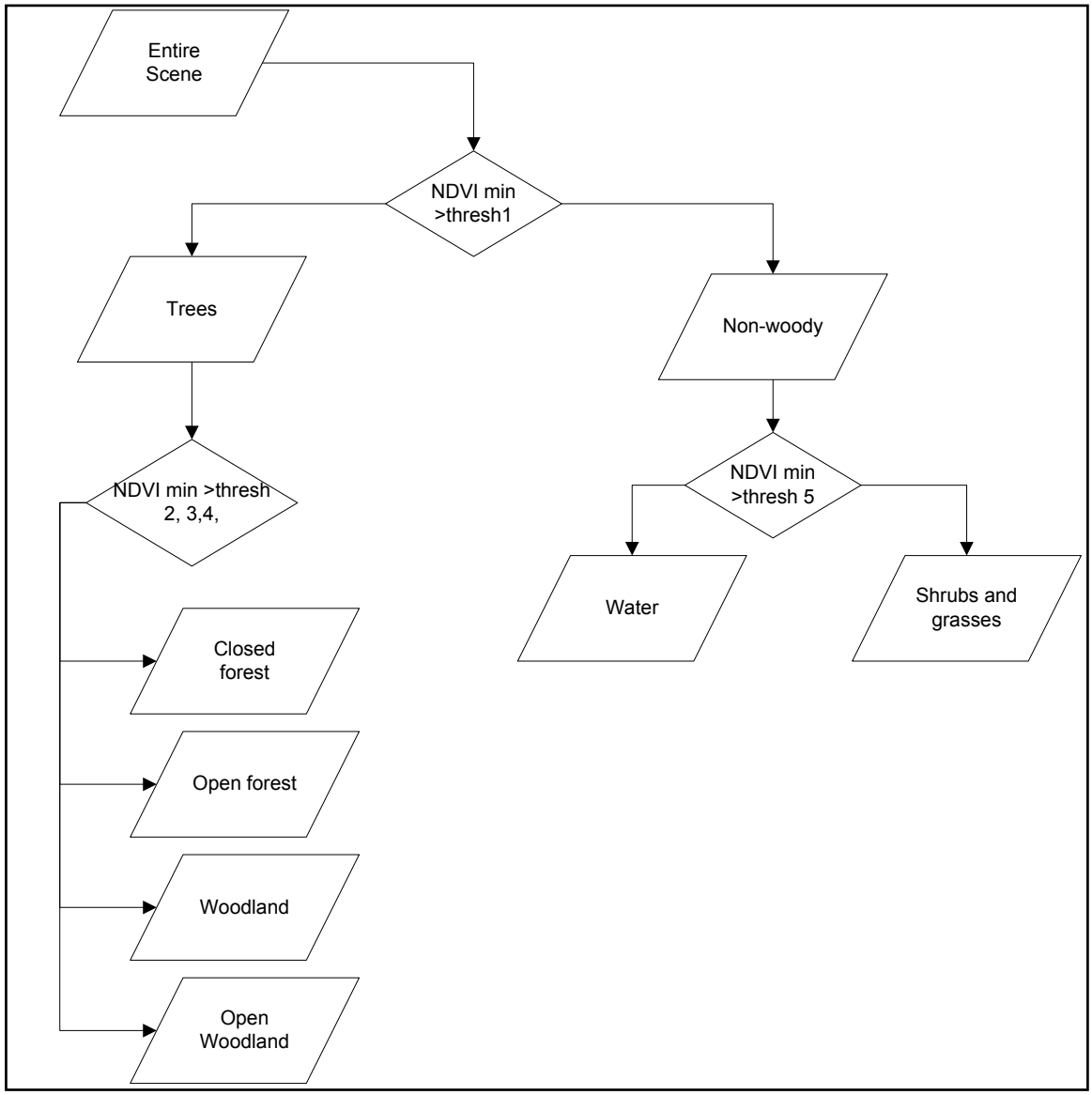



**Figure 17-27.** *Flow chart representing the segmentation process.*

For example the class 'open forest' in the LIDAR raster corresponds to a range of NDVI values and this range of values has a maximum, mean, minimum, standard deviation etc. The mean value for this population can be thought of as the average dry season NDVI for open forest. The threshold between classes (i.e. the value at which an area switched from being labelled as open forest to closed forest) was calculated using Equation 102:

$$\left(\frac{\bar{x}_1 - \bar{x}_2}{2}\right)$$

**Equation 102**

Where $x_1$ is the average dry season NDVI of the higher canopy cover class and $x_2$ is the average dry season NDVI of the lower canopy cover class. Equation 102 was used to calculate the inter-class lower thresholds for open woodland, woodland and open forest. A different equation was used to determine the threshold that discriminated open forest from closed forest for two reasons. Firstly, closed forest populations are typically quite narrow and hence contain many mixed pixels at the Landsat scale. Secondly, due to close proximity to the river course, close forest populations are prone to the inclusion of water mixed pixels. NDVI statistics calculated for these vegetation communities thus resulted in an artificial lowering of the NDVI threshold. To account for this influence Equation 103 was used.

$$\left(\frac{(\bar{x}_1 + \sigma_1) - \bar{x}_2}{2}\right)$$

**Equation 103**

Where $x_1$ and $\sigma_1$ and is the average and standard deviation of dry season NDVI of closed forest cover class and $x_2$ is the average dry season NDVI of open forest. The inter-class threshold values are listed in Table 17-7. These thresholds can also be used to track changes in vegetation canopy cover over time. For example a stand of trees may maintain an open forest canopy density during wetter years or years with high river flow but fall back to a woodland canopy density during drought years.

**Table 17-7.** *Annual minimum NDVI thresholds used to differentiate non-woody and woody cover, and different woody vegetation structural classes.*

| Targets to be discriminated | Threshold value |
|---|---|
| Non-Woody vs. Woody | 0.14 |
| Open Woodland vs. Woodland | 0.15 |
| Woodland vs. Open Forest | 0.19 |
| Open Forest vs. Closed Forest | 0.48 |

The vegetation classification generated using the Landsat segmentation approach was compared with the LiDAR vegetation classification (Figure 17-28). At first glance the two datasets look considerably different but this is largely due to a resolution issue; LiDAR-derived vegetation structure was mapped at a 5 m scale while Landsat-derived vegetation structure was at a 30 m scale. This is demonstrated in Figure 17-28. Aggregation of Landsat data into 'stand of trees' scale polygons was an essential simplification of the data, enabling an automated assessment of temporal changes of a stand of trees. In some areas this aggregation led to marked visual differences at a regional scale between the LiDAR map and the NDVI based map, however closer inspection (Figure 17-28) of the data reveals that the NDVI map provides a consistent labelling regime appropriate for Landsat-scale observations. Note how the LiDAR data in Figure 17-28 inset shows a relatively dense stand of trees and shrubs, all with an open forest canopy density (foliage density >30%) as a stand of open forest. When viewed at the 'whole of study area' scale it appears the NDVI based map is over-estimating the extent of open forest, but closer inspection shows that the area contains significant areas of individual trees with 'open forest' canopy density and hence a high canopy density when viewed at a 30 m scale. Wetland areas that maintained a high minimum NDVI throughout 2009 were manually removed from the forest layers using the LIDAR data as a reference.

For each polygon (i.e. stand of trees or water body) detailed statistics were recorded (Table 17-8) however, because of the uneven number of observations per year (i.e. some years have 10 scenes other years have 1), annual statistics were calculated (Table 17-9). These annualized statistics form the primary basis for the vegetation condition assessment. However, in the years when the total number of Landsat scenes was particularly low (e.g. two scenes in 2003) statistics could be seasonally biased. In this instance, statistics for 2003 could not be used. Additionally, a number of scenes during 2007 corresponded with winter rain events that, although small in relation to long-term averages, were quite large for the drought period. As a consequence of this annual statistics for 2007 reflect the associated spike in vegetation condition relating to these rainfall events and could likewise not be used in the temporal analysis.

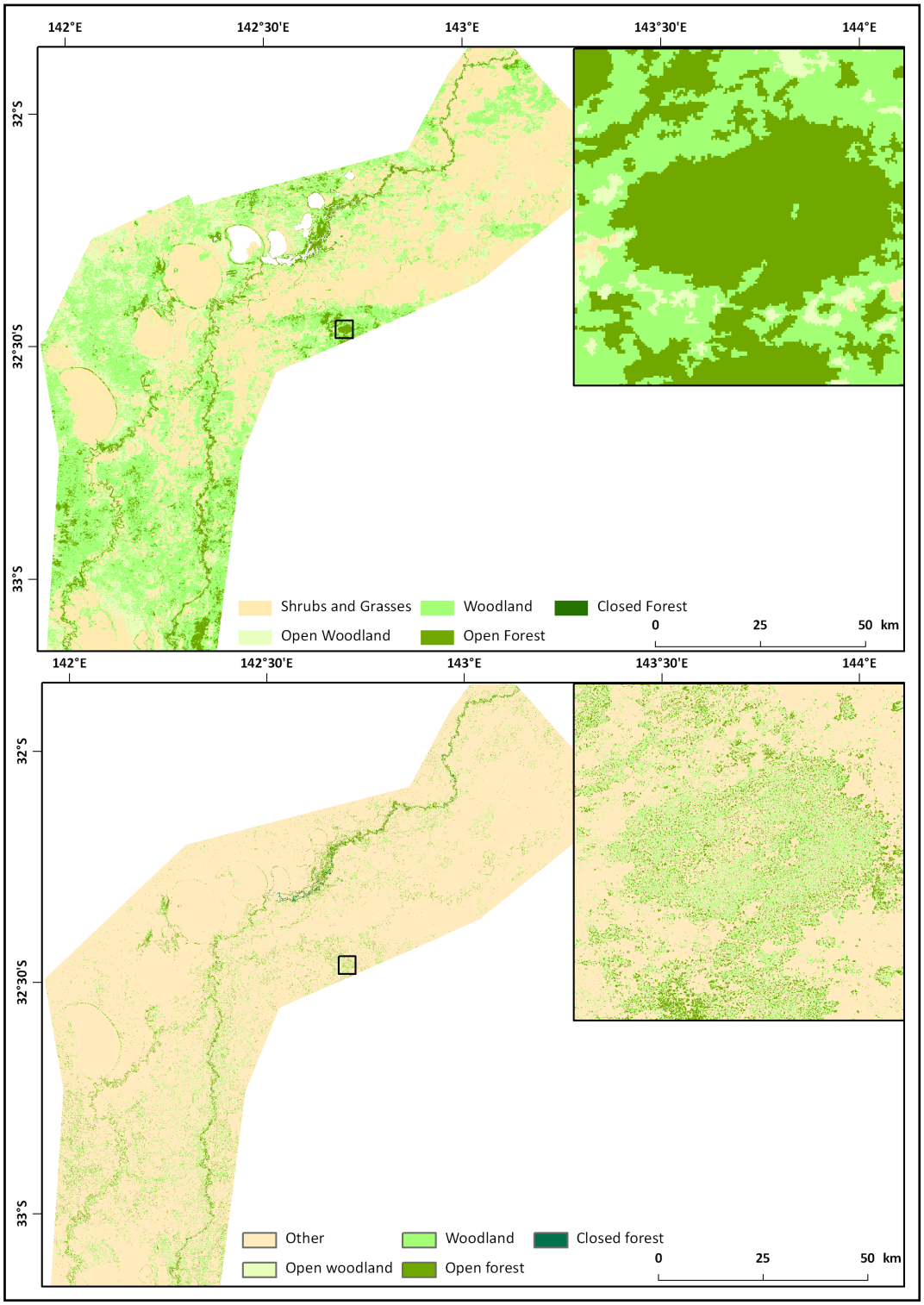



**Figure 17-28.** *Final Landsat derived vegetation classification (top) and LiDAR derived vegetation structure mapping (bottom). Inset images show a detailed comparison of the NDVI-derived (top) and LiDAR-derived (bottom) vegetation maps.*

**Table 17-8.** *Example of scene by scene Landsat NDVI statistics.*

| Polygon ID | Date | NDVI max | NDVI mean | NDVI min | % inundated | % open water |
|---|---|---|---|---|---|---|
| 1 | 11/11/2011 | 0.65 | 0.62 | 0.59 | 20 | 10 |
| 1 | 08/09/2011 | 0.54 | 0.51 | 0.48 | 0 | 0 |
| 1 | 01/01/1987 | 0.66 | 0.63 | 0.61 | 15 | 5 |

**Table 17-9.** *Example of annualized NDVI statistics.*

| Polygon ID | Year | Annual maximum NDVI | Annual average NDVI | Annual minimum NDVI |
|---|---|---|---|---|
| 1 | 2011 | 0.65 | 0.62 | 0.59 |
| 1 | 2010 | 0.54 | 0.51 | 0.48 |
| 1 | 1987 | 0.66 | 0.63 | 0.61 |

*Validation*

As the LiDAR-derived structural map was generated from relatively precise elevation and canopy density measurements obtained at a sub-10 m horizontal resolution, it was felt that in the absence of detailed field investigations, this dataset could be used to assess the relative accuracy of the Landsat NDVI product.

The Landsat-derived vegetation map was subsample to 5 m spatial resolution to match the LiDAR-derived structural map and pixels were correctly aligned to ensure accurate comparison. Classes within both datasets were coded in the same fashion and compared systematic across the whole study area. If the two codes were exactly the same a good match was assigned. This only represented 4% of the population but was concentrated along the riparian zone (see Figure 17-29) where the study was principally focused. Relationships deemed to be moderate and poor are shown in Table 17-10. A moderate match was observed for 89% of the study area, with the remaining 7% exhibiting a poor match. This is predominantly areas that were classified as open forest in the Landsat product and other (i.e. grasslands, shrublands or quite commonly water) with LiDAR. Spatially, a poor match is typically observed on lunettes where shrublands exhibit a similar greenness spectral signature to open forest; and associated with the narrow riparian zone and lake-fringe where vegetation density (i.e. open forest or woodland to bare ground or grasslands) varies on a meter scale, and thus not captured at a Landsat scale. Consequently greater uncertainty is associated with those areas shown in orange in Figure 17-29.

***Table 17-10.*** *Combination of vegetation structural classes considered to be a moderate or poor match. This is based on the structural similarities between the two classes.*

| Moderate match | Poor match |
|---|---|
| Other/woodland | Other/closed forest |
| Other/open woodland | Other/open forest |
| Open forest/closed forest | Woodland/closed forest |
| Open forest/woodland | Open woodland/closed forest |
| Open forest/open woodland | |
| Woodland/open woodland | |

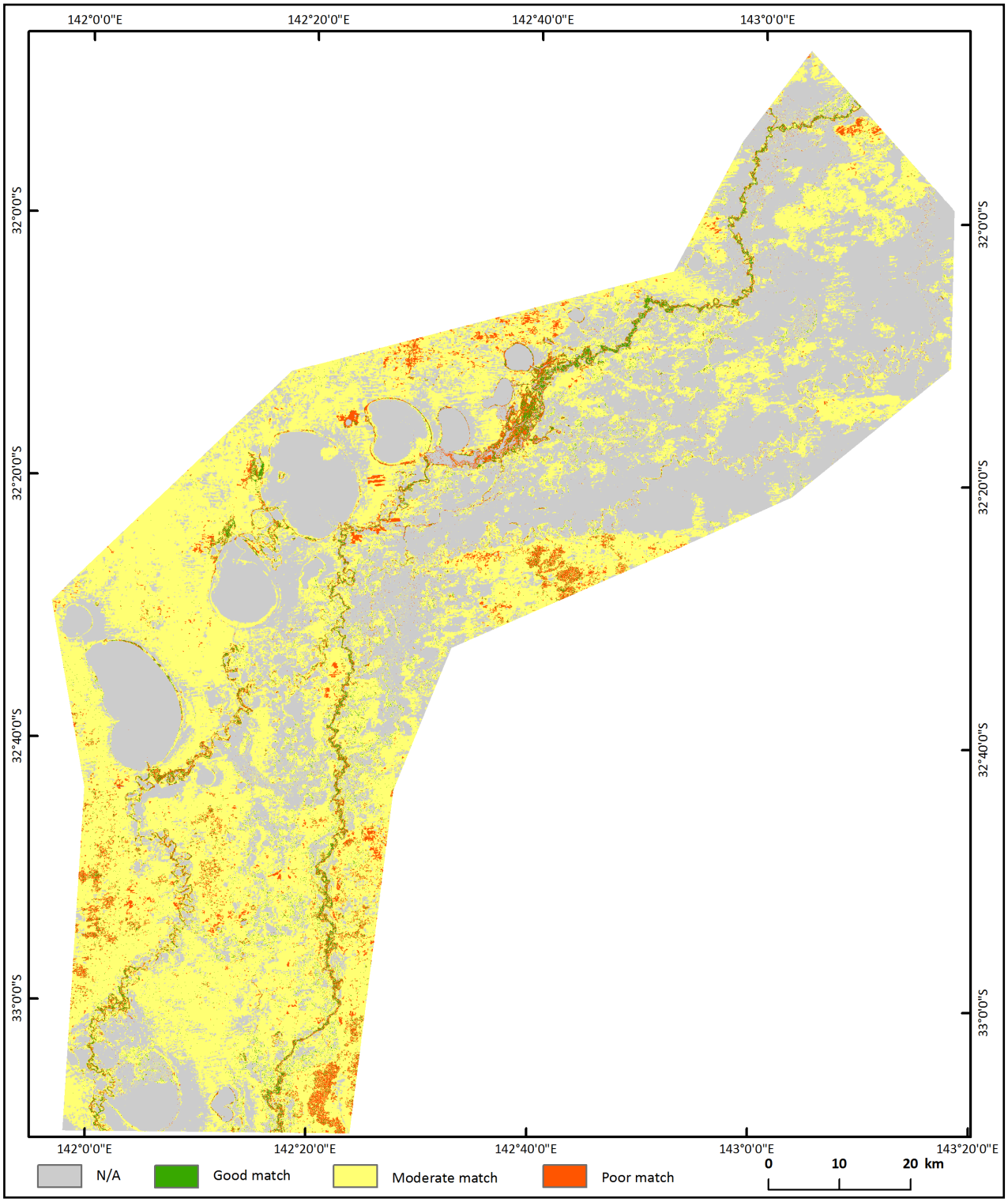



***Figure 17-29.*** *Comparison between Landsat and LiDAR-derived vegetation mapping products. Those areas shown in grey are not of interest – they are classified as 'other' in both datasets – and have not been considered in the calculation of percentages.*

*Limitations and uncertainty*

The vegetation structural classification was derived from LiDAR data acquired towards the end of a severe drought; acquisition occurred between June 19th and August 5th 2009. Had the LiDAR been acquired towards the end of a wet period, canopy information for the same vegetation community would have been quite different. Paired wet and dry LiDAR data could have provided an estimation of the degree of canopy change in response to climate variability and been a further means of validating the accuracy of the Landsat vegetation mapping. However in the absence of additional LiDAR data (which is quite expensive), the 2009 LiDAR was compared with annual minimum Landsat NDVI data from the same year. In this fashion, both canopy and NDVI data reflected the same prolonged climatic conditions. There still remains some uncertainty about how significantly the drought affected canopy density and whether similar degree of influence was detected by NDVI.

The Landsat vegetation mapping was not validated by field data which is a significant limitation of the dataset. Instead it relied on the establishment of a relationship between canopy and height information obtained from LiDAR and Landsat NDVI data. On comparing the two datasets a good to moderate match was observed for 93% of the area of interest. Less confidence is associated with the Landsat NDVI time series data for the remaining 7%. Furthermore, a number of years between 1987 and 2011 have less than four available Landsat scenes (per row). This contributes towards the uncertainty of the NDVI results obtained for these years, particularly beyond the area where the two scenes overlap. Years of particular concern are 1987, 2009, 2010 and 2011 (full study area); 1991, 1998 and 1999 (southern portion of study area); and 2003 (northern portion). That being said, while only a few images were available for 2009, 2010 and 2011, these scenes are fairly indicative of the overall trend in vegetation greenness, with a strong positive response in relation to increased rainfall.

Landsat TM and +ETM imagery has a spatial resolution of 30 m and as such the spectral response over this area is 'averaged'. A single pixel may include many different land cover types including tree canopy, understorey vegetation, bare ground and other attributes such as water bodies. Under such situations, it is difficult to determine what part of the pixel is contributing the most to the various spectral characteristics or changes detected using Landsat time series data. Researchers are attempting to resolve this issue by calculating fractional cover, which is an estimation of the proportion of a pixel covered by each member of a pre-defined set of vegetation or land cover types (e.g. Guerschman *et al*., 2009; Scarth *et al*., 2011). Due to time considerations this technique was not applied in the present study. Instead, the authors attempted to resolve the issue by using annual minimum NDVI values which are analogous to 'dry season' conditions where the spectral influence of understorey vegetation is considered to be reduced. This approach encountered issues in years with limited Landsat coverage (e.g. 2003 and 2007) where the influence of rainfall (particularly on the understorey) still appeared to be evident in the spectral response. The uncertainty associated with these two years was considered to be so high they were removed from the time series to avoid introducing bias.

#### 17.2.3.3 ***Drought-specific Temporal Analysis***

The tree layer appears to be a relatively important component of NDVI during the dry season when the field layer is largely senescent, with maximum contribution occurring at the end of the dry season. The annual minimum NDVI values are analogous to 'dry season' NDVI values and provide the best opportunity to discriminate ephemeral/rain-green vegetation from evergreen vegetation. To further eliminate the influence of rainfall, vegetation dynamics during the millennium drought were investigated, specifically 1) condition of vegetation at the end of the drought (2009), 2) overall trend in condition from the beginning of the drought (2002 for floodplain and riparian vegetation and 2004 for lake vegetation) to the end of the drought, and 3) variability of condition throughout the drought period.

*Vegetation condition in 2009*

For the purposes of this analysis, 2009 was selected as the end of the drought period as it was the last full year in which heavy precipitation did not occur (the drought broke towards the end of 2010). In addition, Landsat imagery was available for seven different dates in 2009 as opposed to two in 2010. Annual NDVI minimum values were averaged for each unique vegetation community. These values ranged from 0.000089 to 0.553038. The vegetation structural thresholds shown in Table 17-7 were used to classify each unique

vegetation community into a structural class (closed forest, open forest, woodland, open woodland) indicative of condition.

Analysis of annual minimum NDVI over the entire time series showed a consistently similar temporal pattern between woodlands and open woodlands with only a slight offset in annual minimum NDVI value (e.g. Figure 17-30). Consequently, for graphical representation (Figure 17-31), these two classes were grouped together. Open forest communities represented the greatest percentage of vegetation, with annual minimum NDVI values ranging from 0.19 to 0.48. Consequently, this class was further sub-divided (based on equal interval) into open forest of low, moderate and high condition as shown in Table 17-11 and Figure 17-31. Ground truth data would be able to provide some sense of the accuracy of these divisions. This product indicates which vegetation communities were in better condition than others after a lengthy drought period where rainfall was minimal. Vegetation of better condition is thought to have had access to additional such as river water or groundwater. This product is however only a single point in time. It does not provide an indication of overall trends in vegetation condition over the drought. Consequently a second product was developed.

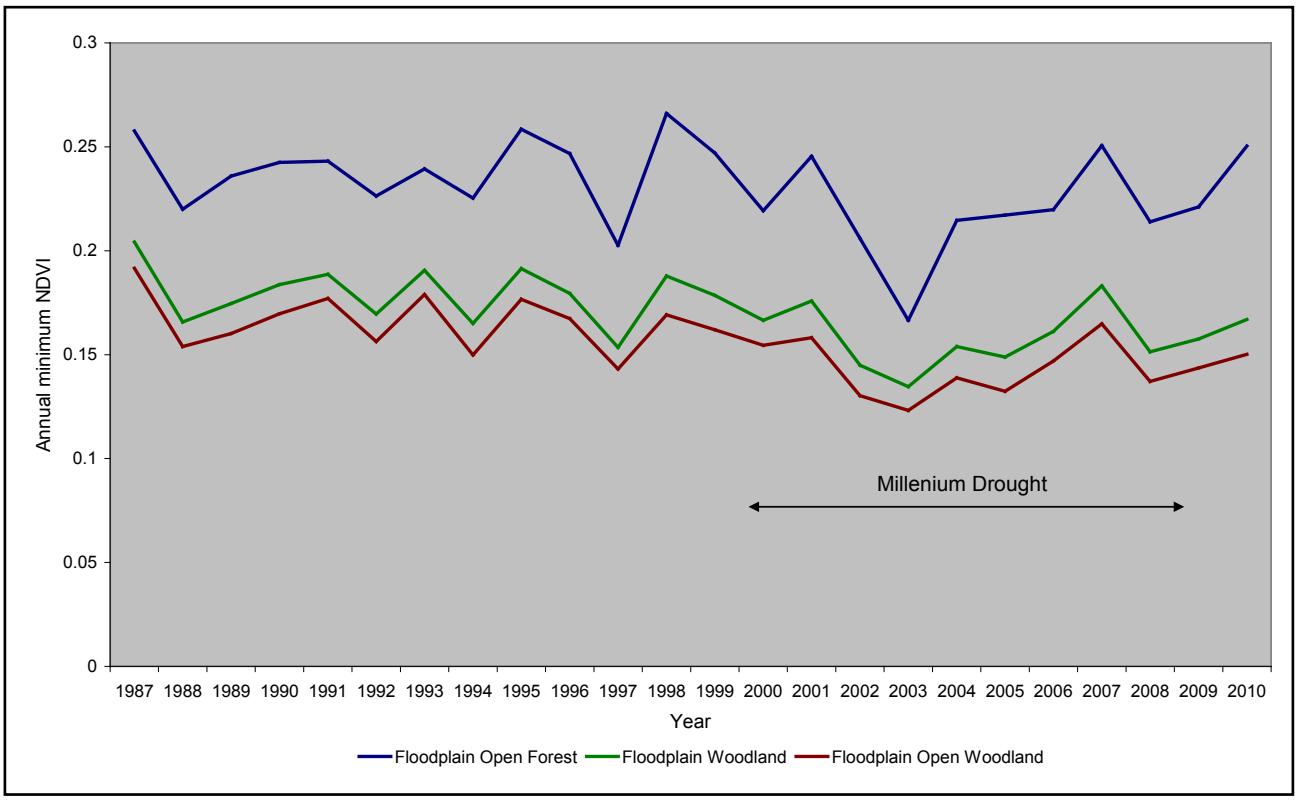



**Figure 17-30.** *Time series profile of floodplain vegetation, showing the close similarly between woodland and open woodland communities, in comparison to open forest communities.*

**Table 17-11.** *Annual minimum NDVI thresholds used to further sub-divide the open forest vegetation structural class.*

| Classification | NDVI range |
|---|---|
| Open Forest, Low Condition | 0.19-0.29 |
| Open Forest, Moderate Condition | 0.29-0.39 |
| Open Forest, High Condition | 0.39-0.48 |

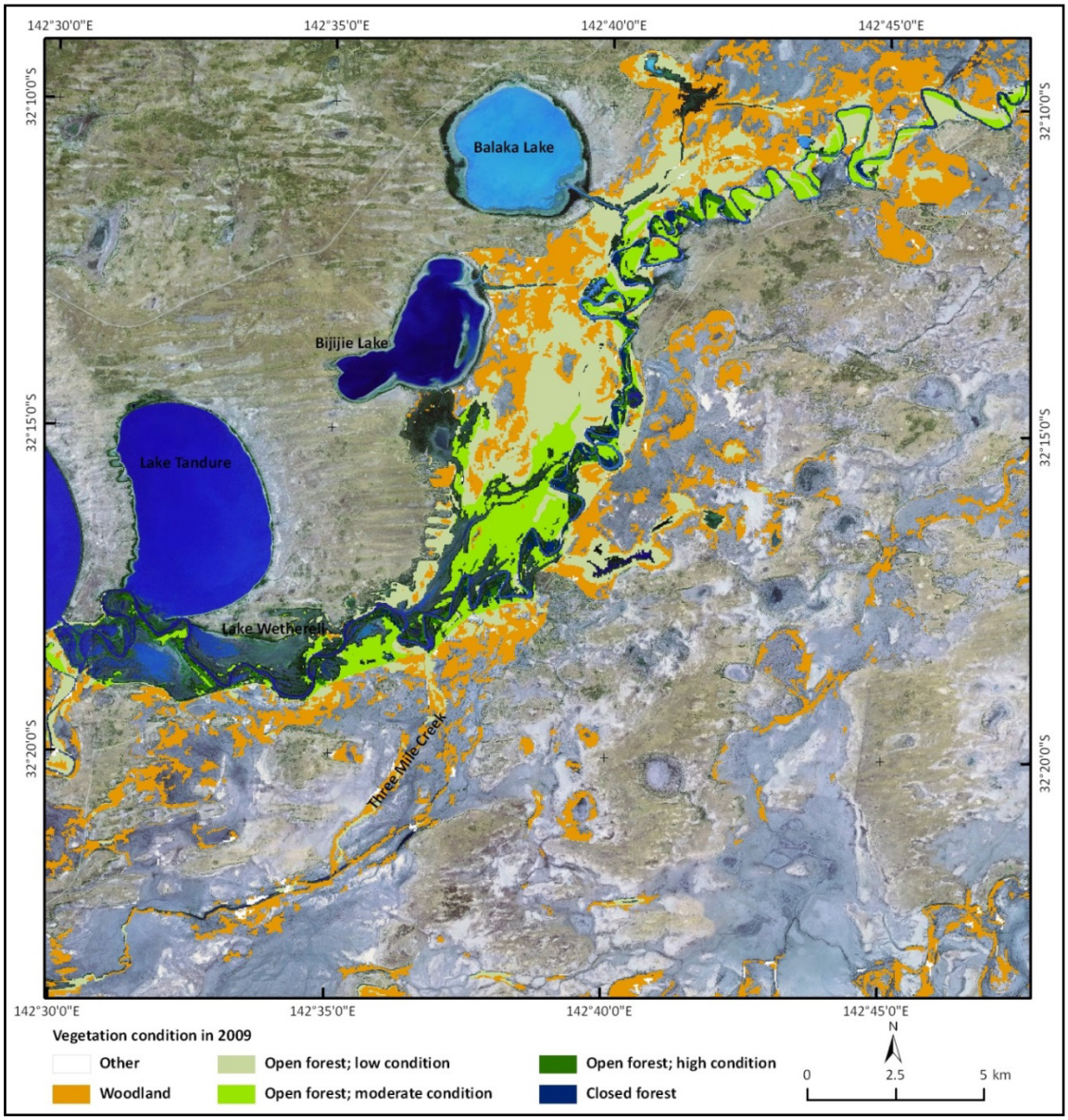



**Figure 17-31.** *Condition of vegetation at the conclusion of the drought (2009).*

*Comparison between vegetation condition at beginning and end of drought*

In order to observe the overall trend in vegetation condition over the drought period two relevant time periods needed to be selected – one that represents vegetation exposed to prolonged dry conditions (i.e. 2009) and one that represents vegetation subjected to good favourable-term conditions (prior to the commencement of the drought), but not responding to recent rainfall events. 2002 was selected as the most appropriate year. However water was held in Lakes Menindee and Cawndilla during this time and associated lake-fringing vegetation was supported by this water. To avoid this complication, 2004 was selected at the 'beginning' of the drought for all lake-fringing vegetation. Annual minimum NDVI values in 2002 or 2004 were subtracted from 2009 values to produce a trend value. Trend values range from -0.30 to 0.33; positive values represent an overall increase in vegetation condition and negative values represent a decrease over time. In order to compare these trends spatially, the results were classified into five standard deviation classes: ± ½ standard deviation representing no/minimal change; ± ½ to 1½ standard deviations representing moderate change; and ± greater than 1½ standard deviations representing considerable change in vegetation condition over time. This classification approach is shown in Figure 17-32. Vegetation communities that apparently exhibit and increase in condition over the course of the drought are typically associated with a reliable source of water.

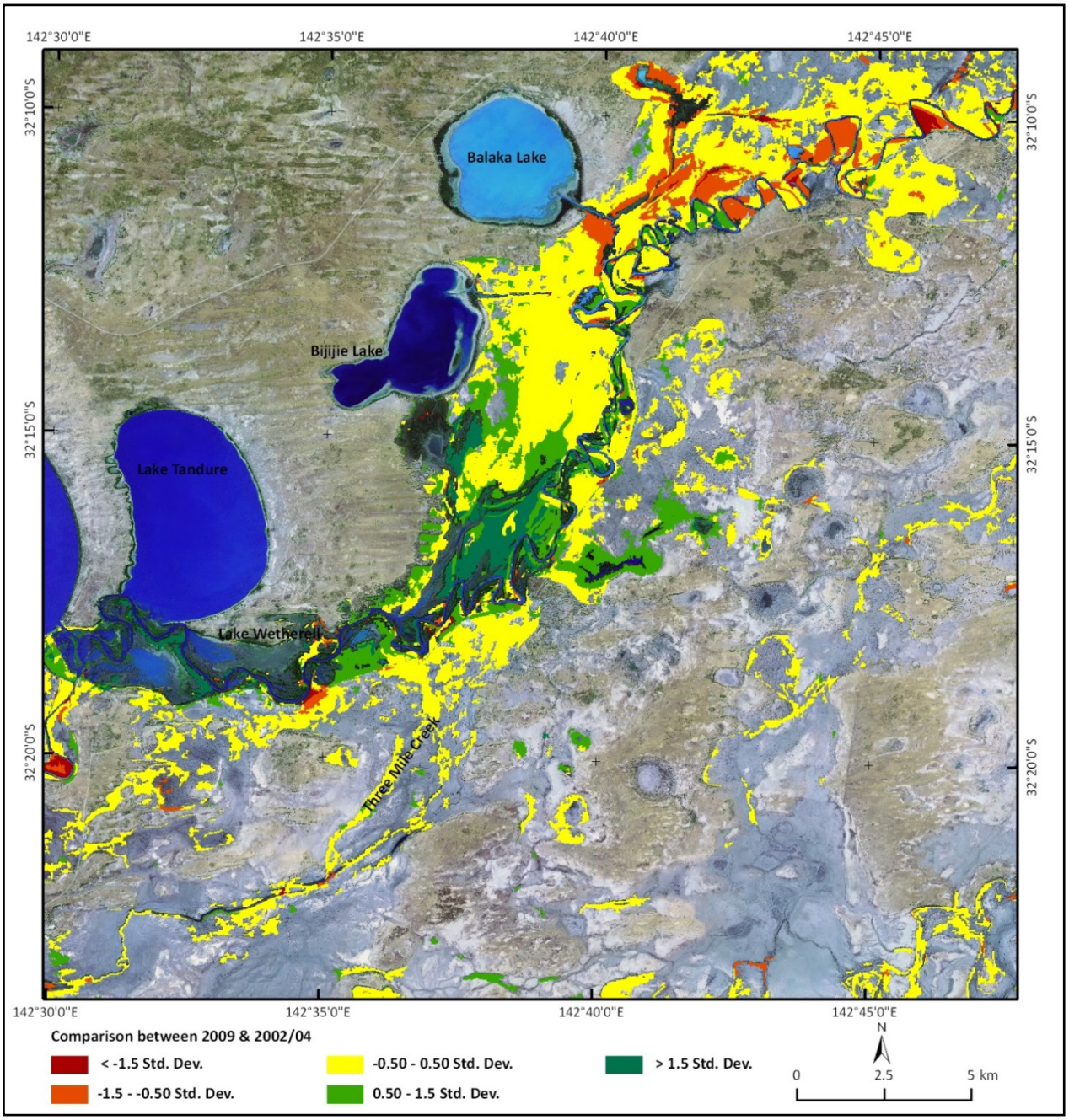



**Figure 17-32.** *Comparison of vegetation condition at the beginning and end of the drought.*

This product however does not provide any information about the amount of variability in condition experienced over time which may provide some indication of the water source being exploited by vegetation. Consequently, at third product was developed.

*Variability in vegetation condition throughout drought*

The amount of variability in vegetation condition on an annual basis over the course of the drought provides an indication of the variability of source water. Where vegetation condition remains largely consistent throughout the drought, a reliable water source is believed to have been accessed. Where vegetation condition changes markedly from one year to the next, it may be a result of varying volumes of water. To this end, the variability in vegetation condition was accessed over the course of the drought. Standard deviation of vegetation condition over the course of the drought (2002-2009) was estimated from annual minimum NDVI values from 2002, 2004, 2005, 2006, 2008 and 2009 using Equation 104 where $x$ is the sample mean average and $n$ is the sample size:

$$\left(\frac{(\bar{x}_1 + \sigma_1) - \bar{x}_2}{2}\right)$$

**Equation 104**

The standard deviation calculated for each vegetation community ranged from 0.001267 to 0.232286. These values were classified into three classes: low, moderate and high (relative) variability in vegetation condition during the drought. The relevant class breaks are shown in Table 17-23. This classification approach is shown in Figure 17-33. Vegetation communities that exhibit minimal variation are likely to have been supported by consistently available water, for example groundwater.

**Table 17-12.** *Classification of variability in vegetation condition based on calculated standard deviations.*

| Variability | Standard Deviation |
|---|---|
| Low | <0.012 |
| Moderate | 0.012-0.021 |
| High | >0.021 |

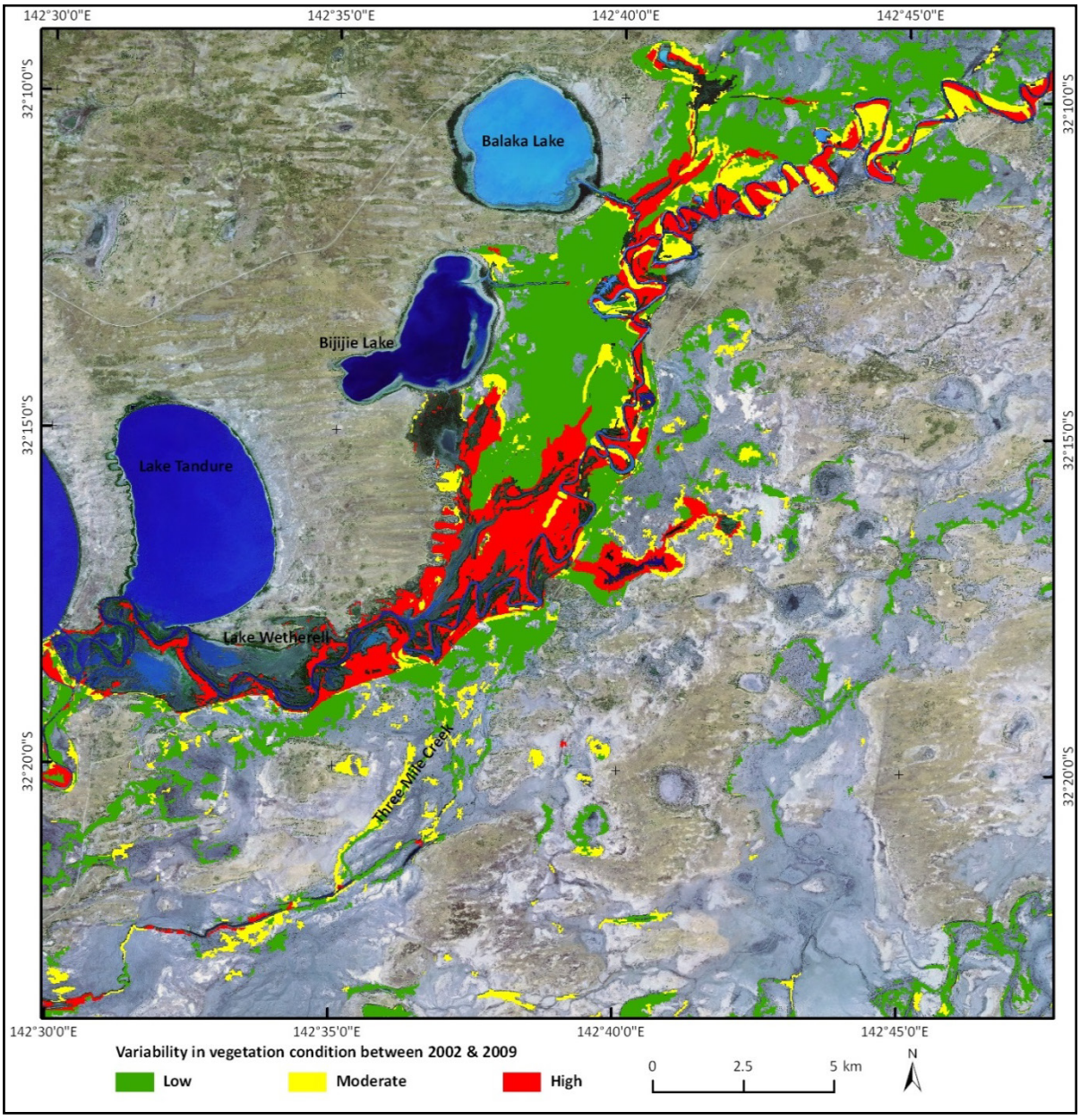



**Figure 17-33.** *Indication of the variability in vegetation condition through the drought period (2002-2009).*

*Water volume and reliability matrix*

The three aforementioned products – condition in 2009, drought condition trend (2009 versus 2002/04), and drought condition variability – were combined to produce a fourth product indicative of source water volume and reliability.

A weight value was applied to each class in the different products (see Table 17-13 and Table 17-14). The overall trend and variability in vegetation condition during the drought were combined to provide an estimate of source water reliability (Table 17-13). If there was little change between 2002 (or 2004) and 2009, and little variability across the whole drought period, then source water was presumed to be high. If considerable change occurred and condition was quite variable, low source water reliability was assigned.

Vegetation condition classes: woodland, open forest (low, moderate and high condition) and closed forest were loosely related to the amount of available water; canopy density has been demonstrated to correlate with the amount of available surface and groundwater (Jones *et al*., 2008). Inferred source water reliability was then combined with inferred qualitative volume of water to derive a water volume/reliability matrix (Table 17-14). This classification scheme is shown in Figure 17-34.

**Table 17-13.** *Two variables a) overall trend in condition between the beginning and end of the drought and b) amount of variability in vegetation condition throughout the drought, classified and combined to provide c) an indication of source water reliability. SD indicates standard deviation.*

| a) | Class | Weight Value |
|---|---|---|
| **2009vs2002/4** | <-1.5 SD | **3** |
| | -1.5–-0.5 SD | **2** |
| | -0.5–0.5 SD | **1** |
| | 0.5–1.5 SD | **2** |
| | >1.5 SD | **3** |

+

| b) | Class | Weight Value |
|---|---|---|
| **Variability** | <=0.012 | **1** |
| | 0.013–0.017 | **2** |
| | >0.021 | **3** |

=

| c) | Reliability of water source |
|---|---|
| 2-3 | High |
| 4 | Moderate |
| 5-6 | Low |

**Table 17-14.** *Vegetation condition at the end of the drought used as an indicator of available water volumes (qualitative) combined with water source reliability to create a matrix of water volume and reliability.*

| a) | NDVI value | Vegetation Class | Volume of water | Weight value |
|---|---|---|---|---|
| **2009 NDVI** | <0.14 | Other | n/a | Null |
| | 0.14-0.19 | **Woodlands** | Very low | 5 |
| | 0.19-0.29 | **Open forest, low condition** | Low | 4 |
| | 0.29-0.39 | **Open forest, moderate condition** | Moderate | 3 |
| | 0.39-0.48 | **Open forest, high condition** | High | 2 |
| | >0.48 | **Closed forest** | Very high | 1 |

+

| b) | Reliability of water source |
|---|---|
| 1 | **High** |
| 2 | **Moderate** |
| 3 | **Low** |

=

| c) | CF | OFH | OFM | OFL | W |
|---|---|---|---|---|---|
| H | 1,1 | 2,1 | 3,1 | 4,1 | 5,1 |
| M | 1,2 | 2,2 | 3,2 | 4,2 | 5,2 |
| L | 1,3 | 2,3 | 3,3 | 4,3 | 5,3 |

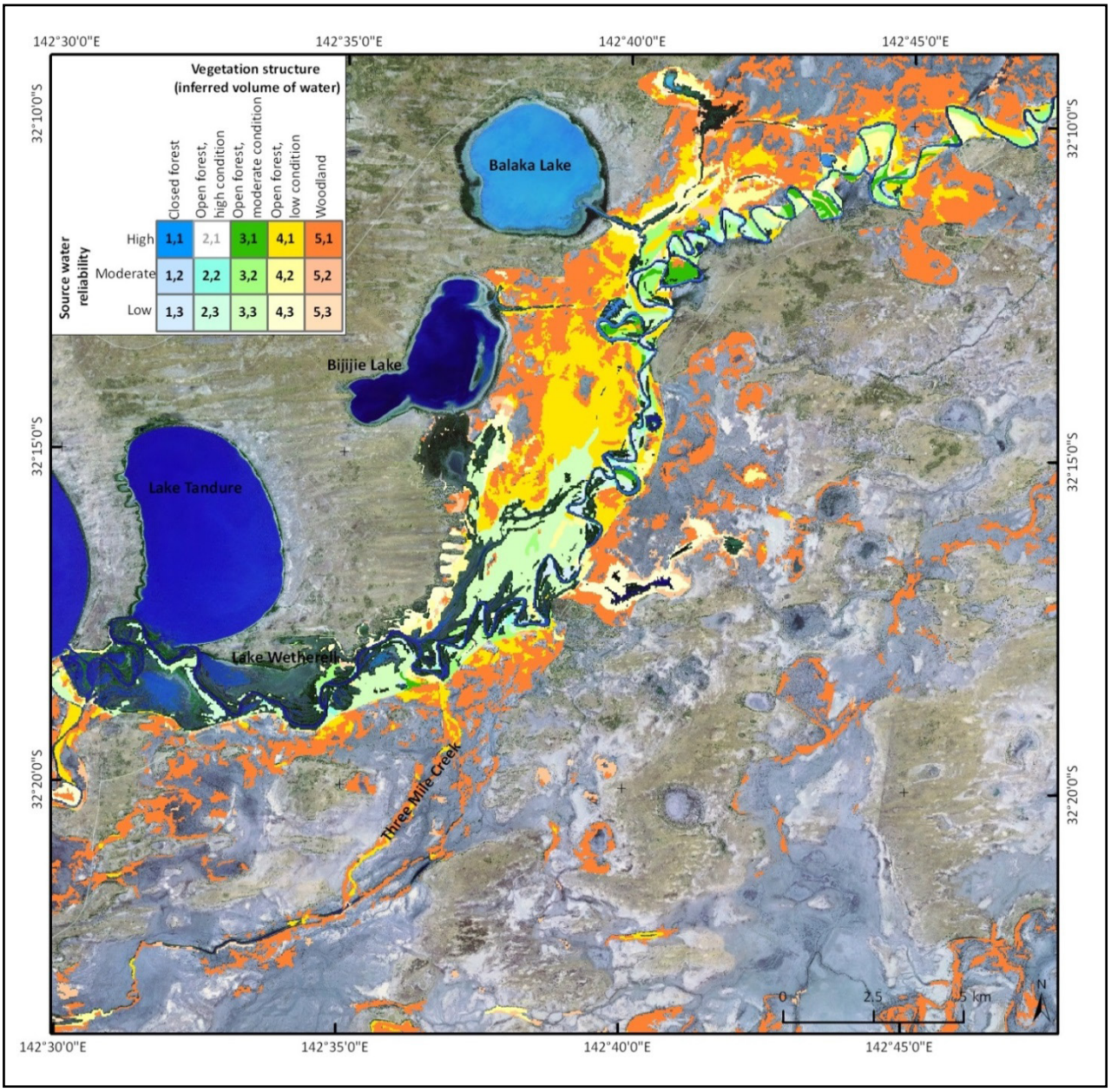



**Figure 17-34.** *Inferred volume and reliability of source water.*

These variables were integrated with hydrologic, hydrogeologic, hydrogeochemical and geophysical data to interpret spatial and temporal vegetation dynamics of woody vegetation. This included analysis of lake-fringing, riparian zone and floodplain vegetation, as well as vegetation within Kinchega National Park, and both the groundwater resource and managed aquifer recharge target sites.

*Limitations and uncertainty*

As with the other dataset, ground truth data would have been able to provide some sense of the accuracy, particularly in relation to the identification of NDVI thresholds for vegetation condition. Field observations cannot be obtained retrospectively though so the opportunity to validate this particular dataset may have passed.

#### 17.2.3.4 *Landsat derived inundation mapping*

Section 17.1 details the inundation mapping generated as part of the BHMAR Project. Relevant to the vegetation assessment study is when, for how long and how frequently vegetation communities have been subject to inundation in the past. This is important when assessing vegetation condition over time as too much or not enough water can have a significant impact. Consequently, in addition to simplifying mapping the spatial extent of surface water (in the case of the Landsat products) or modelling surface water extent against river level data (in the case of the LiDAR products), the timing and frequency of inundation was investigated.

The open water class for each Landsat scene was integrated to create maps that show the maximum observed inundated extent and frequency of inundation on a per year basis (where both extent and frequency are functions of the number of available cloud free scenes for that year). Figure 17-35 shows an example of this product for 2010. As a consequence of this inherent limitation in the Landsat inundation frequency mapping, the LiDAR DEM data was used to model inundation based on local elevation in conjunction with historic river level data.

Potential flood extents were derived by elevation slicing of the adjusted levelled DEM between 5.5 m (the point at which overbank flow occurs at Weir 32) to 8.0 m (maximum recorded river level height). These raster surfaces were then compared with the historical record to generate a flood frequency surface per year, summarizing how many days any single Landsat pixel was inundated (Figure 17-36). As Lakes Wetherell, Tandure, Pamamaroo, Cawndilla and Menindee are regulated, frequencies for these lakes are not truly indicative. Additionally, as the flood surfaces were generated strictly based on elevation, they do not take into account impediments to flow or the depletion of water as it moves through the landscape. For example Lake Tandou has been banked off since 1979 for irrigation and consequently does not experience inundation except in extreme flood cases.

This data was used in the interpretation of vegetation condition (Lawrie *et al*., 2012b).

### 17.2.4 Future Recommendations

There are some limitations of the Landsat vegetation mapping, primarily arising from the inability to quantify the extent of uncertainty. A single-look, dry climate LiDAR vegetation structural map was essentially used to calibrate the Landsat NDVI vegetation categories. The collection of additional LiDAR data for a wet period could be used to more robustly calibrate the Landsat NDVI and provide a better understanding of how changes in hydrologic regimes alter vegetation characteristics. For example, what is the sensitivity of canopy density to prolonged dry conditions with respect to NDVI sensitivity? Hence there still remains some uncertainty about how significantly the drought affected canopy density and whether similar degree of influence was detected by NDVI.

Furthermore, both the LiDAR and Landsat vegetation mapping products would benefit from additional ground truth data which would be used to quantitatively assess the suitability of the methodology used and the accuracy of the derived products. Field observations would also provide valuable input at a much higher resolution than that provided by the 30 m Landsat. Similarly, aerial photography could be used to improve our understanding of vegetation dynamics at an individual tree level. This imagery would also be more readily compared to the historic 1940s aerial photography to better quantify the extent of historic land cover change. As was evident when comparing the two sets of field observations with the LiDAR-derived vegetation structural mapping, it is important to capture field observations at the time of, or as close to image acquisition (e.g. LiDAR or Landsat). This has implications for the usefulness of any field observations collected in the future that are not paired appropriately with LiDAR or Landsat imagery.

Finally, while NDVI is the most commonly used vegetation index in the remote sensing literature for vegetation studies, there are other indices that could provide complimentary input such as vegetation water content indices. Similarly fractional cover could be used to determine the proportion of an area covered by each vegetation or land cover type.

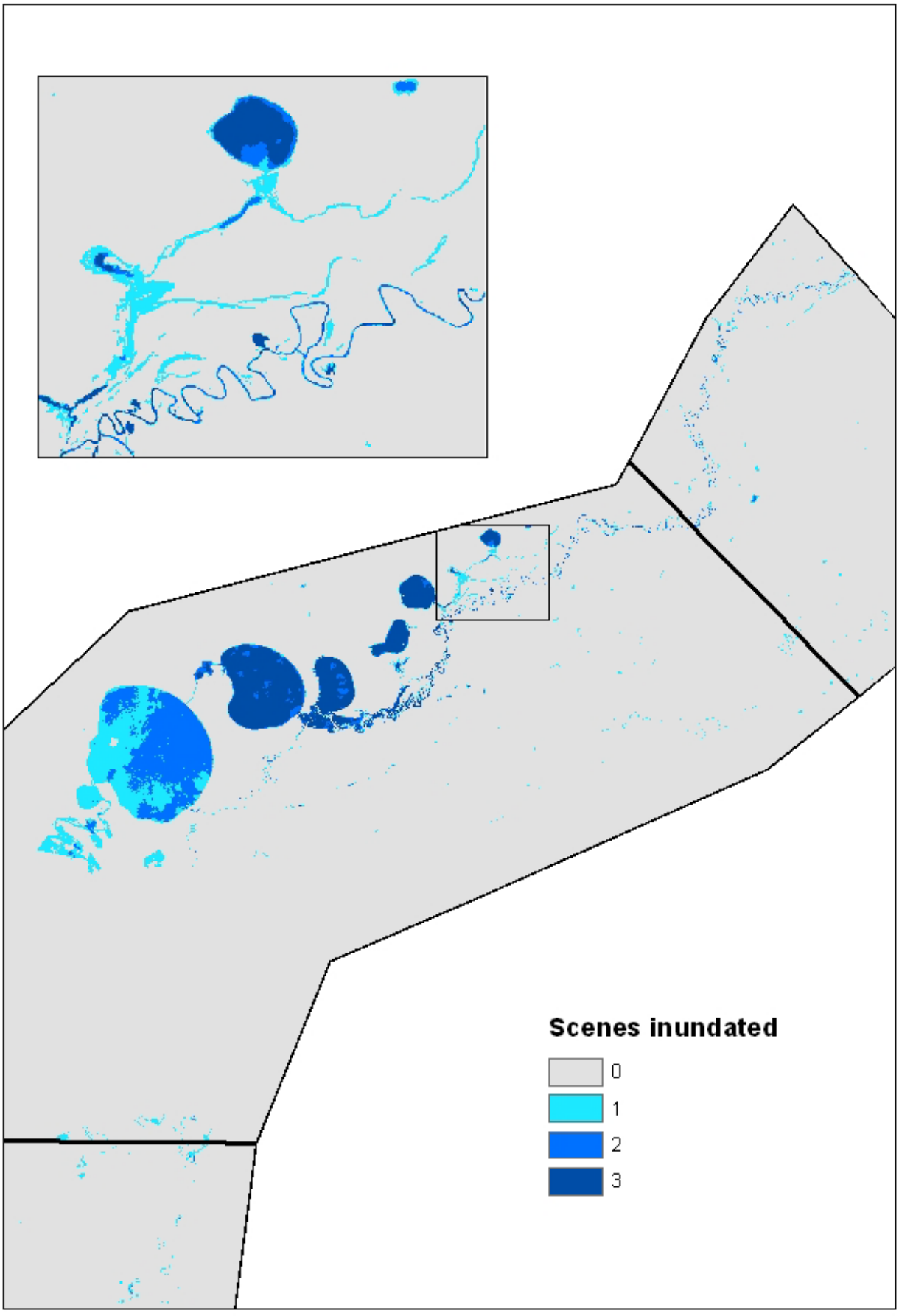



**Figure 17-35.** *Flood frequency for 2010 as generated from the Landsat flood inundation surfaces.*

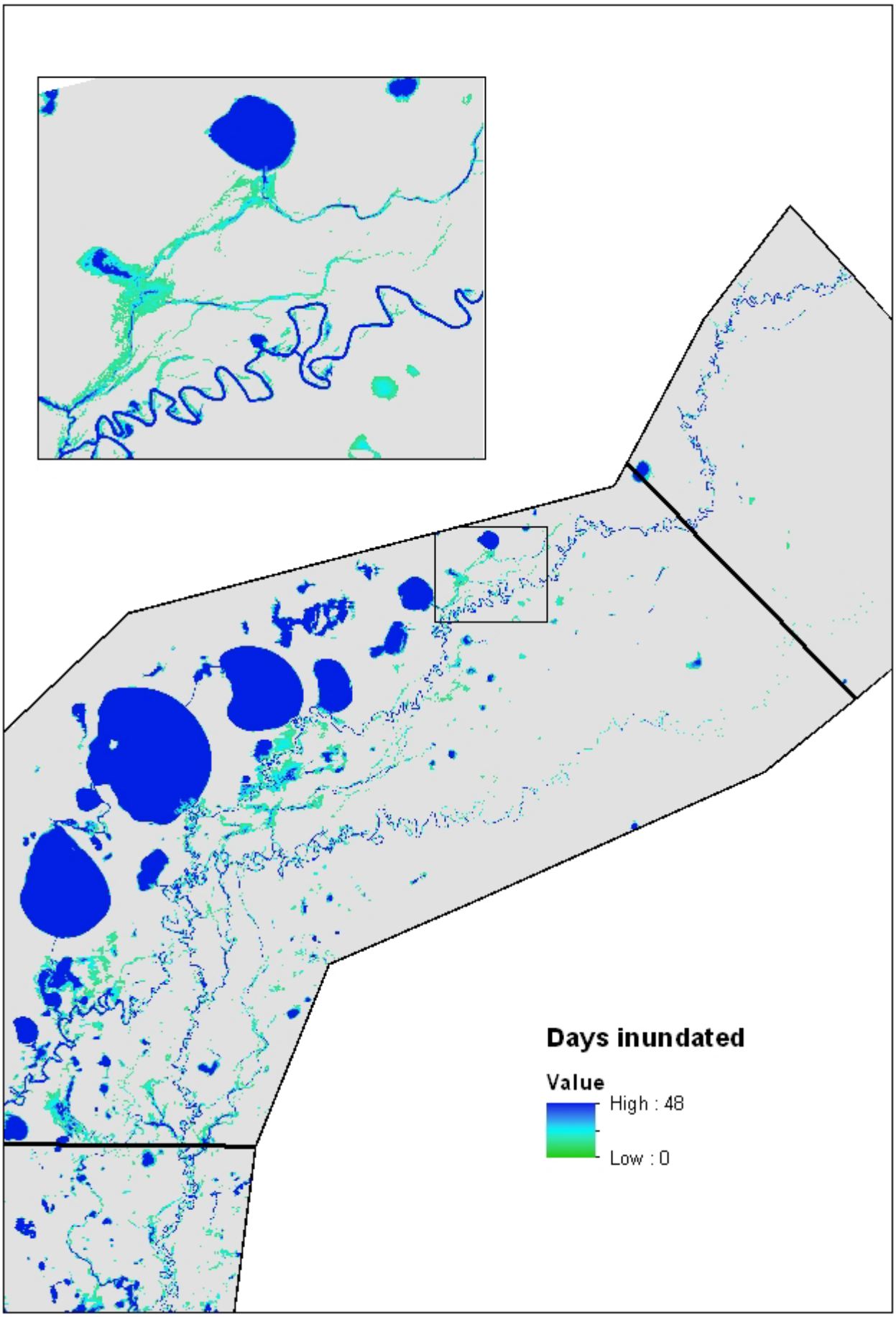



**Figure 17-36.** *Flood frequency for 2010 as generated from the LiDAR DEM potential flood inundation surfaces.*

## 17.3 LINEAMENTS AND STRUCTURAL MAPPING

### 17.3.1 Structural Mapping Using the AEM Inversion Products

Recognition of discrete faults and fold structures in the BHMAR study area was made possible with the final inversions (Figure 17-37; Figure 17-38). In the previous AEM inversions, regularisation and lateral parameter correlation parameters were not optimized for the local hydrostratigraphy and complex structural architecture of the area.

This is evident in Figure 17-37 and Figure 17-38, where the Blanchetown Clay aquitard (electrically conductive), is offset along a discrete fault (bottom panels). Previously, there was insufficient confidence in the layer boundary mapping to either identify or map these structures with any degree of confidence. Figure 17-38 is the same flight line section, showing the results of the WANDA inversion with different regularization constraints. The final inversion procedure used 'loose' regularization constraints and a new lateral parameter correlation procedure to enable details of the hydrostratigraphy and structure to be revealed. Because the final inversion utilised a new lateral parameter correlation procedure and 'loose' regularization settings, a number of additional checks were made on the final AEM inversion (including assessment of data residuals), to ensure that no artefacts were created during the inversion procedure. This gave additional confidence to the mapping of units such as the Blanchetown Clay.

Of equal importance, new lateral correlation methods were developed in the inversion procedures so that a strictly horizontal correlation in the inversions was possible. For the first time, this means that stratigraphic layers do not automatically follow topography when inverted (Figure 17-39). These improvements in inversion procedures have provided confidence in the ability to map a multi-layered hydrostratigraphy, and to identify faults (Figure 17-40; Figure 17-41). Due to depth of investigation limits of the AEM system, and saline (conductive) groundwater in some of the Calivil Formation, it is not possible to map the Calivil Formation-Renmark interface everywhere in the study area. Figure 17-41 is an example where a fault discontinuity mapped at the Blanchetown Clay horizon is also evident in the Calivil Formation-Upper Renmark Group interface.

To map the structures in detail, AEM sections were displayed in Profile Analyst, and vertical displacements or changes in dip of the Blanchetown Clay were marked as a point at about the mean level of Blanchetown Clay on either side of the structure (Figure 17-42). The xyz locations of the points were exported as .csv files, for display as xy points on maps in ArcGIS (Figure 17-40) and to display on 3D Blanchetown Clay surfaces. Features were only identified as faults when features could be mapped across multiple flight lines. For the latter, the xy location of the point was intersected with the elevation of the surface so that a fault point could be marked on the surface. The density of points used to create a contoured map of the elevation of the top of the Blanchetown Clay surface is shown in Figure 17-43 (BHMAR study area). In total, >60,000 picks on formation tops and off-sets were identified in Profile Analyst. The density of points for mapping the top Blanchetown Clay layer at the borefield scale is shown in Figure 17-45, with an interpretation showing the contoured top surface and interpreted faults shown in Figure 17-46.

Displacements vary from sharp, faulted offsets to warps over a distance of several hundred metres (Figure 17-47), with up to 20 m vertical displacement over a single structure (Figure 17-38). The interpretation was confirmed by drilling data.

The AEM mapping reveals that rather than being flat lying the Blanchetown Clay is warped and tilted at a range of scales, with elevation of the top surface varying by ~ 60 m in elevation across the project area (Lawrie *et al*., 2012b; Figure 17-44). These lacustrine deposits filled in an undulating palaeo-topography, and have been eroded in a number of locations and these issues partially explain variations in thickness of the unit including minor variations in the elevation of the top surface (<10 m), but not the 50-60 m differences in elevation mapped across the study area.

Furthermore, in addition to being warped and tilted, the Blanchetown Clay is sharply offset in a number of locations, with vertical displacements of up to 20 m noted (Lawrie *et al*., 2012b; Figure 17-38). Offsets were recorded during systematic interpretation of all the AEM flight line sections and a map of the offset locations combined with the contoured top Blanchetown Clay surface. The pattern of folding and faulting mapped in

the Blanchetown Clay is consistent with the faulting of similar materials used in sandbox and clay laboratory deformation experiments (McClay & Dooley, 1995).

Using this approach, individual offsets in the Blanchetown Clay were found to occur in linear zones of varying length that cross several flight line sections (Figure 17-47). These linear offset zones have been interpreted as geological faults, with vertical displacements of 5-20 m mapped across many of these structures. Interpretation of flight line sections reveals that these faults do not always terminate abruptly, with monoclinal warps mapped in zones 200-400 m beyond mapped fault offsets (Figure 17-41).

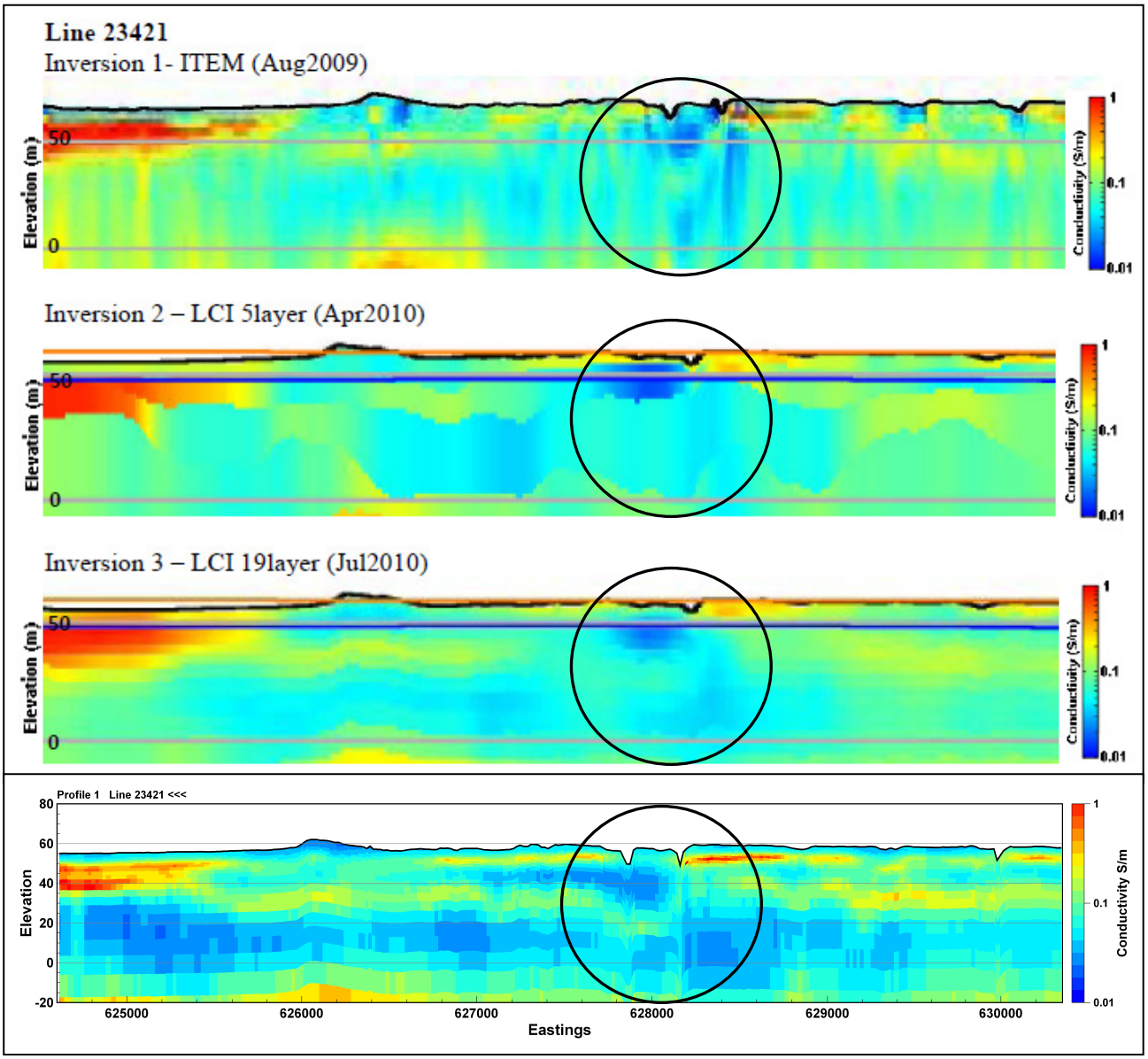



**Figure 17-37.** *Series of conductivity depth sections for one flight line (23421) showing different inversions, with the final inversions in the bottom two panels. The figure illustrates the improvements in mapping the hydrostratigraphy and faults by optimizing the inversion constraints. The final inversion product (bottom image) clearly shows the offset in conductive layers (clay aquitard) in the middle of the area circled. Previously, there was insufficient confidence in the layer boundary mapping to either identify or map these structures with any degree of confidence. Discrete fault offsets are only evident in the bottom two panels.*

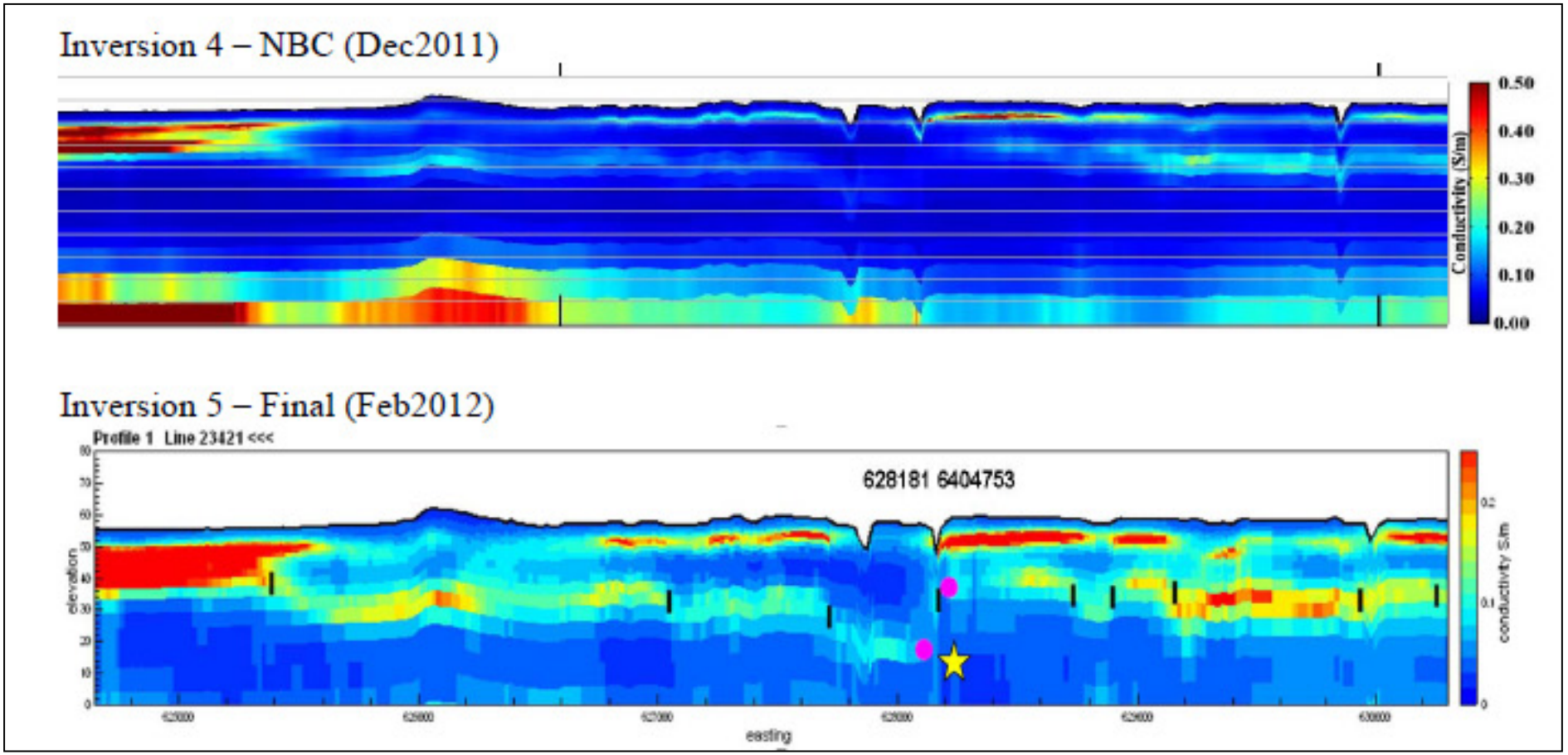



**Figure 17-38.** *Two conductivity depth sections produced using the new Wave Number Domain Approximate (WANDA) inversion procedure with a 1D multi-layer model and constraints in 3D. The top image was produced using standard 'tight' regularisation constraints, while the bottom section was produced using 'loose' regularisation settings. Comparison of borehole induction logs with adjacent AEM fiduciary points confirms high confidence levels in the final inversion (bottom section). The bottom image shows the location of a fault offsetting the Blanchetown Clay aquitard (pink dots). Inter-aquifer leakage is facilitated between the overlying unconfined aquifer and the Calivil Formation aquifer (yellow star) at this location.*

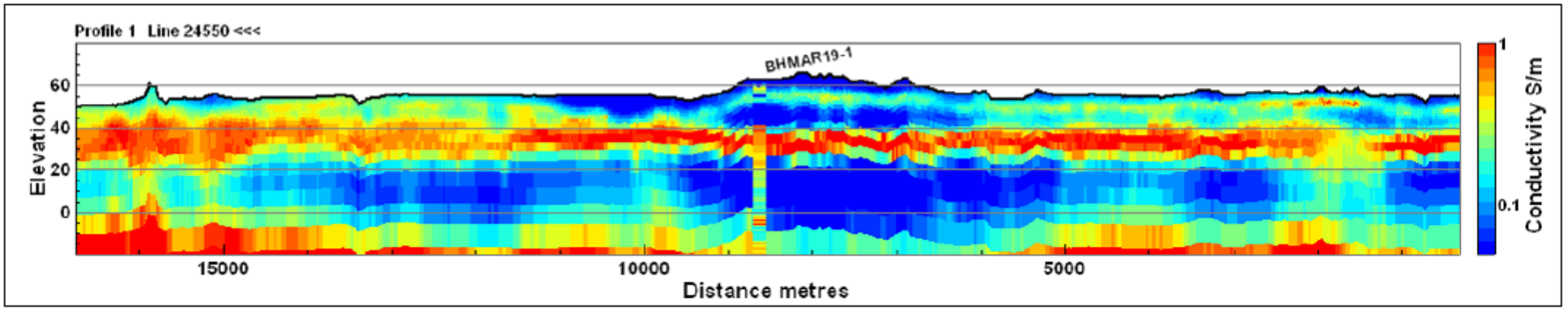



**Figure 17-39.** *Conductivity depth section produced using the new lateral parameter correlation procedures. The strong conductive layer in the middle of the figure is the Blanchetown Clay. It is flat-lying, and is not influenced by the overlying dune (topographic high) in the middle of the line.*

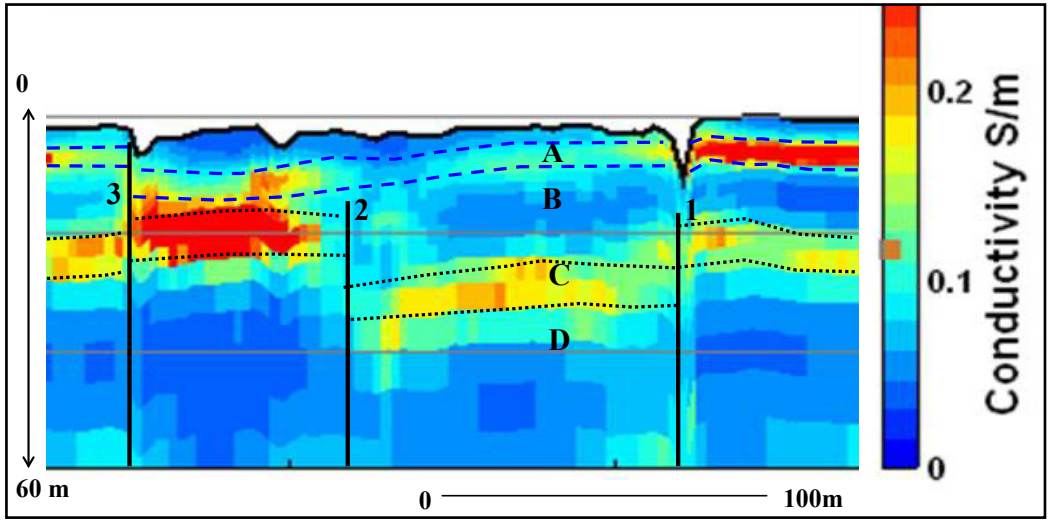



**Figure 17-40.** *Conductivity depth section for Line 23261. Discrete sharp offsets in the Blanchetown Clay (layer C) are evident in the conductivity depth section. A thickness increase in layer B (Coonambidgal Formation aquifer) is also evident across these faults.*

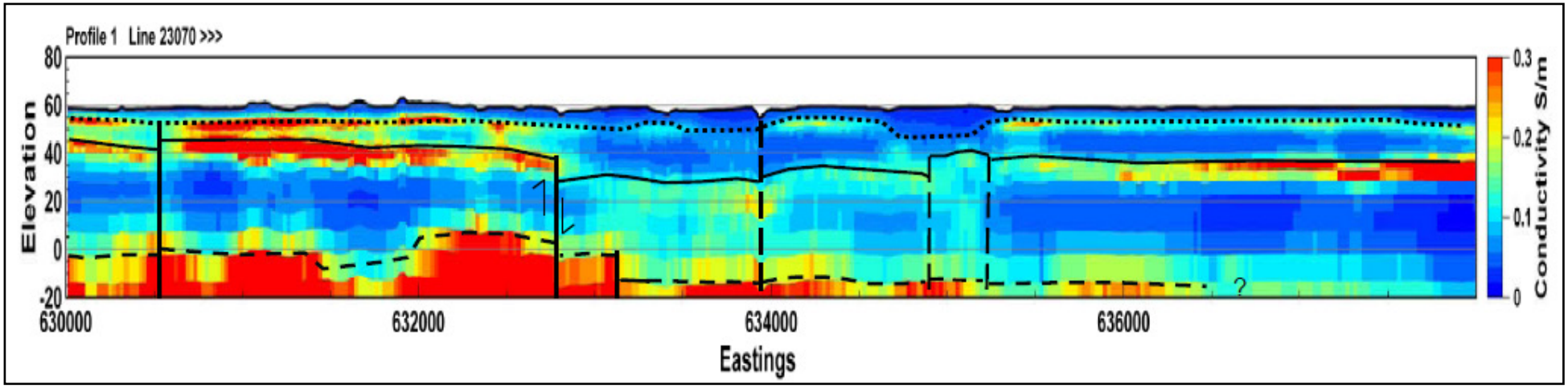



**Figure 17-41.** *Conductivity depth section showing an interpretation of the hydrostratigraphy and faulting. The upper surface of the near-surface aquitard (conductive layer (black dots)), the top of the Blanchetown Clay (conductive) layer is shown with a solid black line, and the approximate location of the top of the Renmark Group (conductive layer) is represented by a dotted black line. Due to depth of investigation limits of the AEM system, and saline (conductive) groundwater in some of the Calivil Formation, it is not possible to map the Calivil Formation-Renmark interface everywhere in the study area. Faults are indicated with vertical black lines.*

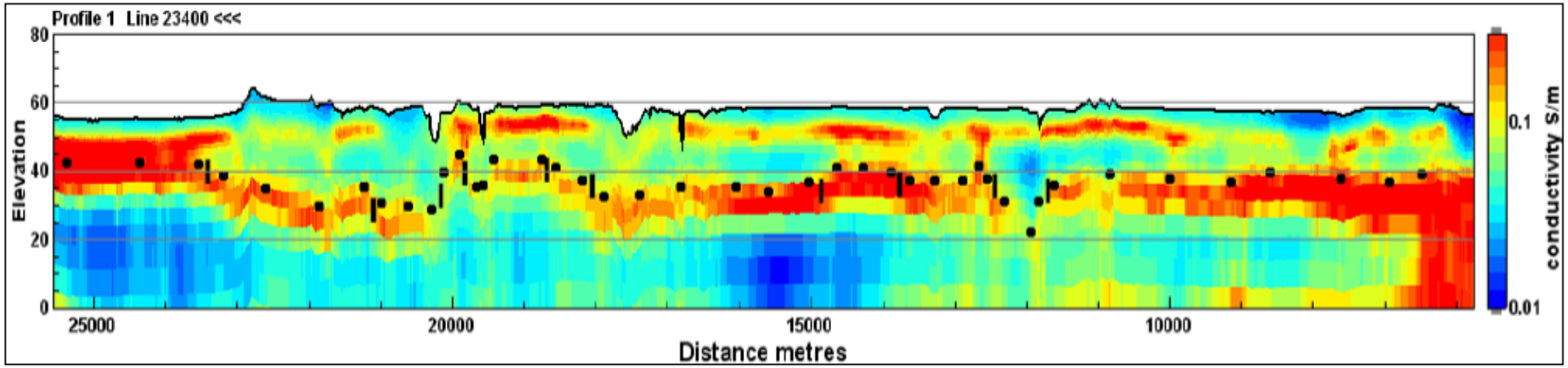



**Figure 17-42.** *Top picks (black dots) for the Blanchetown Clay (upper confining aquitard) and fault picks (vertical black lines) in a conductivity depth section (black lines). Offsets in the Blanchetown Clay were picked in individual flight line sections and then checked on adjacent flight lines and map views. Features were only identified as faults when features could be mapped across multiple flight lines.*

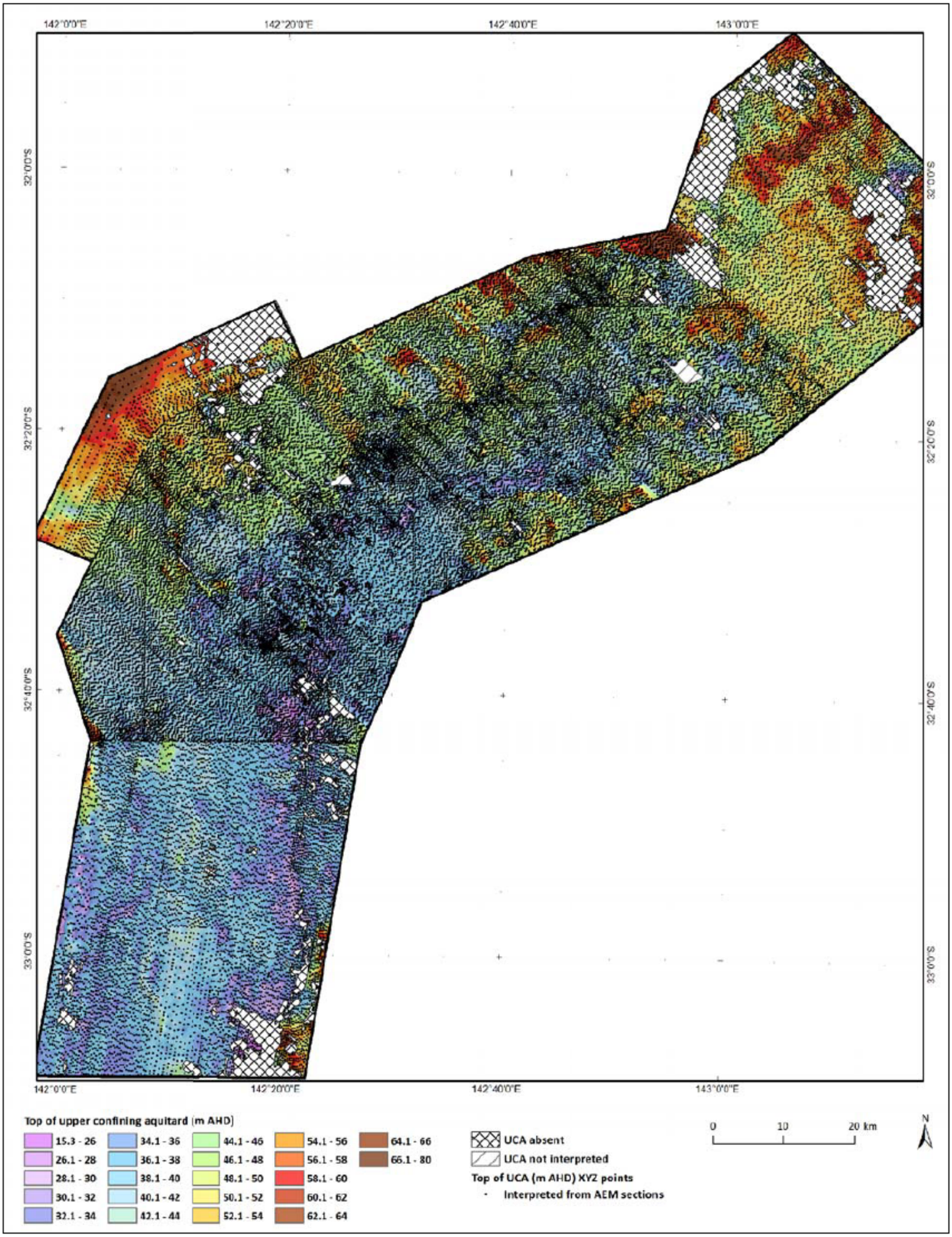



**Figure 17-43.** *Density of data points acquired from mapping the top of the Blanchetown Clay, and areas of 'holes' this surface (cross-hatched areas). The data were obtained from interpreting the top surface in flight line conductivity sections across the BHMAR study area. The data points are displayed on top of a map (colour contoured) of the depth to the top of the Blanchetown Clay layer.*

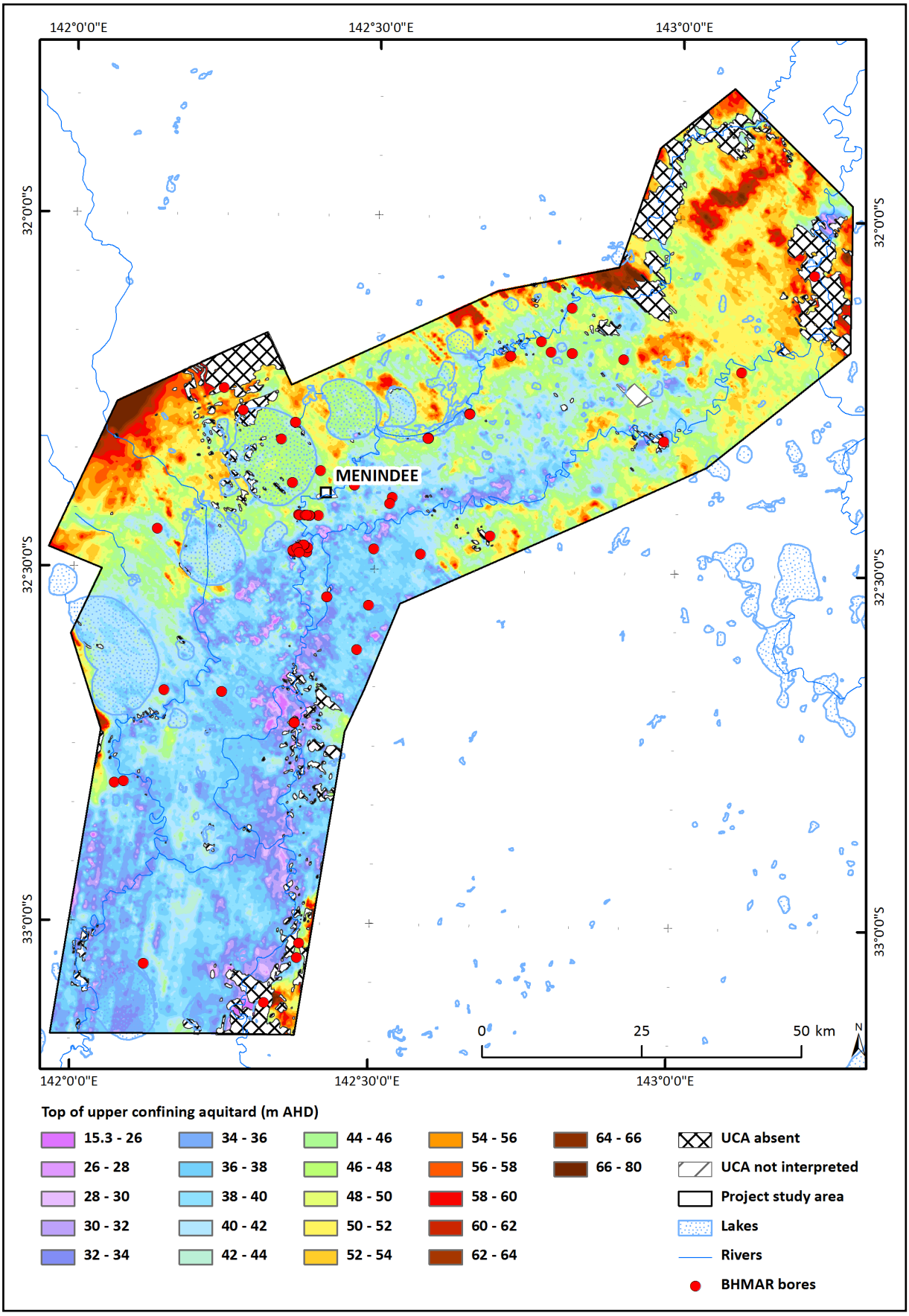



**Figure 17-44.** *Elevation of top of the Upper Confining Aquitard (predominantly Blanchetown Clay) in metres AHD.*

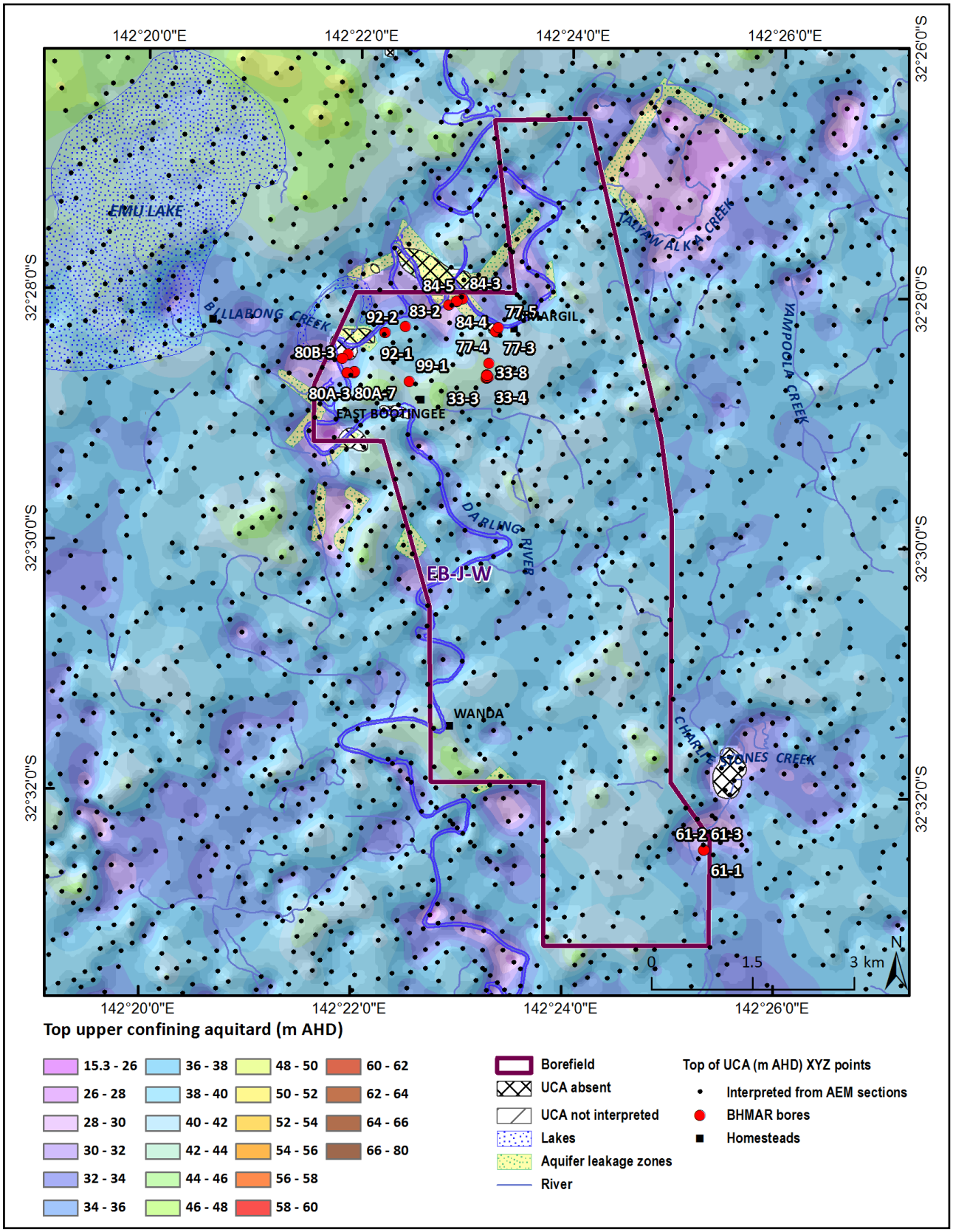



**Figure 17-45.** *Density of data points acquired from mapping the top of the Blanchetown Clay, and areas of 'holes' this surface (cross-hatched areas) at the borefield scale. The data were obtained from interpreting the top surface in flight line conductivity sections. The data points are displayed on top of a map (colour contoured) of the depth to the top of the Blanchetown Clay layer.*

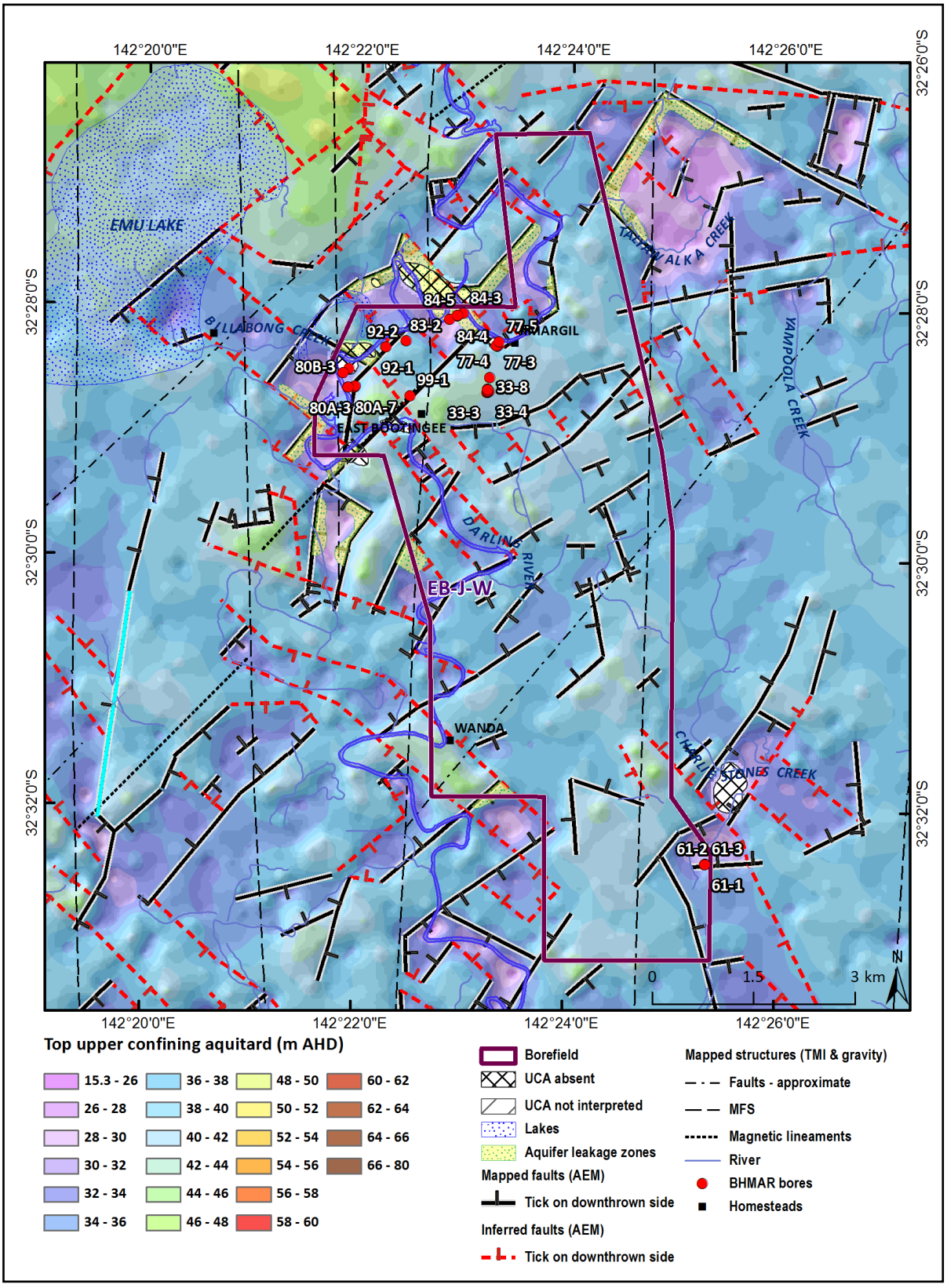



**Figure 17-46.** *Map showing faults offsetting the upper confining aquitard at the Jimargil potential borefield site. Individual flight line conductivity depth sections were used to identify faults and the tops (and base) of the upper confining aquitard produced. Mapped faults include those identified from flight line section picks alone, from interpretation of maps of the upper confining aquitard, and from interpretation of Total Magnetic Intensity images that show the location of basement faults. Locations where fault offsets are sufficient to be likely points for inter-aquifer leakage are marked with yellow stars.*

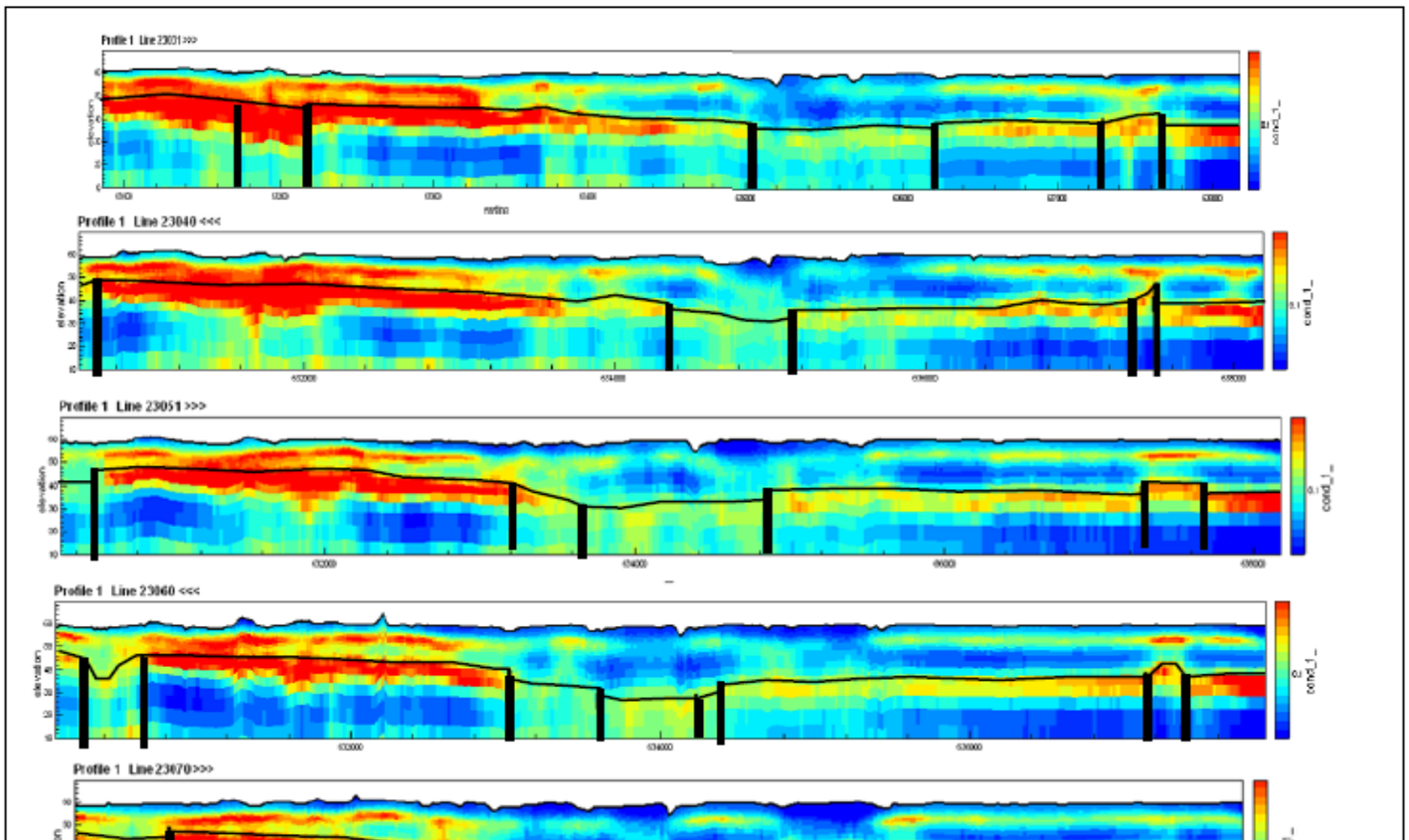



**Figure 17-47.** *Tiled conductivity depth sections with 200 m spacing between flight lines for an area near Menindee. Fault offsets of the top of the upper confining aquitard (Blanchetown Clay- shown with a thicker black line) are evident.*

### 17.3.2 Recognition of Lineaments on LiDAR

The BHMAR Project LiDAR was used to recognise and document lineaments in the surface landscape features, where expressed as anomalous straight-line trends. After some trial and error comparisons, it was determined that a greyscale hill-shaded LiDAR image was most effective for the recognition of features. The whole of the project area was examined on-screen in ArcMap at relatively close scale (~1:25 000) using 10 m resolution LiDAR data and lines were marked over linear features. At times, closer scale examination using 1 m resolution LiDAR was used. Two types of features were mapped:

- Relatively short (typically 0.5-2 km) straight sections of individual landscape elements, most commonly river reaches but also including, lake shorelines, valley margins and topographic highs. These are designated by unbroken lines in the GIS file.
- Longer (typically 3-20 km) straight sections mostly including more than one landscape element, including multiple river reaches, lake shorelines, valley margins and topographic highs. These are designated by broken lines in the GIS file.

The Lower Darling Valley has a thick Cenozoic marine, lacustrine, fluvial and aeolian sedimentary sequence which has buried the basement bedrock. The surface geomorphology consists of a fluvial, lacustrine and aeolian landscape overlying early Quaternary Blanchetown Clay lacustrine mud. Therefore there are no bedrock-related elements such as structure, bedding, jointing etc which can constrain the geomorphic expression of the surface units. However, the AEM interpretation of the Blanchetown clay has identified a number of structural features including faulting and deformation in the Blanchetown Clay and underlying valley-fill units. In some cases the AEM indicates these structures extend to the surface. Therefore, where there are anomalous linear constraints evident in surface units it is possible that it is due to deformation of the underlying Blanchetown clay that extends to the surface.

Some examples of the types of features recognised are presented in the following Figure 17-48 to Figure 17-53.

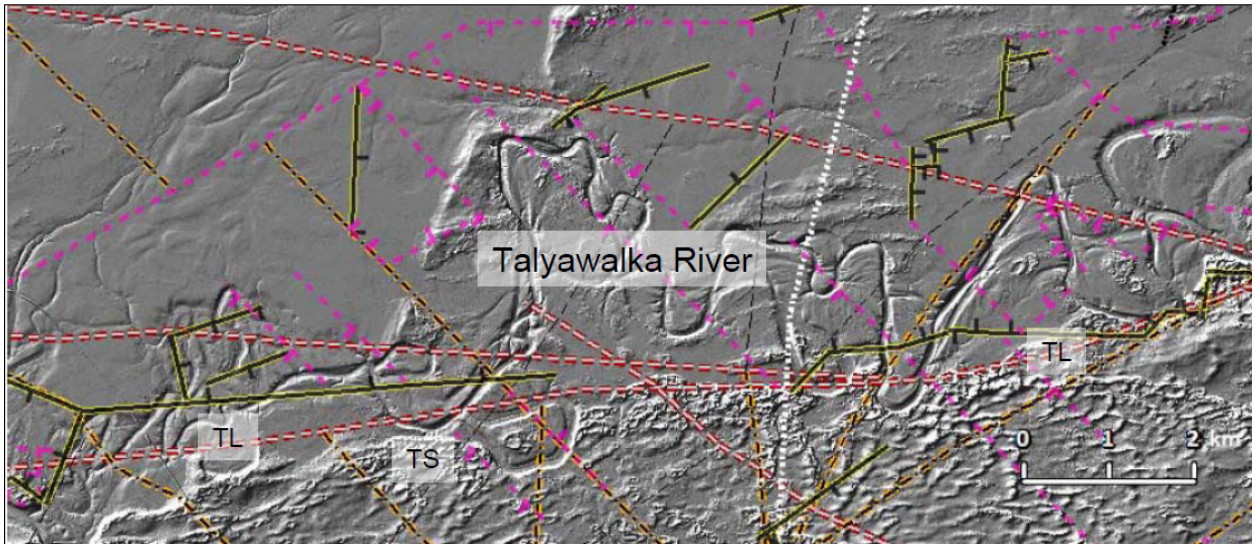



**Figure 17-48.** *LiDAR image showing the Talyawalka Scarp (TS) which is effectively coincident with a basement shear zone (TL – one of several sub-parallel basement shear zones (broken white lines with red border). It is postulated that the relief on the scarp is related to Neogene structural reactivation of the basement structure. The Talyawalka Creek effectively follows this major lineament. En-echelon half graben structures are delineated by extensional faults mapped at the Blanchetown Clay layer (solid black and dotted pink lines). A number of other scarps present in the image may also be related to tectonism.*

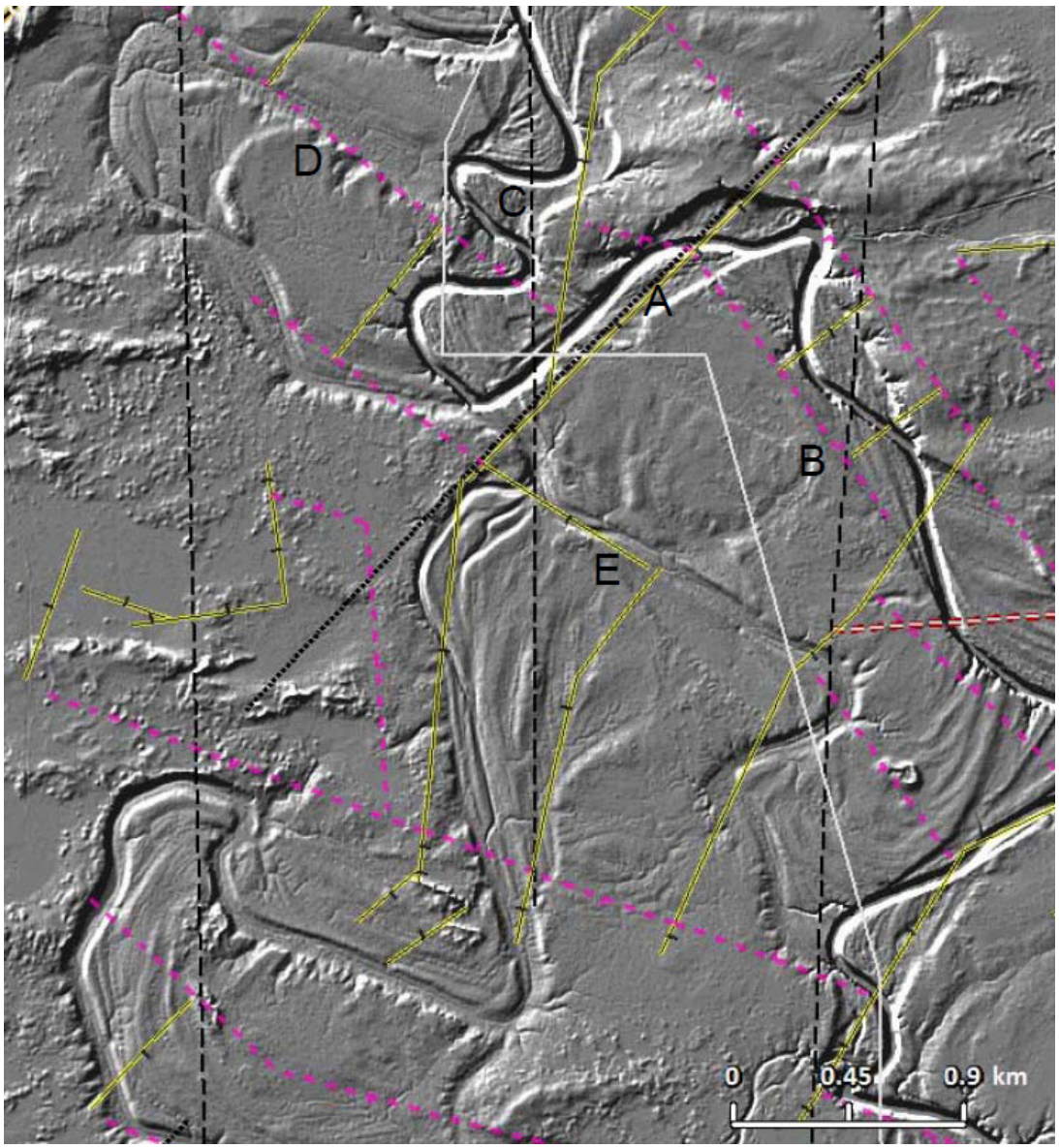



**Figure 17-49.** *LiDAR image of the Darling River near Bootingee showing unusual drainage pattern with numerous straight-line segments and box-like pattern in the river course. A number of straight line scarps (A-E) that parallel the river course are observed to be coincident with mapped faults in the underlying geology. Scarp A is coincident with both faults mapped in the AEM (black with yellow border) and with lineaments in airborne magnetic data (dotted black line). Scarps B, D and E, are coincident with faults mapped in the AEM data, while scarp C and river course, are coincident with an underlying strike-slip fault mapped in the magnetic basement. The drainage pattern is more reminiscent of an incised upland rather than an active low gradient floodplain. The drainage pattern is attributed to neotectonics.*

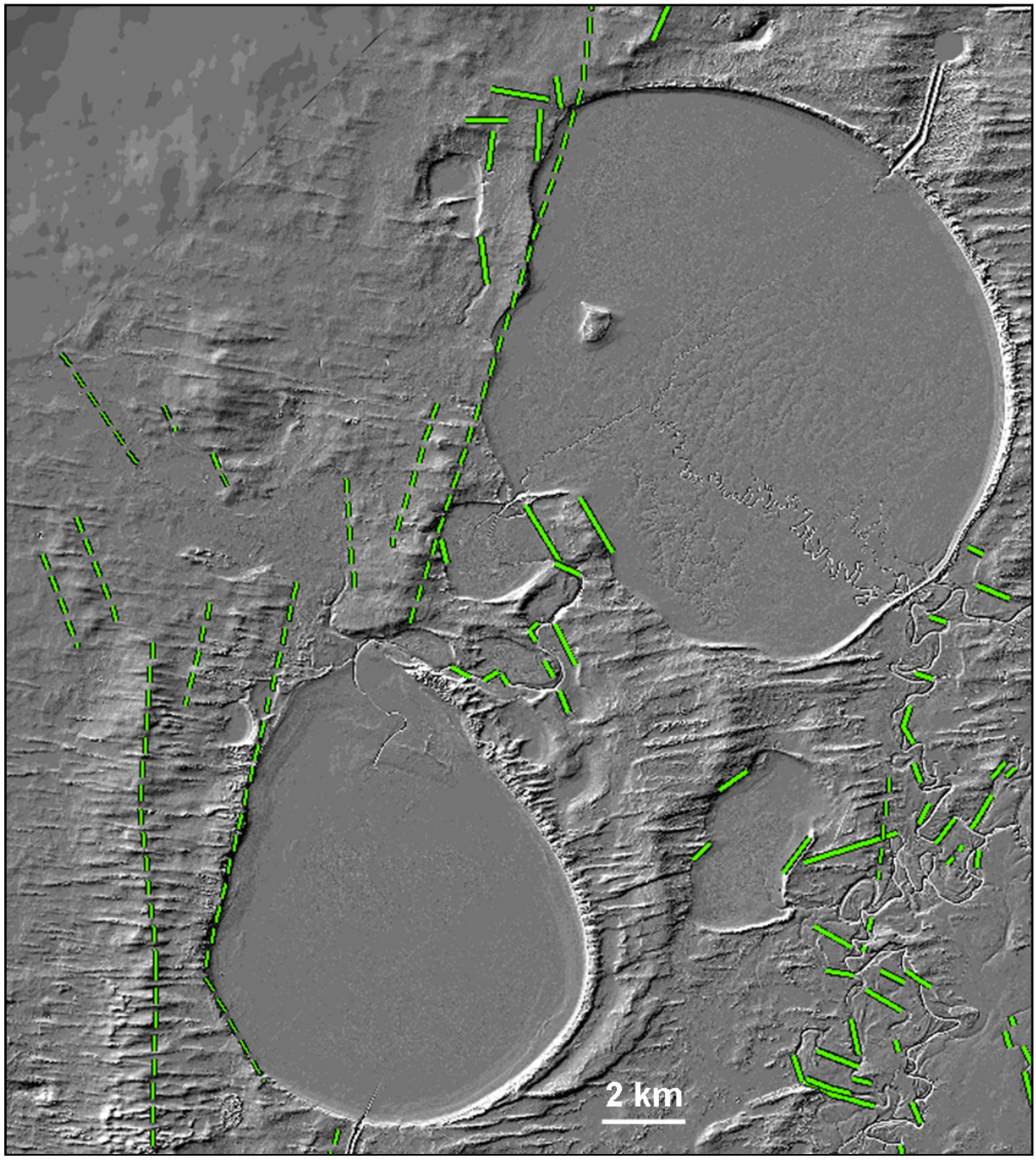



**Figure 17-50.** *View of Lakes Menindee and Cawndilla and the north western part of GWR1. The Darling River in the Jimargil-East Bootingee area is shown in the south-eastern corner. In the western portion of the view, elongate lineaments (dashed lines) extending across landscape elements constrain much of the western margins of both large lakes as well as a straight north-south ridge west of Lake Cawndilla. In between the lakes, shorter lineaments defined by individual landscape elements constrain the nature of the lakes and floodouts of Cawndilla Creek, which connects Lake Cawndilla and Menindee. Similar lineaments define portions of the shoreline of Emu Lake between the Darling River and Cawndilla Lake, as well as constrain many of the river reaches in the Jimargil East-Bootingee area.*

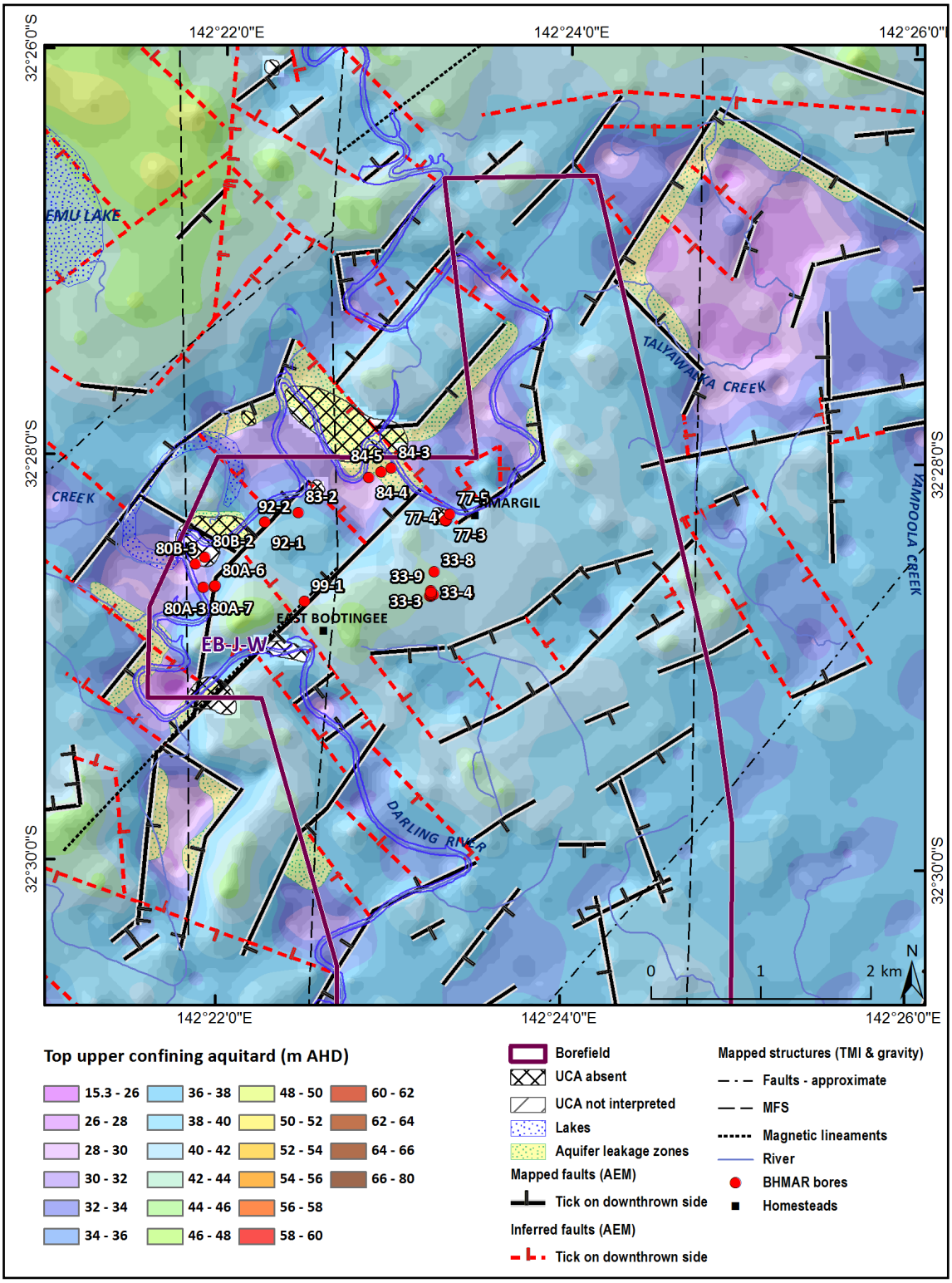



**Figure 17-51.** *Map of the top Blanchetown Clay surface showing contoured elevations and interpreted faults. This image also shows potential inter-aquifer leakage zones (pale yellow stipple) which occur at sites where the unconfined Coonambidgal Formation aquifer is juxtaposed against the semi-confined Calivil Formation aquifer and/or where the Blanchetown Clay has been eroded (cross-hatched pattern) on the footwall zones of some of the larger faults. Rapid recharge of the Calivil Formation is recorded in a number of the bores close to these zones.*

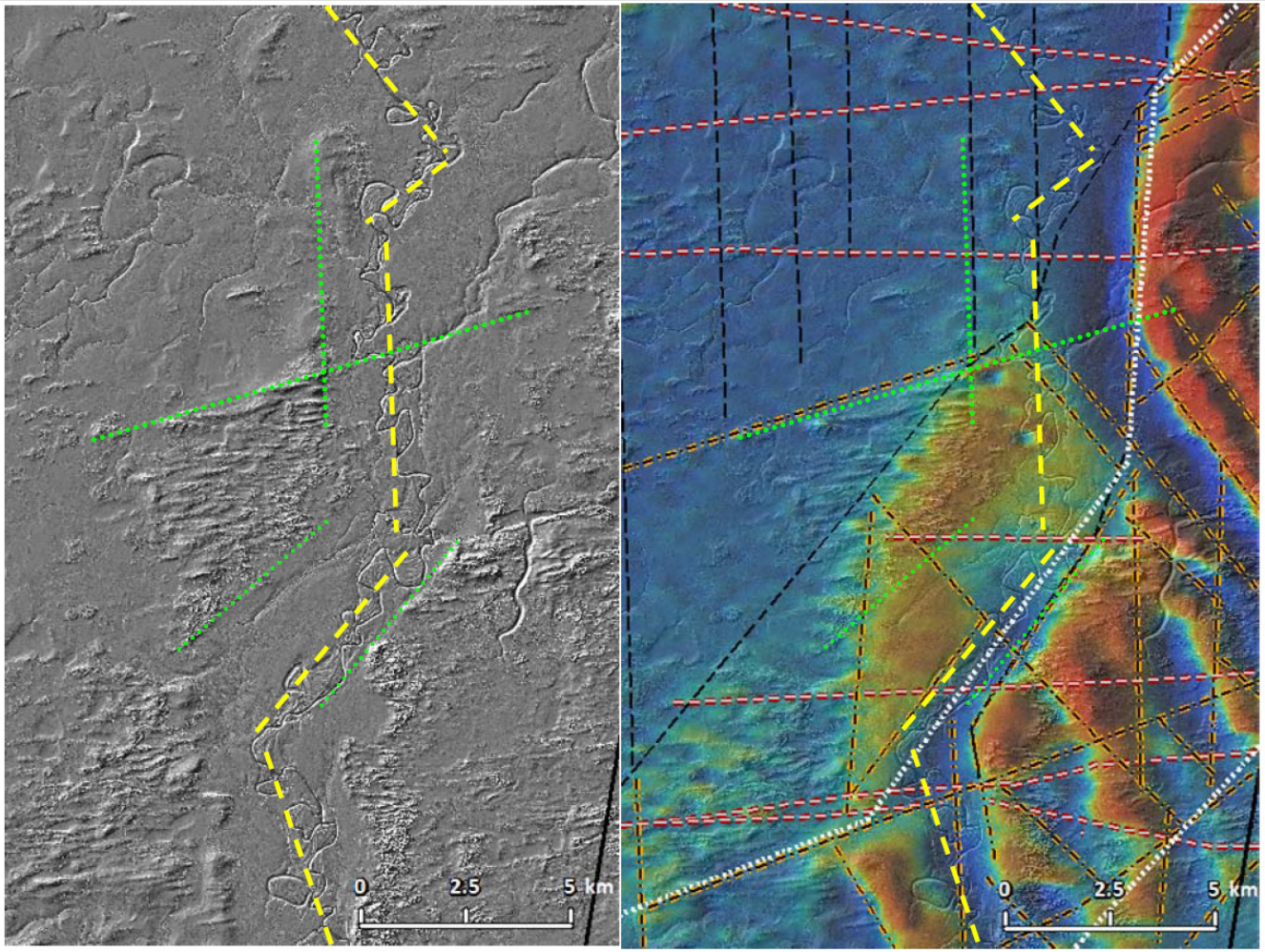



**Figure 17-52.** *The left hand image is a LiDAR image with lineaments mapped for a reach of the lower Yampoola Creek floodplain east of the Darling River and south of Menindee township. A number of elongate linear trends can be seen in the flood-scour channels. While flood-scour channels are much less sinuous than channels of laterally-migrating meandering rivers, these multiple elongate linear channel trends are anomalous. Also shown are three conspicuously straight valley-margin sections on the eastern margin of the floodplain. The green traces are surface scarps, the yellow traces are along the course of the Darling River. The right hand image shows the same area with the backdrop being the Total Magnetic Intensity (TMI) 1st Vertical Derivative (VD) draped over the LiDAR image. The lineaments from the LiDAR image are effectively coincident with faults mapped in the TMI (black lines) and regional gravity data (white dotted line). These data are interpreted as showing evidence for neotectonics in this area through reactivation of basement structures.*

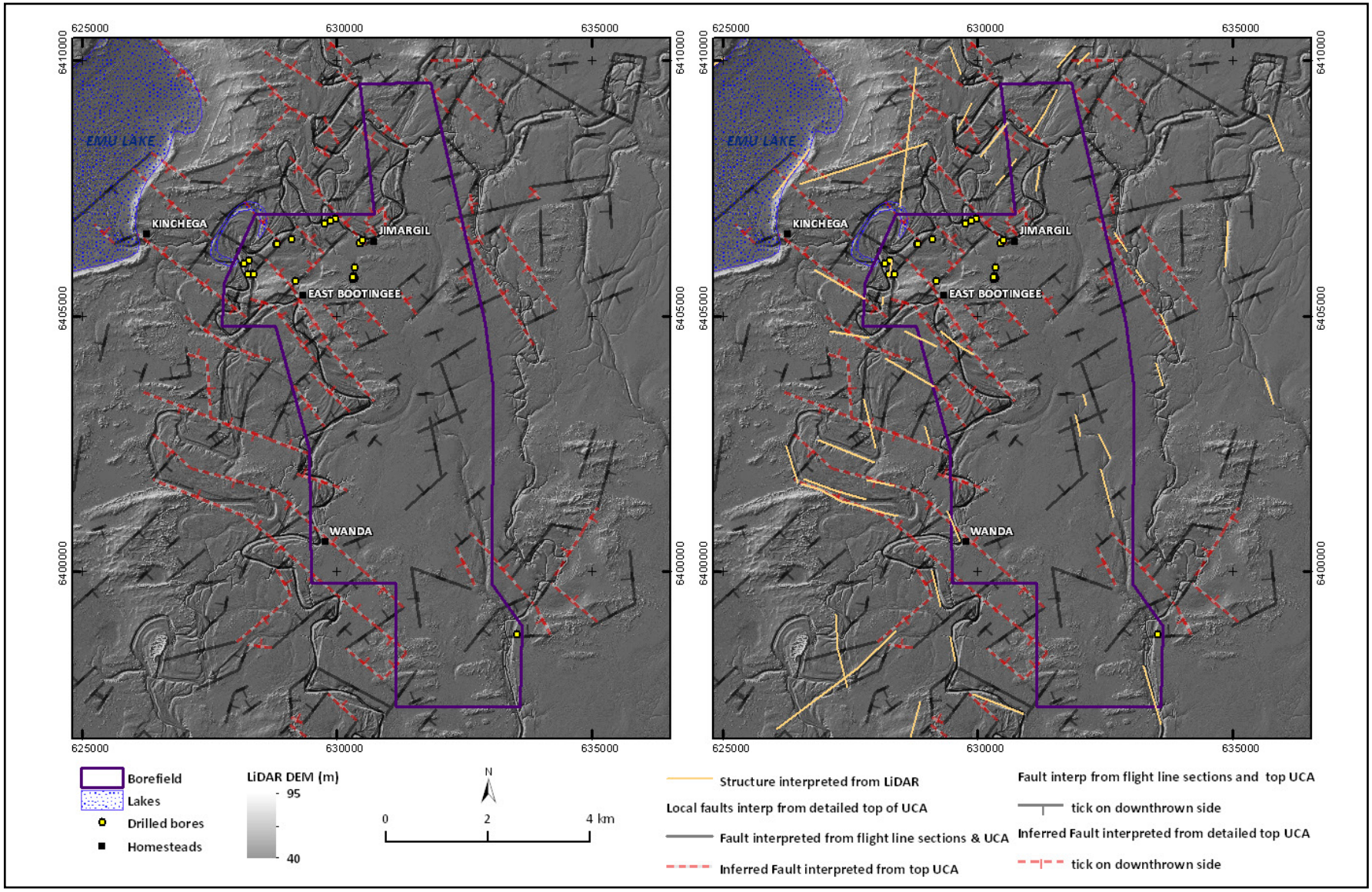



**Figure 17-53.** *The Jimargil-East Bootingee borefield showing a comparison between lineaments interpreted from the LiDAR and faults interpreted from AEM flight line section analysis of the upper-confining aquifer (UCA). There are many agreements indicating the likelihood that some structures interpreted at depth continue to the surface. Because the UCA is at 20-30 m depth matching lineaments will not overlap unless the structure is vertical.*

## 17.4 SURFACE GEOMORPHOLOGY AND LANDFORM MAPPING

### 17.4.1 Landform Mapping

Historically, geomorphic and landform mapping relied heavily on field mapping and aerial photograph interpretation (e.g. Paijmans, 1970; Parry & Beswick, 1973). However with the availability of early Landsat data and later with advances in high-resolution digital elevation models (DEMs), geomorphology and landform mapping is more commonly being undertaken remotely with small-scale field mapping used as validation. For example, Stark (2006) compared LiDAR with other, lower resolution DEMs, concluding the level of detail, type and number of geomorphic features seen in the LiDAR far surpassed the other DEMs. Other authors have similarly seen the advantage of LiDAR DEM for geomorphic or landform mapping (e.g. Newell & Clark, 2008; Clarke *et al*., 2010). Siart *et al*. (2009) used a combination of DEM, satellite imagery (Quickbird) and GIS datasets to map geomorphic features in Central Crete while Hossein *et al*. (2008) combined a DEM with ASTER satellite imagery in a quantitative approach to landform classification. By combining elevation data with multispectral (or hyperspectral) imagery, landform features can be discriminated both by their relative position (elevation) within the landscape and their physical characteristics. More recently, the availability of Google Earth imagery and software has further revolutionised the ability to map features directly from satellite and aerial imagery, as detailed by many papers in Smith *et al*. (2011), especially that of Seijmonsbergen *et al*. (2011).

In this study, we build extensively on previous work by the group, for example Kernich *et al*. (2009), Clarke *et al*. (2010) and Pain *et al*. (2011) to map landforms of the Darling River floodplain and adjacent area upstream and downstream of Menindee were mapped at two scales using LiDAR and SPOT imagery and some field validation. Landform patterns and elements were described using the terminology and definitions of Speight (2008) and Pain (2008). A landform map of the whole study area was compiled at approximately 1:80,000 for a usable scale of 1:100,000. Mapped landform units were initially identified and digitised visually using Google Earth (imagery includes Digital Globe, CNES/SPOT and MapData Sciences Pty Ltd), using paper plots of the LiDAR images as a guide. This line work was then imported into ArcGIS where it was edited, converted into polygons, and assigned landform related attributes. Linear landform features, including channels and lunette crests, were also mapped in Google Earth. Limited field observations were used to assist this map compilation.

A second more detailed map of the central focus area, surrounding the township of Menindee and the adjacent Menindee Lakes, was compiled at 1:25,000 for a usable scale of 1:30,000. This map shows landform elements at sufficient detail to highlight borrow pits, individual scrolls and oxbow lakes. The key dataset for compilation of landform maps at this scale was LiDAR. Prior to landform identification, the LiDAR DEM was levelled to eliminate the floodplain tilt. This is discussed in some detail in Section 17.1.2.1.

Once the LiDAR was levelled, an interactive contour tool in ArcGIS™ was used to map units using specific breaks in elevation associated with landform features, e.g. channel banks and dune bases, as identified in the visual images. Further editing was required to refine this line work and convert features into polygons. Landform attributes were then assigned to these features. A greater number of landform classes were developed at this finer scale than for the regional scale.

The two landform maps (regional and detailed) were merged (Figure 17-54) and as a consequence there is some discontinuity where the two datasets interact. Additionally, the regional map shows landform patterns and the central area map show elements. The scale of presentation means that the central area map is not simply a subset of the regional map, because it was compiled quite separately, and without using the regional map polygons.

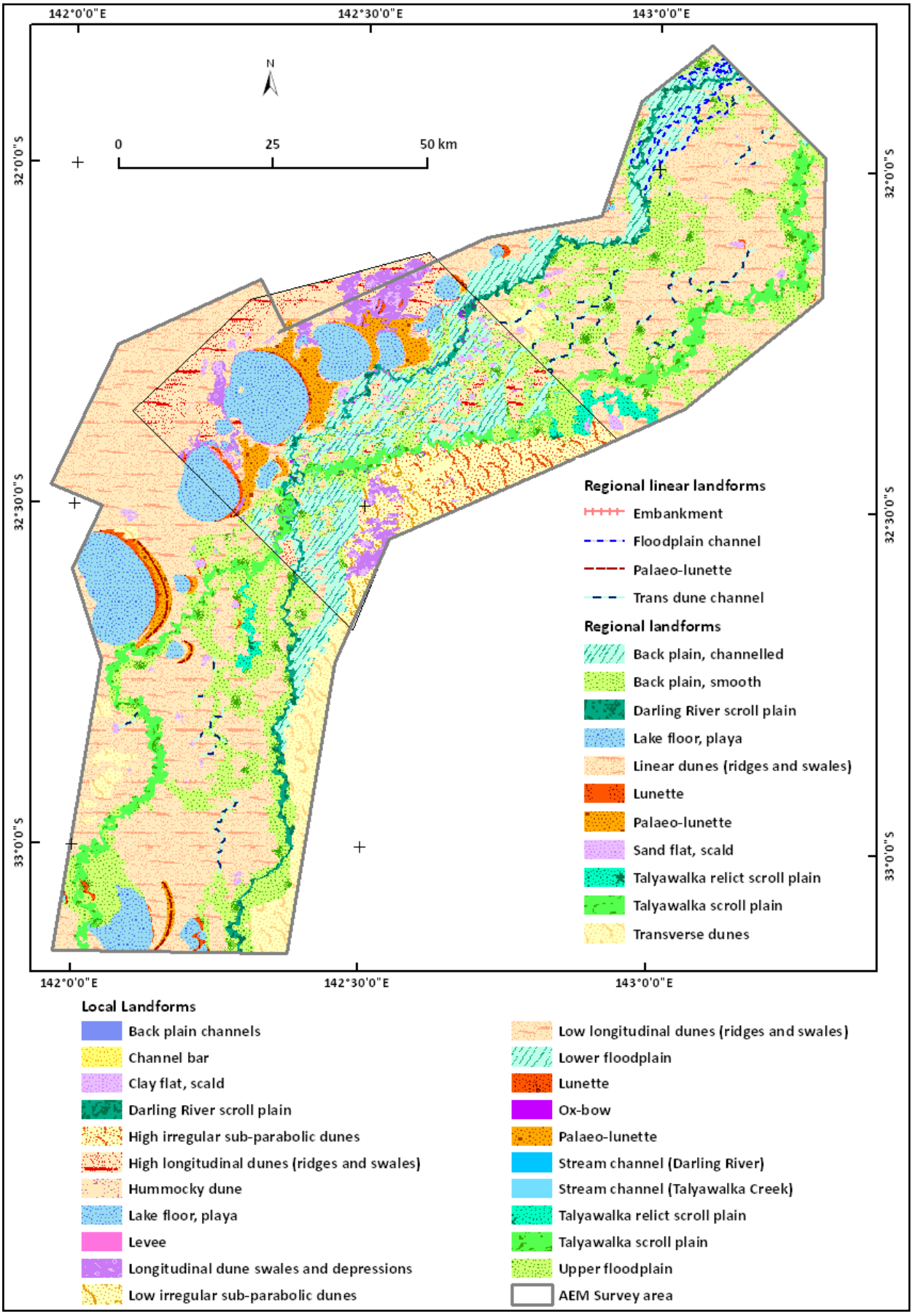



**Figure 17-54.** *Landform mapping with combined regional and detailed products.*

### 17.4.2 Surface-materials Mapping

Multispectral and hyperspectral imagery are often used to map surface materials. Salama *et al*. (1994) used multispectral Landsat TM satellite imagery and aerial photography to map surface materials in Western Australia. More advanced hyperspectral SEBASS airborne imagery was used by Vaughan *et al*. (2003) to map surface minerals in Nevada. Other hyperspectral imagery such as HyMap or ASTER has been similarly used to map surface materials (e.g. Dehaan & Taylor, 2004; Rowan & Mars, 2003; Ninomiya *et al*., 2005). Other studies (e.g. Kernich *et al*., 2009, Lawrie *et al*., 2010a, Pain *et al*., 2011) utilised airborne radiometrics to inform the surface materials mapping process.

ASTER imagery was investigated as part of Phase 1 (Lawrie *et al*., 2009a). A small test case found that the surface materials identified using multispectral SPOT imagery matched more closely to the geomorphic mapping than surface materials mapped using ASTER. In addition, multispectral imagery was more easily obtainable than hyperspectral and overall less noisy. Radiometric data in the BHMAR project area, identified in Phase 1 (Lawrie *et al*., 2009a) was too sparse due to wide flight line spacing, and the landscape too complex for the previously mentioned method to be effective. Consequently, the key dataset for generating the surface-materials mapping was SPOT.

SPOT imaging system operates in either panchromatic (PAN) or multispectral (XS) mode. The PAN sensor on SPOT operates at 2.5 m, 5 m or 10 m resolution from 0.51–0.73 μm while the XS mode provides 10 m or 20 m resolution in three spectral bands covering the ranges 0.5–0.59 μm, 0.61–0.68 μm and 0.79–0.89 μm (Kruse, 1999).

The SPOT imagery used in this project was re-sampled from 2.5 m to 10 m to reduce file size and processing time while still maintaining suitable image detail. A Principal Component algorithm for regolith mapping (using the three multispectral bands) was applied in ER Mapper. An ISOCLASS unsupervised classification was then applied to this imagery, generating 20 classes, with a standard deviation of 2.5 and minimum distance between class means of 2.2. This resulted in the generation of 20 classes that could be assigned preliminary cover/landform classes (Table 17-15) using the SPOT imagery. This was a first pass assessment of the imagery, which was subsequently followed by a more refined classification.

To validate the landform/cover classification, field data were incorporated. This included a systematic program of shallow subsurface sampling (hand augers, tractor pits and natural exposures) at 32 sites and 45 drillholes (sonic and mud rotary). Opportunistic data from field reconnaissance and vehicular traverses were also included. Refer to Section 12.1 for further information about the surface sampling fieldwork.

In the case of subsurface sampling sites, surface-material attributes were assigned simplified textural classes that could be related to the cover/landform classes derived from the SPOT unsupervised classification. A similar process was applied to the borehole data, however it was recognised that sub-surface materials information was more useful than that provided by the sonic drilling, which was in turn more reliable than that provided by the mud rotary. This point data was then compared with the SPOT classes to develop a surface-material classification (Table 17-15). These classes form the basis of the detailed site-specific surface-materials maps. Surface-material classes were simplified and a number were grouped together (Table 17-15) to produce the regional surface-materials maps. The surface-materials map (including field sites used for validation) is shown in Figure 17-55.

**Table 17-15.** *Landform/cover and surface materials classification approaches.*

| Landform/cover class | Surface-materials class | Surface-materials simplified |
|---|---|---|
| Modern scroll plain vegetated wetland | Woodlands: sandy clay to grey clay | Sandy clay and clay |
| Vegetated areas (woodlands and shrublands) | Hard grey sandy silty clay | Sandy silty clay |
| Sandy dunes | Red-orange aeolian sand | Red- orange aeolian sand |
| Water in lakes and channels | Grey silty sand to fine sandy clay | Clayey sand and silt |
| Lakes and channels | Grey clayey fine sand | Clayey sand |
| Sandy dunes | Clayey-silty sand within dune depressions/swales | Clayey silty sand |
| Sandy dunes | Sandy dune fields: fine to medium silty sand and clay | Silty sand |
| Sandy | Sand, silty or clayey sand | Silty sand |
| Sandy dunes transition | Light brown silty sand and clay within floodplain | Silty sand |
| Dry vegetation | Vegetated dunes: sand, silty or clayey sand | Clayey sand |
| Lush vegetation | Dark grey fine sandy clay within floodplain, clayey sand on dunes | Clayey sand |
| Vegetation (wet) | Vegetated areas: moist sandy clay and clay | Sandy clay and clay |
| Sandy dunes darker colour | Red-orange aeolian sand to sandy silt | Red- orange aeolian sand |
| Vegetation (grasslands) | Vegetated areas: sand, clayey sand to sandy clay | Clayey sand |
| Clay-rich plain to sand transition | Clayey sand | Clayey sand |
| Vegetation (shrubland) | Thin sand over sandy clay | Sand over sandy clay |
| Clay-rich reworked plain material - light and dry | Fine white sand and silt | Fine white sand and silt |
| Floodplain drainage depressions | Sandy silt or sandy clay | Sandy silt |
| Floodplain drainage depressions | Clayey sand in channels and lake fans, grey clay within floodplain | Sandy clay |
| Smooth floodplain channels and drainage depressions | Dark brown or grey clay, brown silty clay | Sandy silty clay |

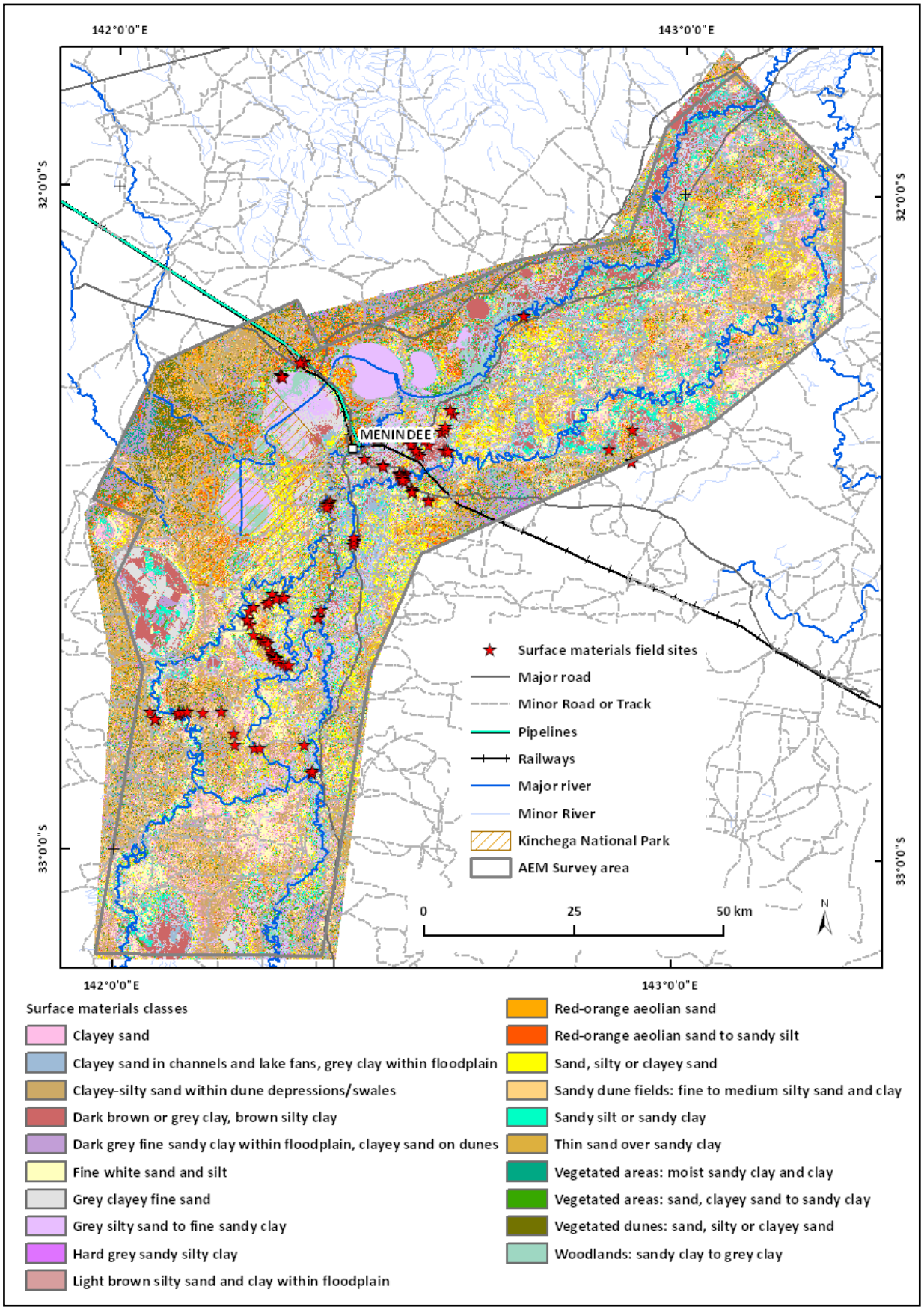



**Figure 17-55.** *Surface materials map including field sites used for validation.*

## 17.5 IDENTIFYING THE BLANCHETOWN CLAY

### 17.5.1 Introduction

The Blanchetown Clay is a useful marker horizon that generally has higher electrical conductivity than the sediments above and below, however there are exceptions where there is less of an electrical conductivity contrast, due to factors such as freshening of pore fluid salinities. Overall, the AEM data could be effectively used to map the distribution of the Blanchetown Clay. The program Encom Profile Analyst (Pitney Bowes Software) was used to display AEM flight line sections with borehole electrical conductivity logs superimposed. The borehole electrical conductivity logs indicated at what level the Blanchetown Clay was present, and in almost all cases this information could be reconciled with a near-continuous, electrically conductive layer in the AEM which was taken to represent the Blanchetown Clay. This assumption is reasonable, given the origin of the Blanchetown Clay as a lacustrine deposit of the palaeo mega Lake Bungunnia, the demonstrated continuity of the unit in the Murray River area, and its predicted presence in the Menindee area (see discussion in Section 17.5).

The distribution and thickness of the AEM conductive layer was mapped by picking representative points of the top and bottom of the conductive layer on the sections, saving the x, y and z coordinates of these points, and then gridding the points in Arc. The electrical conductivity of the Blanchetown Clay and the contrast with the enclosing sediments varies markedly, depending on moisture content of the sediments and its salinity. It was found that various colour scales had to be used to clearly differentiate the electrically conductive layer at different localities, ranging from plotting data on log scales in some stretches with maxima of between 0.5 and 3 S/m, and linear stretches from 0 to maxima of between 0.15 and 2 S/m. In places the minimum electrical conductivity for a colour stretch was set above zero to aid clear depiction of the conductive layer. It was found that the conductive layer had low AEM standard deviation, mostly below 0.32 ms/m, and sections of AEM standard deviation were also used to confirm the location of the conductive layer.

Previously reported thickness and elevations of the Blanchetown Clay were also used to assist in interpretation. The unit is generally around 10 m thick in the drilled boreholes, which is in accord with the recorded thickness in exposures and drillhole intersections to the south. Brown & Stephenson (1991) record a general thickness of "a few metres", but McLaren & Wallace (2010) record 8 measured sections with thickness varying from about 10 to 20 m. Elevations of palaeo shorelines of Lake Bungunnia range between 32 and 60 m AHD (McLaren & Wallace, 2010; McLaren *et al*., 2012), limiting the top of the Blanchetown Clay to between possibly as low as 25 m and as high as 60 m AHD if there have been no tectonic movements to raise or lower the unit. The top of the mapped conductive layer generally falls within these limits, except where it is reaches about 80 m in the far northwest of the study area in an area interpreted from study of geomorphology and basement structures to be a neotectonic horst (see Section 17.3).

### 17.5.2 Methodology

Picks of the top of the Blanchetown Clay were made in late 2011 and early 2012, using the late 2011 inversion of the AEM. When the final inversion became available in February 2012, theses were checked for accuracy against this inversion, and amended if necessary. The picks were made at a variety of spacing along flight lines (mostly 1-2 km) to show the main variations in elevation, along every second, or in many cases, every flight line (Figure 17-56, Figure 17-57).

Picks of the bottom of the Blanchetown Clay were made at approximately the same coordinates as a corresponding top pick. This was so that a thickness grid could be constructed from points of interpreted thickness (by subtracting elevation of the bottom pick from the top pick) rather than subtracting one gridded surface from another, with the danger that this latter method might give thickness anomalies due to gridding from points at different coordinates. An area encompassing Menindee and the Jimargil/Bootingee site was trialled initially, and top, base and thickness grids constructed using the paired picks. These gridded data were thought to be a reasonable representation of the Blanchetown Clay, so the method was continued. Bottom picks were then made for the remainder of the area. Due to time constraints, picks were made on

only every 4th line for much of the area (Figure 17-58). The points were exported from Profile Analyst as .csv files which could be edited to remove any spurious bottom picks without a paired top pick before importing into Arc.

Picks were also made of the edges of possible holes in the Blanchetown Clay (Figure 17-59). These were exported, and plotted as maps of points in Arc software. Using a grid of maximum electrical conductivity between 15 and 30 m (the depth range within which the Blanchetown Clay generally occurs) as a guide, map polygons of possible holes were drawn by "joining the dots".

There was no clear interpretation possible in some areas, due to what appeared to be poor AEM imaging or conflicting possible interpretations. These areas were also depicted as map polygons of no interpretation. Data were checked to ensure that bottom picks were paired with top picks, and that none of these pairs fell within the "hole" or "no interpretation" polygons. The top surface was gridded from top picks. Thickness was determined from the paired top and bottom picks, by difference in elevation. The thickness was then gridded.

The bottom surface was determined by subtracting the gridded thickness from the top surface. It would have been possible to make a difference approach to determining this bottom surface, by gridding the bottom picks. However, over much of the area there are more top than bottom picks. Furthermore, the base of the unit is often more gradational, due to the presence of a fine-textured muddy unit at the top of the Calivil Formation in some locations. Given that it was observed that the elevation of the conductivity anomaly was much more variable than its thickness, with local variations in elevation over hundreds of metres but variations in thickness more likely to occur on a scale of kilometres, it was considered that a grid of the bottom picks would show less detail than the top.

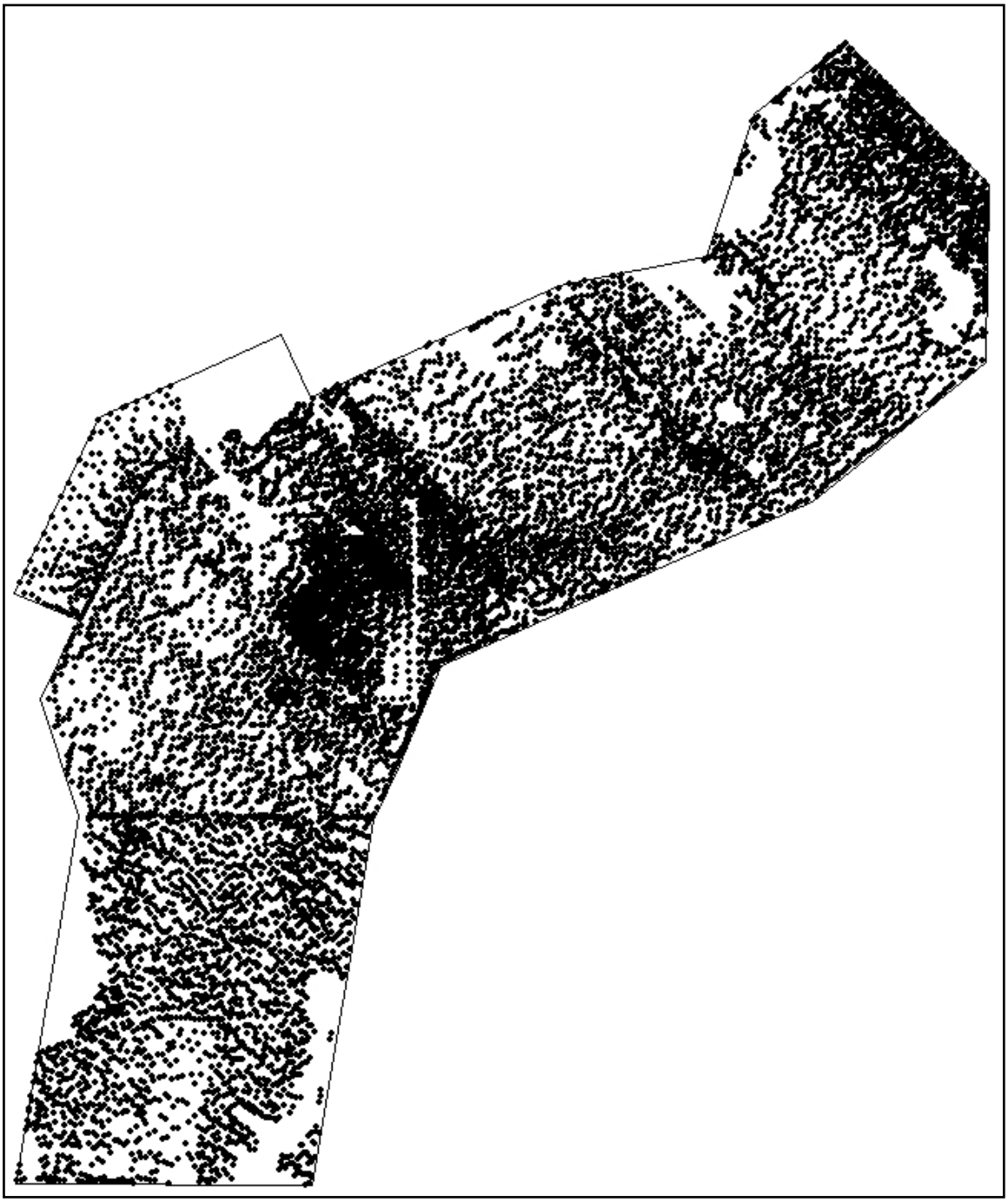


**Figure 17-56.** *Map of coordinates of picks for the top of the Blanchetown Clay electrical conductivity anomaly. Areas without picks are either areas with no interpretation or interpreted holes in the Blanchetown Clay.*

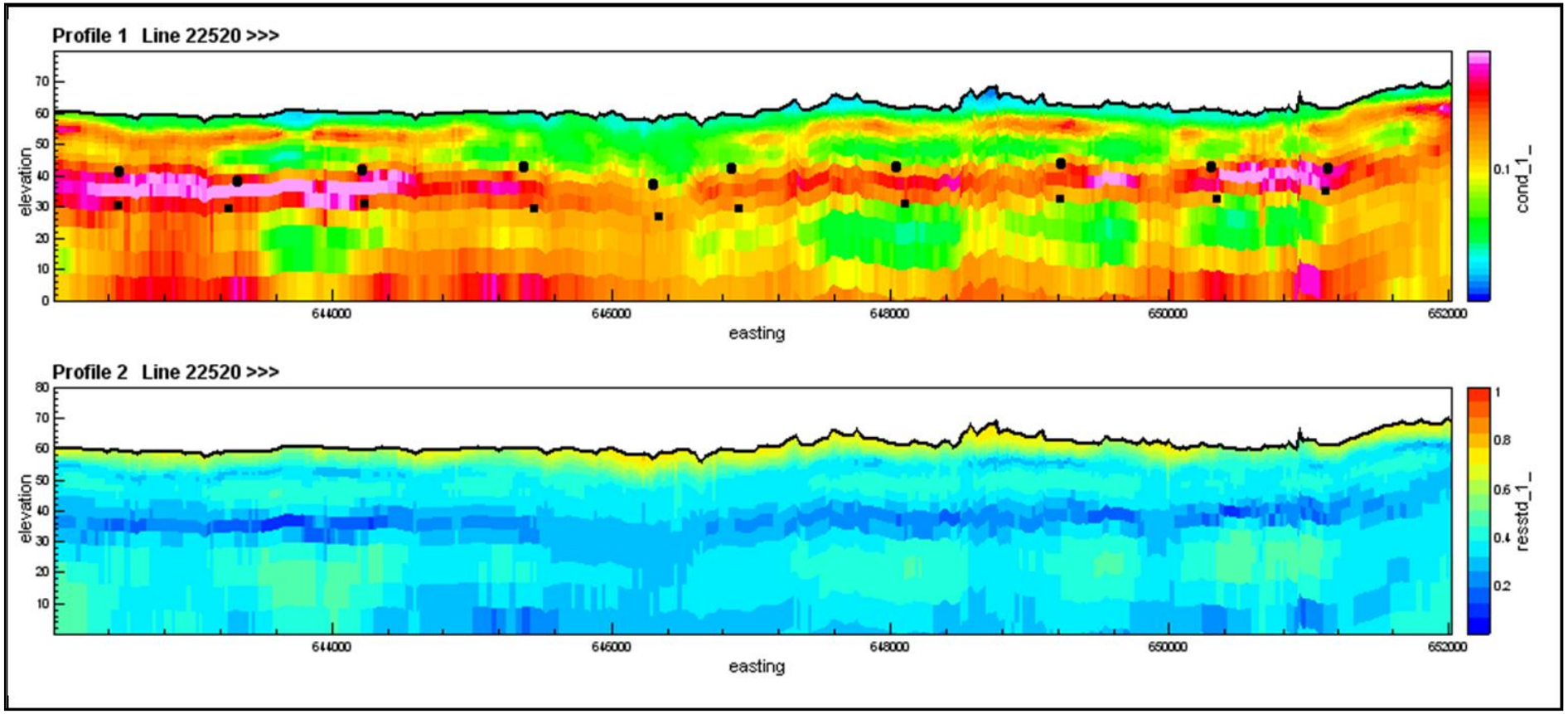



**Figure 17-57.** *The top image shows an AEM conductivity depth section along part of flight line 22520 showing top and bottom picks for Blanchetown Clay conductivity anomaly. Vertical scale 0-80 m AHD, horizontal distance about 7 km, conductivity colour stretch 0-0.1 linear and 0.1-0.8 S/m log. The bottom figure is a conductivity analysis depth section showing estimates of the relative uncertainty on the related conductivities for all conductivity depth (model) sections The standard deviation colour stretch is 0-1 linear for the bottom image.*

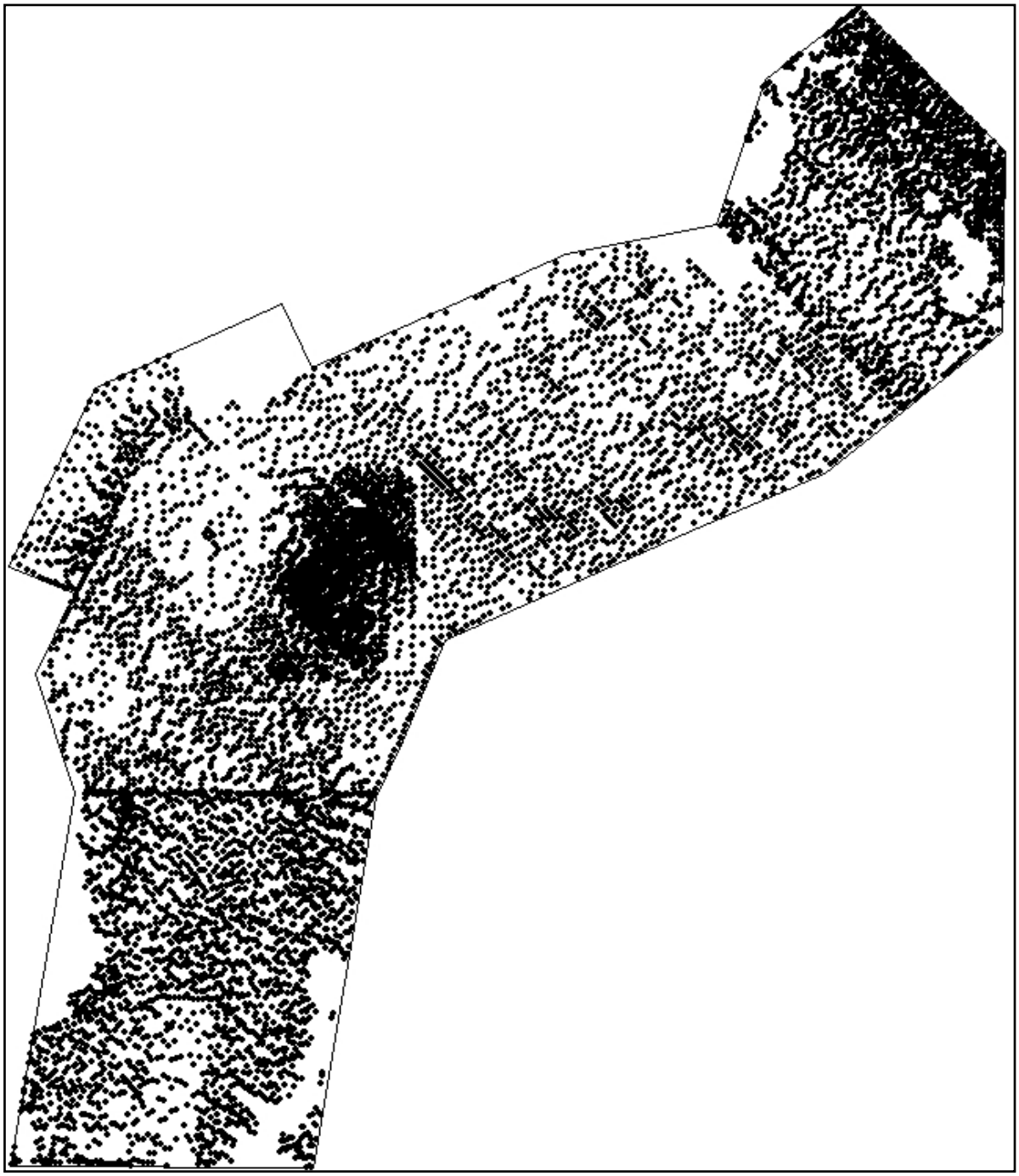


**Figure 17-58.** *Map of coordinates picks for the base of the Blanchetown Clay electrical conductivity anomaly. Areas without picks are either areas with no interpretation or interpreted holes in the Blanchetown Clay.*

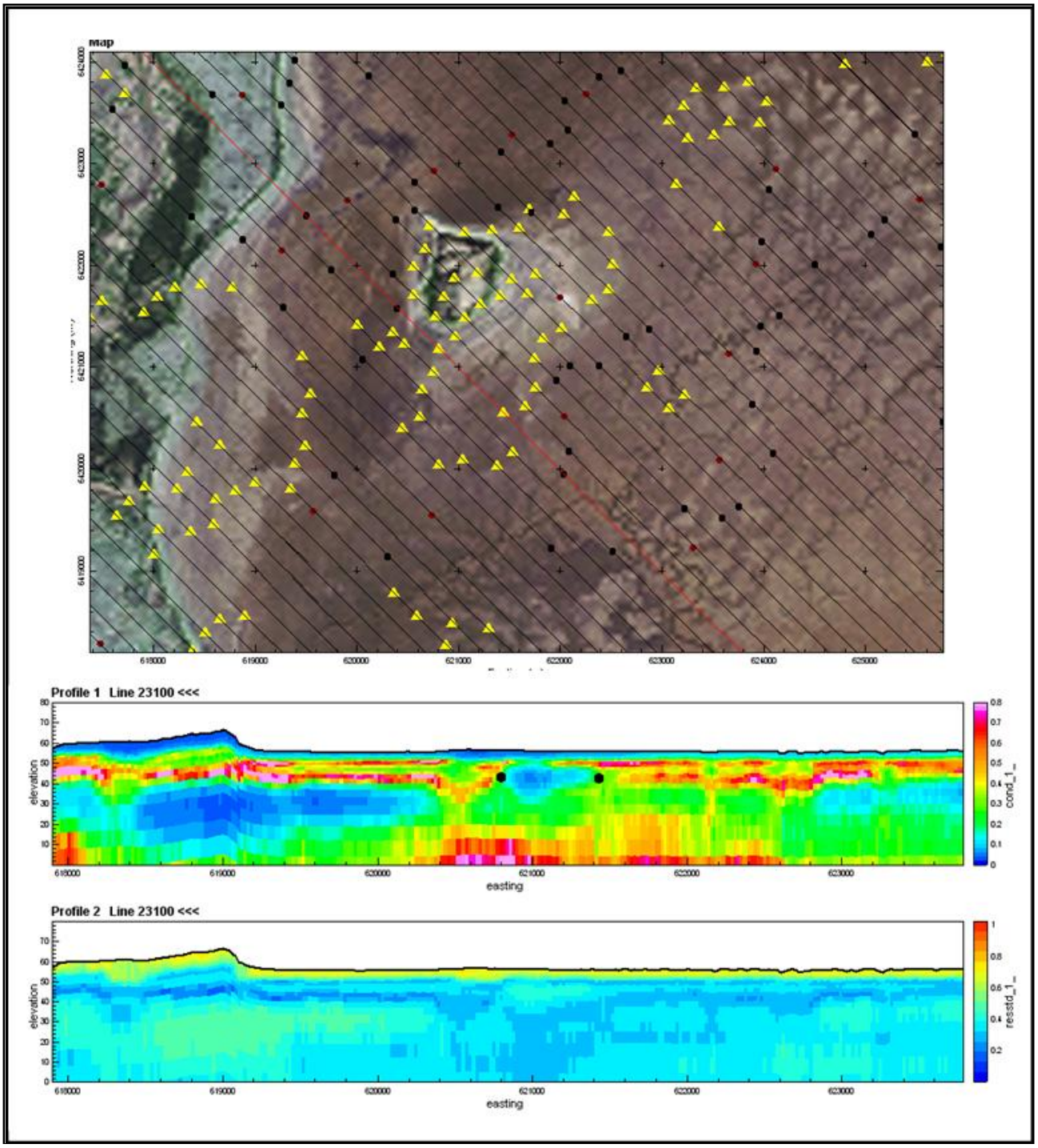



**Figure 17-59.** *Map of flight lines over SPOT image and AEM conductivity section along part of flight line 223100 beneath Menindee Lake. Two discontinuous shallow conductivity anomalies are shown across the lake floor, the shallow one (6-9 m depth) is interpreted to represent an evapotranspiration salt concentration at the water table in sediments of the Willotia beds, the deeper (12-20 m depth) represents the Blanchetown Clay. A hole in the Blanchetown Clay has been interpreted in this section, marked by two black dots. These points and similar holes in adjacent sections are shown as yellow triangles on the map. Hole polygons were constructed in Arc by joining the yellow markers to form a closed shape. Vertical scale 0-80 m AHD; horizontal distance along section about 8 km; linear colour stretch 0-0.8 S/m for conductivity section; and 0-1 for standard deviation.*

There are several caveats to be made about these interpretations:

- The interpretations are made on conductivity data. In some boreholes the top of the underlying Calivil Formation is also conductive, and thus may be included within the anomaly. For example, at site BHMAR33, the Blanchetown Clay is interpreted to be absent, but an electrical conductivity anomaly is still present, due to higher electrical conductivity of the top of the Calivil Formation (Appendix 1, Halas *et al*. 2012a refer to Strater logs for hole BHMAR33-1 for example).
- The Blanchetown Clay is locally very electrically resistive, and in places cannot be distinguished on the AEM sections. Low electrical conductivities in the Blanchetown Clay is observed where the unit is undersaturated and groundwater salinities are low. Plots of electrical conductivity and pore fluid composition, grain size, mineralogy and gravimetric water content confirmed this interpretation. This is the case at BHMAR35-1. There is a large area around this borehole which cannot be interpreted because of lack of clarity.
- The presence of 'holes' in the Blanchetown Clay depends on operator interpretation. Rather than using a discrete cut-off electrical conductivity value to map holes, each possible location was assessed on its own merits, including whether the Blanchetown Clay electrical conductivity anomaly became so indistinct that there appeared to be a clear connection between sediments of similar conductivity above and below. This approach was aided by the use of borehole-scale plots of electrical conductivity and pore fluid composition, grain size, mineralogy and gravimetric water content confirmed this interpretation
- The interpretations are dependent on the accuracy of the original AEM data and their inversion. All picks were made using the final WANDA inversions.
- The vertical location of the pick on the section is influenced by the interpreter. Generally, the picks were made part way through the gradient from low to high electrical conductivity rather than the extremities or core of the high electrical conductivity layer. Greater confidence in picks is obtained where the Blanchetown Clay occurs at shallow depths where the layer boundaries are more clearly defined.
- The depth of the electrical conductivity anomaly and thus thickness of the AEM layers affects the accuracy of picks. Drilling data shows that the Blanchetown Clay varies in thickness from zero up to 17 m. Resolution analysis of the Blanchetown Clay layer shows that the SkyTEM system resolves the Blanchetown Clay layer with a high confidence, particularly at shallow depths. Apparent thickness increases in the layer with depth are largely a function of AEM signal diffusion and loss of resolution with depth.
- The electrical conductivity anomaly beneath local short wavelength topographic features such as channels and dunes was observed to have local variations in elevations following the topography, i.e. at constant depth. This is interpreted to be mostly a result of the data processing and acquisition, and not reflect the actual geometry of the Blanchetown Clay. Therefore, picks were not made beneath short wavelength features deemed by the interpreter to be affected by these features. In other instances, the elevation of the anomaly beneath larger topographic features was also observed to be sub-parallel the ground surface. In some of these locations the electrical conductivity distribution was validated by drilling, and indicates a link between the present landscape and structural modification of the underlying stratigraphy (e.g. Figure 17-60). However, in other cases, the electrical conductivity anomaly clearly continued at a near constant elevation beneath landscape features, such as at borehole BHMAR19-1, where the elevation of the conductivity anomaly matches the position of the Blanchetown Clay in the drillhole (Figure 17-61).
- The Blanchetown Clay electrical conductivity anomaly was not observed in some upland tracts in the south of the AEM area, and in some areas north of the Darling River upstream of Menindee. Ground validation of thin electrical conductors observed in the AEM data were identified these as near-surface clay deposits of the Woorinen Formation. Further ground validation is required to constrain interpretations in these areas (Figure 17-62).

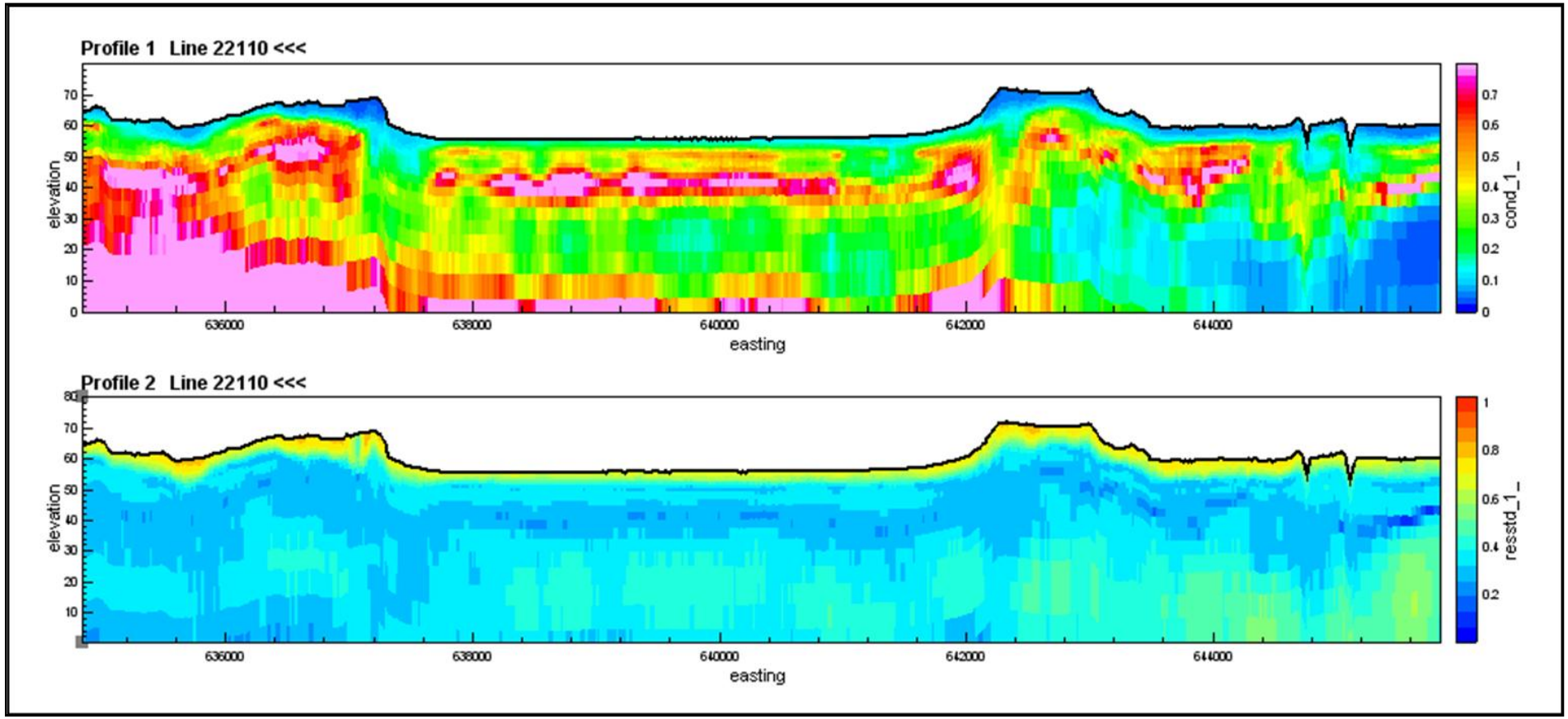



**Figure 17-60.** *AEM conductivity section along part of flight line 22110 across Lake Pamamaroo. The Blanchetown Clay conductivity anomaly (approx. 40-50 m AHD under the lake) rises under the lunette and high ground to the northwest of the lake. This is geometry considered not to be geologically sound, and picks were not made in the elevated areas with apparent tops at up to 60 m AHD. Vertical scale 0-80 m AHD, horizontal scale approx. 16 km, linear colour stretch 0-0.8 S/m for conductivity section, and 0-1 for standard deviation.*

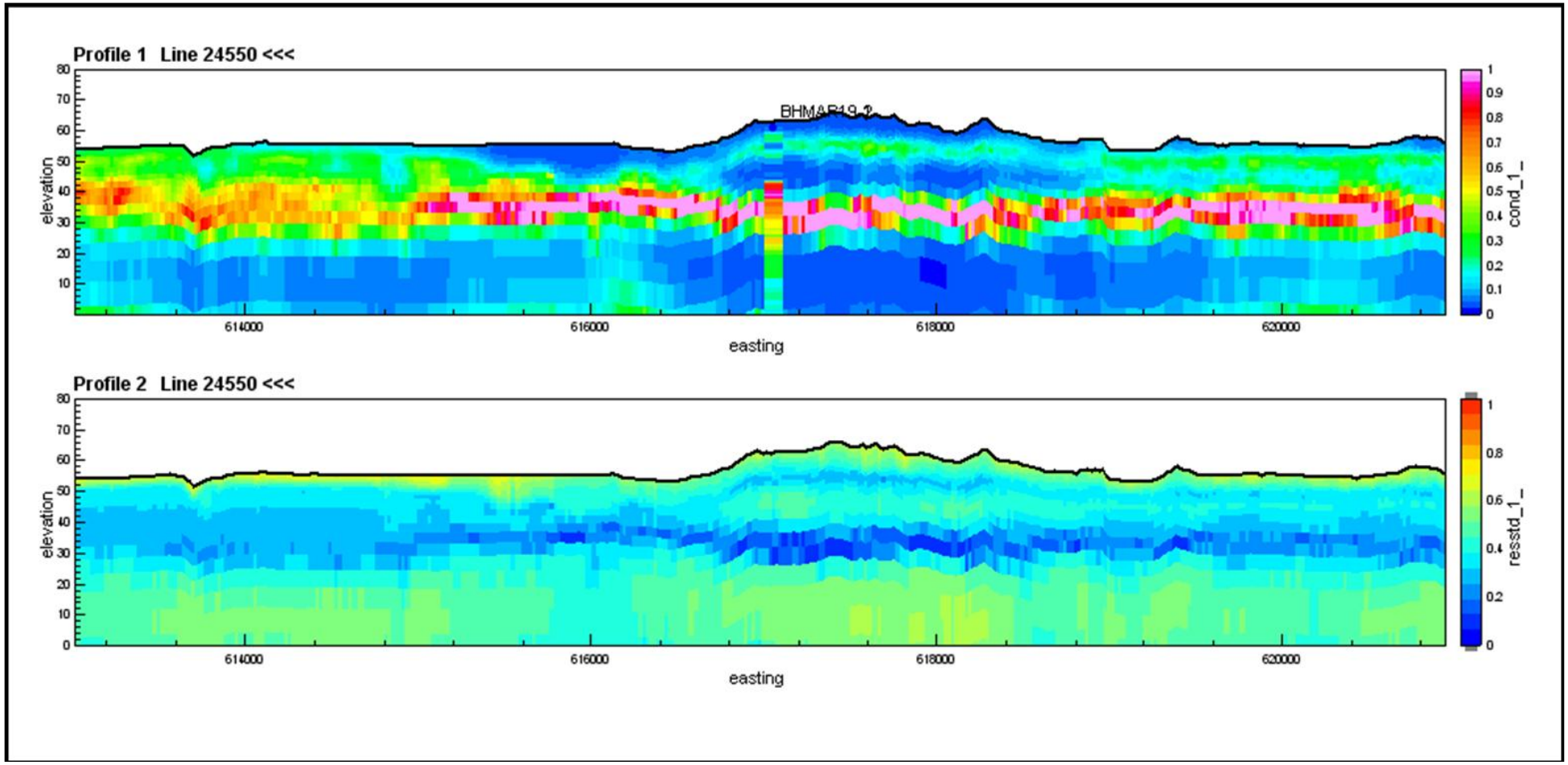



**Figure 17-61.** *AEM conductivity section along part of flight line 24550. The Blanchetown Clay conductivity anomaly (approx. 30-42 m AHD) in the vicinity of the rise at drill site BHMAR19 does not follow topography. The AEM anomaly is a little deeper than the anomaly in the downhole conductivity log, which is a combination of BHMAR19-1 and 19-2, as part of the log in 19-1 is corrupted by steel casing left in the hole by drillers. Vertical scale 0-80 m AHD, horizontal scale approx. 11 km, linear colour stretch 0-1 S/m for conductivity section and drillhole bar, and 0-1 for standard deviation.*

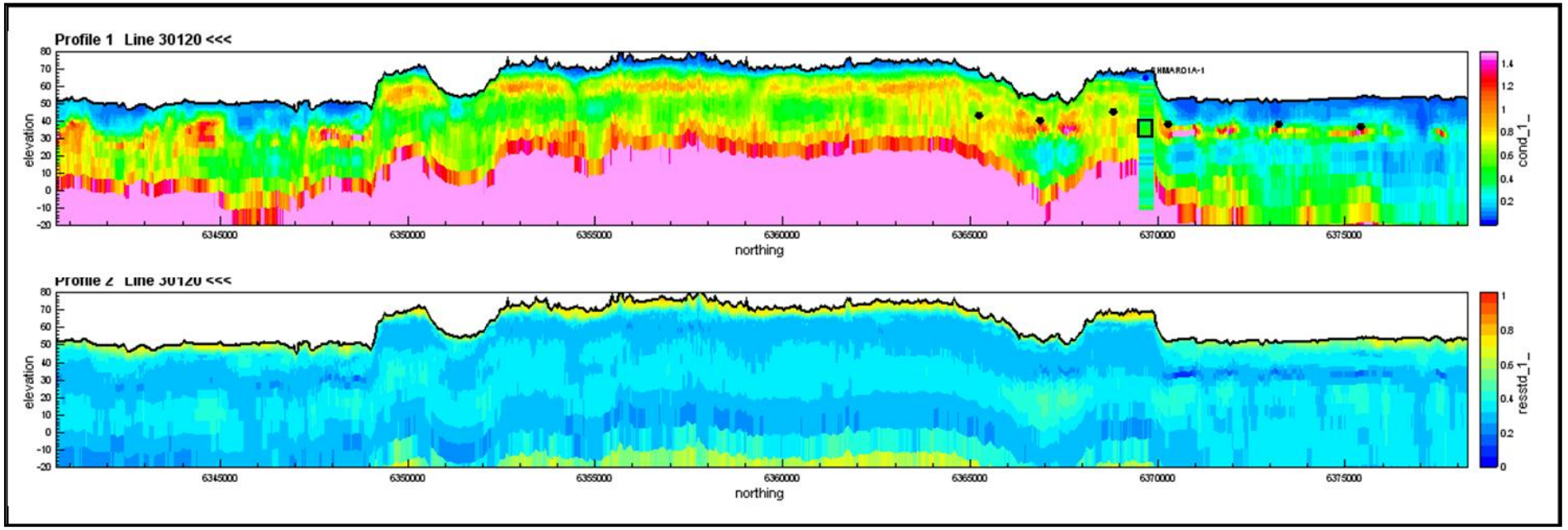



**Figure 17-62.** *AEM conductivity section along part of flight line 30120 in the southwest of the area. The Blanchetown Clay conductivity anomaly shows as high conductivity segments in the south (left) and north parts of the section beneath the floodplain of the Darling Anabranch (confirmed in drillhole BHMAR74-1 about 1 km to the east of this flight line in the north), but appears to disappear under the high dune covered area to the south. The shallow conductor in these sections is Woorinen Formation clays. Top picks for the Blanchetown Clay conductivity anomaly are shown in the northern part of the section. The conductivity profile for drillhole BHMAR01A-1 (projected about 200 m) is present near the edge of the high country. The Blanchetown Clay is interpreted to be at 31-41 m AHD (outlined as a black box on the profile) in this hole, although there is not a clear conductivity anomaly apparent at the colour stretch used. The area with conductivity anomaly at about 60-70 m AHD under the high ground is considered to not be an area of upfaulted Blanchetown Clay, but represent an area where the an anomaly at depth cannot be detected by the AEM system or where the sediments beneath the Blanchetown Clay have similar conductivity to the clay, and thus no interpretation can be made. Vertical scale -20 to 80 m AHD, horizontal distance about 38 km, linear colour stretch 0-1.5 S/m for conductivity and 0-1 for standard deviation.*

## 17.6 STRATIGRAPHIC MAPPING

Ten stratigraphic units are present in the AEM survey area to the depth of approximately 70 m and include the youngest Coonambidgal Formation to the oldest Remark Group (Table 17-16). The detailed depositional environments of these units are described in Lawrie *et al*. (2012b). In terms of choosing the datum for mapping, the pros and cons of both depth and elevation slices were considered.

In terms of the geological model, elevation slices provides an accurate depiction in 3D. However, a 17 m difference in floodplain elevation exists across the study area from the upper to the lower reaches of the Darling River. In general at any specific elevation, younger stratigraphic units would be observed in the north while older units would be observed in the south. Consequently, reconciling the stratigraphic units across the study area would be difficult if elevation slices were used. In comparison, the drawback of using depth slice is the persistence of topographic effects at lower depths. However, this effect is minimal in areas of low surface relief and with the progressive thickness of depth slices. To keep a coherent stratigraphic picture across the study area, especially at near surface higher elevations, depth slice intervals were selected as the preferred approach. Hence, 20 AEM depth slices were used in the stratigraphic mapping, starting from the surface to 72.3 m depth (Table 17-17), with thicknesses ranging from 0.9 m to 11.3 m (Table 17-17).

**Table 17-16.** *Stratigraphic units present in the study area starting with the youngest.*

| Stratigraphic Unit | Stratigraphic Code | Sedimentary Environment |
|---|---|---|
| Coonambidgal | Qac | Fluvial |
| Woorinen | Qdw | Aeolian |
| Menindee | Qam | Fluvial |
| Lunette | Qdl | Aeolian |
| Willotia | Qaw | Fluvial, colluvial |
| Blanchetown Clay | Qpc | Lacustrine |
| Calivil | Tpc | Fluvial |
| Loxton-Parilla Sands | Tps | Shallow marine and beach complex |
| Renmark | Ter | Fluvial |
| Undifferentiated Devonian | Dum | Terrestrial sedimentary environment |

**Table 17-17.** *AEM depth slice intervals and thicknesses.*

| Depth From (m) | Depth to (m) | Thickness |
|---|---|---|
| 0 | 1.6 | 1.6 |
| 1.6 | 2.8 | 1.2 |
| 2.8 | 3.5 | 0.7 |
| 3.5 | 4.4 | 0.9 |
| 4.4 | 5.3 | 0.9 |
| 5.3 | 6.4 | 1.1 |
| 6.4 | 7.7 | 1.3 |
| 7.7 | 9.2 | 1.5 |
| 9.2 | 11.0 | 1.8 |
| 11.0 | 13.1 | 2.1 |
| 13.1 | 15.6 | 2.5 |
| 15.6 | 18.5 | 2.9 |
| 18.5 | 22.0 | 3.5 |
| 22.0 | 26.1 | 4.1 |
| 26.1 | 30.9 | 4.8 |
| 30.9 | 36.7 | 5.8 |
| 36.7 | 43.5 | 6.8 |
| 43.5 | 51.5 | 8 |
| 51.5 | 61.0 | 9.5 |
| 61.0 | 72.3 | 11.3 |

The stratigraphic mapping comprises three parts: near surface younger Quaternary units from 0 to 22 m; the Pliocene Blanchetown Clay; and deeper Tertiary units from 22 to 72.3 m. Each part was mapped differently and brought together in a GIS environment.

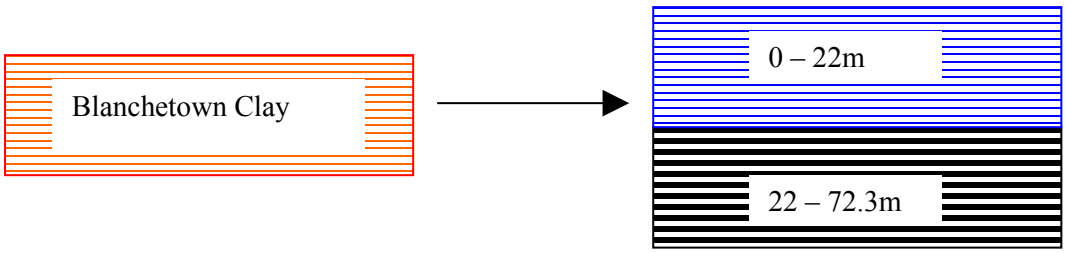



**Figure 17-63.** *Schematic diagram showing the mapping of stratigraphic units using 3 parts: the mapping of shallow and deeper depth slices, and the insertion of the middle Blanchetown Clay unit followed by a final reconciliation of all stratigraphic units.*

### 17.6.1 Blanchetown Clay

The upper confining aquitard, which mainly consist of Blanchetown Clay and part of the conductive upper Calivil Formation, was mapped from AEM cross sections using Encom Profile Analyst. Both the top and bottom surfaces of this unit were delineated in elevation (m AHD). To incorporate this data into the stratigraphic map, the elevation was translated into depth, using the LiDAR DEM, to subtract the top surface and the bottom surface separately. The result was two grids: 'depth to top of' and 'depth to bottom of' the upper confining aquitard. Using ArcGIS expressions, these two depth surfaces were matched with the depth slices to determine the absence or presence of the upper confining aquitard for each depth slice interval. Where Blanchetown Clay is absent within the specific depth slice, the expressions also demarcate if it overlies or underlies, is completely absent or not mappable. The resulting grids were converted into polygons and attributed according to the relative position of Blanchetown Clay with respect to the depth slice, i.e. not mappable, absent, below, above and present within the depth slice. Where Blanchetown Clay is absent, geological interpretation was carried out to determine if Blanchetown Clay was eroded or never been deposited. If the former is the case, the areas will be occupied by younger sediments, and if the latter is the case, the areas will be occupied by older sediment such as Calivil Formation. In areas where it is not possible to map the Blanchetown Clay based on AEM conductivity cross section and in the absence of validation bores, these areas are assigned as not mappable.

### 17.6.2 Mapping the Deeper Intervals

To map the stratigraphy of the Tertiary units, 52 project boreholes, both sonic and mud-rotary drilled bores, and 25 local and regional stratigraphic interpreted cross sections (Table 17-18, Figure 17-64) were referenced.

**Table 17-18.** *The 25 regional cross sections referenced for stratigraphic mapping. These sections can be found in Appendix 5a (Apps et al., 2012b).*

| | | | | |
|---|---|---|---|---|
| A – A1 | G – G1 | M – M1 | S – S1 | AA – AA1 |
| B – B1 | H – H1 | N – N1 | V – V1 | |
| C – C1 | I – I1 | O – O1 | W – W1 | |
| D – D1 | J – J1 | P – P1 | X – X1 | |
| E – E1 | K – K1 | Q – Q1 | Y – Y1 | |
| F – F1 | L – L1 | R – R1 | Z – Z1 | |

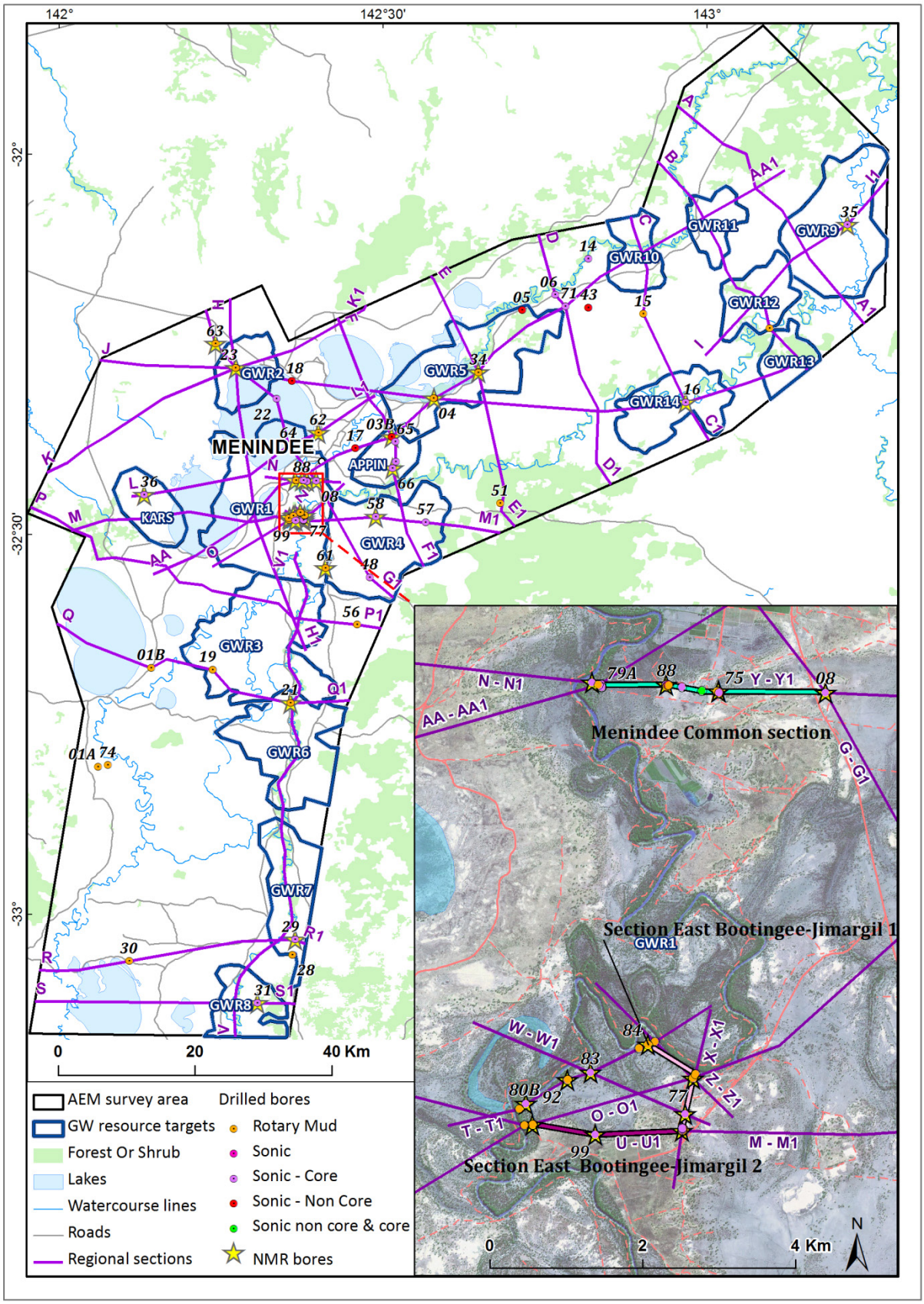



**Figure 17-64.** *Traverse of local and regional AEM conductivity and stratigraphic interpretation cross sections and the location of validation boreholes with site identification number.*

The depth slices from 22.0 m to 72.3 m were digitised based on conductivity thresholds, the same as those used for texture class mapping (refer to Section 17.7). Merged across each depth slice was the elevation contour gridded at 11 m above the floodplain. Starting from the basal layer (61.0 to 72.3 m depth) and moving upwards, the stratigraphic information at each bore location was transcribed to the polygon where the bore was sited. Stratigraphic information of each cross section was then systematically checked and polygons were attributed in sequence, starting from the northeast section (cross section A-A1) and ending in the southwest section (cross section S-S1) of the study area. The interpretation was then checked and updated where necessary with the stratigraphic information on the other cross sections that ran along or oblique to the axis of the valley.

Due to the relatively thick interval (11.3 m), there were several areas where transition from Calivil Formation to Renmark Group, or Loxton-Parilla Sands to Renmark Group occurred. These areas were mapped as Tpc – Ter or Tps – Ter to reflect the presence of disconformity surface within the layer. Additionally, topographic effects were detected in the interpretation of depth slice 61.0-72.3 m however this was restricted to the south as shown in Figure 17-65. Due to the high relief of the regional uplands with respect to the floodplain, the stratigraphic unit was Calivil Formation rather than Loxton-Parilla Sands or Renmark Group (Figure 17-155). The depressions associated with Lakes Mindona and Yartla resulted in Renmark Group partly present beneath the Loxton-Parilla Sands.

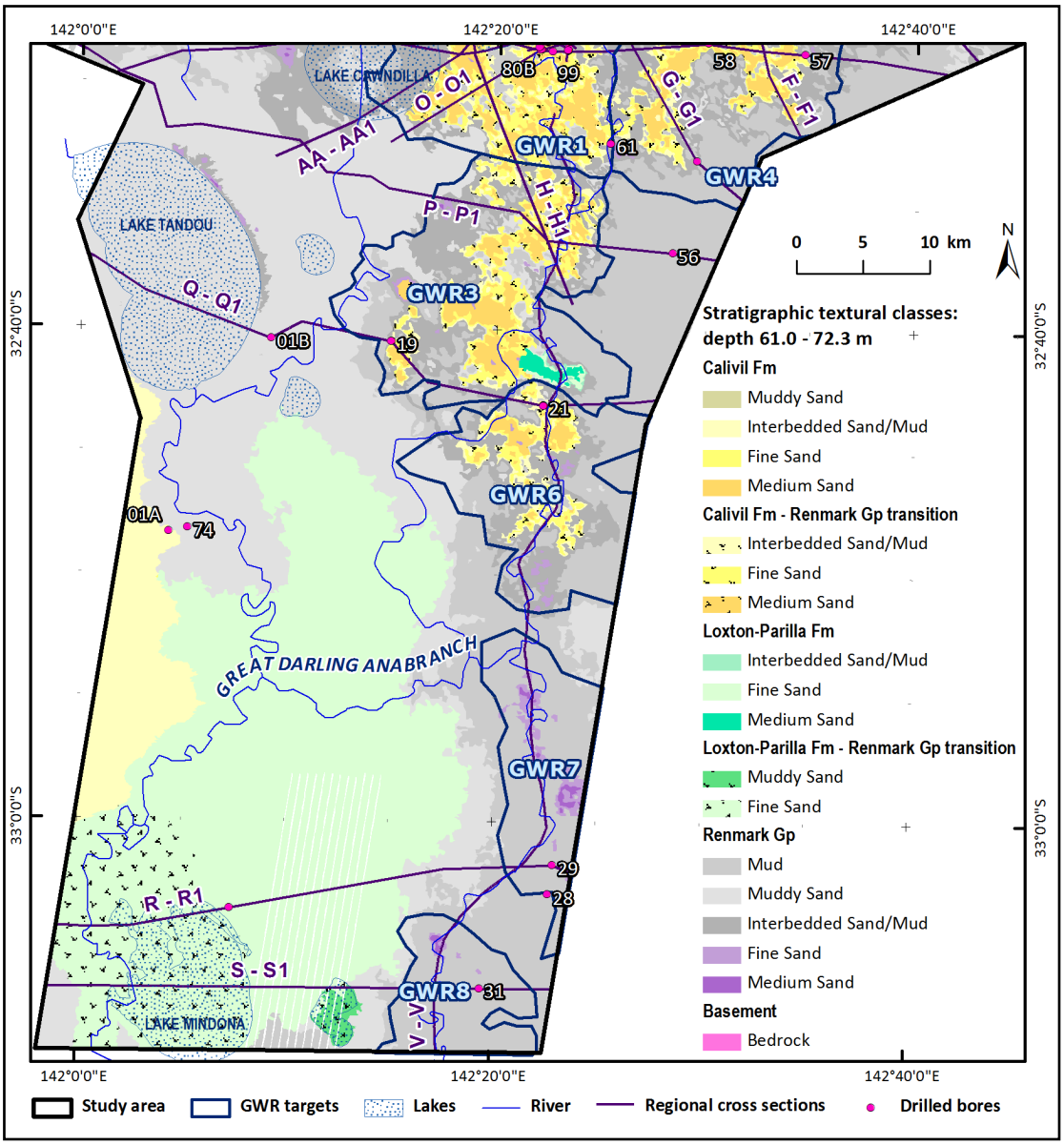



**Figure 17-65.** *Stratigraphic units present at 61.0 m to 72.3 m depths in the southern part of the study area. Bore locations and the regional cross sections are also shown.*

### 17.6.3 Mapping the Shallower Intervals

Some stratigraphic units were predominantly associated with landform features expressed at the surface. These include regional dune fields, dunes on various floodplains (i.e. lower, upper and relict), lunettes, palaeo-lunettes, lakes and other smaller depressions. In contrast, other stratigraphic unit such as Willotia sediment may occur solely in the subsurface, obscured by overlying fluvial and aeolian sediments. Thus information from the geomorphic map was used to establish the three stratigraphic-landscape domains: Coonambidgal Formation scroll plains; Menindee Formation floodplain; and Willotia bed unit underlying the regional dune fields (Woorinen Formation) and dune complexes on floodplain.

There are significant height differences amongst the dunes and lunettes, and the surfaces of each aeolian unit can also varies across a short distance. Since depth slices drape uniformly across the landscape, it is necessary to determine the spatial extent of these surface features with respect to depths. For example, Woorinen Formation associated with a small dune 3 m high may be absent between 5.4 m to 6.3 m depths whereas a large palaeo-lunette 12 m high may still be present at that depths.

As such, relative elevation with respect to a datum was useful in determining whether a geomorphic feature still existed at specific depth intervals. To achieve this, the lowest part of the floodplain was chosen as an arbitrary datum. Taking the elevation of the point data along the floodplain and extrapolate across the study area helped generate a datum plain. A residual elevation grid was then calculated by subtracting the surface elevation and the elevation of the datum plain. The resulting grid was a variation in local relief with respect to the lowest parts of the floodplain, and ranged from < 1 m to > 18 m across the study area. Contour intervals of 2 m to 4 m were selected from this residual elevation grid and union with the depth slice intervals from 0 m to 22 m depths (Table 17-19).

Combining the geomorphic data and residual elevation grid contours with the depth intervals allowed the spatial extent of the surface features and the transition from one formation to the next to be established. The 52 project boreholes, both sonic and mud-rotary drilled bores, and 25 local and regional stratigraphic interpreted cross sections (Table 17-18) were also referenced to ascertain the depths of the transition. In the absence of bore information, other transition, such as thin sediment of the Menindee Formation overlying Willotia beds, was established using information obtained from interpreted AEM cross sections.

The stratigraphic units assigned to the depth slices include Woorinen, Coonambidgal and Menindee Formations, undifferentiated Quaternary lunettes, and Willotia beds.

**Table 17-19.** *Relative height above lowest part of the floodplain and the grid used to delineate surfaces across the respective depth slice interval.*

| Depth from (m) | Depth to (m) | Residual Elevation (m) |
|---|---|---|
| 0 | 1.6 | 0 |
| 1.6 | 2.8 | 2 |
| 2.8 | 3.5 | 4 |
| 3.5 | 4.4 | 4 |
| 4.4 | 5.3 | 6 |
| 5.3 | 6.4 | 6 |
| 6.4 | 7.7 | 8 |
| 7.7 | 9.2 | 12 |
| 9.2 | 11.0 | 12 |
| 11.0 | 13.1 | 14 |
| 13.1 | 15.6 | 14 |
| 15.6 | 18.5 | 18 |
| 18.5 | 22.0 | >18 |

### 17.6.4 Reconciling the Stratigraphic units

Following the mapping of the Quaternary and Tertiary units, the Blanchetown Clay layers were unioned with the stratigraphic depth slices. Where Blanchetown Clay was present, the attribute of the polygons were renamed as Blanchetown Clay. There is no change in stratigraphy if Blanchetown Clay was absent. Where Blanchetown Clay occurred below the depth interval of interest, the polygons were attributed using the appropriate Quaternary unit. On the other hand, if Blanchetown Clay occurred above the depth interval of interest, the polygons were attributed with the appropriate Tertiary unit.

#### 17.6.4.1 *Uncertainty*

In the southern part of the study area, lack of borehole information and the high apparent conductivity of the sediments made differentiation of both lithological and stratigraphic interpretation difficult. Where stratigraphic demarcation based on conductivity was not possible, the stratigraphy was mapped based on geological knowledge. For example, the Pliocene shoreline regressed towards the south and Loxton-Parilla Sands gave way to Calivil Formation at shallower depths.

Major faults with abrupt changes to lithology and stratigraphy were observed in the AEM depth slices. These boundaries were incorporated into the stratigraphic map. On the other hand, minor faults with subtle vertical displacement of stratigraphic units may not be obvious in AEM depth slices, especially in thicker intervals. Under such circumstances, the mappable stratigraphy is the dominant unit and may include part of the other stratigraphy within the same polygon.

## 17.7 MAPPING HYDRAULIC TEXTURAL CLASSES

Hydraulic texture classes of surface and shallow sediments were mapped in an effort to:

- Locate possible areas where vertical recharge to shallow aquifers may take place, especially in low lying scroll plains and floodplains adjacent to the Darling River and creeks subjected to flooding.
- Determine the hydraulic connectivity between river, creeks and shallow aquifers to establish the likelihood of bank recharge.
- Ascertain the thickness of the mud-rich sediment to establish areas suitable for implementing artificial passive recharge technique.

Two main aquifers are present in the study area; the first is the sand-rich channels at the base of the Coonambidgal and Menindee Formations between 7 m and 17 m depths. Beneath these formations is the conspicuously mud-rich Upper Confining (Blanchetown Clay) aquitard, which overlies the Calivil Formation (and Loxton-Parilla Sands in the south). The Calivil Formation may include a mud-rich upper sequence and a bottom sandy sequence extending to 50 m or 70 m depths. The Lower Confining (Renmark Group) Aquitard underlies the Semi-Confined (Calivil Formation and Loxton-Parilla Sands) Aquifer and was also mapped in some areas.

### 17.7.1 Input Datasets

Several datasets and information were used in the mapping of hydraulic textural classes, including:

- 14 AEM depth slice grids from the surface to 22.0 m depth for shallow unconfined aquifer mapping, and 7 AEM depth slice grids from 22.0 m to 72.3 m depths for semi-confined aquifer mapping,
- LiDAR digital elevation model (DEM) at 5 m resolution and shuttle radar topography mission (SRTM) 1 second DEM,
- Geomorphic map as ArcGIS polygon shapefile, and
- Borehole lithological information at 52 sites (12 mud-rotary and 40 sonic-cored holes).

The areas cover by AEM, LIDAR and geomorphic maps all differ slightly. The AEM data is a continuous datasets throughout the study area except for the north-western and the southernmost sections where more widely spaced flight lines were flown, resulting in "stripes" of data with no data in-between (Figure 17-66). This affects all depth slices grids. The geomorphic map has similar coverage to the AEM data except in the north-northwest where the map extends beyond the survey area (Figure 17-66). In addition, the polygons are continuous and do not contains "strips" of no data. LiDAR DEM has similar coverage to the AEM except in the northwest corner over the high regional dune fields (Figure 17-66). This area was patched with the 1 second SRTM data as discussed in Section 5.

Borehole lithological information from both sonic coring and mud-rotary methods were used to validate the lithology maps. However, due to the high level of detail obtained using the sonic coring technique compared to the mud-rotary method, higher level of confidence was given to the lithological information obtained from the sonic cores. For each bore log, the lithology were summarised into five hydraulic texture classes (see Appendix 1, Halas *et al*., 2012a): mud, muddy sand, fine sand, medium sand and coarse to very coarse sand. As the main aim of mapping the lithology was to ascertain the spatial distribution of aquifers and aquitards, the sediments mapped were grouped into these five hydraulic texture classes. Mud and muddy sand correspond with aquitards whereas fine, medium, and coarse to very coarse sand form the transmissive aquifers.

The top three AEM depth slices (i.e. 0.0 – 0.5 m, 0.5 – 1.0 m, and 1.0 – 1.6 m) are only half a metre thick and highly resistive because they are minimal saturated. These depths are also not typically well resolved with airborne method. To get a better representation of the electrical conductivity, a new grid (0-1.6 m) was generated based on the average conductivity values of these three AEM depth slices. This new depth slice grid, together with the individual depth slices down to 22.0 m, formed the 14 depth slice layers (Apps *et al.,* 2012c).

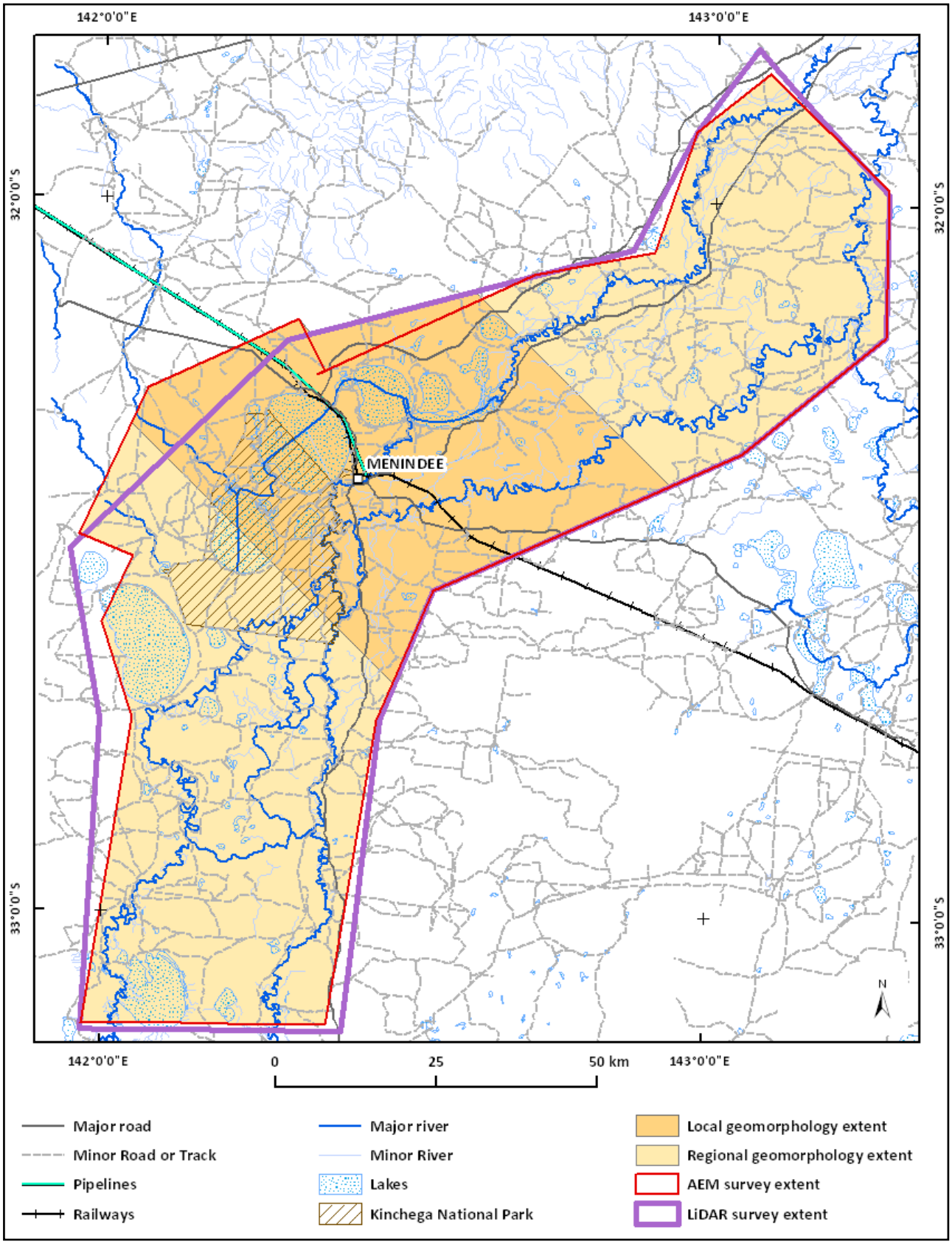



**Figure 17-66.** *Extent of AEM survey, geomorphic mapping and LiDAR DEM.*

## 17.7.2 Methodology

### 17.7.2.1 *Near-surface Sediments*

The 14 AEM depth slice layers were the main datasets used to map the hydraulic texture classes. To use the AEM data however, the causal relationship between apparent conductivity values and the five hydraulic texture classes was first established. To do so, the grid values for each conductivity depth slice at the location of each bore were obtained. The data was then sorted according to the individual hydraulic texture class. For every depth slice and texture class, statistical analysis was carried out to determine the range, percentiles and average apparent conductivity values (Figure 17-67).

The percentiles and average conductivity provided the thresholds to discriminate between the two hydraulic texture classes. For the first couple of depth slices from surface to 5.3 m, it was possible to differentiate between medium and fine sand, but it was not possible to separate between mud and muddy sand. From 6.4 m to 22 m, it was only possible to distinguish between the main texture groups (i.e. mud and sands), but not possible to separate amongst the texture classes within each group (e.g. fine versus medium sand) (Figure 17-68).

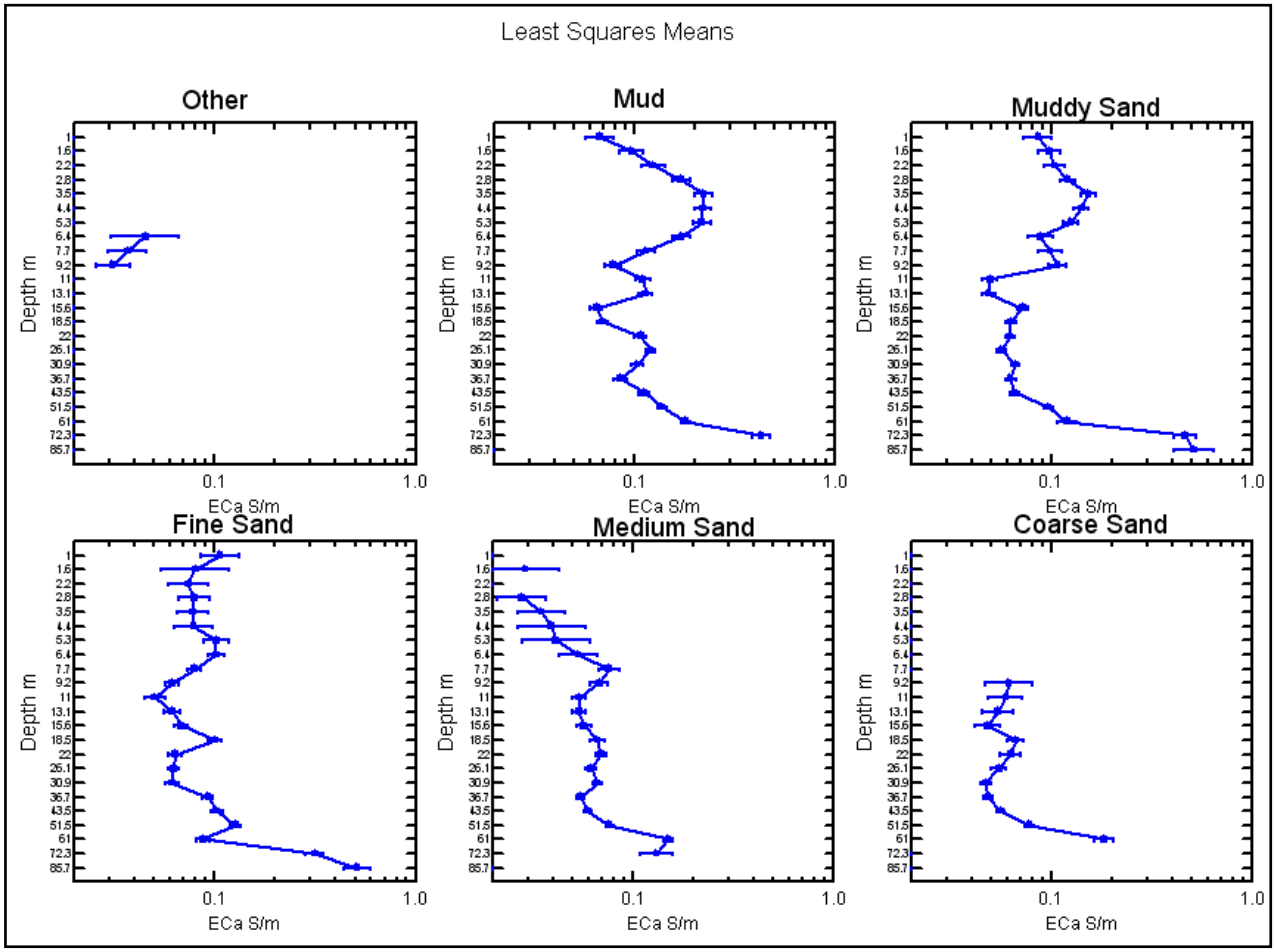



**Figure 17-67.** *Average apparent conductivity values for each hydraulic texture class in each depth slice.*

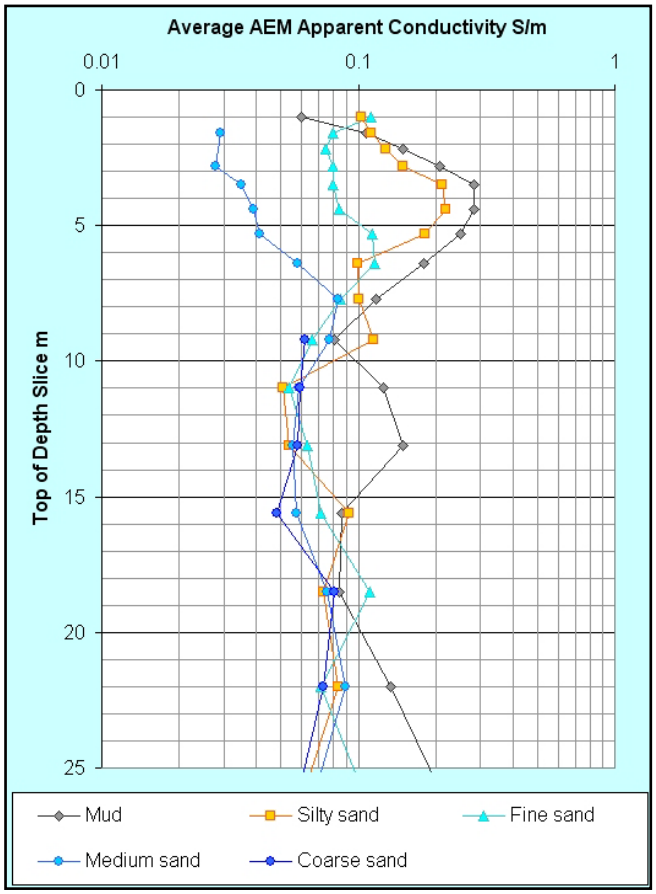



**Figure 17-68.** *Averaged AEM apparent conductivity for each hydraulic texture class at each depth slice interval.*

Other threshold values were selected based on the apparent conductivity patterns observable for each depth slice grid. These values may not relate to variation in lithology, but rather to the water content and salinity. Ten of the depth slice grids, from 0 m to 11 m had three thresholds whereas the other depth slice grids, from 11 m to 22 m had four thresholds (Table 17-20). Using ERMapper, the AEM grids were turned into rasters based on these threshold value classes. Each class was given a grid code, from 1 to 5 for the most resistive to the most conductive class respectively (Figure 17-69). The rasters were converted into shape files with the grid codes.

The electrical conductivity values amongst the texture classes for AEM depth grids 15.6 m to 18.5 m are very similar. This implies that using threshold values alone is insufficient to discriminate between the mud and the sands. Therefore, borehole lithological information from 52 sites is used to validate the apparent conductivity thresholds for each depth grid and spatially across the study area.

Electrical conductivity of similar range appears to form patterns relating to geomorphic features. For example, patterns associated with lunettes, dunes and lakes are recognisable from the AEM depth slice grids. Thus, the mapped geomorphic units are used to divide the depth slices into spatial domains (Figure 17-70). In all, 18 domains corresponding to individual geomorphic units are selected (Table 17-21).

**Table 17-20.** *The 14 AEM depth slice grids and the threshold values used in the hydraulic texture class mapping of the near surface sediment.*

| AEM Grid Depth from (m) | AEM Grid Depth to (m) | Conductivity Threshold S/m | Conductivity Threshold S/m | Conductivity Threshold S/m | Conductivity Threshold S/m |
|---|---|---|---|---|---|
| 0 | 1.6 | 0.02 | 0.046 | 0.126 | |
| 1.6 | 2.2 | 0.02 | 0.06 | 0.12 | |
| 2.2 | 2.8 | 0.035 | 0.07 | 0.15 | |
| 2.8 | 3.5 | 0.035 | 0.08 | 0.19 | |
| 3.5 | 4.4 | 0.04 | 0.08 | 0.20 | |
| 4.4 | 5.3 | 0.045 | 0.08 | 0.19 | |
| 5.3 | 6.4 | 0.05 | 0.11 | 0.25 | |
| 6.4 | 7.7 | 0.06 | 0.15 | 0.3 | |
| 7.7 | 9.2 | 0.09 | 0.15 | 0.35 | |
| 9.2 | 11.0 | 0.07 | 0.13 | 0.35 | |
| 11.0 | 13.1 | 0.07 | 0.15 | 0.36 | 0.90 |
| 13.1 | 15.6 | 0.07 | 0.15 | 0.4 | 1.00 |
| 15.6 | 18.5 | 0.065 | 0.15 | 0.4 | 1.00 |
| 18.5 | 22.0 | 0.05 | 0.18 | 0.4 | 1.00 |

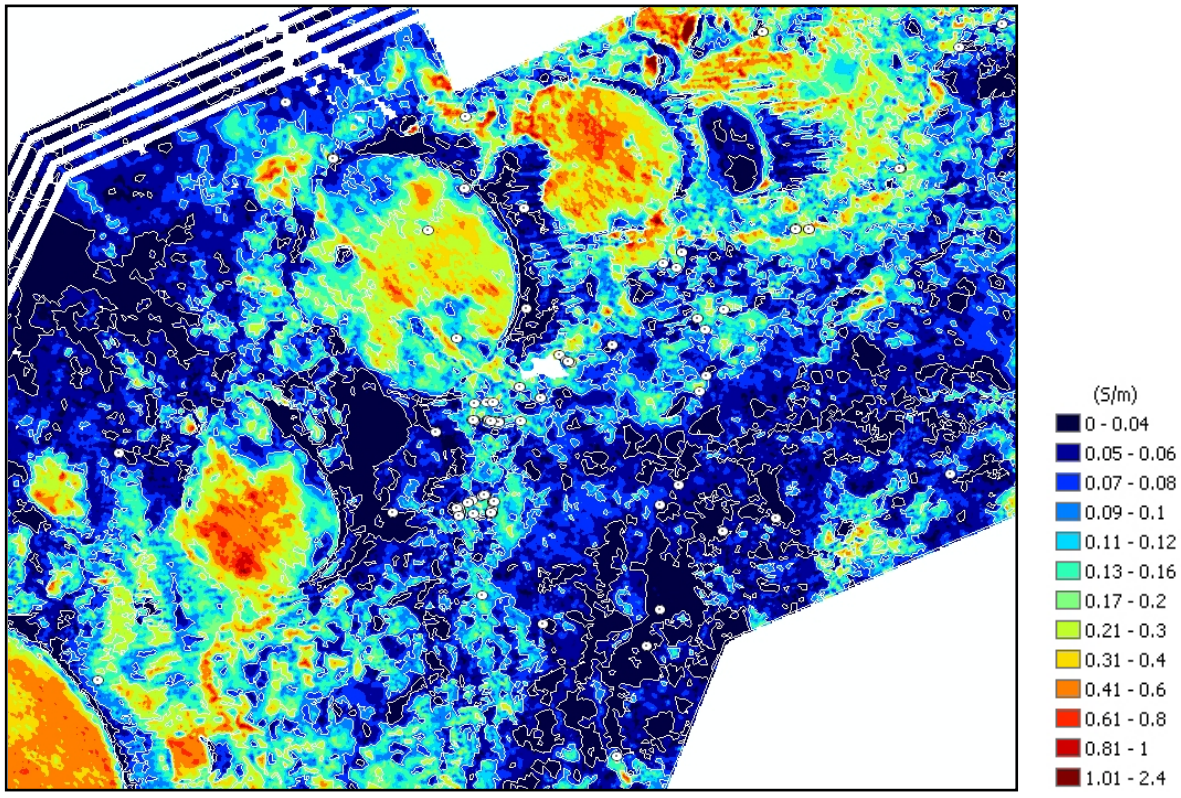



**Figure 17-69.** *AEM apparent conductivity depth slice, 2.8 m to 3.5 m, overlain by AEM conductivity threshold classes as polygons with white outline.*

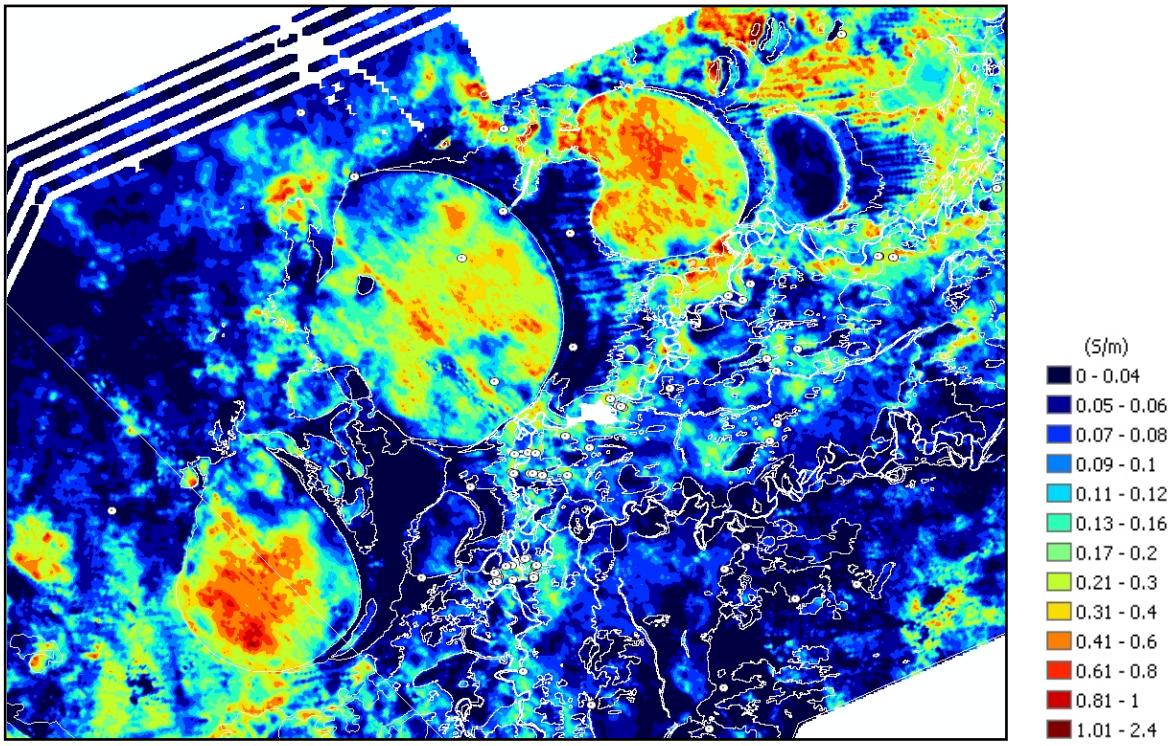



**Figure 17-70.** *AEM depth slice grid 2.8 m – 3.5 m overlain with geomorphic unit polygons (white outline).*

**Table 17-21.** *Geomorphic units and codes for dividing the AEM threshold grids into spatial domains. Also shown are the bore sites with lithological information.*

| Geomorphic Code | Geomorphic Units | Validation Sites (BHMAR) |
|---|---|---|
| Qac | All scroll plains | 16, 79A, 80A, 80B, 84, 92, 99 |
| Qac1 | Ox-bows, channels | |
| Qam | Lower Floodplain | 4, 21, 34, 65 |
| Qam1 | Floodplain depressions | |
| Qam2 | Upper floodplains | 3B, 8, 21, 28, 33, 35, 43, 58, 61, 66, 71, 74, 77, 14, 15 |
| Qam3 | Relict floodplain | 48, 56 |
| Qam4 | Floodplain bar | |
| Qaw | Large lakes | 18, 22, 64 |
| Qaw1 | Clay flat | |
| Qdl | Palaeo-lunette | 1B, 62 |
| Qdl1 | Lunette | |
| Qdw | Longitudinal dunes | |
| Qdw0 | Irregular large depressions | |
| Qdw1 | Hummocky dunes | 41, 66 |
| Qdw2 | Low longitudinal dunes | 1A, 6, 17, 19, 23, 30, 36, 53, |
| Qdw3 | High longitudinal dunes | 5, 63 |
| Qdw4 | Sub-parabolic dunes | 29, 31, 57 |
| Qdw5 | Regional sub-parabolic dunes | 51 |

Note: Some sites consist of single bore, but other sites may contain nested bores, e.g. 79A-2 and 79-6.

Two issues with regards to the use of geomorphic units to demarcate spatial domains are identified. The first is the thickness of the sediment associated with the surface feature. Sediments that make up the floodplain and scroll plains can be up to 18 m thick. However, some geomorphic features such as floodplain depressions and ox-bows may compose of sediment no more than two metres thick. Underlying these sediments are the various floodplain and scroll plains deposits. The second issue is the relative elevation of the geomorphic features. High palaeo-lunettes can reach up to 10 m tall and will be present in depth slice 9.2 m to 11 m. However, the entire polygon may consist of high dune ridges and low swales and slopes. Thus, to accurately depict the elevation within each polygon, a residual analysis on the LiDAR data was carried out. The relative elevations with respect to the scroll plains range from negative 7 m to positive 50 m (Figure 17-71). The negative 7 m include large lakes and channels, whereas the positive 50 m are the regional longitudinal and sub-parabolic dune fields. This relative elevation grid is divided into seven classes (Table 17-22) and polygons using these elevation thresholds are generated. To reflect the presence or absence, and the size of geomorphic domains within each depth slice, specific elevation threshold is merged with the corresponding depth range of the AEM threshold grids (Table 17-22).

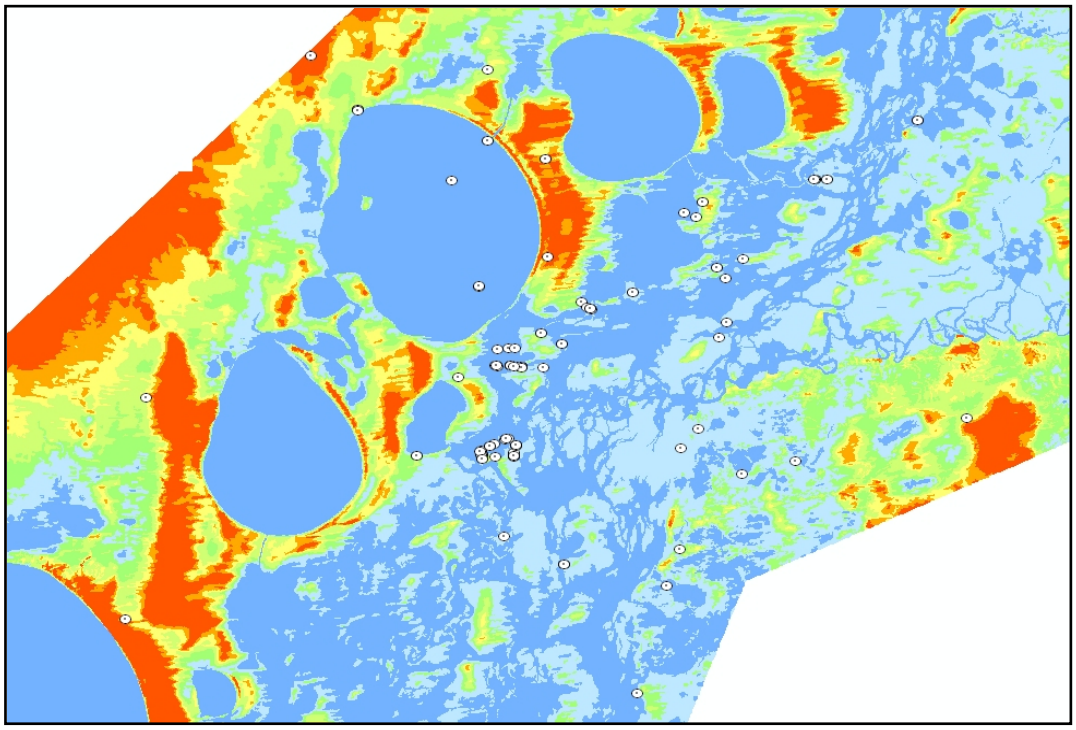


**Figure 17-71.** *Relative elevation with respect to the scroll plains based on residual analysis of the LiDAR DEM data.*

**Table 17-22.** *Elevation classes of the relative elevation grids and the corresponding AEM depth slices.*

| Elevation Class | Relative Elevation from (m) | Relative Elevation to (m) | AEM Depth Slices, Depth from (m) | AEM Depth Slices, Depth to (m) |
|---|---|---|---|---|
| 1 | -7 | 7.5 | 0 | 1.6 |
| 2 | 7.5 | 9.5 | 1.6 | 3.5 |
| 3 | 9.5 | 11.5 | 3.5 | 5.3 |
| 4 | 11.5 | 14 | 5.3 | 7.7 |
| 5 | 14 | 16 | 7.7 | 11.0 |
| 6 | 16 | 18 | 11.0 | 13.1 |
| 7 | 18 | 50 | 13.1 | 22.0 |

Based on borehole lithological information (Table 17-21), a set of supervised classification matrix is created to tabulate the hydraulic texture classes across every AEM threshold category and geomorphic domains for each depth slice (Table 17-23 and Table 17-24). Geomorphic classes in Table 17-21 have been populated from the surface to 22 m depth, as these units have thicker or laterally continuous sediments. In contrast, geomorphic units in Table 17-24 have thin or localised sediments, and these units are merged with the neighbouring units below 2.2 m depth. For example from 2.2 m to 2.8 m depths, polygons of hummocky dunes developed on, or surrounded by, the upper floodplain are assigned the upper floodplain classification.

Most of the geomorphic domains have at least 1 borehole to validate against. Geomorphic categories such as scroll plains, lower and upper floodplains and low longitudinal dunes have several validating bore sites. Other geomorphic units such as ox-bows, floodplain depressions and bars do not have any validation site. Information from field observation and soil sampling are thus used to tabulate the matrix. For example, field observation indicates that hummocky dunes are sandy, similar to the sub-parabolic dunes, but has limited thickness of no more than 3 m.

**Table 17-23.** *Hydraulic texture classes populated across the AEM threshold and geomorphic domain matrix.*

| Depth From m | Depth To m | AEM Threshold S/m | AEM Threshold S/m | AEM Grid Code | Qac *Hyd Class* | Qam *Hyd Class* | Qam2 *Hyd Class* | Qam3 *Hyd Class* | Qaw *Hyd Class* | Qdl *Hyd Class* | Qdl1 *Hyd Class* | Qdw1 *Hyd Class* | Qdw2 *Hyd Class* | Qdw3 *Hyd Class* | Qdw4 *Hyd Class* | Qdw5 *Hyd Class* |
|---|---|---|---|---|---|---|---|---|---|---|---|---|---|---|---|---|
| 0 | 1.6 | min | 0.02 | 1 | 2 | 2 | 3 | 3 | 2 | 3 | 3 | 3 | 3 | 3 | 3 | 3 |
| 0 | 1.6 | 0.02 | 0.046 | 2 | 1 | 1 | 2 | 2 | 2 | 2 | 3 | 3 | 3 | 2 | 3 | 3 |
| 0 | 1.6 | 0.046 | 0.126 | 3 | 1 | 1 | 1 | 1 | 1 | 2 | 2 | 2 | 3 | 2 | 3 | 2 |
| 0 | 1.6 | 0.126 | max | 4 | 1 | 1 | 1 | 1 | 1 | 2 | 2 | 2 | 2 | 2 | 2 | 2 |
| 1.6 | 2.2 | min | 0.02 | 1 | 2 | 2 | 3 | 2 | 2 | 3 | 3 | 3 | 3 | 3 | 3 | 3 |
| 1.6 | 2.2 | 0.02 | 0.06 | 2 | 2 | 1 | 2 | 2 | 2 | 2 | 3 | 3 | 3 | 2 | 3 | 2 |
| 1.6 | 2.2 | 0.06 | 0.12 | 3 | 1 | 1 | 1 | 1 | 1 | 2 | 2 | 2 | 3 | 2 | 3 | 1 |
| 1.6 | 2.2 | 0.12 | max | 4 | 1 | 1 | 1 | 1 | 1 | 2 | 2 | 2 | 2 | 2 | 2 | 1 |
| 2.2 | 2.8 | min | 0.035 | 1 | 3 | 2 | 3 | 3 | 2 | 2 | 3 | 3 | 3 | 2 | 3 | 2 |
| 2.2 | 2.8 | 0.035 | 0.07 | 2 | 2 | 1 | 2 | 2 | 2 | 2 | 3 | 3 | 3 | 1 | 3 | 1 |
| 2.2 | 2.8 | 0.07 | 0.15 | 3 | 1 | 1 | 1 | 1 | 1 | 2 | 2 | 2 | 3 | 1 | 2 | 1 |
| 2.2 | 2.8 | 0.15 | max | 4 | 1 | 1 | 1 | 1 | 1 | 2 | 2 | 2 | 2 | 1 | 1 | 1 |
| 2.8 | 3.5 | min | 0.035 | 1 | 3 | 3 | 3 | 3 | 2 | 2 | 3 | 3 | 3 | 2 | 3 | 2 |
| 2.8 | 3.5 | 0.035 | 0.08 | 2 | 2 | 2 | 2 | 2 | 2 | 2 | 3 | 2 | 3 | 1 | 2 | 1 |
| 2.8 | 3.5 | 0.08 | 0.19 | 3 | 1 | 1 | 1 | 1 | 1 | 1 | 2 | 2 | 3 | 1 | 1 | 1 |
| 2.8 | 3.5 | 0.19 | max | 4 | 1 | 1 | 1 | 1 | 1 | 1 | 2 | 2 | 2 | 1 | 1 | 1 |
| 3.5 | 4.4 | min | 0.04 | 1 | 3 | 3 | 3 | 3 | 2 | 2 | 3 | 3 | 4 | 2 | 3 | 2 |
| 3.5 | 4.4 | 0.04 | 0.08 | 2 | 2 | 2 | 1 | 2 | 2 | 2 | 3 | 2 | 4 | 2 | 2 | 1 |
| 3.5 | 4.4 | 0.08 | 0.2 | 3 | 2 | 1 | 1 | 1 | 1 | 1 | 2 | 2 | 3 | 1 | 1 | 1 |
| 3.5 | 4.4 | 0.2 | max | 4 | 1 | 1 | 1 | 1 | 1 | 1 | 2 | 2 | 2 | 1 | 1 | 1 |
| 4.4 | 5.3 | min | 0.045 | 1 | 3 | 3 | 3 | 3 | 2 | 2 | 3 | 3 | 4 | 2 | 3 | 2 |
| 4.4 | 5.3 | 0.045 | 0.08 | 2 | 2 | 2 | 1 | 3 | 2 | 1 | 3 | 2 | 4 | 2 | 2 | 1 |
| 4.4 | 5.3 | 0.08 | 0.19 | 3 | 2 | 1 | 1 | 2 | 1 | 1 | 2 | 2 | 3 | 1 | 1 | 1 |
| 4.4 | 5.3 | 0.19 | max | 4 | 1 | 1 | 1 | 1 | 1 | 1 | 2 | 2 | 2 | 1 | 1 | 1 |
| 5.3 | 6.4 | min | 0.05 | 1 | 3 | 3 | 3 | 3 | 2 | 2 | 3 | 3 | 4 | 2 | 3 | 2 |
| 5.3 | 6.4 | 0.05 | 0.11 | 2 | 2 | 2 | 1 | 3 | 2 | 1 | 3 | 3 | 3 | 2 | 2 | 1 |
| 5.3 | 6.4 | 0.11 | 0.25 | 3 | 2 | 2 | 1 | 2 | 1 | 1 | 2 | 3 | 3 | 1 | 2 | 1 |
| 5.3 | 6.4 | 0.25 | max | 4 | 1 | 1 | 1 | 1 | 1 | 1 | 2 | 3 | 2 | 1 | 1 | 1 |
| 6.4 | 7.7 | min | 0.06 | 1 | 3 | 3 | 3 | 3 | 2 | 2 | 3 | 4 | 4 | 2 | 3 | 2 |
| 6.4 | 7.7 | 0.06 | 0.15 | 2 | 3 | 2 | 1 | 3 | 2 | 1 | 2 | 4 | 3 | 2 | 3 | 1 |
| 6.4 | 7.7 | 0.15 | 0.3 | 3 | 2 | 1 | 1 | 2 | 1 | 1 | 2 | 4 | 3 | 1 | 1 | 1 |
| 6.4 | 7.7 | 0.3 | max | 4 | 1 | 1 | 1 | 1 | 1 | 1 | 1 | 3 | 1 | 1 | 1 | 1 |

| Depth From m | Depth To m | AEM Threshold S/m | AEM Threshold S/m | AEM Grid Code | Qac Hyd Class | Qam Hyd Class | Qam2 Hyd Class | Qam3 Hyd Class | Qaw Hyd Class | Qdl Hyd Class | Qdl1 Hyd Class | Qdw1 Hyd Class | Qdw2 Hyd Class | Qdw3 Hyd Class | Qdw4 Hyd Class | Qdw5 Hyd Class |
|---|---|---|---|---|---|---|---|---|---|---|---|---|---|---|---|---|
| 7.7 | 9.2 | min | 0.09 | 1 | 3 | 3 | 3 | 5 | 3 | 2 | 3 | 4 | 4 | 2 | 3 | 2 |
| 7.7 | 9.2 | 0.09 | 0.15 | 2 | 2 | 3 | 3 | 3 | 2 | 1 | 2 | 3 | 3 | 1 | 3 | 1 |
| 7.7 | 9.2 | 0.15 | 0.35 | 3 | 1 | 1 | 1 | 1 | 1 | 1 | 2 | 3 | 3 | 1 | 1 | 1 |
| 7.7 | 9.2 | 0.35 | max | 4 | 1 | 1 | 1 | 1 | 1 | 1 | 1 | 3 | 1 | 1 | 1 | 1 |
| 9.2 | 11 | min | 0.07 | 1 | 3 | 4 | 3 | 5 | 3 | 2 | 3 | 4 | 4 | 2 | 3 | 2 |
| 9.2 | 11 | 0.07 | 0.13 | 2 | 1 | 3 | 1 | 2 | 2 | 1 | 2 | 3 | 3 | 1 | 2 | 1 |
| 9.2 | 11 | 0.13 | 0.35 | 3 | 1 | 3 | 1 | 1 | 1 | 1 | 2 | 3 | 3 | 1 | 1 | 1 |
| 9.2 | 11 | 0.35 | max | 4 | 1 | 1 | 1 | 1 | 1 | 1 | 1 | 3 | 1 | 1 | 1 | 1 |
| 11 | 13.1 | min | 0.07 | 1 | 4 | 4 | 3 | 5 | 3 | 2 | 3 | 3 | 3 | 2 | 3 | 2 |
| 11 | 13.1 | 0.07 | 0.15 | 2 | 1 | 3 | 3 | 3 | 3 | 1 | 2 | 3 | 3 | 1 | 2 | 1 |
| 11 | 13.1 | 0.15 | 0.36 | 3 | 1 | 1 | 1 | 1 | 1 | 1 | 2 | 3 | 3 | 1 | 1 | 1 |
| 11 | 13.1 | 0.36 | 0.9 | 4 | 1 | 1 | 1 | 1 | 1 | 1 | 1 | 3 | 3 | 1 | 1 | 1 |
| 11 | 13.1 | 0.9 | max | 5 | 1 | 1 | 1 | 1 | 1 | 1 | 1 | 1 | 1 | 1 | 1 | 1 |
| 13.1 | 15.6 | min | 0.07 | 1 | 4 | 4 | 3 | 4 | 3 | 2 | 3 | 4 | 3 | 2 | 4 | 3 |
| 13.1 | 15.6 | 0.07 | 0.15 | 2 | 1 | 1 | 1 | 1 | 1 | 1 | 2 | 3 | 2 | 1 | 2 | 1 |
| 13.1 | 15.6 | 0.15 | 0.4 | 3 | 1 | 1 | 1 | 1 | 1 | 1 | 2 | 1 | 1 | 1 | 1 | 1 |
| 13.1 | 15.6 | 0.4 | 1 | 4 | 1 | 1 | 1 | 1 | 1 | 1 | 1 | 1 | 1 | 1 | 1 | 1 |
| 13.1 | 15.6 | 1 | max | 5 | 1 | 1 | 1 | 1 | 1 | 1 | 1 | 1 | 1 | 1 | 1 | 1 |
| 15.6 | 18.5 | min | 0.065 | 1 | NA | 3 | 3 | 3 | 4 | 3 | 3 | 3 | 3 | 2 | 4 | 3 |
| 15.6 | 18.5 | 0.065 | 0.15 | 2 | NA | 1 | 3 | 1 | 2 | 1 | 2 | 1 | 2 | 1 | 2 | 3 |
| 15.6 | 18.5 | 0.15 | 0.4 | 3 | NA | 1 | 2 | 1 | 1 | 1 | 1 | 1 | 1 | 1 | 1 | 1 |
| 15.6 | 18.5 | 0.4 | 1 | 4 | NA | 1 | 5 | 1 | 1 | 1 | 1 | 1 | 1 | 1 | 1 | 1 |
| 15.6 | 18.5 | 1 | max | 5 | NA | 1 | 2 | 1 | 1 | 1 | 1 | 1 | 1 | 1 | 1 | 1 |
| 18.5 | 22 | min | 0.05 | 1 | NA | 3 | 3 | 3 | 4 | 3 | 3 | 3 | 2 | 2 | 4 | 4 |
| 18.5 | 22 | 0.05 | 0.18 | 2 | NA | 2 | 1 | 1 | 2 | 1 | 2 | 1 | 1 | 1 | 4 | 4 |
| 18.5 | 22 | 0.18 | 0.4 | 3 | NA | 1 | 1 | 1 | 1 | 1 | 1 | 1 | 1 | 1 | 1 | 1 |
| 18.5 | 22 | 0.4 | 1 | 4 | NA | 1 | 1 | 1 | 1 | 1 | 1 | 1 | 1 | 1 | 1 | 1 |
| 18.5 | 22 | 1 | max | 5 | NA | 2 | 1 | 1 | 1 | 1 | 1 | 1 | 1 | 1 | 1 | 1 |

Notes: Refer to Figure 17-21 for geomorphic domain codes.

Cells in yellow are validated against borehole lithological information.

Codes for Hydraulic Texture Class are: 1 - Mud; 2 - Muddy Sand; 3 - Fine Sand; 4 - Medium Sand; and 5 - Coarse to very coarse sand.

**Table 17-24.** *Hydraulic texture classes populated across the AEM threshold and geomorphic domain matrix. These geomorphic domains consist of thin sediment and are therefore only applicable for the first two depth slice grids down to 2.2 m depth. Thereafter, these geomorphic domains were amalgamated into the surrounding domains shown in Table 17-23.*

| Depth From m | Depth To m | AEM Threshold S/m | AEM Threshold S/m | AEM Grid Code | Qac1 *Hyd Class* | Qam1 *Hyd Class* | Qam4 *Hyd Class* | Qaw1 *Hyd Class* | Qdw0 *Hyd Class* | Qdw *Hyd Class* |
|---|---|---|---|---|---|---|---|---|---|---|
| 0 | 1.6 | min | 0.02 | 1 | 2 | 3 | 3 | 2 | 3 | 3 |
| 0 | 1.6 | 0.02 | 0.046 | 2 | 1 | 2 | 3 | 2 | 2 | 3 |
| 0 | 1.6 | 0.046 | 0.126 | 3 | 1 | 1 | 2 | 1 | 2 | 2 |
| 0 | 1.6 | 0.126 | max | 4 | 1 | 1 | 1 | 1 | 1 | 1 |
| 1.6 | 2.2 | min | 0.02 | 1 | 2 | 3 | 3 | 2 | 3 | 3 |
| 1.6 | 2.2 | 0.02 | 0.06 | 2 | 1 | 2 | 3 | 2 | 2 | 3 |
| 1.6 | 2.2 | 0.06 | 0.12 | 3 | 1 | 1 | 2 | 1 | 2 | 2 |
| 1.6 | 2.2 | 0.12 | max | 4 | 1 | 1 | 1 | 1 | 1 | 1 |

Notes. Refer to Figure 17-21 for geomorphic domain codes.

Cells in yellow are validated against borehole lithological information.

Codes for Hydraulic Texture Class are: 1 - Mud; 2 - Muddy Sand; 3 - Fine Sand; 4 - Medium Sand; and 5 - Coarse to very coarse sand.

17.7.2.2 ***Deeper Sediments***

Deeper sediments are those contained within the lower part of the upper confining aquitard (i.e. Blanchetown Clay and mud-rich upper Calivil Formation), the main aquifer (Calivil Formation) and the lower confining aquitard (Renmark Formation). The seven AEM depth slices used to delineate the textural classes of these sediment starts from 22.0 m and finish at 72.3 m depths.

There are three main electrical conductivity (EC) domains present in the study area. Very resistive areas (<0.02 S/m) are mostly associated with Palaeozoic basement rock. Resistive domains are mainly present in the central area with a few isolated areas distributed in the south and northeast proximal to the Darling River or Talyawalka Creek. The remaining areas are conductive, especially in the southern part of the study area. The statistical analysis used to determine the threshold values for texture classes in the deeper sediments is the same as the statistical method used to delineate the conductivity threshold of textural classes for the near surface sediment (refer to Section 17.7.2.1). Based on 23 sonic bores across 20 sites (Table 17-25) across the resistive domains, the average conductivity for each depth slice is determined (Figure 17-72). A set of thresholds were determine to discriminate the hydraulic texture class at each depth slice (Table 17-26). In some depth intervals, the average conductivities of textural classes may be very similar, thus it is not always possible to distinguish individual texture class based on threshold values alone. For example, for depth slice 22.0 m to 26.1 m, the threshold 0.045 S/m is used to differentiate between the Palaeozoic rock from the sediment, and 0.1 S/m sets the limit between mud and the other texture classes. In such case, mapping of the texture classes between 0.045 S/m and 0.1 S/m will take into account the spatial conductivity patterns, geological concept and validated using borehole lithological information and downhole gamma logs across the 20 sites.

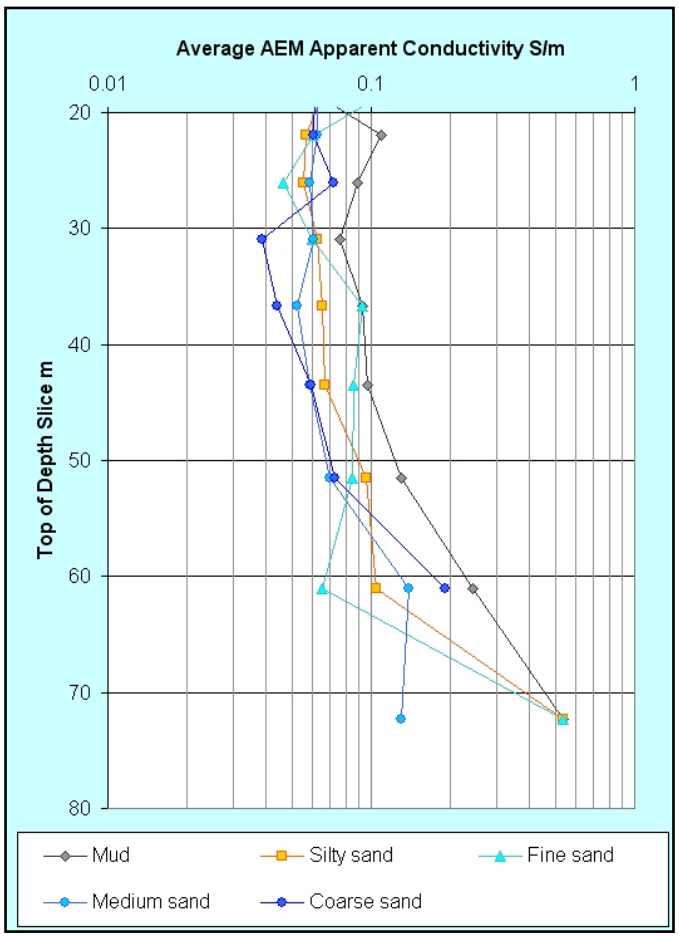



**Figure 17-72.** *Averaged AEM conductivity for each hydraulic texture class at each depth slice interval.*

In contrast to the resistive domains, the majority of the bores in conductive areas were drilled using the mud rotary rig; the slurry returns are not suitable for statistical analysis. The five applicable sonic bores do not provide enough data to perform a statistically robust analysis for each AEM depth slice. Consequently, the results from these bores are use as qualitative validation of the textural classes in each depth slice only.

**Table 17-25.** *The twenty BHMAR sites used to derive the textural class conductivity thresholds.*

| South | Central | Northeast |
|---|---|---|
| 21, 29, 31 | 33, 58, 61, 75, 77, 79A, 80A, 80B, 83, 84, 88, 92, 99 | 4, 16, 34, 35 |

**Table 17-26.** *The seven AEM depth slice grids and the threshold values used in the hydraulic texture class mapping of the deeper sediment.*

| AEM Grid Depth from (m) | AEM Grid Depth to (m) | Conductivity Threshold S/m | Conductivity Threshold S/m | Conductivity Threshold S/m | Conductivity Threshold S/m | Conductivity Threshold S/m | AEM Grid Depth from (m) |
|---|---|---|---|---|---|---|---|
| 22.0 | 26.1 | 0.045 | 0.1 | 0.2 | 0.8 | >0.8 | |
| 26.1 | 30.9 | 0.08 | 0.16 | 0.48 | 1.0 | >1.0 | |
| 30.9 | 36.7 | 0.06 | 0.1 | 0.25 | 0.82 | >0.82 | |
| 36.7 | 43.5 | 0.07 | 0.13 | 0.25 | 0.9 | >0.9 | |
| 43.5 | 51.5 | 0.025 | 0.075 | 0.2 | 0.9 | 2.0 | >2.0 |
| 51.5 | 61.0 | 0.05 | 0.12 | 0.9 | 3 | >3.0 | |
| 61.0 | 72.3 | 0.065 | 0.11 | 0.2 | 1.0 | 3.0 | >3.0 |

Using ERMapper, the AEM grids were turned into rasters based on these threshold value classes. Each class was given a grid code, from 1 to 6 for the most resistive to the most conductive class respectively. The rasters were converted into shape files with the grid codes. Since AEM depth slice is generated based on LiDAR DEM, up to 50 m difference in local relief between the highest dune field and lowest river channel will influenced the distribution of texture class within each depth slice. Thus, the contour boundary between elevated regional dune field and the adjacent floodplain is merged with the AEM threshold shape files.

This boundary allows the differentiation of lithology and stratigraphy in areas of high electrical conductivity but a lack of contrast between adjacent polygons. Example of such a case is in conductive area situated beneath the dune field with equally conductive area beneath adjacent floodplain.

Whilst most polygons correspond to a hydraulic texture class, further examination of the borehole lithological logs indicate the presence of interbedded sediment, i.e. a mixture of fine and coarse textured layers within a depth interval. This is more common with thicker depth slice interval. Thus new texture class “interbedded” is used to demarcate these units, which in general, comprises mud and medium sand (texture code 14) or muddy sand and fine sand (texture code 23). In the case of interbedded transmissive sand, e.g. medium sand with interbedded coarse sand, the polygon is assigned with dominant texture class, i.e. medium sand in this case. Likewise, low transmissive aquitard comprising interbedded mud and muddy sand are assigned using the main texture class.

In the central area, the statistical approach of assigning hydraulic texture classes to the corresponding threshold ranges work well. This is largely attributed to the consistently low salinity (0.00 – 0.08 S/m) associated with the transmissive sand. When salinity is constant, variation in apparent electrical conductivity is associated with a change in porosity and texture. Thus, areas with slightly elevated conductivities (0.05 – 0.16 S/m) are most likely to be fine textured or interbedded sediments.

Away from the central area however, it is more difficult to ascertain the hydraulic texture classes as the salinity of groundwater and the range of apparent conductivity increases (0.1 – >3.0 S/m). In such case, the lithology records from bores, which include both sonic and mud-rotary, are used to validate the conductivity threshold classes within a local area.

Across the survey area, AEM and interpreted stratigraphic cross sections helped define the sedimentary facies. Cross sections are used to constraint the thickness and depths of the upper and lower confining aquitards, interpretation of faults and outlining potential palaeochannels and beach strand system. Geomorphic patterns such as lacustrine, palaeochannels, conductive beach strand system and resistive bedrock are interpreted from AEM depth slices. Linear conductivity boundaries indicate the presence of faults.

However, large tracts of moderately conductive areas with no borehole to validate are present across the study area. The lithologies in these areas have been interpolated with bore constraint lithology from proximal polygons of same conductivity threshold classes. From the available bore lithological records, the lithologies may vary across the study area within the same conductivity threshold class and depth slice.

The resulting combination of conductivity threshold ranges and texture classes for the seven depth slices are summarised in Table 17-27 to Table 17-33. The number of polygons within each threshold is indicative of the importance or association between lithology and conductivity. However, this is not definitive as polygons vary in areas and 1 large polygon may cover the same areas to a dozen of smaller polygons.

An example of the AEM apparent conductivity threshold for depth slice 43.5 m to 51.5 m is shown in Figure 17-73 and the interpreted hydraulic texture classes associated with each conductivity threshold range are shown in Figure 17-74.

**Table 17-27.** *AEM threshold values, hydraulic texture classes and number of polygons (N) present in depth slice 22.0 - 26.1 m.*

| From S/m | To S/m | Texture Class | Texture Code | N |
|---|---|---|---|---|
| 0.0 | 0.045 | Basement | 0 | 1 |
| 0.0 | 0.045 | Interbedded | 13 | 71 |
| **0.0** | **0.045** | Medium Sand | 4 | 105 |
| **0.0** | **0.045** | Coarse Sand | 5 | 2 |
| **0.045** | **0.1** | Mud | 1 | 4 |
| **0.045** | **0.1** | Interbedded | 13 | 296 |
| **0.045** | **0.1** | Muddy Sand | 2 | 356 |
| **0.045** | **0.1** | Medium Sand | 4 | 22 |
| **0.045** | **0.1** | Coarse Sand | 5 | 1 |
| 0.1 | 0.2 | Mud | 1 | 412 |
| 0.1 | 0.2 | Interbedded | 13 | 133 |
| 0.1 | 0.2 | Muddy Sand | 2 | 262 |
| 0.1 | 0.2 | Medium Sand | 4 | 8 |
| 0.2 | 0.8 | Mud | 1 | 517 |
| 0.2 | 0.8 | Interbedded | 13 | 13 |
| 0.2 | 0.8 | Muddy Sand | 2 | 346 |
| 0.2 | 0.8 | Medium Sand | 4 | 10 |
| >0.8 | | Mud | 1 | 791 |
| >0.8 | | Interbedded | 13 | 3 |
| >0.8 | | Muddy Sand | 2 | 12 |
| >0.8 | | Medium Sand | 4 | 1 |

**Table 17-28.** *AEM threshold values, hydraulic texture classes and number of polygons (N) present in depth slice 26.1 - 30.9 m.*

| From S/m | To S/m | Texture Class | Texture Code | N |
|---|---|---|---|---|
| 0.0 | 0.08 | Basement | 0 | 4 |
| 0.0 | 0.08 | Mud | 1 | 5 |
| 0.0 | 0.08 | Interbedded | 13 | 229 |
| 0.0 | 0.08 | Muddy Sand | 2 | 237 |
| 0.0 | 0.08 | Fine Sand | 3 | 78 |
| 0.0 | 0.08 | Medium Sand | 4 | 46 |
| 0.0 | 0.08 | Coarse Sand | 5 | 11 |
| **0.08** | **0.16** | Mud | 1 | 366 |
| **0.08** | **0.16** | Interbedded | 13 | 42 |
| **0.08** | **0.16** | Muddy Sand | 2 | 301 |
| **0.08** | **0.16** | Fine Sand | 3 | 11 |
| **0.08** | **0.16** | Medium Sand | 4 | 22 |
| 0.16 | 0.48 | Mud | 1 | 815 |
| 0.16 | 0.48 | Interbedded | 13 | 1 |
| 0.16 | 0.48 | Muddy Sand | 2 | 183 |
| 0.48 | 1.0 | Mud | 1 | 957 |
| 0.48 | 1.0 | Muddy Sand | 2 | 2 |
| 0.48 | 1.0 | Medium Sand | 3 | 1 |
| >1.0 | | Mud | 1 | 578 |

**Table 17-29.** *AEM threshold values, hydraulic texture classes and number of polygons (N) present in depth slice 30.9 – 36.7 m.*

| From S/m | To S/m | Texture Class | Texture Code | N |
|---|---|---|---|---|
| 0.0 | 0.06 | Basement | 0 | 5 |
| 0.0 | 0.06 | Mud | 1 | 13 |
| 0.0 | 0.06 | Interbedded | 14 | 216 |
| 0.0 | 0.06 | Muddy Sand | 2 | 17 |
| 0.0 | 0.06 | Interbedded | 23 | 7 |
| 0.0 | 0.06 | Fine Sand | 3 | 14 |
| 0.0 | 0.06 | Medium Sand | 4 | 200 |
| 0.0 | 0.06 | Coarse Sand | 5 | 51 |
| 0.06 | 0.1 | Basement | 0 | 3 |
| 0.06 | 0.1 | Mud | 1 | 72 |
| 0.06 | 0.1 | Interbedded | 14 | 120 |
| 0.06 | 0.1 | Muddy Sand | 2 | 378 |
| 0.06 | 0.1 | Interbedded | 23 | 35 |
| 0.06 | 0.1 | Fine Sand | 3 | 5 |
| 0.06 | 0.1 | Medium Sand | 4 | 32 |
| 0.06 | 0.1 | Coarse Sand | 5 | 7 |
| 0.1 | 0.25 | Basement | 0 | 1 |
| 0.1 | 0.25 | Mud | 1 | 641 |
| 0.1 | 0.25 | Interbedded | 14 | 123 |
| 0.1 | 0.25 | Muddy Sand | 2 | 40 |
| 0.1 | 0.25 | Interbedded | 23 | 4 |
| 0.1 | 0.25 | Fine Sand | 3 | 12 |
| 0.1 | 0.25 | Medium Sand | 4 | 42 |

| | | | | |
|---|---|---|---|---|
| 0.1 | 0.25 | Coarse Sand | 5 | 7 |
| 0.25 | 0.82 | Mud | 1 | 706 |
| 0.25 | 0.82 | Interbedded | 14 | 17 |
| 0.25 | 0.82 | Muddy Sand | 2 | 249 |
| 0.25 | 0.82 | Fine Sand | 3 | 1 |
| 0.25 | 0.82 | Medium Sand | 4 | 13 |
| 0.25 | 0.82 | Coarse Sand | 5 | 1 |
| >0.82 | | Mud | 1 | 472 |
| >0.82 | | Muddy Sand | 2 | 1 |
| >0.82 | | Coarse Sand | 5 | 3 |

**Table 17-30.** *AEM threshold values, hydraulic texture classes and number of polygons (N) present in depth slice 36.7 – 43.5 m.*

| From S/m | To S/m | Texture Class | Texture Code | N |
|---|---|---|---|---|
| 0.0 | 0.07 | Basement | 0 | 10 |
| 0.0 | 0.07 | Mud | 1 | 1 |
| 0.0 | 0.07 | Interbedded | 14 | 103 |
| 0.0 | 0.07 | Muddy Sand | 2 | 14 |
| 0.0 | 0.07 | Interbedded | 23 | 71 |
| 0.0 | 0.07 | Fine Sand | 3 | 8 |
| 0.0 | 0.07 | Medium Sand | 4 | 225 |
| 0.07 | 0.13 | Basement | 0 | 3 |
| 0.07 | 0.13 | Mud | 1 | 206 |
| 0.07 | 0.13 | Interbedded | 14 | 91 |
| 0.07 | 0.13 | Muddy Sand | 2 | 289 |
| 0.07 | 0.13 | Interbedded | 23 | 20 |
| 0.07 | 0.13 | Fine Sand | 3 | 37 |
| 0.07 | 0.13 | Medium Sand | 4 | 70 |
| 0.13 | 0.25 | Mud | 1 | 590 |
| 0.13 | 0.25 | Interbedded | 14 | 174 |
| 0.13 | 0.25 | Muddy Sand | 2 | 45 |
| 0.13 | 0.25 | Interbedded | 23 | 121 |
| 0.13 | 0.25 | Fine Sand | 3 | 17 |
| 0.13 | 0.25 | Medium Sand | 4 | 5 |
| 0.25 | 0.9 | Basement | 0 | 1 |
| 0.25 | 0.9 | Mud | 1 | 401 |
| 0.25 | 0.9 | Interbedded | 14 | 97 |
| 0.25 | 0.9 | Muddy Sand | 2 | 193 |
| 0.25 | 0.9 | Interbedded | 23 | 3 |
| 0.25 | 0.9 | Fine Sand | 3 | 96 |
| 0.25 | 0.9 | Medium Sand | 4 | 6 |
| >0.9 | | Mud | 1 | 158 |
| >0.9 | | Interbedded | 14 | 112 |
| >0.9 | | Muddy Sand | 2 | 108 |
| >0.9 | | Fine Sand | 3 | 30 |
| >0.9 | | Medium Sand | 4 | 4 |

**Table 17-31.** *AEM threshold values, hydraulic texture classes and number of polygons (N) present in depth slice 43.5 – 51.5 m.*

| From S/m | To S/m | Texture Class | Texture Code | N |
|---|---|---|---|---|
| 0.0 | 0.025 | Basement | 0 | 18 |
| 0.0 | 0.025 | Medium Sand | 4 | 2 |
| 0.0 | 0.025 | Coarse Sand | 5 | 61 |
| 0.025 | 0.075 | Basement | 0 | 34 |
| 0.025 | 0.075 | Mud | 1 | 9 |
| 0.025 | 0.075 | Interbedded | 14 | 105 |
| 0.025 | 0.075 | Muddy Sand | 2 | 20 |
| 0.025 | 0.075 | Medium Sand | 4 | 275 |
| 0.025 | 0.075 | Coarse Sand | 5 | 1 |
| 0.075 | 0.2 | Basement | 0 | 3 |
| 0.075 | 0.2 | Mud | 1 | 351 |
| 0.075 | 0.2 | Interbedded | 14 | 161 |
| 0.075 | 0.2 | Muddy Sand | 2 | 164 |
| 0.075 | 0.2 | Fine Sand | 3 | 45 |
| 0.075 | 0.2 | Medium Sand | 4 | 10 |
| 0.075 | 0.2 | Coarse Sand | 5 | 1 |
| 0.2 | 0.9 | Mud | 1 | 196 |
| 0.2 | 0.9 | Interbedded | 14 | 174 |
| 0.2 | 0.9 | Muddy Sand | 2 | 172 |
| 0.2 | 0.9 | Fine Sand | 3 | 321 |
| 0.2 | 0.9 | Medium Sand | 4 | 14 |
| 0.9 | 2.0 | Mud | 1 | 27 |
| 0.9 | 2.0 | Interbedded | 14 | 26 |
| 0.9 | 2.0 | Muddy Sand | 2 | 180 |
| 0.9 | 2.0 | Fine Sand | 3 | 183 |
| >2.0 | | Mud | 1 | 8 |
| >2.0 | | Muddy Sand | 2 | 23 |
| >2.0 | | Fine Sand | 3 | 183 |

**Table 17-32.** *AEM threshold values, hydraulic texture classes and number of polygons (N) present in depth slice 51.5 – 61.0 m.*

| From S/m | To S/m | Texture Class | Texture Code | N |
|---|---|---|---|---|
| 0.0 | 0.05 | Basement | 0 | 24 |
| 0.0 | 0.05 | Interbedded | 13 | 4 |
| 0.0 | 0.05 | Muddy Sand | 2 | 17 |
| 0.0 | 0.05 | Medium Sand | 4 | 29 |
| 0.0 | 0.05 | Interbedded | 41 | 15 |
| 0.0 | 0.05 | Coarse Sand | 5 | 99 |
| 0.05 | 0.12 | Basement | 0 | 4 |
| 0.05 | 0.12 | Mud | 1 | 146 |
| 0.05 | 0.12 | Interbedded | 13 | 49 |
| 0.05 | 0.12 | Muddy Sand | 2 | 152 |
| 0.05 | 0.12 | Fine Sand | 3 | 22 |
| 0.05 | 0.12 | Medium Sand | 4 | 130 |
| 0.05 | 0.12 | Interbedded | 41 | 188 |
| 0.05 | 0.12 | Coarse Sand | 5 | 5 |
| 0.12 | 0.9 | Basement | 0 | 1 |

| | | | | |
|---|---|---|---|---|
| 0.12 | 0.9 | Mud | 1 | 256 |
| 0.12 | 0.9 | Interbedded | 13 | 28 |
| 0.12 | 0.9 | Muddy Sand | 2 | 110 |
| 0.12 | 0.9 | Fine Sand | 3 | 147 |
| 0.12 | 0.9 | Medium Sand | 4 | 9 |
| 0.12 | 0.9 | Interbedded | 41 | 36 |
| 0.9 | 3.0 | Mud | 1 | 34 |
| 0.9 | 3.0 | Muddy Sand | 2 | 204 |
| 0.9 | 3.0 | Fine Sand | 3 | 214 |
| 0.9 | 3.0 | Interbedded | 41 | 178 |
| >3.0 | | Muddy Sand | 2 | 45 |
| >3.0 | | Fine Sand | 3 | 200 |
| >3.0 | | Interbedded | 41 | 8 |

**Table 17-33.** *AEM threshold values, hydraulic texture classes and number of polygons (N) present in depth slice 61.0 – 72.3 m.*

| From S/m | To S/m | Texture Class | Texture Code | N |
|---|---|---|---|---|
| 0.0 | 0.065 | Basement | 0 | 34 |
| 0.0 | 0.065 | Mud | 1 | 2 |
| 0.0 | 0.065 | Interbedded | 14 | 9 |
| 0.0 | 0.065 | Muddy Sand | 2 | 6 |
| 0.0 | 0.065 | Medium Sand | 4 | 214 |
| 0.065 | 0.11 | Basement | 0 | 4 |
| 0.065 | 0.11 | Mud | 1 | 56 |
| 0.065 | 0.11 | Interbedded | 14 | 325 |
| 0.065 | 0.11 | **Muddy Sand** | **2** | 216 |
| 0.065 | 0.11 | **Fine Sand** | **3** | 115 |
| 0.065 | 0.11 | **Medium Sand** | **4** | 1 |
| 0.11 | 0.2 | Basement | 0 | 1 |
| 0.11 | 0.2 | Mud | 1 | 577 |
| 0.11 | 0.2 | Interbedded | 14 | 25 |
| 0.11 | 0.2 | **Muddy Sand** | **2** | 63 |
| 0.11 | 0.2 | **Fine Sand** | **3** | 4 |
| 0.2 | 1.0 | Mud | 1 | 440 |
| 0.2 | 1.0 | Interbedded | 14 | 31 |
| 0.2 | 1.0 | **Muddy Sand** | **2** | 290 |
| 0.2 | 1.0 | **Fine Sand** | **3** | 27 |
| 1.0 | 3.0 | Mud | 1 | 195 |
| 1.0 | 3.0 | Interbedded | 14 | 42 |
| 1.0 | 3.0 | **Muddy Sand** | **2** | 307 |
| 1.0 | 3.0 | **Fine Sand** | **3** | 165 |
| >3.0 | | Mud | 1 | 19 |
| >3.0 | | Interbedded | 14 | 15 |
| >3.0 | | **Muddy Sand** | **2** | 250 |
| >3.0 | | **Fine Sand** | **3** | 76 |
| >3.0 | | Interbedded | 41 | 1 |

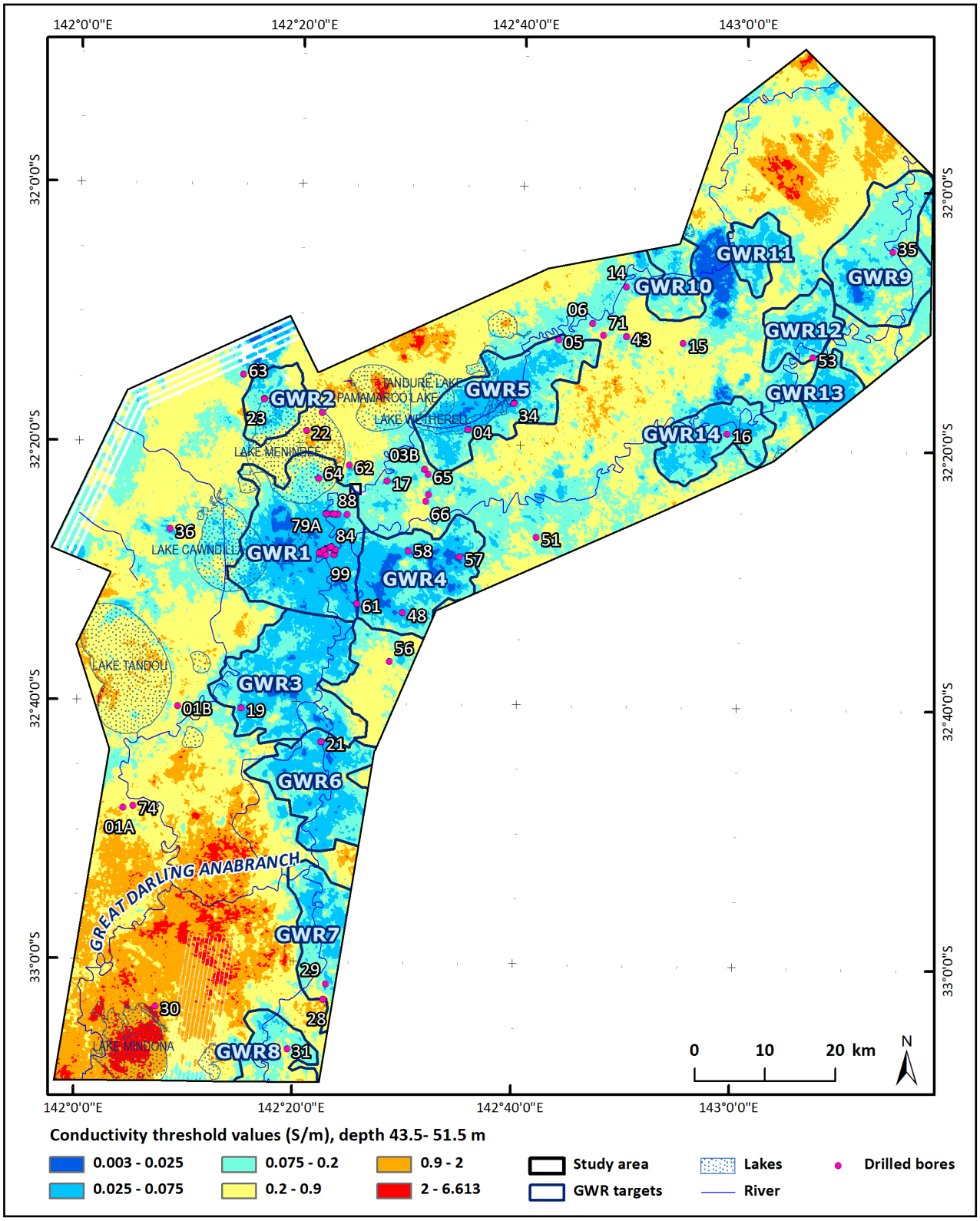



**Figure 17-73.** *AEM apparent conductivity depth slice, 43.5 m to 51.5 m, with threshold classes. Dots and numbers represent validation bore sites.*

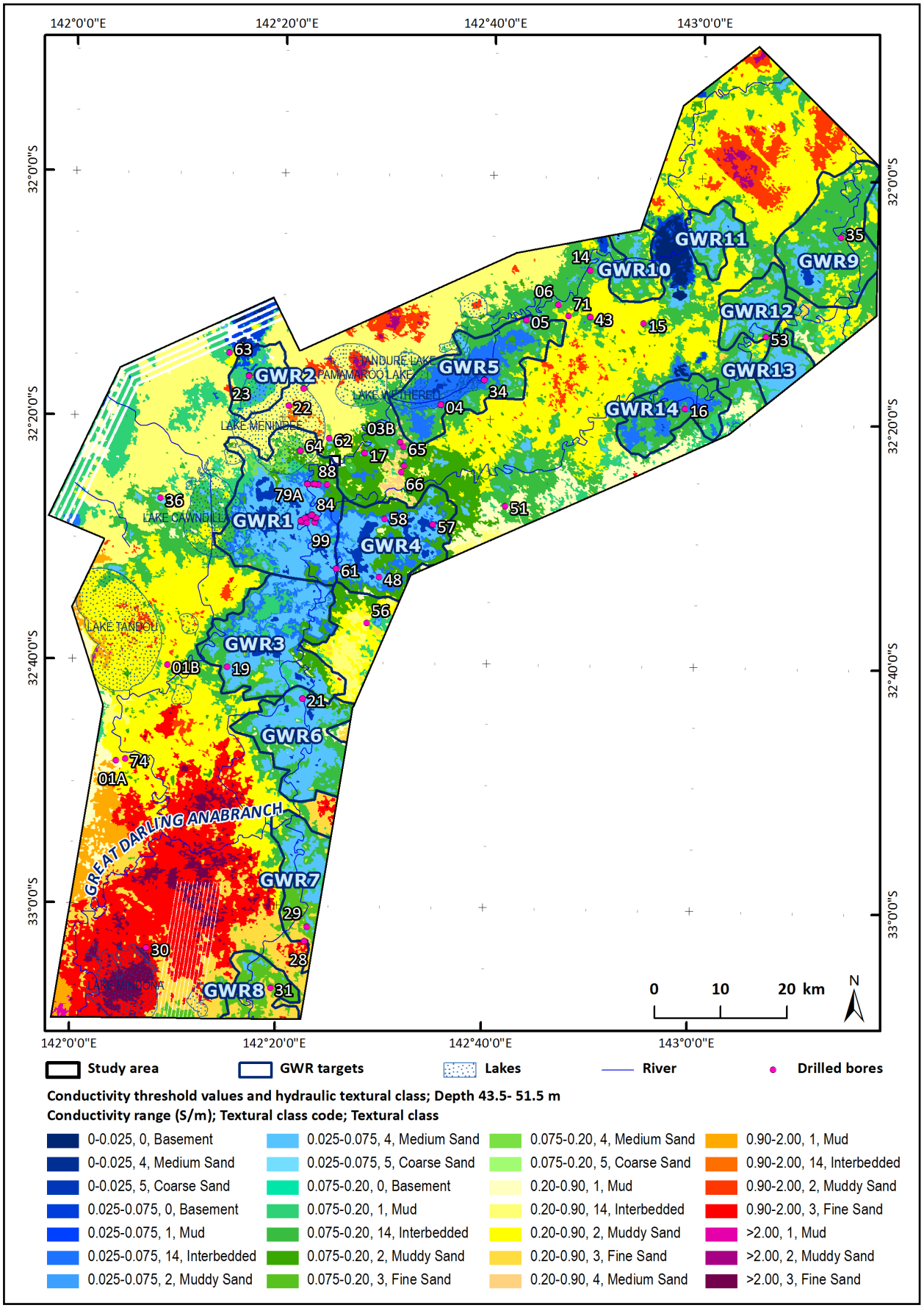



**Figure 17-74.** *AEM depth slice 43.5 m to 51.5 m with interpreted texture classes based on AEM conductivity threshold ranges. Dots and numbers represent validation bore sites.*

## 17.8 HYDROSTRATIGRAPHIC MAPPING

Hydrostratigraphically there are five units of interest within the project area: two aquifers - shallow unconfined and semi-confined aquifers; and three aquitards: near-surface, upper confining and lower confining aquitards. The various stratigraphic units (as discussed in Section 17.6) were attributed to these five specific hydrostratigraphic units based on hydraulic textural classes and depth (Table 17-34). For example, mud-rich sediment (hydraulic texture class code of 1 or 2) of the Willotia beds and the mud-facies of the Coonambidgal and Menindee Formations collectively form the near surface aquitard. In contrast, the basal sand (hydraulic texture class code of 3, 4 or 5) of the Menindee and Coonambidgal Formations and the sandy deposit of the Willotia beds form the shallow unconfined aquifer. Figure 17-75 shows the textural composition of the Coonambidgal Formation, Menindee Formation and Willotia beds.

**Table 17-34.** *Assigning of hydrogeological units based on stratigraphy, hydraulic texture class and depth. 1=mud; 2=muddy sand; 3=fine sand; 4=medium sand; 5=coarse to very coarse sand; 13=interbedded mud and fine sand; 14=interbedded mud and medium sand; 23=interbedded muddy sand and fine sand; and 41=interbedded medium sand overlying mud.*

| Hydrostratigraphy | Stratigraphic Unit | Hydraulic Texture Class Code | Calivil Wt | UCA |
|---|---|---|---|---|
| Near surface aquitard | Menindee, Coonambidgal, Willotia | 1, 2, 13 | | |
| Shallow unconfined aquifer | Menindee, Coonambidgal, Willotia | 3, 4, 5, 14, 23, 41 | | |
| Upper confining aquitard | Blanchetown, Calivil, Loxton-Parilla Sands | 1, 2, 3, 4, 5, 13, 14, 23, 41 1, 2, | | |
| Unsaturated semi-confined aquifer | Calivil, Loxton-Parilla Sands, Calivil over Renmark, Loxton-Parilla Sands over Renmark | 3, 4, 5, 13, 14, 23, 41 | Below | Above |
| Saturated semi-confined aquifer | Calivil, Loxton-Parilla Sands, Calivil over Renmark, Loxton-Parilla Sands over Renmark | 3, 4, 5, 13, 14, 23, 41 | Above | Above |
| Lower confining aquitard | Renmark, Calivil over Renmark, Loxton-Parilla Sands over Renmark | 1, 2 | | |
| Unsaturated lower-confined aquifer | Renmark | 3, 4, 5, 14, 23, 41 | Below | |
| Saturated lower-confined aquifer | Renmark | 3, 4, 5, 14, 23, 41 | Above | |
| Other | Woorinen Formation, Lunette, palaeo-lunette | 0 | | |
| Not Applicable | Devonian Sedimentary Rock | 0 | | |

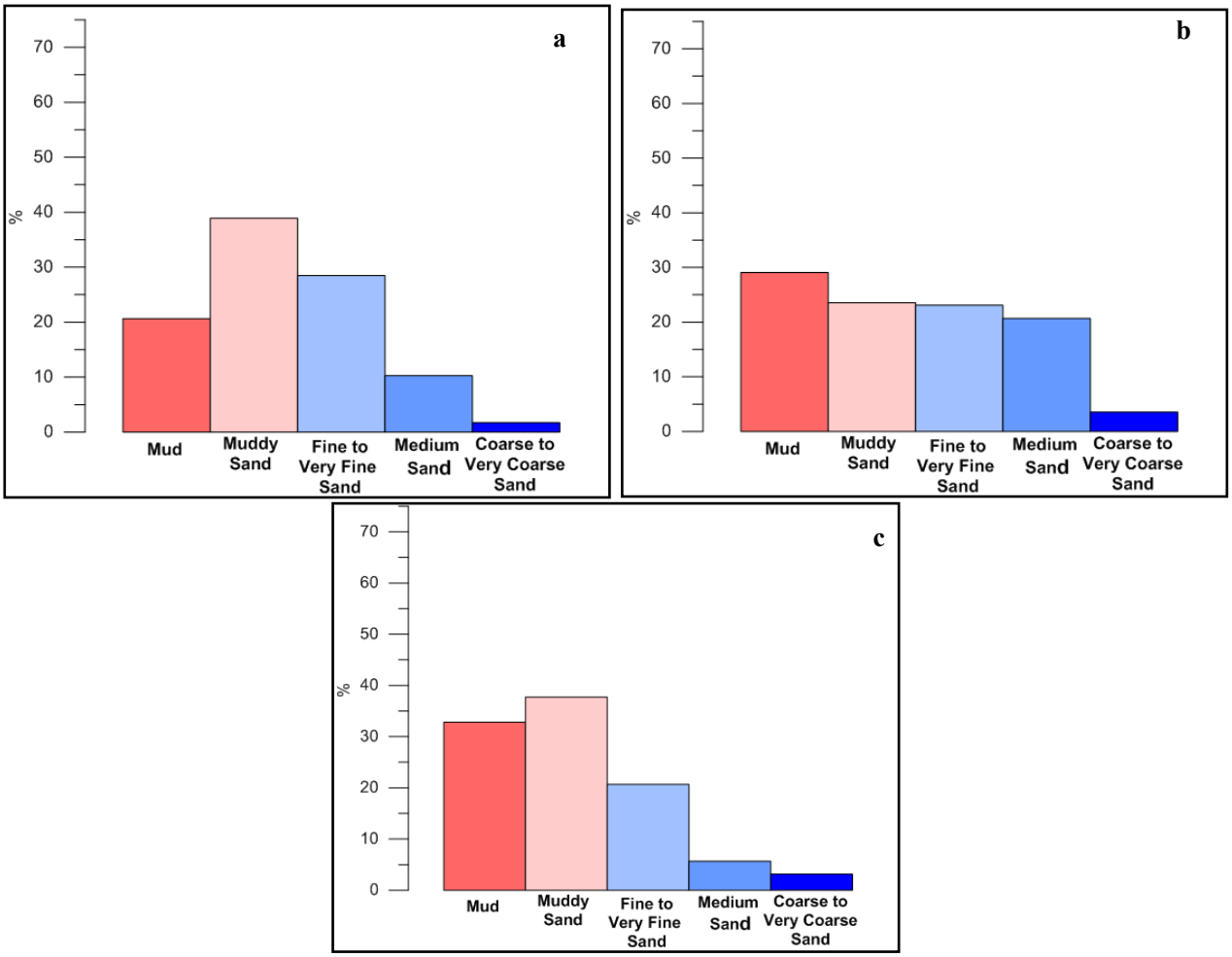



**Figure 17-75.** *Textural composition of the a) Coonambidgal Formation, b) Menindee Formation and c) Willotia beds.*

The upper confining aquitard, mainly consisting of Blanchetown Clay (hydraulic texture class codes, 1 or 2) was mapped by identifying a specific conductive layer in AEM cross sections (refer to Section 17.5). Validating this conductive layer with borehole lithological information suggests the presence of underlying stratigraphic unit such as mud facies of the Calivil Formation with hydraulic texture class codes 1, 2 or 13, which also form part of the upper confining aquitard.

Although limited in occurrence, sandy beds (hydraulic texture class codes of 3, 4 or 5), are observed in Blanchetown Clay. If these units occur at shallow depths (< 18 m) they are considered part of the shallow unconfined aquifer. However, when occurring at depths of more than 18 m, these sediments (hydraulic texture class codes 3, 4, 5, 14 or 23) may form part of the semi-confined aquifer. The dominantly sand-rich Calivil Formation and Loxton-Parilla Sands form the bulk of the semi-confined aquifer. The hydraulic texture class codes include 3, 4 and 5 for homogenous beds and 14 and 23 for interbeds. In areas where the basal sand or gravely sand of the Calivil Formation or Loxton-Parilla Sands overlie Renmark Group within a depth slice interval, the hydraulic texture class code is 41 and these units are considered as part of the semi-confined aquifer. In other areas however, basal sand of Calivil Formation or Loxton-Parilla Sands are absent or thinly bedded with mud. These units also overlie Renmark sediment within the same depth interval, and the combined hydraulic texture class codes are 1, 2 and 13. These deposits are thus assigned to the lower confining aquitard. The majority of the Renmark Group sediments are fine textured with hydraulic texture class codes 1, 2 and 13. These deposits form the lower confining aquitard. However, local sand-rich Renmark Group palaeochannels are present, including interbedded mud, muddy sand and sand. This suite of sediment, with hydraulic class codes 3, 4, 14, 23 or 41 forms part of the semi-confined aquifer.

Two more categories are included in the hydrostratigraphic maps. These include ‘other’ and ‘not applicable’ (Table 17-34). The ‘other’ category denotes modern and Quaternary aeolian deposit of the Woorinen

Formation and undifferentiated Quaternary lunette. The sediments are rarely saturated. Local perched water lenses may be present but the sediment is not considered as part of the aquifer systems. The other category 'not applicable' is applied to the Palaeozoic fractured rock aquifer. Whilst the saprolite may be relatively transmissive (BHMAR23-1), the overall transmissivity of the crystalline bedrock is postulated to be low. Not much is also known about the density and connectivity of the fractures within the Palaeozoic sedimentary sequence, and the fluid interaction between the saprolite and the surrounding Renmark Group sediment.

### 17.8.1 Thickness and Depth to Top of Hydrostratigraphic Units

To determine the depth to the various aquifers and aquitards, GIS queries were applied to specific hydrostratigraphic units (as shown in Table 17-34) within each depth slice. Conditional statements dictate the shallowest depth slice information be returned for each grid cell. Depth slices were queried in sequence from shallowest to deepest until the specific hydrostratigraphic unit was encountered. Subsequently the corresponding (top) depth interval and spatial extent were extracted, generating the depths to the individual aquifer and aquitard maps (Figure 17-76, Figure 17-77, Figure 17-78 and Figure 17-79). Depth to the top of the upper confining aquitard (Figure 17-77) may be slightly different to the surfaces discussed in Section 17.5. These two products have been derived differently, with the surface shown in Figure 17-77 incorporating both the cross sectional interpretation (Section 17.5) and planar AEM depth slice interpretation (Section 17.6) as discussed in Section 17.5.

Formation (i.e. Calivil Formation) and hydrostratigraphic unit (i.e. semi-confined aquifer) thickness was calculated as the summation of the each depth interval thickness where the specific unit was present. Where two different formations overly one another within a single depth slice interval (e.g. Calivil Formation over Renmark Group), it is assumed that each unit is of equal thickness; half the depth slice thickness is thus assigned to each unit.

Aquifer thickness was calculated for both the shallow unconfined aquifer (Figure 17-80) and the semi-confined aquifer (Figure 17-81) while formation thickness was calculated for all recognised stratigraphic units. In the case of the near-surface mud drape, additional products were created. These include full thickness of the hydrostratigraphic unit (Figure 17-82), as well as percent mud from surface to 5 m (corresponding to the average incised depth of Talyawalka Creek, Figure 17-83) and to 9 m (corresponding to the average incised depth of the Darling River, Figure 17-84).

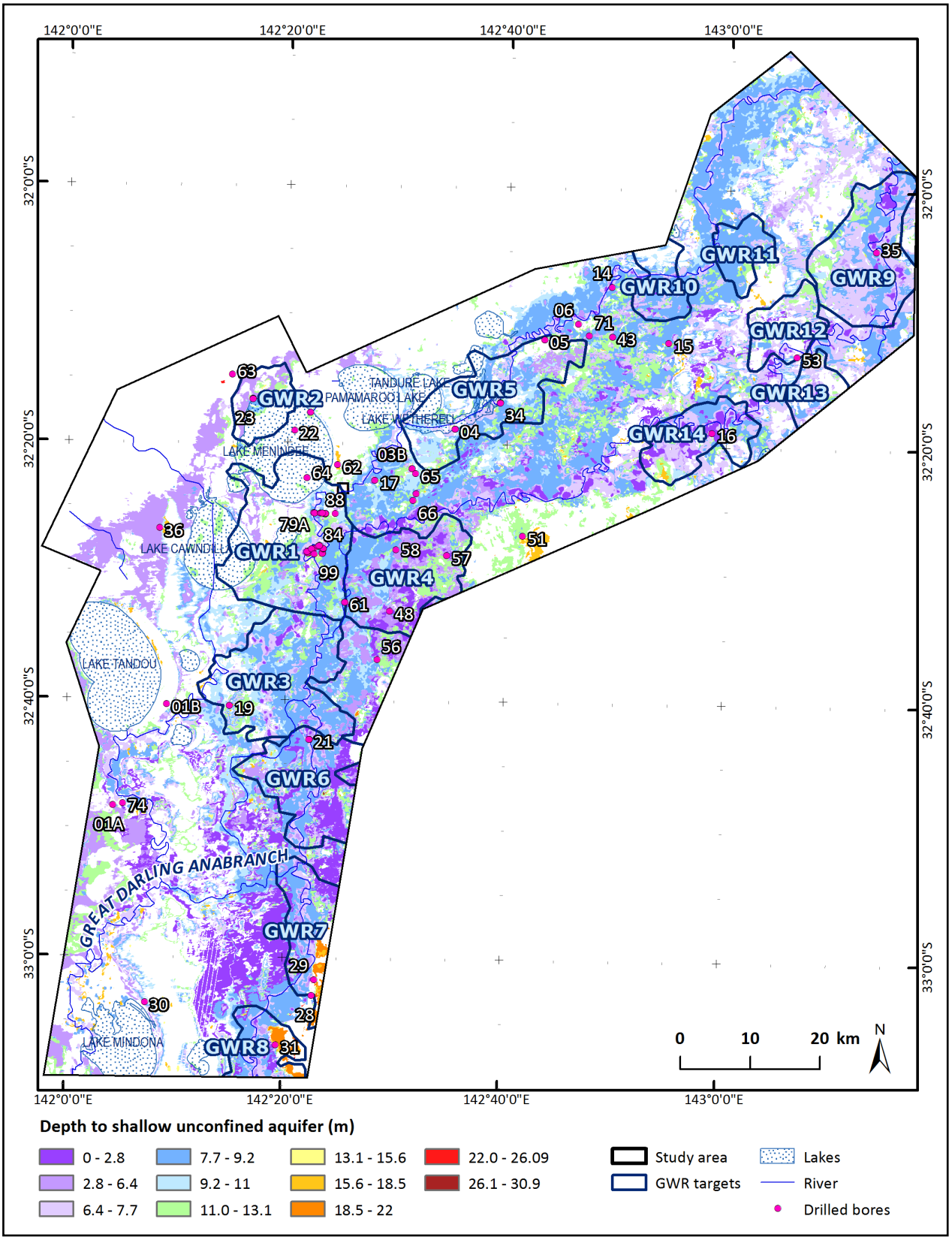



**Figure 17-76.** *Depth to the top of the shallow unconfined aquifer.*

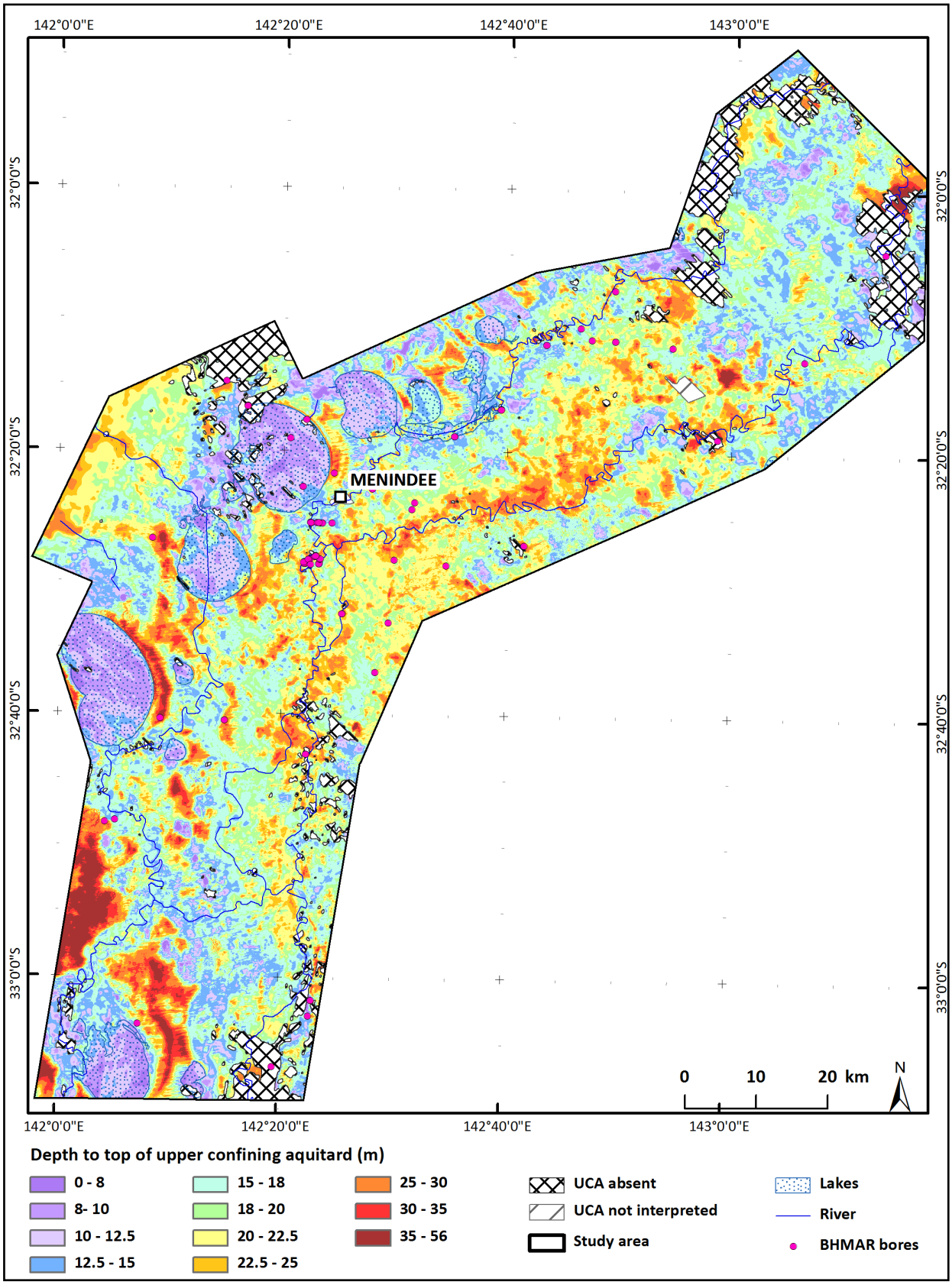



**Figure 17-77.** *Depth to the top of the upper confining aquitard.*

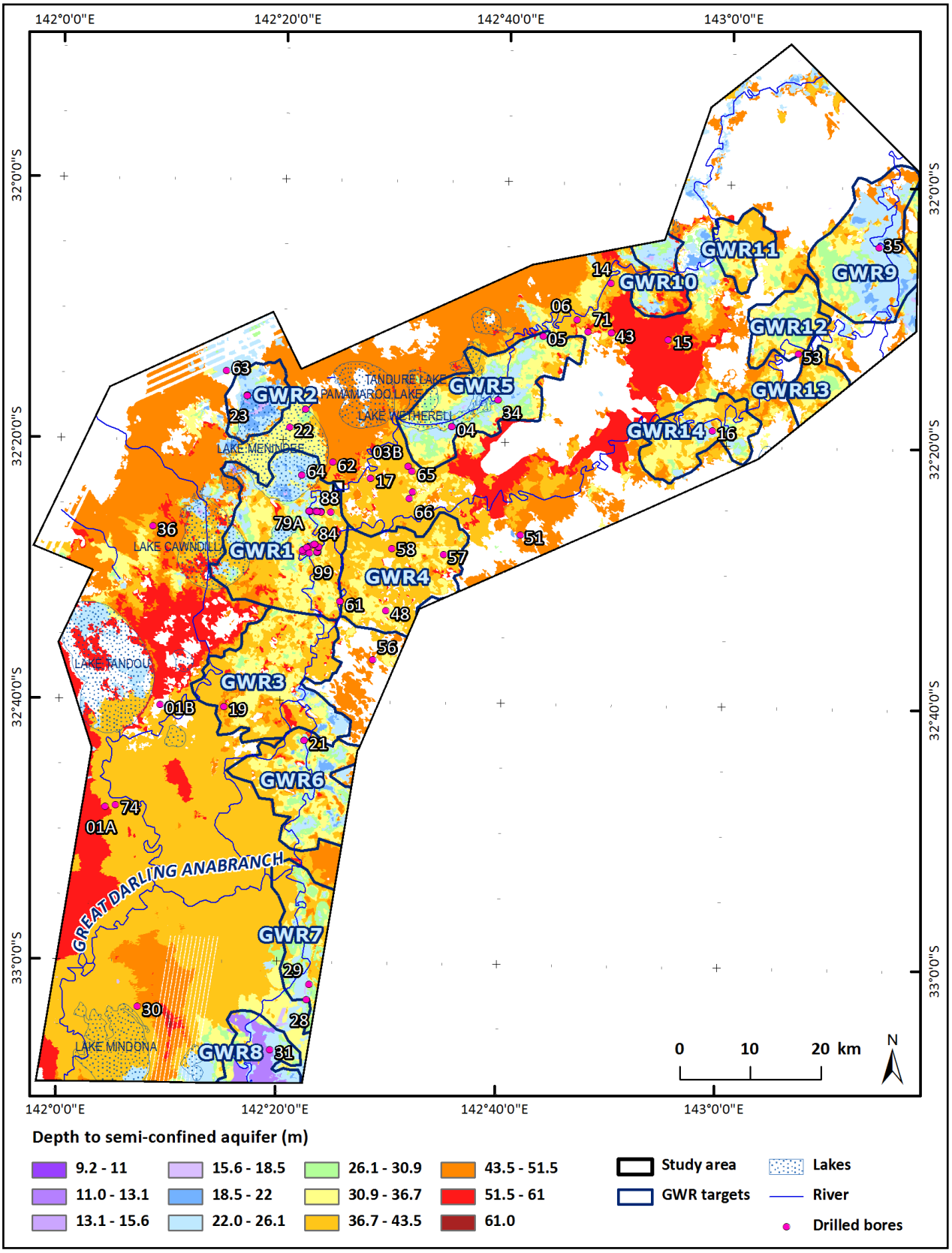



**Figure 17-78.** *Depth to the top of the semi-confined aquifer.*

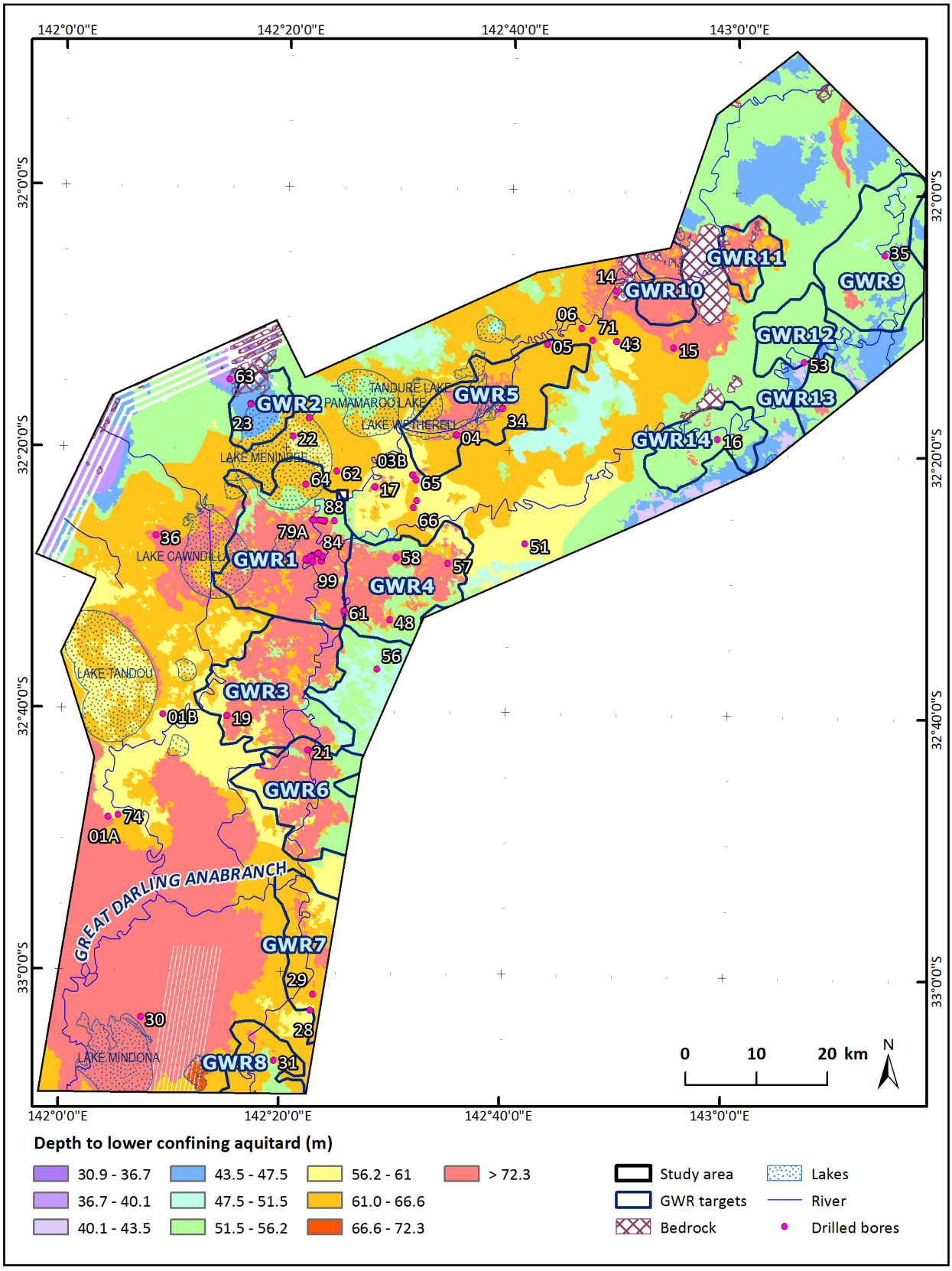



**Figure 17-79.** *Depth to the top of the lower confining aquitard.*

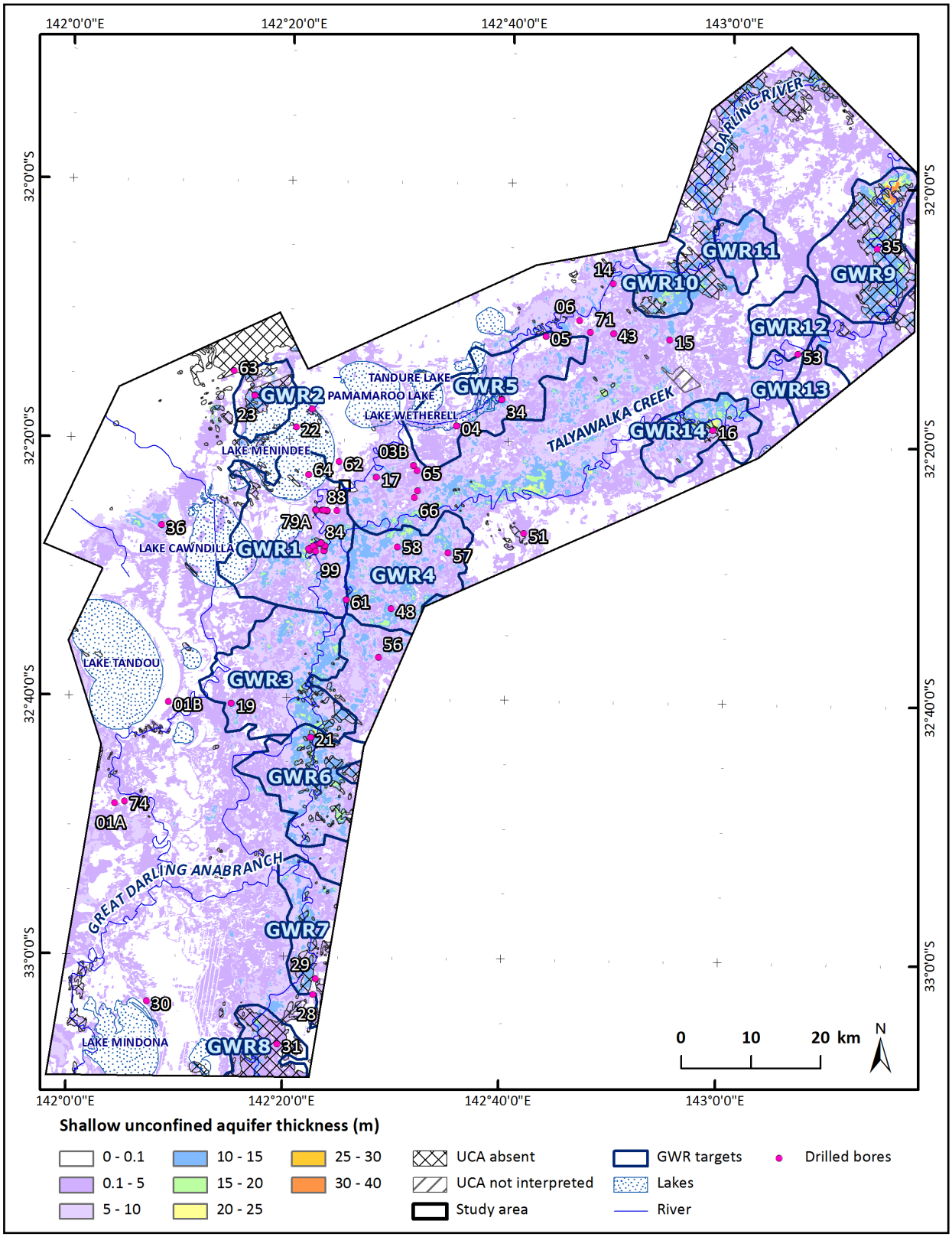



**Figure 17-80.** *Thickness of the shallow unconfined aquifer.*

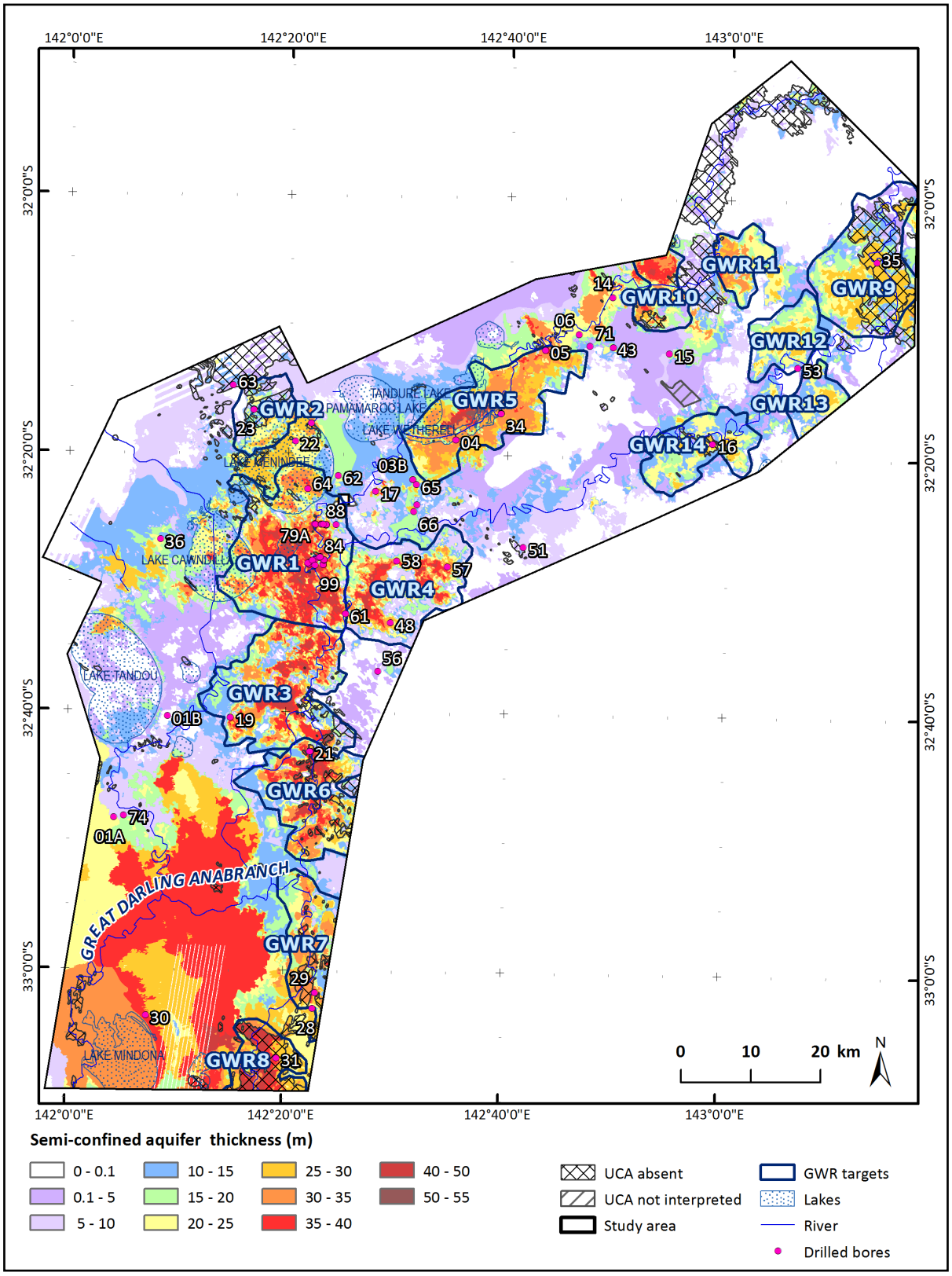



**Figure 17-81.** *Thickness of the semi-confined aquifer.*

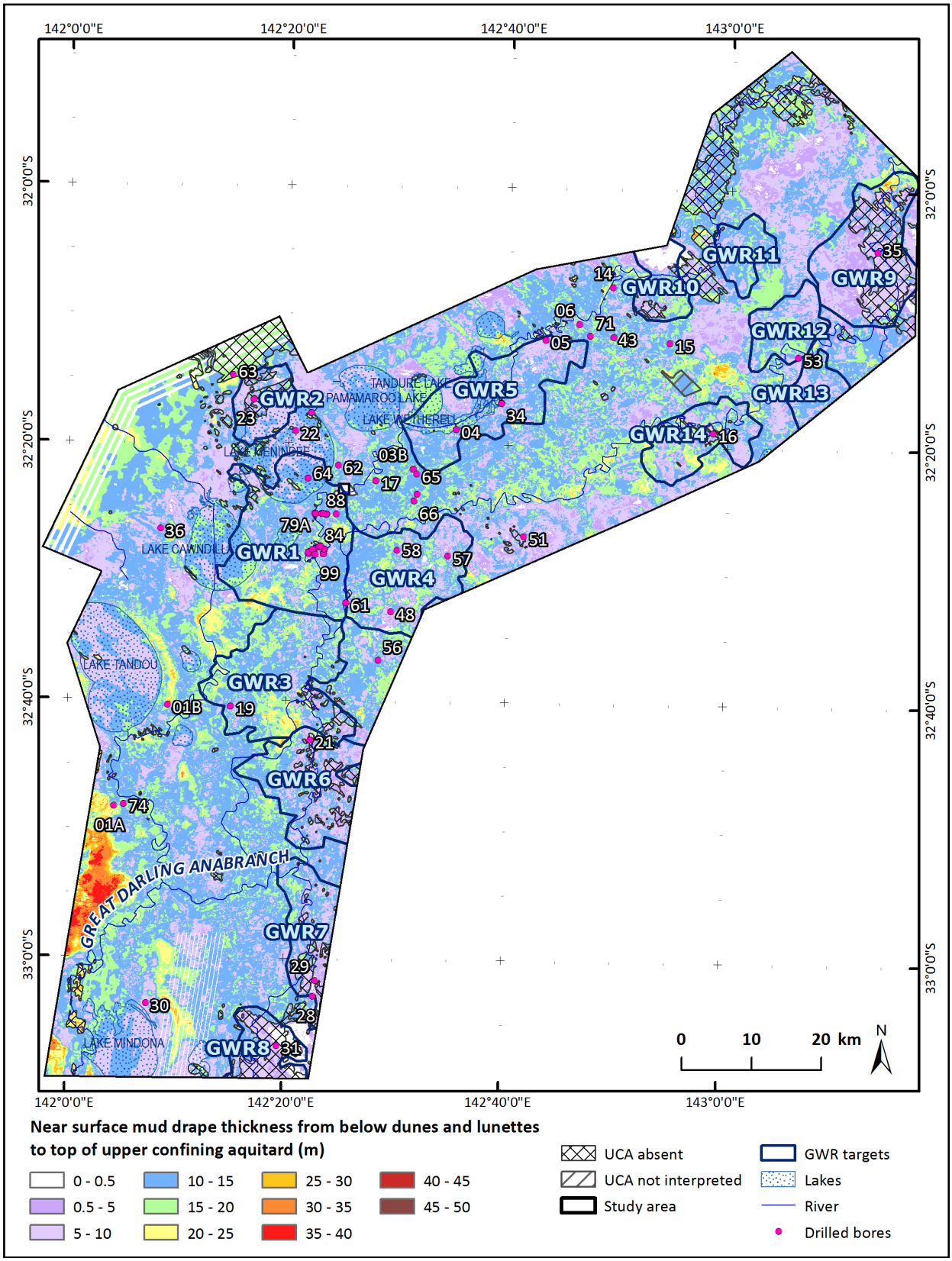



**Figure 17-82.** *Near-surface aquitard thickness.*

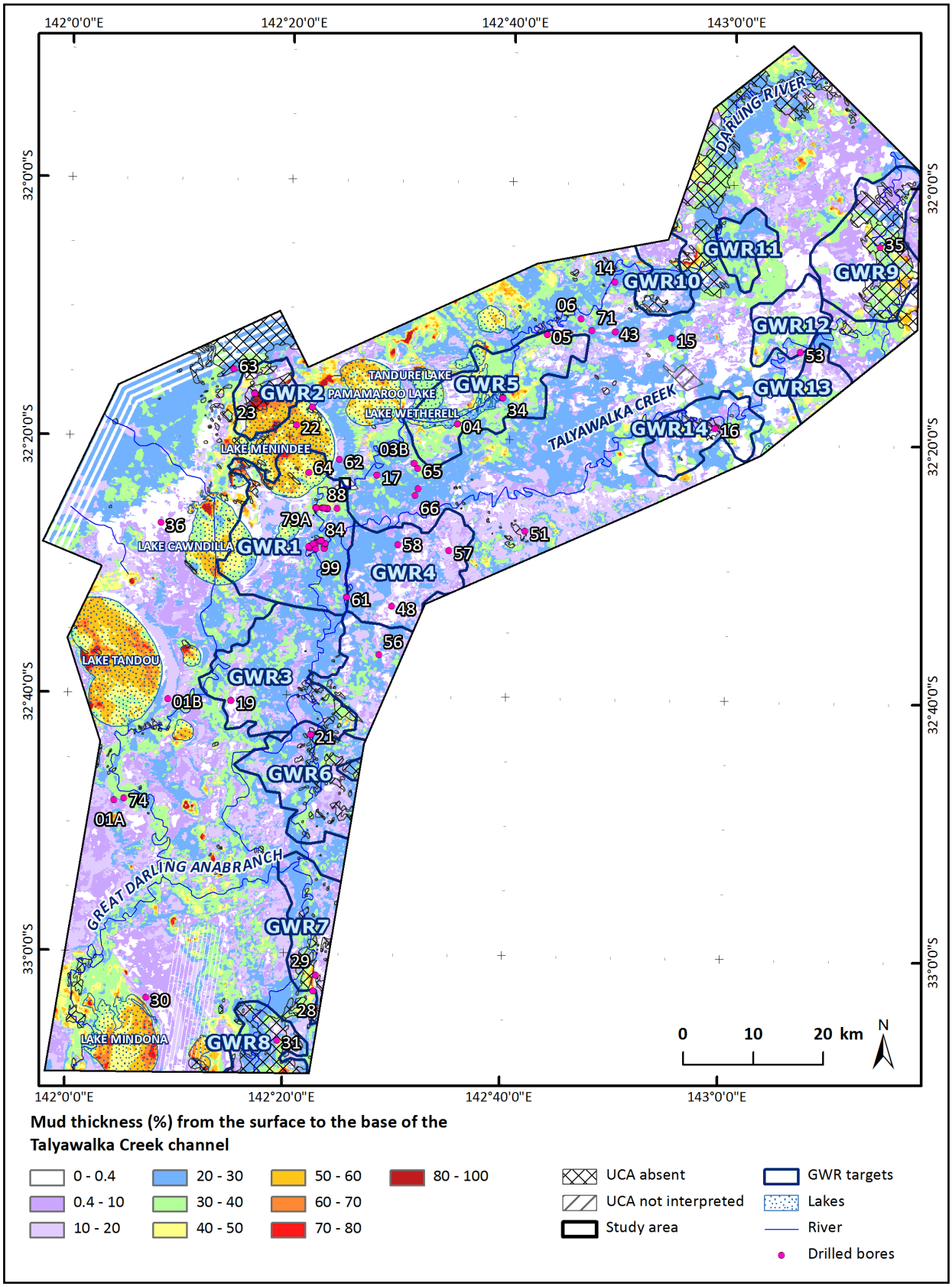



**Figure 17-83.** *Percent mud between ground surface and 5 m depth (nominal base of Talyawalka Creek).*

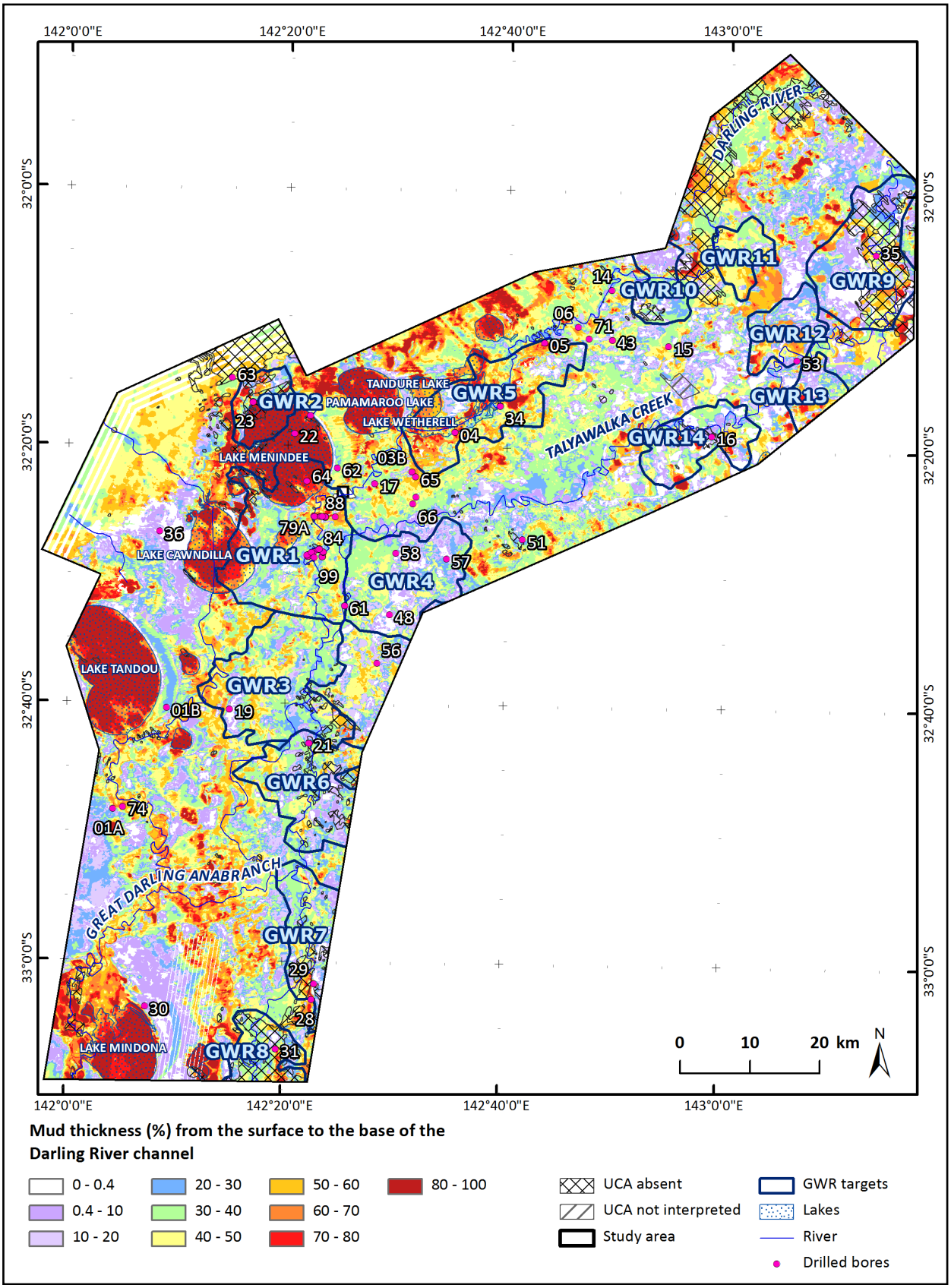



**Figure 17-84.** *Percent mud between ground surface and 9 m depth (nominal base of the Darling River).*

## 17.9 HYDRAULIC CONDUCTIVITY OF SEDIMENTS

Two principal datasets were used to derive the hydraulic conductivity of the sediments. These include the AEM 30 layers lateral constraint inversion depth slice grids and the calculated hydraulic conductivity ($K_{SDR}$) derived from borehole NMR logs (refer to Section 7.3).

For each depth slice, the AEM grid values at each bore location were extracted. The majority of NMR logs started from 1 m below natural ground surface, except for seven bores which started at specific depths (Table 17-35). The NMR data were collected at every 0.5 m interval, whereas the AEM depth slices increase in thickness with depth. As such, the apparent conductivity value from each AEM depth slice may correspond to two or more $K_{SDR}$ (Table 17-36).

**Table 17-35.** *NMR borehole data acquired using the Javelin logging system for the BHMAR project including borehole, drilling method and logged interval.*

| Borehole | Drilling method | NMR logged interval (m) |
|---|---|---|
| BHMAR3B-1 | Sonic coring | 1-60 |
| BHMAR04-1 | Sonic coring | 1-70 |
| BHMAR08-1 | Sonic coring | 1-59 |
| BHMAR16-1 | Sonic coring | 1-60 |
| BHMAR21-1 | Sonic coring | 1-80 |
| BHMAR23-1 | Sonic coring | 1-95 |
| BHMAR29-1 | Sonic coring | 1-60 |
| BHMAR31-1 | Sonic coring | 1-60 |
| BHMAR33-1 | Sonic coring | 1-64 |
| BHMAR33-8 | Sonic coring | 14-53.5 |
| BHMAR34-1 | Sonic coring | 1-60 |
| BHMAR35-1 | Sonic coring | 1-54 |
| BHMAR36-1 | Sonic coring | 15-85 |
| BHMAR58-1 | Sonic coring | 2-75 |
| BHMAR61-1 | Sonic coring | 2-70 |
| BHMAR62-1 | Mud rotary | 15-65 |
| BHMAR63-1 | Mud rotary | 5-45 |
| BHMAR66-1 | Sonic coring | 17-62 |
| BHMAR75-3 | Mud rotary | 1-89.5 |
| BHMAR75-5 | Sonic coring | 1-52.5 |
| BHMAR77-2 | Sonic coring | 1-65 |
| BHMAR79A-6 | Sonic coring | 1-71 |
| BHMAR80A-2 | Sonic coring | 1-65 |
| BHMAR80B-2 | Sonic coring | 1-72 |
| BHMAR83-2 | Sonic coring | 1-65 |
| BHMAR84-2 | Sonic coring | 1-59 |
| BHMAR88-3 | Sonic coring | 1-71 |
| BHMAR92-1 | Sonic coring | 1-70 |
| BHMAR99-1 | Sonic coring | 1-63 |

**Table 17-36.** *AEM depth slice and the corresponding number of NMR derived hydraulic conductivity values.*

| Depth From (m) | Depth To (m) | Thickness | Number of $K_{SDR}$ Sample |
|---|---|---|---|
| 1.0 | 1.6 | 0.6 | 1 |
| 1.6 | 2.2 | 0.6 | 1 |
| 2.2 | 2.8 | 0.6 | 1 |
| 2.8 | 3.5 | 0.7 | 2 |
| 3.5 | 4.4 | 0.9 | 2 |
| 4.4 | 5.3 | 0.9 | 2 |
| 5.3 | 6.4 | 1.1 | 2 |
| 6.4 | 7.7 | 1.3 | 2 |
| 7.7 | 9.2 | 1.5 | 3 |
| 9.2 | 11.0 | 1.8 | 4 |
| 11.0 | 13.1 | 2.1 | 4 |
| 13.1 | 15.6 | 2.5 | 5 |
| 15.6 | 18.5 | 2.9 | 6 |
| 18.5 | 22.0 | 3.5 | 7 |
| 22.0 | 26.1 | 4.1 | 8 |
| 26.1 | 30.9 | 4.8 | 10 |
| 30.9 | 36.7 | 5.8 | 11 |
| 36.7 | 43.5 | 6.8 | 14 |
| 43.5 | 51.5 | 8 | 16 |
| 51.5 | 61.0 | 9.5 | 19 |
| 61.0 | 72.3 | 11.3 | 22 |
| 72.3 | 85.7 | 13.4 | 27 |

### 17.9.1 Data Exclusion

The $K_{SDR}$ only holds true in the saturated zone, where total porosity is equivalent to total water (i.e. sum of bound and free water). Hence, only the $K_{SDR}$ values below the shallow water table, mostly between 9 m to 13 m, are included in calculation of the hydraulic conductivities. Since the majority of the NMR logs only reach 60 m to 70 m depths, in most cases the AEM depth slices between 51.5 m and 85.7 m will not have the maximum number of $K_{SDR}$ samples. In some bores, there is no data at all between 82.3 m to 85.7 m.

In the preceding NMR section, it was noted that NMR logs in mud-rotary constructed bores return a consistently lower $K_{SDR}$ value. Thus, the $K_{SDR}$ of the three mud-rotary bores were excluded in the mapping.

### 17.9.2 AEM and Lithology

Empirical data has shown that under an environment with consistent salinity and degree of saturation, there is a causal relationship between the apparent conductivity of AEM and lithology (refer to Section 17.7.2). Threshold values of the apparent conductivity can be used to demarcate between sand and mud, but it is not possible to further subdivide into other subtle texture class. As such, the lithologies depicted on the map using AEM threshold values are grouped into aquifer and aquitard only. ‘Aquifer’ includes hydraulic texture classes of fine sand, medium sand and coarse to very coarse sand (Section 17.7.2.2), whereas ‘aquitard’ includes hydraulic texture classes of mud and sandy mud.

### 17.9.3 Map of Hydraulic Conductivity

Summary statistics, including the mean, were carried out on the NMR data for each AEM depth slice. The NMR variables include bound and free water content, reported as volume percent, and $K_{SDR}$ is in m/day. At each bore location for the individual depth slice, the bound and free water are displayed in a pie chart, and the size is directly proportionate to the hydraulic conductivity. The $K_{SDR}$ is also labelled as numbers adjacent to the chart. The spatial distribution of the bores varies widely, ranging from 1 km to 3 km per bore, to 5 km to 20 km per bore. As such, depending on the scale of the map and the order of magnitude of $K_{SDR}$, if a cluster of bores are present, the NMR data are displayed as offset charts and labels (Figure 17-85).

## 17.10 TRANSMISSIVITY

Transmissivity is the rate which groundwater flows horizontally through an aquifer. The transmissivity ($T$) of a confined aquifer was calculated from the hydraulic conductivity ($K$) of the sediment across a defined unit thickness as shown in Equation 105. For an unconfined aquifer, only the thickness of the saturated part is considered (Freeze & Cherry, 1979).

$T$ (m$^2$/d) = $K$ (m/d) x *thickness* (m)

**Equation 105**

The borehole NMR logs are the principal data used to derive the hydraulic conductivity of the sediment. These logs provide the bound, free and total water, and the $T_2$ mean log ($T_{2ML}$), i.e. exponential function of the signal relaxation with time (refer to Section 7.3). The Schlumberger-Doll Research Equation (Equation 106) was used to calculate the hydraulic conductivity ($K_{SDR}$) from the formation factor ($C$), $T_{2ML}$ and total porosity (Coates *et. al*., 1999). The formation factor is texture specific; the presence of a range of sedimentary textures suggests the need to group the sediment into five hydraulic texture classes: mud; muddy sand; fine sand; medium sand; and coarse to very coarse sand. Based on slug test and laboratory permeameter analysis results, the formation factor was determined for each of the hydraulic texture class. In accordance with downhole lithological information and respective $C$ values, the $K_{SDR}$ was calculated for each borehole and subsequently sorted into the five hydraulic texture classes. The transmissivity across the screen interval was calculated for each bore and compared with the transmissivity of the slug test; results show a spread of two orders of magnitude (Figure 17-86), most likely attributed to the inherent errors of both methods (Section 13.2).

$K_{SDR} = C\,\varphi^{n}\,(T_{2ML})^2$

**Equation 106**

where $\varphi$ is the NMR total porosity, $n$ is related to the cementation (an exponent of 2 was used in the BHMAR study), $T_{2ML}$ is the logarithmic mean of the $T_2$ distributions, and $C$ is a formation coefficient that depends on the formation type and is related to tortuosity.

Hydraulic texture class is the key parameter to classify the lithological units. The NMR data, including $K_{SDR}$, for all the boreholes in the saturated zone were compiled and sorted into the five hydraulic texture classes. Statistical parameters denoting the range, quartiles and median of the $K_{SDR}$ were calculated for each of the hydraulic texture class and graphically presented (Figure 17-87).

The hydraulic conductivity results (Figure 17-87) show that a range from 3 to 7 orders of magnitude is present between the minimum and maximum values across the five hydraulic texture classes. However, these ranges do not represent the majority of the population. The more probable range of K within each hydraulic texture class should lie between the 1$^{st}$ and 3$^{rd}$ quartiles, which are 1 to 2 orders in magnitude. The design of the NRM probe allows hydraulic conductivity measurements to be taken for a half metre interval which can be converted to transmissivity by multiplying the thickness – in this case 0.5 m.

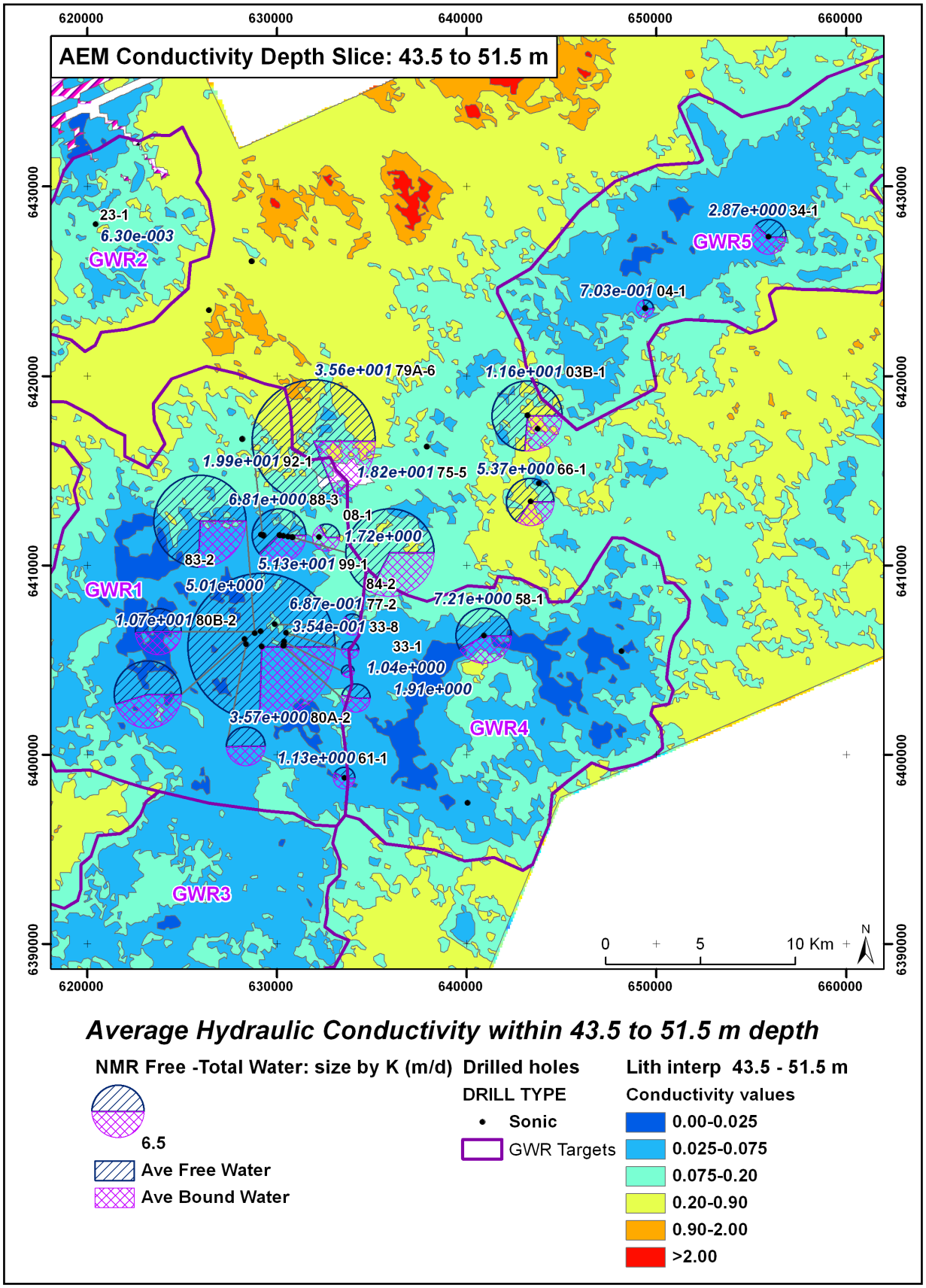



**Figure 17-85.** *Borehole NMR data, including the bound and free water, and hydraulic conductivity for 43.5 to 51.5 m AEM depth slice. Also included are the groundwater resource (GWR) targets and the distribution of aquifer and aquitard. The NMR data in this figure were collected in 2011 using the Javelin tool with an inter-echo spacing of 2.5 ms. Subsequent laboratory and field tests have demonstrated that this setting underestimates the free and total water content, and derived porosities, and should only be used on a semi-quantitative comparative basis. The NMR data may also be unreliable in zones where there is significant iron-(hematite) coating of quartz grains.*

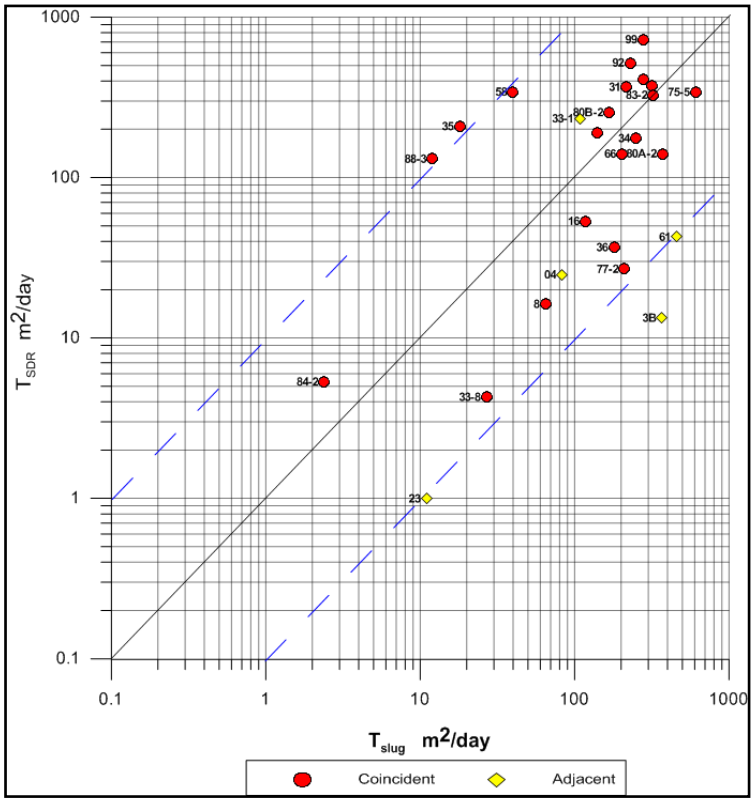



**Figure 17-86.** *Calculated transmissivity (TSDR), based on the final hydraulic classes NMR derived $C_{ave}$ values, versus transmissivity (TSlug) from the slug tests.*

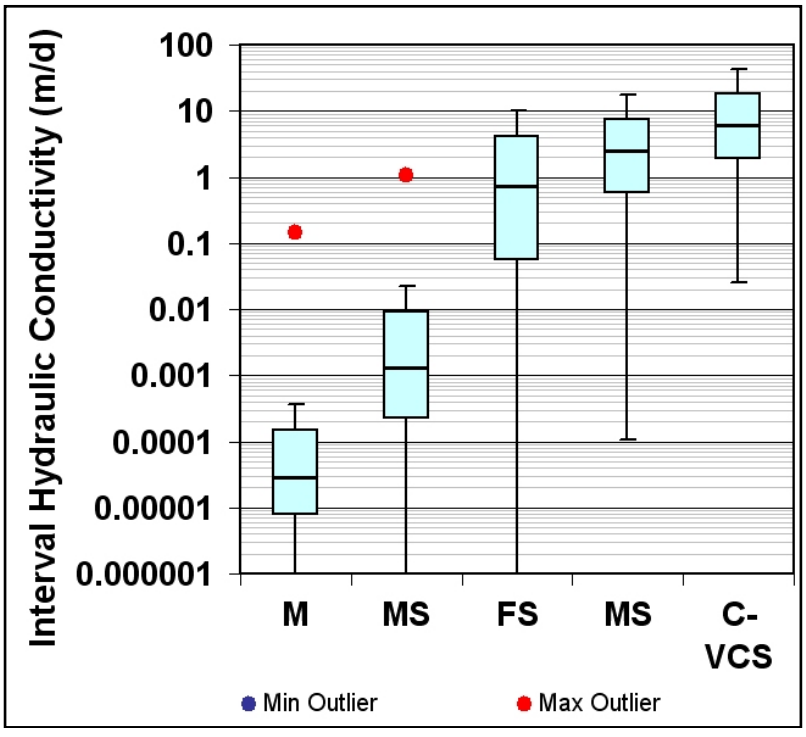



**Figure 17-87.** *Box and whisker plots of hydraulic conductivity for five hydraulic textural classes: mud (M), muddy sand (MS), fine sand (FS), medium sand (MS), and coarse to very coarse sand (C-VCS).*

Transmissivity of sediments can then be mapped spatially based on the mapped spatial distribution of the sedimentary hydraulic texture classes interpreted from AEM data and validated using borehole lithological information. To depict the range of possible transmissivity values of the study area across each depth interval, three sets of maps are generated. These include lower and upper estimate of transmissivity and the range, in orders of magnitude, between these estimates. These transmissivity maps were generated by multiplying the statistically derived hydraulic conductivity of the mapped sedimentary hydraulic texture classes with the thickness of the corresponding depth interval as shown in Equation 107.

$T$ ($m^2$/d) = $K$ (m/d) x t*hickness* (m) of mapped hydraulic texture class interval

**Equation 107**

The thicknesses component required to convert hydraulic conductivity to transmissivity was obtained from the thickness of the AEM depth slice. These increased with depth and range from 0.5 m to 12.3 m. For texturally uniform sediment, the transmissivity of each hydraulic texture class was calculated using the K between the 1st and 3rd quartiles (Table 17-37). However borehole lithological information indicates the common occurrence of vertical textural heterogeneity within a depth interval. Consequently a new set of hydraulic texture class, i.e. interbedded sediment, were included in the lithological mapping. The interpretation of AEM data and mapping of hydraulic texture classes is discussed in Sections 17.7.2.1 and 17.7.2.2 for shallow and deeper sediments respectively.

**Table 17-37.** *Four types of interbedded units and the code assigned to each texture combination.*

| Interbedded | Code | Low estimate of K (m/d) | High estimate of K (m/d) |
|---|---|---|---|
| Mud | 1 | 1st quartile of mud | 3rd quartile of mud |
| Muddy sand | 2 | 1st quartile of muddy sand | 3rd quartile of muddy sand |
| Fine sand | 3 | 1st quartile of fine sand | 3rd quartile of fine sand |
| Medium sand | 4 | 1st quartile of medium sand | 3rd quartile of medium sand |
| Coarse sand | 5 | 1st quartile of coarse sand | 3rd quartile of coarse sand |
| Mud and fine sand | 13 | 1st quartile of mud | 1st quartile of fine sand |
| Mud and medium sand | 14 | 1st quartile of mud | 1st quartile of medium sand |
| Muddy sand and fine sand | 23 | 1st quartile of muddy sand | median of fine sand |
| Medium sand overlying mud | 41 | median of mud | median of medium sand |

Four types of interbedded units were identified: mud and fine sand; mud and medium sand; muddy sand and fine sand; and medium sand overlying mud. To differentiate amongst these units, the hydraulic texture class numbering convention used binary code to represent the two dominant textures (Table 17-37). The order within the code does not indicate dominant or subordinate relationship amongst the textures, but rather indicate that the two texture classes may occur in varying proportion spatially. The exception is for code 41, which denotes the presence of a conspicuous medium sand overlying mud. This code is assigned to sand of the semi-confined aquifer overlying the lower confining mud aquitard.

Based on the hydraulic conductivity statistical parameters shown in Figure 17-87, upper and lower estimates of hydraulic conductivity were selected for the interbedded units as shown in Table 17-37. These values are a combination of the K values of the two dominant hydraulic texture classes. However, due to the presence of finer-textured sediments with lower hydraulic conductivity, the overall transmissivity of interbedded units will be lower than that of the coarser textured sediment. To reflect this, the upper estimate of K values for an interbedded unit was more appropriately represented by the 1st quartile or median of the coarser textured bed rather than the 3rd quartile. For the low estimate of interbedded mud and fine sand; and mud and medium sand, the K value at 1st quartile was chosen. For the high estimate, the 1st quartiles of fine sand and medium sand were selected respectively. For interbedded muddy sand and fine sand, the 1st quartile K value of muddy sand was used to estimate the low transmissivity, whereas the median K value of fine sand was selected for the high estimate. For the interbedded medium sand overlying lower confining aquitard, the median K value of mud was chosen for the lower estimate whereas the median K value of medium sand was used for the higher estimate.

A set of examples of the lower and upper estimated transmissivities and the range between these limits are shown in Figure 17-88 to Figure 17-90. These transmissivities are for depth intervals 51.5 m to 61.0 m and classified as either aquifer or aquitard material. Interpreted geological structures are also shown and transmissivity was not calculated for Devonian sedimentary rock.

By incorporating hydrostratigraphic information, principally the distribution and thickness of the shallow, unconfined aquifer and the semi-confined aquifer, an additional suite of AEM products was derived. In order to achieve this, two separate GIS queries were run, one for each aquifer. Based on the hydrostratigraphic mapping scheme discussed in Section 17.8, the conditional expression identified the presence or absence of the relevant stratigraphic unit within each depth slice and when present summed the respective transmissivity. This was undertaken for lower (Q1) and upper (Q3) estimates of transmissivity as shown in Figure 17-92 and Figure 17-93 for the shallow unconfined aquifer and Figure 17-94 and Figure 17-75 for the semi-confined aquifer.

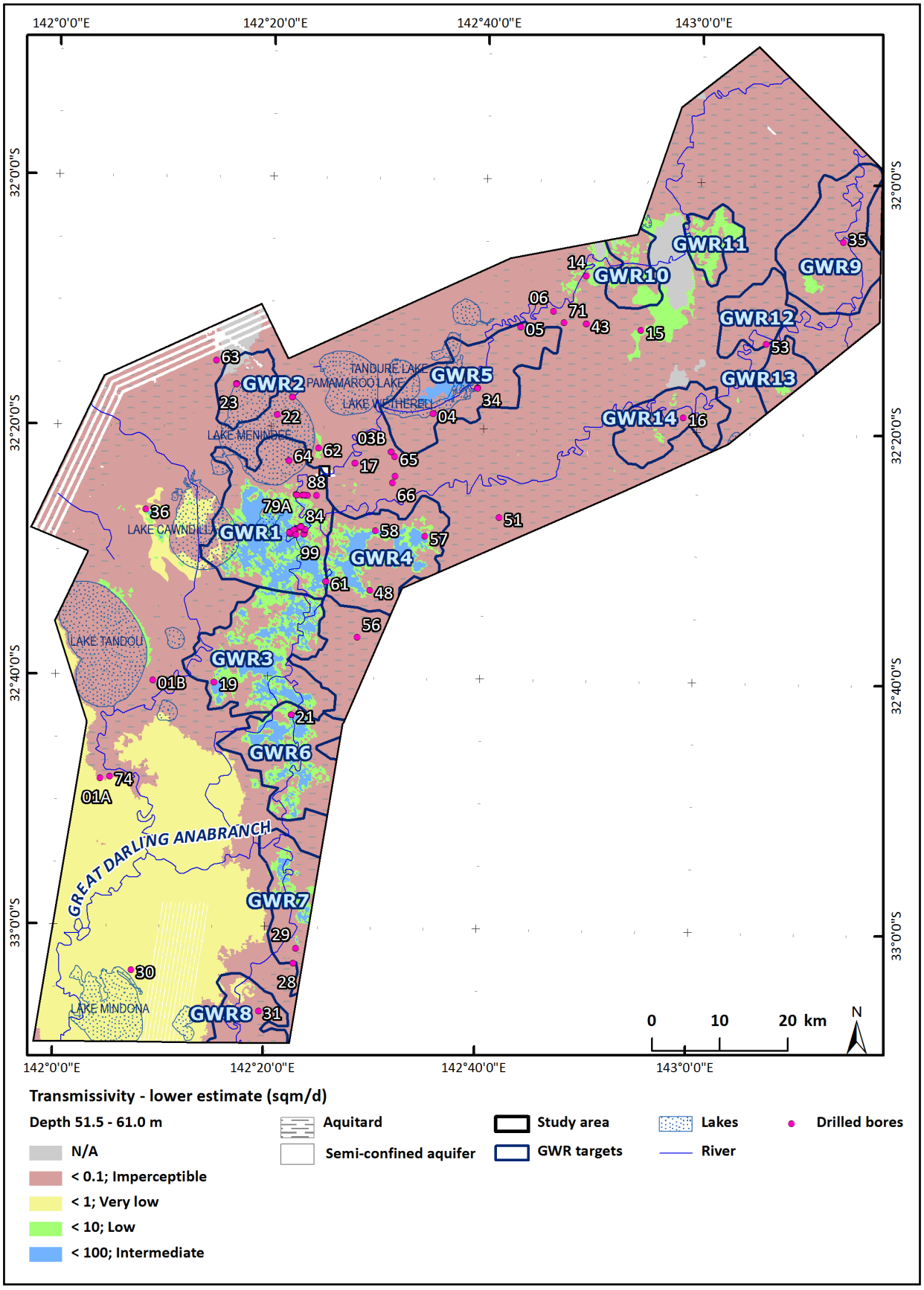



**Figure 17-88.** *Lower estimate of transmissivity ($m^2$/d) across the study area for 51.5 m to 61.0 m depth slice.*

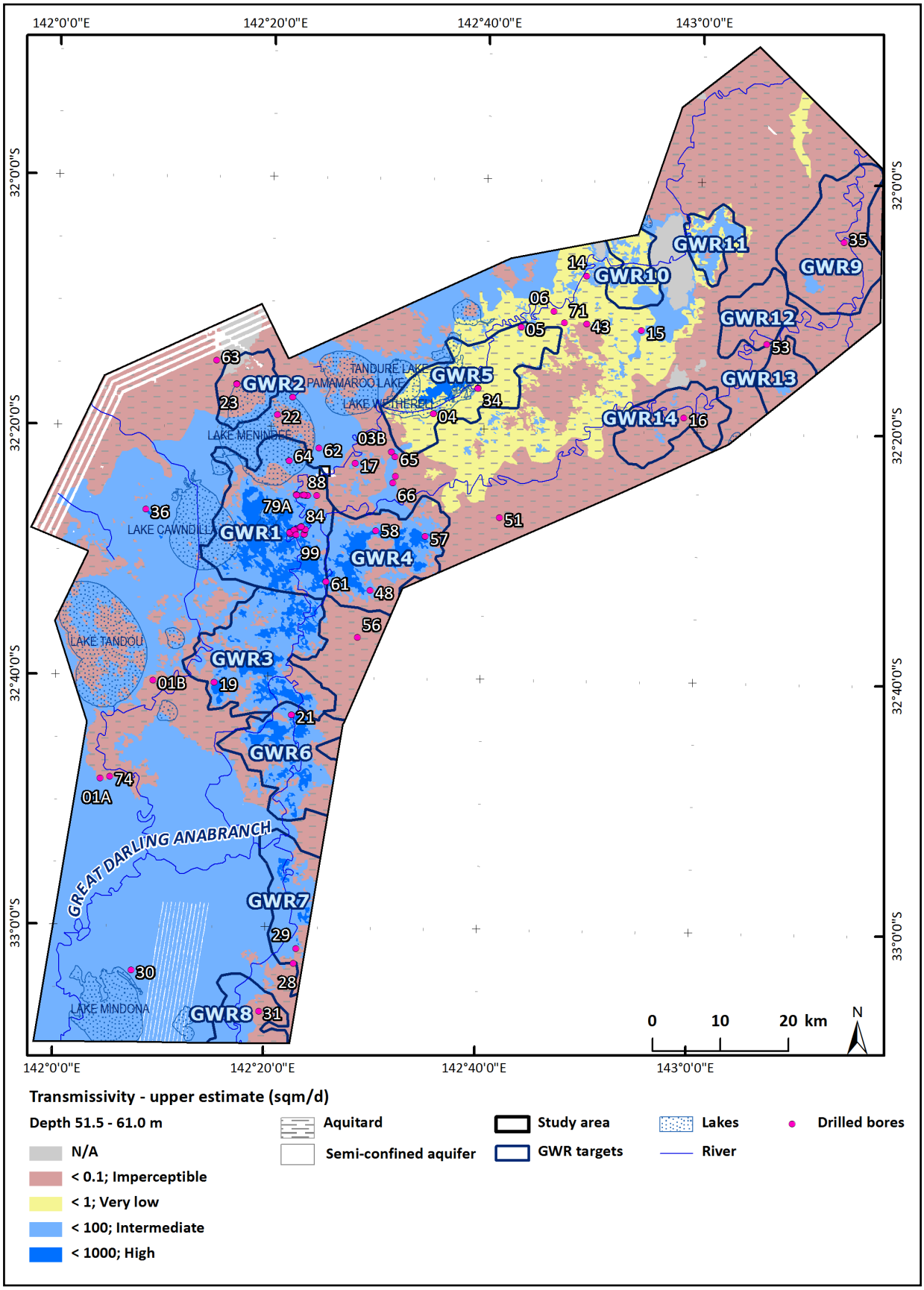



**Figure 17-89.** *Upper estimate of transmissivity ($m^2$/d) across the study area for 51.5 m to 61.0 m depth slice.*

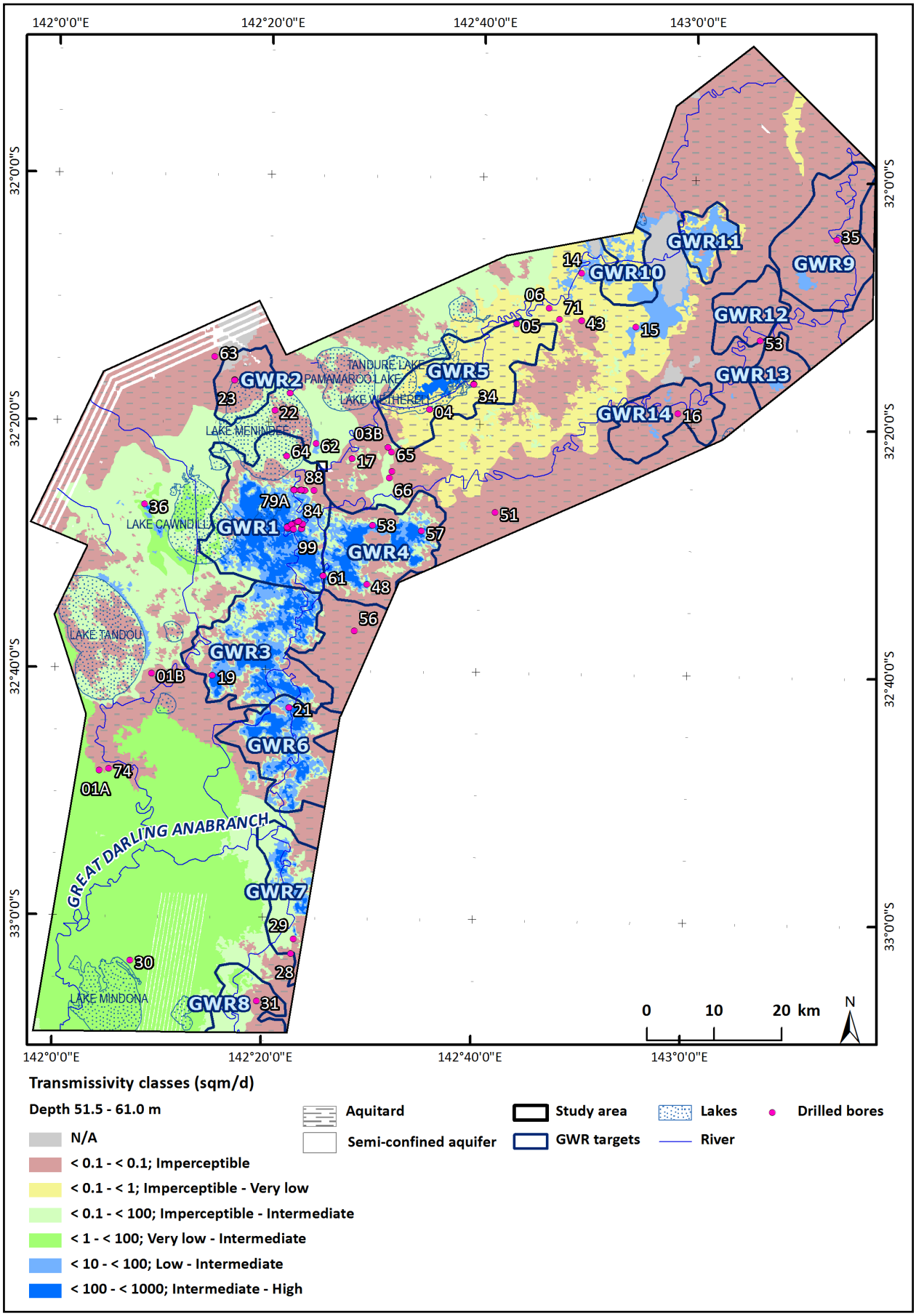



**Figure 17-90.** *Range between lower and upper estimate of transmissivity ($m^2/d$) across the study area for 51.5 m to 61.0 m depth slice.*

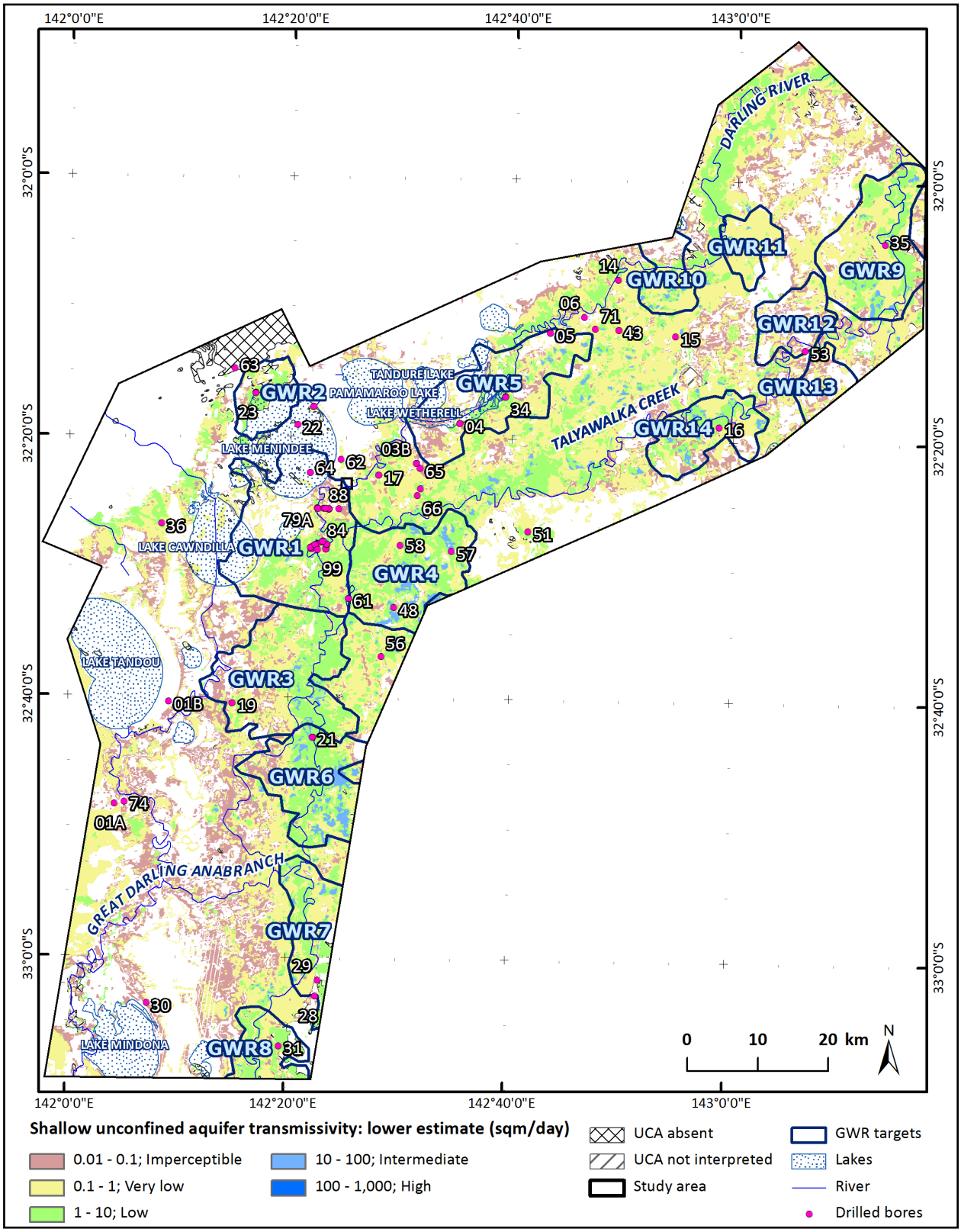



**Figure 17-91.** *Lower estimate of transmissivity ($m^2/d$) across the study area for the shallow unconfined aquifer.*

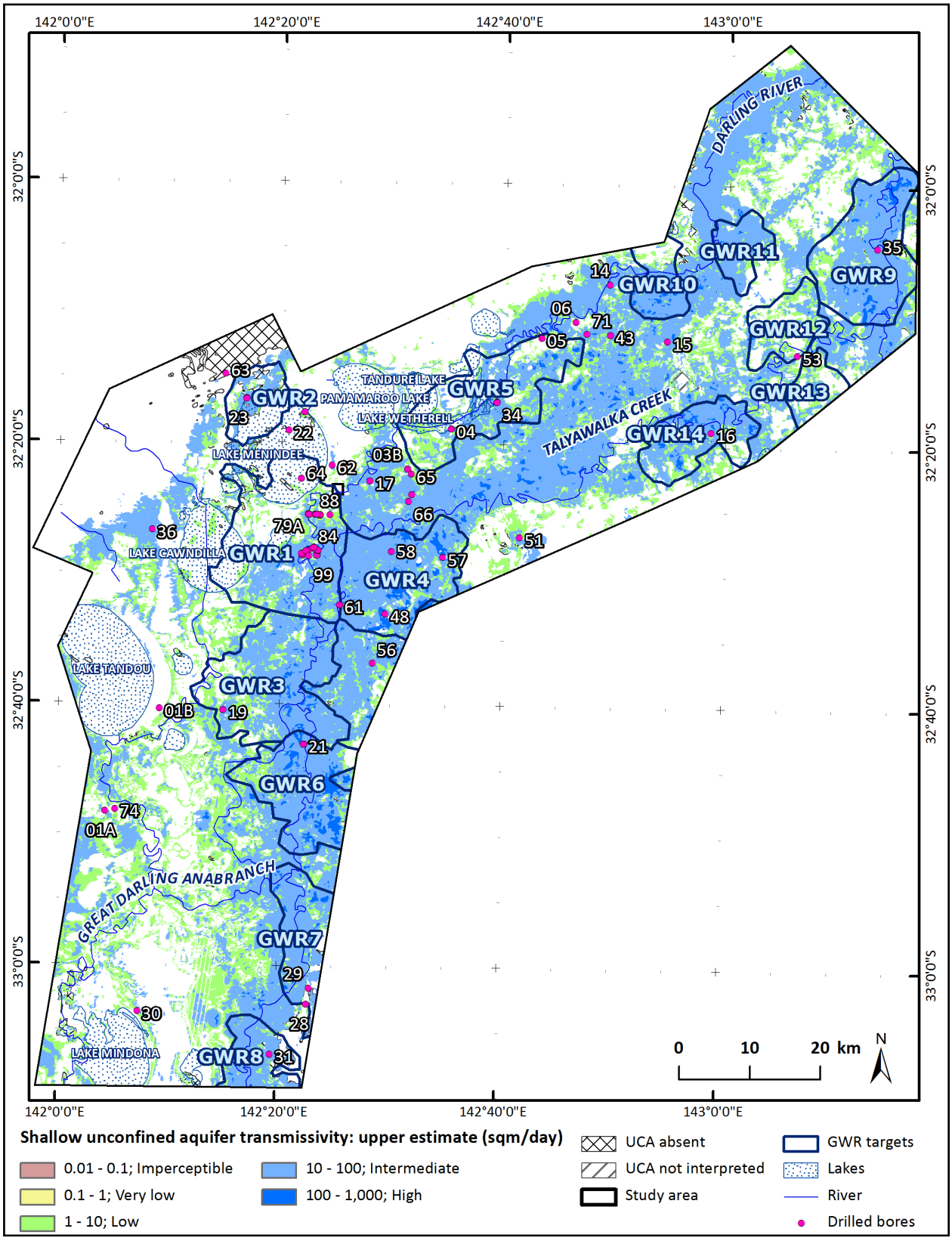



**Figure 17-92.** *Upper estimate of transmissivity ($m^2/d$) across the study area for the shallow unconfined aquifer.*

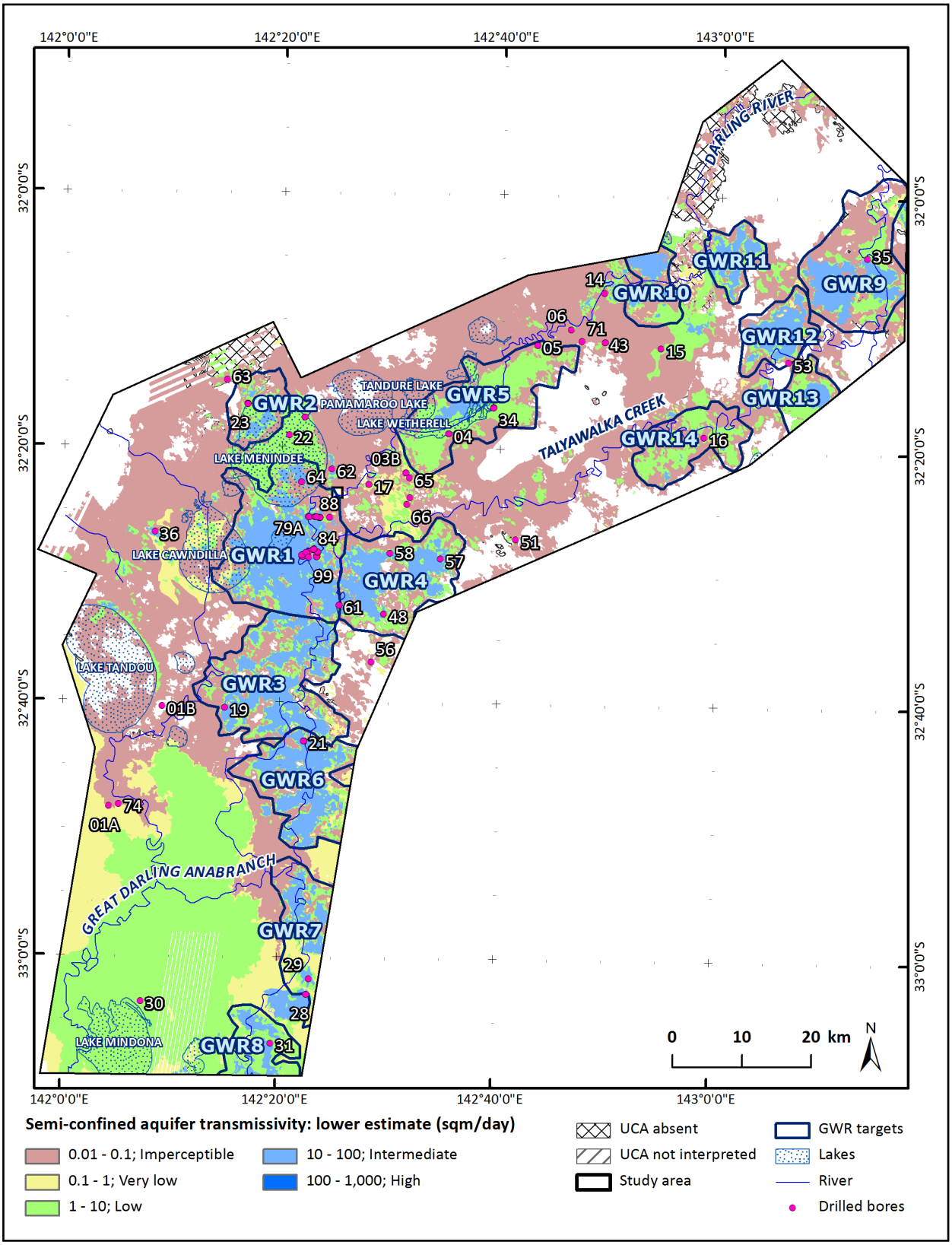



**Figure 17-93.** *Lower estimate of transmissivity ($m^2/d$) across the study area for the semi-confined aquifer.*

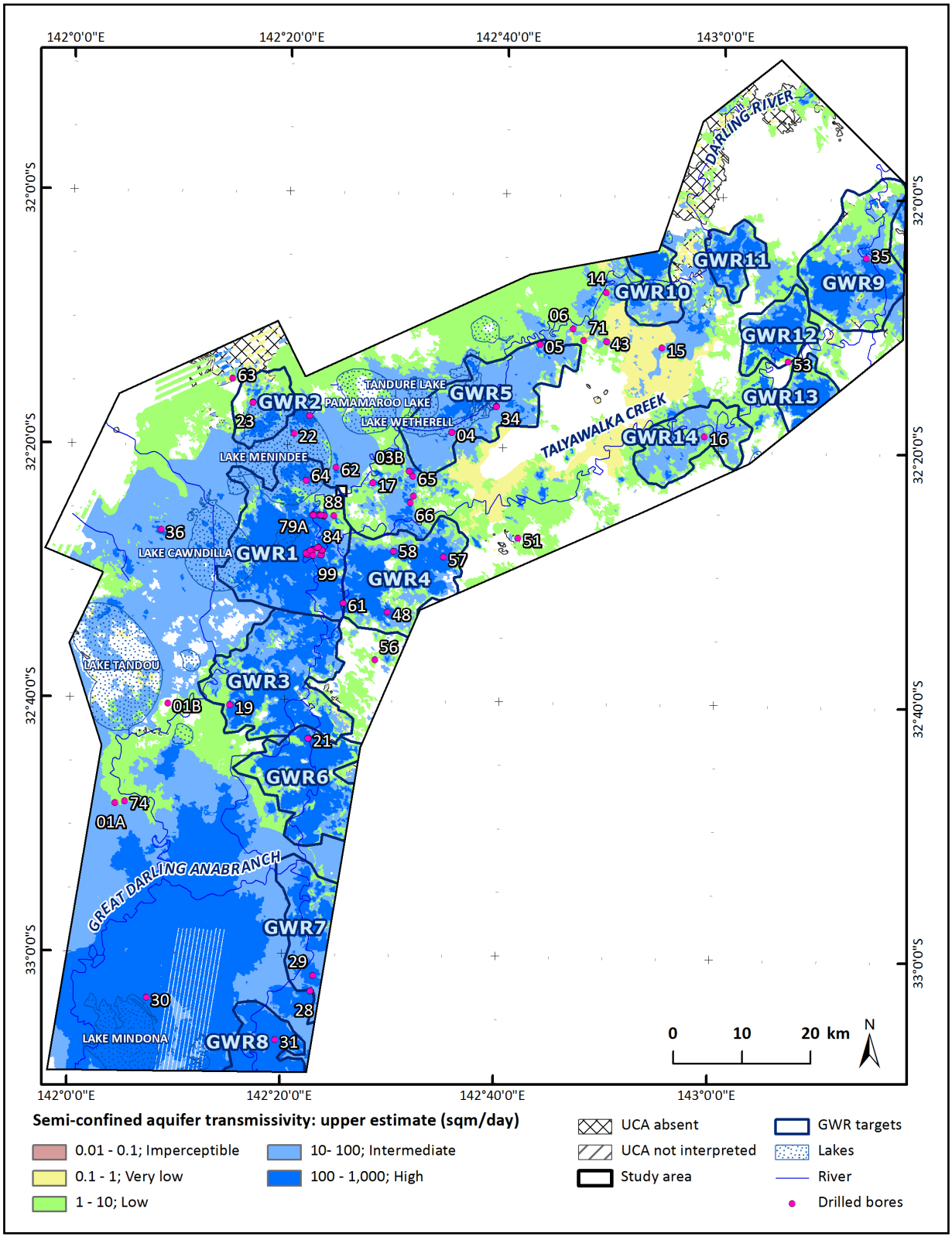



**Figure 17-94.** *Upper estimate of transmissivity ($m^2/d$) across the study area for the semi-confined aquifer.*

## 17.11 EFFECTIVE POROSITY

Estimation of groundwater storage volumes in the target Calivil Formation aquifer requires estimates of the effective porosity of the aquifer material, largely comprised of fine sand, medium sand, coarse to very coarse sand and gravel. Preliminary estimates of groundwater storage volumes relied on the use of the mobile water data from the NMR survey in 2011 as a surrogate for effective porosity. Subsequent comparison of the 2011 NMR data with the gravimetric water content of sonic core samples indicated that the NMR survey could be underestimating downhole water content.

Through dialog with experts in the use of NMR, the manufacturers of NMR instruments, and academic researchers it was inferred that the mismatch between the NMR and gravimetric data may be due to either a calibration error in the NMR instrument, the influence of strong magnetic effects induced by iron minerals or coatings, or the possibility of the instrument not fully detecting water in very small pore spaces.

This prompted additional analysis on selected Lexan-encapsulated sonic core samples to provide more robust measurements of total and effective porosity. A field program was also undertaken in 2013 to re-log several of the BHMAR boreholes with the current available version of the Javelin NMR instrument. The objective was to provide comparative data to enable recalibration of the larger 2011 NMR survey data.

### 17.11.1 NMR Datasets

The 2011 NMR survey involved a total of 29 bores being logged using the Javelin probe JP-250G. Of these bores, 3 were drilled using mud rotary rig and 26 by the sonic rig (Table 17-38). The system setup, calibration of the tool and processing of the data are documented in Section 7.3.4. Visual inspection of the NMR data for the mud rotary bores showed consistently lower mobile and total water contents compared to those of nearby sonic bores. Therefore, only data from the sonic bores was included in the comparative analysis with laboratory porosity measurements and the subsequent 2013 NMR survey data.

The second NMR bore logging program was conducted in April 2013 to investigate the potential under-estimation of water contents and to enable re-calibration of the 2011 NMR data. A total of 10 bores were logged using the improved Javelin system at an inter-echo spacing of 0.0015 seconds, with three bores also logged with an inter-echo spacing of 0.00225 seconds (Table 17-39). The calibration and processing of the data are discussed in Section 7.3.

The subset of 2011 NMR data relevant to the 2013 NMR logging (BHMAR77-2, 80A-2 and 99-1) were compared and a systematic offset was found to be present in the mobile and total water contents between the two datasets. Using the same logging and processing parameters (such as inter-echo spacing and $T_2$ cut off) the offset was estimated to be 20%. As explained in Section 7.3, a factor of 1.2 was subsequently used to recalibrate the 2011 NMR data.

**Table 17-38.** *Summary of the NMR borehole data acquired in 2011 using the Javelin logging system.*

| Borehole | Drilling method | NMR logged From (m) | NMR logged To (m) |
|---|---|---|---|
| BHMAR3B-1 | Sonic coring | 2 | 60 |
| BHMAR04-1 | Sonic coring | 2 | 70 |
| BHMAR08-1 | Sonic coring | 1 | 59 |
| BHMAR16-1 | Sonic coring | 2 | 60 |
| BHMAR21-1 | Sonic coring | 2 | 80 |
| BHMAR23-1 | Sonic coring | 2 | 95 |
| BHMAR29-1 | Sonic coring | 2 | 60 |
| BHMAR31-1 | Sonic coring | 2 | 60 |
| BHMAR33-1 | Sonic coring | 2 | 64 |
| BHMAR33-8 | Sonic coring | 14 | 53.5 |
| BHMAR34-1 | Sonic coring | 2 | 60 |
| BHMAR35-1 | Sonic coring | 2 | 54 |
| BHMAR36-1 | Sonic coring | 15 | 85 |
| BHMAR58-1 | Sonic coring | 2 | 75 |
| BHMAR61-1 | Sonic coring | 2 | 70 |
| BHMAR62-1 | Mud rotary | 15 | 65 |
| BHMAR63-1 | Mud rotary | 5 | 45 |
| BHMAR66-1 | Sonic coring | 17 | 62 |
| BHMAR75-3 | Mud rotary | 1 | 89.5 |
| BHMAR75-5 | Sonic coring | 2 | 52.5 |
| BHMAR77-2 | Sonic coring | 2 | 65 |
| BHMAR79A-6 | Sonic coring | 2 | 71 |
| BHMAR80A-2 | Sonic coring | 2 | 65 |
| BHMAR80B-2 | Sonic coring | 2 | 72 |
| BHMAR83-2 | Sonic coring | 2 | 65 |
| BHMAR84-2 | Sonic coring | 2 | 59 |
| BHMAR88-3 | Sonic coring | 2 | 71 |
| BHMAR92-1 | Sonic coring | 2 | 70 |
| BHMAR99-1 | Sonic coring | 2 | 63 |

**Table 17-39.** *Summary of the NMR borehole data acquired in 2013 using the Javelin logging system.*

| Borehole | Inter-echo Spacing (seconds) | NMR logged From (m) | NMR logged To (m) |
|---|---|---|---|
| BHMAR88-3 | 0.00150 | 10 | 71 |
| BHMAR66-1 | 0.00150 | 16 | 71 |
| BHMAR79A-6 | 0.00150 | 8.5 | 70.5 |
| BHMAR92-1 | 0.00150 | 9.5 | 76 |
| BHMAR3B-1 | 0.00150 | 12.5 | 73 |
| BHMAR77-2 | 0.00150 | 10.5 | 64 |
| BHMAR80A-2 | 0.00150 | 8 | 64 |
| BHMAR33-9 | 0.00150 and 0.00225 | 3 | 62 |
| BHMAR75-8 | 0.00150 and 0.00225 | 3 | 54 |
| BHMAR99-1 | 0.00150 and 0.00225 | 24 | 61 |

### 17.11.2 Laboratory Porosity Measurements

A total of 425 gravimetric water content measurements were undertaken on selected samples of the BHMAR sonic cores. These data were acquired within two months of the cores being collected. As these are expressed by mass, they need to be divided by the particle density to derive a volumetric measure that is comparable with the NMR total and free water content data.

For the sand and gravelly sand, quartz is the dominant mineral so the density of quartz (2.65 g/cm$^3$) was used to convert the gravimetric water to volume percent. There were semi quantitative XRD results for three mud and stiff clay samples. The XRD data showed that up to 30% montmorillonite was present with the remainder composed of kaolinite. Given the density of kaolinite is ≈ 2.6 g/cm$^3$ and montmorillonite is ≈2.0 g/cm$^3$, the resulting composite particle density for the mud was calculated as 2.42 g/cm$^3$ based on these proportions. For the muddy sand, the mud fraction can contain 10% montmorillonite and the rest mostly quartz. Thus the composite particle density of muddy sand is approximately ≈ 2.58 g/cm$^3$. These densities were used in the calculation of volumetric gravimetric water contents for samples across the textural classes.

The volumetric gravimetric data provides a benchmark for the total water content derived from the NMR logging. However, there can be sampling bias as the samples are from a limited section of the core. The cores may have been disturbed during sampling. This is possible although it is limited as the sonic cores can proved some of the best results in unconsolidated sediments. These sampling biases can be partially reduced by a large number of samples. Each of the core samples was assigned a hydraulic class to be compared with the NMR data. Figure 17-95 is a set of box plots illustrating the populations of gravimetric data from the BHMAR sonic cores. There may be greater uncertainty in the class 4 (medium sands) and the class 5 (coarse sand to gravel) due to the evaporation or drainage of some water during the laboratory testing.

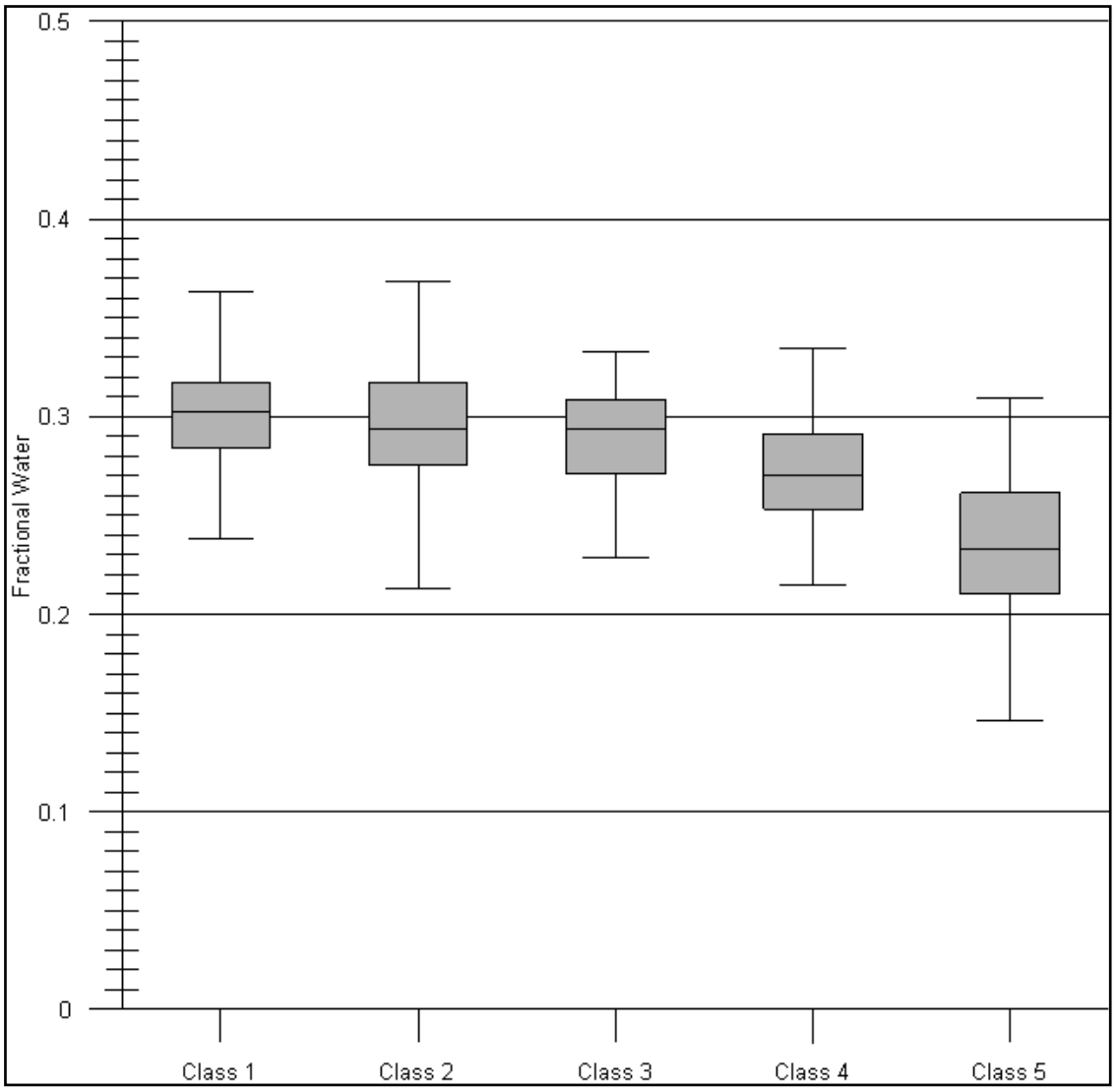



**Figure 17-95.** *Box plot of the gravimetric water content data by hydraulic class. Class 1 is Mud, class 2 is muddy sand, class 3 is fine sand, class 4 is medium sand, and class 5 is coarse sand to gravel.*

### 17.11.3 Comparison of NMR and Porosity Datasets

A point-by-point comparison can be made between the gravimetric data and the NMR total water content downhole. Figure 17-96 is such a plot for BHMAR88-3. In Figure 17-96, a general reasonable correlation can be seen with the gravimetric data and the NMR total water in the lower section of the downhole log, but a poor correlation in the upper section. Upon further inspection it can be shown that the areas where the gravimetric data are poorly correlated is in the fine-grained intervals. Figure 17-97 is a plot of the same NMR log from BHMAR88-3 with a symbol colour coded for the hydraulic class. For comparison, the NMR mobile water for BHMAR83-3 is also plotted. As would be expected the mobile water is lower than the gravimetric water contents in all but one sample. This one sample being higher than the gravimetric data could be related to the water loss due to drying before analysis.

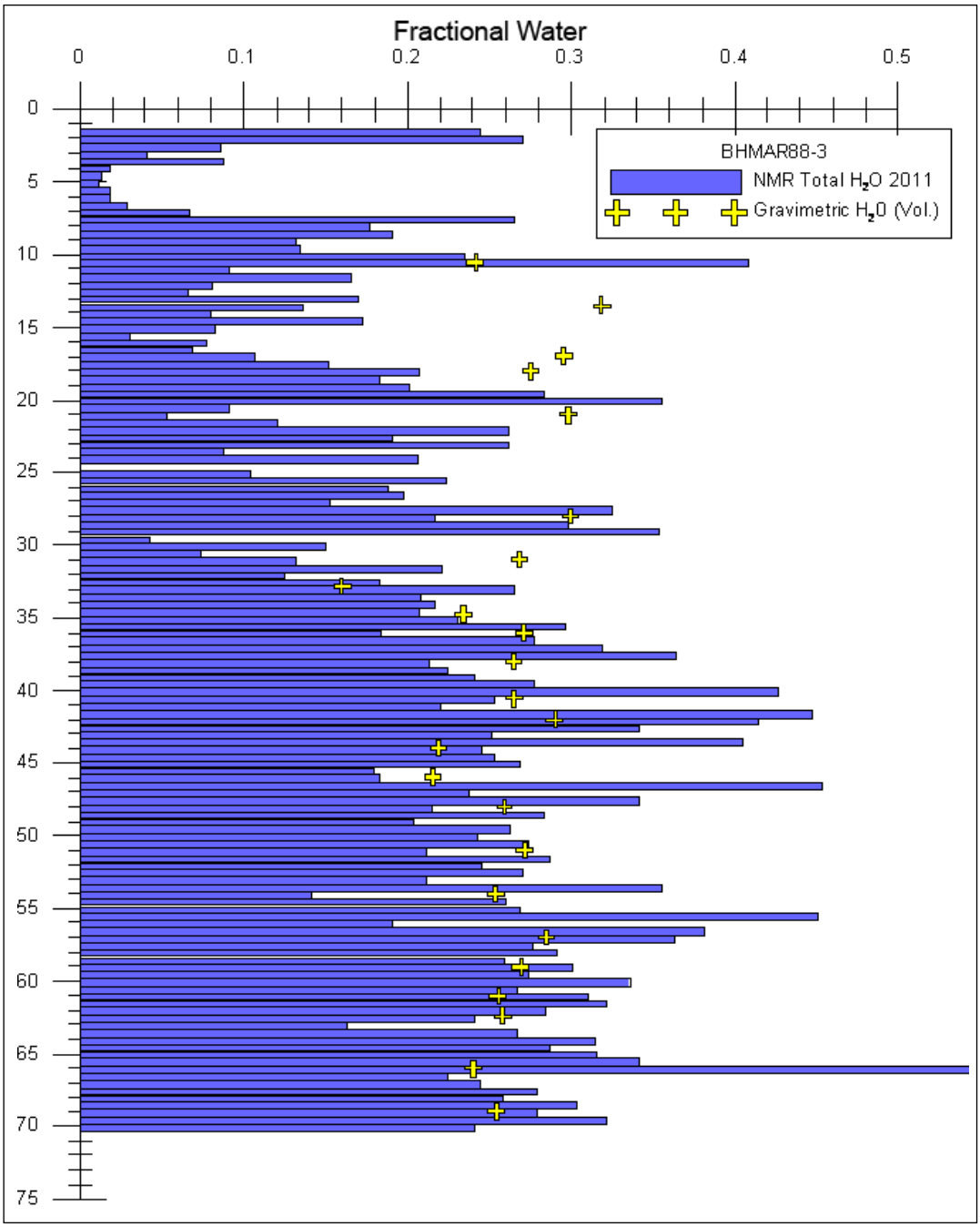



**Figure 17-96.** *Downhole plot of gravimetric data (yellow crosses) and NMR total water for BHMAR88-3.*

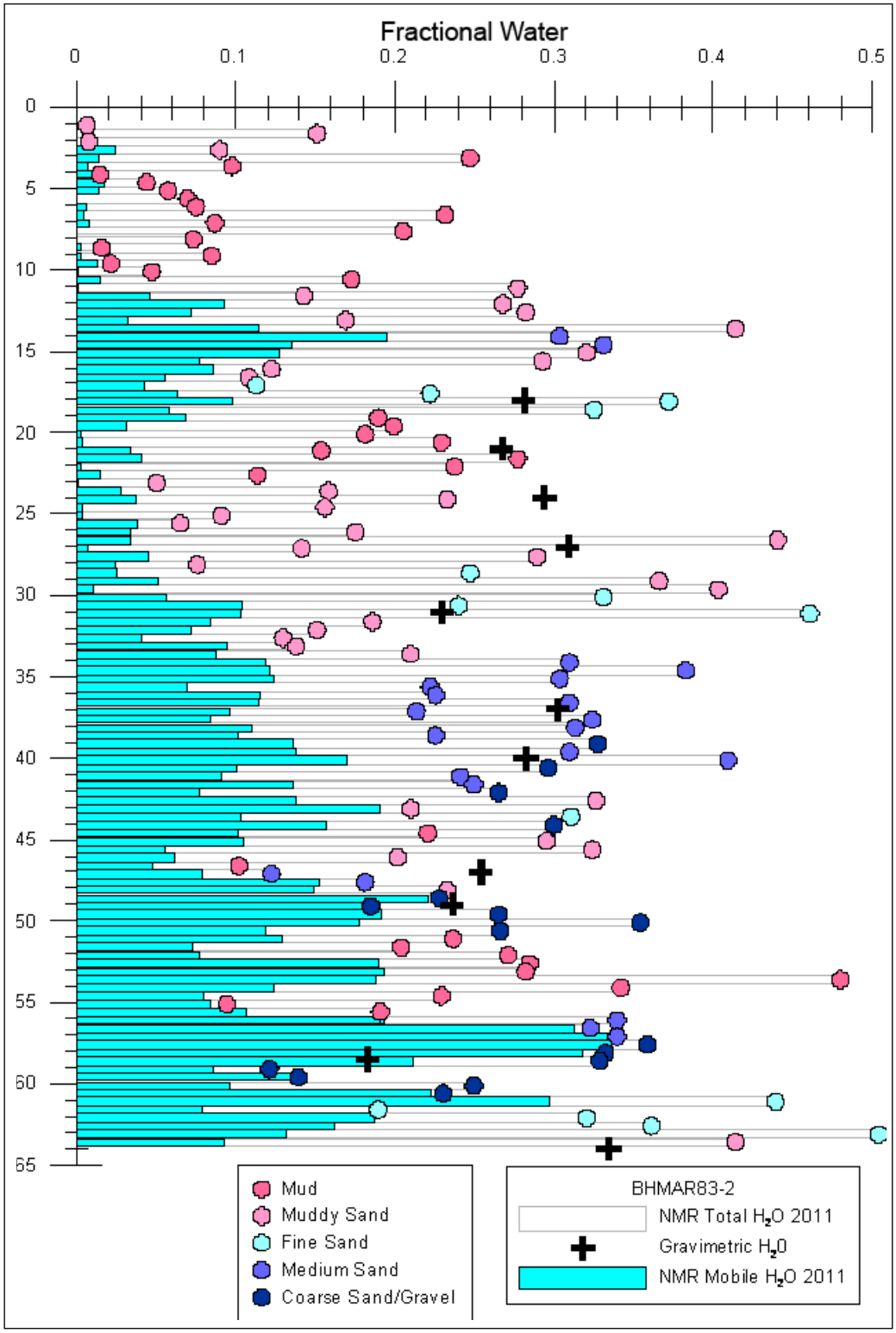



**Figure 17-97.** *Downhole plot of gravimetric data (black crosses), 2011 NMR total water (grey horizontal bars) and 2011 mobile water (light blue) coded by texture class (coloured circles) for BHMAR83-2.*

A set of 25 Lexan-encapsulated sonic core samples were analysed for total and effective porosity. This included several different tests that are summarized in Hignett (2013) and documented in Section 7.3. These samples are from selected intervals from BHMAR33-9 and BHMAR75-8. The water loss at specific matric potentials and total porosity (in volume percent) was used to directly compare with the NMR data. The assumption is that total porosity would relate to NMR total water and that the porosity estimated from the matric potential of a suction 10 to 70-kPa would relate more to the effective porosity. The porosity of the 200 kPa matric potential should also relate closely to the total porosity in coarse grained sediments and should diverge in fine grained sediments. Figure 17-98 is the distribution of the porosity tests for hydraulic classes 5 to 3 (Coarse sand to gravel, medium sand, and fine sand, respectively). Figure 17-99 illustrates the box plots for the hydraulic classes 2 and 1 (muddy sand and mud, respectively). For the mud samples, no data was available for the 10 and 70 kPa suction matric potential. These plots show the progressive decrease in effective porosity as represented by the 10 and 70 kPa data with decreasing grain size.

The next step was to compare the recalibrated 2011 NMR data and the 2013 NMR data with the laboratory porosity measurements for each hydraulic texture class. Table 17-40 summarizes the comparisons made between the various laboratory porosity measurements with the NMR total water and mobile water data derived from the two surveys.

**Table 17-40.** *Comparison of NMR and laboratory porosity data.*

| **NMR Total Water** | **Laboratory measurements** | | |
|---|---|---|---|
| | **200 kPa matric potential porosity** | **Total Porosity** | **Gravimetric** |
| **2011 corrected** | X | X | X |
| **2013** | X | X | X |
| **NMR mobile water** | | **10 kPa matric potential porosity** | **70 kPa matric potential porosity** |
| **2011 corrected** | | X | X |
| **2013** | | X | X |

Figure 17-100 to Figure 17-104 are box plots for each hydraulic class of the distribution of the porosity values compared with the NMR total water datasets. Figure 17-105 to Figure 17-109 are analogous box plots for each hydraulic class of the distribution of the laboratory porosity data compared with the NMR mobile water datasets. The NMR data relating to the unsaturated zone and also the mud rotary boreholes were excluded from this analysis. Note that the rec-calibrated 2011 NMR survey data are plotted in these figures.

The NMR total water box plots for the coarse sand to gravel (Class 5) are plotted in Figure 17-100. The NMR total water data show similar distributions for both the 2013 and 2011 NMR surveys, both exhibiting median values of 0.28. The 200 kPa matric potential and total porosities are similar but slightly elevated in comparison, with median values of 0.32 and 0.31 respectively. The gravimetric data is lower than the other distributions with the median value of 0.23. This is interpreted to be due to water losses during the gravimetric analysis of the coarse grained sediment, due to their free-draining nature.

The NMR total water data for the 2013 and 2011 NMR surveys show similar distributions for the Class 4 medium sands (Figure 17-101), both with median values of 0.29. The 2011 data show a larger range, which can be attributed to the larger population. The 200 kPa matric potential and total porosity are somewhat similar but are elevated compared with the NMR data, median values of 0.33 and 0.36 respectively. It is assumed that these are related to the limited porosity samples compared to the larger NMR datasets. The median value (0.27) of the gravimetric data is lower than the other distributions, but it is higher than the median value for class 5 textures. This supports the statement above that the coarse grained sediments dried while undergoing analysis.

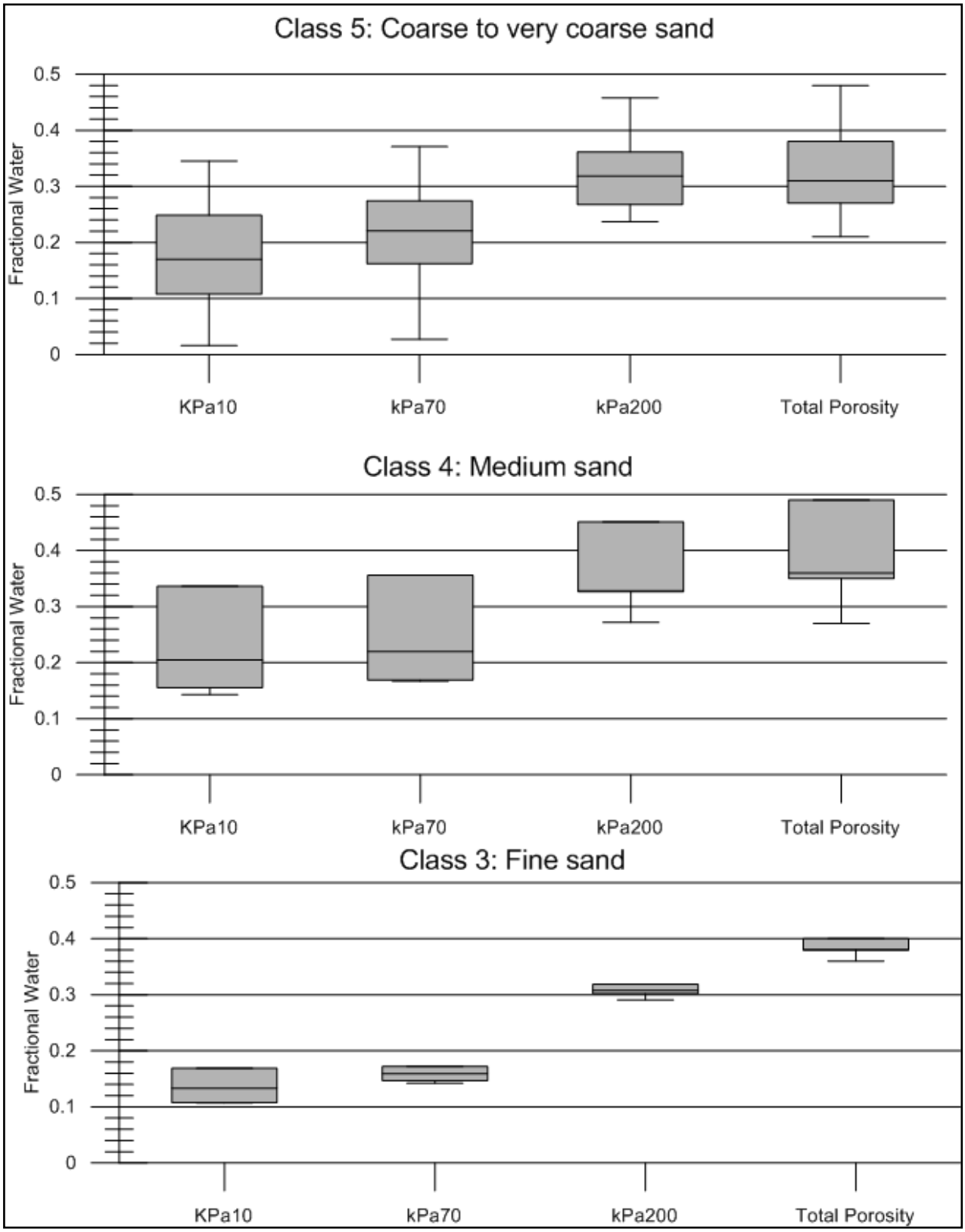



**Figure 17-98.** *Box plots of the porosity values from the matric potential of 10, 70, 200 kPa of suction and the calculated total porosity for texture classes 5, 4, and 3.*

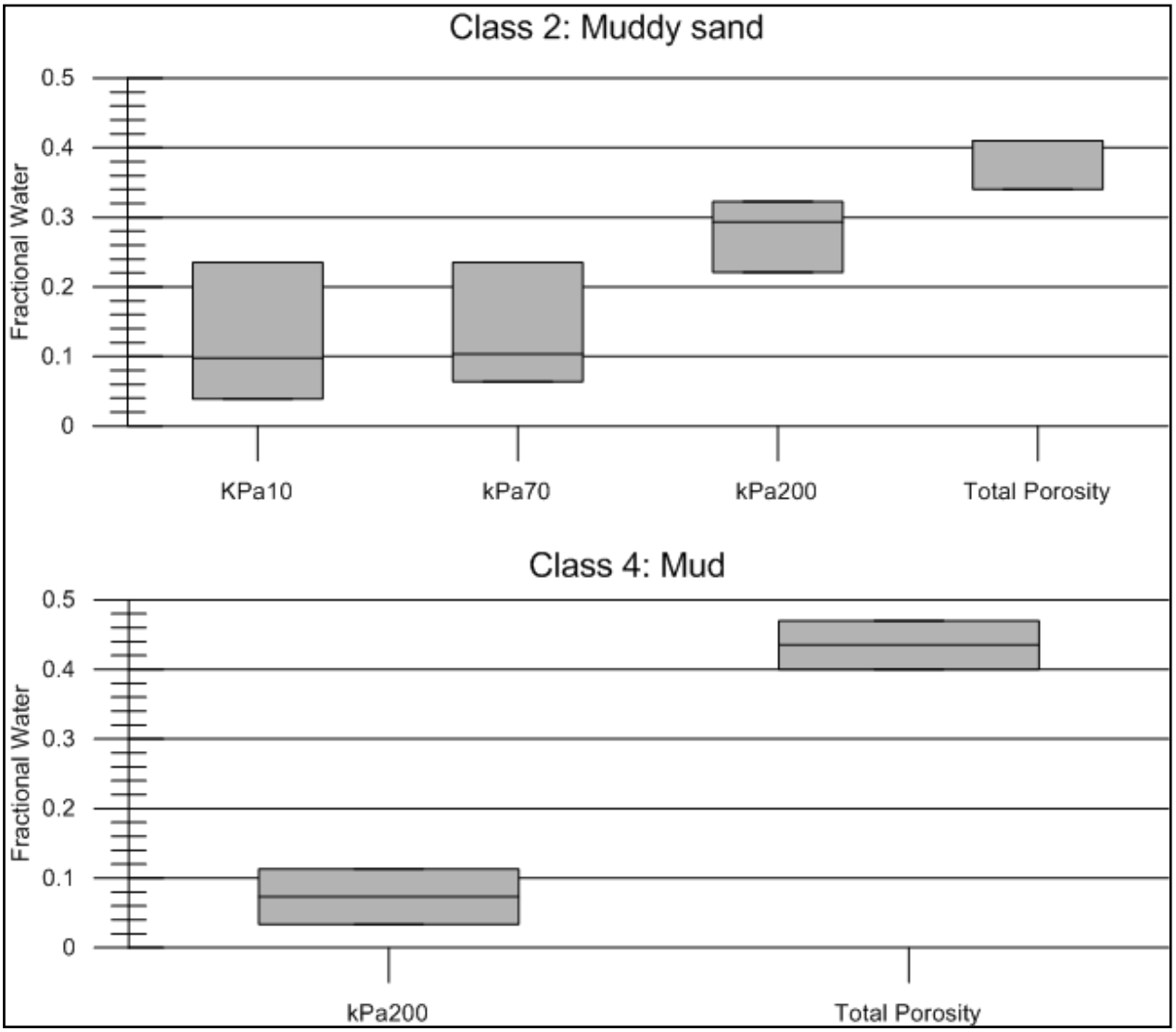



**Figure 17-99.** *Box plots of the porosity values from the matric potential of 10, 70, 200 kPa of suction and the calculated total porosity for texture classes 2 and 1. No porosity values for the matric potential of 10 and 70-kPa due to the high matric potential of the fine grained sediments.*

For the fine sands (Class 3), the NMR total water data also show similar distributions for both the 2013 and 2011 surveys, with median values of 0.29 and 0.31 respectively (Figure 17-102). The 2011 data has a larger distribution, which can be attributed to the larger population. The laboratory total porosity and 200 kPa matric potential are significantly different, with median values of 0.38 and 0.31 respectively. This is probably due to the higher matric potential of the fine-grained sediments. The total porosity is significantly higher than the other distributions. This is probably based on a small population of samples (n=4). The gravimetric data is overlapping well with the NMR data with a median value of 0.29. The gravimetric water losses inferred for the coarse sands would be assumed lower in the fine-grained sediments.

There are also similar distributions for the 2013 and 2011 NMR total water data for the Class 2 muddy sands (Figure 17-94), with median values of 0.23 and 0.22 respectively. The 2011 data show a larger distribution, which can be attributed to the larger population. What is evident is that the median values (0.29 and 0.41) of the laboratory data are all-greater than the upper quartile of the NMR distributions. This would suggest that the NMR is not adequately characterising the total water contents of the fine grained sediments, most likely due to the impact of $T_2$ decays less than the 1.5 ms and the low signal to noise of the fast decays. The laboratory total porosity and 200 kPa matric potential are significantly different, most likely due to the higher matric potential of the fine-grained sediments. The total porosity is also significantly higher than the other distributions. This may be based on a small population of samples, but may also represent an upper bound on

the total porosities. The gravimetric data with a median of 0.29 is also elevated when compared with the NMR data. The water loss issue linked to the coarse sand would be assumed lower in the muddy sands. The gravimetric data also indicates that the NMR tool is not adequately measuring total water content in these finer sediments.

For the Class 1 muds, the NMR total water data show a separation in the distributions for the 2013 and 2011 surveys, with the 2013 median value slightly lower, 0.18 as compared to 0.19. This is not expected with the smaller inter-echo spacing of the 2013 data. The 2011 data show a larger distribution, which can be attributed to the larger population. The difference in the distributions is indicating a possible impact of noise with the use of a higher regularization for the 2013 data. The laboratory total porosity and 200 kPa matric potential are significantly different (median values of 0.07 and 0.43), due to the higher matric potential of the fine-grained sediments. The total porosity is also significantly higher than the other distributions. The gravimetric data (median value of 0.30) is also elevated when compared with the NMR data. Water loss during gravimetric analysis of the free-draining coarse sands is assumed to be not an issue for the muds. The difference between the NMR data and both the total porosity and gravimetric water contents indicates that the NMR tool is not measuring all the total water in the muds. This is interpreted to due to the impact of $T_2$ decays less than the 1.5 ms and the low signal to noise in the fast decays.

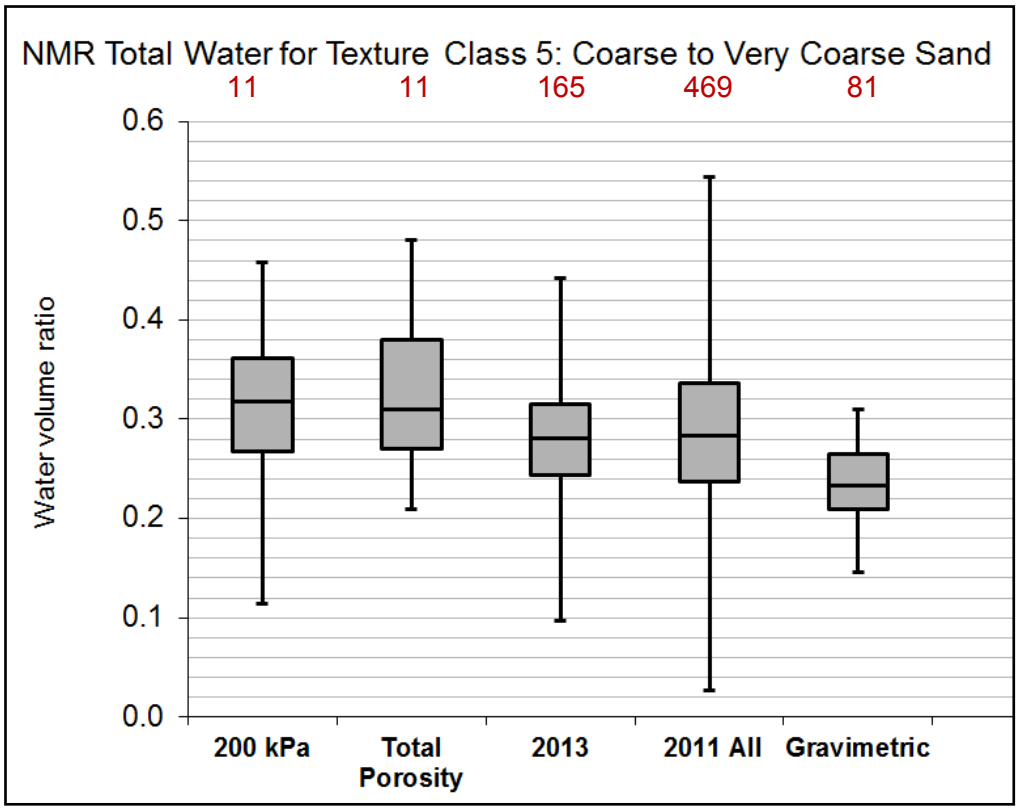



**Figure 17-100.** *NMR total water compared with laboratory measurements of total porosity for texture class 5: Coarse sand to gravel. Red numbers indicate number of samples.*

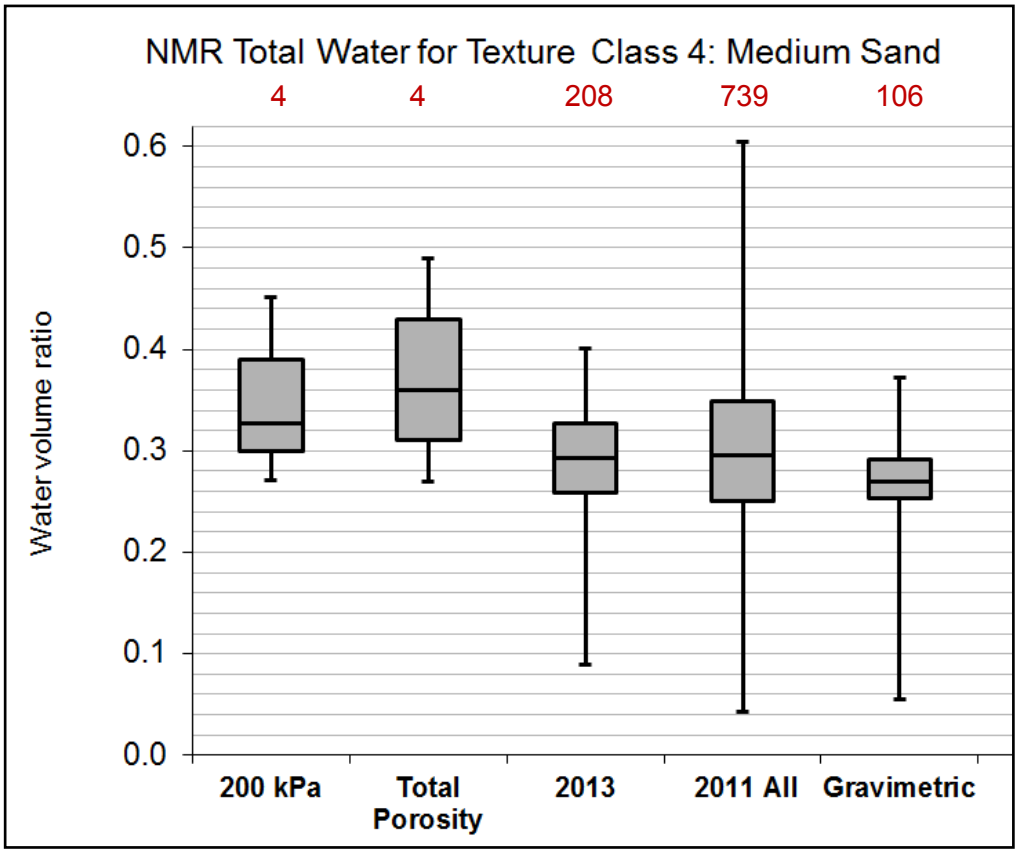



**Figure 17-101.** *NMR total water compared with laboratory measurements of total porosity for texture class 4: Medium sand. Red numbers indicate number of samples.*

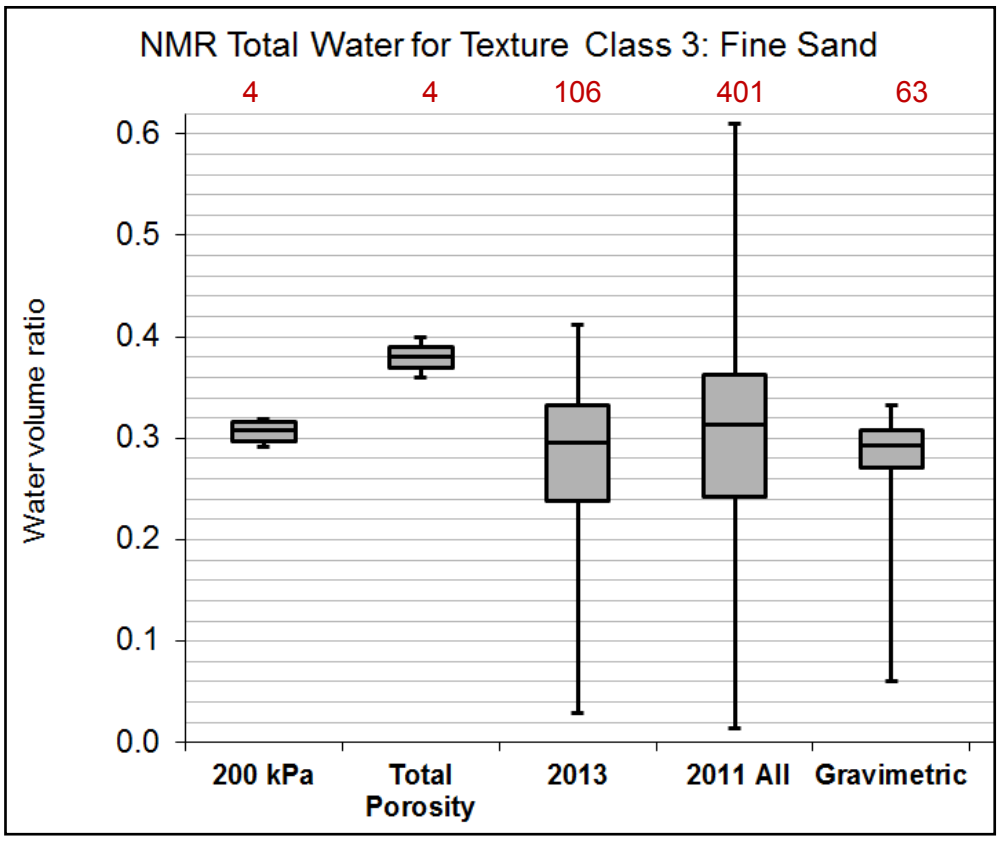



**Figure 17-102.** *NMR total water compared with laboratory measurements of total porosity for texture class 3: Fine sand. Red numbers indicate number of samples.*

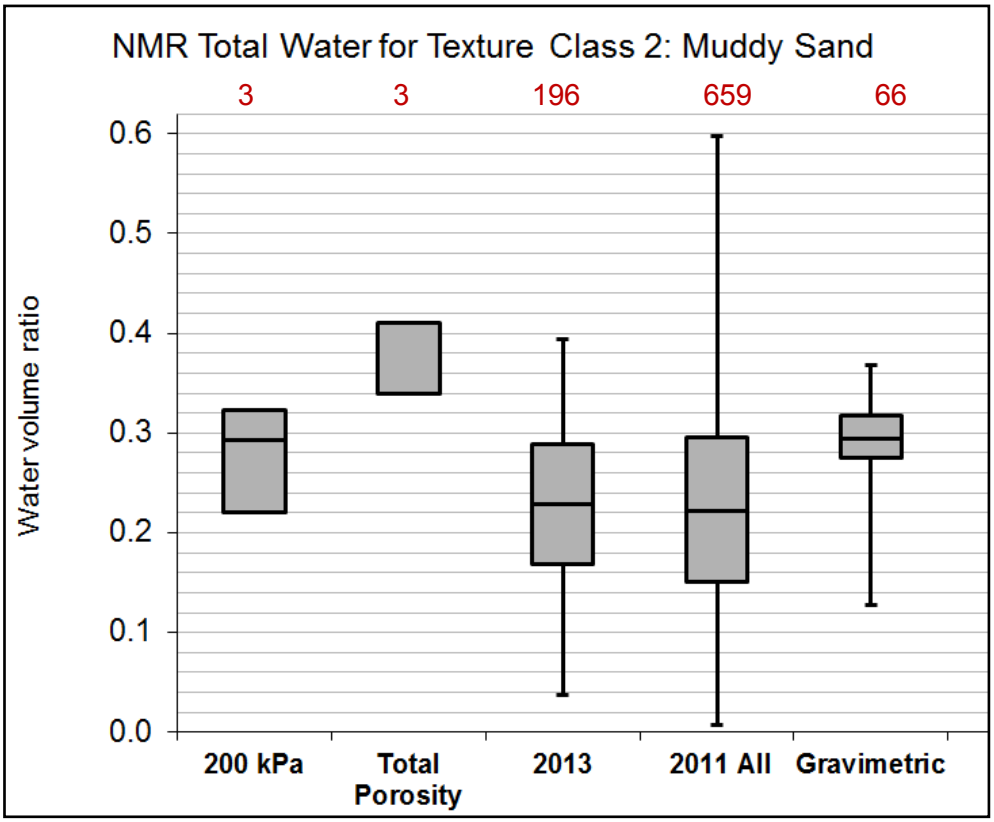



**Figure 17-103.** *NMR total water compared with laboratory measurements of total porosity for texture class 2: Muddy sand. Red numbers indicate number of samples.*

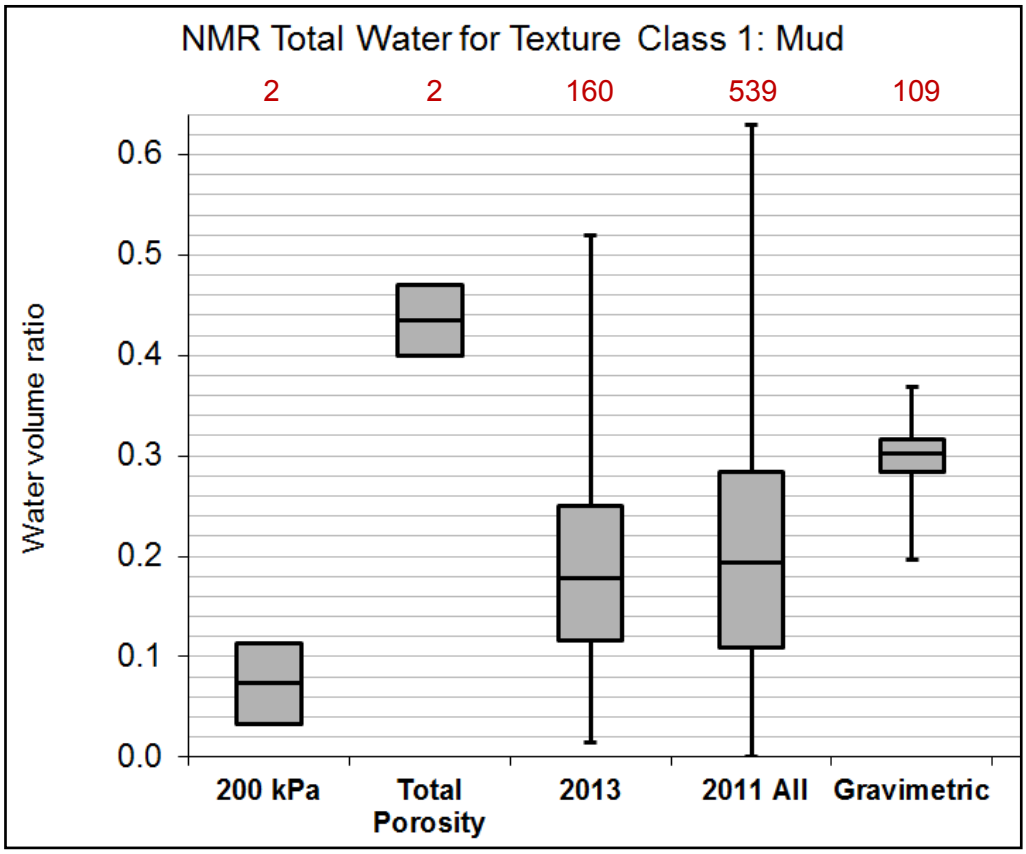



**Figure 17-104.** *NMR total water compared with laboratory measurements of total porosity for texture class 1: Mud. Red numbers indicate number of samples.*

In terms of mobile water contents, Figure 17-105 plots the NMR data for the 2011 and 2013 surveys with the laboratory porosity data for the Class 5 coarse sand to gravel. The NMR mobile water data show differences in the distributions for the 2013 and 2011 surveys, with median values of 0.22 and 0.16 respectively. These differences may reflect the differences in the populations. However there is significant overlap in the box plots. The laboratory matric potentials for 10 and 70 kPa display a difference in their distributions as does the NMR distributions. This may be indicating that the 70 kPa values are more representative of the effective porosity. As with the NMR there is significant overlap in the matric potential distributions. Overall, the mobile water distributions in Class 5 coarse sand to gravel show reasonable agreement with the distributions for the matric potential at 10 and 70 kPa, with the range in the median values being 0.06.

For Class 4 medium sands, the medians of the NMR mobile water data for the 2013 and 2011 surveys are 0.22 and 0.16, respectively (Figure 17-106). The differences in the box plots probably reflect the different population sizes. There is significant overlap in the distributions. The measurements of matric potential of 10 and 70 kPa are similar. Overall, the NMR mobile water in medium sands are showing reasonable agreement with the matric potentials at 10 and 70 kPa, with a range in the median value of 0.05.

There is only a slight difference (0.02) between the median values of the 2013 and 2011 NMR mobile water contents for Class 3 fine sands (Figure 17-107). The 2011 data spread is much wider, probably due to the larger sample population. The matric potential of 10 and 70 kPa display similar and tight distributions, but these distributions are based on very few samples. With a maximum difference between medians of 0.02, the relative consistency between the NMR and matric potential data provides confidence in the 2013 NMR and re-calibrated 2011 NMR mobile water contents.

There are differences in the median values for the 2013 and 2011 NMR mobile water contents for Class 2 muddy sands, but there is also significant overlap in the box plots (Figure 17-108). The matric potential of 10 and 70 kPa display similar distributions and median values, but these distributions are based on very few samples.

For Class 1 muds, the NMR mobile water data show similar median values and distributions for the 2011 and 2013 surveys (Figure 17-109). However, caution should be used in using the data from mud units due to the low signal to noise and the limitation in seeing clay-bound water. There was no laboratory based matric potentials of 10 and 70 kPa measured for the muds.

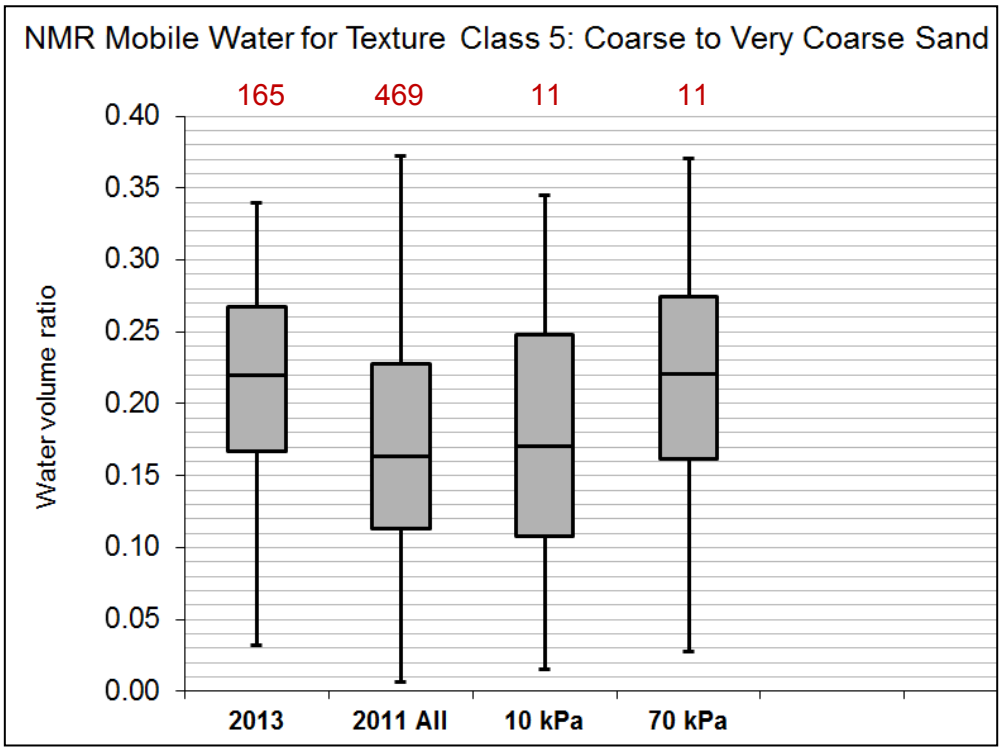



**Figure 17-105.** *NMR mobile water compared with laboratory measurements of total porosity for texture class 5: Coarse sand to gravel. Red numbers indicate number of samples.*

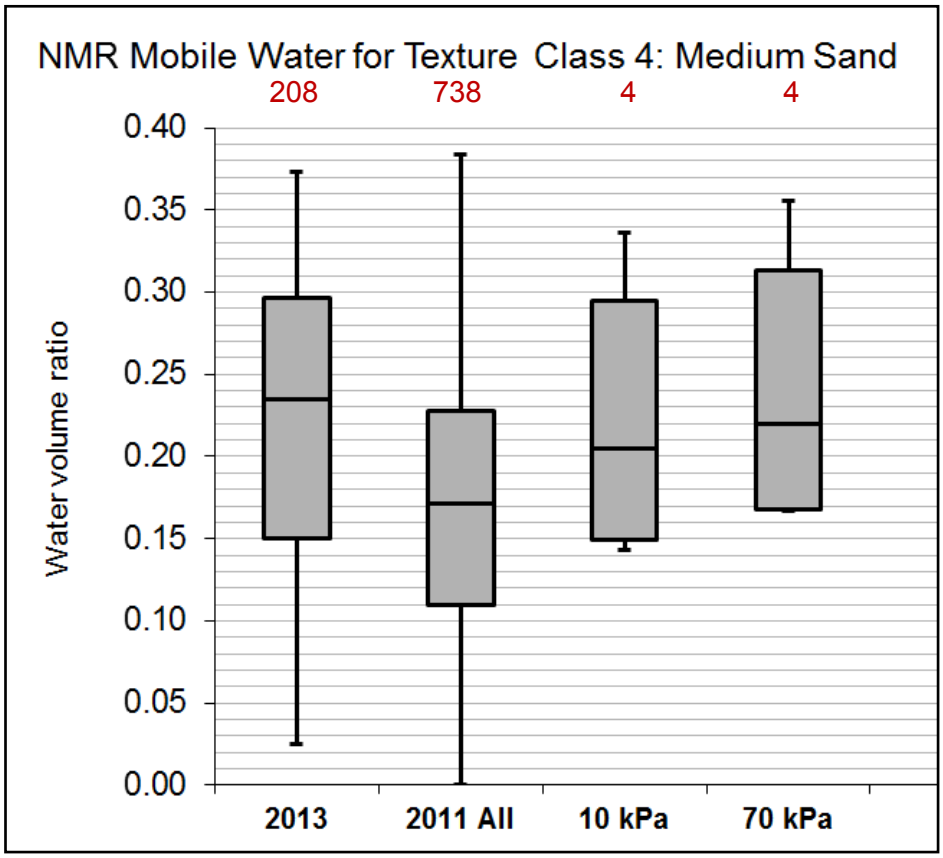



**Figure 17-106.** *NMR mobile water compared with laboratory measurements of total porosity for texture class 4: Medium sand. Red numbers indicate number of samples.*

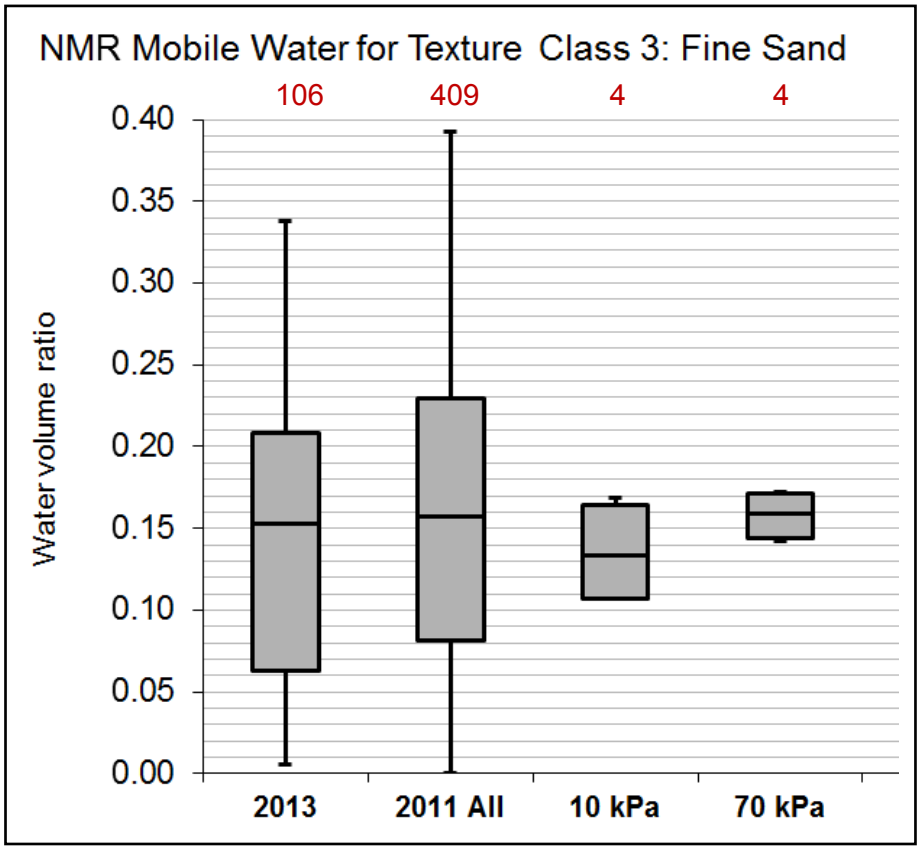



**Figure 17-107.** *NMR mobile water compared with laboratory measurements of total porosity for texture class 3: Fine sand. Red numbers indicate number of samples.*

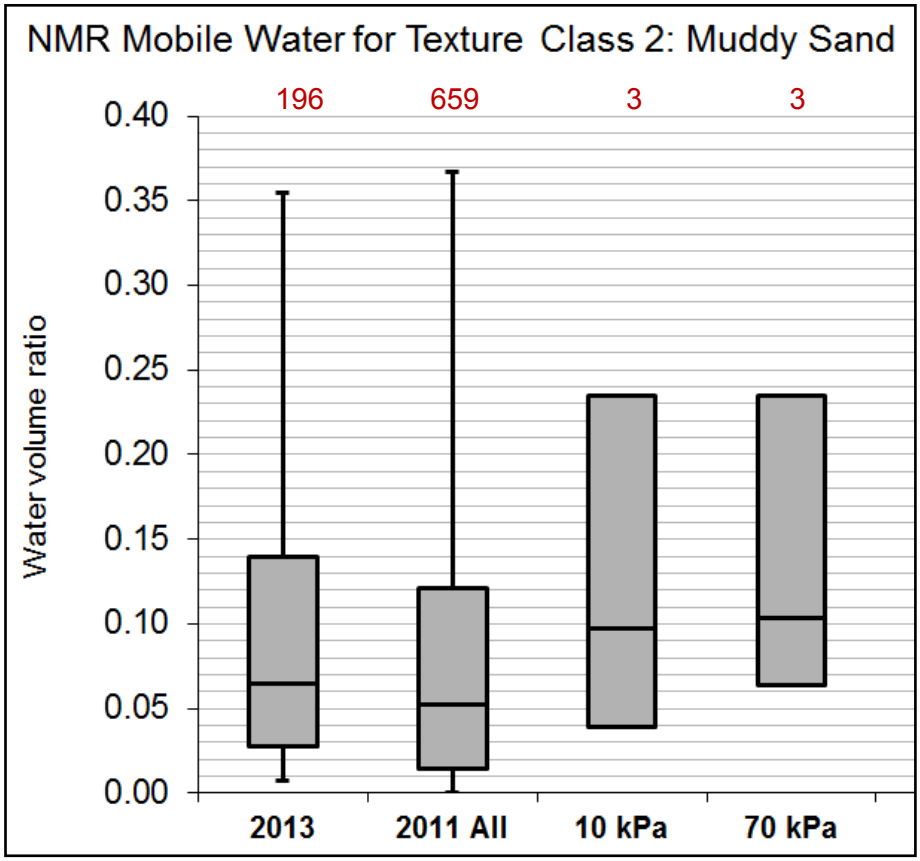



**Figure 17-108.** *NMR mobile water compared with laboratory measurements of total porosity for texture class 2: Muddy sand. Red numbers indicate number of samples.*

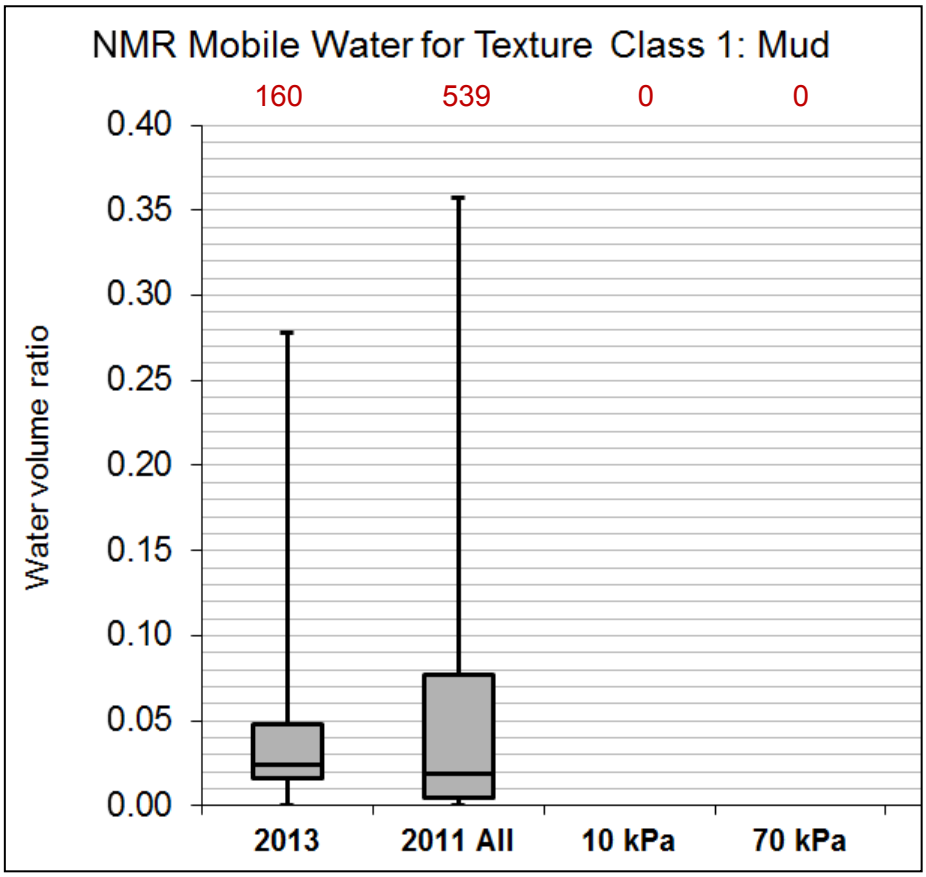



**Figure 17-109.** *NMR mobile water compared with laboratory measurements of total porosity for texture class 1: Mud. Red numbers indicate number of samples. Other numbers indicated values of the box plot parameters.*

Figure 17-110 to Figure 17-115 specifically focus on the NMR and laboratory porosity data for the boreholes BHMAR33-9 and BHMAR75-8. This is because these are the boreholes with the Lexan-encapsulated core, from which the total porosity and matric potential measurements were taken. Hence, these provide the most direct comparison between the NMR and porosity datasets. Box plots of the NMR total and free water contents at both 1.5 ms and 2.25 ms echo spacing are shown.

Figure 17-110 to Figure 17-115 show that in many cases the distributions of the laboratory porosities overlap with the NMR measurements from both the 1.5 and the 2.25 ms echo-spacing. The box plots however do illustrate the sensitivity of the distributions to a low number of data points and the internal scatter in the measurements. The data show that the selection of a 33 ms $T_2$ cut-off correlates well with the porosity measurements from the cores, with the distributions overlapping. There is substantial scatter in the total porosity that was not observed in the larger populations summarized in Figure 17-100 to Figure 17-105. Due to the limited data sets, the median values would be biased by any skewness in the small population. An assessment was followed using a larger dataset to compensate for the natural noise and scatter that are expected from all the technologies.

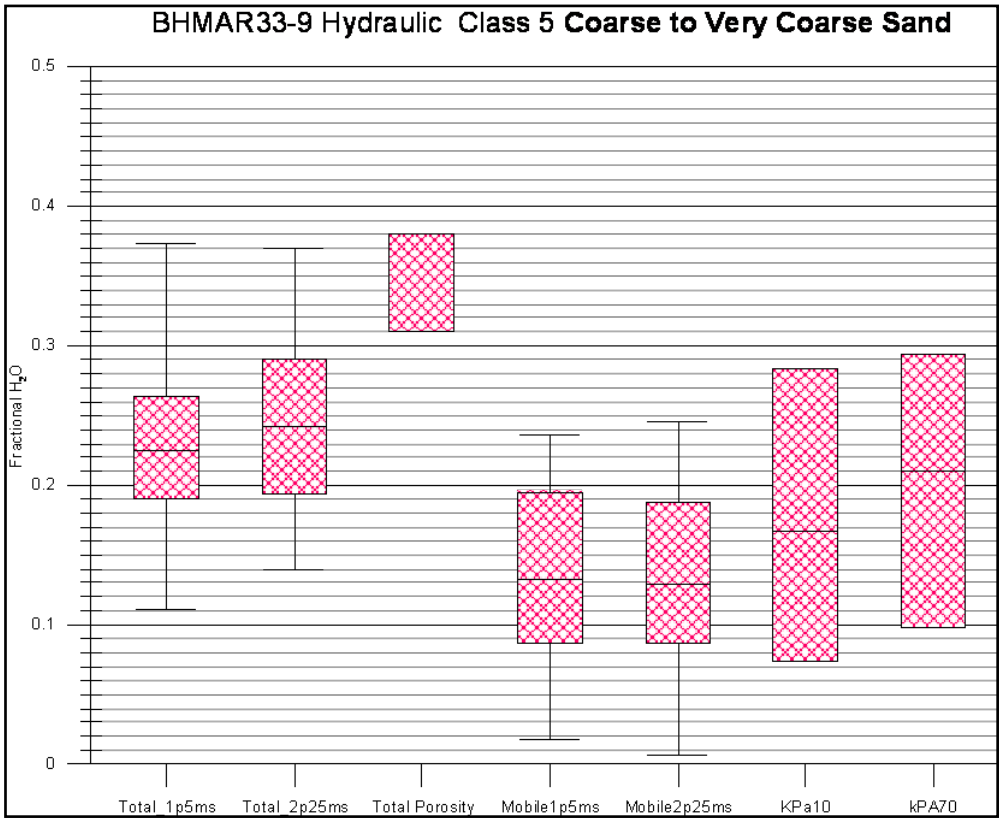



**Figure 17-110.** *Box plots of the NMR total water and mobile water distributions for the two different inter-echo spacing versus the distributions of the laboratory porosity measurements, for texture class 5: Coarse sand to gravel for BHMAR33-9.*

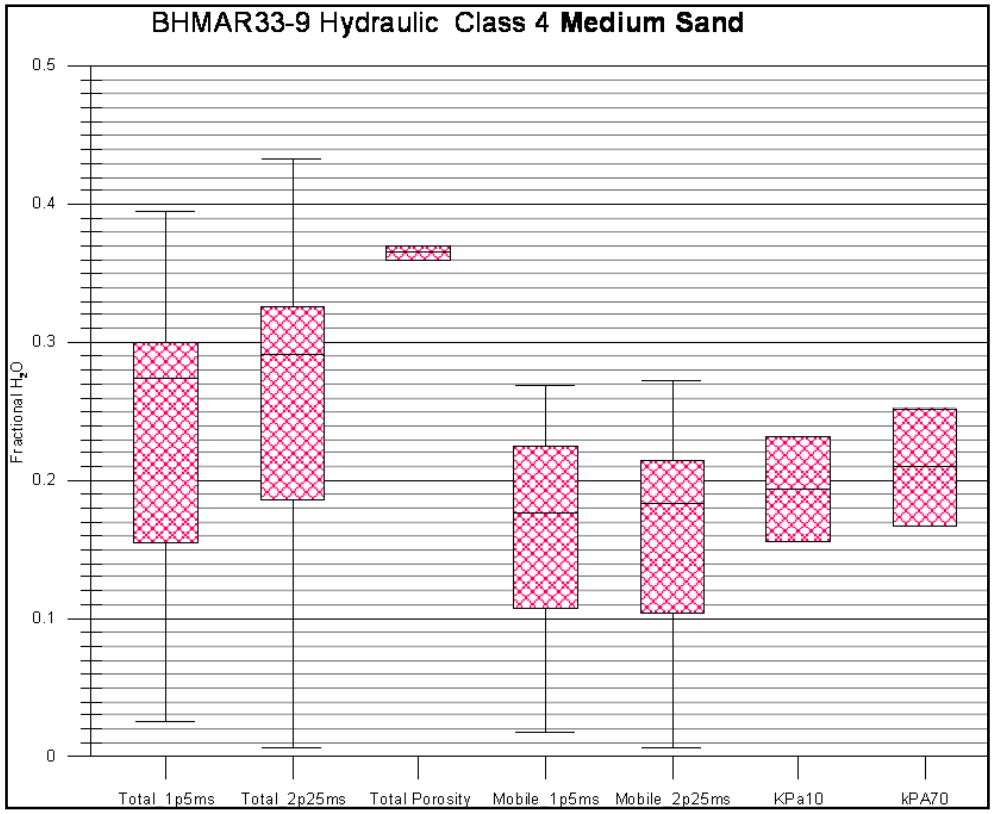



**Figure 17-111.** *Box plots of the NMR total water and mobile water distributions for the two different inter-echo spacing versus the distributions of the laboratory porosity measurements, for texture class 4: Medium sand for BHMAR33-9.*

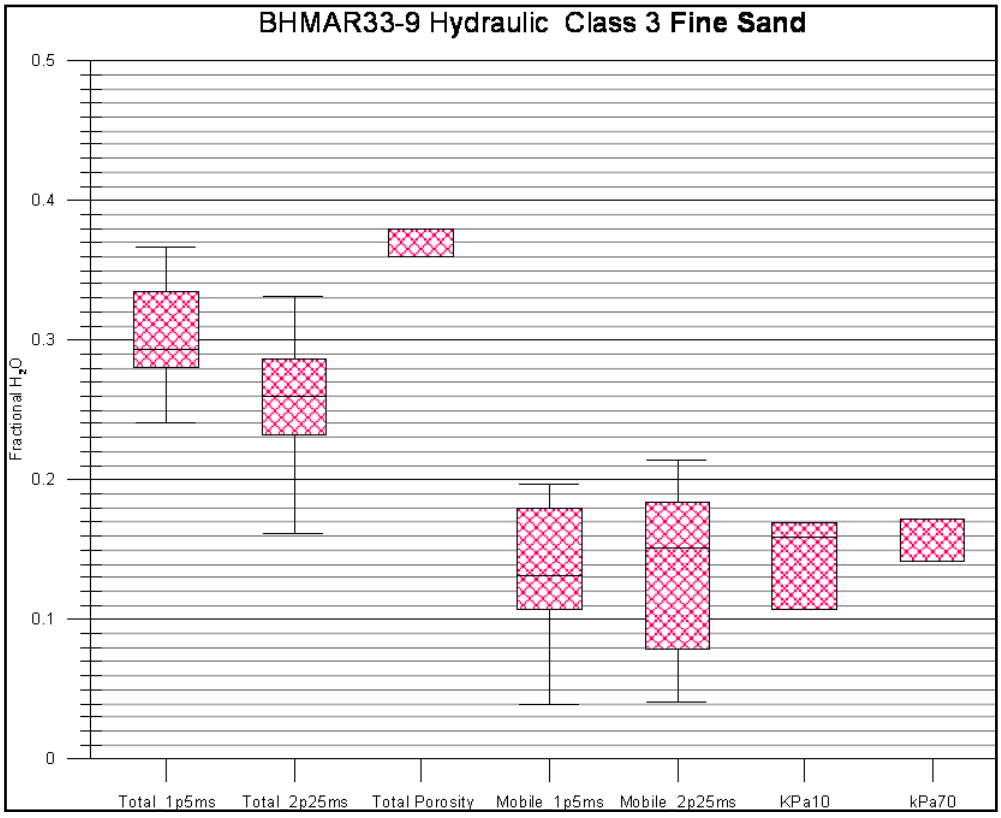



**Figure 17-112.** *Box plots of the NMR total water and mobile water distributions for the two different inter-echo spacing versus the distributions of the laboratory porosity measurements, for texture class 3: Fine sand for BHMAR33-9.*

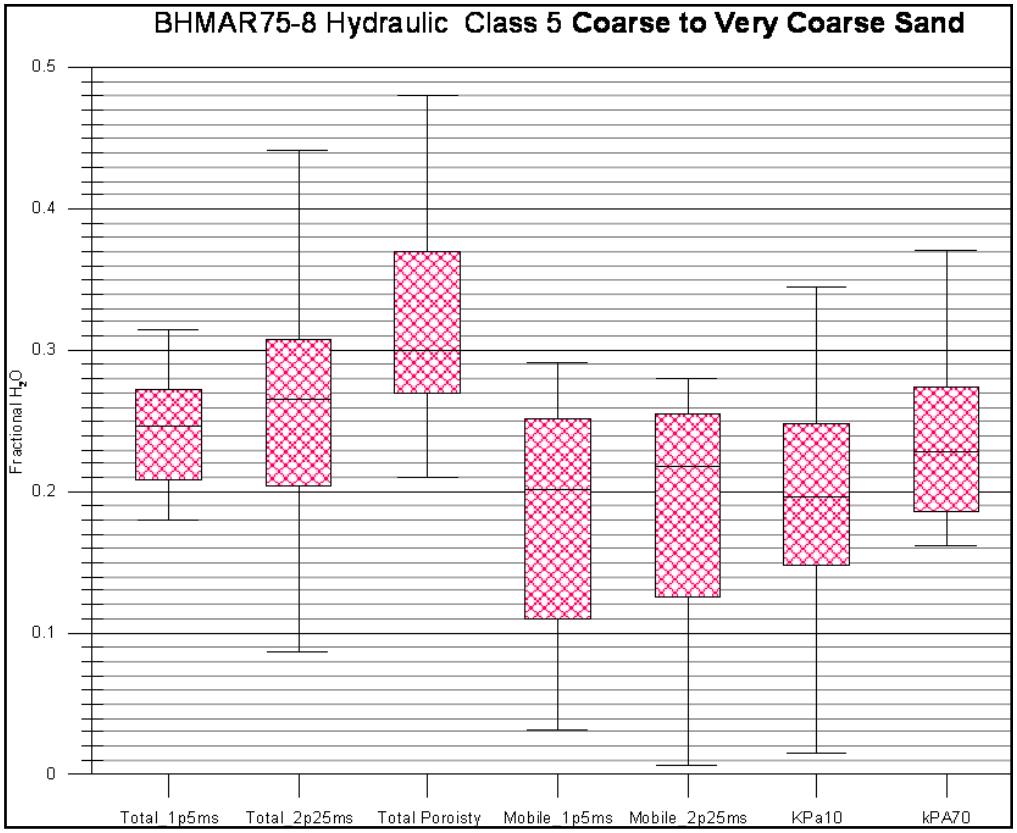



**Figure 17-113.** *Box plots of the NMR total water and mobile water distributions for the two different inter-echo spacing versus the distributions of the laboratory porosity measurements, for hydraulic class 5: Coarse sand to gravel for BHMAR75-8.*

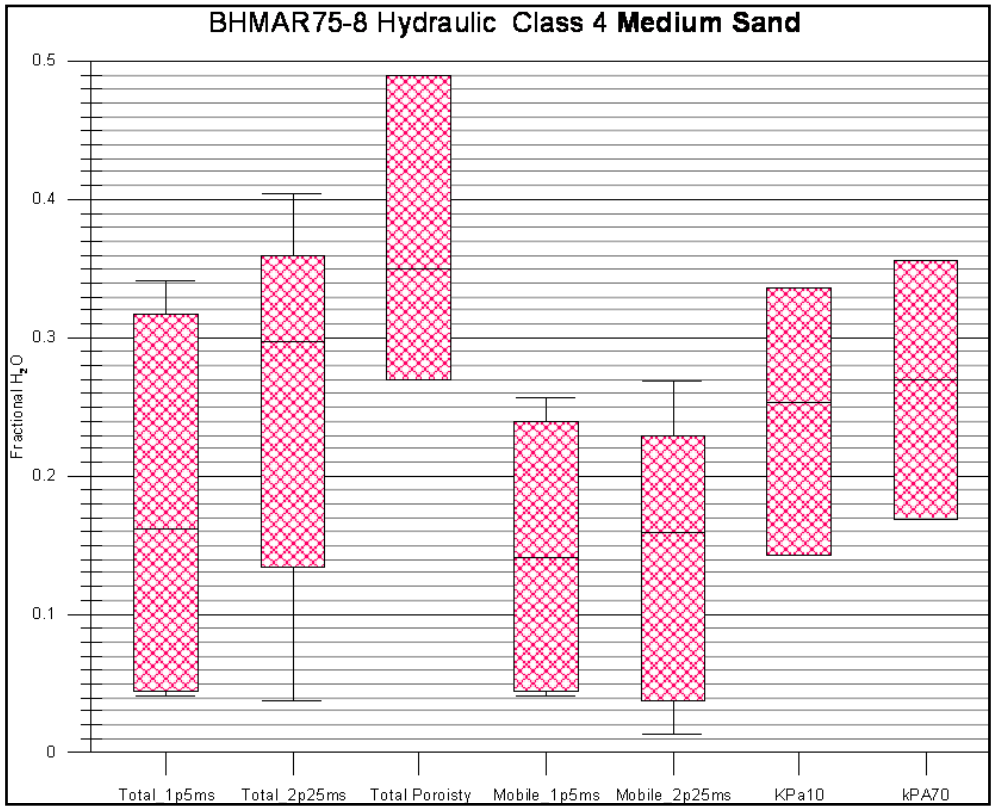



**Figure 17-114.** *Box plots of the NMR total water and mobile water distributions for the two different inter-echo spacing versus the distributions of the laboratory porosity measurements, for texture class 4: Medium sand for BHMAR75-8.*

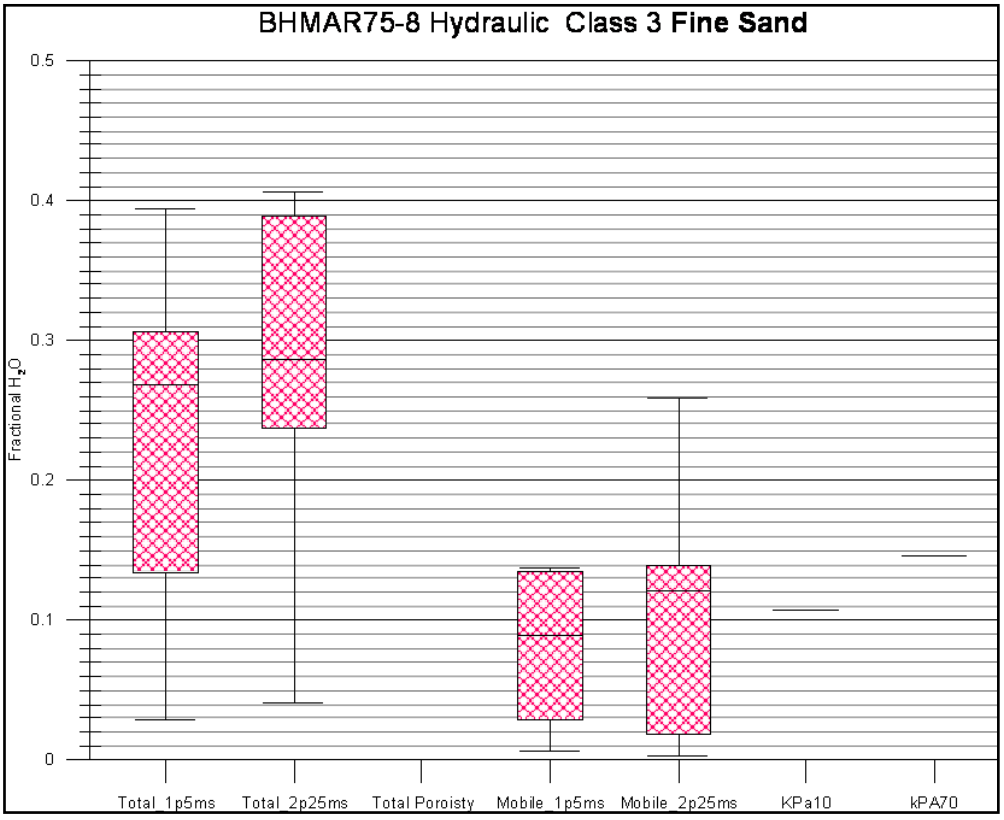



**Figure 17-115.** *Box plots of the NMR total water and mobile water distributions for the two different inter-echo spacing versus the distributions of the laboratory porosity measurements, for texture class 3: Fine sand for BHMAR75-8.*

Figure 17-116 to Figure 17-120 shows the box plots of the NMR mobile water for the 5 texture classes ranging from Class 5 coarse sand to gravel, to Class 1 mud. The data were subdivided into 5 groupings as summarised in Table 17-41. The first borehole dataset is the 2013 NMR mobile water content data. The '2011_Match' dataset is the corresponding re-calibrated 2011 NMR mobile water data for the 8 bores that were NMR logged in 2013. Note that the Lexan-encapsulated bores BHMAR33-9 and 75-8 are excluded from both these groups as these bores were not logged during the 2011 NMR program. With similar population size, these two groups should provide a direct comparison between the 2013 NMR survey and the recalibrated 2011 data. The next group, '2011 Central' focuses on bores from the central GWR1 target and includes the recalibrated 2011 mobile water data for 14 bores. The '2011 All 'group is the recalibrated 2011 mobile water data for all 26 NMR-logged bores across the BHMAR study area. The 'Lexan' group is the two Lexan bores (BHMAR 33-9 and 75-8) that were NMR-logged in 2013 and had Lexan-encapsulated core samples analysed for matric potential water content. Also included in the box plots are the matric potential data at 10 kPa and 70 kPa for these core samples. The NMR data relating to downhole unsaturated zone and also the NMR data for bores drilled using the mud rotary rig were excluded in this analysis. Summary statistics were calculated for each of these groups and on the basis of the 5 texture classes, as reported in Table 17-42 to Table 17-46.

**Table 17-41.** *Comparative groupings of NMR mobile water content survey data.*

| 2013 | 2011 Match | 2011 Central | 2011 All | Lexan |
|---|---|---|---|---|
| BHMAR3B-1 | BHMAR3B-1 | | BHMAR3B-1 | |
| | | | BHMAR04-1 | |
| | | BHMAR08-1 | BHMAR08-1 | |
| | | | BHMAR16-1 | |
| | | | BHMAR21-1 | |
| | | | BHMAR23-1 | |
| | | | BHMAR29-1 | |
| | | BHMAR33-1 | BHMAR31-1 | |
| | | | BHMAR33-1 | |
| | | BHMAR33-8 | BHMAR33-8 | |
| | | | | BHMAR33-9 |
| | | | BHMAR34-1 | |
| | | | BHMAR35-1 | |
| | | BHMAR58-1 | BHMAR36-1 | |
| | | | BHMAR58-1 | |
| BHMAR61-1 | BHMAR61-1 | | BHMAR61-1 | |
| | | | BHMAR66-1 | |
| | | BHMAR75-5 | BHMAR75-5 | |
| | | | | BHMAR75-8 |
| BHMAR77-2 | BHMAR77-2 | BHMAR77-2 | BHMAR77-2 | |
| BHMAR79A-6 | BHMAR79A-6 | BHMAR79A-6 | BHMAR79A-6 | |
| BHMAR80A-2 | BHMAR80A-2 | BHMAR80A-2 | BHMAR80A-2 | |
| | | BHMAR80B-2 | BHMAR80B-2 | |
| | | BHMAR83-2 | BHMAR83-2 | |
| | | BHMAR84-2 | BHMAR84-2 | |
| BHMAR88-3 | BHMAR88-3 | BHMAR88-3 | BHMAR88-3 | |
| BHMAR92-1 | BHMAR92-1 | BHMAR92-1 | BHMAR92-1 | |
| BHMAR99-1 | BHMAR99-1 | BHMAR99-1 | BHMAR99-1 | |

For the Class 5 coarse sand to gravel (Figure 17-116), the lower and upper quartile for the 2013 and matching 2011 group are almost identical (0.137 vs. 0.139; 0.252 vs. 0.257 respectively), whereas the medians are different (0.178 vs. 0.220). Examining the data from the Lexan group shows considerable differences in median values between the Lexan bores and the other 2013 NMR bores. This points out that the variability of water content within each bore is intrinsically large and a bigger population is better able to represent the range of mobile water compared to the potential bias in a small population. Scaling up to the

2011 Central and 2011 All groups, with data population increasing to 245 and 469, the lower, median and upper quartile decrease slightly. The mean and the median are similar, suggesting a normally distributed population. This again highlights the need for a larger population which is more robust against sample bias. The matric potential at 10 kPa was expected to match better to the Lexan class. However, comparing the NMR mobile water median value of the Lexan bores to the matric potential results suggest a better match for the matric potential at 70 kPa rather than at 10 kPa. This is partly attributed to the high permeability of the coarse textured sediment that hinders the accurate laboratory measurement of the water content at full saturation (Hignett, pers. comm. 2013).

The comparative box plots for the Class 4 medium sands are plotted in Figure 17-117. The median values between the 2013 and matching 2011 NMR mobile water are very similar (0.178 vs. 0.164). This supports the comparability between the 2013 and recalibrated 2011 mobile water results. The 2011 Central and 2011 All groups have median values of 0.188 and 0.172 respectively, which are very similar. In fact, the four populations, i.e. 2013, 2011_Match, 2011_Central and 2011_All with sample sizes ranging from 285 to 738, have similar lower and upper quartiles and median values. This suggests that the natural scatter of mobile water content for the medium sand is much lower compared to the coarse sand. Nonetheless, the inter-quartile range of the 2011_All data is the lowest (0.119) amongst the four population classes, suggesting that the larger population is more statistically robust. The mobile water median values of the two Lexan boreholes and the laboratory matric potentials match well (0.201 for Lexan, 0.204 at 10 kPa, 0.220 at 70 kPa), but the range and quartiles do not as there are only 4 laboratory samples. This highlights the natural scatter between small populations which can be a bias due to any anomalous result present. Nonetheless, the good match between two separate techniques, i.e. less than an order of magnitude, suggests a reasonable comparability between the two data sets.

For the Class 3 fine sands, the mobile water median values of the data classes 2013 and 2011_Match are similar (0.162 and 0.146), and the different lower and upper quartile vary (Figure 17-118). The 2011_Match has a smaller inter-quartile range and less scatter. This shows that both the 2013 and corrected 2011 data are compatible and the calibration issue has been largely resolved for this texture class. As the population size progressively increases from 108 to 409 for the 2011_Match, 2011_Central, and 2011_All, so does the range. Nevertheless, the median and inter-quartile range remains similar. Median values are 0.146, 0.132, 0.157 and inter-quartile values are 0.125, 0.144, and 0.148 respectively. This shows that the scatter has increased slightly for the entire population, which also resulted in a slight increase in the median. The median values of the matric potentials at 10 kPa are slightly higher than the NMR mobile water for the Lexan boreholes (0.133 and 0.115 respectively) which is expected from the small number of laboratory samples (N = 4). Nonetheless, the data has a small spread suggesting the consistency of the mobile water in the fine sand. The value at 10 kPa is more comparable to the central population group, where the Lexan bores are situated.

The median values of NMR mobile water for the Class 2 muddy sands are consistently low across the five NMR population classes (Figure 17-119). The median values range from 0.041 to 0.076. However, the classes all contain high maximum values similar to the fine to coarse sand texture classes. Mineralogical differences may occur amongst the muddy sand and could account for the high mobile water content. Those that contain clay minerals would have lower mobile water whereas those that contain quartz silt, albeit the much smaller pore sizes may have relatively high amount of mobile water. The range in the matric potential data, despite only 3 samples being analysed, suggest that effective porosity is variable for this texture class.

The median values of mobile water are low for the Class 1 muds (0.013 to 0.029) and are especially low for the central area and across the entire BHMAR study area (Figure 17-120). Similar to the muddy sand, the mud groups may contain a small proportion of high mobile water. This may be attributed to the mineral composition. Stiff clay that contains kaolinite and a high proportion of shrink-swell montmorillonite will result in very low mobile water. On the other hand, a texture that is predominantly made up of quartz silt may have higher mobile water content. No matric potential analysis was undertaken on the muds, as the method is appropriate for coarser sediments.

Overall, the NMR and laboratory matric potential results at 10 kPa and 70 kPa are consistent and compatible with the NMR mobile water data across the 5 groups. Median, lower and upper quartiles vary slightly amongst the groups and this scatter is considered as natural variability. The effect of local bias on the median

and quartile values due to smaller populations have been identified. A larger population will be able to capture the natural variation of mobile water contents. Hence, the summary statistics of the largest population, in this case the 2011_All data, are thus most representative of the mobile water in a heterogeneous aquifer system.

The mobile water of the corrected 2011 data, which consist of 26 NMR-logged bores, including 14 bores located in the central GWR1 target area and 12 bores distributed elsewhere across the BHMAR study area, is assessed to be the most representative of effective porosity of the target semi-confined aquifer. As such, this data, excluding the unsaturated zone values and the 3 bores drilled using the mud-rotary rig, are used as a surrogate for effective porosity.

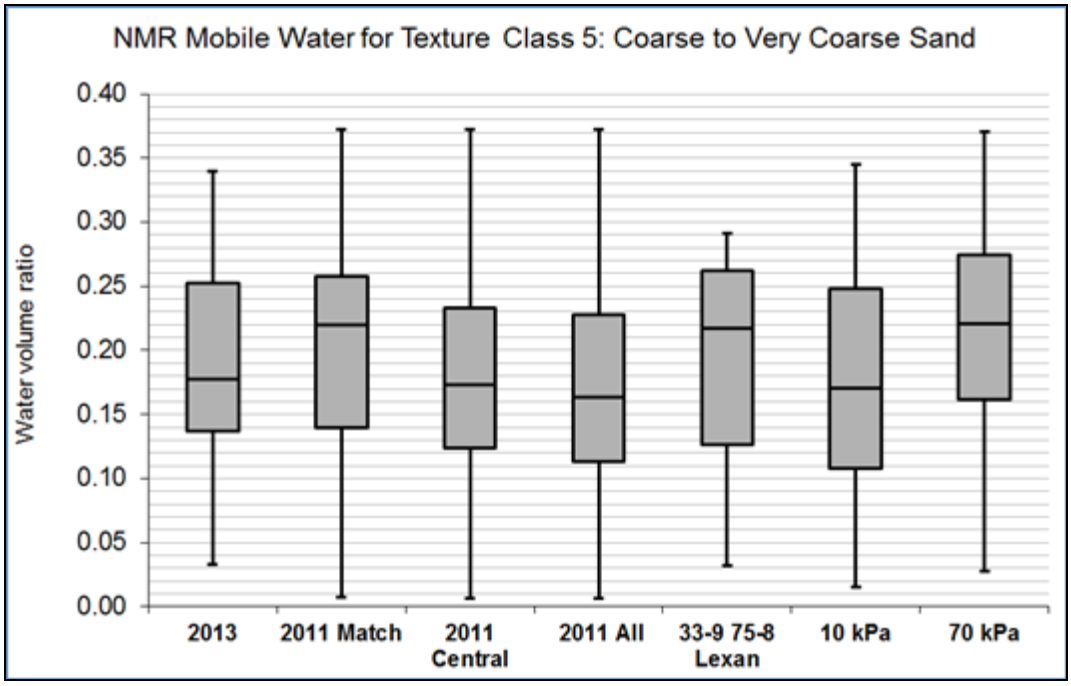



**Figure 17-116.** *Box plots of NMR mobile water distribution for texture class 5 (coarse sands to gravels) across various data groups. Also included are the laboratory porosities at 10 kPa and 70 kPa matric potentials.*

**Table 17-42.** *Summary statistics of NMR mobile water for Class 5 coarse sand to very coarse sand for 5 data populations. Also included are the laboratory porosities at 10 kPa and 70 kPa matric potentials.*

| | 2013 | 2011 Match | 2011 Central | 2011 All | Lexan | 10 kPa | 70 kPa |
|---|---|---|---|---|---|---|---|
| **Maximum** | 0.340 | 0.372 | 0.372 | 0.372 | 0.291 | 0.345 | 0.371 |
| **Upper Quartile** | 0.252 | 0.257 | 0.233 | 0.228 | 0.262 | 0.248 | 0.274 |
| **Median** | 0.178 | 0.220 | 0.173 | 0.163 | 0.217 | 0.170 | 0.220 |
| **Lower Quartile** | 0.137 | 0.139 | 0.124 | 0.113 | 0.126 | 0.108 | 0.162 |
| **Minimum** | 0.033 | 0.008 | 0.007 | 0.007 | 0.032 | 0.016 | 0.027 |
| **Inter Quartile** | 0.115 | 0.118 | 0.109 | 0.115 | 0.136 | 0.141 | 0.112 |
| **Mean** | 0.187 | 0.199 | 0.176 | 0.168 | 0.196 | 0.184 | 0.212 |
| **Mode** | 0.13 | 0.2304 | 0.2304 | 0.1368 | N/A | N/A | N/A |
| **Standard Deviation** | 0.073 | 0.078 | 0.076 | 0.076 | 0.074 | 0.092 | 0.090 |
| **Count** | 143 | 129 | 245 | 469 | 54 | 11 | 11 |

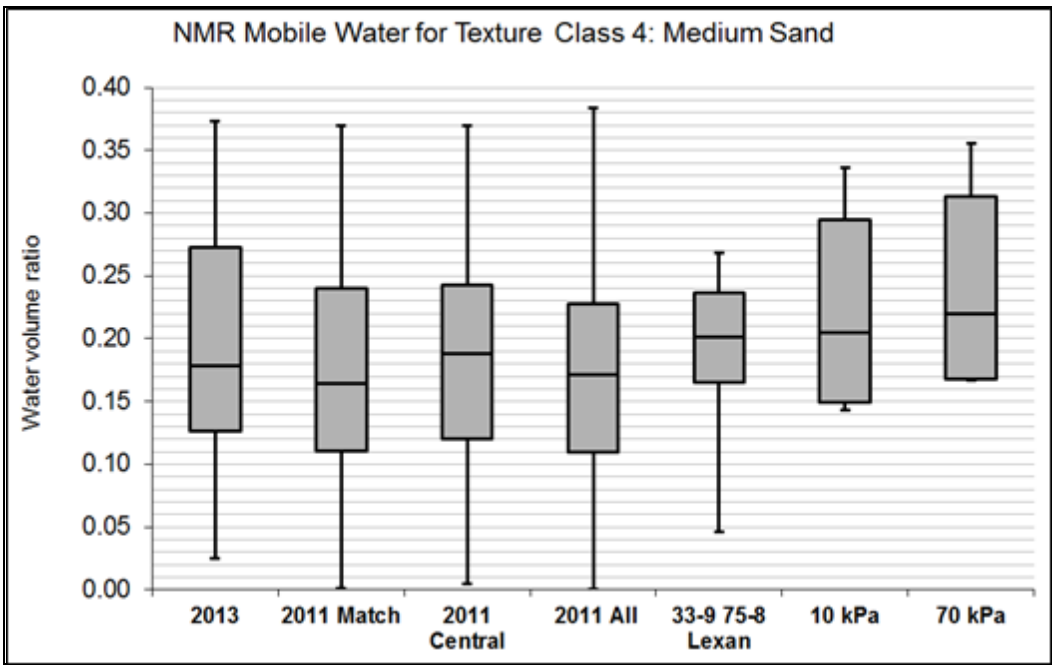



**Figure 17-117.** *Box plots of NMR mobile water distribution for texture class 4 (medium sands) across various data groups. Also included are the laboratory porosities at 10 kPa and 70 kPa matric potentials.*

**Table 17-43.** *Summary statistics of NMR free water for Class 4 medium sands for 5 data populations. Also included are the laboratory porosities at 10 kPa and 70 kPa matric potentials.*

| | 2013 | 2011 Match | 2011 Central | 2011 All | Lexan | 10 kPa | 70 kPa |
|---|---|---|---|---|---|---|---|
| **Maximum** | 0.373 | 0.370 | 0.370 | 0.384 | 0.268 | 0.336 | 0.356 |
| **Upper Quartile** | 0.273 | 0.240 | 0.242 | 0.228 | 0.236 | 0.295 | 0.313 |
| **Median** | 0.178 | 0.164 | 0.188 | 0.172 | 0.201 | 0.204 | 0.220 |
| **Lower Quartile** | 0.127 | 0.111 | 0.121 | 0.109 | 0.165 | 0.149 | 0.168 |
| **Minimum** | 0.025 | 0.001 | 0.005 | 0.000 | 0.046 | 0.143 | 0.167 |
| **Inter Quartile** | 0.146 | 0.129 | 0.122 | 0.119 | 0.072 | 0.146 | 0.145 |
| **Mean** | 0.194 | 0.173 | 0.182 | 0.170 | 0.193 | 0.222 | 0.240 |
| **Mode** | 0.12 | 0.2004 | 0.2004 | 0.144 | N/A | N/A | N/A |
| **Standard Deviation** | 0.088 | 0.083 | 0.082 | 0.083 | 0.054 | 0.079 | 0.079 |
| **Count** | 285 | 311 | 340 | 738 | 24 | 4 | 4 |

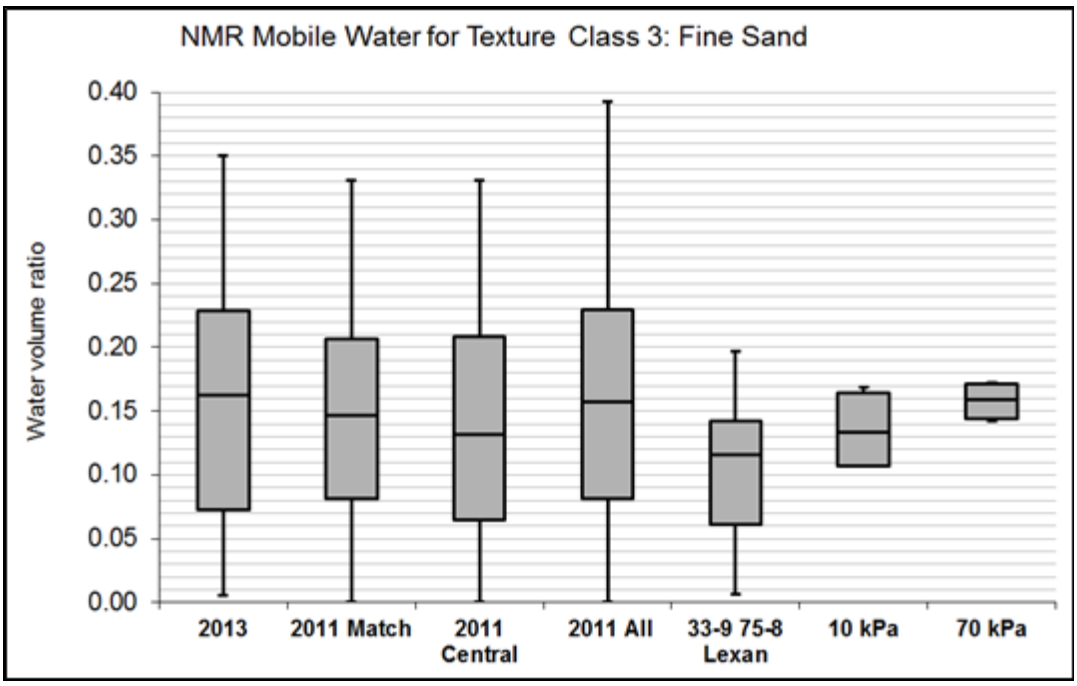



**Figure 17-118.** *Box plots of NMR mobile water distribution for texture class 3 (fine sands) across various data groups. Also included are the laboratory porosities at 10 kPa and 70 kPa matric potentials.*

**Table 17-44.** *Summary statistics of NMR mobile water for Class 3 fine sands for 5 data populations. Also included are the laboratory porosities at 10 kPa and 70 kPa matric potentials.*

| | 2013 | 2011 Match | 2011 Central | 2011 All | Lexan | 10 kPa | 70 kPa |
|---|---|---|---|---|---|---|---|
| **Maximum** | 0.350 | 0.331 | 0.331 | 0.392 | 0.197 | 0.169 | 0.172 |
| **Upper Quartile** | 0.229 | 0.206 | 0.209 | 0.229 | 0.142 | 0.164 | 0.172 |
| **Median** | 0.162 | 0.146 | 0.132 | 0.157 | 0.115 | 0.133 | 0.159 |
| **Lower Quartile** | 0.073 | 0.082 | 0.065 | 0.081 | 0.061 | 0.107 | 0.144 |
| **Minimum** | 0.006 | 0.000 | 0.000 | 0.000 | 0.006 | 0.107 | 0.142 |
| **Inter Quartile** | 0.156 | 0.125 | 0.144 | 0.148 | 0.081 | 0.057 | 0.027 |
| **Mean** | 0.160 | 0.144 | 0.139 | 0.158 | 0.111 | 0.136 | 0.158 |
| **Mode** | 0.0999 | 0.1572 | 0.1992 | 0.000 | N/A | N/A | N/A |
| **Standard Deviation** | 0.093 | 0.088 | 0.087 | 0.100 | 0.057 | 0.029 | 0.014 |
| **Count** | 112 | 108 | 168 | 409 | 22 | 4 | 4 |

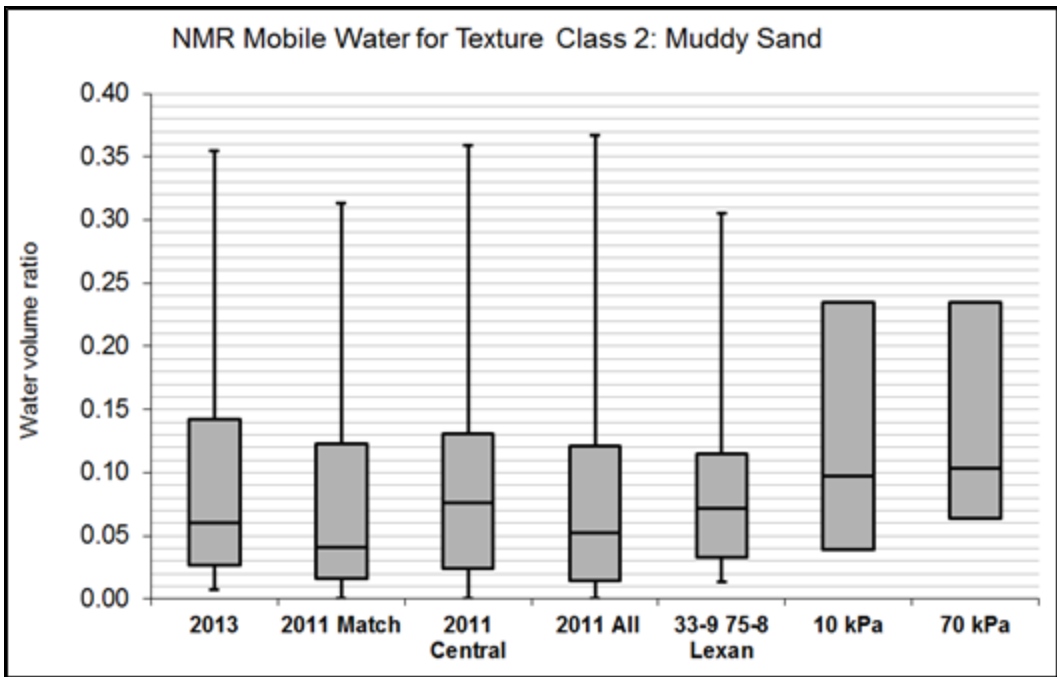



**Figure 17-119.** *Box plots of NMR mobile water distribution for texture class 2 (muddy sands) across various data groups. Also included are the laboratory porosities at 10 kPa and 70 kPa matric potentials.*

**Table 17-45.** *Summary statistics of NMR mobile water for Class 2 muddy sands for 5 data populations. Also included are the laboratory porosities at 10 kPa and 70 kPa matric potentials.*

| NMR Data Mobile Water | 2013 | 2011 Match | 2011 Central | 2011 All | Lexan | 10 kPa | 70 kPa |
|---|---|---|---|---|---|---|---|
| **Maximum** | 0.354 | 0.313 | 0.359 | 0.367 | 0.305 | 0.235 | 0.235 |
| **Upper Quartile** | 0.142 | 0.123 | 0.131 | 0.121 | 0.115 | 0.235 | 0.235 |
| **Median** | 0.061 | 0.041 | 0.076 | 0.052 | 0.072 | 0.097 | 0.104 |
| **Lower Quartile** | 0.027 | 0.016 | 0.024 | 0.014 | 0.033 | 0.039 | 0.064 |
| **Minimum** | 0.007 | 0.000 | 0.000 | 0.000 | 0.014 | 0.039 | 0.064 |
| **Inter Quartile** | 0.115 | 0.107 | 0.107 | 0.107 | 0.081 | 0.196 | 0.171 |
| **Mean** | 0.091 | 0.073 | 0.088 | 0.076 | 0.095 | 0.124 | 0.134 |
| **Mode** | N/A | 0 | 0.02148 | 0.000 | N/A | N/A | N/A |
| **Standard Deviation** | 0.079 | 0.072 | 0.072 | 0.075 | 0.087 | 0.082 | 0.073 |
| **Count** | 179 | 221 | 359 | 659 | 35 | 3 | 3 |

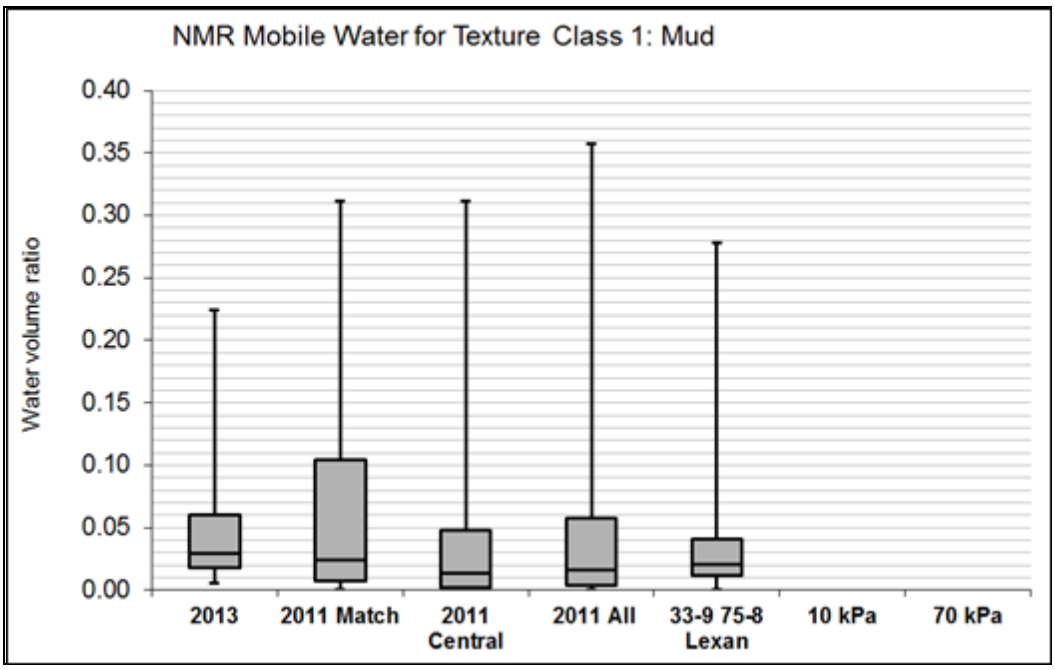



**Figure 17-120.** *Box plots of NMR mobile water distribution for hydraulic texture class 1 (muds) across various data groups. Also included are the laboratory porosities at 10 kPa and 70 kPa matric potentials.*

**Table 17-46.** *Summary statistics of NMR mobile water for Class 1 muds for 5 data populations. Also included are the laboratory porosities at 10 kPa and 70 kPa matric potentials.*

| NMR Data Mobile Water | 2013 | 2011 Match | 2011 Central | 2011 All | Lexan | 10 kPa | 70 kPa |
|---|---|---|---|---|---|---|---|
| **Maximum** | 0.224 | 0.312 | 0.312 | 0.358 | 0.278 | | |
| **Upper Quartile** | 0.061 | 0.105 | 0.048 | 0.058 | 0.041 | | |
| **Median** | 0.029 | 0.024 | 0.013 | 0.016 | 0.021 | | |
| **Lower Quartile** | 0.018 | 0.007 | 0.002 | 0.004 | 0.011 | | |
| **Minimum** | 0.005 | 0.000 | 0.000 | 0.000 | 0.001 | | |
| **Inter Quartile** | 0.043 | 0.097 | 0.046 | 0.054 | 0.030 | | |
| **Mean** | 0.052 | 0.063 | 0.041 | 0.048 | 0.054 | | |
| **Mode** | 0.02 | 0 | 0 | 0.000 | N/A | | |
| **Standard Deviation** | 0.052 | 0.078 | 0.062 | 0.072 | 0.073 | | |
| **Count** | 165 | 145 | 321 | 659 | 51 | 0 | 0 |

## 17.12 DIFFUSION RATE WITHIN UPPER CONFINING AQUITARD

The maintenance of a zone of fresh shallow groundwater due to river leakage may induce a persistent salinity gradient for diffusion of salt from the upper confining aquitard sequence to be maintained. Hence, an understanding of possible diffusion rates in the context of the geological timeframes relating to the various river migration phases is required.

The diffusion of solute through water under steady state conditions is defined by Fick's first law:

$F = -D\, dC/dx$

**Equation 108**

Where $F$ is the mass flux of solute per unit area per unit time ($m^3/m^2/s$), $D$ is the diffusion coefficient ($m^2/s$), $C$ is solute concentration ($g/m^3$), $dC/dx$ is the concentration gradient ($g/m^3/m$). The negative sign indicates movement from greater to lesser solute concentrations (Fetter, 2001). For major ions, $D$ ranges between $1x10^{-9}$ and $2x10^{-9}$ $m^2/s$ at 25 ºC. Li &Gregory (1974) report a value of $1.2x10^{-9}$ $m^2/s$ for seawater diffusing into distilled water.

An effective diffusion coefficient ($D_e$) is used to translate to diffusion through porous media, rather than only through a liquid phase:

$D_e=\omega D$

**Equation 109**

Where $\omega$ is an empirical coefficient, with typical values ranging 0.01-0.5 inferred from laboratory studies (Freeze & Cherry, 1979). Using the seawater diffusion coefficient of Li & Gregory (1974) as a reference, this would equate to a range of $D_e$ of $1.2x10^{-11}$ to $6x10^{-10}$. To derive a reasonable effective diffusion coefficient, the most commonly used is the empirical relationship with porosity $ø$ (Groen *et al.*, 2000):

$D_e = Dø^m$

**Equation 110**

Across a number of studies, values for $D_e$ range between $5x10^{-10}$ and $13x10^{-10}$ $m^2/s$ (Groen *et al.*, 2000). In compacted clays, $m$ is relatively high. For example $m$~2 was used for clay-rich tills, with porosities ranging 0.3-0.35 resulting in $D_e/D$ ratios of ~0.1 (Remenda *et al.*, 1996). The $m$ exponent is closer to unity in less consolidated clays (Appelo & Postma, 1993).

Diffusion depends on the relative concentration gradient ($C/C_0$) for the solute so that diffusion time ($t$) can be derived from:

$$\frac{C}{C_0} = erfc\left(\frac{x}{2\sqrt{D_e t}}\right)$$

**Equation 111**

Where *erfc* is the complementary error function and $x$ is distance (Crank, 1956). Equation 111 forms the basis for estimating diffusion rates through the upper confining aquitard sequence. In this context, the relative concentration gradient ($C/C_0$) relate to end member salinities within the upper confining aquitard and $x$ is the vertical distance within the profile where diffusion has occurred during time, $t$.

Equation 110 was used as the basis to derive a reasonable estimate of the effective diffusion coefficient $D_e$. Figure 17-121 summarises a sensitivity analysis undertaken by varying the power exponent $m$ for various porosity $ø$ values, the latter ranging between 0.3 and 0.7. This would suggest that a range in $D_e$ of between $2x10^{-10}$ and $8x10^{-10}$ $m^2/s$ (with an average of $5x10^{-10}$ $m^2/s$) would be reasonable as an initial estimate, in the absence of field data.

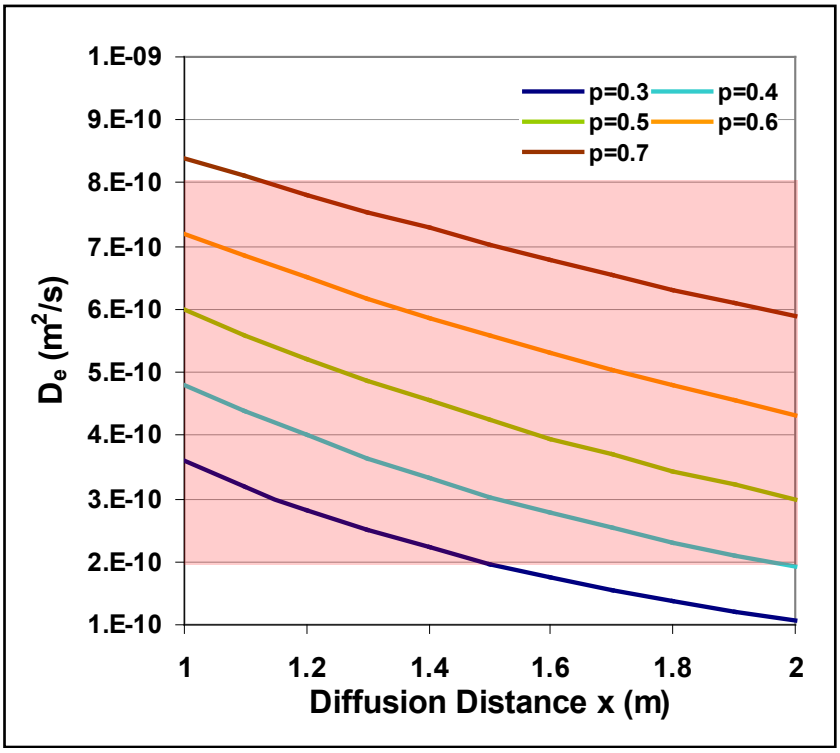



**Figure 17-121.** *Relationship between power exponent (m) and effective dispersion coefficient ($D_e$) for various porosities ranging between 0.3 to 0.7. Red shaded area is the $D_e$ range between $2x10^{-10}$ and $8x10^{-10}$.*

The pore fluid data can be used to estimate the relative concentration gradient ($C/C_0$). Figure 17-122 is a box and whisker plot for pore fluid salinity (TDS, mg/L) for samples obtained from the Blanchetown Clay formation. These have been grouped, in conjunction with the available groundwater, surface water and rainfall samples, into classes defined by fuzzy k-means (refer Section 14.5.1). Table 17-47 provides a statistical summary for these groupings of pore fluids. Of these classes, 8e is the freshest and has the closest affinity with river leakage, and 8f is the most saline and representative of regional evolved groundwaters which tend to occur at depth or peripheral to modern drainage. The statistics for these two classes were used to define the relative concentration gradient. For example, the median salinity for the fresh end-member (Group 8e, 152 mg/L) and the saline end-member (Group 8f, 20860 mg/L) derived a relative concentration gradient of 0.007 (Table 17-47).

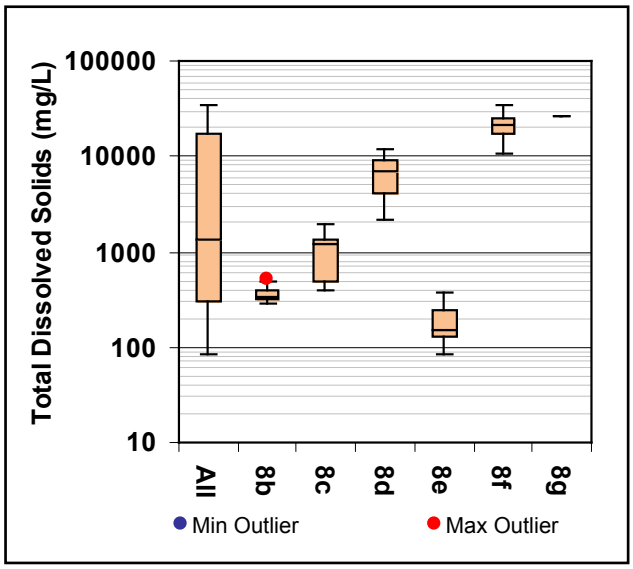



**Figure 17-122.** *Box and whisker plot of salinity (mg/L) of Blanchetown Clay pore fluids, classified by fuzzy k-means.*

***Table 17-47*** *Summary statistics for salinity of Blanchetown Clay pore fluids classified by fuzzy k-means.*

| | All | 8b | 8c | 8d | 8e | 8f | 8g | 8e/8f |
|---|---|---|---|---|---|---|---|---|
| **Count** | 87 | 10 | 13 | 8 | 17 | 26 | 1 | |
| **Minimum** | 84 | 283 | 385 | 2110 | 84 | 10541 | 26953 | |
| **$Q_1$** | 300 | 312 | 497 | 3993 | 127 | 17090 | 26953 | .005 |
| **Median** | 1314 | 344 | 1184 | 6885 | 152 | 20860 | 26953 | .007 |
| **$Q_3$** | 17058 | 386 | 1314 | 9311 | 245 | 25580 | 26953 | .014 |
| **Maximum** | 35033 | 526 | 1935 | 11868 | 369 | 35033 | 26953 | |

Figure 17-123 plots the results of using Equation 111 with an effective diffusion coefficient $D_e$ of $5x10^{-10}$ $m^2/s$. The diffusion distance over varying time frames from 100 years to 1 million years is shown in Figure 17-123a. Also plotted is the expected range of the relative concentration gradient ($C/C_0$) based on the first quartile, median and third quartile statistics for the fresh and saline end members of the Blanchetown Clay pore fluids (Table 17-47). This plot suggests that over 1000 years the diffusion distance in the Blanchetown Clay profile is about 5 m and over 100,000 years is about 17 m.

Figure 17-123b uses the same equation and parameters, but relates to timeframes ascribed to the Coonambidgal Formation lateral migration phases (refer Section 12.2, Lawrie *et al*., 2012b), to provide some hydrogeological context. The age ranges for these phases are:

- Coonambidgal 1: 5-7 to 2.2 ka
- Coonambidgal 2: 21.3 to 17.9 ka
- Coonambidgal 3: 32 to 25 ka
- Coonambidgal 4: 50 to 40 ka

The onset of the migration phase (i.e. the oldest age) is used in this analysis. Figure 17-123b would suggest that diffusion associated with leakage from river reaches where only the Coonambidgal 1 phase occurs would be in the order of about 7 m, in contrast with about 15 m in reaches where the geomorphological history goes back to the Coonambidgal 4 migration phase.

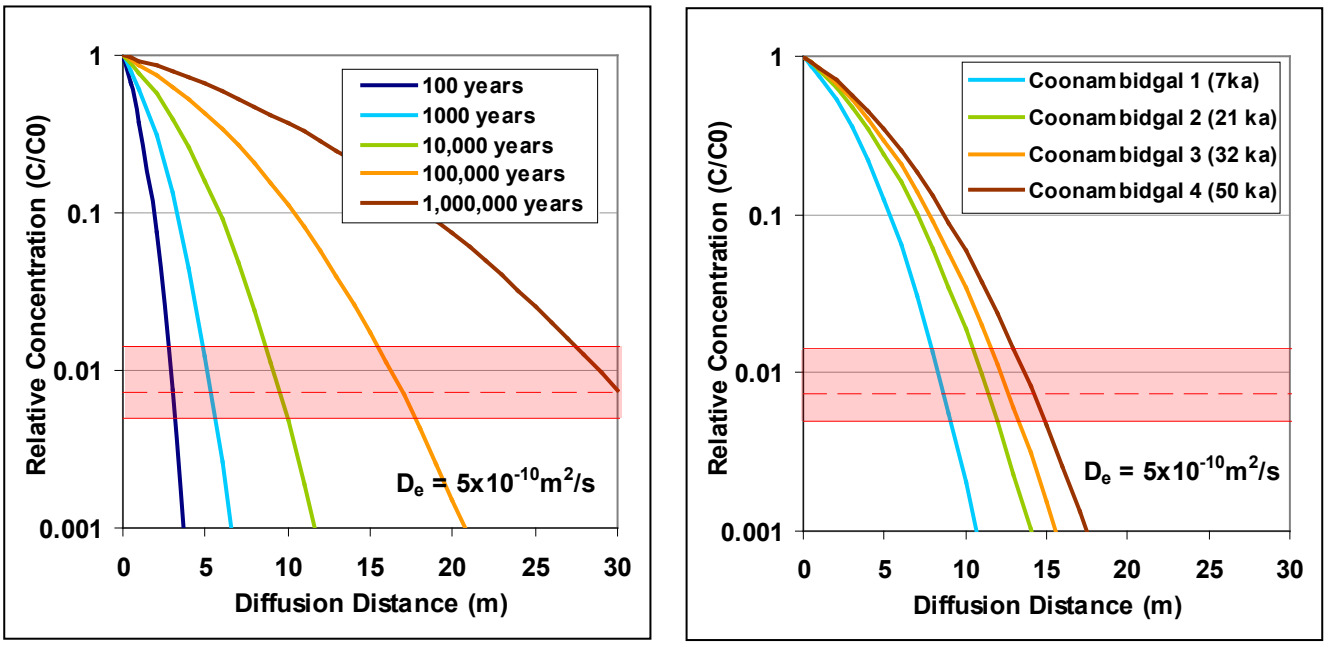



**Figure 17-123** *Diffusion distance over different time frames for Blanchetown Clay (a) 100 years to 1 million years (b) timeframes relating to Coonambidgal lateral migration phases. The red shaded area represents the expected range of concentration gradient ($C/C_0$) based on the pore fluid statistics (Table 17-47).*

Equation 111 is also used to generate Figure 17-124 which plots diffusion distance against diffusion time. In this case, different combinations of *De* and *C/C0* were used to derive a likely range for the upper confining aquitard. These combinations are reported in Table 17-48. The low estimate corresponds to a power trend of $t=2.554x^4$ and the high estimate of $t=1.087x^4$ where $t$ is diffusion time (years) and $x$ is the diffusion distance (m). These power trends have been applied to the mapped thickness of the upper confining aquitard to generate an estimate of diffusion rates spatially across the study area (Figure 17-125 and Figure 17-126).

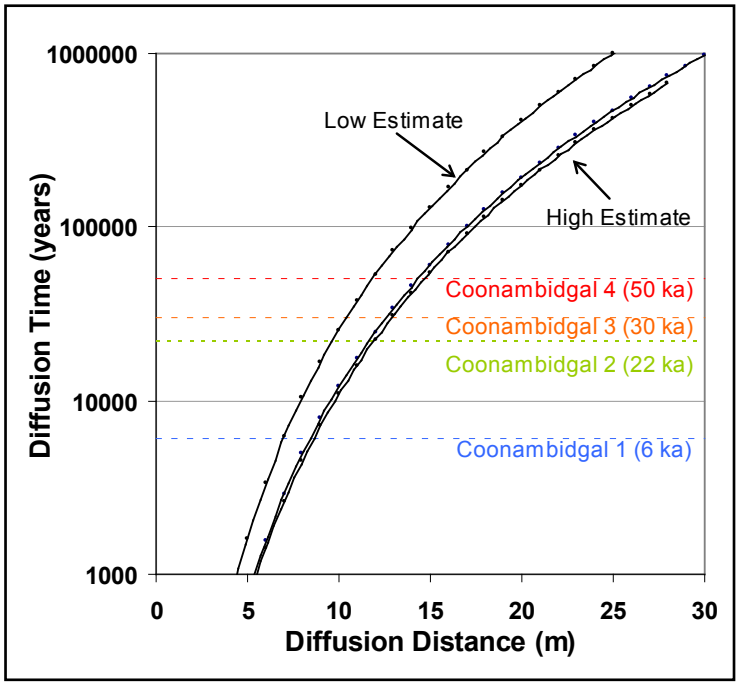



**Figure 17-124.** *Plots of diffusion distance against diffusion time for the upper confining aquitard.*

**Table 17-48.** *Combinations of $D_e$ and $C/C_0$ used to derive diffusion distances in the upper confining aquitard.*

| | $D_e$ | $C/C_0$ |
|---|---|---|
| **Low** | $2x10^{-10}$ | 0.005 |
| **Average** | $5x10^{-10}$ | 0.007 |
| **High** | $8x10^{-10}$ | 0.014 |

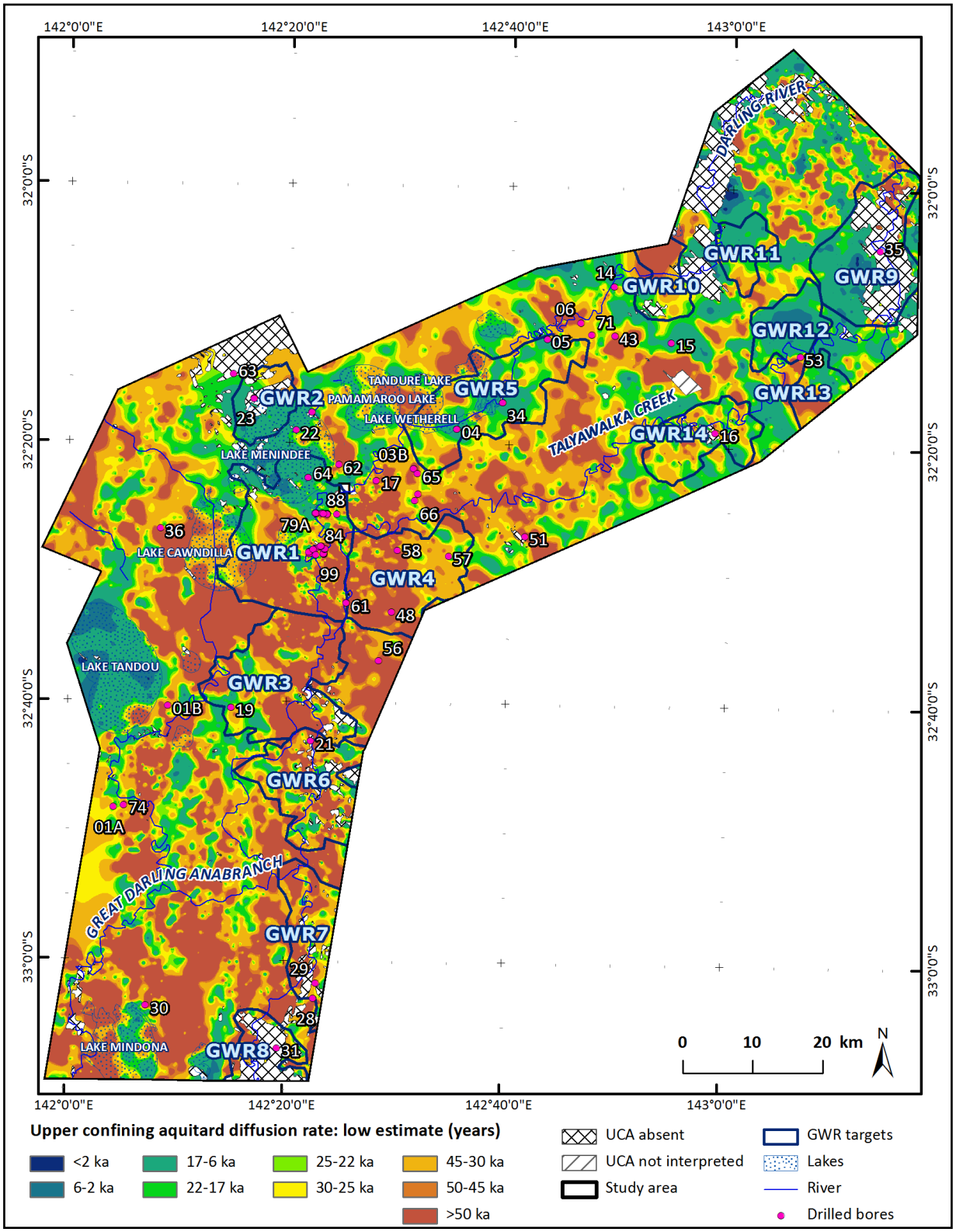



**Figure 17-125.** *Time required for complete diffusion of the upper confining aquitard using a low estimate ($t$=2.554x$^4$), where t is the diffusion rate in time and x is the thickness of the upper confining aquitard. Rates of diffusion have been classified into periods corresponding with the different Coonambidgal Phases.*

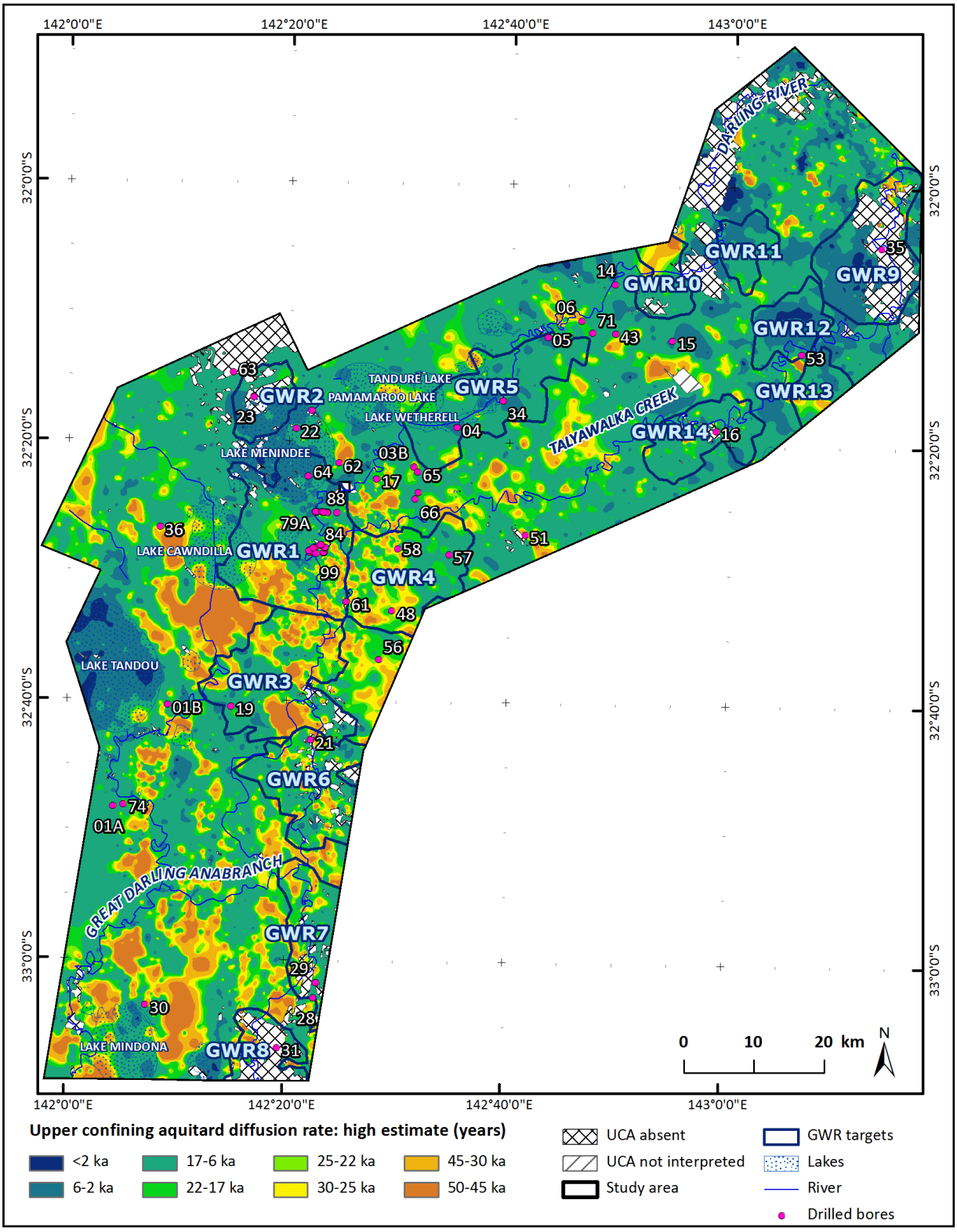



**Figure 17-126.** *Time required for complete diffusion of the upper confining aquitard using a high estimate ($t$=1.087x$^4$), where t is the diffusion rate in time and x is the thickness of the upper confining aquitard. Rates of diffusion have been classified into periods corresponding with the different Coonambidgal Phases.*

## 17.13 GROUNDWATER VOLUME ESTIMATION

Data acquisition by the BHMAR project, particularly the AEM survey (Appendix 3, Apps *et al.*, 2012c), sonic drilling (Appendix 1, Halas *et al.,* 2012a; Appendix 2, Spulak *et al*., 2012), pore fluid chemical analysis (Appendix 6, Somerville *et al.,* 2012) and the NMR downhole geophysics (Appendix 3, Apps *et al.,* 2012b) has provided an opportunity to improve the characterisation of groundwater salinity in the Darling River floodplain. Figure 17-127 summarises the workflow used to map groundwater salinity and to estimate groundwater storage volumes for particular salinity thresholds within target or borefield areas. As indicated in Figure 17-127, there are three main components of the workflow (1) defining groundwater salinity thresholds based on AEM conductivity (2) the calculating of bulk volumes and (3) the estimation of effective porosities to translate bulk volumes to groundwater storage volumes.

### 17.13.1 Groundwater Salinity Thresholds

The groundwater salinity mapping and groundwater volume estimates are reported relative to water quality criteria. The objective was to map good quality (<600 mg/L), acceptable quality (600-1200 mg/L) and brackish (1200-3000 mg/L) groundwater salinity within the target and borefield areas. The first two salinity thresholds (600 and 1200 mg/L) are based on the ADWG 2011 drinking water guidelines This mapping requires establishing a relationship between groundwater salinity and the bulk conductivities as mapped by the AEM depth slices.

In the BHMAR project area, Lewis *et al*. (2008) previously reported that of the 198 bores in the Darling alluvial aquifers, only half (84 of the 198) have salinity information, and that information is provided in broad categories of 0–500 mg/L, 0–1000 mg/L, 0–14,000 mg/L, 1000–10,000 mg/L and 10,000–100,000 mg/L, rather than specific measurements. Salinity-yield mapping (from Lewis *et al*., 2008; adapted from Brodie, 1994) indicated broad regional variation in groundwater salinity (Lawrie *et al*., 2009a). The distribution of bores and corresponding salinity values indicates that groundwater freshens proximal to surface water bodies, such as the Darling River. A general positive relationship between increasing depth and salinity is also apparent. These findings are consistent with previous investigations of the Darling floodplain (Brodie, 1994; Kellett, 1994; Jewell, 2007), and support the generalised conceptual understanding of groundwater systems in this region. However, Lawrie *et al*. (2009a) demonstrated that the data reliability for these maps is poor due to a paucity of data points from which these maps were drawn. Nevertheless, the salinity yield mapping provided a useful starting point for framing the BHMAR project study area and for planning the AEM survey.

AEM surveys maps the bulk electrical conductivity of the variably saturated geological profile. Hence, the AEM conductivity signal is a mix of contributions from the air, fluid and solid phases. For example, Archie's Law is a pioneering empirical relationship between bulk conductivity and rock and fluid properties:

$$C_t = \frac{1}{a} C_w \phi^m S_w^n$$

**Equation 112**

Where $C_t$ is the electrical conductivity of the fluid saturated rock material, $C_w$ is the electrical conductivity of the fluid phase (groundwater), $\phi$ is porosity, $S_w$ is the moisture content, $m$ is the exponent relating to cementation (typically 1.8-2), $n$ is the saturation exponent (typically ~2) and $a$ is the tortuosity factor (Archie, 1942). Hence, an understanding of the distribution of porosity, moisture content (such as position of the watertable) and degree of cementation is required. This relationship assumes that the rock material is non-conductive, so the presence of clay minerals, sulfides or graphite needs to be factored in. Other mixing models developed to understand the relationship between bulk conductivity and rock and fluid properties include those of Waxman & Smits (1968), Jin *et al*. (2007) and Kennedy (2007). This means that there is not usually a direct relationship between the AEM data and the mapping of groundwater salinity.

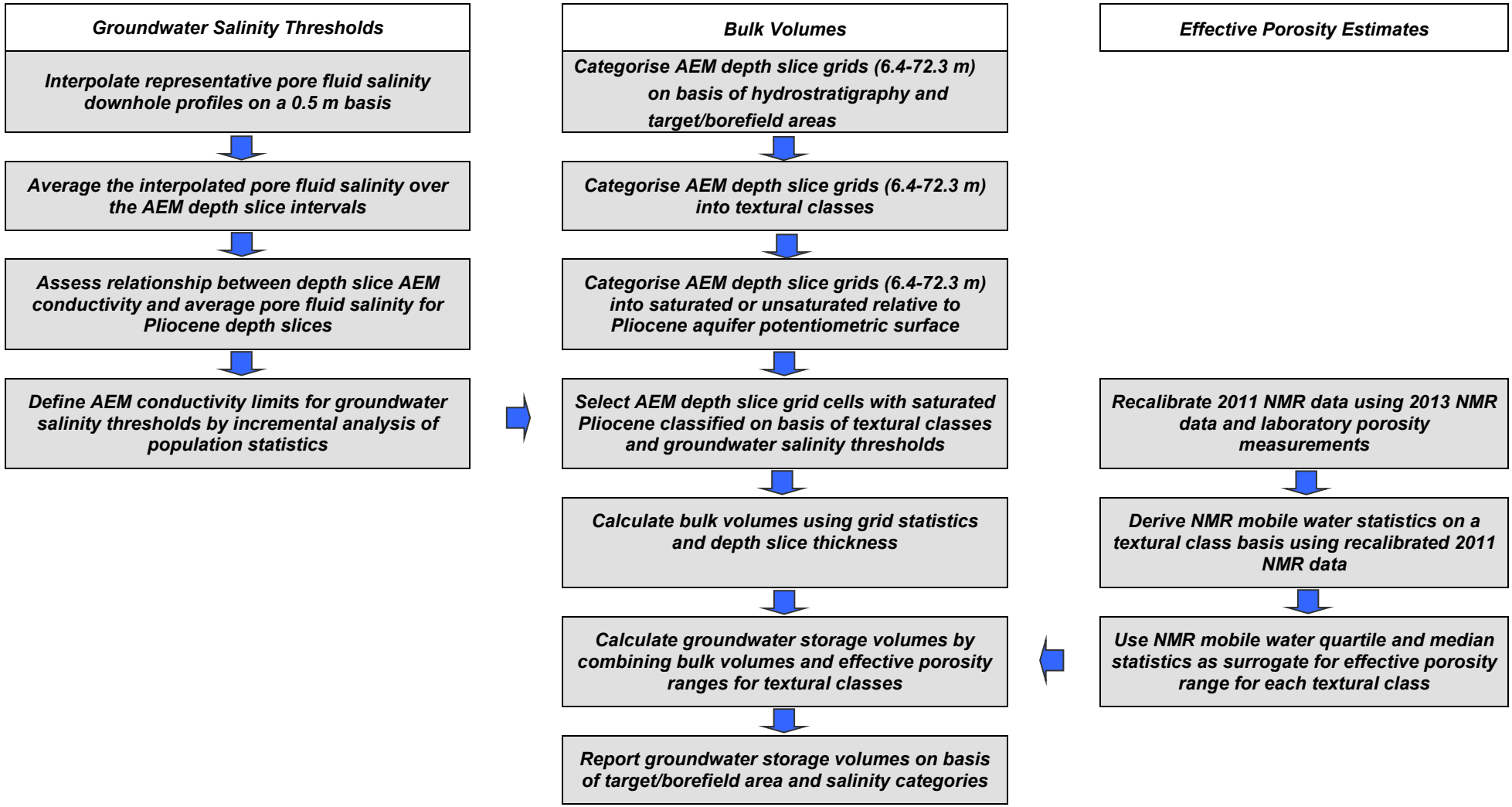



**Figure 17-127.** *Workflow for estimating target/borefield groundwater storage volumes for salinity thresholds.*

Various approaches have been taken to translate AEM conductivity into groundwater salinity mapping. For a regional AEM survey in western Queensland, Mullen & Kellett (2004) found a poor fit between pore fluid salinities and predictions based on expanded versions of Archie's Law, such as the theoretical relationships of Bussian (1983) and Sen *et al*. (1988). Their preferred approach was to use the results of a regression analysis ($R^2$ ~0.65) between measured groundwater salinity and the AEM conductivity at the relevant depth. Similar linear regression between AEM bulk conductivity and pore fluid chemistry data have been used in other studies (Paine, 2003; Cresswell *et al*., 2004). Palamara *et al*. (2010) used AEM conductivity and additional borehole observations, such as lithology, lithostratigraphy, weathering and depth to derive salt store mapping by linear regression. De Souza Filbo *et al*. (2010) applied a geostatistical approach using both kriging and stochastic methods to generate groundwater EC maps from helicopter electromagnetic data for a fractured rock aquifer study in northeast Brazil.

It is important to note that AEM is a conductivity mapping tool primarily, and although there is a relationship observed between the inverted AEM data and borehole induction data (Figure 17-128), there is greater uncertainty in mapping more resistive features. This is illustrated in uncertainty analysis of the inverted data (Figure 17-129). Particular caution must therefore be exercised in mapping 'good' (<600 mg/L) to 'acceptable' (600-1200 mg/L) groundwater quality as defined by ADWG2011, as this has greater uncertainties than more conductive features.

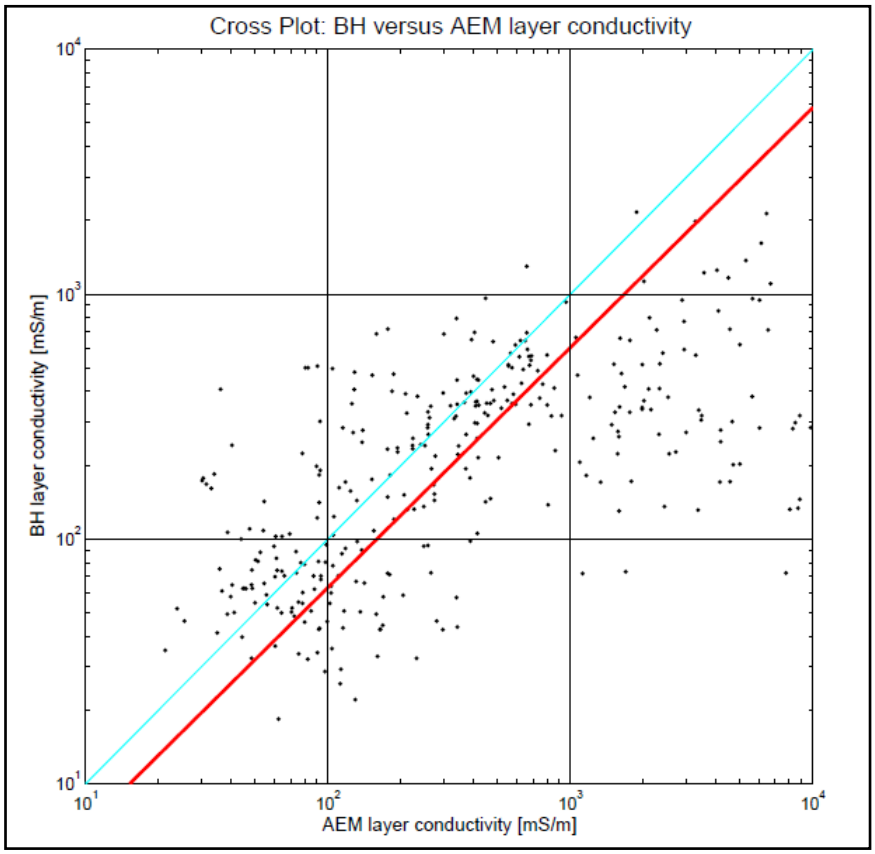



**Figure 17-128.** *Cross plot on a logarithmic scale of the AEM model conductivity as a function of the borehole model (BH) conductivity. The 1:1 correlation line is shown with a thin cyan line while the least squares linear fit, taking uncertainties on both parameters into account, is indicated with a thicker red line. The error bars have been omitted for clarity.*

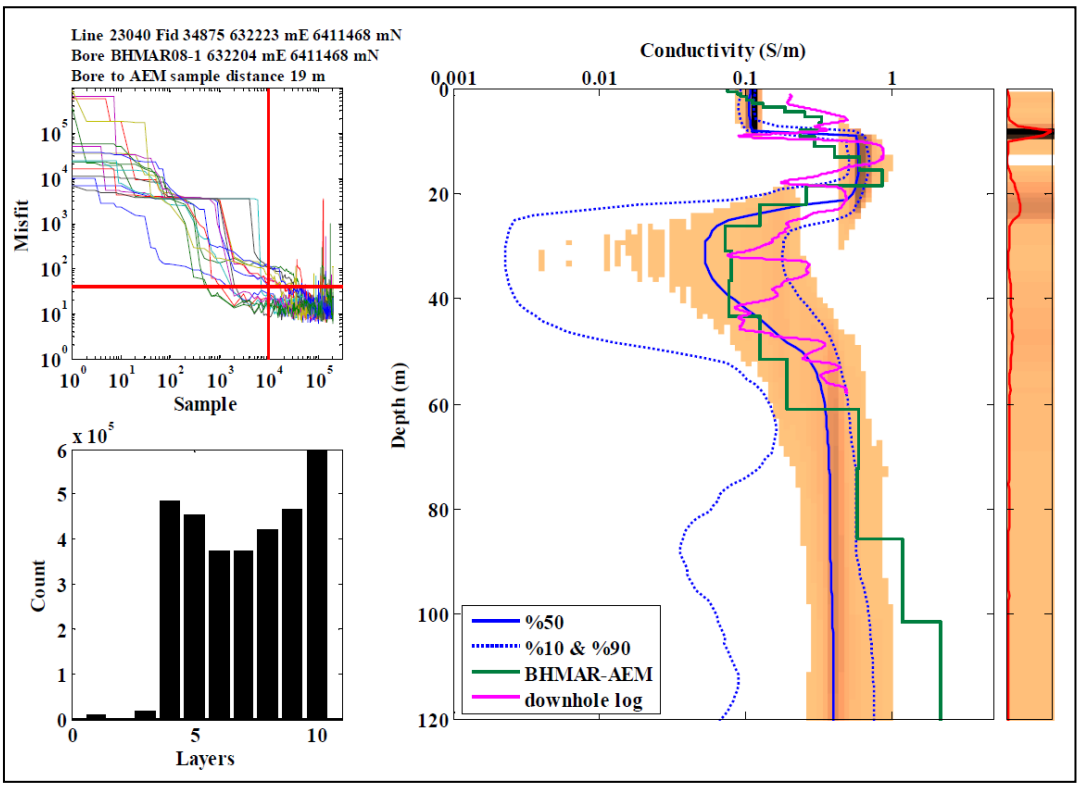



**Figure 17-129.** *Reversible Jump Markov Chain Monte Carlo (RJ-McMC) inversion of one of 9 representative sections in the AEM data. The centre panel shows the model domain down to 120 m depth with the nearest downhole conductivity log (magenta) and the 30 layer inversion model (green) produced by the gradient based inversion algorithm applied to the whole BHMAR data set.*

The salinity measurements of pore fluid samples extracted from specific sonic-cored samples was the starting point for the groundwater salinity mapping and storage volume estimates. Figure 17-130 provides an example of the analysis undertaken on the downhole pore fluid salinity data. Any suspect samples, typically saturation extracts, were excluded from a representative downhole profile. The downhole induction log was used as a guide to this selection process. Using the Excel Forecast function, the selected samples were used to interpolate downhole pore fluid salinity on a 0.5 m basis. These interpolated data points were then averaged over the AEM depth slice intervals.

This enabled, for each depth slice, a comparison between the AEM conductivity at the bore location and the averaged pore fluid salinity. This relationship is poor (Figure 17-131) as the AEM is measuring a bulk conductivity signal that integrates the contributions from a relatively large volume that is a mix of air, fluid and geological material. For the shallow stratigraphic units (Qdw, Qac, Qam, and Qaw) there is a tendency for pore fluid salinity to be significantly higher than the AEM conductivity for the relevant depth slice. This is because of the relatively resistive environment found above the watertable, probably due primarily to the unsaturated conditions. Some depth slices have relatively high AEM conductivities than what would be anticipated from the average pore fluid salinity. These tend to be deeper depth slices, mostly in the Renmark Group, and this is likely to be due to the greater uncertainties in resolving the AEM conductivity at these depths, or perhaps particular lithological characteristics of this formation.

In terms of groundwater resource assessment, the target is the semi-confined aquifer which predominantly consists of Calivil Formation (Lawrie *et al*., 2012d). Table 17-49 summarises the proportion, in each AEM depth slice interval for the sonic bores that are within the Calivil Formation. This shows that Calivil Formation pore fluids are dominant for the six AEM depth slices between 22 and 61 m. On this basis, the analysis was restricted to these six depth slices and Figure 17-132 plots this subset of data.

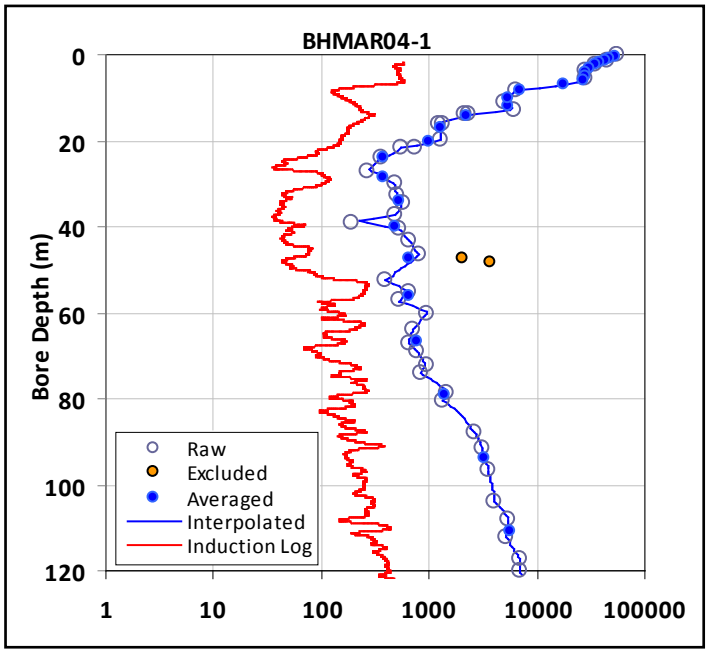



**Figure 17-130.** *Example of interpolating pore fluid salinity (TDS, mg/L) and deriving averages for AEM depth slices. The red line is the downhole induction log (mS/m) for the BHMAR04-1 bore and the blue line is the interpolated pore fluid salinity (TDS, mg/L).*

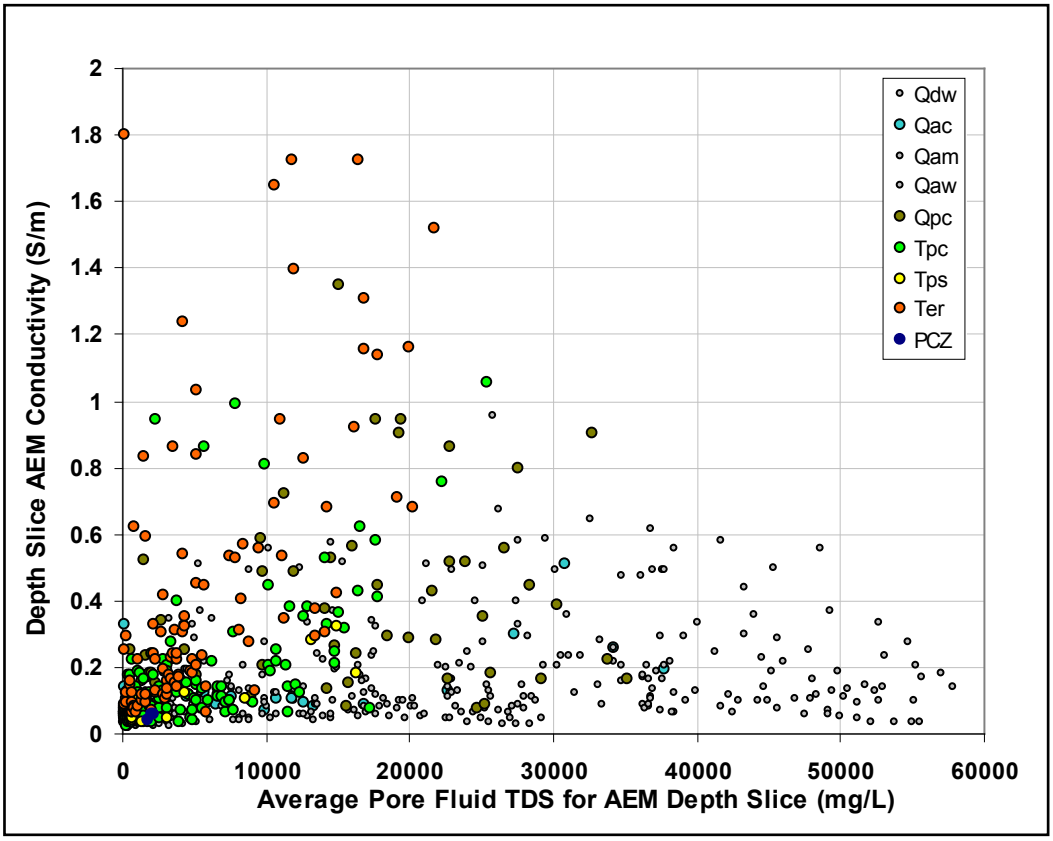



**Figure 17-131.** *Relationship between average pore fluid salinity (TDS, mg/L) and corresponding AEM depth slice conductivity value. Categorisation is based on the dominant stratigraphic unit in the AEM depth slice including Woorinen Formation (Qdw), Coonambidgal Formation (Qac), Menindee Formation (Qam), Willotia beds (Qaw), Blanchetown Clay (Qpc), Calivil Formation (Tpc), Loxton-Parilla Sands (Tps), Renmark Group (Ter) and pre-Tertiary (PCZ).*

The next step was to identify AEM conductivity thresholds that could be used as surrogates to map groundwater salinity zones for the depth slices of interest. Table 17-50 summarises the approach taken to categorise the data plotted in Figure 17-130, namely the average pore fluid salinity and corresponding AEM conductivity at the sonic hole locations for the AEM depth slices 22-61 m. Table 17-50 shows the number of data points within increments of AEM conductivity (e.g. 0.03-0.04 S/m) that have pore fluid salinities <600 mg/L, <1200 mg/L and <3000 mg/L. The challenge is to have an AEM conductivity threshold that captures as many of the data points that are within the TDS limit (e.g. <600 mg/L), without capturing too many that are above this. Using the 600 mg/L limit as an example, the 0.03 S/m threshold would be ideal as 100% of the data points are <600 mg/L (Table 17-50). The issue is that only three data points are within this increment of AEM conductivity. Using a 0.04 S/m threshold captures another 10 data points <600 mg/L but 9 data points are above this value. This would make 0.04 S/m the practical limit for mapping good quality groundwater as 41% of the data points are > 600 mg/L. As shown in Table 17-50, the cumulative percentage of <600 mg/L data points (column 7) progressively decreases as more AEM increments are incorporated. For the acceptable quality limit (<1200 mg/L), a threshold of 0.06 S/m is recommended as the proportion of samples below 1200 mg/L (96%) is good. For the next AEM increment (0.06-0.07 S/m) the proportion of samples within 1200 mg/L is reduced to 73%. Again, the cumulative percentage of <1200 mg/L data points (column 11) progressively decreases from this increment onwards. Using the same logic, a 0.09 S/m threshold is recommended for the brackish limit of 3000 mg/L (Table 17-50). Figure 17-133 is an example of these AEM conductivity thresholds applied to a specific AEM depth slice.

This approach is deliberately conservative to target relatively low AEM conductivity thresholds to represent good to acceptable quality groundwater salinity. Referring to Figure 17-130, it can be argued that higher AEM conductivity thresholds could be used to capture a greater population of incidences within the pore fluid salinity threshold (say 600 mg/L). However, in doing this, greater incidences of more saline pore fluids are also captured. The objective is to reduce the probability that the mapping of good quality groundwater is in reality incorporating zones of brackish to saline groundwater.

**Table 17-49:** *Proportion of pore fluid data points in AEM depth slices that are within the Calivil Formation.*

| AEM Depth Slice (m) | Depth From | Total Count | Calivil Count | %Calivil |
|---|---|---|---|---|
| 6.4-7.7 | 6.4 | 37 | 0 | 0 |
| 7.7-9.2 | 7.7 | 38 | 0 | 0 |
| 9.2-11 | 9.2 | 39 | 0 | 0 |
| 11-13.1 | 11 | 40 | 0 | 0 |
| 13.1-15.6 | 13.1 | 41 | 2 | 5 |
| 15.6-18.5 | 15.6 | 43 | 8 | 19 |
| 18.5-22 | 18.5 | 43 | 18 | 42 |
| 22-26.1 | 22 | 44 | 31 | 70 |
| 26.1-30.9 | 26.1 | 47 | 39 | 83 |
| 30.9-36.7 | 30.9 | 46 | 42 | 91 |
| 36.7-43.5 | 36.7 | 47 | 45 | 96 |
| 43.5-51.5 | 43.5 | 46 | 42 | 91 |
| 51.5-61 | 51.5 | 43 | 27 | 63 |
| 61-72.3 | 61 | 36 | 3 | 8 |
| 72.3-85.7 | 72.3 | 28 | 2 | 7 |
| 85.7-101.5 | 85.7 | 18 | 0 | 0 |
| 101.5-120.3 | 101.5 | 14 | 0 | 0 |

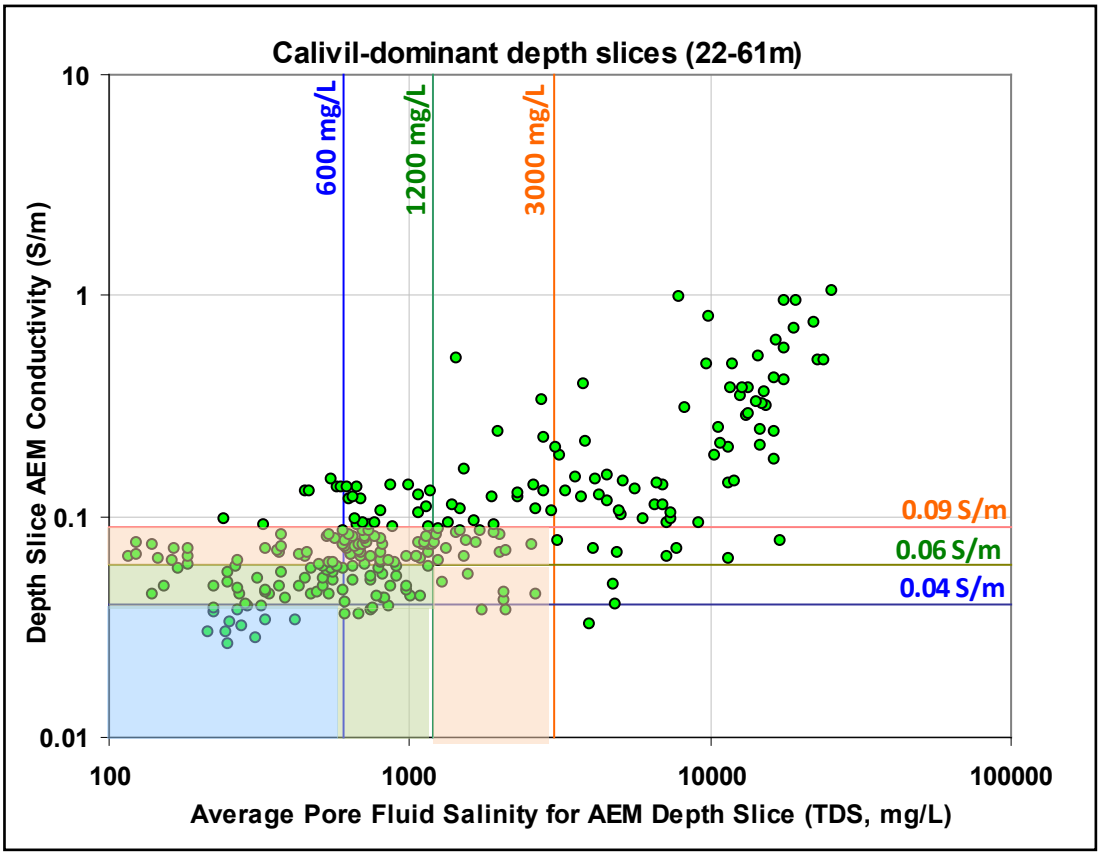



**Figure 17-132:** *Relationship between average pore fluid salinity (TDS, mg/L) and corresponding AEM depth slice conductivity value for Calivil-dominant AEM depth slices (22-61 m). Thresholds for pore fluid salinity (600, 1200 and 3000 mg/L) and for depth slice AEM conductivity (0.04, 0.6 and 0.09 S/m) also plotted.*

**Table 17-50**: *Statistics of average pore fluid salinities (TDS, mg/L) relating to increments of AEM conductivity (S/m), for Calivil-dominant AEM depth slices (22-61 m).*

| AEM Inc. | Inc. Count | Cum. Count | Count <600 | Count >600 | Inc.% <600 | Cum.% <600 | Count <1200 | Count >1200 | Inc.% <1200 | Cum.% <1200 | Count <3000 | Count >3000 | Inc.% <3000 | Cum.% <3000 | Threshold |
|---|---|---|---|---|---|---|---|---|---|---|---|---|---|---|---|
| **0-0.03** | 3 | 3 | 3 | 0 | 100 | 100 | 3 | 0 | 100 | 100 | 3 | 0 | 100 | 100 | |
| **.03-.04** | 19 | 22 | 10 | 9 | 53 | 59 | 15 | 4 | 79 | 82 | 17 | 2 | 89 | 91 | **0.04** |
| **.04-.05** | 31 | 53 | 17 | 14 | 55 | 57 | 26 | 5 | 84 | 83 | 30 | 1 | 97 | 94 | |
| **.05-.06** | 26 | 79 | 15 | 11 | 58 | 57 | 25 | 1 | 96 | 87 | 26 | 0 | 100 | 96 | **0.06** |
| **.06-.07** | 37 | 116 | 8 | 29 | 22 | 46 | 27 | 10 | 73 | 83 | 32 | 5 | 86 | 93 | |
| **.07-.08** | 36 | 152 | 14 | 22 | 39 | 44 | 30 | 6 | 83 | 83 | 34 | 2 | 94 | 93 | |
| **.08-.09** | 19 | 171 | 3 | 16 | 16 | 41 | 12 | 7 | 63 | 81 | 19 | 0 | 100 | 94 | **0.09** |
| **.09-0.1** | 14 | 185 | 2 | 12 | 14 | 39 | 7 | 7 | 50 | 78 | 10 | 4 | 71 | 92 | |
| **0.1-0.11** | 9 | 194 | 0 | 9 | 0 | 37 | 3 | 6 | 33 | 76 | 6 | 3 | 67 | 91 | |
| **0.11-0.12** | 5 | 199 | 0 | 5 | 0 | 36 | 1 | 4 | 20 | 75 | 2 | 3 | 40 | 90 | |
| **0.12-0.13** | 9 | 208 | 0 | 9 | 0 | 35 | 3 | 6 | 33 | 73 | 6 | 3 | 67 | 89 | |
| **0.13-0.14** | 13 | 221 | 4 | 9 | 31 | 34 | 9 | 4 | 69 | 73 | 11 | 2 | 85 | 89 | |
| **0.14-0.15** | 6 | 227 | 1 | 5 | 17 | 34 | 1 | 5 | 17 | 71 | 1 | 5 | 17 | 87 | |
| **0.15-0.16** | 2 | 229 | 0 | 2 | 0 | 34 | 0 | 2 | 0 | 71 | 0 | 2 | 0 | 86 | |
| **0.16-0.17** | 1 | 230 | 0 | 1 | 0 | 33 | 0 | 1 | 0 | 70 | 1 | 0 | 100 | 86 | |
| **0.17-0.18** | 0 | 230 | | | | 33 | | | | 70 | | | | 86 | |
| **0.18-0.19** | 3 | 233 | 0 | 3 | 0 | 33 | 0 | 3 | 0 | 70 | 0 | 3 | 0 | 85 | |
| **0.19-0.20** | 0 | 233 | | | | 33 | | | | 70 | | | | 85 | |
| **0.2-0.25** | 10 | 243 | 0 | 10 | 0 | 32 | 0 | 10 | 0 | 67 | 2 | 8 | 20 | 82 | |

Notes: Inc. = increment; Cum. = cumulative

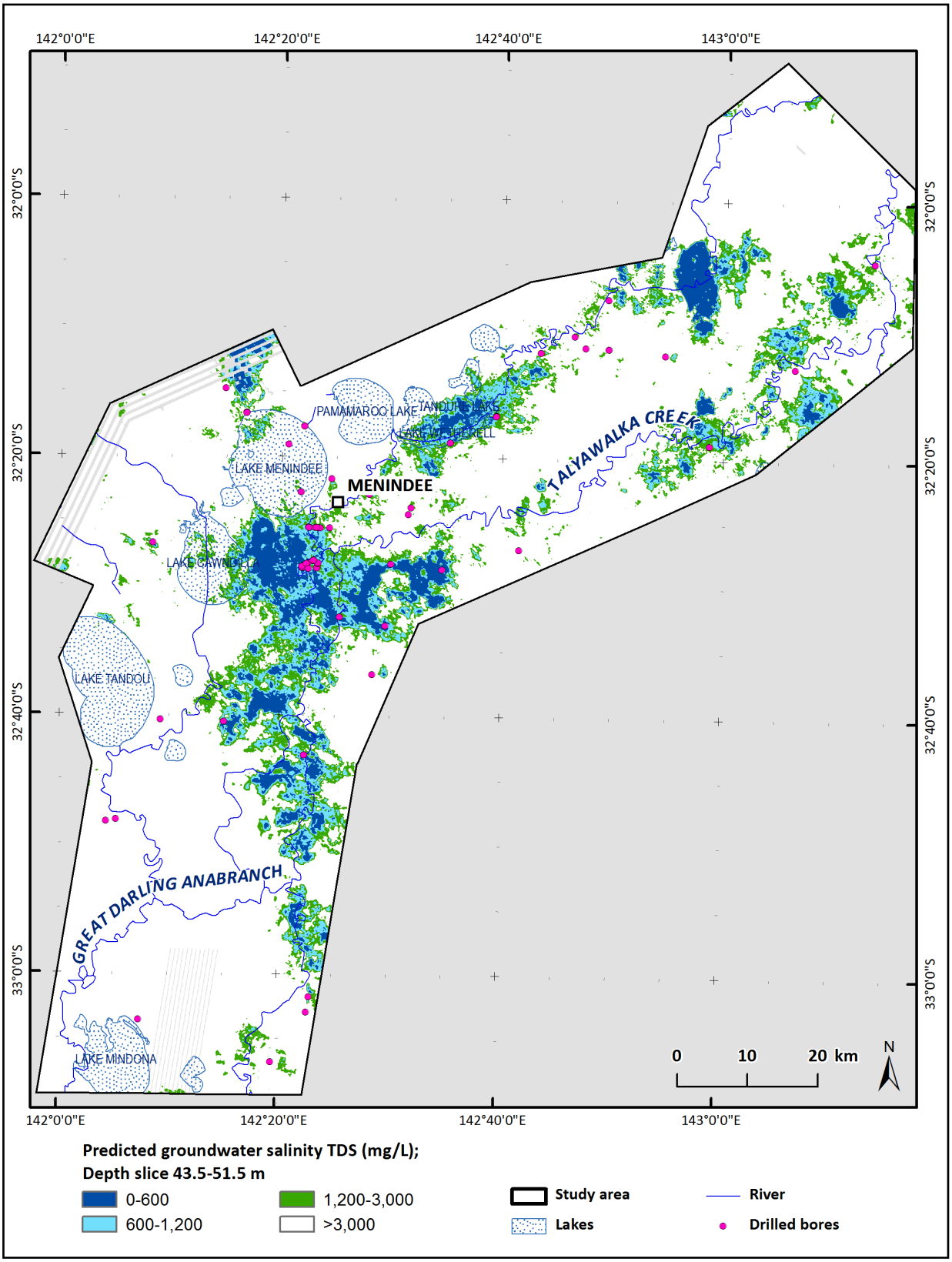



**Figure 17-133.** *Predicted groundwater salinity mapping for the AEM depth slice 43.5-51.5 m based on AEM conductivity thresholds.*

### 17.13.2 Aquifer Bulk Volumes

The groundwater volume estimates are focussed on the target Pliocene aquifer, specifically where the Calivil Formation or Loxton-Parilla Sands is saturated and hosts the coarser-textured sediments. Calculating the bulk volume (sediment + groundwater) for this component of the hydrostratigraphy was undertaken by querying and combining ArcGIS gridded versions of the AEM depth slice conductivities and other key mapping (Figure 17-127). The hydrostratigraphic mapping of the AEM depth slices were used to select the Calivil Formation and Loxton-Parilla target sequence. The mapping of textural classes of the AEM depth slices was used to remove zones of finer-textured material (such as sandy muds and muds) from the volume estimates. A gridded version of the interpreted Pliocene aquifer potentiometric surface was used to classify the Pliocene sequence as saturated or unsaturated.

The Pliocene aquifer was identified in 14 AEM depth slices (6.4-72.3 m) across the BHMAR study area. Using the gridded datasets, the coarser-grained saturated Pliocene sequence could then be selected on an AEM depth slice basis. The following are the classification rules that were applied:

- If stratigraphic unit = Woorinen Formation or Lunette (Qdw, Qdl) then hydrogeology = 1 (Other)
- If stratigraphic unit = Coonambidgal Formation, Menindee Formation, Willotia beds (Qac, Qam, Qaw) and Textural class = Mud or Muddy Sand then hydrogeology = 3 (Near surface mud drape aquitard)
- If stratigraphic unit = Coonambidgal Formation, Menindee Formation, Willotia beds (Qac, Qam, Qaw) and Textural class = Interbedded Sand and Mud then hydrogeology = 3 (Near surface mud drape aquitard)
- If stratigraphic unit = Coonambidgal Formation, Menindee Formation, Willotia beds (Qac, Qam, Qaw) and Textural class = Interbedded sediments or Sands then hydrogeology = 2 (Shallow unconfined aquifer)
- If stratigraphic unit = Blanchetown Clay (Qpc) and Textural class = Sands (fine, medium, coarse, very coarse) then hydrogeology = 8 (Upper confining aquitard sands)
- If stratigraphic unit = Blanchetown Clay (Qpc) and Textural class = Interbedded sediments (23&41) then hydrogeology = 9 (Upper confining aquitard interbeds)
- If stratigraphic unit = Blanchetown Clay (Qpc) and Textural class = Interbedded sediments (13&14) then hydrogeology = 6 (Upper confining aquitard)
- If stratigraphic unit = Blanchetown Clay (Qpc) and Textural class = mud or muddy sand then
- hydrogeology = 6 (Upper confining aquitard)
- If stratigraphic unit = Calivil Formation, Calivil Formation/Renmark Group, Loxton-Parilla Sands, Loxton-Parilla Sands/Renmark Group and Textural class = Sands (fine, medium, coarse, very coarse) or interbeds and Calivil WL position is Below and UCA is Above then hydrogeology = 4 (Semi-confined aquifer, unsaturated)
- If stratigraphic unit = Calivil Formation, Calivil Formation/Renmark Group, Loxton-Parilla Sands, Loxton-Parilla Sands/Renmark Group and Textural class = Sands (fine, medium, coarse, very coarse) or interbeds and Calivil WL position is Above and UCA Above then hydrogeology = 5 (Semi-confined aquifer, saturated)
- If stratigraphic unit = Calivil Formation and Textural class = Mud or Muddy Sand or Loxton-Parilla Sands and HYDCLASS = Mud or Muddy Sand then hydrogeology = 6 (Upper confining aquitard)
- If stratigraphic unit = Calivil Formation/Renmark Group and Textural class = Mud or Muddy Sand or Loxton-Parilla Sands/Renmark Group and Textural class = Mud or Muddy Sand then hydrogeology = 7 (Lower confining aquitard)
- If stratigraphic unit = Renmark Group and Textural class = Mud or Muddy Sand then hydrogeology = 7 (Lower confining aquitard)

- If stratigraphic unit = Renmark Group and Textural class = Sands (fine, medium, coarse, very coarse) or interbeds and Calivil WL position is Below then hydrogeology = 10 (Lower confined aquifer unsaturated)
- If stratigraphic unit = Renmark Group and Textural class = Sands (fine, medium, coarse, very coarse) or interbeds and Calivil WL position is above then hydrogeology = 11 (Lower confined aquifer saturated) else hydrogeology = 0 (N/A)

This grid algebra resulted in the identification of saturated Pliocene aquifer extents for the relevant AEM depth slices (n=14). Aquifer bulk storage volumes (GL) were subsequently calculated for each AEM depth slice by multiplying the number of relevant grid cells by the area of the cell (10x10 m), the thickness (of the AEM depth slice in m) and also a unit conversion factor. This process was carried out in ArcGIS using spatial analyst grid processing tools. These subsets of depth slice grids could then be categorised into groundwater salinity classes using the thresholds as defined by the analysis of AEM bulk conductivity and pore fluid salinity.

### 17.13.3 Effective Porosity

An estimate of effective porosity is required to convert the bulk volumes (assigned to AEM depth slices and groundwater salinity classes) to an estimate of the groundwater storage volume. The process of comparing different NMR survey data with laboratory porosity measurements is documented in Section 11. This comparison resulted in the use of recalibrated mobile (free) water content data from the 2011 NMR survey as the surrogate used for effective porosity. This NMR dataset was classified on the basis of the textural classes identified downhole, enabling NMR mobile water content statistics to be generated for each of the textural classes. The lower quartile, median and upper quartile were used to represent a low, medium and high estimate of effective porosity for each textural class. This recognises the geological heterogeneity within the target aquifer sequence. As well as the 5 textural classes, it was also necessary to assign effective porosities to interbedded sediments (Table 17-51) to account for the varying proportions of sand (aquifer material) and silts/clay (non-aquifer material).

These effective porosity statistics were used to convert the bulk volumes derived from the ArcGIS grid analysis to groundwater storage estimates. These estimates are reported on the basis of groundwater salinity classes for the target areas as well as the borefield areas.

**Table 17-51.** *Effective porosity statistics and associated scaling factors for each of the textural classes.*

| Textural Class | Effective Porosity Surrogate (Recalibrated 2011 mobile water ) | | | Porosity Factor |
|---|---|---|---|---|
| | Lower Quartile (low estimate) | Median (medium estimate) | Upper Quartile (high estimate) | |
| **Basement** | n/a | n/a | n/a | 0 |
| **Class 1 Mud** | n/a | n/a | n/a | 0 |
| **Class 2 Muddy Sand** | n/a | n/a | n/a | 0 |
| **Class 3 Fine Sand** | .081 | .157 | .229 | 1 |
| **Class 4 Medium Sand** | .109 | .172 | .228 | 1 |
| **Class 5 Coarse Sand to Gravels** | .113 | .163 | .228 | 1 |
| **Interbedded (mud & fine sand)** | .081 | .157 | .229 | 0.1 |
| **Interbedded (mud & medium sand)** | .109 | .172 | .228 | 0.5 |
| **Interbedded (muddy sand and fine sand)** | .081 | .157 | .229 | 0.4 |
| **Interbedded (medium sand overlying mud)** | .109 | .172 | .228 | 0.5 |

### 17.13.4 Groundwater Volume Estimates

The groundwater salinity thresholds were used to classify the AEM bulk conductivity depth slices into surrogate maps of groundwater salinity. In this way, 14 groundwater resource targets (GWR1-14) were identified across the BHMAR study area (Figure 17-134). The target boundaries represent broad envelopes around the multi-depth zones of groundwater freshening and are used for reporting purposes (Lawrie *et al*., 2012d). The groundwater storage volumes estimated for these targets are reported in Table 17-45.

It is important to emphasise that these derived storage volumes are indicative only, providing order-of-magnitude estimates to help prioritise targets and to make recommendations for future phases of investigation. These storage volume estimates are required to assess the MAR potential of the target aquifer, in the context of providing a MAR scheme of adequate storage and recovery efficiency. It is also important to emphasise that these groundwater storage volumes do not equate to the groundwater volume that can be extracted. The extractable groundwater volume would be significantly smaller than the groundwater storage estimates and depends on several factors including the:

- Assessment of the magnitude and risk of negative impacts associated with any groundwater extraction. These impacts can include ingress of saline (or poor quality) groundwater into the productive aquifer, decline in the viability of any identified groundwater dependent ecosystem, or reduction in groundwater access by existing licensed users.
- Nature and distribution of the more transmissive parts of the Calivil Formation, with the thicker sand and gravel palaeochannel deposits being the target for groundwater extraction.
- Conceptual understanding and quantification of groundwater recharge, flow and discharge processes.
- Economics and logistics of borefield or MAR design. This includes possible constraints such as land tenure, heritage clearances and proximity to existing infrastructure.

**Table 17-52.** *Estimated groundwater volumes in BHMAR groundwater resource targets.*

| GWR Target | Predicted Groundwater Salinity | Lower Quartile Groundwater Volume (GL) | Median Groundwater Volume (GL) | Upper Quartile Groundwater Volume (GL) |
|---|---|---|---|---|
| GWR1 | < 600 mg/L | 250 | 390 | 530 |
| GWR1 | 600 - 1,200 mg/L | 250 | 390 | 520 |
| GWR1 | 1,200 - 3,000 mg/L | 140 | 230 | 310 |
| **GWR1 Subtotal** | **<3,000 mg/L** | **640** | **1010** | **1360** |
| GWR2 | < 600 mg/L | 20 | 30 | 50 |
| GWR2 | 600 - 1,200 mg/L | 20 | 30 | 40 |
| GWR2 | 1,200 - 3,000 mg/L | 10 | 10 | 20 |
| **GWR2 Subtotal** | **<3,000 mg/L** | **50** | **70** | **110** |
| GWR3 | < 600 mg/L | 110 | 170 | 230 |
| GWR3 | 600 - 1,200 mg/L | 200 | 320 | 420 |
| GWR3 | 1,200 - 3,000 mg/L | 160 | 270 | 360 |
| **GWR3 Subtotal** | **<3,000 mg/L** | **470** | **760** | **1010** |
| GWR4 | < 600 mg/L | 140 | 220 | 300 |
| GWR4 | 600 - 1,200 mg/L | 120 | 190 | 250 |
| GWR4 | 1,200 - 3,000 mg/L | 80 | 120 | 160 |
| **GWR4 Subtotal** | **<3,000 mg/L** | **340** | **530** | **710** |
| GWR5 | < 600 mg/L | 70 | 110 | 140 |
| GWR5 | 600 - 1,200 mg/L | 110 | 180 | 240 |
| GWR5 | 1,200 - 3,000 mg/L | 80 | 130 | 170 |
| **GWR5 Subtotal** | **<3,000 mg/L** | **260** | **420** | **550** |
| GWR6 | < 600 mg/L | 80 | 130 | 170 |

| | | | | |
|---|---|---|---|---|
| GWR6 | 600 - 1,200 mg/L | 160 | 250 | 330 |
| GWR6 | 1,200 - 3,000 mg/L | 120 | 200 | 270 |
| **GWR6 Subtotal** | **<3,000 mg/L** | **360** | **580** | **770** |
| GWR7 | < 600 mg/L | 20 | 40 | 50 |
| GWR7 | 600 - 1,200 mg/L | 60 | 100 | 130 |
| GWR7 | 1,200 - 3,000 mg/L | 60 | 100 | 130 |
| **GWR7 Subtotal** | **<3,000 mg/L** | **140** | **240** | **310** |
| GWR8 | < 600 mg/L | 20 | 30 | 50 |
| GWR8 | 600 - 1,200 mg/L | 30 | 50 | 70 |
| GWR8 | 1,200 - 3,000 mg/L | 50 | 80 | 120 |
| **GWR8 Subtotal** | **<3,000 mg/L** | **100** | **160** | **240** |
| GWR9 | < 600 mg/L | 60 | 100 | 140 |
| GWR9 | 600 - 1,200 mg/L | 60 | 90 | 120 |
| GWR9 | 1,200 - 3,000 mg/L | 60 | 100 | 130 |
| **GWR9 Subtotal** | **<3,000 mg/L** | **180** | **290** | **390** |
| GWR10 | < 600 mg/L | 20 | 30 | 50 |
| GWR10 | 600 - 1,200 mg/L | 20 | 30 | 40 |
| GWR10 | 1,200 - 3,000 mg/L | 30 | 40 | 60 |
| **GWR10 Subtotal** | **<3,000 mg/L** | **70** | **100** | **150** |
| GWR11 | < 600 mg/L | 10 | 20 | 20 |
| GWR11 | 600 - 1,200 mg/L | 40 | 60 | 80 |
| GWR11 | 1,200 - 3,000 mg/L | 40 | 60 | 90 |
| **GWR11 Subtotal** | **<3,000 mg/L** | **90** | **140** | **190** |
| GWR12 | < 600 mg/L | 40 | 60 | 80 |
| GWR12 | 600 - 1,200 mg/L | 40 | 60 | 90 |
| GWR12 | 1,200 - 3,000 mg/L | 30 | 40 | 60 |
| **GWR12 Subtotal** | **<3,000 mg/L** | **110** | **160** | **230** |
| GWR13 | < 600 mg/L | 20 | 30 | 30 |
| GWR13 | 600 - 1,200 mg/L | 30 | 50 | 70 |
| GWR13 | 1,200 - 3,000 mg/L | 20 | 30 | 40 |
| **GWR13 Subtotal** | **<3,000 mg/L** | **70** | **110** | **140** |
| GWR14 | < 600 mg/L | 10 | 20 | 20 |
| GWR14 | 600 - 1,200 mg/L | 40 | 60 | 80 |
| GWR14 | 1,200 - 3,000 mg/L | 40 | 70 | 90 |
| **GWR14 Subtotal** | **<3,000 mg/L** | **90** | **150** | **190** |
| | | | | |
| **All Targets Subtotal** | **<600 mg/L** | **900** | **1400** | **1900** |
| **All Targets Subtotal** | **600-1,200 mg/L** | **1200** | **1900** | **2500** |
| **All Targets Subtotal** | **1,200 - 3,000 mg/L** | **900** | **1500** | **2000** |
| **All Targets Total** | **<3,000 mg/L** | **3000** | **4700** | **6400** |

Notes: These groundwater volumes are indicative estimates only. Groundwater storage volumes do not equate to extractable groundwater volumes, which would be a smaller proportion of these estimates.

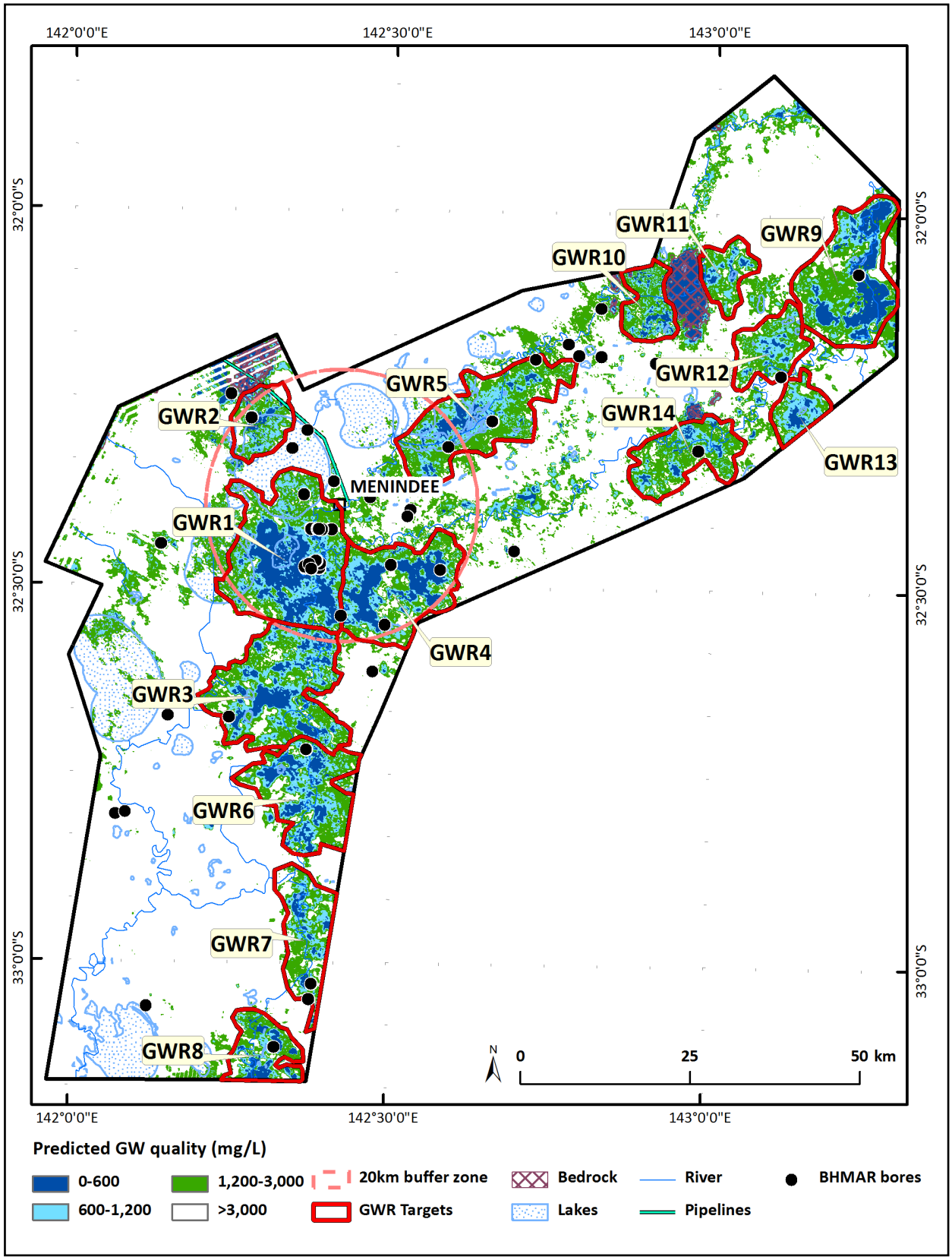



**Figure 17-134.** *Map of the BHMAR project area showing the distribution of groundwater resource (GWR) targets in Pliocene (Calivil and Loxton-Parilla Sand Formation) aquifers. The boundaries marked are the maximum spatial extent of the aquifer with predicted salinities <3000 mg/L. This maximum spatial extent is defined by the combined plotting of all the depth slices most relevant to the Calivil Formation (22-61 m).*

### 17.13.5 Uncertainty Analysis of Groundwater Storage Volume Estimates

Uncertainty in the estimates of stored groundwater volumes can be largely attributed to four key sources of data variability. Firstly, the primary data for the volume estimates are the AEM bulk conductivity depth slices, which are in turn dependent on the method and constraints used in the AEM inversion process. As discussed in Section 6, various iterations of AEM inversions have been implemented in the project to significantly increase the robustness of the dataset as the basis for various interpreted products.

Secondly, there is uncertainty in the relationship between the AEM bulk conductivity and groundwater salinity, due to other attributing factors to bulk conductivity such as sediment texture, mineralogy and water saturation. The bulk-fluid conductivity relationship determines the spatial distribution of the various classes of groundwater salinity. Section 17.13.1 describes the approach taken to derive AEM bulk conductivity values for groundwater salinity thresholds. Figure 17-132 shows the significant scatter between pore fluid salinity and the relevant AEM depth slice conductivity.

Thirdly, the effective porosity estimates used to convert bulk volumes to groundwater volumes are subject to uncertainty. This relates to the variability of effective porosity both within and across textural classes, the errors associated with the laboratory measurements and the uncertainty associated with extrapolating these laboratory measurements to the borefield and target scale. The process of deriving effective porosity estimates for textural classes is outlined in Section 11.8**.** The use of the NMR free water data as a surrogate allows sufficient data density to define low and high values to represent the inherent variability of effective porosity within the textural classes.

Fourthly, there is uncertainty in the hydrostratigraphic, textural and saturation mapping. The key focus of the volume estimates are the coarser textured saturated sediments in the Pliocene (Calivil Formation and Loxton-Parilla Sands) aquifer sequence. The mapping of hydrostratigraphy, texture classes and saturation on an AEM depth slice basis is used to identify these sediments of interest.

A sensitivity analysis was undertaken to explore some of these sources of uncertainty. This analysis was undertaken at both the target and borefield scale, using the bulk volume estimates, rather than the final groundwater volumes. This is because the conversion of bulk to groundwater volumes is based solely on effective porosity, which in turn has been estimated as a range to represent the inherent variability within textural classes. The uncertainty analysis used a baseline of:

- The WANDA2012 Loosely Constrained AEM inversion, which is the final inversion for the interpreted products of the project. This and the other AEM inversions are described in Table 17-53.
- 'Version 3' thresholds used to map AEM bulk conductivity to groundwater salinity (Table 17-54). These were used for the groundwater volume estimates summarised in Table 17-45.
- Application to the 6 AEM depth slices between 22 and 61 m, representing the bulk of the Calivil Formation and Loxton-Parilla sequence
- No constraints relating to stratigraphy, texture or saturation.

The uncertainty analysis was undertaken by changing different elements of the approach (such as AEM inversion or groundwater quality thresholds) one at a time, then comparing the bulk volume results with those calculated for the baseline.

**Table 17-53.** *AEM inversions used in bulk volume analysis.*

| Inversion | Description |
|---|---|
| WANDA 2012 Loose Constrained | 30-layer fast approximate inversion using the WANDA inversion code with loose regularization settings |
| WANDA 2012 Tight Constrained | 30-layer fast approximate inversion using the WANDA inversion code with conventional, tight regularization settings |
| LCI-19 2010 Unconstrained | 19-layer full inversion produced using the Aarhus Workbench |

**Table 17-54.***Versions of groundwater quality thresholds used in bulk volume uncertainty analysis.*

| Version | Groundwater Salinity (mg/L) | AEM bulk conductivity (S/m) |
|---|---|---|
| 1 | 600 | 0.04 |
| 1 | 1200 | 0.07 |
| 1 | 3000 | 0.09 |
| 2 | 600 | 0.035 |
| 2 | 1200 | 0.065 |
| 2 | 3000 | 0.09 |
| 3 | 600 | 0.04 |
| 3 | 1200 | 0.06 |
| 3 | 3000 | 0.09 |

#### 17.13.5.1 *Target-Scale Uncertainty Analysis*

Figure 17-135 to Figure 17-140 show the results of the uncertainty analysis at the groundwater resource (GWR) target scale, where singular changes have been to the baseline approach and the bulk volumes compared. In these plots, the bulk volumes are categorised on the basis of the groundwater quality thresholds ('good' < 600 mg/L, 'acceptable' 600-1200 mg/L, 'brackish' 1200-3000 mg/L and 'saline' > 3000 mg/L). The orange full line is the equivalence (1:1) line. The 2:1 and 1:2 orange large-dashed lines represent where the baseline bulk volumes are twice or half of the modified approach, respectively. The orange short-dashed lines represent order-of-magnitude (10:1 and 1:10) changes.

Figure 17-135 plots the difference in calculated bulk volumes when the AEM inversion used is changed from the baseline WANDA 2012 Loose Constrained inversion to the LCI-19 2010 Unconstrained inversion generated in the early stages of the project. This plot shows the significant departure of bulk volumes, notably for the good and acceptable quality groundwater classes. For some targets, the use of the LCI-19 Unconstrained inversion has reduced the bulk volumes assigned to the fresh groundwater class by one or even two orders of magnitude. A similar effect is apparent when tight constraints (rather than the loose constraints of the baseline) are applied to the WANDA 2012 inversion (Figure 17-136). With this change in the constraints, there have been order-of-magnitude decreases in the bulk volumes relating to the fresh (< 600 mg/L) category.

Figure 17-137 and Figure 17-138 show the results when different thresholds are used to translate AEM bulk conductivity to groundwater salinity. Figure 17-137 plots the change in bulk volumes when the groundwater salinity thresholds are changed from Version 3 to Version 2. This equates to the 600 mg/L threshold decreasing from 0.04 S/m to 0.035 S/m and the 1200 mg/L threshold increasing from 0.06 S/m to 0.065 S/m (Figure 17-136). The changes to bulk volumes are bounded by the 2:1 and 1:2 lines and are not as extreme as evident when changes to the AEM inversion have been made (Figure 17-135 and Figure 17-136). The bulk volumes for the <600 mg/L category decreases, as expected with the decrease in the AEM bulk conductivity threshold, accommodated by systematic increases in the bulk volumes for the 600-1200 mg/L class. Similar magnitude changes to bulk volumes are evident when the groundwater salinity thresholds are changed from Version 3 to Version 1 (Figure 17-138). This equates to the 1200 mg/L threshold decreasing from 0.07 S/m to 0.06 S/m (Table 17-54). In this case, the <600 mg/L and >3000 mg/L bulk volumes are identical as the same AEM thresholds are applied.

Figure 17-139 represents the impact of incorporating limitations defined by the hydrostratigraphy, texture and saturation. These factors have been incorporated in the final volume estimates, to limit the analysis to coarser textured saturated zones in the Calivil Formation and Loxton-Parilla Sands. An example of this is excluding, on an AEM depth slice basis, any areas that have been mapped as muds or muddy sands. Figure 17-139 shows that the exclusion of these finer textured classes has had the greatest impact on the most saline groundwater quality class (>3,000 mg/L). This reflects the tendency, within the bounds of the target areas at least, that the more saline groundwater is hosted in the muds and muddy sands. As the fresher groundwater is

typically associated with the coarser textured aquifer material, the impact of these textural constraints is significantly less for the good and acceptable quality classes.

Figure 17-140 explores changes in the bulk volume estimates brought about by changing the AEM depth slices being considered in the analysis. In both sets of analysis, factors relating to hydrostratigraphic, texture and saturation classifications are incorporated. However, the range in AEM depth slices was changed from a baseline of 22-61 m to 6.4-72.3 m. Figure 17-140 shows that the majority of bulk volumes have increased because of the larger depth range. This increase is relatively small, when compared with the impacts of other factors, such as changing the AEM inversion (Figure 17-135 and Figure 17-136). The depth range of 22-61 m is interpreted to be a reasonable estimate for the bulk of the Calivil Formation and Loxton-Parilla Sands across the various target areas.

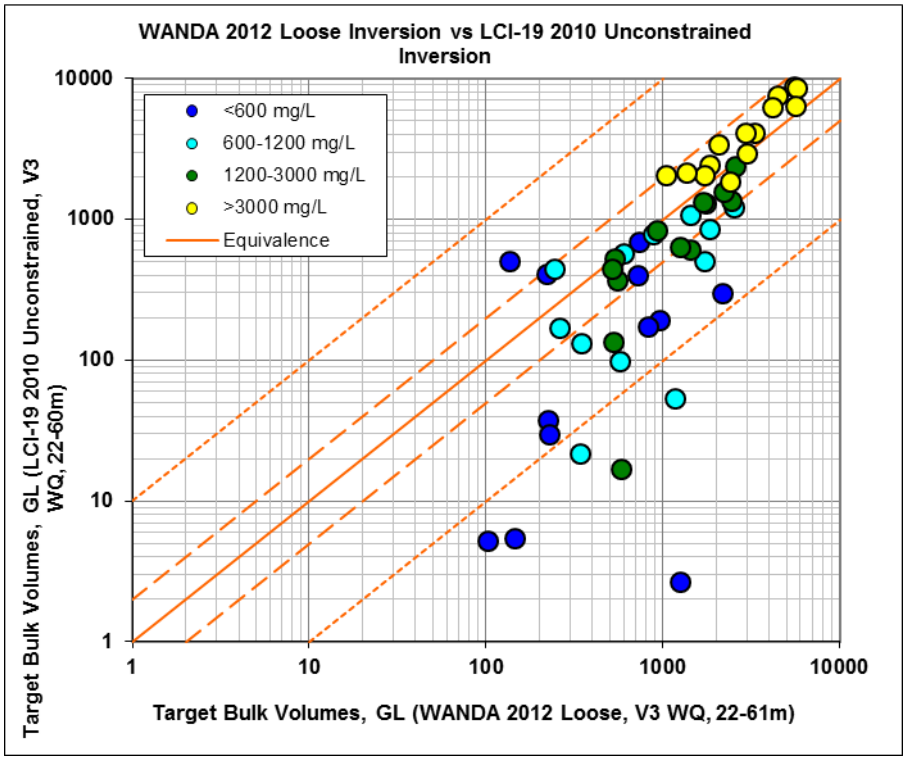



**Figure 17-135.** *Comparison of target bulk volumes calculated from different AEM inversions. The baseline uses the WANDA 2012 Loosely Constrained AEM inversion, Version 3 groundwater quality thresholds (0.04, 0.06, 0.09 S/m) for 22-61 m AEM depth slices. In this comparison, the AEM inversion has been changed to the LCI-19 2010 Unconstrained AEM inversion. The orange full, large- dashed and small-dashed lines are 1:1, 2:1 (or 1:2) and 1:10 (or 10:1) relationships, respectively.*

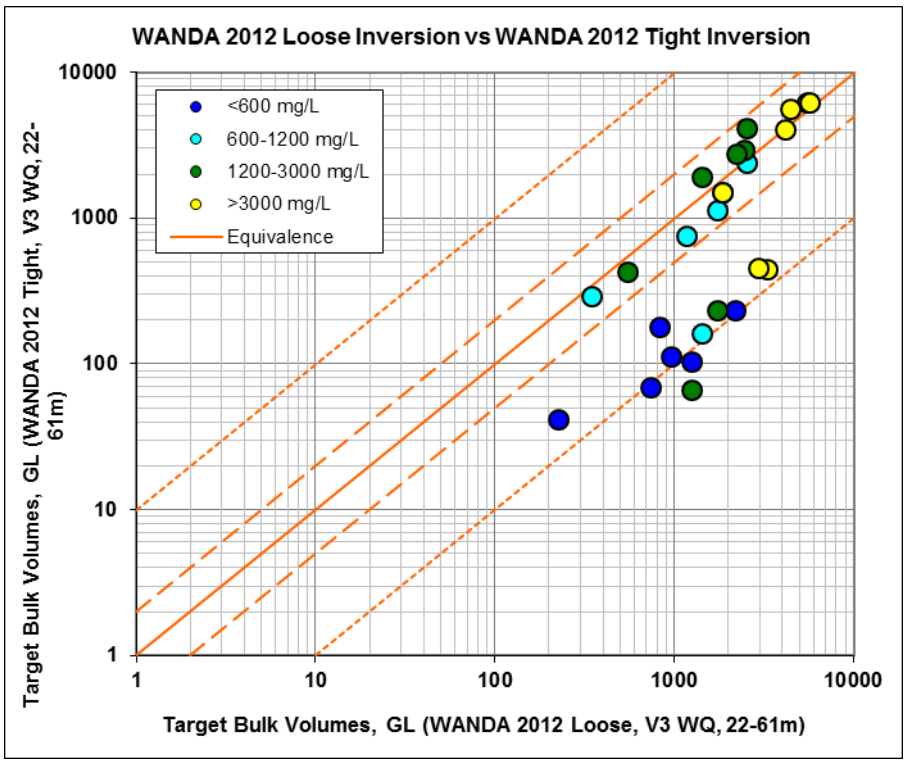



**Figure 17-136.** *Comparison of target bulk volumes calculated from AEM inversions using different constraints. The baseline uses the WANDA 2012 Loosely Constrained AEM inversion, Version 3 groundwater quality thresholds (0.04, 0.06, 0.09 S/m) for 22-61 m AEM depth slices. In this comparison, the AEM inversion has been changed to the WANDA 2012 Tightly Constrained AEM inversion. The orange full, large- dashed and small-dashed lines are 1:1, 2:1 (or 1:2) and 1:10 (or 10:1) relationships, respectively.*

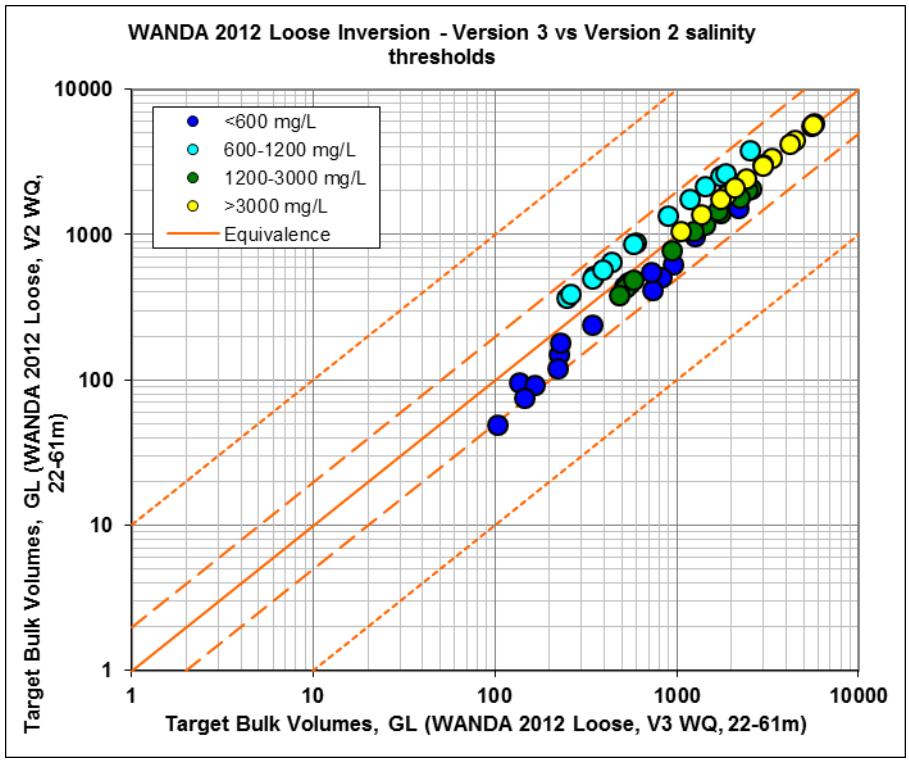



**Figure 17-137.** *Comparison of target bulk volumes calculated using different groundwater salinity thresholds. The baseline uses the WANDA 2012 Loosely Constrained AEM inversion, Version 3 groundwater salinity thresholds (0.04, 0.06, 0.09 S/m) for the 22-61 m AEM depth slices. In this comparison, salinity thresholds have been changed to Version 2 (0.035, 0.065, 0.09 S/m). The orange full, large- dashed and small-dashed lines are 1:1, 2:1 (or 1:2) and 1:10 (or 10:1) relationships, respectively.*

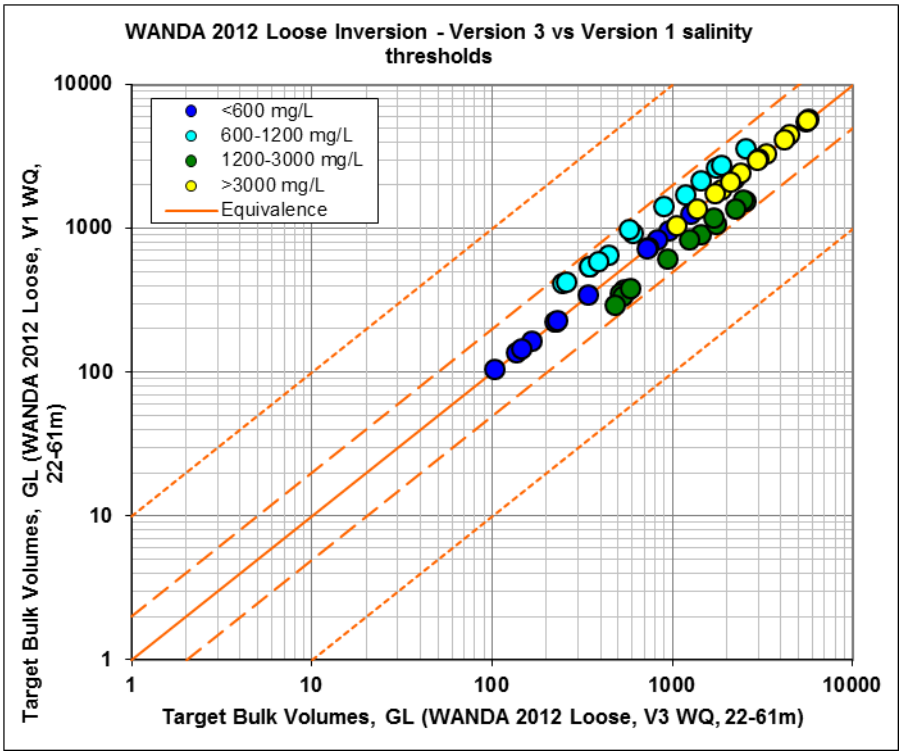



**Figure 17-138.***Comparison of target bulk volumes calculated using different groundwater salinity thresholds. The baseline uses the WANDA 2012 Loosely Constrained AEM inversion, Version 3 groundwater salinity thresholds (0.04, 0.06, 0.09 S/m) for the 22-61 m AEM depth slices. In this comparison, salinity thresholds have been changed to Version 1 (0.04, 0.07, 0.09 S/m). The orange full, large- dashed and small-dashed lines are 1:1, 2:1 (or 1:2) and 1:10 (or 10:1) relationships, respectively.*

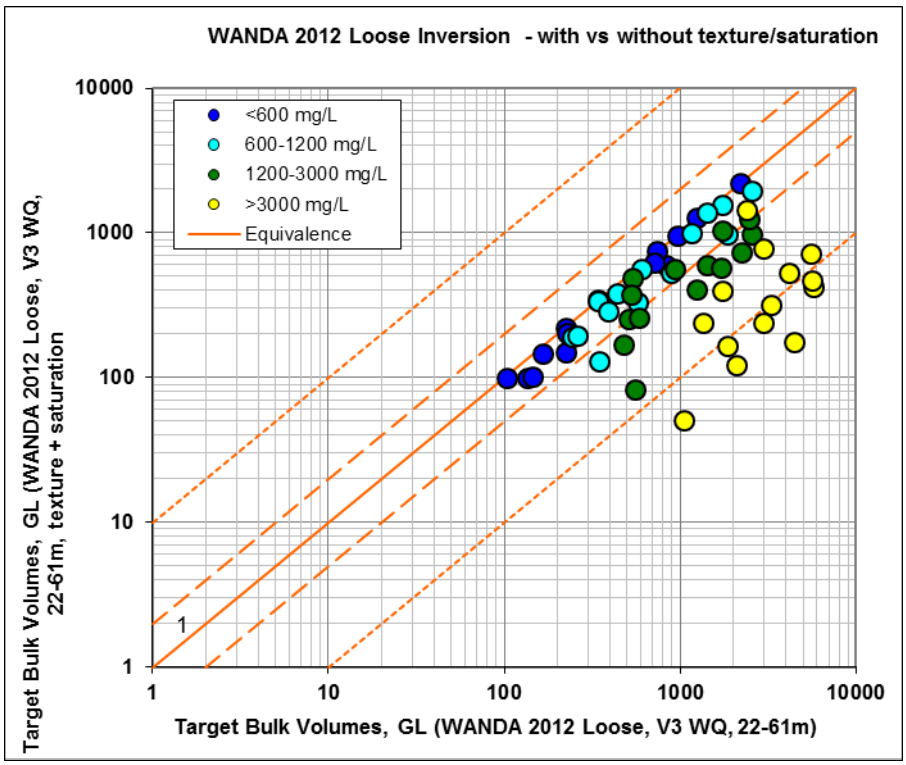



**Figure 17-139.***Comparison of target bulk volumes calculated with (and without) applying additional limits based on texture and saturation classes. Both the methods used the WANDA 2012 Loosely Constrained AEM inversion, Version 3 groundwater quality thresholds (0.04, 0.06, 0.09 S/m) for 22-61 m AEM depth slices. The orange full, large- dashed and small-dashed lines are 1:1, 2:1 (or 1:2) and 1:10 (or 10:1) relationships, respectively.*

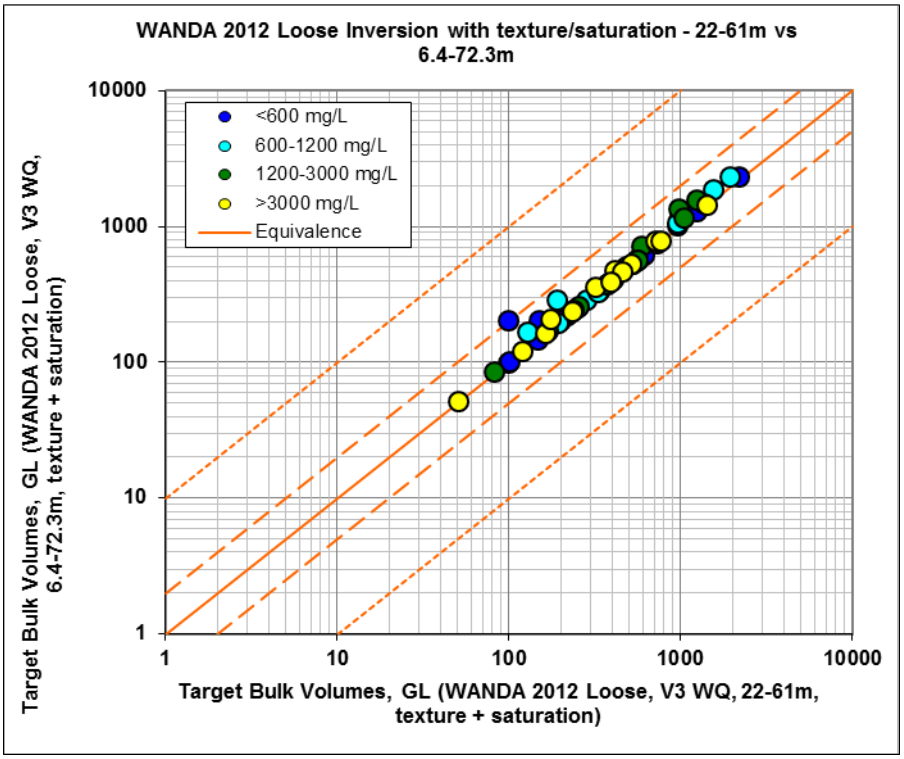



**Figure 17-140.** *Comparison of target bulk volumes calculated using different ranges in the AEM depth slices. The baseline uses the WANDA 2012 Loosely Constrained AEM inversion, Version 3 groundwater quality thresholds (0.04, 0.06, and 0.09 S/m, with texture and saturation classes included and for the 22-61 m AEM depth slices. In this comparison, the AEM depth slices have been changed to 6.4-72.3 m. The orange full, large- dashed and small-dashed lines are 1:1, 2:1 (or 1:2) and 1:10 (or 10:1) relationships, respectively.*

### 17.13.5.2 *Borefield-Scale Uncertainty Analysis*

Figure 17-141 to Figure 17-146 summarise the results of the uncertainty analysis undertaken for the borefield scale, using the same approaches as taken for the groundwater target scale (Figure 17-135 to Figure 17-140). Similar impacts to calculated bulk volumes can be seen when various changes are made to the elements making up the analysis. For example, major reductions in bulk volumes relating to fresh and acceptable quality classes occur when the LCI-19 Unconstrained AEM inversion is used instead of the baseline WANDA 2012 Loose Constrained AEM inversion (Figure 17-141). This is also most notably the case for the bulk volumes for the fresh (< 600 mg/L) class, when additional constraints are placed on the WANDA 2012 inversion (Figure 17-142). Tightening the constraints on the AEM inversion has the greatest effect at the low (fresh) and high (very saline) ends of the bulk conductivity spectrum.

The impact of changing the AEM conductivity thresholds used to map the various groundwater quality classes at the borefield scale (Figure 17-143 and Figure 17-144) are of similar relativities to that evident for the groundwater targets (Figure 17-137 and Figure 17-138). Adding hydrostratigraphic, textural and saturation constraints to the borefield bulk volume calculations (Figure 17-145) gives a similar response to that at the target scale (Figure 17-139). The significant reduction in bulk volumes for the >3000 mg/L class (and to a lesser extent the 1200-3000 mg/L class) is because these have relatively more finer textured sediments (muds and muddy sands) which have been excluded from the calculations with textural constraints. In contrast, the bulk volumes for the fresh (< 600 mg/L) class largely remain the same as these are largely contained in fine to coarse sands. For Figure 17-146, the hydrostratigraphic, textural and saturation constraints are incorporated in both bulk volume calculations, but the AEM depth slice range has been changed from the baseline 22-61 m to a broader 7.7-72.3 m. Figure 17-146 shows that the relative increase in bulk volumes due to the greater depth range becomes larger as the groundwater salinity increases. This is because the more saline groundwaters (1200-3000 mg/L and >3000 mg/L) in the Pliocene aquifer are being captured with the incorporation of AEM depth slices above 22 m and below 61 m. In contrast, the bulk of the good quality (<600 mg/L) groundwater in the Pliocene aquifer is within the baseline 22-61 m depth range.

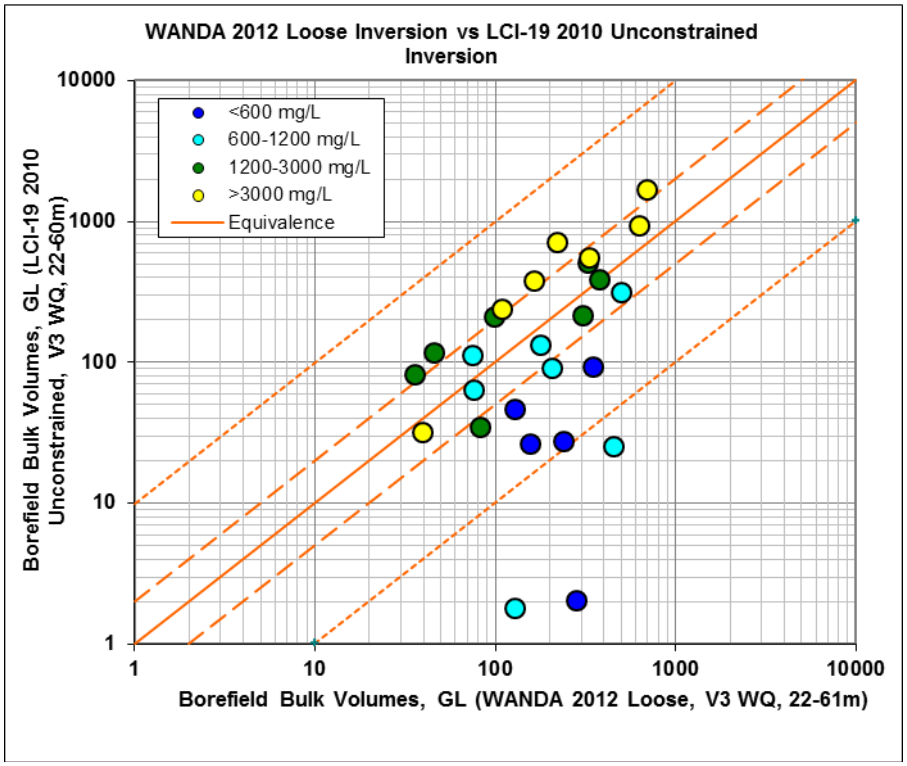



**Figure 17-141.** *Comparison of borefield bulk volumes calculated from different AEM inversions. The baseline uses the WANDA 2012 Loosely Constrained AEM inversion, Version 3 groundwater quality thresholds (0.04, 0.06, 0.09 S/m) for 22-61 m AEM depth slices. In this comparison, the AEM inversion has been changed to the LCI-19 2010 Unconstrained AEM inversion. The orange full, large- dashed and small-dashed lines are 1:1, 2:1 (or 1:2) and 1:10 (or 10:1) relationships, respectively.*

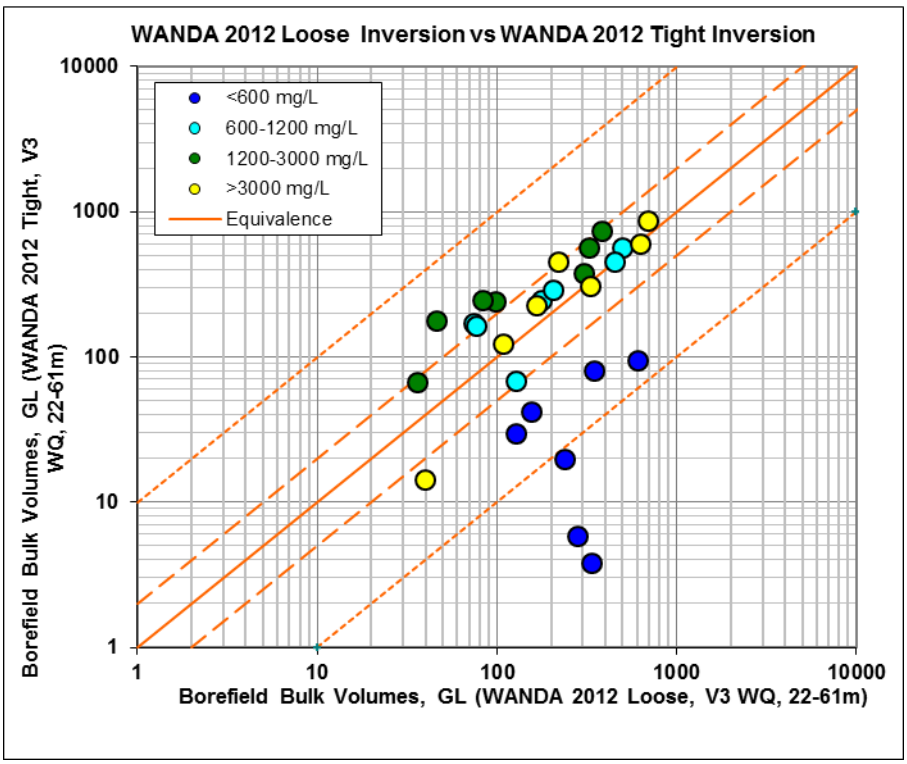



**Figure 17-142.** *Comparison of borefield bulk volumes calculated from AEM inversions using different constraints. The baseline uses the WANDA 2012 Loosely Constrained AEM inversion, Version 3 groundwater quality thresholds (0.04, 0.06, 0.09 S/m) for 22-61 m AEM depth slices. In this comparison, the AEM inversion has been changed to the WANDA 2012 Tightly Constrained AEM inversion. The orange full, large- dashed and small-dashed lines are 1:1, 2:1 (or 1:2) and 1:10 (or 10:1) relationships, respectively.*

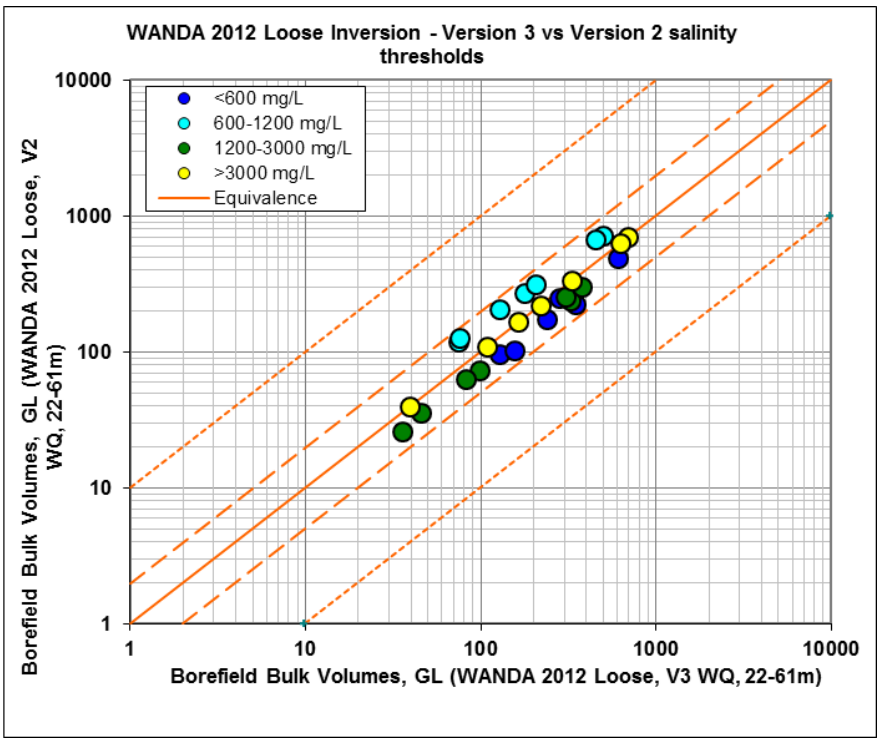



**Figure 17-143.** *Comparison of borefield bulk volumes calculated using different groundwater salinity thresholds. The baseline uses the WANDA 2012 Loosely Constrained AEM inversion, Version 3 groundwater salinity thresholds (0.04, 0.06, 0.09 S/m) for the 22-61 m AEM depth slices. In this comparison, salinity thresholds have been changed to Version 2 (0.035, 0.065, 0.09 S/m). The orange full, large- dashed and small-dashed lines are 1:1, 2:1 (or 1:2) and 1:10 (or 10:1) relationships, respectively.*

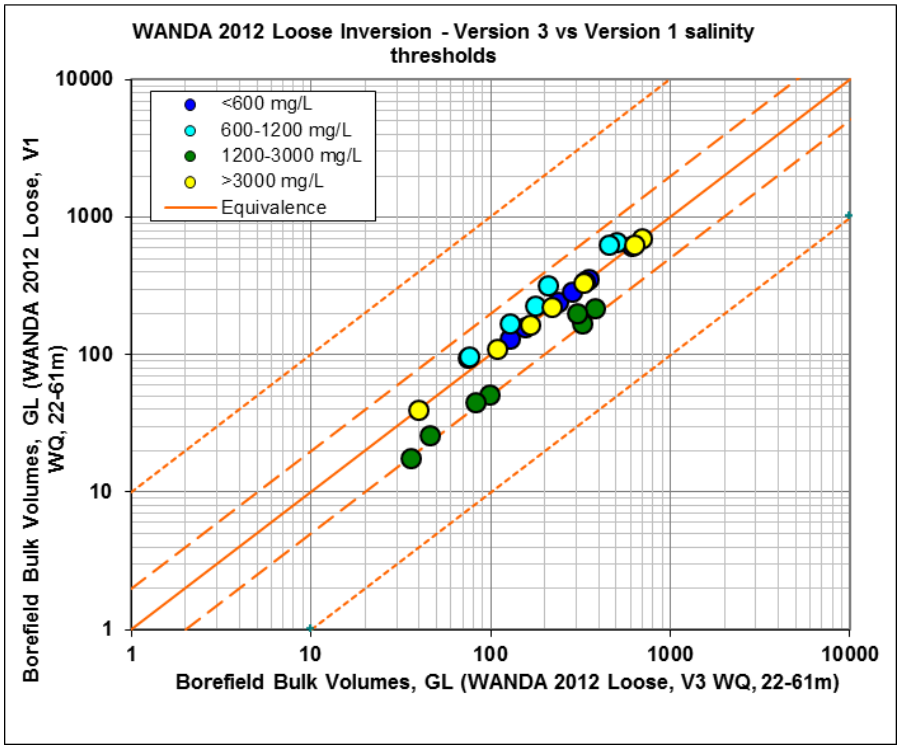



**Figure 17-144.** *Comparison of borefield bulk volumes calculated using different groundwater salinity thresholds. The baseline uses the WANDA 2012 Loosely Constrained AEM inversion, Version 3 groundwater salinity thresholds (0.04, 0.06, 0.09 S/m) for the 22-61 m AEM depth slices. In this comparison, salinity thresholds have been changed to Version 1 (0.04, 0.07, 0.09 S/m). The orange full, large- dashed and small-dashed lines are 1:1, 2:1 (or 1:2) and 1:10 (or 10:1) relationships, respectively.*

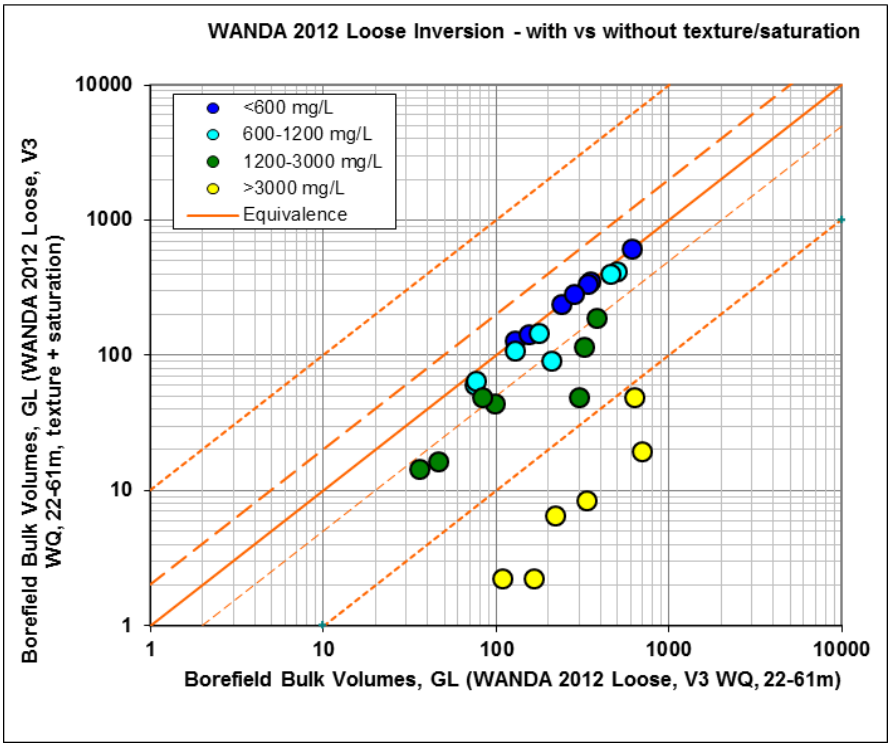



**Figure 17-145.** *Comparison of borefield bulk volumes calculated with (and without) applying additional limits based on texture and saturation classes. Both the methods used the WANDA 2012 Loosely Constrained AEM inversion, Version 3 groundwater quality thresholds (0.04, 0.06, 0.09 S/m) for 22-61 m AEM depth slices. The orange full, large-dashed and small-dashed lines are 1:1, 2:1 (or 1:2) and 1:10 (or 10:1) relationships, respectively.*

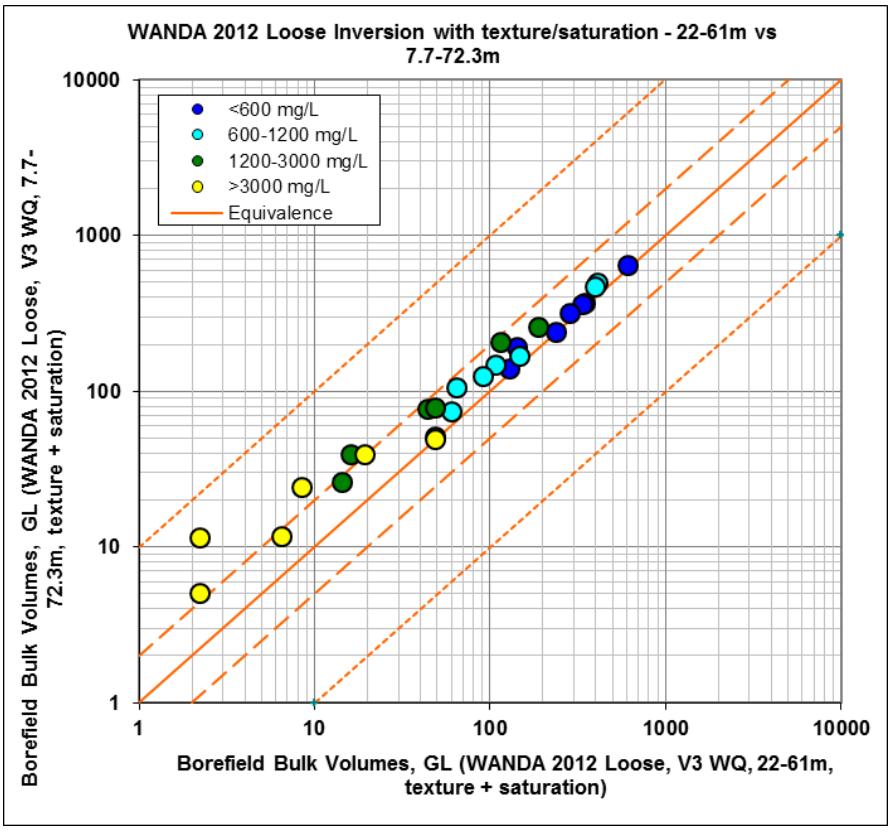



**Figure 17-146.** *Comparison of borefield bulk volumes calculated using different ranges in the AEM depth slices. The baseline uses the WANDA 2012 Loosely Constrained AEM inversion, Version 3 groundwater quality thresholds (0.04, 0.06, and 0.09 S/m, with texture and saturation classes included and for the 22-61 m AEM depth slices. In this comparison, the AEM depth slices have been changed to 6.4-72.3 m. The orange full, large- dashed and small-dashed lines are 1:1, 2:1 (or 1:2) and 1:10 (or 10:1) relationships, respectively.*

#### 17.13.5.3 *Uncertainty Analysis Discussion*

Uncertainty analysis of the bulk volumes relating to the various groundwater salinity classes highlighted the relative importance of the different components making up the bulk volume calculations. The bulk volumes for the better quality groundwaters ('good' < 600 mg/L and 'acceptable' 600-1200 mg/L) are particularly sensitive to the method and constraints placed on the AEM inversion. For example, order-of-magnitude reductions in bulk volumes result for good quality groundwaters when the constraints are tightened on the WANDA 2012 AEM inversion (Figure 17-136). This is because such constraints have a greater effect on the extremes of the AEM bulk conductivity spectrum, with the <600 mg/L class focusing on the low extreme (<0.04 S/m).

The other order-of-magnitude scale reduction of bulk volumes occur when hydrostratigraphic, textural and saturation constraints are incorporated. However, such reductions of this scale only occur for the saline groundwater class of > 3000 mg/L (Figure 17-139). This is because of the greater prevalence in the saline class of finer textures (muds and sandy muds) which are excluded from the bulk volume calculations when these constraints are incorporated. In contrast, the fresh groundwater class (<600 mg/L) tends to be hosted in the fine to coarse sands, so the effects of adding textural limits is not as significant.

The influence of changing the AEM bulk conductivity thresholds that are mapped to groundwater salinity is relatively lower, when compared with that of changing AEM inversions and constraints. However, this influence can still be significant. For example, changing the AEM bulk conductivity threshold for <600 mg/L groundwater salinity from 0.04 S/m to 0.035 S/m can halve the resulting bulk volume estimate for some targets (Figure 17-137).

Bulk volumes do increase by incorporating more AEM depth slices into the analysis (Figure 17-140), but this factor appears to have the least impact on the bulk volume estimate.

The uncertainty analysis highlights and prioritises the potential sources of uncertainty in the bulk volume estimates. Considering the scale of this uncertainty and that these sources of potential error are additive, the resulting bulk volumes (and in turn the derived groundwater storage volume estimates) should only be considered as indicative.

## 17.14 CALCULATING THE SALT STORE IN THE UNSATURATED ZONE

The amount of salt stored in the soil and unsaturated zone is transient and the time of residence varies. Salt store in the soils, aeolian and fluvial sediment in the unsaturated zone is influenced by evapotranspiration, recharge rates, permeability, degree of saturation, abundance of clay minerals and type, and the composition of salt, i.e. monovalent and divalent ions, in the solution. The aim of this section is to estimate the amount of salt in the unsaturated sediment that has the potential to become mobilise.

Datasets used in calculating the salt store of sediment include AEM depth slice grids, pore fluid salinity, NMR data and borehole lithological information. On the floodplain and older scroll plain, the water table is shallow, approximately 13 m depth, but away from the river channel, the water table can be substantially lower (up to 20 m depth). Thus AEM depth slices from the surface to 22 m depths were selected for this analysis. Pore fluids were extracted from the sediment using the hydraulic press method. The fluids were analysed using ion-chromatography and inductively coupled plasma – mass spectrometry (ICP-MS) techniques. The total dissolved solutes (TDS) or salinity, is the summed of major and minor cations and anions expressed as milligrams per litre. Borehole lithological information were summarised into five hydraulic texture classes, from mud to very coarse sand and gravel. The total water content of the NMR data, which consists of mobile and capillary water, is selected for the calculation of salt store, and is expressed as a volume fraction of the measured space. Similar to the use of NMR data for calculation of hydraulic conductivity (Section 7.3), the varying thickness of AEM depth slices and the constant NMR reading at every half metre dictates that one or more NMR data may corresponds to a single AEM grid value. Each grid is 50 m by 50 m in area and the thickness varying according to the AEM depth slice.

The salt store of sediment is expressed as the amount of dissolved salt in tonnes per hectare, and is a function of the water content of the sediment. Salt present in solid phases such as halite, gypsum and calcite, which are not extracted during the hydraulic pressing, is not represented in this model.

### 17.14.1 Calculations

Pore fluid Salinity in mg/l is equivalent to mg/kg or g/t of fluid. To get tonne of salt per tonne fluid, the salinity is divided by a million. Multiplying the salinity concentrations by the volume of fluid (i.e. NMR total water) give salt store in tonnes.

TDS (mg/l) = TDS (mg/kg)

= TDS (g/t)

= TDS x $10^{-6}$ (t/t)

*Salt Store (t) = TDS x $10^{-6}$ (t/t) x Total Water*

**Equation 113**

The AEM grids consist of voxet, each has dimension of 50 m by 50 m by thickness of the depth slice. Since 1 hectare equals four voxets, salt store is multiplied by four and expressed as tonnes per hectare dissolved salt.

*Salt Store (t/ha) = 4 x TDS x $10^{-6}$ (t/t) x Total Water*

**Equation 114**

To use AEM data to model the salt store, causal relationship between apparent conductivity and salt store is first established.

Empirical data from the near surface AEM depth slices (1.6 m to 5.3 m) show a wide spread of data without any apparent causal relationship. Grouping the data into hydraulic texture classes show that majority of the scatter is derived from mud and muddy sand, ranging from low conductivity with low salt store, high conductivity with low salt store and moderate conductivity with high salt store. In comparison, sand-rich sediment has low electrical conductivity and low salt store (Figure 17-56).

Grouping the data with respect to water content provide an obvious association (Figure 17-57). Dry sediment with water content lower than 15 vol% has low salt store, regardless of the apparent conductivity. On the other hand, sediment with moderate to high water content (> 15 vol%, maximum of 49 vol%) has low to high salt stores. The linear regression equations from both groups are used to model the range of potential salt stores with respect to the amount of water present in the sediment.

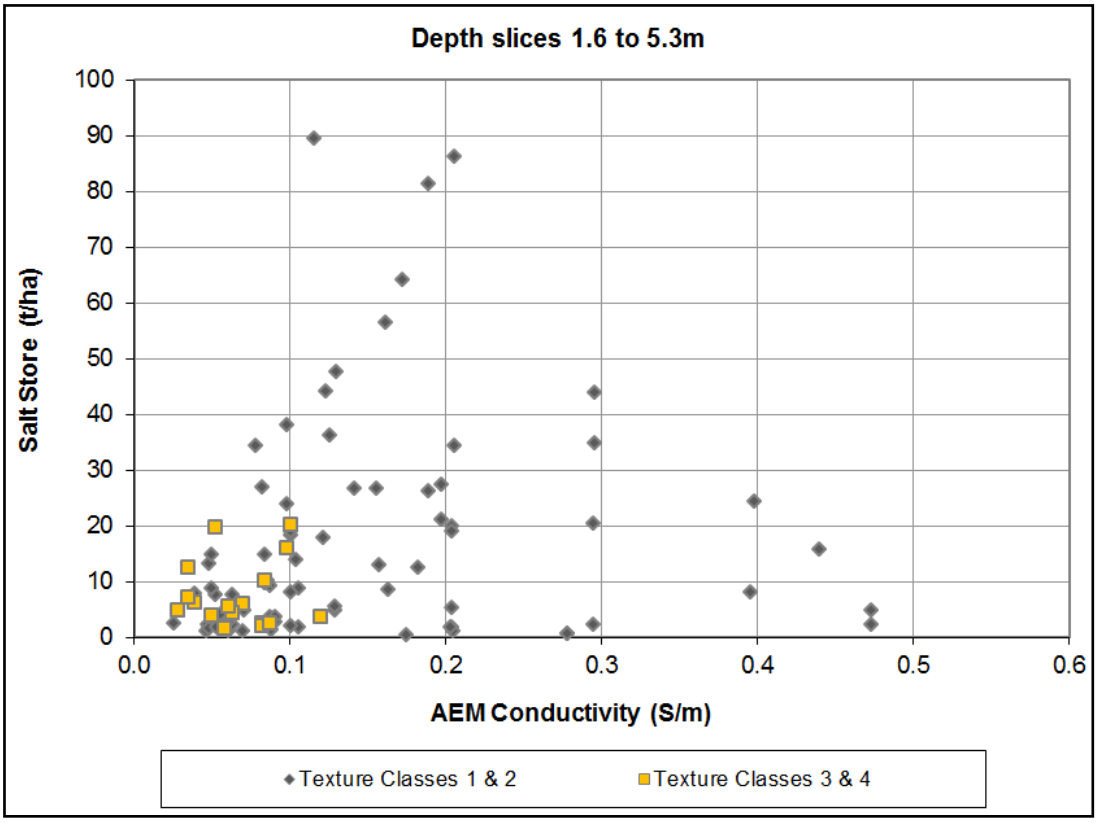



**Figure 17-147.** *Salt store and electrical conductivity of mud-rich and sand-rich sediments. The former includes texture classes 1 and 2 and the latter includes texture classes 3 and 4.*

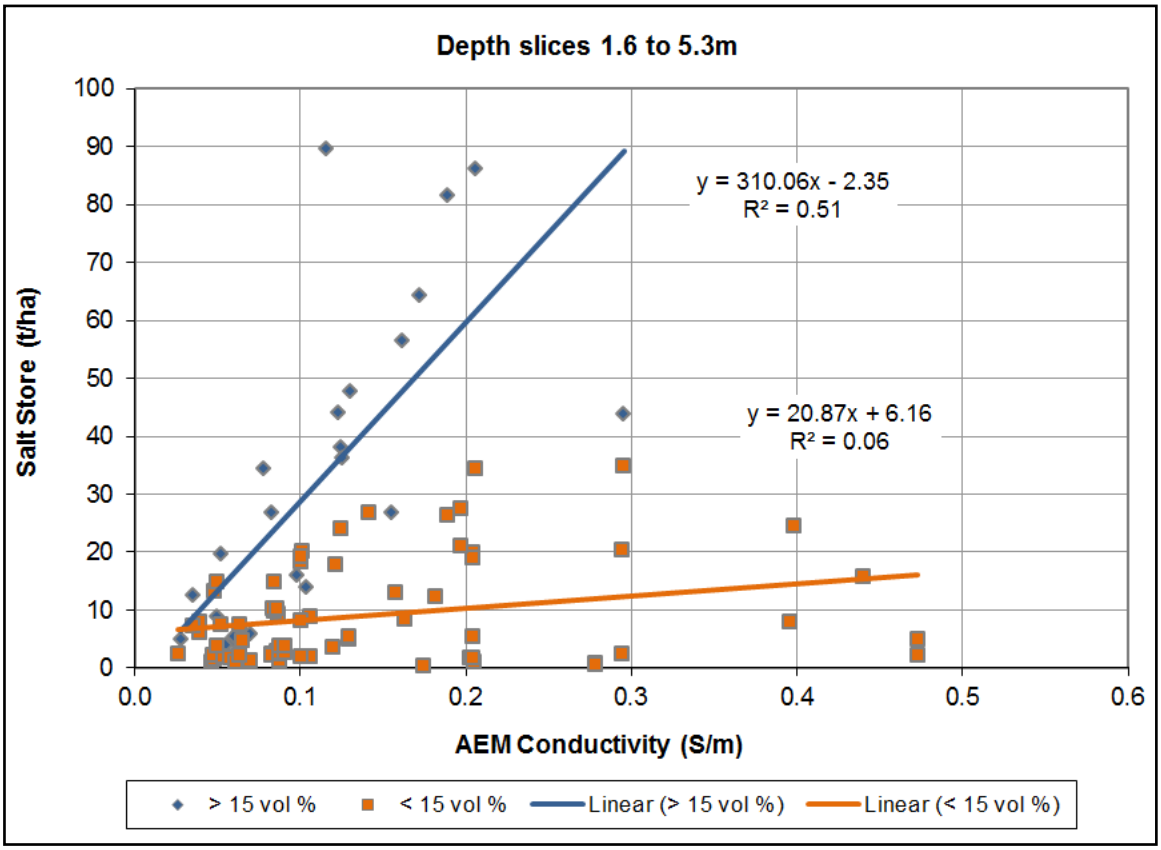



**Figure 17-148.** *Salt store and electrical conductivity of sediment grouped according to water contents (NMR derived total water). AEM conductivities are from depth slices 1.6 m to 5.3 m.*

For wet sediment (total water > 15 vol%):

*Salt Store (t/ha) = 0.178 x EC (S/m)*

**Equation 115**

For dry sediment (total water < 15 vol%):

*Salt Store (t/ha) = 0.009 x EC (S/m) + 0.004*

**Equation 116**

Applying the same criteria to AEM depth slices 5.3 m to 13.1 m, a very subtle trend is present due to the low salt store (0.018 t/ha) (Figure 17-149). Due to the spread of data with a fair degree of overlap in salt stores at low conductivity, the linear equations from both groups depict a range of potential salt stores with high uncertainty.

For wet sediment (total water > 15 vol%):

*Salt Store (t/ha) = 0.032 x EC (S/m)*

**Equation 117**

For dry sediment (total water < 15 vol%):

*Salt Store (t/ha) = 0.006 x EC (S/m) + 0.002*

**Equation 118**

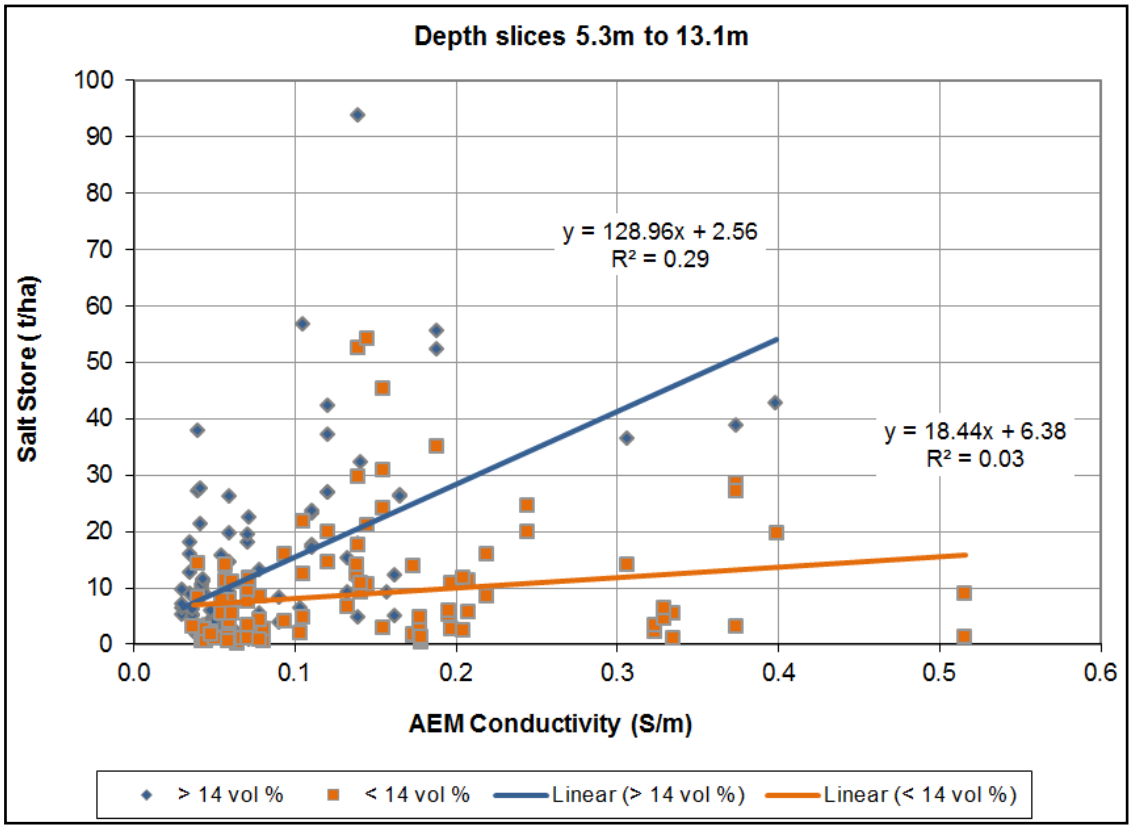



**Figure 17-149.** *Salt store and electrical conductivity of sediment grouped according to water contents (NMR derived total water). AEM conductivities are from depth slices 5.3 m to 13.1 m.*

For data associated AEM depth slices 13.1 m to 22.0 m, majority of the salt store is very low (< 0.002 t/ha) (Figure 17-59). For sediment with high water content, positive correlation between conductivity and salt stores hinges on five data points only. Nonetheless, salt store from sediment with low water content consistently remains consistent lower. The linear regression equations from both groups are used as a semi-quantitative relationship to demarcate the range of salt stores for these AEM depth slices. Thus, the linear regression equations from both groups can be used to demarcate the range of salt stores for these AEM depth slices.

For wet sediment (total water > 15 vol%):

*Salt Store (t/ha) = 0.013 x EC (S/m)*

**Equation 119**

For dry sediment (total water < 15 vol%):

*Salt Store (t/ha) = 0.004 x EC (S/m)*

**Equation 120**

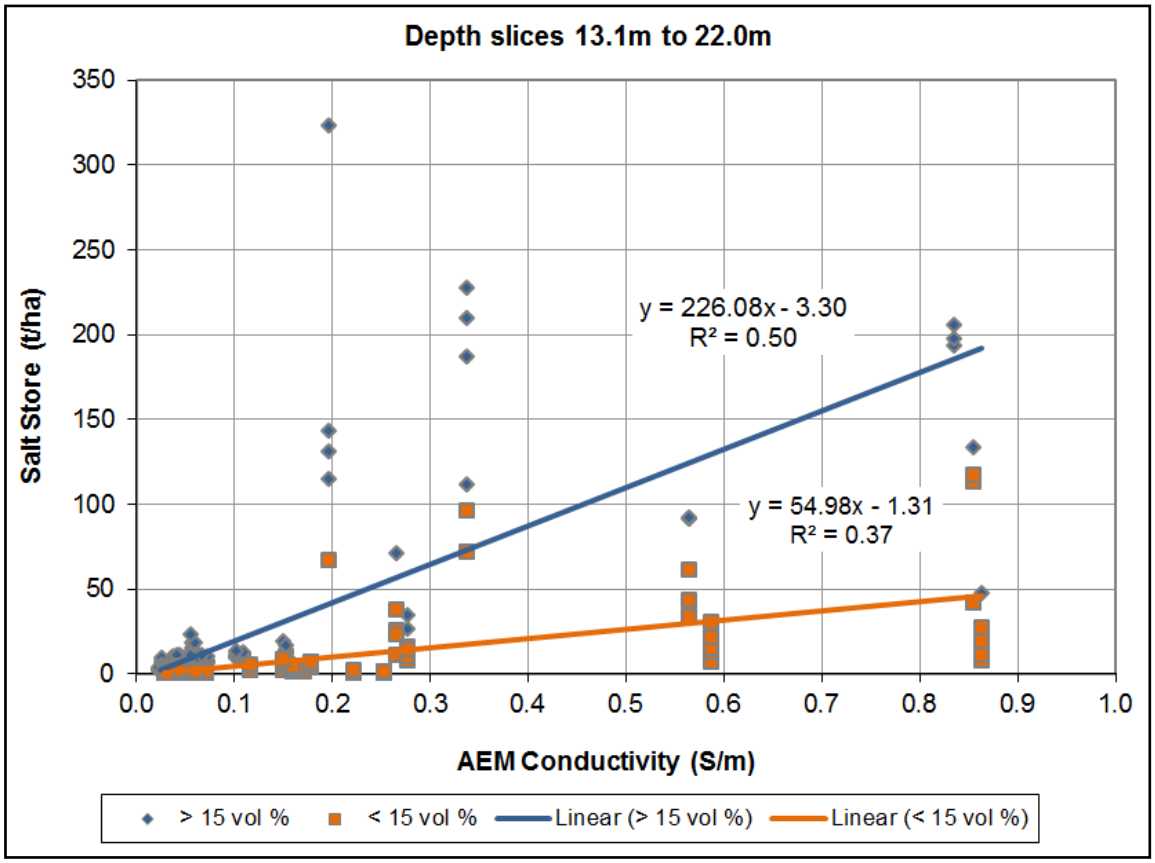



**Figure 17-150.** *Salt store and electrical conductivity of sediment grouped according to water contents (NMR derived total water). AEM conductivities are from depth slices 13.1 m to 22.0 m.*

## 17.15 RECHARGE POTENTIAL MAPPING

### 17.15.1 Introduction

There are a number of different methods for mapping recharge across the landscape. Where field groundwater sampling programs or hydrographic monitoring are extensive, recharge can be calculated using quantitative methods (e.g. chloride mass balance, water table fluctuation etc) and mapped spatially (e.g. Edmunds *et al*., 2002; Yin *et al*., 2011). This mapping approach is limited by the density of field measurements. In the case of the BHMAR Project, insufficient borehole density existed for this approach to be effective. However, where borehole data, hydrochemical analyses and groundwater hydrographs were available, these datasets were used in deriving recharge estimates, as discussed in Section 17.15.2.

Other studies focus more on resolving the water balance (e.g. Yin *et al*., 2011; Szilagyi *et al*., 2011). Szilagyi *et al*. (2011) utilised the difference between monthly evapotranspiration (ET) and monthly precipitation (P) grids made available from PRISM and MODIS satellites to map mean annual groundwater recharge. Diffuse recharge across the landscape by rainfall has been determined as a minor component of the overall groundwater recharge process for the BHMAR Project study area (Lawrie *et al*., 2012b), and as such, applying a similar methodology to Szilagyi *et al*. (2011) would not provide a realistic indication of the spatial distribution of groundwater recharge.

Numerical groundwater models such as MODFLOW can also derive recharge distributions across space and time (e.g. Lubczynski & Gurwin, 2005). The power of these models is that all available data can be incorporated, providing a 3D understanding of hydrogeology and groundwater processes. Such models are data intensive and are recommended as a critical component for any future phases of the project (Lawrie *et al*., 2012e).

Finally, other authors have taken a combined geographic information system (GIS) and remote sensing (RS) approach. Tweed *et al*. (2007) were able to map both groundwater recharge and discharge areas in a basalt aquifer using a number of indicative datasets such as topography, depth to water table, rainfall and groundwater EC. Similarly, Shaban *et al*. (2006) weighted and combined lineaments, drainage, lithology, karstic domains and land cover/land use to map recharge potential in Occidental Lebanon. While the parameters used in these studies are not necessarily applicable to the BHMAR Project, they provide a structured framework for mapping.

### 17.15.2 Recharge Mapping

In keeping with the approach of Tweed *et al*. (2007), recharge potential mapping focused on identifying the various recharge processes relevant to the BHMAR Project area, namely (in order of estimated magnitude): lateral bank recharge, recharge pathways via faults or holes in the upper confining aquitard, and surface infiltration associated with flooding or localised rainfall (as shown conceptually in Lawrie *et al*., 2012b). Based on this, the key surface and subsurface indicators of recharge were identified as:

- AEM depth-slice interpretation showing distribution of fresh groundwater resources (Figure 17-151; Section 17.5);
- Hydrochemical and hydraulic analyses including radiocarbon (oxygen and deuterium), stable isotopes, fuzzy-k means analysis and hydrographic data (Sections 14 and 15);
- Holes in the upper confining aquitard as mapped from the AEM (Figure 17-152; Section 17.5;
- Thickness of the shallow unconfined aquifer (Figure 17-154; Section 17.5);
- Percentage mud in the near surface (Figure 17-153; Section 17.5);
- Tectonic structures (Section 17.3); and
- Availability of source water, either potential flood inundation (Figure 17-155; Section 17.1) or existing surface water bodies (e.g. lakes or rivers).

These various datasets were combined to assess the potential for groundwater recharge, focusing on potential pathways (e.g. faults, holes, lateral bank recharge) combined with evidence of recharge (e.g. fresh groundwater, hydrographic response to flooding, greater presence of modern carbon, particular isotopic signature) described in Table 17-55, Table 17-56 and Table 17-57. This approach could be applied across the whole study area, at specific targets or even at the borefield scale.

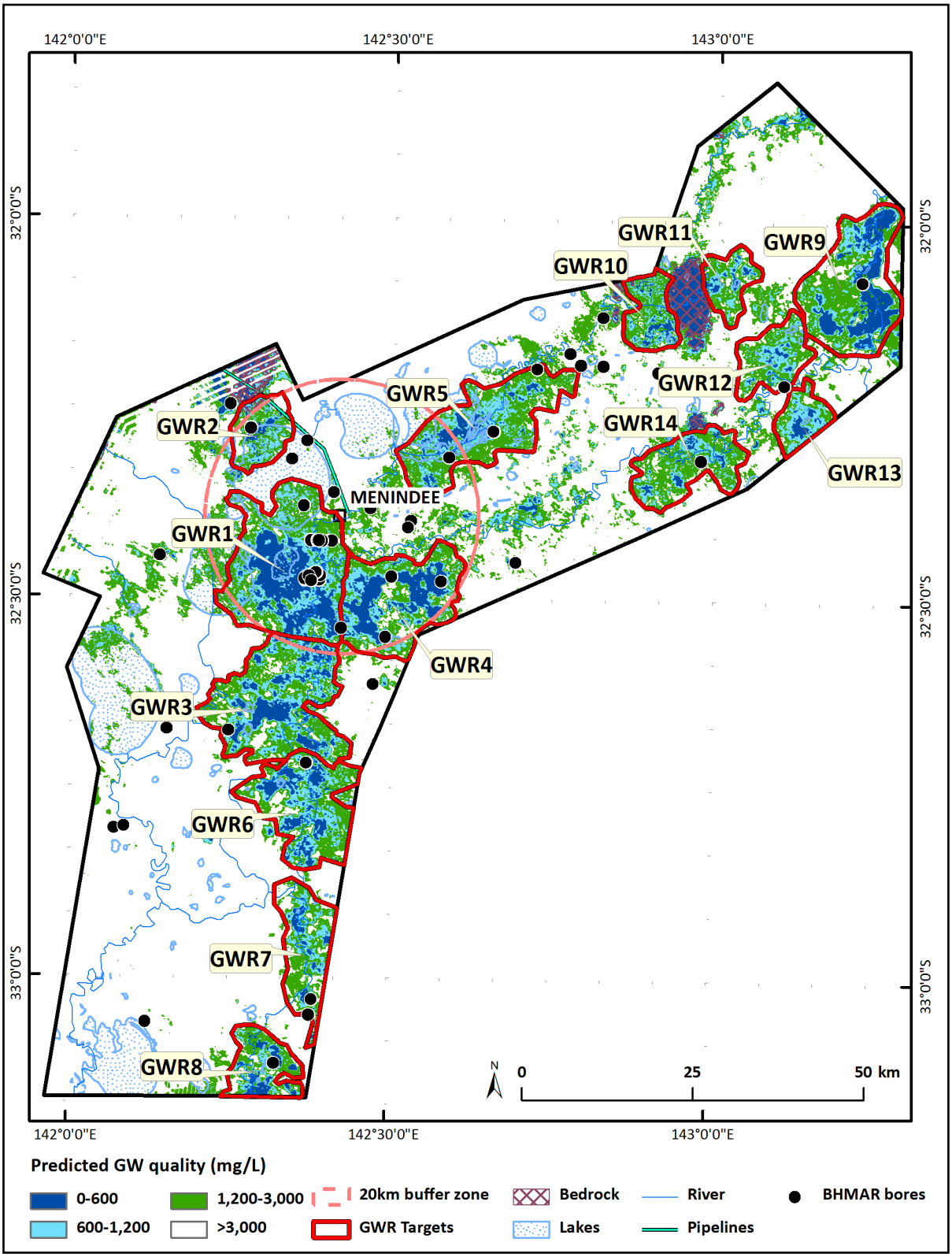



**Figure 17-151.** *Predicted groundwater salinity map for the BHMAR project area.*

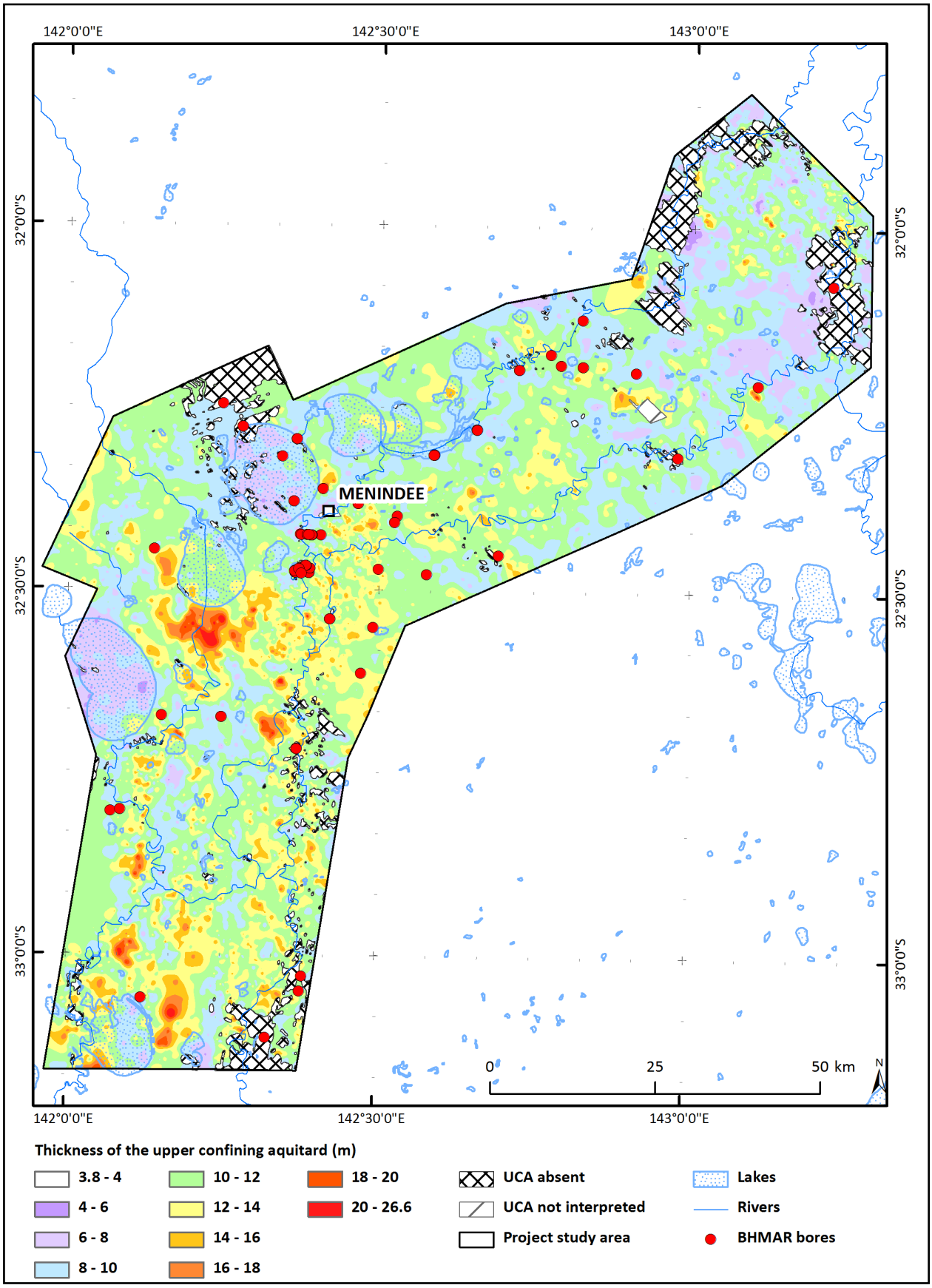



**Figure 17-152.** *Thickness of the upper confining aquitard including areas where it is absent or non-interpreted.*

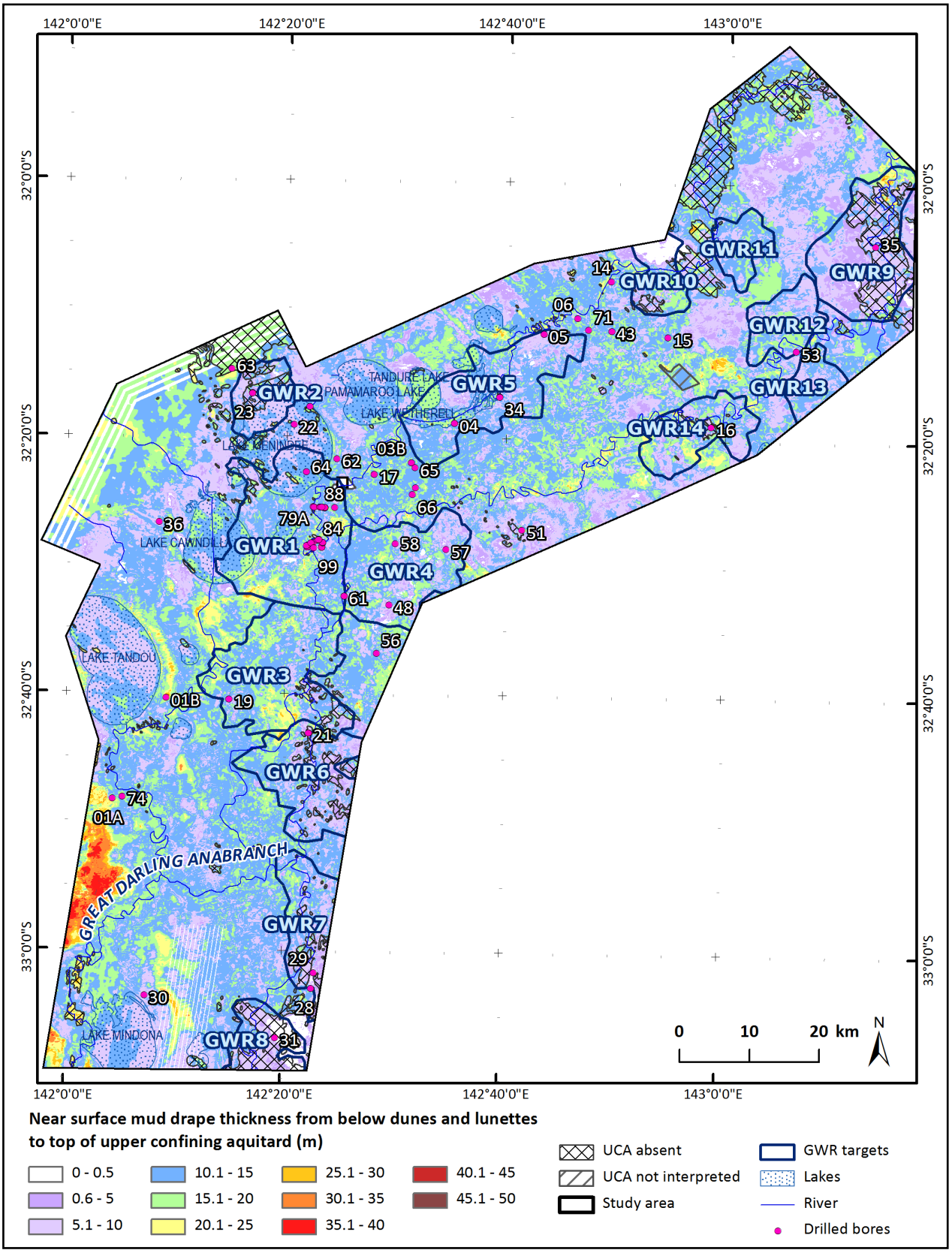



**Figure 17-153.** *Thickness of the upper aquitard (clay-drape).*

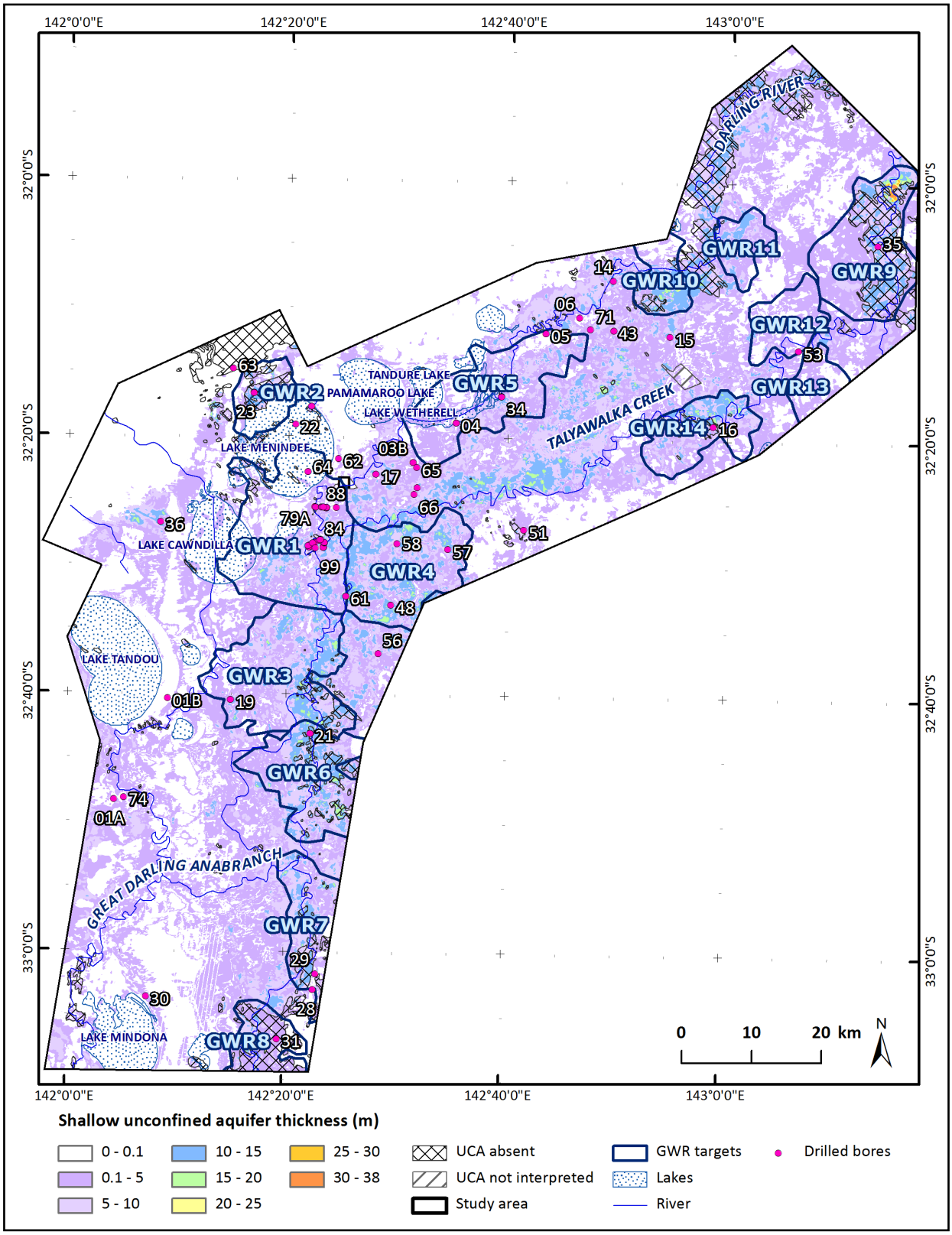



**Figure 17-154.** *Thickness of the shallow unconfined aquifer.*

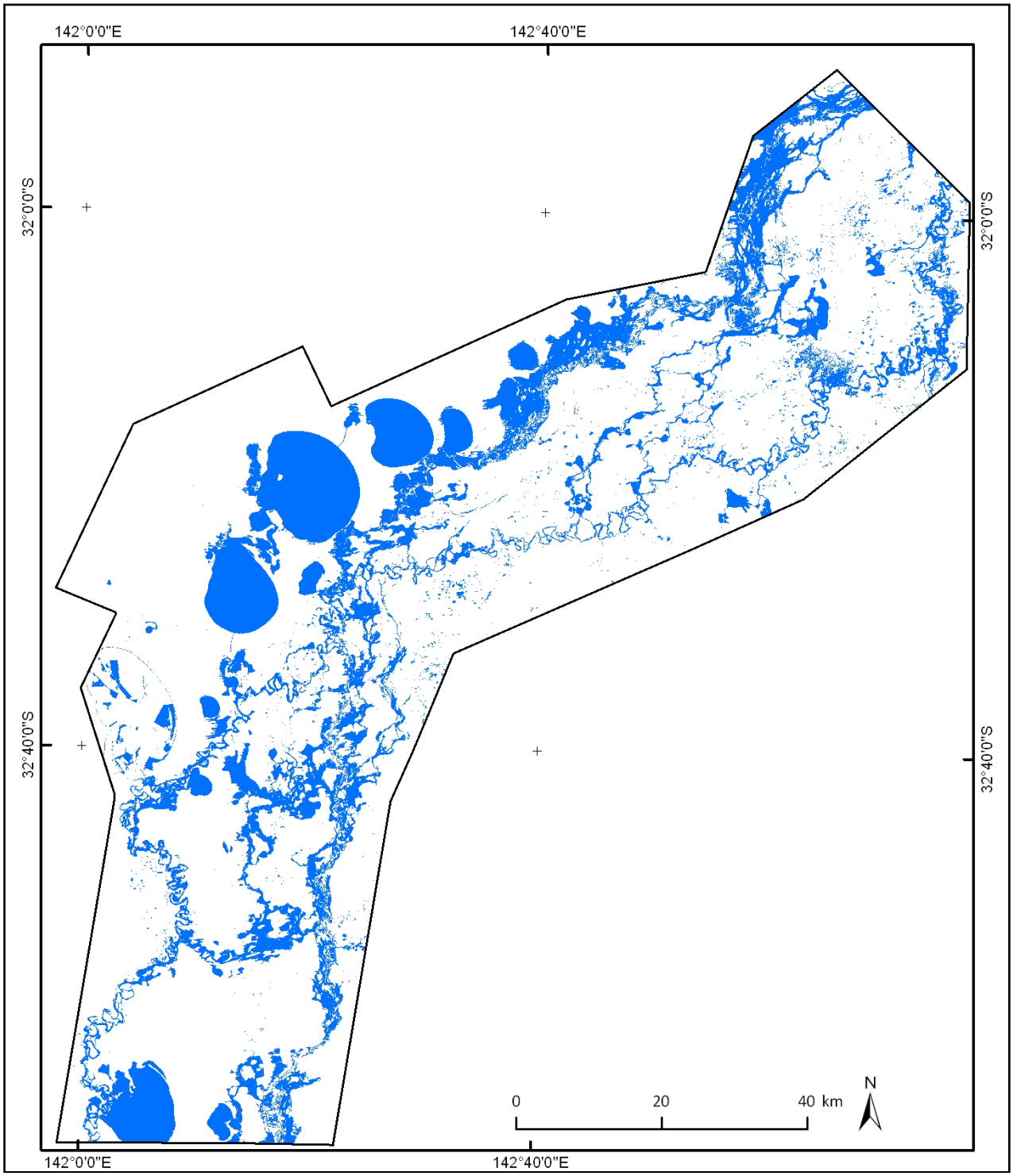



**Figure 17-155.** *Extent of flooding during one of the largest recorded floods for the area - the 1990 flood, as derived from Landsat imagery.*

**Table 17-55.** *Presence or absence of surface water (river, lake or flood waters) and recharge pathways (faults, holes in the upper confining aquitard) at each groundwater resource target. Where either one of these factors is absent, palaeorecharge is inferred.*

| Variable | Groundwater Resource (GWR) Targets | | | | | | | | | | | | | |
|---|---|---|---|---|---|---|---|---|---|---|---|---|---|---|
| | 1 | 2 | 3 | 4 | 5 | 6 | 7 | 8 | 9 | 10 | 11 | 12 | 13 | 14 |
| **Source water** | Y | Y | Y | N | Y | Y | Y | Y | Y | Y | Y | Y | N | Y |
| **Recharge pathway** | Y | Y | Y | N | Y | Y | Y | Y | Y | Y | N | N | N | Y |
| **M=Modern recharge; P=Palaeorecharge** | M | M | M | P | M | M | M | M | M | M | P | P | P | M |

**Table 17-56.** *Amount of hydrograph response observed from bores within each groundwater resource target. - indicated where either an associated bores was not in existence or water levels were not monitored at the particular bore.*

| Variable | Code | Groundwater Resource (GWR) Targets | | | | | | | | | | | | | |
|---|---|---|---|---|---|---|---|---|---|---|---|---|---|---|---|
| | | 1 | 2 | 3 | 4 | 5 | 6 | 7 | 8 | 9 | 10 | 11 | 12 | 13 | 14 |
| **Water level rise** | 0=none; 1=<0.5 m; 2=0.5-1 m; 3=>1 m | 3 | 3 | - | 1 | 3 | 1 | 2 | 1 | 0 | - | - | - | - | 0 |
| **Aquifer transmissivity factor** | 1=very low (0.1-1); 2=low (1-10); 3=intermediate (10-100); 4=high (100-1000)[1] | 4 | 1 | 3 | 4 | 4 | 4 | 4 | 4 | 3 | - | - | - | - | 3 |
| **Water level response** | Watertable rise*transmissivity factor | 12 | 3 | 3 | 4 | 12 | 4 | 8 | 4 | 0 | - | - | - | - | 0 |

Note: [1]Krasny (1993).

**Table 17-57.** *Calculated recharge potential for each groundwater resource target. Classification colours correspond to the classes mapped in Figure 17-156.*

| Variable | Code | Groundwater Resource (GWR) Targets | | | | | | | | | | | | | |
|---|---|---|---|---|---|---|---|---|---|---|---|---|---|---|---|
| | | 1 | 2 | 3 | 4 | 5 | 6 | 7 | 8 | 9 | 10 | 11 | 12 | 13 | 14 |
| **Watertable response** | | 12 | 3 | 3 | 4 | 12 | 4 | 8 | 4 | 0 | - | - | - | - | 0 |
| **Vertical recharge[1]** | 1=low; 2=medium; 3=high | 3 | 3 | 3 | 1 | 3 | 3 | 1 | 1 | 2 | - | - | - | - | 2 |
| **Percentage modern carbon (Calivil)** | 1=<30%; 2=30-60%; 3=60-90%; 4=>90% | 3 | 3 | 1 | 1 | 3 | 4 | 4 | 2 | 3 | - | - | 1 | - | 2 |
| **Recharge potential** | ∑watertable response, vertical recharge & pMC | 18 | 9 | 7 | 6 | 18 | 11 | 13 | 7 | 5 | - | - | - | - | 4 |
| **Classification[2]** | | 1 | 1 | 2 | 4 | 1 | 1 | 1 | 2 | 3 | 5 | 4 | 4 | 4 | 3 |

Note: [1]Based on fuzzy-k means analysis.

2 Classification codes: 1= modern recharge evident; 2= modern recharge probable, requires more data; 3= modern recharge possible but very slow rates; 4= no evidence of modern recharge, palaeo-resource (defined from Table); 5= insufficient data.

### 17.15.3 Application

Initially, the presence of potential (1) surface source water such as modern drainage, lake storages or flood waters, and (2) recharge pathways due to absent or thin near-surface aquitards, faults, or holes in the upper confining aquitard, were assessed for each groundwater resource target. If either was absent, then modern recharge was inferred to be limited. If hydrochemical analyses were available, this was used to either confirm or contradict this assumption. GWR4 is an example of a groundwater palaeo-resource as it lacks connectivity with surface water features, has no apparent leakage mechanism to the Calivil Formation aquifer, had low modern carbon and minimal hydrographic response to flooding. Targets GWR11, 12 and 13 are also inferred to be palaeo-resources (Figure 17-156) however drilling and groundwater analysis is required to confirm this assessment. Insufficient data existed to make a determination about GWR10. Analysis was likewise applied to the other targets, taking into consideration all available datasets. The final interpretation is shown in Figure 17-156, summarised in Lawrie *et al*. (2012e) and expanded on in Lawrie *et al*. (2012b). Similar analysis was applied at a potential borefield scale and discussed in Lawrie *et al*. (2012c).

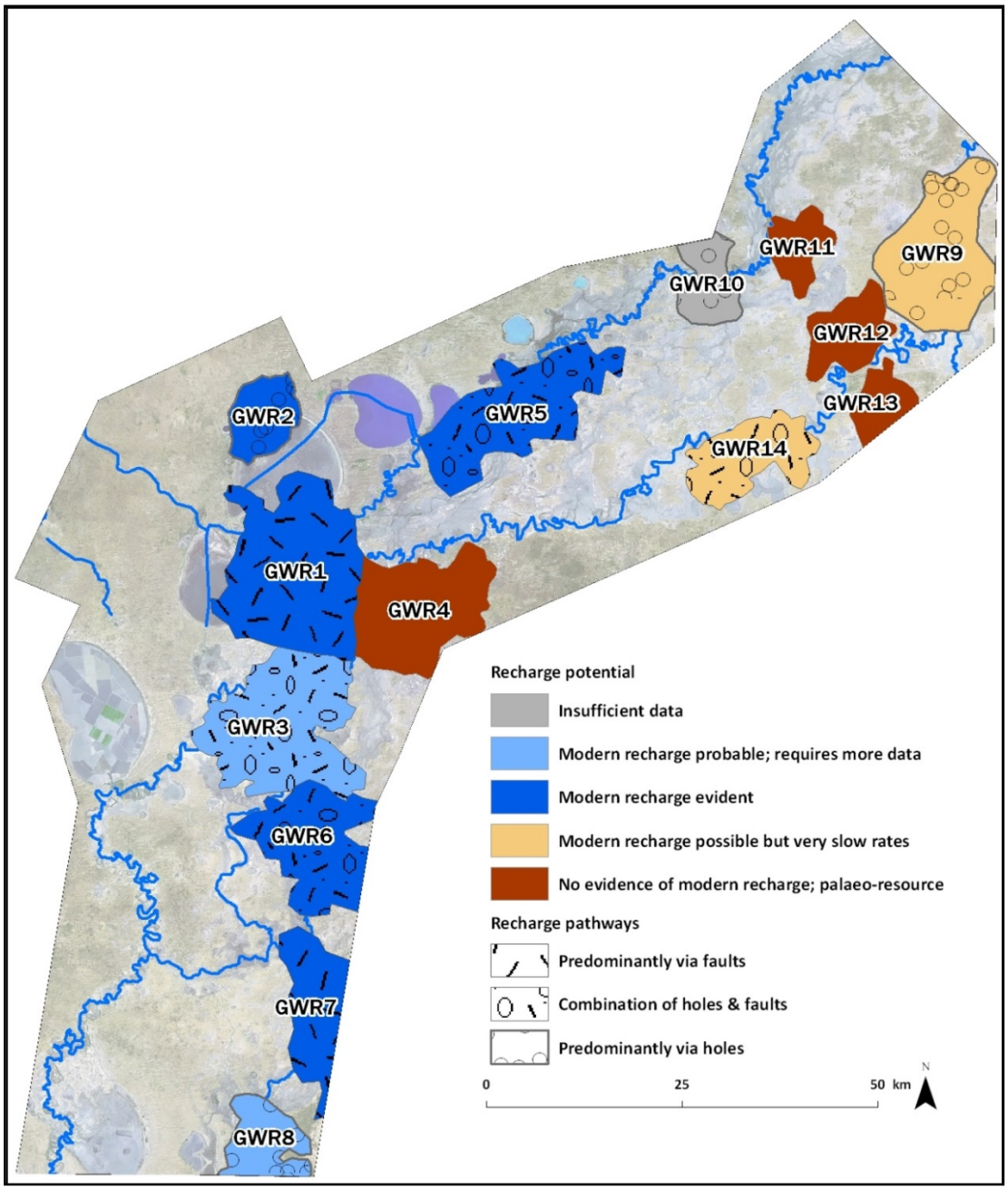



**Figure 17-156.** *Recharge potential and pathway classification applied to the 14 groundwater resource targets.*

## 17.16 GRAPHIC DISPLAY OF BOREHOLE GEOLOGICAL, GEOPHYSICAL AND GEOCHEMICAL DATA

Golden Softwares Strater®2 and Strater®3 were used to produce down-hole graphical displays of geological, geophysical and geochemical data. Strater® displays raw, filtered and inverted data as borehole, well logs, maps and cross-sections. Examples are shown in Figure 17-157 to Figure 17-161 below.

### 17.16.1 Data Collation

Strater® accepts a wide range of data formats which are displayed in tables with set characteristics or types. Data can either be loaded from the desired file or copied directly into the new Strater® table. The Load feature was used to import large data sets whereas relatively small data sets were copied directly into the new table.

When importing data into Strater® the relevant data type was selected. In general, these data are grouped into variable with single depth (x), variable with depth intervals (x1 – x2), variable as text, and variable corresponding to height (z) (Table 17-58).

**Table 17-58.** *The data types used in Strater®.*

| Single Depth | Depth Interval | Lithology | Well-Construction | Collars |
|---|---|---|---|---|
| NMR derived | Stratigraphy | Lithology | Borehole Design | Borehole Information |
| Chemistry | Munsell colour | | | |
| Gamma | | | | |
| Induction Conductivity | | | | |
| Grainsize | | | | |

### 17.16.2 Production of Strater Logs

Once the data was imported into Strater® tables and assigned a data type the graphical logs could be produced. All Strater® logs were produced with a header section in which the crucial information such as Bore ID, Location, standing water level (SWL), logging date and data type was displayed. Once the remainder of information was added a legend was created using the draw legend feature. The project was then saved as template file and used as a temple for the remaining borehole logs of the same type.

#### 17.16.2.1 *Main Logs*

The main Page displays vital information for the respective borehole such as well construction, stratigraphy, lithology, gamma, grainsize and NMR derived data, including bound and free water and the calculated hydraulic conductivity. Each of these logs were linked to the depth scale (normally positioned on the right hand side of the page) in order to maintain a constant scale for all logs. The “Scheme editor” was also used to customize the presentation for all logs.

#### 17.16.2.2 *Fluid and Solid Phase Chemistry Logs*

The downhole chemistry logs (major and trace elements in the solid phase and major and trace ions in solution) were plotted using simple downhole bar logs and their respective data ranges adjusted according to the minimum and maximum values in the data set. In addition, the lithology, induration stratigraphy,

grainsize (with anomalous values highlighted), hydraulic classes, Munsell colours, well-construction, together with borehole induction conductivity and gamma logs, were also displayed. NMR logs were shown for those bores where it was measured.

### 17.16.3 Textural Bar Graph Anomalies

During the production of the Strater Logs for the sonic-cored holes, the lithology column was generated automatically from summary files of lithology descriptions derived from the laboratory logging sheets and the bar charts in the grain-size percentage column were generated automatically from the laser and sieve textural analyses. Routine checking of the Starter Logs resulted in identification of 53 instances in 24 logs where textural bar charts were inconsistent with the equivalent lithology category. Investigation of these anomalies revealed that there were three different categories of anomalous results:

- Incorrectly transcribed lithology descriptions. In these examples, the core photographs and laboratory logging sheets were consistent with the textural bar-charts but not with the lithology category, which was subsequently found to have been incorrectly transcribed to the Strater source file. The anomaly was removed by amending the lithology category to the correct type.
- Coarser texture in bar charts due to undispersed clay or carbonate-cemented aggregates. In these cases the bar charts indicated granules and/or sand domination in mud-dominated lithologies. This problem with the sediment textural analysis protocol not successfully dispersing some mud-rich lithologies had already been recognised and investigated by a specific experimental program of size analyses (See Section 11.3.1). Anomalous textural bar charts due to this issue are indicated on the graphical logs (Figure 17-157).
- Unexplained anomalies. In a small number of samples the reason for anomalies between the textural bar graphs and the associated lithology was not able to be explained. In these cases the core photography and the Laboratory log sheets were consistent with the lithological category indicating a possible problem with the laboratory textural analyses. These possibilities include a malfunction during the laser machine run, a mislabelled sample or processing of the wrong sample. Unexplained anomalous textural bar charts are indicated on the graphic logs (Figure 17-157).

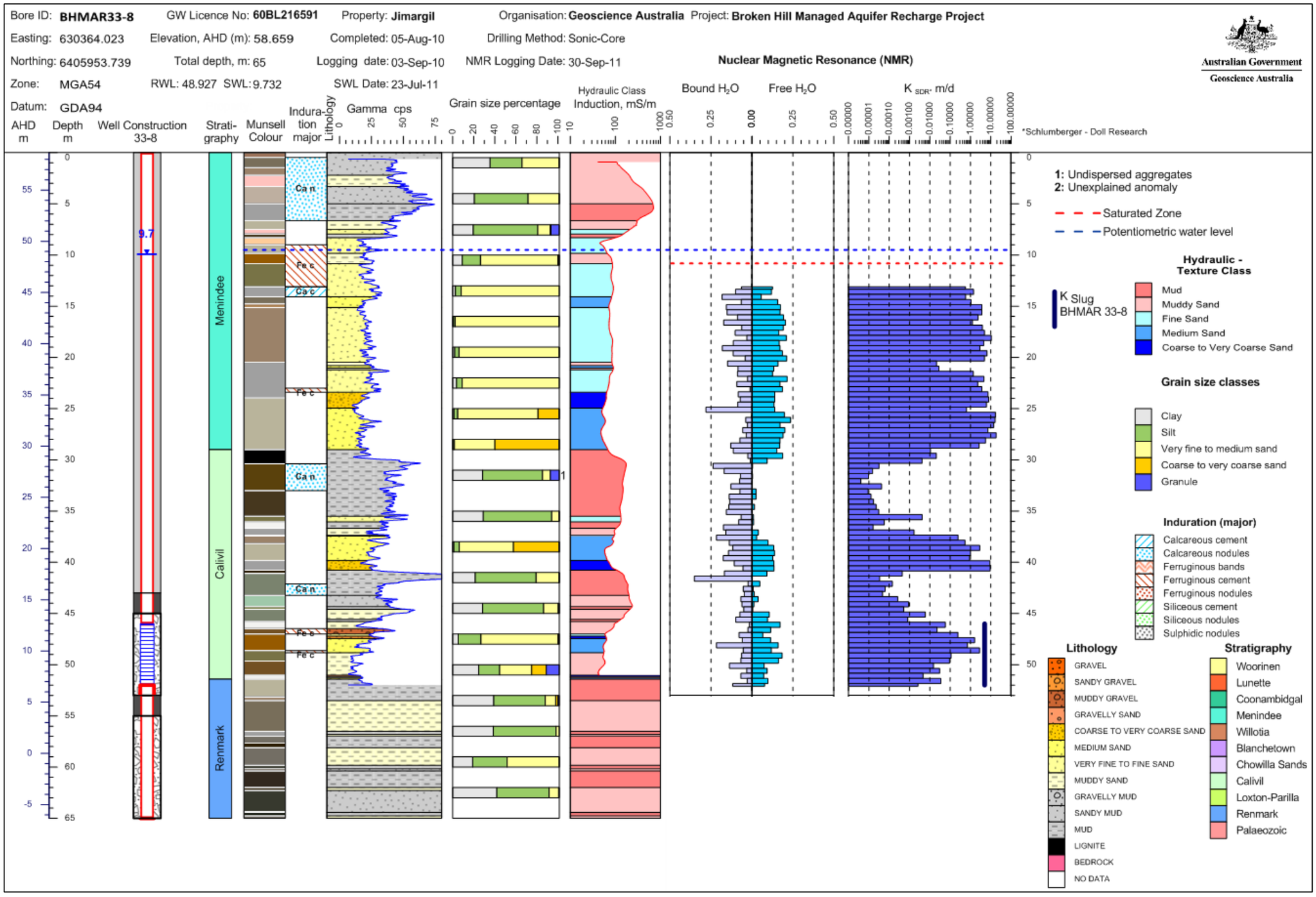



**Figure 17-157.** *Borehole graphical logs including well construction details, stratigraphy, lithology and hydraulic conductivity. Where NMR was acquired, results are also included, as here. Anomalous grainsize values, where present are indicated*




**Figure 17-158.** *Borehole graphical logs including hydrochemical major ion data obtained from pore fluid analysis.*

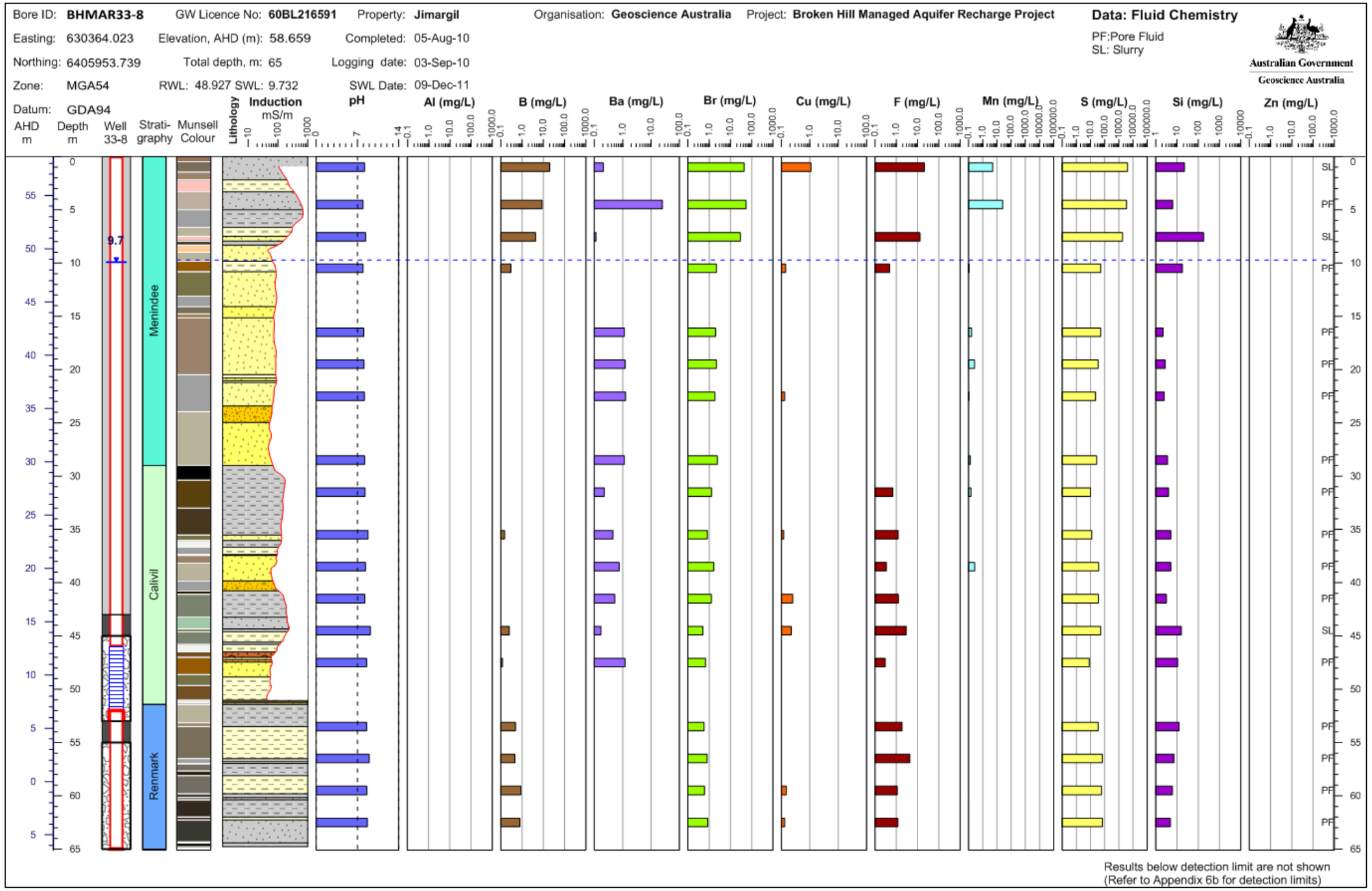



**Figure 17-159.** *Borehole graphical logs including hydrochemical trace ion data obtained from pore fluid analysis.*

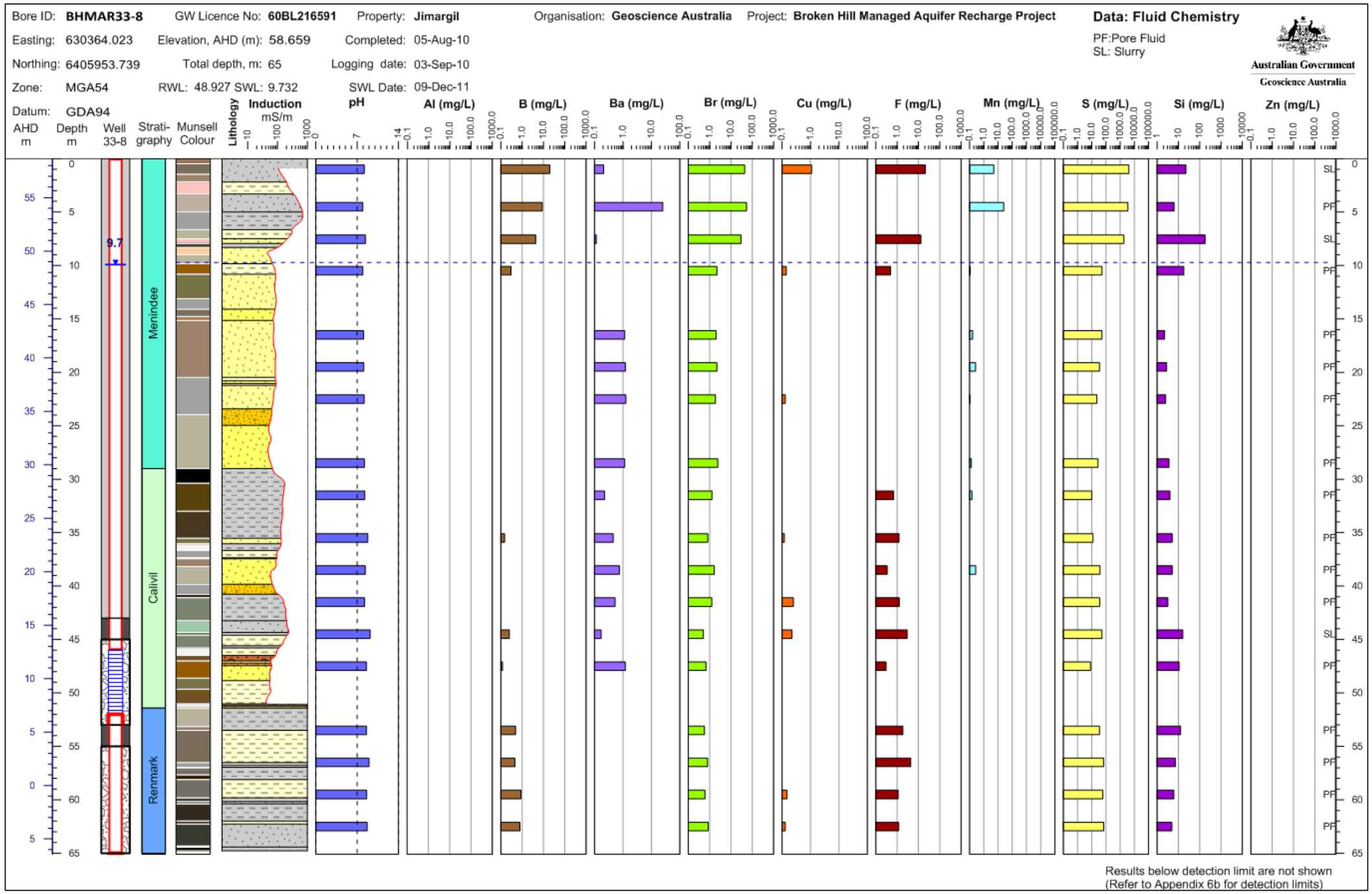



**Figure 17-160.** *Borehole graphical logs including solid major element geochemistry.*

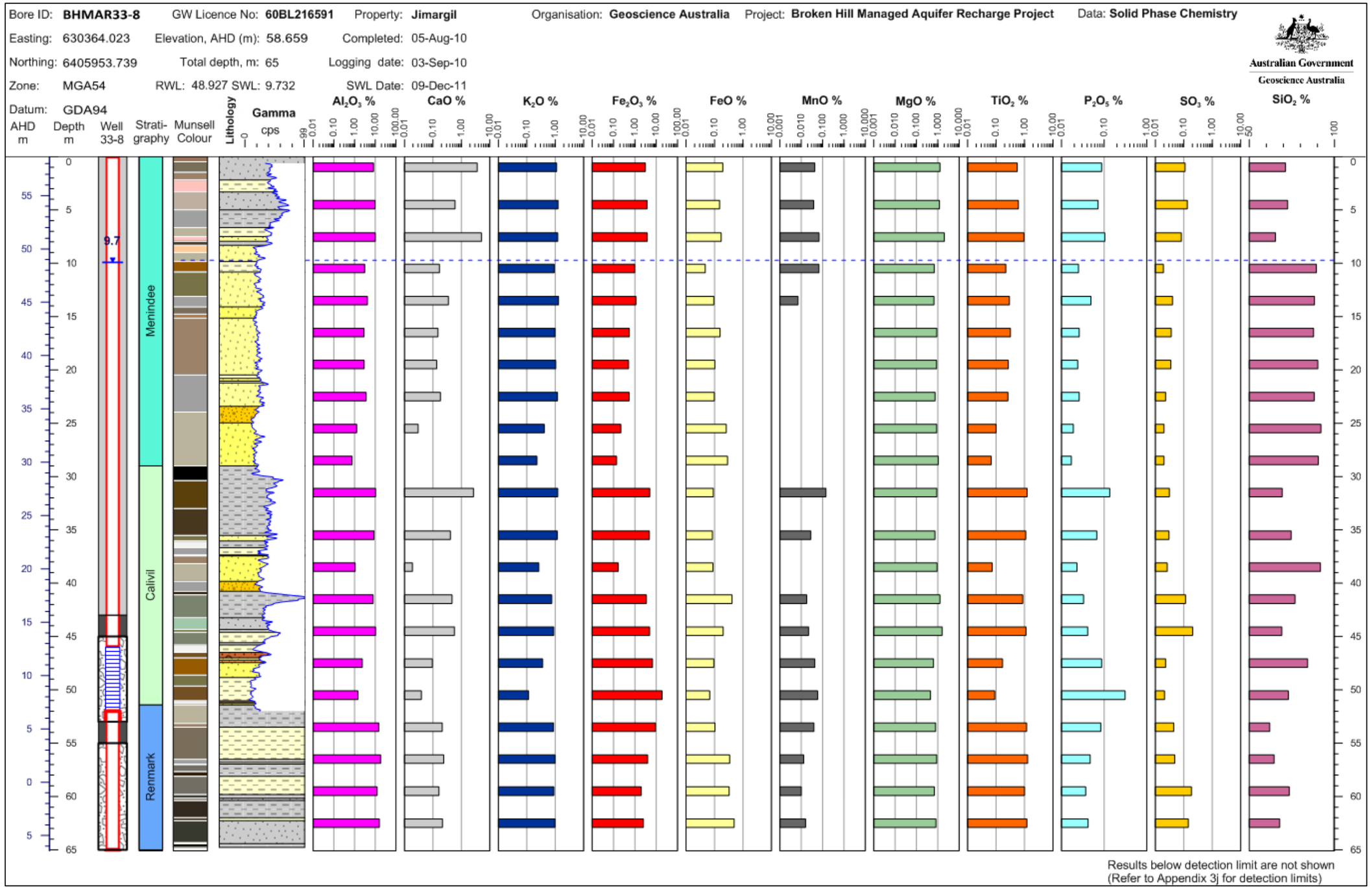



**Figure 17-161.** *Borehole graphical logs including solid trace element geochemistry.*

## 17.17 3D GEOLOGICAL MODEL AND VISUALISATION

The management of water and groundwater resources is increasingly dependent on the integration of large complex datasets to visualise and model hydrological systems. In Australia, the Broken Hill Managed Aquifer Recharge (BHMAR) project, has involved the integration of high resolution LiDAR, remote sensing (Landsat, SPOT), airborne electromagnetic (AEM, e.g. Figure 17-162 ), ground and in-river electrical surveys, and point datasets from surface sites and lines (from drillholes). Products derived from the integration of these datasets include 3D maps of hydrostratigraphy, groundwater quality, hydraulic conductivity, 2D displays of data (e.g. potentiometric surface maps), 3D volume shapes of groundwater resources and managed aquifer storage targets, and lithological, hydrogeochemical and hydrological data in drillholes.

To facilitate effective communication of such large and complex geoscience datasets and project results to a wide range of stakeholders, Geoscience Australia (GA) has recently developed an interactive 3D virtual globe viewer. The interactive virtual globe is built on NASA's open source World Wind Java Software Development Kit (SDK) and provides users with easy and rich access to geoscientific data.

The BHMAR project required further development of the existing viewer platform in order to display complex 3D hydrogeological, hydrogeophysical and hydrogeochemical data (points, lines, 2D surface and 3D shapes). The final product includes support for a variety of geo-referenced raster data formats, as well as vector data such as ESRI shapefiles and native support for a variety of GOCAD data types including TSurf, SGrid, Voxet and PLine. It also supports well and borehole data including attribute-based styling of log features and the ability to include legends and descriptions of data within the user interface. An easy-to-use interface has been customised for navigation of data in 3D space using a virtual globe model, with powerful keyframe based animation tools used to generate flythrough animations for use in knowledge communication workshops. The products will be distributed as data layers via the internet and as a stand-alone DVD package.

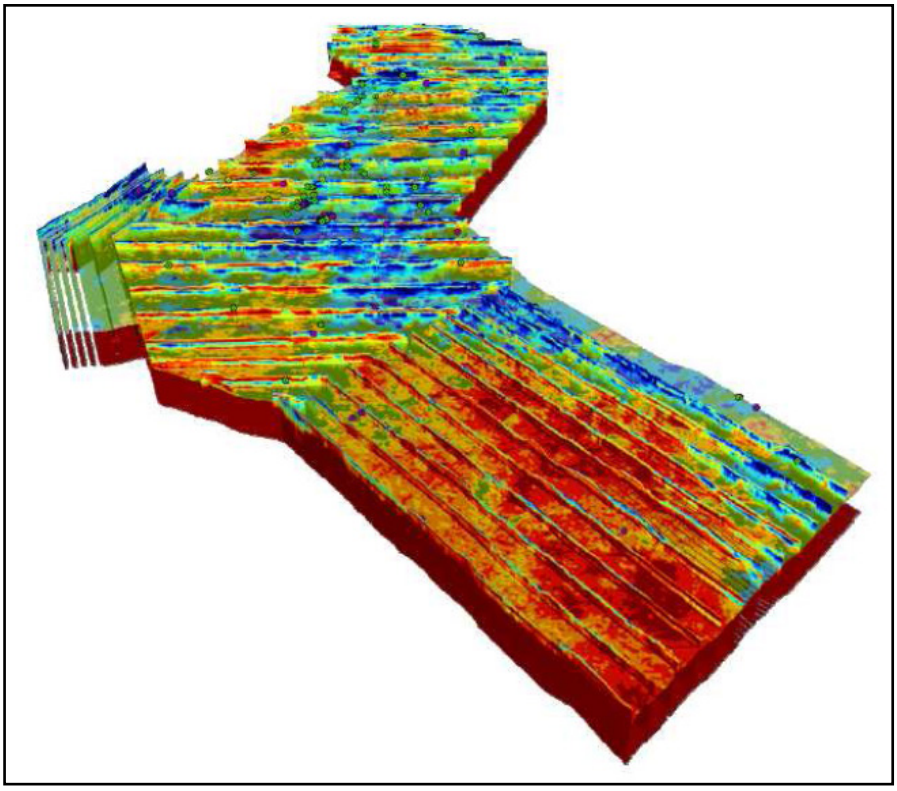


**Figure 17-162.** *Perspective view of BHMAR Project AEM 3D conductivity model. A conductivity depth slice (43-51 m) is shown here with AEM conductivity cross section. Coloured dots represent the different types of boreholes drilled as part of the BHMAR project (green = sonic, cored; yellow = sonic, non-cored; purple = rotary mud).*

# 18 Conclusions

1. The BHMAR study area was recognised prior to commencement of the project as a data-poor area from the perspective of identifying and assessing suitable groundwater targets. A comprehensive review of pre-existing biophysical (e.g. geological, hydrogeological, hydrogeophysical, hydrogeochemical, landscape, vegetation, cultural and environmental) data found relevant to the identification and assessment of potential MAR and groundwater resource targets helped to identify critical data gaps and assisted with the design of a data acquisition strategy. In detail, the principal findings of the review of pre-existing data were:
    i. At face value, there were a significant number (3,292) of pre-existing bores in the potential study areas. However, analysis showed that the vast majority of these bores contained limited geological and hydrogeological data for the zones of interest, and did not greatly assist with the identification and assessment of MAR and/or groundwater resource targets.
    ii. Greater than 90% of pre-existing bores assessed across 6 potential study areas were shallow bores (<30 m depths). Only 0.2% (18 bores) had some lithological data (mainly drillers logs) for the priority Calivil Formation aquifer in the final BHMAR study area, and only 6 of these bores contained reliable/useable geological/hydrogeological data.
    iii. Only 152 bores were recorded as having PVC casing that would enable borehole hydrogeophysical studies to be conducted. Less than a dozen bores had any borehole geophysical data. No core materials for the key aquifer and aquitard intervals existed for the study area, severely limiting assessment of the aquifers and aquitards.
    iv. There was sufficient groundwater salinity data from shallow bores and a few deeper bores to state with reasonable certainty that a dilution aureole was developed in proximity to the Darling River and Talyawalka Creek. However, the data density and depth meant that it was not possible to recognise groundwater or MAR targets in the Calivil Formation aquifer using these data.
    v. There was insufficient major and trace element hydrogeochemical data to carry out MAR risk assessments, or to determine groundwater processes.
    vi. Limited pre-existing pump test data gave some confidence that the Calivil Formation aquifer may have suitable aquifer properties in some locations, although pre-existing data was insufficient to target locations with suitable properties.
    vii. Pre-existing groundwater models for the BHMAR study area were based on a paucity of hydrogeological and geological data, and a limited understanding of groundwater processes including recharge and inter-aquifer leakage. The groundwater models were insufficiently parameterised to assist with the groundwater or MAR assessments.
    viii. Pre-existing regional-scale hydrogeological maps for the study area are superior to the geological maps of the same area. While they are of limited use due to the extrapolation between widely spaced boreholes, there are useful cross-sections as well as salinity-yield mapping that assisted with determining the extent of the project area and aided with the design of new data acquisition strategies.
    ix. Pre-existing borehole and ground geophysical data were of limited areal extent and ground penetration and provided limited insights into the stratigraphy and groundwater. Regional airborne magnetic and gamma radiometric data over the BHMAR study area is sourced from a patchwork of surveys and specifications. There are no data gaps, however there is no high-resolution data, with the best data being course (400 m +) regional line spacing data in a portion of the study area. The regional gravity and airborne magnetic data provided useful insights into key basement structures. There were no airborne electromagnetic (AEM) data for the project area. Regional seismic data targeted deeper crustal structures and basins, and did not provide any shallow (<1 km depth) information, although some of the deeper crustal information provided insights into basement structures.
2. A data acquisition program was undertaken utilising the national MAR guidelines as a reference framework. A phased approach to data acquisition was undertaken, with regional scale data acquired in an initial campaign designed to map and assess groundwater resources and MAR opportunities in 4 main aquifers:

- Shallow (0-30 m) alluvial (unconfined) sand aquifers associated with the Darling River and its Anabranches (Coonambidgal and Menindee Formations).
- Intermediate depth (30-100 m) Pliocene Calivil Formation and Loxton-Parilla Sands (semi-confined to confined) aquifers. These were the primary target.
- Deeper level (180-250 m) Renmark Group Formation (confined) aquifers.
- Shallow (<100 m) Palaeozoic (Devonian and older) basement aquifers, in buried basement highs (sandstone, weathered zone and fractured rock aquifers).

To identify potential MAR and/or groundwater resource targets in these 4 aquifers, the BHMAR Project acquired the following key datasets:

- A 31,834 line km airborne electromagnetic (AEM) survey using the SkyTEM heliTEM system;
- A high resolution LiDAR digital elevation survey (15cm vertical resolution) over the ~7,500 $km^2$ project area;
- 100 bores in a 7.5 km drilling program, including 60 sonic bores (Figure D);
- Construction of a piezometer network, including installation of automated data loggers in 40 bores, with groundwater levels manually checked every 3-4 months;
- A hydrochemical sampling program of rainfall, surface water, groundwater and pore fluids. This entailed analysis of 1600 hydrochemical samples (25 analytes and including trace metals);
- Isotopic characterisation of rainfall, river, lake and groundwater;
- A program of groundwater age dating using radiocarbon $^{14}C$ and chlorofluorocarbon CFC tracers;
- Limited (7-day) pump tests, and more extensive borehole slug tests;
- Ground resistivity and IP surveys of potential borefield sites;
- In-river mapping of the Darling River bed using multi-beam sonar (echosounder) and sub-bottom profiler methods to map river bed bathymetry and composition;
- Borehole geophysics including gamma, induction, and nuclear magnetic resonance (NMR) logging;
- Age dating of geological materials involving optically stimulated luminescence (OSL), radiocarbon and palynology);
- Laboratory column tests to assess ASR clogging potential;
- Laboratory permeameter and porosity testing of drillcore materials;
- Geochemical analysis (major and trace elements and trace metals) of drillcore materials;
- Scanning electron electron microscopy (SEM), x-ray diffraction (XRD), potable infrared mineral analyser (PIMA) and Hylogging multi-spectral analysis of drillcore materials for mineralogical analysis;
- Limited groundwater and water-rock interaction modelling;
- Surface geomorphic mapping, trenching and hand augering; and
- Mapping of Indigenous cultural heritage sites.

Due to cultural heritage sensitivities, it was not possible to proceed with a high-resolution seismic reflection survey in the target areas.

The datasets were acquired as part of a phased approach, with additional data collected as critical data gaps were identified within specific MAR targets.

3. In the BHMAR study, an evolution in project management from multi-disciplinary, to inter-disciplinary and finally a trans-disciplinary approach was critical to developing a robust hydrogeological conceptual model as well as the successful completion of pre-commissioning maximal and residual risk assessments for a proposed MAR site at Jimargil.
4. Previously, the high cost of investigations, low level of knowledge of risk, and time taken to fill hydrogeological knowledge gaps have been a deterrent to development of MAR options, especially in pioneering projects in greenfield and/or more remote locations like Menindee. To overcome these issues,

the project used AEM to map a large, data-poor area (7,541.5 km$^2$) of the Darling floodplain. AEM data acquisition was completed within a nine-week period, with data available to target drilling and field investigations in the same timeframe. It is our understanding that this is the first use of AEM for MAR identification and assessment.

5. The use of airborne electromagnetics (AEM) for hydrogeological investigations often requires high-resolution data. Optimisation of AEM data therefore requires careful consideration of AEM system suitability, calibration, validation and inversion methods. Over the past decade, several new airborne electromagnetic (AEM) systems have become available for commercial surveying, and when a new survey involving AEM is planned, one of the crucial choices is to select an appropriate system for the mapping task. In this study, the choice of an appropriate AEM system for a given task was based on a staged approach utilising:
    i. A derivative analysis approach to comparing various AEM systems, including forward modelling of system responses, based on geo-electric models derived from ground TEM and borehole induction profiles in the candidate areas (Lawrie *et al*., 2008, 2009a);
    ii. A comparative analysis of candidate systems, consisting of both theoretical considerations and field studies including AEM test lines (Christensen *et al*., 2009; Lawrie *et al*., 2009c; Christensen & Lawrie, 2012).
6. This study has demonstrated the importance of selecting the most appropriate AEM system and optimizing the AEM inversions for generating a wide range of customized interpretation products.
    i. New inversion code (WANDA) has been developed for rapid inversion of the AEM data. This permitted rapid trialling of different constraints.
    ii. A lateral correlation procedure was developed to correlate AEM data strictly horizontally.
    iii. Development of the WANDA inversion code enabled rapid experimentation with regularization and lateral smoothing constraints, and combined with numerical modelling, this enabled the settings to be adjusted until there was a close match with the known geology, even in the shallow sub-surface.
    iv. New procedures were developed for borehole induction logging and calibration. These provided greater confidence in the borehole geophysical conductivity measurements. This method offers an extension of previous calibration methods in that it uses a suite of calibration experiments to derive a statistically robust transfer function between measured voltage and conductivity.
    v. Hover tests were used in conjunction with a ground geophysical (WalkTEM) survey to assist with AEM data calibration and inversion.
    vi. A new, more consistent concept with an uncertainty-normalised quantitative measure of misfit was developed for the comparison between AEM inversion model conductivities and borehole conductivity logs and applied to 92 boreholes within the BHMAR area. With the exception of about 10% of the boreholes, the estimated average difference is of the same order of magnitude as the uncertainty of the parameters. An $R^2 > 0.98$ was obtained for new bores used as inversion constraints, while an $R^2 > 0.94$ was obtained for FID point comparisons with bores distributed throughout the project area that were not used as inversion constraints.
    vii. Bayesian inference via a reversible jump Markov Chain Monte Carlo (RJ-McMC) inversion for nine selected AEM data sets provided useful (quantitative) assessment of the final inversion models. Sixteen independent Markov chains were sampled in parallel in the inversion of each data set. In each chain 200,000 samples were acquired. Models were accumulated into the posterior probability and change-point histograms after the burn-in period of 10,000 samples. Therefore a total of 3.04 million (190,000 x 16) samples were acquired after the burn-in period. Overall, the borehole conductivity log and the AEM inversion model lie around the centre of the McMC likelihood interval, with a few exceptions. This analysis provided increased confidence in the final WANDA inversions.
7. A suite of customized interpretation products were produced through integration of AEM data with other project datasets, notably the information from 40 new rotary mud and 60 sonic-cored holes. Data obtained from the drilling program includes: sedimentary facies, textures (including grain size), mineralogy, redox state and whole rock geochemistry; hydrogeophysical data (nuclear magnetic resonance (NMR), induction and gamma logs); hydraulic data (from slug and pump tests), hydrochemistry (from groundwater and pore fluid samples), and hydrodynamic data from the monitoring

of groundwater levels in 40 boreholes pre- and post-flooding in 2010-2011. Customised interpretation products developed through integration of the modelled conductivity data integrated with these datasets include maps of lithostratigraphy, hydrostratigraphy, sedimentary textural classes, structures including neotectonic elements, groundwater salinity, zones of inter-aquifer leakage, aquifer porosity, aquifer transmissivity, and MAR and groundwater storage volumes.

8. In the Broken Hill Managed Aquifer Recharge project, a new method has been developed for surface-materials and geomorphic mapping. These have been essential for assisting hydrogeological investigations, including recharge predictions, salinity hazard and the identification of potential infiltration basins. Prior to landform identification, the LiDAR DEM data was levelled using trend surfaces to eliminate regional slope (~20 m). As a consequence of this, an ArcGIS interactive contour tool could be used to identify specific breaks in elevation associated with landform features. Multivariate image analysis of elevation, high resolution SPOT and Landsat-derived wetness further enhanced the contrast between geomorphic elements to confirm mapping boundaries. While specific landforms can be characterised by particular surface materials, these sediments can vary within a single geomorphic feature. Consequently, SPOT multispectral satellite imagery was used to identify surface materials using principal component analysis and unsupervised classification. This approach generated 20 classes; each assigned a preliminary cover/landform attribute using SPOT imagery. Field data (surface and borehole sample, and observations at shallow pits) were used to refine the classification approach. Interactive mapping using a de-trended DEM provided a rapid, effective and accurate alternative to time consuming manual landform digitisation. The combination of these two new products – surface-materials and geomorphic maps – has assisted in the identification of potential recharge sites and naturally occurring infiltration sites. Overall, this innovative approach significantly increased the speed and the level of detail of geomorphic mapping when compared to previous methods.
9. Mapping of geological structures across the BHMAR study area has entailed a multi-scale mapping approach involving the analysis of AEM, airborne magnetic, regional gravity, LiDAR, landsat (vegetation condition) and geomorphology data in cross-sections and maps. Identification of Neogene tectonics was facilitated by the identification (in the AEM data) of structural off-sets in the lacustrine Blanchetown Clay. The correspondence of faults in multiple, independent datasets, validated by drilling data, provided increased confidence in the structural analysis.
10. Ground direct current/induced polarization (DC/IP) surveys were undertaken largely to assess borefield scale heterogeneity in the hydrogeological system, and in particular, to determine whether the AEM system was mapping 'holes' in the confining aquitards. These ground surveys were limited by access, cultural heritage and environmental issues, with the survey design compromised in a number of locations because of these factors. In particular, it was not possible to extend the surveys either side of boreholes in a number of locations, limiting the utility of borehole datasets for calibration purposes. One particular issue of note is that the IP data (and borehole nuclear magnetic resonance (NMR) data) may be affected by the extensive ferruginisation of the aquifer materials. Further tests are required to establish the effects on the IP (and NMR) response. Two inversions of the ground DC/IP surveys were carried out. These inversions did not match the AEM or borehole IP data particularly well, and further inversions are required using different inversion constraints. One issue of note is that the upper confining aquitard in the Jimargil area is particularly indurated and relatively dry, and this was not factored into the inversion interpretation. The inversions did however appear to reveal some heterogeneity in the hydrogeological system at a scale not observed in the AEM data.
11. In the BHMAR project, sensitivity analysis was used to help define uncertainty for key parameters, such as estimates of aquifer storage volumes at both the regional target and potential borefield scale. These parameters are critical to economic viability of a project (which is not addressed in any National Water Quality Management Strategy (NWQMS) Guidelines). The new multi-scale methodology developed to estimate groundwater quality and storage volumes, was applied to the Pliocene aquifers. This methodology is a significant improvement on previous approaches that rely upon extrapolation from limited borehole data.
12. Difficulty in obtaining regulatory permissions for long-term pump tests necessitated the use of alternative methods for gathering information on the hydraulic properties of aquifers and aquitards. The nuclear magnetic resonance (NMR) borehole logging method provided surrogates for effective porosity and hydraulic conductivity at a downhole resolution not possible using traditional methods. While the results for coarse textured sand and gravels matched other hydraulic conductivity data, effective porosity measurements (using the matric potential method) derived from Lexan-encapsulated core materials

demonstrated that the NMR method significantly over-estimates hydraulic conductivities in fine-textured materials (fine sands, silts and muds).

13. Sonic drilling has been used successfully to obtain 4.5 km of core materials in the BHMAR study area. Although the method effectively fluidises unconsolidated materials, with consequential loss of some detailed bedding information, core recoveries of over 99% were obtained in the unconsolidated sands and gravels, inter-layered clay-sand sequences and indurated layers and bedrock to depths of 206 m. The core was sufficiently well preserved to allow ±5 cm accuracy in the location of geological contacts, thinly interbedded sand and silt units. Preservation of small-scale sedimentary structures such as ripples, root casts, intra-clasts, and burrows aided detailed facies interpretation. The sonic cored material also proved an ideal sampling medium for geological analyses, such as grainsize distribution (sieve and laser), bulk density, X-ray fluorescence, X-ray diffraction and palynology. It was also useful in laboratory tests requiring relatively intact samples, such as permeameter and porosity measurements and column tests to assess clogging potential in MAR studies. Pore fluids were also extracted from core sub-samples using hydraulic presses, for analysis of electrical conductivity (EC), pH, alkalinity and major cations and anions. Although not indicative of in situ conditions, the pore fluid chemistry could be used to identify potential water-rock interactions that could occur with the injection of oxygenated water into the aquifer during MAR operations.
14. A new remote sensing vegetation mapping approach was developed at part of the BHMAR Project. This method utilised 25 years of historic Landsat imagery, processed to highlight medium and long-term trends in vegetation condition. This study combined Landsat Normalised Difference Vegetation Index (NDVI) time series data with hydrogeological, hydrogeochemical and hydrogeophysical data to assess the relative importance of hydrological processes and groundwater characteristics. This new methodology has resulted in a greater understanding of processes driving the spatial distribution of woody vegetation as well as observed changes to condition. More broadly, this vegetation assessment methodology provides a case study for the type of integrated remote sensing temporal analysis required to better understand vegetation variability, in particular a focus on vegetation behaviour during water-limited conditions. Furthermore, the results of this assessment have tantalisingly alluded to the importance of structural features in vegetation distribution and condition that may be applicable elsewhere in the Murray-Darling Basin.
15. In this study, predictive flood modelling and flood-risk assessment used a static modelling approach and a 1 m resolution LiDAR Digital Elevation Model (DEM). To produce accurate predictions of flood inundation and calculations of flood volume in a range of flooding scenarios, a number of steps were undertaken:
    i. The DEM was initially levelled to the Darling River floodplain by subtracting an interpolated floodplain elevation trend surface from the DEM. This produced a de-trended flood plain surface.
    ii. The levelled DEM surface was then adjusted to the water level reading at the Darling River gauging station (Site 425012), upstream of Weir 32, at the time when the LiDAR was acquired.
    iii. Flood extents were then derived by elevation slicing of the adjusted levelled DEM up to any chosen river level. River-level readings from historical and current events were extracted from the NSW Office of Water real time river data website[8].
    iv. The flood-depth dataset is an inverted version of the flood extent grid. Predicted flood depth and extent were classified by depth/elevation slice ranges of the adjusted de-trended DEM with 25 and 50 cm increments.
    v. Predicted flood extents were validated by comparisons to satellite images from the 1990 floods, and photographs of inundation from recent flood events. In all cases, imagery and photo validation proved that predicted extents are accurate. The flood-risk predictions were then applied to a number of river level scenarios. These included:
        a. Examination of the extent of flooding at the highest historical level;

[8] http://waterinfo.nsw.gov.au/water.shtml?ppbm=SURFACE_WATER&rs&3&rskm_url

b. Determination of the river level required to completely inundate the Coonambidgal Formation scroll plain in the GWR1 study area (probable maximum recharge potential); and

c. An assessment of flood impacts in 0.5 m increments from 5.5 to 7 m of river level rise at the Site 425012 gauging station.

vi. This flood inundation modelling only shows the theoretical extent of inundation due to river-level rise based only on elevation and does not take into account flow pathways and impediments to flow or loss of water due to evaporation, soil wetting, and leakage via faults or surface cracks. This may lead to an overestimation, however results of the quantitative validation suggest this only affects a small percentage of the landscape. However modelling the impact of flooding in and around the Menindee Lakes is problematic as the lakes are regulated and do not necessarily, fill under natural flood conditions.

vii. The accuracy of flood modelling decreases with distance from the river gauge station. Validation of the methodology in the central section of the project area indicates good accuracy. More broadly, there appears to be under-estimation in the north, particularly in relation to Talyawalka Creek; and over-estimation in the south, along both the Darling River and the Darling Anabranch. In these areas, flood extent can instead be derived from the Landsat water classification.

viii. There are also limitations with utilising Landsat imagery for flood modelling. Landsat has a repeat cycle of approximately every 16 days, and is affected by cloud cover – both of which limit the number of suitable scenes for analysis. As a consequence of this, Landsat images are not always available for key flood events. Landsat also has a spatial resolution of 30 m as opposed to the LiDAR DEM using in this study (5 m spatial resolution). This causes issues with mixed pixel responses, for example when a single pixel is in reality both wet and dry. The water body extraction algorithm can only essentially assign wet or not wet. Finally, the ability of Landsat to detect surface water can be affected by dense canopy cover (Wang *et al*., 2002). Only the Darling River channel is associated with anything other than open forest hence this is unlikely to affect the analysis considerably. These products are also unable to provide any information about the depth of water inundating any surface which is a strength of the LiDAR products.

ix. Overall, the flood modelling methodology used in this project successfully predicted the extent and depth of water coverage in the central project area of the Darling floodplain under different scenarios, and to identify the geomorphic features prone to inundation in different flooding regimes. The flood predictions were also used as inputs to recharge potential mapping and for borefield and pipeline planning.

16. A comprehensive hydrochemistry campaign involved the sampling of cumulative rainfall, surface water (river, lake storages and treated water supply), groundwater and pore fluids extracted from the sonic core.

i. A field sampling protocol involving low-flow pump operation, monitoring of field parameters, the taking of routine, replicate and spiked samples, sample preservation and storage and chain of custody processes was established for the project.

ii. The suite of hydrochemical analyses was comprehensive and included field parameters, major and minor ions, trace metals, nutrients, organic carbon and radon. These were used to assess the quality of groundwater and potential MAR source water against the national drinking water guidelines (ADWG 2011). More specific analyses such as pesticide screens were also undertaken on selected samples.

iii. The analysis suite also included supplementary parameters useful for the MAR risk assessment. This included the field spectrophotometry of specific ions (ferrous iron, total iron and sulfide), biodegradable dissolved organic carbon, total suspended solids and particle size distribution. These data were also used in the assessment of potential MAR-related issues such as metal remobilisation and clogging. This assessment involved geochemical modelling using the PHREEQC code (Parkhurst & Appelo, 1999).

iv. Many of these water quality parameters (such as major ions, trace metals, EC, pH) can also be used in the hydrochemical assessment of key groundwater processes such as recharge. These data was supplemented by the analysis of stable isotopes (oxygen-18 and deuterium), radiocarbon, chlorofluorocarbons and strontium isotopes. The stable isotopes for groundwaters were particularly useful as the data could be integrated with pre-existing monitoring for rainfall and Darling River surface water. The radiocarbon analyses best captured the spectrum of groundwater ages evident within the shallow and semi-confined aquifers.

17. A new methodology, integrating fuzzy-k means (FCM) cluster analysis with conventional hydrochemical and hydrodynamic analysis provides invaluable new insights into groundwater processes. Surface water and groundwater sampling with pore fluid analysis of cored sediments, combined with fuzzy-k means (FCM) cluster analysis, provides a novel, relatively simple but powerful tool to assist with interpretation of groundwater processes.
    i. Pore fluids were extracted from sediments from 60 sonic-cored bores, and together with rainfall, surface water and groundwater samples, provided a hydrochemical dataset with over 1600 samples and 25 analytes.
    ii. The FCM cluster analysis used analytes that were present in at least 60% of samples and resulted in samples being classified into eight classes (or hydrochemical facies). Pore fluids and groundwater with the greatest affinity to the surface water samples were easily identified. In this way, sites with significant active recharge, principally by river leakage, were mapped.
    iii. Downhole plots of the pore fluid FCM classes provided additional insights into groundwater processes. Comparing the FCM classification of pore fluids within the target (semi)confined aquifer with those from the overlying clay aquitard and shallow aquifer allowed the assessment of vertical inter-aquifer leakage or diffusion processes. The FCM cluster analysis also assigns indices to each sample as indicators of how well it relates to each of the eight classes. A simple recharge index was calculated from these FCM indices.
    iv. In summary, fuzzy-k means (FCM) cluster analysis, combined with conventional hydrochemical and hydrodynamic analysis provides invaluable new insights into groundwater recharge processes.
18. MAR assessment requires the hydraulic characterisation of key aquifers and aquitards, involving the estimation of parameters such as effective porosity, hydraulic conductivity, transmissivity and storativity. For the BHMAR project, various approaches at different scales were applied.
    i. A slug test was routinely undertaken following the construction of each of the 100 project bores. A time series of the groundwater level response during the test was collected using a pressure transducer and processed for input into AQTESOLV, for interpretation, curve fitting and transmissivity estimation of the screened interval. The method provided a relatively cheap, rapid and consistent approach to estimating aquifer properties.
    ii. Two aquifer pump tests were undertaken using production bores constructed into the Calivil Formation aquifer at Jimargil, supplemented by monitoring bores established in the overlaying shallow aquifer, the target aquifer and the underlying Renmark Formation. These tests were limited to 7 days due to regulatory constraints. However, the tests provided useful insights into the level of aquifer confinement, the degree of potential inter-aquifer leakage as well as estimates of key aquifer hydraulic properties that were incorporated into preliminary groundwater flow and solute transport modelling.
    iii. As discussed above, nuclear magnetic resonance (NMR) logging provided a complimentary dataset to these more traditional approaches. The logging could provide a downhole hydraulic conductivity profile at 0.5 m resolution, whilst the slug and pump tests provided aggregated properties of the screened aquifer interval. The logging was also logistically simpler compared to the requirements of an aquifer pump test (including suitable production and monitoring bores and appropriate disposal of pumped groundwater).
    iv. The collection of lexan-encapsulated sonic core allowed the opportunity to have laboratory measurements of porosity and permeability undertaken on relatively undisturbed columns of sediments across a range of textural classes. Due to scale issues, this data was particularly useful in validating the NMR logging.

19. Pressure transducer loggers have been installed in a subset of the monitoring bores constructed by the project. Barometric loggers have also been installed to enable correction of the time-series groundwater level data.
    i. Loggers have been installed in bores screened in different aquifers, along different reaches of the Darling River and Talyawalka Creek and at varying distances from potential sources of surface water leakage. The network is designed to characterise the groundwater response to episodic flood events and associated filling of the Menindee Lakes.
    ii. The network was installed prior to the 2010-11 Darling River flood and this provided an opportunity to monitor groundwater replenishment following a significant drought period. The borehole hydrograph data provided evidence for actual recharge into the Calivil Formation, although the aquifer is ostensibly overlain by a significant regional aquitard.
    iii. The groundwater level data, combined with manual measurements and historic data was used in the contouring of the shallow watertable and Pliocene Sands potentiometric surfaces.
20. Preliminary groundwater flow and solute transport modelling has been undertaken for the Jimargil borefield site.
    i. Two simple models were constructed to represent the radial conditions at sites BHMAR33 and 80A, which were the production bores used in the aquifer pump tests. The estimates of aquifer and aquitards hydraulic properties from the pump tests were used as input parameters for FEFLOW radial models at these two locations.
    ii. The models considered an ASR scenario of two years of continuous injection of fresh source water (EC= 250 µS/cm), followed by 2 years of storage and 2 years of recovery at the same rate as the injection. Two model runs used injection/recovery rates of 25L/s and 50 L/s.
    iii. The modelling was undertaken early in the site investigations and helped scope the requirements and scale of a potential MAR borefield and in the MAR risk assessment process.
21. To define the water quality criteria and minimum pre-treatment requirements to allow recharge at an acceptable scale during Aquifer Storage and Recovery, a new methodology was developed using laboratory column studies. In these studies, four types of treated source water were used at constant temperature (19°C) with light excluded, to determine the potential for near-well clogging for a proposed ASR scheme. Due to time constraints, a limited number of representative geological materials were packed into cylinders for this experiment. Overall, this method provided some useful results, however an improvement in the confidence in the results would likely be obtained if the results were performed on undisturbed lexan core, and run over a greater time period.
22. The potential for geochemical reactions to cause aquifer clogging or detrimental water quality changes was assessed for MAR options at the priority Jimargil borefield site.
    i. The assessment used ambient groundwater quality from the target Calivil Formation aquifer, as well as from the shallow unconfined aquifers; Darling River source water quality; and mineralogy and geochemistry of sonic-cored aquifer samples. PHREEQC was used to examine the impact of mixing and interaction between these end-members. This methodology enabled the potential for chemical and physical clogging of the aquifer, and potential for metal mobilisation under a range of different pe redox states within the Calivil Formation aquifer.
    ii. This evaluation has also provided insights into source water pre-treatment requirements, the use of redox mapping to optimise MAR bore-field design, appropriate monitoring for assessing aquifer clogging and water quality changes, and the appropriate contingency plans for treatment of recovered water if required.
23. The BHMAR projects used various approaches to assess different recharge mechanisms to the shallow watertable aquifers and the target Calivil Formation aquifer.
    i. The routine measurement of chloride concentration in groundwater and pore fluid samples enabled the application of the chloride mass balance method to estimate steady-state diffuse recharge from rainfall. This is a simple and rapid technique that has minimal data requirements.
    ii. The watertable fluctuation method is also a simple approach and was applied using the hydrographic responses observed in boreholes monitoring the shallow watertable aquifers near the Darling River or Menindee Lakes. Assigning an appropriate specific yield represented the greatest source of uncertainty for the method.

iii. The steady state groundwater mounding equation of Hantush (1967) was used based on the geometry and hydraulic properties of representative cross sections for the shallow unconfined aquifer orthogonal to the Darling River.

iv. Radiocarbon depth models to estimate steady state recharge rates to the unconfined aquifer (Walker & Cook, 1991) and the semi-confined aquifer (Cook & Bohlke, 2000) were applied, using the comprehensive groundwater radiocarbon ($^{14}C$) analyses.

24. The BHMAR project provided the opportunity to apply and test the national MAR guidelines (NRMMC-EPHC-NHMRC, 2009) in the evaluation of a range of MAR options, and a proposed large –scale ASR scheme. Key points about the MAR guideline methodologies are briefly summarised below, however detailed discussion and conclusions can be found in Lawrie *et al*., (2012c).

i. Overall, the project found that the guidelines provided a very useful framework for entry-level and pre-commissioning MAR assessments. However, the guidelines assume that a potential MAR site has already been identified, necessitating the development of new methodologies to map and select MAR sites in a data-poor, hydrogeologically complex area.

ii. The project found the application of the entry-level assessment framework from the MAR guidelines to be a particularly useful tool for the assessment of multiple targets. The degree of difficulty assessments were particularly helpful in the identification of critical data and knowledge gaps and the prioritisation of candidate sites.

iii. At an early stage in investigations, the BHMAR project developed a method for evaluating aquifer suitability for MAR using conceptual targets based on the pre-existing understanding of hydrostratigraphy and recharge processes (Lawrie *et al*., 2009). This was useful in identifying targets not just in terms of aquifers with appropriate storage, but also the presence of bounding aquitards and potential recharge mechanisms. These conceptual models were also used to define the requirements of the data acquisition program. This was a useful process as it enabled the definition and prioritisation of a range of potential MAR targets, rather than having project success relying on assessment of a single target.

iv. In parallel with the above approach, the BHMAR project developed a technical risk assessment (TRA) methodology to prioritise regional investigations and evaluate the viability of MAR options in different aquifers (Lawrie *et al*., 2009). This TRA matrix was based on the two key criteria of:

- Likelihood of technical success – accounting for the probability that the required groundwater resource is likely to be present, discoverable with the available technology, and the water supply alternative can be implemented.
- Likelihood of negative consequences – accounting for the potential and significance of impacts to the water resource, ecosystems and other groundwater users if the option was to be implemented.

This approach was successfully used to assess the relative viability of various options, defined by a combination of target formations, water supply strategy and the ability to map and characterise the targets. This allowed elimination of a number of options at an early stage, as well as the identification of critical data gaps. Broader than a MAR human health and environmental risk assessment, the matrix approach was useful in prioritising aquifer targets and aided design of the data acquisition program and assessing the suitability of various technologies (such as AEM survey requirements).

25. Acquisition of a high-resolution LiDAR dataset has been essential in developing a range of geomorphic, geological and hydrogeological interpretation and planning products. For example, the LiDAR dataset provides a high resolution surface datum over which remote sensing data (e.g. Landsat) data be draped for vegetation structure and health mapping, and a datum at an appropriate high resolution to reference the sub-surface datasets including AEM, ground geophysical, and borehole data.

i. Ground validation has demonstrated that the LiDAR data is an accurate representation of the terrain at the time of the survey. However, due to localised flooding at the time of survey (which provided returns from the surface of turbid waters), the LiDAR data is inaccurate in some small, partially inundated landscapes around Lake Wetherell.

ii. Fundamental vertical accuracy (at 95% confidence level) of the LiDAR derived 5 m DEM dataset was found to be 0.52 m, due to inherent inaccuracies of the methodology, insufficient

and erroneous ground control points and cumulative errors including the transformation to the vertical reference datum and re-sampling procedures. These vertical inaccuracies need to be factored in to flood modelling, and in utilisation of LiDAR datasets as an absolute height datum. Even considering this factor, flood inundation extent mapping of the central project area has a 93% compatibility with corresponding Landsat TM 5 imagery.

iii. Three digital elevation models (DEMs) were used within the BHMAR Project: 1, 5 and 10 m spatial resolution. These surfaces were fundamental to the interpretation of both surface and subsurface geomorphic, geological and hydrogeological features. BHMAR Project spatial analysis datasets could not have been generated from pre-existing elevation data (e.g. SRTM DEM) due to inadequate spatial resolution and vertical accuracy.

   a. The 1 m DEM has the greatest accuracy and highest level of detail but is a very large file which impacts on processing time. It was consequently only used at the borefield scale for the generation of products such as flood inundation and river incision where minor topographic variation was important.

   b. The 5 m DEM was more appropriate at the target scale. This product still retained good spatial resolution but was considerably smaller in size and thus quicker to process. This DEM was used for geomorphic mapping, AEM-derived products such as depth to formations and stratigraphic units and interpreted cross sections, and also displaying topography.

   c. The 10 m DEM was re-sampled twice thus has slight greater inherent vertical error of the three DEM products. This is was particularly evident where topographic variation was considerable over a small area (i.e. river banks). Consequently this surface was used at the regional scale and when combined with coarse resolution products such as the depth to the watertable.

   d. The acquisition of a high resolution LiDAR dataset has also enabled:

      - Key elements of the floodplain geomorphology to be mapped. The LiDAR dataset has also been critical in guiding the siting of pits and trenches for dating of the near-surface geomorphic units.
      - Fault scarps to be identified in the landscape. The high resolution of the dataset further enables the timing of faulting relative to scroll plain deposition to be ascertained.
      - Integration of river bed mapping with floodplain elevation data.
      - Flood inundation modelling to be carried out at a range of scales, including local borefield scales.
      - Assessment of infiltration options for MAR.
      - Assessment of the potential impact of groundwater extraction and MAR on groundwater dependent vegetation.
      - Cultural heritage and environmental surveys to be carried out with a high degree of spatial accuracy. This was essential for planning all field activities.
      - Design of conceptual borefields.
      - Planning of surface water engineering works at the MLS.

26. In this study, two hyperspectral instruments were used on sonic-cored drillhole materials to assess the value of hyperspectral methods for hydrogeological investigations. The Portable Infrared Mineral Analyser (PIMA) was used on individual samples, and was used to cross-check SWIR results from the Hylogger. Further validation of the methods was carried out using XRD analysis of selected samples. The Hylogger core scanner provides continuous coverage down the logged sonic cores in the visible to near-infrared (VNIR), short wavelength infrared (SWIR), and thermal infrared (TIR) bands. The Hylogging method successfully mapped the distribution of clays and oxides in both the aquitards and aquifers.
27. A number of issues have been identified with using laser grain size analysis of BHMAR core materials. More specifically, samples from mud- and clay-sized textural classes, as determined by laser grain size analysis, were found to often contain sand-sized or larger mud- and clay-particle aggregates if they have been dried (either naturally of in the laboratory) or contain secondary carbonate (or other) cementation.

Air drying is sufficient to produce aggregates and it should be noted that the same process turns wet mud into adobe bricks. The study has concluded that standard minimal dispersion regime used in the GA Sedimentology Laboratory does not disaggregate these secondary particles. However, the standard dispersion regime does successfully determine the correct modal grainsize of the clay-fraction of samples that contain significant sand-sized clay- and mud-aggregates.

28. To facilitate effective communication of large and complex geoscience datasets and project results to a wide range of stakeholders, the BHMAR project an interactive 3D virtual globe viewer built on NASA's open source World Wind Java Software Development Kit (SDK) was developed to display complex 3D hydrogeological, hydrogeophysical and hydrogeochemical data (points, lines, 2D surface and 3D shapes).

Overall, the 3D hydrogeological systems approach has successfully delineated key functional elements of the Darling Floodplain hydrogeological system (e.g. aquifers, aquitards and faults), mapped heterogeneity (and 'holes') within the aquitards, and hydraulic classes and transmissivities within the main aquifers, as well as groundwater salinities (Lawrie *et al*., 2012b). An even greater heterogeneity of the hydrogeological system is revealed by ground geophysics and drilling data at a borefield scale.

The new datasets, knowledge and hydrogeological conceptual models generated in the project have provided a reliable basis for the identification, characterisation and initial assessment of groundwater resources and MAR options. In particular, AEM data, informed by facies analysis of sonic cores, have been used to target high-yielding palaeochannels, greatly assisting with the rapid identification and prioritisation of groundwater resources and MAR targets.

The products and knowledge generated will also provide important inputs to assist with the parameterisation of groundwater flow and solute transport models that are critical to the next steps in the assessment of MAR and groundwater extraction options in the area. It is our understanding that this is the first use of a trans-disciplinary approach utilising AEM for MAR identification and assessment.

Lessons from the BHMAR study in terms of MAR site identification, characterisation and assessment, have the potential to reduce the timeframes for similar studies, and the scientific investigative costs, even in data-poor areas. Hydrogeological systems mapping approach and the integrated workflows developed in the BHMAR Project, can provide rapid and comprehensive assessments of MAR options, in comparison with more traditional methods. In particular, the integrated use of AEM, ground electrical methods, and borehole NMR, enables the rapid characterisation of complex hydrogeological systems, including the key groundwater storage parameters necessary for assessing MAR options. This methodology has the potential for application in many Australian landscapes (and more broadly).

Overall, a multi-scale approach provides a reliable platform for the development of new geological and hydrogeological conceptual models, and a framework for understanding complex hydrogeological and hydrogeochemical processes (Lawrie *et al*., 2012b). Using a holistic systems analysis approach, integration of the 3D mapping with hydrochemical and hydrodynamic data provides critical new insights into surface-groundwater interactions. This approach has been fundamental to developing a new understanding of recharge processes, and the identification of potential recharge and groundwater flow pathways.

# 19 Recommendations

1. A number of recommendations are made about the use of AEM technology for the high resolution mapping of near-surface hydrogeological systems and the identification and assessment of MAR targets:
    i. AEM data acquisition should be considered as part of any data acquisition strategy in data-poor areas. These data can map large near-surface areas rapidly, maximising the likelihood of identifying multiple MAR targets.
    ii. The mapping and assessment of MAR targets often requires high-resolution geophysical data to resolve the complexities of the hydrogeological system. Traditional derivative analysis approaches for AEM technology selection are inadequate for assessing the ability of candidate systems to map MAR targets. A comparative analysis of candidate systems, consisting of both theoretical considerations and field studies including test lines over representative hydrostratigraphic targets is recommended.
    iii. Optimisation of AEM data for MAR investigations should also involve careful consideration of AEM data acquisition strategy, AEM system calibration, validation and inversion methods.
    iv. It is recommended that a phased approach to AEM data acquisition be trialled to decrease the costs of acquiring AEM data for MAR target mapping. Depending on the nature of the target and the size of the area of investigation, initial reconnaissance mapping of MAR targets could utilise wide line-spaced data to identify potential MAR targets in Australia's major river basins.
        a. As shown in this study, one risk of using this phased approach is that wide line-spacing data may identify targets that on closer inspection may not pass assessments. To minimise these risks, a swath-mapping approach, with 3-5 closely-spaced (e.g. 200 m) flight lines separated by wider line spaced data (e.g. 1-2 km), could be trialled to give more opportunity for key elements of the hydrogeological system to be mapped and assessed.
        b. It should be noted however, that for logistic reasons, it is not always possible to acquire data in phased approaches, however the potential benefits of using such an approach for MAR mapping and assessment should be investigated in future investigations.
        c. The area surveyed should be sufficient to allow for assessment of multiple targets, given the likelihood of failure of some targets on hydrogeological, economic, environmental or social factors.
        d. Depending on the hydrogeological system, it is likely that high density line spacing and/or follow up high resolution ground geophysics would be required to provide sufficient data to resolve the complexities of many Australian hydrogeological systems.
2. An initial assessment concluded that the BHMAR project required a high resolution DEM with a vertical resolution <0.20 m absolute vertical accuracy for the purposes of aquifer potentiometric mapping, flood modelling, and to map key landscape and geomorphic features across the Darling floodplain. However, this was translated as an absolute vertical accuracy of < 0.2 m (RMSE) or < 0.39 m (FVA - Fundamental Vertical Accuracy) when the contract with the provider was finalised. To avoid confusion in the future, it is recommended that all vertical accuracies should be reported as Fundamental Vertical Accuracy (FVA) representing 95% confidence levels, rather than RMSE values representing 1 sigma or 68% confidence levels. The latter are inadequate for hydrological and hydrogeological applications in most Australian landscape settings. Based largely on the BHMAR project experiences, a number of additional recommendations are made with regard to the acquisition, processing, calibration and validation of remote sensing technologies used for high-resolution elevation surveys.
    i. The selection of the appropriate elevation survey technology has to be driven by a clear understanding of project requirements. There are a range of satellite and aircraft-mounted systems available, all with different resolution and accuracy capabilities.
        a. It is recommended that future projects clearly identify the immediate project requirements, while also paying some heed to the likely future uses of the datasets as part of the project planning phase. Publically-funded datasets should generally anticipate that these datasets will be used for a range of purposes beyond the initial scope, and attempt to adhere to the highest standards in terms of precision, accuracy and metadata description.

b. For hydrological investigations, it is recommended that particular attention be paid to the vertical accuracy requirements and definitions. In most Australian floodplain landscapes it is recommended that datasets with < 0.2 m vertical accuracies with respect to an application appropriate vertical reference datum, e.g. the national Geoid model, are obtained.

c. It is recommended that guidelines be drafted providing clear guidance on the resolution capabilities of different systems (precision and accuracy), the limitations of the techniques, and the steps that are required to calibrate these datasets. Such guidelines are required to better inform stakeholders on the potential and limitations of the different technology platforms, and to provide some guidance on the ancillary steps required to ensure the datasets are fit for purpose and adequately calibrated.

ii. Complementary techniques. There are a number of elevation mapping techniques that provide different measurements of surface (and sub-surface) datums with geoscience applications. The following recommendations are made:

a. For hydrological investigations, it is recommended that InSAR techniques be deployed where measurements of temporal variations in land surface heights are required. This includes instances of subsidence and /or 'floodplain breathing'.

b. More specifically, it is recommended that inSAR techniques be trialled in the BHMAR study area to assess the degree of floodplain breathing as a consequence of episodic flooding.

c. It is also recommended that inSAR techniques be trialled in the BHMAR study area to assess the capability of InSAR techniques for mapping watertable fluctuations in unconfined aquifers under Australian landscape conditions.

iii. Ground techniques such as Global Navigation Satellite System (GNSS), geodetic levelling, ground based gravity and other geodetic observing techniques might also complement InSAR mapping techniques. To provide reference surfaces for hydrological applications.

a. Currently, the Australian Height Datum (AHD m.s.l.) is used as the reference surface for elevation applications across Australia. While AHD meets the needs of most users, and is used extensively throughout Australia, there must be a recognition within the hydrological community that is not suited for many hydrological applications due to its errors and its definition (m.s.l.) that results in a north–south slope (~1 m) arising as a consequence of sea surface topography. It is therefore recommended that for hydrological applications an appropriate vertical reference datum be adopted. This might be the national Geoid model, which is derived from the national gravity network.

b. Efforts should be made to capture and archive all elevation surfaces in an ellipsoidal datum, as described in the ICSM LiDAR Acquisition and Tender Templateiii, to future proof their use and facilitate their future improvement as the national Geoid model and height datum is improved.

c. Ellipsoid-geoid transformations are an important source of error in digital elevation modelling applications. In part, this error stems from limitations in the national Geoid model. It is recommended that further observational and modelling efforts be directed toward improvement of the Australian national Geoid model. The contribution of errors associated with the ellipsoid-Geoid transformation in elevation mapping applications is currently poorly understood and also requires additional research.

iv. There are a number of recommendations made with respect to the acquisition of airborne LiDAR and derived products. The current ICSM LiDAR Specifications and Tender Template[9] should be modified to incorporate learnings from the BHMAR project. These changes include:

a. Clearly stating the requirement for vertical accuracy in terms of Fundamental Vertical Accuracy (FVA). An FVA of < +/-20cm 95% confidence interval (1.96 x RMSE) is the most appropriate for hydrological modelling in floodplain environments.

[9] http://www.icsm.gov.au/elevation/LiDAR_Specifications_and_Tender_Template.pdf

b. Incorporate options for derived products, specifically for hydrological modelling. All derived surfaces should be provided with ellipsoidal and orthometric heights. Orthometric heights should be relative to the AUSGeoid Gravity Model, not the Australian Height Datum 1971 (AHD).

c. Improved requirements for ground control.

- Aircraft trajectories must be computed with reference to local base stations and precise ephemeris data (ITRF), and then subsequently transformed to GDA94.
- Where existing CORS are not within range to ensure fixed ambiguity solutions for trajectories, new base station sites are to be established with permanent marking. The Precise Point Positioning (PPP) technique is not acceptable either as a primary or fall-back solution.
- The GDA94 ellipsoid heights for these sites are to be determined using the AUSPOS Online GPS Processing Service (final orbit product) with a minimum of two 6 hour observations sessions.
- If the setup is a tripod, then it must be reset with a different height between sessions. Refer also to Section 13.4 below for GNSS base station data delivery requirements.

d. A minimum standard for LiDAR classification of Level 3 ground correction should be stipulated to ensure that all derivative surfaces provide the best possible representation of the ground surface.

e. A minimum point density of 2 points per square metre is recommended at nadir to improve the chances of obtaining a ground measurement.

f. There should be a requirement to capture coincident imagery to ensure Level 3 classification is achieved and assist with water masking.

3. Darling Floodplain strategic science site. The BHMAR project area is the most data-rich site in Australia from a hydrology-hydrogeology-geomorphology-neotectonics perspective. A groundwater observation network (40 bores) has been established, and sites established for the trialling of new geophysical and remote sensing technologies.
   i. It is recommended this site be recognised as a strategic science site for the trialling of a range of new geophysical, remote sensing technologies, and science methods.
   ii. More specifically, it is recommended that a number of monitoring sites (e.g. tiltmeters, microseismic monitoring stations, GNSS reference station) be established at strategic locations within this area to provide baseline stations for future technology and science trials.
   iii. It is also recommended that InSAR techniques be trialled in the BHMAR study area to assess the degree of floodplain breathing as a consequence of episodic flooding.
   iv. It is also recommended that inSAR techniques be trialled in the BHMAR study area to assess the capability of InSAR techniques for mapping watertable fluctuations in unconfined aquifers under Australian landscape conditions.
4. With regard to the flood modelling, the paucity of river gauge data, and issues with the vertical accuracy of the LiDAR dataset limit the accuracy of the modelled flood extent surfaces. Flood predictions could be improved by:
   i. Developing an automated process for removing areas disconnected from the river;
   ii. Collecting additional ground control points to recalibrate the LiDAR dataset may be useful if sub-20cm vertical resolution is required. This would have to take into account temporal shifts in the elevation of the land surface during the 2010-11 flooding.
   iii. Using alternative mapping and prediction methods. These methods could include:
      a. Generation of continuous surface flow networks in discretized stretches of the river. This could also be trialled in the northern and southern portions of the BHMAR Project area to reduce over- and under-estimation.

b. Hydrodynamic modelling utilising the extensive data obtained over the course of the BHMAR Project.

5. For mapping and assessing vegetation condition, particularly with respect to groundwater dependent vegetation (GDV), it is recommended that:
   i. A temporal, integrated approach similar to that utilised in the BHMAR study be applied when considering any new (or modified) groundwater developments including for urban supply, irrigation or mining/extraction purposes such as coal or coal seam gas.
   ii. Furthermore, it is strongly recommended that any such study be undertaken in conjunction with a vegetation field program, measuring compatible biophysical parameters under varying climatic/seasonal conditions. This will result in a more robust, quantitative analysis. Other, complimentary remote methods could also be undertaken to strengthen the analysis and increase the spatial resolution such as aerial photography, different satellite or airborne imagery (e.g. Quickbird) or derived products (e.g. fractional cover).
6. A trans-disciplinary systems approach, and integrated workflows developed in the BHMAR Project, should be considered for future hydrogeological investigations and the assessment of MAR options in Australia, and in shallow sedimentary systems in particular. These methods provide the integrative framework required to address the many inter-related issues encountered in assessing MAR options, particularly in hydrogeologically and hydrogeochemically complex areas.
7. Structural mapping in the BHMAR study area and in the larger area covering the Western Murray Porous Rock Aquifer, combined with other recent tectonic studies, have revealed that Neogene tectonics (and neotectonics) may be more extensive than previously thought in the Murray-Darling Basin and Australia more generally. Neogene and more recent faulting activity may play an important role in inter-aquifer leakage and recharge processes. It is therefore recommended that future hydrogeological and MAR studies should consider tectonic studies as an integral part of future investigations and assessments.
8. The key learnings and recommendations from applying various methods to estimate recharge are outlined below.
   i. There are many different methods for estimating groundwater recharge. Some of these provide estimates of potential recharge or deep drainage, which is the flux below the root zone that has the potential to reach the watertable over varying periods of time. Other methods focus on groundwater responses where recharge accessions have actually reached the watertable. Many of these methods apply only to the unconfined aquifer and cannot be extrapolated to estimating groundwater recharge to confined or semi-confined aquifers. An understanding of the geometry and structure of the hydrostratigraphy, including any overlying aquitards is recommended to ensure that the recharge method is appropriate.
   ii. It is important to understand the assumptions inherent in any recharge estimation method and the implications of these on method suitability. This is important to ensure that the recharge method is appropriate to the conceptual model developed for the groundwater system. For example, the groundwater chloride mass balance method assumes that the chloride in groundwater originates from rainfall, with no other subsurface chloride sources. It also assumes that surface water leakage to the aquifer is absent. With river/lake leakage interpreted as the dominant recharge mechanism, these assumptions are not met for the BHMAR study area so the derived potential recharge estimates are not valid. A verification of the underlying assumptions of the recharge method against the conceptual model is recommended.
   iii. Recharge to the Calivil Formation is dominated by episodic leakage during high river flows and via structurally controlled disruptions to the regional overlying aquitards. This results in significant variations in recharge rates in both space and time, resulting in significant challenges in terms of extrapolating point-based recharge estimates. To address this spatial and temporal variability in recharge, it is recommended that a transient groundwater flow model be constructed and calibrated to the hydrographic responses to a series of flood events.
9. The hydrographic network established by the BHMAR project enabled comprehensive monitoring of the groundwater response to the 2010-11 Darling River flood. This provided a critical dataset that provided evidence that recharge is predominantly the result of river leakage during high flow events. Based on the importance of long-term hydrographic monitoring of critical episodic events it is therefore recommended that:

i. The newly established hydrographic and barometric network should be maintained in the study area, to monitor the groundwater response to streamflow events of varying magnitude on both Talyawalka Creek and the Darling River;

ii. Current bore data loggers should be upgraded to include improved temperature sensors, and key bore monitoring stations telemeterised to provide real-time monitoring of groundwater levels.

vi. Stream gauges be established for Talyawalka Creek to assist with measuring the frequency and magnitude of flows, and to calculate losses to the groundwater system.

vii. Additional stream gauges are required for the Darling River upstream of Lake Wetherell to enable losses to the groundwater system to be calibrated.

viii. Trial the installation of additional logger technologies in the monitoring bores to collect time series data of complimentary parameters (such as groundwater electrical conductivity).

10. A number of recommendations are made with respect to water sampling and analysis:

i. In future sonic drilling programs, investigate further the use of suitable field methods or instrumentation (such as hand-held meters) to measure key hydrochemical parameters including EC, pH and Eh at the time of drilling and core retrieval.

ii. Establish protocols for the appropriate preservation of core material, notably to reduce exposure to the atmosphere. This is important to retain the integrity of redox-sensitive species in the pore fluids and to reduce post-drilling water-rock interactions as much as possible. Different approaches could be taken depending on whether conventional plastic sleeves or more specialised lexan tubing is used in core collection.

iii. Expand the routine hydrochemical analysis of pore fluids to include the stable isotopes of oxygen-18 and deuterium to help provide insights into groundwater flow paths and processes. This will require reviewing of pore fluid extraction and preservation protocols to ensure suitable sample integrity, particularly the minimisation of post-drilling evaporation.

iv. Integrate with the existing regular sampling of the Darling River and Menindee Lakes by Country Water staff, to enable regular surface water samples for complimentary analyses, particularly for water stable isotopes.

v. Extend the groundwater sampling regime to the collection of dissolved or entrained gases, particularly carbon dioxide and methane. Gas analyses can provide insights on biogenic processes such as methanogenesis and assist in the mapping of redox zones in the aquifer. This is important in assessing and managing risks such as clogging and metal remobilisation associated with injection of treated source water.

vi. The project borehole network provides the opportunity to trial alternative approaches to groundwater sampling, considering the routine use of low-flow pumping during the BHMAR project.

11. Recommendations with respect to the use of tracers and age dating include:

i. Trial alternative groundwater age dating techniques (such as sulfur hexafluoride $SF_6$) to test and extend the interpretations based on the use of carbon-14 and chlorofluorocarbon analyses.

ii. When using chlorofluorocarbon as a tracer tool, analysis of CFC-113 is recommended in addition to the conventional analysis of CFC-11 and CFC-12. This would improve evaluation of groundwater mixing fractions between the fresh river leakage and the saline regional groundwaters.

iii. Investigate the use of heat as a tracer for interactions between the river (or lakes) and the shallow unconfined aquifer. This can include the installation of infrastructure to monitor temperature in the river and also within the near-river sediments.

12. Hydraulic testing of aquifers in the target borefield has involved the extensive use of slug tests and two short-term pump tests. This has been supplemented by downhole profiles of hydraulic properties derived from NMR logging, as well as permeameter and porosity testing on selected core samples. The next phase of investigations could include the following recommendations:

i. Implement longer-term (> 1 month) aquifer pump tests in the potential borefield target to quantify key aquifer hydraulic properties (such as transmissivity and storativity), assess inter-aquifer leakage and river-aquifer connectivity.

ii. Such aquifer pump tests should not only include monitoring of groundwater levels in monitoring bores in the target Calivil Formation, the overlying unconfined aquifer and the underlying Renmark Formation, but also monitoring of the hydrochemistry of the pumped groundwater. This includes regular field chemistry measurements (e.g. EC, pH, Eh, alkalinity, $Fe^{2+}$ etc.), water quality indicators (major ions, trace metals, nutrients etc.) and isotopes (oxygen-18, deuterium etc.). This hydrochemistry data can be used to assess the potential mobilisation of poor quality groundwater with pumping and the identification of groundwater flow paths.

iii. The existing infrastructure of production and monitoring bores can equally be used in aquifer injection trials at the Jimargil borefield site. Like the aquifer pump tests, this would involve monitoring the hydraulic response in the shallow watertable aquifer, the target Calivil Formation aquifer and the underlying Renmark Formation aquifer. Hydrochemical monitoring and sampling would also be undertaken to map the progress of the injectant plume and secondary processes such as redox, water-rock and source water-groundwater reactions. Monitoring of injection flow rates would be used to assess potential clogging. Such an injection trial would preferably involve the temporary installation of a mobile treatment plant to replicate the use of appropriately treated Darling River source water, as envisaged in an operational MAR scheme.

iv. The monitoring bore network provides an opportunity to trial other approaches to hydraulic characterisation. One such approach is using an electromagnetic borehole flowmeter to measure variations in hydraulic conductivity within the screened interval. This would provide independent data to better define the conversion of NMR logging data to downhole estimates of hydraulic conductivity.

13. Recommendations with respect to hydrographic Monitoring and analysis are:
    i. Continue to collect time-series groundwater level and barometric data from the existing project monitoring network. The monitoring of the groundwater response to flood events of varying magnitude is required to better quantify recharge dynamics.
    ii. Trial the installation of additional logger technologies in the monitoring bores to collect time series data of complimentary parameters (such as groundwater electrical conductivity or temperature).
14. Unfortunately due to time and resource constraints, both phases of geomorphic mapping were only completed in the central, higher priority area. It is thus recommended that detailed geomorphic mapping be finalised across the entire BHMAR study area. More broadly, in areas where the trend in the floodplain dictates, it is recommended that the regional digital elevation model be levelled prior to geomorphic mapping. This will then facilitate the generation of both rapid and highly detailed geomorphic mapping of the floodplain using a semi-automated contouring tool.
15. With respect to grain size analysis, the following recommendations are made:
    i. To improve the reliability of the laser grain size analysis, stronger pre-treatment regimes (including acid) and dispersion protocols can more effectively disaggregate secondary particles but must necessarily add to laboratory time and therefore costs. In future, stronger pre-treatment (including acid) and dispersion regimes should be used for mud- and clay-rich samples which are dry or are known to have dried in the past and/or contain secondary cementation. Moisture analyses and quantitative XRD mineralogy determinations can help inform the decision to select samples requiring these processes. Sand-sized sediments have issues with repeatability of results, due to the difficulty of obtaining representative samples because of the small sample requirements of the measuring instrument. This constraint is likely to increase with coarser textured samples.
    ii. New laboratory procedures are recommended for sample preparation prior to carrying out laser grain size analysis of core materials. More specifically, representative samples should be tested prior to routine analyses to determine the most appropriate disaggregation method for a batch of samples; routine treatment with HCl where carbonate cementation is possible. Methodologies should also be established for dealing with non-carbonate cementation; and sample splitting methods are necessary to ensure statistically representative sub-sampling.
16. Clogging tests

17. The following recommendations are based on the successful trialling of in-river surveys and sampling by the BHMAR project.
    i. The data and observations from the in-river survey were critical in finessing the conceptual model for river-aquifer connectivity in the Jimargil target area. This data included mapping of river bathymetry which could be compared against the existing understanding of underlying hydrostratigraphy, as well as the identifying and sampling of riverbed depressions.
    ii. The survey boat is a useful platform where additional data collection could be incorporated. This could include systematic photography of the river banks, regular river water sampling and the towing of water quality sondes (such as EC, pH and DO). Reconnaissance survey data could then be used to target more detailed investigations such as shallow coring or the installation of pressure or temperature loggers in the water column and river sediments. Such data is important in understanding the spatial and temporal changes in groundwater-surface water connectivity. The in-river data also has relevance to other disciplines (such as aquatic ecology, engineering and landscape remediation)
18. Preliminary groundwater modelling was undertaken as part of Phase 3 investigations of the Jimargil borefield target, for which the following recommendations are based:
    i. The use of rapid, simple but robust (parsimonious) groundwater flow and solute transport models is recommended at relatively early stages of data acquisition and interpretation. Such models are useful in (1) a sensitivity analysis to define key data gaps, (2) in testing the validity of a range of potential conceptual models about the hydrogeological system and key groundwater processes and (3) in scoping the broad MAR requirements and potential impacts such defining the required target size or highlighting zones of inter-aquifer leakage;
    ii. A review of the available data and conceptual understanding be made at a decision point concerning the development of a more sophisticated 3D multi-layered transient groundwater flow and solute transport model to support any future borefield design and operation. Such modelling will need to take account of (1) the episodic flow-dependent nature of river leakage including change in river bed conductance (2) the localised nature of recharge to the target Calivil Formation aquifer via structural or erosional gaps in the overlying Blanchetown Clay (3) the preferential distribution of Calivil Formation aquifer sands and gravels in palaeovalley fill (4) the mapping of the shallow aquifer as generations of alluvial deposits that are structurally controlled and disrupted (5) the distribution of native vegetation that has been interpreted to have a degree of dependency on shallow groundwater (6) possible variability in the hydraulic connectivity between the target Calivil Formation aquifer and the underlying Renmark Formation (7) the potential with pumping for vertical and lateral ingress from mapped zones of brackish to saline groundwater.
19. To improve the reliability of the laser grain size analysis, stronger pre-treatment regimes (including acid) and dispersion protocols can more effectively disaggregate these secondary particles but must necessarily add to laboratory time and therefore costs. In future, stronger pre-treatment (including acid) and dispersion regimes should be used for mud- and clay-rich samples which are dry or are known to have dried in the past and/or contain secondary cementation. Moisture analyses and quantitative XRD mineralogy determinations can help inform the decision to select samples requiring these processes. Sand-sized sediments have issues with repeatability of results, due to the difficulty of obtaining representative samples because of the small sample requirements of the measuring instrument. This constraint is likely to increase with coarser textured samples.
20. New laboratory procedures are recommended for sample preparation prior to carrying out laser grain size analysis of core materials. More specifically, representative samples should be tested prior to routine analyses to determine the most appropriate disaggregation method for a batch of samples; routine treatment with HCl where carbonate cementation is possible. Methodologies should also be established for dealing with non-carbonate cementation; and sample splitting methods are necessary to ensure statistically representative sub-sampling.
21. The MAR guidelines (NRMMC-EPHC-NHMRC, 2009) are a component of the National Water Quality Management Strategy (NWQMS) and as such have a specific focus on human health and environment protection. Experience in the BHMAR project suggests that there is a strong case that the MAR guidelines be complemented by supporting documentation that would provide complementary advice on a broader range of issues not covered in the existing Guidelines. This supporting

documentation, covering MAR site selection and best practice advice on the adequacy of geological and hydrogeological data for MAR site assessment, may include:

i. Advice on technical risk assessment frameworks for selecting the most appropriate technologies and methods for MAR mapping and assessment.

ii. This document should also provide 'best practice' advice on how to assess the adequacy of geological and hydrogeological data, and the inherent variability of key geological and hydrogeological parameters, be written to guide MAR proponents. This document should also address issues such as the potential impact on the level of confidence in proceeding through the MAR assessment stages. This should include guidance on the data density and data quality required to map critical geological, hydrochemical and hydraulic properties could also be provided in the supporting document.

iii. Advice on assessing the uncertainty associated with the hydrogeological and hydrochemical characterisation, including sensitivity analysis approaches, would also be useful.

iv. This document should stress the importance of assessing multiple targets. This was highlighted by the failure of many sites in the BHMAR study. Failure to identify multiple candidate sites may lead to significant delays in MAR project implementation, if scientific investigations required to address the questions in Stage 2 assessments are undertaken sequentially rather than concurrently

v. Advice on how groundwater flow and solute transport modelling could be incorporated into the MAR assessment process is also warranted. As the case for the BHMAR project, relatively simple models constructed early in the process can greatly assist with the MAR viability or degree of difficulty assessment and the defining of key information gaps. As data acquisition proceeds, more sophisticated models could be constructed to provide a more realistic evaluation of operational options and potential third party or environmental impacts.

vi. The document would aim more broadly to assist proponents with all stages of MAR selection and assessment.

22. A trans-disciplinary systems approach, and integrated workflows developed in the BHMAR Project, should be considered for future hydrogeological investigations and the assessment of MAR options in Australia, and in shallow sedimentary systems in particular. These methods provide the integrative framework required to address the many inter-related issues encountered in assessing MAR options, particularly in hydrogeologically and hydrogeochemically complex areas.

# References


AAM Hatch. 2009. Lower Darling LiDAR Data Capture Project. Final Project Report. 35p. (Unpublished).

Abraham, J.D., Kress, W.H., Cannia, J.C., Steele, G.V., Smith, B.D. & Woodward, D. 2008. Examination of magnetic resonance soundings in the central Platte River Basin for groundwater model enhancements. Eos Transactions AGU 89(53), Fall Meeting Supplemental, Abstract NS43B-1194.

Abraham, J.D., Cannia, J.C, Bedrosian, P.A., Johnson, M.R., Ball, L.B. & Sibray, S.S. 2011a. Airborne Electromagnetic Mapping of the base of the aquifer in areas of Western Nebraska. U.S. Geological Survey Scientific Investigations Report 2011-5219.

Abraham, J., Cannia, J., Irons, T., Steele, G., Williams, G. & Woodward, D. 2011b. Magnetic Resonance Soundings in the Central Platter River Basin for groundwater models. In: Abstracts from the Environmental Engineering Geophysical Society's Annual Symposium on the Application of Geophysics to Environmental and Engineering Problems April 10-14, Charleston, SC.

Abraham, J.D., Minsley, B.J., Bedorsian, P.A., Smith, B.D. & Cannia, J.C. 2012. Airborne Electromagnetic survey for groundwater characterization. Australian Society of Exploration Geophysicists 22nd International Conference and Exhibition, February 26-29, 2012, Brisbane, Australia.

Abramowitz, M. & Stegun, I.A. (eds) 1972. Handbook of mathematical functions with formulas, graphs, and mathematical tables. New York: Dover Publications, 1064 pp.

ADWG. 2011, Australian Drinking Water Guidelines 2011. National Water Quality Management Strategy. National Health and Medical Research Council – Natural Resource Management Ministerial Council. http://www.nhmrc.gov.au/guidelines/publications/eh52

Akumu, C.E., Pathirana, S., Baban, S. & Bucher, D. 2010. Monitoring coastal wetland communities in north-eastern NSW using ASTER and Landsat satellite data. Wetlands Ecological Management, 18, 357-365.

Allan, D., Flaum, C., Ramakrishnan, T.S., Fairhurst, D., Pritchard, T., Bedford, J., Gubelin, G., Heaton, N., Minh, C.C., Ramamoorthy, R., Castelijns, K., Norville, M.A. & Seim, M.R. 2000. Trends in NMR logging. Oilfield Review, 2-20.

Allen, D. 2005. A review of geophysical equipment applied to groundwater and soil investigations. ANCID/Sustainable Irrigation Travel Fellowship Report, 77pp.

Alumbaugh, D.L. & Newman, G.A. 2000. Image appraisal for 2-D and 3-D electromagnetic inversion. Geophysics, 65, 1455.

Alvarado, R.J., Damgaard, A., Hansen, P., Raven, M., Heidler, R., Hoshun, R., Kovats, J., Morriss, C., Rose, D. & Wendt, W. 2003. Nuclear magnetic resonance logging while drilling. Oilfield Review 15, 40-51.

An, Z., Bowler, J.M., Opdyke, N.D., Macumber, P.G. & Firman, J. B. 1986. Palaeomagnetic stratigraphy of Lake Bungunnia: Plio- Pleistocene precursor of aridity in the Murray Basin, southeastern Australia. Palaeogeography, Palaeoclimatology, Palaeoecology 54, 219–239.

APHA (American Public Health Association) 2005. Standard methods for the examination of water and wastewater. 21st Ed, Eaton, A.D., Clesceri, L.S., Rice, E.W., Greenberg, A.E., Franson, M.A.H. Washington.

Appelo, C.A.J. & Postma, C. 1999. Geochemistry, groundwater and pollution. Balkema, Netherlands.

Apps, H.E., Clarke, J.D.A., Gow, L. & Halas, L. 2012a. BHMAR Project Appendix 8: Recharge models and data. Geoscience Australia Record 2012/16. Geocat 73824.

Apps, H.E., Halas, L., Knox, K., Cook, B., Beaudreau, D., Tan, K.P., Gibson, D., Smith, M., Lawrie, K.C., Brodie, R.S., Brodie, R.C., Abraham, J., Christensen, N.B., Gow, L., Magee, J.W. & Clarke, J.D.A. 2012b. BHMAR Project Appendix 5: AEM-based interpretation products: maps and cross-sections. Geoscience Australia Record 2012/16. Geocat 73824.

Apps, H.E., Lawrie, K.C., Christensen, N.B., Brodie, R.C., Smith, M. & Knox, K. 2012c. BHMAR Project Appendix 4: AEM data: acquisition reports, inversion and calibration, and basic conductivity map and cross-section products. Geoscience Australia Record 2012/16. Geocat 73824.

Apps, H.E., Lawrie, K.C., Halas, L., Atkinson, I., Clarke, J.D.A., Wintle, C. & Wilson, O. 2012d. BHMAR Project Appendix 10: Ground and in-river geophysics and supporting data. Geoscience Australia Record 2012/16. Geocat 73824.

Apps, H.E., Magee, J.W. & Clarke, J.D.A. 2012e. BHMAR Project Appendix 7: Age dating (contractor reports). Geoscience Australia Record 2012/16. Geocat 73824.

Apps, H.E., Schoning, G., Tan, K.P., Clarke, J.D.A., Magee, J.W., Gibson, D., Halas, L., Gow, L. & Davies, A. 2012f. BHMAR Project Appendix 3: Borehole geophysical and geological data. Geoscience Australia Record 2012/16. Geocat 73824.

Apps, H.E., Tan, K.P. & Brodie, R.S. 2012g. BHMAR Project Appendix 13. Borehole hydraulic data (contractor reports). Geoscience Australia Record 2012/16. Geocat 73824.

Apps, H.E. & Gibson, D. 2012. BHMAR Project Appendix 12: Drilling construction, location and remediation data and reports. Geoscience Australia Record 2012/17. Geocat 73824.

Apps, H.E. & Lawrie, K.C. 2012. BHMAR Project Appendix 11: CSIRO MAR reports. Geoscience Australia Record 2012/16. Geocat 73824.

Archie, G.E. 1942. The electrical resistivity log as an aid in determining some reservoir characteristics. Transactions American Institute of Mechanical Engineers 146, 54-67.

Armston, J.D., Denham, R.J., Danaher, T.J., Scarth, P.F. & Moffiet, T.N. 2009. Prediction and validation of foliage projective cover from Landsat-5 TM and Landsat-7 ETM+ imagery. Journal of Applied Remote Sensing 3, 1-28.

Auken, E. & Christiansen, A.V. 2004. Layered and laterally constrained 2D inversion of resistivity data. Geophysics 69, 752-761.

Auken, E., Christiansen, A.V., Jacobsen, B.H., Foged, N. & Sørensen, K.I. 2005. Piecewise 1D laterally constrained inversion of resistivity data. Geophysical Prospecting 53, 497-506.

Auken, E., Pellerin, L., Christensen, N.B. & Sørensen, K.I. 2006. A survey of current trends in near-surface electrical and electromagnetic methods. Geophysics 71, G249-G260.

Auken, E., Christiansen, A.V., Westergaard, J.H., Kirkegaard, C., Foged, N. & Viezzoli, A. 2009. An integrated processing scheme for high-resolution airborne electromagnetic surveys, the SkyTEM system. Exploration Geophysics 40, 184-192.

Barron, O.V., Crosbie, R.S., Charles, S.P., Dawes, W.R., Ali, A., Evans, W.R., Cresswell, R., Pollock, D., Hodgson, G., Currie, D., Mpelasoka, F., Pickett, T., Aryal, S., Donn, M. & Wurcker, B. 2011. Climate change impact on groundwater resources in Australia. Waterlines Report, National Water Commission, Canberra.

Bedrosian, P.A., Densmore-Judy, J., Martin, P., Burgess, M., Langenheim, V. & Jachens, R. 2012. Faulting and groundwater in arid environments: Airborne electromagnetics in support of framework hydrology in the northern Mojave Desert, southern California. 22nd ASEG Conference, Brisbane, Australia. (Ext. Abs.).

Bergman, D.J., LaTorraca, G.A. & Dunn, K.J. 1995. Magnetic susceptibility contrast effects on NMR $T_2$ logging, Society of Petrophysicists and Well Log Analysts, Annual Logging Symposium.

Bird, M.I., Ayliffe, L.K., Fifield, L.K., Cresswell, R., Turney, C.S.M., Barrows, T.T. & David, B. 1999. Radiocarbon dating of 'old' charcoal using a wet oxidation-stepped combustion procedure. Radiocarbon 41, 127-40.

Bird, M.I., Turney, C.S.M., Fifield, L.K., Jones, R., Ayliffe, L.K., Palmer, A., Cresswell, R.G. & Robertson, S. 2002. Radiocarbon analysis of the early archaeological site of Nauwalibila I, Arnhem Land, Australia: implications for sample suitability and stratigraphic integrity. Quaternary Science Reviews 21, 1061-1075.

Black, J.H. 2010. The practical reasons why slug tests (including falling and rising head tests) often yield the wrong value of hydraulic conductivity. Quarterly Journal of Engineering Geology and Hydrogeology 43, 345-358.

Bodin, T., Sambridge, M. & Gallagher, K. 2009. A self-parameterizing partition model approach to tomographic inverse problems. Inverse Problems 25, 055009 (22 pp).

Bodin, T. & Sambridge, M. 2009. Seismic tomography with the reversible jump algorithm. Geophysical Journal International 178, 1411-1436.

Bouwer, H. 2002. Artificial recharge of groundwater: hydrogeology and engineering. Hydrogeology Journal 10, 121-142.

Bouwer, H. & Rice R.C. 1976. A slug test method for determining hydraulic conductivity of unconfined aquifers with completely or partially penetrating wells. Water Resources Research 12, 3, 423-428.

Bowler, J.M. 1980. Quaternary chronology and palaeohydrology in the evolution of Mallee landscapes. In: Storrier, R.R. & Stannard, M.E. (eds) Aeolian landscapes in the semi-arid zone of south eastern Australia, 17-36. Australian Society of Soil Science, Riverina Branch.

Bowler, J.M, Kotsonis, A. &. Lawrence, C.A. 2006. Environmental evolution of the Mallee Region, western Murray Basin. Proceedings of the Royal Society of Victoria 118, 161-210.

Brodie, R. & Sambridge, M. 2006. A holistic approach to inversion of frequency-domain airborne EM data. Geophysics 71, G301-G312.

Brodie, R. & Sambridge, M. 2012. Transdimensional Monte Carlo Inversion of AEM Data. 22nd International Geophysical Conference and Exhibition, Australian Society of Exploration Geophysicists, Extended Abstracts.

Brodie, R.S. 1994. MENINDEE Hydrogeological Map (1:250 000 scale). Murray Basin Hydrogeological Map Series. Canberra, Australian Geological Survey.

Bronk Ramsay, C. 2009. Bayesian analysis of radiocarbon dates. Radiocarbon 51, 337-360. http://c14.arch.ox.ac.uk/embed.php?File=oxcal.html

Brown, C.M. & Stephenson, A.E. 1991. Geology of the Murray Basin, South Eastern Australia. BMR Bulletin 235.

Brown, R.J.S. & Gamson B.W. 1960. Nuclear magnetism logging. Transactions of the American Institute of Mining and Metallurgical Engineers 219, 201-219.

Brownstein, K.R. & Tarr C.E. 1979. Importance of classical diffusion in NMR studies of water in biological cells. Physical Review A 19, 2446-2453.

Bussian A.E. 1983. Electrical conductance in a porous medium. Geophysics 48, 1258-1268.

Butler, J.J. 1998. The design, performance and analysis of slug tests. Lewis Publishers, 252 pp.

Butler, J.J., Duffield, G.M. & Kelleher, D.L. 2007. Field guide for slug testing and data analysis. Midwest Geosciences Group.

Caldwell, N., de Hoog, M., Navin, J., Lawrie, K., Brodie, R.S., Apps, H. & Halas, L. 2012. Fly-through movie. Broken Hill Managed Aquifer Recharge Project, Geocat 63827.

Carman, P.C. 1956. Flow of gases through porous media, Academic Press, New York.

Carr, H.Y. & Purcell E.M. 1954. Effects of diffusion on free precession in nuclear magnetic resonance experiments. Physical Review 94, 630-638.

Carslaw, H.S. & Jaeger, J.C. 1959. Conduction of heat in solids. Oxford University Press, London.

Cartus, O., Kellndorfer, J., Rombach, M. & Walker, W. 2012. Mapping canopy height and growing stock volume using Airborne LiDAR, ALOS PALSAR and Landsat ETM+. Remote Sensing 4, 3320-45.

Chamberlain, T. & Wilkinson, K. (eds), 2004. Salinity investigations using airborne geophysics in the Lower Balonne area, Southern Queensland. Queensland Department of Natural Resources and Mines, 257p.

Chang, C.I. 2003. Hyperspectral imaging: techniques for spectral detection and classification. Kluwer Academic/Plenum Publishers, New York, pp 370.

Chen, J., Kemna, A. & Hubbard, S.S. 2008. A comparison between Gauss-Newton and Markov-chain Monte Carlo-based methods for inverting spectral induced-polarization data for Cole-Cole parameters. Geophysics 73, F247-F259.

Chen, Q., Marble, A.E., Colpitts, B.G. & Balcom, B.J. 2005. The internal magnetic field distribution and single exponential magnetic resonance free induction decay, in rocks. Journal of Magnetic Resonance 175, 300-308.

Chen, S., Li, L., Zhang, G. & Chen, J. 2011. Magnetic resonance for downhole complex-lithology earth formation evaluation. New Journal of Physics 13, 14.

Chen, S., Ostroff, G. & Georgi, D.T. 1998. Improving estimation of NMR log $T_2$ cutoff value with core NMR and capillary pressure measurements. Pure and Applied Geophysics 162, 549-570.

Chiew, F., Wang, Q.J., McConachy, F., James, R., Wright, W. & de Hoedt, G. 2002. Evapotranspiration maps for Australia. Hydrology and Water Resources Symposium, Melbourne, 20-23 May, 2002, Institution of Engineers, Australia. http://www.bom.gov.au/climate/averages/climatology/evapotrans/text/evapotranspiration-paper.pdf

Chopra, P., Papp, E. & Gibson, D. 2002. Geophysical well-logging, In: Papp, E. (ed.) Geophysical and remote sensing methods for regolith exploration. CRC LEME Open File Report 144, 105–115.

Christensen, N.B. 1990. Optimized Fast Hankel Transform Filters. Geophysical Prospecting 38, 545-568.

Christensen, N.B. 2002. A generic 1-D imaging method for transient electromagnetic data. Geophysics 67, 438-447.

Christensen, N.B. 2011. Integrated geophysical inversion and interpretation in the Broken Hill Area. Aarhus University Report to Geoscience Australia. (Unpublished).

Christensen, N.B. 2012. Wave Number Domain Approximate Inversion procedure. Aarhus University Report to Geoscience Australia. (Unpublished).

Christensen, N.B. & Lawrie, K. 2012. Resolution analyses for selecting an appropriate airborne electromagnetic (AEM) system. Exploration Geophysics 43, 213-227. http://dx.doi.org/10.1071/EG12005

Christensen, N.B. & Tølbøll, R.J. 2009. A lateral model parameter correlation procedure for one-dimensional inverse modelling. Geophysical Prospecting 57, 919-929. DOI: 10.1111/j.1365-2478.2008.00756.x

Christensen, N.B., Reid, J.E. & Halkjaer, M. 2009. Fast, laterally smooth inversion of airborne time-domain electromagnetic data. Near Surface Geophysics 7, 599–612.
Christiansen, A.V. & Auken, E. 2012. A global measure for depth of investigation. Geophysics 77, WB171-WB177.
Clarke, J.D.A., Gibson, D. & Apps, H. 2010. The use of LiDAR in applied interpretive landform mapping for natural resource management, Murray River alluvial plain, Australia. International Journal of Remote Sensing 31, 6275-96.
Clarke, J., Wong, V., Gibson, D., Apps, H., Luckman, J., Pain, C. & Lawrie, K. 2007a. Geomorphology and surface materials: Robinvale to Boundary Bend. CRC LEME Restricted Report 259R.
Clarke, J. Wong, V., Pain, C., Apps, H., Gibson, D., Luckman, J. & Lawrie, K. 2007b. Geomorphology and surface materials: Lindsay to Wallpolla. CRC LEME Restricted Report 261R.
Clifton, C., Cossens, B. & McAulay, C. 2007. A framework for assessing the environmental water requirements of groundwater dependent ecosystems. Report 1 Assessment Toolbox. Canberra.
Coates, G.R., Marschall, D., Mardon, D. & Galford, J. 1997. A new characterization of bulk-volume irreducible using magnetic resonance. The Log Analyst 39, 51-63.
Coates, G. R., Xiao, L. & Prammer, M. G. 1999. NMR logging principles and applications. Houston, TX, USA. Halliburton Energy Services.
Cohen, M.H. & Mendelson, K.S. 1982. Nuclear magnetic relaxation and the internal geometry of sedimentary rocks. Journal of Applied Physics 53, 1127-1135.
Cole, K.S. & Cole, R.H. 1941. Dispersion and absorption in dielectrics. Journal of Chemical Physics 9, 341-351.
Conway, B. 2008. Minor uplift from groundwater recharge in Phoenix area http://arizonageology.blogspot.com.au/2008/07/minor-uplift-in-groundwater-recharge.html
Cook, A. & Merwade, V. 2009. Effect of topographic data, geometric configuration and modeling approach on flood inundation mapping. Journal of Hydrology 377, 131-42.
Cook, P.G. & Bohlke, J-K. 2000. Determining timescales for groundwater flow and transport. In: Cook, P.G & Herczeg, A.L. (eds), Environmental tracers in subsurface hydrology. Kluwer.
Cooper, H.H., Bredehoeft, J.D. & Papadopulos, S.S. 1967. Response of a finite-diameter well to an instantaneous charge of water. Water Resources Research 3, 1, 263-269
Crank, J. 1956. The mathematics of diffusion. Oxford University Press, Oxford, pp 347.
Cresswell, R.G., Dent, D.L., Jones, G.L. & Galloway, D.S. 2004. Three dimensional mapping of salt stores in the southeast Murray- Darling Basin, Australia 1. Steps in calibration of airborne electromagnetic surveys. Soil Use Management 20, 133–143.
Cresswell, R.G., Mullen, I.C., Kingham, R. Kellett, J., Dent, D.L. & Jones, G.L. 2007. Airborne electromagnetics supporting salinity and natural resource management decisions at the field scale in Australia. International Journal of Applied Earth Observation and Geoinformation 9, 91-102.
Crosbie, R.S., Jolly, I.D., Leaney, F.W. & Petheram, C. 2010. Can the dataset of field based recharge estimations in Australia be used to predict recharge in data poor areas? Hydrology and Earth Systems Sciences 14, 2023-2038.
CSIRO. 2011. Analysis of $^{222}$Rn concentrations in surface water and groundwater samples. http://www.clw.csiro.au/services/isotope/documents/Rn-analysis.pdf
CSIRO. Undated. HyLogging Systems hyperspectral mineralogical logging and imaging of drill core and chips. Address when accessed 12/12/11 http://www.csiro.au/files/files/py3w.pdf
Cunningham, S.C., MacNally, R., Read, J., Baker, P.J., White, M., Thomson, J.R. & Griffioen, P. 2009. A robust technique for mapping vegetation condition across a major river system. Ecosystems 12, 207-219.
Cunningham, S.C., MacNally, R., White, M., Read, J., Baker, P.J., Thomson, J. & Griffioen, P. 2007. Mapping the current condition of River Red Gum (*Eucalyptus camaldulensis* Dehnh.) stands along the Victorian Murray River floodplain. A report to the Northern Victorian Catchment Management Authorities and the Department of Sustainability and Environment.
Daigle, H. & Dugan, B. 2009. Extending NMR data for permeability estimation in fine-grained sediments. Marine and Petroleum Geology 26, 1419-1427.
Daigle, H. & Dugan, B. 2011. An improved technique for computing permeability from NMR measurements in mudstones. Journal of Geophysical Research 116, B08101.
Davis, S.N., Whittemore, D.O. & Fabryka-Martic, J. 1998. Use of chloride/bromide ratios in studies of potable water. Groundwater 36, 2, 338-350
de Hoog, M., Navin, J., Lawrie, K., Apps, H., Halas, L., Brodie, R.S. 2012. WORLDWIND virtual globe model. Broken Hill Managed Aquifer Recharge Project, Geocat 63827.

de Moel, H., Van Alphen, J. & Aerts, J.C.J.H. 2009. Flood maps in Europe - methods, availability and use. Natural Hazards and Earth System Science 9, 289-301.
de Souzo Fillho, O.A., Silva, A.M., Remacre, A.Z., Sancevero, S.S., McCafferty, A.E. & Perrotta, M.M. 2010. Using helicopter electromagnetic data to predict groundwater quality in fractured crystalline bedrock in a semi-arid region, Northeast Brazil. Hydrogeology Journal 18, 905-916.
Dehaan, R. & Taylor, G.R. 2003. Image-derived spectral end members as indicators of salinisation. International Journal of Remote Sensing 24, 775–794.
Dehaan, R.L. & Taylor, G.R. 2004. A remote-sensing method of mapping soils and surficial lags from a deeply weathered arid region, near Cobar, NSW, Australia. Geochemistry - Exploration, Environment, Analysis 4, 99-112.
Delaunay, B. 1934. Sur la sph`ere vide, Izvestia Akademii Nauk SSSR, Otdelenie Matematicheskikh i Estestvennykh Nauk 7, 793-800.
Deming, W.E. & Birge, R.T. 1934. On the statistical theory of errors. Review of Modern Physics 6, 119-161.
Diersch, 2002. FEFLOW Reference Manual. WASY Berlin.
Dillon, P., Toze, S., Pavelic, P., Vanderzalm, J., Barry, K., Ying, G-G., Kookana, R., Skjemstad, J., Nicholson, B., Miller, R., Correll, R., Prommer, H., Greskowiak, J. & Stuyfzand, P. 2005. Water quality improvements during aquifer storage and recovery at ten sites. In: UNESCO (ed.) Recharge systems for protecting and enhancing groundwater resources. Proceedings of the 5th International Symposium on Management of Aquifer Recharge (ISMAR5), Berlin, 11–16 June 2005, 85–94. http://unesdoc.unesco.org/images/0014/001492/149210e.pdf
Dillon, P., Page, D., Pavelic, P., Toze, S., Vanderzalm, J., Barry, K., Levett, K., Regel, R., Rinck-Pfeiffer, S., Pitman, C., Purdie, M., Marles, C., Power, N. & Wintgens, T. 2008a. City of Salisbury's progress towards being its own drinking water catchment. Proceedings of the IWA conference Singapore Water Week, June 2008.
Dillon, P., Page, D., Vanderzalm, J., Pavelic, P., Toze, S., Bekele, E., Sidhu, J., Prommer, H., Higginson, S., Regel, R., Rinck-Pfeiffer, S., Purdie, M., Pitman, C. & Wintgens, T. 2008b. A critical evaluation of combined engineered and aquifer treatment systems in water recycling. Water Science and Technology 57, 753-762.
Dillon, P., Pavelic, P., Page, D., Beringen, H. & Ward, J. 2009. Managed aquifer recharge. Waterlines Report Series No. 13, February 2009.
Dlubac, K., Knight, R.J., Song, Y., Bachman, N., Grau, B., Cannia, J.C. & Williams, J. 2011. Obtaining permeability estimates from NMR logging data in an unconsolidated groundwater aquifer. 2011 Fall Meeting, AGU, San Francisco, California, December 5-9.
Dlubac, K., Knight, R.J., Song, Y., Bachman, N., Grau, B., Cannia, J.C. & Williams, J. 2013. The use of NMR logging to obtain estimates of hydraulic conductivity in the High Plains aquifer, Nebraska, USA. Water Resources Research, 49, DOI: 10.1002/wrcr.20151
Doble, R., Connor, J., Ariyaratne, C., Matthew, M., Evans, R., McEwan, K., Stenson, M., Sauffacher, M. & Walker, G. 2005. River Murray corridor systems model. Year 2 Interim progress report - Task A.CSIRO Water for a Healthy Country Flagship report. Adelaide: CSIRO.
Doble, R., Connor, J., Stenson, M., Elmahdi, A. & Walker, G. 2008. Future landscape scenarios in the lower River Murray, south-eastern Australia and their implications for river salinity and floodplain health. International Salinity Forum, 30 March - 3 April 2008, Adelaide. http://www.internationalsalinityforum.org/14_final.html
Doll, W.E., Nyquist, J.E., Beard, L.P. & Gamey, T.J. 2000. Airborne geophysical surveying for hazardous waste site characterization on the Oak Ridge Reservation, Tennessee. Geophysics 65, 1372-1387.
Doody, T.M., Holland, K.L., Benyon, R.G. & Jolly, I.D. 2009. Effect of groundwater freshening on riparian vegetation water balance. Hydrological Processes 23, 3485-3499.
Doody, T. & Overton, I. 2009. Environmental management of riparian tree health in the Murray-Darling Basin, Australia. Transactions on Ecology and the Environment 124, 197-206.
d'Ozouville, N., Auken, E., Sorensen, K., Violette, S. Marsily, G. de, Deffontaines, B. & Merlen, G. 2008. Extensive perched aquifer and structural implications revealed by 3D resistivity mapping in a Galapagos volcano. Earth and Planetary Science Letters 269, 518-522.
Du, B. 2000. Comparison of crosswell diffraction tomography to Kirchoff migration. Exploration Geophysics 31, 366-371.
Dunn, K.-J., Bergman, D.J. & Latorraca, G.A. 2002. Nuclear magnetic resonance petrophysical and logging applications. Oxford, United Kingdom: Elsevier Science.

Edmunds, W.M., Fellman, E., Goni, I.B. & Prudhomme, C. 2002. Spatial and temporal distribution of groundwater recharge in northern Nigeria. Hydrogeology Journal 10, 205-15.

Edwards, D. & MacAuley, S. 2008. Airborne electromagnetic surveying for answering environmental /land management questions: a case study from the Lower Macquarie Catchment, NSW, Australia. AEM 08, Helsinki, Finland. (ext abs) 08-05, 2p.

Eldridge, S.R., Thorburn, P.J., McEwan, K.L. & Hatton, T.J. 1993. Health and structure of Eucalyptus communities on Chowilla and Monoman islands of the River Murray floodplain, South Australia. Divisional Report - CSIRO Australia, Division of Water Resources 93.

ESCAVI. 2003. Australian vegetation attribute manual. National Vegetation Information System, version 6.0. Canberra, Department of the Environment and Heritage.

Evans, R., Murrihy, E., Bastiaanssen, W. & Molloy, R. 2009. Using satellite imagery to measure evaporation from storages- solving the great unknown in water accounting. Irrigation and Drainage Conference 2009, Irrigation Australia Ltd, Swan Hill, Vic, Australia, 18 – 21 Oct. 2009.

Feng, Y. & Wang, J. 2008. GPS RTK performance characteristics and analysis. Journal of Global Positioning Systems 7, 1-8.

Fetter, C.W. 2001. Applied hydrogeology. 4th Edition, Prentice-Hall, New Jersey.

Fiandaca, G., Auken, E., Christiansen, A.V. & Gazoty, A. 2012. Full decay forward response modelling and direct inversion for Cole-Cole parameters. Geophysics, 77, 3, E213-E225.

Fitterman, D.V. & Deszcz-Pan, M. 1998. Helicopter EM mapping of saltwater intrusion in Everglades National Park, Florida. Exploration Geophysics 29, 240-243.

Fitzpatrick, A. & Munday, T.J. 2005, Forward modelling airborne electromagnetic data for application in mapping the Coffin Bay groundwater lens. CRCLEME restricted report.

Fogel, N. & Sorensen, C. 2010. Processing and inversion of the Broken Hill SkyTEM survey using the Aarhus Workbench. Hydrogeophysics Group, Aarhus University.

Freeze, R.A. & Cherry, J.A. 1979, Groundwater. Prentice Hall, Upper Saddle River, New Jersey, 604 pp.

Fuller, D.O., Prince, S.D. & Astle, W.L. 1997. The influence of canopy strata on remotely sensed observations of savanna-woodlands. International Journal of Remote Sensing 18, 14, 2985-3009.

Gao, B. 1996. NDWI - A Normalised Difference Water Index for remote sensing of vegetation liquid water from space. Remote Sensing of Environment 58, 257-266.

Gaveau, D.L.A. & Hill, R.A. 2003. Quantifying canopy height underestimation by laser pulse penetration in small-footprint airborne laser scanning data. Canadian Journal of Remote Sensing 29, 650-7.

Gazoty, A., Fiandaca, G., Pedersen, J., Auken, E. & Christiansen, A.V. 2012. Mapping of landfills using time-domain spectral induced polarization data - The Eskelund case study. Near Surface Geophysics, 10, 6, 575-586.

George, R.J. 1998. An evaluation of airborne geophysics for catchment management, Toolibin Catchment, Western Australia. Unpublished (see www.ndsp.gov.au).

George, R.J., Beasley, I., Gordon, D., Heislers, D., Speed, R., Brodie, R., McConnell, C. & Woodgate, P. 1998. Evaluation of airborne geophysics for catchment management. National Report to AFFA on National Airborne Geophysics Project (unpublished).

George, R.J. & Green, A. 2000. Position paper on airborne geophysics for salinity and land management: Sustainable Land and Water Resources Management Committee (SLWRMC), Airborne Geophysics Advisory Group.

George, R.J., Campbell, C., Woodgate, P., Farrell, S. & Taylor, P.J. 2000. Complementary data and cost benefit analysis of utilising airborne geophysics for salinity management purposes. Land and Water Australia project no. RM17.

George, R. J. & Woodgate, P. 2002, Critical factors affecting the adoption of airborne geophysics for management of dryland salinity. Exploration Geophysics 33, 84-89.

George, R.J., Lawrie, K.C. & Woodgate, P. 2003. Convince me all your bloody data and maps are going to help me manage salinity any better: A review of remote sensing methodology for salinity mapping. Proceedings of the 9th PURSL (Productive Use and Rehabilitation of Saline Land) Conference, Yeppoon, Qld. 29th September to 2nd October 2003. National Dryland Salinity Program.

Ghorbani, A., Camerlynck, C., Florsch, N., Cosenza, P. & Revil, A. 2007. Bayesian inference of the Cole-Cole parameters from time- and frequency-domain induced polarization. Geophysical Prospecting 55, 589-605.

Gillespie, R., Fifield, L.K., Levchenko, V. & Wells, R. 2008. New $^{14}C$ ages on cellulose from Diprotodon gut contents: explorations in oxidation chemistry and combustion. Radiocarbon 50, 75-81.

Godefroy, S., Korb, J., Fleury, M. & Bryant, R. 2001. Surface nuclear magnetic relaxation and dynamics of water and oil in macroporous media. Physical Review E, 64, 1-13.

Gow, L., Apps, H.E., Halas, L., Tan, K.P., Lawrie, K.C., Brodie, R.S., Gibson, D., Magee, J.W., Somerville, P., Smith, M., Clarke, J.D.A., Schoning, G., Halas, V., Spulak, R., Beudreau, D., Cook, B., Knox, K., Lymburner, L., McIntyre A., Christensen, N.B., Brodie, R.C., Abraham, J., Jaycock, J., Davies, A. & Ley-Cooper, Y. 2012a. Broken Hill Managed Aquifer Recharge Project GIS. GeoCat no. 73825.

Gow, L., Lymburner, L., Halas, L., McIntyre, A., Magee, J.W. & Beaudreau, D. 2012b. BHMAR Project Appendix 9: Remote sensing /vegetation health analysis background data and intermediate products. Geoscience Australia Record 2012/16. Geocat 73824.

Green, A.A. & Munday, T. 2004. Forward modelling airborne electromagnetic data for the Riverland, S.A. CRC LEME Open File Report 171, 36 pp. http://crcleme.org.au/Pubs/OPEN%20FILE%20REPORTS/OFR%20171-180/OFR171.pdf

Groen, J., Velstra, J. & Meesters, A.G.C.A. 2000. Salinization processes in paleowaters in coastal sediments of Suriname: Evidence from $\delta^{37}$Cl analysis and diffusion modelling. Journal of Hydrology, 234(1-2), 1-20.

Grün, R. 2009. The "Age" programme for the calculation of luminescence age estimates. Ancient TL 27, 45-46.

Grunewald, E. & Knight, R. 2009. A laboratory study of NMR relaxation times and pore coupling in heterogeneous media. Geophysics 74, E215.

Grunewald, E. & Knight R. 2011. A laboratory study of NMR relaxation times in unconsolidated heterogeneous sediments: Geophysics 76, 4, G73-G83.

Guerschman, J.P., Hill, M.J., Renzullo, L.J., Barrett, D.J., Marks, A.S. & Bortha, E.J. 2009. Estimating fractional cover of photosynthetic vegetation, non-photosynthetic vegetation and bare soil in the Australian tropical savanna region upscaling the EO-1 Hyperion and MODIS sensors. Remote Sensing for Environment 113, 928-45.

Güler, C. & Thyne, G.D. 2004. Delineation of hydrochemical facies distribution in a regional groundwater system by means of fuzzy c-means clustering. Water Resources Research 40, W12503.

Gyulai, Á & Ormos, T. 1999. A new procedure for the interpretation of VES data: 1.5-D simultaneous inversion method. Journal of Applied Geophysics 64, 1–17.

Halas, L., Halas, V., Schoning, G., Tan, K.P., Clarke, J.D.A., Gibson, D., Somerville, P., Spulak, R., Magee, J.W., Smith, M., Smith, M., Boston, K., Brodie, R.S., Lawrie, K.C. & Apps, H.E., 2012a. BHMAR Project Appendix 1: Graphical display of borehole geological and geophysical logs and hydrogeochemical data. Geoscience Australia Record 2012/16. Geocat 73824.

Halas, L., Apps, H., Lawrie, K., Brodie, R.S. & Tan, K.P. 2012b. 3D GoCAD Model. Broken Hill Managed Aquifer Recharge Project. Geocat, 63827.

Hantush, M.S. 1967. Growth and decay of ground water mounds in response to uniform percolation. Water Resources Research 3, 227-234.

Healy, R.W. & Cook, P.G. 2002. Using groundwater levels to estimate recharge. Hydrogeology Journal 10, 1, 91-109.

Hendrick, N. & Hearn, S. 1999. Polarisation analysis: What is it? Why do you need it? How do you do it? Exploration Geophysics 30, 177-190.

Henry, J.B., Chastanet, P., Fellah, K. & Desnos, Y.L. 2006. Envisat multi-polarized ASAR data for flood mapping. International Journal of Remote Sensing 27, 1921-9.

Herczeg, A.L., Rattray, K.J., Dillon, P.J., Pavelic, P. & Barry, K.E. 2004. Mineral-solution interactions during 5-years of Aquifer Storage and Recovery in a confined carbonate aquifer. Ground Water 42, 438-445.

Hess, L.L., Melack, J.M., Filoso, S. & Wang, Y. 1995. Realtime mapping of inundation on the Amazon floodplain with SIR-C/X-SAR synthetic aperture radar. IEEE Transactions on Geoscience and Remote Sensing 33, 896-904.

Hignett, C. 2013. Water holding properties of section of aquifer for Geoscience Australia. Technical Report, Daw Park, South Australia, Australia, Soil Water Solutions, Aps.

Hirsch, H.G., Hoffmann-Riem, H., Biber-Klemm, S., Grossenbacher-Mansuy, W., Joye, D., Pohl, C., Wiesmann, U. & Zemp, E. (eds) 2008. Handbook of trans-disciplinary research. New York, Springer, 2008.

Holben, B. 1986. Characteristics of maximum-value composite images from temporal AVHRR data. International Journal of Remote Sensing 7, 1417-1434.

Hönig, M. & Tezkan, B. 2007. 1D and 2D Cole-Cole-inversion of time-domain induced-polarization data. Geophysical Prospecting 55, 117-133.

Hopkinson, C., Chasmer, L., Zsigovics, G., Creed, I., Sitar, M., Treitz, P. & Maher, R. 2004. Errors in LiDAR ground elevation and wetland vegetation height estimates. International Archives of Photogrammetry, Remote Sensing, and Spatial Information Sciences 36, 108-13.
Horritt, M.S., Bates, P.D. & Mattinson, M.J. 2006. Effects of mesh resolution and topographic representation in 2D finite volume models of shallow water fluvial flow. Journal of Hydrology 329, 306-14.
Hossein, S., Bonnell, R., Sharifi, R., Mehuys, G., Namdar, M. & Ale-Ebrahim, S. 2008. Landform classification from a digital elevation model and satellite imagery. Geomorphology 100, 453-64.
Hudson, P.F. & Colditz, R.R. 2003. Flood delineation in a large and complex alluvial valley, lower Panuco Basin, Mexico. Journal of Hydrology 280, 229-45.
Huete, A.R. 1985. Spectral response of a plant canopy with different soil backgrounds. Remote Sensing of Environment 25, 295-309.
Hui, F., Xu, B., Huang, H., Yu, Q. & Gong, P. 2008. Modelling spatial-temporal change of Poyang Lake using multitemporal Landsat imagery. International Journal of Remote Sensing 29, 5767-84.
Hvorslev, M.J. 1951. Time lag and soil permeability in ground-water observations. Bulletin No. 36, Waterways Experimental Station. Corps of Engineers, U.S. Army, Vicksburg, Mississippi, 1-50.
Hyder, Z., Butler, Jr. J.J., McElwee, C.D. & Liu, W. 1994. Slug tests in partially penetrating wells. Water Resources Research, 30, 11, 2945-2957.
ICSM. 2008. ICSM guidelines for digital elevation data. Version 1.0. http://www.icsm.gov.au/elevation/ICSM-GuidelinesDigitalElevationDataV1.pdf
Inman, J.R. Jr, Ryu, J. & Ward, S.H. 1975. Resistivity inversion. Geophysics 38, 1088–1108.
Irons, T.P., Hobza, C.M., Steele, G.V., Abraham, J.D., Cannia, J.C. & Woodward, D.D. 2012. Quantification of aquifer properties with surface nuclear magnetic resonance in the Platte River valley, central Nebraska, using a novel inversion method. U.S. Geological Survey Scientific Investigations Report 2012–5189, 50 pp. http://pubs.usgs.gov/sir/2012/5189/
Islam, A.S., Bala, S.K. & Haque, M.A. 2010. Flood inundation map of Bangladesh using MODIS time-series images. Journal of Flood Risk Management 3, 210-22.
Jewell, C.M.J. 2007. Options for use of the Menindee and Broken Hill aquifers. Consultants report for Country Energy. C.M Jewell and Associates Pty Ltd, Wentworth Falls.
Jin, G., Torres-Verdín, C., Devarajan, S., Toumelin, E. & Thomas, E.C. 2007. Pore-scale analysis of the Waxman-Smits shaly-sand conductivity model. Petrophysics 48, 104–120.
Johnson, A.I. 1967. Specific yield - Compilation of specific yields for various materials. U.S. Geological Survey Water-Supply Paper 1662-D, 74 pp.
Jolly, I.D., Gow, L., Davies, P., O'Grady, A. & Leaney, F.W. 2011. Recharge and discharge estimation in data poor areas: User guide for the recharge and discharge estimation spreadsheets and MapConnect. CSIRO, Water for a Healthy Country National Research Flagship.
Jones, K.B., Edmonds, C.E., Slonecker, E.T., Wickham, J.D., Neale, A.C., Wade, T.G., Riitters, K.H. & Kepner, W.G. 2008. Detecting changes in riparian habitat conditions based on patterns of greenness change: A case study from the Upper San Pedro River Basin, USA. Ecological Indicators 8, 89-99.
Jurgens, B.C., McMahon, P.B., Chapelle, F.H. & Eberts, S.M. 2009. An Excel workbook for identifying redox processes in ground water. US Geological Survey Open-File Report 2009-1004.
Kaufman, Y.J. & Tanre, D. 1992. Atmospherically resistant vegetation index (ARVI) for EOS-MODIS. IEEE Transactions on Geoscience and Remote Sensing 30, 261-270.
KBR (Kellogg Brown & Root Pty Ltd). 2010. Weaber Plain groundwater modelling report Stage 1 results. Report prepared for LandCorp, Western Australia.
Keating, K. & Knight, R. 2007. A laboratory study to determine the effect of iron oxides on proton NMR measurements. Geophysics 72, E27–E32, doi:10.1190/1.2399445.
Keating, K. & Knight, R. 2008. A laboratory study of the effect of magnetite on NMR relaxation rates. Journal of Applied Geophysics 66, 188–196.
Keating, K., Knight, R. & Tufano, K. 2008. Nuclear magnetic resonance relaxation measurements as a means of monitoring iron mineralization processes. Geophysical Research Letters 35, L19405.
Kellett, J.R. 1994. MANARA Hydrogeological Map (1:250 000 scale). Murray Basin Hydrogeological Map Series. Australian Geological Survey Organisation, Canberra.
Kemna, A., Binley, A. & Slater, L. 2004. Crosshole IP imaging for engineering and environmental applications. Geophysics 69, 97-107.
Kennedy, D. 2007. The porosity-water saturation-conductivity relationship: An alternative to Archie's Model. Petrophysics 48, 5, 335-261.

Kennett-Smith, A., Cook, P.G. & Walker, G.R. 1994. Factors affecting groundwater recharge following clearing in the south western Murray Basin. Journal of Hydrology, 154, 85-105.

Kenyon, W.E., Kleinberg, R.L., Straley, C., Gubelin, G. & Morriss, C. 1995. Nuclear magnetic resonance imaging – technology for the 21st century. Oilfield Review 7, 19-33.

Kenyon, W.E. 1992. Nuclear magnetic resonance as a petrophysical measurement. Nuclear Geophysics 6, 153-171. Later revised and published in 1997 under the title, Petrophysical principles of applications of NMR logging, in The Log Analyst 38, 21–43.

Kenyon, W.E., Straley, C. & Willemsen, J.F. 1988. A three-part study of NMR longitudinal relaxation properties of water-saturated sandstones. Society of Petroleum Engineers Formation Evaluation 3, 3, 622-636.

Kernich, A., Pain, C., Clarke, J. & Fitzpatrick, A. 2009. Geomorphology of a dryland fluvial system: the Lower Balonne River, southern Queensland. Australian Journal of Earth Sciences 56, S139-S53.

Keys, W.S. 1997. A practical guide to borehole geophysics in environmental investigations. CRC Press, Boca Raton, Florida, USA, 176 pp.

Klein, J.T. 2008. Evaluation of inter-disciplinary and trans-disciplinary research: a literature review. American Journal of Preventive Medicine 35, 2S, S116 –S123.

Kleinberg, R.L., Flaum, C., Griffin, D.D., Brewer, P.G., Malby, G.E., Peltzer, E.T. & Yesinowski, J.P. 2003. Deep sea NMR: methane hydrate growth habit in porous media and its relationship to hydraulic permeability, deposit accumulation, and submarine slope stability. Journal of Geophysical Research 108, 2508.

Kloppman, W., Negrel, P., Casanova, J., Klinge, H., Schelkes, K. & Guerrot, C. 2001. Halite dissolution derived brines in the vicinity of a Permian salt dome (N German Basin): Evidence from boron, strontium, oxygen and hydrogen isotopes. Geochimica et Cosmochimica Acta 65, 22, 4087-41401.

Knight, R., Grunewald, E., Irons, T., Dlubac, K., Song, Y., Bachman, H.N., Grau, B., Walsh, D., Abraham, J.D. & Cannia, J. 2012. Field experiment provides ground truth for surface nuclear magnetic resonance measurement. Geophysical Research Letters 39, L03304.

Konikow, L.F. & Bredehoeft, J.D. 1992. Ground-water models cannot be validated. Advances in Water Resources 15, 75-83.

Kruse, F.A. 1999. Visible-infrared sensors and case studies. In: Rencz, A.N. (ed.) Manual of remote sensing, 3 Ed., Vol 3: Remote sensing for the earth sciences. p 567-611. John Wiley and Sons, New York.

Kuosmanen, V., Laitinen, J. & Arkimaa, H. 2005. A comparison of hyperspectral airborne Hymap and spaceborne Hyperion data as tools for studying the environmental impact of talc mining in Lahnaslampi, NE Finland. Proceedings of 4th EARSeL Workshop on Imaging Spectroscopy. New quality in environmental studies. EARSeL and Warsaw University, Warsaw 2005

Lane, R. & Pracilio, G. 2000. Visualisation of sub-surface conductivity derived from airborne EM. Symposium on the Application of Geophysics to Engineering and Environmental Problems (SAGEEP) 2000, 101-111.

Lane, R., Green, A., Golding, C., Owers, M., Pik, P., Plunkett, C., Sattel, D. & Thorn, B. 2000. An example of 3D conductivity mapping using the TEMPEST airborne electromagnetic system: Exploration Geophysics 31, 162-172.

Lane, R., Brodie, R. & Fitzpatrick, A. 2004. Constrained inversion of AEM data from St George, Queensland, Australia. CRCLEME Open File Report 163.

Lawrie, K.C., Munday, T.J., Dent, D.L., Gibson, D.L., Brodie, R.C., Wilford, J., Reilly, N.S., Chan, R.A. & Baker, P. 2000. A 'Geological Systems' approach to understanding the processes involved in land and water salinisation in areas of complex regolith - the Gilmore Project, central-west NSW. AGSO Research Newsletter 32, 13-32.

Lawrie, K.C., Gray, M. Fitzpatrick, A., Wilkes, P., Lane, R., Pain C. & Lambert, I. 2003a. Assessing cost-effective salinity mapping strategies using a landscape-based approach for methodology and technology selection. Submission to National Review of Salinity Mapping Methods and Technologies in the Australian Context. CRC LEME Open File Report.

Lawrie, K.C., Gray, M., Fitzpatrick, A., Wilkes P. & Lane, R. 2003b. Reducing the acquisition costs of airborne electromagnetics surveys for salinity and groundwater mapping. Preview, October 2003.

Lawrie, K.C. 2006a. Improving the outcomes of salinity management in Australia's regolith landscapes: lessons learned from 5 years of research in CRC LEME, and new opportunities identified. CRC LEME Regolith Symposium, Handorf. Ext. Abs. In: Fitzpatrick, R.W. & Shand, P. (eds) Regolith 2006- Consolidation and Dispersion of Ideas. CRC LEME, Perth, Western Australia, 206-208.

Lawrie, K.C. 2006b. Land use questions and models of AEM targets. Report by technical working group chair on proposed River Murray Corridor (South Australian border to Gunbower) Victorian AEM mapping project. CRC LEME Restricted Report 265r, 27 pp.

Lawrie, K.C. 2008a. Recent advances in the application of hydrogeophysics and regolith geoscience for groundwater and salinity mapping and management. AESC 2008. (Abstract Keynote Address).

Lawrie, K. 2008b. To what extent can recent advances in salinity mapping and assessment create new salinity management and policy opportunities? 2nd International Salinity Forum (Plenary Address) Extended Abstract.

Lawrie, K.C., Reid, M., Tan, K.P., Clarke, J., Pain, C., Halas, L. & Apps, H. 2006. Land use questions and AEM targets for the BRS River Murray Corridor Project. CRC LEME Restricted Report 265R.

Lawrie, K.C., Clarke, J.D.A., Cullen, K., Brodie, R.S., Munday, T., Hatch, M., Apps, H.E, Fitzpatrick, A., Cahill, K., Lane, R., Richardson, M., Ransley, T. & English, P. 2008. Broken Hill Managed Aquifer Recharge Project, Phase 1: Progress report against the project plan and project scope. Geoscience Australia Professional Opinion 2008/06.

Lawrie, K.C., Munday, T., Clarke, J.D.A., Fitzpatrick, A., Cullen, K., Apps, H.E., Brodie R.S., Ransley, T., Cahill, K., Lane, R., Richardson, M., English, P. & Hatch, M. 2009a. Broken Hill Managed Aquifer Recharge Project, Phase 1: Final Report. Geoscience Australia Professional Opinion 2009/03.

Lawrie, K.C., Brodie, R.C., Gibson, D., Kuske, T.J., Halas, L., Tan, K.P., Cullen, K., Brodie R.S. Hannah, A. & Richardson, M. 2009b. Broken Hill Managed Aquifer Recharge Project, Phase 2: Report on AEM system selection. Geoscience Australia Professional Opinion 2009 (Unpublished).

Lawrie, K.C., Brodie, R.S., Gibson, D.L., Ley-Cooper, Y., Davis, A., Magee, J.W., Cullen, K., Halas, L. & Apps, H. 2009c. Broken Hill Managed Aquifer Recharge Project, Phase 2. Conceptual managed aquifer recharge and groundwater resource targets identified from preliminary analysis of airborne electromagnetic data. Geoscience Australia Professional Opinion 2009.

Lawrie, K.C., Tan, K.P., Halas, L., Cullen, K., Pain, C.F., Brodie, R.C., Apps, H., Wong, V., Reid, M., Clarke, J.C. & Gibson, D. 2009d. River Murray Corridor (RMC) Salinity Mapping and Interpretation Project: Report on the Barr Creek to Gunbower Island Region. Geoscience Australia Professional Opinion 2009/13, pp 186.

Lawrie, K.C., Tan, K.P., Clarke, J.C., Munday, T.J., Fitzpatrick, A., Brodie, R.S., Pain, C.F., Apps, H., Cullen, K., Halas, L., Kuske, T.J. & Cahill, K. & Davis, A. 2009e. Utilising time domain airborne electromagnetics (AEM) to map aquifer systems and salinity hazard in the Ord Valley, Western Australia. Geoscience Australia Professional Opinion 2009, 400p.

Lawrie, K.C., Tan, K.P., Clarke, J.C., Munday, T.J., Fitzpatrick, A., Brodie, R.S., Apps, H., Halas, L., Cullen, K., Pain, C.F., Kuske, T.J., Cahill, K. & Davis, A. 2010a. Using the SkyTEM time domain airborne electromagnetics (AEM) system to map aquifer systems and salinity hazard in the Ord Valley, Western Australia. Geoscience Australia Professional Opinion 2010/01.

Lawrie, K.C., Brodie R.S., Dillon, P., Gibson, D., Clarke, J.D.A., Tan, K.P., Page, D., Magee, J.W., Halas, L., Vanderzalm, J., Apps, H.E., Davis, A., Ley-Cooper, A.Y., Smith, M.S., Miotlinski, K., Somerville, P., Gow, L., Boston, K., Smith, M., Barry, K., & Levett, K., 2010c. Broken Hill Managed Aquifer Recharge Project Phase 3a: Assessment of managed aquifer recharge viability at Menindee Lakes. Interim Report. Geoscience Australia Professional Opinion 2010/08. pp 468.

Lawrie, K.C., Brodie R.S., Dillon, P., Tan, K.P., Halas, L., Christensen, N.B., Ley-Cooper, A.Y., Davis, A., Somerville, P., Smith, M.S., Apps, H.E., Magee, J.W., Gibson, D., Clarke, J.D.A., Page, D., Vanderzalm, J., Miotlinski, K., Barry, K., & Levett, K., & Gow, L. 2011. Securing Broken Hill's water supply: Assessment of groundwater extraction and conjunctive water supply options at Menindee Lakes. Geoscience Australia Professional Opinion, 2011/02, 55 pp.

Lawrie, K.C., Brodie R.S., Tan, K.P., Gibson, D., Magee, J.W., Clarke, J.D.A., Halas, L., Gow, L, Somerville, P., Apps, H.E., Christensen, N.B., Brodie, R.C., Abraham, J., Smith, M, Page, D., Dillon, P., Vanderzalm, J., Miotlinski, K., Hostetler, S., Davis, A., Ley-Cooper, A.Y., Schoning, G., Barry, K. & Levett, K. 2012a. BHMAR Project: Data acquisition, processing, analysis and interpretation methods. Geoscience Australia Record 2012/11. Geocat 73819.

Lawrie, K.C., Brodie R.S., Tan, K.P., Gibson, D., Magee, J.W., Clarke, J.D.A., Halas, L., Gow, L, Somerville, P., Apps, H.E., Smith, M, Christensen, N.B., Abraham, J., Hostetler, S. and Brodie, R.C. 2012b. BHMAR Project: Geological and hydrogeological framework and conceptual model. Geoscience Australia Record 2012/12. Geocat 73820.

Lawrie, K.C., Brodie R.S., Dillon, P., Tan, K.P., Gibson, D., Magee, J.W., Clarke, J.D.A., Somerville, P., Gow, L., Halas, L., Apps, H.E., Page, D., Vanderzalm, J., Abraham, J., Hostetler, S., Christensen, N.B., Miotlinski, K., Brodie, R.C., Smith, M., Schoning, G., Barry, K. & Levett, K. 2012c. BHMAR Project: Assessment of conjunctive water supply options involving managed aquifer recharge options at Menindee Lakes. Geoscience Australia Record 2012/13. Geocat 73821.

Lawrie, K.C., Brodie R.S., Tan, K.P., Somerville, P., Gibson, D., Magee, J.W., Clarke, J.D.A., Abraham, J., Gow, L., Halas, L., Apps, H.E., Hostetler, S., Christensen, N.B., Smith, M., Brodie, R.C. & Schoning, G. 2012d. BHMAR Project: Assessment of potential groundwater resources and underground storage options in the Darling Floodplain. Geoscience Australia Record 2012/14. Geocat 73822.

Lawrie, K.C., Halas, L. & Apps, H.E. 2012f. BHMAR Project Appendix 14: LIDAR acquisition and processing contractor reports. Geoscience Australia Record 2012/16. Geocat 73824.

Lawrie, K.C., Brodie R.S., Dillon, P., Tan, K.P., Gibson, D., Magee, J.W., Clarke, J.D.A., Somerville, P., Gow, L., Halas, L., Apps, H.E., Page, D., Vanderzalm, J., Abraham, J., Hostetler, S., Christensen, N.B., Miotlinski, K., Brodie, R.C., Smith, M., Schoning, G., Barry, K. & Levett, K. 2012e. BHMAR Project: Securing Broken Hill's water supply: Assessment of conjunctive water supply options involving managed aquifer recharge and/or groundwater extraction at Menindee Lakes- Summary Report. Geoscience Australia Record 2012/16. Geocat 73823.

Leaney, F.W., Crosbie, R.S., O'Grady, A., Jolly, I.D., Gow, L., Davies, P., Wilford, J. & Kilgour, P. 2011. Recharge and discharge estimation in data poor areas: Scientific reference guide. CSIRO: Water for a Healthy Country National Research Flagship.

Leaney, W.S. 1990. Parametric wavefield decomposition and applications. 60th Meeting, Society of Exploration Geophysicsts, San Francisco, Expanded Abstracts, 1097-1100.

Lewis, S.J., Roberts, J., Brodie, R.S., Gow, L., Kilgour, P., Ransley, T., Coram, J.E. & Sundaram, B. 2008. Assessment of groundwater resources in the Broken Hill region. Geoscience Australia Professional Opinion 2008/05.

Ley-Cooper, Y. & Macnae, J. 2007. Amplitude and phase correction of helicopter EM data. Geophysics 72, 3, F119–F126.

Li, X. & Götze, H-J. 1999. Comparison of some gridding methods. The Leading Edge 18, 8, 898-900.

Li, Y.-H. & Gregory, S. 1974. Diffusion of ions in sea water and in deep-sea sediments. Geochimica et Cosmochimica Acta 38, 703–714.

Lillesaeter, O. 1982. Spectral reflectance of partly transmitting leaves: Laboratory measurements and mathematical modelling. Remote Sensing of Environment 12, 247-254.

Liu, G. & Becker, A. 1990. Two dimensional mapping of sea-ice keels with airborne electromagnetics, Geophysics 55, 2, 239-248.

Loke, M.H., Chambers, J.E. & Ogilvy, R.D. 2006. Inversion of 2-D spectral induced polarization imaging data. Geophysical Prospecting 54, 287-301.

Lu, Z. & Danskin, W.R. 2001. InSAR analysis of natural recharge to define structure of a ground-water basin, San Bernardino, California. Geophysical Research Letters 28, 2661-2664.

Lubczynski, M.W. & Gurwin, J. 2005. Integration of various data sources for transient groundwater modelling with spatio-temporally variable fluxes: Sardon study case, Spain. Journal of Hydrology 306, 71-96.

LWBC. 2003. Minimum construction requirements for water bores in Australia. Edition 2. Revised September, 2003. Land and Water Biodiversity Committee.

Lymburner, L., Mueller, N. & Islam, A. 2008. Assessing the accuracy of flood mapping techniques using coincident MODIS and Landsat TM scenes. In: Proceedings of the 14th ARSP Conference, Darwin, Northern Territory.

Macnae, J.C. 2007. Developments in broadband airborne electromagnetics in the past decade. In: Milkereit, B. (ed.) Proceedings of Exploration 07: Fifth Decennial International Conference on Mineral Exploration. 9-12 September, Toronto, Canada, 387-398 pp. Prospectors and Developers Association of Canada, Toronto, Canada.

Macnae, J., King, A., Stolz, E., Osmakoff, A & Blaha, A. 1998. Fast AEM data processing and inversion, Exploration Geophysics 29, 163-169.

Magee, J.W., Apps, H.E. & Knox, K. 2012. BHMAR Project Appendix 15: Cultural heritage and environmental clearance surveys. Geoscience Australia Record 2012/16. Geocat 73824.

Malinverno, A. 2002. Parsimonious Bayesian Markov chain Monte Carlo inversion in a nonlinear geophysical problem. Geophysical Journal International 151, 675-688.

Martinez, K. & Pitcher, D. 2008. Water resources applications with the VTEM system. AEM 2008. 5th International Conference on Airborne Electromagnetics, Finland, 28-30 May 2008. Extended Abstract.
Mauger, A.J. & Hore, S. 2009. Integrating mineralogical interpretation of HyLogger data with HyMap mineral mapping, Mount Painter, South Australia. Innovations in Remote Sensing and Photogrammetry Lecture Notes in Geoinformation and Cartography 271-280
Mauger, A.J. & Huntington, J.F. 2005. Hylogging applications in exploration. Extended Abstracts Mineral Exploration Through Cover Conference, Mawson Laboratories, University of Adelaide, Adelaide, South Australia. CRC LEME 2005.
Maunsell. 2007. Darling River Water Savings Project, Part A Report. Report to NSW Department of Natural Resources and National Water Commission, 62 pp.
McCormac, F.G., Hogg, A.G., Blackwell, P.G., Buck, C.E., Higham, T.F.G. & Reimer, P.J. 2004. SHCal04 Southern Hemisphere Calibration 0 - 11.0 cal kyr BP. Radiocarbon 46, 1087-1092.
McElwee, C.D. & Zenner, M. 1998. A nonlinear model for analysis of slug-test data. Water Resources Research 34, 1, 55-66
McGaughey, R. 2007. FUSION/LDV: Software for LiDAR data analysis and visualization. USDA Forest Service, Pacific Northwest Research Station.
McLaren, S. & Wallace, M.W. 2010. Plio-Pleistocene climate change and the onset of aridity in southeastern Australia. Global and Planetary Climate Change 71, 55-72.
McLaren, S., Wallace, M.W., Pillans, B.J., Gallagher, S.J., Miranda, J.A. & Warne, M.T. 2009. Revised stratigraphy of the Blanchetown Clay, Murray Basin: age constraints on the evolution of paleo Lake Bungunnia. Australian Journal of Earth Sciences 56, 259 – 270.
McLaren, S. Wallace, M.W. & Reynolds, T. 2012 The Late Pleistocene evolution of palaeo megalake Bungunnia, southeastern Australia: A sedimentary record of fluctuating lake dynamics, climate change and the formation of the modern Murray River. Palaeogeography, Palaeoclimatology, Palaeoecology 317–318, 114–127.
MDBA. 2010. Guide to the proposed plan: overview. Murray-Darling Basin Authority, Canberra.
MDBA, 2011. Proposed Basin Plan. Murray-Darling Basin Authority, Canberra.
MDBA, 2012. Basin Plan – Water Act 2007. Commonwealth of Australia, Murray-Darling Basin Authority, Canberra.
MDBC, 2003. Preliminary investigations into observed River Red Gum decline along the River Murray below Euston, Technical Report 03/03. Murray-Darling Basin Commission.
Meiboom, S. & Gill, D. 1958. Modified spin-echo method for measuring nuclear relaxation times. Review of Scientific Instruments 29, 688-691.
Meinzer, O.E. 1923. The occurrence of groundwater in the United States with a discussion of principles. US Geological Survey Water Supply Paper 489, 321 pp.
Menke, W. 1989. Geophysical data analysis: Discrete inverse theory. Academic Press Inc.
Miall, A.D. 1996. The geology of fluvial deposits. Springer, Berlin.
Minsley, B.J. 2011. A trans-dimensional Bayesian Markov chain Monte Carlo algorithm for model assessment using frequency-domain electromagnetic data. Geophysical Journal International 187, 252-272.
Miotlinski, K., Page, D., Vanderzalm, J. & Dillon, P. 2010. Groundwater modelling of Broken Hill Managed Aquifer Recharge to estimate ASR recovery efficiency and effects on water levels. Client report. CSIRO Land and Water.
Moench, A.F. 1985. Transient flow to a large-diameter well in an aquifer with storative semiconfining layers. Water Resources Research 21, 1121-1131.
Moench, A.F. 1997. Flow to a well of finite diameter in a homogeneous, anisotropic water-table aquifer. Water Resources Research 33, 1397-1407.
Moore, D.M. & Reynolds, R.C. 1997. X-ray diffraction and the identification and analysis of clay minerals. 2nd ed, Oxford University Press.
Moran, J. & Kunz, K. 1962. Basic theory of induction logging and application to study of two-coil sondes. Geophysics 27, 6, 829–858.
Mullen, I. & Kellett, J. 2004. Groundwater salinity interpretation using airborne electromagnetics in the Lower Balonne area, Southern Queensland, Australia. Bureau of Rural Sciences, Canberra.
Mullen, I.C., Wilkinson, K.E., Cresswell, R.G. & Kellett, J. 2007. Three-dimensional mapping of salt store in the Murray-Darling Basin, Australia 2. Calculating landscape salt loads from airborne electromagnetic and laboratory data. International Journal of Applied Earth Observation and Geoinformation 9, 103-115.
Munday, T.J. 2008. Regolith geophysics. In: Scott, K.M & Pain, C.F. (eds) Regolith Geology. 219-250. CSIRO.

Munday, T., Walker, G., Cresswell, R., Wilford, J., Barnett, S. & Cook, P. 2003a. South Australian Salt Mapping and Management Support Project – An example of the considered application of airborne geophysics in natural resource management. 16th ASEG Conference, Adelaide.

Munday, T., Green, A., Brodie, R., Lane, R., Sattel, D., Barnett, S., Cook, P. & Walker, G. 2003b. Developing recharge reduction strategies in the Riverland of South Australia using airborne electromagnetic data – a case study in tailoring airborne geophysics given a particular target and a desired set of outcomes. 16th ASEG Conference, Adelaide.

Munday, T.J., Hill, A.J., Wilson, T., Hopkins, B., Telfer, A.L., White, G.J. & Green, A.A. 2004. Combining geology and geophysics to develop a hydrologic framework for salt interception in the Loxton Sands aquifer, central Murray Basin, Australia. CRC LEME Open File Report 180/CSIRO Exploration and Mining Report P2004/86, 20pp.

Munday, T., Fitzpatrick, A., Noble, R., Berens, V., Hatch, M. & Cahill, K. 2006. The combined use of air, ground and 'in river' electromagnetics in defining spatial processes of salinisation across ecologically important floodplain areas - Lower River Murray, SA. Regolith 2006: Consolidation and Dispersion of Ideas, Proceedings of the CRC LEME Regolith Symposium, November 2006, CRC LEME, Perth 249-255.

Munday, T., Fitzpatrick, A., Cahill, K., Hatch, M., Berens, V. & Overton, I. 2007. Spatio-temporal monitoring of floodplain environments using electromagnetic methods: A scaled approach to understanding surface water - groundwater interactions on the Chowilla Floodplain, SA. Proceedings Volume, Symposium on the Application of Geophysics to Engineering and Environmental Problems (20th SAGEEP). 1-5 April 2007, Denver, Colorado, USA.

Munsell Color. 2000. Munsell soil colour charts. Gretag Macbeth, New Windsor, New York.

Murray, A.S. & Wintle, A.G. 2000. Luminescence dating of quartz using an improved single-aliquot regenerative dose protocol. Radiation Measurements 32, 57-73.

Nash J.M., Collins, B.N., Loughlin, S.E., Soolbrig, M., Harvey, R., Krishnan-Sarin, S., Unger, J., Miner, C., Rukstalis, M., Shenassa, E., Dube, C. & Spirito, A. 2003. Training the trans-disciplinary scientist: a general framework applied to tobacco use behaviour. Nicotine and Tobacco Research 5, 1S, S41–S53.

Neuzil, C.E. 1986. Groundwater flow in low permeability environments. Water Resources Research 22, 1163-1195

Neuzil, C.E. 1994. How permeable are clays and shales? Water Resources Research 30, 145-150.

Newell, W.L. & Clark, I. 2008. Geomorphic map of Worcester County, Maryland, interpreted from a LiDAR-based, digital elevation model. In: Open-File Report - U.S. Geological Survey, 34. U. S. Geological Survey, Reston, VA, USA.

Newman, G.A., Hohmann, G.W. & Anderson, W.L. 1986. Transient electromagnetic response of a three-dimensional body in a layered-earth. Geophysics 51, 1608-1627.

NHMRC-NRMMC. 2011. Australian Drinking Water Guidelines Paper 6 National Water Quality Management Strategy. National Health and Medical Research Council, National Resource Management Ministerial Council, Commonwealth of Australia, Canberra.

Nielsen, M.T., Hagensen, T., Chalikakis, K. & Legchenko, A. 2011. Comparison of transmissivities from MRS and pumping tests in Denmark. Near Surface Geophysics 9, 2, 211-223.

Ninomiya, Y., Fu, B. & Cudahy, T.J. 2005. Detecting lithology with Advanced Spaceborne Thermal Emission and Reflection Radiometer (ASTER) multispectral thermal infrared "radiance-at-sensor" data. Remote Sensing of Environment 99, 127-39.

Norrish, K. & Chappell, B.W. 1977. X-ray fluorescence spectrometry. In: Zussman, J. (ed.) Physical methods in determining mineralogy. pp. 201-72. Academic Press, London.

Norrish, K. & Hutton, J.T. 1969. An accurate X-ray spectrographic method for the analysis of a wide range of geological samples. Geochimica et Cosmochimica Acta 33, 431-53.

NRMMC-EPHC-NHMRC. 2008. Australian Guidelines for Water Recycling: Managing Health and Environmental Risks. Phase 2A: Augmentation of drinking water supplies. Environment Protection and Heritage Council, National Health and Medical Research Council, and Natural Resource Management Ministerial Council. www.ephc.gov.au/taxonomy/term/39

NRMMC-EPHC-NHMRC. 2009. Australian Guidelines for Water Recycling: Managing Health and Environmental Risks. Phase 2C: Managed aquifer recharge. Environment Protection and Heritage Council, National Health and Medical Research Council, and Natural Resource Management Ministerial Council. www.ephc.gov.au/taxonomy/term/39

Oldenburg, D.W. & Li, Y. 1999, Estimating depth of investigation in DC resistivity and IP surveys. Geophysics 64, 403-416.

Omuto, C.T. 2011. A new approach for using time-series remote-sensing images to detect changes in vegetation cover and composition in drylands: a case study of eastern Kenya. International Journal of Remote Sensing 32, 6025-45.

Page, D., Dillon, P., Vanderzalm, J., Bekele, E., Barry, K., Miotlinski, K. & Levett, K. 2010. Managed aquifer recharge case study risk assessments. CSIRO Water for a Healthy Country Flagship Report, Dec 2010, 144 pp. http://www.clw.csiro.au/publications/waterforahealthycountry/2010/wfhc-MAR-case-study-risk-assessments.pdf

Paijmans, K. 1970. Land evaluation by air photo interpretation and field sampling in Australian New Guinea. Photogrammetria 26, 77-100.

Paillet, F.L. 2000. A field technique for estimating aquifer parameters using flow log data. Groundwater 38, 510-521.

Pain, C.P. 2008. Field guide for describing regolith and landforms. CRC LEME, Bentley.

Pain, C.F., Clarke, J.D. & Wong, V.N. 2011. Applied geomorphic mapping for land management in the River Murray corridor, SE Australia. In: Smith, M.J., Paron, P. & Griffiths, J.S. (eds) Geomorphological Mapping: Methods and Applications.

Paine, J.G. 2003. Determining salinization extent, identifying salinity sources, and estimating chloride mass using surface, borehole, and airborne electromagnetic induction methods. Water Resources Research 39, 1059.

Paine, J.G., Collins, E.W., Nance, H.S. & Niemann, K.L. 2009. Combining airborne electromagnetic induction and hydrochemistry to quantify salinity contributions to a large basin stream, Colorado River, Texas, USA. Near Surface Geophysics 7, 4, 271-284.

Palamara, D., Rodriguez, V., Kellett, J. & Macaulay, S. 2010. Salt mapping in the Lower Macquarie area, Australia, using airborne electromagnetic data. Environmental Earth Sciences 61, 3, 613-623.

Parkhurst, D.L. & Appelo, C.A.J. 1999. User's Guide to PHREEQC (version 2) - A Computer Program for speciation, reaction path, advective transport, and inverse geochemical calculations. Report 99-4259, U.S. Geological Survey, Water Resources Investigations Report 99-4259, 312 pp.

Parry, J.T. & Beswick, J.A. 1973. The application of two morphometric terrain-classification systems using air-photo interpretation methods. Photogrammetria 29, 153-86.

Pedersen, J. & Fiandaca, G. 2011. ERT/IP data processing and inversion. Aarhus University Report to Geoscience Australia - January, 2011, 56 pp.

Pelton, W.H., Ward, S.H., Hallof, P.G., Sill, W.R. & Nelson, P.H. 1978. Mineral discrimination and removal of inductive coupling with multifrequency induced-polarization. Geophysics 43, 588-609.

Peterson, B.E. & Nelson, K. 2009. Vegetation change detection and quantification-linking Landsat imagery and LiDAR data. In: Civco, D.L. (ed.) International Workshop on the Analysis of Multi-Temporal Remote Sensing Images, 5th Conference: Paper.

Poppenga, S.K., Worstell, B.B., Stoker, J.M. & Greenlee, S.K. 2010. Using selective drainage methods to extract continuous surface flow from 1-meter LiDAR-derived digital elevation data. USGS Scientific Investigations Report 2010-5059, 12 pp.

Prescott, J.R. & Hutton, J.T. 1994. Cosmic ray contribution to dose rates for luminescence and ESR dating: large depths and long-term variations. Radiation Measurements 23, 497-500.

Puls, R.W. & Barcelona, M.J. 1996. Low flow (minimal drawdown) ground water sampling procedures. USEPA/ORD EPA/540/S-95/504. Washington, DC. US Environmental Protection Agency.

Quinonez-Pinon, R., Mendoza-Duran, A. & Valeo, C. 2007. Design of an environmental monitoring program using NDVI and cumulative effects assessment. International Journal of Remote Sensing 28, 1643-1664.

Rasmussen, W.C. & Andreasen, G.E. 1959. Hydrologic budget of the Beaverdam Creek Basin, Maryland. US Geological Survey Water Supply Paper 1472, 106 pp.

Rayment, G.E. & Lyons, D.J. 2010. Soil Chemical Methods - Australasia. CSIRO Publishing

Reid, J., Eade, R. & Kemp, T. 2009. SkyTEM final processed data: Broken Hill Managed Aquifer Recharge Project Part B, Geoforce Report to Geoscience Australia, 158 pp.

Reid, J., Fitzpatrick, A. & Godber, K. 2010. An overview of the SkyTEM airborne EM system with Australian examples. Preview, April 2010, 26-37.

Reid, M., Gill, B., Cheng, X., Fawcett, J., Hekmeijer, P., Clark, P. & Hood, A. 2008. Overview of groundwater trends and dryland salinity in Victoria. 2nd International Salinity Forum. http://www.internationalsalinityforum.org/Final%20Papers/reid_E1.pdf

Remenda, V.H., van der Kamp, G. & Cherry, J.A. 1996. Use of vertical profiles of $\delta^{18}O$ to constrain estimates of hydraulic conductivity in a thick, unfractured aquitard. Water Resources Research 32(10), 2979.

Richardson, S., Evans, R., Hawarth, D. & Prider, J. 2007. Tri-State hydrogeological benchmark assessment. Resource & Environmental Management Pty. Ltd. (Unpublished Report).
Ritman, K.T. 1995. Structural vegetation data: a specifications manual for the Murray Darling Basin Project M305.
Roach, I.C. (ed.) 2012. The Frome airborne electromagnetic survey, South Australia: implications for energy, minerals, and regional geology. Geoscience Australia Record 2012/40.
Rodrigues, E., Morris, C.S. & Belz, J.E. 2006. A global assessment of the SRTM performance. Photogrammetric Engineering and Remote Sensing 72, 249-60.
Rosenfield, P.L. 1992. The potential of trans-disciplinary research for sustaining and extending linkages between the health and social sciences. Social Science and Medicine 35, 1343–57.
Rowan, L.C. & Mars, J.C. 2003. Lithologic mapping in the Mountain Pass, California area using Advanced Spaceborne Thermal Emission and Reflection Radiometer (ASTER) data. Remote Sensing of Environment 84, 350-66.
Salama, R.B., Tapley, I., Ishii, T. & Hawkes, G. 1994. Identification of areas of recharge and discharge using Landsat-TM satellite imagery and aerial photography mapping techniques. Journal of Hydrology 162, 119-41.
Sattel, D. 1998. Conductivity information in three dimensions: Exploration Geophysics 29, 157-162.
Sattel, D. 2005. Inverting airborne electromagnetic (AEM) data with Zohyd's method. Geophysics 70, G77-7.1.
Scanlon, T.M., Albertson, J.D., Caylor, K.K. & Williams, C.A. 2002. Determining land surface fractional cover from NDVI and rainfall site series for a savanna ecosystem. Remote Sensing of Environment 82, 376-388.
Scarth, P., Roder, A. & Schmidt, M. 2011. Tracking grazing pressure and climate interaction - the role of Landsat fractional cover in time series analysis. In: 15th Australasian Remote Sensing and Photogrammetry Conference, Alice Springs.
Schmidt, D.A. & Burgmann, R. 2003. Time-dependent land uplift and subsidence in the Santa Clara valley, California, from a large interferometric synthetic aperture radar data set. Journal of Geophysical Research 108, B9, 2416, doi:10.1029/2002JB002267, 2003
Seevers, D.O. 1966. A nuclear magnetic method for determining the permeability of sandstones. Society of Petrophysicists and Well-Log Analysts, Transactions of the 7th Annual Logging Symposium 1966, Conference Paper, 14 pp.
Seijmonsbergen, A.C., Hengl, T. & Anders, N.S. 2011. Semi-automated identification and extraction of geomorphological features using digital elevation data. In: Smith, M.J., Paron, P. & Griffiths, J.S. (eds) Geomorphological Mapping: Methods and Applications, 297.
Sen, P.N., Goode, P.A. & Sibbit, A.M. 1988. Electrical conduction in clay bearing sandstones at low and high salinities. Journal of Applied Physics 63, 4832-4840.
Serban, D.Z. & Jacobsen, B.H. 2001. The use of broadband prior covariance for inverse palaeoclimate estimation. Geophysical Journal International 147, 29-40.
Shaban, A., Khawlie, M. & Abdallah, C. 2006. Use of remote sensing and GIS to determine recharge potential zones: the case of Occidental Lebanon. Hydrogeology Journal 14, 433-43.
Siart, C., Bubenzer, O. & Eitel, B. 2009. Combining digital elevation data (SRTM/ASTER), high resolution satellite imagery (Quickbird) and GIS for geomorphological mapping: A multi-component case study on Mediterranean karst in Central Crete. Geomorphogy 112, 106-21.
Sibson, R. 1981. A brief description of natural neighbour interpolation (Chapter 2). In: Barnett, V. (ed.) Interpreting Multivariate Data. Chichester: John Wiley. pp. 21-36.
Siemon, B. & Steuer, A. 2011. Airborne geophysical investigation of groundwater resources in Northern Sumatra after the tsunami of 2004. The Tsunami Threat - Research and Technology. N.-A. Mörner, InTech.
Siemon, B., Christiansen, A.V. & Auken, E. 2009. A review of helicopter-borne electromagnetic methods for groundwater exploration. Near-Surface Geophysics 7, 629-646.
SKM. 2009. Darling River Water Savings Project - Part B, Stage 1 – Preliminary environmental issues of Part A schemes. Technical Report for the NSW Department of Water and Energy.
SKM. 2010. Darling River Water Saving Project – Part B draft final report (unpublished). Report for NSW Office of Water and Department of the Environment, Heritage and the Arts.
Slater, L.D. & Glaser, D.R. 2003. Controls on induced polarization in sandy unconsolidated sediments and application to aquifer characterization. Geophysics 68, 1547-1558.
Slater, L.D. & Lesmes, D. 2002. IP interpretation in environmental investigations. Geophysics 67, 77-88.

Smith, B.D., Smith, D.V., Hill, P.L. & Labson, V.F. 2003. Helicopter electromagnetic and magnetic survey data and maps, Seco Creek Area, Medina and Uvalade Counties, Texas. US Geological Survey Open-File Report. 53 pp.

Smith, B.D., Cain, M.J., Clark, A.K., Moore, D.W., Faith, J.R. & Hill, P.L. 2005. Helicopter electromagnetic and magnetic survey data and maps, northern Bexar County, Texas. US Geological Survey Open-File Report. 122 pp.

Smith, B.D., Smith, D.V. & Blome, C.D. 2008. Helicopter electromagnetic surveys of carbonate karstic aquifers with emphasis on recent applications by the U.S. Geological Survey. In: Proceedings of 5th International Conference on Airborne Electromagnetics, Haikko Manor, Finland, 4 pp.

Smith, M.J., Paron, P. & Griffiths, J.S. 2011. Geomorphological mapping: Methods and applications. Elsevier Science Limited.

Somerville, P., Brodie, R.S., Gow, L., Halas, L. & Apps, H.E. 2012. BHMAR Project Appendix 6: Hydrological, climate, hydrochemical and hydrodynamic data. Geoscience Australia Record 2012/16. Geocat 73824.

Song, Y.Q. 2010. Recent progress of nuclear magnetic resonance applications in sandstones and carbonate rocks. Vadose Zone Journal 9, 828-834.

Sonneveld, C., Van Den Ende, J. & De Bes, S.S. 1990. Estimating the chemical compositions of soil solutions obtained by saturation extracts or specific 1:2 by volume extracts. Plant and Soil 122, 169-175.

Sørensen, K.I. & Auken, E. 2004. SkyTEM - a new high-resolution helicopter transient electromagnetic system. Exploration Geophysics 35, 194-202.

Speight, J.G. 2008. Landform. In: Australian soil and land survey field handbook. Third edition (NCST, Australian Collaborative Land Evaluation Program, Canberra.

Spies, B.R. 1989. Depth of investigation in electromagnetic sounding methods. Geophysics 54, 872–888.

Spies, B. & Woodgate P. 2005. Salinity mapping methods in the Australian context. Land and Water Australia, Department of the Environment and Heritage and Department of Agriculture Fisheries and Forestry, June 2005. 236 pp. http://www.nrm.gov.au/publications/salinity-mapping

Spulak, R., Schoning, G., Halas, V., Long, R., Rousseau, J. & Clarke, J.D.A. 2012. BHMAR Project Appendix 2: Core photographs. Geoscience Australia Record 2012/17. Geocat 73824.

Stark, J.M. 2006. Use of LiDAR in geomorphic mapping and interpretation of coastal, fluvial, glacial and anthropogenic landforms. 64 pp.

Stevenson, J., Gillespie, R., Hope, G., Jacobsen, G., Fallon, S. & Levchenko, V. 2010. The archaic and puzzling record of Lake Xere Wapo, New Caledonia. In: Haberle, S., Stevenson, J. & Prebble, M. (eds) Altered ecologies: fire, climate and human influence on terrestrial landscapes. Terra Australis 32, 381-393.

Stokols, D., Fuqua,, J., Gress, J., Harvey, R., Phillips, K., Baezconde-Garbanati, L., Unger, J., Palmer, P., Clark, M.A., Colby, S.M., Morgan, G. & Trochim, W. 2003. Evaluating trans-disciplinary science. Nicotine and Tobacco Research 5, 1S, S21–S39.

Stokols, D., Hall, K.L., Taylor, B.K., Moser, R.P. 2008. The science of team science: Overview of the field and introduction to the Supplement. American Journal of Preventive Medicine 35, 2S, S77–S89.

Straley, C., Morriss, C.E., Kenyon, W.E. & Howard, J.J. 1995. NMR in partially saturated rocks: laboratory insights on free fluid index and comparison with borehole logs. Log Analyst 36, 40-65.

Supper, R., Ahl, A., Motschka, K., Ottowitz, D., Bauer, P., Alonso, G.M., Jochum, B. & Gondwe, B. 2009. Spatial mapping of submerged cave systems by means of airborne electromagnetics: Results from the 2008 mapping campaign in the area around Tulum, Yucatan. Symposium on the Application of Geophysics to Engineering and Environmental Problems 22, 499-510.

Systat Software 2008. SigmaPlot for Windows version 11.0.

Szilagyi, J., Zlotnik, V.A., Gates, J.B. & Jozsa, J. 2011. Mean mapping annual groundwater recharge in the Nebraska Sand Hills, USA. Hydrogeology Journal 19, 1503-13.

Tan, K.P., Apps, H., Halas, L., Gibson, D. & Lawrie, K. 2005. Utilizing airborne electromagnetic data to model the subsurface salt load in a catchment, Bland Basin, NSW. In: Zerger, A. & Argent, R.M. (eds) MODSIM 2005 International Congress on Modelling and Simulation. Modelling and Simulation Society of Australia and New Zealand, December 2005, 1478-1484 pp. ISBN: 0-9758400-2-9. http://www.mssanz.org.au/modsim05/papers/ascough_1.pdf

Tan, K.P., Lawrie, K.C., Halas, L., Pain, C.F., Clarke, J.D., Gibson, D., Apps, H., Cullen, K., Brodie, R.C. & Wong, V. 2009. Methodology for the customised products developed as part of the River Murray Corridor Victorian AEM mapping project, Geoscience Australia, Professional Opinion 2009/12, 75 pp.

Tan, K.P., Clarke, J.D.A., Halas, L., Lawrie, K.C., Apps, H.E., Brodie, R.C., Costelloe, M., Sumner, J., Fell-Smith, S., Christensen, N.B., Schoning, G.L., Halas, V. & Lewis, S.J. 2012. Northern Territory coastal

plain: Mapping seawater intrusion in coastal plain aquifers using airborne electromagnetic data. Geoscience Australia Record, 2012/41, Canberra. pp 218.
Tappert, M., Rivard, B., Giles, D., Tappert, R. & Mauger, A. 2011. Automated drill core logging using visible and near-infrared reflectance spectroscopy: a case study from the Olympic Dam IOCG deposit, South Australia. Economic Geology 106, 289-296.
Tarantola, A. 1987. Inverse problem theory, methods for data fitting and model parameter estimation. Elsevier, Amsterdam.
Tarantola, A. & Valette, B. 1982. Generalized nonlinear inverse problems solved using the least squares criterion. Reviews of Geophysics and Space Physics 20, 219-232.
Tartakovsky, D.M., Guadagnini, A. & Guadagnini, L. 2000. Effective hydraulic conductivity and transmissivity for heterogeneous aquifers. Mathematical Geology 32, 751-759.
Taylor-Wood, E., McCormick, S., Mueck, S., Richardson, M. & Jukic, M. 2001. Report for the Menindee Lakes Ecologically Sustainable Development Project Steering Committee. Vegetation/habitat mapping of inundated areas of Menindee Lakes. Project no: 3445.
Theiss Services. 2002. Topographic survey of Lake Wetherell: Final report. In: Menindee Lakes ESD Project.
Thompson, A.J.B., Hauff, P.L. & Robitaille, A.J. 1999. Alteration mapping in exploration: application of short-wave infrared (SWIR) spectroscopy. Society of Exploration Geophysics Newsletter 39, 16-27.
Thoms, M.C. & Sheldon, F. 2000. Water resource development and hydrological change in a large dryland river: the Barwon–Darling River, Australia. Journal of Hydrology 228, 10–21.
Thomson, S., Fountain, D. & Watts, T. 2007. Airborne geophysics - evolution and revolution. In: Milkereit, B. (ed.) Proceedings of Exploration 07: Fifth Decennial International Conference on Mineral Exploration, 9-12 September, Toronto, Canada. 19-37. Prospectors and Developers Association of Canada, Toronto, Canada.
Timur, A. 1969. Pulsed nuclear magnetic resonance studies of porosity, movable fluid and permeability of sandstones. Journal of Petroleum Technology 21, 775–786.
Traverse, A. 1988. Palaeopalynology, Unwin Hyman, London
Turney, C.S.M., Bird, M.I., Fifield, L.K., Roberts, R.G., Smith, M.A., Dortch, C.E., Grun, R., Lawson, E., Ayliffe, L.K., Miller, G.H., Dortch, J. & Cresswell, R.G. 2001a. Early human occupation at Devil's Lair, southwestern Australia 50,000 years ago. Quaternary Research 55, 3-13.
Turney, C.S.M., Kershaw, A.P., Moss, P., Bird, M.I., Fifield, L.K., Cresswell, R.G., Santos, G.M., di Tada, M.L., Hausladen, P.A. & Zhou, Y. 2001b. Redating the onset of burning at Lynch's Crater (North Queensland): implications for human settlement in Australia. Journal of Quaternary Science 16, 767-771.
Tweed, S.O., Leblanc, M., Webb, J.A. & Lubczynski, M.W. 2007. Remote sensing and GIS for mapping groundwater recharge and discharge areas in salinity prone catchments, southeastern Australia. Hydrogeology Journal 15, 75-96.
Van der Kamp, G. 2001. Methods for determining the *in situ* hydraulic conductivity of shallow aquitards - an overview. Journal of Hydrology 9, 5-6.
Vanderzalm, J.L., Le Gal La Salle, C. & Dillon, P.J. 2006. Fate of organic matter during aquifer storage and recovery (ASR) of reclaimed water in a carbonate aquifer. Applied Geochemistry 21, 1204-1215.
Vanderzalm, J., Barry, K., Miotlinski, K. & Page, D. 2012. Broken Hill MAR: Geochemical evaluation – revision including monitoring data collected until 31/8/2011. CSIRO: Water for a Healthy Country National Research Flagship.
Vaughan, R.G., Calvin, W.M. & Taranik, J.V. 2003. SEBASS hyperspectral thermal infrared data: surface emissivity measurement and mineral mapping. Remote Sensing of Environment 85, 48-63.
Viezzoli, A., Auken, E., & Munday, T., 2009. Spatially constrained inversion for quasi 3D modelling of airborne electromagnetic data - an application for environmental assessment in the Lower Murray Region of South Australia: Exploration Geophysics 40, 173-183.
Viezzoli, A., Christiansen, A.V., Auken, E. & Sorensen, K. 2008. Quasi-3D modeling of airborne TEM data by spatially constrained inversion. SEG, 2008. Geophysics 73, F105-F113.
Viezzoli, A., Abraham, J., Bedrosian, P., Cannia, J., Minsley, B. & Brown, B. 2011. Fast and effective groundwater mapping from 10 to 300 m depth with accurate processing and inversion of SkyTEM data. In: Environmental Engineering Geophysical Society's Annual Symposium on the Application of Geophysics to Environmental and Engineering Problems April 10-14, Charleston, South Carolina, USA.
Vista Clara. 2011. Javelin manual and documentation, Revision 1.0, June 2011, Mukilteo, Washington, USA: Vista Clara, Inc.

Vista Clara. 2013. Javelin manual and documentation, Revision 1.3: April 2013, Mukilteo, Washington, USA: Vista Clara, Inc.
Vogel, J.C. 1966. Investigations of groundwater flow with radiocarbon. Proceedings of Symposium on Isotope Hydrology, 1966. IAEA Vienna, 355-367.
Vollath, U., Landau, H., Chen, X., Doucet, K. & Pagels, C. 2002. Network RTK versus single base RTK - understanding the error characteristics. In: ION GPS, Portland, Oregon.
Wagenseil, H. & Samimi, C. 2007. Woody vegetation cover in Namibian savannahs: A modelling approach based on remote sensing. Erdkunde 61, 325-334.
Walker, G.R. & Cook, P.G. 1991. The importance of considering diffusion when using carbon-14 to estimate groundwater recharge to an unconfined aquifer. Journal of Hydrology 128, 41-48.
Walker, G., Cresswell, R., Munday, T. & Liddicoat, C. 2004. South Australian Salinity Mapping and Management Support Project: Final Report (Overall Project Summary Report), South Australia. Department of Water, Land and Biodiversity Conservation. Report, DLWBC 2004/39.
Walker, J. & Hopkins, M.S. 1990. Vegetation. In: McDonald, R.C., Isbell, R.F., Speight, J.G., Walker, J. & Hopkins, M. (eds). Australian soil and land survey. Field handbook. 2nd Edition. Melbourne: Inkata Press.
Walsh, D.O., Grunewald, E., Turner, P. & Frid, I. 2010. Javelin: A slimhole and microhole NMR logging tool: FastTimes 15, 67-72.
Walsh, D.O. 2012. NMR principles and application, CSIRO NMR Groundwater Workshop, February 23rd, Perth, WA.
Wang, C., Feng, Y., Higgins, M. & Cowie, B. 2010. Assessment of commercial network RTK user positioning performance over long inter-station distances. Journal of Global Positioning Systems 9, 78-89.
Wang, E., Miles, M., Schultz, T., Cook, P., Maschmedt, D., Munday, T., Leaney, T., Walker, G., Barnett, S. 2005. Targeting dryland areas in the Mallee for controlling groundwater recharge and salt load to the Murray River. Report to Client No.#/2005. CSIRO: Canberra.
Wang, Y. 2004. Seasonal change in the extent of inundation on floodplains detected by JERS-1 Synthetic Aperture Radar data. International Journal of Remote Sensing 25, 2497-508.
Wang, Y., Colby, J.D. & Mulcahy, K.A. 2002. An efficient method for mapping flood extent in a coastal floodplain using Landsat TM and DEM data. International Journal of Remote Sensing, 23, 3681-3696.
Ward, S.H. & Hohmann, G.W. 1987. Electromagnetic theory for geophysical applications. In: Nabighian, M.N. (ed.) Electromagnetic methods in applied geophysics, pp. 131-311. Investigations in Geophysics 3, Society of Exploration Geophysicists.
Wasser, L., Day, R., Chasmer, L. & Taylor, A. 2013. Influence of vegetation structure on LiDAR-derived canopy height and fractional cover in forested riparian buffers during leaf-off and leaf-on conditions. PLoS ONE 8, e54776.
Waxman, M.H. & Smits, L.J.M. 1968. Electrical conductivities in oil-bearing shaly sands. Transactions American Institute Mining Petroleum Engineers 243, 2, 107–122.
Wei, Y. & Howe, B. 2008. Chowilla Floodplain Groundwater Model [online]. In: Lambert, M., Daniell, T.M. & Leonard, M. (eds) Proceedings of Water Down Under 2008. Modbury, SA, Engineers Australia, Causal Productions, 2008, 1260-1271. http://search.informit.com.au/documentSummary;dn=586280161662294;res=IELENG
White, W.N. 1932. A method of estimating groundwater supplies based on discharge by plants and evaporation from soil – results of investigations in Escalante Valley, Utah. US Geological Survey Water Supply Paper 659, 106 pp.
Wilson, G.A., Cox, L.H. & Zhdanov, M.S. 2010. Practical 3D inversion of airborne electromagnetic data. Preview 146, 29-33.
Wilson, M., Bates, P., Alsdorf, D., Forsberg, B., Horritt, M., Melack, J., Frappart, F. & Famiglietti, J. 2007. Modeling large-scale inundation of Amazonian seasonally flooded wetlands. Geophysical Research Letters 34, L15404.
Wohling, D.L., Leaney, F.W. & Crosbie, R.S. 2012. Deep drainage estimates using multiple linear regression with percent clay content and rainfall. Hydrology and Earth System Sciences 16, 563-572. doi:10.5194/hess-16-563-2012, 2012.
Wood, W.W. 1999. Use and misuse of the chloride-mass balance method in estimating groundwater recharge. Groundwater 37, 1, 2-3.
Yang, K., Huntington, J.F., Browne, R.R.L. & Ma, C. 2000. An infrared spectral reflectance study of hydrothermal alteration minerals from the Te Mihi sector of the Wairakei geothermal system, New Zealand. Geothermics 29, 377-392.

Yin, L., Hu, G., Huang, J., Wen, D., Dong, J., Wang, X. & Li, H. 2011. Groundwater-recharge estimation in the Ordoz Plateau, China: comparison of methods. Hydrogeology Journal 19, 1563-75.
York, D., Evensen, N., Martinez, M. & Delgado, J. 2004. Unified equations for the slope, intercept, and standard errors of the best straight line. American Journal of Physics 72, 3, 367-375.
Yoshioka, K. & Zhdanov, M.S. 2005. Three-dimensional nonlinear regularized inversion of the induced polarization data based on the Cole-Cole model. Physics of the Earth and Planetary Interiors 150, 29-43.
Yuval & Oldenburg, D.W. 1997. Computation of Cole-Cole parameters from IP data. Geophysics 62, 436-448.
Zhao, B., Yan, Y., Guo, H.D., He, M., Gu, Y. & Li, B. 2009. Monitoring rapid vegetation succession in estuarine wetland using time series MODIS-based indicators: An application in the Yangtze River Delta area. Ecological Indicators 9, 346-356.

# Acknowledgements

The BHMAR Project was commissioned and managed by the Australian Government Department of Environment, Water, Heritage and the Arts (DEWHA), which subsequently became the Department of Sustainability, Environment, Water, Population and Communities (SEWPaC) and in turn the Department of the Environment (DoE). Through these changes, the project has been directed by Richard McLoughlin and Mary Harwood, and the project team would like to express their appreciation for their unwavering support. Current and former DoE staff, notably Lee Harris, Geraldine Cusack, Warren Sillick, Angela Robinson and Frank Cita are thanked for their marvellous efforts in facilitating the project, and providing clear guidance to the Geoscience Australia (GA) team.

The BHMAR project has involved a very significant data acquisition phase on a scale not undertaken on-shore by Geoscience Australia for >30 years. Moreover, the relatively short timeframes available for data acquisition challenged all involved, both within the formal Geoscience Australia project team as well as those who volunteered or were seconded from other parts of the organisation. Of course, none of these efforts would have been successful if it were not for the heroic efforts of a significant number of external participants, and it is the latter whom we wish to thank first.

**External participants**

The BHMAR project area is one of great cultural and environmental sensitivity. The guidance and practical assistance we received in this study from Noeline Ferguson, Coordinator at the Menindee Land Council (MLC), other Elders in the MLC, and members of the Indigenous Community is greatly appreciated. Noeline organised for members of the Indigenous community to assist with carrying out cultural and heritage assessments of field sites, and then provided staff to work in gruelling conditions, on both day and night shifts, as drilling field assistants. Dennis Sloan, Menindee Land Council Contractor, is particularly thanked for taking on so much of the workload helping with the drilling. Other MLC contractors also assisted with a range of other fieldwork activities, and their efforts are greatly commended.

Sarah Martin, Archaeologist, is thanked for providing initial introductions to the MLC and for carrying out the initial cultural heritage site assessments for the drilling. Wilfred Shawcross is also thanked for stepping in to provide additional advice and clearances on the cultural and heritage issues surrounding the drilling sites.

The drilling activities would not have taken place without the considerable efforts of two New South Wales (NSW) Agencies: the NSW Office of Water, and the NSW Land and Property Management Authority. Staff from both agencies pulled out all the stops to help us obtain the requisite licences for drilling in our tight timeframes, despite the extra workload that this produced. The assistance of Peter Winton from the NSW Office of Water in Buronga, and the team of Shaun Baker, Donna Basham and Elizabeth Burke from the NSW Land and Property Management Authority are particularly thanked for working extra time for us to obtain the clearances we required. The guidance and assistance from the local NSW and Country Energy/Water staff at Menindee is also greatly appreciated. Barry Philp is particularly thanked for his on-going willingness to assist in all practical ways.

The assistance of local landowners, too numerous to mention individually, has been critical to the success of the field program. Without their support for the project, we could not have completed the field program in the allotted timeframe. However, Sandy Crombie needs special mention. As Idleview property owner, Sandy provided accommodation in Menindee when we were working in more remote locations. Sandy has gone above and beyond the call of duty with her assistance in providing accommodation for the field parties travelling to Menindee. The Menindee Hotel and Motel are also thanked for showing great flexibility in accommodating to our evolving field program. Richard Unsworth, from the Grape Exchange provided fantastic assistance with storing the core in refrigeration containers while the core truck was in Canberra unloading. Landholders Stewart Oates and John Caskey provided land access and drilling-related earthworks and rehabilitation on their own land.

AEM data acquisition can be fraught with delays, and was recognised as a significant project risk. So it is with great pleasure that we can thank the team from Geoforce (ably supported by HeliWest), who delivered a

high quality AEM dataset in record time. We would like to thank Eric Wedepohl and the field crews and data processing team in Perth for running a very professional field operation. James Reid is particularly thanked for his technical and scientific advice to members of the project team, and for going that extra step to identify and solve issues as they arose.

It is a credit to the Boart Longyear Company that they have been able to carry out such a large sonic drilling program in a short period of time using such a relatively new technology in difficult drilling conditions. Ken Patterson and Scott Barnes are thanked for their excellent communication and flexibility in delivering this program. The efforts of the various drillers, particularly Denzel and Mike who flew in from the USA to lead the drilling teams with great skill and tenacity in completing the program in exhausting conditions. Simon Barwald and Duncan Black (formerly of Boart Longyear) provided drilling services.

Compression of various field activities into a remarkably short timeframe meant that Geoscience Australia had to enlist the assistance of geological contractors to assist with drilling activities. David Jenkins, CEO of Terrasearch, provided enormous support by supplying contractors, sometimes within 24 hours. David Tognon, Contract Geologist/Hydrogeologist worked on both the sonic rig as the onsite Geologist and on the mud rig for drilling and development of the bores. He worked tirelessly in intense conditions from mid November 2009 through to March 2010. Kevin D'Arcy, Contract Geologist worked on both the sonic rig as the onsite Geologist and the mud rig in some of the hottest weeks Menindee saw that summer, November and December 2009. They provided reliable and always friendly and professional service, and their efforts are greatly appreciated.

Congratulations go to Terry O'Shaughnessy and the rest of the Impax Group team for successfully organising and implementing the pump tests at the Jimargil site, providing such critical data for our assessments. Rod Harwood (Environmental Strategies) provided a wealth of experience in pump test operation and data interpretation. Lucy Lytton and Anne Riesz took time out from their busy schedules at the Murray-Darling Basin Authority (MDBA) to help out as on-site hydrogeologists during the pump tests as well as subsequent water sampling. It was also comforting to have the hydrogeological experience of Mark Hocking (Hocking et al) during our field activities. Steve Hostetler (FrOGTech) helped crunch the numbers in terms of pump test analysis, as well as much-needed and timely contributions in hydrochemical, hydrographic and hydrological analysis.

When one of our geophysics team went off on paternity leave, it was with great relief that first CSIRO and then Zonge Engineering stepped in to assist. Kevin Cahill is thanked for giving up the delights of a Perth office for coming once more to Menindee in the heat of summer, while Kelly Keates, Managing Director of Zonge Engineering is thanked for providing the services of the excellent Nkhil Dhyan, at such short notice to assist with our borehole geophysical logging program. Kelly Keates, Simon Mann, Anton Khrapov (Zonge Engineering and Research Organisation) provided ground geophysical investigations. David Walsh (Vista Clara), Andrew Fitzpatrick (CSIRO), Mike Hatch and Kevin Cahill assisted with downhole geophysical logging.

Safety in the field is always a top concern and it was with great relief when we discovered the services of Complete Ute and Van hire, who supplied us on short notice with safe and fully kitted vehicles in excellent condition. Customer service was A1, and a credit to Rob and Steve Harris. Andrew Pressler (West State Training and agent for Complete Ute and Van Hire) assisted with vehicle hire and other field logistics.

We would also like to acknowledge the services of Justin and Brett Green, Tolbra Earthmovers, who provided contract services for the digging of pits for the sonic drilling and also assisted in the rehabilitation of the bores. Bernard Blore as well as Brett and Justin Green carried out drilling-related earthworks and rehabilitation. Nathan White, Roadmaster, Canberra, provided/providing storage of the core in refrigeration.

Staff from Aarhus University have come to the rescue at a couple of critical points in the project to date. Niels B. Christensen is particularly thanked for a massive effort in writing new inversion software and in developing procedures for calibrating and validating the AEM inversion products. Without Niels' efforts we would not have been able to reconcile the various strands of the project and would not have been able to develop a coherent hydrogeological conceptual model. At earlier stages in the project, Aarhus University

also stepped in to re-process the datasets and carry out full inversions when necessary due to unforeseen circumstances. The efforts of Esben Auken, Camilla Sorensen, Gianluca Fiandaca and Nikoli Foghed are greatly appreciated in these tasks. Niels Christensen's contribution to the write-up of the reports is also greatly appreciated. Jared Abraham (formerly USGS, now XRI Geophysics) also guided us through the intricacies of AEM data acquisition and its interpretation. Jared was also instrumental in moving forward our first foray into NMR logging, helping us make sense of all that data. His contribution to the reports is also greatly appreciated.

Importantly, we would be remiss not to mention the efforts and advice of member of the project steering committee. Peter Dillon from CSIRO is Australia's expert in MAR, and the team greatly appreciate the time he has taken to assist the project leadership team with scientific and technical guidance, and for his strong overall support for the project. Peter and Declan Page, Joanne Vanderzalm and Konrad Miotlinski (CSIRO) are also thanked for their contributions in MAR risk assessment, geochemical interpretation and numerical modelling. Mike Williams from NSW Office of Water, is also thanked for his uncompromising advice and constant reality checks! Andy Green is thanked for giving of his precious time for advice on all matters geophysical and for his participation in Steering Committee meetings. Phil Commander and Don Woolley provided the all-important peer reviews of Interim reports, while Phil also peer reviewed the final reports. The USGS is also greatly thanked for undertaking an exhaustive peer review of the BHMAR reports. Jodie Eimers is thanked for facilitating the process, while Jim Leenhouts coordinated the review by 14 USGS staff members. Addressing the review comments added significantly to the time required to finalise the reports, however the comments greatly improved the quality of the science within the reports, and the efforts of the USGS review team are to be highly commended.

**GA volunteers and secondees**

Delays in commencement of the project, compounded by delays in obtaining field clearances for drilling, meant that a number of extra Geoscience Australia staff were brought in from different corners of the organisation to assist with field and laboratory activities.

Raymond DeGraaf, Marine Mechanical Manager, Petroleum and Marine Division (PMD), has gone above and beyond providing staff and his own time to go into the field for us and to drive the core truck to and from Canberra/Menindee. Ray and his team continually came through for us whenever we had a need they always provided assistance even if it meant working extra hours and harder in their own jobs so that they could help us out. Ray also assisted in sourcing a refrigerated storage container to store the core at GA.

The efforts of those listed next, were essential for assisting with delivery of the field program: Andrew Hislop (PMD) assisted with driving the core truck as well as site preparation and clearances and rehabilitation of the bores; Dave Holdway (PMD) and Andre Clive (GEMD) also drove the core truck; Craig Wintle (PMD) was also a core truck driver and also assisted with the site preparation and clearances as well as rehabilitation of the bores; Mark Sharah (PMD) and Matthew Carey (PMD) assisted with borehole rehabilitation, data logging and water sampling; Anthony Schofield (OEMD) assisted us with a shift as the day time supervising Geologist on the sonic rig; Chris Consoli (PMD) assisted us with a shift as the night time supervising Geologist on the sonic rig; Gerard Stewart (OEMD) assisted with doing a shift on the site preparation and clearances as well as rehabilitation of the bores; Pauline English (GEMD) assisted us with a shift as the day time supervising Geologist on the sonic rig. Tehani Kuske helped out in all manner of activities while on her graduate rotation.

With a critical shortage of GIS staff, Greg Scott kindly volunteered the excellent services of Danielle Beaudreau, Kristen Knox and Brad Cook, all of whom put in many hours producing map figures that appear in this and other reports. The 3D visualisation (Worldwind) and movie fly-through team of James Navin, Michael de Hoog, Neil Caldwell and Michael O'Rourke are thanked for their considerable efforts in simplifying complex datasets and portraying these in an effective manner. Laurent Ailliers is greatly thanked for constructing the GoCAD model.

**The 'Official' project team**

The BHMAR report write-up team is recognized in the authorship of the individual reports. Within GA, current and former BHMAR Project Team members who contributed to interim reports and activities, but are

not authors in this report include: Aaron Davis, Yusen Ley-Cooper, Michael Smith, Rebecca Norman, Anthony Pressler, Luke Wallace, Martin Smith, Katherine Boston, Pauline English, Tim Ransley, and Kristen Cullen.

Most importantly, we would like to acknowledge the efforts of Tenai Luttrell, project coordinator, who played a pivotal role in being able to find staff and contract resources when all other efforts looked forlorn. Tenai coordinated the field resources to ensure that multiple field parties had flights and/or vehicles to get them safely to their destinations, and that they had a bed to sleep in when they arrived. Tenai also assisted with arranging drilling permissions, and with managing the project's financial resources. A stellar effort, and all that while working part-time. Tenai was also assisted by Kim Forbes, Samantha Murray, and Sally Moon. Kriton Glenn is thanked for stepping in as acting project leader for a 2 month period.

In the laboratories, Stuart McEwen (PMD Laboratory Manager and Project Leader), and his team provided a very professional service, designing effective workflows that have seen a very steady flow of results to the interpretation team. Stuart also provided assistance and direction with the lab analysis and arranged the Analytical Equipment Service Agreements. Christian Thun (Laboratory Manager, PMD) provided assistance and direction with the lab analysis of cores coming into GA. He also assisted with the recruitment of various lab assistants that were required due to the extra workload. Tony Watson (PMD Laboratory) supervised laboratory analysis, provided QA/QC on laboratory analysis, and supervised equipment procurement and maintenance, training and procedure development.

Alexandra Plazinska and Janice Trafford provided assistance in relation to pore fluid samples and core samples under very tight deadlines. Kylia Wall provided laboratory analysis assistance, training and procedure development, while Amber Green, Billie Poignand, Gregory O'Connell and Mathew Brown also provided sterling service in Geoscience Australia laboratory analysis. Jonathon Rousseau, Viktoria Halas and Rick Long assisted with core sampling, assisted by Ross Spulak and Gerhard Schoning, who also greatly assisted with fieldwork. Gerhard, Ross and Victoria also greatly assisted with preparation of Strater logs and cross-sections and preparation of Report Appendices. Liz Webber and Bill Pappas (Inorganic Geochemistry Laboratory) worked on XRF, XRD and ICP analysis of Broken Hill samples.

The efforts of Robert Apps, Contracts Manager in Geoscience Australia rate a special mention. Robert brought a wealth of experience to the tendering and the management of contracts in general, and he managed to streamline processes and ensure external contracts were implemented with no fuss delay. The late Trish Yates is also remembered for her efforts in shepherding this project through the financial and contracts side of things at the commencement of this project.

Murray Richardson is thanked for his very effective management of the AEM acquisition program, while Ian Atkinson and his team are thanked for carrying out the in-river surveys. Leo Lymburner and Elexis McIntyre are thanked for their terrific contribution to the Landsat processing and interpretation.

Phil Tickle and Hamish Anderson are also thanked for managing the LiDAR acquisition program, while Hamish, Jonah Sullivan and John Dawson are thanked for their work in determining the accuracy of the LiDAR dataset. Peter Maher assisted with obtaining land owner permissions and official clearances from the Land and Property Management Authority and NSW Office of Water and coordinated the cultural and heritage clearances. Tanya Fomin (OEMD) provided advice and information in relation to a possible Seismic Survey.

John Jaycock, Tim Ransley and Ross Spulak also spent an enormous amount of time in the field assisting with the drilling and water and groundwater sampling programs, while Heike Apps is thanked for foregoing family commitments, and virtually taking up residence at Menindee for several months prior to her retirement.

Jane Coram, and Matt Hayne at an earlier stage in the project, are thanked for helping to ensure the BHMAR team had the necessary internal resources to undertake this project.

# Glossary

**Aeolian.** Applied to landforms or sedimentary materials which are formed or transported by the action of wind.

**Aeolian.** Wind depositional environments.

**Airborne Electromagnetic (AEM).** A geophysical survey method that measures the electromagnetic properties of geological material by use of geophysical sensors carried by airplane or helicopter. Electric conductivity and magnetic susceptibility are calculated, and because these properties vary depending on the nature of the rock, water saturation, salinity and other parameters, the resultant maps are used for estimation of the nature of underground rock Formations, ground water, contamination and other geological and environmental changes.

**Alluvial/alluvium.** Non-marine sediments deposited by the action of water.

**Anabranch.** A distributary channel divergent from a main stream and either rejoining downstream or remaining separate and diminishing in size until becoming indistinct.

**Anastomosing Rivers.** Have multiple, relatively stable, interconnecting channels.

**Aquifer.** A geological formation, group of formations or part of a formation which is sufficiently porous and permeable to store, and allow the movement of groundwater. Aquifers can also be defined in terms of yielding quantities of groundwater for consumptive use or for ecosystems.

**Aquifer storage and recovery (ASR).** ASR is a type of managed aquifer recharge (MAR) that involves the injection of water into a well for storage in an aquifer and recovery from the same well. The aquifer may be confined or unconfined.

**Aquifer storage, transport and recovery (ASTR).** ASTR is a type of managed aquifer recharge (MAR) that involves injection of water into a well for storage in an aquifer and recovery from a different well, generally to provide additional water treatment.

**Aquitard.** Saturated geological unit that can store large volumes of water but cannot transmit significant quantities of water to production wells. Also can be called a 'confining bed'.

**Bank filtration.** In bank filtration, groundwater is extracted from a well or caisson near or under a river or lake by inducing infiltration from the surface water body, thereby improving water quality.

**Basement.** Bedrock that underlies the geological materials of interest.

**Bioturbation.** The displacement and mixing of sediment particles by plants and animals.

**Biogenic carbonate.** Calcium carbonate directly precipitated by biological processes, such as shells, corals.

**Bore Yield.** The amount of water that can be abstracted from a bore (either by pumping or natural artesian flow) over a specific time interval. Bore yields are usually measured in litres per second (L/s).

**Cenozoic.** Geological Era extending from 65.5 million years ago to the present.

**Clast.** A rock fragment or grain resulting from the breakdown of larger rocks.

**Colluvial.** Gravity deposits in slope depositional environments.

**Conductivity (σ).** How the earth or a geological Formation conducts electricity. Conductivity is usually measured in milli-Siemens per metre (mS/m). It is the reciprocal of resistivity.

**Conductor.** Used to describe anything in the ground more conductive than the surrounding geological material. Conductors are most often clays, graphite, metallic mineralization or saline groundwater.

**Confined Aquifer.** An aquifer that is overlain and underlain by impervious layers (aquitards), and is not associated with the water table.

**Conjunctive Water Use.** Coordinated management of surface-water and groundwater resources.

**Core/coring.** Drilling method that recovers intact samples of subsurface materials.

**Crevasse.** A crevasse is a break in a river levee through which flood waters and sediments split out onto the floodplain, forming a crevasse-splay deposit.

**Darcian Vertical Infiltration.** Vertical infiltration is determined by applying Darcy's Law which describes the flow of a fluid through a porous medium.

**Deflation.** Erosion of sediment and resultant ground-surface lowering by wind action.

**Depth of exploration.** The maximum depth at which the geophysical system can detect the target and this maximum depth depends on a variety of characteristics. This term often refers to the resolution depth of the strongest conductive target.

**Devonian.** Geological Period extending from 416 to 359 million years.

**Discharge (Groundwater).** The flow of groundwater to surface water, bores, and between aquifers or the sea.

**Discharge (Stream).** Amount of water flowing in the stream.

**Distributary.** A stream that branches off and flows away from a main stream channel. Often called an anabranch in Australia.

**Drawdown.** Watertable lowering.

**Electrical conductivity (EC).** The ability of electrical current to pass through a substance. EC is commonly used to estimate the amount of soluble salt in solution. EC measurements can be made with a range of devices on ground and stream water, soils, and soil-paste extracts. Units of electrical conductivity are commonly given in mS/m, dS/m or µS/cm; 100 mS/m = 1 dS/m = 1000 µS/cm. Here, S is the symbol for siemens, and the prefixes d is deci ($10^{-1}$), c is centi ($10^{-2}$), m is milli ($10^{-3}$) and µ is micro ($10^{-6}$).

**Electromagnetic (EM).** Comprised of a time-varying electrical and magnetic field. Radio waves are common electromagnetic fields. In geophysics, an electromagnetic system is one that transmits a time-varying primary field to induce eddy currents in the ground, and then measures the secondary field emitted by those eddy currents.

**Ephemeral.** Watercourses (streams) that are active for only a short period of time.

**Exceedance Threshold.** In water quality standards it is the limit between acceptable and unacceptable amounts of a particular water component or characteristic.

**Extensional Fault.** A normal fault characterised by vertical movement on an inclined plane that vertically thins and horizontally extends portions of the Earth's crust. In normal faults the hanging wall (rock above the fault plane) moves downward relative to the footwall (rock below the fault plane).

**Facies.** Characteristics or bodies of sediments recognised by the depositional environment.

**Fault Scarp.** A break in slope at the earth's surface caused by relative uplift along a fault.

**Ferruginised.** Geological material that has gained iron following its original formation. Commonly, iron-rich groundwater solutions may precipitate iron under favourable hydrochemical conditions.

**Fiducial, or fid.** Timing mark on a survey record. Originally these were timing marks on a profile or film; now the term is generally used to describe 1-second timing records in digital data and on maps or profiles.

**Flood-out Lakes.** Lakes adjacent to a stream that fill and empty via a connecting channel or channels.

**Floodplain.** A low-lying area adjacent to a river or stream subjected to inundation when that stream floods. Floodplains are often sites of deposition of fine-grained sediments.

**Fluvial.** River depositional environment.

**Footprint** This is a measure of the area of sensitivity under the aircraft of an airborne geophysical system; depends on the altitude of the system, the orientation of the transmitter and receiver, the separation between the receiver and transmitter, the conductivity of the ground and the strength of the contrasting anomaly.

**Fractured Rock Aquifer**. Aquifers that store groundwater in the fractures, joints, bedding planes and cavities of the rock mass.

**Fuzzy-k Means.** A statistical cluster-analysis method.

**Gamma logging.** Down-hole geophysical logging techniques that maps the gamma radiation released by naturally occurring uranium, thorium and radioactive potassium.

**Gaining Stream.** A stream or river-reach into which groundwater flows via the stream bed and/or banks.

**Geodynamics.** Dynamics of the Earth produced by large-scale processes such as plate tectonics.

**Geological Basement.** Rock mass below a sedimentary platform or cover; or more generally, any rock below sedimentary rocks or sedimentary basins that are metamorphic or igneous in origin.

**Geophysics.** The study of the Earth by quantitative physical methods, such as magnetics, electromagnetics, gamma ray spectrometry (radiometrics), seismology and gravity.

**Gigalitre (GL).** 1000 megalitres or 1 billion litres

**Glacial-Interglacial Cycles.** Earth ice-age climate cycles that have seen ice-sheets advance (glacial) and contract (interglacial) on timescales of up to 100 thousand years over the past 2.5 million years.

**Global Meteoric Water Line.** Worldwide average relationship between hydrogen and oxygen isotope ratios in natural terrestrial waters.

**Graben.** A depressed or down-thrown block bounded on at least two sides by faults. See also **half graben.**

**Groundwater.** Water stored below ground that saturates the pore spaces, cavities or fractures within geological material. The upper surface of this saturated zone is the water table.

**Groundwater Management Unit**. A hydraulically connected groundwater system that is defined and recognised by Australian State and Territory agencies for management purposes.

**Groundwater Models.** Simulations of groundwater flow or other groundwater characteristics. **Numerical groundwater models** use mathematical equations to simulate the hydraulics of groundwater flow processes.

**Groundwater Mounding.** Outward and upward expansion of the watertable caused by water injection.

**Half-Graben.** An asymmetric depressed or down-thrown block bounded on only one side by a fault.

**Hazard.** Something with the potential to cause harm. For example, salinity when above a health or other guideline threshold is considered a hazard when it has the potential to move or be moved to where it can threaten assets such as agriculture, infrastructure, water resources and biodiversity.

**Head (or hydraulic head).** A measurement of water pressure representing the total energy at the entrance of a piezometer. Usually measured as a water surface elevation. Differences in Head between two or more points can be used to determine the hydraulic gradient and direction of groundwater flow. Synonymous with Hydraulic Head.

**Holocene.** Most recent Geological Epoch extending from 12 000 years ago to the present.

**Horst.** A raised or up-thrown block bounded by faults or grabens, which remains stationary or is uplifted while the land has dropped on either side.

**Hummocky dunes.** Low irregular dune forms.

**Hydraulic Classes.** Hierarchical grouping of sediments according to their hydraulic properties.

**Hydraulic Conductivity (K).** Hydraulic conductivity is the volume of water flowing through a 1 $m^2$ cross-sectional area of an aquifer under a hydraulic gradient of 1 m/1 m (100%) in a given time (usually 1 day).

**Hydraulic Gradient.** With regard to an aquifer, the rate of change of pressure head per unit of distance of flow at a given point and in a given direction.

**Hydraulic loading.** Increased head pressure due to increased water depth.

**Hydrochemistry.** Study of the chemical characteristics of water.

**Hydrodynamics.** Study of the motion of fluids, especially noncompressible fluids, under the influence of internal and external forces.

**Hydrogeology.** The study of geological properties of rocks, soils, and sediments as they relate to groundwater movement and storage.

**Hydrogeophysics.** Geophysical measurement of hydrological parameters and processes.

**Hydrograph (Stream).** Graphical representation showing the variation in time in the water level and/or flow in a surface water body.

**Hydrograph (Bore).** Graphical representation showing the variation in time in the groundwater level within a bore.

**Hydrostratigraphy.** The identification of mappable stratigraphic units on the basis of hydraulic properties (aquifer / aquitard).

**Infiltration basins or ponds.** Infiltration structures that are usually constructed off-stream where diverted surface water infiltrates (through an unsaturated zone) to the underlying unconfined aquifer.

**Infrabasins.** Bedrock sedimentary basins underlying the geological sequence of interest.

**Inter-disciplinary Research.** An interactive process whereby researchers work jointly, each drawing from their own discipline-specific perspective, to address a common research problem. See also **uni-disciplinary research, multi-disciplinary research and trans-disciplinary research.**

**Inversion or Inverse Modelling.** A process of converting geophysical data to an earth model; theoretical models iteratively compare the earth response to the data measured, until the model fits closely.

**Isotope.** A different chemical species of a chemical element with a different atomic mass. Used in hydrogeologic applications to date and understand the origin and evolution of groundwater.

**Lacustrine.** Lake depositional environments and deposits.

**Laterally constrained inversion (LCI).** A geophysical inversion process whereby the theoretical models are changed to fit the measured response along the direction of the flight path of an AEM survey.

**Lateral Migration.** Erosion and subsequent deposition of sand and gravel channel and bed-load by meandering rivers.

**Lateral infiltration.** Horizontal movement of water from a river into its banks.

**Layered earth.** A common geophysical model which assumes that the earth is horizontally layered – the physical parameters are constant to infinite distance horizontally, but change vertically.

**Levees.** Natural levees are raised banks adjacent to channels formed by initial rapid over-bank deposition of the coarsest suspended sediment during floods. Artificial levees are man-made flood-control embankments.

**LiDAR.** *Li*ght *D*etection *A*nd *R*anging. A highly accurate topographic surveying method using an aircraft-founded laser scanner to measure variations in altitude.

**Lineament.** A linear feature in a landscape that expresses an underlying geological structure such as a fault.

**Lithification.** The process of consolidation, compaction and hardening to form rocks from sediments.

**Lithology.** Physical characteristics of a rock or sediment.

**Local Meteoric Water Line.** Relationship between hydrogen and oxygen isotope ratios in natural precipitation in a given area.

**Losing Stream.** A stream or river reach where the stream bed leaks surface water to an underlying aquifer.

**Lunette.** Elongated, crescent-moon shaped dune built up by wind on the downwind margin of a lake.

**Macropore.** Relatively large cavities in rock, soil or sediment; water flow is not impeded by capillarity.

**Magnetic survey.** Geophysical mapping of the distribution of magnetic materials in the earth. Magnetic surveys can be carried out on the ground or from aircraft (**Airborne**).

**Managed Aquifer Recharge (MAR).** The purposeful recharge of water to aquifers for subsequent recovery or environmental benefit.

**Meanders.** Tight bends in a river channel that can either be fixed or migrating.

**Microfauna.** Microscopic organisms.

**Miocene.** Geological Epoch extending from 23 to 5.3 million years ago.

**Megalitre (ML).** 1,000,000 litres.

**Morphostratigraphic unit.** A body of sediment that is identified primarily from the surface form it displays with such units including both landform and lithologic information in their definition.

**Multi-disciplinary Research.** A sequential process whereby researchers in different disciplines work independently, each from their own discipline-specific perspective, with a goal of eventually combining efforts to address a common research problem. See also **uni-disciplinary research, inter-disciplinary research** and **trans-disciplinary research**.

**Neotectonics. S**tudy of current or recent motions and deformations of the Earth's crust.

**Nick Point**. A point at which there is a sudden break of slope in the long profile of a river.

**Noise.** That part of a geophysical signal that is being measured that is derived internal to the equipment or from external sources deemed to be meaningless.

**Nuclear Magnetic Resonance (NMR) Logging.** A type of down-hole geophysical logging that uses the NMR response of the sediment to directly determine its porosity and permeability.

**Numerical dating.** Assigning of an actual age in thousands or millions of years to geological materials.

**Oligocene.** Geological Epoch extending from 33.9 to 23 million years ago.

**Optically Stimulated Luminescence (OSL).** System of dating sediments that measures progressive increase in energy accumulated in crystals due to damage from natural environmental radiation.

**Overbank Flow.** River flow during a flood that extends beyond the channel.

**Palaeo-.** Prefix meaning old or ancient often now-defunct.

**Palaeovalley.** The preserved remnants of an ancient drainage system, now infilled with sediment and no longer forming an active surface drainage feature. Palaeovalleys can contain aquifers and have active groundwater flow systems.

**Palaeochannel.** Preserved remnants of the channel of an ancient fluvial system.

**Palaeozoic.** Geological Era extending from 542 to 251 million years ago.

**Palynology.** The study of pollen and other resistant plant, protist, and fungi microfossils.

**Pedogenesis.** Modification of original deposits or rocks by soil-forming processes.

**Permeability.** The ability of a material, such as rock or sediment, to allow the passage of a liquid such as water. Permeable gravel and sand allow free movement of groundwater whereas impermeable clays do not and can be considered barriers to groundwater movement.

**Permeameter.** Instrument for measuring water infiltration rates through soil or sediment.

**Piezometer.** A bore used specifically to monitor water levels or hydraulic head within an aquifer.

**Pleistocene.** Geological Epoch extending from 2.5 million to 12 thousand years ago.

**Pliocene.** Geological Epoch extending from 5.3 to 2.5 million years ago.

**Point Bars.** Depositional areas on the inside of river meander beds where bed-load sand and gravel are deposited as the meander migrates laterally.

**Porosity.** A measure of the water-bearing capacity of an aquifer. Water movement depends on both the size and interconnectivity of voids.

**Potentiometric Surface.** A surface that represents the hypothetical level that water under pressure within a confined aquifer would rise to if tapped by a bore.

**Primary field.** The EM field emitted by a transmitter. This field induces eddy currents in (energizes) the conductors in the ground, which then create their own secondary fields.

**Progradation.** Seaward movement of a shoreline by deposition of sediment.

**Pump Test.** A hydrological assessment undertaken when an aquifer is 'stressed' by pumping or injecting water and noting the water drawdown (or rise) level over space and time.

**Quaternary.** Geological Period extending from 2.5 million years ago to the present.

**Receiver.** The signal detector of a geophysical system. This term is most often used in active geophysical systems that transmit. In AEM surveys it is most often a coil (see also transmitter).

**Recharge.** The entry into the saturated zone of water made available to the watertable surface, together with associated flow away from the watertable within the saturated zone.

**Recovery efficiency.** The fraction or percentage of injected water that can be recovered.

**Redox.** Variations in chemical state between oxidation and reduction.

**Regolith.** The entire unconsolidated or secondarily re-cemented cover that overlies more coherent bedrock, that has been formed by weathering, erosion, transport and/or deposition of the older material.

**Regression.** A term used in geology, to mean the withdrawal of the sea from a large area of land.

**Regularization.** Regularization of the solution to the inversion of AEM data with a multi-layer model involves imposing smoothness constraints on the vertical variability of the conductivity. The smoothness constraint limits the variability of the subsurface conductivity model thus excluding models that are erratic or geologically unrealistic. When the constraints are set tightly, the model becomes smoother than when the constraints are set loosely.

**Resistivity (ρ).** The strength with which the earth or a geological Formation resists the flow of electricity, typically the flow induced by the primary field of the electromagnetic transmitter. Normally expressed in ohm-metres, it is the reciprocal of conductivity.

**Reverse Osmosis.** A filtration method that removes many types of molecules and ions from solutions (such as brackish to saline groundwater) by applying pressure to pass the solution through a selective membrane.

**Reversible Jump Markov Chain Monte Carlo (RJ-McMC) analysis.** A computational statistical technique that can assess model sampling validity even if the number of parameters in the model is unknown.

**Riedel shears.** Characteristic sets of small faults with various orientations, which occur within the overlying cover in the early stages of strike-slip fault formation and displacement within basement rocks or where an active strike-slip zone lies within an area of continuing sedimentation.

**Riparian.** Of, on, or relating to the banks of a natural stream.

**Risk.** The likelihood that harm will occur from exposure to a hazard. For example, salinity risk is a measure of the chance that a salt hazard will cause harm to an asset at some time in the future.

**Runoff.** Overland flow of rainfall not absorbed by the soil. This is a major component of the water cycle and a primary agent of erosion.

**Salinity ingress.** Saline groundwater entering an area previously occupied by fresh groundwater.

**Salinity Up-coning.** The vertical rise of saline water into a production well.

**Salt stores.** Vertical and spatial distribution of soil and sediment salinity.

**Saturation (water).** The condition whereby water fills all available pore space in rock, sediment or soil.

**Scour Channels.** Floodplain channels formed by erosion, commonly relatively straight and non-depositional.

**Scroll bars.** Scroll bars are sub-parallel curving ridges found on meander point bar deposit surfaces, formed by progressive migration of a meander. Scroll bars nearest the river are the youngest. Scroll bars form a scroll tract or **scroll-plain** tract along the river course.

**Secondary field.** The field created by conductors in the ground, as a result of electrical currents induced by the primary field from the electromagnetic transmitter. Airborne electromagnetic systems are designed to create and measure a secondary field.

**Semi-confined aquifer.** An aquifer that is partly overlain and completely underlain by impervious layers.

**Signal.** That component of a measurement that the user wants to see – the response from the targets, from the earth, etc. (see also noise).

**Sodicity.** A measure of the amount of available sodium in water or soil.

**Spatially constrained inversion (SCI).** A geophysical inversion process whereby the theoretical models that are changed to fit the measured response a spatial sense (both horizontally and vertically). A *borehole-constrained SCI (or LCI)* is where a spatially constrained inversion whereby data from borehole conductivity logs are added to the starting SCI or LCI models.

**Spectrometry.** Measurement across a range of energies, where amplitude and energy are defined for each measurement. In gamma-ray spectrometry, the number of gamma rays is measured for each energy window, to define the spectrum.

**Spectrum.** In gamma ray spectrometry, the continuous range of energy over which gamma rays are measured. In time-domain electromagnetic surveys, the spectrum is the energy of the pulse distributed across an equivalent, continuous range of frequencies.

**Spring.** A naturally occurring groundwater discharge feature.

**Strike-slip Faulting.** Where a fault surface is usually near vertical and the footwall moves laterally (either left or right) with very little vertical motion. Strike-slip fault types are defined by the direction of movement of the ground on the opposite side of the fault from an observer and those with left-lateral motion also known as sinistral faults and those with right-lateral motion also known as dextral faults.

**Sub-Artesian Aquifer.** An aquifer containing groundwater under pressure that rises to a level greater than that at which it is first encountered, when tapped by a bore, but does not reach the surface.

**Sustainable Yield.** The level of groundwater extraction measured over a specified planning timeframe that would, if exceeded, compromise key environmental assets, ecosystem functions or the productive base of the resource associated with the aquifer. Also referred to as the environmentally sustainable level of extraction.

**Swale.** Low point between adjacent dune crests.

**Tectonics.** The study of structures in the Earth's crust.

**Tectonic inversion.** Reactivation of a fault in the opposite direction to its original movement.

**Thalweg.** The line defining the lowest points along the length of a river bed or channel.

**Total Dissolved Solids (TDS).** The amount of material dissolved in water (mostly inorganic salts).

**Transcurrent Fault.** A fault with a near-vertical surface that moves laterally with very little vertical motion. **Sinistral faults** have left-lateral motion and **dextral faults have** right-lateral motion.

**Trans-disciplinary Research.** An integrative process in which researchers work jointly to develop and use a shared conceptual framework that synthesizes and extends discipline-specific theories, concepts, methods, or all three to create new models and language to address a common research problem. See also **uni-disciplinary research, inter-disciplinary research** and **multi-disciplinary research.**

**Transgression.** A term used in geology, to mean the invasion of a large area by the sea.

**Transient.** Time-varying. Usually in this study used to describe a very short period pulse of electromagnetic field.

**Transmissivity (T).** The capacity of a rock to transmit water under pressure. Expressed as the volume of water flowing through a cross-sectional area of an aquifer that is 1 m x the aquifer thickness under a hydraulic gradient of 100% in a given amount of time (usually 1 day). Transmissivity is equal to the hydraulic conductivity (K) times the aquifer thickness.

**Trans-tensional Region.** An area that experiences both extensive and transtensive shear and is characterised by both extensional structures (normal faults, grabens) and strike-slip faults.

**Trough.** Elongated sedimentary basin where sediments accumulate.

**Turbidity.** Water opacity or clouding due to suspended sediment or particles.

**Unconfined Aquifer.** A type of aquifer in which the upper boundary is defined by the water table. Unconfined aquifers can be recharged from infiltration of rainfall or by leakage from surface water bodies.

**Uni-disciplinary Research.** Researchers from a single discipline work together to address a common research problem.

**Up-coning.** A situation where a well, located close to saline water underlying freshwater, is pumped at a rate sufficient to cause the salt water to be drawn into the well in an upward shaped cone or mound.

**Vertical Aggradation** or **Accretion.** Deposition of overbank muds on flood plains adjacent to river channels during flood events.

**Vertical Infiltration.** Downward movement of water from the surface into soil or sediment.

**Waterlogging.** Permanent wetting of the surface due to groundwater rise.
**Well clogging.** Filling of sediment pores adjacent to a well due to injection of water; reduces permeability.
**Wetting Profile.** Moisture penetration depth in soil or sediment.